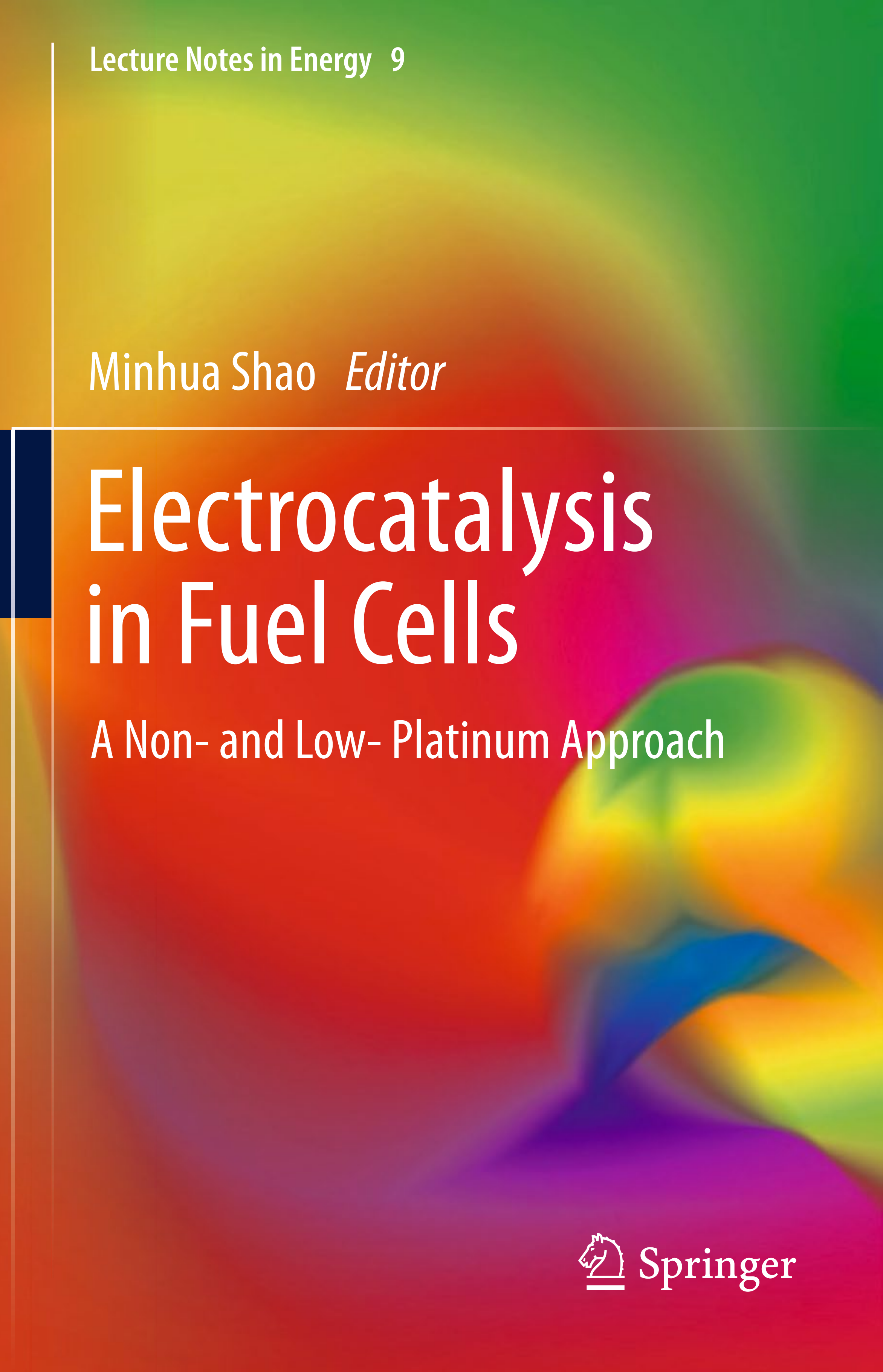

Lecture Notes in Energy 9

Minhua Shao *Editor*

Electrocatalysis in Fuel Cells

A Non- and Low- Platinum Approach

Springer

Lecture Notes in Energy 9

For further volumes:
http://www.springer.com/series/8874

Minhua Shao
Editor

Electrocatalysis in Fuel Cells

A Non- and Low- Platinum Approach

Springer

Editor
Minhua Shao
UTC Power
South Windsor
CT, USA

ISSN 2195-1284 ISSN 2195-1292 (electronic)
ISBN 978-1-4471-4910-1 ISBN 978-1-4471-4911-8 (eBook)
DOI 10.1007/978-1-4471-4911-8
Springer London Heidelberg New York Dordrecht

Library of Congress Control Number: 2013934980

© Springer-Verlag London 2013
This work is subject to copyright. All rights are reserved by the Publisher, whether the whole or part of the material is concerned, specifically the rights of translation, reprinting, reuse of illustrations, recitation, broadcasting, reproduction on microfilms or in any other physical way, and transmission or information storage and retrieval, electronic adaptation, computer software, or by similar or dissimilar methodology now known or hereafter developed. Exempted from this legal reservation are brief excerpts in connection with reviews or scholarly analysis or material supplied specifically for the purpose of being entered and executed on a computer system, for exclusive use by the purchaser of the work. Duplication of this publication or parts thereof is permitted only under the provisions of the Copyright Law of the Publisher's location, in its current version, and permission for use must always be obtained from Springer. Permissions for use may be obtained through RightsLink at the Copyright Clearance Center. Violations are liable to prosecution under the respective Copyright Law.
The use of general descriptive names, registered names, trademarks, service marks, etc. in this publication does not imply, even in the absence of a specific statement, that such names are exempt from the relevant protective laws and regulations and therefore free for general use.
While the advice and information in this book are believed to be true and accurate at the date of publication, neither the authors nor the editors nor the publisher can accept any legal responsibility for any errors or omissions that may be made. The publisher makes no warranty, express or implied, with respect to the material contained herein.

Printed on acid-free paper

Springer is part of Springer Science+Business Media (www.springer.com)

Preface

Low temperature fuel cells are electrochemical devices that convert chemical energy directly to electricity. They have great potential for both stationary and transportation applications and are expected to help address the energy and environmental problems that have become prevalent in our society. Despite their great promise, commercialization has been hindered by lower than predicted efficiencies and the high cost of electrocatalysts in the electrodes.

Highly dispersed Pt nanoparticles (2–3 nm) on carbon black are commonly used as electrocatalysts for both fuel oxidation (anode) and oxygen reduction (cathode) reactions in low temperature fuel cells. In a hydrogen fuel cell, hydrogen oxidation is an extremely fast reaction and requires low Pt catalyst loading (<0.05 mg/cm^2). For more than five decades, the predominant work has been focused on the development of novel catalysts for the oxygen reduction reaction (ORR), which has sluggish kinetics and is responsible for the high overpotential observed in the low current region. Significant progress on Pt reduction (from >1.0 mg/cm^2 to ~ 0.4 mg/cm^2) in the cathode has been achieved by optimizing the membrane electrode assembly (MEA) over the past two decades. However, the rising price of Pt continues to offset this effort.

In direct alcohol fuels cells (DAFCs), some simple organic molecules such as methanol, ethanol, formic acid, and ethylene glycol are used as alternative fuels. Besides the slow kinetics of ORR in the cathode, the slow alcohol oxidation reaction on Pt is another major contribution to low DAFC performance.

Recent intensive research efforts have led to the development of less expensive and more abundant electrocatalysts for fuel cells. This book aims to summarize recent advances of electrocatalysis in oxygen reduction and alcohol oxidation, with a particular focus on low- and non-Pt electrocatalysts. The book is divided into two parts containing 24 chapters total. All the chapters were written by leading experts in their fields from Asia, Europe, North America, South America, and Africa. The first part contains six chapters and focuses on the electro-oxidation reactions of small organic fuels. The subsequent eighteen chapters cover the oxygen reduction reactions on low- and non- Pt catalysts.

Chapter 1 discusses the current status of electrocatalysts development for methanol and ethanol oxidation. Chapter 2 presents a systematic study of electrocatalysis of methanol oxidation on pure and Pt or Pd overlayer-modified tungsten carbide, which has similar catalytic behavior to Pt. Chapters 3 and 4 outline the understanding of formic acid oxidation mechanisms on Pt and non-Pt catalysts and recent development of advanced electrocatalysts for this reaction. The faster kinetics of the alcohol oxidation reaction in alkaline compared to acidic medium opens up the possibility of using less expensive metal catalysts. Chapters 5 and 6 discuss the applications of Pt and non-Pt-based catalysts for direct alcohol alkaline fuel cells.

Chapters 7–12 focus on the electrocatalysis of carbon-based non-precious metal catalysts. The unique properties and fuel cell applications of various carbon based catalysts are intensively discussed in these chapters. Chapter 7 summarizes the fundamental studies on the electrocatalytic properties of metallomacrocyclic and other non-macrocyclic complexes. Chapter 8 and 9 review the progress made in the past 5 years of pyrolyzed carbon-supported nitrogen-coordinated transition metal complexes. Chapter 10 gives a comprehensive discussion on the role of transitional metals in the ORR electrocatalysts in acidic medium. Chapter 11 introduces modeling tools such as density functional theory (DFT) and ab initio molecular dynamics (AIMD) simulation for chemical reaction studies. It also presents a theoretical point of view of the ORR mechanisms on Pt-based catalysts, non-Pt metal catalysts, and non-precious metal catalysts. Chapter 12 presents an overview on recent progresses in the development of carbon-based metal-free ORR electrocatalysts, as well as the correlation between catalyst structure and their activities.

Chapter 13 and 14 summarize the development of transitional metal oxides and transition metal chalcogenides for ORR, respectively. Chapter 15 is the only chapter in this book dedicated to the ORR catalysis of alkaline fuel cells. Electrocatalytic properties of various non-Pt catalysts including Ag, Pd, transition metal macrocycles, metal oxides, and multifunctional materials are presented. Fundamental issues related to the design of low-cost, high-performance electrocatalysts for alkaline fuel cells are discussed. Chapter 16 and 17 review the recent advances on the study of ORR on Au and Pd-based catalysts, respectively.

Chapters 18–21 discuss core–shell and advanced Pt alloy catalysts (which also can be considered to have a core–shell structure). Chapter 18 studies the fundamentals of Pt core–shell catalysts synthesized by selective removal of transition metals from transition metal-rich Pt alloys. Chapter 19 outlines the advances of core–shell catalysts synthesized by both electrochemical and chemical methods. The performance, durability, and challenges of core–shell catalyst in fuel cell applications are also discussed. Chapter 20 reviews the recent analyses of the various aspects intrinsic to the core–shell structure including surface segregation, metal dissolution, and catalytic activity, using DFT, molecular dynamics, and kinetic Monte Carlo. Chapter 21 presents the recent understanding of activity dependences on specific sites and local strains in the surface of bulk and core–shell nanoparticle based on DFT calculation results.

The last three chapters are dedicated to improving the durability of the catalyst/electrode. Chapter 22 reports the development and evaluation of bimetallic Pt–Ru (Ir) oxygen evolution catalysts on 3M's nanostructured thin film (NSTF). This type of catalyst may significantly reduce carbon corrosion and Pt dissolution during transient conditions of fuel cells. Chapter 23 discusses the unique properties of carbide-modified carbon as the support for fuel cell catalysts. The final chapter gives a comprehensive review of novel materials other than carbon black as catalyst support. The interactions between the supports and catalysts are intensively discussed in the last two chapters.

I believe this book includes most of the state-of-the-art development of low cost and high performance catalysts and our understanding of fuel cell reactions. I hope that this book can be a comprehensive reference for those who are interested in the related areas. I truly believe that some of the technologies described in this book will be applied in the mass-produced fuel cells in the not-too-distant future.

I would like to thank all the authors of each chapter for their great contributions and efforts to this project. I would also like to acknowledge the invitation from Dr. Anthony Doyle, Senior Editor at Springer to edit the book, and Ms. Christine Velarde and Grace Quinn for their kind help in the preparation of this book. Finally, I would like to express my appreciation to my family for their understanding and support of my work.

South Windsor, CT Minhua Shao

Contents

List of Contributors

Radoslav Adzic Chemistry Department, Brookhaven National Laboratory, Upton, NY, USA

N. Alonso-Vante IC2MP UMR-CNRS 7285, University of Poitiers, Poitiers, France

Ermete Antolini Scuola di Scienza dei Materiali, Cogoleto, Genova, Italy

Instituto de Química de São Carlos, USP, São Carlos, SP, Brazil

Ljiljana L. Atanasoska Corporate Research Analytical Laboratory, 3M Company, St. Paul, MN, USA

Radoslav T. Atanasoski 3M Company, Fuel Cell Components Program, St. Paul, MN, USA

Perla B. Balbuena Artie McFerrin Department of Chemical Engineering and Materials Science and Engineering Program, Texas A&M University, College Station, TX, USA

Sarah Ball Johnson Matthey Technology Centre, Blount's Court, Sonning Common, Reading, Berkshire, UK

Akshay Bauskar The Center for Manufacturing Research, Department of Chemical Engineering, Tennessee Tech University, Cookeville, TN, USA

Rafael Callejas-Tovar Artie McFerrin Department of Chemical Engineering, Texas A&M University, College Station, TX, USA

Jingguang G. Chen Department of Chemical Engineering, University of Delaware, Newark, DE, USA

Rongrong Chen Indiana University Purdue University Indianapolis, Indianapolis, IN, USA

Xin Chen College of Environmental and Energy Engineering, Beijing University of Technology, Beijing, P. R. China

Zhongwei Chen Department of Chemical Engineering, Waterloo Institute for Nanotechnology, Waterloo Institute for Sustainable Energy, University of Waterloo, Waterloo, ON, Canada

David A. Cullen Materials Science and Technology Division, Oak Ridge National Lab, Oak Ridge, TN, USA

Liming Dai Department of Macromolecular Science and Engineering, Case School of Engineering, Case Western Reserve University, Cleveland, Ohio, USA

Jean-Pol Dodelet INRS-Énergie Matériaux et Télécommunications, Varennes, QC, Canada

Lior Elbaz Alon Los Alamos National Laboratory, Los Alamos, NM, USA

Juan M. Feliu Instituto de Electroquímica, Universidad de Alicante, Alicante, Spain

Lin Gan The Electrochemical Energy, Catalysis, and Materials Science Laboratory, Department of Chemistry, Chemical Engineering Division, Technical University Berlin, Berlin, Germany

Kuanping Gong San Jose Lab, Corporate Research Institute, Samsung Cheil Industries Inc., San Jose, California

Junsong Guo Indiana University Purdue University Indianapolis, Indianapolis, IN, USA

Enrique Herrero Instituto de Electroquímica, Universidad de Alicante, Alicante, Spain

Drew Higgins Department of Chemical Engineering, Waterloo Institute for Nanotechnology, Waterloo Institute for Sustainable Energy, University of Waterloo, Waterloo, ON, Canada

Andrew Hsu Charles W. Davidson College of Engineering, San José State University, San José, CA, USA

Akimitsu Ishihara Yokohama National University, Green Hydrogen Research Center, Hodogaya-ku, Yokohama, Japan

Meng Li Chemistry Department, Brookhaven National Laboratory, Upton, NY, USA

Justus Masa Analytische Chemie – Elektroanalytik & Sensorik, and Center for Electrochemical Sciences – CES, Ruhr-Universität Bochum, Bochum, Germany

Mkhulu Kenny Mathe Materials Science and Manufacturing, Council for Scientific and Industrial Research (CSIR), Brummeria, Pretoria, South Africa

Zachary J. Mellinger Department of Chemical Engineering, University of Delaware, Newark, DE, USA

Belabbes Merzougui Center of Excellence in Nanotechnology (CENT) & Department of Chemistry, King Fahd University of Petroleum and Minerals (KFUPM), Dhahran, Saudi Arabia

Remegia Mmalewane Modibedi Materials Science and Manufacturing, Council for Scientific and Industrial Research (CSIR), Brummeria, Pretoria, South Africa

Oki Muraza Center of Excellence in Nanotechnology (CENT) and Department of Chemical Engineering, King Fahd University of Petroleum and Minerals (KFUPM), Dhahran, Saudi Arabia

William E. Mustain Department of Chemical and Biomolecular Engineering, University of Connecticut, Storrs, CT, USA

Kenneth Ikechukwu Ozoemena Energy and Process Unit, Materials Science and Manufacturing, Council for Scientific and Industrial Research (CSIR), Pretoria, South Africa

Department of Chemistry, University of Pretoria, Pretoria, South Africa

Ken-ichiro Ota Yokohama National University, Green Hydrogen Research Center, Hodogaya-ku, Yokohama, Japan

Amra Peles United Technologies Research Center, East Hartford, CT, USA

Joelma Perez Universidade de São Paulo, IQSC, São Carlos, SP, Brazil

Peter G. Pickup Memorial University, St. John's, NL, Canada

Mohammad Qamar Center of Excellence in Nanotechnology (CENT), King Fahd University of Petroleum and Minerals (KFUPM), Dhahran, Saudi Arabia

Ahsanulhaq Qurashi Center of Excellence in Nanotechnology (CENT) and Department of Chemistry, King Fahd University of Petroleum and Minerals (KFUPM), Dhahran, Saudi Arabia

Cynthia Ann Rice The Center for Manufacturing Research, Department of Chemical Engineering, Tennessee Tech University, Cookeville, TN, USA

Wolfgang Schuhmann Analytische Chemie – Elektroanalytik & Sensorik, and Center for Electrochemical Sciences – CES, Ruhr-Universität Bochum, Bochum, Germany

Minhua Shao UTC Power, South Windsor, CT, USA

Zheng Shi NRC-Institute for Fuel Cell Innovation,Vancouver, British Columbia, Canada

Sujan Shrestha Department of Chemical and Biomolecular Engineering, University of Connecticut, Storrs, CT, USA

José Solla-Gullón Instituto de Electroquímica, Universidad de Alicante, Alicante, Spain

Peter Strasser The Electrochemical Energy, Catalysis, and Materials Science Laboratory, Department of Chemistry, Chemical Engineering Division, Technical University Berlin, Berlin, Germany

Francisco J. Vidal-Iglesias Instituto de Electroquímica, Universidad de Alicante, Alicante, Spain

Andrzej Wieckowski Chemistry Department, The University of Illinois, Urbana-Champaign, IL, USA

Gang Wu Los Alamos National Laboratory, Los Alamos, NM, USA

Dingduo Xia Peking University, Haidian District, Beijing, P. R. China

José H. Zagal Departamento de Química de los Materiales, Facultad de Químicay Biología, Universidad de Santiago de Chile, Santiago, Chile

Piotr Zelenay Materials Physics & Applications Division, Los Alamos National Laboratory, Los Alamos, NM, USA

Jiujun Zhang NRC Energy, Mining & Environment Portfolio, National Research Council Canada, Vancouver, BC, Canada

Sheng Zhang Department of Macromolecular Science and Engineering, Case School of Engineering, Case Western Reserve University, Cleveland, Ohio, USA

Chapter 1
Low-Platinum-Content Electrocatalysts for Methanol and Ethanol Electrooxidation

Meng Li and Radoslav R. Adzic

Abstract Methanol and ethanol, having high energy density, likely production from renewable sources, and ease of storage and distribution, are ideal combustibles for fuel cells wherein their chemical energy can be converted directly into electrical energy. However, the slow, incomplete oxidation of methanol and ethanol on platinum-based anodes as well as the high price and limited reserves of platinum has hampered the practical application of direct alcohol fuel cells. Extensive research efforts have been dedicated to developing high-activity electrocatalysts. This chapter presents an overview of the recent progress in methanol and ethanol electrocatalysis on platinum-based materials, with special attention focused on the research effort to reduce platinum content.

1.1 Introduction

Hydrogen is the most convenient fuel for fuel cell applications, because of its fast oxidation kinetics and the high efficiency of a hydrogen/oxygen fuel cell; however, hydrogen is not a primary fuel, meaning it has to be produced from other sources, such as, natural gas reforming, oil or coal gasification, and water electrolysis [1]. The clean and efficient production of hydrogen and the difficulties with its storage and large-scale distribution have greatly hindered the wider application and commercialization of hydrogen-fed fuel cells.

Alcohols (e.g., methanol and ethanol) are considered as potential alternatives to hydrogen, because they are liquid under ambient temperature and pressure, which makes their storage and distribution simple [2–4]. Moreover, alcohols have a high energy density (6–9 kWh/kg), and they can be obtained from renewable sources. The

---

M. Li • R.R. Adzic (✉)
Chemistry Department, Brookhaven National Laboratory, Upton, NY 11973, USA
e-mail: adzic@bnl.gov

M. Shao (ed.), *Electrocatalysis in Fuel Cells*, Lecture Notes in Energy 9,
DOI 10.1007/978-1-4471-4911-8_1,

direct methanol fuel cell (DMFC) gained most attention at first because methanol is the simplest alcohol (with only one carbon atom) and its electrocatalysis is also the simplest. Compared to methanol, ethanol possesses advantages such as low toxicity, easy logistics, and likely production in large quantities from renewable sources such as agricultural products. In addition, it has higher energy density than methanol (8.0 vs. 6.1 kWh/kg). However, the practical application of the direct ethanol fuel cell (DEFC) is more difficult than that of the DMFC, because of the slower kinetics of ethanol electrooxidation than that of methanol.

Platinum and Pt-based materials are currently the best electrocatalysts for these reactions. The price and the limited reserves of Pt are the prime obstacles to adequately developing this major field. Extensive research efforts have been devoted to the development of highly active and cost-effective electrocatalysts. This chapter describes recent advances in electrocatalysts for anodic reactions in low-temperature fuel cells that use methanol and ethanol as fuels in acidic media. Special attention is focused on the effort to decrease Pt content in the catalysts. Electrocatalysts employed in alkaline fuel cells are not discussed as they have been adequately covered in Chap. 5.

1.2 Electrocatalysts for Methanol and Ethanol Oxidation in Acidic Media

1.2.1 Methanol and Ethanol Electrooxidation on Bulk Platinum Electrode

Methanol electrooxidation and ethanol electrooxidation are complex reactions occurring in a pattern of parallel reaction pathways (Fig. 1.1) [5–14]. Although detailed reaction mechanisms remain obscure, a number of reaction intermediates and products have been identified by spectroscopic methods such as in situ Fourier transform infrared spectroscopy (FTIR), on-line differential electrochemical mass spectrometry (DEMS), and other techniques [6, 12–14].

The complete oxidation of methanol yields CO_2 and six electrons per methanol molecule:

$$CH_3OH + H_2O \rightarrow CO_2 + 6H^+ + 6e^- \tag{1.1}$$

Methanol has a low theoretical oxidation potential (0.02 V) comparable to that of hydrogen (0.0 V), and in principle it can be an efficient fuel at low temperatures. However, methanol decomposition on Pt produces surface-poisoning species and leads to a low activity. Adsorbed CO (CO_{ad}) has been identified in many studies as the primary poisoning species [8, 9]. Oxidizing CO requires oxygen atoms, usually supplied by the dissociation of water. However, Pt does not chemisorb H_2O at potentials lower than 0.7 V, and thus, pure Pt is a poor electrocatalyst at low

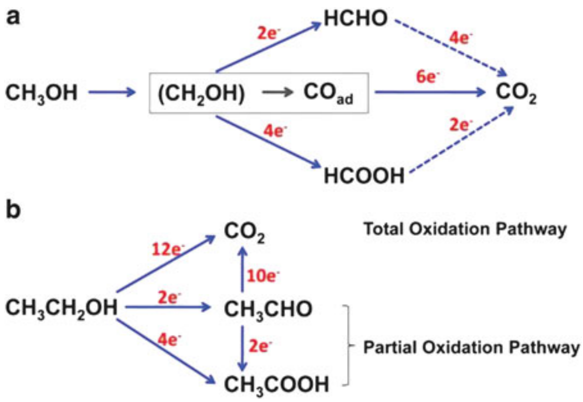

Fig. 1.1 Schematic representations of the parallel pathways for methanol (**a**) and ethanol (**b**) electrooxidation on Pt electrode [5, 6]

potentials. A high rate of oxidation on pure Pt occurs only at high potentials without technological interest. The tardiness of the methanol oxidation reaction (MOR) at the anode is more prominent than that of the oxygen reduction reaction (ORR) at the cathode, so adversely affecting the performance of DMFCs.

The total ethanol oxidation reaction (EOR) can be described as

$$CH_3CH_2OH + 3H_2O \rightarrow 2CO_2 + 12H^+ + 12e^- \quad (1.2)$$

The EOR has a useful thermodynamic potential of 0.08 V. The kinetics of the EOR is more sluggish than that of MOR on Pt since the number of electrons exchanged doubles and the activation of the C−C bonds is more difficult than that of C−H bonds. There is a consensus that carbon dioxide (CO_2), acetaldehyde (CH_3CHO), and acetic acid (CH_3COOH) are the main products of the oxidation of ethanol in acidic solution. Similarly, Pt itself is rapidly poisoned by the strongly adsorbed intermediates generated from the dissociative adsorption of ethanol. Moreover, breaking the C–C bond for a total oxidation to CO_2 is the major problem in ethanol electrocatalysis. The ethanol partial oxidation pathway dominates on the pure Pt catalyst, which causes a decrease in number of electrons extracted from ethanol fuel and consequently a considerable lowering of the fuel utilization efficiency [12–14].

1.2.2 Structure Modification of Platinum Electrocatalysts

Significant structure sensitivity has been found for alcohol oxidation on well-defined Pt single-crystal surfaces as well as on nanoparticle Pt catalysts. This activity dependence of the Pt surfaces on crystallographic orientation offers the possibility of selecting the surface structure for the optimal activity [15–34].

The onset potential for methanol bulk oxidation increases in the order of Pt(111) $<$ Pt(110) $<$ Pt(100). The largest current is associated with the peak at 0.8 V on the Pt(100) plane [15]. However, from a practical point of view, this oxidation takes place at too high a potential because a cell with such electrode would have too low voltage. In that respect, Pt(111) plane could be considered as the most active MOR catalyst among the three low-index planes. Similar performances have been observed during EOR, and Pt(111) is the most active among the three basal planes [14–21].

Tripkovic, Koper, Feliu, and Korzeniewski groups carried out systematic electrochemical study on a series of high-index Pt single-crystal surfaces to understand the role surface steps and defects played in methanol and ethanol electrooxidation [22–28]. The study of Pt[n(111) × (110)]-type electrodes (having (111) terraces with (110) monoatomic steps) shows that the overall oxidation rate of both methanol and ethanol increases with an increasing (110)-type step density. Moreover, spectroscopic studies reveal a dual effect from (110)-type steps on the EOR: at potentials below 0.7 V, the step catalyzes the C–C bond cleavage and the oxidation of CO_{ad}; at high potentials, the step also catalyzes the oxidation of ethanol to acetic acid and acetaldehyde. The study of Pt[n(111) × (100)]-type electrodes shows that the presence of (100)-type steps on the (111) terraces has no significant enhancement of the activity of the surfaces [25, 26].

For practical Pt electrocatalysts in the form of nanoparticles dispersed on a conductive support such as carbon black, it is expected that the higher surface area would bring higher activity. Decreasing Pt particle size is an important way to increase the surface area, improve Pt utilization, and reduce Pt loading. Although it was expected that surfaces with higher step densities would mimic smaller particles, the contrary is observed for particles in the nanometer range: MOR activity decreases with smaller particle size [29]. Moreover, a great variance is observed in results from different groups [22, 23, 29–31]. It has to be noted that different synthetic methods can profoundly affect the morphology of resulting nanoparticles as well as the support.

Guided by the finding from single-crystal model catalysts studies, Pt nanoparticles enclosed with high-index facets have been designed. Sun et al. developed an electrochemical shape-controlled method and successfully synthesized tetrahexahedral Pt nanocrystals (THH Pt NCs) enclosed by (730), (210), and/or (520) surfaces that have a large density of atomic steps and dangling bonds [32]. THH Pt NCs with a defined size that can be varied from 20 to 200 nm are grown on the glassy carbon electrode and exhibit much enhanced (up to 400 %) catalytic activity for equivalent Pt surface areas for electrooxidation of formic acid and ethanol. The same group improved the synthetic method and synthesized high-index faceted Pt NCs (Fig. 1.2) supported on carbon black (HIF–Pt/C) with a size 2–10 nm comparable to that of commercial catalysts by using a square-wave potential method [33].

Zhou et al. synthesized the one-dimensional (1D) Pt nanowire electrocatalyst, which exhibited greatly enhanced activity and efficiency in the EOR (Fig. 1.3), a negatively

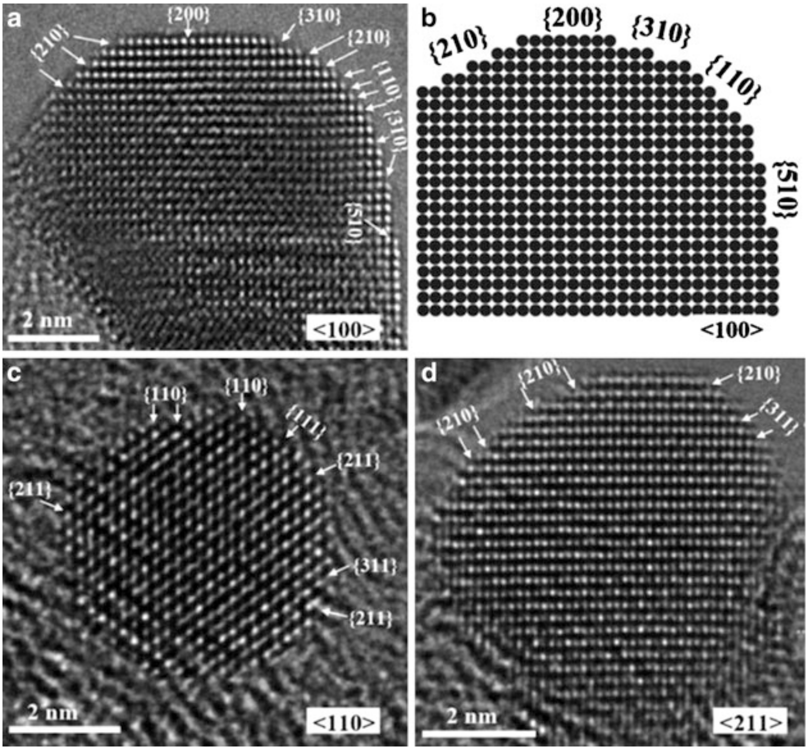

Fig. 1.2 Aberration-corrected high-resolution transmission electron microscopy (HR-TEM) images of HIF-Pt/C catalysts, showing the high density of atomic steps [33]

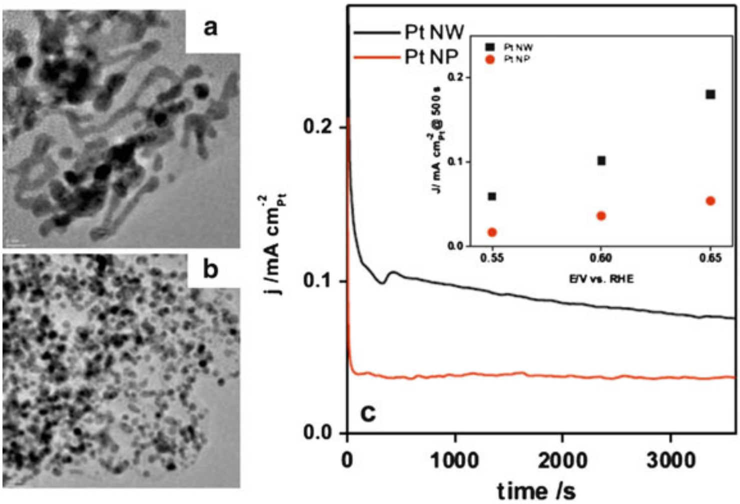

Fig. 1.3 TEM images of Pt nanowires (**a**) and Pt nanoparticles (**b**); comparison of current–time plots (**c**) during EOR on Pt nanowires (*black*) and nanoparticles in 0.2 M ethanol in 0.1 M $HClO_4$ solution at 0.65 V for 3,600 s reaction time. Inset in (**c**) shows comparison of current densities measured at three different potentials (0.55 V, 0.60 V, and 0.65 V) at 500 s reaction time [34]

shifted onset potential for ~0.22 V, and a high current density with at least a twofold enhancement compared with the 0D counterparts (i.e., Pt nanoparticles) [34]. The enhanced catalytic performance of 1D nanostructures in the EOR has been attributed to the likely interplay between balanced terrace-step sites for ethanol adsorption and reaction and a facilitated removal of chemisorbed CO on the nanowires.

1.2.3 Cocatalysts Modified Platinum Electrocatalysts

Pure platinum is an inadequate electrocatalyst for alcohol oxidation, and thus, efforts to improve Pt have been concentrated on the addition of cocatalysts [35–38]. Different approaches have been developed, for instance, adatom- or adlayer-modified Pt [37–45], Pt–M alloy [46–62], Pt–MO (metal oxide) [63–69], Pt–M intermetallic [70], M–Pt core–shell nanostructures [71–74], and the like. The promotional effect from the cocatalyst is often attributed to the bifunctional effect (promoted mechanism) [37] and the electronic effect (ligand effect or intrinsic mechanism) [38]. According to the bifunctional effect, the oxidative removal of the strongly adsorbed poisoning species is facilitated in the presence of an oxyphilic cocatalyst (e.g., Ru, Sn, Ir, Re, Os, Pb, Bi, and Mo) by supplying oxygen atoms at an adjacent site at a lower potential than that accomplished by pure Pt. The electronic effect postulates that the presence of the cocatalyst modifies the electronic structure of Pt and, as a consequence, the adsorption strength of poisoning species and oxygen-containing species. Moreover, the addition of the cocatalysts reduces Pt content in the electrocatalysts. Among various anode electrocatalysts developed, the most extensively investigated ones are Pt–Ru- and Pt–Sn-based catalysts.

1.2.3.1 Pt–Ru-Based Electrocatalysts

Pt–Ru electrocatalysts are generally considered to be the most active binary catalysts for the MOR. Several commercial Pt–Ru alloy nanoparticles supported on carbon black have been available for applications in DAFCs. The catalytic effect has been observed using different kinds of Pt–Ru materials, such as adsorbed Ru on bulk Pt [46, 47], UHV-evaporated Ru on bulk Pt [46, 47], Pt–Ru electrodeposits [48, 49], Pt–Ru alloys [50–60], and Pt–RuO_2 [63–66].

Supported Pt–Ru alloy nanoparticle catalysts are usually prepared by impregnation [50, 51] and colloidal methods [52–54]. The impregnation method is a simple procedure; however, the resulting nanoparticles have a large average size and a broad distribution. The colloidal methods can produce very small and homogeneously distributed nanoparticles but the methodologies are more complex. Microemulsion method is a new synthetic route and the main advantage is the ease in controlling metallic composition and particle size within a narrow distribution by varying synthesis conditions [55–57].

The Pt–Ru alloy catalyst with a Pt:Ru atomic ratio of 1:1 is generally considered as the best MOR catalysts in terms of activity and stability [58]. Lamy et al. [59]

reported the best composition of Pt–Ru alloy for MOR depended on electrode potentials. A Ru-rich catalyst showed higher performance at low potentials, while a Pt-rich one worked better at higher potentials. Contrary to the current understanding, the mixed-phase electrocatalyst containing Pt metal and hydrous ruthenium oxides were reported to be more active than the Pt–Ru bimetallic alloy catalyst [60, 63–65]. Wieckowski and co-workers first demonstrated the spontaneous deposition of a noble metal on another noble-metal surface by the deposition of Ru adlayers on a Pt(*hkl*) single crystal [66, 75]. Using the spontaneous deposition method, Pt nanoparticles were decorated with Ru to obtain a Pt/Ru catalyst, and the optimized Pt/Ru catalyst was twice as active as the commercial Pt–Ru alloy catalyst. However, Pt content in the Pt/Ru catalyst is high, so the approach to decorate Ru nanoparticle surfaces by Pt adatoms/adlayers seems beneficial to reduce Pt loading. Hwang et al. [76] prepared Pt-decorated Ru nanoparticle catalysts by a redox-transmetalation process; the catalysts showed higher mass activity for methanol oxidation than did commercial Pt–Ru catalysts. Sasaki et al. synthesized electrocatalysts comprising a monolayer amount of Pt on Ru nanoparticles by galvanic displacement of a Cu adlayer (detailed discussion in Sect. 2.4) [77].

Pt–Ru catalysts also received much attention in ethanol oxidation [48, 67, 78, 79]. Iwasita et al. [48] investigated the EOR activity of Pt–Ru electrodeposits as a function of their atomic composition and demonstrated that the catalytic activity of Pt–Ru is strongly dependent on the Ru content. The optimum Pt:Ru composition was suggested to be 3:2. At low Ru concentration, there are insufficient Ru sites to effectively assist the oxidation of adsorbed residues, while ethanol adsorption can be inhibited when Ru concentration is too high (i.e., >ca. 40 %) due to the diminution of Pt sites.

Some work was carried to modify Pt–Ru catalysts by adding a third or even a fourth constituent. These Pt–Ru-based ternary or quaternary electrocatalysts such as Pt–Ru–Os, Pt–Ru–W, Pt–Ru–Ni, Pt–Ru–Mo, Pt–Ru–Pb, Pt–RuO_2–IrO_2, and Pt–Ru–Os–Ir showed improved catalytic activities than Pt–Ru binary catalysts [61, 80–85].

1.2.3.2 Pt–Sn-Based Electrocatalysts

Pt–Sn electrocatalysts only show modest improvement in catalyzing MOR compared to pure Pt catalysts, despite the superior performance of Sn as a cocatalyst for enhancing CO oxidation [86]. Generally, comparisons between Pt–Ru and Pt–Sn catalysts indicated that the former are more active for the MOR, and DMFCs with Pt–Ru/C anode catalysts demonstrated substantially better performance compared to one with Pt–Sn/C catalysts under similar operating conditions [62, 87–89].

Pt–Sn electrocatalysts have been considered as the most active binary catalyst for the EOR, and their superior performance has been confirmed in fuel cell measurements [89–91]. Sn promotes the EOR activity of Pt and works even better than Ru. Polyol method [92, 93] and "Bönneman" method [94, 95] were employed to synthesize alloy Pt–Sn/C and Pt–SnO_x/C catalysts, and Jiang et al. [68] claimed that the greater activity was from Pt–SnO_x/C due to the presence of both sufficiently large Pt ensembles for ethanol dehydrogenation and C–C bond splitting and of SnO_x for OH generation. Considerable research has been devoted to optimizing Pt–Sn electrocatalysts. Lamy et al. [95] found the alloy Pt–Sn/C catalysts with 10–20 at.% of Sn exhibited best activity at low potentials. Results from Jiang et al. showed that the Pt–SnO_x/C catalyst with an atomic ratio Pt/Sn of 1 was the most active among four with different Pt/Sn ratios. An integrated surface science and electrochemistry study of the SnO_x/Pt(111) model catalysts was carried out by Zhou et al. [69], and the results showed a "volcano" dependence of the EOR activity on the surface composition with the highest activity appearing at a SnO_x coverage of 37 %. Despite the improved overall EOR activity from Pt–Sn catalysts, on-line DEMS studies have shown that acetic acid and acetaldehyde represent the dominant products with CO_2 formation contributing only 1–3 % [68].

Pt–Sn-based systems like Pt–Sn–Ru, Pt–Sn–Ir, Pt–Sn–Ni, and Pt–Sn–Ce were also studied to improve the electrocatalytic activity of Pt–Sn catalysts [69, 96–100].

Other catalysts including Pt–M (where M represents metals other than Ru or Sn, e.g., W, Pd, Rh, Re, Mo, Ti, and Ce) and Pt–MO (where MO represents a metal oxide like WO_3, TiO_2, and CeO_2) have been investigated for the electrocatalysis of alcohols [35, 36].

1.2.3.3 Electrocatalysts with Novel Nanostructures

The use of Pt–Ru and Pt–Sn electrocatalysts has been found to introduce a stability problem: during extended period of fuel cell operation, the catalyst surface becomes depleted of Ru and Sn [70]. It was reported that Ru can nucleate in other parts of the cell and facilitate degradation of the membrane. Ordered intermetallic systems, in general, provide predictable control over structural, geometric, and electronic effects and high structure stability. DiSalvo et al. [70] studied a wide range of ordered intermetallic phases, and the PtBi, PtIn, and PtPb ordered intermetallic phases appeared to be very promising fuel cell anode electrocatalysts.

Most recently, Pt-based electrocatalysts with novel nanostructures such as nanowire, nanotube, hollow, core–shell, and nanodendrite structures have been investigated [71–74, 101]. One-dimensional ternary PtRuM (M = Ni, Co, and W) nanowire catalysts were synthesized, and these catalysts outperform Pt–Ru commercial catalyst and have a low noble-metal content due to the incorporation of an Earth-abundant element [101].

1.2.4 Platinum Monolayer Electrocatalysts

Adzic et al. [102] developed a new approach for designing and synthesizing electrocatalysts that can dramatically reduce the required Pt content while affording possibilities to enhance their catalytic performance. These electrocatalysts consist of a monolayer (one-atom thick) of Pt on extended or supported nanoparticle metal or metal–alloy surfaces. The Pt-monolayer (Pt_{ML}) approach has several attractive features: (a) close to complete Pt utilization since all Pt atoms are present on the surface and involve in catalytic reactions; (b) tailored electrocatalytic properties consequent upon the combined geometric effect (substrate-induced strain) and ligand effect (the electronic interaction between Pt_{ML} and the substrate); (c) enhanced stability because of the decreased oxidation of the Pt_{ML} resulting from the interaction with the suitable substrate; and (d) direct activity correlations between catalytic and physical properties of the Pt_{ML} as all Pt atoms involved in the reaction are sampled by the measuring technique [102].

The Pt_{ML}/Ru electrocatalysts were inaugurated for fuel cell anode reactions, and the catalysts were synthesized by two methods. The first method facilitated the formation of submonolayer-to-multilayer Pt deposits on Ru surfaces via the electroless (spontaneous) deposition of Pt on Ru [103–107]. The coverage and morphology of the Pt deposit on Ru depended on the concentration of platinum ions and the time of deposition. The activity and selectivity of the electrocatalyst was fine-tuned by changing the coverage (the cluster size) of the Pt deposit, and the optimized $PtRu_{20}$/C (with atomic ratio of Pt:Ru as 1:20) electrocatalyst demonstrated superior CO tolerance and stability compared to conventional Pt–Ru/C alloy catalyst [104].

The second synthetic method involves depositing submonolayer-to-monolayer amount of Pt on Ru by the galvanic displacement of an underpotentially deposited (UPD) Cu adlayer; thus, the Pt coverage on Ru can be efficiently controlled by varying Cu coverage (Fig. 1.4). Scanning tunneling microscopy (STM) study of the resulting Pt_{ML}/Ru(1010) surface revealed that Pt was deposited as a small three-dimensional (3D) island on Ru [77]. In some other Pt–M binary systems, for instance, Pt on Pd, a pseudomorphic monolayer of Pt was formed by the displacement of a Cu UPD layer [102]. The Pt_{ML} electrocatalysts comprising different coverage of Pt deposit on carbon-supported Ru nanoparticle supports with 10 nmol Ru content were synthesized, and electrochemical study showed that 3.9 nmol Pt afforded the most active surface for methanol electrooxidation (Fig. 1.5a). Figure 1.5b compared Pt mass activities for methanol oxidation on commercial PtRu/C and the optimized partial Pt monolayer on Ru/C, denoted as Pt_{ML}/Ru/C electrocatalysts; the latter exhibited a threefold higher Pt mass activity. The effect of the size of Ru nanoparticles on the MOR activity of Pt_{ML}/Ru/C electrocatalysts was investigated, and the optimal size was found to be around 3 nm. Chronoamperometric measurements at 0.67 V showed that the loss of activity with time for the Pt_{ML}/Ru/C electrocatalyst is 2.5 times slower than that for commercial PtRu/C electrocatalyst (Fig. 1.6). The difference is caused by the weaker CO bonding to the Pt_{ML}/Ru than to the Pt–Ru alloy and also by a more efficient bifunctional mechanism. An interesting finding was that the incorporation of another oxyphilic metal into the Pt_{ML} by depositing mixed-metal M + Pt monolayer (where M = Ir, Pd, Os, and Rh) on Ru/C did not surpass the Pt_{ML}/Ru/C electrocatalyst in catalyzing methanol oxidation.

Most recently, Pt_{ML} electrocatalysts were systematically studied for the electrooxidation of methanol and ethanol [108]. Pt_{ML} was deposited on different substrates via the galvanic displacement of a Cu UPD monolayer, employing five single-crystal surfaces (Au(111), Pd(111), Ir(111), Rh(111), and Ru(0001))

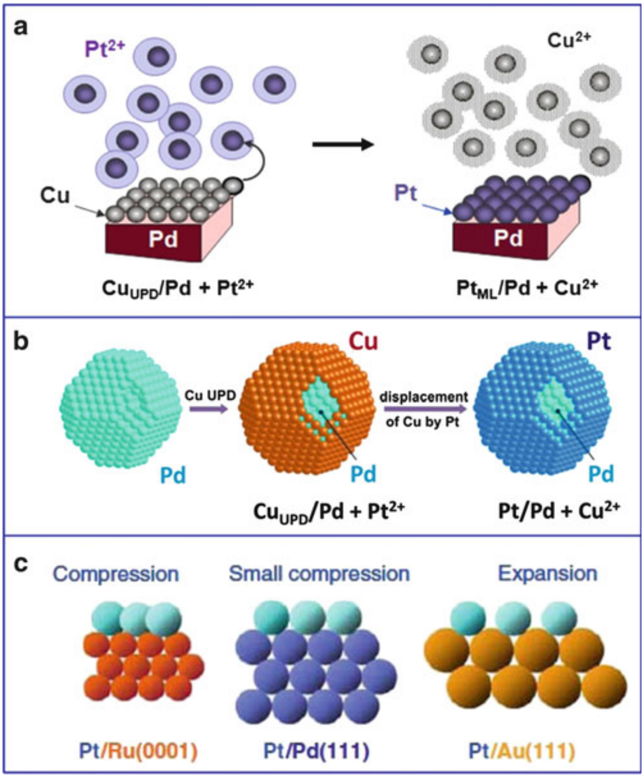

Fig. 1.4 Pt_{ML} deposition by galvanic displacement of a Cu UPD adlayer on the substrates of bulk Pd electrode (**a**) and Pd nanoparticle (**b**). Models of pseudomorphic monolayers of Pt on three different substrates (**c**) inducing compressive strain (Ru(0001) and Pd(111)) and expansive strain (Au(111)) [102]

as substrates. Taking as examples a Pt_{ML}/Au(111) surface, where Au exerts on Pt a tensile strain, and a Pt_{ML}/Pd(111) surface where Pt is under compressive strain, a significant enhancement in the catalytic activity associates with the tensile strain, and decreased activity associates with the compressive strain. During the MOR (Fig. 1.7a), the Pt_{ML}/Au(111) exhibited a negatively shifted potential at the onset of the reaction and over sevenfold enhancement in peak current density with respect to Pt(111) (the most active low-index plane of Pt). Similarly, during the EOR (Fig. 1.7b), the stretched Pt_{ML} supported on Au(111) demonstrates slightly negatively shifted reaction-onset potential and over fourfold increase in peak current density. Along with more electrochemical studies, a trend is observable indicating that increased lattice compression lowers reactivity. Spectroscopic study showed the enhanced MOR activity in Pt_{ML}/Au(111) was due to the formation of COH_{ads}, instead of poisoning CO_{ads}, and the promoted oxidation of COH_{ads} directly to CO_2. The high EOR activity on Pt_{ML}/Au(111) was attributed to the fast kinetics of partial oxidation pathway leading to acetic acid and acetaldehyde.

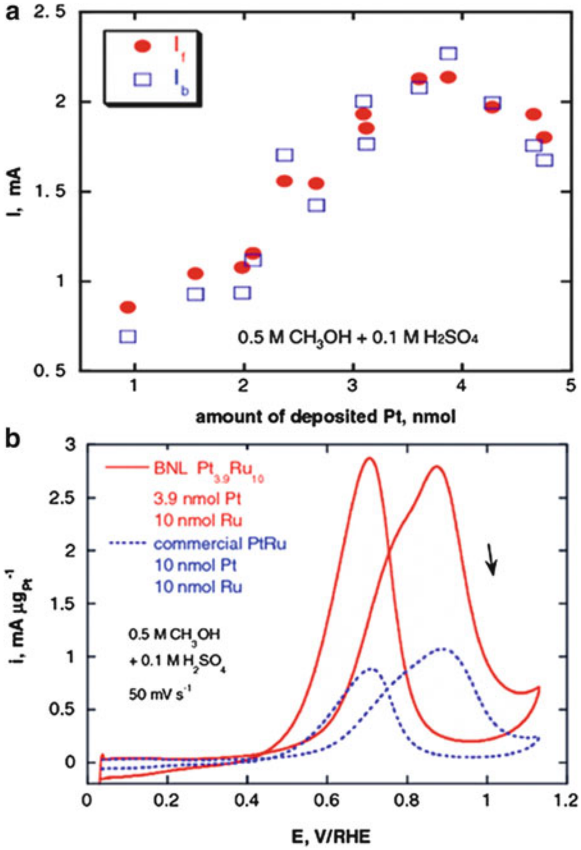

Fig. 1.5 Methanol oxidation peak currents as a function of Pt coverage (4 nmol as 2D islands is approximately 0.8 of a monolayer), where If and Ib represent peak currents at forward and backward scans, respectively (**a**) Pt mass activity for methanol oxidation on commercial PtRu and Pt_{ML}/Ru electrocatalysts (**b**) [77] (reproduced with permission from J. Electrochem. Soc. 155, B183 (2008). Copyright 2003, The Electrochemical Society)

DFT calculations were carried out to gain better understanding of the methanol electrooxidation on the surfaces of Pt_{ML} supported on different substrates. The onset potential for methanol electrooxidation on the Pt_{ML}/metal surfaces was estimated by calculating the binding energies and free energies of CO and OH (Fig. 1.8). The DFT-predicted trend in reactivity agreed well with the experimental observations, showing in decreasing sequence, Pt_{ML}/Au(111) > Pt(111) > Pt_{ML}/Pd(111) > Pt_{ML}/Ir(111) > Pt_{ML}/Rh(111) > Pt_{ML}/Ru(0001); Pt_{ML}/Au(111) displays the highest activity, where Pt_{ML} is stretched by over 4 % and exhibits enhanced reactivity in the dehydrogenative adsorption of alcohol molecules (Pt–CO) and the dissociation of water (Pt–OH formation). That is, the strain effect due to the Au support results in a Pt with moderate activity, being able to bind the adsorbates

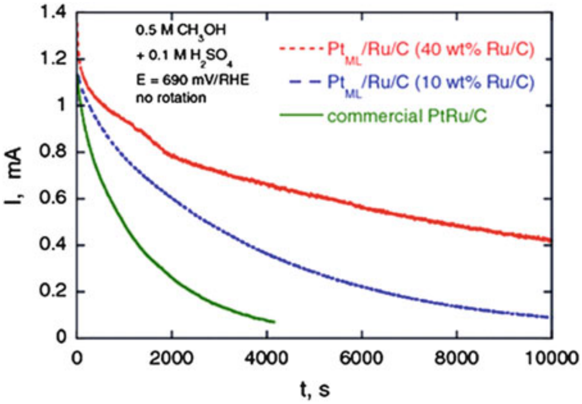

Fig. 1.6 Time dependence of the Pt_{ML}/Ru electrocatalysts' activity at 0.69 V with two different compositions indicated in the graph and a commercial PtRu/C catalyst for methanol oxidation [77] (reproduced with permission from J. Electrochem. Soc. 155, B185 (2008). Copyright 2003, The Electrochemical Society)

strongly enough to activate methanol, yet weakly enough to prevent CO poisoning and allow the formation of CO_2.

Several Pt_{ML} nanocatalysts comprising Pt_{ML} supported on mono- or bimetallic nanoparticle cores were studied (Fig. 1.9), and the activity for both methanol and ethanol electrooxidation reactions increased in the order of Pt_{ML}/Pd/C < Pt/C < Pt_{ML}/Au/C. Hence, a qualitatively similar trend is observed as with single-crystal surfaces, viz., dilated Pt_{ML} enhances activity, while activity in compressed Pt_{ML} is decreased. Pt_{ML} supported on Pd–Au bimetallic alloy nanoparticles demonstrated an activity in between of Pt_{ML}/Pd/C and Pt_{ML}/Au/C, which also suggested a tunable activity can be obtained from Pt_{ML} by manipulating its lateral strain. Nanoparticles are generally enclosed by a mixture of (111) and (100) planes and have certain surface density of low coordinated sites. The size, shape, and structure of nanoparticle supports can affect the reactivity, selectivity, and stability of Pt_{ML} in a complex way. However, with advanced synthetic nanotechnology methods, designing suitable, low-cost nanoparticle supports with enhancing properties is quite feasible.

1.2.5 Ternary Electrocatalysts for Oxidizing Ethanol to Carbon Dioxide

The major challenge for the electrocatalysis of ethanol is to facilitate its total oxidation to CO_2 at low potentials, which cannot be achieved by existing Pt-based binary catalysts. Adzic et al. developed the multifunctional ternary Pt–Rh–SnO_2 electrocatalyst which is effective in splitting the C–C bond in ethanol at room

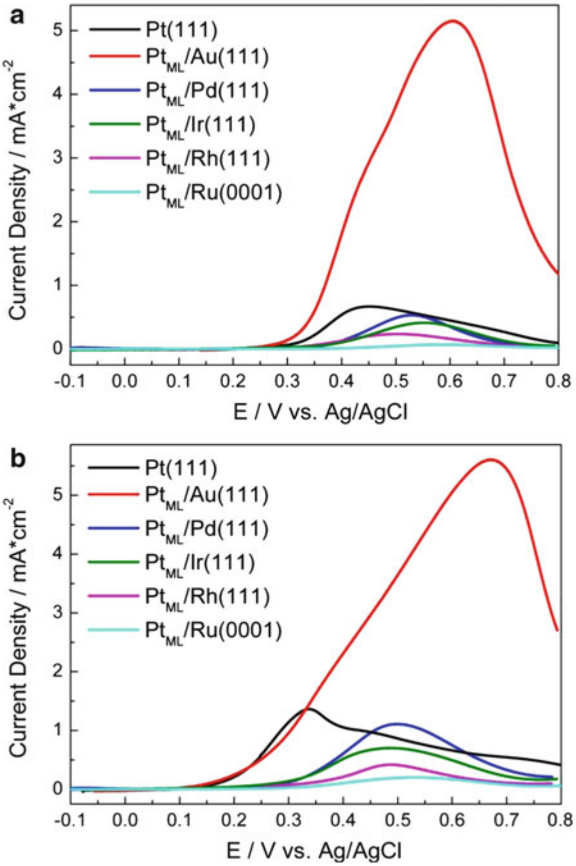

Fig. 1.7 Positive voltammetric scans for Pt(111) and Pt$_{ML}$ supported on five different substrates (Au(111), Pd(111), Ir(111), Rh(111), and Ru(0001)) in 0.1 M $HClO_4$ containing 0.5 M methanol (**a**) or 0.5 M ethanol (**b**) with scan rate 10 mV/s [108]

temperature, and the catalytic property of the ternary catalyst is attributed to the synergistic effect between all three constituents (where Pt is for ethanol dehydrogenerative adsorption, SnO_2 supplies oxygen-containing species, and Rh is responsible for C–C bond cleavage) [109–115].

The model catalyst $RhSnO_2/Pt(111)$ and $PtRhSnO_2/C$ nanoparticle catalyst were synthesized; both demonstrated unprecedented activity for the EOR with the onset of reaction occurring at low overpotentials [109]. In situ infrared reflection-absorption spectra (IRRAS) recorded during EOR with both catalysts demonstrated the enhanced CO_2 production compared to pure Pt and binary $PtSnO_2$ catalysts. DFT investigation of ethanol decomposition over a model $RhPt/SnO_2(110)$ catalyst suggested the optimal reaction pathway is $^*CH_3CH_2OH \rightarrow {}^*CH_3CHO + H^* \rightarrow {}^*CH_2CH_2O + 2H^* \rightarrow {}^*CH_2 + {}^*CH_2O + 2H^*$.

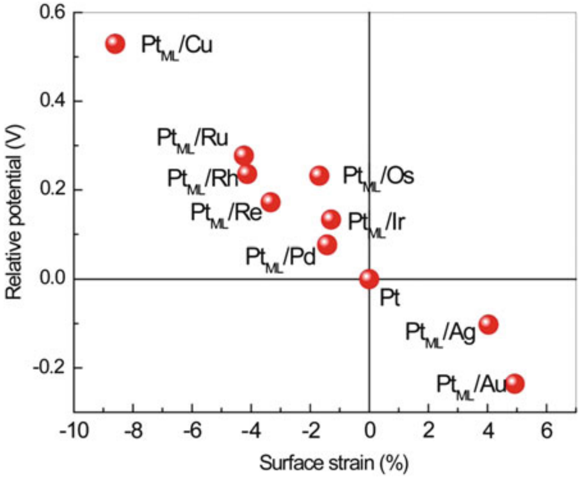

Fig. 1.8 DFT investigations of methanol oxidation on Pt_{ML} supported on different substrates. The DFT-calculated variation of the lowest potential to proceed methanol electrooxidation on the Pt_{ML} supported on Cu(111), Ru(001), Rh(111), Re(001), Pd(111), Os(001), Ir(111), Ag(111), and Au(111) surfaces with the surface strain. The surface stain was calculated by $[d(Pt_{ML/surf}) - d(Pt)]/d(Pt)$, where d is Pt–Pt bond length. The potential and surface strain were expressed with respect to the case of Pt(111) [108]

Most recently, a series of carbon-supported ternary SnOM′/SnO_2 NP electrocatalysts comprising SnO_2 NP cores decorated with multi-metallic nanoislands (MM′ = PtIr, PtRh, IrRh, PtIrRh) were prepared using a seeded-growth approach as synthetic analogues to the PtRh/SnO_2(110) model catalyst in the earlier DFT study [109, 112]. The composition and architecture of these catalysts were established using an array of characterization techniques including Z-contrast scanning transmission electron microscope (STEM) (Fig. 1.10), X-ray diffraction (XRD), and more techniques.

Electrochemical measurements (Fig. 1.11) and in situ IRRAS studies (Fig. 1.12) were carried out to investigate the catalytic properties of the MM′/SnO_2/C electrocatalysts. Both EOR reactivity and selectivity towards CO_2 formation of several of these MM′/SnO_2/C NP catalysts are significantly higher than those of Pt/C and PtSnO_2/C. Among the systems studied, PtIr/SnO_2/C catalyst with highest Ir content, i.e., the catalyst with atomic ratio Pt:Ir:Sn of 1:1:1, showed the most negative EOR onset potential and considerably improved capability in C–C bond splitting. PtRh/SnO_2/C electrocatalysts with a suitable Rh content, i.e., catalysts with atomic ratio Pt:Rh:Sn of 1:1/2:1 and 1:1/3:1, exhibit the highest selectivity towards ethanol total oxidation. The dependency between chemical composition and catalytic properties was attributed to the combined ensemble effect and ligand effect. The PtIrRh/SnO_2/C electrocatalyst (with atomic ratio Pt:Ir:Rh:Sn of 1:1:1:1) displays lower activity compared to PtRh/SnO_2/C and PtIr/SnO_2/C electrocatalysts,

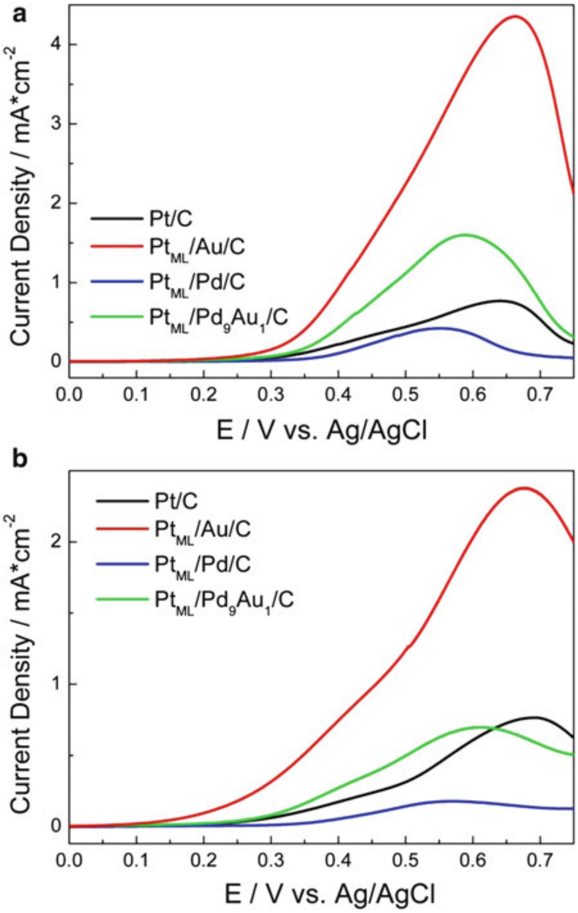

Fig. 1.9 Positive voltammetric scans for Pt/C and Pt$_{ML}$ supported on different nanoparticle substrates in 0.1 M $HClO_4$ containing 0.5 M methanol (**a**) or 0.5 M ethanol (**b**) with scan rate 10 mV/s [108]

and the IrRh/SnO_2/C electrocatalyst (with atomic ratio Ir:Rh:Sn of 1:1:1) is the poorest of all. The CO_2 production efficiency of the above catalysts decreases in the following order: PtRh/SnO_2 (with atomic ratio Pt:Rh:Sn of 1:1/2:1 and 1:1/3:1) > PtIrRh/SnO_2 (with atomic ratio Pt:Ir:Rh:Sn of 1:1:1:1) > PtIr/SnO_2 (with atomic ratio Pt:Ir:Sn of 1:1:1).

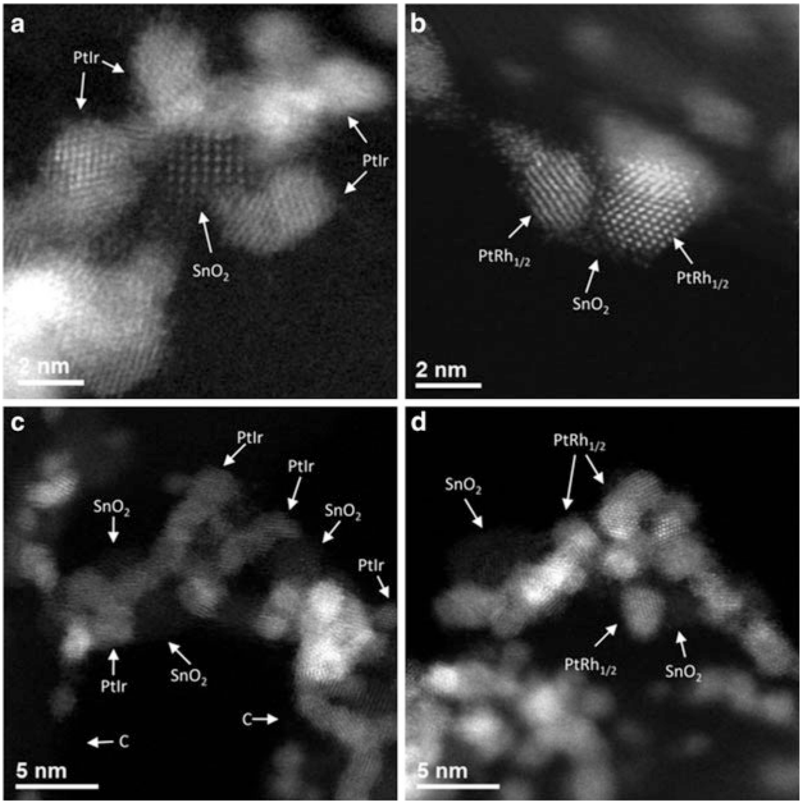

Fig. 1.10 Representative high-resolution Z-contrast AC-STEM images of PtIr/SnO_2/C (**a** and **c**), and $PtRh_{1/2}$/SnO_2/C (**b** and **d**) electrocatalysts [112]

1.2.6 Alternative to Pt-Based Electrocatalysts

Ir- and Rh-based catalysts have been investigated for ethanol oxidation reaction in acidic media, and there have been some interesting and reasonably promising results [116–118]. Lamy et al. [116] carried out in situ FTIR study on polycrystalline Ir and Rh electrodes and showed ethanol oxidation on Ir leading selectively to either acetic acid or acetaldehyde, while Rh is a better catalyst in the total oxidation of ethanol to CO_2. Cao et al. [117] studied carbon-supported Ir_3Sn nanoparticle electrocatalyst, and the fuel cell test results showed that the overall performance of Ir_3Sn/C was comparable to that of the Pt_3Sn/C catalyst.

The combined DFT and kinetic Monte Carlo (kMC) simulations conducted by Choi et al. [118] propose that ethanol on Rh(111) is decomposed into C and CO, with the cleavage of the C–C bonds (Fig. 1.13).

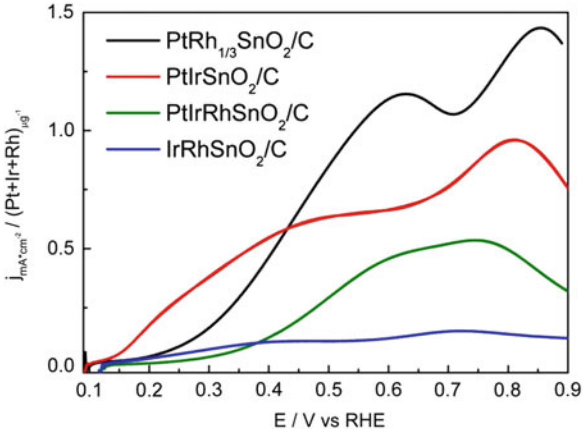

Fig. 1.11 Anodic polarization curves of PtIr/SnO_2/C (with atomic ratio Pt:Ir:Sn of 1:1:1), $PtRh_{1/3}$/SnO_2/C (with atomic ratio Pt:Rh:Sn of 1:1/3:1), IrRh/SnO_2/C (with atomic ratio Ir:Rh:Sn of 1:1:1), and PtIrRh/SnO_2/C (with atomic ratio Pt:Ir:Rh:Sn of 1:1:1:1) electrocatalysts in 0.1 M $HClO_4$ with 0.5 M ethanol with scan rate 10 mV/s. The total noble-metal mass (Pt + Rh + Ir) specific current densities were employed in the comparison, and all measurements were carried out at room temperature [112]

1.3 Conclusions and Future Directions

This chapter summarized the fundamental aspects and recent advances in electrocatalysts for the oxidation reactions of methanol and ethanol occurring at fuel cell anodes. Pt-based electrocatalysts are still considered to be the most viable for the anodic reactions in acidic media. The major drawback, however, is the price and limited reserves of Pt. To lower the Pt loading, the core–shell structure comprising Pt shells is more beneficial than the alloy structure, since all the Pt atoms on the nanoparticle surfaces can participate in the catalytic reactions (and those in cores do not); particularly, the Pt submonolayer/monolayer approach would be an ultimate measure to minimize the Pt content. The architectures in nanoscale also have a significant effect on the reactivity and durability [119, 120] and thus should be explored continuously in a future. As for the ethanol oxidation, Rh addition is shown to enhance the selectivity towards C–C bond splitting; however, Rh is even more expensive than Pt, and thus, the Rh content has to be very low, or less expensive constituents replacing Rh are necessary to be found.

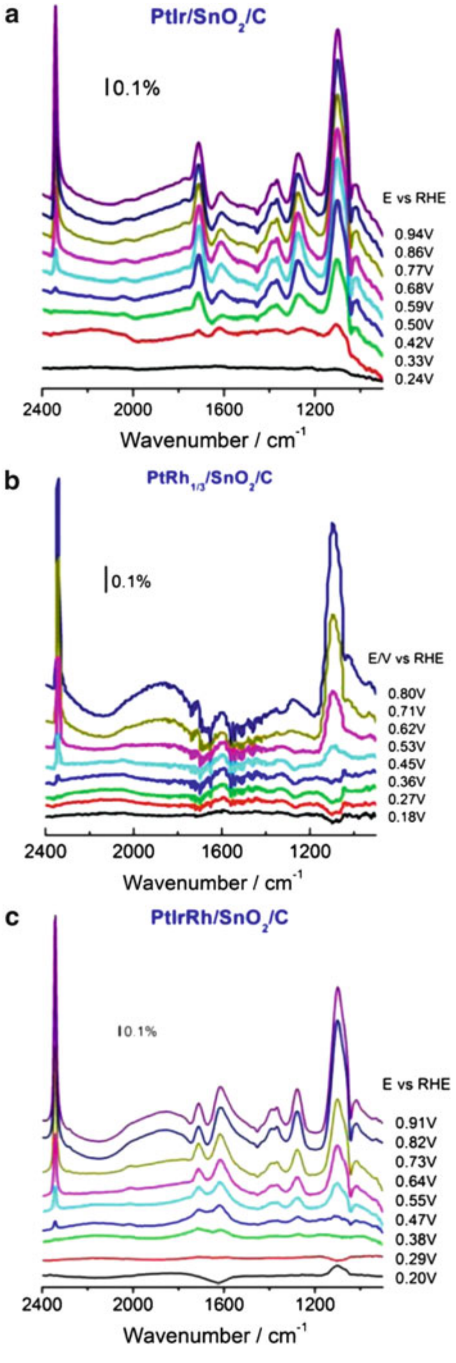

Fig. 1.12 In situ IRRAS spectra recorded during EOR on three MM′/SnO_2/C NP electrocatalysts: (**a**) PtIr/SnO_2/C, (**b**) $PtRh_{1/3}$/SnO_2/C, and (**c**) PtIrRh/SnO_2/C [112]

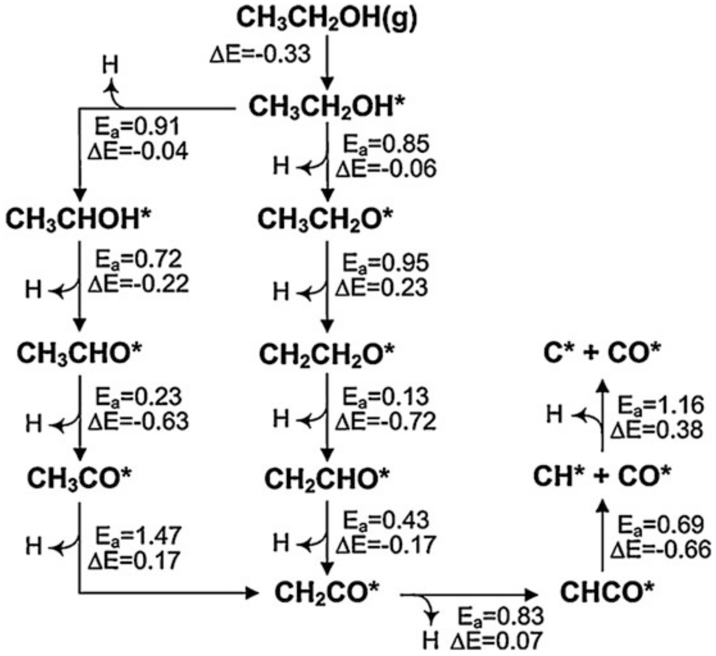

Fig. 1.13 Proposed reaction pathways for ethanol decomposition on Rh(111). Energy is in units of eV [118]

References

1. Gosselink JW (2002) Pathways to a more sustainable production of energy: sustainable hydrogen—a research objective for Shell. Int J Hydrogen Energ 27:1125–1129
2. Aricò AS, Baglio V, Antonucci V (2009) Direct methanol fuel cells: history, status and perspectives. In: Liu H, Zhang J (eds) Electrocatalysis of direct methanol fuel cells. Wiley-VCH Verlag GmbH & Co. KGaA, Weinheim
3. Lamy C, Leger J-M, Srinivasan S (2001) Direct methanol fuel cells—from a 20th century electrochemist's dream to a 21st century emerging technology. In: Bockris JO'M (ed) Modern aspects of electrochemistry. Plenum, New York, NY
4. Lamy C, Coutanceau C, Leger J-M (2009) The direct ethanol fuel cell: a challenge to convert bioethanol cleanly into electric energy. In: Barbaro P, Bianchini C (eds) Catalysis for sustainable energy production. Wiley-VCH Verlag GmbH & Co. KGaA, Weinheim
5. Batista EA, Hoster H, Iwasita T (2003) Analysis of FTIRS data and thermal effects during methanol oxidation on UHV-cleaned PtRu alloys. J Electroanal Chem 554–555:265–271
6. Camara GA, Iwasita T (2005) Parallel pathways of ethanol oxidation: the effect of ethanol concentration. J Electroanal Chem 578:315–321
7. Wasmus S, Kuver A (1999) Methanol oxidation and direct methanol fuel cells: a selective review. J Electroanal Chem 461:14–31
8. Iwasita T (2002) Electrocatalysis of methanol oxidation. Electrochim Acta 47:3663–3674
9. Batista EA, Malpass GRP, Motheo AJ, Iwasita T (2004) New mechanistic aspects of methanol oxidation. J Electroanal Chem 571:273–282

10. Vigier F, Rousseau S, Coutanceau C, Leger J-M, Lamy C (2006) Electrocatalysis for the direct alcohol fuel cell. Top Catal 40(1–4):111–121
11. Lamy C, Belgsir EE, Leger J-M (2001) Electrocatalytic oxidation of aliphatic alcohols: application to the direct alcohol fuel cell (DAFC). J Appl Electrochem 31:799–809
12. Jusys Z, Kaiser J, Behm RJ (2003) Methanol electrooxidation over Pt/C fuel cell catalysts: dependence of product yields on catalyst loading. Langmuir 19:6759–6769
13. Wang H, Jusys Z, Behm RJ (2004) Ethanol electrooxidation on a carbon-supported Pt catalyst: reaction kinetics and product yields. J Phys Chem B 108:19413–19424
14. Shao MH, Adzic RR (2005) Electrooxidation of ethanol on a Pt electrode in acid solutions: in situ ATR-SEIRAS study. Electrochim Acta 50:2415–2422
15. Adzic RR, Tripkovic AV, O'Grady WE (1982) Structural effects in electrocatalysis. Nature 296:10–11
16. Xia XH, Iwasita T, Ge F, Vielstich W (1996) Structural effects and reactivity in methanol oxidation on polycrystalline and single crystal platinum. Electrochim Acta 41:711–718
17. Xia XH, Liess H-D, Iwasita T (1997) Early stages in the oxidation of ethanol at low-index single crystal platinum electrodes. J Electroanal Chem 437:233–240
18. Lamy C, Leger J-M, Clavilier J, Parsons R (1983) Structural effects in electrocatalysis: a comparative study of the oxidation of CO, HCOOH, and CH_3OH on single crystal Pt electrodes. J Electroanal Chem 150:71–77
19. Morin M-C, Lamy C, Leger J-M, Vasquez J-L, Aldaz A (1990) Structural effects in electrocatalysis: oxidation of ethanol on platinum single crystal electrodes. Effect of pH. J Electroanal Chem 283:287–302
20. Chang S-C, Leung L-W H, Weaver MJ (1990) Metal crystallinity effects in electrocatalysis as probed by real-time FTIR spectroscopy: electrooxidation of formic acid, methanol, and ethanol on ordered low-index platinum surfaces. J Phys Chem 94:6013–6021
21. Colmati F, Tremiliosi-Filho G, Gonzalez ER, Berna A, Herrero E, Feliu JM (2008) Surface structure effects on the electrochemical oxidation of ethanol on platinum single crystal electrodes. Faraday Discuss 140:379–397
22. Lai SCS, Lebedeva NP, Housmans THM, Koper MTM (2007) Mechanisms of carbon monoxide and methanol oxidation at single-crystal electrodes. Top Catal 46:320–333
23. Housmans THM, Koper MTM (2003) Methanol oxidation on stepped Pt[n(111) × (110)] electrodes: a chronoamperometric study. J Phys Chem B 107:8557–8567
24. Lai SCS, Koper MTM (2008) Electro-oxidation of ethanol and acetaldehyde on platinum single-crystal electrodes. Faraday Discuss 140:399–416
25. Tripkovic AV, Popovic KD (1996) Oxidation of methanol on platinum single crystal stepped electrodes from [110] zone in acid solution. Electrochim Acta 41(15):2385–2394
26. Colmati F, Tremiliosi-Filho G, Gonzalez ER, Berna A, Herrero E, Feliu JM (2009) The role of the steps in the cleavage of the C–C bond during ethanol oxidation on platinum electrodes. Phys Chem Chem Phys 11:9114–9123
27. Shin J, Tornquist WJ, Korzeniewski C, Hoaglund CS (1996) Elementary steps in the oxidation and dissociative chemisorptions of ethanol on smooth and stepped surface planes of platinum electrodes. Surf Sci 364:122–130
28. Tarnowski DJ, Korzeniewski C (1997) Effects of surface step density on the electrochemical oxidation of ethanol to acetic acid. J Phys Chem B 101:253–258
29. Park S, Xie Y, Weaver MJ (2002) Electrocatalytic pathways on carbon-supported platinum nanoparticles: comparison of particle-size-dependent rates of methanol, formic acid, and formaldehyde electrooxidation. Langmuir 18(15):5792–5798
30. Arenz M, Mayrhofer KJJ, Stamenkovic V, Blizanac BB, Tomoyuki T, Ross PN, Markovic NM (2005) The effect of the particle size on the kinetics of CO electrooxidation on high surface area Pt catalysts. J Am Chem Soc 127(18):6819–6829
31. Maillard F, Savinova ER, Stimming U (2007) CO monolayer oxidation on Pt nanoparticles: further insights into the particle size effects. J Electroanal Chem 599(2):221–232

32. Tian N, Zhou Z-Y, Sun S-G, Ding Y, Wang ZL (2007) Synthesis of tetrahexahedral platinum nanocrystals with high-index facets and high electro-oxidation activity. Science 316:732–735
33. Zhou ZY, Huang Z-Z, Chen D-J, Wang Q, Tian N, Sun S-G (2010) High-index faceted platinum nanocrystals supported on carbon black as highly efficient catalysts for ethanol electrooxidation. Angew Chem Int Ed 49(2):411–414
34. Zhou W-P, Li M, Koenigsmann C, Ma C, Wong SS, Adzic RR (2011) Morphology-dependent activity of Pt nanocatalysts for ethanol oxidation in acidic media: nanowires versus nanoparticles. Electrochim Acta 56(27):9824–9830
35. Liu H, Song C, Zhang L, Zhang J, Wang H, Wilkinson DP (2006) A review of anode catalysis in the direct methanol fuel cell. J Power Sources 155(2):95–110
36. Antolini E (2007) Catalysts for direct ethanol fuel cells. J Power Sources 170:1–12
37. Watanabe M, Motoo S (1975) Electrocatalysis by ad-atoms: Part II Enhancement of the oxidation of methanol on platinum by ruthenium ad-atoms. J Electroanal Chem 60: 267–273
38. Van Veen JAR, Frelink T, Visscher W (1995) On the role of Ru and Sn as promotors of methanol electro-oxidation over Pt. Surf Sci 335:353–360
39. Del Colle V, Berna A, Tremiliosi-Filho G, Herrero E, Feliu JM (2008) Ethanol electrooxidation onto stepped surfaces modified by Ru deposition: electrochemical and spectroscopic studies. Phys Chem Chem Phys 10:3766–3773
40. Souza-Garcia J, Herrero E, Feliu JM (2010) Breaking the C–C bond in the ethanol oxidation reaction on platinum electrodes: effect of steps and ruthenium adatoms. ChemPhysChem 11: 1391–1394
41. Wang H, Baltruschat H (2007) DEMS study on methanol oxidation at poly- and monocrystalline platinum electrodes: the effect of anion, temperature, surface structure, Ru adatom, and potential. J Phys Chem C 111(19):7038–7048
42. Campbell SA, Parsons R (1992) Effect of Bi and Sn adatoms on formic acid and methanol oxidation at well defined platinum surfaces. J Chem Soc Faraday Trans 88:833–841
43. Janssen MMP, Moolhuysen J (1976) Binary systems of platinum and a second metal as oxidation catalysts for methanol fuel cells. Electrochim Acta 21(11):869–878
44. Kokkinidis G (1986) Underpotential deposition and electrocatalysis. J Electroanal Chem Interfacial Electrochem 201(2):217–236
45. Bittins-Cattaneo B, Iwasita T (1987) Electrocatalysis of methanol oxidation by adsorbed tin on platinum. J Electroanal Chem Interfacial Electrochem 238(1–2):151–161
46. Iwasita T, Hoster H, John-Anacker A, Lin WF, Vielstich W (2000) Methanol oxidation on PtRu electrodes: influence of surface structure and Pt – Ru atom distribution. Langmuir 16(2):522–529
47. Hoster H, Iwasita T, Baumgärtner H, Vielstich W (2001) Pt–Ru model catalysts for anodic methanol oxidation: influence of structure and composition on the reactivity. Phys Chem Chem Phys 3:337–346
48. Camara GA, Lima RBD, Iwasita T (2004) Catalysis of ethanol electrooxidation by PtRu: the influence of catalyst composition. Electrochem Commun 6(8):812–815
49. Tsai M-C, Yeh T-K, Tsai C-H (2006) An improved electrodeposition technique for preparing platinum and platinum–ruthenium nanoparticles on carbon nanotubes directly grown on carbon cloth for methanol oxidation. Electrochem Commun 8(9):1445–1452
50. Radmilovic V, Gasteiger HA, Ross PN (1995) Structure and chemical composition of a supported Pt–Ru electrocatalyst for methanol oxidation. J Catal 154(1):98–106
51. Yang B, Lu Q, Wang Y, Zhang L, Lu J, Liu P (2003) Simple and low-cost preparation method for highly dispersed PtRu/C catalysts. Chem Mater 15:3552–3557
52. Guo JW, Zhao TS, Prabhuram J, Chen R, Wong CW (2005) Preparation and characterization of a PtRu/C nanocatalyst for direct methanol fuel cells. Electrochim Acta 51:754–763

53. Bonnemann H, Brinkmann R, Kinge S, Ely TO, Armand M (2004) Chloride free Pt- and PtRu-nanoparticles stabilised by “Armand’s ligand” as precursors for fuel cell catalysts. Fuel Cells 4:289–296
54. Park KC, Jang IY, Wongwiriyapan W, Morimoto S, Kim YJ, Jung YC, Toya T, Endo M (2010) Carbon-supported Pt–Ru nanoparticles prepared in glyoxylate-reduction system promoting precursor–support interaction. J Mater Chem 20:5345–5354
55. Liu Y, Qiu X, Chen Z, Zhu W (2002) A new supported catalyst for methanol oxidation prepared by a reverse micelles method. Electrochem Commun 4:550–553
56. Solla-Gullon J, Vidal-Iglesias FJ, Montiel V, Aldaz A (2004) Electrochemical characterization of platinum–ruthenium nanoparticles prepared by water-in-oil microemulsion. Electrochim Acta 49:5079–5088
57. Xiong L, Manthiram A (2005) Catalytic activity of Pt–Ru alloys synthesized by a microemulsion method in direct methanol fuel cells. Solid State Ionics 176:385–392
58. Dinh HN, Ren X, Garzon FH, Zelenay P, Gottesfeld S (2000) Electrocatalysis in direct methanol fuel cells: in-situ probing of PtRu anode catalyst surfaces. J Electroanal Chem 491:222–233
59. Dubau L, Coutanceau C, Garnier E, Leger J-M, Lamy C (2003) Electrooxidation of methanol at platinum–ruthenium catalysts prepared from colloidal precursors: atomic composition and temperature effects. J Appl Electrochem 33:419–429
60. Rolison DR, Hagans PL, Swider KE, Long JW (1999) Role of hydrous ruthenium oxide in Pt − Ru direct methanol fuel cell anode electrocatalysts: the importance of mixed electron/proton conductivity. Langmuir 15(3):774–779
61. Gurau B, Viswanathan R, Liu R, Lafrenz TJ, Ley KL, Smotkin ES, Reddington E, Sapienza A, Chan BC, Mallouk TE, Sarangapani S (1998) Structural and electrochemical characterization of binary, ternary, and quaternary platinum alloy catalysts for methanol electro-oxidation. J Phys Chem B 102:9997–10003
62. Morimoto Y, Yeager EB (1998) Comparison of methanol oxidations on Pt, PtRu and PtSn electrodes. J Electroanal Chem 444:95–100
63. Long JW, Stroud RM, Swider-Lyons KE, Rolison DR (2000) How to make electrocatalysts more active for direct methanol oxidation—avoid PtRu bimetallic alloys! J Phys Chem B 104:9772–9776
64. Cao L, Scheiba F, Roth C, Schweiger F, Cremers C, Stimming U, Fuess H, Chen L, Zhu W, Qiu X (2006) Novel nanocomposite Pt/RuO_2·xH_2O/carbon nanotube catalysts for direct methanol fuel cells. Angew Chem Int Ed 45:5315–5319
65. Suffredinia HB, Tricolib V, Avacaa LA, Vatistasb N (2004) Sol–gel method to prepare active Pt–RuO_2 coatings on carbon powder for methanol oxidation. Electrochem Commun 6(10):1025–1028
66. Chrzanowski W, Wieckowski A (1997) Ultrathin films of ruthenium on low index platinum single crystal surfaces: an electrochemical study. Langmuir 13:5974–5978
67. Suffredini HB, Tricoli V, Vatistas N, Avaca LA (2006) Electro-oxidation of methanol and ethanol using a Pt–RuO_2/C composite prepared by the sol–gel technique and supported on boron-doped diamond. J Power Sources 158(1):124–128
68. Jiang L, Colmenaresa L, Jusysa Z, Sunb GQ, Behma RJ (2007) Ethanol electrooxidation on novel carbon supported Pt/SnO_x/C catalysts with varied Pt:Sn ratio. Electrochim Acta 53: 377–389
69. Zhou WP, Axnanda S, White MG, Adzic RR, Hrbek J (2011) Enhancement in ethanol electrooxidation by SnO_x nanoislands grown on Pt(111): effect of metal oxide-metal interface sites. J Phys Chem C 115:16467–16473
70. Casado-Rivera E, Volpe DJ, Alden L, Lind C, Downie C, Va´zquez-Alvarez T, Angelo ACD, DiSalvo FJ, Abruna HD (2003) Electrocatalytic activity of ordered intermetallic phases for fuel cell applications. J Am Chem Soc 126:4043–4049
71. Guo S, Dong S, Wang E (2010) Three-dimensional Pt-on-Pd bimetallic nanodendrites supported on graphene nanosheet: facile synthesis and used as an advanced nanoelectrocatalyst for methanol oxidation. ACS Nano 4(1):L547–555

72. Guo S, Fang Y, Dong S, Wang E (2007) High-efficiency and low-cost hybrid nanomaterial as enhancing electrocatalyst: spongelike Au/Pt core/shell nanomaterial with hollow cavity. J Phys Chem C 111(45):17104–17109
73. Wang H, Xu C, Cheng F, Zhang M, Wang S, Jiang SP (2008) Pd/Pt core-shell nanowire arrays as highly effective electrocatalysts for methanol electrooxidation in direct methanol fuel cells. Electrochem Commun 10(10):1575–1578
74. Zeng J, Yang J, Lee JY, Zhou W (2006) Preparation of carbon-supported core-shell Au–Pt nanoparticles for methanol oxidation reaction: the promotional effect of the Au core. J Phys Chem B 110:24606–24611
75. Chrzanowski W, Kim H, Wieckowski A (1998) Enhancement in methanol oxidation by spontaneously deposited ruthenium on low-index platinum electrodes. Catal Lett 50:69–75
76. Chen CH, Sarma LS, Wang DY, Lai FJ, Al Andra CC, Chang SH, Liu DG, Chen CC, Lee JF, Hwang BJ (2010) Platinum-decorated ruthenium nanoparticles for enhanced methanol electrooxidation. ChemCatChem 2:159–166
77. Sasaki K, Adzic RR (2008) Monolayer-level Ru- and NbO_2-supported platinum electrocatalysts for methanol oxidation. J Electrochem Soc 105:B180–B186
78. Dong L, Gari RRS, Li Z, Craig MM, Hou S (2010) Graphene-supported platinum and platinum–ruthenium nanoparticles with high electrocatalytic activity for methanol and ethanol oxidation. Carbon 48(3):781–787
79. Fujiwara N, Friedrich KA, Stimming U (1999) Ethanol oxidation on PtRu electrodes studied by differential electrochemical mass spectrometry. J Electroanal Chem 472(2):120–125
80. Tanaka S, Umeda M, Ojima H, Usui Y, Kimura O, Uchida I (2005) Preparation and evaluation of a multi-component catalyst by using a co-sputtering system for anodic oxidation of ethanol. J Power Sources 152:34–39
81. Wang Z, Yin G, Zhang J, Sun Y, Shi P (2006) Co-catalytic effect of Ni in the methanol electro-oxidation on Pt–Ru/C catalyst for direct methanol fuel cell. Electrochim Acta 51: 5691–5697
82. Park KW, Choi JH, Kwon BK, Lee SA, Sung YE, Ha HY, Hong SA, Kim HS, Wieckowski A (2002) Chemical and electronic effects of Ni in Pt/Ni and Pt/Ru/Ni alloy nanoparticles in methanol electrooxidation. J Phys Chem B 106:1869–1877
83. Oliveira Neto A, Franco EG, Arico E, Linardi M, Gonzalez ER (2003) Electro-oxidation of methanol and ethanol on Pt–Ru/C and Pt–Ru–Mo/C electrocatalysts prepared by Bönnemann's method. J Eur Ceram Soc 23:2987–2992
84. Li G, Pickup PG (2006) The promoting effect of Pb on carbon supported Pt and Pt/Ru catalysts for electro-oxidation of ethanol. Electrochim Acta 52:1033–1037
85. Calegaro ML, Suffredini HB, Machado SAS, Avaca LA (2006) Preparation, characterization and utilization of a new electrocatalyst for ethanol oxidation obtained by the sol–gel method. J Power Sources 156:300–305
86. Stamenkovic VR, Arenz M, Lucas CA, Gallagher ME, Ross PN, Markovic NM (2003) Surface chemistry on bimetallic alloy surfaces: adsorption of anions and oxidation of CO on $Pt_3Sn(111)$. J Am Chem Soc 125:2735–2745
87. Wang K, Gasteiger HA, Markovic NM, Ross PN (1996) On the reaction pathway for methanol and carbon monoxide electrooxidation on Pt–Sn alloy versus alloy surfaces. Electrochim Acta 41:2587–2593
88. MacDonald JP, Gualtieri B, Runga N, Teliz E, Zinola CF (2008) Modification of platinum surfaces by spontaneous deposition: methanol oxidation electrocatalysis. Int J Hydrogen Energ 33:7048–7061
89. Zhou WJ, Zhou B, Li WZ, Zhou ZH, Song SQ, Sun GQ, Xin Q, Douvartzides S, Goula M, Tsiakaras P (2004) Performance comparison of low-temperature direct alcohol fuel cells with different anode catalysts. J Power Sources 126:16–22
90. Wang Q, Sun GQ, Jiang LH, Xin Q, Sun SG, Jiang YX, Chen SP, Jusys Z, Behm RJ (2007) Adsorption and oxidation of ethanol on colloid-based Pt/C, PtRu/C and Pt_3Sn/C catalysts: in situ FTIR spectroscopy and on-line DEMS studies. Phys Chem Chem Phys 9:2686–2696

91. Colmati F, Antolini E, Gonzalez ER (2006) Effect of temperature on the mechanism of ethanol oxidation on carbon supported Pt, PtRu and Pt_3Sn electrocatalysts. J Power Sources 157:98–103
92. Song SQ, Zhou WJ, Zhou ZH, Jiang LH, Sun GQ, Tsiakaras P, Xin Q, Leonditis V, Kontou S, Tsiakaras P (2005) Direct ethanol PEM fuel cells: the case of platinum based anodes. Int J Hydrogen Energ 30:995–1001
93. Jiang L, Sun G, Sun S, Liu J, Tang S, Li H, Zhou B, Xin Q (2005) Structure and chemical composition of supported Pt–Sn electrocatalysts for ethanol oxidation. Electrochim Acta 50: 5384–5389
94. Bonneman H, Britz P, Vogel W (1998) Structure and chemical composition of a surfactant stabilized Pt_3Sn alloy colloid. Langmuir 14:6654–6657
95. Lamy C, Rousseau S, Belgsir EM, Coutanceau C, Léger JM (2004) Recent progress in the direct ethanol fuel cell: development of new platinum–tin electrocatalysts. Electrochim Acta 49:3901–3908
96. Zhou WJ, Li WZ, Song SQ, Zhou ZH, Jiang LH, Sun GQ, Xin Q, Poulianitis K, Kontou S, Tsiakaras P (2004) Bi- and tri-metallic Pt-based anode catalysts for direct ethanol fuel cells. J Power Sources 131(1–2):217–223
97. Antolini E, Colmatia F, Gonzalez ER (2007) Effect of Ru addition on the structural characteristics and the electrochemical activity for ethanol oxidation of carbon supported Pt–Sn alloy catalysts. Electrochem Commun 9:398–404
98. Sine G, Smida D, Limat M, Foti G, Comninellis C (2007) Microemulsion synthesized Pt/Ru/Sn nanoparticles on BDD for alcohol electro-oxidation. J Electrochem Soc 154:B170–B174
99. Neto AO, Dias RR, Tusi MM, Linardi M, Spinace EV (2007) Electro-oxidation of methanol and ethanol using PtRu/C, PtSn/C and PtSnRu/C electrocatalysts prepared by an alcohol-reduction process. J Power Sources 166:87–91
100. Ribeiro J, dos Anjos DM, Kokoh KB, Coutanceau C, Léger J-M, Olivi P, de Andrade AR, Tremiliosi-Filho G (2007) Carbon-supported ternary PtSnIr catalysts for direct ethanol fuel cell. Electrochim Acta 52(24):6997–7006
101. Koenigsmann C, Wong SS (2011) One-dimensional noble metal electrocatalysts: a promising structural paradigm for direct methanol fuel cells. Energy Environ Sci 4:1161–1176
102. Adzic RR, Zhang J, Sasaki K, Vukmirovic MB, Shao M, Wang JX, Nilekar AU, Mavrikakis M, Valerio JA, Uribe F (2007) Platinum monolayer fuel cell electrocatalysts. Top Catal 46:249–262
103. Brankovic SR, McBreen J, Adzic RR (2001) Spontaneous deposition of Pt on the Ru(0001) surface. J Electroanal Chem 503:99–104
104. Brankovic SR, Wang JX, Adzic RR (2001) Pt submonolayers on Ru nanoparticles a novel low Pt loading, high CO tolerance fuel cell electrocatalyst. Electrochem Solid-State Lett 4: A217–A220
105. Brankovic SR, Marinkovic NS, Wang JX, Adzic RR (2002) Carbon monoxide oxidation on bare and Pt-modified Ru(1010) and Ru(0001) single crystal electrodes. J Electroanal Chem 532:57–66
106. Brankovic SR, Wang JX, Adzic RR (2001) New methods of controlled monolayer-to-multilayer deposition of Pt for designing electrocatalysts at an atomic level. J Serb Chem Soc 66(11–12): 887–898
107. Wang JX, Brankovic SR, Zhu Y, Hanson JC, Adzic RR (2003) Kinetic characterization of PtRu fuel cell anode catalysts made by spontaneous Pt deposition on Ru nanoparticles. J Electrochem Soc 150:A1108–A1117
108. Li M, Liu P, Adzic RR (2012) Platinum monolayer electrocatalysts for anodic oxidation of alcohols. J Phys Chem Lett 3:3480–3485
109. Kowal A, Li M, Shao M, Sasaki K, Vukmirovic MB, Zhang J, Marinkovic NS, Liu P, Frenkel AI, Adzic RR (2009) Ternary Pt/Rh/SnO_2 electrocatalysts for oxidizing ethanol to CO_2. Nature Mater 8:325–330
110. Li M, Kowal A, Sasaki K, Marinkovic NS, Su D, Korach E, Liu P, Adzic RR (2010) Ethanol oxidation on the ternary Pt–Rh–SnO_2/C electrocatalysts with varied Pt:Rh:Sn ratios. Electrochim Acta 55:4331–4338

111. Li M, Marinkovic NS, Sasaki K (2012) In situ characterization of ternary Pt–Rh–SnO_2/C catalysts for ethanol electrooxidation. Electrocatal 3:376–385
112. Li M, Cullen D, Sasaki K, Marinkovic NS, More K, Adzic RR (2013) Ternary electrocatalysts for oxidizing ethanol to carbon dioxide: making Ir capable of splitting C-C bond. J Am Chem Soc 135:132–141
113. Kowal A, Gojković SL, Leed KS, Olszewski P, Sung Y-E (2009) Synthesis, characterization and electrocatalytic activity for ethanol oxidation of carbon supported Pt, Pt–Rh, Pt–SnO_2 and Pt–Rh–SnO_2 nanoclusters. Electrochem Commun 11(4):724–727
114. Du W, Wang Q, LaScala CA, Zhang L, Su D, Frenkel AI, Mathura VK, Teng X (2011) Ternary PtSnRh–SnO_2 nanoclusters: synthesis and electroactivity for ethanol oxidation fuel cell reaction. J Mater Chem 21:8887–8892
115. Colmati F, Antolini E, Gonzalez ER (2008) Preparation, structural characterization and activity for ethanol oxidation of carbon supported ternary Pt–Sn–Rh catalysts. J Alloy Compd 456:264–270
116. de Tacconi NR, Lezna RO, Beden B, Hahn F, Lamy C (1994) In-situ FTIR study of the electrocatalytic oxidation of ethanol at iridium and rhodium electrodes. J Electroanal Chem 379:329–337
117. Cao L, Sun G, Li H, Xin Q (2007) Carbon-supported IrSn catalysts for a direct ethanol fuel cell. Electrochem Commun 9:2541–2546
118. Choi Y, Liu P (2011) Understanding of ethanol decomposition on Rh(111) from density functional theory and kinetic Monte Carlo simulations. Catal Today 165:64–70
119. Wang JX, Inada H, Wu L, Zhu Y, Choi Y-M, Liu P, Zhou W-P, Adzic RR (2009) Oxygen reduction on well-defined core-shell nanocatalysts: particle size, facet, and Pt shell thickness effects. J Am Chem Soc 131:17298–17302
120. Cai Y, Ma C, Zhu Y, Wang JX, Adzic RR (2011) Low-coordination sites in oxygen-reduction electrocatalysis: their roles and methods for removal. Langmuir 27:8540–8547

Chapter 2
Metal-Modified Carbide Anode Electrocatalysts

Zachary J. Mellinger and Jingguang G. Chen

Abstract Fuel cells are being extensively studied to help ease the potential energy crisis. There have been many recent advances in direct methanol fuel cells (DMFC). These devices have shown promise for portable power applications because of the high gravimetric energy density of methanol. One major limitation of the technology is its extensive use of platinum in its anode catalyst. This chapter will provide a review of the work done to eliminate or significantly decrease the amount of platinum in DMFC catalysts by replacing platinum with tungsten monocarbide (WC) and monolayer coverages of platinum or palladium on WC.

2.1 Introduction

While there has been much progress in DMFC technology, there are still technical hurdles that remain for large-scale commercialization. One of the challenges with the anode electrocatalyst is the high cost and low abundance of the leading catalyst materials: Pt and Ru. Another challenge is the strong binding of CO molecules to Pt and Ru, which leads to CO poisoning of the active sites and slow kinetics for the electrooxidation of methanol [1]. The commercialization of DMFC depends upon new catalytic materials being developed that are more cost-effective and show a higher CO tolerance. This can be achieved by either finding a new catalyst or modifying the current catalysts.

A potential alternative electrocatalyst is tungsten carbide, which has attracted attention from researchers since Levy and Boudart discovered that tungsten carbides had similar catalytic behavior to Pt [2]. The Levy and Boudart study has led to many groups researching tungsten carbides as alternatives to Pt for

---

Z.J. Mellinger • J.G. Chen (✉)
Department of Chemical Engineering, University of Delaware, Newark, DE 19716, USA
e-mail: jgchen@UDel.Edu

M. Shao (ed.), *Electrocatalysis in Fuel Cells*, Lecture Notes in Energy 9,
DOI 10.1007/978-1-4471-4911-8_2,

catalytic and electrocatalytic applications [3–5]. Some of the initial studies focused on single-crystal surfaces in an ultrahigh vacuum (UHV) environment [6–11] and density functional theory (DFT) calculations [12]. Studies were also being performed using Pt- and Pd-modified tungsten carbides. Replacing Pt with Pd is desirable as Pd is cheaper and more abundant than Pt as is discussed in one of the chapters. Pt- and Pd-modified tungsten carbides are also promising potential electrocatalysts because having an electrocatalytically active support decreases the precious metal loading needed while possibly adding a synergistic effect between the materials.

Our research group attempted to bridge the "materials gap" and "pressure gap" between fundamental surface science studies and industrially applicable catalysts. This bridging was needed because while single-crystal and UHV studies have provided fundamental insights into the catalytic behavior of tungsten carbides and metal-modified tungsten carbides, an industrially applicable catalyst would have the form of carbide catalysts on large surface area supports. Our group first investigated the reaction pathways of methanol on single-crystal surfaces of tungsten carbide and Pt-modified tungsten carbide [6–11]. Then those single-crystal results were extended to the synthesis, characterization, and electrochemical evaluation of polycrystalline tungsten carbide and metal-modified tungsten carbide films [11, 13–22]. Electrochemical studies were performed in acid as well as basic solutions as pH and type of solution affect the performance of electrocatalysts. Finally, supported particles of tungsten carbide and Pt-modified tungsten carbide were tested in full-cell measurements [23]. These studies bridged the "materials gap" and "pressure gap" between DFT and UHV studies on model surfaces and the evaluation of relevant supported electrocatalysts throughout the literature [23–30].

2.2 Theoretical and Experimental Studies on Single-Crystal Surfaces

2.2.1 DFT Studies

DFT studies of single-crystal and polycrystalline surfaces have provided a fundamental understanding of the reaction pathways of methanol decomposition on tungsten carbide and metal-modified tungsten carbide surfaces. The binding energies of methanol and methoxy species are shown in Table 2.1 on different surfaces [14, 16, 31, 32]. For both methanol and methoxy, tungsten carbide showed the highest binding energy, and adding a monolayer of Pt or Pd decreased the binding energy closer to that of the pure metals. The methanol and methoxy binding energies are similar to the literature for Pd(111) [33–36] and Pt(111) [37, 38]. The trend in Table 2.1 predicts that metal-modified WC surfaces should show activity more similar to the parent metals than to tungsten carbide. Additionally, metal-modified

Table 2.1 Binding energies of methanol and methoxy on metals, tungsten carbide, and metal-modified tungsten carbide surfaces

	Binding energy (kcal/mol)				
	Methanol	Methoxy			
	Binding site				
	Atop	Atop	fcc	hcp	Bridge
Pt(111) [32]	−4.50	−31.80			
Pd(111) [14]	−5.56	−33.79	−38.00	−37.69	−37.22
WC(0001) [16]	−19.07		−51.16		
Pt/WC(0001) [16]	−8.37		−5.35		
Pt [31]	−4.86	−34.91	−32.95	−31.33	−31.93
WC [14, 31]	−15.86	−66.38	−81.94	−91.09	−73.95
Pt/WC [31]	−10.59	−49.49	ns	−48.97	−48.9
Pd/WC [14]	−8.58	−48.62	−55.33	−54.84	−52.25

ns not stable

tungsten carbide surfaces should show higher total activity than parent metals because of the higher methanol and methoxy binding energies. These DFT studies provided the basis for selecting relevant model surfaces for UHV experiments.

2.2.2 TPD Studies on Single-Crystal Surfaces

For the UHV experiments, surface preparation and characterization of C/W(111) have been described in detail previously [8]. Clean W(111) was dosed with ethylene at 120 K and then annealed to 1,200 K, producing C/W(111). The Pt/C/W(111) surface was synthesized by depositing Pt by evaporative deposition by resistively heating a W wire which was wrapped with Pt wire [10]. Previous studies using Auger electron spectroscopy (AES) had determined that Pt grows on tungsten carbide through a layer-by-layer mechanism [39, 40]. This growth mechanism means that submonolayer coverages of Pt form regions of monolayers on the tungsten carbide surfaces, as opposed to forming nanoparticles. Thus, Pt could be deposited onto the carbide surface with precise control over the surface coverage. Temperature-programmed desorption (TPD) and high-resolution electron energy loss spectroscopy (HREELS) were used to determine the decomposition pathways of methanol on Pt (111) [17, 41], C/W(111) [16, 17], Pt/C/W(111) [16, 17], C/W(110) [11], Pt/C/W (110) [11], and Pd(111) [14, 42, 43]. Methanol has been found to decompose via the following net reaction pathways under UHV conditions:

$$\mathrm{aCH_3OH \rightarrow aC_{ad} + aO_{ad} + 2aH_2 \quad (complete\ decomposition)} \tag{2.1}$$

$$\mathrm{bCH_3OH \rightarrow bCO + 2bH_2 \quad (reforming,\ desired\ reaction)} \tag{2.2}$$

$$\mathrm{cCH_3OH \rightarrow cCH_4 + cO_{ad} \quad (methane\ production)} \tag{2.3}$$

Table 2.2 Activity of methanol decomposition on single-crystal surfaces of metals, tungsten carbides, and metal-modified tungsten carbides

Methanol activity (ML)				
Surface	Reforming	Decomposition	CH_4	Total
Pt(111) [41]	~0	~0	~0	~0
Pd(111) [14]	0.079[a]	0.000[a]	0	0.079[a]
C/W(111) [9]	0.087	0.155	0.038	0.28
0.6 ML Pt/C/W(111) [10]	0.091	0.086	0	0.177
C/W(110) [6]	0.06	0.176	0.068	0.304
0.5 ML Pt/C/W(110) [11]	0.049	0.174	0	0.223

[a] [42]

where *a*, *b*, and *c* denote the amount of methanol molecules undergoing each pathway. The reforming pathway is the desired reaction as this extracts the most hydrogen from the fuel while not coking up the catalyst surface. The CO product can be further reacted on the surface to produce CO_2 to release two more electrons. The production of CO in the reforming reaction pathway is the reason why CO tolerance is an important characteristic of an anode DMFC catalyst. Also, the removal of the methane production pathway is critical for the efficient utilization of methanol because it leads to losing four of the six electrons available from the methanol electrooxidation reaction.

The quantification of the TPD results for the reactions of methanol on various single-crystal surfaces is shown in Table 2.2. The methods used to quantify the TPD results are described in the literature [44]. These results indicate that there is a synergistic effect by supporting submonolayer coverage Pt on WC(111) and WC(110); the Pt-modified WC single-crystal surfaces still had a high activity for methanol decomposition while eliminating the production of the undesirable methane production pathway. The selectivity toward the reforming reaction pathway was higher for the Pt-modified surfaces when compared to the metal single crystals.

2.2.3 Vibrational Studies of Single-Crystal Surfaces

To further characterize the intermediates on the surfaces, vibrational studies using HREELS were performed with methanol dosed between 90 and 100 K on the single-crystal surfaces. The results of the HREELS experiments are summarized in Table 2.3. The HREELS spectra of methanol on various surfaces include an O–H stretching mode at ~3,200 cm^{-1}, a symmetric and asymmetric C–H stretching modes at ~3,000 cm^{-1}, CH_3 deformation features at ~1,475 cm^{-1}, a CH_3 rocking mode at ~1,150 cm^{-1}, a CO stretch at ~1,000 cm^{-1}, an O–H deformation at ~700 cm^{-1}, and a metal-O stretch at ~400 cm^{-1}. The spectra on the carbon-modified tungsten surfaces showed that the methanol adsorbed as methoxy, indicative that the tungsten carbide surfaces adsorbed methanol dissociatively breaking the O–H bond. The Pt-modified surfaces still showed a weak O–H stretching mode at around 3,200 cm^{-1}

Table 2.3 HREELS assignments for methanol on single-crystal surfaces (in cm^{-1})

Mode	Gas phase	Liquid phase[a]	Pt (111)[c]	Pd (111)[d]	C/W (111)[e]	0.6 ML Pt/C/W (111)[f]	C/W (110)[g]	0.5 ML Pt/C/W (110)[g]
ν(OH)			3,220			3,470		
$\nu_{as}(CH_3)$	3,000	2,980	2,930	3,015	2,956	2,976	2,936	2,963
	2,960[a]	2,946		2,865			2,821	
ν(M–CO)								
$\delta(CH_3)$	1,455; 1,477[a]	1,480	1,410	1,430	1,454	1,454	1,448	1,461
				1,375				
$\rho(CH_3)$	1,124[b]			1,140	1,157	1,150	1,157	1,150
ν(CO)	1,033[a]	1,030	970	1,005	1,035	1,028	1,028	1,025
δ(OH)			680					
ν(M–O)				325		670		

[a] [32]
[b] [62]
[c] [41]
[d] [43]
[e] [8]
[f] [10]
[g] [11]

which indicated that at least some of the methanol adsorbed molecularly on those surfaces. This was confirmed as the spectrum of Pt(111) showed a strong O–H stretching feature as nearly all the methanol adsorbed molecularly [41]. In contrast, Pd(111), which will be further examined later, adsorbed methanol as a methoxy intermediate [43].

As the surfaces were heated, the intermediates that were left adsorbed to the surfaces were investigated for the different single-crystal surfaces. For the C/W (111) and C/W(110) surfaces, the methoxy was found to react without producing any other surface intermediates. The Pt-modified surfaces reacted at a lower temperature than the pure carbides. The methanol on Pt(111) mostly desorbed from the surface by 300 K [41]. These conclusions from the single-crystal studies were then applied to study polycrystalline foils which are much more realistic surfaces than the idealized single crystals.

2.3 Surface Science and Half-Cell Measurements on Polycrystalline Surfaces

Studies of the clean and Pt-modified carburized W single crystals provided a fundamental understanding of how methanol decomposition proceeds under UHV conditions. These studies suggest that tungsten carbide-based electrocatalysts, especially metal-modified tungsten carbides, are promising anode catalyst materials to replace Pt in the DMFC. These conclusions are further examined on more applicable polycrystalline foils. These foils are better representations of the complex morphology of real catalysts. These materials also can be more easily used to electrochemically evaluate the catalysts. In these experiments, chronoamperometry (CA), cyclic voltammetry (CV), X-ray photoelectron spectroscopy (XPS), TPD, and HREELS have been used to analyze the activity and selectivity of these polycrystalline films toward the electrooxidation of methanol. These samples were synthesized by either carburizing a polycrystalline tungsten foil [14] or by depositing WC on a carbon substrate [19, 22]. These different WC thin films were characterized by a combination of various techniques including X-ray diffraction (XRD), AES, and XPS. The samples were found to be phase-pure WC in the bulk as well as on the surface. The Pt- and Pd-modified surfaces were synthesized either by evaporative deposition [14] or incipient wetness impregnation [45] and were characterized by AES and XPS. Pd has been found to follow a layer-by-layer growth mechanism on WC [14]. Electrochemical studies were performed as described previously [14, 20].

2.3.1 TPD Studies of Methanol on Polycrystalline Surfaces

The TPD quantification results of methanol on WC and metal-modified WC are summarized in Table 2.4. These results show that modifying the polycrystalline WC foil with Pt takes away the methane production pathway. The 0.5 ML Pt/WC surface had a higher selectivity toward the reforming reaction and a much higher activity than the pure Pt foil. The 1 ML Pt/WC surface also had a higher activity than Pt foil but with a lower selectivity toward the reforming reaction. For the Pd-modified WC surfaces, even a low Pd loading such as 0.5 ML Pd significantly reduced the methane production pathway, while it was completely removed with 1 ML Pd. While not having as high of a selectivity toward reforming as Pd(111), there was a much greater overall and reforming activity for the 0.5 ML Pd/WC surface. The 1 ML Pd/WC surface also had a higher reforming activity than Pd(111). Another property that was examined for these polycrystalline surfaces through TPD was the CO tolerance. The CO TPD results of CO dosed on to Pd(111), Pt, tungsten monocarbide (WC), Pt/WC, and Pd/WC surfaces are compared in Fig. 2.1 [14, 15]. These results show that supporting the Pt and Pd with WC decreased the CO desorption temperature, suggesting an increase in the CO tolerance of the catalysts. Another property that increased CO tolerance was the ability for a surface to dissociate water. Tungsten carbides and Pt-modified tungsten carbides are more active toward water dissociation than Pt(111) [11].

2.3.2 Vibrational Studies of Polycrystalline Surfaces

HREELS measurements were performed to further examine the reaction pathways of methanol that were observed on the polycrystalline WC and metal-modified WC surfaces. Table 2.5 shows the HREELS vibrational features of the polycrystalline

Table 2.4 Activity of methanol decomposition on polycrystalline surfaces of metals, tungsten carbides, and metal-modified tungsten carbides

Methanol activity (ML)				
Surface	Reforming	Decomposition	CH_4	Total
Pt [16]	0.006	0.04	0	0.046
WC [14, 16]	0.02	0.182	0.023	0.225
0.5 ML Pt/WC [16]	0.018	0.107	0	0.125
1 ML Pt/WC [16]	0.006	0.079	0	0.085
0.5 ML Pd/WC [14]	0.183	0.083	0.011	0.277
1 ML Pd/WC[14]	0.053	0.152	0	0.205

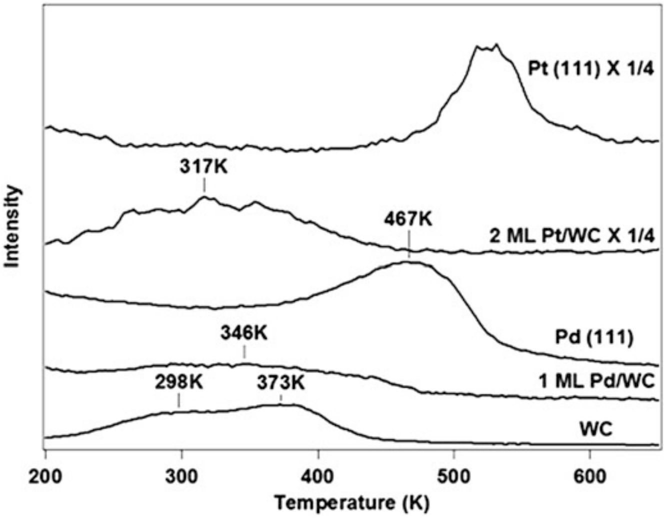

Fig. 2.1 CO TPD on Pt(111), 2 ML Pt/WC, Pd(111), 1 ML Pd/WC, and WC following adsorption of CO at 100 K

Table 2.5 HREELS assignments for methanol on polycrystalline surfaces (in cm^{-1})

Mode	Gas phase	Liquid phase[a]	Pt[c]	WC[d]	0.5 ML Pt/WC[c]	1 ML Pd/WC[d]
ν(OH)			3,626		3,606	3,301
$\nu_{as}(CH_3)$	3,000; 2,960[a]	2,980; 2,946	2,970; 3,369	2,936	2,929; 3,277	2,936
ν(M-CO)			1,860; 2,036	2,043	2,036	2,043
δ(CH3)	1,455; 1,477[a]	1,480	1,454	1,441	1,444	1,448
ρ(CH3)	1,124[b]		1,150	1,150	1,136	1,143
ν(CO)	1,033[a]	1,030[c]	1,021	1,015	1,021	1,028
δ(OH)					717	737

[a] [32]
[b] [62]
[c] [16]
[d] [14]

surfaces following methanol adsorption. Similar to the single-crystal surfaces, WC was found to adsorb methanol as a methoxy intermediate. When the WC surface was heated up to ~350 K, the C–O bond was broken which confirmed what the TPD results showed with the presence of the methane production pathway [14, 16]. The polycrystalline Pt surface showed that the adsorbed molecular methanol reacted through an aldehyde intermediate. Above 300 K, the Pt surface showed an increase in the aldehyde feature as well as a C–O stretching peak [16]. The Pt-modified WC surfaces also showed that the methanol reacted through the aldehyde intermediate; however, with this surface, the C–H bond broke before the C–O bond [16]. The Pt-modified WC showed that the origin of the synergistic effect of supporting Pt on WC can be attributed to the different chemical properties of the modified surface [17]. For the Pd-modified WC surfaces, there was a weak O–H stretching mode. There was no η^2-formaldehyde intermediate as was seen on the Pd(111) surface [43]. The methoxy on Pd-modified WC reacted at a lower temperature than on the WC surface [14]. The reaction temperature for methoxy on Pd/WC [14] was lower than that of Pt/WC [16], Au/WC [31], and Ni/WC [31] and was similar to Rh/WC [31]. Overall, the metal-modified catalysts decomposed methoxy at a lower temperature with a greater selectivity toward the reforming reaction pathway. The metal-modified surfaces also showed an increased CO tolerance when compared with the parent metals. These surface science experiments were then extended to electrochemical testing of the activity, selectivity, and stability of the surfaces.

2.3.3 Electrochemical Evaluation of Polycrystalline WC and Metal-Modified WC

2.3.3.1 CO Stripping Experiments

The surface science studies of both single-crystal and polycrystalline surfaces suggest that WC and metal-modified WC are promising DMFC anode electrocatalysts. The next step is to bridge the “pressure gap” and test the polycrystalline catalysts in atmospheric pressure. The first set of experiments examined the CO tolerance of the polycrystalline catalysts in an electrochemical environment through CO stripping voltammetry as described earlier [15]. Pt foil, Pt supported on carbon paper, WC on carbon paper, and Pt-modified WC on carbon paper were exposed to CO followed by two consecutive cyclic voltammograms. The first scan stripped off the CO, showing at what potential CO was oxidized and removed from the sample. The second scan provided a clean scan of the surface from which to compare the first “poisoned” scan. For Pt foil and Pt supported on carbon paper, the results were similar with CO stripping peaks at ~0.75 V (all potentials are recorded versus the normal hydrogen electrode) in a 0.05 M solution of H_2SO_4. For the sample of WC supported on carbon paper, a broad peak at ~0.45 V was observed. For the Pt-modified WC on carbon paper, there was a peak at ~0.75 V as well the start of CO oxidation as low as ~0.28 V.

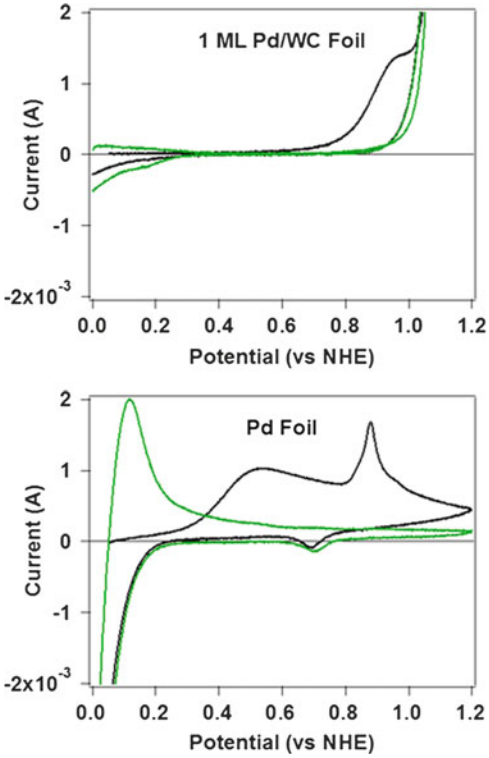

Fig. 2.2 CO stripping voltammetry on 1 ML Pd/WC foil and Pd foil

These results confirmed that using WC as a substrate increases the CO tolerance of the Pt catalyst [15].

This same procedure was performed for a Pd foil and 1 ML Pd/WC in a 0.05 M H_2SO_4 environment. The results of this CO stripping voltammetry are shown in Fig. 2.2. The two peaks on the Pd foil CO stripping scan show the CO being oxidized from the steps (~0.55 V) and terraces (~0.88 V) of the foil [46]. For the 1 ML Pd/WC surface, the oxidation peak starts below the potential at which the Pd foil terrace sites start to oxidize CO. This figure also suggests that using WC as a substrate increases the CO tolerance of the precious metal.

2.3.3.2 Methanol Electrooxidation on WC and Metal-Modified WC in Acidic and Alkaline Media

CV and CA experiments were performed to examine the electrochemical activity of Pt, Pd, WC, Pt/WC, and Pd/WC activity toward methanol electrooxidation. Experiments were performed with Pt, 0.8 ML Pt/WC, and WC samples in a 0.2 M CH_3OH and 0.05 M H_2SO_4 electrochemical environment [20]. The Pt foil showed methanol oxidation peaks at ~0.9 V on the forward scan at ~0.7 V on the

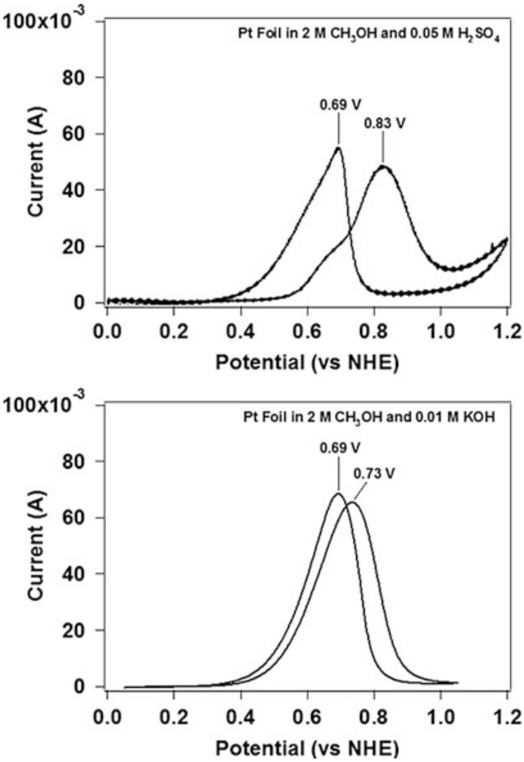

Fig. 2.3 Methanol CV of Pt foil in acidic and alkaline environments

reverse scan. The WC surface exhibited a methanol oxidation peak at ~0.65 V on the forward scan and no features on the reverse scan. The 0.8 ML Pt/WC surface showed similar features to the WC surface but with greater stability of the curves. CA was also performed on the three surfaces at a potential of 0.65 V. These results showed that the WC and 0.8 ML Pt/WC surfaces had a significantly higher steady state current than the Pt foil [20]. The higher steady state current for WC and 0.8 ML Pt/WC can be at least partially explained by the higher CO tolerance.

Experiments were performed with Pd, WC, and 1 ML Pd/WC surfaces in a 2 M CH_3OH and 0.01 M KOH environment [14]. An alkaline solution was chosen for the palladium experiments as Pd-based catalysts in this environment have been shown to have a higher CO tolerance and an increased activity for methanol oxidation when compared to Pt-based catalysts [29, 47–50]. As a means of comparison between acidic and alkaline CV, Pt foil samples were tested using CV in a 0.01 M KOH as well as a 0.05 M H_2SO_4 solution, both with 2 M CH_3OH. The results are shown in Fig. 2.3 with both of the spectra having peaks on the forward and reverse scans but at different potentials. The Pt foil in the alkaline environment shows slightly higher currents. The Pd foil surface shows a methanol oxidation peak at 0.86 V on the forward scan and 0.77 V on the reverse scan. The WC CV experiments in alkaline media showed no activity toward methanol oxidation. The 1 ML Pd/WC foil showed similar methanol oxidation activity as Pd foil with oxidation peaks at 0.89 V on the forward scan and 0.71 V on the reverse scan. The CA experiments showed that the 1 ML Pd/WC surface had a higher steady state activity and maintained a higher stability over a 2-h scan when compared to Pd foil [14]. Again, this higher steady state activity and stability can be at least partially explained by the higher CO tolerance of the 1 ML Pd/WC surface.

2.3.3.3 Electrochemical Stability of WC and Metal-Modified WC

Surface stability in an electrochemical environment is one of the critical requirements in developing an effective electrocatalyst. XPS measurements were performed before and after the electrochemical experiments to directly probe the oxidation state of the surface metal atoms. Some of these experiments were performed with a setup that allowed the surface to be kept in a UHV environment between experiments as described previously [18, 20]. XPS experiments investigate whether a surface is irreversibly oxidized or dissolved from the surface during the electrochemical experiments. For all the experiments on WC and metal-modified WC, phase-pure WC was confirmed before experiments were performed. It was found that for CV of clean WC, the surface could be ramped up to ~0.8 V for 30 cycles in a 0.05 M H_2SO_4 environment without showing surface oxidation [18]. Pt deposited on WC was found to help protect the WC from forming surface oxides, even when ramped up to a potential of 1.2 V. In these experiments, the Pt loading was not found to decrease after the CV experiments [15]. These experiments confirmed that there is a synergistic effect for the Pt/WC surface with the samples showing a higher CO tolerance than Pt and with greater stability and activity than WC [15]. For the alkaline environment experiments, there was little oxidation on the surface after the 2-h CA experiments on the WC and 1 ML Pd/WC surfaces. With the 1 ML Pd/WC surface, there was a 20 % loss in Pd on the surface after the 2-h experiment. This loss was either due to agglomeration or dissolution of the Pd metal. The electrochemical experiments on Pt-modified WC were then expanded to full-cell testing of WC and Pt/WC nanoparticles.

2.4 Full-Cell Measurements of Supported Catalysts

Supported nanoparticles are the main catalysts used in current fuel cell devices. The combined DFT, single crystal, polycrystalline, and electrochemical experiments demonstrated that WC and Pt/WC have catalytic properties that are promising for use as anode DMFC electrocatalysts. These fundamental results still left questions unanswered as to how these materials could be incorporated into a realistic device. These questions led to studies of WC and Pt/WC nanoparticles in a fuel cell test station [23]. The WC nanoparticles were obtained from Japan New Metals Company. The Pt/WC nanoparticles were prepared with a 10 wt% Pt loading using incipient wetness impregnation [45]. In preparing the membrane electrode assembly (MEA), the nanoparticles were coated on a Nafion 117 membrane. This combination was then hot pressed along with the gas diffusion layer into the MEA, which was then evaluated using an Arbin Instruments fuel cell test stand [23].

2.4.1 Characterization of WC Nanoparticles

The WC nanoparticles were characterized using XRD, XPS, and scanning electron microscopy (SEM). XRD and XPS were used to confirm that the nanoparticles were phase-pure WC in the bulk and on the surface, respectively. SEM was then used to confirm the WC particle size. The XPS results also revealed that ~25 % of the tungsten signal for the WC nanoparticles were due to tungsten oxides and that there was some carbonaceous carbon on the surface. After the synthesis of the Pt/WC nanoparticles, the amount of the tungsten signal that was now tungsten oxides increased to ~50 % [23].

2.4.2 Fuel Cell Evaluation of WC and Pt/WC Nanoparticle Anode Electrocatalysts

Power density and polarization curves for the Pt/WC nanoparticles are shown in Fig. 2.4 [23] with a summary of the data in Table 2.6 [23]. These curves were generated by withdrawing specific current density values for 5-min intervals. The output of the MEA was monitored within the normal temperature ranges for DMFC evaluation [51–54]: 323 K, 333 K, and 343 K. As the temperature increased, so did the MEA performance, suggesting that the reaction was kinetically limited. With the increase in temperature from 323 K to 343 K, the power density of the MEA was increased from 6.8 mW/cm^2 to 14.5 mW/cm^2. The open-circuit voltage for the Pt/WC nanoparticles also increased with temperature going from 460 mV at 323 K to 500 mV at 343 K. On Pt/WC, the electrooxidation of methanol was found to be reaction limited as the position of the maximum power density was within the linear region of the polarization curve. Also, the polarization curves lack of a mass transfer limited regime suggested that the cell performance was likely limited by the surface area of the anode electrocatalyst. The Pt/WC nanoparticle MEA was also compared to an MEA with a Pt/Ru anode electrocatalyst. The results in Table 2.6 show that, on the basis of power per mg of metal loading, the Pt/WC MEA delivered about the same power as the Pt/Ru MEA. The MEAs for the WC and Pt/WC catalysts were not optimized, leaving the possibility for significant improvement. These results showed that as a realistic catalyst in a full-cell test station, Pt/WC showed promise as an alternative DMFC electrocatalyst to Pt and Pt/Ru catalysts.

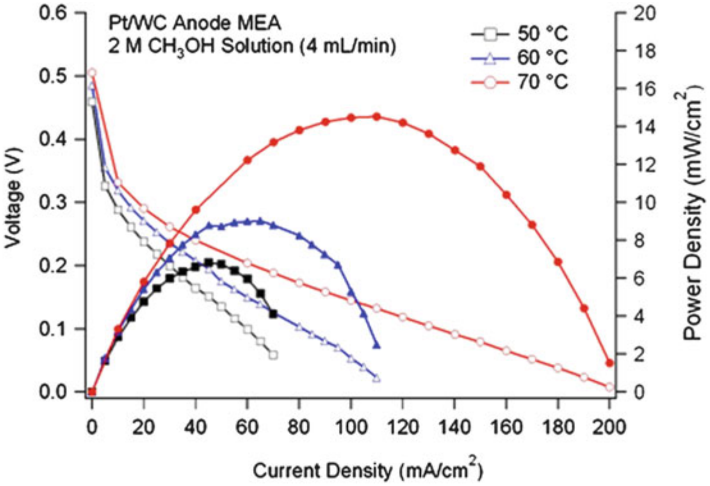

Fig. 2.4 Power density and polarization curves of a Pt/WC anode MEA with a 2 M methanol concentration and a flow rate of 4 ml/min at various operating temperatures [23]

Table 2.6 Maximum power density and cell voltage values at various temperatures for Pt/WC and Pt/Ru anode MEAs

	Anode MEA (2 M CH_3OH, 4 ml/min)		
	Temperature (K)	Power density (mW/cm^2)	Power per mg Pt at anode (mW/mg Pt)
Pt/WC nanoparticles	323	6.8	17.0
	333	9.1	22.8
	343	14.5	36.3
Pt/Ru nanoparticles	323	67.5	16.9
	333	98.4	24.6
	343	120.1	30.0

2.5 Conclusions

This chapter describes the research approach of combining DFT, UHV surface science studies, half-cell electrochemical evaluation, and full-cell testing to identify DMFC electrocatalysts with desirable properties. These different studies bridged both the “materials gap” and “pressure gap” by applying the fundamental understanding gained from theoretical and surface science studies to industrially relevant supported nanoparticle electrocatalysts. For the purpose of finding anode electrocatalysts for DMFC, this approach illustrates the potential to substitute WC-supported Pt or Pd for the Pt/Ru anode electrocatalyst. These results also suggest WC, Pt/WC, and Pd/WC are active and stable electrocatalysts which can be explored for other electrocatalytic applications [13, 39, 55–61].

References

1. Liu H, Song C, Zhang L, Zhang J, Wang H, Wilkinson DP (2006) A review of anode catalysis in the direct methanol fuel cell. J Power Sources 155:95–110
2. Levy RB, Boudart M (1973) Platinum-like behavior of tungsten carbide in surface catalysis. Science 181(4099):547–549
3. Chen JG (1996) Carbide and nitride overlayers on early transition metal surfaces: preparation, characterization, and reactivities. Chem Rev 96:1477–1498
4. Hwu HH, Chen JG (2005) Surface chemistry of transition metal carbides. Chem Rev 105: 185–212
5. Oyama ST (1996) The chemistry of transition metal carbides and nitrides. Blackie Academic and Professional, London
6. Hwu HH, Chen JG (2003) Potential application of tungsten carbides as electrocatalysts: 4. Reactions of methanol, water, and carbon monoxide over carbide-modified W(110). J Phys Chem B 107:2029–2039
7. Hwu HH, Chen JG (2003) Potential application of tungsten carbides as electrocatalysts. J Vac Sci Technol A 21:1488–1493
8. Hwu HH, Chen JG, Kourtakis K, Lavin JG (2001) Potential application of tungsten carbides as electrocatalysts. 1. Decomposition of methanol over carbide-modified W(111). J Phys Chem B 105:10037–10044
9. Hwu HH, Polizzotti BD, Chen JG (2001) Potential application of tungsten carbides as electrocatalysts. 2. Coadsorption of CO and H_2O on carbide-modified W(111). J Phys Chem B 105:10045–10053
10. Liu N, Kourtakis K, Figueroa JC, Chen JG (2003) Potential application of tungsten carbides as electrocatalysts: III. Reactions of methanol, water, and hydrogen on Pt-modified C/W(111) surfaces. J Catal 215:254–263
11. Zellner MB, Chen JG (2005) Potential Application of tungsten carbides as electrocatalysts: synergistic effect by supporting Pt on C/W(110) for the reactions of methanol, water, and CO. J Electrochem Soc 152:A1483–A1494
12. Kitchin JR, Nørskov JK, Barteau MA, Chen JG (2005) Trends in the chemical properties of early transition metal carbide surfaces: A density functional study. Catal Today 105:66–73
13. Esposito DV, Chen JG (2011) Monolayer platinum supported on tungsten carbides as low-cost electrocatalysts: opportunities and limitations. Energy Environ Sci 4:3900–3912
14. Mellinger ZJ, Kelly TG, Chen JG (2012) Pd-modified tungsten carbide for methanol electro-oxidation: from surface science studies to electrochemical evaluation. ACS Catal 2:751–758
15. Mellinger ZJ, Weigert EC, Stottlemyer AL, Chen JG (2008) Enhancing CO tolerance of electrocatalysts: electro-oxidation of CO on WC and Pt-modified WC. Electrochem Solid-State Lett 11(5):B63–B67
16. Stottlemyer AL, Liu P, Chen JG (2010) Comparison of bond scission sequence of methanol on tungsten monocarbide and Pt-modified tungsten monocarbide. J Chem Phys 133:104702
17. Stottlemyer AL, Weigert EC, Chen JG (2011) Tungsten carbides as alternative electrocatalysts: from surface science studies to fuel cell evaluation. Ind Eng Chem Res 50: 16–22
18. Weigert EC, Esposito DV, Chen JG (2009) Cyclic voltammetry and XPS studies of electrochemical stability of clean and Pt-modified tungsten and molybdenum carbide (WC and Mo_2C) electrocatalysts. J Power Sources 193:501–506
19. Weigert EC, Humbert MP, Mellinger ZJ, Ren Q, Beebe TP Jr, Bao L, Chen JG (2008) Physical vapor deposition synthesis of tungsten monocarbide (WC) thin films on different carbon substrates. J Vac Sci Tech A 26:23–28
20. Weigert EC, Stottlemyer AL, Zellner MB, Chen JG (2007) Tungsten monocarbide as potential replacement of platinum for methanol electrooxidation. J Phys Chem C 111:14617–14620
21. Weigert EC, Zellner MB, Stottlemyer AL, Chen JG (2007) A combined surface science and electrochemical study of tungsten carbides as anode electrocatalysts. Top Catal 46:349–357

22. Zellner MB, Chen JG (2005) Surface science and electrochemical studies of WC and W_2C PVD films as potential electrocatalysts. Catal Today 99:299–307
23. Weigert EC, Arisetty S, Advani SG, Prasad AK, Chen JG (2008) Electrochemical evaluation of tungsten monocarbide (WC) and platinum-modified WC as alternative DMFC electrocatalysts. J New Mater Electrochem Syst 11:243–251
24. Angelucci C, Deiner L, Nart F (2008) On-line mass spectrometry of the electro-oxidation of methanol in acidic media on tungsten carbide. J Solid State Electrochem 12:1599–1603
25. Ganesan R, Lee JS (2005) Tungsten carbide microspheres as a noble-metal-economic electrocatalyst for methanol oxidation. Angew Chem Int Ed 44:6557–6560
26. Joo JB, Kim JS, Kim P, Yi J (2008) Simple preparation of tungsten carbide supported on carbon for use as a catalyst support in a methanol electro-oxidation. Mater Lett 62:3497–3499
27. Meng H, Shen PK, Wei Z, Jiang SP (2006) Improved performance of direct methanol fuel cells with tungsten carbide promoted Pt/C composite cathode electrocatalyst. Electrochem Solid-State Lett 9:A368–A372
28. Nagai M, Yoshida M, Tominaga H (2007) Tungsten and nickel tungsten carbides as anode electrocatalysts. Electrochim Acta 52:5430–5436
29. Wang ZB, Zuo PJ, Liu BS, Yin GP, Shi PF (2009) Stable PtNiPb/WC catalyst for direct methanol fuel cells. Electrochem Solid-State Lett 12:A13–A15
30. Zhao Z, Fang X, Li Y, Wang Y, Shen PK, Xie F, Zhang X (2009) The origin of the high performance of tungsten carbides/carbon nanotubes supported Pt catalysts for methanol electrooxidation. Electrochem Commun 11:290–293
31. Kelly TG, Stottlemyer AL, Ren H, Chen JG (2011) Comparison of O–H, C–H, and C–O bond scission sequence of methanol on tungsten carbide surfaces modified by Ni, Rh, and Au. J Phys Chem C 115:6644
32. Skoplyak O, Menning CA, Barteau MA, Chen JG (2007) Experimental and theoretical study of reactivity trends for methanol on Co/Pt(111) and Ni/Pt(111) bimetallic surfaces. J Chem Phys 127:114707
33. Chen Z-X, Neyman KM, Lim KH, Rösch N (2004) CH_3O Decomposition on PdZn(111), Pd(111), and Cu(111). A theoretical study. Langmuir 20:8068–8077
34. Jiang RB, Guo WY, Li M, Fu DL, Shan HH (2009) Density functional investigation of methanol dehydrogenation on Pd(111). J Phys Chem C 113:4188–4197
35. Schennach R, Eichler A, Rendulic KD (2003) Adsorption and desorption of methanol on Pd (111) and on a Pd/V surface alloy. J Phys Chem B 107:2552–2558
36. Zhang CJ, Hu P (2001) A first principles study of methanol decomposition on Pd(111): mechanisms for O–H bond scission and C–O bond scission. J Chem Phys 115:7182–7186
37. Greeley J, Mavrikakis M (2002) A first-principles study of methanol decomposition on Pt(111). J Am Chem Soc 124:7193–7201
38. Greeley J, Mavrikakis M (2004) Competitive paths for methanol decomposition on Pt(111). J Am Chem Soc 126:3910–3919
39. Esposito DV, Hunt ST, Stottlemyer AL, Dobson KD, McCandless BE, Birkmire RW, Chen JG (2010) Low-cost hydrogen-evolution catalysts based on monolayer platinum on tungsten monocarbide substrates. Angew Chem Int Ed 49:9859–9862
40. Humbert MP, Menning CA, Chen JG (2010) Replacing bulk Pt in Pt–Ni–Pt bimetallic structures with tungsten monocarbide (WC): Hydrogen adsorption and cyclohexene hydrogenation on Pt–Ni–WC. J Catal 271:132–139
41. Sexton BA (1981) Methanol decomposition on platinum (111). Surf Sci 102:271–281
42. Davis JL, Barteau MA (1987) Decarbonylation and decomposition pathways of alcohols on Pd(111). Surf Sci 187(3):387–406
43. Davis JL, Barteau MA (1990) Spectroscopic identification of alkoxide, aldehyde, and acyl intermediates in alcohol decomposition on Pd(111). Surf Sci 235:235–248
44. Stottlemyer AL, Ren H, Chen JG (2009) Reactions of methanol and ethylene glycol on Ni/Pt: Bridging the materials gap between single crystal and polycrystalline bimetallic surfaces. Surf Sci 603:2630–2638

45. Bozzini B, Gaudenzi GPD, Fanigliulo A, Mele C (2004) Electrochemical oxidation of WC in acidic sulphate solution. Corros Sci 46:453–469
46. El-Aziz AM, Kibler LA (2002) Influence of steps on the electrochemical oxidation of CO adlayers on Pd(111) and on Pd films electrodeposited onto Au(111). J Electroanal Chem 534: 107–114
47. Antolini E (2009) Palladium in fuel cell catalysis. Energy Environ Sci 2:915–931
48. Lee Y-W, Ko A-R, Han S-B, Kim H-S, Kim D-Y, Kim S-J, Park K-W (2010) Cuboctahedral Pd nanoparticles on WC for enhanced methanol electrooxidation in alkaline solution. Chem Commun 46:9241–9243
49. Lu J, Bravo-Suarez JJ, Takahashi A, Haruta M, Oyama ST (2005) In situ UV–vis studies of the effect of particle size on the epoxidation of ethylene and propylene on supported silver catalysts with molecular oxygen. J Catal 232:85–95
50. Singh RN, Singh A, Anindita X (2009) Electrocatalytic activity of binary and ternary composite films of Pd, MWCNT and Ni, Part II: Methanol electrooxidation in 1 M KOH. Int J Hydrogen Energy 34:2052–2057
51. Carrette L, Friedrich KA, Stimming U (2001) Fuel cells—fundamentals and applications. Fuel Cells 1:5–39
52. Cheng X, Peng C, You M, Liu L, Zhang Y, Fan Q (2006) Characterization of catalysts and membrane in DMFC lifetime testing. Electrochim Acta 51:4620–4625
53. Reshetenko TV, Kim H-T, Krewer U, Kweon HJ (2007) The effect of the anode loading and method of MEA fabrication on DMFC performance. Fuel Cells 3:238–245
54. Wee J-H (2006) Which type of fuel cell is more competitive for portable application: direct methanol fuel cells or direct borohydride fuel cells? J Power Sources 161:1–10
55. Bozzini B, Gaudenzi GPD, Busson B, Humbert C, Six C, Gayral A, Tadjeddine A (2010) In situ spectroelectrochemical measurements during the electro-oxidation of ethanol on WC-supported Pt-black, based on sum-frequency generation spectroscopy. J Power Sources 195(13):4119–4123
56. Bozzini B, Gaudenzi GPD, Tadjeddine A (2010) In situ spectroelectrochemical measurements during the electro-oxidation of ethanol on WC-supported Pt-black. Part II: Monitoring of catalyst aging by in situ Fourier transform infrared spectroscopy. J Power Sources 195(24): 7968–7973
57. Esposito DV, Dobson KD, McCandless BE, Birkmire RW, Chen JG (2009) Comparative study of tungsten monocarbide and platinum as counter electrodes in polysulfide-based photoelectrochemical solar cells. J Electrochem Soc 156:B962–B969
58. Esposito DV, Hunt ST, Kimmel YC, Chen JG (2012) A new class of electrocatalysts for hydrogen production from water electrolysis: metal monolayers supported on low-cost transition metal carbides. J Am Chem Soc 134:3025–3033
59. Hsu IJ, Kimmel YC, Jiang XJ, Willis BG, Chen JG (2012) Atomic layer deposition synthesis of platinum–tungsten carbide core–shell catalysts for the hydrogen evolution reaction. Chem Commun 48:1063–1065
60. Hu FP, Shen PK (2007) Ethanol oxidation on hexagonal tungsten carbide single nanocrystal-supported Pd electrocatalyst. J Power Sources 173:877–881
61. Kimmel YC, Esposito DV, Birkmire RW, Chen JG (2012) Effect of surface carbon on the hydrogen evolution reactivity of tungsten carbide (WC) and Pt-modified WC electrocatalysts. Int J Hydrogen Energy 37:3019–3024
62. Falk M, Whalley E (1961) Infrared spectra of methanol and deuterated methanols in gas, liquid, and solid phases. J Chem Phys 34:1554–1568

Chapter 3
Electrocatalysis of Formic Acid Oxidation

Cynthia Ann Rice and Andrzej Wieckowski

Abstract Direct liquid fuel cells for portable electronic devices are plagued by poor efficiency due to high overpotentials and accumulation of intermediates on the electrocatalyst surface. Direct formic acid fuel cells have a potential to maintain low overpotentials if the electrocatalyst is tailored to promote the direct electrooxidation pathway. Through the understanding of the structural and environmental impacts on preferential selection of the more active formic acid electrooxidation pathway, a higher performing and more stable electrocatalyst is sought. This chapter overviews the formic acid electrooxidation pathways, enhancement mechanisms, and fundamental electrochemical mechanistic studies.

3.1 Introduction

The ever-increasing energy demands of portable electronic devices have overburdened the power supply capabilities of today's state-of-the-art battery technologies. The markets for small personal electronic devices are driven by three dominant criteria: (1) reduced volume, (2) decreased weight, and (3) increased uninterrupted power. Batteries are essentially "energy storage devices" due to their finite storage capacity that scales with energy density. Fuel cells are potentially a competitive alternative to batteries, promoting efficient conversion of chemical energy directly to electrical energy. Fuel cells are capable of "hot" refueling, permitting 24/7 operation. For personal portable electronic devices, based on current

---

C.A. Rice (✉)
The Center for Manufacturing Research, Department of Chemical Engineering, Tennessee Tech University, Cookeville, TN 38505, USA
e-mail: criceyork@tntech.edu

A. Wieckowski (✉)
The University of Illinois at Urbana-Champaign, Urbana, IL 61801, USA
e-mail: awieckow@illinois.edu

M. Shao (ed.), *Electrocatalysis in Fuel Cells*, Lecture Notes in Energy 9,
DOI 10.1007/978-1-4471-4911-8_3, © Springer-Verlag London 2013

fuel cell technologies, proton exchange membrane fuel cells (PEMFC) using direct liquid fuel-oxygen (anode/cathode) are currently the most viable, meeting criteria 1 and 2 above.

High sustainable power densities demanded by criterion 3 remains a challenge. Anode fuel type and catalyst selection are pivotal in attaining high overall conversion efficiencies and power densities. Hydrogen fuel is capable of high conversion efficiencies, but for portable devices the requirement of onboard compressed gas storage or reforming has negative implications to criteria 1 and 2. Direct liquid fuel cells (DLFC) have the advantages of easy transport and handling but typically suffer from poor conversion efficiencies, high fuel crossover through the PEM, toxicity, and poor leak detection [1]. Direct formic acid fuel cells (DFAFC) overcome several of the issues of DLFCs, having low fuel crossover, low toxicity, and a putrid odor for fast leak detection. The first DFAFC was demonstrated in 1996 on a phosphoric acid-doped polybenzimidazole (PBI) membrane at 170 °C [2]. In the early 2000s, Masel et al. began working on DFAFCs with Nafion™ (sulfonated tetrafluoroethylene) membranes, operating below 60 °C [3–10]. A drawback of DFAFCs in terms of liquid fuels is the low volumetric energy density of formic acid (2,104 Wh L^{-1}) as compared to methanol (4,900 Wh L^{-1}). This deficiency in DFAFCs is compensated by the 6× reduction in crossover through the Nafion™ membrane, allowing substantially higher fuel concentrations—5 to 12 M formic acid versus only 1–2 M for methanol [9, 11, 12]. For a formic acid-oxygen fuel cell, the theoretical open circuit voltage (OCV) is 1.48 V at 25 °C determined from the formal potentials of the anode and cathode half-cell reactions, respectively ($E_{\mathrm{cell}} = E_{\mathrm{cathode}} - E_{\mathrm{anode}} = 1.23\ \mathrm{V} - (-0.25\ \mathrm{V}) = 1.48\ \mathrm{V}$). The theoretical OCV for formic acid is larger than either hydrogen or direct methanol fuel cells: 1.23 V and 1.21 V, respectively. The magnitude of parasitic overpotentials and conversion efficiencies for formic acid electrooxidation are dependent on catalyst composition and size since they dictate the dominant reaction pathways.

(All cited potentials are versus a reversible hydrogen reference electrode (RHE) unless otherwise stated.)

Formic acid is produced in nature (biofuels), commercially, and as a byproduct of commercial synthesis. Renewable, carbon neutral, synthesis processes are also under investigation to form formic acid from CO_2 [13]. Reagent grade formic acid requires further purification to remove ppm levels of common substituent impurities, i.e., methyl formate, methanol, and acetic acid [14].

3.2 Review of Reaction Pathways

Since around 1960, the formic acid electrooxidation mechanism has been investigated, resulting in several review articles [15–18]. Formic acid electro-oxidation studies have been carried out on pure metal electrodes, such as platinum (Pt) [19], palladium (Pd) [20], gold [21–23], rhodium [24, 25], and iridium [26]. Studies have also been performed on alloys, intermetallics, and adatoms. The conversion efficiency is determined by the rate of a series of steps: (a) reactant adsorption, (b) electrooxidation, and (c) product desorption. The electrooxidation

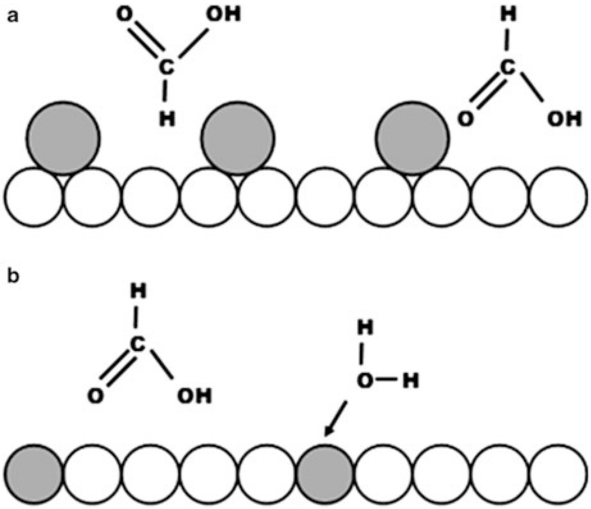

Fig. 3.1 Catalyst-mediated formic acid electrooxidation mechanisms: (**a**) ensemble/third-body effect and (**b**) bifunctional mechanism. The catalyst atoms: (*open circle*) commonly Pt or Pd and (*filled circle*) secondary metal atom

pathway selection (step b) is controlled by the initial adsorption orientation of formic acid either in the CH-down or CH-up configuration (step a; see Fig. 3.1a) [27–29]. The subsequent electrooxidation (step b) occurs via either a dual [30] or triple [19, 31] pathway mechanism: the direct dehydrogenation and the indirect dehydration reactions. It has been suggested by Behm et al. [19, 31] and Osawa et al. [32, 33] that a third reaction pathway through a bridge-bonded formate ($HCOO_{ad}$) intermediate is possible. Their attenuated total reflection Fourier transform infrared (ATR-FTIR) spectroscopic measurements demonstrated a fast formate "adsorption–desorption equilibrium," limiting appreciable formate conversion to CO_2 [19, 31].

The direct dehydrogenation pathway favors high turnover efficiencies at low overpotentials through a direct conversion of formic acid to the carbon dioxide (CO_2) product [Eq. (3.1)]:

$$HCOOH \rightarrow \text{active intermediate} \rightarrow CO_2 + 2H^+ + 2e^- \quad (3.1)$$

Alternatively, the indirect dehydration pathway forms a strongly adsorbed carbon monoxide (CO_{ads}) reaction intermediate via an initial non-Faradic step [Eq. (3.2a)]. To complete further oxidation of CO_{ads}, an additional activated hydroxyl species (OH_{ads}) is required. OH_{ads} is typically formed on a separate catalytic surface site [Eq. (3.2b)] at higher overpotentials. The two adsorbed intermediates diffuse across the catalyst surface to combine and complete the conversion sequence [Eq. (3.2c)]. The limited availability of OH_{ads} results in the accumulation of CO_{ads} that blocks the catalyst surface, limiting the turnover efficiency [34, 35]:

$$HCOOH + M(1)^0 \rightarrow M(1)\text{–}CO_{ads} + H_2O \quad (3.2a)$$

$$M(2)^0 + H_2O \rightarrow M(2)\text{–}OH_{ads} + H^+ + e^- \quad (3.2b)$$

$$M(1)\text{–}CO_{ads} + M(2)\text{–}OH_{ads} \rightarrow M(1)^0 + M(2)^0 + CO_2 + H^+ + e^- \quad (3.2c)$$

Typically, the metals (M) that participate in either electrooxidation reactions (3.2a) or (3.2b) in the dehydration pathway to form CO_{ads} [Eq. (3.2a)] and OH_{ads} [Eq. (3.2b)] at low overpotentials are not the same, completing the electrooxidation reaction through a complementary bifunctional mechanism [36]. The dual M catalysts are either comprised of alloys or adatoms. The overpotential of Eq. (3.2a) is low, as compared to formic acid's formal potential (E_{anode}). Unfortunately, the requirement of an activated OH_{ads} species imposes a penalty on the conversion efficiency through overpotentials exceeding 0.3 V even on ruthenium (Ru) surface sites. For formic acid electrooxidation, the dominance of one reaction pathway versus the other is dependent on the physical and electronic characteristics of the catalyst, thus catalyst optimization is pivotal in reducing overpotentials by promoting the dehydrogenation pathway [Eq. (3.1)] and restricting accumulation of adsorbed reaction intermediates.

The presence of the dual pathway mechanism was experimentally verified in an elegant differential electrochemical mass spectroscopy (DEMS) study performed by Willsau et al. [37] (Fig. 3.2). Isotopically labeled $H^{13}COOH$ was oxidized at a polycrystalline Pt electrode at 0.25 V forming a partial surface coverage of adsorbed ^{13}CO. While maintaining the potential, the solution was replaced with $H^{12}COOH$ followed by a positive potential scan to 1.5 V. The resulting DEMS response showed an immediate low potential loss of $^{12}CO_2$, followed by a combined $^{13}CO_2$ loss above 0.5 V. The presence of the $^{12}CO_2$ oxidation peak at voltages below 0.5 V confirms the presence of an alternative, less strongly adsorbed reaction intermediate because of the inability of Pt to activate OH_{ads} required in the dehydration pathway [Eq. (3.2b)] at low voltages.

3.3 Enhancement Mechanisms

The catalytic enhancement mechanisms commonly described to facilitate the electrooxidation of hydrocarbon fuels are (a) the ensemble or third-body effect, (b) the bifunctional mechanism, and (c) the electronic effect [15, 16, 38]. Figure 3.1 shows a graphical description of (a) the third-body effect and (b) bifunctional mechanism. The third-body effect is typically attributed to enhancement of the dehydrogenation pathway by adatoms or alloys due to a steric hindrance facilitating preferential orientation of adsorbing formic acid in the CH-down direction, step (a) [27–29]. Alternatively, the dehydration pathway turnover frequency is accelerated by increased availability of activated hydroxyl groups [Eq. (3.2b)] at lower overpotentials through the bifunctional mechanism. Ultimately, the bifunctional mechanism is incapable of producing significant reductions in the overpotentials required for increased turnover efficiencies compared to the dehydrogenation pathway. The electronic effect could manifest itself either as a reduced CO_{ads} bond strength or a preferential reactant adsorption orientation promoting the dehydrogenation reaction pathway.

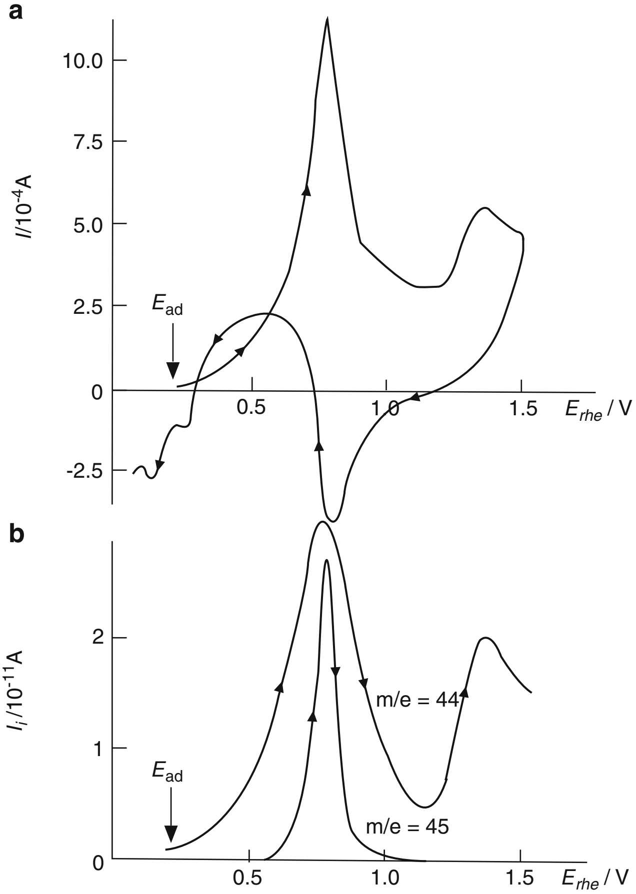

Fig. 3.2 Formic acid cyclic voltammetry (**a**) coupled with differential electrochemical mass spectroscope (**b**) on Pt in 0.5 M H_2SO_4. Initially, $H^{13}COOH$ was pre-adsorbed at 0.25 V to form a sub-monolayer of Pt–$^{13}CO_{ads}$. After exchanging the solution with 10 mM $H^{12}COOH$, the voltage was scanned at 12.5 mV s^{-1}, resulting in an initial low-voltage mass signal for $^{12}CO_2$ ($m/e = 44$) via the dehydrogenation pathway and an additional signal for $^{13}CO_2$ due to the dehydration pathway [37]

3.4 Platinum and Palladium Electrocatalysts Reactivity

The electrooxidation of formic acid has been evaluated on single crystal, polycrystalline, unsupported nanoparticle and supported nanoparticle Pt- or Pd-based electrodes.

3.4.1 Single Crystal

Formic acid electrooxidation has been studied on both Pt [39–41] and Pd [42] single-crystal surfaces. Herein we compare the work of Iwasita et al. [41] and Hoshi et al. [42] on Pt and Pd single crystals, respectively. The cyclic voltammograms were

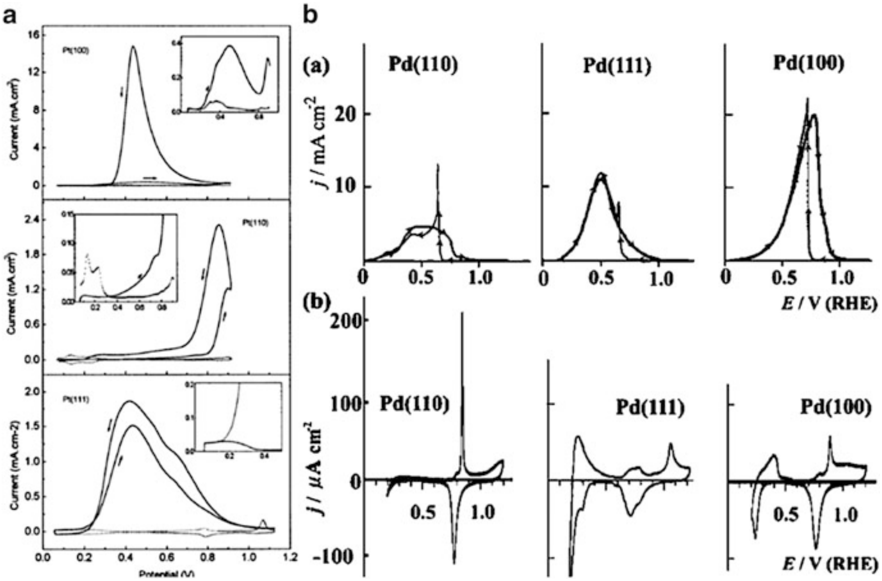

Fig. 3.3 Single-crystal cyclic voltammograms of (**A**) Pt [41] and (**B**) Pd [42] for (110), (111), and (100) facets. The electrooxidation of 0.1 M formic acid is evaluated on the various faceted surfaces in 0.1 M $HClO_4$ supporting electrolyte at scan rates of 50 mV s^{-1} and 20 mV s^{-1}, respectively. In (**A**) the *dashed lines* are for the background cyclic voltammograms of the different faceted Pd single crystals in 0.1 M $HClO_4$ alone, as are the designated (b) plots in (**B**) for Pt (reprinted with permission from [41] and [42], respectively)

performed under similar conditions, i.e., in 0.1 M $HClO_4$ supporting electrolyte solution and 0.1 M formic acid at room temperature. On the three types of single crystals studied (Fig. 3.3), the formic acid electrooxidation reaction pathway is impacted by (a) competitive adsorption of both hydrogen and oxygen, (b) availability of adsorbed oxygen, and (c) shifting of the d-band centers of the metal surface atoms due to changes in the interatomic bond lengths. The portion of the cyclic voltammograms most relevant to fuel cell operations is the low-voltage anodic sweep, <0.4 V.

Selecting 0.4 V vs. RHE as a potential relevant to operating DFAFCs, Pt has the following anodic scan single crystal orientation dependence: Pt(110) 0.015 mA cm^{-2} < Pt(100) 0.31 mA cm^{-2} < Pt(111) 1.8 mA cm^{-2} [41]. The overall performance at 0.4 V on Pd single crystals is higher than that of Pt, with preference on different facets: Pd(100) 2.7 mA cm^{-2} < Pd(110) 4.5 mA cm^{-2} < Pd(111) 8 mA cm^{-2} [42]. The symmetry between the forward anodic and reverse cathodic sweep currents is similar for all Pd single-crystal electrodes and asymmetric for Pt with the cathodic sweep current significantly higher than that of the anodic. Formic acid electrooxidation on both Pt and Pd is suppressed at the higher potentials during the anodic sweep due to competitive adsorption of OH_{ads} blocking the surface sites on both catalyst types. The Pd cyclic voltammogram profile supports the dominance of the dehydrogenation pathway on all facets. The lack of significant current densities in the anodic sweep

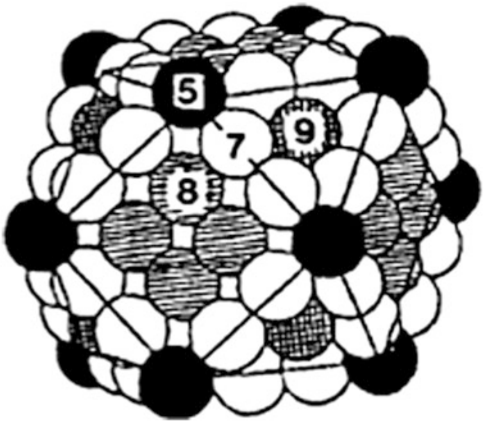

Fig. 3.4 Cuboctahedral nanoparticle (~1.5 nm). Types of surface atoms corner (*filled circle*), edge (*open circle*), and terrace (*hashed circle*). The numeric values represent the coordination of adjacent atoms [43]

for both Pt(100) and Pt(110) suggests the increase propensity of the dehydration pathway on these surface. For the Pt(100) surface, the current density response is asymmetric with relatively little activity in the anodic sweep and an amplified intensity exceeding that of the other two facets in the reverse sweep.

3.4.2 Nanoparticle: Size Effect

The electrooxidation of formic acid is a heterogeneous reaction involving only surface atoms, thus it is cost effective to reduce the particle size, increasing the dispersion (ratio of the number surface atoms to the total number of atoms) of the catalyst. As particle size decreases, the relative abundance of corners and edges increases, accompanied by a decrease in extended surface terraces that results in undercoordinated catalysts with altered d-band energetic and interatomic lattice spacing; all of which are potentially negatively impacting specific activity (current per unit surface area). Metal nanoparticles are typically described by a cuboctahedral geometry, shown in Fig. 3.4 [43]. Nanoparticle sizes below 10 nm require stabilization by an electrically conducting support (typically carbon) introducing possible metal–support interactions.

Park et al. compared methanol versus formic acid electrooxidation on polycrystalline Pt and on two sizes of carbon-supported Pt (2.0 nm vs. 8.8 nm) (Fig. 3.5) [44]. The potentials were referenced to a saturated calomel electrode (SCE) (RHE, 0.242 V) in 0.05 M H_2SO_4 at a scan rate of 50 mV s^{-1}. The cyclic voltammograms were normalized to a 1 cm^2 Pt "effective area." They observed a reduction in methanol activity for particles smaller that 4 nm and an opposite effect for formic acid; see Fig. 3.5. The disparity between methanol and formic acid size-dependent performance trends is due to methanol preferentially adsorbing onto three adjacent Pt atoms found on Pt(111)-faceted surfaces during the C–H bond dissociation step

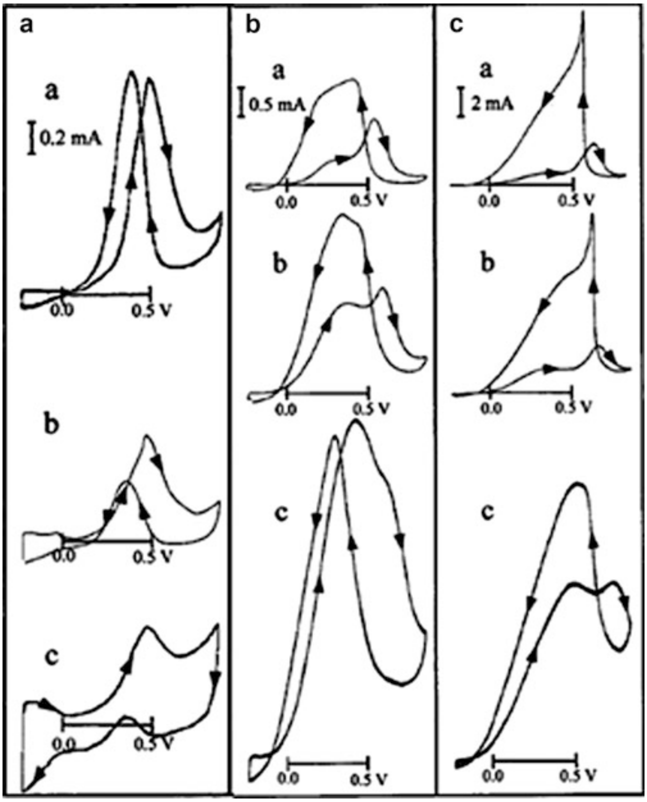

Fig. 3.5 Cyclic voltammograms on (a) polycrystalline Pt, (b) Pt(8.8 nm)/C, and (c) Pt(2.0 nm)/C in 0.05 M H_2SO_4 at 50 mV s^{-1} versus SCE. Electroactive species in solution (**A**) 0.01 M methanol, (**B**) 0.01 M formic acid, and (**C**) 0.1 M formic acid. The active surface area of each electrode was measured in pure electrolyte solution and normalized to 1 cm^2 Pt (modified from Park et al. [44])

to form CO_{ads} [45]. Adzic et al. attributed these differences to a facet-dependent bond strength for the adsorbed methanol intermediate [40]. As particle size decreases, the number of adjacent surface sites needed for adsorption decreases resulting in a decrease in the maximum current density. Additionally, the available surface sites are further diminished by OH_{ads} at elevated potentials, resulting in a reduction in methanol adsorption onto the catalyst surface during the reverse potential sweep.

Formic acid adsorption onto Pt requires either multiple sites for the dehydration pathway or only one to activate C–H bond for the dehydrogenation pathway [46]. The onset of formic acid electrooxidation has been shown to be effected by both Pt particle size and reactant concentration (Fig. 3.5B, C). The dehydration pathway is favored on both the polycrystalline and 8.8 nm Pt catalyst surfaces during the forward scan, as is apparent from the low currents and high overpotentials. The higher potentials are required to form the activated hydroxyl complexes required to oxidize the passivating CO moieties to CO_2, similar to methanol. The formic acid

Fig. 3.6 Size-dependent current densities acquired at (**A**) 0.4 V and (**B**) 0.2 V versus RHE from cyclic voltammograms anodic scan (5 mV s^{-1}) on carbon-supported Pd nanoparticles (Pd/C) in 3 M formic acid and 0.1 M $HClO_4$ [48]

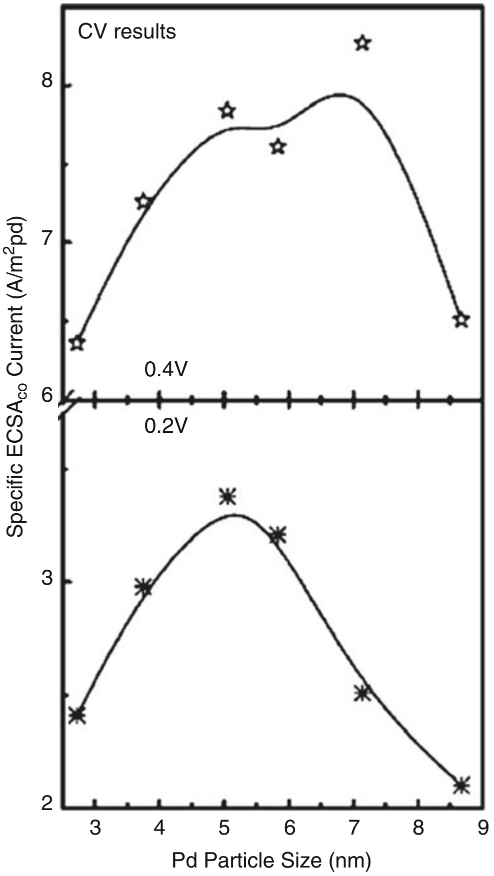

electrooxidation rate on the 2.0 nm Pt nanoparticles is significantly enhanced, resulting in reduced overpotentials during the forward scan. The authors attribute this to the reduction in the abundance of contiguous terrace binding sites promoting the dehydrogenation reaction pathway. The maximum current was higher in 0.1 M formic acid (Fig. 3.5C), but the onset potential was unexpectedly shifted to higher overpotentials for the reaction to proceed.

On Pd catalyst, the dehydrogenation pathway is dominant at low overpotentials in the positive scan [30, 47]. The Pd particle size dependence of formic acid electrooxidation was studied by Zhou et al. with carbon-supported nanoparticles (SA = 240 m^2 g^{-1}) ranging from 2.7 to 9 nm [48]. In this study, X-ray photoelectron spectroscopy was used to decouple the particle size effects on the surface binding energy and corresponding valency of the Pd species (Pd^0, Pd^{2+}, and Pd^{4+}). As the particle size decreased, the Pd^0 surface species was reduced by a factor of 2 and the Pd^{2+} increased by a third. The Pd^{4+} was observed at low percentages for particles under 4 nm. The formic acid cyclic voltammograms support the dominance of the dehydrogenation pathway on the Pd nanoparticle catalysts. As shown in Fig. 3.6, the most active Pd/C size is (a) around 6.5 nm at 0.4 V but (b) only 5.2 nm at 0.2 V versus RHE in 3 M formic acid and 0.1 M $HClO_4$.

Although Pd has superior initial performance at low overpotential, it is quickly deactivated over time. Pan et al. from Tekion Inc. showed that at 40 °C in a DFAFC environment 30 % of the power was lost in the first 3 h of operation [49]. The degradation is attributed to the accumulation of CO_{ads}-like species on the Pd nanoparticle surface during continuous operation [49–52]. Reactivation of the surface has been demonstrated by both electrochemical [49, 53, 54] and non-electrochemical [51] methods. This activity instability drives the search for more stable and active catalysts.

3.5 Modeling Insights

Several modeling efforts have been published probing the formic acid electro-oxidation pathway mechanisms, specifically trying to quantify the energetics of each step [27, 28, 46, 55, 56]. Recent density functional theory (DFT) calculations by Neurock et al. and Wang et al. have shown the CH-down adsorption configuration results in a lower energy electrooxidation pathway of formic acid on Pt [28, 46]. In a recent theoretical study by Gao et al., the impact of the energetically favored formic acid electrooxidation pathways was probed due to the relative presence of water at the Pt(111) interface: (a) two water molecules versus (b) a bilayer network of water molecules [55]. They concluded that in the more realistic solvated environment, formic acid electrooxidation proceeds via a *dual-path mechanism* including the direct path with a transient CO_2*-adsorbed intermediate species and an indirect path that proceeds through an HCOO* species. Unfortunately, the models are for idealized planer single-crystal surfaces and are lacking connections to the more active nanoparticle surfaces—6.5 nm on Pd and 4 nm on Pt. To find the ideal catalyst structure to exclusively promote the dehydrogenation reaction, a firm relationship must be drawn between catalyst reactivity and physical atomic catalyst structure through the following sequence:

1. Surface solvation
2. Nanoparticle-faceted terraces, corners, and edges' presence
    (a) Third-body effect
3. Adatoms and alloying component addition
    (a) Third-body effect
    (b) Electronic effect
4. Surface coverage must be correlated to formic acid feed concentrations.
5. Impact of inner catalyst/ionomer agglomerate acidity.
6. CO_2 removal rate from the ionomer shell of the agglomerate.

In a relatively simple model by Leiva et al., the impact of adatom coverage in terms of a nearest-neighbor electronic effect versus a third-body effect was developed and compared to experimental results for both bismuth (Bi)- and antimony (Sb)-modified Pt single-crystal surfaces, shown in Fig. 3.7 [56]. One of

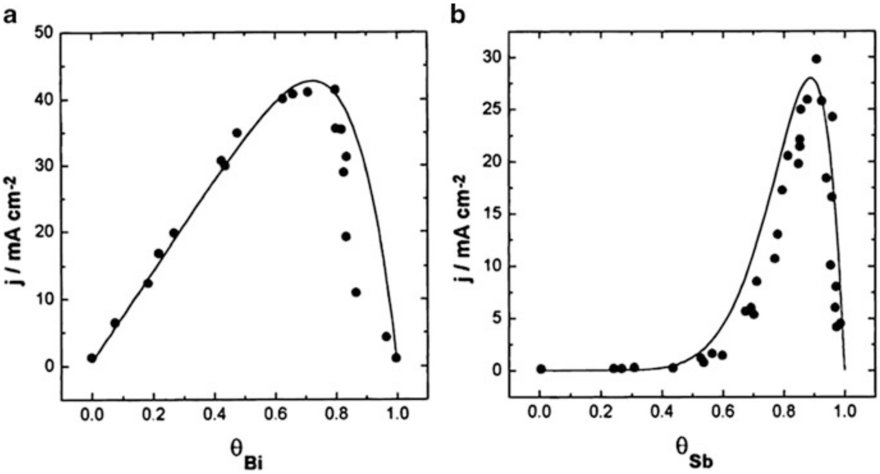

Fig. 3.7 Adatom coverage-dependent current densities acquired at 0.5 V versus RHE from cyclic voltammograms anodic scan (50 mV s^{-1}) on Pt single-crystal electrodes in 0.25 M formic acid and 0.5 M H_2SO_4. The experimental results (*filled circle*) are compared to the theoretically (*continuous line*) predicted activity. (**A**) Pt(111)/bismuth and (**B**) Pt(100)/antimony [56]

the fundamental assumptions of the model was that formic acid only adsorbs onto Pt atoms. The experimental current density measurements were made at 0.5 V, 50 mV s^{-1} in 0.25 M formic acid, and 0.5 M H_2SO_4. The different adatom surface coverages (θ) resulted in significantly different current density trends. The addition of a slight fraction of Bi induced an immediate increase in performance, with a maximum between θ of 0.7 and 0.8. While the performance did not increase for Sb-modified surfaces until $\theta > 0.4$. The Bi enhancement was found to be consistent with an electronic effect proportional to the number of Bi–Pt pairs. The lack of impact at low coverages of Sb followed their predicted trend due to steric hindrance promoting CH-down adsorption through a third-body effect at elevated coverages.

Peng et al. combined electrochemical surface-enhanced infrared spectroscopy (EC-SEIRAS) and DFT calculations to probe the Sb adatom enhancement mechanism on polycrystalline Pt surfaces [27]. The forward cyclic voltammogram in 0.1 M formic acid and 0.5 M H_2SO_4 showed a 2.7× decrease in CO_{ads} at potentials below 0.2 V versus RHE for a 0.6 monolayer (ML) Sb, with a tenfold current increase at 0.5 V in the forward scan. They concluded at coverages >0.25 ML that the $[Sb]^{\delta+}[Pt]^{\delta-}$ dipole interaction enhances CH-down adsorption. This is consistent with Leiva et al.'s work presented above. They additionally attributed this coverage dependence to a decrease in the Pt–CO_{ads} bond strength with increased Sb coverage.

Demirci investigated the degree of segregation and shifting of d-band centers by metal alloy combinations to improve the direct liquid fuel cell catalyst activity through electronic promotion of the dehydrogenation pathway [57]. He focused on Pt- and Pd-based catalyst for formic acid electrooxidation and looked at the potential impact of surface adatom adsorption of other 3d, 4d, and 5d transition metals. The criteria he imposed for improved catalytic activity on Pt and Pd

Table 3.1 Comparison of shifts in d-band center (eV)/separation energies of ad-metals (impurities) to Pt and Pd

	V	Cu	Nb	Pd	Ag	Ta	Pt	Au
Pt	/A1	−0.33/n	/A2	0.19/A1	0.5/A2	/A1	0	0.46/A2
Pd	/S1	/S1	/A1	0	0.14/A1	/S1	−0.17/n	0.17/A1

The separation energies are designated S for segregation, A for antisegregation, and n for no segregation—1, 2, and 3 as moderate, strong, and very strong, respectively [55]

surfaces were that the second metal did not segregate and a positive shift in the d-band center of Pt. The results from Demirci's work are listed in Table 3.1. The positive shift in the d-band center is predicted to enhance the adsorption of the "active intermediate" species [Eq. (3.1)]. Unfortunately, the relative d-band shifts were not provided for all the secondary metals of interest in Table 3.1. The Pd cross entries designated with S1 are predicted to segregate in the presence of the ad-metal. The predicted performance enhancement of Pd adatoms onto Pt and Au has been experimentally demonstrated by Wieckowski's group [6, 58–60]. Significant work has been preformed with gold (Au) incorporated onto both Pt and Pd catalyst, supporting Demirici's prediction [61–64].

3.6 Electrocatalyst Performance Studies

Controlled electrochemical experiments are designed to probe select aspects of the formic acid electrooxidation reaction as a function of material selection and/or experimental conditions. Unfortunately, the selected experimental technique employed imposes deviations from a complex three-dimensional catalyst layer used in an operational DFAFC and thus results in inconsistencies between techniques. Assuming the current–potential relationship is always directly correlated to Faraday's law for charge and CO_2 production, the assessment techniques can be broken down into three general categories: (1) indirect correlation, (2) desorbed product detection, and (3) direct catalyst surface analysis.

General Electrochemical Setup. Catalytic studies to probe formic acid electrooxidation efficiencies are commonly not performed in a complex fuel cell, but using a three-electrode electrochemical cell at room temperature, consisting of a working (catalyst of interest), a counter (Pt mesh), and a reference electrode. Potentials are typically referenced against an RHE, saturated calomel electrode (SCE), or silver/silver chloride (Ag/AgCl).

The supporting electrolyte type and concentration of formic acid impact the observed overpotentials. The two most commonly used supporting electrolytes are either H_2SO_4 or $HClO_4$. Specific bisulfate anion adsorption onto Pt surface sites from H_2SO_4 adversely increases the onset potential of formic acid electrooxidation. The top of Fig. 3.8 shows an unfavorable increase in the onset potential for OH_{ads} in the anodic cycle by ~0.1 V on a Pt (~2.3 nm)/C catalyst in the presence of 0.1 M H_2SO_4 versus 0.1 M $HClO_4$ [65]. In the presence of 0.5 M formic acid, the initial response in the forward anodic sweep at potentials below 0.4 V versus SCE is

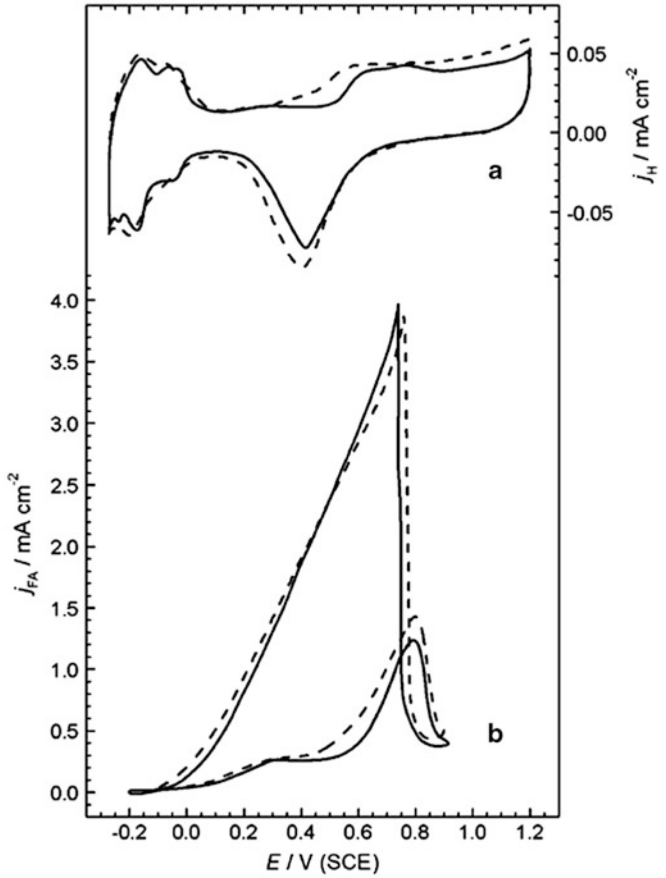

Fig. 3.8 Comparison of cyclic voltammetric features in 0.1 M H_2SO_4 (*solid line*) and 0.1 M $HClO_4$ (*dashed line*) on Pt/C (47.5 wt% from Tanaka Precious Metal Group) at 50 mV s^{-1}. (**a**) Base electrolyte and (**b**) 0.5 M formic acid and base electrolyte [65]

relatively unaffected by the electrolyte. This may be attributed to the combined surface coverage of bisulfate and CO_{ads} having relatively little impact on the availability of the single adsorption sites required for the dehydrogenation pathway. The onset and maximum current density for the second peak in the forward scan is negatively impacted by the presence of bisulfate.

The formic acid electrooxidation current density may be impacted by temperature, formic acid concentration, rotation rate of the working electrode (0–1,000 rpm), upper potential limit, and contamination from the reference electrode. The upper potential limit in the cyclic voltammogram, depending on catalyst type, impacts the magnitude of the reverse scan current density due to the promotion of the dehydration path through the formation of OH_{ads} at higher potentials [66]. Masel's group has shown an increase in turnover efficiency of formic acid electrooxidation with increasing pH for both Pt and Pd catalyst [67].

Purity of the formic acid fuel can have significant effects on the initial and sustained catalyst performance. Commercial synthesis of formic acid contains residual precursors due to incomplete conversion or purification such as methanol, methyl formate, and formaldehyde [68]. In a recent paper by Law et al., the impact of ppm-level common catalyst poisoning substituents on steady-state DFAFC performance was investigated: methyl formate ($CH_3OC(O)H$), methanol, and acetic acid (CH_3COOH) [14]. At contamination levels of 50 ppm, an accelerated DFAFC decay at 200 mA cm^{-2} was observed for all contaminates measured. To remove undesirable contaminates from the supplied standard commercial grade formic acid at minimal cost penalties, a patent from the Masel group demonstrates improved performance for formic acid pretreated by freeze distillation [68].

3.6.1 Indirect Correlation

Several types of indirect measurements may be used to infer the physical and/or chemical phenomena inducing changes in the formic acid electrooxidation activity. Using *in-vacuum* X-ray diffraction (XRD) and X-ray photoelectron spectroscopy (XPS) to complement electrochemical evaluations, Yu and Pickup have evaluated the change in electron density due to adatom addition of Bi [69] and Sb [70] individually onto Pt/C to assess coverage-dependent changes. Their results supported segregation of the adatom to the surface with no observable alloying.

Electrochemical impedance spectroscopy (EIS) is a powerful technique for probing reaction kinetics and mass transport limitations within a finite electrochemical system. EIS has been applied to both ex situ electrochemical cell [12, 71–76] and in situ fuel cell [11, 51, 77–79] formic acid systems. The discussion herein is limited to testing in a two-electrode electrochemical cell: electrode 1 (counter and reference electrodes)/electrode 2 (sense and working electrodes). The frequency range of interest is typically 10 kHz to 0.01 Hz at the acquisition interval of ten points per decade with an ac perturbation amplitude of 10 mV. The ac perturbation is superimposed upon a constant applied dc potential. The results are typically represented in a Nyquist plot, with the imaginary component ($-Z''$) versus the real component (Z'). The high-frequency intercept (R_I) is dominated by electrolyte resistance and contact resistance; in the electrochemical cell, these contributions are minimal and approach zero. The arc is a combination of charge transfer resistance (R_{ct}) and double-layer capacitance (C_{dl}). The C_{dl} is represented in an equivalent circuit model as a capacitive phase element (CPE_{dl}) due to the impact of formic acid increasing the extent of solvation of ions across the Helmholtz layer [80]. Additional circuit elements may be included to account for electrooxidation of adsorbed reaction intermediate species. Mass transport resistances are typically not observed in a two-electrode electrochemical cell.

Wang et al. compared formic acid electrooxidation EIS Nyquist plots for Pt/C and PtPd(alloy)/C catalyst (Fig. 3.9a, b, respectively) [12]. The results were acquired in 0.5 M formic acid and 0.5 M $HClO_4$ over a range of applied dc potentials from 0.1 to 0.7 V versus Ag/AgCl (+0.199 V vs. RHE). The Nyquist

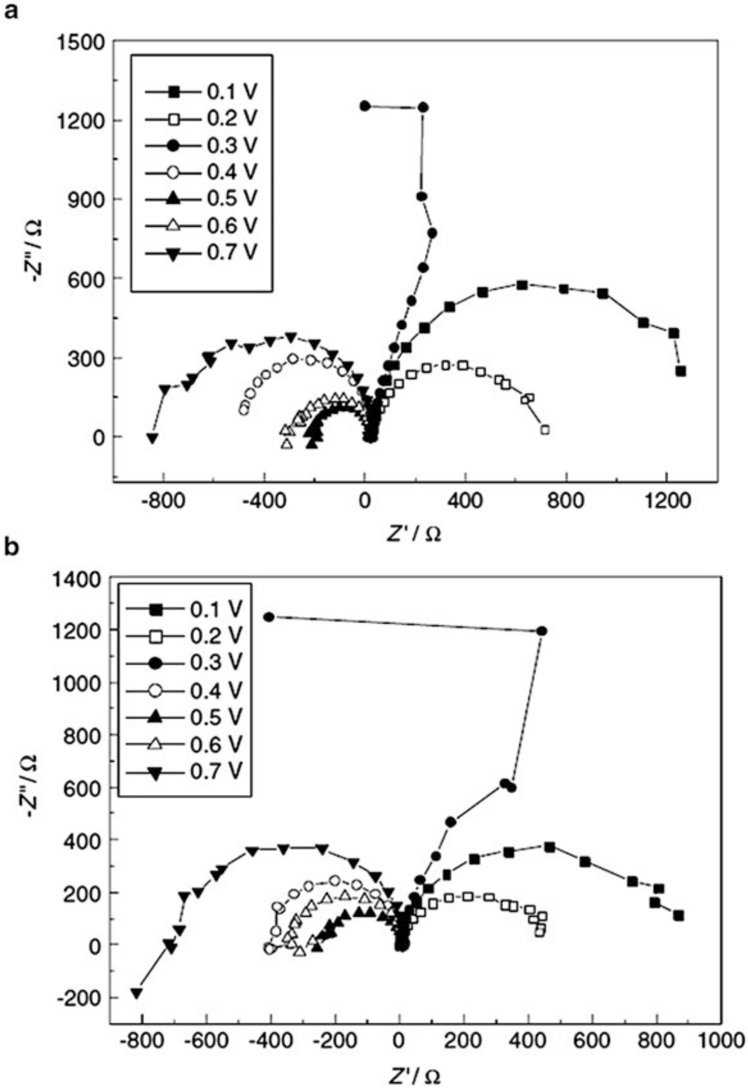

Fig. 3.9 Nyquist plot of (**a**) Pt/C and (**b**) PtPd/C (alloy) at 25 °C in 0.5 M $HClO_4$ and 0.5 M formic acid as a function of applied potential [vs. Ag/AgCl/KCl(sat)] [12]

plots show activity in two quadrants, dependent on the applied potential and the dominant reaction mechanism. The arc in quadrant (Z', $R_I \rightarrow +$) decreases as the potential is increased from 0.1 to 0.2 V for both catalyst types, which is consistent with a decrease in the R_{ct} of the reaction. As the potential increases to 0.3 V, the radius of the arc increases beyond that observed for 0.1 V. The transitioning to the second quadrant (Z', $R_I \rightarrow -$) has been attributed to the contribution of the dehydration reaction (3.2c), [12] being consistent with the anodic sweep of Wang's cyclic voltammograms (Fig. 10 in [12]) for the Pt/C and PtPd/C, which exhibited similar peak trends with the activity of the PtPd/C catalyst and which is significantly higher for the identical applied potentials. The lower potential peak current below 0.5 V is attributed to the dehydrogenation reaction pathway, while the current from the dehydration pathway reaches a maximum between 0.6 and 0.8 V. Suo and coworkers studied Pd/C and attributed the increase in the arc in the second quadrant at higher applied potential to a blocking effect of surface oxide species [76]. Wang found that the R_{ct} was smaller for the PtPd/C catalyst, but it followed the general trends of Pt/C in terms of arc location dependence on applied potential.

Electrochemical quartz crystal microbalance. To monitor adsorbate accumulation on catalyst surfaces from formic acid electrooxidation and advance mechanistic understanding, an electrochemical quartz crystal microbalance (EQCM) can be used to simultaneously measure current and mass [22, 66, 81–83]. The dampening of the vibration frequency (Δf) of an AT-cut 9 MHz piezoelectric crystal is directly proportional to mass accumulation (Δm) on the catalyst surface through the Sauerbrey equation $\left(\Delta f = -f_0^2 2(\mu_q \rho_q)^{-1/2} \Delta m / A\right)$ [84], where f_0 is the base frequency, μ_q is the quartz shear modulus, ρ_q is the density of the quartz, and A is the active area. The detection limit can be as low as ±0.4 ng cm^{-2} [85].

In a three-electrode electrochemical arrangement, in the absence of formic acid, the Δm's on polycrystalline Pt working electrodes during potential cycling are associated with H-adsorption–desorption, double-layer alignment, and oxide formation/reduction [85]. In the presence of 0.1 M formic acid and 0.2 M $HClO_4$ at 50 mV s^{-1}, Tian and Conway observed competitive adsorption between CO_{ads} [Eq. (3.2a)] and Ox_{ads} [Eq. (3.2b)] formation [66]. They observed strong symmetry between the current- and mass-dependent potential response on the forward anodic sweep. Figure 3.10 shows the effect of sequentially increasing the upper potential limit (0.6–1.4 V vs. RHE) during cyclic voltammetric measurements (from 0.05 V) on the (a) current and (b) mass response in 0.2 M $HClO_4$ and 0.2 M formic acid [66]. *Positive scan*—The forward anodic scan is unaffected by the previous upper potential limit. As the potential increases in the positive direction, the emergence of a second peak with a maximum current at 1.05 V is observed without a corresponding increase in mass (decrease in frequency); this observation is attributed to the favorable autocatalytic low oxide layer coverage facilitating step 3 [Eq. (3.2c)] in the indirect reaction pathway. Above 1.05 V the mass increases which corresponds to the accumulation of an oxide layer on the Pt surface and inhibition of formic acid adsorption. The growth of an oxide layer is shifted by about 200 mV in the presence of formic acid. *Negative scan*—While the reverse negative going scan shows a strong dependence on the upper potential limit, when the potential is limited to less than 0.8 V, the current in the reverse scan is only slightly higher than that in the forward scan; the current peak near 0.6 V shifts to higher potentials with increasing upper potential limits. A distinct current spike is observed for upper potential limits of 1.05 V and greater which coincides with the increase in mass due to surface oxide accumulation. As the surface oxide layer becomes more well developed at higher

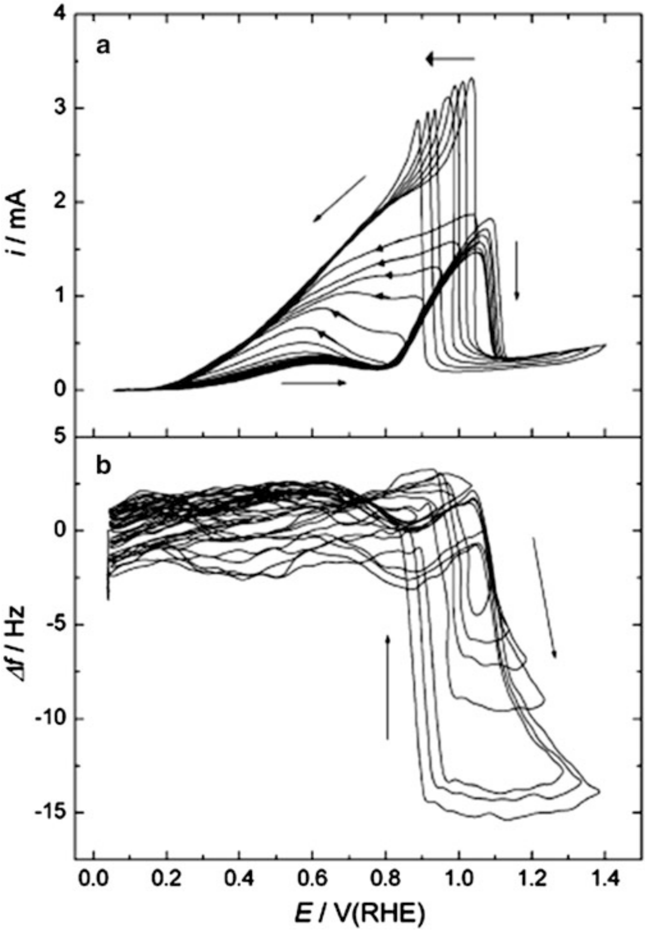

Fig. 3.10 Cyclic voltammetry using a electrochemical quartz crystal microbalance of formic acid electrooxidation on a polycrystalline Pt surface in 0.2 M formic acid and 0.2 M $HClO_4$ at 50 mV s^{-1} (**a**) current and (**b**) frequency (corresponding to negative mass changes) response. The upper potential limit is sequentially increased with each subsequent cycle [66]

upper potential limits, the subsequent formic acid anodic spike decreases in intensity and is negatively shifted.

3.6.2 Desorbed Product Detection

Several research groups have used differential electrochemical mass spectroscopy (DEMS) to monitor product conversion during formic acid electrooxidation [2, 21, 37, 86–88]. In Fig. 3.2, the origins of the CO_2 product formation pathway is investigated by using isotopically labeled formic acid [37].

3.6.3 Direct Catalyst Surface Analysis

The in situ study in electrochemical cells of the catalyst surface is challenging due to low surface sensitivity through the electrolyte. Several surface-sensitive techniques have been employed to probe the abundance and/or state of adsorbed surface species formed during formic acid electrooxidation: broadband sum frequency generation [89, 90], surface-enhanced Raman spectroscopy [21], scanning tunneling microscopy [91], and Fourier transform infrared spectroscopy [19, 26, 27, 31, 32, 41, 92–99].

Fourier transform infrared spectroscopy (FTIR) is a powerful technique to probe real-time adsorbed surface species (reactants, intermediates, products) and solution constituents due to selected molecular dipole bond vibrations induced by tuned incident radiation [100]. FTIR has been used to study the formic acid electrooxidation reaction mechanism in situ by stepping or scanning the potential where species of interest are generated, from either high potentials where the intermediate species are completely oxidized (a clean surface, >1 V vs. RHE) or low potentials where the intermediate species approaches the coverage limit (blocked surface, <0.05 V vs. RHE) [100]. The three observed reaction intermediates for formic acid electrooxidation are linearly bonded CO_L, bridge-bonded CO_B, and bridge-bonded formate ($HCOO_{ad}$) with vibrational bands at 2,052–2,080 cm^{-1}, 1,810–1,850 cm^{-1}, and 1,320 cm^{-1}, respectively [27, 98]. The vibration frequencies of the adsorbates are influenced by the electronic characteristics and electrochemical potential of the electrode surface. Additional peaks of lesser intensity are observed for the water adlayer and sulfate/bisulfate at the electrode interface [27, 98].

The initial studies in this area were done in external infrared reflection adsorption spectroscopy (IRAS) mode [26, 41, 92–97], where the incident beam was passed through an optical window, a 1–100 μm ultra thin solution layer, then reflected off the electrode where it transverses back through the aforementioned layers at an incident angle to a detector. The solution layer is minimized to reduce solution interference at the expanse of induced mass transport effects. To enhance surface sensitivity and alleviate mass transport restrictions, attenuated total reflection surface-enhanced infrared adsorption spectroscopy (ATR-SEIRAS) has been used [19, 27, 31, 32, 98, 99]. The radiation passes through the backside of a hemicylindrical Si prism that has a metal film on the front to act as the working electrode and the incident infrared radiation goes to a detector [33, 101].

Considering the work by Pang et al., they clearly demonstrate the positive impact of antimony (Sb) adatoms on Pt for enhanced formic acid electrooxidation; see Fig. 3.11 [27]. They studied a surface coverage of 60 % Sb ($\theta_{Sb} = 0.6$) on polycrystalline Pt in 0.5 M H_2SO_4 and 0.1 M formic acid at 10 mV s^{-1} versus RHE. Figure 3.11a shows the normal current response for formic acid electrooxidation on polycrystalline Pt with the corresponding detection of the extent of coverage of the surface by reaction intermediates, CO_L, CO_B, and formate. At low potentials in the positive potential scan, CO_L is the dominant surface species, with negligible current

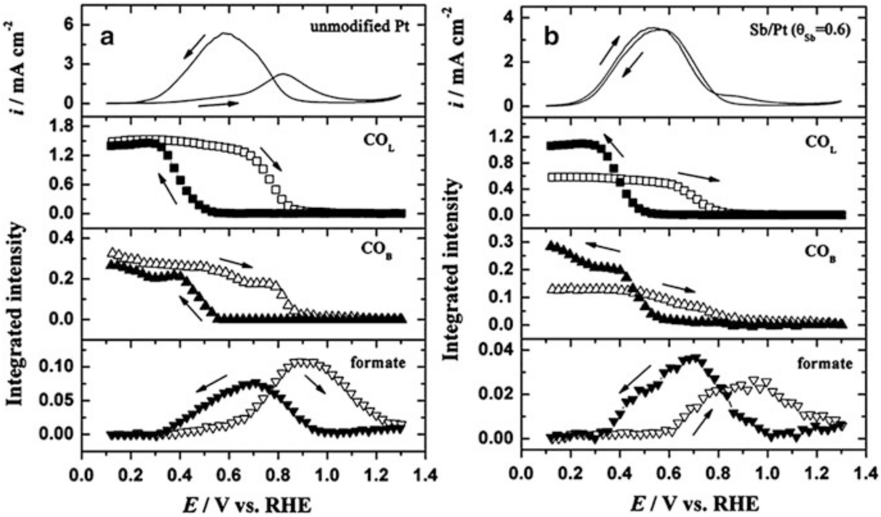

Fig. 3.11 A time-resolved series of selected ART-FTIR integrated peak intensities as measured during potential cycling on (**a**) polycrystalline Pt and (**b**) 60 % antimony (Sb) adatom covered polycrystalline Pt in 0.5 M H_2SO_4 and 0.1 M formic acid at 10 mV s^{-1}. From the top-down the series of plots are as follows: the current response, CO_L, CO_B, and formate [27]

generation. As CO_{ads} is removed from the surface at potentials >0.4 V, the current increases slightly and formate begins to appear on the surface. Above 0.7 V both CO_{ads} species are rapidly removed from the surface and the current increases. In the reverse negative potential scan, the asymmetric current profile has increased and shifted toward lower potentials; the CO_L and CO_B are not detected until the potential is decreased below 0.55 V. Conversely, the Sb-modified surface (Fig. 3.11b) exhibits a symmetric current profile with favorably intensity shifted to lower potentials. The initial CO_L and CO_B intensities at 100 mV are reduced by at least 50 %. The initial rise in current is unaffected by the presence of CO_{ads} and simultaneously decreases with CO_{ads} desorption due to surface oxidation. This observation clearly demonstrates the dominance of the dehydrogenation (direct) pathway on an Sb-modified Pt surface. The rise in CO_L and CO_B intensities in the reverse scan is potentially linked with loss of Sb due to oxidation at elevated potentials.

3.7 Conclusions

The type, structure, and electron density clearly determine the reactivity of a catalyst toward formic acid electrooxidation. The catalyst characteristics that promote reactant adsorption in the CH-down orientation exhibit enhanced activity through the dehydrogenation reaction pathway. Pd catalyst initially favors the dehydrogenation pathway but suffers for 30 % activity loss within only 3 h of continuous operation due to accumulation of reaction intermediates on the surface.

A smaller percentage of Pt surface sites participate in the dehydrogenation pathway, limiting activity to high overpotentials that promote OH_{ads} formation to complete the dehydration reaction.

Size of the Pt and Pd catalyst plays an important role in catalytic activity, due to reduction in the abundance of contiguous surface sites and crystallographic facets as the size of nanoparticles are reduced. Geometrically, the reduction in contiguous Pt sites enhances reactivity, with an optimal size of 2 nm. Alternatively, for Pd as the particle size decrease the abundance of unfavorable oxidation states increase, adversely impacting reactivity; the optimal size at 0.4 V is 6.5 nm.

Separate modeling efforts have evolved to include solvation, electronic alterations in the d-band center, and the third-body effect. The findings suggest a combination of a positive electronic shift in the d-band center and third-body effect promotes the dehydration pathway. There exists a need for a cohesive hybrid model that also includes nanoparticle attributes.

References

1. Gasteiger HA, Garche J (2008) Fuel cells. In: Ertl G (ed) Handbook of heterogeneous catalysis, 2nd edn. Weinheim, Wiley-VCH, pp 3081–3121
2. Weber M, Wang JT, Wasmus S, Savinell RF (1996) Formic acid oxidation in a polymer electrolyte fuel cell. J Electrochem Soc 143:L158–L160
3. Ha S, Rice CA, Masel RI, Wieckowski A (2002) Methanol conditioning for improved performance of formic acid fuel cells. J Power Sources 112:655–659
4. Rice C, Ha S, Masel RI, Waszczuk P, Wieckowski A (2002) Characteristics of formic acid fuel cells. In: Proceedings of the 40th power sources conference, pp 254–257
5. Rice C, Ha S, Masel RI, Waszczuk P, Wieckowski A, Barnard T (2002) Direct formic acid fuel cells. J Power Sources 111:83–89
6. Waszczuk P, Barnard TM, Rice C, Masel RI, Wieckowski A (2002) A nanoparticle catalyst with superior activity for electrooxidation of formic acid. Electrochem Commun 4:732
7. Masel RI, Rice CA, Waszczuk P, Wieckowski A (2003) Fuel cells and fuel cells catalysts. US Patent 7,132,188
8. McGovern MS, Garnett EC, Rice C, Masel RI, Wieckowski A (2003) Effects of Nafion as a binding agent for unsupported nanoparticle catalysts. J Power Sources 115:35–39
9. Rhee Y-W, Ha SY, Masel RI (2003) Crossover of formic acid through Nafion membranes. J Power Sources 117:35–38
10. Rice C, Ha S, Masel RI, Wieckowski A (2003) Catalysts for direct formic acid fuel cells. J Power Sources 115:229–235
11. Uhm S, Lee HJ, Lee J (2009) Understanding underlying processes in formic acid fuel cells. Phys Chem Chem Phys 11:9326–9336
12. Wang X, Hu J-M, Hsing IM (2004) Electrochemical investigation of formic acid electro-oxidation and its crossover through a Nafion membrane. J Electroanal Chem 562:73–80
13. Masel RI (2012) Novel catalyst mixtures for electrochemical conversion of carbon dioxide to formic acid. US Patent Application WO2012006240A1
14. Law WL, Platt AM, Wimalaratne PDC, Blair SL (2009) Effect of organic impurities on the performance of direct formic acid fuel cells. J Electrochem Soc 156:B553–B557
15. Parsons R, VanderNoot T (1988) The oxidation of small organic molecules: a survey of recent fuel cell related research. J Electroanal Chem Interfacial Electrochem 257:9–45

16. Jarvi TD, Stuve EM (1998) Fundamental aspects of vacuum and electrocatalytic reactions of methanol and formic acid on platinum surfaces. In: Lipkowski J, Ross PN (eds) Electrocatalysis. Wiley-VCH, New York, NY, pp 75–133
17. Vielstich W (2003) CO, formic acid, and methanol oxidation in acid electrolytes-mechanisms and electrocatalysis. In: Bard AJ, Stratmann M (eds) Encyclopedia of electrochemistry. Wiley-VCH Verlag GmbH & Co. KGaA, Weinheim, pp 466–511
18. Ross PN Jr (1998) The science of electrocatalysis on bimetallic surfaces. In: Lipkowski J, Ross PN (eds) Electrocatalysis. Wiley-VCH, New York, NY, pp 43–74
19. Chen YX, Heinen M, Jusys Z, Behm RJ (2006) Bridge-bonded formate: active intermediate or spectator species in formic acid oxidation on a Pt film electrode? Langmuir 22: 10399–10408
20. Larsen R, Ha S, Zakzeski J, Masel RI (2006) Unusually active palladium-based catalysts for the electrooxidation of formic acid. J Power Sources 157:78–84
21. Beltramo GL, Shubina TE, Koper MTM (2005) Oxidation of formic acid and carbon monoxide on gold electrodes studied by surface-enhanced Raman spectroscopy and DFT. ChemPhysChem 6:2597–2606
22. Chen S-l, Wu B-l, Cha C-s (1997) An EQCM investigation of oxidation of formic acid at gold electrode in sulfuric acid solution. J Electroanal Chem 431:243–247
23. Chen W, Tang Y, Bao J, Gao Y, Liu C, Xing W, Lu T (2007) Study of carbon-supported Au catalyst as the cathodic catalyst in a direct formic acid fuel cell prepared using a polyvinyl alcohol protection method. J Power Sources 167:315–318
24. Hahn F, Beden B, Lamy C (1986) In situ infrared reflectance spectroscopic study of the adsorption of formic acid at a rhodium electrode. J Electroanal Chem Interfacial Electrochem 204:315–327
25. Wieckowski A, Sobkowski J, Zelenay P (1977) The potential dependence and kinetics of formic acid adsorption on rhodium electrodes. J Electroanal Chem Interfacial Electrochem 84:109–116
26. Gómez R, Weaver MJ (1997) Electrochemical infrared studies of monocrystalline iridium surfaces Part I: Electrooxidation of formic acid and methanol. J Electroanal Chem 435: 205–215
27. Peng B, Wang H-F, Liu Z-P, Cai W-B (2010) Combined surface-enhanced infrared spectroscopy and first-principles study on electro-oxidation of formic acid at Sb-modified Pt electrodes. J Phys Chem C 114:3102–3107
28. Wang H-F, Liu Z-P (2009) Formic acid oxidation at Pt/H2O interface from periodic DFT calculations integrated with a continuum solvation model. J Phys Chem C 113:17502–17508
29. Luo Q, Feng G, Beller M, Jiao H (2012) Formic acid dehydrogenation on Ni(111) and comparison with Pd(111) and Pt(111). J Phys Chem C 116:4149–4156
30. Capon A, Parsons R (1973) The oxidation of formic acid on noble metal electrodes: II A comparison of the behaviour of pure electrodes. J Electroanal Chem Interfacial Electrochem 44:239–254
31. Chen YX, Heinen M, Jusys Z, Behm RJ (2006) Kinetics and mechanism of the electrooxidation of formic acid–spectroelectrochemical studies in a flow cell. Angew Chem Int Ed 45:981–985
32. Samjeske G, Osawa M (2005) Current oscillations during formic acid oxidation on a Pt electrode: insight into the mechanism by time-resolved IR spectroscopy. Angew Chem Int Ed 44:5694–5698
33. Miki A, Ye S, Osawa M (2002) Surface-enhanced IR absorption on platinum nanoparticles: an application to real-time monitoring of electrocatalytic reactions. Chem Commun 14: 1500–1501
34. Beden B, Lamy C (1988) Infrared reflectance spectroscopy. In: Gale RJ (ed) Spectroelectrochemistry: theory and practice. Plenum, New York, NY, p 189
35. Bewick A, Pons B (1985) In: Clark RJH, Hester RE (eds) Advances in infrared and raman spectroscopy. Wiley, Chichester, p 360

36. Watanabe M, Motoo S (1975) Electrocatalysis by ad-atoms: Part II. Enhancement of the oxidation of methanol on platinum by ruthenium ad-atoms. J Electroana Chem Interfacial Electrochem 60:267–273
37. Willsau J, Heitbaum J (1986) Analysis of adsorbed intermediates and determination of surface potential shifts by dems. Electrochim Acta 31:943–948
38. Motoo S, Watanabe M (1980) Electrocatalysis by ad-atoms: Part VII. Enhancement of CO oxidation on platinum by As ad-atoms. J Electroanal Chem Interfacial Electrochem 111:261–268
39. Clavilier J, Parsons R, Durand R, Lamy C, Leger JM (1981) Formic acid oxidation on single crystal platinum electrodes. Comparison with polycrystalline platinum. J Electroanal Chem 124:321–326
40. Adzic RR, Tripkovic AV, O'Grady WE (1982) Structural effects in electrocatalysis. Nature 296:137–138
41. Iwasita T, Xia X, Herrero E, Liess H-D (1996) Early stages during the oxidation of HCOOH on single-crystal Pt electrodes as characterized by infrared spectroscopy. Langmuir 12: 4260–4265
42. Hoshi N, Kida K, Nakamura M, Nakada M, Osada K (2006) Structural effects of electrochemical oxidation of formic acid on single crystal electrodes of palladium. J Phys Chem B 110:12480–12484
43. Benfield RE (1992) Mean coordination numbers and the non-metal-metal transition in clusters. J Chem Soc Faraday Trans 88:1107–1110
44. Park S, Xie Y, Weaver MJ (2002) Electrocatalytic pathways on carbon-supported platinum nanoparticles: comparison of particle-size-dependent rates of methanol, formic acid, and formaldehyde electrooxidation. Langmuir 18:5792–5798
45. Chrzanowski W, Kim H, Wieckowski A (1998) Enhancement in methanol oxidation by spontaneously deposited ruthenium on low-index platinum electrodes. Catal Lett 50:69–75
46. Neurock M, Janik M, Wieckowski A (2008) A first principles comparison of the mechanism and site requirements for the electrocatalytic oxidation of methanol and formic acid over Pt. Faraday Discuss 140:363–378
47. Pavese A, Solis V, Giordano MC (1988) Electrocatalytic oxidation of formic acid on Pd + Pt alloys of different bulk composition in acidic medium. J Electroanal Chem 245(1–2): 145–156
48. Zhou W, Lee JY (2008) Particle size effects in Pd-catalyzed electrooxidation of formic acid. J Phys Chem C 112:3789–3793
49. Pan Y, Zhang R, Blair SL (2009) Anode poisoning study in direct formic acid fuel cells. Electrochem Solid St Lett 12:B23–B26
50. Zhou WP, Lewera A, Larsen R, Masel RI, Bagus PS, Wieckowski A (2006) Size effects in electronic and catalytic properties of unsupported palladium nanoparticles in electrooxidation of formic acid. J Phys Chem B 110:13393–13398
51. Zhou Y, Liu J, Ye J, Zou Z, Ye J, Gu J, Yu T, Yangc A (2010) Poisoning and regeneration of Pd catalyst in direct formic acid fuel cell. Electrochim Acta 55:5024–5027
52. Zhang H-X, Wang S-H, Jiang K, Andre T, Cai W-B (2012) In situ spectroscopic investigation of CO accumulation and poisoning on Pd black surfaces in concentrated HCOOH. J Power Sources 199:165–169
53. Zhu Y, Khan Z, Masel RI (2005) The behavior of palladium catalysts in direct formic acid fuel cells. J Power Sources 139:15–20
54. Jung WS, Han J, Ha S (2007) Analysis of palladium-based anode electrode using electrochemical impedance spectra in direct formic acid fuel cells. J Power Sources 173:53–59
55. Gao W, Keith JA, Anton J, Jacob T (2010) Theoretical elucidation of the competitive electro-oxidation mechanisms of formic acid on Pt(1 1 1). J Am Chem Soc 132:18377–18385
56. Leiva E, Iwasita T, Herrero E, Feliu JM (1997) Effect of adatoms in the electrocatalysis of HCOOH oxidation. A theoretical model. Langmuir 13:6287–6293

57. Demirci UB (2007) Theoretical means for searching bimetallic alloys as anode electrocatalysts for direct liquid-feed fuel cells. J Power Sources 173:11–18
58. Babu PK, Kim HS, Chung JH, Oldfield E, Wieckowski A (2004) Bonding and motional aspects of CO adsorbed on the surface of Pt nanoparticles decorated with Pd. J Phys Chem B 108:20228–20232
59. Lu G-Q, Crown A, Wieckowski A (1999) Formic acid decomposition on polycrystalline platinum and palladized platinum electrodes. J Phys Chem B 103:9700–9711
60. Spendelow JS, Wieckowski A (2004) Noble metal decoration of single crystal platinum surfaces to create well-defined bimetallic electrocatalysts. Phys Chem Chem Phys 6: 5094–5118
61. Yin M, Huang Y, Lv Q, Liang L, Liao J, Liu C, Xing W (2011) Improved direct electrooxidation of formic acid by increasing Au fraction on the surface of PtAu alloy catalyst with heat treatment. Electrochim Acta 58:6–11
62. Zhang S, Shao Y, Yin G, Lin Y (2010) Facile synthesis of PtAu alloy nanoparticles with high activity for formic acid oxidation. J Power Sources 195:1103–1106
63. Park I-S, Lee K-S, Yoo SJ, Cho Y-H, Sung Y-E (2010) Electrocatalytic properties of Pd clusters on Au nanoparticles in formic acid electro-oxidation. Electrochim Acta 55: 4339–4345
64. Mazumder V, Lee Y, Sun S (2010) Recent development of active nanoparticle catalysts for fuel cell reactions. Adv Funct Mater 20:1224–1231
65. Lovic JD, Tripkovic AV, Gojkovic SL, Popovic KD, Tripkovic DV, Olszewski P, Kowal A (2005) Kinetic study of formic acid oxidation on carbon-supported platinum electrocatalyst. J Electroanal Chem 581:294–302
66. Tian M, Conway BE (2008) Electrocatalysis in oscillatory kinetics of anodic oxidation of formic acid: At Pt; nanogravimetry and voltammetry studies on the role of reactive surface oxide. J Electroanal Chem 616:45–56
67. Haan JL, Masel RI (2009) The influence of solution pH on rates of an electrocatalytic reaction: formic acid electrooxidation on platinum and palladium. Electrochim Acta 54: 4073–4078
68. Masel RI, Zhu Y, Khan Z, Man M (2006) Low contaminant formic acid fuel for direct liquid fuel cell. US Patent 20060059769
69. Yu X, Pickup PG (2011) Carbon supported PtBi catalysts for direct formic acid fuel cells. Electrochim Acta 56:4037–4043
70. Yu X, Pickup PG (2010) Pb and Sb modified Pt/C catalysts for direct formic acid fuel cells. Electrochim Acta 55:7354–7361
71. Kristian N, Yu Y, Gunawan P, Xu R, Deng W, Liu X, Wang X (2009) Controlled synthesis of Pt-decorated Au nanostructure and its promoted activity toward formic acid electro-oxidation. Electrochim Acta 54:4916–4924
72. Lu Y, Chen W (2012) PdAg alloy nanowires: facile one-step synthesis and high electrocatalytic activity for formic acid oxidation. ACS Catal 2:84–90
73. Liu Z, Guo B, Tay SW, Hong L, Zhang X (2008) Physical and electrochemical characterizations of PtPb/C catalyst prepared by pyrolysis of platinum(II) and lead(II) acetylacetonate. J Power Sources 184:16–22
74. Maxakato NW, Ozoemena KI, Arendse CJ (2010) Dynamics of electrocatalytic oxidation of ethylene glycol, methanol and formic acid at MWCNT platform electrochemically modified with Pt/Ru nanoparticles. Electroanalysis 22:519–529
75. Seland F, Tunold R, Harrington DA (2008) Impedance study of formic acid oxidation on platinum electrodes. Electrochim Acta 53:6851–6864
76. Suo Y, Hsing IM (2009) Size-controlled synthesis and impedance-based mechanistic understanding of Pd/C nanoparticles for formic acid oxidation. Electrochim Acta 55:210–217
77. Uhm S, Chung ST, Lee J (2008) Characterization of direct formic acid fuel cells by impedance studies: in comparison of direct methanol fuel cells. J Power Sources 178:34–43

78. Kang Y, Ren M, Yuan T, Qiao Y, Zou Z, Yang H (2010) Effect of Nafion aggregation in the anode catalytic layer on the performance of a direct formic acid fuel cell. J Power Sources 195:2649–2652
79. Kang S, Lee J, Lee JK, Chung S-Y, Tak Y (2006) Influence of Bi modification of pt anode catalyst in direct formic acid fuel cells. J Phys Chem B 110:7270–7274
80. Conway BE (2003) Electrochemical capacitors their nature, function, and applications. Electrochemistry Encyclopedia. http://electrochem.cwru.edu/encycl/art-c03-elchem-cap.htm
81. Chung S-Y, Uhm S-H, Lee J-K, Kang S-J, Tak Y-S, Lee J-Y (2007) Electrocatalytic oxidation of HCOOH on Pt-based anodes. J Ind Eng Chem 13:339–344
82. Inzelt G, Kertesz V (1996) Effect of poly(aniline) pseudocapacitance on potential and EQCM frequency oscillations arising in the course of galvanostatic oxidation of formic acid on platinum. Electrochim Acta 42:229–235
83. Uhm S, Yun Y, Tak Y, Lee J (2005) EQCM analysis of Bi oxidation mechanism on a Pt electrode. Electrochem Commun 7:1375–1379
84. Hepel M (1999) Electrode-solution interface studies with electrochemical quartz-crystal nanobalance. In: Wieckowski A (ed) Interfacial electrochemistry: theory, experiment, and applications. Marcel Dekker, Inc., Postdam
85. Jerkiewicz G, Vatankhah G, S-i T, Lessard J (2011) Discovery of the potential of minimum mass for platinum electrodes. Langmuir 27:4220–4226
86. Casado-Rivera E, Gal Z, Angelo ACD, Lind C, DiSalvo FJ, Abruna HD (2003) Electrocatalytic oxidation of formic acid at an ordered intermetallic PtBi surface. ChemPhysChem 4:193–199
87. Miura A, Wang H, Leonard BM, Abruna HD, Di SFJ (2009) Synthesis of intermetallic PtZn nanoparticles by reaction of Pt nanoparticles with Zn vapor and their application as fuel cell catalysts. Chem Mater 21:2661–2667
88. Xia XH, Iwasita T (1993) Influence of underpotential deposited lead upon the oxidation of formic acid in perchloric acid at platinum electrodes. J Electrochem Soc 140:2559–2565
89. Behrens RL, Lagutchev A, Dlott DD, Wieckowski A (2010) Broad-band sum frequency generation study of formic acid chemisorption on a Pt (1 0 0) electrode. J Electroanal Chem 649:32–36
90. Behrens RL, Wieckowski A (2009) Electrochemical and spectroscopic studies of small organic molecule oxidation on low index platinum electrodes. Central Regional Meeting of the American Chemical Society, Cleveland, OH
91. Rodriguez-Lopez J, Bard AJ (2010) Scanning electrochemical microscopy: surface interrogation of adsorbed hydrogen and the open circuit catalytic decomposition of formic acid at platinum. J Am Chem Soc 132:5121–5129
92. Chang SC, Leung LWH, Weaver MJ (1990) Metal crystallinity effects in electrocatalysis as probed by real-time FTIR spectroscopy: electrooxidation of formic acid, methanol, and ethanol on ordered low-index platinum surfaces. J Phys Chem 94:6013–6021
93. Yang Y-Y, Zhou Z-Y, Sun S-G (2001) In situ FTIRS studies of kinetics of HCOOH oxidation on Pt(110) electrode modified with antimony adatoms. J Electroanal Chem 500:233–240
94. Beden B, Bewick A, Lamy C (1983) A study by electrochemically modulated infrared reflectance spectroscopy of the electrosorption of formic acid at a platinum electrode. J Electroanal Chem Interfacial Electrochem 148:147–160
95. Lamy C, Leger JM (1991) Electrocatalytic oxidation of small organic molecules at platinum single crystals. J Chim Phys Phys -Chim Biol 88:1649–1671
96. Arenz M, Stamenkovic V, Ross PN, Markovic NM (2004) Surface (electro-)chemistry on Pt (111) modified by a pseudomorphic Pd monolayer. Surf Sci 573:57–66
97. Arenz M, Stamenkovic V, Schmidt TJ, Wandelt K, Ross PN, Markovic NM (2003) The electro-oxidation of formic acid on Pt–Pd single crystal bimetallic surfaces. Phys Chem Chem Phys 5:4242–4251
98. Chen YX, Ye S, Heinen M, Jusys Z, Osawa M, Behm RJ (2006) Application of in-situ attenuated total reflection-fourier transform infrared spectroscopy for the understanding of

complex reaction mechanism and kinetics: formic acid oxidation on a Pt film electrode at elevated temperatures. J Chem Phys B 110:9534–9544

99. Samjeske G, Miki A, Ye S, Osawa M (2006) Mechanistic study of electrocatalytic oxidation of formic acid at platinum in acidic solution by time-resolved surface-enhanced infrared absorption spectroscopy. J Chem Phys B 110:16559–16566
100. Bard AJ, Faulkner LR (2006) Electrochemical methods: fundamentals and applications. Wiley, New York
101. Miki A, Ye S, Senzaki T, Osawa M (2004) Surface-enhanced infrared study of catalytic electrooxidation of formaldehyde, methyl formate, and dimethoxymethane on platinum electrodes in acidic solution. J Electroanal Chem 563:23–31

Chapter 4
Recent Advances in Electrocatalysis of Formic Acid Oxidation

Cynthia Ann Rice, Akshay Bauskar, and Peter G. Pickup

Abstract Direct formic acid fuel cells offer an alternative power source for portable power devices. They are currently limited by unsustainable anode catalyst activity, due to accumulation of reaction intermediate surface poisons. Advanced electrocatalysts are sought to exclusively promote the direct dehydrogenation pathway. Combination and structure of bimetallic catalysts have been found to enhance the direct pathway by either an electronic or steric mechanism that promotes formic acid adsorption to the catalyst surface in the CH-down orientation. Catalyst supports have been shown to favorably impact activity through either enhanced dispersion, electronic, or atomic structure effects.

4.1 Introduction

Fundamental anode catalyst research is imperative for improved direct formic acid fuel cell (DFAFC) performance and stability; such that an intimate understanding of the interplay between structural, morphological, and physicochemical properties is needed. The primary base catalysts found to be active for formic acid electrooxidation are either platinum (Pt) or palladium (Pd). The cyclic voltammograms in Fig. 4.1 compare the activity of carbon-supported Pt to Pd towards formic acid electrooxidation. The anodic (forward) scan, relevant to DFAFC performance, is relatively inactive on Pt/C until the applied potential

---

C.A. Rice (✉) • A. Bauskar
The Center for Manufacturing Research, Department of Chemical Engineering, Tennessee Tech University, Cookeville, TN 38505, USA
e-mail: criceyork@tntech.edu

P.G. Pickup (✉)
Chemistry Department, Memorial University, St. John’s, NL, Canada A1B 3X7,
e-mail: ppickup@mun.ca

M. Shao (ed.), *Electrocatalysis in Fuel Cells*, Lecture Notes in Energy 9,
DOI 10.1007/978-1-4471-4911-8_4, © Springer-Verlag London 2013

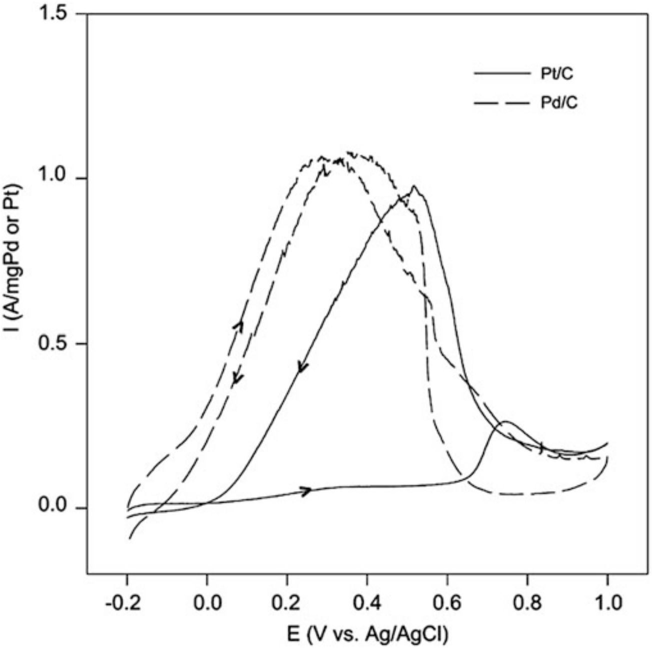

Fig. 4.1 Cyclic voltammograms on Pt(4 nm)/C and Pd(5 nm)/C in 3 M formic acid and 1 M H_2SO_4 at 10 mV s^{-1} [101]

exceeds 0.8 V vs. RHE (ca. 0.6 V vs. Ag/AgCl), due to the dominance of the indirect dehydration pathway [(3.2) in Chap. 3]. Conversely, on the Pd/C catalyst, large currents are immediately observed at very low potentials, because initially the reaction on a Pd surface is almost exclusively by the nonpoison-forming direct dehydrogenation pathway [(3.1) in Chap. 3].

The reason for Pd's enhanced activity is due to the breakage of the H–COOH bond by adsorption in the CH-down orientation, while Pt promotes the breakage of the HC(O)–OH bond by adsorption in the CH-up orientation [1–4]. Although Pd is significantly more active than Pt, it lacks sustained high performance. Pd has the propensity to generate intermediate species that slowly stifle the direct pathway [5–8], as well as to lose active area due to Pd dissolution in an acid environment [9, 10]. Research and development activities for advanced anode catalysts for DFAFCs are driven by the need for increased activity, sustained activity during long-term operation of the cell, and reduced cost. To that end secondary metals have been incorporated into the Pt- or Pd-based catalyst. Table 4.1 enumerates several precious and non-precious metals that have been investigated in combination with either Pt or Pd [11]. Group III elements have a distinct cost advantage over Groups I and II. Since none of these have completely eliminated the activity loss for Pd-based (Pt-free) catalysts, and some (notably Bi, Pb, and Sb) result in greatly enhanced and stable performances for Pt-based catalysts, there is substantial activity in the further

Table 4.1 Groupings of secondary metals having been incorporated into Pt- or Pd-based anode catalysts for formic acid electrooxidation (adapted from [11])

	Elements	Classification	Remarks
Group I	Au, Ir, Pd, Pt, Ru	Precious metals	Enhancement of Pt
Group II	Cr, Cu, Fe, Mo, Nb, V	Transition non-precious metals	Thermodynamic properties
Group III	Bi, Pb, Sb, Sn	Post-transition metals	Reduced cost

development of both of these types of catalyst. In the case of Pt-based catalysts, the focus is now on the development of supported, low Pt loading catalysts (e.g., Pt on carbon; Pt/C), and the search for novel support materials that increase activity [12, 13].

Catalyst activity towards formic acid electrooxidation is strongly influenced by preparation method and nanoparticle size. As discussed in the previous chapter, the optimal sizes for Pt/C and Pd/C are 4 nm and 5.2–6.5 nm, as determined by Park et al. [14] and Zhou et al. [15], respectively. This chapter is segregated into two sections: bimetallic catalysts and catalyst supports. The section on bimetallic catalysts is subdivided into adatoms, alloys, and intermetallics.

4.2 Bimetallic Catalysts

The goal of the addition of a secondary metal is to enhance activity and/or stability. Adatoms are adsorbed onto preformed catalyst surfaces. While for both alloys and intermetallics, the composition of a base metal (typically Pt or Pd) is altered by the addition of a secondary metal as part of the preparation procedure. The key difference between the two is that alloys are characterized by a random mixture of at least two metallic solid solution phases, while intermetallics are defined as ordered solid solution phases with fixed stoichiometry and identical atomic unit cells. The resulting intermetallics have uniform geometries, resulting in control of the electronic environment [16].

4.2.1 Adatoms

A common method for improving formic acid electrooxidation activity is through the incorporation of foreign adatoms in sub- or monolayer coverages onto metal electrocatalyst surfaces (substrates). Adatoms are usually deposited onto the metal surface either by under potential deposition (UPD) or by irreversible adsorption [17]. The two dominant reaction enhancement mechanisms for the direct dehydrogenation pathway, as described in Sect. 3.3 of the previous chapter for formic acid electrooxidation, are the third-body and electronic effects. The type of enhancement mechanism due to adatom addition is dependent on the substrate/adatom

Table 4.2 Activity of Pt(111) adatom electrodes, from anodic portion of cyclic voltammogram in 0.25 M formic acid and 0.5 M H_2SO_4 (except Te in 0.1 M formic acid) at 50 mV s^{-1}

Adatom on Pt(111)	Optimal coverage (θ)	I at 0.4 V (mA cm^{-2})	Anodic peak E (V)	Anodic peak I (mA cm^{-2})	Primary enhancement mechanism	References
Pure	n/a	0.57	0.53	1.12		[20]
Se	0.28	0.1	0.71	3.4	Third body	[39]
As	0.31	0.35	0.54	4.6	Electronic	[35]
Te	0.3	0.9	0.75	6.2	Electronic	[38]
Pd	0.28	1.5	0.50	2	Third body	[5]
Pd/Pt(100)	0.7	14	0.22	55	Electronic	[5]
Bi	0.82	15.5	0.495	35	Electronic	[20]

Potentials (E) vs. RHE and current (I)

configuration and/or electronic interaction. Results in the literature suggest that both effects promote the adsorption of formic acid in the CH-down direction which is a predetermining factor for the direct reaction pathway [2–4].

The most commonly investigated substrates have been Pt and Pd, ranging from well-defined single-crystal surfaces to nanoparticles. Bismuth (Bi) has been the most extensively tested adatom [18–28]. Other adatoms that have also exhibited performance enhancements are lead (Pb) [29–31], antimony (Sb) [2, 22, 29, 32, 33], arsenic (As) [34, 35], gold (Au) [36], tellurium (Te) [37, 38], selenium (Se) [39], ruthenium (Ru) [40], and palladium (Pd) [5, 40, 41]. Researchers have seen that, for the various adatoms, higher coverages promote the direct reaction pathway.

4.2.1.1 Single-Crystal Surfaces

To illustrate the primary effects of adatom addition, single-crystal electrodes are discussed here. Feliu and Herrero have extensively studied formic acid electrooxidation on Pt single-crystal substrates modified with an array of various adatoms. They have established a connection between the electronegativity of the adatoms in relation to Pt and the type of active enhancement mechanism incurred as a function of adatom coverage [42]. Their results support inhibition of the indirect pathway on Pt(111) terraces and they have demonstrated that CO_{ads} formation occurs at step and defect sites. For Pt(111) substrates decorated with electropositive adatoms, such as Bi, Pb, Sb, and Te, the electronic enhancement is extended to the second or third Pt atom shell from the adatom. While for electronegative adatoms, in respect to Pt, the third-body effect dominates with increased coverages, such as S and Se.

Table 4.2 highlights the extensive work done in Feliu's group on adatom-decorated Pt(111) substrates—specifically Se, As, Te, Pd, and Bi. Cyclic voltammogram results are compared for the first forward sweep in 0.25 M formic acid and 0.5 M H_2SO_4 at 50 mV s^{-1} vs. RHE. Two distinct phenomena can be differentiated based on their results: (a) formic acid electrooxidation activity at low overpotentials and (b) the amount of surface poison. For Se, As, and Te, the optimal coverage was found to be around 0.3. Coverages in excess of 0.3 for these adatoms resulted in a decrease in overall performance. We have selected a potential of 0.4 V to evaluate fuel cell relevant anode catalyst activity, where the indirect dehydration pathway does not significantly contribute to the current density. At 0.4 V for these three modifiers, an increase in current density over the Pt(111) baseline was observed only for Te, while for Se and As the current density decreased. The peak current density with these modifiers was observed above 0.5 V and higher than that of the Pt(111) baseline. To evaluate the extent of poison formation as a function of adatom coverage, the electrodes were held at 0.1 V for an extended period of time in formic acid containing electrolyte, after which the solution was exchanged with pure electrolyte and a cyclic voltammogram was initiated to strip off CO_{ads}. Formic acid dissociation to CO_{ads} was found to only occur on the Pt substrate, thus the adatoms do not directly participate in the reaction. The CO_{ads} on Se-decorated surfaces decreased linearly with increasing adatom coverages, consistence with a primarily third-body effect, i.e., higher coverages are required to induce steric inhibition of the CH-up adsorption in the indirect pathway [43]. Conversely Te follows the trend of an electronic effect promoting CH-down adsorption for the direct pathway up to 6–8 Pt atom away from the adatom. For As-decorated surfaces, the magnitude of the electronic effect is diminished by adatom desorption at open-circuit potentials in the presence of formic acid, as is also found for Sn- and Pb-decorated Pt surfaces [42].

For Pd- and Bi-decorated surfaces, higher coverages resulted in enhanced performances. For $\theta_{Pd} = 0.28$, the observed current density at 0.4 V was nearly three times that of the Pt(111) baseline, but there was only marginal improvement at the peak potential which was only slightly lower than at pure Pt. In comparison, Bi has an optimal coverage at 0.82 with a 27 times increase in activity at 0.4 V relative to Pt. The CO_{ads} stripping coverage dependence followed the linear decrease characteristic of a third-body effect for Pd on Pt(111) (albeit at a steeper slope than Sb), while Bi produced an exponential decrease consistent with an electronic enhancement. The optimal coverage of Pd increased to 0.7 on Pt(110) and the current density at 0.4 V was comparable to that of the optimal Bi-modified surface. The key difference for the Pd/Pt(100) combination is that the maximum peak potential is shifted to 0.22 V with a current density of 55 mA cm^{-2}.

4.2.1.2 Nanoparticles

The driving force for small nanoparticle catalysts is reduced cost by minimizing inactive non-surface atoms, which is the basis of most low Pt approaches. Yu and Pickup investigated the coverage dependence of Pb and Sb on commercial 40 wt% Pt supported on carbon in situ in a formic acid/O_2 fuel cell [29]. They found optimal coverages of 0.7 for both types of adatoms. The performance of both PtSb/C and PtPb/C far exceeded that of Pt/C. After nearly a 2 h hold at 0.6 V under fuel cell operation, the performance increase over Pt/C was 15- and 12.8-fold, respectively. Figure 4.2 is a comparison of fuel cell performance at 0.6 V as a function of adatom

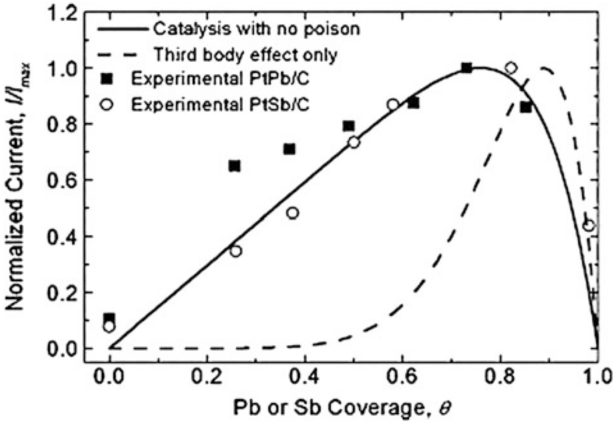

Fig. 4.2 Plot of direct formic acid fuel cell performance at 0.6 V for Pt/C anodes as a function of Pb and Sb adatom coverages. The experimental data is compared to the two formic acid electrooxidation models proposed by Leiva: (*solid line*) electronic enhancement and (*dashed line*) third-body effect [29]

coverage. This cell voltage corresponds to a relatively low anode overpotential in a region where the direct pathway would exclusively contribute to the measured power density. The results are compared to the model developed by Leiva et al. [44] for the two dominant formic acid electrooxidation enhancement mechanisms—third body (dashed line) vs. electronic (solid line). The results follow the trend line for an electronic enhancement, whereas Leiva et al. [44] reported that increasing the coverage of Sb on a Pt(100) single crystal displayed a third-body enhancement effect (Fig. 3.7 in Chap. 3). The divergence in dominant enhancement mechanism for an Sb-decorated Pt substrate is potentially twofold: (a) the facet structure of the Pt substrate and/or (b) the dispersion of the Sb. The Pt/C nanoparticles used in Yu and Pickup's work were 2.5 nm in diameter, possessing typical cuboctahedral features depicted in Fig. 4.3 with fractal Pt(111) and Pt(110) contiguous terraces and an abundance of low coordination corners and edges. Also, their decoration method was via chemical deposition as opposed to under potential deposition, which may produce an alternative more active adatom dispersion on a per Pt basis, in comparison to that prepared by Lee et al. by UPD [33].

Wieckowski's group has studied formic acid electrooxidation on Pt nanoparticles decorated with controlled amounts of Pd and Pd+Ru adatoms [41]. They reported two orders of magnitude increase in the reactivity of the Pd-decorated catalyst compared to pure Pt towards formic acid oxidation. Also, it was concluded that the impact of CO_{ads} on the Pt/Pd catalyst through the dual pathway mechanism is much lower even though the potential required to remove CO_{ads} from the surface was the highest.

Bi et al. boosted the performance of Pt nanoparticles towards formic acid electrooxidation by depositing sub-monolayer Au clusters [36]. The modified Pt nanoparticles exhibited a 23-fold increase in specific activity. This enhancement in

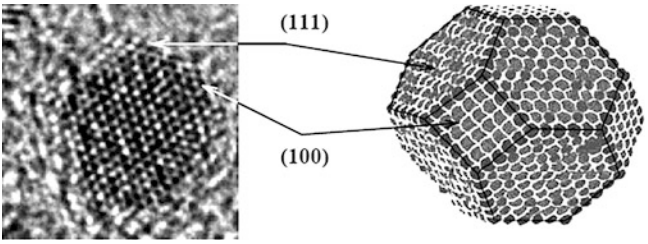

Fig. 4.3 (*Left*) High-resolution TEM image of a Pt/C nanoparticle. (*Right*) Pictorial proposed representation of the cuboctahedral Pt nanoparticle, with Pt(111)- and Pt(100)-faceted terraces identified [102]

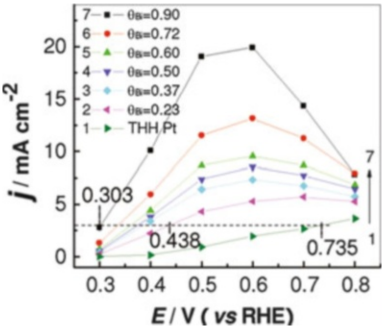

Fig. 4.4 Current density at 60 s after transient potential holds on 81 nm tetrahexahedral (THH) Pt nanoparticles as a function of Bi coverage. The dashed line is for a 3 mA cm^{-2} performance target [18]

catalytic activity was attributed to the inhibition of the indirect reaction pathway by the third-body effect.

Bismuth has attracted significant interest as a Pt/C modifier for formic acid electrooxidation [21, 24, 26, 27]. A wide range of stable and well-characterized electrode surfaces modified by irreversible Bi adatom adsorption on Pt have been reported in the literature for a range of Bi coverages (θ). Chen et al. have explored Bi adatom decoration on 81 nm tetrahexahedral Pt nanoparticles that while composed of (100) and (110) facets that are the least active for formic acid electrooxidation, they are bound by {730} and vicinal high-index facets that are extremely active [18]. They have measured current densities of 10 mA cm^{-2} for Bi coverages up to 0.9 at 0.4 V in 0.25 M formic acid and 0.5 M H_2SO_4 solution; see Fig. 4.4. They also showed steady-state activity at 0.3 V of 2.8 mA cm^{-2} after 1 min vs. 0.0003 mA cm^{-2} for the non-modified Pt baseline.

Kim et al. [24] reported a detailed analysis on formic acid electrooxidation on 3 nm Pt/C modified by irreversible adsorption of Bi. They ascribed the enhancement in catalytic activity to promotion of the direct pathway, which is dependent on the oxidation state and coverage of the Bi. For Bi coverage on Pt above 0.54, the oxidation rate of formic acid increased by a factor of 8. The amounts of CO and

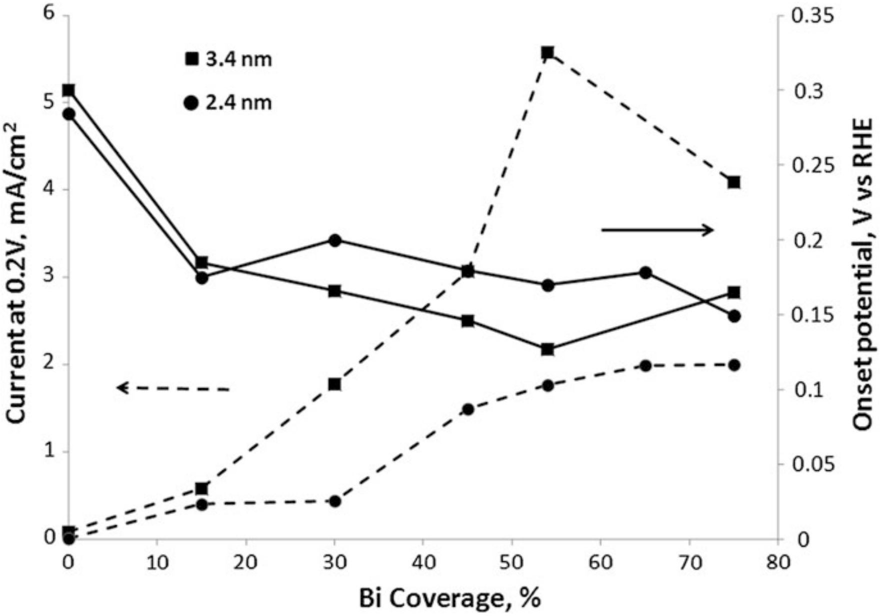

Fig. 4.5 Anodic current density acquired during a cyclic voltammogram at 0.2 V vs. RHE for 3.4 nm and 2.4 nm Pt/C as a function of Bi coverage, in 0.1 M formic acid and 0.1 M $HClO_4$. Onset potential for formic acid electrooxidation of Bi-modified Pt electrodes (unpublished work from Rice's group)

poison were proportional to Bi coverage with a negative slope indicating the blocking of Pt sites by Bi for CO adsorption thereby impeding the dehydration pathway predominantly by the third-body enhancement effect. At a θ_{Bi} of 0.75, the anodic current density at 0.55 V vs. RHE was around 4.5 mA cm^{-2} after a 33 min hold, demonstrating an eightfold increase over the Pt baseline.

Bauskar and Rice have recently investigated an alternative method of adsorbing adatoms onto Pt/C substrates using a solution surface potential method amenable to mass scale-up [28]. Figure 4.5 tracks the change in formic acid electrooxidation current at 0.2 V vs. RHE as a function of Bi coverage for two commercial Pt/C nanoparticle sizes (2.4 nm and 3.4 nm). The performance is compared on a specific surface area basis to limit undesirable mass activity effects. The larger nanoparticles exhibit higher per surface atom activity at Bi coverages above 0.15. The initial rise in activity of the 3.4 nm Pt/C with Bi coverages up to 0.45 is indicative of an electronic enhancement, while the jump at around 0.54 would suggest a coverage-dependent shift in the dominant enhancement mechanism to third body. In contrast the activity-coverage-dependent features of the 2.4 nm Pt/C lack strong characteristics of either mechanism. Onset potentials for the unmodified Pt/C nanoparticles are similar, although slightly less for the 2.4 nm than 3.4 nm particles. Upon adsorption of 0.15 of a layer of Bi, the onset potential drops by nearly 0.11 V for both nanoparticle sizes, from 0.3 V to less than 0.2 V. Subsequent increases in Bi coverage induce a slight additional decrease in the onset potential to around 0.15 V. Similar studies on Bi-modified mesoporous platinum microelectrodes resulted in a 0.15 V lower onset potential with respect to an unmodified mesoporous platinum microelectrode [21].

Scale-up for mass production can also potentially be achieved by reductive chemical deposition of metals such as Bi [27], Pb [29], and Sb [29] onto preformed Pt/C. For Bi, it was found that optimum performance occurred at very low surface coverage (ca. 0.15), which is not consistent with the third body or electronic enhancement models that work with other Bi on Pt catalysts or Pt/C modified with Sb and Pb in the same way [27]. However, it is consistent with observations that a Bi coverage as low as 0.04 can suppress CO formation on Pt(111) [34, 42]. These observations highlight the sensitivity of the enhancement mechanism to the way in which adatoms are deposited on the Pt surface, as well as possible differences in the structures of the modified Pt particles.

4.2.2 Alloys

In keeping with the focus of this book, “A Non and Low Platinum Approach,” we have elected to restrict our discussion of recent catalyst advances here to either carbon-supported Pt or non-Pt-containing alloyed catalysts. The interested reader is directed to the following papers and review articles [45] on unsupported Pt alloys: PtHg [46], PtCd [46], PtCu [47], PtTi [48], and PtFe/Au [49]. To reduce cost, the reduction in the relative amounts Pt and Pd is desirable while approaching or exceeding the initial activity of Pd.

Pt/C-based—The introduction of a second metal to Pt has resulted in performance increases in a number of cases. For carbon-supported lead (Pb) alloyed with Pt (PtPb/C) in a nearly 1:1 atomic ratio, Huang et al. showed that for a 5.9 nm average PtPb particle size the anodic performance increased 74-fold over commercial Pt/C at 0.4 V vs. RHE [50, 51]. Unfortunately, the magnitude of the initial enhancement was not maintained under chronoamperometric testing; within the first few seconds of the hold, there was a substantial decrease in performance and after holding for only 30 min the performance difference to that of Pt/C was less than threefold.

Obradovic et al. investigated two different PtAu/C preparation methods [52]. They observed a 39-fold increase in activity at 0.4 V vs. RHE for a PtAu-modified Au(18.3 nm)/C core over the Pt(2.5 nm)/C baseline. The performance enhancement was only transitory, resulting in a rapid loss in performance. Chen et al. synthesized a systematic series of Pt_xAu_{x-1}/C alloys with sizes ranging from 4.5 to 5.5 nm. For the 1:1 Pt to Au alloy ($Pt_{0.5}Au_{0.5}/C$) at 0.1 V vs. SCE (0.344 V vs. RHE), an 8.8-fold improvement was observed over Pt/C [53]. The activities of both catalysts decayed at similar rates, but after 30 min the $Pt_{0.5}Au_{0.5}/C$ was able to maintain a 9.2-fold improvement.

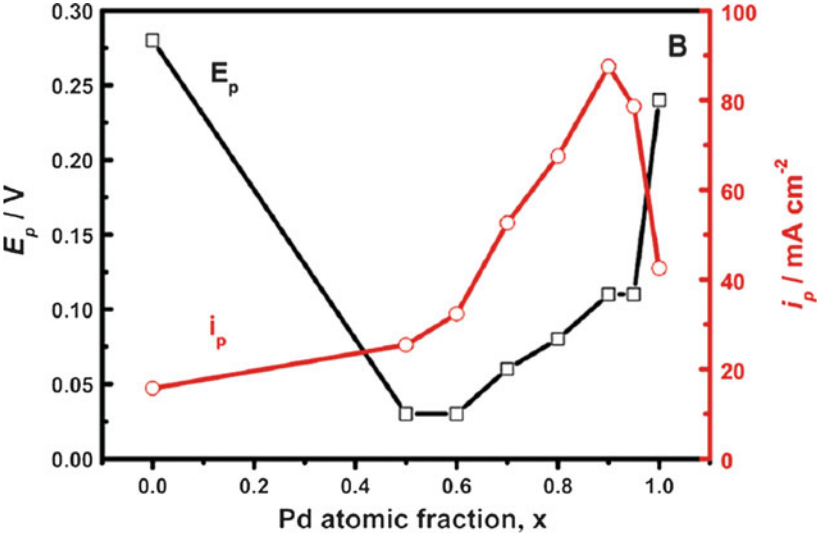

Fig. 4.6 Maximum anodic peak potential (E_p) vs. SCE (0.244 V vs. RHE) and peak current density (I_p) acquired during a cyclic voltammogram at 50 mV s^{-1}for Pd_xPt_{1-x}/C atomic fractions, in 0.5 M formic acid and 0.5 M H_2SO_4 [55]

Carbon-supported PtSb alloy catalysts have been shown to provide high and stable performances for formic oxidation in DFAFCs over 2 h periods [54]. Optimum performances were obtained for 1.8 nm particles with a 0.29 mol fraction of Sb.

Several groups have explored replacing a fraction of Pt with less expensive Pd [55–57]. Zhang et al. have systematically prepared and evaluate Pd_xPt_{1-x}/C, with atomic fractions of $x = 0.5$–1 for a narrow size distribution of 3.2–3.8 nm and compared their performances to Pt/C, as shown in Fig. 4.6 [55]. Pt/C was the least active in regard to peak potential (E_p) and peak current density (I_p). The lowest Pd content tested was $Pd_{0.5}Pt_{0.5}/C$, which resulted in a favorable 0.25 V decrease in anodic peak potential (E_p) with a slight increase in current density (I_p). As the Pd fraction was increased, E_p trended back towards the value for Pt, but I_p continued to increase, reaching a maximum for $Pd_{0.9}Pt_{0.1}/C$. For this composition, the current was 5.9- and 2.1-fold higher relative to Pt/C and Pd/C, respectively.

An attempt to produce PtBi alloy nanoparticles on carbon produced highly active catalysts for formic acid oxidation, although XRD showed no evidence of alloy formation [27]. Highest performances were obtained with a Bi:Pt mole ratio of just 0.07.

Pd/C-based—Metals, metalloids, and nonmetals have been alloyed with Pd in order to increase its activity and/or prevent or minimize its activity decay during formic acid oxidation. Increases in activity with boron (B) [58] and phosphorous (P) [59–61] have been attributed to a reduction in the 3d electron density and an increase

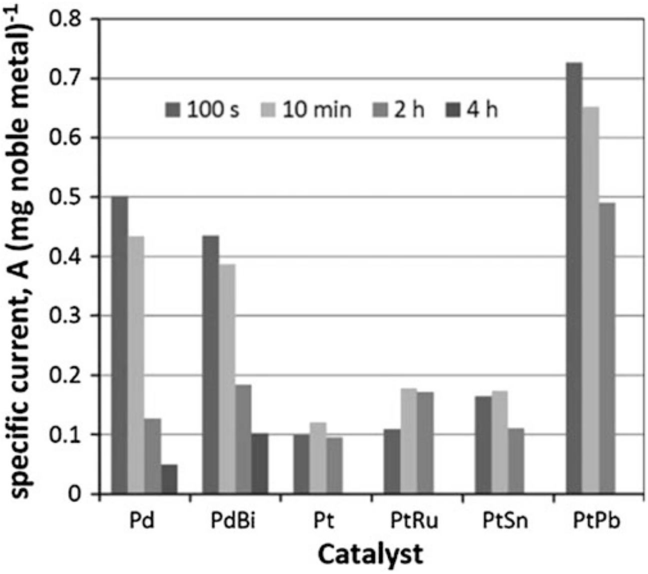

Fig. 4.7 Specific current acquired from DFAFC chronoamperometric holds at 0.3 V for selected catalyst combinations, 5 M formic acid at 0.2 ml min^{-1} and O_2 at 100 ml min^{-1} on the anode and cathode, respectively. Alloys—PdBi(4:1)/C and PtRu(1:1)/C. Adatoms—PtSn(8:1)/C and PtPb (8:1)/C [71]

in the percentage of metallic Pd [59]. The increases in activity were modest, between 1.3 and 1.9 times, while decay rates during potential holds were similar to those for unmodified Pd/C, albeit at higher current density values.

Several research groups have explored the addition of cobalt (Co) to Pd [62–66]. Wang et al. found that the addition of a third metal (iridium (Ir)) to a PdCo/C catalyst resulted in further enhanced activity [65]. At 0.294 V vs. RHE (0.05 V vs. SCE), the current density increases were 1.5- and 2.5-fold for Pd_2Co/C and Pd_4Co_2Ir/C, respectively, over that of Pd/C. The stabilities of the catalysts were evaluated at 0.344 V vs. RHE (0.10 V vs. SCE) and after a 16.7 min hold the Pd_4Co_2Ir/C current density was 18.4 times that of Pd/C, however, with a continued decreasing slope.

Tin (Sn)/Pd carbon-supported alloys have shown enhanced activity and stability [67–71]. Although Sn is completely inactive towards formic acid electrooxidation, a decrease in the 3d electronic density has been observed. An atomic ratio of Sn to Pd of 1:1 resulted in the highest overall performance for particles of similar sizes [69, 70]. For the aforementioned PdSn/C results, the current density increased 2- to 2.3-fold at 0.4 V vs. RHE. During constant potential holds, the Pd/C has a continued decrease, while the PdSn/C alloys stabilize after 500 s [70].

Alloying bismuth (Bi) with Pd/C has resulted in a slight decrease in performance but an increase in stability during a constant DFAFC operation at 0.3 V (Fig. 4.7) [71]. Unfortunately after 2 h of continued operation, the performance of PdBi/C

Table 4.3 Activity of extended surface intermetallics, from anodic portion of cyclic voltammogram in 0.125 M formic acid and 0.1 M $HClO_4$ (except Pt_3Sn and PtSb in 0.25 M formic acid) at 10 mV s^{-1}

Electrode	Onset *E* (V)	Anode peak *E* (V)	Anode peak *I* (mA cm^{-1})
Pt	0.317	0.847	0.5
PtBi	0.357	0.752	3.8
PtIn	0.247	0.697	0.93
Pt_3Sn	0.297	0.577	0.35
Pt_2Sn_3		0.627	0.02
PtSb	0.197	0.457	0.1

Potentials (*E*) vs. RHE and current (*I*) (modified from [16])

approached that of Pt/C, while a PtRu/C catalyst had improved activity. The last two catalysts included in Fig. 4.7 are for Sn and Pb adatom-decorated Pt/C, for which Sn only minimally increased activity and Pb had a significant impact, exceeding the performance of Pd with much better performance stability.

4.2.3 Intermetallics

Transformation of alloys into ordered intermetallics through various thermal treatments results in a tuning mechanism of the structural, geometric, and electronic character of the catalyst. The inner atomic bond distances are altered with the addition of a secondary metal.

The DiSalvo group at Cornell University has intensely studied intermetallics for formic acid electrooxidation and observed significant enhancements in turnover efficiencies [16, 46, 72–79]. Table 4.3 compares the activity of several extended intermetallic surfaces in comparison to a Pt baseline [16]. The onset potential relevant to enhanced reactivity through the direct dehydrogenation pathway was most impacted by the addition of Sb. The introduction of both Sn and Sb into the Pt unit cell negatively impacted the anodic peak current. While Bi increased the peak current, it had an adverse impact on the onset potential. It increased the onset potential by 0.06 V and nearly doubled the peak current. The key challenges related to intermetallics for DFAFCs are surfactant-free synthesis methods and reduced nanoparticle sizes (>10 nm) to improve mass activity of the catalyst [74, 75, 80]. Mastumoto et al. compared the mass activity of PtPb 10–20 nm intermetallic particles to a commercial nanocatalyst [79]. During a 9 h hold at 0.197 V vs. RHE, the PtPb intermetallic catalyst demonstrated over a twofold sustained mass activity over that of Pd.

4.3 Catalyst Supports

There have been a number of recent reviews of supports for fuel cell catalysts [12, 13, 81]. Although these focus on oxygen reduction and methanol oxidation, they provide an excellent overview of the breadth of support materials that are available, mechanistic information, and include some examples for formic acid oxidation. Various types of high surface area carbons have been most commonly used as supports for formic acid oxidation catalysts. However, there is now growing interest in the use of various metals, metal oxides, and conducting polymers.

Several studies have been performed on alternative extended carbon support structures: Pd/graphite rods [82], Pd/nanotubes [83], and Pd/nanofibers [84]. However, it is difficult to distinguish between catalyst size and atomic structure differences. Zhang et al. attributed the performance enhancements to an increase in the relative abundance of the more active Pd(111) facet [82].

Iridium alloyed on Pt has been tested on different supports: Pt_xIr_{1-x}/Au [85] and PtIr/Ti [86]. Chen and Chen have demonstrated an initial performance increase for $Pt_{0.5}Ir_{0.5}$/Au, with an average particle size of 2 nm, of 9.4-fold at 0.459 V vs. RHE [85]. Unfortunately, the performance decayed quickly and within 30 min had decreased to a value only twofold higher than that of Pt/C. NanoPtSn/Ti surfaces were prepared resulting in cyclic voltammetric profiles similar to Pt/C [87]. For the aforementioned results, it is difficult to decouple the impacts of metal–support interactions.

The most widely studied conducting polymer support is polyaniline (PANI), which has been shown to decrease the poisoning of Pt by CO_{ads} [88]. Gharibi et al. have recently explored the factors responsible for the enhanced formic acid oxidation activity of Pt supported on a carbon/PANI composite [89]. They concluded that improvements in both electron and proton conductivities, as well as the increased methanol diffusion coefficient and decreased catalyst poisoning, could be involved. A carbon nanotubes/PANI composite [90], poly(*o*-methoxyaniline) [91], and polyindole [92] have recently been reported as effective supports for formic acid oxidation at Pt nanoparticles, while polycarbazole [93] has also been used to support PtRu nanoparticles.

Because of its lower cost relative to Pt, there is growing interest in the development of supported Pd catalysts for formic acid oxidation. Synergies between Pd and PANI supports are well documented [94], while poly(diphenylamine-co-3-aminobenzonitrile) [95] has recently been shown to provide enhanced and more stable activities. Addition of 3-aminobenzonitrile to poly(diphenylamine) was found to improve the dispersion of the Pd, while both polymers eliminated the current decay seen over 1 h for carbon supported Pd.

Pb oxide [96], W oxide [97, 98], and Ce oxide [99] have been shown to notably promote formic acid oxidation at Pt and/or Pd. In the case of Pb oxide, a Pd-Pt-PbO_x/C catalyst was shown to be less susceptible to poisoning than Pd/C, exhibiting a superior performance after ca. 800 s at 0.15 V vs. Ag/AgCl [100].

4.4 Conclusions

Considerable progress has been made in the development of supported Pt-based catalysts for formic acid oxidation, with a variety of Pt alloy, intermetallic, and surface-modified catalysts showing impressive increases in performance relative to Pt/C. The use of Au, Bi, Pb, or Sb as the second metal has been shown to be particularly beneficial, although it is not clear yet whether any of these metals combined with Pt will provide sufficient long-term durability, nor which type of modification of the Pt structure (alloy, intermetallic, or surface modified) is most suitable.

The high cost of Pt continues to be a significant issue. This has been partially addressed by the use of a variety of supports, which allow better dispersion of the Pt in small particles (1–4 nm) with high area/mass ratios. Replacement of a significant fraction of the Pt with a second metal is also an effective way of decreasing the required loading of Pt, as in $Pd_{0.9}Pt_{0.1}/C$, $Pt_{0.5}Au_{0.5}/C$, and the PtPb and PtSb intermetallics.

Improvements in Pd-based catalysts have been modest in comparison with the advances in Pt-based catalysts, although this needs to be considered in the context of the far superior activity of pure Pd over pure Pt. Slow loss of activity, over a period of hours, remains a problem for all Pd-based catalysts, to the point where Pt-based catalysts provide better performances over long time periods.

Future advances in the catalysis of formic acid oxidation will benefit from further development of our understanding of the fundamental processes involved via single crystal and computational studies. Refinement of synthesis methods to produce nanoparticles with the most active and durable geometries and structures will allow fine-tuning of catalysts. Continued discovery of support effects and advances in the understanding of such effects will create additional opportunities to improve performances, lower costs, and enhance durability.

References

1. Arenz M, Stamenkovic V, Schmidt TJ, Wandelt K, Ross PN, Markovic NM (2003) The electro-oxidation of formic acid on Pt–Pd single crystal bimetallic surfaces. Phys Chem Chem Phys 5:4242–4251
2. Peng B, Wang H-F, Liu Z-P, Cai W-B (2010) Combined surface-enhanced infrared spectroscopy and first-principles study on electro-oxidation of formic acid at Sb-modified Pt electrodes. J Phys Chem C 114:3102–3107
3. Wang H-F, Liu Z-P (2009) Formic acid oxidation at Pt/H_2O interface from periodic DFT calculations integrated with a continuum solvation model. J Phys Chem C 113:17502–17508
4. Luo Q, Feng G, Beller M, Jiao H (2012) Formic acid dehydrogenation on Ni(111) and comparison with Pd(111) and Pt(111). J Phys Chem C 116:4149–4156
5. Llorca MJ, Feliu JM, Aldaz A, Clavilier J (1994) Formic acid oxidation on Pdad + Pt(100) and Pdad + Pt(111) electrodes. J Electroanal Chem 376:151–160

6. Babu PK, Kim HS, Chung JH, Oldfield E, Wieckowski A (2004) Bonding and motional aspects of CO adsorbed on the surface of Pt nanoparticles decorated with Pd. J Phys Chem B 108:20228–20232
7. Baldauf M, Kolb DM (1996) Formic acid oxidation on ultrathin Pd films on Au(hlk) and Pt (hkl) electrodes. J Phys Chem 100:11375–11381
8. Pan Y, Zhang R, Blair SL (2009) Anode poisoning study in direct formic acid fuel cells. Electrochem Solid St Lett 12:B23–B26
9. Solla-Gullon J, Montiel V, Aldaz A, Clavilier J (2002) Electrochemical and electrocatalytic behavior of platinum–palladium nanoparticle alloys. Electrochem Commun 4:716–721
10. Hartley FR (1991) The occurrence, extraction, properties and uses of the platinum group metals in studies in inorganic chemistry. In: Hartley FR (ed) Chemistry of the platinum group metals: recent developments, vol 11. Elsevier, Amsterdam, p 642
11. Uhm S, Lee HJ, Lee J (2009) Understanding underlying processes in formic acid fuel cells. Phys Chem Chem Phys 11:9326–9336
12. Wang Y-J, Wilkinson DP, Zhang J (2011) Non-carbon support materials for polymer electrolyte membrane fuel cell electrocatalysts. Chem Rev 111:7625–7651
13. Sharma S, Pollet BG (2012) Support materials for PEMFC and DMFC electrocatalysts-A review. J Power Sources 208:96–119
14. Park S, Xie Y, Weaver MJ (2002) Electrocatalytic pathways on carbon-supported platinum nanoparticles: comparison of particle-size-dependent rates of methanol, formic acid, and formaldehyde electrooxidation. Langmuir 18:5792–5798
15. Zhou WP, Lewera A, Larsen R, Masel RI, Bagus PS, Wieckowski A (2006) Size effects in electronic and catalytic properties of unsupported palladium nanoparticles in electrooxidation of formic acid. J Phys Chem B 110:13393–13398
16. Casado-Rivera E, Volpe DJ, Alden L, Lind C, Downie C, Vazquez-Alvarez T, Angelo ACD, DiSalvo FJ, Abruna HD (2004) Electrocatalytic activity of ordered intermetallic phases for fuel cell applications. J Am Chem Soc 126:4043–4049
17. Parsons R, VanderNoot T (1988) The oxidation of small organic molecules: a survey of recent fuel cell related research. J Electroanal Chem Interfacial Electrochem 257:9–45
18. Chen Q-S, Zhou Z-Y, Vidal-Iglesias FJ, Solla-Gullon J, Feliu JM, Sun S-G (2011) Significantly enhancing catalytic activity of tetrahexahedral Pt nanocrystals by Bi adatom decoration. J Am Chem Soc 133:12930–12933
19. Clavilier J, Femandez-Vega A, Feliu JM, Aldaz A (1989) Heterogeneous electrocatalysis on well-defined platinum surfaces modified by controlled amounts of irreversibly adsorbed adatoms: Part III. Formic acid oxidation on the Pt (100)–Bi system. J Electroanal Chem Interfacial Electrochem 261:113–125
20. Clavilier J, Fernandez-Vega A, Feliu JM, Aldaz A (1989) Heterogeneous electrocatalysis on well defined platinum surfaces modified by controlled amounts of irreversibly adsorbed adatoms: Part I. Formic acid oxidation on the Pt (111)–Bi system. J Electroanal Chem Interfacial Electrochem 258:89–100
21. Daniele S, Bergamin S (2007) Preparation and voltammetric characterisation of bismuth-modified mesoporous platinum microelectrodes. Application to the electrooxidation of formic acid. Electrochem Commun 9:1388–1393
22. Herrero E, Feliu JM, Aldaz A (1994) Poison formation reaction from formic acid on Pt(100) electrodes modified by irreversibly adsorbed bismuth and antimony. J Electroanal Chem 368:101–108
23. Kang S, Lee J, Lee JK, Chung S-Y, Tak Y (2006) Influence of Bi modification of Pt anode catalyst in direct formic acid fuel cells. J Phys Chem B 110:7270–7274
24. Kim B-J, Kwon K, Rhee CK, Han J, Lim T-H (2008) Modification of Pt nanoelectrodes dispersed on carbon support using irreversible adsorption of Bi to enhance formic acid oxidation. Electrochim Acta 53:7744–7750
25. Maciá MD, Herrero E, Feliu JM (2003) Formic acid oxidation on Bi–Pt(1 1 1) electrode in perchloric acid media. A kinetic study. J Electroanal Chem 554–555:25–34

26. Saez A, Exposito E, Solla-Gullon J, Montiel V, Aldaz A (2012) Bismuth-modified carbon supported Pt nanoparticles as electrocatalysts for direct formic acid fuel cells. Electrochim Acta 63:105–111
27. Yu X, Pickup PG (2011) Carbon supported PtBi catalysts for direct formic acid fuel cells. Electrochim Acta 56:4037–4043
28. Bauskar A, Rice CA (2013) Bi modified Pt/C for enhanced formic acid electro-oxidation. Electrochim Acta 93:152–157
29. Yu X, Pickup PG (2010) Pb and Sb modified Pt/C catalysts for direct formic acid fuel cells. Electrochim Acta 55:7354–7361
30. Xia XH, Iwasita T (1993) Influence of underpotential deposited lead upon the oxidation of formic acid in perchloric acid at platinum electrodes. J Electrochem Soc 140:2559–2565
31. Uhm S, Chung ST, Lee J (2007) Activity of Pt anode catalyst modified by underpotential deposited Pb in a direct formic acid fuel cell. Electrochem Commun 9:2027–2031
32. Fernandez-Vega A, Feliu JM, Aldaz A, Clavilier J (1989) Heterogeneous electrocatalysis on well defined platinum surfaces modified by controlled amounts of irreversibly adsorbed adatoms: Part II. Formic acid oxidation on the Pt (100)-Sb system. J Electroanal Chem Interfacial Electrochem 258:101–113
33. Lee JK, Jeon H, Uhm S, Lee J (2008) Influence of underpotentially deposited Sb onto Pt anode surface on the performance of direct formic acid fuel cells. Electrochim Acta 53:6089–6092
34. Herrero E, Fernández-Vega A, Feliu JM, Aldaz A (1993) Poison formation reaction from formic acid and methanol on Pt(111) electrodes modified by irreversibly adsorbed Bi and As. J Electroanal Chem 350:73–88
35. Fernandez-Vega A, Feliu JM, Aldaz A, Clavilier J (1991) Heterogeneous electrocatalysis on well-defined platinum surfaces modified by controlled amounts of irreversibly adsorbed adatoms: Part IV. Formic acid oxidation on the Pt(111)–As system. J Electroanal Chem Interfacial Electrochem 305:229–240
36. Bi X, Wang R, Ding Y (2011) Boosting the performance of Pt electro-catalysts toward formic acid electro-oxidation by depositing sub-monolayer Au clusters. Electrochim Acta 56:10039–10043
37. Herrero E, Llorca MJ, Feliu JM, Aldaz A (1995) Oxidation of formic acid on Pt(100) electrodes modified by irreversibly adsorbed tellurium. J Electroanal Chem 383:145–154
38. Herrero E, Llorca MJ, Feliu JM, Aldaz A (1995) Oxidation of formic acid on Pt(111) electrodes modified by irreversibly adsorbed tellurium. J Electroanal Chem 394:161–167
39. Llorca MJ, Herrero E, Feliu JM, Aldaz A (1994) Formic acid oxidation on Pt(111) electrodes modified by irreversibly adsorbed selenium. J Electroanal Chem 373:217–225
40. Rice C, Ha S, Masel RI, Wieckowski A (2003) Catalysts for direct formic acid fuel cells. J Power Sources 115:229–235
41. Waszczuk P, Barnard TM, Rice C, Masel RI, Wieckowski A (2002) A nanoparticle catalyst with superior activity for electrooxidation of formic acid. Electrochem Commun 4:732
42. Feliu JM, Herrero E (2010) Formic acid oxidation. In: Vielstich W, Lamm A, Gasteiger HA (eds) Handbook of fuel cells—fundamentals, technology and applications. Wiley, Chichester
43. Neurock M, Janik M, Wieckowski A (2008) A first principles comparison of the mechanism and site requirements for the electrocatalytic oxidation of methanol and formic acid over Pt. Faraday Discuss 140:363–378
44. Leiva E, Iwasita T, Herrero E, Feliu JM (1997) Effect of adatoms in the electrocatalysis of HCOOH oxidation. A theoretical model. Langmuir 13:6287–6293
45. Yu X, Pickup PG (2008) Recent advances in direct formic acid fuel cells (DFAFC). J Power Sources 182:124–132
46. Ghosh T, Zhou Q, Gregoire JM, van Dover RB, DiSalvo FJ (2010) Pt−Cd and Pt−Hg phases as high activity catalysts for methanol and formic acid oxidation. J Phys Chem C 114:12545–12553

47. Yang H, Dai L, Xu D, Fang J, Zou S (2010) Electrooxidation of methanol and formic acid on PtCu nanoparticles. Electrochim Acta 55:8000–8004
48. Abe H, Matsumoto F, Alden LR, Warren SC, Abruña HD, DiSalvo FJ (2008) Electrocatalytic performance of fuel oxidation by Pt3Ti nanoparticles. J Am Chem Soc 130:5452–5458
49. Chen W, Kim J, Sun S, Chen S (2007) Composition effects of FePt alloy nanoparticles on the electro-oxidation of formic acid. Langmuir 23:11303–11310
50. Huang Y, Zheng S, Lin X, Su L, Guo Y (2012) Microwave synthesis and electrochemical performance of a PtPb alloy catalyst for methanol and formic acid oxidation. Electrochim Acta 63:346–353
51. Liu Z, Guo B, Tay SW, Hong L, Zhang X (2008) Physical and electrochemical characterizations of PtPb/C catalyst prepared by pyrolysis of platinum(II) and lead(II) acetylacetonate. J Power Sources 184:16–22
52. Obradovic MD, Rogan JR, Babic BM, Tripkovic AV, Gautam ARS, Radmilovic VR, Gojkovic SL (2012) Formic acid oxidation on Pt–Au nanoparticles: relation between the catalyst activity and the poisoning rate. J Power Sources 197:72–79
53. Chen G, Li Y, Wang D, Zheng L, You G, Zhong C-J, Yang L, Cai F, Cai J, Chen BH (2011) Carbon-supported PtAu alloy nanoparticle catalysts for enhanced electrocatalytic oxidation of formic acid. J Power Sources 196:8323–8330
54. Yu X, Pickup PG (2011) Codeposited PtSb/C catalysts for direct formic acid fuel cells. J Power Sources 196:7951–7956
55. Zhang H-X, Wang C, Wang J-Y, Zhai J-J, Cai W-B (2010) Carbon-supported Pd–Pt nanoalloy with low Pt content and superior catalysis for formic acid electro-oxidation. J Phys Chem C 114:6446–6451
56. Feng L, Si F, Yao S, Cai W, Xing W, Liu C (2011) Effect of deposition sequences on electrocatalytic properties of PtPd/C catalysts for formic acid electrooxidation. Catal Commun 12:772–775
57. Li X, Hsing IM (2006) Electrooxidation of formic acid on carbon supported Pt_xPd_{1-x} (x=0–1) nanocatalysts. Electrochim Acta 51:3477–3483
58. Wang J-Y, Kang Y-Y, Yang H, Cai W-B (2009) Boron-doped palladium nanoparticles on carbon black as a superior catalyst for formic acid electro-oxidation. J Phys Chem C 113:8366–8372
59. Sun H, Xu J, Fu G, Mao X, Zhang L, Chen Y, Zhou Y, Lu T, Tang Y (2012) Preparation of highly dispersed palladium-phosphorus nanoparticles and its electrocatalytic performance for formic acid electrooxidation. Electrochim Acta 59:279–283
60. Yang G, Chen Y, Zhou Y, Tang Y, Lu T (2010) Preparation of carbon supported Pd–P catalyst with high content of element phosphorus and its electrocatalytic performance for formic acid oxidation. Electrochem Commun 12:492–495
61. Zhang L, Tang Y, Bao J, Lu T, Li C (2006) A carbon-supported Pd–P catalyst as the anodic catalyst in a direct formic acid fuel cell. J Power Sources 162:177–179
62. Mazumder V, Chi M, Mankin MN, Liu Y, Metin O, Sun D, More KL, Sun S (2012) A facile synthesis of MPd (M = Co, Cu) nanoparticles and their catalysis for formic acid oxidation. Nano Lett 12:1102–1106
63. Morales-Acosta D, Ledesma-Garcia J, Godinez LA, Rodriguez HG, Alvarez-Contreras L, Arriaga LG (2010) Development of Pd and Pd–Co catalysts supported on multi-walled carbon nanotubes for formic acid oxidation. J Power Sources 195:461–465
64. Sangarunlert W, Sukchai S, Pongtornkulpanich A, Nathakaranakule A, Luschtinetz T (2011) Technical and economic evaluation of a formic acid/hydrogen peroxide fuel cell system with Pt-M/C as anode catalyst. J Fuel Cell Sci Technol 8:061005–061007
65. Wang R, Liao S, Ji S (2008) High performance Pd-based catalysts for oxidation of formic acid. J Power Sources 180:205–208
66. Wang X, Xia Y (2008) Electrocatalytic performance of PdCo-C catalyst for formic acid oxidation. Electrochem Commun 10:1644–1646

67. Habibi B, Delnavaz N (2012) Electrosynthesis, characterization and electrocatalytic properties of Pt–Sn/CCE towards oxidation of formic acid. RSC Adv 2:1609–1617
68. DandanTu WB, Wang B, Deng C, Gao Y (2011) A highly active carbon-supported PdSn catalyst for formic acid electrooxidation. Appl Catal B 103:163–168
69. Zhang Z, Ge J, Ma L, Liao J, Lu T, Xing W (2009) Highly active carbon-supported PdSn catalysts for formic acid electrooxidation. Fuel Cells 9:114–120
70. Liu Z, Zhang X (2009) Carbon-supported PdSn nanoparticles as catalysts for formic acid oxidation. Electrochem Commun 11:1667–1670
71. Yu X, Pickup PG (2011) Screening of PdM and PtM catalysts in a multi-anode direct formic acid fuel cell. J Appl Electrochem 41:589–597
72. Alden LR, Han DK, Matsumoto F, Abruna HD, DiSalvo FJ (2006) Intermetallic PtPb nanoparticles prepared by sodium naphthalide reduction of metal-organic precursors: electrocatalytic oxidation of formic acid. Chem Mater 18:5591–5596
73. Casado-Rivera E, Gal Z, Angelo ACD, Lind C, DiSalvo FJ, Abruna HD (2003) Electrocatalytic oxidation of formic acid at an ordered intermetallic PtBi surface. Chemphyschem 4:193–199
74. Ghosh T, Leonard BM, Zhou Q, DiSalvo FJ (2010) Pt alloy and intermetallic phases with V, Cr, Mn, Ni, and Cu: synthesis as nanomaterials and possible applications as fuel cell catalysts. Chem Mater 22:2190–2202
75. Leonard BM, Zhou Q, Wu D, DiSalvo FJ (2011) Facile synthesis of PtNi intermetallic nanoparticles: influence of reducing agent and precursors on electrocatalytic activity. Chem Mater 23:1136–1146
76. Liu Y, Lowe MA, DiSalvo FJ, Abruna HD (2010) Kinetic stabilization of ordered intermetallic phases as fuel cell anode materials. J Phys Chem C 114:14929–14938
77. Roychowdhury C, Matsumoto F, Zeldovich VB, Warren SC, Mutolo PF, Ballesteros M, Wiesner U, Abruña HD, DiSalvo FJ (2006) Synthesis, characterization, and electrocatalytic activity of PtBi and PtPb nanoparticles prepared by borohydride reduction in methanol. Chem Mater 18:3365–3372
78. Volpe D, Casado-Rivera E, Alden L, Lind C, Hagerdon K, Downie C, Korzeniewski C, DiSalvo FJ, Abruna HD (2004) Surface treatment effects on the electrocatalytic activity and characterization of intermetallic phases. J Electrochem Soc 151:A971–A977
79. Matsumoto F, Roychowdhury C, DiSalvo FJ, Abruna HD (2008) Electrocatalytic activity of ordered intermetallic PtPb nanoparticles prepared by borohydride reduction toward formic acid oxidation. J Electrochem Soc 155:B148–B154
80. Li X, An L, Wang X, Li F, Zou R, Xia D (2012) Supported sub-5 nm Pt–Fe intermetallic compounds for electrocatalytic application. J Mater Chem 22:6047–6052
81. Antolini E (2010) Composite materials: an emerging class of fuel cell catalyst supports. Appl Catal B 100:413–426
82. Zhang B, Ye D, Li J, Zhu X, Liao Q (2012) Electrodeposition of Pd catalyst layer on graphite rod electrodes for direct formic acid oxidation. J Power Sources 214:277–284
83. Morgan RD, Salehi-khojin A, Masel RI (2011) Superior formic acid oxidation using carbon nanotube-supported palladium catalysts. J Phys Chem C 115:19413–19418
84. Qin Y-H, Jia Y-B, Jiang Y, Niu D-F, Zhang X-S, Zhou X-G, Niu L, Yuan W-K (2012) Controllable synthesis of carbon nanofiber supported Pd catalyst for formic acid electrooxidation. Int J Hydrogen Energy 37:7373–7377
85. Chen W, Chen S (2011) Iridium–platinum alloy nanoparticles: composition-dependent electrocatalytic activity for formic acid oxidation. J Mater Chem 21:9169–9178
86. Yi Q, Chen A, Huang W, Zhang J, Liu X, Xu G, Zhou Z (2007) Titanium-supported nanoporous bimetallic Pt–Ir electrocatalysts for formic acid oxidation. Electrochem Commun 9:1513–1518
87. Yi Q, Zhang J, Chen A, Liu X, Xu G, Zhou Z (2008) Activity of a novel titanium-supported bimetallic PtSn/Ti electrode for electrocatalytic oxidation of formic acid and methanol. J Appl Electrochem 38:695–701

88. Laborde H, Leger JM, Lamy C (1994) Electrocatalytic oxidation of methanol and C1 molecules on highly dispersed electrodes. Part 1. Platinum in polyaniline. J Appl Electrochem 24:219–226
89. Gharibi H, Kakaei K, Zhiani M (2010) Platinum nanoparticles supported by a Vulcan XC-72 and PANI doped with trifluoromethane sulfonic acid substrate as a new electrocatalyst for direct methanol fuel cells. J Phys Chem C 114:5233–5240
90. Shi J, Zhang Z-Y, Hu Y-Q, Hua Y-X (2010) Incorporation of 4-aminobenzene functionalized multi-walled carbon nanotubes in polyaniline for application in formic acid electrooxidation. J Appl Polym Sci 118:1815–1820
91. Ren F, Zhou W, Du Y, Yang P, Wang C, Xu J (2011) High efficient electrocatalytic oxidation of formic acid at Pt dispersed on porous poly(o-methoxyaniline). Int J Hydrogen Energy 36:6414–6421
92. Zhou W, Wang C, Xu J, Du Y, Yang P (2011) High efficient electrooxidation of formic acid at a novel Pt-indole composite catalyst prepared by electrochemical self-assembly. J Power Sources 196:1118–1122
93. Zhou W, Xu J, Du Y, Yang P (2011) Polycarbazole as an efficient promoter for electrocatalytic oxidation of formic acid on Pt and Pt-Ru nanoparticles. Int J Hydrogen Energy 36:1903–1912
94. Moghaddam RB, Pickup PG (2011) Support effects on the oxidation of formic acid at Pd nanoparticles. Electrocatalysis 2:159–162
95. Philips MF, Gopalan AI, Lee K-P (2011) Enhanced electrocatalytic performance of cyano groups containing conducting polymer supported catalyst for oxidation of formic acid. Catal Commun 12:1084–1087
96. Buzzo GS, Niquirilo RV, Suffredini HB (2010) Active Pt–PbO_x/C anodes to promote the formic acid oxidation in presence of sulfuric acid. J Braz Chem Soc 21:185–190
97. Zhang Z, Huang Y, Ge J, Liu C, Lu T, Xing W (2008) WO_3/C hybrid material as a highly active catalyst support for formic acid electrooxidation. Electrochem Commun 10:1113–1116
98. Feng L-G, Yan L, Cui Z-M, Liu C-P, Xing W (2011) High activity of Pd–WO_3/C catalyst as anodic catalyst for direct formic acid fuel cell. J Power Sources 196:2469–2474
99. Wang Y, Wang S, Wang X (2009) CeO_2 promoted electrooxidation of formic acid on Pd/C nano-electrocatalysts. Electrochem Solid-State Lett 12:B73–B76
100. Niquirilo RV, Teixeira-Neto E, Buzzo GS, Suffredini HB (2010) Formic acid oxidation at Pd, Pt and PbO_x-based catalysts and calculation of their approximate electrochemical active areas. Int J Electrochem Sci 5:344–354
101. Liu Z, Hong L, Tham MP, Lim TH, Jiang H (2006) Nanostructured Pt/C and Pd/C catalysts for direct formic acid fuel cells. J Power Sources 161:831–835
102. Markovic NM, Schmidt TJ, Stamenkovic V, Ross PN (2001) Oxygen reduction reaction on Pt and Pt bimetallic surfaces: a selective review. Fuel Cells 2:105

Chapter 5
Anode Catalysts for Alkaline Direct Alcohol Fuel Cells and Characteristics of the Catalyst Layer

Ermete Antolini and Joelma Perez

Abstract The faster kinetics of the alcohol oxidation reaction in alkaline direct alcohol fuel cells (ADAFCs), opening up the possibility of using less expensive metal catalysts, as silver, nickel, and palladium, makes the alkaline direct alcohol fuel cell a potentially low-cost technology compared to acid direct alcohol fuel cell technology, which employs platinum catalysts. In this work an overview of catalysts for ADAFCs, and of testing of ADAFCs, fuelled with methanol, ethanol, and ethylene glycol, formed by these materials, is presented.

5.1 Introduction

Among different types of fuel cells, alkaline fuel cells (AFCs) are the most matured. Alkaline fuel cells have numerous advantages over proton-exchange membrane fuel cells on both cathode kinetics and ohmic polarization. The less-corrosive nature of an alkaline environment ensures a potential greater longevity. The kinetics of the ORR reaction is more facile in alkaline medium than in some acid medium such as H_2SO_4 using Pt catalysts [1] and $HClO_4$ using Ag catalysts [2]. The inherently faster kinetics of the oxygen reduction reaction in an alkaline fuel cell allows the use of non-noble and low-cost metal electrocatalysts such as silver and nickel, making the AFC a potentially low-cost technology compared to PEMFCs, which employ platinum catalysts. Thus, a resurgence of interest in AFCs has occurred in recent years [3–7]. A serious problem of AFCs was the progressive

---

E. Antolini (✉)
Scuola di Scienza dei Materiali, Via 25 aprile 22, 16016 Cogoleto, Genova, Italy
e-mail: ermantol@libero.it

J. Perez
Universidade de São Paulo, IQSC, São Carlos, SP, Brazil

M. Shao (ed.), *Electrocatalysis in Fuel Cells*, Lecture Notes in Energy 9,
DOI 10.1007/978-1-4471-4911-8_5, © Springer-Verlag London 2013

carbonation of the alkaline electrolyte due to CO_2 from air or the oxidation product of the fuel, addressed mainly by the application of alkaline anion-exchange membranes (AAEMs) [8–10]. Indeed, a boost in the research regarding AFC is related to the development of alkaline anion-exchange membranes. Alkaline fuel cells using AAEMs have several important advantages over conventional AFCs: (1) since there is no mobile cation, there is no precipitated carbonate; (2) no electrolyte weeping; (3) reduced alcohol crossover; (4) potentially simplified water management, due to the fact that the water is produced at the anode and consumed at the cathode; and (5) potentially reduced corrosion [11].

The development of alternative power sources is an important issue at present. Direct alcohol fuel cells (DAFCs) have attracted considerable interest in their application to alternative power sources for automobile and portable consumer electronics [12]. Liquid fuels, such as low molecular weight alcohols, have several advantages compared to pure hydrogen, because they can be easily handled, stored, and transported. Furthermore, they have relatively high mass energy density, comparable to that of gasoline. Methanol is a promising fuel for DAFCs [13], but other low molecular weight alcohols such as ethanol [14] and ethylene glycol [15] are also candidates. At present, DAFCs are mostly using acidic proton-exchange membrane. With strong acidic electrolyte membrane, CO_2 generated in anodic reaction can be easily removed. A major contribution to the relatively low DAFC performance is from kinetic constraints in the alcohol oxidation reaction in acid media. Improved alcohol oxidation kinetics can be facilitated using basic media [16]. In addition, the ionic current in alkali fuel cells is due to conduction of hydroxide ions and is the reverse direction to that in proton-conducting systems. As such, the direction of the electroosmotic drag is reversed, reducing the alcohol permeation rate [17]. Accordingly, the approach is to develop an alkali analogue of the DAFC. The recent development of polymeric membrane presenting a good anionic conductivity opens a new research area to conceive solid fuel cells working with an electrolytic membrane different from the common proton-exchange membrane. Several DAFCs which use an alkaline anion-exchange membrane as a polymer electrolyte membrane have already been reported [8, 17–19]. An advantage of using alkaline fuel cells, rather than the traditional acidic fuel cells, is the potential use of non-Pt catalysts in the electrodes. The development of new anode and cathode catalyst systems is more likely in alkaline media because of the wide range of options for the materials support and catalyst, as compared to acidic media which offer more limited materials choice. Alternatives to platinum have been investigated, showing good performance, comparable sometimes to platinum itself.

In this work an overview of anode catalysts for alkaline direct alcohol fuel cells, and reports of the testing of these materials in alkaline direct alcohol fuel cells fuelled with C_1 (methanol) and C_2 (ethanol and ethylene glycol) alcohols, is presented.

5.2 Anode Catalysts

5.2.1 Catalysts for Methanol Oxidation in Alkaline Media

The use of alkali electrolytes not only leads to better polarization characteristics of methanol oxidation on platinum compared to acid media but also opens up the possibility of using non-noble, less expensive metal catalysts for the process.

5.2.1.1 Pt and Pt-Based Catalysts

Platinum has the highest catalytic activity for the methanol oxidation reaction (MOR) of any of the pure metals both in acid and in alkaline media. An excellent review on the MOR on Pt and Pt-based catalysts in alkaline media was done by Spendelow and Wieckowski [20]. Concisely, the enhanced activity in alkaline media results from the lack of specifically adsorbing spectator ions in alkaline solutions, and the higher coverage of adsorbed OH at low potential, which is required for methanol oxidation [20].

The rate-limiting step during the MOR on Pt in alkaline media is a chemical step involving reaction of adsorbed MOR intermediates (such as CO or CHO) and adsorbed OH [21]. The final product of the MOR in alkaline media, carbonate or formate, is a subject of some controversy. Tripkovic et al. [22] carried out a comparative study of methanol oxidation on a Pt(100) surface in various alkaline solutions. They found that Pt(100) adsorbs OH and “poisoning species.” The “poisoning species,” produced in methanol oxidation, participate in the reaction at higher potentials but block the surface partially at lower potentials. A dual-path reaction mechanism, common to all the alkaline solutions used, was proposed based on the assumptions that HCO is a reactive intermediate and that a formate is a reaction product in the main path, while CO_2 is a product of “poisoning species” oxidation in a parallel reaction path. Tripkovic et al. [23] performed the electrochemical oxidation of methanol, ethanol, *n*-propanol, and *n*-butanol at the Pt(111). They observed that reversible OH_{ad} species were produced in a fast process of OH^- adsorption as opposite to irreversible OH_{ad} species, which could be generated only during a time-dependent adsorption. The reversibly adsorbed OH species are the active intermediates in alcohol oxidation, while the irreversible adsorbed OH species are the inactive, strongly bound intermediates, acting as a “poison” in the alcohol oxidation. Spendelow and Wieckowski [20] concluded that the different final reaction products reported in the literature for the MOR on Pt(111) simply reflect the different potential ranges in which the MOR is examined.

A lot of papers have been addressed to the methanol oxidation on Pt–Ru catalyst in acidic media, and excellent reviews have been done by Spendelow et al. [24] and Petrii [25]. Conversely, few works have been addressed to the MOR on Pt–Ru catalysts in alkali media. Firstly, Petrii et al. [26] compared the polarization curves of methanol electrooxidation in an alkaline solution under steady-state conditions on Pt–Ru (Pt:Ru atomic ratio 9:1) deposited on platinum with those on a platinized-platinum electrode. They found that the overvoltage of methanol oxidation on Pt–Ru is 60–70 mV lower than on Pt/Pt at a current density of 2.5 mA cm^{-2}. Rauhe et al. [27] performed methanol electrooxidation on poor alloyed Pt–Ru (1:1) in Cs_2CO_3 electrolytes at 100–140 °C and ambient pressures. They found that Pt–Ru/C provided enhanced performance, compared to Pt/C. Performance curves, based on unit catalyst mass, for Pt–Ru/C at 120 °C matched or exceeded previously reported performance data for supported Pt or Pt black in concentrated Cs_2CO_3 electrolytes at 120–150 °C at 8 atm and for supported Pt–Ru in concentrated H_3PO_4 electrolytes at 200 °C. Tripkovic et al. [16, 28] investigated the kinetics of methanol oxidation on supported Pt and Pt–Ru (Pt:Ru = 3:2 and 2:3) catalysts in 0.5 M H_2SO_4 and 0.1 NaOH at 22 and 60 °C. At room temperature, the Pt–Ru catalysts were slightly more active than Pt for methanol oxidation in alkaline solution, suggesting a promoter effect of Ru on OH^- adsorption. Higher activity of Pt_3Ru_2 than Pt_2Ru_3 catalyst was observed, ascribed to the higher rate of methanol dehydrogenation/adsorption on Ru-less rich alloy. At higher temperatures, a negligible difference in the kinetics between Pt and Pt–Ru catalysts was observed. Jayashree et al. [29] compared the performance of an air-breathing laminar flow-based direct methanol fuel cell (LFFC) operated in acidic or alkaline media at room temperature with a bulk Pt–Ru (1:1) alloy as the anode catalyst. Figure 5.1 from ref. [29] shows polarization and power density curves for the LFFCs operated in acidic and alkaline media under identical operating conditions. As can be seen in Fig. 5.1, the performance of LFFCs operated in alkaline media was higher than that of LFFCs in acidic media. A maximum power density of 11.8 and 17.2 mW cm^{-2} was found for operation in acidic and alkaline media, respectively.

Besides Ru, a variety of alloyed metals, metal adatoms, and metal oxides have been investigated as MOR promoters on Pt in alkaline media. Kadirgan et al. [30] investigated the electrocatalytic oxidation of methanol on Pt–Pd alloy electrodes of different compositions in acid, neutral, and alkaline solutions. In alkaline solution, the exchange current densities for the MOR presented a pronounced maximum for a surface composition of about 15 at.% in palladium. This synergistic effect is important, since the exchange current densities are up to ten times greater than for platinum. Conversely, in acid and neutral media, there is no such maximum, and the exchange current densities decrease monotonically from pure platinum to pure palladium. This enhanced MOR electroactivity in alkaline media at the Pt–Pd catalyst was explained on the basis of a decrease of electrode poisoning.

Gold is recognized to adsorb oxygen-containing species in alkaline solution at a more negative potential than in acidic solution, so, based on the bifunctional theory of electrocatalysis, the presence of gold atoms is expected to enhance the electrocatalytic activity of platinum electrode for methanol oxidation in alkaline solution but not in acidic solution [31]. Watanabe and Motoo [31] observed the activity maximum for the MOR on Pt–Au alloys at 40 at.% Au. The activity was enhanced about 2.5 times compared with that of Pt in alkaline solution. On the contrary, no enhancement was exhibited in acidic solution by alloying. More recently, nanosized gold has been reported to have the excellent catalytic activity

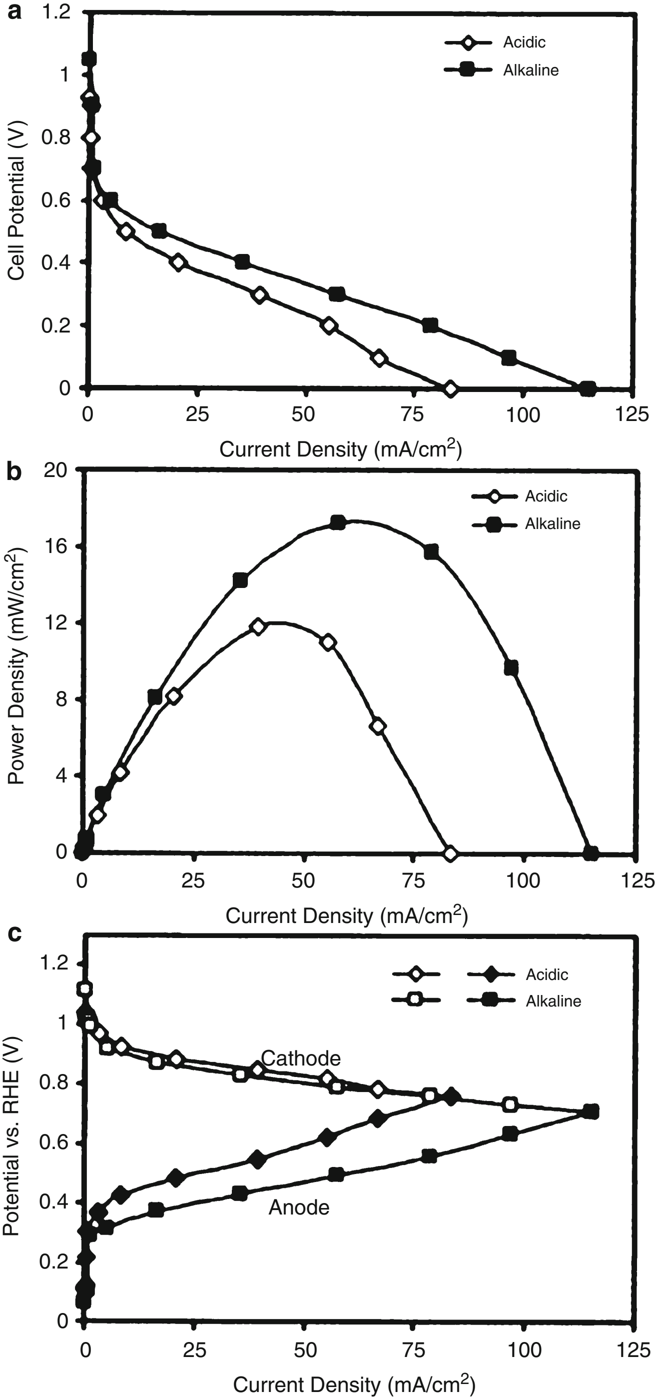

Fig. 5.1 Polarization (*filled symbols*) and power density (*open symbols*) curves for an air-breathing, direct methanol LFFC operated in either alkaline or acidic media at room temperature. Reprinted from ref. [29]

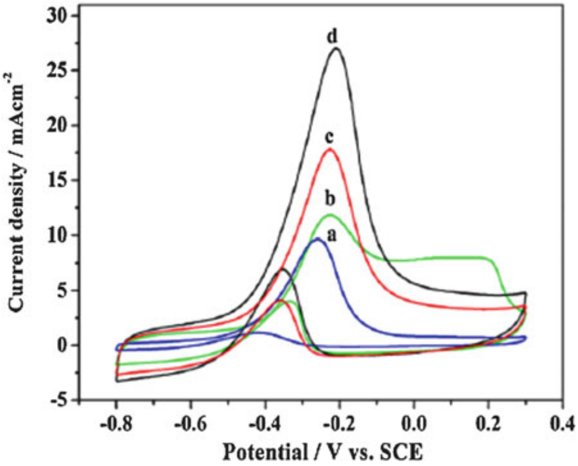

Fig. 5.2 Cyclic voltammograms of Pt/G (a), PtAu/G (b), PtPd/G (c), and PtPdAu/G (d) catalysts in 1.0 M KOH containing 1.0 M CH_3OH solutions with a scan rate of 50 mV s^{-1}. Reproduced from ref. [37]

for CO oxidation [32, 33]; thus, it could be suitable to decrease the poisoning effect of CO_{ads} at the Pt-based catalyst surface. So, the cocatalytic effect of gold for methanol electrooxidation at Pt-based catalysts has attracted many attentions [34–36]. Luo et al. [34] investigated the MOR activities in alkaline electrolytes of Au–Pt/C catalysts with different composition ranging from 10 to 90 % Au. The catalysts with 65–85 % Au exhibited maximum electrocatalytic activities. The findings revealed important insights into the participation of CO_{ads} and OH_{ads} on Au sites in the catalytic reaction of Pt in the Au–Pt alloys with 75 % Au.

Zhang et al. [37] synthesized ternary PtPdAu alloy nanoparticles on graphene sheets via a chemical reduction method. This catalyst exhibited high catalytic activity and stability for MOR in alkaline medium. Cyclic voltammograms (CVs) for PtPdAu/G, PtPd/G, PtAu/G, and Pt/G electrodes in 1.0 M KOH and 1.0 M CH_3OH solutions are shown in Fig. 5.2. As can be seen in Fig. 5.2, the onset potential of MOR on PtPdAu/G was the lowest, indicating an effective decrease of the overpotential of the methanol electrooxidation reaction. Moreover, the current of methanol oxidation on the PtPdAu/G electrode was the highest, 1.5, 2.3, and 2.8 times as high as that of PtPd/G, PtAu/G, and Pt/G, respectively.

Noble (Au) [31] and non-noble (Cd, Pb, Bi, Tl) [21] metal adatoms were investigated as MOR promoters on Pt in alkaline media. When these metals are present in alkaline solutions at low concentrations, methanol oxidation on Pt electrodes is enhanced in the low potential range of interest for fuel cell anodes. At higher concentrations of these species, methanol oxidation is suppressed due to excessive coverage by foreign metal adatoms. The ad-electrode Au–Pt presented the same electrocatalytic characteristics for methanol oxidation as the Au–Pt alloy electrode. This finding indicates the surface composition to play predominant roles in the methanol oxidation [31].

Recently, some metal oxides (CeO_2, NiO, V_2O_5) [38–41] have been tested as promoters for the MOR in alkaline media on Pt. Oxide-promoted Pt showed higher MOR activity than Pt alone. The higher activity and better poison resistance of the

Pt–M_xO_y catalysts were attributed to the synergistic effect between Pt and oxide promoter. Pt electrocatalytic properties for the methanol oxidation reaction in alkaline electrolyte can be enhanced significantly by the copresence of Ag, as compared with monometallic Pt catalyst [42]. The data clearly demonstrate that the Ag oxide plays an important role in promoting the catalysis of Pt towards methanol electrooxidation via a synergistic effect, and this promoting effect of Ag oxide also depends on the composition and/or the proximity of Ag and Pt [42].

Perovskites were also investigated as promoters of the MOR on Pt. The perovskite-modified ($La_{1-x}Sr_xCoO_3$ and $La_{1-x}Sr_xMnO_3$) Pt/C electrodes were more active than the Pt/C electrode for methanol electrooxidation in alkaline solution. The higher electrocatalytic activities of the perovskite-modified Pt/C compared with Pt/C alone were ascribed to the advantageous role of the perovskite oxides in promoting the formation of the active platinum oxides/hydroxides, providing oxy-species at a less positive potentials [43].

5.2.1.2 Pt-Free Catalysts

Among different metals, nickel is the most investigated Pt-alternative anode catalysts for methanol oxidation in alkaline media. Since nickel placed in contact with a solution of aqueous alkali has been shown to become covered with a layer of nickel hydroxide, the surface change is normally written as

$$\mathrm{Ni(OH)_2} \rightarrow \mathrm{NiOOH} + \mathrm{H^+} + \mathrm{e^-} \tag{5.1}$$

although it is recognized that the oxidation state of the nickel in the oxide layer probably changes continuously between two and four over a range of potentials [44]. The oxidation of primary alcohols at Ni/NiOOH electrodes in alkaline medium leads to the formation of organic acids [44]:

$$\mathrm{RCH_2OH} + \mathrm{NiOOH} \rightarrow \mathrm{RCOOH} + \mathrm{Ni(OH)_2} \tag{5.2}$$

A general mechanism of the oxidation of primary alcohols at Ni/NiOOH electrodes in alkaline medium was proposed by Fleischmann et al. [44]. Kowal et al. [45] investigated the electrochemical oxidation of methanol at Ni hydroxide electrodes in alkaline electrolytes. They found that methanol oxidation commences in the potential region where multilayers of NiOOH are formed on the electrode surface, and occurs in two stages, with predominantly formate being formed in the potential window 0.36–0.44 V (vs. SCE), followed by further oxidation to carbonate at potentials above approx. 0.45 V. Rahim et al. [46] observed that the reaction of the electrooxidation of methanol in alkaline medium on Ni dispersed on graphite electrodes is activation controlled proceeding by direct chemical reaction with NiOOH for thin nickel oxides and by charge transfer with the electrode for thick oxides. Recently, a novel titanium-supported nanoscale nickel catalyst (nanoNi/Ti) with flaky structures was prepared by Yi et al. [47]. Cyclic voltammograms in alkaline solutions showed that the oxidation current of methanol on the nanoNi/Ti was much higher than that on a polycrystalline nickel. Chronoamperometric measurements indicated that the steady-state current on the nanoNi/Ti was significantly higher than on conventional Ni and linearly proportional to the methanol concentration. The results showed that this novel nickel electrode can be used repeatedly and possess stable electrocatalytic activity for the methanol oxidation.

In addition to the pure nickel electrode, different nickel-based electrodes, like nickel alloy and nickel complex-modified carbon electrodes, have been tested for methanol oxidation in alkaline media. The MOR activity of Ni can be enhanced by alloying with Ru and Cu. Kasakov et al. [48] observed that the electrocatalytic activity of Ni–Ru alloys for methanol oxidation in alkaline solutions is higher than that of Ni and Ru alone and rises with the Ru content increasing to 80 %. Gobal et al. [49, 50] investigated the redox process and electrocatalytic activities towards the MOR in alkaline media of nickel and nickel–copper alloy-modified glassy carbon electrodes. The addition of copper to the electrodeposited nickel is a very effective method of suppressing the formation of γ-NiOOH species, less effective for the MOR than β-NiOOH species, during prolonged cycling processes in alkaline medium. The methanol electrooxidation at the Ni–Cu alloy (40 % Cu)-modified electrode was significantly larger than that at pure Ni.

Research into developing new electrode materials is also directed towards the use of macrocyclic complexes of some metals in the form of conductive polymers. An immobilized polymeric film containing a reversible redox center acts as a fast electron-transfer mediator for a solution species, which is oxidized or reduced slowly or not at all at the naked electrode. Macrocyclic complexes of nickel are of particular interest as modifying agents because in basic media, nickel redox centers show high catalytic activity towards the oxidation of some small organic compounds [51, 52]. Thus, Ni-complex-modified electrode systems have been tested for the MOR in alkaline solutions [52–58]. All these systems showed a MOR activity in NaOH solution higher or comparable to that of bare Ni. One of the main advantages of redox polymers with the coordinated redox couple is the higher chemical stability of the attached redox center compared with electrostatically incorporated sites. The physical stability of the polymer films is also very often satisfactory, due to the insolubility of the polymers in the aqueous electrolytes.

Palladium and gold are active for methanol oxidation in alkaline media [30, 31, 59–61], but their activity is remarkably lower than that of platinum [39, 62]. The MOR activity of Pd can be enhanced by the presence of a second metal, as in binary Pd–Au [31] and Pd–Ni catalysts (with Ni either alloyed [63, 64] or in the oxide form [65]). The MOR activity of Au, instead, can be increased by using specific metal structures, as continuous gold films deposited on the surface of ultrafine PAni fibers [66] or isle-like Au nanoparticle formed on modified ITO electrodes [67].

The perovskite oxides of the general compositions ABO_3 and A_2BO_4 with excellent electrical conductivities and electrocatalysis were considered as possible materials for the application as anode materials in direct methanol fuel cells (DMFCs). White and

Sammells [68] observed that perovskite electrocatalysts are active towards methanol oxidation during CV measurements in H_2SO_4. On this basis, perovskite oxides have been investigated as electrocatalysts for methanol oxidation in alkaline media. A series of rare-earth cuprates with overall composition $Ln_{2-x}M_xCu_{1-y}M_y'O_{4-\delta}$ (where Ln = La and Nd; M = Sr, Ca, and Ba; M′ = Ru and Sb: $0.0 \leq x \leq 0.4$; and $y = 0.1$) were tested as anode electrocatalysts for methanol oxidation in alkaline media by Raghuveer et al. [69]. These materials showed significant activity for the MOR at higher potentials. The linear correlation between Cu^{3+} content and methanol oxidation activity suggested that the active sites for adsorption of methanol are Cu^{3+} ions. These materials showed better tolerance towards the poisoning by the intermediates of methanol oxidation compared to that of conventional noble metal electrocatalysts. The lattice oxygen in these oxides could be considered as active oxygen to remove CO intermediates of methanol oxidation reaction. The high values of Tafel slopes obtained for rare-earth cuprates compared to that of platinum in the methanol adsorption region suggest that the adsorption of methanol is the rate-determining step on these oxides. Yu et al. [70] investigated the electrocatalytic activity of $La_{1-x}Sr_xMO_{3-\delta}$, where M = Co and Cu, towards methanol oxidation in 1 M NaOH. The methanol oxidation onset potential for $La_{1-x}Sr_xCoO_{3-\delta}$ was 0.42 V, 0.03 V lower than that for $La_{1-x}Sr_xCuO_{3-\delta}$. However, the electrocatalytic activity for methanol oxidation of $La_{1-x}Sr_xCuO_{3-\delta}$ was much higher than that of $La_{1-x}Sr_xCoO_{3-\delta}$. The authors ascribed the higher electrocatalytic activity for $La_{1-x}Sr_xCuO_{3-\delta}$ to the capability of Cu ions for the absorption of methanol and the existence of a large amount of oxygen vacancies facilitating oxygen ion (O^{2-}) transport into the proximity of adsorbed methanol oxidation intermediates at the reaction site. Singh et al. [71] studied the MOR activity in an alkaline solution at 25 °C of $La_{2-x}Sr_xNiO_4$ ($x = 0$, 0.25, 0.5, and 1.0). The results showed that all the $La_{2-x}Sr_xNiO_4$ are quite active for the MOR in alkaline medium and the electrocatalytic activity increases with x. All the perovskites investigated did not indicate any poisoning by the methanol oxidation intermediates/products. The MOR activity of $La_{2-x}Sr_xNiO_4$ was compared with that of pure Pt. The onset potential for electrooxidation of methanol on Pt was significantly lower than that on $La_{2-x}Sr_xNiO_4$; however, the observed apparent current densities are considerably low at Pt compared to that on $La_{2-x}Sr_xNiO_4$. The observed low oxidation current densities on Pt can be caused to the poisoning of the direct methanol fuel cells electrode surface by the oxidation intermediates. To improve the electrocatalytic activities of $La_{2-x}Sr_xNiO_4$ catalysts, the electrodes were modified by finely dispersed nickel particles [72]. The results showed that the apparent electrocatalytic activities of the modified oxide electrodes are much higher than those of unmodified electrodes under similar experimental conditions. The highest activity was obtained with the Ni-modified $La_{1.5}Sr_{0.5}NiO_4$ electrode. At 0.55 V (vs. Hg|HgO) in 1 M KOH/1 M CH_3OH at 25 °C, this electrode delivered a current density of over 200 mA cm^{-2}. According to the authors, such high methanol oxidation current densities have not been reported on any other non-platinum electrode in alkaline solution.

5.2.2 *Catalysts for Ethanol Oxidation in Alkaline Media*

Among pure metals, palladium is the more active catalyst for the ethanol oxidation reaction (EOR) in alkaline media. Conversely to ethanol oxidation in acid media, in alkaline media, the EOR activity of Pd is remarkably higher than that of Pt [38]. Xu et al. [73] compared the EOR activity in alkaline medium of Pt and Pd supported on carbon Vulcan and carbon microspheres (CMS) by cyclic voltammetry. The onset potential for ethanol oxidation on Pd shifted at lower potentials with respect to that on Pt. The current density peak on Pd was higher than on Pt. These results indicate that the activity for ethanol oxidation is higher on Pd than on Pt independently of the type of support, also if the difference is more significant for the catalysts supported on CMSs. Liang et al. [74] studied the mechanism of the EOR on Pd by CV measurements. They found that acetate is the final product and acetaldehyde is an active intermediate. The content of the carbonate ions in the solution indicated that less than 5 % of the ethanol was converted to the carbonate ions. This result indicates that, as in the case of ethanol oxidation in acid medium on Pt [14], the cleavage of the C–C bond is rather difficult on the Pd catalyst and acetate ions are the main product of the EOR. They also found that the dissociative adsorption of ethanol proceeds rather quickly and the rate-determining step is the removal of the adsorbed ethoxy by the adsorbed hydroxyl.

As nanowire arrays have attracted more interest due to their excellently physical and chemical properties, highly ordered Pd nanowire arrays, prepared by a template-electrodeposition method, were investigated as catalysts for ethanol oxidation in alkaline media [75]. The activity of Pd nanowire arrays for ethanol oxidation was not only higher than that of Pd film but also higher than that of a commercial Pt–Ru/C. This nanowire array structure has high electrochemical active surface and permits liquid alcohol to diffuse into the catalyst layer easily, resulting in the reduction of liquid sealing effect.

To improve the electrocatalytic activity of platinum and palladium, the ethanol oxidation on different metal adatom-modified, alloyed, and oxide-promoted Pt- and Pd-based electrocatalysts has been investigated in alkaline media. Firstly, El-Shafei et al. [76] studied the electrocatalytic effect of some metal adatoms (Pb, Tl, Cd) on ethanol oxidation at a Pt electrode in alkaline medium. All three metal adatoms, particularly Pb and Tl, improved the EOR activity of Pt. More recently, Pt–Ni nanoparticles, deposited on carbon nanofiber (CNF) network by an electrochemical deposition method at various cycle numbers such as 40, 60, and 80, have been tested as catalysts for ethanol oxidation in alkaline medium [77]. The Pt–Ni alloying nature and Ni to Pt atomic ratio increased with increasing of cycle number. The performance of PtNi80/CNF for the ethanol electrooxidation was better than that of the pure Pt40/CNF, PtNi40/CNF, and PtNi60/CNF.

The electrocatalytic activities of a wide range of intermetallic bulk compounds for ethanol oxidation in alkaline media have been investigated by Matsumoto [78], and the results have been compared to those of pure polycrystalline Pt and Pd electrodes. Among all of the examined bulk electrodes, the PtPb, PtBi, and $PtBi_2$

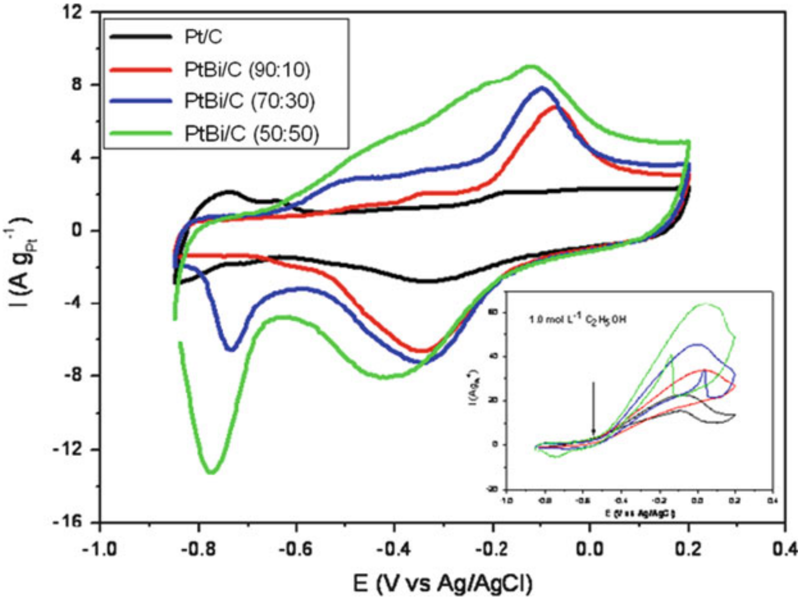

Fig. 5.3 Cyclic voltammograms (CV) of Pt/C and Pt–Bi/C electrocatalysts in 1.0 mol L^{-1} KOH with a sweep rate of 10 mV s^{-1}. (*Inset*) CVs in 1.0 mol L^{-1} KOH containing 1.0 mol L^{-1} of ethanol. Reproduced from ref. [79]

intermetallic compounds appeared to be the most promising electrocatalysts. PtPb had the lowest onset potential for EtOH oxidation, which was 20–30 mV less than that of pure Pt and Pd. The current densities of PtPb were at least seventeen times larger than those of pure Pt and Pd. Tusi et al. [79] observed a high EOR activity of Pt–Bi/C electrocatalysts in alkaline medium. The cyclic voltammograms (CV) of Pt/C and Pt–Bi/C electrocatalysts in alkaline medium are shown in Fig. 5.3. The CV of Pt–Bi/C electrocatalysts showed that the hydrogen adsorption region was greatly reduced compared to the Pt/C electrocatalyst. The electrooxidation of ethanol (Fig. 5.3, inset) started at around −0.55 V for all electrocatalysts, and the current values in the potential range of −0.5 to 0.2 V increase rapidly with the increase of Bi content in the samples.

Gold/platinum (Au/Pt) bimetallic nanodendrites were successfully synthesized through seeded growth method using preformed Au nanodendrites as seeds and ascorbic acid as reductant and tested for ethanol oxidation in alkaline media [80]. The peak current density of ethanol electrooxidation on the Au_3Pt_1 nanodendrites-modified glassy carbon electrode (Au_3Pt_1 electrode) was about 16, 12.5, and 4.5 times higher than those on the polycrystalline Pt electrode, polycrystalline Au electrode, and Au nanodendrites-modified glassy carbon electrode (Au dendrites electrode), respectively. In the same way than for methanol oxidation, ternary PtPdAu catalysts showed high activity for ethanol oxidation in alkaline media [81, 82]. Addition of Pd and Au into Pt matrix drastically reduces the charge transfer resistance and promotes the electrocatalytic activity towards the ethanol oxidation.

Bimetallic Pd–M (M = Ru, Au, Sn, and Cu) catalysts [83–85] have been tested for ethanol oxidation in alkaline media. Chen et al. [83] found that the catalytic activity of Pd–Ru is considerably higher than that of Pd towards the oxidation of methanol, ethanol, and ethylene glycol. The activity sequence of Pd–Ru towards the alcohol oxidation was ethanol > ethylene glycol > methanol, and Pd–Ru with 1:1 atomic ratio exhibited the highest activity. They also compared the activities of Pd–Ru and Pt–Ru catalysts for alcohol oxidations in alkaline media. For the oxidation of methanol and ethylene glycol, the activity of Pd–Ru was lower than that of Pt–Ru. For ethanol oxidation, instead, the activity of Pd–Ru was higher than that of Pt–Ru. At potentials ranging from 0.3 to 0.4 V, the mass specific activity of Pd–Ru was almost four times that on Pt–Ru. He et al. [84] prepared Pd_4Au/C and $Pd_{2.5}Sn/C$ catalysts and compared their EOR activity with that of a commercial Pt/C. The results indicated that although Pt/C showed better kinetics for ethanol oxidation, as manifested by the more negative onset potential and larger instantaneous current density, Pd_4Au/C and $Pd_{2.5}Sn/C$ were more tolerant to poisoning. Among the catalysts investigated, Pd_4Au/C displayed the best EOR activity in alkaline media. Jou et al. [85] compared the EOR activity in an alkaline solution of a Pd–Cu-coated ITO electrode (Pd:Cu 90:10) with that of a Pd-coated ITO electrode. The onset potential for ethanol oxidation on the Pd–Cu-coated electrode was 150 mV more negative than that observed on the Pd-coated electrode. The results indicated that the Pd–Cu alloy electrode has higher EOR activity and better capability against poisoning than Pd.

Du et al. [86] investigated the EOR activity in alkaline media of PdSn catalysts. Among various PdSn catalysts, $Pd_{86}Sn_{14}/C$ catalysts showed much enhanced current densities in cyclic voltammetric and chronoamperometric measurements, compared to commercial Pd/C. Density functional theory calculations indicated that PdSn alloy structures would result in lower reaction energies for the dehydrogenation of ethanol, compared to the pure Pd crystal. Various Pd–Tb/C electrocatalysts with different Pd/Tb ratios were synthesized and tested for ethanol oxidation in alkaline media [87]. It was found that Pd–Tb/C catalysts have higher activity and durability for ethanol oxidation than Pd/C. This may be attributed to the promotion effect of Tb on OH^- adsorption. The highest performance was observed for 10 % Pd–2 % Tb/C in terms of the highest activity, stability, and lowest activation energy for ethanol oxidation.

PdAg alloys containing different amounts of Ag (8, 21, and 34 at.%) were prepared in order to evaluate their catalytic activity towards the ethanol oxidation [88]. It was found that alloying Pd with Ag leads to an increase of the EOR kinetics, relative to Pd. Among the alloys under study, the 21 at.% Ag content alloy presents the highest catalytic activity for the EOR.

The effect of addition of various oxides to carbon-supported Pt and Pd catalysts on ethanol oxidation in alkaline media was investigated [89–96]. The addition of oxides such as CeO_2 [89, 92, 94, 95], ZrO_2 [90], MgO [91], Co_3O_4 [92, 95], Mn_3O_4 [92, 95], NiO [92–95], and In_2O_3 [96] remarkably improved the EOR activities of Pt/C and, in particular, Pd/C and moved the onset potentials towards lower values. The effect of the content of oxide in Pt/C and Pd/C catalysts on the EOR activity is

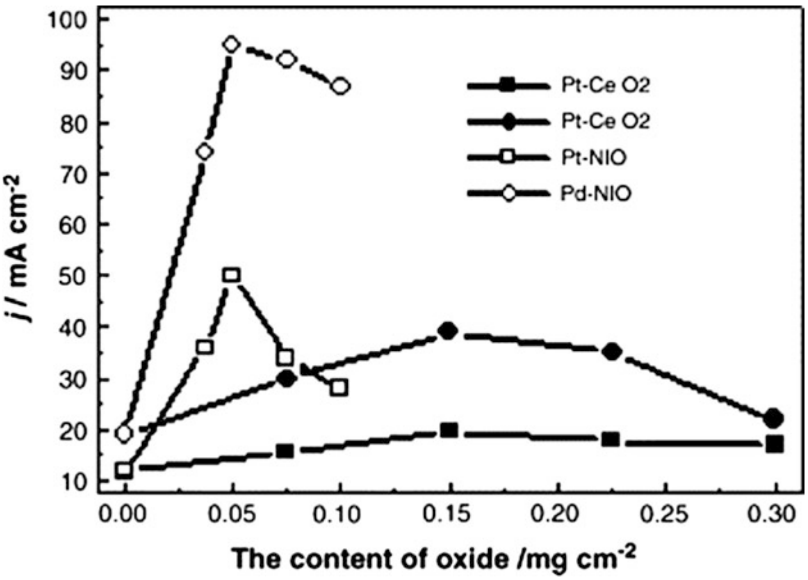

Fig. 5.4 Effect of the content of oxide in Pt/C and Pd/C catalysts for ethanol electrooxidation in 1.0 M KOH solution containing 1.0 M ethanol with a sweep rate of 50 mV s^{-1}, Pt or Pd loading: 0.3 mg cm^{-2}. Reproduced from ref. [94]

shown in Fig. 5.4 from ref. [93]. The electrocatalysts with the weight ratio of Pt or Pd to CeO_2 of 2:1 and Pt or Pd to NiO of 6:1 showed the highest electrochemical catalytic activity for ethanol oxidation. According to Xu et al. [91], it is possible that oxide functions as Ru does in Pt-oxide and Pd-oxide catalysts because OH_{ad} species could easily form on the surface of oxide. The formation of OH_{ad} species at lower potential can transform CO-like poisoning species on the surface of noble metal to CO_2 or other products. In particular, among various oxide-promoted Pd catalysts, Pd–NiO showed the highest EOR activity, with the lowest onset potential and the highest peak current density [92].

Spontaneous deposition of noble metals onto less-noble metal particles or metal surfaces is an alternative method to electroless and electrodeposition techniques for manufacturing electroactive materials [97]. Recently, it was discovered that Raney nickel materials can be successfully employed as supports for noble metal catalysts to give effective anodes in aqueous ammonia electrolyzers [98]. On these bases, Bambagioni et al. [99] prepared Pd-based catalysts by the spontaneous deposition of Pd on Ni–Zn and Ni–Zn–P alloys supported on carbon. An advantage of Ni–Zn materials as substrates for spontaneous deposition procedures is just the presence of Zn, which is more electropositive than Ni and therefore prone to undergo transmetallation with Pd^{II} or Pd^{IV}. The analytical and spectroscopic data showed that the surface of Pd–(Ni–Zn)/C and Pd–(Ni–Zn–P)/C contains very small (0.5–1 nm), highly dispersed, and crystalline palladium clusters as well as single palladium sites, likely stabilized by interaction with oxygen atoms from Ni–O moieties. The ethanol oxidation reaction on Pd–(Ni–Zn)/C and Pd–(Ni–Zn–P)/C was compared with that of a conventional carbon-supported Pd. The results obtained in the half cell indicated that the EOR activity of Pd–(Ni–Zn)/C and Pd–(Ni–Zn–P)/C is only slightly superior to that of Pd/C, but the chronopotentiometric tests showed lower overpotentials on Pd–(Ni–Zn)/C and Pd–(Ni–Zn–P)/C electrodes.

A new group of Ru–Ni and Ru–Ni–Co catalysts for ethanol oxidation in alkaline media was investigated by Kim and Park [100, 101]. The electrooxidation of ethanol on thermally prepared ruthenium oxide in alkaline solution was firstly investigated by Hsieh et al. [102]. The redox couple of ruthenate (Ru(VI)) and perruthenate (Ru(VII)) on the RuO_2 electrode surface was observed during the oxidation of ethanol. As previously reported, a redox couple of nickel, i.e., nickel hydroxide ($Ni(OH)_2$) and nickel oxyhydroxide (NiOOH), was shown to be involved in the oxidation of alcohols at nickel electrodes in alkaline media [44]. On this basis, the RuO_2 system on the Ni support is expected to possess high electrocatalytic activity during oxidation of organic compounds. As reported by Kim and Park [100], the RuO_2–Ni electrode showed higher activity for ethanol oxidation in 1 M NaOH than the Ni electrode. The net anodic peak current densities for ethanol oxidation at the RuO_2–Ni electrode were 6.3 and 1.7 times larger than those observed at the Ni electrode, in 0.1 and 0.5 M ethanol, respectively. A synergistic effect between Ru and Ni oxides was proposed.

Electrochemical deposition is the most common method of making nickel hydroxide electrodes. Commonly, nickel hydroxide is precipitated from a solution of nickel nitrate and sodium nitrate dissolved in an ethanol–water mixture. The sodium nitrate provides excess nitrate to enhance the precipitation, and the presence of the ethanol changes the surface-tension characteristics of the precipitation process, improving adhesion of precipitate to the current collector [103]. For this reason, in a next work, Kim and Park [101] used the sodium nitrate to prepare the base nickel electrode and Ni electrodes with Ru and Co as additives. CVs of these electrodes in alkaline media are shown in Fig. 5.5. The nickel electrodes containing Ru and/or Co showed higher EOR activity than Ni alone. The ethanol oxidation onset potentials shifted to more negative values, and the current densities were higher than pure Ni. The Ni–Co–Ru electrode, with an anodic peak potential more negative than that of nickel by about 70 mV and an anodic current density of about 1.4 times higher than that of Ni electrode, showed the best electrochemical characteristics. Addition of cobalt lowers the oxidation potential, while ruthenium increases the current density for the anodic process and shifts the oxygen evolution potential to a more negative value. When both ruthenium and cobalt are used as additives, the redox potential shifts to an even more negative value than that for Ni with Co and Na. XANES data for the Ni and Co K-edges of these composite electrodes revealed that both Ni and Co are in the Ni^{3+}–Ni^{4+} and Co^{3+}–Co^{4+} mixed states, respectively, depending on applied potentials.

An Italian company, Acta, has recently reported good activity for the EOR, with complete oxidation to CO_2 or carbonate, on anodes consisting of small nanoparticles or clusters of Ni–Fe–Co alloys in a matrix of hydrazine-based polymer, with the trade name HYPERMEC™ [20].

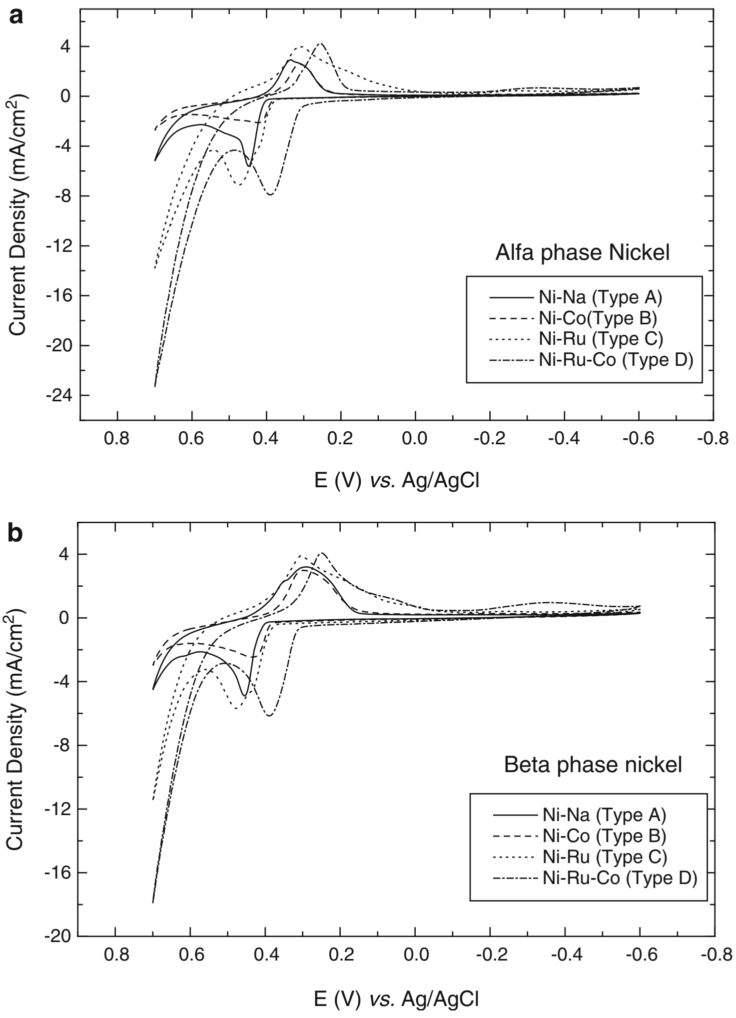

Fig. 5.5 CVs of various electrodes electrochemically prepared (**a**) α-phase and (**b**) β-phase nickel electrodes in 1.0 M KOH at a scan rate of 5 mV s^{-1}. Reprinted from ref. [101]

5.2.3 Catalysts for Ethylene Glycol Oxidation in Alkaline Media

Ethylene glycol (EG) is of particular importance as an energy carrier for fuel cells because of its high-energy densities, ease of transport, favorable storage, low vapor pressure, nontoxic nature, and ready availability. Starting from the middle of 1970s, the anodic oxidation of ethylene glycol in alkaline media has been extensively investigated both from an electrocatalytic point of view and for its possible use in fuel cells. The overall oxidation reaction, which needs up to ten electrons per molecule when the final state of oxidation (i.e., CO_2) is reached, proceeds through several consecutive and parallel steps, involving different reaction intermediates. Platinum is commonly used as catalyst for EG oxidation, also if gold presents higher current densities than Pt [104]. Chang et al. [105] studied the electrooxidation pathways of ethylene glycol in alkaline aqueous solution on gold and platinum. The electrooxidation on gold featured the successive formation of partially oxidized C_2 solution species en route to oxalate and carbonate production. The latter species was produced predominantly via the formation of the dialdehyde glyoxal. In contrast, ethylene glycol electrooxidation on platinum exhibited markedly different kinetics and product distributions to those for the partially oxidized C_2 species, inferring that at least carbonate production from ethylene glycol occurred largely through sequences of chemisorbed, rather than solution-phase, intermediates. Hahn et al. [106] investigated the adsorption of ethylene glycol at a platinum electrode in aqueous medium. The adsorption appeared to be dissociative at any pH. However, striking changes occurred in the composition of the adsorbed layer when the pH varied from acid to alkaline solutions. Linearly bonded CO was dominant at pH ~1, whereas almost equal amounts of bridge-bonded and linearly bonded CO species were found at pH ~13. Christensen and Hamnett [107] investigated the electrooxidation of ethylene glycol at Pt electrodes in acidic and basic solutions by in situ FTIR spectroscopy. In acid, the main products were glycolic acid and CO_2, and the reaction is shown to proceed through a relatively small number of reactive sites. These active sites were poisoned at intermediate potentials, and the poisoning species were identified as terminally bonded CO. In alkali, the main products are glycolate, oxalate, and CO_3^{2-}. Production of glycolate and carbonate appeared to take place via the same intermediate, but oxalate was apparently produced by further oxidation of desorbed glycolate. Poisoning also took place in alkali medium.

Matsuoka et al. [108] investigated the electrochemical oxidation of ethylene glycol at 400 and 500 mV on platinum in alkaline solution. By analyzing the oxidation products, they concluded that there were two paths for ethylene glycol oxidation: poisoning and non-poisoning paths. The poisoning path led to the production of C_1 compounds and the non-poisoning path gave oxalate. Most of the C–C bond cleavage in ethylene glycol could not take place below 400 mV, which would prevent CO poisoning of platinum. On the other hand, the C–C bond of ethylene glycol was cleaved in ethylene glycol oxidation at 500 mV, which led to CO poisoning.

The electrocatalytic activity of platinum for the ethylene glycol oxidation reaction (EGOR) can be improved using binary systems obtained either by alloying platinum with different metals or by modifying a platinum surface by foreign metal adatoms. Kohlmuller [109] observed that the intermetallic compound Pt_3Pb exhibited an activity approximately ten times higher than pure platinum in the anodic oxidation of ethylene glycol to oxalic acid in 6 M KOH. Dalbay and Kadirgan [110] investigated the electrocatalytic oxidation of ethylene glycol on Pt, Pd, and Pt–Pd alloy electrodes of different compositions in alkaline solution. The exchange current density of Pt–Pd alloys went through a maximum at about 20 at.% Pd, greater than those for pure metals, so indicating a synergistic effect.

This effect was ascribed to a decrease of strongly bound residue of ethylene glycol. Kadirgan et al. [111] investigated seven different foreign metal adatoms (Bi, Cd, Cu, Pb, Re, Ru, T1) as activity modifiers of a platinum electrode for the EGOR in alkaline medium. All these metal adatoms increased the electrocatalytic activity of the Pt electrode for the optimum foreign metal concentrations in solution. This enhanced activity, which can reach very high values, close to diffusion-limited current densities with the best foreign metals (Pb and Bi), was explained through the bifunctional theory of electrocatalysis. Conversely, in acid medium the presence of the same adatoms does not enhance the electrocatalytic activity of Pt. El-Shafei et al. [112] studied the electrochemical oxidation of ethylene glycol on Pt, Pd, and Au electrodes in alkaline medium in the absence and in the presence of metal adatoms. For pure-metal electrodes, the maximum current density was obtained at the Au electrode. However, in the presence of metal adatoms, enhancement of catalytic activity changed its order to Pt $>$ Au $>$ Pd. The three different electrodes showed maximum catalytic activity when modified with Pb adatoms. More recently, Demarconnay et al. [113] observed that the addition of Bi to platinum leads to decrease the onset potential of EG electrooxidation of about 70 mV and to achieve higher current densities. The ternary catalyst Pt–Pd–Bi/C does not change the onset potential of EG oxidation, but leads to increase the current densities compared to Pt–Bi/C. They found that the addition of foreign atoms to platinum led to decrease the ability of the catalyst to break the C–C bond, likely due to dilution of surface platinum atoms. But, in the same time, catalyst containing Pd and Bi seems to activate the oxidation of EG to oxalate compared to pure platinum. They proposed that Bi mainly favors the adsorption of OH species but also affects the product distribution by changing the composition of chemisorbed species, whereas Pd only limits the poisoning of Pt sites by changing the composition of chemisorbed species. Recently, the electrocatalytic activities of Pt/C, Pt–Ru/C, and Pt–Ni/C for the oxidation of ethylene glycol in a basic solution have been evaluated by CV and quasi-steady-state polarization [114]. Based on the results of Tafel slopes from quasi-steady-state polarization, the catalytic activities for ethylene glycol oxidation are in the order of Pt–Ru/C $>$ Pt–Ni/C $>$ Pt/C. The analysis of intermediate products for ethylene glycol oxidation by higher performance liquid chromatography (HPLC) demonstrates that the degree of ethylene glycol oxidation is dependent on catalysts. Pt–Ru/C shows the highest current densities for ethylene glycol oxidation but shows lower fuel utilization. On the other hand, Pt–Ni/C shows higher ability to cleavage C–C bonds but is suffered from catalyst poisoning. To improve the tolerance for catalyst poisoning, we construct a novel Pt–Ni–SnO_2/C catalyst, compare its catalytic activities, and evaluate the intermediates. Pt–Ni–SnO_2/C shows superior catalytic activities for ethylene glycol oxidation, resulting in the highest degree of complete electrooxidation of ethylene glycol to CO_2. Electrocatalytic activities of the resultant Pt–Ni–SnO_2/C were studied by CV and Tafel plots as shown in Fig. 5.6. Pt–Ni–SnO_2/C showed superior catalytic activities for ethylene glycol oxidation than Pt–Ni/C and Pt/C. Therefore, it is confirmed that the addition of SnO_2 nanoparticles is effective to improve the tolerance for catalyst poisoning of Pt–Ni/C. The HPLC analysis for intermediates

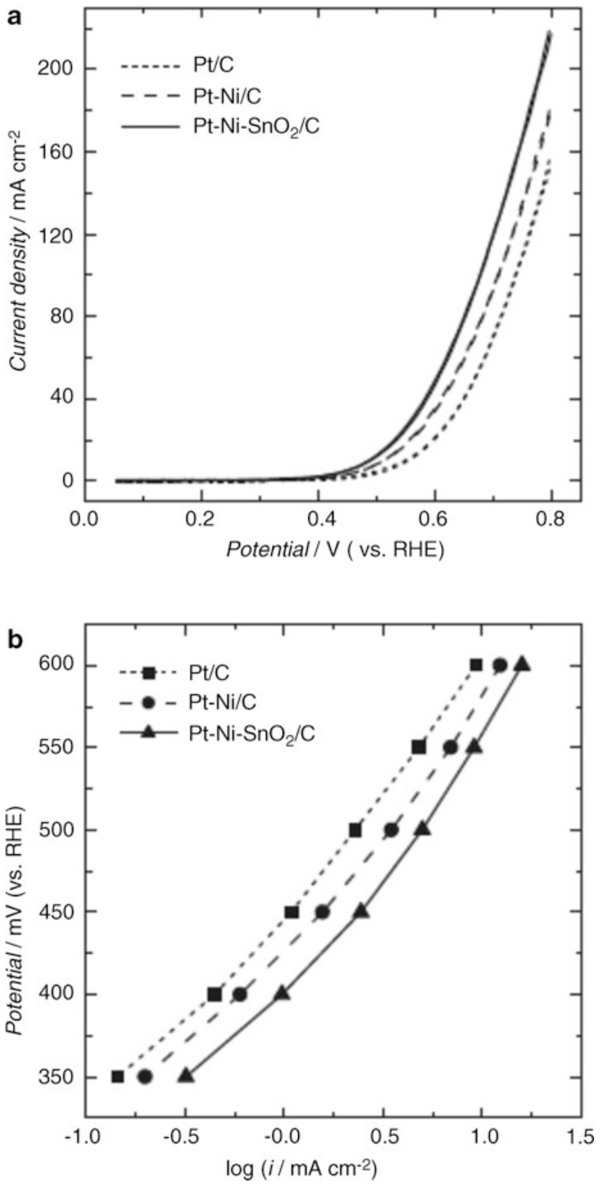

Fig. 5.6 (**a**) Cyclic voltammograms and (**b**) Tafel plots of Pt/C, Pt–Ni/C, and Pt–Ni–SnO$_2$/C catalysts in an aqueous solution of 1 mol dm^{-3} KOH and 1 mol dm^{-3} ethylene glycol. Reproduced from refs. [94, 114]

for ethylene glycol oxidation shows that the amount of formate production decreased and the degree of complete oxidation increased by Pt–Ni–SnO$_2$/C. However, SnO$_2$ nanoparticles did not reduce the formation of glycolate. These results indicate that the addition of SnO$_2$ nanoparticles had a specific effect of improving the tolerance for catalyst poisoning.

It was demonstrated that gold is a very good catalyst for the electrochemical oxidation of aldehydes and alcohols in alkaline solutions [104]. However, the potentials at which the maximum current densities occur are too positive for practical applications in fuel cells. These difficulties may be overcome using gold–platinum alloys, as reported by Beden et al. [115]. They carried out the oxidation of ethylene glycol on a Pt–Au electrode (48.4 at.% Au surface composition) by CV. During the positive sweep, the EG oxidation occurs in two main peaks: the first one at 0.76 V/RHE, in the same potential range as that for EG oxidation on pure Pt, and the second one at 1.18 V/RHE, corresponding to oxidation on pure Au. However, the current densities obtained with Pt–Au alloy electrodes were much higher than those on pure metals, particularly in the Pt region of the alloy, since the current density for this alloy was about eight times greater. The catalytic activity of the Au region of the alloy was also enhanced but only by a factor of two. This high activity was ascribed to synergistic effects between Pt and Au. They also observed that underpotential deposition of Pb adatoms on a Pt–Au alloy electrode greatly enhances the EGOR activity in alkaline medium of this alloy. The synergistic effect between Pt and Au was observed also by El-Shafei et al. [116]. They studied the EGOR at Pt, Au, and Pt–Au alloy deposited electrochemically on a glassy carbon (GC) substrate. Pt–Au/GC showed higher activity compared with that of Pt/GC and Au/GC. The current density obtained on Pt–Au/GC electrodes in the Pt region was much higher than that on the Pt/GC electrode, resulting in a catalytic factor of about 5 at the optimum alloy composition (40 at.% Pt). More recently, Jin et al. [117] investigated the EGOR on platinum–gold catalysts by CV. They observed the presence of a large oxidation peak in the potential range of pure platinum and a second small peak in the potential range of pure gold. Given that similar peak current densities have been reported for Pt and Au electrodes [118] and that the Pt–Au nanoparticles were prepared with a 1:1 atomic ratio, a synergistic effect of Au presence on the Pt activity, but not of Pt presence on Au activity for EG oxidation, can be inferred. Gold has higher electronegativity than platinum, so the interaction between platinum and gold in the Pt–Au nanoparticles may change the distribution of electrons in platinum, making the adsorption of ethylene glycol and hydroxyl on platinum easier. Summarizing, both Au and Pt are good electrocatalysts for EG oxidation, but in Pt–Au alloys, gold overall acts as promoter of the EGOR on Pt.

Kadirgan et al. [119] investigated the electrochemical oxidation of ethylene glycol on gold and adatom-modified gold electrodes in alkaline medium. As in the case of Pt, the influence of different metal adatoms (Bi, Cd, Cu, Pb, Re, Ru, Tl) on the catalytic properties of Au electrodes was considered. In contrast to the case in acid medium, the spectroscopic results showed clearly that almost no C–C bond scission occurs during adsorption in alkaline medium. Depending on the potential of electrolysis, the major products of the reaction were found to be glycolate alone or a mixture of glycolate, oxalate, carbonate, and formate. Compared to Au alone, only the Au–Bi and Au–Pb electrodes appeared to be relatively interesting. These systems shifted the polarization curves towards more negative potentials, reducing the overvoltage by about 100 mV but without changing the magnitude of the current density. Recently, Matsuoka et al. [120] deposited ultrafine gold on α-Fe_2O_3/Pt/C electrodes. Compared to Pt/C catalyst for ethylene glycol oxidation, the Au/α-Fe_2O_3/Pt/C electrode showed higher catalytic activity for the oxidation of ethylene glycol in alkaline solution in the potential range lower than 500 mV.

5.3 Tests in ADAFC

5.3.1 General Overview

As previously reported, the reaction kinetics and catalytic activities of the anodic oxidation of alcohols and the cathodic reduction of O_2 in alkaline media are significantly higher than those in acidic media. With the recent development of polymeric membranes presenting a good anionic conductivity, the feasibility of using anion-exchange membranes on fuel cells with alcohol as the fuel was investigated. Several tests on ADAFCs using an alkaline anion-exchange membrane as the electrolyte have been reported [8, 17, 19, 113, 121–139]. The results suggest the potential application of anion-exchange membranes in direct alcohol fuel cells. The first tests on ADAFCs with AAEM were carried out by Ogumi et al. [130] and Yu and Scott [17, 131]. Ogumi et al. [130] investigated ADAFCs formed by Pt/C as anode and cathode catalysts and a commercial ammonium-type anion-exchange membrane (AHA) by Tokuyama Co. The fuel supplied was 1 M methanol or EG in 1 M KOH at 50 °C. Cell voltages were around 100 mV higher for EG compared to methanol. Yu and Scott [17] carried out fuel cell tests using the conventional hot-pressed MEAs with carbon-supported Pt catalysts and a commercial quaternized cross-linked fluorinated polymer membrane (Morgane®-ADP, Solvay). Using 2 M methanol in 1 M NaOH as the fuel at 60 °C and a Pt loading of 2.1 mg cm^{-2}, a maximum power density (MPD) of 11 mW cm^{-2} was attained.

NaOH was added in the fuel stream because, as reported by Prabhuram and Manoharan [140], the MOR performance increases on going from a highly acidic range to a highly alkaline range. The same authors compared ADAFCs with platinized Ti mesh or Pt/C as the anode material, Pt/C as the cathode material, and the Morgane®-ADP membrane at 60 °C in 2 M CH_3OH and 1 M NaOH and a similar Pt loading [131]. The cell with the platinized Ti mesh anode showed a higher MPD than that of the cell with Pt/C.

Matsuoka et al. [8] tested ADAFCs formed by Pt–Ru/C as anode catalyst, Pt/C or Ag/C as cathode catalyst, and the AHA membrane by Tokuyama Co. The cells operated at 50 °C and were fuelled with four polyhydric alcohols and methanol for comparison. These alcohols (1 M) were dissolved in 1 M KOH aqueous solution. The maximum power densities were in the order of ethylene glycol > glycerol > methanol > erythritol > xylitol. The direct ethylene glycol fuel cell showed the highest power density. Alkaline direct alcohol fuel cells using silver as a cathode catalyst showed good performance; however, the open-circuit voltage of a cell with a silver catalyst was ca. 150 mV lower than that of a cell with a platinum catalyst under the same conditions. The performance of alkaline direct ethylene glycol fuel cells using Ag/C was improved by increasing the concentration of ethylene glycol. The performance of a cell with 3 or 5 M ethylene glycol solution was comparable to that of a cell using Pt/C catalyst in the large current density region (>40 mA cm^{-2}). Couteanceau et al. [19] tested alkaline direct alcohol fuel cells, fuelled with methanol (ADMFCs) and ethylene glycol (ADEGFC), using Pt/C 40 % as anode and cathode catalyst and the Morgane®-ADP membrane. They demonstrated the necessity to add sodium hydroxide to methanol and EG aqueous solutions in order to obtain significant performance. 4 M of NaOH added seems to be an optimum value, and a maximum of 18 mW cm^{-2} was observed at room temperature. In the case of the ADEGFC, with a concentration of 2 M ethylene glycol and 4 M sodium hydroxide, a maximum of 19 mW cm^{-2} of power density was obtained at 20 °C, a value very close to that observed for methanol. In addition to the previous works, further papers addressed to the use of ethylene glycol as the fuel in ADAFCs [113, 121, 122]. Different anode and cathode catalysts were tested. The best results were obtained using a ternary Pt–Pb–Pd/C catalyst as anode material [113] and a binary Pt–Pb/C catalyst as cathode material [121].

In all the previous works, commercial quaternized membranes were used as solid electrolyte in ADAFCs. In the following part of this paragraph, tests on ADAFCs prepared using homemade AAEMs are reported. Varcoe and Slade [125] prepared ADMFCs using a homemade quaternized ETFE-based membrane and Pt–Ru and Pt black as anode and cathode materials, respectively. Moreover, unlike from the previous ADAFC tests, aqueous methanol without MOH added was used as the fuel. Peak power densities of 1.5 mW cm^{-2} at 50 °C increasing to 8.5 mW cm^{-2} at 80 °C (with additional reactant pressurization) were obtained. According to the authors, these results represent the highest peak power performances obtained with metal cation-free quaternary ammonium-functionalized alkaline MEAs and demonstrate that the presence of M^+OH^- in an aqueous methanol fuel is not needed to obtain a functioning ADMFC. Yang et al. [126] tested an ADMFC composed of MnO_2/BP2000 as the cathode catalyst, Pt–Ru black as the anode catalyst, and an alkaline cross-linked non-quaternized PVA/SSA membrane. The MPD of the ADMFC goes from 2.38 mW cm^{-2} at 30 °C to 4.13 mW cm^{-2} at 60 °C and 1 atm in 2 M KOH + 2 M CH_3OH solution. The ADMFC with the same catalysts but a hybrid membrane obtained by adding ceramic fillers such as TiO_2 and HAP to PVA, better performed than the cell with PVA only. The MPD of the ADMFC increased from 2.38 to 9.25 mW cm^{-2} using PVA/TiO_2 [127], to 11.48 mW cm^{-2} using PVA/HAP [128]. Regarding the ADAFC with the PVA/TiO_2 hybrid membrane fuelled with different alcohols, the MPDs were also in the order of methanol > ethanol > 2-propanol. It has to be remarked, however, that Pt–Ru is the best catalyst for the MOR in alkaline media, while the best catalyst for the EOR is Pd. This should explain the better performance of ADMFC than that of ADEFC. Summarizing, these ADAFCs consisting of a low-cost air cathode electrode (MnO_2 is a non-precious metal catalyst), a Ti-based Pt–Ru anode electrode, and a PVA-based solid polymer membrane (PVA is a cheap non-perfluorosulfonated polymer membrane, as compared to the expensive Nafion® membrane) can be considered a low-cost system, with respect to the acidic DAFC.

Hou et al. prepared ADAFCs with Pt–Ru/C as the anode catalyst, Pt/C as the cathode catalyst, and KOH-doped PBI as the anion-exchange membrane, then these cells were tested at 90 °C using a KOH + ethanol [123] or methanol [124] solution. The PBI/KOH membrane exhibited excellent endurance both in basic solution and at higher temperature. The maximum power densities of ADEFC and ADMFC were about 61 and 31 mW cm^{-2}, respectively. The much lower performance of ADMFC than that of ADEFC under the same conditions should be attributed to the presence of CO_2, formed by complete methanol oxidation in the ADMFC, which reacts with KOH, causing carbonation of the membrane and collapsing electrode pores. Conversely, ethanol tends to be oxidized incompletely, because most of the C–C bonds cleavage in ethanol molecule cannot take place, minimizing the negative effect of carbonation.

The performances of ADAFCs with different catalysts and membranes are reported in Table 5.1.

5.3.2 Comparison Between Alkaline and Acid Direct Alcohol Fuel Cells

In some papers the performance of alkaline fuel cells with anion-exchange membranes has been compared with that of acid fuel cells with proton-exchange membranes. Varcoe et al. [129] tested three ADAFCs formed by Pt–Ru as anode catalyst, Pt black as cathode catalyst, by two AAEM, an ETFE-based radiation-grafted AAEM (AAEM-E), and a thicker commercial cross-linked quaternary ammonium-type AAEM (AAEM-C), and, for comparison, by a Nafion®-115 membrane. All the types of cells were fuelled with aqueous solutions of methanol, ethanol, and ethylene glycol. Poorer power densities of alkaline DAFCs were observed with respect to the performances of the acid DAFCs and were due overall to the absence in OH^- in the fuel stream. The power performance substantially decreased with the Nafion®-containing cells when replacing methanol with ethanol and ethylene glycol. Conversely, the AAEM-based cells exhibited no such decrease in peak power densities: higher MPDs were observed with the C_2 alcohols on testing of the thicker AAEM. Fujwara et al. compared the performance of a direct ethanol fuel cell with a Pt–Ru anode and a Pt cathode using an anion-exchange membrane (AAEM, Tokuyama Co.) with a direct ethanol fuel cell with the same catalysts and a cation-exchange membrane (CEM, Nafion®-117). The cell voltage and power density versus current density of AEM- and CEM-type DEFCs are shown in Fig. 5.7. The maximum power density of the cell significantly increased from 6 to 58 mW cm^{-2} at room temperature and atmospheric pressure when the electrolyte membrane was changed from CEM to AAEM. The anode and cathode polarization curves showed a decrease in the anode potential and an increase in the

Table 5.1 Performance, as maximum power density (MPD), of some Pt-containing ADAFCs with different catalysts and AAEMs. Only temperature is reported in operating conditions, but it has to be remarked that MPD depends also on other parameters such as catalyst loading, gas flow, and pressure

Fuel	Anode	Cathode	Electrolyte	Temperature (°C)	MPD (mW cm^{-2})	Ref.
Methanol + KOH	Pt/C	Pt/C	AHA Tokuyama	50	5.5	[130]
EG + KOH					9.2	
Methanol + NaOH	Pt/C	Pt/C	Morgane®-ADP, Solvay	60	6.8	[17]
Methanol + NaOH	Pt/Ti	Pt/C	Morgane®-ADP, Solvay	60	7.8	[131]
Methanol + KOH	Pt–Ru/C	Pt/C	AHA Tokuyama	50	6.2	[8]
		Pt/C			9.5	
EG + KOH (1 M)		Ag/C			8.1	
EG + KOH (3 M)						
Methanol + NaOH	Pt/C	Pt/C	Morgane®-ADP, Solvay	20	18	[19]
EG + NaOH					19	
EG + NaOH	Pt/C	Pt/C	Morgane®-ADP, Solvay	20	19	[113]
					22	
	PtPb/C				28	
	PtPbPd/C					
EG + NaOH	Pt/C	Pt/C	Morgane®-ADP, Solvay	20	19	[121]
		PtPb/C			23.5	
EG + KOH	Pt–Ru/C	Pt/C	A-006, Tokuyama	80	25	[122]
					20	
		Ag/C			18	
		LaSrMnO/C				
Methanol	Pt–Ru	Pt black	QAETFE	50	1.5	[125]
				80	8.5	
Methanol + KOH	Pt–Ru black	MnO_2/C	PVA/SSA	30	2.38	[126]
				60	4.13	
Methanol + KOH	Pt–Ru black	MnO_2/C	PVA/TiO_2	25	9.25	[127]
Ethanol + KOH					8.0	
Methanol + KOH	Pt–Ru black	MnO_2/C	PVA/HAP	25	11.48	[128]
Ethanol + KOH	Pt–Ru/C	Pt/C	PBI/KOH	75	49.20	[123]
				90	60.95	
Methanol + KOH	Pt–Ru/C	Pt/C	PBI/KOH	90	31	[124]
Methanol	Pt–Ru	Pt black	AAEM-C	50	1.17	[129]
					1.71	
Ethanol					1.57	
EG						
Ethanol + KOH	Pt–Ru	Pt black	AAEM, Tokuyama	20	58	[132]
Methanol + KOH	Pt–Ru/C	Pt/C	AAEM, Tokuyama	20	6.8	[133]

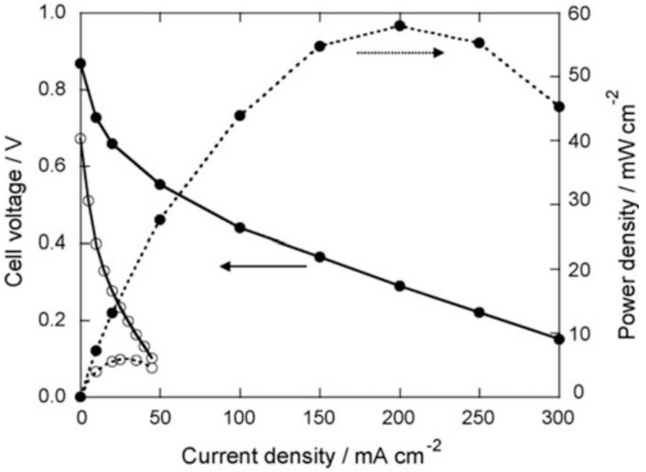

Fig. 5.7 Cell voltage and power density versus current density plots of DEFCs using an AEM and 1 M ethanol + 0.5 M KOH solution (●) or a CEM and 1 M ethanol aqueous solution (○), as an electrolyte membrane and a fuel, respectively, at room temperature and atmospheric pressure. Anode: 3 mg cm^{-2} Pt–Ru black, cathode: 3 mg cm^{-2} Pt black, and cathode gas: humidified O_2. Reproduced from ref. [132]

cathode potential for the cell with AAEM compared to the cell with CEM. Kim et al. [133] compared the performance of direct methanol fuel cells using alkaline and acid-exchange membranes. In both the cells, the anode was Pt–Ru/C and the cathode Pt/C. The cell with AAEM exhibited a higher open-circuit voltage and superior cell performance than those in cell using Nafion®-117. In 1 M methanol solution, the MPD of the cell with AAEM was 6.8 mW cm^{-2}, while that of the cell with Nafion®-117 was 5.2 mW cm^{-2}. In addition, by using homemade Pd–Sn/C catalyst as a cathode catalyst on ADMFC, the membrane electrode assembly (MEA) using Pd–Sn/C catalyst as cathode showed a higher performance than the usual commercially available Pt/C catalyst in high methanol concentration.

5.3.3 Pt-Free ADAFCs

Considering the high cost and the limited availability of platinum, the development of Pt-free fuel cells is necessary. Very recently, tests were carried out on Pt-free ADAFCs [134–139], in particular on cells with Pd-based catalysts as anode materials and ethanol as the fuel, being Pd the best catalyst for ethanol oxidation. These ADAFCs presented high performance, and particularly, Bianchini et al. [134] reported exceptionally high values of power density (55 mW cm^{-2} at 20 °C and 170 mW cm^{-2} at 80 °C) for the ADEFC formed by a Tokuyama A-006 anion-exchange membrane, Pd–(Ni–Zn)/C as anode catalyst and Fe–Co as cathode catalyst. Ethanol oxidation occurs by the selective conversion of ethanol into potassium acetate with negligible formation of CO_3^{2-}, avoiding in this way catalyst poisoning or membrane carbonation. For comparative purposes, electrodes coated with Pd/C were successfully used to selectively oxidize ethanol to acetic acid in alkaline media in both half cells and ADEFC, yet neither the power output (28 mW cm^{-2} at 20 °C and 120 mW cm^{-2} at 80 °C) nor the electrochemical stability was comparable to those exhibited by the Pd–(Ni–Zn)/C electrode. This finding suggests that the Ni–Zn alloy exerts a beneficial action on the activity of the Pd sites. Also, Modestov et al. [135] attained a power density of about 100 mW cm^{-2} at 80 °C with an ADEFC formed by Ru-V/C as anode catalyst, Co-TMPP as cathode catalyst, and a KOH/PBI membrane. The performance of this ADEFC single cell was remarkably higher than that of the ADEFC, employing the same KOH/PBI membrane and Pt-based electrodes (61 mW cm^{-2} at 90 °C) [123]. Finally, it has to be promptly pointed out that the corresponding acid DEFCs, with more expensive Pt-based catalysts, exhibit MPD values lower than 100 mW cm^{-2}. Very recently, Shen et al. [136] tested an ADEFC formed by a Tokuyama A201 anion-exchange membrane, Pd/C or Pd_2Ni_3/C, synthesized by simultaneous Pd and Ni reduction using $NaBH_4$, as anode catalyst, and non-platinum HYPERMEC™ catalyst by Acta, as cathode catalyst. The measurements were made by feeding 1.0 M ethanol/1.0 M KOH and 3.0 M ethanol/5.0 M KOH to the fuel cell at 60 °C. In both conditions, the ADEFC with a Pd_2Ni_3/C anode better performed than that with Pd/C in terms of both open-circuit voltage (OCV) and power density. By feeding 3.0 M ethanol mixed with 5.0 M KOH, the cell with the Pd_2Ni_3/C catalyst as an anode, the OCV was 0.89 V and the peak power density was 90 mW cm^{-2}, while in the case of Pd/C, the OCV was 0.79 V and the peak power density was 67 mW cm^{-2}.

The performances of some platinum-free ADAFCs are reported in Table 5.2.

5.3.4 Presence of OH^- in the Fuel Stream

As previously reported, generally MOH (M = K, Na) was added in the fuel stream because the activity for alcohol oxidation on different catalysts increases on going from an acidic range to an alkaline range. Beden et al. [21] studied the MOR on a platinum electrode in 10^{-3}, 10^{-2}, 10^{-1}, 0.5, and 1 M NaOH solutions with different concentrations of methanol (10^{-3}, 10^{-2}, 10^{-1}, and 1 M CH_3OH). They observed an increase in the MOR activity as the hydroxyl ion concentration in solution is increased for a given methanol concentration, and a decrease in the MOR activity once the hydroxyl/methanol concentration ratio is greater than unity. Analogously, Prabhuram and Manoharan [140] investigated the MOR activity on platinum electrodes in electrolytes containing different concentrations of alkali (1, 6, and 11 M KOH) and methanol (1, 6, and 11 M CH_3OH). They reported that methanol oxidation on Pt electrodes increases only up to 6 M KOH solution. At higher

Table 5.2 Performance, as maximum power density (MPD), of some Pt-free ADAFCs with different catalysts and AAEMs

Fuel	Anode	Cathode	Electrolyte	Temperature (°C)	MPD (mW cm^{-2})	Ref.
Ethanol + KOH	Pd–(Ni–Zn)/C	Fe–Co HYPERMEC™	A-006, Tokuyama	20	58	[134]
				80	170	
Ethanol + KOH	RuV/C	Co-TMPP/C	PBI	80	90 air	[135]
					110 O_2	
Ethanol (1 M) + KOH (1 M)	Pd_2Ni_3/C	Fe–Co HYPERMEC™	A201, Tokuyama	60	44	[136]
Ethanol (3 M) + KOH (5 M)				60	90	
Ethanol + KOH	Ni–Fe–Co HYPERMEC™	Fe–Co HYPERMEC™	A201, Tokuyama	40	60	[137]
Methanol + KOH	Pd/MWCNT	Fe–Co HYPERMEC™	A-006, Tokuyama	20–22	7	[138]
					18	
Ethanol + KOH					5	
EG + KOH						

concentrations, the activity declines. Also, they observed that the MOR performance depends on the methanol concentration of a given pH solution. The 6 M KOH/6 M CH_3OH mixture yields the highest MOR performance. It appears that CHO species do not become bonded on the platinum electrodes in the equimolar mixture 6 M KOH/6 M CH_3OH. They concluded that by choosing the proper ratio of OH^- ions and CH_3OH, it is possible to remove completely the intermediate organic species and/or poisonous species that retard the MOR rate on the electrode surface. Yu et al. [141] found that the activity of methanol oxidation on Pt/Ti in aqueous alkaline systems increased with pH or OH species coverage on the electrode surface. A reaction order of close to 0.5 was obtained for both NaOH and CH_3OH/NaOH solutions indicating that adsorption of methanol and OH^- on the platinized electrode follows Termkin isotherm. In the high potential region, a poisoning effect was observed at CH_3OH/OH^- concentration ratio greater than 1, which could have arisen from an excess of methanol at the electrode surface and/or depletion of OH^- at the electrode surface. The onset potential for methanol oxidation varied with the concentration of NaOH, shifting cathodic with increasing NaOH concentration from 0.1 to 2 M, at a fixed 2 M CH_3OH solution. All the mentioned studies were performed in a half cell. However, in an ADMFC, i.e., in the presence of an anion-exchange membrane, the effect of OH^- and hydroxyl/methanol concentrations can be different. According to Coutanceau et al. [19], taking into account that the anionic membrane used in ADMFC is an ionic conductor needing a constant concentration of OH^- to maintain its conductivity, the amount of added sodium hydroxide is a critical point. If it is not sufficient, some hydroxyl species would be taken from the membrane to form carbonate and the conductivity of the membrane will drop rapidly. However, if the concentration of OH^- is too high, it becomes difficult to stabilize working conditions of the ADMFC, and the observed performances decrease rapidly with time. To investigate an effect of ion conductivity on cell performance, Kim et al. [133] investigated the behavior of an ADMFC operating with various KOH concentrations in anode fuel. Figure 5.8 from ref. [133] shows the polarization curves of an ADMFC operating with 2 M CH_3OH and various KOH concentrations. The current density at a cell voltage of 0.1 V increased from 39 to 65 mA cm^{-2} as KOH concentration solution increases from 1 to 3 M. Moreover, the MPD in 3 M KOH was about two times larger than that in 1 M KOH, from 5.9 to 11.5 mW cm^{-2}. In the same way, Li et al. [139], to study the influence of the electrolyte on ADEFC performance, tested 1.0 and 5.0 M ethanol aqueous solutions with various KOH concentrations. From polarization curves for different KOH concentrations ranging from 1.0 to 11.0 M at a fixed ethanol concentration of 1.0 M, they observed that the voltage increases with increasing KOH concentration in the low current density region (lower than 150 mA cm^{-2}). This suggests that in the low current density region, the concentration of OH^- ion is the predominant factor that determines the anode potential. This result was further confirmed by the increase of the OCV with increasing KOH concentration. It has to be pointed out that the increase in KOH concentration is limited by its solubility in ethanol solutions. With an ethanol concentration of 1.0 M, the KOH concentration cannot be higher than 13.0 M. Unlike the results

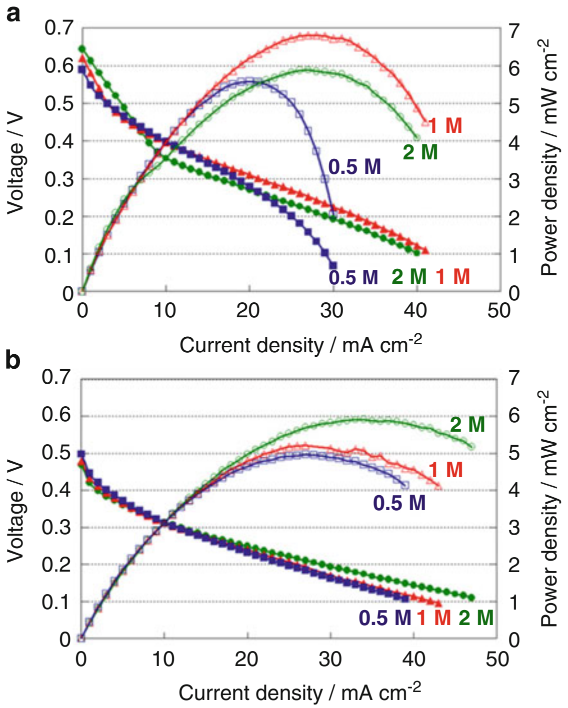

Fig. 5.8 Polarization curves of MEA with anion-exchange membrane (Tokuyama Co.) (anode: Pt–Ru/C, 1.8 mg cm^{-2}, anionic ionomer: 28 %; cathode: Pt/C, 2.0 mg cm^{-2}, anionic ionomer: 27 %) in 2 M CH_3OH containing various concentration of KOH (1 M (● and ○), 2 M (■ and □), and 3 M (▲ and △)). Reproduced from ref. [133]

obtained in the low current density region, in the high current density region, when the KOH concentration is increased above 5.0 M, the voltage falls. Similar results were obtained by increasing the ethanol concentration to 5.0 M. Regarding the ADEGFCs, also if MOH is commonly added in the fuel stream, analogous detailed investigations are not present in literature.

On the other hand, Varcoe et al. [142] asserted that the addition of MOH into the fuel stream is not desirable for two principal reasons: (1) The MOH constitutes a further chemical component reducing the energy density of the fuel and making this fuel supply highly caustic. (2) The presence of M^+ in the system will lead to the formation of precipitates of carbonate/bicarbonate on reaction of the OH^- with CO_2.

5.3.5 *Effect of the Polymer Binder in the Catalyst Layer*

In preparing the electrodes for low-temperature fuel cells that use membrane electrolytes, a polymer binder is essential to bind discrete catalyst particles to form a porous catalyst layer that simultaneously facilitates the transfer of ions, electrons, and reactants/products. Firstly, polytetrafluoroethylene (PTFE) was used as the binder in the catalyst layer of PEMFCs, but PTFE does not conduct protons. The substitution of PTFE with Nafion®, which is a perfluorosulfonic acid polymer with high proton conductivity, was a decisive pathway in the development of the low-temperature fuel cell technology [143]. In acidic fuel cells, Nafion® has proved to be the best binder for both the anode and cathode catalyst layers. Regarding the ADAFCs, PTFE or Nafion® was added to the catalyst layer to serve as a binder [17–19]. Although both PTFE and Nafion® can bind catalyst particles so as to form a catalyst layer, they cannot conduct hydroxide ions. Hence, these two polymer materials are not a good choice as the binder for preparing MEAs for ADAFCs. Recently, an anion-conducting ionomer, named A3, has been developed by Tokuyama as a binder for ADAFCs, and the effect of the presence of A3 in the catalyst layer on cell performance has been investigated [133, 136, 144]. Kim et al. prepared MEAs with various contents of A3 in the anode catalyst layer to evaluate the effect of the ion conductivity of the catalyst layer. The MPD of ADMFCs fuelled with 1 M CH_3OH containing 1 M KOH increased with increasing ionomer content in the anode catalyst layer (in the range 10–35 wt%). In the same way, Bunazawa and Yamazaki [144] investigated the influence of A3 content in the anode and cathode catalyst layers of ADMFCs. The ionomer contents of MEAs were 30, 39.2, 45.4, and 51.7 wt% both for the anode and the cathode. The MEA with 45.4 wt% of ionomer content showed the highest performance when both non-alkaline (CH_3OH (1 M)) and alkaline (CH_3OH (1 M) + NaOH (0.5 M)) fuels were used. Comparing to the MEA with 45.4 wt% of ionomer, the MEA with 39.2 wt% of ionomer showed higher OCV, but the *I*–*V* curve was sharp. This indicates that the OH^- transfer of this MEA was low because of the low ionomer content. On the other hand, MEAs with 51.7 and 56.3 wt% of ionomer showed higher activation polarization because the ionomer content was at a surplus and the reactant supply was impeded. Unlike the results previously reported [133, 144], Li et al. [136] observed that in the presence of KOH in the fuel, the ADEFC performance decreased with increasing A3 content in the catalyst layer from 0 to 30 wt% over the whole current density region, including the activation, ohmic, and concentration-controlled regions. The maximum current density was 65 mA cm^{-2} with 30 wt% A3, whereas it was 138 mA cm^{-2} without ionomer in the anode catalyst layer. According to the authors, as film-like structures are likely formed when A3 is incorporated into the catalyst layer, the active sites may be covered by A3 films, leading to a decrease in the active surface area. The A3 films also increase the transport resistance of hydroxide ions, electrons, and fuel in the catalyst layer. When the anode was fed with 3 M ethanol solution without added KOH, the cell performance varied with ionomer content, and the best performance was achieved with 10 wt% of ionomer. The use of the A3 ionomer could extend the active surface area of the anode catalyst layer as it can conduct hydroxide ions, which is beneficial to anode performance. On the other hand, excessive A3 ionomer in the anode catalyst layer hinders the transfer of ethanol and electrons to catalytic sites and thus lowers the anode performance.

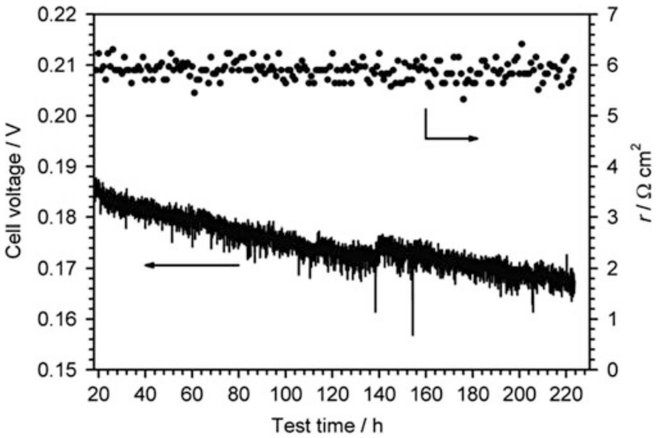

Fig. 5.9 Medium-term test with an AAEM-MEA (4 mg cm^{-2} Pt–Ru anode and 4 mg cm^{-2} Pt black cathode both with the alkaline interface). Test conditions: 50 °C, 0.1 A discharge, cathode: 2 dm^{3} min^{-1} air (RH = 100 %), anode: methanol (2 M, 2 cm^{3} min^{-1}), no back pressures. Reprinted from ref. [9]

5.3.6 *Duration Tests*

Long-term durability of MEAs is always a question for any fuel cell and in particular in the case of the ADAFCs, where one of the major causes of the degrading performance is the precipitation of large solid metal carbonate crystals, formed by the interaction of hydroxide ions with carbon dioxide, either in the air stream or formed as part of fuel oxidation in the electrolyte-filled pores of the electrode. However, few tests on durability have been carried out on ADAFCs. Moreover, it is important to remark that these studies were performed without MOH presence in the system [9, 19] or without CO_2 formation by alcohol oxidation [134], i.e., in the absence of carbonation. Varcoe et al. [9] carried out a 233 h durability test on an ADMFC, formed by an alkaline cross-linked quaternized poly(vinylbenzyl)-based membrane and by Pt–Ru and Pt blacks as anode and cathode catalysts, respectively, and fuelled with a 2 M CH_3OH aqueous solution. As can be seen in Fig. 5.9, the cell voltage stabilized to a very low degradation rate of 95 ± 10 μV h^{-1} (with no associated increase in cell area resistance). After this 233 h test, the methanol/O_2 performance was reevaluated, and the MPD increased from 0.9 to 1.1 mW cm^{-2}, indicating that performance was recoverable. The ion-exchange capacity of the membrane after the 233 h test had reduced by less than 5 %. In contrast, the performance of a KOH electrolyte AFC (6 mol dm^{-3}) degraded rapidly over the course of 70 h at 60 °C and 94 h at 30 °C, due to carbonate precipitation at the anode, when fuelled with methanol. According to the authors, the above observations demonstrate that elimination of M^{n+} cations in such systems minimizes performance losses due to carbonation, thereby allowing alcohols to be used in AFCs.

In the same way, Scott et al. [17] tested the stability of an ADMFC, formed by a Morgane®-ADP hydroxide ion-conducting membrane, and Pt–Ru/C and Pt/C as catalysts, and fuelled with an aqueous solution of CH_3OH. The cell was tested for 12 days at a fixed current density (20 mA cm^{-2}) at 60 °C without any significant loss in performance. Bianchini et al. [134] performed a galvanostatic experiment at 60 °C on an ADEFC formed by a Tokuyama A-006 anion-exchange membrane, Pd–(Ni–Zn)/C and Fe–Co as anode and cathode catalysts, respectively, and fuelled with a 2 M KOH solution of ethanol. After a conditioning time of 1 h at the OCV of 0.75 V, the cell was held to a constant current density of 20 mA cm^{-2} for 217 h showing a modest 15 % decay of the cell voltage. The high stability of this ADEFC has to be ascribed to negligible formation of carbonate, as detected by NMR, which is consistent with the selective acetate formation (no C–C bond cleavage) on the anode side and negligible atmospheric CO_2 uptake on the cathode side.

5.4 Conclusions

The use of alkali electrolytes not only leads to better polarization characteristics of alcohol oxidation on platinum compared to acid media but also opens up the possibility of using non-noble, less expensive metal catalysts for the process. Platinum has the highest catalytic activity for the methanol oxidation reaction of any of the pure metals in alkaline media. To increase the MOR activity of Pt, Pt-based binary and ternary catalysts, such as Pt–Ru, PtAu, and PtPdAu, have been investigated, showing enhanced catalytic activity than pure Pt. Among different metals, nickel has been the most investigated Pt-alternative anode catalyst for methanol oxidation in alkaline media. In addition to the pure nickel electrode, different nickel-based electrodes, like nickel alloy and nickel complex-modified carbon electrodes, have been tested for methanol oxidation in alkaline media. Conversely to ethanol oxidation in acid media, in alkaline media the EOR activity of Pd is remarkably higher than that of Pt. Among pure metals, palladium is the more active catalyst for the ethanol oxidation in alkaline media. To improve the electrocatalytic activity of platinum and palladium, the ethanol oxidation on different metal adatom-modified, alloyed, and oxide-promoted Pt- and Pd-based electrocatalysts has been investigated in alkaline media. Moreover, a new group of Ru–Ni and Ru–Ni–Co catalysts for ethanol oxidation in alkaline media has been investigated with encouraging results. Platinum is commonly used as catalyst for ethylene glycol oxidation, also if gold presents higher current densities than Pt. The electrocatalytic activity of platinum for ethylene glycol oxidation can be improved using binary systems obtained either by alloying platinum with different metals or by modifying a platinum surface by foreign metal adatoms.

The comparison of the performance of ADAFCs, formed by the same catalysts and membrane but fuelled with different fuels, to establish a ranking of fuels is hazardous, considering that the activity for alcohol oxidation depends on the anode catalyst. The correct comparison should be carried out using the best catalyst for each fuel, and not the same catalyst for all the fuels compared. Regarding the comparison of methanol with ethanol, unlike acidic direct alcohol fuel cells, where DMFC performance $\gg$ DEFC performance, in alkaline media ADEFC performance $\geq$ ADMFC performance (notwithstanding the use of Pt-based anode catalysts, being Pd the best catalyst for the EOR in alkaline media) [123, 124, 127, 129]. Indeed, using Pd as anode catalyst ADEFC performance $\gg$ ADMFC performance [137]. Regarding ADAFCs with Pt-based anode catalysts, fuelled with methanol and ethylene glycol, the performance of ADEGFCs was higher than that of ADMFCs [8, 19, 129, 130]. Summarizing, in direct alcohol fuel cells, the choice of the liquid fuels at the anode can be expanded to include alcohols other than methanol.

On the basis of the performances of various types of ADAFCs, the most relevant observation is the mandatory presence of OH ions in the fuel stream. Up to date, in the absence of OH^- in the alcohol solution, the cell performance is very poor and far from a possible industrial application. The addition of MOH into alcohol supply, however, is not desirable for different reasons, such as corrosion, electrode weeping, mechanic electrode destruction by carbonate crystals, and catalyst decomposition [145]. Therefore, in addition to short-time tests, durability tests on ADAFCs fuelled with alcohol + MOH in the presence of CO_2 have to be carried out, to find a MOH content, resulting in a good compromise between the positive effect on cell performance and the negative effect on the durability.

Generally, the presence of an anionic binder in the catalyst layer improves the cell performance, and the optimum ionomer content goes through a maximum. However, as film-like structures are likely to form when the ionomer is incorporated into the catalyst layer, the active sites may be covered by ionomer films, leading to a decrease in the active surface area and, as a consequence, in the cell performance.

In conclusion, all of these observations indicate that there is still much room to improve ADAFC performance by developing novel materials and, on the other hand, by optimizing the operational conditions of the fuel cell. Future work should look into a wider range of potential low-cost materials and composites with novel structures and properties, presenting catalytic activity comparable to that of noble metals. The development of new catalyst systems is more likely in alkaline media because of the wide range of options for the materials support and catalyst, as compared to acidic media which offer more limited materials choice. Moreover, efforts have to be addressed to meet the durability targets required for commercial application. More work is needed to optimize the operational fuel cell conditions, by achieving suitable chemical (OH^- concentration, hydroxyl/alcohol ratio in the fuel stream) and physical (temperature, pressure, flow rate) parameters.

References

1. Markovic N, Gasteiger H, Ross PN (1997) Kinetics of oxygen reduction on Pt(hkl) electrodes: implications for the crystallite size effect with supported Pt electrocatalysts. J Electrochem Soc 144(5):1591–1597
2. Blizanac BB, Ross PN, Markovic NM (2007) Oxygen electroreduction on Ag(111): the pH effect. Electrochim Acta 52(6):2264–2271
3. Kordesch K, Hacker V, Gsellmann J, Cifrain M, Faleschini G, Enzinger P, Fankhauser R, Ortner M, Muhr M, Aronson RR (2000) Alkaline fuel cells applications. J Power Sources 86 (1–2):162–165
4. Gouerec P, Poletto L, Denizot J, Sanchez-Cortezon E, Miners JH (2004) The evolution of the performance of alkaline fuel cells with circulating electrolyte. J Power Sources 129(2): 193–204
5. Gulzow E, Schulze M, Gerke U (2006) Bipolar concept for alkaline fuel cells. J Power Sources 156(1):1–7
6. Lin BYS, Kirk DW, Thorpe SJ (2006) Performance of alkaline fuel cells: a possible future energy system? J Power Sources 161(1):474–483
7. Duerr M, Gair S, Cruden A, McDonald J (2007) Dynamic electrochemical model of an alkaline fuel cell stack. J Power Sources 171(2):1023–1032
8. Matsuoka K, Iriyama Y, Abe T, Matsuoka M, Ogumi Z (2005) Alkaline direct alcohol fuel cells using an anion exchange membrane. J Power Sources 150:27–31
9. Varcoe JR, Slade RCT, Lam How Yee E (2006) An alkaline polymer electrochemical interface: a breakthrough in application of alkaline anion-exchange membranes in fuel cells. Chem Commun 13:1428–1429
10. Yang CC, Hsu ST, Chien WC, Shih MC, Chiu SJ, Lee KT, Wang CL (2006) Electrochemical properties of air electrodes based on MnO2 catalysts supported on binary carbons. Int J Hydrogen Energy 31(14):2076–2087
11. Bidault F, Brett DJL, Middleton PH, Brandon NP (2009) Review of gas diffusion cathodes for alkaline fuel cells. J Power Sources 187(1):39–48
12. Dillon R, Srinivasan S, Arico AS, Antonucci V (2004) International activities in DMFC R&D: status of technologies and potential applications. J Power Sources 127(1–2):112–126
13. Wasmus S, Kuver A (1999) Methanol oxidation and direct methanol fuel cells: a selective review. J Electroanal Chem 461(1–2):14–31
14. Antolini E (2007) Catalysts for direct ethanol fuel cells. J Power Sources 170(1):1–12
15. Peled E, Livshits V, Duvdevani T (2002) High-power direct ethylene glycol fuel cell (DEGFC) based on nanoporous proton-conducting membrane (NP-PCM). J Power Sources 106(1–2):245–248
16. Tripkovic AV, Popovic KD, Grgur BN, Blizanac B, Ross PN, Markovic NM (2002) Methanol electrooxidation on supported Pt and PtRu catalysts in acid and alkaline solutions. Electrochim Acta 47(22–23):3707–3714
17. Yu EH, Scott K (2004) Development of direct methanol alkaline fuel cells using anion exchange membranes. J Power Sources 137(2):248–256
18. Scott K, Yu E, Vlachogiannopoulos G, Shivare M, Duteanu N (2008) Performance of a direct methanol alkaline membrane fuel cell. J Power Sources 175(1):452–457
19. Coutanceau C, Demarconnay L, Lamy C, Leger JM (2006) Development of electrocatalysts for solid alkaline fuel cell (SAFC). J Power Sources 156(1):14–19
20. Spendelow JS, Wieckowski A (2007) Electrocatalysis of oxygen reduction and small alcohol oxidation in alkaline media. Phys Chem Chem Phys 9(21):2654–2675
21. Beden B, Kadirgan F, Lamy C, Leger JM (1982) Oxidation of methanol on a platinum-electrode in alkaline-medium – effect of metal Ad-atoms on the electrocatalytic activity. J Electroanal Chem 142(1–2):171–190

22. Tripkovic AV, Popovic KD, Momcilovic JD, Drazic DM (1998) Kinetic and mechanistic study of methanol oxidation on a Pt(100) surface in alkaline media. J Electroanal Chem 448(2):173–181
23. Tripkovic AV, Popovic KD, Lovic JD (2001) The influence of the oxygen-containing species on the electrooxidation of the C-1-C-4 alcohols at some platinum single crystal surfaces in alkaline solution. Electrochim Acta 46(20–21):3163–3173
24. Spendelow JS, Babu PK, Wieckowski A (2005) Electrocatalytic oxidation of carbon monoxide and methanol on platinum surfaces decorated with ruthenium. Curr Opin Solid State Mater Sci 9(1–2):37–48
25. Petrii OA (2008) Pt-Ru electrocatalysts for fuel cells: a representative review. J Solid State Electron 12(5):609–642
26. Petry OA, Podlovchenko BI, Frumkin AN, Lal H (1965) Behaviour of platinized-platinum and platinum-ruthenium electrodes in methanol solutions. J Electroanal Chem 10(4):253–269
27. Rauhe BR, Mclarnon FR, Cairns EJ (1995) Direct anodic-oxidation of methanol on supported platinum ruthenium catalyst in aqueous cesium carbonate. J Electrochem Soc 142(4): 1073–1084
28. Tripkovic AV, Strbac S, Popovic KD (2003) Effect of temperature on the methanol oxidation at supported Pt and PtRu catalysts in alkaline solution. Electrochem Commun 5(6):484–490
29. Jayashree RS, Egas D, Spendelow JS, Natarajan D, Markoski LJ, Kenis PJA (2006) Air-breathing laminar flow-based direct methanol fuel cell with alkaline electrolyte. Electrochem Solid State Lett 9(5):A252–A256
30. Kadirgan F, Beden B, Leger JM, Lamy C (1981) Synergistic effect in the electrocatalytic oxidation of methanol on platinum + palladium alloy electrodes. J Electroanal Chem 125(1): 89–103
31. Watanabe M, Motoo S (1975) Electrocatalysis by Ad-atoms. 1. Enhancement of oxidation of methanol on platinum and palladium by gold Ad-atoms. J Electroanal Chem 60(3):259–266
32. Haruta M, Date M (2001) Advances in the catalysis of Au nanoparticles. Appl Catal A Gen 222(1–2):427–437
33. Valden M, Lai X, Goodman DW (1998) Onset of catalytic activity of gold clusters on titania with the appearance of nonmetallic properties. Science 281(5383):1647–1650
34. Luo J, Njoki PN, Lin Y, Mott D, Wang LY, Zhong CJ (2006) Characterization of carbon-supported AuPt nanoparticles for electrocatalytic methanol oxidation reaction. Langmuir 22(6):2892–2898
35. Zeng JH, Yang J, Lee JY, Zhou WJ (2006) Preparation of carbon-supported core-shell Au-Pt nanoparticles for methanol oxidation reaction: the promotional effect of the Au core. J Phys Chem B 110(48):24606–24611
36. Guo X, Guo DJ, Qiu XP, Chen LQ, Zhu WT (2008) A simple one-step preparation of high utilization AuPt nanoparticles supported on MWCNTs for methanol oxidation in alkaline medium. Electrochem Commun 10(11):1748–1751
37. Zhang YZ, Gu YE, Lin SX, Wei JP, Wang ZH, Wang CM, Du YL, Ye WC (2011) One-step synthesis of PtPdAu ternary alloy nanoparticles on graphene with superior methanol electrooxidation activity. Electrochim Acta 56(24):8746–8751
38. Xu CW, Zeng R, Shen PK, Wei ZD (2005) Synergistic effect of CeO2 modified Pt/C catalysts on the alcohols oxidation. Electrochim Acta 51(6):1031–1035
39. Shen PK, Xu CW, Zeng R, Liu YL (2006) Electro-oxidation of methanol on NiO-promoted Pt/C and Pt/C catalysts. Electrochem Solid State 9(2):A39–A42
40. Wang JS, Xi JY, Bai YX, Shen Y, Sun J, Chen LQ, Zhu WT, Qiu XP (2007) Structural designing of Pt-CeO_2/CNTs for methanol electro-oxidation. J Power Sources 164(2): 555–560
41. Justin P, Rao GR (2009) Enhanced activity of methanol electro-oxidation on Pt-V_2O_5/C catalysts. Catal Today 141(1–2):138–143
42. Feng YY, Bi LX, Liu ZH, Kong DS, Yu ZY (2012) Significantly enhanced electrocatalytic activity for methanol electro-oxidation on Ag oxide-promoted PtAg/C catalysts in alkaline electrolyte. J Catal 290:18–25

43. Biswas PC, Enyo M (1992) Electrooxidation of methanol on graphite-supported perovskite-modified Pt electrodes in alkaline-solution. J Electroanal Chem 322(1–2):203–220
44. Fleischmann M, Korinek K, Pletcher D (1971) Oxidation of organic compounds at a nickel anode in alkaline solution. J Electroanal Chem 31(1):39–49
45. Kowal A, Port SN, Nichols RJ (1997) Nickel hydroxide electrocatalysts for alcohol oxidation reactions: an evaluation by infrared spectroscopy and electrochemical methods. Catal Today 38(4):483–492
46. Rahim MAA, Hameed RMA, Khalil MW (2004) Nickel as a catalyst for the electro-oxidation of methanol in alkaline medium. J Power Sources 134(2):160–169
47. Yi QF, Huang W, Zhang JJ, Liu XP, Li L (2008) Methanol oxidation on titanium-supported nano-scale Ni flakes. Catal Commun 9(10):2053–2058
48. Kazakov VA, Titova VN, Yavich AA, Petrova NV, Tarasevich MR (2004) Electrocatalytic properties of electrolytic Ni/Ru and Fe/Ru in the methanol oxidation. Russ J Electrochem 40 (6):679–682
49. Danaee I, Jafarian M, Forouzandeh F, Gobal F, Mahjani MG (2008) Electrocatalytic oxidation of methanol on Ni and NiCu alloy modified glassy carbon electrode. Int J Hydrogen Energy 33(16):4367–4376
50. Jafarian M, Moghaddam RB, Mahjani MG, Gobal F (2006) Electro-catalytic oxidation of methanol on a Ni-Cu alloy in alkaline medium. J Appl Electrochem 36(8):913–918
51. Casella IG, Cataldi TRI, Salvi AM, Desimoni E (1993) Electrocatalytic oxidation and liquid-chromatographic detection of aliphatic-alcohols at a nickel-based glassy-carbon modified electrode. Anal Chem 65(21):3143–3150
52. Ciszewski A (1995) Catalytic oxidation of methanol on a glassy carbon electrode electrochemically modified by a conductive Ni-II-curcumin film. Electroanalysis 7(12):1132–1135
53. Ciszewski A, Milczarek G (1997) Glassy carbon electrode modified by conductive, polymeric nickel(II) porphyrin complex as a 3D homogeneous catalytic system for methanol oxidation in basic media. J Electroanal Chem 426(1–2):125–130
54. Golikand AN, Asgari M, Maragheh MG, Shahrokhian S (2006) Methanol electrooxidation on a nickel electrode modified by nickel-dimethylglyoxime complex formed by electrochemical synthesis. J Electroanal Chem 588(1):155–160
55. Golabi SM, Nozad A (2004) Electrocatalytic oxidation of methanol on a nickel-porphyrin IX complex modified glassy carbon electrode in alkaline medium. Electroanalysis 16(3): 199–209
56. Cardoso WS, Dias VLN, Costa WM, Rodrigues ID, Marques EP, Sousa AG, Boaventura J, Bezerra CWB, Song CJ, Liu HS, Zhang JJ, Marques ALB (2009) Nickel-dimethylglyoxime complex modified graphite and carbon paste electrodes: preparation and catalytic activity towards methanol/ethanol oxidation. J Appl Electrochem 39(1):55–64
57. Golikand AN, Raoof J, Baghayeri M, Asgari M, Irannejad L (2009) Nickel electrode modified by N,N-bis(salicylidene)phenylenediamine (Salophen) as a catalyst for methanol oxidation in alkaline medium. Russ J Electrochem 45(2):192–198
58. Taraszewska J, Roslonek G (1994) Electrocatalytic oxidation of methanol on a glassy-carbon electrode modified by nickel-hydroxide formed by ex-situ chemical precipitation. J Electroanal Chem 364(1–2):209–213
59. AvramovIvic M, Jovanovic V, Vlajnic G, Popic J (1997) The electrocatalytic properties of the oxides of noble metals in the electro-oxidation of some organic molecules. J Electroanal Chem 423(1–2):119–124
60. Borkowska Z, Tymosiak-Zielinska A, Shul G (2004) Electrooxidation of methanol on polycrystalline and single crystal gold electrodes. Electrochim Acta 49(8):1209–1220
61. Hernandez J, Solla-Gullon J, Herrero E, Aldaz A, Feliu JM (2006) Methanol oxidation on gold nanoparticles in alkaline media: unusual electrocatalytic activity. Electrochim Acta 52(4): 1662–1669
62. Bunazawa H, Yamazaki Y (2009) Ultrasonic synthesis and evaluation of non-platinum catalysts for alkaline direct methanol fuel cells. J Power Sources 190(2):210–215

63. Kumar KS, Haridoss P, Seshadri SK (2008) Synthesis and characterization of electrodeposited Ni-Pd alloy electrodes for methanol oxidation. Surf Coating Technol 202 (9):1764–1770
64. Liu ZL, Zhang XH, Hong L (2009) Physical and electrochemical characterizations of nanostructured Pd/C and PdNi/C catalysts for methanol oxidation. Electrochem Commun 11(4):925–928
65. Wang ML, Liu WW, Huang CD (2009) Investigation of PdNiO/C catalyst for methanol electrooxidation. Int J Hydrogen Energy 34(6):2758–2764
66. Guo B, Zhao SZ, Han GY, Zhang LW (2008) Continuous thin gold films electroless deposited on fibrous mats of polyacrylonitrile and their electrocatalytic activity towards the oxidation of methanol. Electrochim Acta 53(16):5174–5179
67. Ballarin B, Cassani MC, Scavetta E, Tonelli D (2008) Self-assembled gold nanoparticles modified ITO electrodes: the monolayer binder molecule effect. Electrochim Acta 53(27): 8034–8044
68. White JH, Sammells AF (1993) Perovskite anode electrocatalysis for direct methanol fuel-cells. J Electrochem Soc 140(8):2167–2177
69. Raghuveer V, Thampi KR, Xanthopoulos N, Mathieu HJ, Viswanathan B (2001) Rare earth cuprates as electrocatalysts for methanol oxidation. Solid State Ionics 140(3–4):263–274
70. Yu HC, Fung KZ, Guo TC, Chang WL (2004) Syntheses of perovskite oxides nanoparticles $La_{1-x}Sr_xMO_{3-\delta}$ (M = Co and Cu) as anode electrocatalyst for direct methanol fuel cell. Electrochim Acta 50(2–3):811–816
71. Singh RN, Sharma T, Singh A, Anindita, Mishra D, Tiwari SK (2008) Perovskite-type $La_{2-x}Sr_xNiO_4$ (0 <= x <= 1) as active anode materials for methanol oxidation in alkaline solutions. Electrochim Acta 53(5):2322–2330
72. Singh RN, Singh A, Mishra D, Anindita, Chartier P (2008) Oxidation of methanol on perovskite-type $La_{2-x}Sr_xNiO_4$ (0 <= x <= 1) film electrodes modified by dispersed nickel in 1 M KOH. J Power Sources 185(2):776–783
73. Xu CW, Cheng LQ, Shen PK, Liu YL (2007) Methanol and ethanol electrooxidation on Pt and Pd supported on carbon microspheres in alkaline media. Electrochem Commun 9(5): 997–1001
74. Liang ZX, Zhao TS, Xu JB, Zhu LD (2009) Mechanism study of the ethanol oxidation reaction on palladium in alkaline media. Electrochim Acta 54(8):2203–2208
75. Wang H, Xu CW, Cheng FL, Jiang SP (2007) Pd nanowire arrays as electrocatalysts for ethanol electrooxidation. Electrochem Commun 9(5):1212–1216
76. Elshafei AA, Elmaksoud SAA, Moussa MNH (1992) Effect of some Ad-atoms on the electrocatalytic oxidation of ethanol on a platinum-electrode in alkaline-medium. J Electroanal Chem 336(1–2):73–83
77. Soundararajan D, Park JH, Kim KH, Ko JM (2012) Pt-Ni alloy nanoparticles supported on CNF as catalyst for direct ethanol fuel cells. Curr Appl Phys 12(3):854–859
78. Matsumoto F (2012) Ethanol and methanol oxidation activity of PtPb, PtBi, and PtBi2 intermetallic compounds in alkaline media. Electrochemistry 80(3):132–138
79. Tusi MM, Polanco NSO, da Silva SG, Spinace EV, Neto AO (2011) The high activity of PtBi/C electrocatalysts for ethanol electro-oxidation in alkaline medium. Electrochem Commun 13(2):143–146
80. Han XY, Wang DW, Liu D, Huang JS, You TY (2012) Synthesis and electrocatalytic activity of Au/Pt bimetallic nanodendrites for ethanol oxidation in alkaline medium. J Colloid Interface Sci 367:342–347
81. Dutta A, Mahapatra SS, Datta J (2011) High performance PtPdAu nano-catalyst for ethanol oxidation in alkaline media for fuel cell applications. Int J Hydrogen Energy 36(22): 14898–14906
82. Datta J, Dutta A, Mukherjee S (2011) The beneficial role of the Cometals Pd and Au in the carbon-supported PtPdAu catalyst toward promoting ethanol oxidation kinetics in alkaline fuel cells: temperature effect and reaction mechanism. J Phys Chem C 115(31):15324–15334

83. Chen YG, Zhuang L, Lu JT (2007) Non-Pt anode catalysts for alkaline direct alcohol fuel cells. Chinese J Catal 28(10):870–874
84. He QG, Chen W, Mukerjee S, Chen SW, Laufek F (2009) Carbon-supported PdM (M = Au and Sn) nanocatalysts for the electrooxidation of ethanol in high pH media. J Power Sources 187(2):298–304
85. Jou LS, Chang JK, Twhang TJ, Sun IW (2009) Electrodeposition of palladium-copper films from 1-ethyl-3-methylimidazolium chloride-tetrafluoroborate ionic liquid on indium tin oxide electrodes. J Electrochem Soc 156(6):D193–D197
86. Du WX, Mackenzie KE, Milano DF, Deskins NA, Su D, Teng XW (2012) Palladium-tin alloyed catalysts for the ethanol oxidation reaction in an alkaline medium. ACS Catal 2(2): 287–297
87. Nguyen ST, Tan DSL, Lee JM, Chan SH, Wang JY, Wang X (2011) Tb promoted Pd/C catalysts for the electrooxidation of ethanol in alkaline media. Int J Hydrogen Energy 36(16):9645–9652
88. Oliveira MC, Rego R, Fernandes LS, Tavares PB (2011) Evaluation of the catalytic activity of Pd-Ag alloys on ethanol oxidation and oxygen reduction reactions in alkaline medium. J Power Sources 196(15):6092–6098
89. Xu CW, Shen PK (2005) Electrochemical oxidation of ethanol on Pt-CeO2/C catalysts. J Power Sources 142(1–2):27–29
90. Bai YX, Wu JJ, Xi JY, Wang JS, Zhu WT, Chen LQ, Qiu XP (2005) Electrochemical oxidation of ethanol on Pt-ZrO2/C catalyst. Electrochem Commun 7(11):1087–1090
91. Xu CW, Shen PK, Ji XH, Zeng R, Liu YL (2005) Enhanced activity for ethanol electro oxidation on Pt-MgO/C catalysts. Electrochem Commun 7(12):1305–1308
92. Shen PK, Xu CW (2006) Alcohol oxidation on nanocrystalline oxide Pd/C promoted electrocatalysts. Electrochem Commun 8(1):184–188
93. Hu FP, Chen CL, Wang ZY, Wei GY, Shen PK (2006) Mechanistic study of ethanol oxidation on Pd-NiO/C electrocatalyst. Electrochim Acta 52(3):1087–1091
94. Xu CW, Shen PK, Liu YL (2007) Ethanol electrooxidation on Pt/C and Pd/C catalysts promoted with oxide. J Power Sources 164(2):527–531
95. Xu CW, Tian ZQ, Shen PK, Jiang SP (2008) Oxide (CeO2, NiO, Co(3)O(4) and Mn3O4)-promoted Pd/C electrocatalysts for alcohol electrooxidation in alkaline media. Electrochim Acta 53(5):2610–2618
96. Chu DB, Wang J, Wang SX, Zha LW, He JG, Hou YY, Yan YX, Lin HS, Tian ZW (2009) High activity of Pd-In2O3/CNTs electrocatalyst for electro-oxidation of ethanol. Catal Commun 10(6):955–958
97. Brankovic SR, McBreen J, Adzic RR (2001) Spontaneous deposition of Pd on a Ru(0001) surface. Surf Sci 479(1–3):L363–L368
98. Vitse F, Cooper M, Botte GG (2005) On the use of ammonia electrolysis for hydrogen production. J Power Sources 142(1–2):18–26
99. Bambagioni V, Bianchini C, Filippi J, OberhauserIal W, Marchionni A, Vizza F, Psaro R, Sordelli L, Foresti ML, Innocenti M (2009) Ethanol oxidation on electrocatalysts obtained by spontaneous deposition of palladium onto nickel-zinc materials. Chemsuschem 2(1):99–112
100. Kim JW, Park SM (1999) Electrochemical oxidation of ethanol at thermally prepared RuO2-modified electrodes in alkaline media. J Electrochem Soc 146(3):1075–1080
101. Kim JW, Park SM (2003) In situ XANES studies of electrodeposited nickel oxide films with metal additives for the electro-oxidation of ethanol. J Electrochem Soc 150(11):E560–E566
102. Shieh DT, Hwang BJ (1995) Kinetics for electrooxidation of ethanol on thermally prepared ruthenium oxide in alkaline-solution. J Electrochem Soc 142(3):816–823
103. Ta KP, Newman J (1998) Mass transfer and kinetic phenomena at the nickel hydroxide electrode. J Electrochem Soc 145(11):3860–3874
104. Beden B, Cetin I, Kahyaoglu A, Takky D, Lamy C (1987) Electrocatalytic oxidation of saturated oxygenated compounds on gold electrodes. J Catal 104(1):37–46

105. Chang SC, Ho YH, Weaver MJ (1991) Applications of real-time FTIR spectroscopy to the elucidation of complex electroorganic pathways – electrooxidation of ethylene-glycol on gold, platinum, and nickel in alkaline-solution. J Am Chem Soc 113(25):9506–9513
106. Hahn F, Beden B, Kadirgan F, Lamy C (1987) Electrocatalytic oxidation of ethylene-glycol. 3. In-situ infrared reflectance spectroscopic study of the strongly bound species resulting from its chemisorption at a platinum-electrode in aqueous-medium. J Electroanal Chem 216(1–2): 169–180
107. Christensen PA, Hamnett A (1989) The oxidation of ethylene-glycol at a platinum-electrode in acid and base – an in situ FTIR study. J Electroanal Chem 260(2):347–359
108. Matsuoka K, Iriyama Y, Abe T, Matsuoka M, Ogumi Z (2005) Electro-oxidation of methanol and ethylene glycol on platinum in alkaline solution: poisoning effects and product analysis. Electrochim Acta 51(6):1085–1090
109. Kohlmuller H (1977) Anodic-oxidation of ethylene-glycol with noble-metal alloy catalysts. J Power Sources 1(3):249–256
110. Dalbay N, Kadirgan F (1991) Electrolytically Co-deposited platinum palladium electrodes and their electrocatalytic activity for ethylene-glycol oxidation – a synergistic effect. Electrochim Acta 36(2):353–356
111. Kadirgan F, Beden B, Lamy C (1983) Electrocatalytic oxidation of ethylene-glycol. 2. Behavior of platinum-Ad-atom electrodes in alkaline-medium. J Electroanal Chem 143(1–2):135–152
112. Elshafei AA, Shabanah HM, Moussa MNH (1993) Catalytic influence of underpotentially deposited submonolayers of different metals in ethylene-glycol oxidation on various noble-metal electrodes in alkaline-medium. J Power Sources 46(1):17–27
113. Demarconnay L, Brimaud S, Coutanceau C, Leger JM (2007) Ethylene glycol electrooxidation in alkaline medium at multi-metallic Pt based catalysts. J Electroanal Chem 601(1–2):169–180
114. Miyazaki K, Matsumiya T, Abe T, Kurata H, Fukutsuka T, Kojima K, Ogumi Z (2011) Electrochemical oxidation of ethylene glycol on Pt-based catalysts in alkaline solutions and quantitative analysis of intermediate products. Electrochim Acta 56(22):7610–7614
115. Beden B, Kadirgan F, Kahyaoglu A, Lamy C (1982) Electrocatalytic oxidation of ethylene-glycol in alkaline-medium on platinum-gold alloy electrodes modified by underpotential deposition of lead adatoms. J Electroanal Chem 135(2):329–334
116. Elshafei AA, Elmaksoud SAA, Fouda AS (1995) Noble-metal-modified glassy-carbon electrodes for ethylene-glycol oxidation in alkaline-medium. J Electroanal Chem 395(1–2): 181–187
117. Jin CC, Song YS, Chen ZD (2009) A comparative study of the electrocatalytic oxidation of ethylene glycol on PtAu nanocomposite catalysts in alkaline, neutral and acidic media. Electrochim Acta 54(16):4136–4140
118. Moller H, Pistorius PC (2004) The electrochemistry of gold-platinum alloys. J Electroanal Chem 570(2):243–255
119. Kadirgan F, Bouhiercharbonnier E, Lamy C, Leger JM, Beden B (1990) Mechanistic study of the electrooxidation of ethylene-glycol on gold and adatom-modified gold electrodes in alkaline-medium. J Electroanal Chem 286(1–2):41–61
120. Matsuoka K, Iriyama Y, Abe T, Matsuoka M, Ogumi Z (2005) Electrocatalytic oxidation of ethylene glycol in alkaline solution. J Electrochem Soc 152(4):A729–A731
121. Demarconnay L, Coutanceau C, Leger JM (2008) Study of the oxygen electroreduction at nanostructured PtBi catalysts in alkaline medium. Electrochim Acta 53(8):3232–3241
122. Miyazaki K, Sugimura N, Matsuoka K, Iriyama Y, Abe T, Matsuoka M, Ogumi Z (2008) Perovskite-type oxides La1-xSrxMnO3 for cathode catalysts in direct ethylene glycol alkaline fuel cells. J Power Sources 178(2):683–686
123. Hou HY, Sun GQ, He RH, Wu ZM, Sun BY (2008) Alkali doped polybenzimidazole membrane for high performance alkaline direct ethanol fuel cell. J Power Sources 182(1):95–99
124. Hou HY, Sun GQ, He RH, Sun BY, Jin W, Liu H, Xin Q (2008) Alkali doped polybenzimidazole membrane for alkaline direct methanol fuel cell. Int J Hydrogen Energy 33(23): 7172–7176

125. Varcoe JR, Slade RCT (2006) An electron-beam-grafted ETFE alkaline anion-exchange membrane in metal-cation-free solid-state alkaline fuel cells. Electrochem Commun 8(5): 839–843
126. Yang CC, Chiu SJ, Chien WC (2006) Development of alkaline direct methanol fuel cells based on crosslinked PVA polymer membranes. J Power Sources 162(1):21–29
127. Yang CC, Chiu SJ, Lee KT, Chien WC, Lin CT, Huang CA (2008) Study of poly(vinyl alcohol)/titanium oxide composite polymer membranes and their application on alkaline direct alcohol fuel cell. J Power Sources 184(1):44–51
128. Yang CC, Lin CT, Chiu SJ (2008) Preparation of the PVA/HAP composite polymer membrane for alkaline DMFC application. Desalination 233(1–3):137–146
129. Varcoe JR, Slade RCT, Yee ELH, Poynton SD, Driscoll DJ (2007) Investigations into the ex situ methanol, ethanol and ethylene glycol permeabilities of alkaline polymer electrolyte membranes. J Power Sources 173(1):194–199
130. Ogumi Z, Matsuoka K, Chiba S, Matsuoka M, Iriyama Y, Abe T, Inaba M (2002) Preliminary study on direct alcohol fuel cells employing anion exchange membrane. Electrochemistry 70(12): 980–983
131. Yu EH, Scott K (2004) Direct methanol alkaline fuel cell with catalysed metal mesh anodes. Electrochem Commun 6(4):361–365
132. Fujiwara N, Siroma Z, Yamazaki SI, Ioroi T, Senoh H, Yasuda K (2008) Direct ethanol fuel cells using an anion exchange membrane. J Power Sources 185(2):621–626
133. Kim J, Momma T, Osaka T (2009) Cell performance of Pd-Sn catalyst in passive direct methanol alkaline fuel cell using anion exchange membrane. J Power Sources 189(2): 999–1002
134. Bianchini C, Bambagioni V, Filippi J, Marchionni A, Vizza F, Bert P, Tampucci A (2009) Selective oxidation of ethanol to acetic acid in highly efficient polymer electrolyte membrane-direct ethanol fuel cells. Electrochem Commun 11(5):1077–1080
135. Modestov AD, Tarasevich MR, Leykin AY, Filimonov VY (2009) MEA for alkaline direct ethanol fuel cell with alkali doped PBI membrane and non-platinum electrodes. J Power Sources 188(2):502–506
136. Shen SY, Zhao TS, Xu JB, Li YS (2010) Synthesis of PdNi catalysts for the oxidation of ethanol in alkaline direct ethanol fuel cells. J Power Sources 195(4):1001–1006
137. Li YS, Zhao TS, Liang ZX (2009) Effect of polymer binders in anode catalyst layer on performance of alkaline direct ethanol fuel cells. J Power Sources 190(2):223–229
138. Bambagioni V, Bianchini C, Marchionni A, Filippi J, Vizza F, Teddy J, Serp P, Zhiani M (2009) Pd and Pt-Ru anode electrocatalysts supported on multi-walled carbon nanotubes and their use in passive and active direct alcohol fuel cells with an anion-exchange membrane (alcohol = methanol, ethanol, glycerol). J Power Sources 190(2):241–251
139. Li YS, Zhao TS, Liang ZX (2009) Performance of alkaline electrolyte-membrane-based direct ethanol fuel cells. J Power Sources 187(2):387–392
140. Prabhuram J, Manoharan R (1998) Investigation of methanol oxidation on unsupported platinum electrodes in strong alkali and strong acid. J Power Sources 74(1):54–61
141. Yu EH, Scott K, Reeve RW, Yang LX, Allen RG (2004) Characterisation of platinised Ti mesh electrodes using electrochemical methods: methanol oxidation in sodium hydroxide solutions. Electrochim Acta 49(15):2443–2452
142. Varcoe JR, Slade RCT (2005) Prospects for alkaline anion-exchange membranes in low temperature fuel cells. Fuel Cells 5(2):187–200
143. Antolini E, Giorgi L, Pozio A, Passalacqua E (1999) Influence of Nafion loading in the catalyst layer of gas-diffusion electrodes for PEFC. J Power Sources 77(2):136–142
144. Bunazawa H, Yamazaki Y (2008) Influence of anion ionomer content and silver cathode catalyst on the performance of alkaline membrane electrode assemblies (MEAs) for direct methanol fuel cells (DMFCs). J Power Sources 182(1):48–51
145. Cifrain M, Kordesch KV (2004) Advances, aging mechanism and lifetime in AFCs with circulating electrolytes. J Power Sources 127(1–2):234–242

Chapter 6
Palladium-Based Nanocatalysts for Alcohol Electrooxidation in Alkaline Media

Remegia Mmalewane Modibedi, Kenneth Ikechukwu Ozoemena, and Mkhulu Kenny Mathe

Abstract Direct alcohol alkaline fuel cells (DAAFCs) are potential power sources for a variety of portable applications as they provide unique advantages over hydrogen-based fuel cell devices. Alcohols (such as methanol, ethanol, ethylene glycol, and glycerol) have high volumetric energy density and are easier to store and transport than hydrogen. Palladium-based nanocatalysts have continued to receive much research attention because of their cost advantages, relative abundance, and unique properties in the electrocatalytic oxidation of alcohols in alkaline media compared to platinum catalysts. Recent efforts have focused on the discovery of palladium-based electrocatalysts with little or no platinum for oxygen reduction reaction (ORR). This chapter is an overview of the recent developments in the employment of palladium-based nanocatalysts, containing little or no platinum, for the electrooxidation of alcohols in alkaline media.

6.1 Introduction

The research and development of nanostructured electrode materials for improved performance of the direct alcohol fuel cells (DAFCs) in alkaline electrolytes has continued to grow. Palladium-based nanocatalysts, in particular, have continued to receive much research attention because of their unique properties in alcohol electrooxidation in alkaline media compared to their platinum-based counterparts [1].

R.M. Modibedi • M.K. Mathe
Materials Science and Manufacturing, Council for Scientific and Industrial Research (CSIR), Meiring Naude Road, Brummeria, Pretoria 0001, South Africa

K.I. Ozoemena (✉)
Materials Science and Manufacturing, Council for Scientific and Industrial Research (CSIR), Meiring Naude Road, Brummeria, Pretoria 0001, South Africa

Department of Chemistry, University of Pretoria, Pretoria 0002, South Africa
e-mail: kozoemena@csir.co.za

M. Shao (ed.), *Electrocatalysis in Fuel Cells*, Lecture Notes in Energy 9,
DOI 10.1007/978-1-4471-4911-8_6,

Palladium is more abundant in nature and sells at half the current market price of platinum. Unlike Pt, the Pd-based electrocatalysts are more active towards the oxidation of a plethora of substrates in alkaline media. The high activity of Pd in alkaline media is advantageous considering that non-noble metals are sufficiently stable in alkaline for electrochemical applications. Importantly, it is believed that the integration of Pd with non-noble metals (as bimetallic or ternary catalysts) can remarkably reduce the cost of the *membrane electrode assemblies* (MEAs) and boost the widespread application or commercialization of DAFCs [1]. Palladium has proved to be a better catalyst for alcohol electrooxidation in alkaline electrolytes than Pt [2]. Palladium activity towards the electrooxidation of low-molecular weight alcohols can be enhanced by the presence of a second or third metal, either alloyed or in the oxide form [3].

As elegantly articulated in a recent review by Bianchini and Shen [1], alkaline media provide unique characteristics for efficient alcohol electrooxidation, including the following (1) the ability to use noble and non-noble metal catalysts; (2) enhanced electrochemical kinetics, at low anodic overpotential; (3) reduced alcohol crossover from the anode to the cathode via electroosmotic drag of hydrated hydroxyl ions; (4) enhanced water management since water is formed at the anode side where aqueous solution already exists, while electroosmotic drag removes water from the cathode preventing waterflooding; (5) reduced risks of corrosion of electrode materials, including catalysts and carbon supports; and (6) reduced risk of adsorption of spectator ions on the MEA that might limit electrocatalysis. Moreover, in the alkaline environment, CO poisoning effect is very weak and it is possible to use cheaper catalyst than Pt [4, 5].

Much effort has been made to enhance the performance of Pd–M (where M = second metal) for alcohol electrooxidation. These efforts were persuaded by the bifunctional mechanism and the electronic/ligand effect, which can be explained by either the electron density, electronegativity, density functional theory, or d-band theory [6–17]. For example, according to the bifunctional theory of electrocatalysis, the oxidation of a primary alcohol to CO_2 and R–COOH (or CO_3^{2-} and R–COO^- in alkaline medium) needs the activation of water under OH adsorbed species at the surface to bring the extra oxygen atom and to complete the oxidation reaction, according to the following chemical reactions (in alkaline medium):

$$\mathrm{RCH_2OH} \rightarrow (\mathrm{RCH_2OH})_{\mathrm{ads}} \tag{6.1}$$

$$(\mathrm{RCH_2OH})_{\mathrm{ads}} + 3\mathrm{OH^-} \rightarrow \mathrm{RCO_{ads}} + 3\mathrm{H_2O} + 3\mathrm{e^-} \tag{6.2}$$

$$\mathrm{OH^-} \rightarrow \mathrm{OH^-}_{\mathrm{ads}} + \mathrm{e^-} \tag{6.3}$$

$$\mathrm{RCO_{ads}} + \mathrm{OH^-}_{\mathrm{ads}} \rightarrow \mathrm{R{-}COOH} \tag{6.4}$$

$$\mathrm{RCOOH} + \mathrm{OH^-} \rightarrow \mathrm{RCOO^-} + \mathrm{H_2O} \tag{6.5}$$

Equations (6.1) and (6.2) describe the dissociative adsorption of alcohol on the catalyst surface. Equation (6.4) represents the rate-determining step, meaning that the degree of alcohol oxidation is dependent on the coverage of the RCO_{ads} and OH_{ads} on the surface of the catalyst.

In this chapter, the authors review some developments in the application of Pd-based nanostructures for the electrocatalytic oxidation of alcohols in alkaline media. Special focus is given to the role of such nanostructures (mono-, bi-, or ternary metallic catalysts) and/or their supporting platforms in lowering the anodic overpotential (onset potential), enhancing the catalytic current density, and improving the stability or lifetime of the catalysts.

6.2 Current Research Trends on Pd-Based Nanoelectrocatalysts for Alcohol Electrooxidation in Alkaline Media

Figure 6.1 presents an insight into the publication trends in the last decade (2002–2011) on the electrooxidation of two major alcohols (methanol and ethanol) in alkaline media at Pd-based nanocatalyst platforms. The nanocatalysts comprised monometallic (Pd alone), bimetallic (Pd–M, where $M =$ metal or metal oxide), and ternary ($Pd–M_1M_2$, where M_1 and M_2 represent different metals or metal oxides) catalysts. Since 2002, there has been a steady publication growth in this research field. The increased research trend may be related to three factors (1) the need to protect the environment from the emission of greenhouse gases emanating from the burning of fossil fuels, (2) high crude oil prices, and (3) the promise of nanoscience and nanotechnology. The last decade has witnessed a steady and unpredictable high crude oil prices, exacerbated by the Asian economic growth, weak US dollar, Iraq war, world economic recession, the Arab uprising termed the *Arab spring*, and global economic sanction on Iran. Without doubt, these factors have encouraged investments in the R&D for advanced renewable energy technologies. For example, the USA introduced the Energy Policy Act of 2005 to encourage investment in renewable technologies [18]. In a similar vein, an Advanced Energy Initiative (AEI) related to climate change was introduced in 2006 by the USA to accelerate renewable energy and technologies [19]. Nanostructured materials exhibit unique (and sometime incredible) physicochemical properties compared to their bulk material counterparts, hence the increased global R&D investments. South Africa, for example, through its Department of Science and Technology (DST) and National Research Foundation (NRF), has continued to make huge financial R&D investments in nanotechnology fields through programs such as the *Emerging Research Areas* (*ERAs*), *National Nanotechnology Equipment Programs* (*NNEPs*), and *National Nanotechnology Flagship Projects* (*NNFPs*).

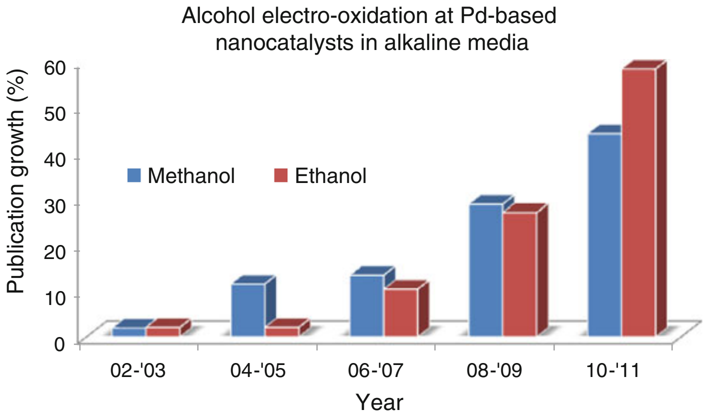

Fig. 6.1 Graphical representation of the publication growth (% growth = number of publications per 2-year period divided by the total number of publications in the last decade, multiplied by 100) from 2002 until 2011 (raw data obtained from the ACS SciFinder Scholar(R) search engine)

6.2.1 Methanol Electrooxidation

Pd activity towards the electrooxidation of methanol is lower than that of Pt in alkaline media. Research activities aiming at improving the activity of Pd for the oxidation of methanol are increasing [20, 21], including Pd-based binary alloyed catalysts. Table 6.1 is a summary of notable reports in the last decade on the Pd nanocatalysts, synthetic strategies, support platforms, and the electrochemical performance (in terms of the onset potential and catalytic current density). For the readers' ease of reference, the major findings in each of the study are highlighted in Table 6.1. Generally, the ratio of the current height of the forward anodic peak to the backward (reverse) peak (I_f/I_b) indicates the tolerance of the catalyst to CO poisoning; the higher the ratio, the better the tolerance to CO poisoning, while the lower the ratio, the more likely that the catalyst is poisoned. Several reports reviewed in this chapter used this current ratio as one of the measures of the electrocatalytic performance of the Pd-based nanocatalysts. Most of the recent reports on methanol electrooxidation in alkaline media are based on monodispersed and bimetallic Pd nanocatalysts [22–41, 43]. A bimetallic nanocatalyst worth mentioning is the Pd–NiO reported by Wang et al. [33]. The presence of the NiO was found to enhance the anti-poison ability of Pd–NiO/C catalyst. The anti-poison ability was ascribed to the three factors (1) the presence of the NiOOH that increases the activity of composite catalyst for methanol oxidation, (2) the catalytic role of NiO for methanol dehydration, and (3) the promotion of large amount of active species PdO (low oxidation state) for methanol oxidation.

Table 6.1 Representative Pd-based nanocatalysts for methanol electrooxidation in alkaline media

Catalyst	Synthesis method	Support	Onset potential (E_s)	Main highlight
Pd [22]	Self-assembly plus hydrazine reduction	S-HCNF	−0.56 V (vs. SCE), same as for vulcan	Same E_s, but current density is higher than at the vulcan
Pd [23]	UHV deposition	WC	0.6 V vs. NHE	Same E_s, but I_f/I_b ratios were 1.78 and 3.18 for the Pd/WC and Pd foils, respectively. Steady-state oxidation current shows higher CO tolerance on Pd/WC than on Pd foils
Pd [24]	Microwave-assisted polyol	PHCSs	−0.3 V (vs. Hg/HgO)	The Pd/PHCS gave higher current density and slight negative shift of the E_s compared with Pd/C at the same Pd loadings
Pd [25]	Microwave-assisted polyol	Graphene	−0.58 V (vs. Hg/HgO)	Same E_s for all supports, but graphene support gave better current density than MWCNT and other nanocarbon supports
Pd–Ni ($Pd_{40}Ni_{60}$) [26]	Dealloying a ternary $Al_{75}Pd_{10}Ni_{15}$ alloy under free corrosion conditions	Vulcan	−0.4 V(vs. Hg/HgO)	Better E_s and current density than nanoporous Pd/vulcan. This is supported by the high I_f/I_b ratio of the $Pd_{40}Ni_{60}$, indicating a better poisoning tolerance
Pd [27]	Electroless plating	Ti electrode	~ −0.50 V (vs. SCE)	Same E_s with flat Pd electrode, but current density is about 3 times higher than that of the Pd electrode
Pd [28]	Polyol/$NaBH_4$ reduction	MnO_2-MWCNT	~ −0.50 V (vs. SCE)	Same E_s but different current densities. I_f/I_b ratio of Pd–MnO_2/MWCNTs catalyst is 18.3, higher than that of Pd/MWCNTs ($I_f/I_b = 4.6$) and Pd/vulcan ($I_f/I_b = 3.8$)
Hollow Pd nanospheres (HPNs) [29]	Galvanic replacement reaction	PDDA-MWCNTs	~ −0.50 V (vs. Ag/AgCl)	Better E_s and current density than Pd nanoparticles. Current density is ~2.5× higher
Pd [30]	Chemical reduction with $NaBH_4$	APZ-MWCNTs	~ −0.50 V (vs. SCE)	Same E_s with acid-functionalized MWCNTs and vulcan carbon supports but better CD. The I_f/I_b ratio of the Pd/APZ-MWCNTs (2.13)

(continued)

Table 6.1 (continued)

Catalyst	Synthesis method	Support	Onset potential (E_s)	Main highlight
				higher than Pd/AO-MWCNTs (1.76) and Pd/C (1.15) catalysts, showing better catalyst tolerance of the APZ-MWCNTs' support
Pd [31]	Microwave-assisted polyol	HPC	~ −0.40 V (vs. Hg/HgO)	Pd/HPC better E_s and current density compared to Pd/C. Current density is about three times that of the Pd/C
Nanoporous palladium (NPPd) [32]	Dealloying of an Al–Pd alloy in an alkaline solution	Carbon powder	~ −0.45 V (vs. Hg/HgO)	NPPd exhibits high activity towards methanol
Pd–NiO [33, 34]	Co-reduction and annealing in air	Vulcan C	~ −0.50 V (vs. SCE)	NiO enhances the anti-poison ability of Pd–NiO/C catalyst. The anti-poison ability of Pd–NiO/C catalyst can be enhanced by three ways (1) the NiOOH on the surface of catalyst improves the activity of composite catalyst for methanol oxidation, (2) the catalytic role of NiO for methanol dehydration, and (3) the promotion of large amount active species PdO (low oxidation state) for methanol oxidation
Pd [35]	Reduction using $NaBH_4$	S-MWCNTs	−0.45 V vs. SCE	Lower E_s and higher current density compared to other types of MWCNTs. S-MWCNTs/Pd catalyst has the highest I_f/I_b, indicating the best CO resistance
Pd–Sn [36]	Microwave-assisted polyol	GNS	The E_s of the Pd–Sn/GNS was more negative than Pd/GNS	Catalytic activity and CO poisoning tolerance of 18 % Pd–2 % Sn/GNS at −0.10 V were 79 % and 40 %, respectively, than Pd/GNS
Pd–Co [37]	Reduction using $NaBH_4$	Carbon black/CNTs	Pd/C and Pd–Co (8:1)/C have same onset potential	Pd–Co (8:1)/C high current density and tolerance to CO poisoning on Pd/C. Higher I_f/I_b was obtained on Pd–Co (8:1)/CNT than Pd–Co (8:1)/C

Pd–Ag [38]	Reduction using $NaBH_4$	C	−0.59 V vs. Hg/HgO	Pd–Ag (1:1)/C displays better catalytic activity and improved tolerance to CO poisoning than other Pd:Ag ratio and Pd/C
Pd–Ni [39]	Reduction using formic acid	Vulcan C	−0.61 V vs. Ag/AgCl	Pd–Ni/C have higher catalytic activity and tolerance to CO poisoning than Pd/C
Pd–Pt [40]	Electrodeposition	Ti foil	−0.53 V vs. SCE	$Pd_{0.8}Pt_{0.2}$/Ti exhibits higher electrocatalytic activity and better tolerance to poisoning than other Pd:Pt molar ratios: Pd/C and Pt/C
Pd–Au [41]	Ultrasonic synthesis in ethylene glycol	Vulcan C	0.630 V vs. RHE	Pd/C and Pd–Au/C showed more positive onset potential and lower current densities than Pt/C. These catalysts are not suitable for methanol oxidation reaction
Pd–Ru [21]	Impregnation and reduction under H_2 atmosphere	Vulcan C	Pd–Ru/C showed a negative shift of ~0.15 V vs. RHE than Pd/C	1:1 atomic ratio Pd–Ru/C was higher than that of Pd, evidenced by a negative shift of 0.15 V in the onset potential
Ni–Pd [42]	Electrodeposition	Ti substrate	Addition of Pd on Ni/Ti improved the onset potential	Slight decrease in the onset potential from 338 to 332 mV vs. SCE with increase in Pd content from 4.5 to 10.8 at.%. But increase in current density with the increase in Pd content was observed

UHV Ultrahigh vacuum, *MWCNTs* multiwalled carbon nanotubes, *S-HCNF* helical carbon nanofibers functionalized with benzyl mercaptan, *WC* tungsten carbide, *PHCSs* porous hollow carbon spheres, *HPC* honeycomb-like porous carbon, *PDDA-MWCNTs* Polydiallyldimethylammonium-functionalized MWCNTs, *APZ-MWCNTs* 2-aminophenoxazin-3-one-functionalized MWCNTs, *S-MWCNTs* sulfonated MWCNTs, *GNS* graphene nanosheets

6.2.1.1 Synthetic Methods and Support Materials

In heterogeneous catalysis, the synthetic strategies are intricately linked to the physicochemical properties of the catalysts. The synthetic method is important in tuning the morphology, particle size, and composition of the catalysts, the degree of alloying, and the electrocatalytic performance. Also, from the various reports, it is evident that the difference between the electrocatalytic performance of one Pd-based nanocatalyst and the other lies mainly in their morphology, particle size, and structure, which are dictated mainly by the synthetic strategy adopted and supporting platform employed by the researchers. Thus, Pd nanocatalysts are reported in various names such as *nanoparticles*, *nanoporous*, *nanocrystalline*, *Raney-like nanoporous*, and *nanospheres*. The various methods that have been used to synthesize monodispersed Pd nanocatalysts include self-assembly technique assisted by chemical reduction using hydrazine as the reductant [22], ultrahigh vacuum deposition [23], microwave-assisted polyol strategies [24, 25, 31], galvanic replacement reaction [29], polyol synthesis using borohydride as the reductant [28], and dealloying [26]. As would be expected, the different morphologies and structures and supporting platforms (carbon, nanocarbons) yield different electrocatalytic performances in terms of the onset potential (E_s/V), catalytic current densities (j/A cm^{-2}), and stability or catalyst lifetime.

For the bimetallic alloyed catalysts, several methods have also been reported. For example, Chen et al. prepared 20 % Pd–Ru/C catalyst using the impregnation method and a reduction under H_2 atmosphere [21]. Pd–Ag/C catalyst with different Ag loadings was obtained by the borohydride reduction method. The modification of Pd with inexpensive metals such as Ag, aimed at improving its reactivity, is based on the d-band theory, which was reported firstly by Norskov and coworkers [7, 10]. The d-band theory as interpreted by Wang et al. [38] on Pd–Ag/C reactivity towards alcohol oxidation states that “when metals with small lattice constants are overlaid or alloyed on metals with larger lattice constants, the d-band center shifts up and vice versa, which subsequently affects the reaction rate. If the d-band center is shifted up, the adsorption ability of the adsorbate onto the metals becomes stronger and may help to improve the electrooxidation of alcohol on the surface of the metals.” The 1:1 Pd–Ag/C catalyst showed better activity than Pd/C for methanol oxidation in alkaline medium. The better performance of Pd–Ag/C was associated with the removal of adsorbed CO by the second metal, thus freeing the active Pd for further oxidation of methanol. The ability of the Pd–Ag/C catalyst to eliminate the adsorbed CO and other poisoning intermediates was explained by the bifunctional mechanism. This effect was confirmed by performing CO stripping studies via chronoamperometry. The onset potential of CO oxidation on the Pd–Ag (1:1)/C catalyst was more negative than that on the Pd/C catalyst. Pd–Au (1:1)/C catalysts was synthesized using of ultrasonic method with citric acid as the surfactant and varying solvents [41]. A well-dispersed Pd–Au having small and uniform particle size was obtained when ethylene glycol was used as a solvent. However, Pd–Au (1:1)/C showed lower activity towards methanol oxidation and higher

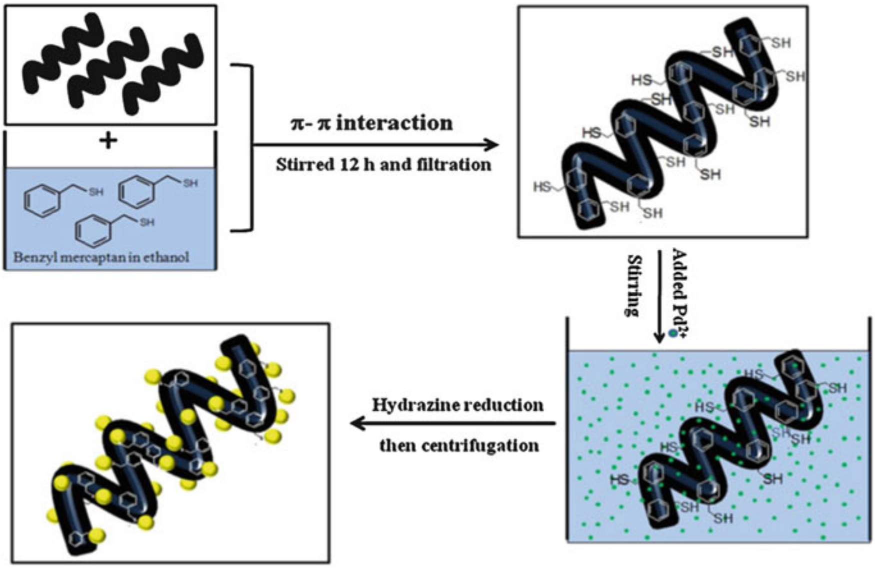

Fig. 6.2 Preparation procedure for Pd-S-HCNFs [22]

activity towards oxygen reduction reaction (ORR). Pd–Ni/C catalyst synthesized by Liu et al. through the chemical reduction method using formic acid as the reducing agent showed more negative onset potential and higher current density than Pd/C catalyst for methanol electrooxidation. On the other hand, the activity of Pd–Ni/C towards methanol oxidation in alkaline medium was found to be lower than that of Pt/C [39]. Carbon black- and carbon nanotube-supported Pd–Co catalysts with different amounts of cobalt were prepared using the sodium borohydride chemical reduction method [37]. Pd–Co (8:1) produced higher electrocatalytic activity towards methanol oxidation in alkaline medium and improved the resistance to CO poisoning. Pd–Co (8:1) supported on carbon nanotubes showed higher current density than the catalyst supported on carbon black. The enhanced activity was described by a bifunctional mechanism. However, the supported Pd–Co catalyst is preferred for use in the oxygen reduction reaction than the alcohol oxidation.

Support materials play an important role on the activity of catalysts and on lowering the amount of metals required in developing catalysts. For example, Hu et al. [22] recently reported the synthesis of S-HCNF-supported Pd nanocatalyst (Pd-S-HCNFs, Fig. 6.2) and compared its activity with Pd/C and found that both support materials gave the same onset potential but the current density at S-HCNF was about 2.3 times higher than that at the commercial carbon.

Shen et al. [24] compared PHCS and carbon as support for Pd nanocatalyst and found that PHCS gave higher (~3 times) current density than carbon. Singh et al. [25] compared graphene and MWCNTs as support for Pd nanocatalyst and found that both support materials gave the same onset potential but the current density at graphene was higher than that at the MWCNTs. CNTs have been studied

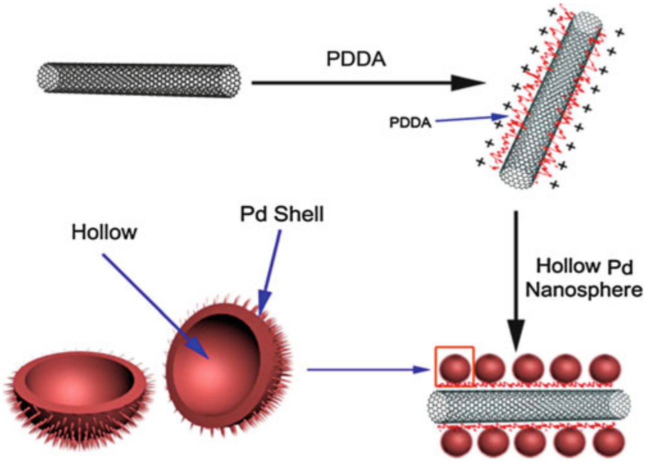

Fig. 6.3 Schematic illustration of assembling HPNs onto the surface of CNTs [29]

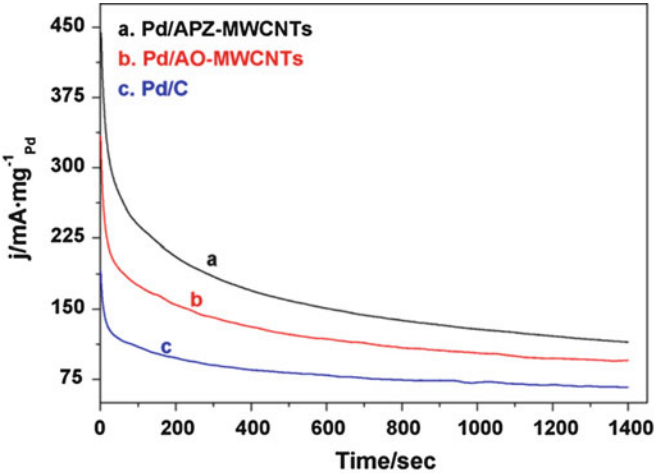

Fig. 6.4 Chronoamperometry collected for 1,400 s at −0.2 V for the Pd/APZ-MWCNTs, Pd/AO-MWCNTs, and Pd/C catalysts' modified electrodes in 0.5 M NaOH + 1.0 M CH_3OH solution [30]

extensively as a support material owing to their high aspect ratio and high specific surface area and are known to improve the catalyst utilization and electrochemical activity in fuel cells. An interesting development is the chemical modification of MWCNTs with MnO_2 [28], polydiallyldimethylammonium chloride (PDDA) (Fig. 6.3) [29], and 2-aminophenoxazin-3-one (APZ) (Fig. 6.4) [30], all of which exhibited higher current density than the unmodified MWCNTs or commercial carbon supports.

Graphene is an sp^2 hybridized two-dimensional monolayer carbon sheets and has low cost as well as high specific surface area than other carbon support materials. Pd–Ag (1:1) was also supported on carbon nanotubes (CNTs) by Wang et al. [38] for the oxidation of methanol. The onset potential for the oxidation of methanol on Pd–Ag (1:1)/C and Pd–Ag (1:1)/CNTs was the same, but higher current density was obtained for the CNTs supported catalyst.

This signifies good properties such as high specific area, big pore volume, and better Pd–Ag dispersion. Ti-based substrates are of interest in fuel cells due to its high chemical stability and conductivity. Lu et al. [40] electrodeposited Pd_xPt_{1-x} ($x = 0$–1) nanocatalysts on Ti foil and determined its activity towards the electrooxidation of alcohols. The results showed that the electrocatalytic activity and stability of nanocatalysts was influenced by the atomic ratios of Pd and Pt. $Pd_{0.8}Pt_{0.2}$/Ti showed better catalytic activity and stability for the electrooxidation of alcohols in alkaline medium, thus, indicating improved kinetics due to synergistic effect by the interaction between Pd and Pt for the electrooxidation of methanol. Also, recently, graphene was used as a support material for Pd–Sn catalyst for the electrooxidation of methanol in alkaline electrolyte. Microwave-assisted polyol reduction method was utilized to synthesise Pd/GNS and Pd–Sn/GNS catalysts. 18 % Pd–2 % Sn/GNS electrode was more efficient and more tolerant to poisoning than 20 % Pd/GNS due to the alloying effect of Sn [36].

6.2.2 *Ethanol Electrooxidation*

The alcohol oxidation process happens to be more problematic as the number of carbon atoms in the alcohol increases. The overall kinetics of alcohol oxidation becomes sluggish, owing to the formation of various intermediates which get strongly adsorbed on the catalyst surface and to the breaking of the C–C bond. Unlike methanol, ethanol oxidation in alkaline media is found to be better on Pd than on Pt [44]. However, research in developing Pd-based binary and ternary alloy catalysts that are active, stable, and low cost as well as to understand the mechanism of alcohol oxidation in alkaline electrolytes still continues. Table 6.2 presents a summary of representative reports in the last decade on the Pd nanocatalysts, synthetic strategies, support platforms, and the electrochemical performance (in terms of the onset potential and catalytic current density). For the readers' ease of reference, the major findings in each of the study are highlighted in the Table 6.2. Unlike the methanol electrooxidation, most studies on ethanol electrooxidation in alkaline employ bimetallic or ternary catalysts to achieve the bifunctional mechanism required for the more difficult ethanol oxidation process [22, 24–26, 29, 32, 45–76].

6.2.2.1 Synthetic Methods and Support Materials

Like the methanol electrooxidation, the activity of Pd for ethanol electrooxidation can be affected by the synthesis method, support material, and the dilution of Pd with another metal or metal oxide. This influence is the indication of a synergetic

Table 6.2 Representative Pd-based nanocatalysts for ethanol electrooxidation in alkaline media

Catalyst	Synthesis method	Support	Onset potential (E_s)	Main highlight
Pd [22]	Self-assembly-assisted hydrazine reduction	S-HCNF	−0.65 V (vs. SCE), same as for the vulcan	Same E_s, but current density is higher than at the vulcan
Pd–Ag [45]	Hydrothermal method	$Nb_xTi_{1-x}O_2$	−0.5 V (vs. Hg/HgO)	Same E_s as the Pd–Ag/vulcan C. Pd–Ag/$Nb_xTi_{1-x}O_2$ exhibited excellent performance for the oxidation of ethanol and higher durability in alkaline solution compared with Pd–Ag/C and Pd–Ag/commercial TiO_2
Pd [46]	Combination of ball-milling and a simple alkali-leaching treatment	Vulcan	−0.5 V (vs. Hg/HgO)	Compared with those traditional Pd catalysts (i.e., Pd nanoparticles, Pd nanowire, and arrays), this new Raney-like nanoporous Pd nanocatalyst shows superior electrocatalytic activity and stability towards electrooxidation of ethanol
Pd–Ag [47]	Co-reduction using urea-assisted ethylene glycol (EG)	RGO	−0.5 V (vs. SCE)	Same E_s as vulcan and MWCNT but higher current density
Pd [24]	Microwave-assisted polyol	PHCSs	−0.5 V (vs. Hg/HgO)	The Pd/PHCS gave about 3 times higher current density and slight negative shift of the E_s compared with Pd/C at the same Pd loadings
Pd–Ru [48]	Hydrothermal method	Ti		$Pd_{87}Ru_{13}$ exhibits high electroactivity towards ethanol oxidation
Pd–Ni [49]	Deposition–precipitation (DP) route along with a relatively low-reduction temperature (390 K) to prevent the aggregation of alloy NPs	Vulcan	−0.5 V (vs. NHE)	5 % CeO_2 efficiently dispersed the Pd–Ni alloy NPs on the C support as well as manipulate the surface composition High I_f/I_b ratio with 5 % CeO_2 Alloy contains some amorphous NiO species on its surface, which are able

				produce OH_{ads} and provides an oxygen source for CO oxidation at low potential and thereby speeds up the decomposition rate for ethanol
Pd [25]	Microwave-assisted polyol	Graphene	−0.5 V (vs. Hg/HgO)	Same E_s for all supports, but graphene support gave better current density than MWCNT and nanocarbon supports
Ru@PtPd [50]	Hydrothermal	Vulcan	−0.6 V (vs. Hg/HgO)	The I_f/I_b ratio of Ru@PtPd/C was 1.5, which is much higher than for PtPd/C, Pd/C, or PtRu/C catalyst
Pd–Ni ($Pd_{40}Ni_{60}$) [26]	Dealloying a ternary $Al_{75}Pd_{10}Ni_{15}$ alloy in a 20 wt.% NaOH solution	Vulcan	−0.83 V (vs. Hg/HgO)	Better E_s and current density than nanoporous Pd/vulcan. This is supported by the high I_f/I_b ratio of the $Pd_{40}Ni_{60}$, indicating enhanced tolerance to poisoning
Pd–Sn Pd–Ru–Sn [51]	Chemical co-reduction	Vulcan	−0.6 V (vs. Ag/AgCl Sat'd KCl)	Pd–Sn/C displayed better electrocatalytic activity and stability towards poisoning than Pd–Ru–Sn/C and Pt–Ru/C nanocatalysts
Ag–Pd [52]	Dealloying a ternary $Mg_{60}Ag_{32}Pd_8$ precursor	Vulcan		The nanoporous $Ag_{80}Pd_{20}$ alloy exhibits superior catalytic activity towards ethanol compared to nanoporous Pd electrode
Pd [29]	Galvanic replacement reaction	PDDA-MWCNTs	~ −0.60 V (vs. Ag/AgCl)	The HPNs showed better E_s and current density than Pd nanoparticles. Current density is ~2.5× higher. Unlike methanol, I_f/I_b ratio is less than 1
Pd–Sn [53]	Electrodeposition from an ionic liquid	Graphite electrode	~ −0.50 V (vs. Ag/AgCl)	Pd–Sn exhibited enhanced performance to Pd. However, when Sn content is more than 25 atom %, the catalytic efficiency drops due to the presence of new Pd–Sn

(continued)

Table 6.2 (continued)

Catalyst	Synthesis method	Support	Onset potential (E_s)	Main highlight
				intermetallic phases in the deposited film
Pd [54]	Microwave-assisted polyol	HCH	~ −0.50 V (vs. Hg/HgO)	The current densities of Pd/HCH is three times that of the Pd/C at the same Pd loadings
Pd–Ni [55]	Co-reduction with $NaBH_4$	CNF	~ −0.60 V (vs. Hg/HgO)	Low in the E_s and a threefold enhancement in the peak current density for Pd–Ni/CNF catalyst compared to Pd/C catalyst with the same Pd loading. The I_f/I_b ratio is less than 1
Pd [31]	Microwave-assisted polyol	HPC	~ −0.50 V (vs. Hg/HgO)	Pd/HPC better E_s and current density compared to Pd/C. Current density is about 3 times that of the Pd/C. The I_f/I_b ratio is less than 1
Pd–Pb [56]	Co-reduction	Carbon black	~ −0.60 V (vs. Hg/HgO)	The E_s on the Pd–Pb/C is more negative than that on the Pd/C. The Pd–Pb (4:1) has a better activity than the Pd/C catalyst. The addition of Pb facilitates the oxidative removal of CO. The promoting effect of Pb is explained by a bifunctional mechanism and d-band theory
Pd [32]	Dealloying of an Al–Pd alloy in an alkaline solution	Carbon powder	~ −0.45 V (vs. Hg/HgO)	NPPd exhibits high catalytic activity for electrooxidation of ethanol
Pd–Ag [57]	Co-reduction with $NaBH_4$	Vulcan	−0.45 V (vs. Hg/HgO)	In this study, the high activity of Pd–Ag/C catalysts towards ethanol oxidation in alkaline media in comparison with Ag/C, Pt/C, and Pd/C was reported. The best performance was observed for the 10 % Pd–10 % Ag/C

Pd–In_2O_3 [58]	Hydrothermal/reduction with NaHB4	MWCNTs	−0.6 V (vs. SCE)	E_s and current density are better than Pd/CNTs. Pd–In_2O_3/CNT electrocatalysts exhibited higher current density that is about twice higher than the Pd/CNTs
Pd@Au [59]	Chemically epitaxial seeded growth method	Vulcan	−0.65 V vs. SCE	The I_f/I_b for Pd/C is smaller than that of Pd@Au/C, suggesting that poisoning of Pd/C is more serious than that of the Pd@Au/C. The anti-poisoning effect of the Pd@Au/C is related to the effect of the Au support which weakens the bonding interaction between the absorption species and Pd
Pd/MO (M = NiO or CeO_2) [60]	Microwave for metal oxide (MO) and chemical reduction for Pd	Vulcan	−0.62 V (vs. Hg/HgO)	Pd–NiO (6:1 by weight)/C gave the best E_s and current density (5 times) compared to the Pd/C or Pd–CeO_2
Nanoporous Pd foam with sub-10 nm dendrites [61]	Electrodeposition		−0.50 V (vs. Hg/HgO)	Excellent current density when foam obtained from NH_4Cl electrolyte
Pd [62]	Reduction by $NaBH_4$	S-MWNTS	−0.50 V vs. SCE	Same E_s and higher current density compared to other types of MWCNTs used. The S-MWCNTs/Pd catalysts show the highest I_f/I_b, suggesting the best CO resistance
Pd–Sn, Pd–Ni [63]	microwave-assisted polyol	Sulfonated MWCNTs	−0.50 V vs. Ag/AgCl on $PdSn_{mix}$, $PdNi_{mix}$, and Pd	$PdNi_{mix}$/S-MWCNTs showed faster charge transfer kinetics than $PdSn_{mix}$/S-MWCNTs
Pd–Ni [64]	Solution phase-based nanocapsule	Vulcan C	−0.801 V vs. Hg/HgO	Pd_4Ni_5/C onset potential on was 180 mV more negative than that of Pd/C and its exchange current density was 33 times higher than that of Pd/C

(continued)

Table 6.2 (continued)

Catalyst	Synthesis method	Support	Onset potential (E_s)	Main highlight
Pd–Bi [65]	Reduction by $NaBH_4$	Vulcan C	Pd–Bi/C (95:05) −0.6 V vs. Ag/AgCl	Pd–Bi/C (95:05) showed higher activity than Pd/C
Pt–Pd–Au [66]	Reduction by $NaBH_4$	Vulcan C	~ −0.45 V vs. MMO	$Pt_{30}Pd_{38}Au_{32}/C$ displayed better catalytic activity and lower charge transfer resistance than Pt/C
Pd–Sn [67]	Modified polyol	Vulcan C		$Pd_{86}Sn_{14}/C$ 1.4 times higher current density than Pd/C (JM) other Pd–Sn alloys

THH Pd NCs tetrahexahedral Pd nanocrystals, *HPC* honeycomb-like porous carbon, *NPPd* nanoporous palladium, *HPNs* hollow Pd nanospheres, *RGO* reduced graphene oxide, *MWCNTs* multiwalled carbon nanotubes, *S-HCNF* helical carbon nanofibers functionalized with benzyl mercaptan, *WC* tungsten carbide, *PHCSs* porous hollow carbon spheres, *HPC* honeycomb-like porous carbon, *PDDA-MWCNTs* polydiallyldimethylammonium-functionalized MWCNTs, *APZ-MWCNTs* 2-aminophenoxazin-3-one-functionalized MWCNTs, *S-MWCNTs* sulfonated MWCNTs, *GNS* graphene nanosheet

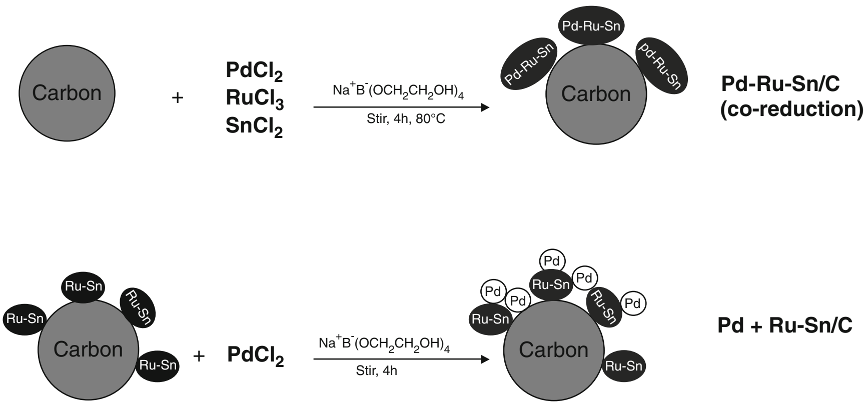

Fig. 6.5 Schematic representation of the preparation routes of Pd–Ru–Sn/C nanocatalyst [51]

effect of the additive or support with Pd on ethanol electrooxidation in alkaline electrolytes. Pd–Ru (1:1)/C was found to have higher activity towards ethanol electrooxidation in alkaline media than Pd/C, with the mass specific activity of almost four times that on Pt–Ru [21].

Pd–Pb/C catalysts with different amounts of Pb were prepared using $NaBH_4$ chemical reduction method in the presence of sodium citrate. Pd–Pb (4:1)/C showed better activity towards ethanol electrooxidation in alkaline electrolyte than Pd/C catalyst. The Arrhenius equation was used to calculate the activation energy, which showed a smaller value, thus implying a faster charge transfer process. The enhanced activity of Pd–Pb/C was explained by a bifunctional mechanism and the d-band theory [56]. Pd_4–Au/C and $Pd_{2.5}$–Sn/C catalysts prepared by He et al. [72] showed lower activity for ethanol electrooxidation in alkaline electrolyte than commercial Pt/C but were more tolerant to poisoning.

$Pd_{2.5}$–Sn/C prepared by Modibedi et al. [51] through the chemical reduction method using a mixture of $NaBH_4$ + ethylene glycol as a reducing agent (Fig. 6.5) displayed better electrocatalytic activity for ethanol oxidation and stability towards poisoning than the E-TEK Inc. Pt–Ru/C catalyst. It was observed that not all the Sn was alloyed with Pd and a small amount existed as SnO_2 on the surface of the catalyst. The changes in the lattice parameters or constants were noted as having an effect on the electrocatalytic activity of the catalysts. Pd–Sn/C catalysts were also synthesized via the polyol reduction method by Du et al. [67]. They obtained a homogeneous alloy formation of Pd and Sn with Sn on the surface being slightly oxidized. DFT calculations were employed together with the electrochemical characterization to understand the electrooxidation of ethanol in alkaline medium on Pd–Sn/C catalysts. Pd–Sn/C with 14 atomic % Sn showed improved current density than the JM Pd/C catalyst.

Tian et al. [53] obtained PdSn via electrochemical deposition from an ionic liquid onto a graphite electrode. Pd–Sn exhibited enhanced performance compared to Pd alone. However, when Sn content is more than 25 atom %, the catalytic efficiency drops due to the presence of new Pd–Sn intermetallic phases in the deposited film. Gao et al. [50] reported the use of a core–shell-structured Ru@PtPd/C, obtained via hydrothermal method, for the electrooxidation of ethanol in alkaline solution. Yi et al. [48] used hydrothermal strategy to obtain Pd–Ru deposited on Ti and proved that $Pd_{87}Ru_{13}/Ti$ exhibits high electroactivity towards ethanol oxidation. Xu et al. [73] developed a series of Pd–Au/C alloy using dimethylformamide co-reduction method under an ultrasonic process. The atomic ratio of Pd to Au was varied from 7:1 to 3:1 and 1:1. Pd_3Au/C showed increased catalytic stability while maintaining the comparable activity than Pd/C catalyst. Au was selected as the promising second metal to form Pd–Au/C alloy because it is the most electronegative metal, which resulted in the electron-withdrawing effect to the neighboring Pd atoms, thus, suggesting that the electronic effect mechanism for ethanol electrooxidation on Pd–Au/C catalyst will be favored. A different form of alloyed Pd–Au/C known as Pd-decorated Au/C (Pd@Au/C) was prepared with successive procedures, in which Au seeds were first synthesized and then Pd was electrodeposited on the surface of Au through the under-potential deposition method. This method has the advantage of minimizing the Pd loading since Pd does not form new nuclei Au. Pd@Au/C showed enhanced anti-poison capability for adsorbed species and stability towards ethanol electrooxidation in alkaline media than Pd/C due to the electronic interaction between the Au and Pd [59]. Nguyen et al. [57] synthesized Pd–Ag/C by the $NaBH_4$ reduction method using citrate as the complexing agent and stabilizer. Pd–Ag/C displayed an excellent activity, enhanced CO tolerance, and better stability than Pt/C and Pd/C catalysts, which was explained by the d-band theory. The sequential electroless deposition method was employed to prepare Pd–Ag alloys on stainless steel disc. The ethanol oxidation performance in alkaline medium was higher on Pd–Ag alloy with 21 at. % Ag than on Pd. This Ag content showed improved tolerance towards poisoning by the adsorbed intermediates. The enhanced performance was described by the bifunctional mechanism [74]. Liu et al. [47] employed co-reduction process to prepare Pd–Ag supported on reduced graphene oxide. Ji et al. [52] prepared Pg–Ag/C by dealloying $Mg_{60}Ag_{32}Pd_8$ precursor and found that the nanoporous $Ag_{80}Pd_{20}$ alloy exhibited superior catalytic activity towards ethanol compared to the nanoporous Pd electrode. Shen et al. [75] followed the same procedure as Nguyen [57] to prepare Pd–Ir/C catalysts. Their results showed that Ir addition improved the ethanol oxidation kinetics on Pd in alkaline electrolyte. The enhanced catalyst activity after Ir addition on Pd was attributed to the bifunctional mechanism. In continuing with their earlier work on Pd–Ir/C, Shen et al. [68] recently reported a ternary Pd–Ir–Ni nanocatalyst which they showed could increase the peak power density by more than 122 % compared with the monometallic Pd nanocatalyst, 69 % compared bimetallic Pd–Ir nanocatalyst, and 44 % as compared with the bimetallic Pd–Ni nanocatalyst.

Pd–Ni/C was synthesized by Shen et al. [76] through the $NaBH_4$ reduction method, and the Ni content was optimized since the high content of Ni will lower the electronic conductivity due to the presence of Ni oxide or hydroxide on the surface, thus resulting in a decrease in activity of the Pd–Ni/C catalyst. The highest activity for ethanol electrooxidation in alkaline electrolyte and stability was obtained on Pd_2Ni_3/C catalyst. The enhanced activity was attributed to the various oxidation states of Ni found around Pd. Maiyalagan et al. [55] synthesized Pd–Ni using $NaBH_4$ reduction method supported on carbon nanofibres (CNFs). CNF-supported Pd catalysts were more active towards ethanol electrooxidation in alkaline medium than Pd/C catalyst. The onset potential on Pd_3Ni/CNF was 200 mV more negative, and a threefold increase in current density was obtained as compared to Pd/C having the same Pd loading. $Pd_{40}Ni_{60}$ nanocrystalline alloy catalyst, which was produced by dealloying $Al_{75}Pd_{10}Ni_{15}$ alloy, showed an increase in ethanol electrooxidation in alkaline medium than on nanoporous Pd [26]. Pd_xNi_y/C catalysts were prepared using a solution phase-based nanocapsule method. This method was chosen based on its ability to control diameter and size distribution of Pd–Ni/C particles as well as to assist in producing contacts between Pd and Ni on the surface of the catalyst. Pd_4Ni_5/C onset potential for ethanol electrooxidation was 180 mV more negative than that of Pd/C, and high current density was obtained [64]. Pd–Bi/C was synthesized by Neto et al. [65], varying the atomic ratios of Pd:Bi via the $NaBH_4$ reduction method. Pd–Bi/C (95:05) electrocatalyst showed higher activity towards ethanol oxidation in alkaline electrolyte than Pd/C described by the effective removal of intermediates by the OH adsorbed species.

Recently, we [63] synthesized various sulfonated multiwalled carbon nanotube (SF-MWCNT)-supported Pd–M (M=Ni and Sn) using microwave-assisted polyol synthesis (Fig. 6.6) and compared their activity towards ethanol electrooxidation. We showed that the bimetallic catalyst (i.e., obtained by simple ultrasonication of the metallic mixtures) gave enhanced electrocatalysis towards alcohol than the alloy counterparts (i.e., obtained by co-reduction of the metals).

X-ray photoelectron spectroscopy was used to prove that Pd–M alloy was obtained using the simple ultrasonication mixing (Fig. 6.7). The Pd $3d_{5/2}$ (alloy) peak gives four contributions which relate to the chemical states: 335.6 ± 0.1 eV (PdSn), 336.4 ± 0.1 eV (Pd_xO_y), 337.9 ± 0.1 (Pd_xO_y), and 338.7 ± 0.1 eV ($PdSO_4$). Interestingly, the Pd $3d_{5/2}$ (mix) peak gives similar contributions at 335.3 ± 0.1 eV (PdSn), 336.4 ± 0.1 eV (Pd_xO_y), and 337.9 ± 0.1 eV (Pd_xO_y). Clearly, the surface chemistry of the $PdSn_{Alloy}$ and $PdSn_{Mix}$ is similar. The same trend of peak evolutions and chemical compounds is observed for both Pd–Ni (alloy) and Pd–Ni (mix). The Pd $3d_{5/2}$ peak of our SF-MWCNT-$PdNi_{mix}$ (335.3 eV) was comparable to the binding energy value (335.4 eV) for Pd–Ni alloy, confirming that ultrasonic-mixing technique formed an alloy.

The ternary catalyst systems are developed in order to illustrate the concept synergy towards the oxidation of alcohols having more than one carbon. Dutta et al. [66] synthesized Pt–Pd–Au/C catalyst using the borohydride reduction method, and

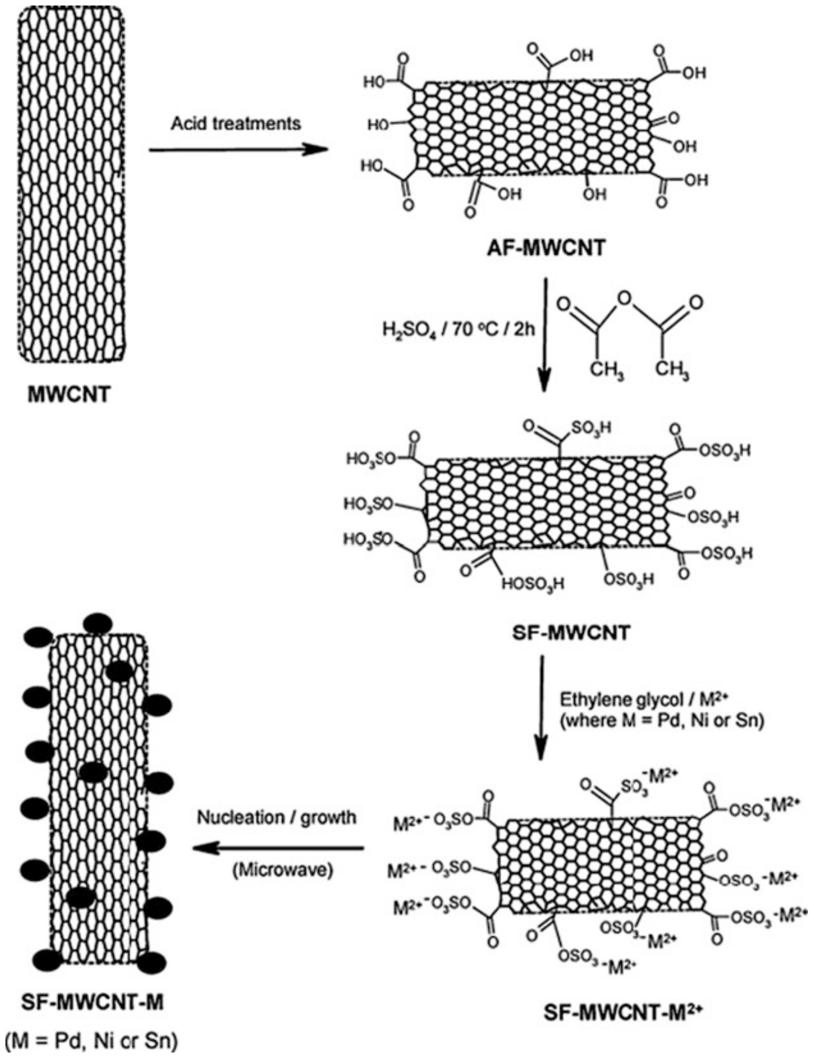

Fig. 6.6 Synthesis route of SF-MWCNT-M (M = Pd, Ni, or Sn) nanocomposites using microwave-assisted strategy [63]

the onset potential was more negative on $Pt_{30}Pd_{38}Au_{32}/C$ than on Pt–Pd/C and Pt–Au/C binary systems. The addition of Pd and Au into the Pt matrix increased the catalyst's efficiency for ethanol electrooxidation and reduced the rate of catalyst poisoning and in addition lowered the loading of Pt in the ternary catalyst. Modibedi et al. [51] showed that the activity of a ternary Pd–Ru–Sn/C catalyst

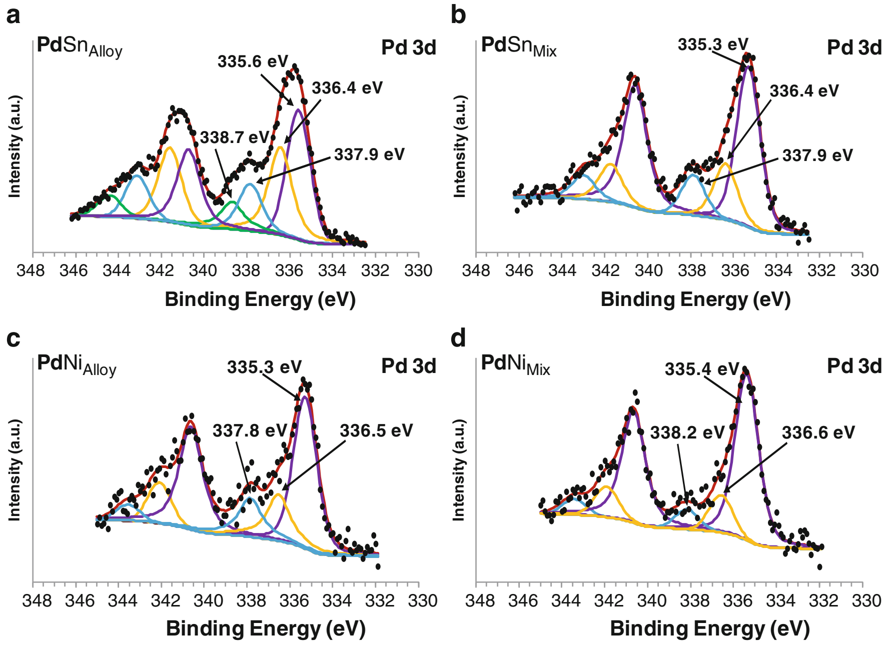

Fig. 6.7 Typical XPS evolutions of Pd 3d of (**a**) PdSn$_{\mathrm{alloy}}$ and (**b**) PdSn$_{\mathrm{mix}}$, and (**c**) PdNi$_{\mathrm{alloy}}$ and (**d**) PdNi$_{\mathrm{mix}}$

towards ethanol oxidation was slightly lower than that of the binary Pd–Sn/C alloyed catalyst but higher than Pd/C and Pt–Ru/C catalysts. Pd$_x$Pt$_{1-x}$ ($x = 0$–1) nanocatalysts on Ti foil prepared by Lu et al. [40] were also tested for ethanol electrooxidation in alkaline medium. The best performance was found when the ratio of Pd to Pt was from 0.5:0.5 to 0.8:0.2 towards ethanol oxidation.

6.2.3 Propanol Electrooxidation

There are few reports on the electrooxidation of 1-propanol and 2-propanol on Pd-based catalysts in alkaline electrolytes. This suggests that more research work on these alcohols is needed because 2-propanol is less toxic than methanol and its electrochemical oxidation is of great interest due to its particular molecular structure. Pd$_x$Pt$_{1-x}$ ($x = 0$–1) nanocatalysts on Ti foil were prepared by Lu et al. [40] using electrochemical methods, and they determined its activity towards the electrooxidation of 2-propanol. Pd$_{0.8}$Pt$_{0.2}$/Ti showed better catalytic activity and stability for the electrooxidation of 2-propanol in alkaline medium based on the bifunctional mechanism. Pd–Au/C catalyst was synthesized by chemical reduction method using NaBH$_4$ as the reducing agent. Pd–Au (4:1)/C showed higher electrocatalytic activity and improved stability for the electrooxidation of 2-propanol in alkaline medium than Pd/C and E-TEK Pt/C electrocatalysts. The promoting mechanism of Au in Pd–Au/C electrocatalyst towards the oxidation of 2-propanol was not clear to the authors [77]. Pd–Au/PPP was prepared by the electrodeposition of Pd–Au nanoparticles on poly(*p*-phenylene) (PPP) films. PPP films were used as the support material owing to the good electrochemical activity and good thermal stability. Adding Au to Pd-based catalyst improved the activity of the catalyst towards isopropanol oxidation. Pd–Au/PPP not only showed higher catalytic activity; it also had better poisoning resistance than Pd–Au deposited on bare glassy carbon electrode [78].

6.2.4 Polyhydric Alcohol Electrooxidation

The benefits of using polyhydric alcohols such as ethylene glycol and glycerol as alternative fuel sources in fuel cells are that these alcohols have low toxicity, are safe to handle, have high specific energy, and are highly soluble in water. EG is considered as the most viable alternative to methanol for FC development which has been investigated in acidic media using Pt-based nanocatalysts [79–81]. However, research in electrooxidation of ethylene glycol and glycerol in alkaline media remains hugely limited. Table 6.3 shows some of the representative works with Pd-based nanocatalysts in alkaline media.

As we did for ethanol [63], we also studied the electrooxidation of ethylene glycol using S-MWCNT-PdSn$_{\mathrm{mix}}$ and S-MWCNT-PdNi$_{\mathrm{mix}}$ and demonstrated that the Pd-based bimetallic nanocatalysts are more efficient catalysts than the monodispersed Pd nanocatalyst (results shown in Fig. 6.8 and summarized in Table 6.4).

6.3 Conclusions and Future Perspectives

Pd-based nanoelectrocatalysts exhibit superior performance towards alcohol electrooxidation in alkaline media compared to the state-of-the-art Pt/C. They give promise as likely replacement to Pt-based catalysts in alkaline media. However, more research is still needed to optimize the plethora of work reported so far in this field. Such future research activities may want to optimize the dilution levels of the Pd with metals or metal oxides for large-scale production and the employment of more conductive and cheap carbon supports. Graphene, known for its high conductivity compared to carbon nanotubes or carbon black, is a promising candidate as supporting platform, especially considering that it is now being produced in large commercial quantities.

Table 6.3 Representative Pd-based nanocatalysts for ethylene glycol and glycerol electrooxidation in alkaline media

Nanocatalyst	Synthesis method	Support	Onset potential (E_s)	Main highlight
Ethylene glycol				
Nanoporous Pd foam with sub-10 nm dendrites [61]	Electrodeposition		−0.50 V (vs. Hg/HgO)	Excellent current density when foam obtained from NH_4Cl electrolyte
Pd [62]	$NaBH_4$	Sulfonated MWCNT	−0.45 V (vs. SCE)	Lower E_s and higher current density compared to other types of MWCNTs. S-MWCNTs/Pd catalyst has the highest I_f/I_b, indicating the best CO resistance
PdSn, PdNi [82]	Microwave polyol	Sulfonated MWCNT	See Table 6.4	See Table 6.4
Glycerol				
Pd [83]	Reduction by $NaBH_4$	Vulcan	~ 0.45 V vs. NHE	The platinum-free $Pd_{0.9}Bi_{0.1}/C$ exhibits similar activity towards glycerol oxidation as Pt/C
Pd–Au [84]	Plasma co-sputtering method on a carbon diffusion layer	Gas diffusion layers (GDLs)	0.5 V vs. RHE	Plasma sputtering method leads to more active bimetallic Pd–Au nanocatalyst than from wet chemistry method. Better E_s (0.5 vs. 0.63 V) and current density (~2.2 times higher)
Pd_xM_{1-x} [43]	*Water-in-oil* microemulsion method, with $NaBH_4$ as reducing agent	Vulcan	0.55 V vs. RHE for $Pd_{0.3}Au_{0.7}/C$	For bimetallic catalysts, the order of activity at low potentials is $Pd_{0.3}Au_{0.7}/C > Pd_{0.5}Au_{0.5}/C > Pd_{0.5}Ni_{0.5}/C$

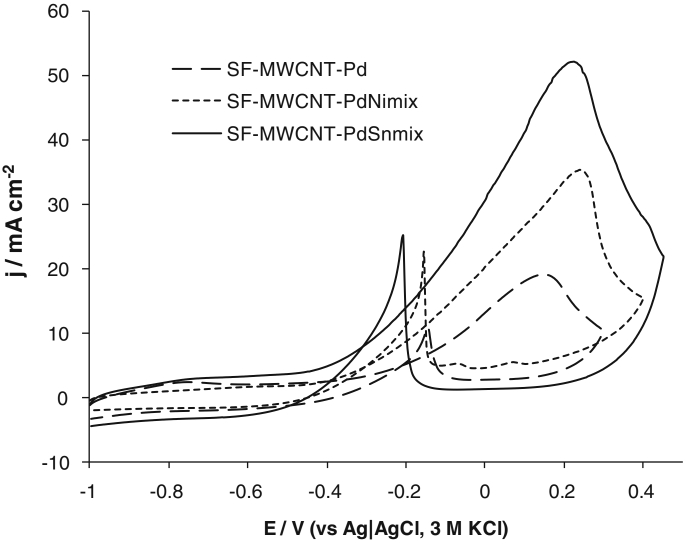

Fig. 6.8 Cyclic voltammograms of SF-MWCNT-Pd, SF-MWCNT-PdNi$_{\text{mix}}$, and SF-MWCNT-PdSn$_{\text{mix}}$ (at the fourth cycle) 0.5 M KOH + 0.5 M EG solutions. Scan rate −50 mV s^{-1}

Table 6.4 Comparison of the electrochemical performances of ethanol oxidation on GCE-SF-MWCNT-Pd, GCE-SF-MWCNT-PdSn$_{\text{mix}}$, and GCE-SF-MWCNT-PdNi$_{\text{mix}}$ nanocomposites measured in a 0.5 M ethylene glycol + 0.5 M KOH solution at a sweep rate of 50 mV s^{-1} ($n = 9$)

	Electrocatalytic performance data			
Electrocatalyst	J_f (mA cm^{-2})	E_{onset} (V)	E_p (V)	I_f/I_b
SF-MWCNT-Pd	19.1 ± 0.02	−0.24 ± 0.02	0.15 ± 0.02	1.82
SF-MWCNT-PdNi$_{\text{mix}}$	35.3 ± 0.02	−0.39 ± 0.02	0.25 ± 0.02	1.57
SF-MWCNT-PdSn$_{\text{mix}}$	51.9 ± 0.02	−0.44 ± 0.02	0.23 ± 0.02	2.10

References

1. Bianchini C, Shen PK (2009) Palladium-based electrocatalysts for alcohol oxidation in half cells and in direct alcohol fuel cells. Chem Rev 109:4183–4206
2. Antolini E, Gonzalez ER (2010) Alkaline direct alcohol fuel cells. J Power Sources 195: 3431–3450
3. Kazemi R, Kiani A (2012) Deposition of palladium submonolayer on nanoporous gold film and investigation of its performance for the methanol electrooxidation reaction. Int J Hydrogen Energy 37:4098–4106
4. Tripkovic AV, Popovic KD, Grgur BN, Blizanac B, Ross PN, Markovic NM (2002) Methanol electrooxidation on supported Pt and PtRu catalysts in acid and alkaline solutions. Electrochim Acta 47:3707–3714
5. Prabhuram J, Manoharan R (1998) Investigation of methanol oxidation on unsupported platinum electrodes in strong alkali and strong acid. J Power Sources 74(1):54–61
6. Hu F, Chen C, Wang Z, Wei G, Shen PK (2006) Mechanistic study of ethanol oxidation on Pd–NiO/C electrocatalyst. Electrochim Acta 52:1087–1091

7. Kadirgan F, Beden B, Lamy C (1983) Electrocatalytic oxidation of ethylene glycol. Part 2. Behavior of platinum ad-atom electrodes in alkaline medium. J Electroanal Chem 143: 135–152
8. Demirci UB (2007) Theoretical means for searching bimetallic alloys as anode electrocatalysts for direct liquid-feed fuel cells. J Power Sources 173:11–18
9. Greeley J, Norskov JK (2005) A general scheme for the estimation of oxygen binding energies on binary transition metal surface alloys. Surf Sci 592:104–111
10. Hammer B, Norskov JK (1995) Electronic factors determining the reactivity of metal surfaces. Surf Sci 343:211–220
11. Lima FHB, Zhang J, Shao MH, Sasaki K, Vukmirovic MB, Ticianelli EA, Adzic RR (2007) Catalytic activity-d-band center correlation for the O_2 reduction reaction on platinum in alkaline solutions. J Phys Chem C 111:404–410
12. Ruban A, Hammer B, Stoltze P, Skriver HL, Norskov JK (1997) Surface electronic structure and reactivity of transition and noble metals. J Mol Catal A Chem 115:421–429
13. Watanabe M, Motoo S (1975) Electrocatalysis by ad-atoms. Part I. Enhancement of the oxidation of methanol on platinum and palladium by gold ad-atoms. J Electroanal Chem 60: 259–266
14. Wang H, Alden LR, Di Salvo FJ, Abruna HD (2009) Methanol electrooxidation on PtRu bulk alloys and carbon-supported PtRu nanoparticle catalysts: a quantitative DEMS study. Langmuir 25:7725–7735
15. Yang J, Zhou Y, Su H, Jiang S (2011) Theoretical study on the effective methanol decomposition on Pd(111) surface facilitated in alkaline medium. J Electroanal Chem 662:251–256
16. Zheng HT, Li Y, Chen S, Shen PK (2006) Effect of support on the activity of Pd electrocatalyst for ethanol oxidation. J Power Sources 163:371–375
17. Jeon TY, Lee KS, Yoo SJ, Cho YH, Kang SH, Sung YE (2010) Effect of surface segregation on the methanol oxidation reaction in carbon-supported Pt-Ru alloy nanoparticles. Langmuir 26:9123–9129
18. http://www.gpo.gov/fdsys/pkg/PLAW-109publ58/pdf/PLAW-109publ58.pdf
19. NEC (2007) Advanced Energy Initiative, 2006. Published by the National Environmental Council for the President of the United States
20. Shen PK, Xu C (2006) Alcohol oxidation on nanocrystalline oxide Pd/C promoted electrocatalysts. Electrochem Commun 8:184–188
21. Chen Y, Zhuang L, Lu J (2007) Non-Pt anode catalysts for alkaline direct alcohol fuel cells. Chin J Catal 28:870–874
22. Hu G, Nitze F, Barzegar HR, Sharifi T, Mikołajczuk A, Tai CW, Borodzinski A, Wågberg T (2012) Palladium nanocrystals supported on helical carbon nanofibers for highly efficient electro-oxidation of formic acid, methanol and methanol in alkaline electrolytes. J Power Sources 209:236–242
23. Mellinger ZJ, Kelly TG, Chen JG (2012) Pd-modified tungsten carbide for methanol electrooxidation: from surface science to electrochemical evaluation. ACS Catal 2:751–758
24. Shen PK, Yan Z, Meng H, Wu M, Cui G, Wang R, Wang L, Sic K, Fu H (2011) Synthesis of Pd on porous hollow carbon spheres as an electrocatalyst for alcohol electrooxidation. RSC Adv 1:191–198
25. Singh RN, Awasthi R (2011) Graphene support for enhanced electrocatalytic activity of Pd for alcohol oxidation. Catal Sci Technol 1:778–783
26. Qi Z, Geng H, Wang X, Zhao C, Ji H, Zhang C, Xu J, Zhang Z (2011) Novel nanocrystalline PdNi alloy catalyst for methanol and ethanol electro-oxidation in alkaline media. J Power Sources 196:5823–5828
27. Hosseini J, Bodaghi A (2011) Preparation of palladium nanoparticles-titanium electrodes as a new anode for direct methanol fuel cells. J Solid State Electrochem 15:795–800
28. Zhao Y, Zhan L, Tian J, Nie S, Ning Z (2010) MnO_2 modified multi-walled carbon nanotubes supported Pd nanoparticles for methanol electro-oxidation in alkaline media. Int J Hydrogen Energy 35:10522–10526

29. Liu Z, Zhao B, Guo C, Sun Y, Shi Y, Yang H, Li H (2010) Carbon nanotube/raspberry hollow Pd nanosphere hybrids for methanol, ethanol, and formic acid electro-oxidation in alkaline media. J Colloid Interface Sci 351:233–238
30. Zhao Y, Yang X, Tian J, Wang F, Zhan L (2010) Highly dispersed Pd nanoparticles on 2-aminophenoxazin-3-one functionalized MWCNTs surface for methanol electro-oxidation in alkaline media. Mater Sci Eng B 171:109–115
31. Yan Z, He G, Zhang G, Meng H, Shen PK (2010) Pd nanoparticles supported on ultra high surface area honey-comb-like carbon for alcohol electrooxidation. Int J Hydrogen Energy 35:3263–3269
32. Wang X, Wang W, Qi Z, Zhao C, Ji H, Zhang Z (2009) High catalytic activity of ultrafine nanoporous palladium for electro-oxidation of methanol, ethanol and formic acid. Electrochem Commun 11:1896–1899
33. Wang M, Liu W, Huang C (2009) Investigation of PdNiO/C catalyst for methanol electrooxidation. Int J Hydrogen Energy 34:2758–2764
34. Shen PK, Xu C, Zeng R, Liu Y (2006) Electro-oxidation of methanol on NiO-promoted Pt/C and Pd/C Catalysts. Electrochem Solid State Lett 9:A39–A42
35. Sun ZP, Zhang XG, Liu RL, Liang YY, Li HL (2008) A simple approach towards sulfonated multi-walled carbon nanotubes supported by Pd catalysts for methanol electro-oxidation. J Power Sources 185:801–806
36. Awasthi R, Singh RN (2012) Optimization of the Pd-Sn/GNS nanocomposite for enhanced electrooxidation of methanol. Int J Hydrogen Energy 37:2103–2110
37. Wang Y, Wang X, Li CM (2010) Electrocatalysis of Pd-Co supported on carbon black or ball-milled carbon nanotubes in alkaline media. Appl Catal B Environ 99:229–234
38. Wang Y, Sheng ZM, Yang H, Jiang SP, Li CM (2010) Electrocatalysis of carbon black- or activated carbon nanotubes-supported Pd-Ag towards methanol oxidation in alkaline media. Int J Hydrogen Energy 35:10087–10093
39. Liu Z, Zhang X, Hong L (2009) Physical and electrochemical characterisations of nanostructured Pd/C and PdNi/C catalysts for methanol oxidation. Electrochem Commun 11:925–928
40. Lu J, Lu S, Wang D, Yang M, Liu Z, Xu C, Jiang SP (2009) Nanostructured PdxPt1-x/Ti anodes prepared by electrodeposition for alcohol electrooxidation. Electrochim Acta 54:5486–5491
41. Bunazawa H, Yamazaki Y (2009) Ultrasonic synthesis and evaluation of non-platinum catalysts for alkaline direct methanol fuel cells. J Power Sources 190:210–215
42. Kumar KS, Haridoss P, Seshadri SK (2008) Synthesis and characterization of electrodeposited Ni–Pd alloy electrodes for methanol oxidation. Surf Coating Technol 202:1764–1770
43. Simoes M, Baranton S, Coutanceau C (2010) Electro-oxidation of glycerol at Pd based nanocatalysts for an application in alkaline fuel cells for chemicals and energy cogeneration. Appl Catal B Environ 93:354–362
44. Xu C, Zeng R, Shen PK, Wei Z (2005) Synergistic effect of CeO2 modified Pt/C catalysts on the alcohols oxidation. Electrochim Acta 51:1031–1035
45. Nguyen ST, Yang Y, Wang X (2012) Ethanol electro-oxidation activity of Nb-doped-TiO2 supported PdAg catalysts in alkaline media. Appl Catal B Environ 113(114):261–270
46. Wang X, Wang W, Qi Z, Zhao C, Ji H, Zhang Z (2012) Novel Raney-like nanoporous Pd catalyst with superior electrocatalytic activity towards ethanol electro-oxidation. Int J Hydrogen Energy 37:2579–2587
47. Liu J, Zhou H, Wang Q, Zeng F, Kuang Y (2012) Reduced graphene oxide supported palladium silver bimetallic nanoparticles for ethanol electro-oxidation in alkaline media. J Mater Sci 47:2188–2194
48. Yi Q, Niu F, Song L, Liu X, Nie H (2011) Electrochemical activity of novel Titanium supported porous binary Pd-Ru particles for ethanol oxidation in alkaline media. Electroanalysis 23:2232–2240

49. Wei YC, Liu CW, Kang WD, Lai CM, Tsai LD, Wang KW (2011) Electro-catalytic activity enhancement of Pd-Ni electrocatalysts for the ethanol electro-oxidation in alkaline medium: the promotional effect of CeO_2 addition. J Electroanal Chem 660:64–70
50. Gao H, Liao S, Liang Z, Liang H, Luo F (2011) Anodic oxidation of ethanol on core shell structured Ru@PtPd/C catalyst in alkaline media. J Power Sources 196:6138–6143
51. Modibedi RM, Masombuka T, Mathe MK (2011) Carbon supported Pd-Sn and Pd-Ru-Sn nanocatalysts for ethanol electrooxidation in alkaline medium. Int J Hydrogen Energy 36:4664–4672
52. Ji H, Frenzel J, Qi Z, Wang X, Zhao C, Zhang Z, Eggeler G (2010) An ultrafine nanoporous bimetallic Ag-Pd alloy with superior catalytic activity. CrystEngComm 12:4059–4062
53. Jou LH, Chang JK, Whang TJ, Sun IW (2010) Electrodeposition of Palladium-Tin alloys from 1-ethyl-3-methylimidazolium chloride-tetrafluoroborate ionic liquid for ethanol electro-oxidation. J Electrochem Soc 157:D443–D449
54. Yan Z, Meng H, Shi L, Li Z, Shen PK (2010) Synthesis of mesoporous hollow carbon hemispheres as highly efficient Pd electrocatalyst support for ethanol oxidation. Electrochem Commun 12:689–692
55. Maiyalagan T, Scott K (2010) Performance of carbon nanofiber supported Pd-Ni catalysts for electro-oxidation of ethanol in alkaline medium. J Power Sources 195:5246–5251
56. Wang Y, Nguyen TS, Liu X, Wang X (2010) Novel palladium-lead (Pd-Pb/C) bimetallic catalysts for electrooxidation of ethanol in alkaline media. J Power Sources 195:2619–2622
57. Nguyen ST, Law HM, Nguyen HT, Kristian N, Wang S, Chan SH, Wang X (2009) Enhancement effect of Ag for Pd/C towards the ethanol electro-oxidation in alkaline media. Appl Catal B Environ 91:507–515
58. Chu D, Wang J, Wang S, Zha L, He J, Hou Y, Yan Y, Lin H, Tian Z (2009) High activity of Pd-In_2O_3/CNTs electrocatalyst for electro-oxidation of ethanol. Catal Commun 10:955–958
59. Zhu LD, Zhao TS, Xu JB, Liang ZX (2009) Preparation and characterization of carbon supported submonolayer palladium decorated gold nanoparticles for the electro-oxidation of ethanol in alkaline media. J Power Sources 187:80–84
60. Xu C, Shen PK, Liu Y (2007) Ethanol electrooxidation on Pt/C and Pd/C catalysts promoted with oxide. J Power Sources 164:527–531
61. Cherevko S, Kulyk N, Chung CH (2012) Nanoporous palladium with sub-10 nm dendrites by electrodeposition for ethanol and ethylene glycol oxidation. Nanoscale 4:103–105
62. Sun ZP, Zhang XG, Liang YY, Li HL (2009) A facile approach towards sulfonate functionalization of multi-walled carbon nanotubes as Pd catalyst support for ethylene glycol electro-oxidation. J Power Sources 191:366–370
63. Ramulifho T, Ozoemena KI, Modibedi RM, Jafta CJ, Mathe MK (2012) Fast microwave-assisted solvothermal synthesis of metal nanoparticles (Pd, Ni, Sn) supported on sulfonated MWCNTs: Pd-based bimetallic catalysts for ethanol oxidation in alkaline medium. Electrochim Acta 59:310–320
64. Zhang Z, Xin L, Sun K, Li W (2011) Pd-Ni electrocatalysts for efficient ethanol oxidation reaction in alkaline electrolyte. Int J Hydrogen Energy 36:12686–12697
65. Neto AO, Tusi MM, de Oliveira Polanco NS, da Silva SG, dos Santos MC, Spinace EV (2011) PdBi/C electrocatalysts for ethanol electro-oxidation in alkaline medium. Int J Hydrogen Energy 36:10522–10526
66. Dutta A, Mahapatra SS, Datta J (2011) High performance PtPdAu nano-catalyst for ethanol oxidation in alkaline media for fuel cell applications. Int J Hydrogen Energy 36:14898–14906
67. Du W, Mackenzie KE, Milano DF, Deskins NA, Su D, Teng X (2012) Palladium tin alloyed catalysts for ethanol oxidation reaction in alkaline medium. ACS Catal 2:287–297
68. Shen SY, Zhao TS, Xu JB, Li YS (2011) High performance of a carbon supported ternary PdIrNi catalyst for ethanol electro-oxidation in anion exchange membrane direct ethanol fuel cells. Energy Environ Sci 4:1428–1433
69. Shi JJ, Yang GH, Zhu JJ (2011) Sonoelectrochemical fabrication of PDDA-RGO-PdPt nanocomposites as electrocatalyst for DAFCs. J Mater Chem 21:7343–7349

70. Guo S, Dong S, Wang E (2010) Pt/Pd bimetallic nanotubes with petal-like surfaces for enhanced catalytic activity and stability towards ethanol electrooxidation. Energy Environ Sci 3:1307–1310
71. Tian N, Zhou ZY, Yu NF, Wang LY, Sun SG (2010) Direct electrodeposition of tetrahexahedral Pd nanocrystals with high index facets and high catalytic activity for ethanol electrooxidation. J Am Chem Soc 132:7580–7581
72. He Q, Chen W, Mukerjee S, Chen S, Laufek F (2009) Carbon-supported PdM (M=Au and Sn) nanocatalysts for the electrooxidation of ethanol in high pH media. J Power Sources 187: 298–304
73. Xu JB, Zhao TS, Shen SY, Li YS (2010) Stabilization of the palladium electrocatalyst with alloyed gold for ethanol oxidation. Int J Hydrogen Energy 35:6490–6500
74. Oliveira MC, Rego R, Fernandes LS, Tavares PB (2011) Evaluation of the catalytic activity of Pd–Ag alloys on ethanol oxidation and oxygen reduction reactions in alkaline medium. J Power Sources 196:6092–6098
75. Shen SY, Zhao TS, Xu JB (2010) Carbon-supported bimetallic PdIr catalysts for ethanol oxidation in alkaline media. Electrochim Acta 55:9179–9184
76. Shen SY, Zhao TS, Xu JB, Li YS (2010) Synthesis of PdNi catalysts for the oxidation of ethanol in alkaline direct ethanol fuel cells. J Power Sources 195:1001–1006
77. Xu C, Tian Z, Chen Z, Jiang SP (2008) Pd/C promoted by Au for 2-propanol electrooxidation in alkaline media. Electrochem Commun 10:246–249
78. Zhou W, Wang C, Xu J, Du Y, Yang P (2010) Enhanced electrocatalytic performance for isopropanol oxidation on Pd–Au nanoparticles dispersed on poly(p-phenylene) prepared from biphenyl. Mater Chem Phys 123:390–395
79. Livshits V, Philosoph M, Peled E (2008) Direct ethylene glycol fuel cell stack: study of oxidation intermediate products. J Power Sources 178:687–691
80. Maxakato NW, Arendse CJ, Ozoemena KI (2009) Insights into the electro-oxidation of ethylene glycol at Pt/Ru nanocatalysts supported on MWCNTs: adsorption-controlled electrode kinetics. Electrochem Commun 11:534–537
81. Maxakato NW, Arendse CJ, Ozoemena KI (2010) Dynamics of electrocatalytic oxidation of ethylene glycol, methanol and formic acid at MWCNT platform electrochemically modified with Pt/Ru nanoparticles. Electroanalysis 22:519–529
82. Ramulifho T, Ozoemena KI, Modibedi RM, Jafta CJ, Mathe MK (2013) Electrocatalytic Oxidation of Ethylene Glycol at Palladium-Bimetallic Nanocatalysts (PdSn and PdNi) Supported on Sulfonate functionalised Multi-walled Carbon Nanotubes. J Electroanal Chem 692:26–30
83. Simoes M, Baranton S, Coutanceau C (2011) Enhancement of catalytic properties for glycerol electrooxidation on Pt and Pd nanoparticles induced by Bi surface modification. Appl Catal B Environ 110:40–49
84. Mougenot M, Caillard A, Simoes M, Baranton S, Coutanceau C, Brault P (2011) PdAu/C catalysts prepared by plasma sputtering for the electro-oxidation of glycerol. Appl Catal B Environ 107:372–379

Chapter 7
Fundamental Studies on the Electrocatalytic Properties of Metal Macrocyclics and Other Complexes for the Electroreduction of O_2

Justus Masa, Kenneth I. Ozoemena, Wolfgang Schuhmann, and José H. Zagal

Abstract The high prospects of exploiting the oxygen reduction reaction (ORR) for lucrative technologies, for example, in the fuel cells industry, chlor-alkali electrolysis, and metal-air batteries, to name but a few, have prompted enormous research interest in the search for cost-effective and abundant catalysts for the electrocatalytic reduction of oxygen. This chapter describes and discusses the electrocatalysis of oxygen reduction by metallomacrocyclic complexes and the prospect of their potential to be used in fuel cells. Since the main interest of most researchers in this field is to design catalysts which can achieve facile reduction of O_2 at a high thermodynamic efficiency, this chapter aims to bring to light the research frontiers uncovering important milestones towards the synthesis and design of promising metallomacrocyclic catalysts which can accomplish the four-electron reduction of O_2 at low overpotential and to draw attention to the fundamental requirements for synthesis of improved catalysts. Particular attention has been paid to discussion of the common properties which cut across these complexes and how they may be aptly manipulated for tailored catalyst synthesis. Therefore, besides discussion of the progress attained with regard to synthesis and design of catalysts with high selectivity towards the four-electron reduction of O_2, a major part of this chapter highlights quantitative structure–activity relationships (QSAR) which govern the activity and stability of these complexes, which when well understood, refined, and carefully implemented

---

J. Masa • W. Schuhmann
Analytische Chemie-Elektroanalytik & Sensorik, and Center for Electrochemical Sciences–CES, Ruhr-Universität Bochum, Universitätsstr 150, D-44780 Bochum, Germany

K.I. Ozoemena
Energy and Process Unit, Materials Science and Manufacturing, Council for Scientific and Industrial Research (CSIR), Pretoria 0001, South Africa

Department of Chemistry, University of Pretoria, Pretoria 0002, South Africa

J.H. Zagal (✉)
Departamento de Química de los Materiales, Facultad de Química y Biología, Universidad de Santiago de Chile, Casilla 40, Correo 33, Santiago 1100773, Chile
e-mail: jose.zagal@usach.cl

M. Shao (ed.), *Electrocatalysis in Fuel Cells*, Lecture Notes in Energy 9,
DOI 10.1007/978-1-4471-4911-8_7, © Springer-Verlag London 2013

should lead to rational design of better catalysts. A brief discussion about nonmacrocyclic copper (I) complexes, particularly Cu(I) phenanthrolines, and those with a laccase-like structure which exhibit promising activity for ORR has been included in a separate section at the end.

7.1 Introduction

Providing adequate, clean, and sustainable energy, from the source of exploitation through eventual disposal, is one of the grand challenges of the twenty-first century. Electrochemical energy storage and conversion systems offer some of the most appealing possibilities for providing clean energy. Of the electrochemical energy systems, fuel cells [1] and metal-air batteries [2] have particularly attracted great research interest. The oxygen reduction reaction (ORR) is one of the key reactions in both of these systems, and Pt is the premium cathode catalyst for the reaction [3]. There is also a growing interest of the importance of ORR in chlor-alkali electrolysis due to its energy saving benefits [4]. Owing to the scarcity of Pt, intensive research has been undertaken aimed at improving both its mass- and area-specific activities through its alloying with less expensive metals and through developments in the synthesis of nanoparticles [5–7]. However, with the awareness that even the most ingenious improvements in catalyst synthesis cannot dispel the issue of Pt scarcity and the potential escalation of its cost upon increased demand, it is a prudent endeavor to explore alternative inexpensive catalysts. Metallomacrocyclic complexes, particularly metalloporphyrins (MPs) and metallophthalocyanines (MPcs), have been widely investigated for ORR since the 1960s [8]. However, due to lack of systematic methodologies for prediction of metallomacrocyclic complexes with satisfactory activity and stability, their performances with regard to both activity and stability generally trail those of catalysts derived from Pt. Of the metallomacrocyclic complexes that have been investigated for ORR, the N_4 metallomacrocyclic complexes, specifically MPs and MPcs, generally exhibit better activity compared to N_2O_2 (Pfeiffer complexes), O_4, N_2S_2, and S_4 macrocyclic chelate complexes [9, 10]. These materials are particularly interesting because of their lower costs compared to noble metals, and their high tolerance to methanol crossover, for the case of methanol fuel cell applications. They are also interesting because they provide models where active centers can be identified, and their catalytic activity can be modulated by changing the structure of the macrocyclic ligand [11]. Several factors influence the activity and stability of metallomacrocyclic complexes for ORR. For a given macrocyclic ligand, ORR will vary with the type of central metal ion [12–15]. Conversely, for a given metal ion, ORR will vary with the nature of substituents on the macrocyclic ligand [16–19], due to the electronic density changes they induce on the metal ion. In addition to these inherent limitations, the ORR activity and stability of a given metallomacrocyclic complex are highly dependent on the pH of the electrolyte. This effect is more pronounced in acidic electrolytes than in alkaline ones [20]. The other factors which

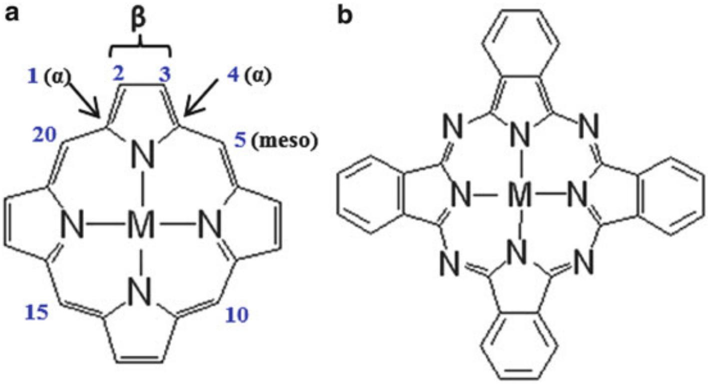

Fig. 7.1 Basic structure of a metalloporphyrin (**a**) and a metallophthalocyanine (**b**)

influence the activity and stability of a given metallomacrocyclic complex include its solubility in a given electrolyte, the method of its immobilization on the electrode, the operating conditions, and whether the ORR is measured with the metallomacrocyclic complex in solution or adsorbed on an electrode [21]. The most commonly used methods for immobilization of metallomacrocyclic complexes on an electrode include dip coating, drop dry, spin coating, electropolymerization, grafting, self-assembled layer(s), sublimation, and spraying. As such, the ORR performance of a given metallomacrocyclic complex may also vary depending on the method of immobilization used. For example, it has been reported in some literature that the potential of the M(III)/M(II) redox couple and oxygen reduction are shifted to more positive values for films formed by electropolymerization compared to films formed by dip coating or drop coating. Therefore, because of the inevitable variations in experimental procedures and conditions from one laboratory to another, it is difficult to make cross-laboratory comparisons of results reported in literature. To avoid delving into this complexity, qualitative and quantitative structure–activity relationships (QSAR) which govern the activity and stability of metallomacrocyclic complexes have been highlighted, which when well understood, refined, and carefully implemented should form a basis for rational design of improved metallomacrocyclic catalysts for oxygen reduction.

MPs and MPcs show very similar physical and chemical properties and they are structurally related to biological catalysts like cytochrome c and hemoglobin. The basic difference between their structures is shown (Fig. 7.1). As it will be discussed in details later, the properties of these complexes are very dependent on the type of central metal (M) and on the nature of substituents on the ligand. It is important to remark that the choice of substituents for the macrocyclic ligands is inexhaustible which leaves plenty of room for tailoring their properties. For example, the properties of metalloporphyrins may be varied widely by means of substitution groups at the β and meso-positions of the ring (Fig. 7.1a). Furthermore, the concepts of supramolecular chemistry and molecular self-assembly offer additional possibilities to vary the properties of metallomacrocyclic [22–24].

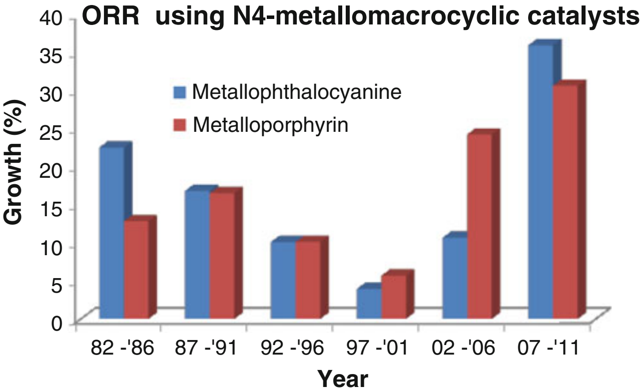

Fig. 7.2 Graphical representation of the publication growth (% growth = number of publications per 5-year period divided by the total number of publications in the last 30 years, multiplied by 100) from 1982 until 2011. Raw data obtained from SciFinder Scholar(R) search engine

Figure 7.2 presents an overview of the intensity of research in the use of MPs and MPcs as electrocatalysts for ORR during the last 4 decades (1982–2011). The graph is interesting as it clearly depicts that intensity of research in ORR follows the trends in global oil prices and world events: increasing as oil prices increase and decreasing as oil prices reduce (see "Oil Price History and Analysis" at http://www.wtrg.com/prices.htm). The 1981/1982 period recorded one of the peak oil prices in history. The increased research interest in ORR using MPs and MPcs in the 1982–1986 period may be related to two major events that led to high oil prices: the Iran/Iraq war and the imposition of price controls by the United States on her domestically produced oil, resulting in the US consumers paying more for imports than domestic production.

The increased research activity in the 1987–1991 period is associated with the spike in oil prices in 1990 due to low production and the uncertainty relating to invasion of Kuwait by Iraqi and the ensuing Gulf war. Crude oil prices were low over the 1992–1996 period (about US$ 20 per barrel). The 1997–2001 period was the period of the Asian financial crisis that led OPEC to increase oil production quota by 10 %. In fact, this period recorded one of the lowest oil prices in history (about US$ 18 per barrel in 1998). It is not surprising that the intensity of research in ORR for fuel cells and metal-air batteries was at its lowest during this period. Since 2002 to date, research in ORR has continued to increase. This is mostly due to the high oil prices as a result of the Asian economic growth, weak US dollar, Iraq war, world economic recession, and the Arab uprising termed the "Arab spring," and the increased awareness that the current energy sources cannot fulfill future energy demands. The increased global awareness about the detrimental effects of using fossil energies to the environment and the fact that fossil energy reserves are finite have also in part contributed to the increased intensity of research in ORR for fuel cells.

Apart from high oil prices, the world has increasingly become concerned about the need for environmental protection by minimizing the emission of greenhouse gases emanating from the burning of coal and oil. To address these environmental concerns, most countries of the world are now investing in Research and Development (R&D) for advancement of renewable energy technologies, which may further explain the recent increased research activities in ORR (2002–2011). For example, the USA introduced the Energy Policy Act of 2005 to encourage investment in renewable technologies (http://www.gpo.gov/fdsys/pkg/PLAW-109publ58/pdf/PLAW-109publ58.pdf). In a similar vein, an Advanced Energy Initiative (AEI) related to climate change was introduced in 2006 by the USA to accelerate renewable energy and technologies and reduce greenhouse gas emissions. The AEI provided for a 22 % increase in funding for clean-energy technology research in clean coal technology, nuclear power, and renewable solar and wind energies [25].

7.1.1 Reaction Pathways for the Reduction of Molecular Oxygen

The electrochemical reduction of oxygen in aqueous solutions is a complex multielectron reaction that occurs via two main pathways: one involving the transfer of two electrons to give peroxide and the so-called direct four-electron pathway to give water. The latter involves the rupture of the O–O bond. The nature of the electrode strongly influences the preferred pathway. Most electrode materials catalyze the reaction via two electrons to give peroxide. The several possible pathways are summarized in Table 7.1.

In strongly alkaline solutions or in organic solvents, O_2 is reduced via the transfer of a single electron to give a superoxide ion: $O_2 + e^- \rightleftarrows O_2^-$ ($E^\circ = -0.33$ V vs. NHE). The maximum free energy or the highest oxidant capacity of O_2 is obtained when this molecule reacts on the cathode of a fuel cell via four-electrons. So there is a need for catalysts that promote the four-electron reduction pathway. Most common electrode materials only promote the two-electron pathway, which releases almost one-half the free energy compared to that of the four-electron pathway. This is due in part to the relatively high dissociation energy of the O–O bond (118 kcal/mol). The four-electron reduction of O_2 to give water involves the rupture of the O–O bond and can involve the interaction of O_2 with one site (single site) or with two active sites simultaneously (dual site) on the electrode surface (Fig. 7.3).

Upon these possible interactions, the energy of the O–O bond decreases, favoring its rupture since electrons accepted by the O_2 molecule will occupy antibonding π^* orbitals. On platinum, O_2 reduction occurs almost entirely via four-electrons [26]. It is likely that on this metal O_2 interacts via the "bridge *cis*" conformation, involving two metal active sites (see Fig. 7.3) since the Pt–Pt separation in certain crystallographic orientations is optimal for this type of interaction. It is then crucial

Table 7.1 Possible pathways for the oxygen reduction in aqueous media

Mode of interaction	ORR pathways	
	Acidic medium	Basic medium
Bridge (or) trans	$O_2 + 2e^- + 2H^+ \rightarrow 2OH_{ads}$	$O_2 + 2e^- + 2H_2O \rightarrow 2OH_{ads} + 2OH^-$
	$2OH_{ads} + 2H^+ + 2e^- \rightarrow 2H_2O$	$2OH_{ads} + 2e^- \rightarrow 2OH^-$
	Overall direct reaction	Overall direct reaction
	$O_2 + 4H^+ + 4e^- \rightarrow 2H_2O$	$O_2 + 2H_2O + 4e^- \rightarrow 4OH^-$
	$E^o = 1.23\ V_{NHE}$	$E^o = 0.401\ V_{NHE}$
End-on	$O_2 + e^- + H^+ \rightarrow HO_{2,ads}$	$O_2 + H_2O + e^- \rightarrow HO_{2,ads} + OH^-$
	$HO_{2,ads} + e^- + H^+ \rightarrow H_2O$	$HO_{2,ads} + e^- \rightarrow HO_2^{\bullet}$
	Overall indirect reaction	Overall indirect reaction
	$O_2 + 2e^- + 2H^+ \rightarrow H_2O_2$	$O_2 + H_2O + 2e^- \rightarrow HO_2^{\bullet} + OH^-$
	$E^o = 0.682\ V_{NHE}$	$E^o = -0.076\ V_{NHE}$
	with $H_2O_2 + 2H^+ + 2e^- \rightarrow 2H_2O$	with $HO_2^{\bullet} + H_2O + 2e^- \rightarrow 3OH^-$
	$E^o = 1.77\ V_{NHE}$	$E^o = 0.88\ V_{NHE}$

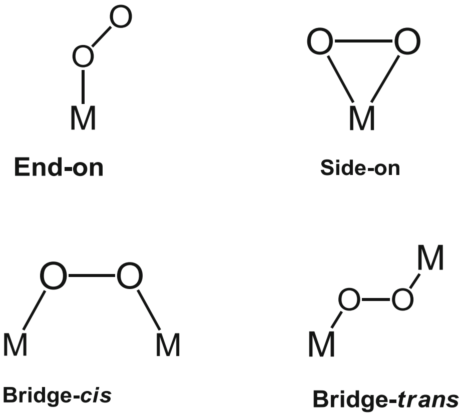

Fig. 7.3 Different spatial configurations for molecular oxygen when it interacts with metal sites

to develop low-cost catalysts that decrease the overpotential of the reduction of O_2 and that can also promote the four-electron reduction.

7.1.2 Evaluation of Catalysts for ORR

It is desirable to evaluate potential catalysts for fuel cell reactions in fuel cell prototypes under the real conditions of application. The standard approach involves profiling the voltage and power output as a function of the current drawn by a load during operation of a fuel cell. A schematic representation of the typical features of the voltage/power–current graphs is shown in Fig. 7.4. Fuel cells generally exhibit a

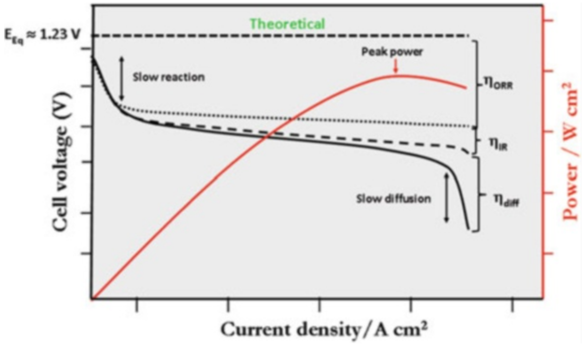

Fig. 7.4 Schematic representation of the typical voltage/power–current curves during operation of a fuel cell

substantial drop in voltage from the theoretically expected maximum voltage, even at their open circuit potential. When a load is applied to the cell, the cell voltage drops further as more and more current is drawn from it. For intermediate current densities, the voltage drops linearly as the current drawn from it is increased as shown in Fig. 7.4. As the current drawn from the cell is increased further up to some point, mass-transport limitation of either reactants, products, or both ensues and a drastic decline in the cell voltage is observed.

The effective voltage E of a fuel cell at a given current density, taking into account the various voltage loses, is given by $E = E_{\mathrm{eq}} - \eta_{\mathrm{ORR}} - \eta_{\mathrm{IR}} - \eta_{\mathrm{diff}}$, where E_{eq} is the theoretical thermodynamic voltage, η_{ORR} is the activation overpotential due to slow electrode reactions, η_{IR} is the overpotential due to ohmic resistances in the cell, and η_{diff} is the overpotential due to slow diffusion of reactants, products, or both. For hydrogen fuel cells, the voltage losses due to electrooxidation of H_2 at the anode are insignificant compared to the voltage losses due to ORR. Therefore, when comparing different catalysts for a given fuel cell configuration, the best catalyst or pair of catalysts for the anodic and cathodic reactions should be the one(s) which exhibit(s) minimum loss in cell voltage at a given current density. Said otherwise, the best catalyst should be the one which operates at the highest efficiency (η), η being defined as the ratio of the operating voltage (E) to the theoretical thermodynamic voltage (E_{eq}): $\eta(\%) = (E/E_{\mathrm{eq}}) \times 100$. In addition to the efficiency criterion, long-term operation of a fuel cell is an equally important requirement. A desirable catalyst should therefore be characterized with a high efficiency and also exhibit minimal loss in activity over long-term use.

However, the costs for installation of a fuel cell prototype are fairly high, and the devise is fairly expensive to operate. Additionally, long-term stability tests are particularly time consuming, which would make preliminary evaluation of catalysts using a fuel cell prototype unnecessarily costly, both resource-wise and time-wise. Preliminary evaluation of catalysts for fuel cells therefore often involves independent investigation of their half-cell reactions. A brief description of the methods that are most commonly used to investigate catalysts for the oxygen half-cell reaction follows in the next section.

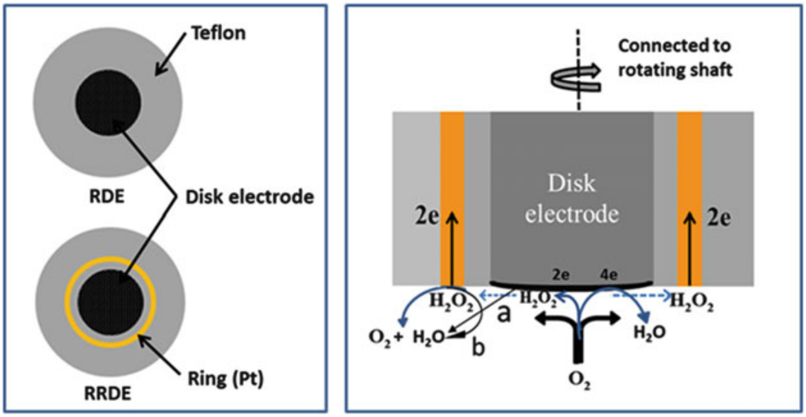

Fig. 7.5 Schematic representation of the RDE and RRDE (*left panel*) and of the possible reactions that take at the RRDE during ORR (*right panel*)

7.1.3 Determination of the Selectivity of O_2 Electroreduction

Ordinarily, the selectivity of ORR is determined by means of rotating disk electrode (RDE) or rotating ring-disk electrode (RRDE) voltammetry. The RDE is designed to boost the diffusion of an electroanalyte in conditions where an electrochemical reaction is limited by diffusion of the analyte to the electrode. In RRDE, a ring (often platinum) surrounds the disk electrode with an insulating material (usually Teflon) between them (Fig. 7.5).

During rotation of the electrode, the electrolyte is tangentially drawn to the disk electrode and radially swept away from it under controlled hydrodynamic conditions. Levich showed that the diffusion limited current (i_d) measured at a smooth disk electrode under controlled rotation is related to the angular velocity speed of rotation of the electrode according to Eq. (7.1) [27]:

$$i_{\mathrm{d}} = 0.62nFAD_0^{2/3}\omega^{1/2}\upsilon^{-1/6}C_0 \tag{7.1}$$

where n is the number of electrons exchanged per molecule, F is the Faraday constant, A is the surface area of the electrode, D_0 is the diffusion coefficient of the electroanalyte, ω is the angular velocity of the electrode, υ is the kinematic viscosity of the electrolyte, and C_0 is the bulk concentration of the electroanalyte. For a reaction which is essentially under diffusion limitation, a graph of i_{d} against $\omega^{1/2}$ yields a straight with a slope $= 0.62nFAD_0{}^{2/3}C_0\upsilon^{-1/6}$ from which n may be determined. Note that the coefficient 0.62 is used when ω is expressed in rad s^{-1}, while 0.21 is used when ω is expressed in revolution per minute (i.e., $0.62 \times (2\pi/60)^{1/2} = 0.21$) [28]. A more commonly used approach employs a modification form of Eq. (7.1), called the Levich-Koutecky analysis [Eq. (7.2)], for reactions which are under mixed kinetic and diffusion control, where i is the measured current, i_k is the kinetic current defined by Eq. (7.3), and i_d is the term in Eq. (7.1):

$$\frac{1}{i} = \frac{1}{i_\mathrm{k}} + \frac{1}{i_\mathrm{d}} \text{ or } \frac{1}{i} = \frac{1}{i_\mathrm{k}} + \frac{1}{B\sqrt{\omega}} \tag{7.2}$$

$$i_\mathrm{k} = knAFC_0 \tag{7.3}$$

From Eq. (7.2), a graph of the inverse of the measured current at a given potential i^{-1} against $\omega^{-1/2}$ gives a straight line with a slope of B^{-1} from which n can be determined and $i_\mathrm{k}{}^{-1}$ as the intercept on the i^{-1} axis [27].

The RRDE is designed in such a way that under the hydrodynamic conditions, an electroactive species generated at the disk may be detected at the ring electrode. The species generated at the disk electrode must therefore be sufficiently long-lived to be able to traverse the radius of the disk electrode and be detected at the ring. For the case of the ORR, the ring electrode is always poised at a potential where any H_2O_2 generated at the disk is oxidized at the ring. The fraction of H_2O_2 generated during ORR is calculated from Eq. (7.4), while the number of electrons transferred (n) is obtained from Eq. (7.5):

$$X\mathrm{H_2O_2} = \frac{2I_\mathrm{R}/N}{I_\mathrm{D} + I_\mathrm{R}/N} \tag{7.4}$$

$$n = \frac{4i_\mathrm{O2}}{i_\mathrm{H2O2}/N + i_\mathrm{O2}} \tag{7.5}$$

where N is the collection efficiency of the ring electrode, I_R is the ring current, I_D is the disk current, while i_O2 is the electrocatalytic oxygen reduction current at the disk, and i_H2O2 is the corresponding ring current due to H_2O_2 oxidation at a specific potential. The value of N is normally supplied by the manufacturer but it is advisable to verify it as often as possible using a suitable redox pair [29].

RDE and RRDE are very convenient voltammetric methods for studying the mechanism and kinetics of ORR and are by far the most widely used methods. However, it is important to bear in mind that the underlying mathematical formulations of these methods are theorized for smooth electrode surfaces under laminar flow hydrodynamics. There are many examples in recent literature where RDE and RRDE have been used to study catalyst films for which turbulent flow hydrodynamics is quite obvious. The collection efficiency of RRDE for microscopically disordered films, for example, very porous materials and irregularly built-up films (as may be the case for catalysts modified with nanocarbons such as carbon nanotubes and graphenes), is likely to be determined erroneously due to sporadic hydrodynamics. Therefore, the quality of a given catalyst film has a great influence on the correctness of results obtained from RDE and RRDE. It is generally recommended that catalyst films for RDE and RRDE studies should be as thin as possible [29]. Thick films may lead to increased mass-transport resistance through the catalyst layer and incomplete utilization of the catalyst which certainly lead to incorrect interpretation of results. These factors have to be considered critically when performing and interpreting RDE and RRDE measurements. A depiction of the possible processes that occur during the electroreduction of oxygen at RRDE electrodes is schematically shown in Fig. 7.4 to draw attention to some possible sources of error in treatment and interpretation of RRDE results. If O_2 is reduced by the transfer of two electrons to form H_2O_2, at least four competing reactions may follow and these include a competition between further electroreduction of H_2O_2 and its disproportionation on the disk, and if the H_2O_2 makes it to the ring, a competition between its electrochemical detection and disproportionation takes place since H_2O_2 is known to disproportionate on Pt surfaces. Therefore, the amount H_2O_2 detected at the ring is likely to be much lower than the amount actually produced because of the competing reactions. The magnitude of the error encountered in the determination of n and H_2O_2 using RRDE is likely to be even larger the less smooth the catalyst film is. However, in the absence of a more reliable method for studying the mechanism and kinetics of ORR, RDE, and RRDE voltammetries continue to be useful and handy. In the face of these drawbacks, several groups have proposed the use of scanning electrochemical microscopy (SECM) to study the selectivity of electrocatalysis of ORR [30–34].

7.2 From Model Structures to Active N_4-Metallomacrocyclic Catalysts

There is a vast amount of scientific literature about ORR catalysis by metallomacrocyclic. As mentioned earlier in the introduction, a variety of factors influence the ORR activity of these complexes, including the method used for immobilization of the complex, the pH of the electrolyte, and the conditions and quality of the experiments among others. As such, there is some ambiguity concerning the ORR selectivity of some complexes. In the next Sects. 2.1–2.4, a discussion of ORR catalysis by N_4-metallomacroyclic complexes is given with special emphasis placed upon those complexes and their design aspects which facilitate the four-electron reduction of oxygen. Nature achieves facile reduction of O_2 to water at very high turnover frequencies in the terminal respiration chain by cytochrome c oxidases (CcO) at their heme (Fe a_3)/Cu (Cu_B) bimetallic active site (Fig. 7.6a). This makes CcO interesting model systems to emulate, in what should be appropriately termed as bioinspired catalyst design. The next section gives a brief insight of the electrocatalysis of oxygen reduction by CcO and the progress attained in the biomimetic design of artificial heme/Cu-like catalysts for oxygen reduction.

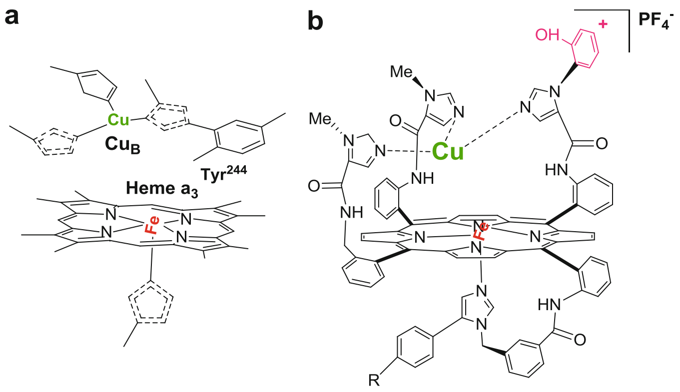

Fig. 7.6 Active structure of cytochrome c oxidase (**a**) and of a synthetic analog of cytochrome c oxidase (**b**) [35]

7.2.1 Oxygen Reduction by Cytochrome c Oxidases

Natural cytochrome c oxidases (CcO) catalyze the reduction of oxygen at their heme a_3/Cu_B (Fig. 7.6a) bimetallic site directly to water without the release of superoxide or peroxide. The Fe–Cu distance in CcO varies in the range of ~4.9–5.3 Å [36], depending on the redox states of the metal ions and ligation thereof, depending on the protein environment.

Recent work by Collman and Ghosh [35] has provided additional evidence that the active site in CcO is comprised of a heme a_3 of an iron porphyrin and Cu (Cu_B) coordinating three histidine groups with one of the histidine groups bound to a posttranslationally modified tyrosine residue (Fig. 7.6b). It is reported that the primary role of the redox centers is to rapidly provide the four electrons needed to reduce oxygen directly to water without the release of toxic superoxide or peroxide species.

The first step of the reduction process involves adsorption of oxygen at the reduced Fe^{II}/Cu^{I} center to form an Fe^{III}–O_2^- superoxide adduct with subsequent formation of an intermediate comprised of oxidized Cu^{II}, an Fe^{IV}=O ferryl radical, and a peripheral phenoxide radical (Fig. 7.7). The oxidized intermediate is then reduced directly to water by simultaneous transfer of four electrons [35].

Tremendous effort has been devoted to synthesize artificial catalysts which can achieve reduction of oxygen directly to water by mimicking the active site of CcO [35]. A key motivation of this endeavor has also been to use the CcO synthetic analogs as biomimetic models to probe the structure and function of CcO in the respiration chain. After an enduring effort spanning about three decades, successful synthesis of a functional heme/Cu analog with the ability to reduce oxygen directly to water at physiological conditions without generation of toxic peroxide and superoxide species was reported [35–39]. It is generally believed that natural enzymes exhibit unique flexibility, with the ability to sustain long range open-to-closed conformational changes, which is necessary for binding and catalyzing the

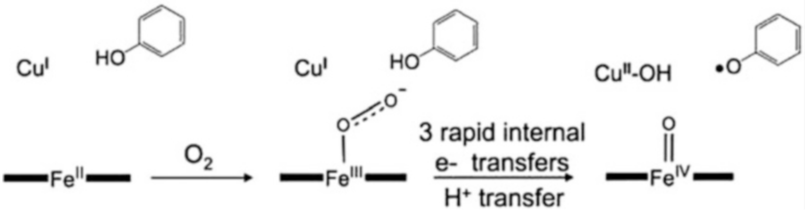

Fig. 7.7 A simplified mechanism leading to formation of the oxidized intermediate in the course of oxygen reduction at the active site of a functional heme/Cu analog of CcO [35]

reaction of small molecules [40]. Synthetic mimics of the heme/Cu active site in CcO must therefore be faultlessly designed with such conformational flexibility as to facilitate adsorption of oxygen, retention of partially reduced oxide species (PROS) intermediates until final products are formed, and release of the products. Artificial analogs of the heme/Cu sites in CcO have tended to be rather rigid, devoid of this conformational flexibility. A number of factors which complicate replication of the heme/Cu site of the CcO system in biomimetic design of functional heme/Cu analogs for oxygen reduction have been discussed [39]. Functional analogs of CcO incorporating dissimilar metal centers other than a heme/Cu active site have also been reported [41]. The success achieved in synthesizing functional CcO analogs and in the elucidation of their mechanism for oxygen reduction not only is useful for understanding the role of CcO in the terminal respiration chain but also gives new impetus to the design of effective molecular catalysts for four-electron reduction of oxygen.

7.2.2 *Oxygen Reduction by Bimetallic Cofacial Porphyrins*

Cofacial metalloporphyrins refers to a molecular arrangement whereby the metal ions of two independent planar metalloporphyrins exist face-to-face with each other. This molecular configuration may arise by spontaneous molecular arrangement, for example, due to π–π stacking, or by employing special synthetic schemes [42]. Dicobalt cofacial diporphyrins hinged on amide bridges were the earliest bimetallic diporphyrins with close semblance to the heme/Cu system that achieved four-electron reduction of oxygen to water in acidic electrolytes at remarkably low overpotentials [43]. Minor alterations in the dicobalt diporphyrin structures are reported to drastically poison the potency of the catalysts or cause them to revert to two-electron oxygen reduction catalysts [44]. Selection of the right anchoring system for the two individual cobalt porphyrin units to achieve just the right interplanar conformational separation between them is one critical factor in designing dicobalt cofacial diporphyrins with the ability to reduce oxygen to water. The first successful bridging system for two dicobalt diporphyrins was reported by Collman et al. [42, 43] and comprised of two diametrically positioned four-atom amide chains. The potential at

Table 7.2 Dicobalt cofacial porphyrins with a high selectivity for direct four-electron reduction of oxygen

Electrocatalyst	Medium	$E_{1/2}$ (V) vs. NHE	n	References
Co_2FTF4	0.5 TFA	0.71	3.9	[43]
Co_2DPB	0.5 TFA	0.70	3.7	[45]
Co_2DPA	–	0.67	3.7	[45]
Co_2DPD	0.5 M $HClO_4$	ca. 0.57	4	[40]
Co_2DPX	0.5 M $HClO_4$	ca. 0.58	4	[40]
$[Ir(OEP)]_2$DDAB	0.5 M H_2SO_4	0.80	4	[46]
$[Ir(OEP)]_2$	0.1 TFA	0.57	4	[47]

DDAB didodecyldimethylammonium bromide, *TFA* trifluoroacetic acid

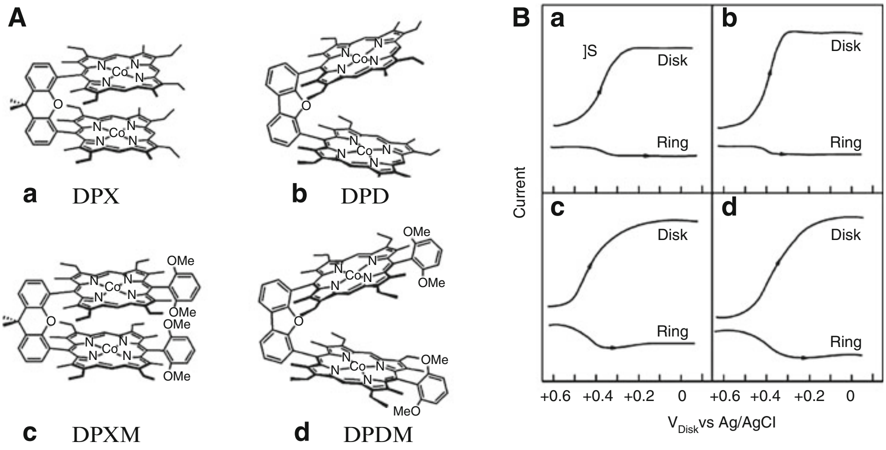

Fig. 7.8 (**A**) Examples of dicobalt cofacial bisporphyrins: *DPX* diporphyrin xanthene (a); *DPD* diporphyrin dibenzofuran (b); *DPXM* diporphyrin xanthene methoxyaryl (c); *DPDM* diporphyrin dibenzofuran methoxyaryl (d). (**B**) Rotating ring-disk voltammograms of O_2 reduction at pyrolytic graphite disks modified with (a), (b), (c), and (d) [48]

which oxygen reduction commences in these complexes is substantially more positive than the standard potential of the O_2/H_2O_2 couple ($E = 0.68$ V vs. SHE) which thermodynamically precludes production of hydrogen peroxide by any mechanism. Table 7.2 shows examples of dimetal cofacial porphyrins which achieve the four-electron reduction of O_2 to water at substantially low overpotentials.

If one or both cobalt atoms were replaced by other metal atoms, hydrogen peroxide was formed either as the main product or as an intermediate. Chang et al. [40] found that dicobalt diporphyrins anchored on dibenzofuran (DBD) and xanthene (DPX), Fig. 7.8A, exhibited remarkable conformational flexibility, and in both cases, the complexes were able to reduce oxygen directly to water despite having large differences (~4 Å) in the interplanar separation of their metal centers. Two other anchoring systems, anthracene and bisphenylene, have also been successfully used to

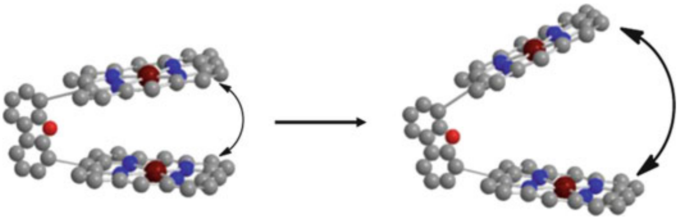

Fig. 7.9 Illustration of the flexibility of dicobalt cofacial porphyrins with a dibenzofuran bridging system showing the "Pac-Man effect." *White* = hydrogen, *gray* = carbon, *red* = oxygen, *blue* = nitrogen, and *crimson* = Co

design four-electron oxygen reduction "pillared" cobalt (II) cofacial diporphyrins, Fig. 7.8A [45, 49]. The flexibility of the dicobalt cofacial porphyrins anchored on DPD and DPX was attributed to the ability of these hinge-like frameworks (or pillared platforms) to considerably open their bite "the Pac-Man effect" as illustrated in Fig. 7.9 in accommodating exogenous ligands.

The effect of the type of anchoring system and porphyrin structure on the ORR activity of dicobalt cofacial diporphyrins can be observed in Fig. 7.8A. The ORR activity is drastically affected by the introduction of 2,6 dimethoxyphenyl groups to the *meso*-position of the porphyrin ring as can be seen by the increased anodic current registered at the ring. It is however not definitively clear whether it is the electronic changes or steric effects which lead to this sharp drop in activity. Some quantitative results showing the effect of the type of anchoring system on the ORR activity of dicobalt cofacial porphyrins have been reported in the review by Collman et al. [50].

The two cobalt centers in dicobalt cofacial diporphyrins have been reported to act in concert in order to achieve four-electron reduction of oxygen [51, 52]. One of the sites reportedly functions as a Lewis acid to stabilize the intermediate(s) in the cavity, ensuring that it does not dissociate before completion of the reaction [53]. To corroborate the dual-site postulate and specificity of the reaction site, a parallel type of mechanism involving both the two- and four-electron reduction was observed when one of the Co(III) centers in Co_2FTF4 was replaced by Al(III) [53]. A simplified scheme of the proposed mechanism of oxygen by dicobalt cofacial porphyrins is shown in Fig. 7.10 [48].

Electrocatalysis of O_2 reduction using bimetallic cofacial diporphyrins bearing dissimilar metal ions has been investigated by some groups. Using anthracene as the bridging system, Ni et al. [54] investigated the influence of the nature of the metal centers including Co–Co, Co–Cu, Co–Fe, Fe–Fe, and Fe–H_2 on the electrocatalysis of ORR by cofacial dimeric porphyrins. The cofacial dimeric porphyrin was found to reduce oxygen to hydrogen product as the final product. The other complexes, namely, Co–Fe, Fe–Fe, and Fe–H_2, were reported to catalyze the reduction of O_2 by a parallel mechanism involving both the two-electron and the four-electron reduction pathways. The researchers reported that for those catalysts which reduced O_2 to water, H_2O_2 was not formed as an intermediate.

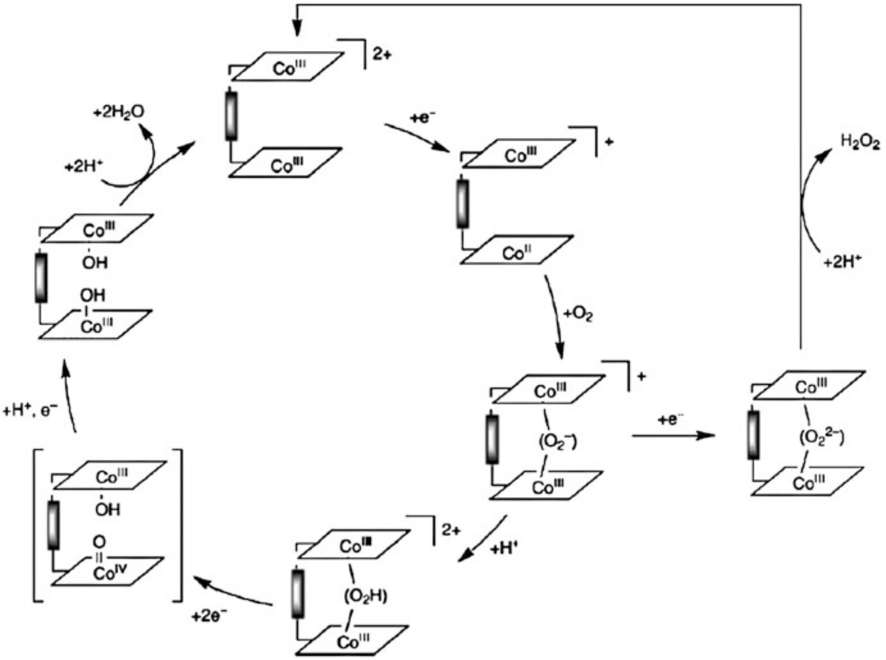

Fig. 7.10 Proposed mechanism for oxygen reduction at an active site of a dicobalt cofacial diporphyrin (adopted from [48])

A major drawback associated with dicobalt cofacial diporphyrins is their drastic decline in activity when adsorbed on other electrode surfaces other than edge-plane graphite (EPG). The catalysts have been reported to revert to two-electron reduction catalysts when adsorbed on other electrode surfaces other than EPG [50]. This has led to the conclusion that axial ligation of surface oxygen groups on EPG to the cobalt ion bears a significant contribution to the ORR activity of these complexes [50]. A second disadvantage is that these complexes are active in limited potential and pH windows outside of which they become readily deactivated. In a particular study which investigated the influence of site availability of these complexes for oxygen adsorption and for axial ligation on their activity for oxygen reduction, that is, whether the sites were located inside or on the outside of the cavity, it was found that four-electron reduction of oxygen was only possible when the sites inside the cavity were both available for interaction with oxygen. As with monomeric mononuclear porphyrins, dicobalt cofacial diporphyrins also gradually lose their activity upon repetitive potential cycling for a few cycles. Pretreatment of the active catalysts with hydrogen peroxide was found to rapidly deactivate them indicating that the mechanism of their deactivation involves chemical attack by peroxide and superoxide species. Despite all these existing drawbacks, the success achieved thus far should stimulate enthusiasm for synthesis of molecular heme/Cu or heme/Cu-like analogs of CcO and dinuclear cofacial porphyrin which can function under the conditions desirable for technological applications. As proposed way back in the original work by Collman et al. [43] it should be possible to modulate the ORR activity of the dicobalt cofacial porphyrins by judicious modification of the porphyrin ring and possibly by exploration of other bridging groups.

7.2.3 ORR by Simple N_4-Metallomacrocyclic Complexes

There is a large amount of literature available about the pathways for oxygen reduction by N_4-metallomacrocyclic complexes, with the reported results conflicting in some cases, which complicates a balanced review of the work. Additionally, the activity and stability of N_4-metallomacrocyclic complexes are affected by a variety of factors as spelt out in the introduction. This makes it difficult to make reliable cross-laboratory comparisons. However, by and large, the number of simple N_4-metallomacrocyclic complexes that can achieve the reduction of oxygen exclusively to water without generation of substantial amounts of hydrogen peroxide is generally very limited. Much of the attention in this section is devoted to research frontiers in view of promising simple N_4-macrocyclic catalysts that can achieve four-electron reduction of oxygen as this is the primary desire of many researchers in the field. To simplify our task, bearing in mind that thorough coverage of all the important works reported over the last four decades by various authors cannot be achieved faultlessly, emphasis of the discussion was placed more on specific structural properties or special catalyst preparation procedures that achieve four-electron reduction of oxygen either (a) in a direct four-electron reduction process, or (b) in a series process via hydrogen peroxide as an intermediate with its further electrochemical reduction to water or dismutation to water and oxygen, or (c) in a parallel type mechanism involving both (a) and (b). Unique cases involving sophisticated modifications, or otherwise, by means of which oxygen is reduced by the transfer of four electrons have also been included in as far as we could access the concerned literature. The rationale for discussing the electrocatalysis of oxygen reduction by these complexes in slight detail was to draw attention to their important properties which furnish them with the unique ability to facilitate the four-electron reduction of oxygen.

7.2.4 Direct Four-Electron Reduction of O_2 by Simple Monomeric N_4-Macrocycles

It has been shown in several studies that the ORR activity of metallomacrocyclic complexes is very dependent on the pH of the electrolyte. Therefore, a given metallomacrocyclic complex may catalyze the reduction of oxygen via the four-electron reduction in a specific pH window, outside of which, it may only afford to it via the two-electron pathway. This is particularly true for Fe and Co porphyrins

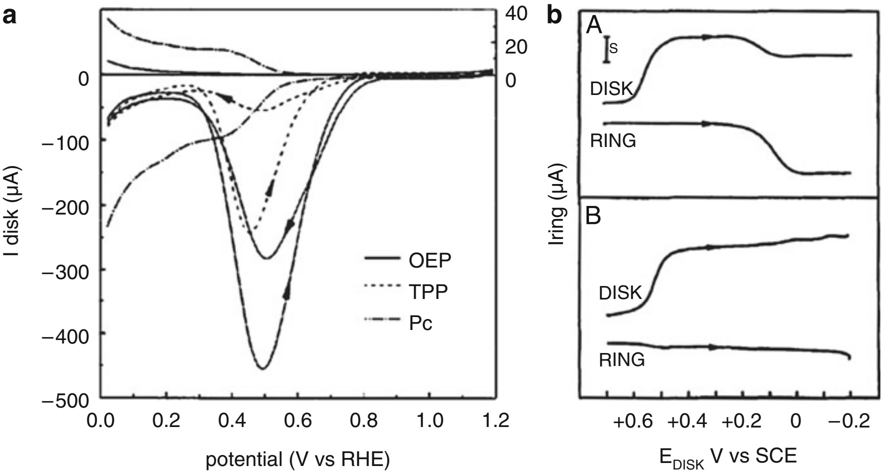

Fig. 7.11 (**a**) Rotating ring-disk voltammograms of iridium chelates irreversibly adsorbed on pyrolytic graphite (Cp) in 0.5 M H_2SO_4 at a rotation of 16 rps and scan rate of 10 mV s^{-1} [56] (reproduced with permission of Elsevier); (**b**) rotating ring-disk voltammograms of a Pt (*ring*) and graphite (*disk*) coated with DDAB and $[Ir(OEP)]_2$ (1.3×10^{-9} mol cm^{-2}) *upper panel* (A) and *lower panel* (B) Pt ring (*uncoated)*-Pt disk in 0.5 M H_2SO_4 saturated with air. The Pt rings were maintained at 1.0 V in both cases [46]

and phthalocyanines. Fe phthalocyanines generally reduce oxygen via the four-electron pathway under alkaline conditions, whereas the two-electron transfer pathway is predominant under acidic conditions. This is quite the oppositee for Co phthalocyanines which show a higher selectivity towards the four electron trasfer pathway in acidic electrolytes wheras they are essentially two-electron reduction catalysts under alkaline conditions. This subject will be discussed in details in Chap. 3. Most simple monomeric, monometallic N_4-metallomacrocyclic complexes can only achieve the reduction of oxygen to hydrogen peroxide by the transfer of two electrons. A few metallo N_4-macrocyclic complexes can however catalyze the reduction of oxygen in a direct four-electron transfer process and they constitute the subject of discussion in this section.

Many iridium porphyrins, specifically Ir(OEP)R, R = H, alkyl or aryl derivatives, and Ir(OEP)I and Ir(OEP)OOH, catalyze the direct four-electron reduction of oxygen at substantially low overpotentials [55]. With the exception of Ir(OEP)H, the rest of the complexes require preconditioning at specific potentials to be activated, the required conditioning potential varying depending on the nature of substituent groups.

According to studies by Collman et al. [47] Ir(OEP)R complexes specifically required conditioning at high positive potentials (>0.8 V vs. NHE), while Ir(OEP)I and Ir(OEP)OOH required conditioning at negative potentials (<−0.2 V vs. NHE) to be activated. As can be seen in Fig. 7.11a, Ir(OEP)H has been reported to exhibit the best activity similar to or better than that observed for dicobalt cofacial

Table 7.3 Metallomacrocyclic complexes with high activity and significantly low overpotentials for oxygen in acidic electrolytes

Electrocatalyst	Medium	$E_{1/2}$ (V) vs. NHE	(n)	References
Ir(OEP)H	0.1 M TFA	0.72/0.8	3.9	[55]
IrTPP	0.1 M TFA	0.48	NR	[47, 56]
Ir(OEP)R, R=OOH, Ph	0.1 M TFA	0.54	NR	[47]
CoP	1 M $HClO_4$	0.75	3.8	[57]
CoTMeP	1 M $HClO_4$	0.64	3.3	[57]
$[CoP(PyRu(NH_3)_5)_4]$	0.5 M $HClO_4$	0.47	NR	[52]
$[CoP(PhCNRu(NH_3)_5)_4]$	0.5 M $HClO_4$	0.58	NR	[52]
$[CoP(py\text{-}CH_3)_4(Os(NH_3)_5)_{\sim 2}]$	0.5 M $HClO_4$	0.59	NR	[52]

NR not reported, *n* number of electrons transferred

porphyrins [47, 55]. It was reported in a study by Shi et al. [46] that the presence of a cationic surfactant (DDAB) improved both the activity and stability of Ir(OEP)H and also widened its active potential window, Fig. 7.11b.

The dimeric form of Ir(OEP), $[Ir(OEP)]_2$, also catalyzes the direct four-electron reduction of oxygen, but unlike its monomer, it does not require any conditioning. As shown in Fig. 7.11a, the iridium chelate complexes become severely but reversibly deactivated at low potentials [56]. Their activity is not however affected by pH as dramatically as the dicobalt cofacial diporphyrin complexes. As with the case for Co_2FTF catalysts, it has been reported that when the Ir(OEP)R catalysts are adsorbed on other electrode surfaces other than EPG, their activity declines to two-electron reduction catalysts. Quite surprisingly, the main product of oxygen reduction was reported to be hydrogen peroxide after pyrolysis of Vulcan supported IrOEP and IrTPP. This is a rather peculiar case since the activity of most N_4-metalloporphyrins increases upon their pyrolysis. It has also been reported that the Ir complexes are unstable in air, losing all their activity after a few months. The four-electron reduction of oxygen by iridium porphyrins has been attributed to a single site which facilitates the adsorption of oxygen on Ir(II)in a side-on configuration, with scission of the O–O bond being a likely step in the mechanism.

Unfortunately, Ir is one of the rarest and most expensive metals which would render its use very costly. Nonetheless, the complex should serve as a suitable model, such that theoretical and experimental knowledge gained from its study may serve to tailor the synthesis of improved catalysts. Table 7.3 lists some metallomacrocyclic complexes which accomplish the reduction of oxygen via the four-electron transfer pathway in acidic electrolytes.

The other monomeric mononuclear porphyrins which mediate the four-electron reduction of oxygen are cobalt porphyrin (CoP) and cobalt *meso*-tetramethyl porphyrin (CoTMeP), with CoP exhibiting a higher activity than CoTMeP [57]. The unexpectedly high activity of CoP has been attributed to its likely spontaneous dimerization to produce a more catalytically active species. The synthesis of CoP or its free base (porphine) is quite challenging specifically regarding the attainable yield and purity, which makes it overly expensive for a nonprecious metal catalyst. Another drawback is that the catalyst is highly susceptible to oxidative degradation which severely affects its merit. In a later study which compared the ORR activity of several *meso*-tetraalkyl cobalt porphyrins by the same group, activity was found to follow the order CoP > CoTmeP > CoTBuP > CoTPrP > CoTEtP > CoPeP [16]. This led to the conclusion that the rate of adsorption of oxygen decreased as the bulkiness of the alkyl substituents increased. At the moment, there is no foreseeable strategy for improving the stability of CoP. Nevertheless, understanding its properties which furnish it with this exceptional activity deserves to be investigated in detail.

7.2.5 Specially Modified N_4-Metallomacrocyclic Complexes

Some studies have shown that certain modification procedures can be used to transform two-electron reduction metalloN_4-macrocyclic complexes into hybrid materials with the capability to reduce oxygen to water, either via the direct four-electron transfer pathway or in the series two-electron transfer pathway. Carbon nanomaterials, carbon nanotubes in particular [58–65], have been reported to significantly increase the catalytic oxygen reduction current, with a substantial reduction of the overpotential for ORR reported in some cases, as shown by the examples in Table 7.4.

Ozoemena's group has recently reported that MOCPcPt (where M = Fe, Ru) (Fig. 7.12a) supported on multiwalled carbon nanotubes afford the reduction of O_2 in a direct four-electron transfer process in 0.1 M NaOH [60, 61, 67]. There was no significant difference between the ORR activity at the FeOCPcPt and RuOCPcPt except that the latter gave a slightly higher kinetic rate constant (~3.6×10^{-2} cm s^{-1}) than the former (~2.8×10^{-2} cm s^{-1}).

The other material design strategies that have been reported to yield four-electron reduction metalloN_4-macrocyclic complexes include the use of supramolecular assembly [68, 69], by exploiting the electrostatic interaction between oppositely charged ions as in the work of D'Souza et al. [70] and Liu et al. [71]. D'Souza et al. reported that a 98 % selectivity of O_2 reduction to water was achieved when a dimeric porphyrin formed by electrostatic coupling of [*meso*-tetrakis(*N*-methylpyridyl) porphyrinato]cobalt tetrachloride ($[Co(TMPyP)]^{4+}$ Cl_4^-) with tetrasodium [*meso*-tetrakis(4-sulfonatophenyl)porphyrinato]cobalt ($[(Na^+)_4Co(TPPS)]^{4-}$) was used as a catalyst for ORR (Fig. 7.12b) [70]. In a related study, Liu et al. reported the formation of a supramolecular complex $[CoTBPyP][SiW_{12}O_{40}]$ by the electrostatic interaction of *meso*-tetrakis(4-*N*-benzylpyridyl)porphyrinatocobalt (CoTBPyP) and a polyoxometalate anion, silicotungstate $(SiW_{12}O_{40})^{4-}$, which was capable of reducing O_2 to water. The application of supramolecular porphyrins for oxygen reduction has been reviewed by Araki and Toma [72].

The multinulear complexes reported by Shi and Anson are another interesting example of specially designed metalloN_4-macrocyclic complexes with exceptional activity for ORR. Cobalt (tetrakis(4-pyridyl)porphyrin), with four $[Ru(NH_3)_5]^{2+}$ and ($[(NH_3)_5Os]^{n+}$ (n) 2, 3) groups around the porphyrin periphery, generally termed as

Table 7.4 Comparative onset potentials and current densities for MPc and MPc-CNT hybrid catalysts

MPc/CNT catalyst	Onset potential/*V* (vs. Ag|AgCl sat. KCl)	E_p/*V* (vs. Ag|AgCl sat. KCl)	Current density (mA cm^{-2})	References
NanoFePc	−0.2	−0.18	−0.6	[66]
NanoFePc-MWCNT	−0.05	−0.15	−1.7	
FeOBSPc	−0.2	−0.22	−0.5	[65]
FeOBSPc-MWCNT	0.0	−0.15	−1.4	
PtFeOCPc	−0.1	−0.30	−0.6	[61]
PtFeOCPc-MWCNT	0.0	−0.10	−1.2	

The current densities were measured at the stated peak potential (E_p/*V* Ag/AgCl, sat. KCl)

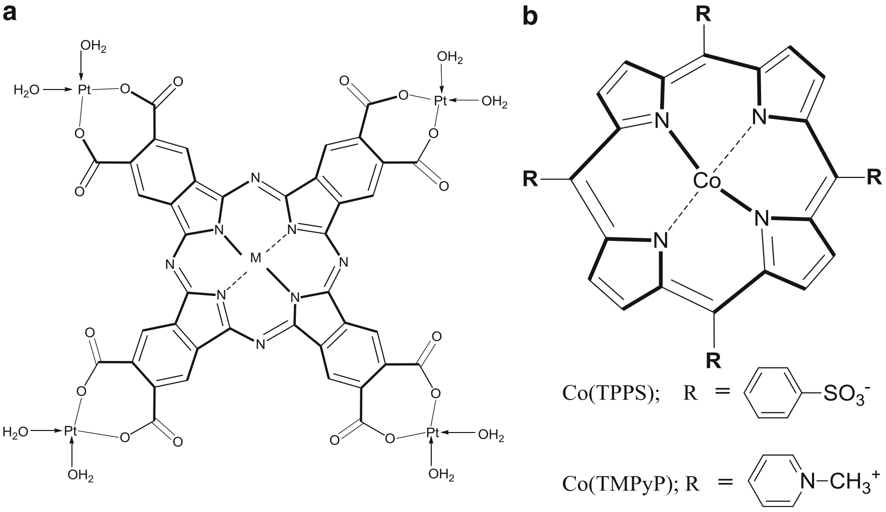

Fig. 7.12 (**a**) Structure of metallo-tetrakis-(diaquaplatinum)octacarboxy phthalocyanine (MOCPcPt, where M = Fe, Ru) and (**b**) structure of Co(TPPS) and Co(TMPyP)

"multinuclear catalysts" reduce oxygen nearly exclusively to water [52, 73–76]. As shown in Fig. 7.13b, the evident increase in the diffusion-limited current for oxygen reduction at the disk and the large decrease in the anodic current at the platinum ring clearly confirm that modification of $CoP(py)_4$ with $[Ru(NH_3)_5]^{2+}$ converts it from a predominantly two-electron O_2 reduction catalyst to a nearly exclusively four-electron reduction catalyst with minimal generation of hydrogen peroxide.

The proposed mechanism for oxygen reduction by the multinuclear ORR catalysts is outlined in Fig. 7.14 for tetraruthenated $[CoP(pyRu(NH_3)_5)_4]^{8+}$ but is also applicable to osmiumated porphyrins.

The mechanism has been proposed to involve π-backdonation from Ru(II) or Os (II) to the oxygen adsorbed porphyrin adduct Co(II)–O_2, where the cobalt porphyrin is the site for oxygen reduction while Ru and Os serve as cocatalysts which affect

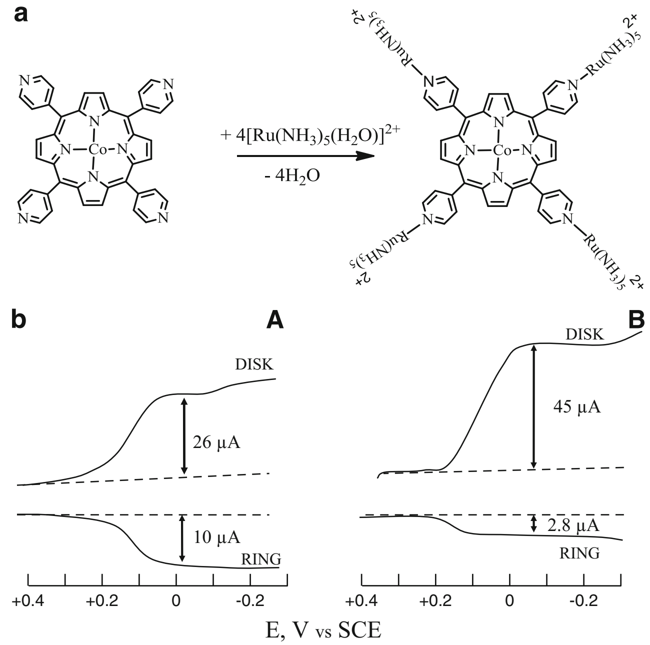

Fig. 7.13 (**a**) Reaction for conversion of $\mathrm{CoP(py)_4}$ to $[\mathrm{Co^{II}P(pyRu^{II}(NH_3)5)^4}]^{8+}$ (adopted from [52]). (**b**) RRDE voltammograms of (A) $\mathrm{CoP(py)_4}$, (B) $[\mathrm{Co^{II}P(pyRu^{II}(NH_3)_5)_4}]^{8+}$ (reproduced from [74])

$$\left[\mathrm{Co^{III}P(pyRu^{III}(NH_3)_5)_4}\right]^{13+} + e^- \rightleftharpoons \left[\mathrm{Co^{II}P(pyRu^{III}(NH_3)_5)_4}\right]^{12+} \tag{1}$$

$$\left[\mathrm{Co^{II}P(pyRu^{III}(NH_3)_5)_4}\right]^{12+} + O_2 \rightleftharpoons \left[\mathrm{O_2CoP(pyRu^{III}(NH_3)_5)_4}\right]^{12+} \tag{2}$$

$$\left[\mathrm{O_2CoP(pyRu^{III}(NH_3)_5)_4}\right]^{12+} + 4e^- \rightleftharpoons \left[\mathrm{O_2CoP(pyRu^{II}(NH_3)_5)_4}\right]^{8+} \tag{3}$$

$$\left[\mathrm{O_2CoP(pyRu^{II}(NH_3)_5)_4}\right]^{8+} + 4e^- + 4H^+ \rightarrow \left[\mathrm{Co^{II}P(pyRu^{II}(NH_3)_5)_4}\right]^{8+} + 2H_2O \tag{4}$$

$$\left[\mathrm{Co^{II}P(pyRu^{II}(NH_3)_5)_4}\right]^{8+} + O_2 \rightleftharpoons \left[\mathrm{O_2CoP(pyRu^{II}(NH_3)_5)_4}\right]^{8+} \tag{5}$$

Fig. 7.14 Proposed mechanism for O_2 reduction by $[\mathrm{CoP(pyRu(NH_3)_5)_4}]^{8+}$ and other related multinuclear complexes (reproduced from [52])

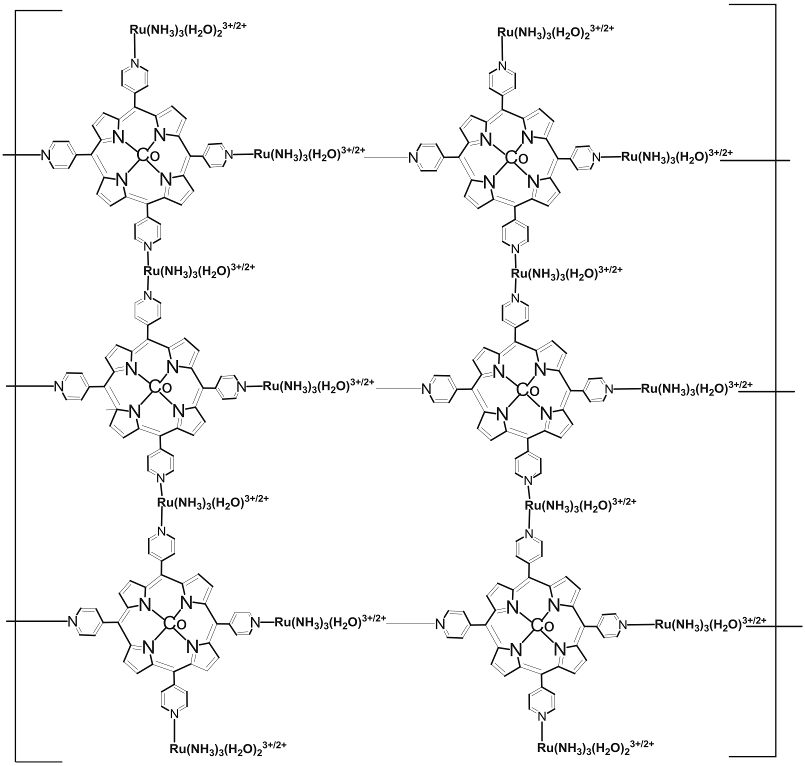

Fig. 7.15 Proposed structure of the supramolecular structure formed by complexation of *meso*-tetrakis((4-pyridyl)porphyrinato)cobalt (CoP(py)$_4$) with $[Ru(NH_3)_3(H_2O)_3]^{2+}$ on a graphite electrode

the relative rates of two competing pathways for oxygen. The first step in the mechanism (1) involves generation of Co(II) porphyrin with subsequent adsorption of oxygen on the active-site Co(II) in the next reaction (2). The next reaction (3) generates the backbonding Ru(II) which drives the reduction of oxygen by four electrons as shown in reaction (4) and finally, regeneration of the Co(II)–O_2 in reaction (5). It has been proposed that the electronic effects produced by the backdonation of the Ru(II) and Os(II) complexes on Co(II)–O_2 might be achieved by other suitable electron-donating nonmetallic functional groups attached to the porphyrin ring. It was however observed that differences in catalytic activity of multinuclear complexes were correlated to the relative backbonding strengths of the coordinated metal complexes but not on their relative reducing strengths.

Anson et al. postulated that their multinuclear catalysts described above may actually be supramolecular porphyrins with a structure similar to that shown in Fig. 7.15.

Most cobalt porphyrins can only reduce oxygen to hydrogen peroxide with no further reduction or dismutation of the peroxide [77]. Some recent studies have proposed a hybrid multifunctional catalyst incorporating a metallomacrocyclic complex and Prussian blue (PB) or horseradish peroxidase (HRP) so that the hydrogen peroxide generated by the metallomacrocycle can be reduced further by the PB/HRP to water. For example, reduction of O_2 to H_2O was achieved by designing a multicomponent-multifunctional catalyst incorporating carbon nanotubes (CNTs), CoPIX, and PB. The CNTs provide a high surface area matrix for dispersion of the catalysts [78].

According to a study by Forshey et al. [79] electrodeposited iron *meso*-tetrakis (*N*-methyl-4-pyridyl)porphyrin and electropolymerized *meso*-tetrakis(2-thienyl) porphyrinato]cobalt(II) (pCoTTP) accomplsih the reduction of O_2 to water. The ability of pCoTTP to reduce O_2 directly to water was attributed to a conducting network of CoTTP nodal points where multiple layers are arranged in such a way that they form suitable Co–Co bifacial binding clefts for O_2, thus allowing four-electron reduction of oxygen to water. A study by Elbaz et al. [80] has reported that Co(III) *meso*-tetra(*o*-aminophenyl)porphyrin (Co(III)TAPP) and Co(III) (*p*-sulfonatedphenyl)porphyrin (Co(III)TPPS) incorporated into aerogel carbon (AEG) electrodes by adsorption or electropolymerization achieved four electrons of oxygen.

7.3 Fundamental Studies of O_2 Electroreduction by N_4-Metallomacrocyclic Complexes

The preceding section focused mostly on qualitative description of the dependence of ORR activity on the structure of N_4-metallomacrocyclic complexes and some special modification procedures which can be used to improve activity. In this section, much of the discussion will focus on quantitative decription of the parameters which influence the ORR activity of N_4-metallomacrocyclic complexes. Specifically, the dependence of activity on the properties of the central metal ion will be dicussed in relation to the driving force of the reaction. In addition to this, the molecular orbital theory and the concept of intermolecular are used to describe the interaction between oxygen the central metal ion in N_4-macrocyclic complexes and how this interaction influences the ORR activity of the complex.

7.3.1 Effect of the Central Metal on the ORR Activity of N_4-Macrocylic Complexes

The electroreduction of oxygen by N_4-macrocylic complexes reaction is very sensitive to the nature of the metal center in the complex. For Fe and Mn phthalocyanines, at low overpotentials a four-electron reduction is observed with rupture of the O–O bond [14, 81–83], without the formation of peroxide. In contrast Co, Ni, and Cu phthalocyanines promote the reduction of O_2 only via two electrons to give peroxide

[14] as the main product of the reaction. Polymerized Co tetraaminophthalocyanines promote the four-electron [84, 85] reduction, whereas polymerized Fe tetraaminophthalocyanines only promote the two-electron reduction [86] in contrast to their monomeric counterparts. The net catalytic activity of metal macrocyclics is linked to the redox potential of M(III)/(II) of the complexes, the more positive the redox potential, the higher the activity. This trend is the opposite to what is expected from a simple redox catalysis mechanism, which is generally observed for the reduction of O_2 catalyzed by immobilized enzymes. The metal-N_4 chelates need to be supported on a conducting support, like carbon or graphitic materials. Long-term stability is a problem with N_4 chelates. Heat treatment in an inert atmosphere increases both the stability and catalytic activity [87–92].

Even though a few studies have been carried out using the complexes in solution [93], most studies have been performed with the metal chelates confined on an electrode surface, generally graphite or carbon supports, since this is closer to the situation in a fuel cell, where catalysts are absent in the electrolyte. Since the support can act as an axial ligand, the properties of the complexes in solution or on the adsorbed state could be different. So most studies discussed here have been carried out with the complexes immobilized on graphite or carbon supports. Smooth electrodes have been used to study mechanistic aspects of the reaction.

7.3.1.1 Interaction of O_2 with Active Sites and the Redox Mechanism

The one-electron reduction of O_2 to give superoxide is an outer-sphere reaction and does not involve the interaction of the molecule with an active site on the electrode surface. The electron transfer process probably occurs at the outer Helmholtz plane. This process is observed in nonaqueous media or in strongly alkaline aqueous solutions and is not relevant to fuel cell development since little free energy is liberated in the process. In contrast, ORR occurring via the transfer of more than one electron (two or four) is an inner-sphere reaction, involving the interaction of the molecule and or intermediates with active sites present on the electrode surface. Since we are interested in discussing the electrocatalytic reduction of O_2, we will focus our attention on the inner-sphere reduction processes.

O_2 interacts with the N_4 catalysts usually binding to the d orbitals of the central metal in the macrocyclic structure. The energy of the interaction will depend on the energy and the electronic density located on those orbitals. Figure 7.16 illustrates some different possible interactions (end-on and side-on) of the orbitals of the oxygen molecule with the orbitals of the metal in the M–N_4 molecule for end-on and side-on interactions, respectively.

For end-on M–O_2 complexes (see Figs. 7.16 and 7.17), the most important interaction for both σ and π bondings occurs with the π^* antibonding orbitals of the O_2. The σ interaction is primarily between the metal $3dz^2$ and the in-plane antibonding $\pi_g{}^s$ orbital on the O_2, where the superscript “s” refers to whether or not the orbital is symmetric (or antisymmetric) in relation to the MO_2 plane. This interaction involves a transfer electron density from the metal to the O_2 molecule.

Fig. 7.16 End-on and side-on interactions of frontier orbitals of O_2 with the frontier orbitals of a metal site (reproduced from [94])

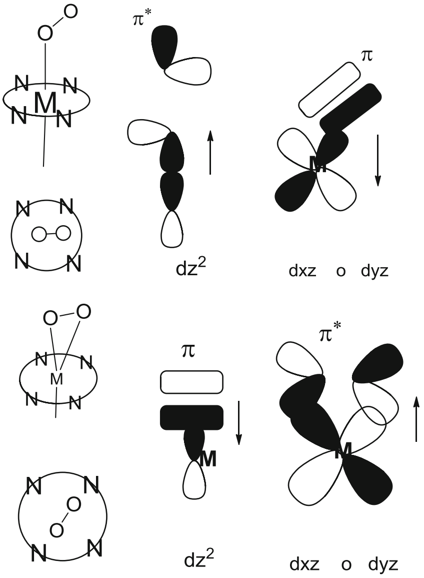

Fig. 7.17 Qualitative molecular orbital diagram for the end-on $M(O_2)PL$ dioxygen adduct. M = Fe, Co; P = porphyrin; L = NH_3 or imidazole (reprinted with permission from American Chemical Society [95])

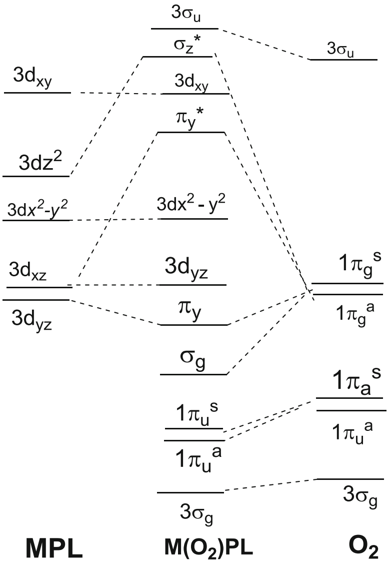

The π interaction is primarily between the metal 3dyz and the $1\pi_g^{a}$ (π antibonding antisymmetric orbital) on the O_2 and can be viewed as a backbonding interaction. In both of these interactions, the π_u^{s} and π_u^{a} (bonding π orbitals symmetric and antisymmetric, respectively) play a lesser role in the composition of the bonding orbitals [95]. In the case of the side-on interaction, a $3dz^2$ orbital of the metal interacts with the $1\pi_s^{u}$ bonding orbital (backbonding interaction) and a 3 dxz with a

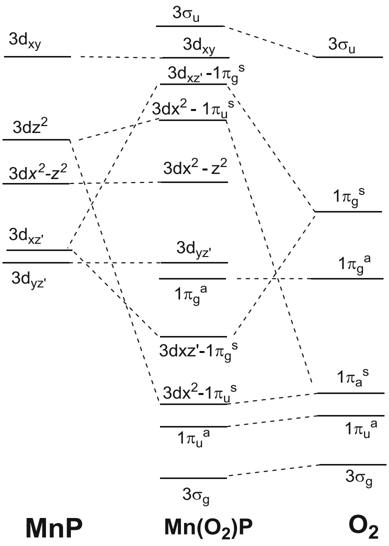

Fig. 7.18 Qualitative molecular orbital diagram for a side-on $Mn(O_2)PL$ dioxygen adduct (reprinted with permission from [95])

$1\pi_g^s$ antibonding orbital of oxygen as shown in Figs. 7.16 and 7.18. Figure 7.19 illustrates the optimized structural configurations for the O_2 adsorbed on FePc and CoPc molecules according to calculations by Wang et al. [96].

The predominating interactions will weaken the O–O bond and increase the O–O distance. The metal in the complex should be in the M(II) state, so, for example, in alkaline solution a step will require the reduction of M(III):

$$\mathrm{M(III)} - \mathrm{OH} + \mathrm{e} \rightleftarrows \mathrm{M(II)} + \mathrm{OH}^- \tag{7.6}$$

An adduct will be formed according to

$$\mathrm{M(II)} + \mathrm{O_2} \rightleftarrows \mathrm{M(III)} - \mathrm{O_2}^- \text{ or } \mathrm{M(II)} - \mathrm{O_2} \tag{7.7}$$

This adduct must be short-lived. Otherwise it will hinder further O_2 molecules from interacting with the active site. The adduct will undergo reduction as follows:

$$\mathrm{M(III)} - \mathrm{O_2}^- + e^- \rightleftarrows \mathrm{M(II)} + \text{intermediates} \tag{7.8}$$

where M(II) is the active site. The last reaction shows the process in alkaline media and could involve M(II)–O_2 instead of M(III)–O_2^- especially when Co is the metal center. In acid media the process will involve a proton. The scheme above is applicable to Mn and Fe complexes. In the case of Co complexes, Co(III) is probably not formed upon its interaction with the oxygen molecule since the Co (III)/Co(II) formal potential is much more positive than the M(III)/(II) formal potentials (M = Mn, Fe). However, step 2 is still important since the catalytically active site is Co(II) [82, 97]. Density functional theory calculations [96] have

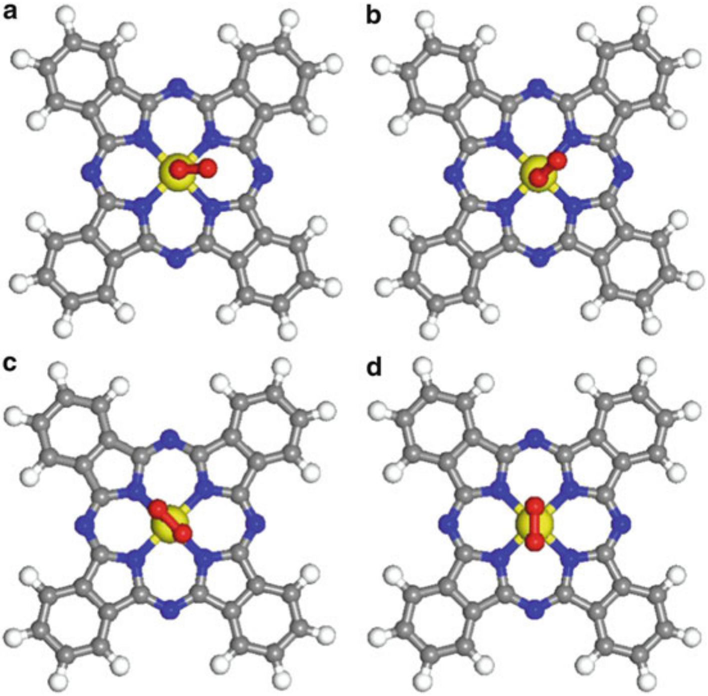

Fig. 7.19 Optimized structural configurations for the O_2 adsorbed on FePc and CoPc molecules. The *upper portion* shows two end-on configurations. The *lower portion* of the figure shows two side-on configurations. The *central yellow sphere* depicts the metal Fe or Co atom, the *central two red spheres* represent the adsorbed O_2 molecule, *blue spheres* represent N atoms, *gray spheres* represent C atoms, and *light white spheres* represent H atoms [96]

shown that that with CoPcs only end-on interaction is possible, whereas for FePc both end-on and side-on interactions are plausible. As it will be discussed further, only Mn and Fe phthalocyanines promote the four-electron reduction of O_2 and this can be attributed to a side-on interaction of O_2, particularly for Fe complexes.

Since the interaction of the oxygen with the active site involves a partial oxidation of the metal in the complex or at least a decrease of electron density in the metal upon interacting with O_2, it is interesting to compare the catalytic activity of metallomacrocyclic with their M(III)/(II) formal potential. Since the formal potentials are sensitive to the pH of the electrolyte, it should be measured in the same media in which the catalytic activity is examined [14, 20, 98]. Further, they should also be measured with the complex adsorbed on the electrode and not in solution phase. When comparing phthalocyanines, the Co and Fe derivatives show the highest activity for the reduction of O_2 but they behave differently. As pointed out above, Co complexes exhibit Co(III)/(II) transition that is far more positive than the onset potential for the reduction of O_2, whereas for Fe complexes the onset potential for the catalytic reduction of O_2 is very close to the Fe(III)/(II) transition [14, 82, 97, 99]. For both types of complexes, there is in situ spectroscopic evidence for the reversible transition involving the M(III)/(II) couples [97, 100, 101]. For example, for Fe phthalocyanine adsorbed on ordinary pyrolytic graphite, Scherson et al. used Fe K-edge XANES (X-ray Absorption Near Edge Structure) recorded in situ in 0.5 M H_2SO_4 to prove the evidence for the redox transition of Fe(III)/(II) involving a metal-based orbital.

Many authors have discussed that a correlation should exist between the formal potential of the catalysts and its activity for ORR and it is yet not clear what sort of correlation should be expected. Reduction of O_2 should be observed at the potential of reduction of the $M(III)O_2^-$ adduct and not at the potential of the M(III)/(II) couple if adduct formation takes place before the transfer of an electron from the electrode. The latter should only be observed if the reaction were outer sphere, where O_2 would only collide with the redox center without the formation of a bond. In the special case of iron phthalocyanines and other macrocyclics, O_2 reduction usually starts at potentials very close to the Fe(III)/(II) couple [82, 102, 103]. In contrast, for cobalt macrocyclics reduction of O_2 begins at potentials much more negative than those corresponding to the Co(III)/(II) couple [14]. Several authors have reported correlations between activity (measured as potential at constant current) and the M(III)/(II) formal potential and volcano-shaped curves have been obtained [14, 15, 104, 105].

This could indicate that the redox potential needs to be located in an appropriate window to achieve maximum activity. In other words, a M(III)/(II) formal potential that is too negative (easily oxidable metal center) or a M(III)/(II) formal potential that is too positive (metal center that is more difficult to oxidize) does not favor the catalysis. However, more recent studies [94, 106–109] have shown that when comparing families of metallophthalocyanines, linear correlations are obtained when plotting log k or log I (rate constant or current at fixed potential) vs. the M(III)/(II) formal potential, as illustrated in Fig. 7.20. First-order rate constants were calculated as $k = I/nAFc$, where I is the current at a given potential, n is the total number of electrons transferred which is 2 for the peroxide pathway and 4 for the reduction to H_2O, A is the area in cm^2, F is the Faraday constant, and c is the oxygen concentration in moles per cm^3. One linear correlation is obtained for Cr, Mn, and Fe complexes and these metals have configurations d^4(Cr), d^5(Mn), and d^6(Fe). Another linear correlation is obtained for Co complexes, which have a configuration d^7. An interesting feature in the data of Fig. 7.20 is that the lines are parallel with a slope close to +0.15 V/decade. It is possible that the straight lines in Fig. 7.20 are part of an incomplete volcano correlation. If so, the slope 0.15 V/decade might have a physical meaning as discussed for the oxidation of thiols [110]. The data in Fig. 7.20 strongly suggest that more positive redox potentials will increase the catalytic activity, and it is good that no volcano correlation is obtained because there seems to be room for improving the catalytic activity of phthalocyanines or other macrocyclics. The M(III)/(II) redox potential of some macrocyclics can be shifted in the positive direction with heat treatment, and this could increase the catalytic activity. For example, when iron tetraphenylporphyrin [92], FeTPP, is heat treated, the Fe(III)/(II) redox transition is shifted from 0.2 V vs. RHE for fresh FeTPP to 0.4 V for FeTPP heat treated at 700 °C. Intermediate redox

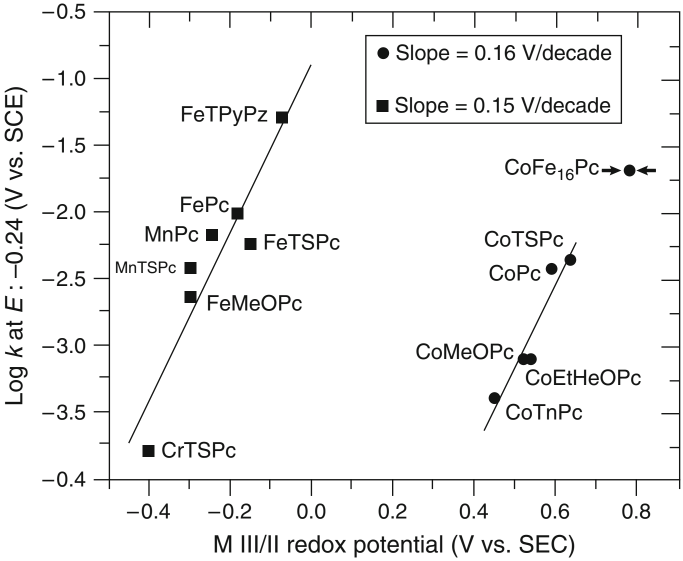

Fig. 7.20 Plot of log *k* (at constant potential vs. the M(III)/(II) formal potential of the MN_4 macrocyclic for the reduction of oxygen in 0.2 M NaOH) (from [106])

potentials are obtained for heat treatments at intermediate temperatures [92], and the catalytic activity increases with heat treatment, showing that a more positive redox potential of the catalyst favors the O_2 reduction reaction rate. In a recent study [111], it has been discussed that the changes in the formal potential of the catalyst could explain the high catalytic activity of ORR that has been obtained by heat treatment of metallomacrocyclics and other starting materials. For example, when comparing data obtained with heat-treated catalysts prepared by very different techniques and starting materials, not necessarily involving metallomacrocyclic complexes [112], a correlation of log *i* (as currents normalized per mass of catalysts) vs. the formal potential of the catalyst gives what could be considered a linear correlation (see Fig. 7.21).

The scatter of the data could be attributed to differences in the porosity of the electrode prepared and also to differences in the number of active sites per unit of surface area. But in spite of this, a clear trend in the figure shows that more positive formal potentials seem to favor the catalytic activity of the different materials. Since the structures of the different catalysts used in the correlation of Fig. 7.21 are not known, no chemical formulas can be given and the numbers correspond exactly to those given in the original paper. More discussion on heat-treated materials will be given on other chapters of this book.

The increase in activity as the M(III)/(II) redox potential of the catalysts is more positive is in contrast to what was previously found in volcano correlations where a maximum activity is observed for intermediate redox potentials not only for the reduction of O_2 but for other reactions such as the oxidation of thiols or of hydrazine [99]. When studying a series of unsubstituted and substituted Mn phthalocyanines,

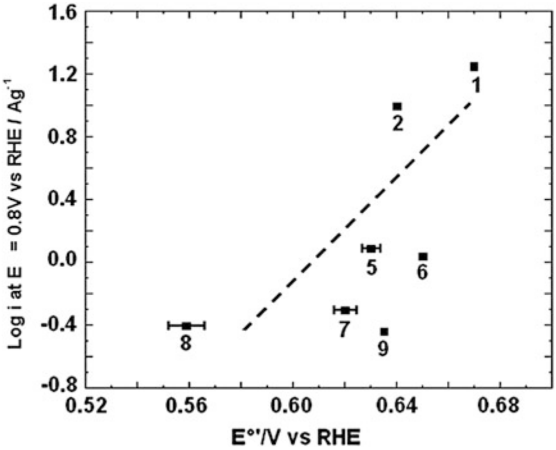

Fig. 7.21 Plot of log i_M (in Ag^{-1}) at $E = 0.8$ V vs. the formal potential of the catalyst for ORR [111, 112]

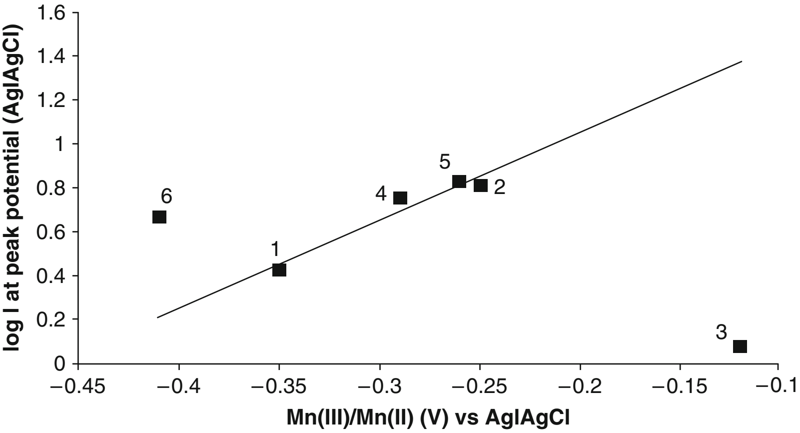

Fig. 7.22 Plot of log *i* vs. MnIII/MnII redox potential for oxygen reduction in pH 5 buffer. Manganese phthalocyanine (MnPc, 1), manganese tetraaminophthalocyanine (MnTAPc, 2), manganese tetrapentoxy pyrrole phthalocyanine (MnTPePyrPc, 3), manganese tetra phenoxy pyrrole phthalocyanine (MnTPPyrPc, 4), manganese tetra mercaptopyrimidine phthalocyanine (MnTMPyPc, 5), and manganese tetra ethoxy thiophene phthalocyanine (MnTETPc, 6) [109]

Nyokong and Sehlotho [109] have also found that the catalytic activity of these complexes increases as the Mn(III)/(II) becomes more positive (see Fig. 7.22) with a slope of 0.24 V/decade. It is very likely that the data in Figs. 7.20, 7.21, and 7.22 are part of an incomplete volcano and this is very important because it means that hypothetically that catalysts with higher activities could be prepared by shifting the formal potential to more positive values.

A possible explanation for the results in Figs. 7.20 and 7.22 (activity decreases as the driving force of the catalyst increases) is that the electronic coupling between the donor (MPc) and the acceptor (O_2) decreases as the electron-donating capacity of the substituents increases, due to a shift in the energy of the frontier orbitals of the metallophthalocyanine [113–115]. The shift in the energy of the frontier orbital with substituents on cobalt phthalocyanines has been calculated by Schlettwein [113] and Cárdenas-Jirón [114–116] using PM3 and ZINDO/S semiempirical theoretical calculations. There are several approaches to estimate the electronic coupling matrix elements between the donor and the acceptor in electron transfer reactions. One of them considers the energy difference between the LUMO (lowest unoccupied molecular orbital) of the electron acceptor and the HOMO (highest occupied molecular orbital) of the electron donor [117] but this requires to know the distance that separates the donor from the acceptor. This is not simple for an inner-sphere reaction where the $M\cdots O_2$ distance could vary from complex to complex. To avoid this difficulty, another reactivity index can be used to explain the data in Fig. 7.20 and this is the concept of molecular hardness which is a commonly used criterion of reactivity in organic reactions as proposed by Pearson [118, 119]. The hardness η of a single molecule is approximately one-half the energy gap of the HOMO–LUMO, so the larger the gap, the greater the hardness, the more stable the molecule (the harder the molecule, the less its reactivity). The opposite corresponds to a molecule with a narrow HOMO–LUMO gap (soft molecule) situation that will correspond to a very reactive molecule. Now for a donor–acceptor pair, it is more convenient to use the concept of donor–acceptor hardness η_{DA} which is one-half the difference between the energy of the LUMO of the acceptor (O_2 molecule) and the energy of the HOMO of the donor (metal complex):

$$\eta_{\mathrm{DA}} = \frac{1}{2}\left(\varepsilon_{\mathrm{LUMOacceptor}} - \varepsilon_{\mathrm{HOMOdonor}}\right) \tag{7.9}$$

The donor–acceptor intermolecular hardness can also be described as one-half the difference between the ionization potential of the donor and the electron affinity of the acceptor:

$$\eta_{\mathrm{DA}} = -\frac{1}{2}\left(\varepsilon_{\mathrm{acceptor}} - \varepsilon_{\mathrm{donor}}\right) \tag{7.10}$$

For a gas phase reaction involving the transfer of a single electron, this will be equivalent to the Gibbs free energy of the process ΔG°. For the special case of Co phthalocyanine in its ground state, the HOMO is occupied with a single electron (doublet state) so it corresponds to a single occupied molecular orbital (SOMO). The same is valid for molecular oxygen, which in its ground state has two unpaired electrons in two degenerate π^* antibonding orbitals. In this case, the formation of an adduct CoPc-O_2 involves the interaction of two SOMOs and η_{DA} is given by

$$\eta_{\mathrm{DA}} = \frac{1}{2}\left(\varepsilon_{\mathrm{SOMOacceptor}} - \varepsilon_{\mathrm{SOMOdonor}}\right) \tag{7.11}$$

Figure 7.23 illustrates the calculated energy levels of the SOMOs of the different cobalt phthalocyanines with respect to the SOMO of oxygen using PM3.

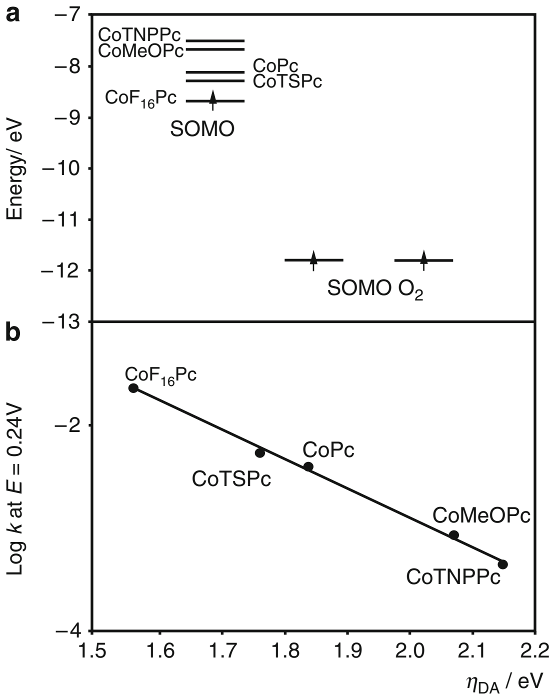

Fig. 7.23 (**a**) Relative energies of frontier orbitals of dioxygen and substituted Co phthalocyanines. For simplicity, only one electron is shown on the SOMO of the CoPcs [115]. (**b**) Plot of log *k* (at constant potential) vs. the donor–acceptor intermolecular hardness for the different O_2–CoPc pairs (reproduced from [114])

Electron-withdrawing substituents (sulfonate, fluoro) on the phthalocyanine ring stabilize the SOMO and the opposite is true for electron-donating groups (methoxy and neopentoxy). So electron-withdrawing groups, even though they decrease the electron density on the cobalt (more positive redox potential), also decrease the gap between the energy of the SOMO of the phthalocyanine and the energy of the SOMO of oxygen. The bottom of Fig. 7.23 shows that log k for O_2 reduction increases as the chemical hardness of the system decreases or as the softness of the system increases (more reactivity). The trend in reactivity is exactly the same as that illustrated in Fig. 7.20. It can be concluded then that hardness could be used as a criterion for reactivity of these systems when comparing complexes that bear the same structure and could explain why, for example, perfluorinated phthalocyanine, which has the most positive redox potential (the most oxidant), is the best catalyst for O_2 reduction in alkaline media in the series of cobalt phthalocyanines examined.

Quantum theories of elementary heterogeneous electron transfer (ET) reactions in polar media have been extended to reactions which proceed through active intermediate electronic surface band states or bands. On the basis of this theoretical framework, Ulstrup [120] has interpreted experimental data obtained for O_2 reduction catalyzed by metal phthalocyanines.

When comparing activities of complexes by plotting constant potential vs. redox potential of the catalyst, linear correlations are also obtained (see Fig. 7.24) and this was predicted theoretically by the work of Ulstrup [120]. The slope of the lines in

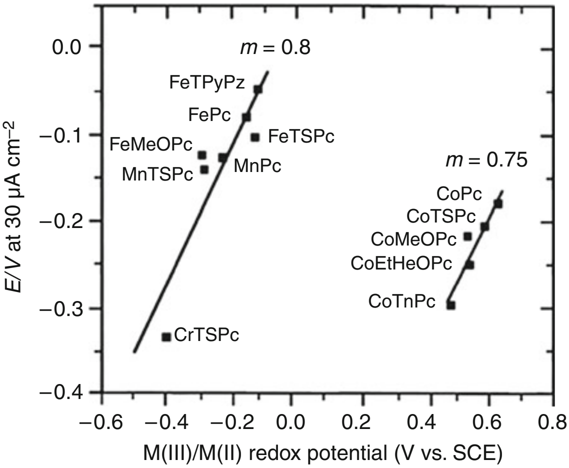

Fig. 7.24 Plot of log *E* (at constant current) vs. the M(III)/(II) formal potential of the MN_4 macrocyclic for the reduction of oxygen in 0.2 M NaOH (from [106])

Fig. 7.24 is less than one, which was also predicted by Ulstrup and is attributed to the excitation of intramolecular modes of relatively low frequencies in the cathodic range. The data shown in Fig. 7.24 is essentially similar to that shown in Fig. 7.20 but the comparison was made at constant current. So essentially, the graph of Fig. 7.20 is a plot of driving force vs. driving force. This carries the assumption that the M(III)/(II) redox potential provides a measure of the driving force of the catalysts. Since catalysts produced by heat treatment, using MN_4 metal macrocyclics as the starting materials, or other ingredients like metal salts and nitrogen-containing compounds show very high activities and stabilities, especially in acidic media, it is interesting to compare activity parameters such as those in Fig. 7.20, that is, potential at constant current vs. the formal potential of the catalyst for this type of catalysts.

A correlation of this sort is illustrated in Fig. 7.25 [111] and includes catalysts reported by several groups in a joint article [112]. It is interesting to note that in spite of the scatter of the data, it seems that a linear correlation does exist, similar to that illustrated in Fig. 7.20. The slope is 1.2, which is not too far from unity as predicted by Ulstrup. If one compares the data in Fig. 7.21 with that in Fig. 7.25, the scatter of the data in Fig. 7.20 is much lower than that in Fig. 7.25 because it was obtained with graphite electrodes modified with monolayers of MN_4 macrocyclics. So the amount of active sites per unit of real area is very similar for all cases, which might not be true for the data in Fig. 7.25, in spite of the normalization of the current for the mass of catalysts per unit of geometric area. However, a trend is observed and again suggests that more positive formal potentials of the catalyst seem to favor the ORR catalytic process. Finally, it is important to point out that the formal potential plotted in Fig. 7.25 does not necessarily involve the M(III)/(II) but might involve metal-free redox functionalities generated after heat treatment as discussed in [112].

Not all metals of the first transition series exhibit the M(III)/(II) processes, so if one compares macrocyclics of different metals, it is convenient to use another parameter, for example, the number of *d* electrons in the metal as shown in

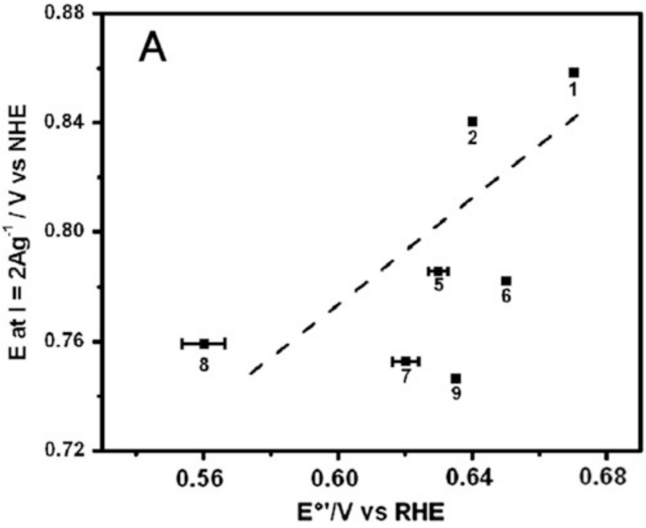

Fig. 7.25 Plot of log *E* (at constant current) vs. the formal potential of catalysts obtained by heat treatment for the reduction of oxygen in 0.05 M H_2SO_4 at 25 °C (reproduced by permission of the Electrochemical Soc [111], data from [112]). The labeling of catalysts is the same as that used in the original reference [112]

Fig. 7.26. In this figure, since different Tafel slopes are obtained for the different catalysts, it is not simple to compare activities as current at constant potential. So instead, as a criterion of activity, potential at constant currents is used.

Figure 7.26 clearly shows that Fe derivatives exhibit the highest activity, followed by Mn and Co and also illustrates a common observation in catalysis that metals with nearly half-filled *d*-energy levels exhibit the highest activity. So a redox type of mechanism does not operate for metals that do not exhibit the M(III)/(II) transition in the potential window examined for O_2 reduction. This is the case for Ni, Cu, and Zn phthalocyanines. It is important to point out that in order to have catalytic activity, the frontier orbital of the MN_4 needs to have some d character as illustrated in Fig. 7.16. The catalysts with higher activity included in Fig. 7.24 (Cr, Mn, Fe, Co) have frontier orbitals with d character, whereas in Ni and Cu phthalocyanines, the frontier orbitals have more ligand character [121]. This is illustrated in Fig. 7.27 [108] that compares the frontier orbitals of CoPc and CuPc. CoPc shows a well-defined dz^2 orbital sticking out of the plane of the phthalocyanine, whereas CuPc does not and shows low activity for O_2 reduction.

There is experimental evidence to support this using tunneling electron microscopy. It has been shown a strong d orbital dependence on the images of metal phthalocyanines (see Fig. 7.28).

Unlike copper phthalocyanine where the metal appears as a hole in the molecular image, cobalt phthalocyanine shows the highest point in the molecular image [122]. The benzene regions of CoPc and CuPc show the same height. So, essentially the

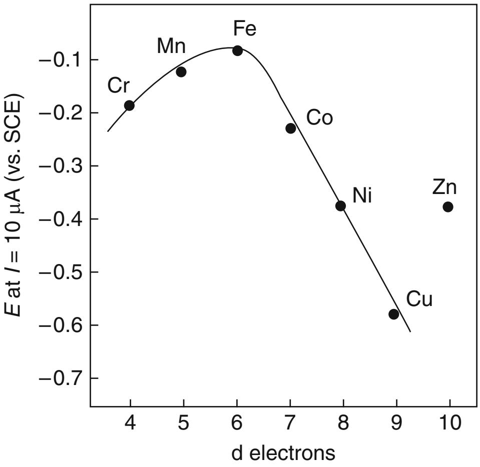

Fig. 7.26 Volcano plot for the electrocatalytic activity of different M-tetrasulfonated phthalocyanines adsorbed on graphite for O_2 reduction in 0.1 m NaOH, as a function of the number of d electrons in the metal (from [15])

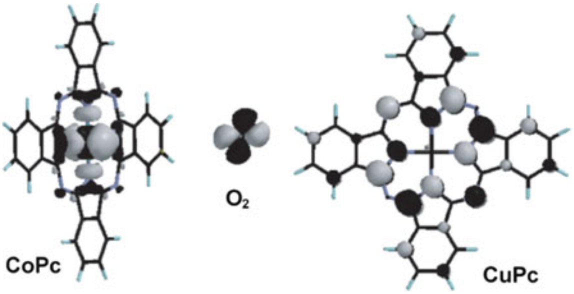

Fig. 7.27 Illustration of the frontier orbitals involved in the interaction of cobalt phthalocyanine with O_2 (reprinted from [108])

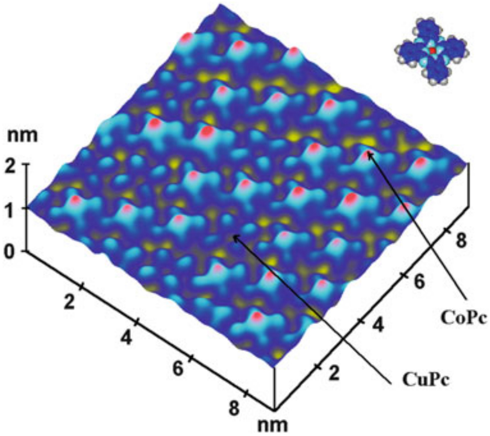

Fig. 7.28 STM surface plot image of CoPc and CuPc coadsorbed on the (111) plane of Au [122]

data using images generated using electron tunneling microscopy is in agreement with the images generated by theoretical calculations.

Even though most authors agree that the M(II) state is the active site for O_2 reduction [15, 20, 65–67, 70, 72, 88, 89, 97–99, 102, 105, 123, 124] for FePc (iron phthalocyanine) and FeNPc (iron naphthalocyanine) [125–127], it has been proposed that Fe(I) could also play a role in the electrocatalytic process. This was based on electroreflectance experiments that indicated that Fe(I) interacts with O_2 whereas Fe (II) does not. However, many authors have shown experimental evidence that O_2 reduction commences at potentials much more positive than those corresponding to the Fe(II)/(I) couple [14, 82, 97, 99]. On the contrary, the reduction currents are observed at potentials close to the potential of the Fe(III)/(II) couple, so it seems unlikely that Fe(I) could be the active site. Worse, as shown from rotating ring-disk experiments, Fe(I) only favors the two-electron reduction in contrast to Fe(II) [82, 88].

The catalytic activity can also depend on the amount of metal complex present on the electrode surface. In general, the amount of catalyst present on the surface is evaluated from cyclic voltammograms, measuring the electrical charge under reversible peaks. This carries the assumption that all adsorbed catalyst gives an electrochemical signal. This might not necessarily be true and there could be a fraction of complexes present on the surface that are electrochemically silent. It is assumed that the "electroactive" adsorbed species are also active for the reduction of O_2.

It has been found that the O_2 reduction currents are directly proportional to the amount of catalyst present [21, 128], when the catalysts is adsorbed on the electrode surface indicating that the reaction is first order in the surface concentration of catalyst. This is not true for cases where the catalyst is incorporated to the surface by vapor deposition or when the catalyst is deposited from solutions and the solvent is completely evaporated [21]. An explanation for these different observations is that when the catalyst is deposited by vapor deposition or from complete evaporation of solutions, multilayers are formed, and the metal active centers are not all completely accessible to the O_2 molecule. Another example of this type of behavior is the case for polymerized multilayers of cobalt tetraaminophthalocyanines, where it has been demonstrated that only the outermost layer is active for the reduction of O_2 [84, 85]. Scherson et al. [129] have reported that when $(FeTMPP)_2O$ is deposited on a porous support, only 30 % of the amount deposited is found to be electrochemically active. Anson et al. [130] have found that for the case of $CoPc(CN)_{16}$ and $CoPcF_{16}$ that were deposited from solutions where the solvent was completely evaporated, again it was found that only 30 % of the amount deposited was electrochemically active. It was concluded that only those molecules that directly exposed to the electrolyte and to the incoming O_2 molecules and at the same time are in electric contact to the electrode are active for the reduction of O_2. These results are not surprising since when multilayers are deposited, not all are necessarily in electrical contact with the electrode, which is not the case for adsorbed layers, where molecules are probably lying flat on the electrode surface, interacting with the π system of the graphitic planes. Van der Putten et al. [131] have observed catalytic activity with vacuum-deposited layers in spite of the fact that these layers are electrochemically silent. As pointed out before when multilayers of metal phthalocyanines are deposited on an electrode surface, only the outermost layer is active for the reduction of O_2 [131] and this is also true for other electrochemical reactions. This shows that multilayers of phthalocyanines or polymerized multilayers of phthalocyanines are rather compact and the inner layers are not accessible to O_2 molecules [85].

7.3.1.2 N_4-Metallomacrocyclic Catalysts for One-Electron Reduction of O_2

An electrode surface that has no active sites should only promote the outer-sphere one-electron reduction of dioxygen. An example of such surface is a defect-free electrode surface that exposes the basal plane of graphite [124]. On the basal plane, all carbon atoms are fully coordinated so they cannot bind an oncoming molecule like O_2. On electrodes modified with adsorbed catalysts, to the best of our knowledge, there is only one report that shows evidence for the one-electron reduction of O_2 in alkaline media. A reversible one-electron reduction of O_2 to produce the stable superoxide ion was observed in an aqueous solution of 1 M NaOH. This electroreduction of O_2 was catalyzed by Cobalt(II) 1,2,3,4, 8,9,10,11, 15,16,17, 18,22,23,24,25-hexadecafluoro-29*H*,31*H*-phthalocyanine (abbreviated as $Co^{II}PcF_{16}$) adsorbed on a graphite electrode [132]. What is curious is that $Co^{II}PcF_{16}$ is the most active catalyst for the two-electron reduction of O_2 in the correlations shown in Figs. 7.17, 7.19, and 7.20, so it is very surprising that it can promote the one-electron reduction of O_2. The OH^- concentration has a very strong effect on the reduction process. Higher OH^- concentrations could stabilize the superoxide ion [124] but 1 M NaOH might not be concentrated enough to achieve this purpose so it could be interetsing to check this experiments by using electron paramagnetic resonance (EPR) techniques to detect any superoxide formation.

7.3.1.3 N_4-Metallomacrocyclic Catalysts for Two- and Four-Electron Reduction of O_2

Most mononuclear Co macrocyclics catalyze the reduction of dioxygen via two electrons to give peroxide [28, 82, 97, 99, 123]. The activity of Fe phthalocyanines in general is higher than those of Co phthalocyanines and the opposite is true for porphyrins, which reveals the importance of the nature of the ligand in determining the catalytic activity [96]. The opposite is true for heat-treated materials [133]. Cobalt complexes are more stable than iron complexes and this trend is maintained after heat treatment [72, 105]. However, iron complexes tend to promote the four-electron reduction of dioxygen and this will be discussed further on.

Lamy et al. [134] and van der Putten et al. [135] conducted spectroscopic investigations of polymer-modified electrodes containing CoTSPc using UV–visible differential reflectance spectroscopy and were able to identify Co(III)/Co(II) transition when varying the electrode potential. They used electron spin resonance on the Ppy (polypyrrole) and Ppy-CoTSPc electrodes in deoxygenated and oxygen-saturated solutions. It was shown that the Co(III)TSPc species is effective in the electroreduction of oxygen and that this species is more stable in oxygen-saturated medium than in deoxygenated medium because of its stabilization under the

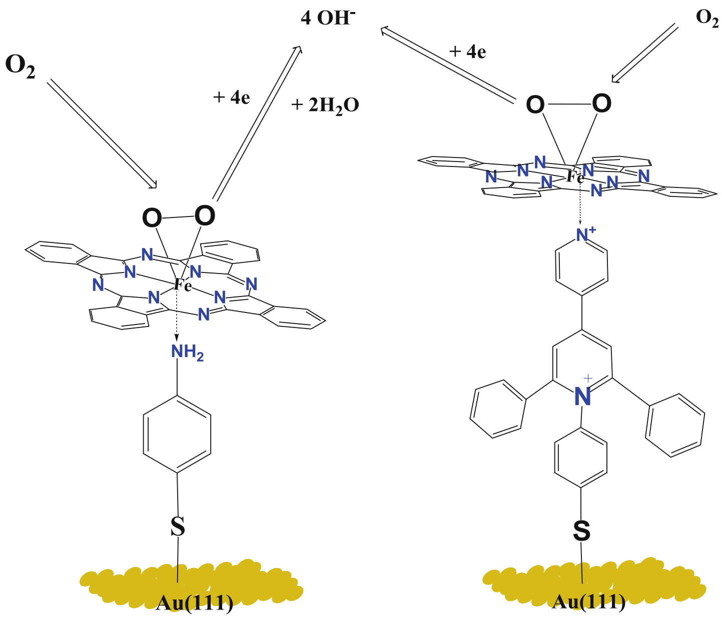

Fig. 7.29 Illustration of the catalytic action of FePc bound to gold via a self-assembled monolayer of axial ligand bound to Au [137]

following form: Co(III)–O_2. In the case of Ppy-CoTSPc film, the polypyrrole matrix undergoes strong interactions with oxygen species and, most likely, with hydrogen peroxide.

Phosphoric acid is one of the electrolytes used in fuel cells although very few studies have focused attention on the activity of metallomacrocyclic complexes in this electrolyte. Vasudevan and Phougat [136] investigated the electrocatalytic activity of cobalt phthalocyanine monomers and polymers with imido and carboxylic group ends. The complexes were mixed with carbon powder and polyethylene powder. The activity of the monomeric compounds was found to be higher than that of polymeric compounds.

However, in recent work, Ponce et al. [137] have shown that when Fe phthalocyanine is anchored on gold via self-assembled axial ligands, the electrocatalytic activity for ORR increases (see Fig. 7.29). The increase in activity seems to be associated to the electron-withdrawing effect of the axial ligand. This will shift the Fe(III)/(II) formal potential in the positive direction which favors the catalysis as shown in Fig. 7.24.

When the catalytic activity of graphite modified with mixtures of different proportions of FeTSPc and CoTSPc was tested for ORR, it was found that the catalysts acted independently, that is, the amount of peroxide generated was directly proportional to the fraction of CoTSPc present on the electrode surface. FeTSPc did not promote the decomposition or reduction of peroxide generated on sites occupied by CoTSPc. However, the possibility for the Fe centers to form hydrogen peroxide and promote its decomposition cannot be ruled out completely since Fe(II) sites are known for their catalase activity [138]. Indeed for some metal complexes van Veen et al. have found that their catalytic activity for peroxide decomposition is directly proportional to its activity for O_2 reduction [139].

Again, as observed with FeTSPc and FePc [77, 87, 140, 141], a prewave is observed for the reduction currents and corresponding to the direct four-electron reduction. In contrast to FeTSPc or FePc, production of peroxide was attributed to reduction of the ligand and not reduction of the metal (Fe(I) formation). For this particular catalyst, it was suggested that dioxygen can bind to the Fe center and to a highly electronegative nitrogen in the ring, which will avoid the desorption of peroxide before it is reduced. This dual-site mechanism would aid charge injection via backbonding from the macrocycle into antibonding orbitals of O_2 or bound peroxide causing the destabilization and further rupture of the O–O bond [142]. At more negative potentials at which reduction of the ligand takes place, this mechanism becomes inoperative, the O_2 molecule only binds to the Fe center, and peroxide can desorb into the solution. In a study involving heat-treated FeTPP [143] and deposited by thick layers on glassy carbon, it was found that the amount of hydrogen peroxide decomposed, compared to the amount of oxygen and hydrogen peroxide reduced, was so small that chemical decompositions were ruled out.

Van den Brink et al. [141] when using vacuum-deposited layers of FePc have found that when examining the catalytic activity of these layers, the first reduction wave scan was very different from subsequent scans, indicating that some reorganization of the deposited layers took place since this phenomenon is not observed on adsorbed layers of FePc. The effect of irreversible changes of FePc when treated under potential load with oxygen is only observed using vacuum-deposited multilayers [125]. Léger et al. pointed out that the structure of FePc films influences their electrocatalytic activity.

XRD studies have shown that non-heat-treated FePc is under the α-phase whereas heat-treated FePc is under the β-phase. Surprisingly, the α-phase shows higher activity than the β-phase (see Fig. 7.30). These authors have also shown using electrochemical quartz crystal microbalance (EQCM) that α-phase FePc probably forms μ-oxo dimers at potentials higher than 700 mV vs. RHE. These μ-oxo dimmers are reduced at the same potential than the monomer of α-phase FePc [142].

Theoretical studies performed by Anderson and Sidik [144] using spin-unrestricted hybrid gradient-corrected density functional calculations have predicted that Fe(II) is the active site for four-electron reduction of oxygen by iron in the N_4Fe systems employed in the calculation, and it may be suggested that the same should be expected for heat-treated iron macrocyclics. The calculations have shown that Fe(II) is favored over Fe(III) because H_2O bonds strongly to the Fe(III) site, preventing O_2 adsorption and water does not bond strongly to Fe(II). On a first step, –OOH bonds more strongly to Fe(II) than to Fe(III), which results in a calculated more reversible potential for its formation over Fe(II). Calculations show that subsequent reduction steps have very reversible potentials over both centers (Fe(II) or Fe(III)). Calculations also show a hydrogen bonding interaction between –(OHOH) bonded to Fe(II) and to a nitrogen lone-pair orbital in the N_4 chelate. This interaction prevents peroxide from

Fig. 7.30 Polarization curves for the oxygen reduction on a α-FePc/C (m) and a β-FePc (d) disk electrode recorded at 2,500 rpm in O_2-saturated 0.5 M H_2SO_4 electrolyte ($T = 20\ °C$, $v = 5\ mV\ s^{-1}$) [142]

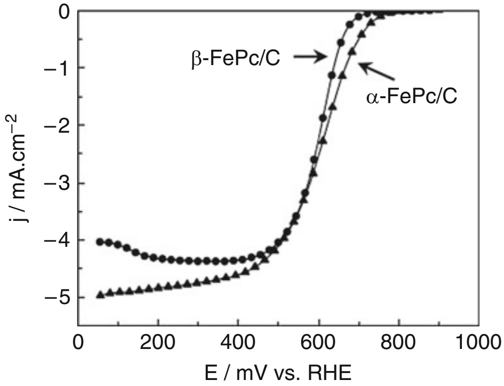

desorbing as a two-electron reduction product. So essentially these studies show that adsorbed hydrogen peroxide in an intermediate formed from N_4Fe–OOH on Fe(II) sites and can be released into the solution at more negative potentials as found experimentally [14, 28].

Most catalysts investigated usually have Fe and Co as metal centers. However, complexes of other metals have also been studied. For example, CrTSPc and MnTSPc exhibit catalytic activity for ORR [14] and they somehow resemble the behavior of Fe complexes, especially MnTSPc, in the sense that it shows a prewave where O_2 reduction proceeds entirely via four electrons to give water. Peroxide is produced at higher polarizations. The lower activity of Cr and Mn phthalocyanines compared to Fe phthalocyanines can be attributed to their low redox potential, that is, they are easily oxidized [82, 105]. The activity of most macrocyclic metal complexes increases after heat treatment [145]. However, the opposite is observed for manganese complexes probably because the metal is lost from the N_4 structure. So, most work dealing with heat-treated materials has focused on Fe and Co macrocycles. Complexes of Mo can only be used in alkaline solution since they are not stable in acid media. MoNPc is less activity than FeNPc as reported by Magner [146].

Very few authors have studied the effect of temperature [147] on the catalytic activity of phthalocyanines. Baker et al. [147] carried out experiments at different temeperatures in an acidic electrolyte to simulate the environment of an operating PEM fuel cell. They conducted experiments in the temperature range of 20–80 °C and using unsubstituted and substituted Fe phthalocyanines. The surface electrochemical responses of the FePc species were characterized with respect to their surface concentrations and adsorbed surface orientations. Depending on the type of substituent, the adsorption mode could be flat, edge-on, as a dimer, or as an agglomerate, suggesting that the substituent has a strong effect on the FePc species' adsorption mode. Substitution also has a significant effect on stability. With respect to their electrocatalytic activity, both temperature, substitution, and possibly mode of adsorption can significantly affect the ORR mechanism. For example, the overall electron transfer number observed can change from 1 to 3 depending on the type of substituent and the reaction temperature. Further research is required to determine if this change in *n* reflects a change in the ORR pathway and/or a decrease in the stability of the adsorbed ORR intermediates. Based on the various approaches found in the literature and the current understanding, a mechanism for the FePc species catalyzed ORR was suggested as follows:

$$\mathrm{FeIIIPc} + e^- \rightleftarrows \mathrm{FeIIPc} \tag{i}$$

$$\mathrm{FeIIPc} + \mathrm{O_2} \rightleftarrows \mathrm{O_2} - \mathrm{FeIIPc} \tag{ii}$$

$$\mathrm{O_2} - \mathrm{FeIIPc} + e^- + \mathrm{H} + \rightleftarrows [\mathrm{HO_2} - \mathrm{FeIIIPc}]\ (\mathrm{r.d.s}) \tag{iii}$$

$$[\mathrm{HO_2} - \mathrm{FeIIIPc}] \rightarrow \mathrm{HO_2}\bullet^- + \mathrm{FeIIIPc}\ (\text{hydroperoxyl radical formation}) \tag{iv}$$

$$[\mathrm{HO_2} - \mathrm{FeIIIPc}] + e^- + 1\mathrm{H}^+ \rightarrow \mathrm{H_2O_2} + \mathrm{FeIIIPc}\ (\mathrm{H_2O_2}\ \text{formation}) \tag{v}$$

$$[\mathrm{HO_2} - \mathrm{FeIIIPc}] + 3e^- + 3\mathrm{H}^+ \rightarrow 2\mathrm{H_2O} + \mathrm{FeIIIPc}\ (\mathrm{H_2O}\ \text{formation}) \tag{vi}$$

It is worth mentioning that Wilkinson et al. [148] have also conducted studies at different temperatures using Fe fluoroporphyrin and reported some kinetic parameters such as activation energies. They found that the results were essentially similar to those found with FePc.

7.4 Oxygen Reduction Catalyzed by Nonmacrocyclic Cu Complexes

Copper (I) complexes exhibit catalytic activity for the four-electron (4-e) reduction of O_2 to water. Natural occurring enzymes like Cu-containing fungal laccase reduce O_2 directly to water very efficiently at very positive potentials, not far from the thermodynamic standard potential of the O_2/H_2O couple. These enzymes involve a trinuclear Cu active site [149–153]. For this reason some authors have investigated the catalytic activity of Cu(I) complexes for ORR, in particular Cu phenanthrolines confined on graphite or glassy carbon surfaces [154–169], with the aim of achieving the total reduction of O_2 via the transfer of four-electrons.

For example, copper(I) 1,10-phenanthroline, Cu(phenP), reduces O_2 almost entirely via the transfer of four electrons and four protons to give water [156, 157, 170]. This is quite interesting since, similarly to what is observed with Fe phthalocyanines [99, 171], the four-electron reduction of O_2 is promoted by single-site catalysts. The O_2 molecule cannot interact simultaneously with two Cu active sites. If this were the case, the order of the reaction in surface concentration would equal to two. Anson et al. [156, 157, 170] checked this and found that the reaction is first order in Cu coverage, suggesting of a mononuclear Cu site as the active catalyst. As mentioned above, Cu-containing fungal laccase enzymes promote the reduction of molecular oxygen directly to water at a trinuclear Cu active site at very low overpotentials [149, 150]. Using specially designed laccase-modified electrodes, Heller et al. [172–174] have measured current densities of 5 mA/cm^2 at overpotentials (vs. the O_2/H_2O couple) as low as −0.070 V at pH 5. As discussed by Chidsey et al. [168], this current density corresponds to a turnover rate of 2.1 O_2 reduced per laccase s^{-1}, or 0.7 O_2 per Cu s^{-1}. In comparison, as pointed out by Chidsey et al. [168], Pt nanoparticle catalysts reduce O_2 with rates of 2.5 O_2 per active surface Pt s^{-1} or 0.25 O_2 per total Pt s^{-1}, at an overpotential of −0.350 V [168, 175]. This normalization allows the comparison of atom efficiency of the catalysts regardless of catalyst loading [166]. With this evidence it is possible to design and prepare Cu complexes that can mimic enzymatic systems using mononuclear Cu complexes.

Anson et al. found that 1,10-phenanthroline (phen) complexes of Cu, adsorbed on the edge-plane orientation of graphite, catalyze the four-electron reduction of O_2 to H_2O [156–159, 170]. They proposed a mechanism for the electrocatalytic four-electron reduction of O_2. Using complexes having three different phen ligands (phen, 2,9-Me2-phen, 5-Cl-phen), they found that reduction of O_2 occurs at potentials negative to the formal Cu (II/I) redox potential of the respective complex strongly suggesting that the active species is the Cu(I) complex [158]. They conducted their studies in the presence of buffers containing acetate, phosphate, and borate. However, the mechanism proposed did not involve the coordination of these anions to the Cu center, even though these anions can affect the potentials and electrocatalytic activity of similar complexes [174]. Chidsey et al. [168] conducted a systematic study of the catalytic activity of several Cuphen complexes for ORR in the presence of acetate. They found that the reduction of Cu(II) on the adsorbed complexes occurs with the concerted dissociation of an acetate ion as $[\text{phenCu(II)}\,\text{AcO}^-]_{ad} + e^- > [\text{phenCu(I)}]_{ad} + \text{AcO}^-$ and that this can happen with any coordinating anion. They found that catalytic currents are observed at potentials very close to the Cu(II)/(I) formal potential of the adsorbed Cu phen complex. This is illustrated in Fig. 7.31. They found that the presence of the anion is crucial in the stability of the catalyst since irreversible degradation of the catalyst is observed if an O_2 reduction experiment is conducted in the absence of acetic acid. The effect of the $E^{\circ\prime}$, the Cu(II)/(I) formal of the catalyst on the ORR activity was studied by investigating some complexes with electron-withdrawing groups located on the phenanthroline ligand as illustrated in Fig. 7.31. As expected, these groups, according to their electron-withdrawing power, shift the Cu(II)/(I) formal potential to more positive values, as seen by the shift of the reversible waves (dotted lines) in Fig. 7.31 assigned to the Cu(II)/(I) transition.

The shift to more positive potential of the Cu(II)/(I) formal potential has a positive effect in the catalytic activity of the complexes since the ORR waves (solid lines) also shift in the same direction, that is, to lower ORR overpotentials. Figure 7.32 illustrates the effect of the formal potential on the catalytic currents. The currents were measured at the formal potential of each catalyst, not at a constant potential, and they are normalized for the amount of catalyst present on

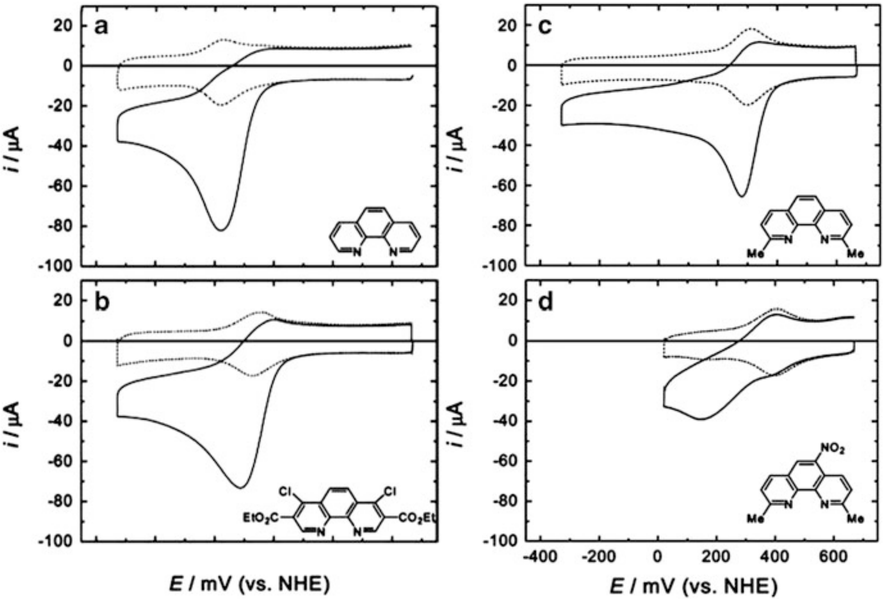

Fig. 7.31 Cyclic voltammograms of edge-plane graphite modified with adsorbed Cu complexes of (**a**) phen, (**b**) 3,8-$(CO_2Et)_2$-4,7-Cl_2-phen, (**c**) 2,9-Me_2-phen, and (**d**) 2,9-Me_2-5-NO_2-phen, in N_2-purged (*dotted lines*) and air-saturated (*continuous lines*) solutions of 0.1 M $NaClO_4$, 0.020 M NaAcO, 0.02 M AcOH, pH 4.8 at 0.1 V s^{-1} as reported by Chidsey et al. [168]

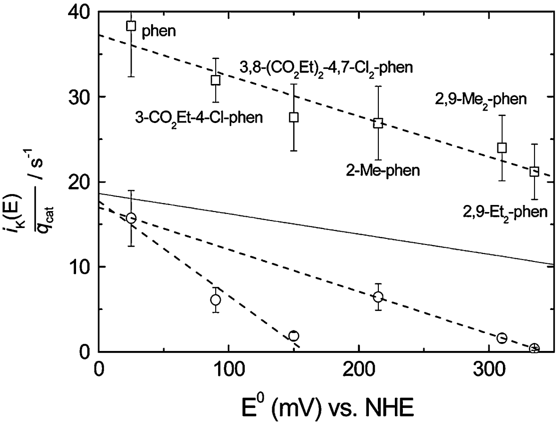

Fig. 7.32 Normalized kinetic currents for Cu complexes adsorbed on the edge-plane of graphite, measured at $E^{\circ\prime}$ (*circles*) and at −0.150 V vs. NHE (*squares*) plotted vs. $E^{\circ\prime}$ for each Cu complex. The *dotted line* is the expected behavior for the kinetic current measured at $E_{1/2}$. All data measured in 0.020 M NaAcO and 0.020 M AcOH pH 4.8, 0.1 M $NaClO_4$ except 2,9-Me_2-phen measured in 0.020 M NaAcO and 0.072 M AcOH pH 4.2, 0.1 M $NaClO_4$

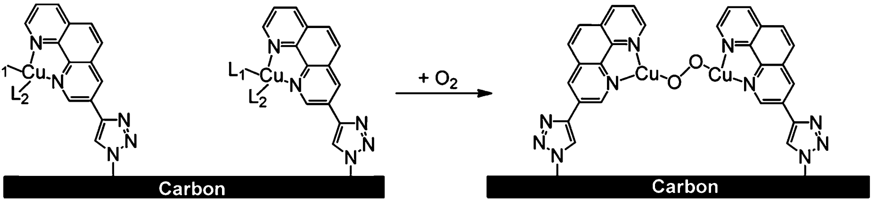

Fig. 7.33 Binding of dioxygen to two proximal Cu centers of 3-ethynyl-phenanthroline covalently attached to an azide-modified glassy carbon electrode according to Chidsey et al. [169]

the surface (the amount of catalyst is proportional to the electrical charge under the reversible peaks, dashed lines, in Fig. 7.31). It could be interesting to compare the currents at constant electrode potential vs. the formal potentials since it would be likely that a similar correlation to that shown in Fig. 7.20 illustrated for ORR on metallophthalocyanines vs. the M(III)/(II) formal potential, judging from the data in Fig. 7.31.

Chidsey et al. [169] have also studied the catalytic activity of a Cu(I) complex of 3-ethynyl-phenanthroline covalently attached to an azide-modified glassy carbon electrode. This catalyst promotes the four-electron reduction of O_2 at pH 4.8 (acetate buffer). In contrast to what is observed by Anson et al. [156–158, 170] using Cu phenanthroline, Chidsey et al. found a second-order dependence of the rates on Cu coverage at moderate overpotentials. This suggests that O_2 interacts with two Cu centers simultaneously, forming a bridge structure, as illustrated in Fig. 7.33.

Copper(I) complexes confined on electrode surfaces are promising catalyst for the four-electron ORR and seem to require the presence of coordinating anions like acetate to stabilize the adsorbed. This is a much less explored field of nonprecious metal catalysts compared to MN_4 macrocyclics for ORR and might be interesting to mimic laccase-like structures as this particular enzyme catalyzes the reduction of O_2 at very low overpotentials [151].

7.5 Conclusions

It can be concluded that in spite of the rather large amount of work published in the literature, there are still many questions that remain unsolved about the electrocatalytic reduction of O_2 mediated by N_4-metallomacrocyclics confined on electrode surfaces. Improving the activity of these complexes beyond the present state-of-the-art catalysts will require development of rigorous qualitative and quantitative structure–activity relationships (QSAR) [176] for judicious tailoring of activity. Some useful trends do exist. For example, it is now well established that Fe and Co macrocyclic complexes are by far the best catalysts for oxygen reduction even though some studies have demonstrated that cofacial Ir complexes are also very active. These complexes are characterized by exhibiting a reversible redox transition involving the M(III)/(II) couple. Some authors have found volcano-shaped correlations between activity (measured as current at constant potential or potential at constant current) vs.

M(III)/(II) formal potential of the catalyst suggesting that an optimal M(III)/(II) redox potential does exist for maximum activity. However, other authors have found only linear correlations between activity and M(III)/(II) redox potential, which indicates that the more positive the redox potential, the higher the activity. In the latter correlations, the activity decreases with increasing the driving force of the catalyst. This finding is important since a priori one would expect that the more negative the M (III)/(II) formal potential, the higher the activity, since this could favor the partial reduction of O_2 upon interacting with the metal center, that is, M(III)-O_2-. It is also possible that the linear correlations found are part of an incomplete volcano. However, in these correlations it was found that Cr, Mn, Fe, and Co complexes, which exhibit a M(III)/(II) transition, give rise to two separated correlations or families of compounds. This is a reflection of the fact that the reduction wave for O_2 reduction on, for example, Mn and Fe complexes starts at a potential very close to the M(III)/(II) formal potential of the catalyst. In contrast, for Co macrocyclics, the reduction wave starts at potentials far more negative than the Co(III)/(II) formal potentials. The proximity of the O_2 reduction wave to the M(III)/(II) for some complexes is also reflected in the observation that a direct four-electron reduction process operates, as observed for Fe and Mn complexes. For most monomeric or monolayers of Co complexes, the onset for O_2 reduction is far removed from the Co(III)/(II) transition and only the peroxide pathway is observed.

Biomimetic catalyst design schemes have been very successful in tailoring the properties of catalysts, for example, as demonstrated for functional heme/Cu analogs and bimetallic cofacial diporphyrins. The knowledge gained thus far provides a promising leeway for the design of efficient N_4-metallomacrocyclic based catalysts for four-electron reduction of oxygen.

Despite Ir- and Ru-based N_4-metallomacrocyclic complexes reporting some of the best activities in acidic and alkaline media, respectively, being rare metals, their advantageous superiority would be offset by their high cost. Nonetheless, these complexes should serve as appropriate models, such that theoretical and experimental knowledge gained from studying them may serve to tailor the synthesis of improved catalysts. Particularly, the energetic aspects that furnish some monomeric complexes the unique ability to reduce oxygen directly to water as opposed to other monomeric complexes warrant detailed investigation.

The relative backdonating power of metal ions attached to the pendant groups of the multinuclear oxygen reduction catalysts discussed in this work is the fundamental parameter for modulating the ORR activity of these complexes. It is therefore possible that the electronic effects introduced due to π backdonation by Ru(II) and Os(II) may also be fulfilled by other groups. This rationale constitutes the prospect for modulation of the ORR activity of these complexes.

The stability of metalloporphyrins and metallophthalocyanines alike is far from satisfactory for any practical application. Whereas there is irrefutable evidence for improved activity upon heat treatment of the N_4-metallomacrocyclic complexes, the loss of their structural merit is obvious. The fact that the performance of nonprecious metal catalysts synthesized by heat treatment of inexpensive nitrogen, carbon, and metal precursors rivals that of heat-treated N_4-metallomacrocyclic complexes, which are relatively more expensive, renders the latter to be noncompetitive precursors [177]. On the other hand, improving the stability and activity of N_4-metallomacrocyclic complexes while conserving their molecular integrity is a difficult task, and indeed very little progress has been reported in line with this.

New material design approaches including exploitation of the synergetic benefits reported for some catalyst supports, for example, carbon nanotubes, graphene, nitrogen-doped carbons, and titanium oxide [178, 179] and other conductive mesoporous materials with high surface areas, among others, might help to solve some of the current challenges. The multicomponent and multifunctional approach [78, 180, 181], where the individual components of a composite catalyst perform specific reactions to ensure complete reduction of oxygen, is worthwhile engendering.

Finally, it is worth mentioning that one of the advantages of MN_4 macrocyclics over Pt catalysts is their tolerance to methanol crossover [14], which is a serious problem in methanol-air fuel cells [83]. For example, Léger et al. have shown that FePc is highly tolerant to methanol [182]. The same is true for CoPc [183]. When methanol crossover from the anode through the electrolytic membrane to the cathode occurs, electroreduction of dioxygen and electrooxidation of methanol occur simultaneously, which is detrimental to the overall performance of the fuel cell since the fuel efficiency decreases and so does the power output. In general MN_4 macrocyclics are poor catalysts for the oxidation of methanol so this reaction should not occur and this would avoid the problems mentioned above.

Cu(I) complexes that somehow mimic natural-occuring laccase represent an interesting class of catalysts since they catalyze the four-electron reduction of O_2 directly to water at rather low overpotentials at pH 4.8 but they lack long-term stability. However, it might be possible to solve this problem in the future.

Acknowledgments J.H. Zagal is grateful to Fondecyt 1100773 and Núcleo Milenio Project P07-006 Iniciativa Científica Milenio del Ministerio de Economía, Fomento y Turismo, for financial support. Justus Masa is grateful to the German Academic Exchange Service (DAAD) for a PhD scholarship.

References

1. Steele BC, Heinzel A (2001) Materials for fuel-cell technologies. Nature 414(6861):345–352
2. Lee J, Kim ST, Cao R, Choi N, Liu M, Lee KT, Cho J (2011) Metal-air batteries with high energy density: Li–Air versus Zn–Air. Adv Energy Mater 1(1):34–50
3. Gasteiger HA, Kocha SS, Sompalli B, Wagner FT (2005) Activity benchmarks and requirements for Pt, Pt-alloy, and non-Pt oxygen reduction catalysts for PEMFCs. Appl Catal B Environ 56(1–2):9–35
4. Spendelow JS, Wieckowski A (2007) Electrocatalysis of oxygen reduction and small alcohol oxidation in alkaline media. Phys Chem Chem Phys 9(21):2654–2675
5. Min M (2000) Particle size and alloying effects of Pt-based alloy catalysts for fuel cell applications. Electrochim Acta 45(25–26):4211–4217
6. Mazumder V, Lee Y, Sun S (2010) Recent development of active nanoparticle catalysts for fuel cell reactions. Adv Funct Mater 20(8):1224–1231

7. Sun Z, Masa J, Liu Z, Schuhmann MM (2012) Highly concentrated aqueous dispersions of graphene exfoliated by sodium taurodeoxycholate: dispersion behavior and potential application as a catalyst support for the oxygen-reduction reaction. Chem Eur J 18:6972–6978
8. Jasinski R (1964) New fuel cell cathode catalyst. Nature 201(492):1212–1213
9. Jahnke H, Schönborn M, Zimmermann G (1976) Organic dyestuffs as catalysts for fuel cells. In: Schäfer F, Gerischer H, Willig F, Meier H, Jahnke H, Schönborn M, Zimmermann G (eds) Physical and chemical applications of dyestuffs, vol 61. Springer, Heidelberg, pp 133–181
10. Alt H, Binder H, Sandstede G (1973) Mechanism of the electrocatalytic reduction of oxygen on metal chelates. J Catal 28(1):8–19
11. Kadish K (1984) Redox tuning of metalloporphyrin reactivity. J Electroanal Chem 168 (1–2):261–274
12. Randin J (1974) Interpretation of the relative electrochemical activity of various metal phthalocyanines for the oxygen reduction reaction. Electrochim Acta 19(2):83–85
13. Richards G, Swavey S (2009) Electrooxidation of Fe, Co, Ni and Cu metalloporphyrins on edge-plane pyrolytic graphite electrodes and their electrocatalytic ability towards the reduction of molecular oxygen in acidic media. Eur J Inorg Chem 35:5367–5376
14. Zagal JH, Páez M, Tanaka A, dos Santos Jr JR, Linkous CA (1992) Electrocatalytic activity of metal phthalocyanines for oxygen reduction. J Electroanal Chem 339(1–2):13–30
15. Vasudevan P, Santosh MN, Tyagi S (1990) Transition metal complexes of porphyrins and phthalocyanines as electrocatalysts for dioxygen reduction. Transit Met Chem 15(2):81–90
16. Yuasa M, Nishihara R, Shi C, Anson FC (2001) A comparison of several meso-tetraalkyl cobalt porphyrins as catalysts for the electroreduction of dioxygen. Polym Adv Technol 12(3–4):266–270
17. Song E, Shi C, Anson FC (1998) Comparison of the behavior of several cobalt porphyrins as electrocatalysts for the reduction of O_2 at graphite electrodes. Langmuir 14(15):4315–4321
18. Ozer D, Harth R, Mor U, Bettelheim A (1989) Electrochemistry of various substituted aminophenyl iron porphyrins: Part II. Catalytic reduction of dioxygen by electropolymerized films. J Electroanal Chem 266(1):109–123
19. Bettelheim A, Ozer D, Harth R, Murray RW (1989) Electrochemistry of various substituted aminophenyl iron porphyrins: Part I. Redox properties of dissolved, adsorbed and electropolymerized species. J Electroanal Chem 266(1):93–108
20. van der Putten A, Elzing A, Visscher W, Barendrecht E (1987) Redox potential and electrocatalysis of O_2 reduction on transition metal chelates. J Electroanal Chem 221(1–2):95–104
21. Elzing A, van der Putten A, Visscher W, Barendrecht E (1986) The cathodic reduction of oxygen at cobalt phthalocyanine. Influence of electrode preparation on electrocatalysis. J Electroanal Chem 200(1–2):313–322
22. Beletskaya I, Tyurin VS, Tsivadze AY, Guilard R, Stern C (2009) Supramolecular chemistry of metalloporphyrins. Chem Rev 109(5):1659–1713
23. Tashiro K, Aida T (2007) Metalloporphyrin hosts for supramolecular chemistry of fullerenes. Chem Soc Rev 36(2):189
24. Sun D, Tham FS, Reed CA, Chaker L, Boyd PD (2002) Supramolecular fullerene-porphyrin chemistry. fullerene complexation by metalated “Jaws Porphyrin” Hosts. J Am Chem Soc 124(23):6604–6612
25. NEC (2007) Advanced energy initiative, 2006. National Environmental Council for the President of the United States
26. Adzic R (1998) Recent advances in kinetics of oxygen reduction. In: Lipkowski J, Ross PN (eds) Electrocatalysis. Wiley-VCH, New York, NY, pp 197–237
27. Bard AJ, Faulkner LR (2001) Electrochemical methods. Fundamentals and applications, 2nd edn. Wiley, New York, NY
28. Zagal JH, Bindra P, Yeager E (1980) A mechanistic study of O_2 reduction on water soluble phthalocyanines adsorbed on graphite electrodes. J Electrochem Soc 127(7):1506

29. Paulus UA, Schmidt TJ, Gasteiger HA, Behm RJ (2001) Oxygen reduction on a high-surface area Pt/Vulcan carbon catalyst: a thin-film rotating ring-disk electrode study. J Electroanal Chem 495(2):134–145
30. Dobrzeniecka A, Zeradjanin A, Masa J, Puschhof A, Stroka J, Kulesza PJ, Schuhmann W (2013) Application of SECM in tracing of hydrogen peroxide at multicomponent non-noble electrocatalyst films for the oxygen reduction reaction. Catal Today 202:55–62
31. Okunola AO, Nagaiah TC, Chen X, Eckhard K, Schuhmann BM (2009) Visualization of local electrocatalytic activity of metalloporphyrins towards oxygen reduction by means of redox competition scanning electrochemical microscopy (RC-SECM). Electrochim Acta 54(22):4971–4978
32. Sánchez-Sánchez CM, Bard AJ (2009) Hydrogen peroxide production in the oxygen reduction reaction at different electrocatalysts as quantified by scanning electrochemical microscopy. Anal Chem 81(19):8094–8100
33. Mezour MA, Cornut R, Hussien EM, Morin M, Mauzeroll J (2010) Detection of hydrogen peroxide produced during the oxygen reduction reaction at self-assembled thiol − porphyrin monolayers on gold using SECM and nanoelectrodes. Langmuir 26(15):13000–13006
34. Sánchez-Sánchez CM, Rodríguez-López J, Bard AJ (2008) Scanning electrochemical microscopy. 60. Quantitative calibration of the SECM substrate generation/tip collection mode and its use for the study of the oxygen reduction mechanism. Anal Chem 80(9):3254–3260
35. Collman J, Ghosh S (2010) Recent applications of a synthetic model of cytochrome c. Inorg Chem 49(13):5798–5810
36. Kim E, Chufán EE, Kamaraj K, Karlin KD (2004) Synthetic models for heme − copper oxidases. Chem Rev 104(2):1077–1134
37. Collman J, Boulatov R, Sunderland CJ, Fu L (2004) Functional analogues of Cytochrome c oxidase, myoglobin, and hemoglobin. Chem Rev 104(2):561–588
38. Collman J, Devaraj NK, Decreau RA, Yang Y, Yan Y, Ebina W, Eberspacher TA, Chidsey CED (2007) A Cytochrome c oxidase model catalyzes oxygen to water reduction under rate-limiting electron flux. Science 315(5818):1565–1568
39. Boulatov R, Collman J, Shiryaeva IM, Sunderland CJ (2002) Functional analogues of the dioxygen reduction site in cytochrome oxidase: mechanistic aspects and possible effects of CuB. J Am Chem Soc 124(40):11923–11935
40. Chang CJ, Deng YQ, Shi CN, Chang CK, Anson FC, Nocera DG (2000) Electrocatalytic four-electron reduction of oxygen to water by a highly flexible cofacial cobalt bisporphyrin. Chem Commun 15:1355–1356
41. Collman J (1997) A functional model related to Cytochrome c oxidase and its electrocatalytic four-electron reduction of O_2. Science 275(5302):949–951
42. Collman J, Elliott CM, Halbert TR, Tovrog BS (1977) Synthesis and characterization of “face-to-face” porphyrins (biometallic ligands/metal-metal interactions/electron spin resonance/dioxygen reduction/dinitrogen reduction). Proc Natl Acad Sci U S A 74(1):18–22
43. Collman J, Denisevich P, Konai Y, Marrocco M, Koval C, Anson FC (1980) Electrode catalysis of the four-electron reduction of oxygen to water by dicobalt face-to-face porphyrins. J Am Chem Soc 102(19):6027–6036
44. Shigehara K, Anson FC (1982) Electrocatalytic activity of three iron porphyrins in the reduction of dioxygen and hydrogen peroxide at graphite cathodes. J Phys Chem 86(14):2776–2783
45. Chang CK, Liu HY, Abdalmuhdi I (1984) Electroreduction of oxygen by pillared cobalt(II) cofacial diporphyrin catalysts. J Am Chem Soc 106(9):2725–2726
46. Shi C, Mak KW, Chan KS, Anson FC (1995) Enhancement by surfactants of the activity and stability of iridium octaethyl porphyrin as an electrocatalyst for the four-electron reduction of dioxygen. J Electroanal Chem 397(1–2):321–324

47. Collman J, Chng LL, Tyvoll DA (1995) Electrocatalytic Reduction of Dioxygen to Water by Iridium Porphyrins Adsorbed on Edge Plane Graphite Electrodes Inorg Chem 34(6):1311–1324
48. Chang CJ, Loh Z, Shi C, Anson FC, Nocera DG (2004) Targeted proton delivery in the catalyzed reduction of oxygen to water by bimetallic pacman porphyrins. J Am Chem Soc 126(32):10013–10020
49. Liu HY, Abdalmuhdi I, Chang CK et al (1985) Catalysis of the electroreduction of dioxygen and hydrogen peroxide by an anthracene-linked dimeric cobalt porphyrin. J Phys Chem 89(4):665–670
50. Collman J, Wagenknecht PS, Hutchison JE (1994) Molecular catalysts for multielectron redox reactions of small molecules—the cofacial metallodiporphyrin approach. Angew Chem Int Ed 33(15–16):1537–1554
51. Durand RR, Bencosme CS, Collman J, Anson FC (1983) Mechanistic aspects of the catalytic reduction of dioxygen by cofacial metalloporphyrins. J Am Chem Soc 105(9):2710–2718
52. Anson FC, Shi C, Steiger B (1997) Novel multinuclear catalysts for the electroreduction of dioxygen directly to water. Acc Chem Res 30(11):437–444
53. Collman J, Hendricks NH, Kim K, Bencosme CS (1987) The role of Lewis acids in promoting the electrocatalytic four-electron reduction of dioxygen. Chem Commun (20):1537
54. Ni CL, Abdalmuhdi I, Chang CK, Anson FC (1987) Behavior of four anthracene-linked dimeric metalloporphyrins as electrocatalysts for the reduction of dioxygen. J Phys Chem 91(5):1158–1166
55. Collman J, Kim K (1986) Electrocatalytic four-electron reduction of dioxygen by iridium porphyrins adsorbed on graphite. J Am Chem Soc 108(24):7847–7849
56. Bouwkamp-Wijnoltz AL, Visscher W, van Veen J (1994) Oxygen reduction catalysed by carbon supported iridium-chelates. Electrochim Acta 39(11–12):1641–1645
57. Shi C, Steiger B, Yuasa M, Anson FC (1997) Electroreduction of O_2 to H_2O at unusually positive potentials catalyzed by the simplest of the cobalt porphyrins. Inorg Chem 36(20):4294–4295
58. Zagal JH, Griveau S, Ozoemena KI, Nyokong T, Bedioui F (2009) Carbon nanotubes, phthalocyanines and porphyrins: attractive hybrid materials for electrocatalysis and electroanalysis. J Nanosci Nanotechnol 9(4):2201–2214
59. Okunola A, Kowalewska B, Bron M, Kulesza PJ, Schuhmann W (2009) Electrocatalytic reduction of oxygen at electropolymerized films of metalloporphyrins deposited onto multiwalled carbon nanotubes. Electrochim Acta 54(7):1954–1960
60. Mamuru SA, Ozoemena KI, Fukuda T, Kobayashi N (2010) Iron(II) tetrakis(diaquaplatinum) octacarboxyphthalocyanine supported on multi-walled carbon nanotube platform: an efficient functional material for enhancing electron transfer kinetics and electrocatalytic oxidation of formic acid. J Mater Chem 20(47):10705
61. Mamuru SA, Ozoemena KI (2010) Iron (II) tetrakis(diaquaplatinum) octacarboxyphthalocyanine supported on multi-walled carbon nanotubes as effective electrocatalyst for oxygen reduction reaction in alkaline medium. Electrochem Commun 12(11):1539–1542
62. Xu Z, Li H, Cao G, Zhang Q, Li K, Zhao X (2011) Electrochemical performance of carbon nanotube-supported cobalt phthalocyanine and its nitrogen-rich derivatives for oxygen reduction. J Mol Catal A: Chem 335(1–2):89–96
63. Yuan Y, Zhao B, Jeon Y, Zhong S, Zhou S, Kim S (2011) Iron phthalocyanine supported on amino-functionalized multi-walled carbon nanotube as an alternative cathodic oxygen catalyst in microbial fuel cells. Biores Technol 102(10):5849–5854
64. Morozan A, Campidelli S, Filoramo A, Jousselme B, Palacin S (2011) Catalytic activity of cobalt and iron phthalocyanines or porphyrins supported on different carbon nanotubes towards oxygen reduction reaction. Carbon 49(14):4839–4847
65. Mamuru SA, Ozoemena KI, Fukuda T, Kobayashi N, Nyokong T (2010) Studies on the heterogeneous electron transport and oxygen reduction reaction at metal (Co, Fe)

octabutylsulphonylphthalocyanines supported on multi-walled carbon nanotube modified graphite electrode. Electrochim Acta 55(22):6367–6375

66. Mamuru SA, Ozoemena KI (2010) Heterogeneous electron transfer and oxygen reduction reaction at nanostructured Iron(II) phthalocyanine and its MWCNTs nanocomposites. Electroanalysis 22(9):985–994
67. Maxakato NW, Mamuru SA, Ozoemena KI (2011) Efficient oxygen reduction reaction using ruthenium tetrakis(diaquaplatinum)octacarboxyphthalocyanine catalyst supported on MWCNT platform. Electroanalysis 23(2):325–329
68. Damos FS, Luz RC, Tanaka AA, Kubota LT (2010) Dissolved oxygen amperometric sensor based on layer-by-layer assembly using host–guest supramolecular interactions. Anal Chim Acta 664(2):144–150
69. Duarte J, Luz R, Damos F, Tanaka AA, Kubota LT (2008) A highly sensitive amperometric sensor for oxygen based on iron(II) tetrasulfonated phthalocyanine and iron(III) tetra-(N-methyl-pyridyl)-porphyrin multilayers. Anal Chim Acta 612(1):29–36
70. D'Souza F, Hsieh Y, Deviprasad GR (1998) Four-electron electrocatalytic reduction of dioxygen to water by an ion-pair cobalt porphyrin dimer adsorbed on a glassy carbon electrode. Chem Commun 9:1027–1028
71. Liu S, Xu J, Sun H, Li D-M (2000) *meso*-Tetrakis(4-N-benzylpyridyl)porphyrin and its supramolecular complexes formed with anionic metal–oxo cluster: spectroscopy and electrocatalytic reduction of dioxygen. Inorg Chim Acta 306(1):87–93
72. Araki K, Toma HE (2006) Supramolecular Porphyrins as Electrocatalysts. In: Zagal JH, Bedioui F, Dodelet JP (eds) N_4-macrocyclic metal complexes. Springer, New York, pp 255–314
73. Shi C, Anson FC (1991) Multiple intramolecular electron transfer in the catalysis of the reduction of dioxygen by cobalt meso-tetrakis(4-pyridyl)porphyrin to which four $Ru(NH_3)_5$ groups are coordinated. J Am Chem Soc 113(25):9564–9570
74. Shi C, Anson FC (1992) Electrocatalysis of the reduction of molecular oxygen to water by tetraruthenated cobalt *meso*-tetrakis(4-pyridyl)porphyrin adsorbed on graphite electrodes. Inorg Chem 31(24):5078–5083
75. Steiger B, Anson FC (1997) [5,10,15,20-tetrakis(4-((pentaammineruthenio)-cyano)phenyl) porphyrinato]cobalt(II) immobilized on graphite electrodes catalyzes the electroreduction of O_2 to H_2O, but the corresponding 4-cyano-2,6-dimethylphenyl derivative catalyzes the reduction only to H_2O_2. Inorg Chem 36(18):4138–4140
76. Shi C, Anson FC (1996) Cobalt meso- tetrakis(N-methyl-4-pyridiniumyl)porphyrin becomes a catalyst for the electroreduction of O_2 by four electrons when $[(NH_3)_5Os]_{n+}$ ($n = 2, 3$) groups are coordinated to the porphyrin ring. Inorg Chem 35(26):7928–7931
77. Zagal JH, Páez M, Sturm J, Ureta-Zanartu S (1984) Electroreduction of oxygen on mixtures of phthalocyanines co-adsorbed on a graphite electrode. J Electroanal Chem 181(1–2):295–300
78. Dobrzeniecka A, Zeradjanin A, Masa J, Stroka J, Goral M, Schuhmann W, Kulesza PJ (2011) ECS Trans 35:33–44
79. Forshey PA, Kuwana T (1983) Electrochemistry of oxygen reduction. 4. Oxygen to water conversion by iron(II)(tetrakis(N-methyl-4-pyridyl)porphyrin) via hydrogen peroxide. Inorg Chem 22(5):699–707
80. Elbaz L, Korin E, Soifer L, Bettelheim A (2008) Electrocatalytic oxygen reduction by Co(III) porphyrins incorporated in aerogel carbon electrodes. J Electroanal Chem 621(1):91–96
81. Zagal JH, Páez MA, Silva JF (2006) Fundamental Aspects on the Catalytic Activity of Metallomacrocyclics for the Electrochemical Reduction of O_2. In: Zagal JH, Bedioui F, Dodelet JP (eds) N_4-Macrocyclic Metal Complexes. Springer, New York, pp 41–82
82. Zagal JH (1992) Metallophthalocyanines as catalysts in electrochemical reactions. Coord Chem Rev 119:89–136
83. Zagal JH (2003) Macrocycles. In: Vielstich W, Lamm A, Gasteiger HA (eds) Handbook of fuel cells-fundamentals, technology and applications, vol. 2, Part 5. Wiley, Chichester

84. Tse Y, Janda P, Lam H, Zhang J, Pietro WJ, Lever ABP (1997) Monomeric and polymeric tetra-aminophthalocyanatocobalt(II) modified electrodes: electrocatalytic reduction of oxygen. J Porphyrins Phthalocyanines 1(1):3–16
85. Pavez J, Paez M, Ringuede BF, Zagal JH (2005) Effect of film thickness on the electroreduction of molecular oxygen on electropolymerized cobalt tetra-aminophthalocyanine films. J Solid State Electrochem 9(1):21–29
86. Ramírez G, Trollund E, Isaacs M, Armijo F, Zagal JH, Costamagna J, Aguirre MJ (2002) Electroreduction of molecular oxygen on poly-iron-tetraaminophthalocyanine modified electrodes. Electroanalysis 14(7–8):540–545
87. Lalande G, Cote R, Guay D, Dodelet JP, Weng LT, Bertrand P (1997) Is nitrogen important in the formulation of Fe-based catalysts for oxygen reduction in solid polymer fuel cells? Electrochim Acta 42(9):1379–1388
88. Bouwkamp-Wijnoltz A, Visscher W, van Veen J (1998) The selectivity of oxygen reduction by pyrolysed iron porphyrin supported on carbon. Electrochim Acta 43(21–22):3141–3152
89. Lefevre M, Dodelet JP, Bertrand P (2002) Molecular oxygen reduction in PEM fuel cells: evidence for the simultaneous presence of two active sites in Fe-based catalysts. J Phys Chem B 106(34):8705–8713
90. Lefèvre M (2003) Fe-based catalysts for the reduction of oxygen in polymer electrolyte membrane fuel cell conditions: determination of the amount of peroxide released during electroreduction and its influence on the stability of the catalysts. Electrochim Acta 48(19):2749–2760
91. Schilling T, Okunola A, Masa J, Schuhmann W, Bron M (2010) Carbon nanotubes modified with electrodeposited metal porphyrins and phenanthrolines for electrocatalytic applications. Electrochim Acta 55(26):7597–7602
92. Bouwkamp-Wijnoltz AL, Visscher W, van Veen JA (2002) On active-site heterogeneity in pyrolyzed carbon-supported iron porphyrin catalysts for the electrochemical reduction of oxygen: an in situ Mossbauer study. J Phys Chem B 106(50):12993–13001
93. Kobayashi N, Nevin WA (1996) Electrocatalytic reduction of oxygen using water-soluble iron and cobalt phthalocyanines and porphyrins. Appl Organomet Chem 10(8):579–590
94. Zagal JH, Aguirre MJ, Basaez L, Pavez J, Padilla L, Toro-Labbé A (1995) Possible explanations for the volcano-shaped plots for the electrocatalytic reduction of O_2 on electrodes modified with N-4 macrocycles. In: Adzic RR, Anson FC, Kinoshita K (eds) Proceedings of the symposium on oxygen electrochemistry, 95–26. The Electrochemical Society Symposium Inc., Pennington, NJ, p 89
95. Bytheway I, Hall MB (1994) Theoretical calculations of metal-dioxygen complexes. Chem Rev 94(3):639–658
96. Wang G, Ramesh N, Hsu A, Deryn C, Rongrong C (2008) Density functional theory study of the adsorption of oxygen molecule on iron phthalocyanine and cobalt phthalocyanine. Mol Simul 34(10–15):1051–1056
97. Scherson DA, Palencsár A, Tolmachev Y, Stefan I (2008) Transition metal macrocycles as electrocatalysts for dioxygen reduction. In: Alkire RC, Kolb DM, Lipkowski J, Ross PN (eds) Electrochemical surface modification: thin films, functionalization and characterization. Wiley-VCH Verlag GmbH & Co. KGaA, Weinheim, Germany
98. Zecevic S, Simic-Glavaski B, Yeager E, Lever ABP, Minor PC (1985) Spectroscopic and electrochemical studies of transition metal tetrasulfonated phthalocyanines. Part V. Voltammetric studies of adsorbed tetrasulfonated phthalocyanines (MTsPc) in aqueous solutions. J Electroanal Chem 196(2):339–358
99. Zagal JH, Griveau S, Francisco Silva J, Nyokong T, Bedioui F (2010) Metallophthalocyanine-based molecular materials as catalysts for electrochemical reactions. Coord Chem Rev 254 (23–24):2755–2791
100. Kim S, Scherson DA (1992) In situ UV–visible reflection absorption wavelength modulation spectroscopy of species irreversibly adsorbed on electrode surfaces. Anal Chem 64(24):3091–3095

101. Stefan IC, Mo Y, Ha SY, Scherson D (2003) In situ Fe K-edge X-ray absorption fine structure of a nitrosyl adduct of iron phthalocyanine irreversibly adsorbed on a high area carbon electrode in an acidic electrolyte. Inorg Chem 42(14):4316–4321
102. Zagal JH, Bedioui F, Dodelet JP (eds) (2006) N_4-macrocyclic metal complexes. Springer, New York
103. Wiesener K, Ohms D, Neumann V, Franke R (1989) N_4 macrocycles as electrocatalysts for the cathodic reduction of oxygen. Mater Chem Phys 22(3–4):457–475
104. van Veen J (1979) Oxygen reduction on monomeric transition metal phthalocyanines in acid electrolyte. Electrochim Acta 24(9):921–928
105. van Veen JA, van Baar JF, Kroese CJ, Coolegem JGF, De Wit N, Colijn HA (1981) Oxygen reduction on transition-metal porphyrins in acid electrolyte. 1. Activity. Phys Chem Chem Phys 85(8):693–700
106. Zagal JH, Gulppi M, Isaacs M, Cárdenas-Jirón G, Aguirre MJ (1998) Linear versus volcano correlations between electrocatalytic activity and redox and electronic properties of metallophthalocyanines. Electrochim Acta 44(8–9):1349–1357
107. Appleby AJ, Zagal JH (2011) Free energy relationships in electrochemistry: a history that started in 1935. J Solid State Electrochem 15(7–8):1811–1832
108. Cardenas-Jiron GI, Gulppi MA, Caro CA et al (2001) Reactivity of electrodes modified with substituted metallophthalocyanines. Correlations with redox potentials, Hammett parameters and donor–acceptor intermolecular hardness. Electrochim Acta 46(20–21):3227–3235
109. Sehlotho N, Nyokong T (2006) Effects of ring substituents on electrocatalytic activity of manganese phthalocyanines towards the reduction of molecular oxygen. J Electroanal Chem 595(2):161–167
110. Bedioui F, Griveau S, Nyokong T, Appleby AJ, Caro CA, Gulppi M, Ochoa G, Zagal JH (2007) Tuning the redox properties of metalloporphyrin- and metallophthalocyanine-based molecular electrodes for the highest electrocatalytic activity in the oxidation of thiols. Phys Chem Chem Phys 9(26):3383–3396
111. Zagal JH, Ponce I, Baez D, Venegas R, Pavez J, Paez M, Gulppi M (2012) A possible interpretation for the high catalytic activity of heat-treated metal-Nx/C macrocycles for O_2 reduction in terms of formal potentials of the catalyst. Electrochem Solid-State Lett 15(6): B1–B3
112. Jaouen F, Herranz J, Lefèvre M, Dodelet JP, Kramm UI, Herrmann I, Bogdanoff P, Maruyama J, Nagaoka T, Garsuch A, Dahn JR, Olson T, Pylypenko S, Atanassov P, Ustinov EA (2009) Cross-laboratory experimental study of non-noble-metal electrocatalysts for the oxygen reduction reaction. ACS Appl Mater Interfaces 1(8):1623–1639
113. Schlettwein D, Yoshida T (1998) Electrochemical reduction of substituted cobalt phthalocyanines adsorbed on graphite. J Electroanal Chem 441(1–2):139–146
114. Zagal JH, Cárdenas-Jirón GI (2000) Reactivity of immobilized cobalt phthalocyanines for the electroreduction of molecular oxygen in terms of molecular hardness. J Electroanal Chem 489(1–2):96–100
115. Cardenas-Jiron GI, Zagal JH (2001) Donor–acceptor intermolecular hardness on charge transfer reactions of substituted cobalt phthalocyanines. J Electroanal Chem 497(1–2):55–60
116. Zagal JH, Gulppi MA, Cárdenas-Jirón G (2000) Metal-centered redox chemistry of substituted cobalt phthalocyanines adsorbed on graphite and correlations with MO calculations and Hammett parameters. Electrocatalytic reduction of a disulfide. Polyhedron 19(22–23):2255–2260
117. Newton MD (1991) Quantum chemical probes of electron-transfer kinetics: the nature of donor-acceptor interactions. Chem Rev 91(5):767–792
118. Pearson RG (1986) Absolute electronegativity and hardness correlated with molecular orbital theory. Proc Natl Acad Sci 83(22):8440–8441
119. Parr RG, Pearson RG (1983) Absolute hardness: companion parameter to absolute electronegativity. J Am Chem Soc 105(26):7512–7516

120. Ulstrup J (1977) Catalysis of the electrochemical reduction of molecular dioxygen by metal phthalocyanines. J Electroanal Chem 79(1):191–197
121. Rosa A, Baerends EJ (1994) Metal-macrocycle interaction in phthalocyanines: density functional calculations of ground and excited states. Inorg Chem 33(3):584–595
122. Hipps KW, Lu X, Wang XD, Mazur U (1996) Metal d-orbital occupation-dependent images in the scanning tunneling microscopy of metal phthalocyanines. J Phys Chem 100(27):11207–11210
123. Jasinski R (1965) Cobalt phthalocyanine as a fuel cell cathode. J Electrochem Soc 112(5):526
124. Yeager E (1984) Electrocatalysis for O_2 reduction. Electrochim Acta 29(11):1527–1537
125. Hinnen C, Coowar F, Savy M (1989) Oxygen reduction in acid media investigations by electroreflectance on adsorbed iron phthalocyanine and naphthalocyanine layers. J Electroanal Chem 264(1–2):167–180
126. van den Ham D, Hinnen C, Magner G, Savy M (1987) Electrocatalytic oxygen reduction: the role of oxygen bridges as a structural factor in the activity of transition-metal phthalocyanines. J Phys Chem 91(18):4743–4748
127. Coowar F, Contamin O, Savy M, Scarbeck G (1988) Electrocatalysis of O_2 reduction to water in different acid media by iron naphthalocyanines. J Electroanal Chem 246(1):119–138
128. Elzing A, van der Putten A, Visscher W, Barendrecht E (1987) The cathodic reduction of oxygen at metal tetrasulfonato-phthalocyanines: influence of adsorption conditions on electrocatalysis. J Electroanal Chem 233(1–2):99–112
129. Fierro CA, Mohan M, Scherson DA (1990) *In situ* Moessbauer spectroscopy of a species irreversibly adsorbed on an electrode surface. Langmuir 6(8):1338–1342
130. Ouyang J, Shigehara K, Yamada A, Anson FC (1991) Hexadecafluoro- and octacyano phthalocyanines as electrocatalysts for the reduction of dioxygen. J Electroanal Chem 297(2):489–498
131. van der Putten A, Elzing A, Visscher W, Barendrecht E (1986) Oxygen reduction on vacuum-deposited and absorbed transition-metal phthalocyanine films. J Electroanal Chem 214(1–2):523–533
132. Song C, Zhang L, Zhang J (2006) Reversible one-electron electro-reduction of O_2 to produce a stable superoxide catalyzed by adsorbed Co(II) hexadecafluoro-phthalocyanine in aqueous alkaline solution. J Electroanal Chem 587(2):293–298
133. Kalvelage H, Mecklenburg A, Kunz U, Hoffmann U (2000) Electrochemical reduction of oxygen at pyrolyzed iron and cobalt N_4-chelates on carbon black supports. Chem Eng Technol 23(9):803–807
134. Coutanceau C, Rakotondrainibe A, Crouigneau P, Léger JM, Lamy C (1995) Spectroscopic investigations of polymer-modified electrodes containing cobalt phthalocyanine: application to the study of oxygen reduction at such electrodes. J Electroanal Chem 386(1–2):173–182
135. Elzing A, van der Putten A, Visscher W, Barendrecht E (1990) Spectroscopic measurements on metal tetrasulphonato-phthalocyanines. J Electroanal Chem 279(1–2):137–156
136. Phougat N, Vasudevan P (1997) Electrocatalytic activity of some metal phthalocyanine compounds for oxygen reduction in phosphoric acid. J Power Sources 69(1–2):161–163
137. Ponce I, Silva JF, Oñate R, Rezende MC, Páez MA, Pavez J, Zagal JH (2011) Enhanced catalytic activity of Fe phthalocyanines linked to Au(111) via conjugated self-assembled monolayers of aromatic thiols for O_2 reduction. Electrochem Commun 13(11):1182–1185
138. Sheldon RA, Kochi JK (1981) Metal-catalyzed oxidations of organic compounds. Academic, New York
139. van den Brink F, Barendrecht E, Visscher W (1980) The cathodic reduction of oxygen: A review with emphasis on macrocyclic organic metal complexes as electrocatalysts. Recl Trav Chim Pays-Bas 99:253–262
140. Elzing A, van der Putten A, Visscher W, Barendrecht E (1987) The mechanism of oxygen reduction at iron tetrasulfonato-phthalocyanine incorporated in polypyrrole. J Electroanal Chem 233(1–2):113–123

141. van den Brink F, Visscher W, Barendrecht E (1984) Electrocatalysis of cathodic oxygen reduction by metal phthalocyanines. Part III. Iron phthalocyanine as electrocatalyst: experimental part. J Electroanal Chem 172(1–2):301–325
142. Baranton S, Coutanceau C, Garnier E, Léger J-M (2006) How does α-FePc catalysts dispersed onto high specific surface carbon support work towards oxygen reduction reaction (orr)? J Electroanal Chem 590(1):100–110
143. Ikeda O, Fukuda H, Tamura H (1986) The effect of heat treatment on group VIIIB porphyrins as electrocatalysts in the cathodic reduction of oxygen. J Chem Soc Faraday Trans 1 82(5):1561
144. Anderson AB, Sidik RA (2004) Oxygen electroreduction on Fe II and Fe III coordinated to N_4 chelates. Reversible potentials for the intermediate steps from quantum theory. J Phys Chem B 108(16):5031–5035
145. Kadish KM, Smith KM, Guilard R (eds) (2003) The porphyrin handbook. Academic, San Diego, Calif, London
146. Magner G (1981) Effects of substitution of iron by molybdenum in the naphthalocyanine structures upon their electrocatalytic properties for O_2 reduction and evolution in alkaline media. J Electrochem Soc 128(8):1674
147. Baker R, Wilkinson D, Zhang J (2008) Electrocatalytic activity and stability of substituted iron phthalocyanines towards oxygen reduction evaluated at different temperatures. Electrochim Acta 53(23):6906–6919
148. Zhang L, Song C, Zhang J, Wang H, Wilkinson DP (2005) Temperature and pH dependence of oxygen reduction catalyzed by iron fluoroporphyrin adsorbed on a graphite electrode. J Electrochem Soc 152(12):A2421
149. Solomon EI, Sundaram UM, Machonkin TE (1996) Multicopper oxidases and oxygenases. Chem Rev 96(7):2563–2605
150. Mirica LM, Ottenwaelder X, Stack TD (2004) Structure and spectroscopy of copper-dioxygen complexes. Chem Rev 104(2):1013–1045
151. Schweiger H, Vayner E, Anderson AB (2005) Why is there such a small overpotential for O_2 electroreduction by copper laccase? Electrochem Solid-State Lett 8(11):A585
152. Gallaway J, Wheeldon I, Rincon R, Atanassov P, Banta S, Barton SC (2008) Oxygen-reducing enzyme cathodes produced from SLAC, a small laccase from *Streptomyces coelicolor*. Biosens Bioelectron 23(8):1229–1235
153. Vayner E, Schweiger H, Anderson AB (2007) Four-electron reduction of O_2 over multiple Cu–I centers: quantum theory. J Electroanal Chem 607(1–2):90–100
154. Sugiyama K, Aoki K (1989) Catalytic reactions of bis(1,10-phenanthroline) cuprous complex with hydrogen-peroxide at glassy-carbon and pyrolytic-graphite electrodes. J Electroanal Chem 262(1–2):211–219
155. Zagal JH, Paez C, Aguirre MJ, Garcia AM, Zamudio W (1993) Catalytic electroreduction of molecular-oxygen on Cu(II)bisdipyridyl and Cu(II)bisphenanthroline complexes adsorbed on a graphite electrode. Bol Soc Chil Quim 38(3):191–199
156. Zhang JJ, Anson FC (1993) Electrocatalysts for the reduction of O_2 and H_2O_2 based on complexes of Cu(II) with the strongly adsorbing 2,9-dimethyl-1,10-phenanthroline ligand. Electrochim Acta 38(16):2423–2429
157. Zhang JJ, Anson FC (1993) Complexes of Cu(II) with electroactive chelating ligands adsorbed on graphite-electrodes - Surface coordination chemistry and electrocatalysis. J Electroanal Chem 348(1–2):81–97
158. Lei YB, Anson FC (1994) Mechanistic aspects of the electroreduction of as catalyzed by copper-phenanthroline complexes adsorbed on graphite-electrodes. Inorg Chem 33(22):5003–5009
159. Lei YB, Anson FC (1995) Dynamics of the Coordination equilibria in solutions containing copper(II), copper(I), and 2,9-dimethyl-1,10-phenanthroline and their effect on the reduction of O_2 by Cu(I). Inorg Chem 34(5):1083–1089

160. Marques AL, Zhang JJ, Lever AB (1995) Poisoning effect of SCN^-, H_2S and HCN on the reduction of O_2 and H_2O_2 catalyzed by a 1:1 surface complex of Cu-1,10-phenanthroline adsorbed on graphite electrodes, and its possible application in chemical analysis. J Electroanal Chem 392(1–2):43–53
161. Losada J, del Peso I, Beyer L (2001) Electrochemical and spectroelectrochemical properties of copper(II) Schiff-base complexes. Inorg Chim Acta 321(1–2):107–115
162. Dias VL, Fernandes EN, da Silva LSM, Marques EP, Zhang J, Marques ALB (2005) Electrochemical reduction of oxygen and hydrogen peroxide catalyzed by a surface copper (II)-2,4,6-tris(2-piridil)-1,3,5-triazine complex adsorbed on a graphite electrode. J Power Sources 142(1–2):10–17
163. Weng YC, Fan FR, Bard AJ (2005) Combinatorial biomimetics. Optimization of a composition of copper(II) poly-L-histidine complex as an electrocatalyst for O_2 reduction by scanning electrochemical microscopy. J Am Chem Soc 127(50):17576–17577
164. Wang M, Xu X, Gao J, Jia N, Cheng Y (2006) Electrocatalytic reduction O_2 at pyrolytic graphite electrode modified by a novel copper(II) complex with 2-[bis(2-aminoethyl)amino] ethanol and imidazole ligands. Russ J Electrochem 42(8):878–881
165. Pichon C, Mialane P, Dolbecq A, Marrot J, Riviere E, Keita B, Nadjo SF (2007) Characterization and electrochemical properties of molecular icosanuclear and bidimensional hexanuclear Cu(II) azido polyoxometalates. Inorg Chem 46(13):5292–5301
166. Hermann A, Silva LS, Peixoto CRM, Oliveira ABD, Bordinhão J, Hörner M (2008) Electrochemical properties of $Cu_4[PhN_3C_6H_4N_3(H)Ph]_4(\mu\text{-}O)_2$, a tetranuclear Copper(II) complex with 1-phenyltriazenido-2-phenyltriazene-benzene as ligand. Eclet Quím 33(3):43–46
167. Thorum MS, Yadav J, Gewirth AA (2009) Oxygen reduction activity of a copper complex of 3,5-diamino-1,2,4-triazole supported on carbon black. Angew Chem Int Ed 48(1):165–167
168. McCrory CCL, Ottenwaelder X, Stack TDP, Chidsey CED (2007) Kinetic and mechanistic studies of the electrocatalytic reduction of O_2 to H_2O with mononuclear Cu complexes of substituted 1,10-phenanthrolines. J Phys Chem A 111(49):12641–12650
169. McCrory CCL, Devadoss A, Ottenwaelder X, Lowe RD, Stack TDP, Chidsey CED (2011) Electrocatalytic O_2 reduction by covalently immobilized mononuclear copper(I) complexes: evidence for a binuclear Cu_2O_2 intermediate. J Am Chem Soc 133(11):3696–3699
170. Zhang JJ, Anson FC (1992) Electrochemistry of the Cu(II) complex of 4,7-diphenyl-1,10-phenanthrolinedisulfonate adsorbed on graphite electrodes and its behavior as an electrocatalyst for the reduction of O_2 and H_2O_2. J Electroanal Chem 341(1–2):323–341
171. Masa J, Ozoemena K, Schuhmann ZJH (2012) Oxygen reduction reaction using N_4-metallomacrocyclic catalysts: fundamentals on rational catalyst design. J Porphyrins Phthalocyanines 16(7):761
172. Barton SC, Kim H, Binyamin G, Zhang Y, Heller A (2001) The "Wired" laccase cathode: high current density electroreduction of O2 to water at +0.7 V (NHE) at pH 5. J Am Chem Soc 123(24):5802–5803
173. Barton SC, Kim H, Binyamin G, Zhang Y, Heller A (2001) Electroreduction of O_2 to water on the "Wired" Laccase Cathode. J Phys Chem B 105(47):11917–11921
174. Soukharev V, Mano N, Heller A (2004) A four-electron O_2-electroreduction biocatalyst superior to platinum and a biofuel cell operating at 0.88 V. J Am Chem Soc 126(27):8368–8369
175. Ralph TR, Hogarth MP (2002) Catalysis for low temperature fuel cells Part I: The cathode challenges. Platinum Metals Rev 46(1):3–14
176. Hu X, Liu C, Wu Y, Zhang Z (2011) Structure–reactivity relationships of metalloporphyrin modified by ionic liquid and its analogue. J Phys Chem C 115(48):23913–23921
177. Masa J, Schilling T, Bron M, Schuhmann W (2011) Electrochemical synthesis of metal–polypyrrole composites and their activation for electrocatalytic reduction of oxygen by thermal treatment. Electrochim Acta 60:410–418

178. Xia W, Masa J, Bron M, Schuhmann W, Muhler M (2011) Highly active metal-free nitrogen-containing carbon catalysts for oxygen reduction synthesized by thermal treatment of polypyridine-carbon black mixtures. Electrochem Commun 13(6):593–596
179. Masa J, Bordoloi A, Muhler M, Schuhmann W, Xia W (2012) Enhanced electrocatalytic stability of platinum nanoparticles supported on a nitrogen-doped composite of carbon nanotubes and mesoporous titania under oxygen reduction conditions. ChemSusChem 5:523–525
180. Mittasch A, Frankenburg W (1950) Early studies of multicomponent catalysts. Adv Catal 2:81–104
181. Dembinska B, Kulesza PJ (2009) Multi-walled carbon nanotube-supported tungsten oxide-containing multifunctional hybrid electrocatalytic system for oxygen reduction in acid medium. Electrochim Acta 54(20):4682–4687
182. Baranton S, Coutanceau C, Roux C et al (2005) Oxygen reduction reaction in acid medium at iron phthalocyanine dispersed on high surface area carbon substrate: tolerance to methanol, stability and kinetics. J Electroanal Chem 577(2):223–234
183. Lu Y, Reddy R (2007) The electrochemical behavior of cobalt phthalocyanine/platinum as methanol-resistant oxygen-reduction electrocatalysts for DMFC. Electrochim Acta 52(7):2562–2569

Chapter 8
Heat-Treated Non-precious-Metal-Based Catalysts for Oxygen Reduction

Lior Elbaz, Gang Wu, and Piotr Zelenay

Abstract Non-precious metal catalysts have shown good activity towards oxygen reduction reaction, both in basic and acidic media. The use of NPMCs in fuel cells and metal–air batteries has been hampered by two main issues: the synthesis complexity, translating into a high fabrication cost, and by relatively low stability when compared to platinum-based catalysts, especially in acidic media. In order to overcome these issues, a new class of non-precious metal oxygen reduction catalysts was developed that involves heat treatment as a key step in the NPMC synthesis. This chapter provides a review of the progress in research on heat-treated non-precious metal catalysts of oxygen reduction since the early 1970s until today. The focus of this chapter is on the activity and morphology of the state-of-the-art heat-treated ORR catalysts and trends in the development of more active and durable materials.

8.1 Introduction

Since the discovery of their ability to catalyze the oxygen reduction reaction (ORR) [1] and up until today, there has been a continuous growth in the interest in macrocyclic compounds as reviewed in the Chap. 7 of this book. Researchers in various fields, from biology to physics and chemistry, have investigated the ORR mechanism and modified the macrocyclic structures to achieve better catalytic performance [2]. While very good catalytic activity was demonstrated under certain conditions [3, 4], mainly at room temperature and in neutral environment, the lack of stability under harsher acidic conditions and at elevated temperatures have made non-precious metal catalysts (NPMCs) for oxygen reduction less attractive for prominent technologies, such as fuel cells, in particular for the polymer electrolyte fuel cells (PEFCs) operating under acidic conditions ($pH < 1$) and at an average temperature of 80 °C.

L. Elbaz • G. Wu • P. Zelenay (✉)
Los Alamos National Laboratory, Los Alamos, NM 87545, USA
e-mail: zelenay@lanl.gov

M. Shao (ed.), *Electrocatalysis in Fuel Cells*, Lecture Notes in Energy 9,
DOI 10.1007/978-1-4471-4911-8_8,

In the case of macrocyclic compounds, such as porphyrins and phthalocyanines, it was concluded that the catalytic ORR sites are the transition metal themselves [5]. It was shown by Jahnke et al. that there is a clear dependence between the type of the metal center and the catalytic activity [1]. The stability of catalysts in this group depends on their ability to maintain their macrocyclic character. That character can be compromised in a reaction with a hydrogen peroxide, an intermediate product of ORR in acidic environment, which is capable of oxidizing and splitting the macrocyclic structure [6]. The stability of this family of catalysts also depends on their ability to resist the dissociation of the transition metal. Metals tend to easily dissociate in their reduced form, resulting in an inactive, protonated, metal-free macrocycle [7]. On top of these inherent stability issues, metalloporphyrins and metallo-phthalocyanines, especially the analogous biomimetic ones [8], are considered to be extremely hard to make because of a high number of the synthesis steps required. This translates into high manufacturing cost, outweighing the benefit of the low initial materials cost.

Over time, many variations of macrocyclic compounds were introduced in order to enhance catalytic activity and stability [9]. One of the more prominent paths taken in the design of such catalysts was based on heat-treating porphyrins and phthalocyanines. The work on heat-treated macrocyclic compounds started in the early 1970s by Jahnke et al. [10] and was followed by the work of Bagotzky [11] and by Wiesner and Fuhrmann [12, 13]. All three groups sought to activate phthalocyanines and porphyrins for oxygen reduction and showed improvements in both the activity and durability of catalysts following the heat treatment. Since then, the work on heat-treated non-precious-metal-based ORR catalysts has progressed in parallel to the research on non-heat-treated metallo-macrocyclic compounds and other transition metal complexes. While the heat treatment of these complexes was shown to increase the activity and stability of catalysts, it also resulted in a loss of their original structure [14] and formation of materials with new, usually poorly defined morphology, the nature of which typically depends on the heat-treatment temperature [15], gas atmosphere [16], and the type of carbon support used [17]. Those significant changes raised fundamental questions regarding the final catalyst structure and the nature of the active site, the two key parameters for the design of future catalysts.

In their extensive work, Jahnke et al. used different chelates to coordinate Co, Mn, Fe, Cu, and Ni. They showed that the most durable ORR catalysts involve Co–N_4 complexes [10]. In order to find inexpensive alternatives to the macrocyclic compounds, various research groups studied the synthesis routes for heat-treated transition metal complexes using less complex ligands, such as polyacrylonitrile [18], tetraazaannulene [19], and phenanthroline [20]. A significant breakthrough was made in the early 2000s by Dodelet et al. who were able to increase the activity of Fe–N–C compounds using two heat-treatment steps at different temperatures and in different gases [21]. While this new category of NPMCs showed ORR activity comparable to that of Pt-based catalysts, it lacked the durability of Pt [22], which became the main challenge for non-precious metal catalysts for oxygen reduction.

8.2 Heat-Treated Macrocyclic Compounds

Heat treatment of macrocyclic compounds was shown to dramatically increase their ORR catalytic properties. The important factors in the heat treatment of catalysts will be discussed in this section together with their effect on the ORR catalysis. Also discussed will be the catalyst structure. The majority of research in this field has focused on the macrocyclic complexes of transition metals, heat-treated in the presence of various carbons. That class of ORR catalysts will be addressed below.

8.2.1 Heat Treatment

8.2.1.1 Conditions

Throughout the years, the heat-treatment conditions for macrocyclic compounds were one of the most extensively studied parameters of NPMC synthesis. It was argued that the right selection of heat-treatment conditions could lead to significant improvements to both the activity and durability of resulting materials. In their first publication on heat-treated transition metal complexes, Jahnke et al. concluded that of the studied ligands (N_2, N_4, O_2, O_4, S_2, and S_4), N_4-ligand containing precursors, e.g., porphyrins and phthalocyanines, are most efficient in inducing the ORR activity [10]. Jahnke et al., as well as other authors, continued that research focusing predominantly on the optimization of heat-treatment conditions for macrocyclic compounds. The most important conditions included the following:

1. Temperature
2. Gas atmosphere
3. Duration

The temperature range used to heat-treat the precursors was at first relatively wide, from 300 to 1,000 °C. Wiesener et al. studied the effect of heat-treatment temperature on the ORR current density at catalysts derived from N_4 macrocycles at a potential of 0.70 V (vs. RHE) in 2.25 M H_2SO_4 (Fig. 8.1) [23]. They found that the optimum temperature for heat-treating cobalt tetraazaannulene (CoTAA) on activated carbons P33 and P33p was around 650 °C.

From that and other published work, it can be concluded that the optimum heat-treatment temperature (from 600 to 800 °C for macrocyclic compounds) and heat-treatment duration are highly dependent on the structure of the precursor and the nature of the transition metal. It can also be concluded that iron-based catalysts require higher temperature to achieve their maximum performance compared to cobalt-based catalysts with the same ligand.

The optimum heat-treatment temperatures to reach best ORR durability and optimum activity of NPMCs were found not to be the same, especially under acidic conditions. Maximum durability tends to be reached following heat treatment at temperatures by up to 300 °C higher than the temperatures yielding catalysts with the highest activity [23].

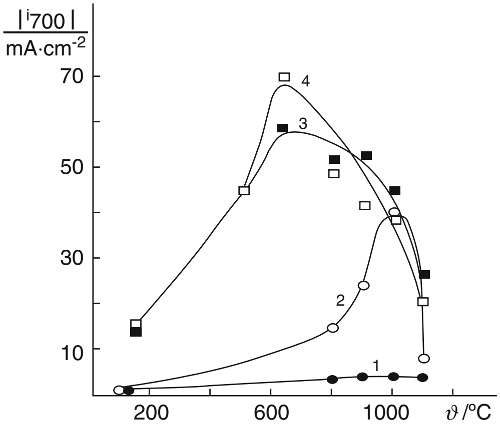

Fig. 8.1 Influence of the heat-treatment temperature on the ORR current at chelate-modified carbon electrodes measured at 0.70 V (vs. RHE). (1) H_2TAA on P33p-carbon support, (2) H_2TAA on P33-carbon support, (3) CoAA on P33p, and (4) CoTAA on P33. Heating rate 4 K min^{-1} (reprinted with permission from the *Journal of Electroanalytical Chemistry* [24])

The effect of the gaseous atmosphere was studied by Tarasevich and Radyuskina who concluded that under N_2, Ar, and He in the temperature range of 500–1,000 °C for different dwell times between 0.3 and 5.0 h, the activity and durability of the studied metalloporphyrins and metallo-phthalocyanines were similar [25]. This was a case for disagreement between different groups who observed dependence between the activity of heat-treated catalysts and the gas used during the heat treatment. For example, Dhar et al. showed the difference in the catalytic activity of heat-treated CoTAA under vacuum, N_2, Ar, and N [26]. They concluded that the most active ORR catalyst was obtained under vacuum with the following decrease in activity: vacuum $>$ N_2 $>$ Ar $>$ N (Fig. 8.2). Dodelet and his collaborators [27] showed that an iron tetra(methoxyphenyl) porphyrin is the most stable, but the least active when heat-treated in Ar, and that it becomes very active and loses its stability when treated in ammonia, an effect attributed to the concurrent increase in the microporous surface area, as well as the N and Fe surface content. The authors raised important questions about the catalyst design and optimum heat-treatment conditions for maximum stability and activity.

It can be concluded that the importance of the gas used during the synthesis is highly dependent on the type of precursor and carbon support employed in the heat treatment.

8.2.1.2 Precursors

One of the most important factors affecting the activity of non-heat-treated transition metal macrocyclic complexes is their structure, more specifically, the ligand, the substituents, and the metal center [28]. The role of those factors closely ties to the mechanism by which the complexes are activated and bind oxygen.

Although metallo-macrocycles are generally unlikely to maintain their original structure after the heat treatment [29], that original structure before the treatment is important as it often affects final distribution of atoms in the catalysts and its

Fig. 8.2 Steady-state current-potential curves in 4 N H_2SO_4 for adsorbed $CoTAABr_2$ on acetylene-black carbon, heat-treated at 500 °C for 30 min in various atmospheres: (1) vacuum, (2) nitrogen, (3) argon, and (4) nitrogen passed over heated Cu (reprinted with permission from *Electrochimica Acta* [26])

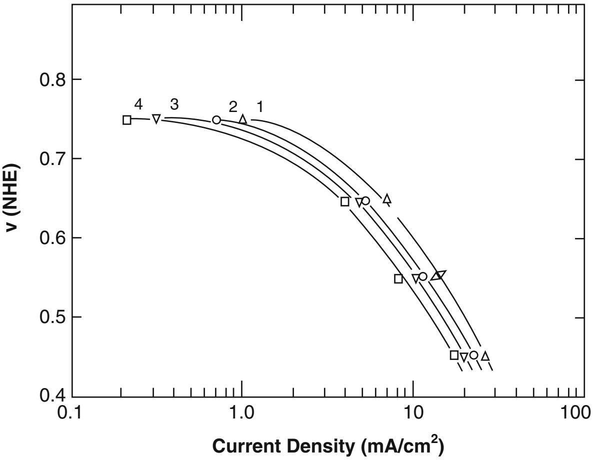

interaction with the carbon support. Van Veen et al. [30] studied 15 different porphyrins and phthalocyanines containing various metal centers and metal-free macrocycles (Fig. 8.3). Other nitrogen precursors, such as phthalocyanine/phenolic resin [31], aminoantipyrine [32], and corrole [33], have been explored in the NPMCs synthesis, showing improved activity and durability for the ORR. From those studies, it appears that heat-treating selected macrocycles improve their ORR catalytic activity and that substituent-dependent ORR activity trends are identical before and after the treatment regardless of the metal center. In general, the governing factors that apply to non-heat-treated transition metal macrocycles discussed in the previous chapter also apply to the heat-treated macrocyclic precursors in this chapter.

8.2.1.3 Metal Center

The ORR performance of NPMCs strongly depends on the transition metal used. In their extensive research, which included 9 metallo-phthalocyanines and 24 metal chelates, Beck et al. demonstrated very strong dependence of the ORR activity on the metal center [34]. The authors concluded that the activity of transition metal complexes decreases in the following order: Fe > Co > Ni > Cu ≅ Mn. In general, a consensus has by now been reached in the non-precious metal research community that iron and cobalt yield the most ORR-active catalysts among transition-metal-based macrocyclic compounds. Alt et al. explained that dependence using the molecular orbital (MO) theory [35]. They found that the $d_z{}^2$ orbital of the metal ion is most likely to bind the oxygen molecule and that an empty $d_z{}^2$ orbital favors the partial electron transition from the metal to the antibonding π^* orbitals of the oxygen during the formation of a chelate–oxygen complex. Thus, the emptier the

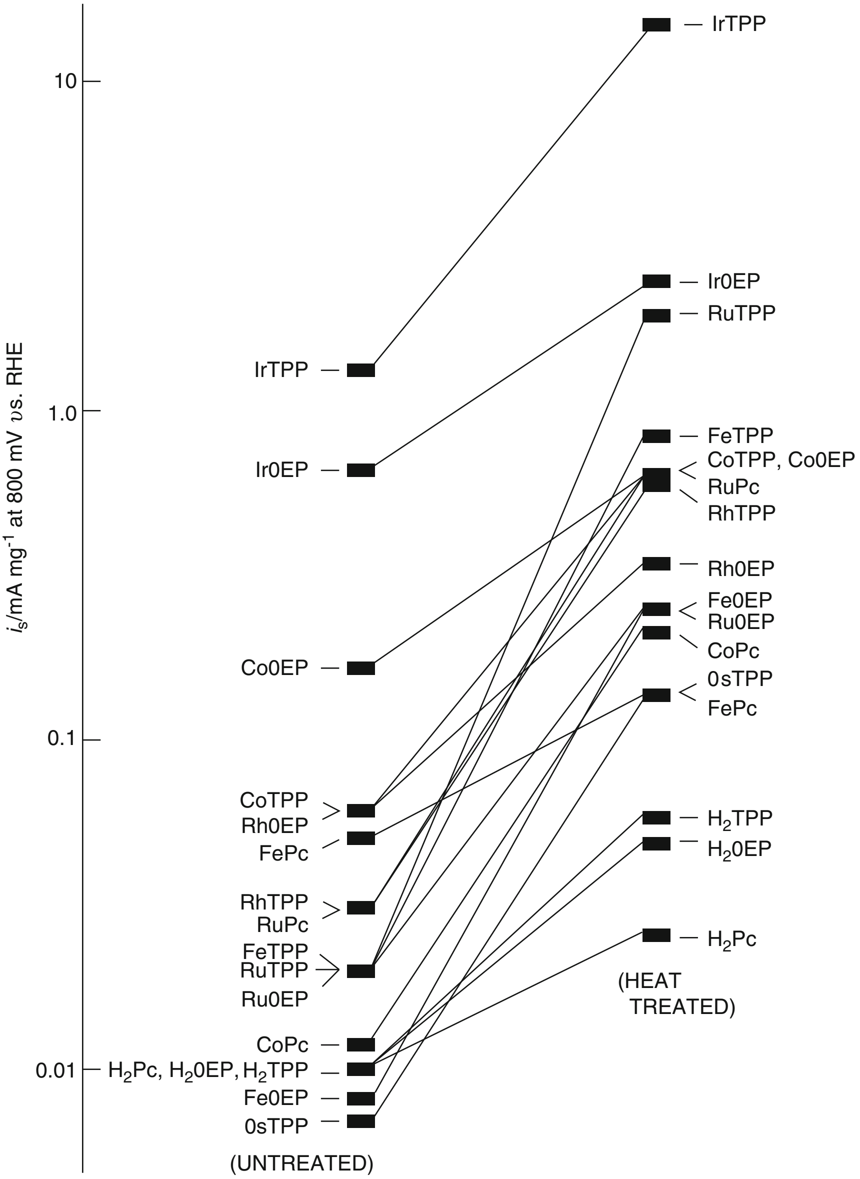

Fig. 8.3 ORR activity of various porphyrins and phthalocyanines before and after heat treatment in an inert gas atmosphere (reprinted with permission from the *Journal of the Chemical Society, Faraday Transactions I* [30])

$d_z{}^2$ orbital is, the more active is the transition metal complex in the ORR. The latter conclusion supports findings of the aforementioned study by Beck et al. Similar trends and explanation appear to hold true for heat-treated transition metal complexes [29].

8.2.2 Structure of Heat-Treated Macrocyclic ORR Catalysts

Although factors governing the synthesis of active and durable heat-treated NPMCs have been well documented in the scientific literature, the final catalyst structure is still not entirely understood, mainly due to the fact that most catalysts are synthesized in the presence of different carbon supports.

The presence of carbon makes it difficult to obtain a clear picture of the molecular structure of heat-treated macrocyclic compounds, even when the most sophisticated techniques are used. Van Veen et al. studied the structure of heat-treated transition metal macrocycles on carbon supports by a wide range of techniques, including Fourier transform infrared (FTIR), electron spin resonance spectroscopy (ESR), Mössbauer spectroscopy, X-ray photoelectron spectroscopy (XPS), extended X-ray absorption fine structure spectroscopy (EXAFS), X-ray diffraction (XRD), transmission electron microscopy (TEM), differential thermal analysis (DTA), thermogravimetric analysis (TGA), and mass spectroscopy [36, 37]. They found that the heat treatment leads to the formation of isolated metal sites in an axially symmetric environment, presumably created by the thermally modified ligand. These results led to a conclusion that thermal treatment does not cause the formation of catalytically active metallic particles. The results of that study also provided support for Fuhrhop's observation of a surface complex originating in a reaction between radicals formed at the metal complex and the carbon support [38]. Van Veen et al. postulated that during the decomposition of complexes in this family of compounds in the temperature range of 300–1,000 °C, the first part of the complex to react with the carbon surface are the ligand substituents, followed by the reaction of the rest of the macrocycle with the carbon support at higher temperatures (with the inner ring of the macrocycle postulated to retain some of its original structure). This leads to the formation of a range of surface complexes responsible for a continuous increase in stability with increasing temperature of the heat treatment.

Vallejos-Burgos et al. studied the structure and activity of a free-base phthalocyanine, Cu phthalocyanine, and Co phthalocyanine after heat-treating the compounds at different temperatures [39]. The structural changes that occurred during the heat treatment are summarized in Fig. 8.4. It is clear from that study that the structural evolution of the macrocycle and carbon support associated with a loss of nitrogen or changes in the microporosity of the support depend on the metal center.

A summary of the interesting research by Wiesener et al. on the loss of nitrogen at different heat-treatment temperatures is given in Table 8.1 [13, 24]. The authors observed a gradual decrease in the nitrogen mass in the catalysts with an increase in the heat-treatment temperature, from 3.05 wt% in the original sample to 1.05 wt% after the short-time heat treatment at 1,000 °C. The loss of nitrogen at 1,000 °C correlates well with a significant decrease in the ORR activity of the catalyst.

Many hypothetical structures of the heat-treated macrocyclic compounds have been proposed in the electrocatalysis literature to date. Most of those structures involve the formation of a covalent bond between the macrocycle and the carbon

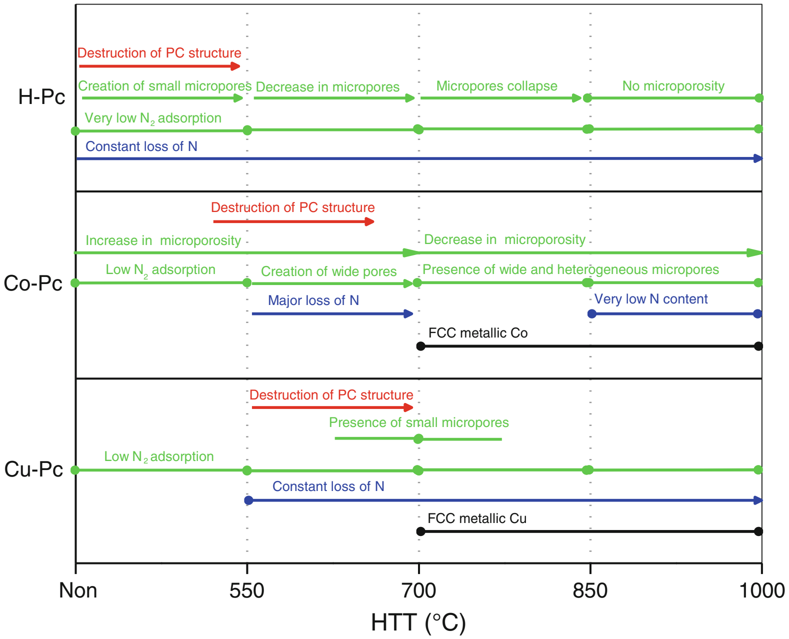

Fig. 8.4 A schematic representation of main structural changes occurring during the heat treatment of various phthalocyanine samples (reproduced from *Fuel* [39])

Table 8.1 Nitrogen content of heat-treated Co(II) dibenzotetraazaannulene on active carbon P33 [24]

Heat-treatment temperature (°C)	Heat-treatment time (h)	Nitrogen mass (%)
None	–	3.05
400	5	2.9
450	5	2.5
500	5	2.4
560	5	2.2
630	5	2.2
700	5	2.1
1,000	Short term	1.05

support [40]. In some cases it was shown that a portion of the macrocycle is imbedded in the support (Fig. 8.5) [41].

The real structure, or structures, of heat-treated ORR catalysts is yet to be revealed. The catalyst makeup is likely to strongly depend on the precursors used, with the structure of catalysts derived from different macrocycle compounds differing from one another due to such factors as the type of a macrocycle, substituent, carbon support, and the metal center. This is an intriguing subject of future research that promises to produce non-precious metal ORR catalysts with much improved activity and performance durability.

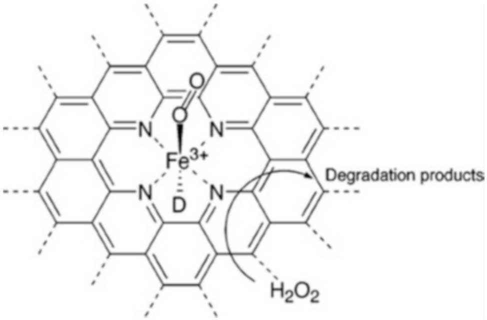

Fig. 8.5 Proposed model structure of the active site and ORR catalysis mechanism after a heat treatment of Fe tetramethoxyphenylporphyrin (FeTMPP) on a Black Pearls® support at 900 °C in Ar (reprinted with permission from the *Journal of Physical Chemistry B* [41])

8.3 Heat-Treated Non-macrocyclic Catalysts for ORR

In spite of a very significant progress achieved with heat-treated macrocyclic compounds as ORR catalysts since the early 1970s, the activity and durability of that family of catalysts are still insufficient for replacing platinum at the fuel cell cathode and in other applications. Furthermore, the complex structure of macrocyclic compounds makes their synthesis expensive and potentially noncompetitive with precious-metal-based catalysts also from the materials cost point of view. For those reasons, much effort has been invested by the electrocatalysis research community in recent years into finding less expensive and catalytically more active non-precious metal ORR catalysts that would not rely on macrocylic compounds as either catalysts or catalyst precursors. In the past decade, there has been a significant improvement both in the activity and of non-macrocyclic catalysts, expected to be manufactured at a fraction of the cost of their macrocyclic counterparts. In this section, we review the precursors, synthesis routes, and applications of this relatively new family of catalysts.

8.3.1 Precursors

Heat-treated transition metal–nitrogen–carbon (M–N–C) NPMCs can be divided into three main groups: (1) catalysts obtained from transition-metal-based macrocycles (discussed above); (2) catalysts derived from metal salts and gaseous nitrogen precursors, such as NH_3; and (3) catalysts synthesized from inorganic metal salts and simple nitrogen-containing molecules [42]. In this section, we will focus on NPMCs from group 3. This group of catalysts has received much attention since 2006, evidenced by a high number of published papers (Fig. 8.6).

Even though the heat treatment of virtually any mixture of nitrogen, metal, and carbon species can yield a material with some ORR activity, the selection of precursors, supports, and synthesis conditions plays a major role in obtaining materials with high activity and long-term durability required of practical catalysts [43, 44].

Fig. 8.6 Published papers associated with group 3 NPMCs from 2006 to 2011

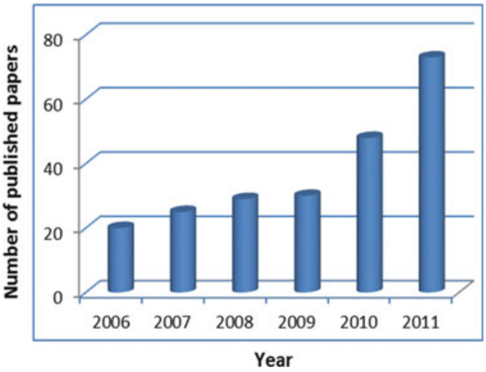

Fig. 8.7 Molecular structure of (**a**) acetonitrile and (**b**) cyanamide

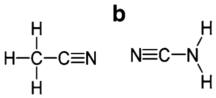

8.3.1.1 Nitrogen Precursors

According to previous research on nitrogen-doped carbons heat-treated at temperatures above 700 °C [45, 46], nitrogen atoms can replace atoms in the carbon lattice. It has been generally recognized that nitrogen-doped sites in graphitic carbon layers can act as reactive centers and enhance the ORR due to favorable morphology modification and high electron density induced by the nitrogen. The catalytic properties of doped N–C structures in M–N–C catalysts were found to be tunable through varying the catalyst synthesis conditions [43, 47]. In particular, nitrogen precursors used in the synthesis were found to be crucial to the formation of catalyst nanostructures. In this part, we divide nitrogen precursors into three different groups: (1) C≡N-based nonaromatic precursors, (2) C-N-based nonaromatic amine precursors, and (3) aromatic precursors.

C≡N-Based Nonaromatic Precursors

Acetonitrile and cyanamide are the most common nitrogen precursors containing C≡N bonds in the catalyst synthesis (Fig. 8.7).

Matter et al. heat-treated at 900 °C acetonitrile together with iron acetate salts supported on Vulcan [46]. The most active catalysts, containing significantly higher amount of the pyridinic nitrogen (as determined by XPS) were formed when Fe was added to the support before the heat treatment. The current-potential ORR polarization plots, obtained using 2 % Fe on Vulcan and heat-treated for 2 h at 900 °C, are shown in Fig. 8.8. Although the measured ORR activity is not as promising in this

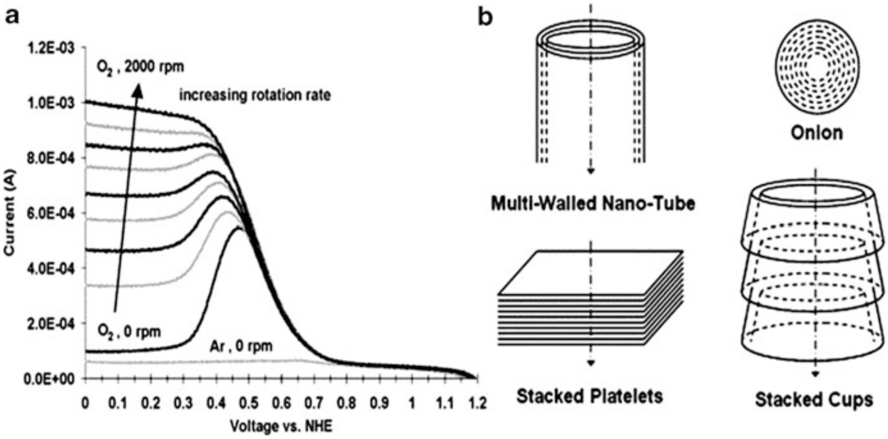

Fig. 8.8 (**a**) ORR activity of Fe catalyst derived from acetonitrile and (**b**) schematic diagrams of common carbon nanostructures demonstrating plane orientation relative to the central axis and resulting edge plane exposure (reprinted from ref. [46] with permission from Elsevier)

case as in some other cases [42], the results highlight the importance of in situ formed carbon nanostructures for the ORR active site formation. Different carbon nanostructures, such as tubes, fibers and onion-like carbon, were observed in the catalysts obtained via the decomposition of acetonitrile. The nanostructures were found to be rich in pyridinic nitrogen and exposed plane edges. As shown in Fig. 8.8, onion-like structures and tubes (especially longer ones) have mostly basal planes exposed, whereas carbon fibers with stacked platelets or cups have significant plane edge exposure. The enhanced catalytic activity of such structures is assumed to be associated with the increased plane-edge exposure in carbon nanostructures, marked by the pyridinic nitrogen.

Cyanamide (CM) was firstly explored at Los Alamos as a precursor of M–N–C oxygen reduction catalysts [48]. The most active catalyst, obtained following a heat treatment at 1,050 °C, showed very high activity relative to previously reported NPMCs, with an open circuit voltage (OCV) value of 1.0 V and a current density of 105 mA cm^{-2} at 0.80 V (*iR*-corrected) in H_2/O_2 fuel cell testing (Fig. 8.9). The reason for choosing cyanamide as a nitrogen precursor was that the compound had been known to act as precursor for graphitic C_3N_4 structures following high-temperature treatment [49]. Although the original motivation for the use of cyanamide was to increase the nitrogen content in the graphitized carbon structure, this was not the outcome. Instead, cyanamide was found to aid in the incorporation of sulfur from the iron-sulfate precursor into the carbon. It was also found that the decomposition of sulfate and evolution of SO_2 are greatly depressed in the presence of cyanamide. This was an indication that the interaction between cyanamide and sulfate (or sulfate-derived species) can stabilize sulfur in the sample, likely through

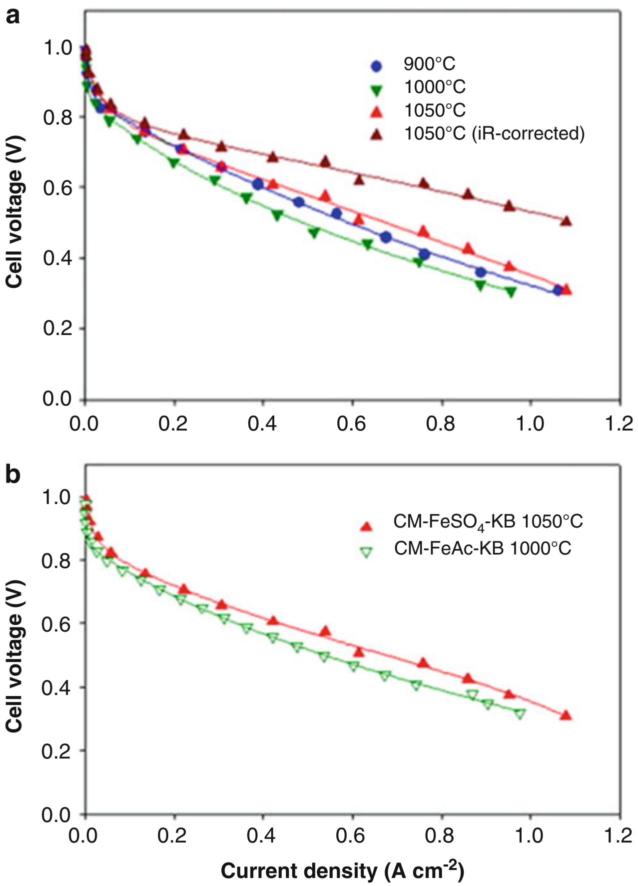

Fig. 8.9 (**a**) Fuel cell polarization plots recorded with CM–$FeSO_4$–KB ORR catalysts obtained at different heat-treatment temperatures; (**b**) fuel cell polarization plots comparison with CM–$FeSO_4$–Ketjenblack heat-treated at 1,050 °C and CM–FeAc–KB heat-treated at 1,000 °C. Nafion®117 membrane; anode: 30 psig H_2, 0.25 mg_{Pt} cm^{-2} (catalyzed cloth GDL, E-TEK); cathode: 30 psig O_2, non-precious catalyst loading 4.0 mg cm^{-2}; 100 % RH anode and cathode humidification; 300/500 standard mL per minute anode/cathode flow rates for H_2 and O_2, respectively; MEA surface area 5 cm^2 (reprinted from ref. [48] with permission from Elsevier)

the formation of C–S bonds. To further determine whether sulfur enhances the ORR activity of the CM-based catalyst, samples were prepared using Fe(II) acetate as the iron source instead of iron sulfate, thus avoiding any sulfur presence. The current density measured with these catalysts at high fuel cell voltages ($>$ 0.8 V) was found to be about half of the value measured with the catalyst prepared using the iron-sulfate precursor (Fig. 8.9b). This difference indicates that sulfur may be responsible for the improved ORR activity of CM-based catalysts.

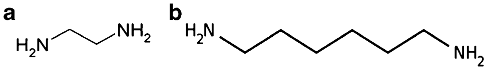

Fig. 8.10 Molecular structures of (**a**) ethylenediamine and (**b**) hexamethylenediamine

C–N-Based Nonaromatic Amine Precursors

Diamines have been one of the most efficient nitrogen precursors used in the NPMC synthesis to date due to their ability to coordinate transition metals and form complexes with four nitrogens (MN_4) [50]. The structures of ethylenediamine (EDA) and hexamethylenediamine (HDA) are shown in Fig. 8.10.

EDA has been used as a nitrogen precursor in the catalyst synthesis ever since it was first introduced by a University of South Carolina research group [50, 51]. Cobalt species were chelated by EDA, giving rise to CoN_4 structures, simpler than the traditional macrocyclic compounds. While the resulting Co–EDA catalyst exhibited improved activity compared to previous reports, it still suffered from poor four-electron selectivity [42]. It was found that a nitric-acid treatment and the resulting formation of quinone-like groups on the carbon surface were key to increasing the dispersion of the Co–EDA complex on supports by creating adsorption sites for the amine [51]. The CoFe–N chelate was then deposited on metal-free carbon-composite support leading to a catalyst with improved ORR activity and durability (Fig. 8.11) [50]. The carbon composite catalyst showed an onset potential for oxygen reduction as high as 0.87 V vs. RHE in H_2SO_4 solution and an H_2O_2 yield of less than 1 %. Current densities as high as 0.27 A cm^{-2} at 0.6 V and 2.3 A cm^{-2} at 0.2 V were demonstrated in fuel cell testing using a catalyst loading of 6.0 mg cm^{-2}. No significant performance decrease was observed for 480 h of continuous fuel cell operation. According to XPS analysis, all metal species were removed from the surface by chemical treatment in 0.5 M H_2SO_4. It was proposed that transition metals facilitate the incorporation of pyridinic and graphitic nitrogen groups into the carbon matrix during the pyrolysis, leading to the formation of catalytically active ORR sites [50].

It was found that precursors containing long hydrocarbon-chain amines resulted in higher ORR activity than short-chain precursors [45, 53]. Similarly to EDA, HDA is capable of coordinating transition metals, such as Co and Fe, to form an interlinked macromolecule. A variation in the Co-to-Fe ratio in the synthesis of the HDA-derived CoFe binary catalysts results in markedly different ORR activity and four-electron selectivity (Fig. 8.12). A binary CoFe(1:3)–N–C catalyst, synthesized with a Co-to-Fe ratio of 1:3, was found to have the most positive onset and half-wave potentials and a low hydrogen peroxide yields (2–3 %). In fuel cell testing, the binary CoFe catalyst performed noticeably better than an Fe-based catalyst, especially at fuel cell voltages lower than 0.80 V. Under these experimental conditions, the best performing catalyst was found to generate a current density of 0.05 A cm^{-2} at 0.8 V and power density as high as 0.42 W cm^{-2} [52].

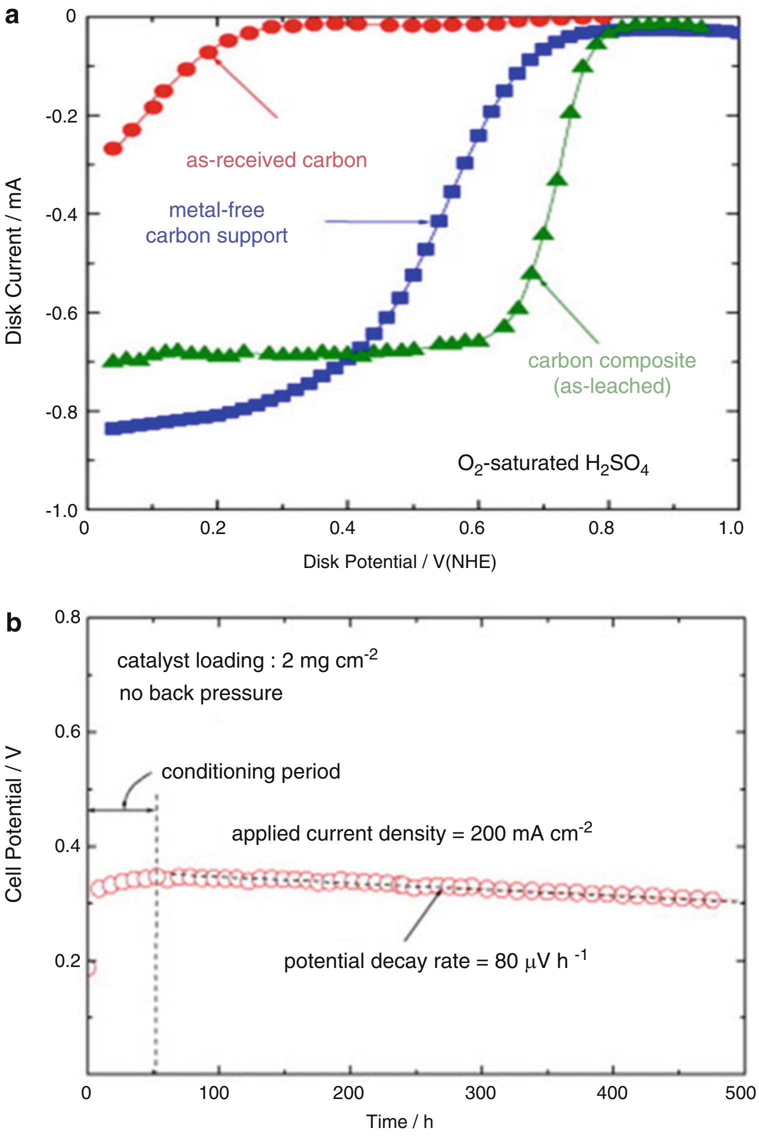

Fig. 8.11 ORR performance of an EDA-derived CoFe composite: (**a**) RDE activity in 0.5 M H_2SO_4 at room temperature and (**b**) fuel cell life tests at 80 °C at a constant current density of 200 mA cm^{-2} using H_2 and O_2 at no back pressure. Cathode catalyst loading: 2.0 mg cm^{-2} (reprinted from reference in [50] with permission from Elsevier)

Aromatic Precursors

It has long been believed that nitrogen–carbon precursors can undergo a metal-assisted graphitization during heat treatment [46]. Due to structural similarities between aromatic molecules and graphite, aromatic precursors of nitrogen have

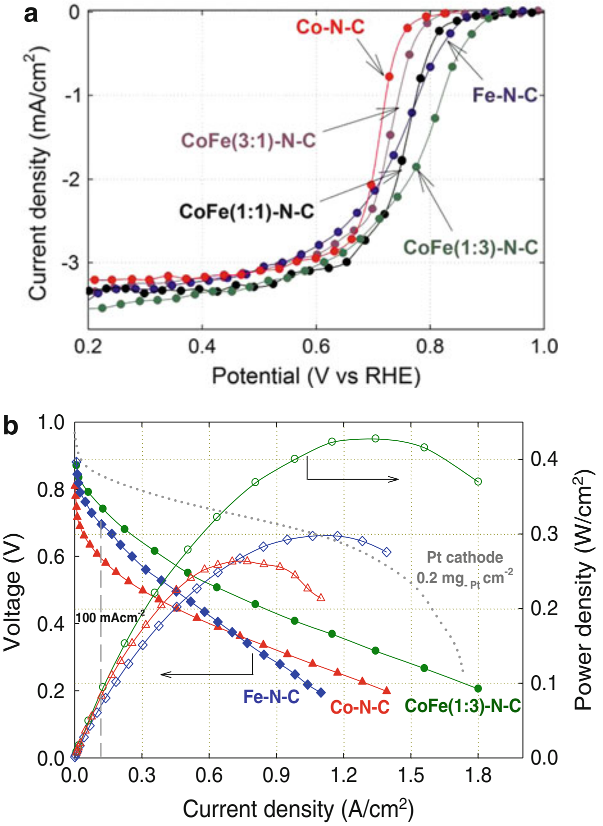

Fig. 8.12 ORR performance of CoFe–N–C NPMCs as a function of the Co-to-Fe ratio in the synthesis. (**a**) RDE measurement in 0.5 M H_2SO_4 at 25 °C and 900 rpm; catalyst loading: 0.6 mg cm^{-2}. (**b**) Fuel cell polarization plots in a H_2–O_2 cell; anode/cathode back pressure: 1.0 bar; cell temperature: 80 °C; anode: 0.25 mg_{Pt} cm^{-2}; membrane: Nafion® 212 (reprinted from ref. [52] with permission from Elsevier)

recently attracted much attention in the synthesis of NPMCs. Three aromatic precursors, nitroaniline [54], melamine [55], and polyaniline [56, 57], are shown in Fig. 8.13.

Researchers at 3M developed NPMCs by heat-treating polynitroaniline obtained via a metal-assisted polymerization of 4-nitroaniline [54]. A possible structure of the polymer derived from nitroaniline is depicted in Fig. 8.13a. The repeating unit in the polymer is quinoxaline, containing pyrazinic rather than pyridinic nitrogen [58]. The results showed that the polymerization of nitroaniline in the presence of certain anhydrous metal salts, followed by a thermal treatment, could create an NPMC with high ORR activity [54]. The nitroaniline-derived catalyst has an ORR onset potential as high as 0.94 V vs. RHE. The ORR activity is maintained throughout a broad linear Tafel region that extends over two orders of magnitude in current density, with a

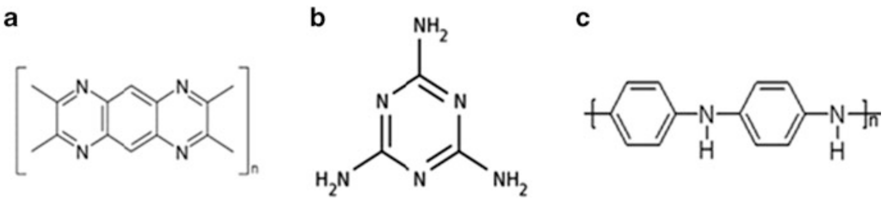

Fig. 8.13 Molecular structures for (**a**) polynitroaniline, (**b**) melamine, and (**c**) polyaniline

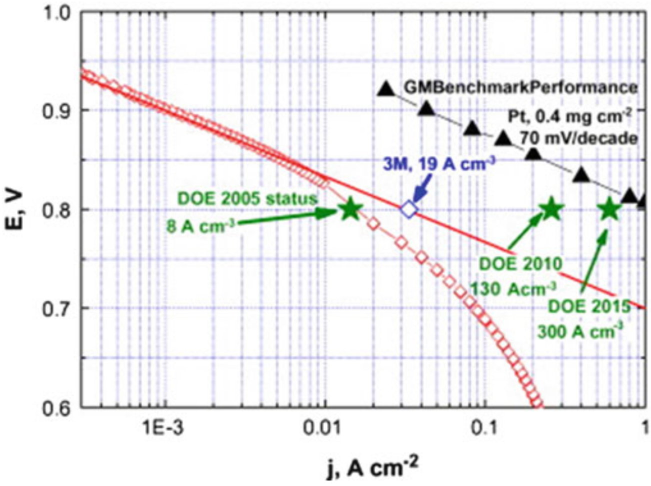

Fig. 8.14 Polarization curves of a 4-nitroaniline precursor-based catalyst. The straight-line slope is 70 mV dec^{-1}, measured at 80 °C with saturated hydrogen at the anode (180 sccm, 300 kPa backpressure) and oxygen at the cathode (335 sccm, 430 kPa backpressure) (reprinted from ref. [54] with permission from Elsevier). Pt reference catalyst data obtained from GM [59]

slope of 70 mV dec^{-1} (Fig. 8.14). The volumetric activity of the nitroaniline-derived catalyst is 19 A cm^{-3} at a fuel cell voltage of 0.8 V. Compared to macrocyclic compounds, the use of nitroaniline is a cost-effective method, amenable to scale-up. However, relatively high toxicity of nitroaniline is a drawback from the point of view of a large-scale synthesis of the catalyst.

Melamine, a trimer of cyanamide, with a 1,3,5-triazine skeleton containing 66 wt% of nitrogen, was first employed as a nitrogen precursor in NPMC synthesis by a Michigan State University group as a means of enhancing the content of doped nitrogen [55]. In a typical approach, solid melamine was ground with Ketjenblack 600JD carbon, containing adsorbed Fe(II) acetate, before it was heat-treated at 800 °C in nitrogen atmosphere. At the final stage of the synthesis, the catalyst was treated in 0.5 M sulfuric acid. The melamine-derived catalyst was found to have superior ORR activity to catalysts derived from other nitrogen precursors, such as bipyridine, pyrazine, and purine (Fig. 8.15) [55].

Fig. 8.15 Oxygen reduction plots at a thin-film RDE with NPMCs derived from various nitrogen precursors: (**a**) steady-state polarization plots, (**b**) *iR*- and mass-transfer corrected Tafel plots (reprinted from ref. [60] with permission from the Electrochemical Society)

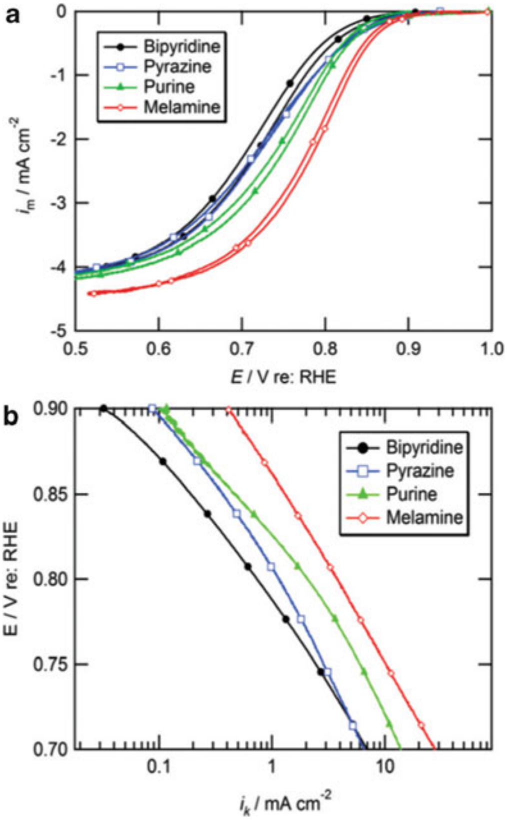

The volumetric current density measured with the melamine-based catalyst was 12.4 A cm^{-3} at 0.8 V. The high ORR activity of the melamine-derived NPMC was attributed to a threefold increase in the bulk nitrogen content. It is worth noting that a 33 % increase in the BET surface area was observed for the melamine-derived catalyst relative to the bipyridine-derived catalyst, suggesting that higher surface area might have contributed to the improved ORR activity. A 50 % increase in nitrogen retention was also observed for melamine-based catalysts, compared to a bipyridine-derived catalyst. However, the direct attribution of enhanced ORR activity of the melamine-based catalyst to the total nitrogen content should be done with care in the context of findings by other authors that ORR activity is not necessarily dependent on the amount of nitrogen content in the catalyst, but rather how nitrogen is incorporated into the carbon [43, 48]. A 100-h performance durability test was performed with the melamine-based catalyst at a fuel cell voltage of 0.5 V using pure H_2 and O_2. The performance loss was less than 10 %, a respectable result by the standards of most NPMCs [55].

Recently, polyaniline (PANI), an inexpensive and nontoxic aromatic polymer, was selected as a precursor of nitrogen and carbon in the NPMC synthesis at Los Alamos [56, 57]. Because of the similarity between the structures of PANI and graphite, the heat treatment of PANI was thought to facilitate the incorporation of

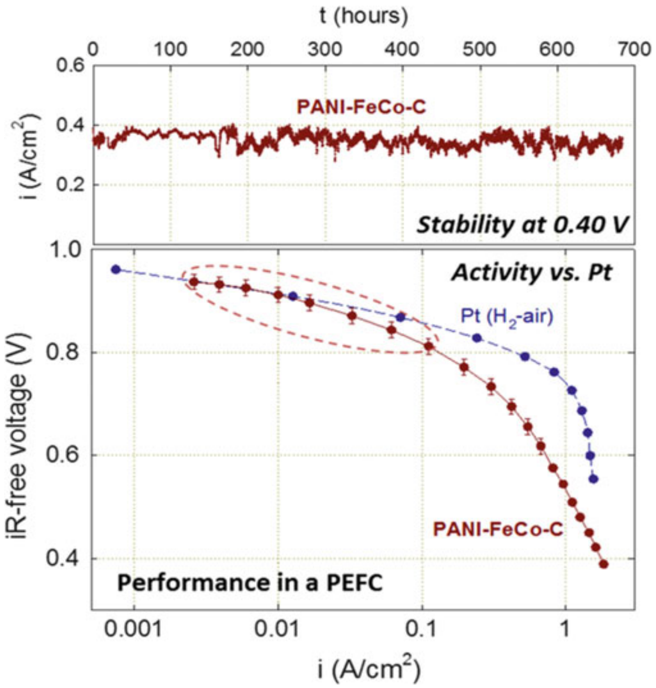

Fig. 8.16 *Bottom*: H_2–O_2 fuel cell polarization plots recorded with ~4 mg cm^{-2} of a PANI–FeCo–C catalyst in the cathode. Performance of an H_2–air fuel cell with a Pt cathode (0.2 mg$_{Pt}$ cm^{-2}) is shown for comparison. *Top*: Long-term performance stability test of the PANI–FeCo–C catalyst in a H_2–air fuel cell at a constant fuel cell voltage of 0.40 V. Anode and cathode gas pressure 2.8 bar; anode loading 0.25 mg$_{Pt}$ cm^{-2}; cell temperature 80 °C (reprinted from ref. [57] with permission from AAAS)

nitrogen-containing active sites into the partially graphitized carbon matrix in the presence of iron and/or cobalt. Furthermore, the use of such a polymer as a nitrogen precursor promised a more uniform distribution of nitrogen sites on the catalyst surface and possible increase in the active-site density. Heat-treated PANI-derived formulations appear to combine high ORR activity with high durability. The most active materials in the group were shown to catalyze the ORR at potentials within ~60 mV of those obtained with state-of-the-art carbon-supported Pt catalysts (Fig. 8.16) [57].

8.3.1.2 Transition Metal Precursors

While some metal-free nitrogen-doped carbon materials are at least to some degree capable of catalyzing the ORR on their own [61], an addition of transition metal(s) appears necessary for achieving high catalytic activity and improved durability of heat-treated NPMCs [62, 63]. The influence of different transition metal ions on

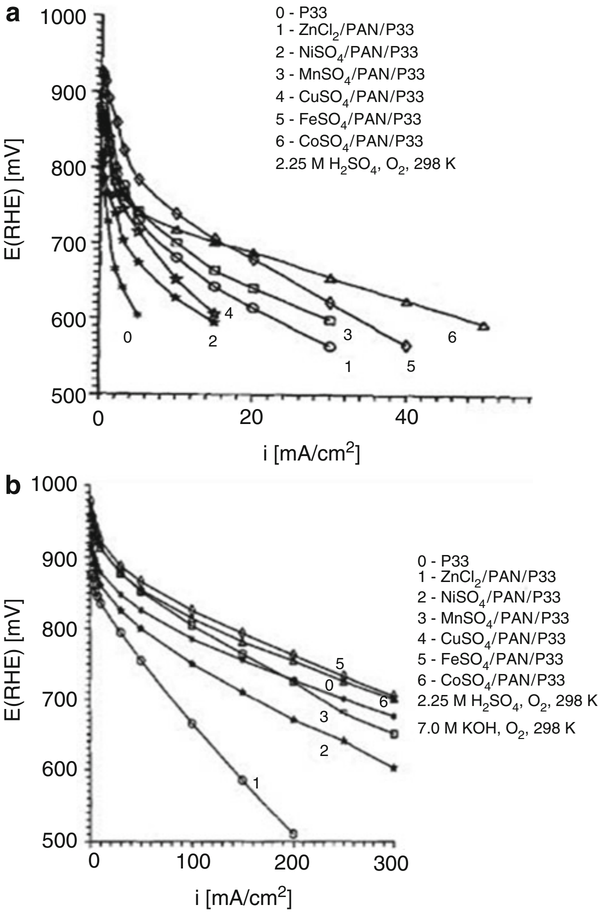

Fig. 8.17 ORR polarization for different catalysts in (**a**) 2.25 M H_2SO_4 and (**b**) 7.0 M KOH at 298 K (reprinted from ref. [64] with permission from Elsevier)

ORR activity of catalysts prepared using heat treatment of polyacrylonitrile was studied in both acid and alkaline solutions [64]. The results indicate that the nature of metallic center in the precursor plays a critical role in the ORR catalysis and can be tied to activity increase after the heat treatment. By now, there is strong experimental evidence that iron and cobalt lead to the formation of the active centers with the highest activity towards the catalysis of ORR regardless of the solution pH (Fig. 8.17). In acidic media, Fe-containing catalysts generally have more positive onset potential than Co catalysts, which suggests a higher intrinsic activity. The Fe-containing catalysts also exhibit the highest four-electron selectivity among the catalysts based on transition metals [64]. In alkaline media, Fe- and Co-based electrocatalysts often show similar activity [64].

While both Fe and Co are generally more efficient in forming active ORR sites than other non-precious metals [63], it is worth noting that the nature of the sites

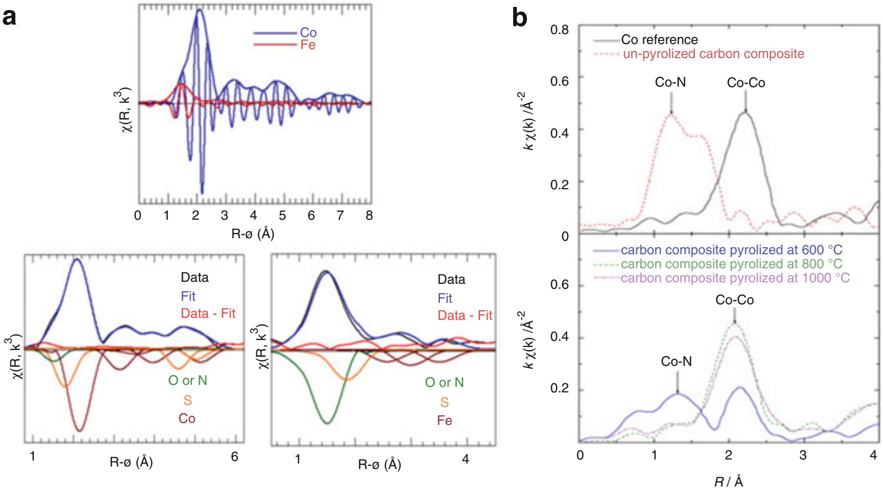

Fig. 8.18 EXAFS of (**a**) PANI–Fe–C and PANI–Co–C catalysts (reproduced from ref. [43] with permission of The Royal Society of Chemistry) and (**b**) EDA–Co–C catalyst (reprinted from ref. [50] with permission from Elsevier)

may be different for the two metals. The active sites generated in the presence of Co appear to have the onset ORR potential similar to that observed in metal-free nitrogen-doped carbon (N–C) catalysts, abundant in CN$_x$ groups (pyridinic, quaternary nitrogens) [50]. There is strong evidence that, unlike Co-derived species, Fe directly participates in the ORR, likely via the formation of Fe–N$_x$ type sites. Such sites have generally higher ORR activity than the metal-free sites formed in Co-based catalysts [43, 65, 66]. As follows from ex situ EXAFS studies of the coordination environment of transition metals in PANI-derived catalysts (Fig. 8.18a), the chemical environment of Fe and Co in such Fe- and Co-based catalysts is quite different. Fe–O/N coordination structures are dominant in Fe-based catalysts (signals from O and N in the local environment of the metal cannot be distinguished in EXAFS), while only small fractions of Co is bound to O/N.

In the case of EDA-derived Co catalysts (Fig. 8.18b), the EXAFS of not heat-treated sample shows the presence of one major peak around the R values of ca. 1.2 Å. That peak can be assigned the Co–N interactions. The Co–N peak weakens and the Co–Co peak becomes more apparent with an increase in the heat-treatment temperature. The CoN$_x$ chelate complexes decompose at high heat-treatment temperatures, 800 °C and higher, which results in the formation of metallic Co species. As a consequence, the Co–N structure is no longer dominant in both heat-treated PANI- and EDA-derived Co catalysts.

Electrochemical kinetic analysis yields different Tafel slope values for Co–N–C (~59 mV dec^{-1}) and Fe–N–C (~87 mV dec^{-1}) catalysts [52, 57], attesting to different ORR mechanism in the case of the two metals. Based on the Tafel slope analysis for the ORR on Pt catalysts by Coutanceau et al. [67], the diffusion of adsorbed oxygen intermediates during the ORR is a likely the rate-determining step

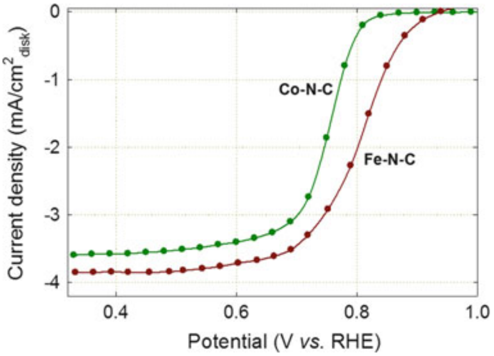

Fig. 8.19 Steady-state ORR polarization plots recorded at an RDE with PANI-derived Co- and Fe-based ORR catalysts in 0.5 M H_2SO_4 at 25 °C and at a rotation rate of 900 rpm (reproduced from ref. [43] by permission of The Royal Society of Chemistry)

on the Co–N–C catalyst. More complicated ORR mechanism on Fe–N–C catalysts is possible, involving both intermediate migration and charge transfer in the rate-determining step [68].

Regardless of the nitrogen precursor used, Fe–N–C catalysts have higher content of quaternary nitrogen compared to Co–N–C catalysts, indicating that nitrogen atoms favor doping at the interior rather than at the edges of the graphene layers in Fe-based catalysts [43, 52]. Generally, the ratio of pyridinic and quaternary nitrogens is expected to reach a steady state during the heat treatment of carbon-containing nitrogen groups [45]. The addition of Fe seems to facilitate the formation of quaternary nitrogen. The differences in the chemical and physical state of the active ORR sites are likely responsible for the lower ORR activity of the Co-based catalysts than Fe-based catalysts in acid media. The disparity in the ORR activity of PANI-derived Co- and Fe-based catalysts in the RDE testing is shown in Fig. 8.19.

Although the intrinsic activity of Co-based catalysts is lower than that of Fe-based catalysts, the use of Co usually leads to more graphitic nanostructures [43, 52], enhancing the electronic conductivity and corrosion resistance. In order to simultaneously take advantage of the apparent high ORR activity of the Fe-based catalysts and better stability of Co-based materials, binary CoFe catalysts were synthesized at Los Alamos. Enhanced activity and durability were indeed demonstrated with EDA–CoFe–C [50], HDA–CoFe–C [52], and PANI–FeCo–C [57] catalysts.

8.3.2 Synthesis Conditions

8.3.2.1 Heat Treatment

The active ORR sites in M–N–C catalysts are believed to be formed during the heat-treatment step, with the resulting activity being strongly dependent on the treatment temperature [42]. The optimum heat-treatment temperature depends on the nitrogen

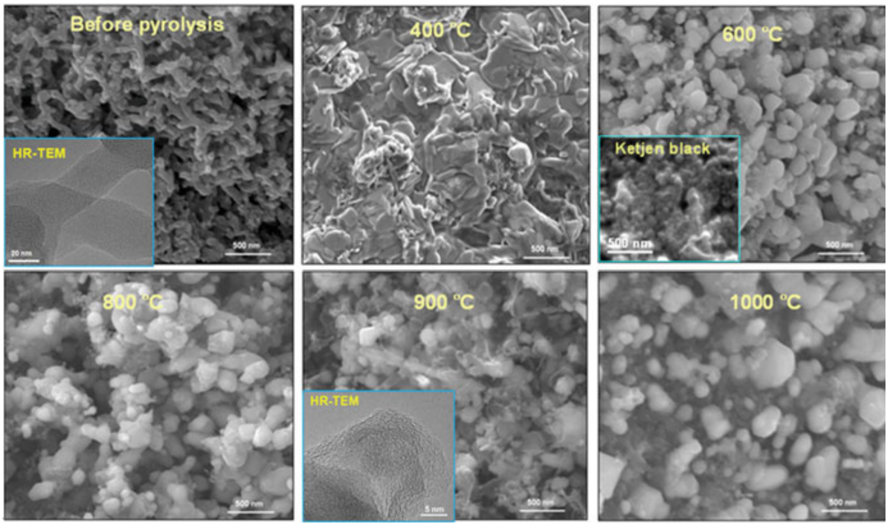

Fig. 8.20 SEM images of PANI–Fe–C catalyst in their final form (after the second heat treatment [43]) as a function of the heat-treatment temperature. Scale bar for all SEM images is 500 nm; scale bar for the HR–TEM inset in the "Before pyrolysis" image is 20 nm; scale bar in the "900 °C" image is 5 nm (reproduced from ref. [43] by permission of The Royal Society of Chemistry)

and transition metal precursors used [22, 42]. It typically falls in the 800–1,100 °C range, sufficient for nitrogen doping into the (partially) graphitized carbon structure. Higher heat-treatment temperatures result in a significant decrease in the number of nitrogen functionalities and reduction in the surface area. For example, the ORR activity of PANI-derived Fe–N–C catalysts has been found to gradually increase with the heat-treatment temperature in the 400–900 °C temperature range and decrease at higher temperatures. The type of carbon nanostructures and catalyst morphology formed during heat treatment at different temperatures may be the factors determining the catalyst performance.

As shown in Fig. 8.20 for PANI-derived Fe–N–C catalysts, the characteristic PANI nanofibers gradually disappear as the heat-treatment temperature increases to 400 °C and the spherical particles begin to form at 600 °C [43]. A higher degree of graphitization is observed at 900 °C, resulting in the formation of graphitic shells often covering sulfide-rich particles (cf. TEM images in Fig. 8.18). Following heat treatment at even higher temperatures, the catalyst morphology becomes highly nonuniform, the particles agglomerate reaching sizes much larger than those in the carbon black originally used in the synthesis, and the surface area significantly decreases. These changes in the carbon structure and morphology, together with their impact on the catalyst ORR performance, point to the importance of the metal-catalyzed transformation of the precursors into new carbon forms in NPMCs.

The effect of heat-treatment temperature on the ORR activity and selectivity of M–N–C catalysts was studied with physical characterization techniques [43]. A correlation between the ORR performance and the BET surface area of a

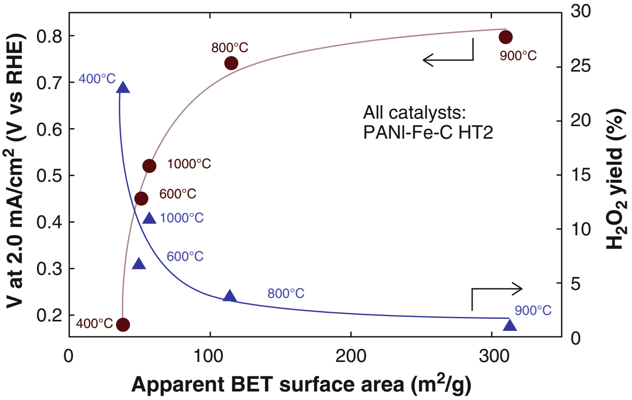

Fig. 8.21 Dependence of the ORR activity and H_2O_2 yield on the BET surface area of a PANI–Fe–C catalyst heat-treated at temperatures ranging from 400 to 1,000 °C (reproduced from ref. [43] by permission of The Royal Society of Chemistry)

PANI–Fe–C catalyst is shown in Fig. 8.21. The surface area increases from ~40 $m^2\ g^{-1}$ for the catalyst heat-treated at 400 °C to ~300 $m^2\ g^{-1}$ for the catalyst treated at 900 °C, before dropping to ~60 $m^2\ g^{-1}$ for the catalyst heat-treated at 1,000 °C [43].

Also dependent on the heat-treatment temperature are the content and relative ratios of different nitrogen functionalities in M–N–C catalysts. An increase in the heat-treatment temperature from 600 to 1,000 °C leads to a decrease in the total nitrogen content but without a significant change in the ORR activity [43]. Those changes are accompanied by an increase in the ratio of quaternary to pyridinic nitrogen [43, 60], suggesting that the ORR activity may not be dependent on the total amount of incorporated nitrogen but on how nitrogen is incorporated into doped nitrogen–carbon hybrid nanostructures. A similar trend was found for Co-based catalysts and TiO_2-supported Fe catalysts [60, 69]. Although pyridinic nitrogen has been often linked to the oxygen reduction activity of NPMC catalysts [46], the quaternary nitrogen content and C–N_x structure distribution, reflected by the ratio of the quaternary to pyridinic nitrogen, appear to play an important role, too [66]. In some cases, an increase in the heat-treatment temperature leads to a decrease in the total nitrogen content and increase in ORR activity. Presently, there is no clear correlation between the absolute content of quaternary or pyridinic nitrogen and the associated active-site density [43].

8.3.2.2 Post-treatment

While ORR active sites are formed during the first heat treatment of NPMC precursors [42], the post-treatment, including the acid leach and the second heat treatment in neutral gas atmosphere (N_2), was shown to be important for the final performance of non-precious metal catalysts [43]. The acid leach results in much

Fig. 8.22 Steady-state ORR polarization plots for PANI–Fe–C catalyst after the first heat treatment at 900 °C (HT1), after the acid leach (AL), and after the second heat treatment at 900 °C (HT2). RDE data in 0.5 M H_2SO_4 at 25 °C. Disk rotation rate: 900 rpm (reproduced from ref. [43] by permission of The Royal Society of Chemistry)

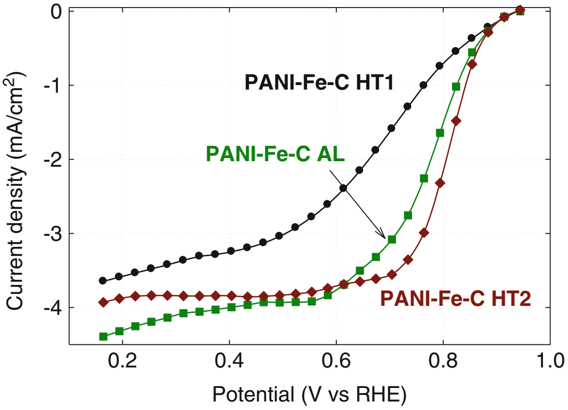

higher ORR activity, thanks to the removal of unstable and unreactive phases from the porous catalyst, which likely leads to an exposure of additional active sites [56]. In the case of a PANI-derived catalyst in Fig. 8.22, the acid leach does not affect the onset ORR potential, indicating no change to the active site. The second heat treatment (after the acid leach) results in further ORR performance improvement. Once again, the onset ORR potential does not change. This implies that neither the acid leach nor the second heat treatment influence the type of active sites present in the catalyst.

It is worth noting that the second heat treatment at 900 °C results in a decrease in the BET surface area (390 vs. 315 $m^2\ g^{-1}$) [43], implying that an increase in the active-site density during the second heat treatment likely offsets the surface area loss. Catalysts with much enhanced ORR activity after the second heat treatment were also demonstrated by Koslowski et al. [70]. The use of reactive gases, especially NH_3, during the second heat treatment was required to generate very significant ORR activity, as previously shown by Fournier et al. [71].

8.3.3 Structure–Property Correlation

M–N–C catalysts are obtained by simultaneously heat-treating precursors of nitrogen, carbon, and transition metal(s) at 700–1,000 °C. The activity and durability of these catalysts greatly depend on the selection of precursors and synthesis chemistry and correlate quite well with the catalyst nanostructure. Although no rational design of active and durable M–N–C catalysts based on a rigorous description of the ORR active site can yet be proposed, some guiding information for the synthesis of future NPMCs is available. It first and foremost stems from the understanding of the effect of nitrogen doping and in situ graphitization of carbonaceous materials in the catalysts.

Various types of nitrogen functionalities, in particular pyridinic and quaternary nitrogen, can be viewed as an n-type dopant of carbon in M–N–C catalysts that can assist in the formation of nanostructures and donate electrons to the carbon [46].

The N–C groups likely behave as one kind of ORR active sites. At the same time, as already stated above, the ORR activity is not governed by the total amount of nitrogen imbedded into the carbon but depends more on how the nitrogen is incorporated into the nitrogen–carbon hybrid nanostructures [43]. The nature of N–C groups in M–N–C catalysts can be controlled by tuning the synthesis conditions, usually aimed at maximizing catalytic activity [43]. Regardless of the nitrogen precursor used, XPS data indicate a higher content of the quaternary nitrogen in Fe–N–C catalysts than in Co–N–C catalysts. This indicates that, in the presence of Fe, nitrogen atoms are likely to be also incorporated in the interior rather than at the edges of the graphene layer.

Apart from possibly participating in the active site, the transition metal in M–N–C catalysts appears to be linked to the formation of new carbon structures by catalyzing graphitization of nitrogen–carbon precursors [46]. The highly graphitic carbon nanostructures may serve as a matrix for the ORR-active nitrogen and/or metal moieties. NPMC research to date suggests that the presence of graphitized carbon phase in some ORR catalysts may play a role in enhancing their stability. Also, the formation of different carbon nanostructures strongly depends on the type of nitrogen precursor, transition metal, heat-treatment temperature, and support used in the catalysts synthesis [43, 52, 60, 72], which can all be correlated to the catalyst performance. Compared to catalysts obtained from other nitrogen precursors, in situ formed nitrogen-doped graphene sheets are particularly abundant in the PANI–Co–C catalyst [57], the effect that may be responsible for an enhanced catalytic activity of the catalyst. Graphene-sheet structures were found not to be as common in Co-based catalysts synthesized using other nitrogen–carbon precursors, such as EDA [50], HDA [52], and cyanamide [48]. The morphology of the HDA–Co–C catalyst is dominated by carbon nanostructures different from graphene sheets, e.g., onion-like carbon nanoshells, which are not particularly ORR active. Well-defined graphitized carbon shells surrounding metal-rich particles were also observed in catalysts derived from Fe(III) tetramethoxyphenyl porphyrin chloride (FeTMPP-Cl), at a relatively high heat-treatment temperature of 1,000 °C. The graphite-shell formation was correlated to an increase in the open cell potential of the catalysts in oxygen-saturated solutions [73]. The significant morphological differences between Fe- and Co-based catalysts possibly attest to the strong effect of the transition metal precursor selection on carbon/nitrogen structures during the heat treatment. It seems that Co is a more effective catalyst of the carbonization process at high temperatures, leading to highly graphitic carbon structures [43]. Although Co appears to facilitate the formation of graphitized carbon structures, potentially helping the catalyst performance, the Co-based catalysts are generally less ORR-active in acid media than the Fe-based ones. This is probably due to the difference in the nature of the ORR active sites formed in the presence of different transition metals. Binary-metal catalysts, involving both Co and Fe, seem to benefit from the unique Co-induced graphene-rich morphology and highly active sites, created in the presence and/or participation of Fe. That unique combination of the two functions has led to catalysts with high ORR activity and, at the same time, improved stability [42].

Carbon nanostructures ex situ introduced into the NPMC may also play a role in improving catalytic activity and durability. Very recently, a highly active and durable NPMC was prepared based on nanotube–graphene (NT–G) complexes treated in NH_3 at 900 °C [74]. The abundance of edges and defect sites was claimed to be responsible for the high ORR activity. The high degree of graphitization of carbon nanotubes, the exfoliation of the outer walls, and the presence of graphene flakes in NT–G could impart high oxidative corrosion resistance of the catalytic sites. The NT–G catalyst showed a significant loss in activity on exposure to cyanide anions, suggesting that high ORR activity stems from iron-containing catalytic sites. Aberration-corrected scanning transmission electron microscopy (STEM) and electron energy loss spectrum (EELS) mapping techniques on the atomic scale revealed the presence of iron atoms on the edges of graphene sheets in close proximity to nitrogen species [74].

8.3.4 Beyond Standard PEFC Cathodes

8.3.4.1 Alkaline Fuel Cells

Alkaline fuel cells present several potential advantages over their acidic counterparts, dominating low-temperature fuel cell applications today. Main advantages include performance improvements and cost reduction, both associated with the use of NPMCs.

Thanks to the -59 mV change in the potential per every pH unit, the operation potential of an ORR catalyst is expected to be by ca. -0.83 V lower in a 1.0 M solution of a strong base than in 1.0 M solution of a strong acid. Such a potential shift impacts the double-layer structure and the electric field at the electrode–electrolyte interface, altering the adsorption strength of neutral species [76]. Decreased anionic adsorption in alkaline media is expected to help the kinetics of electrocatalytic reactions, including the ORR [77]. While improvements in the electrocatalysis can be significant, the better materials stability afforded by the use of alkaline electrolytes is even more important. In particular, a wide variety of NPMCs have shown comparable corrosion resistance in alkaline media to that of precious metals, which makes them particularly suitable for alkaline fuel cells [76].

The presence of nitrogen-doped graphitic carbon has been considered necessary for an efficient multi-electron transfer in the ORR catalysis in alkaline media [78]. An EDA-derived binary CoFe catalyst, heat-treated at 900 °C and acid-leached in 0.5 M H_2SO_4 at 80 °C, was successfully demonstrated in an anion exchange membrane fuel cell (AEMFC) at the University of South Carolina, using an A201 membrane (Tokuyama Corporation, Japan), composed of a hydrocarbon main chain and quaternary ammonium groups as ion-exchange sites [75]. In a fuel cell test, the OCVs were found to be 0.97 and 1.04 V for the EDA–CoFe–C and Pt/C catalysts, respectively. The corresponding maximum power densities were measured at 177 and 196 mW cm^{-2} (Fig. 8.23) [75]. At high potentials, the performance of EDA–CoFe–C was slightly lower than that of Pt/C. At intermediate potentials, both catalysts showed

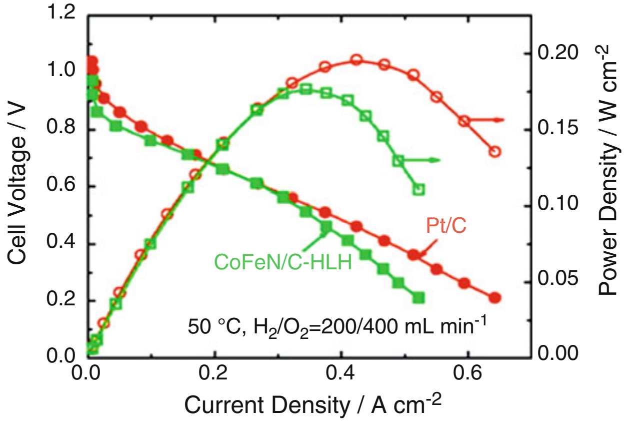

Fig. 8.23 Performance of an H_2–O_2 AEMFC with EDA–CoFe–C and Pt/C cathodes at 50 °C. Cathode catalyst loadings: 4 mg cm^{-2} for EDA–CoFe–C and 0.4 mg$_{Pt}$ cm^{-2} for Pt/C. Anode and cathode gases humidified at 50 °C. Gas flow rates: 200 mL min^{-1} (H_2) and 400 mL min^{-1} (O_2). The A201 membrane thickness 28 μm; ion-exchange capacity 1.8 mmol g^{-1}; conductivity 42 mS cm^{-1} (reprinted from ref. [75] with permission from Elsevier)

very similar activity. The lower performance of EDA–CoFe–C at low potentials may be attributed to high mass transfer and/or ionic resistance in the cathode, caused by a high catalyst loading and considerable thickness of the electrode.

The ORR performance of three different PANI-derived catalysts in an alkaline electrolyte is shown in Fig. 8.24 [79]. The best performing catalyst, PANI–Co–C, containing a large number of Co_9S_8 particles surrounded by nitrogen-doped graphene sheets, shows the activity and performance stability superior to that of a Pt/C reference catalyst. Oxygen is effectively reduced at that catalyst to OH^- in a four-electron reaction mechanism.

8.3.4.2 Methanol Tolerance

Methanol (MeOH) crossover from the anode to the cathode in the direct methanol fuel cell (DMFC) is responsible for significant depolarization of the Pt cathode catalyst. Compared to Pt-based catalysts, NPMCs are poor oxidation catalysts, of methanol oxidation in particular, which makes them highly methanol-tolerant. As shown in Fig. 8.25, the ORR activity of a PANI–Fe–C catalyst in a sulfuric acid solution is virtually independent of the methanol content, up to 5.0 M in MeOH concentration. A significant performance loss is only observed in 17 M MeOH solution (~1:1 water-to-methanol molar ratio), a solution that can no longer be considered aqueous. The changes to oxygen solubility and diffusivity, as well as to the double-layer dielectric environment, are all likely to impact the ORR mechanism and kinetics, which may not be associated with the electrochemical oxidation of methanol at the catalyst surface. Based on the ORR polarization plots recorded at

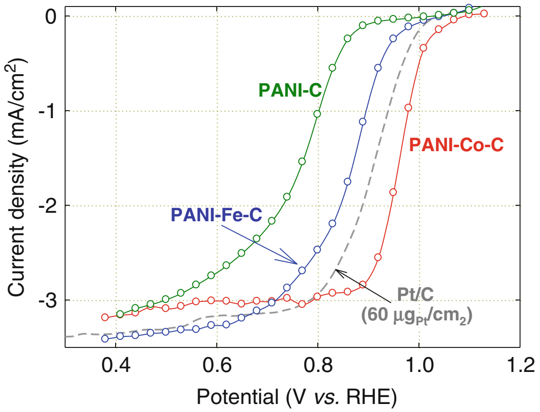

Fig. 8.24 Steady-state ORR polarization plots recorded with three PANI-derived and Pt/C reference catalysts in 0.1 M KOH electrolyte at 25 °C. Polarization data recorded after 1,000 durability cycles in a potential range from 0.6 to 1.0 V vs. RHE in an N_2-saturated solution. RDE rotation rate: 900 rpm (reprinted from ref. [79] with permission from the Electrochemical Society)

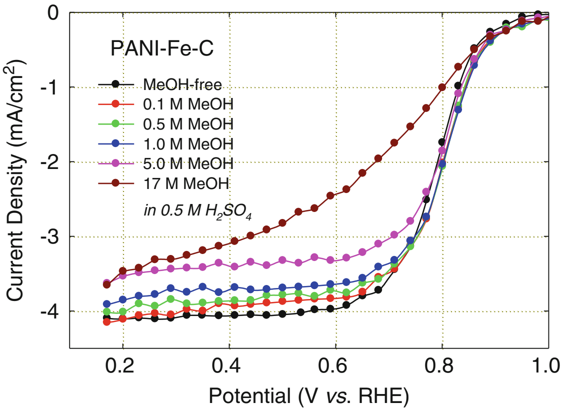

Fig. 8.25 Steady-state ORR polarization plots recorded with a PANI–Fe–C catalyst at an RDE in 0.5 M H_2SO_4 electrolyte at 25 °C and at a rotation speed of 900 rpm as a function of methanol concentration

lower methanol concentrations, the PANI–Fe–C catalyst should be viewed as a potential methanol-tolerant replacement for Pt at the DMFC cathode.

High methanol tolerance of an NPMC was also demonstrated with a heat-treated CoTMPP catalyst [80].

8.3.4.3 Anion Tolerance

A high-temperature (HT) PEFC operating with phosphoric-acid-doped polybenzimidazole (PBI) membrane has several potential advantages over the low-temperature PEFCs utilizing either perfluorosulfonic acid or hydrocarbon membranes. The advantages include faster ORR kinetics at elevated temperatures (150–200 °C), improved CO tolerance, and an ease of the water and heat management [81]. However, the ORR activity of the state-of-the-art Pt catalysts is significantly reduced in HT-PEFCs due to severe poisoning of the catalyst by chemisorbed phosphate ions ($H_2PO_4^-$ and HPO_4^{2-}).

Fig. 8.26 Steady-state ORR polarization plots recorded with (**a**) PANI–Fe(30 wt %)–KJ and (**b**) Pt/C catalyst in 0.5 M H_2SO_4 electrolyte at 25 °C as a function of concentrations of H_3PO_4. RDE rotation rate: 900 rpm

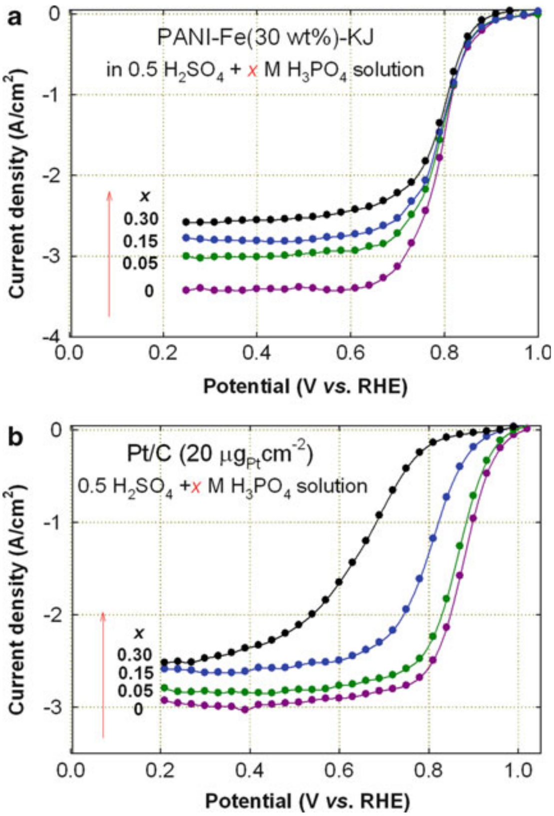

Unlike Pt and Pt alloys, NPMCs do not suffer from the specific adsorption of anions. As shown in Fig. 8.26a, the ORR performance of a PANI–Fe–C catalyst in the kinetic range of the steady-state RDE polarization curves is virtually independent of the solution concentration of H_3PO_4. In the case of a Pt/C catalyst (Fig. 8.26b), a continuous ORR activity loss is observed with an increase in H_3PO_4 concentration due to the chemisorption of phosphate ions. Thanks to their resistance to anions (true also of (bi)sulfate in sulfuric acid solutions), NPMCs represent an attractive alternative to Pt-based catalysts at the HT-PEFC cathode.

8.4 Conclusions

Heat-treated non-precious metal catalysts, synthesized from earth-abundant elements, are capable of catalyzing the ORR and efficiently generating electricity from fuels via a direct electrochemical conversion. Carbon–nitrogen precursors, supports, and in situ formed graphitized carbon play an important role in the catalyst performance.

Advanced catalyst synthesis is likely to focus in the future on (a) novel nitrogen precursors, (b) optimization of the content of transition metal(s) (Fe, Co, and possibly other metals), (c) precursor ratios, (d) functionalization of the catalyst surface (e.g., by NH_3, CO_2, and N_2 treatment), (e) fine-tuning of the heat-treatment conditions (temperature, heating rate, treatment duration, gas atmosphere), and (f) the effect of post-treatment (acid leach, additional heat treatments, etc.). The interaction between the metal and precursors of carbon and nitrogen during the heat treatment will likely be controlled more precisely in the future. The knowledge gained will be used to formulate chemical and morphological requirements for catalysts.

The major challenge of non-precious metal electrocatalysis of oxygen reduction reaction continues to be the lack of knowledge of the active catalytic sites and reaction mechanisms. The difficulties in the identification of the active sites are augmented by the virtual absence of effective NPMC characterization tools for direct probing of the surface of heat-treated catalysts. Further progress in the development of NPMCs will likely depend on the ability to characterize and understand the source(s) of the activity of the catalysts that have been already developed and are under development today.

References

1. Jahnke H, Schoenborn M (1969) Cathodic reduction of oxygen on phthalocyanine-carbon catalysts. Presses Acad Eur: 60–65
2. Kadish KM, Smith KM, Guilard R (eds) (2000) The porphyrin handbook, vol 1, Synthesis and organic chemistry. Academic, Boston
3. Collman JP, Denisevich P, Konai Y, Marrocco M, Koval C, Anson FC (1980) Electrode catalysis of the four-electron reduction of oxygen to water by dicobalt face-to-face porphyrins. J Am Chem Soc 102(19):6027–6036
4. Boulatov R, Collman JP, Shiryaeva IM, Sunderland CJ (2002) Functional analogues of the dioxygen reduction site in cytochrome oxidase: mechanistic aspects and possible effects of CuB. J Am Chem Soc 124:11923–11935
5. Jahnke H, Schoenborn M, Zimmermann G (1973) N4 chelates as catalysts in fuel cells. Thieme: 71–89
6. Berezin BD (1962) Metal phthalocyanines in solution. VI. Effect of the nature of the central ion on the stability of the macroring of phthalocyanine in sulfuric acid solutions. Zh Fiz Khim 36:494–501
7. Tarasevich MR, Radyushkina KA, Andruseva SI (1977) Electrocatalysis of oxygen reduction on organic metallic complexes. Bioelectrochem Bioenerg 4:18–29
8. Collman JP, Ghosh S (2010) Recent applications of a synthetic model of cytochrome c oxidase: beyond functional modeling. Inorg Chem 49:5798–5810
9. Kadish KM, Smith KM, Guilard R (2000) The porphyrin handbook, vol 6, Applications: past, present and future. Academic, New York
10. Jahnke H, Schoenborn M, Zimmermann G (1974) Transition metal chelates as catalysts for fuel cell reactions. Electrochem Soc: 303–318
11. Bagotskii VS, Tarasevich MR, Levina OA, Radyushkina KA, Andruseva SI (1977) Electrocatalysis of the reduction of oxygen on metal chelates in an acid electrolyte. Dokl Akad Nauk SSSR 233:889–891

12. Fuhrmann A, Wiesener K, Iliev I, Gamburzev S, Kaisheva A (1980) Characterization of heat-treated electrocatalytically active tetramethoxyphenylporphyrinatocobalt(II). J Power Sources 6:69–81
13. Wiesener K, Fuhrmann A (1980) Use of tetramethoxyphenylporphyrinatocobalt(II) and its pyrolysis products as catalysts for cathodic oxygen reduction in acidic fuel cells. Z Phys Chem 261:411–424
14. Weng LT, Bertrand P, Lalande G, Dodelet JP (1994) Charaterization of electrocatalysts for oxygen reduction by ToF SIMS. Proceedings of the Int Conf on Sec Ion Mass Spec, Wiley: 442–445
15. Ramaswamy N, Mukerjee S (2010) Electrocatalysis of oxygen reduction on non-precious metallic centers at high pH environments. ECS Trans 33:1777–1785
16. Charreteur F, Jaouen F, Dodelet J-P (2009) Iron porphyrin-based cathode catalysts for PEM fuel cells: influence of pyrolysis gas on activity and stability. Electrochim Acta 54:6622–6630
17. Medard C, Lefevre M, Dodelet JP, Jaouen F, Lindbergh G (2006) Oxygen reduction by Fe-based catalysts in PEM fuel cell conditions: activity and selectivity of the catalysts obtained with two Fe precursors and various carbon supports. Electrochim Acta 51:3202–3213
18. Gupta S, Tryk D, Bae I, Aldred W, Yeager E (1989) Heat-treated polyacrylonitrile-based catalysts for oxygen electroreduction. J Appl Electrochem 19:19–27
19. Yamana M, Darby R, Dhar HP, White RE (1983) Electrodeposition of cobalt tetraazaannulene on graphite electrodes. J Electroanal Chem Interfacial Electrochem 152:261–268
20. Shigehara K, Anson FC (1982) Catalysis of the reduction of dioxygen to water at graphite electrodes coated with two transition metal catalysts acting in series. J Electroanal Chem Interfacial Electrochem 132:107–118
21. Lefèvre M, Proietti E, Jaouen F, Dodelet J-P (2009) Iron-based catalysts with improved oxygen reduction activity in polymer electrolyte fuel cells. Science 324(5923):71–74
22. Chen Z, Higgins D, Yu A, Zhang L, Zhang J (2011) A review on non-precious metal electrocatalysts for PEM fuel cells. Energy Environ Sci 4(9):3167–3192
23. Wiesener K, Ohms D, Neumann V, Franke R (1989) N_4 macrocycles as electrocatalysts for the cathodic reduction of oxygen. Mater Chem Phys 22(3–4):457–461
24. Franke R, Ohms D, Wiesener K (1989) Investigation of the influence of thermal treatment on the properties of carbon materials modified by N_4-chelates for the reduction of oxygen in acidic media. J Electroanal Chem 260(1):63–68
25. Radyushkina KA, Tarasevich MR (1986) Electrocatalytic properties of pyropolymers based on N_4 complexes. Elektrokhimiya 22:1155–1170
26. Dhar HP, Darby R, Young VY, White RE (1985) The effect of heat treatment atmospheres on the electrocatalytic activity of cobalt tetraazaannulenes: preliminary results. Electrochim Acta 30(4):423–429
27. Meng H, Larouche N, Lefevre M, Jaouen F, Stansfield B, Dodelet J-P (2010) Iron porphyrin-based cathode catalysts for polymer electrolyte membrane fuel cells: effect of NH_3 and Ar mixtures as pyrolysis gases on catalytic activity and stability. Electrochim Acta 55:6450–6461
28. Kadish KM, Smith KM, Guilard R (eds) (2000) The porphyrin handbook, vol 9, Database of redox potentials and binding constants. Academic, New York
29. Jahnke H, Schonborn M, Zimmermann G (1976) Organic dyestuffs as catalysts for fuel cells. Top Curr Chem 61:133–181
30. van Veen JAR, van Baar JF, Kroese KJ (1981) Effect of heat treatment on the performance of carbon-supported transition-metal chelates in the electrochemical reduction of oxygen. J Chem Soc Faraday Trans 1: Pys Chem in Cond Phases 77(11):2827–2843
31. Nabae Y, Moriya S, Matsubayashi K, Lyth SM, Malon M, Wu L, Islam NM, Koshigoe Y, Kuroki S, Kakimoto M-a, Miyata S, Ozaki J-i (2010) The role of Fe species in the pyrolysis of Fe phthalocyanine and phenolic resin for preparation of carbon-based cathode catalysts. Carbon 48(9):2613–2624
32. Serov A, Robson MH, Halevi B, Artyushkova K, Atanassov P (2012) Highly active and durable templated non-PGM cathode catalysts derived from iron and aminoantipyrine. Electrochem Commun 22(1):53–56

33. Huang H-C, Shown I, Chang S-T, Hsu H-C, Du H-Y, Kuo M-C, Wong K-T, Wang S-F, Wang C-H, Chen L-C, Chen K-H (2012) Pyrolyzed cobalt corrole as a potential non-precious catalyst for fuel cells. Adv Func Mater 22(16):3500–3508
34. Beck F, Dammert W, Heiss J, Hiller H, Polster R (1973) Electrocatalysis of the oxygen cathode by metal-phthalocyanines and -dibenzotetraazaannulenes. Z Naturforsch Teil A 28: 1009–1021
35. Alt H, Binder H, Sandstede G (1973) Mechanism of the electrocatalytic reduction of oxygen on metal chelates. J Catal 28:8–19
36. Van Veen JAR, Van Baar JF, Kroese KJ (1981) Effect of heat treatment on the performance of carbon-supported transition metal chelates in the electrochemical reduction of oxygen. J Chem Soc Faraday Trans 1(77):2827–2843
37. Van Wingerden B, Van Veen JAR, Mensch CTJ (1988) An extended x-ray absorption fine structure study of heat-treated cobalt porphyrin catalysts supported on active carbon. J Chem Soc Faraday Trans 1(84):65–74
38. Fuhrhop JH (1975) Irreversible reactions at the porphyrin periphery (excluding photochemistry). Porphyrins Metalloporphyrins: 625–666
39. Vallejos-Burgos F, Utsumi S, Hattori Y, García X, Gordon AL, Kanoh H, Kaneko K, Radovic LR (2012) Pyrolyzed phthalocyanines as surrogate carbon catalysts: initial insights into oxygen-transfer mechanisms. Fuel 99(1):106–117
40. Yamanaka I, Onizawa T, Suzuki H, Hanaizumi N, Nishimura N, Takenaka S (2012) Study of direct synthesis of hydrogen peroxide acid solutions at a heat-treated MnCl-porphyrin/activated carbon cathode from H_2 and O_2. J Phys Chem C 116:4572–4583
41. Schulenburg H, Stankov S, Schünemann V, Radnik J, Dorbandt I, Fiechter S, Bogdanoff P, Tributsch H (2003) Catalysts for the oxygen reduction from heat-treated iron(III) tetramethoxyphenylporphyrin chloride: structure and stability of active sites. J Phys Chem B 107(34): 9034–9041
42. Jaouen F, Proietti E, Lefevre M, Chenitz R, Dodelet J-P, Wu G, Chung HT, Johnston CM, Zelenay P (2011) Recent advances in non-precious metal catalysis for oxygen-reduction reaction in polymer electrolyte fuel cells. Energy Environ Sci 4(1):114–130
43. Wu G, Johnston CM, Mack NH, Artyushkova K, Ferrandon M, Nelson M, Lezama-Pacheco JS, Conradson SD, More KL, Myers DJ, Zelenay P (2011) Synthesis-structure-performance correlation for polyaniline-Me-C non-precious metal cathode catalysts for oxygen reduction in fuel cells. J Mater Chem 21(30):11392–11405
44. Jaouen F, Herranz J, Lefèvre M, Dodelet J-P, Kramm UI, Herrmann I, Bogdanoff P, Maruyama J, Nagaoka T, Garsuch A, Dahn JR, Olson T, Pylypenko S, Atanassov P, Ustinov EA (2009) Cross-laboratory experimental study of non-noble-metal electrocatalysts for the oxygen reduction reaction. ACS Appl Mater Interfaces 1(8):1623–1639
45. Pels JR, Kapteijn F, Moulijn JA, Zhu Q, Thomas KM (1995) Evolution of nitrogen functionalities in carbonaceous materials during pyrolysis. Carbon 33(11):1641–1653
46. Matter PH, Zhang L, Ozkan US (2006) The role of nanostructure in nitrogen-containing carbon catalysts for the oxygen reduction reaction. J Catal 239(1):83–96
47. Biddinger EJ, von Deak D, Ozkan US (2009) Nitrogen-containing carbon nanostructures as oxygen-reduction catalysts. Top Catal 52(11):1566–1574
48. Chung HT, Johnston CM, Artyushkova K, Ferrandon M, Myers DJ, Zelenay P (2010) Cyanamide-derived non-precious metal catalyst for oxygen reduction. Electrochem Commun 12(12):1792–1795
49. Chung HT, Johnston CM, Zelenay P (2009) Synthesis and evaluation of heat-treated, cyanamide-derived non-precious catalysts for oxygen reduction. ECS Trans 25(1):485–492
50. Nallathambi V, Lee J-W, Kumaraguru SP, Wu G, Popov BN (2008) Development of high performance carbon composite catalyst for oxygen reduction reaction in PEM Proton Exchange Membrane fuel cells. J Power Sources 183(1):34–42
51. Subramanian NP, Kumaraguru SP, Colon-Mercado H, Kim H, Popov BN, Black T, Chen DA (2006) Studies on Co-based catalysts supported on modified carbon substrates for PEMFC cathodes. J Power Sources 157(1):56–63

52. Wu G, Dai CS, Wang DL, Li DY, Li N (2010) Nitrogen-doped magnetic onion-like carbon as support for Pt particles in a hybrid cathode catalyst for fuel cells. J Mater Chem 20(15): 3059–3068
53. Wu G, Nelson M, Ma SG, Meng H, Cui GF, Shen PK (2011) Synthesis of nitrogen-doped onion-like carbon and its use in carbon-based CoFe binary non-precious-metal catalysts for oxygen-reduction. Carbon 49(12):3972–3982
54. Wood TE, Tan Z, Schmoeckel AK, O'Neill D, Atanasoski R (2008) Non-precious metal oxygen reduction catalyst for PEM fuel cells based on nitroaniline precursor. J Power Sources 178(2):510–516
55. Nallathambi V, Leonard N, Kothandaraman R, Barton SC (2011) Nitrogen precursor effects in iron-nitrogen-carbon oxygen reduction catalysts. Electrochem Solid State Lett 14(6):B55–B58
56. Wu G, Chen ZW, Artyushkova K, Garzon FH, Zelenay P (2008) Polyaniline-derived non-precious catalyst for the polymer electrolyte fuel cell cathode. ECS Trans 16(2):159–170
57. Wu G, More KL, Johnston CM, Zelenay P (2011) High-performance electrocatalysts for oxygen reduction derived from polyaniline, iron, and cobalt. Science 332(6028):443–447
58. Byon HR, Suntivich J, Shao-Horn Y (2011) Graphene-based non-noble-metal catalysts for oxygen reduction reaction in acid. Chem Mater 23(15):3421–3428
59. Gasteiger HA, Kocha SS, Sompalli B, Wagner FT (2005) Activity benchmarks and requirements for Pt, Pt-alloy, and non-Pt oxygen reduction catalysts for PEMFCs. Appl Catal B Environ 56(1–2):9–35
60. Wu G, Nelson MA, Mack NH, Ma SG, Sekhar P, Garzon FH, Zelenay P (2010) Titanium dioxide-supported non-precious metal oxygen reduction electrocatalyst. Chem Commun 46(40): 7489–7491
61. Subramanian NP, Li XG, Nallathambi V, Kumaraguru SP, Colon-Mercado H, Wu G, Lee JW, Popov BN (2009) Nitrogen-modified carbon-based catalysts for oxygen reduction reaction in polymer electrolyte membrane fuel cells. J Power Sources 188(1):38–44
62. Bezerra CWB, Zhang L, Liu H, Lee K, Marques ALB, Marques EP, Wang H, Zhang J (2007) A review of heat-treatment effects on activity and stability of PEM fuel cell catalysts for oxygen reduction reaction. J Power Sources 173(2):891–908
63. Bezerra CWB, Zhang L, Lee K, Liu H, Marques ALB, Marques EP, Wang H, Zhang J (2008) A review of Fe–N/C and Co–N/C catalysts for the oxygen reduction reaction. Electrochim Acta 53(15):4937–4951
64. Ohms D, Herzog S, Franke R, Neumann V, Wiesener K, Gamburcev S, Kaisheva A, Iliev I (1992) Influence of metal ions on the electrocatalytic oxygen reduction of carbon materials prepared from pyrolyzed polyacrylonitrile. J Power Sources 38(3):327–334
65. Lefevre M, Proietti E, Jaouen F, Dodelet JP (2009) Iron-based catalysts with improved oxygen reduction activity in polymer electrolyte fuel cells. Science 324(5923):71–74
66. Ferrandon M, Kropf AJ, Myers DJ, Artyushkova K, Kramm UI, Bogdanoff P, Wu G, Johnston CM, Zelenay P (2012) Multi-technique characterization of a polyaniline-iron-carbon oxygen reduction catalyst. J Phys Chem C 116(30):16001–16013
67. Coutanceau C, Croissant MJ, Napporn T, Lamy C (2000) Electrocatalytic reduction of dioxygen at platinum particles dispersed in a polyaniline film. Electrochim Acta 46(4):579–588
68. Wu G, Li L, Xu B-Q (2004) Effect of electrochemical polarization of PtRu/C catalysts on methanol electrooxidation. Electrochim Acta 50(1):1–10
69. Wu G, Mack NH, Gao W, Ma S, Zhong R, Han J, Baldwin JK, Zelenay P (2012) Nitrogen-doped graphene-rich catalysts derived from heteroatom polymers for oxygen reduction in nonaqueous lithium–O_2 battery cathodes. ACS Nano 6(11):9764–9776
70. Koslowski U, Herrmann I, Bogdanoff P, Barkschat C, Fiechter S, Iwata N, Takahashi H, Nishikori H (2008) Evaluation and analysis of PEM-FC performance using non-platinum cathode catalysts based on pyrolysed Fe- and Co-porphyrins – influence of a secondary heat-treatment. ECS Trans 13(17):125–141
71. Fournier J, Lalande G, Côté R, Guay D, Dodelet JP (1997) Activation of various Fe-based precursors on carbon black and graphite supports to obtain catalysts for the reduction of oxygen in fuel cells. J Electrochem Soc 144(1):218–226

72. Wu G, More KL, Xu P, Wang H-L, Ferrandon M, Kropf AJ, Myers D, Johnston CM, Zelenay P (2013) Carbon-Nanotube-Supported Graphene-Rich Non-Precious Metal Catalyst of Oxygen Reduction with Enhanced Performance Durability. Chem Commun doi: 10.1039/C3CC39121C
73. Gojkovic SL, Gupta S, Savinell RF (1998) Heat-treated iron(III) tetramethoxyphenyl porphyrin supported on high-area carbon as an electrocatalyst for oxygen reduction. J Electrochem Soc 145(10):3493–3499
74. Li Y, Zhou W, Wang H, Xie L, Liang Y, Wei F, Idrobo J-C, Pennycook SJ, Dai H (2012) An oxygen reduction electrocatalyst based on carbon nanotube-graphene complexes. Nat Nanotechnol 7(6):394–400
75. Spendelow JS, Wieckowski A (2007) Electrocatalysis of oxygen reduction and small alcohol oxidation in alkaline media. Phys Chem Chem Phys 9(21):2654–2675
76. Marković NM, Ross PN Jr (2002) Surface science studies of model fuel cell electrocatalysts. Surf Sci Rep 45(4–6):117–229
77. Gong KP, Du F, Xia ZH, Durstock M, Dai LM (2009) Nitrogen-doped carbon nanotube arrays with high electrocatalytic activity for oxygen reduction. Science 323(5915):760–764
78. Li X, Popov BN, Kawahara T, Yanagi H (2011) Non-precious metal catalysts synthesized from precursors of carbon, nitrogen, and transition metal for oxygen reduction in alkaline fuel cells. J Power Sources 196(4):1717–1722
79. Wu G, Chung HT, Nelson M, Artyushkova K, More KL, Johnston CM, Zelenay P (2011) Graphene-enriched Co_9S_8-N-C non-precious metal catalyst for oxygen reduction in alkaline media. ECS Trans 41(1):1709–1717
80. Piela B, Olson TS, Atanassov P, Zelenay P (2010) Highly methanol-tolerant non-precious metal cathode catalysts for direct methanol fuel cell. Electrochim Acta 55(26):7615–7621
81. Lee KS, Yoo SJ, Ahn D, Kim SK, Hwang SJ, Sung YE, Kim HJ, Cho E, Henkensmeier D, Lim TH, Jang JH (2011) Phosphate adsorption and its effect on oxygen reduction reaction for Pt(x)Co(y) alloy and Au(core)-Pt(shell) electrocatalysts. Electrochim Acta 56(24):8802–8810

Chapter 9
Recent Development of Non-precious Metal Catalysts

Drew Higgins and Zhongwei Chen

Abstract The development of high-performance non-precious metal catalysts (NPMC) for use at the cathode of polymer electrolyte membrane fuel cells will provide immense economic advantages over the current platinum-based catalyst technologies, perpetuating the sustainable widespread commercialization of these devices. It is imperative to develop NPMC that can effectively combine excellent oxygen reduction activities, high catalyst utilization, and long-term operational durability. This chapter focuses on recent advances made in the past 3–4 years and research trends in this field, with a particular focus on pyrolyzed carbon-supported nitrogen-coordinated transition metal (Fe and/or Co) complexes which have high potential of replacing conventional platinum-based catalysts.

9.1 Introduction

Depleting fossil fuel reserves and steadily increasing environmental awareness has resulted in the demand for sustainable, environmentally benign energy technologies being at an all-time high. Polymer electrolyte membrane fuel cells (PEMFCs) can efficiently convert chemical to electrical energy with high efficiency and minimal emissions, with immense market opportunity available for these technologies in transportation and backup power supply applications. However, in order to maintain a competitive market presence among emerging energy storage and conversion technologies and to ensure a sustainable long-term commercialization, the overall system costs must be significantly reduced. At the current state of technology, the electrocatalyst layers consisting of platinum nanoparticles supported on high

---

D. Higgins • Z. Chen (✉)
Department of Chemical Engineering, Waterloo Institute for Nanotechnology, Waterloo Institute for Sustainable Energy, University of Waterloo, 200 University Ave. W, Waterloo, ON, Canada N2L 3G1
e-mail: zhwchen@uwaterloo.ca

M. Shao (ed.), *Electrocatalysis in Fuel Cells*, Lecture Notes in Energy 9,
DOI 10.1007/978-1-4471-4911-8_9,

surface area carbons (Pt/C) account for almost half of the entire fuel cell system costs [1]. Despite recent advances in platinum catalyst activity and utilization providing a short-term solution, these improvements can be expected to be offset by the steadily increasing price of platinum materials due to the volatile precious metal market and uneven global distribution. Taking these factors into consideration, Pt/C is not a viable long-term electrocatalyst option for an affordable, sustainable PEMFC market.

Despite being utilized as both cathode and anode catalyst, a dramatically higher platinum loading is required at the cathode in order to facilitate the inherently sluggish oxygen reduction reaction (ORR). Due to the relatively much higher cost of the cathode catalyst layer, a majority of research and development efforts have been directed at replacing Pt/C at the cathode with inexpensive, non-precious metal catalysts (NPMCs). Significant advances have been realized for the utilization of NPMCs in alkaline fuel cells [2–5]; however, the pressing challenge involves the development of NPMCs for utilization in PEMFCs operating under acidic conditions. Several different research approaches have been taken including (1) conductive polymer composites [6, 7], (2) transition metal chalcogenides [8–10], and (3) transition metal oxides, carbides, and nitrides [11], all of which have achieved variable amounts of success. To date, however, the most promising approach has been the development of carbon-supported transition metal-nitrogen complexes prepared by high-temperature pyrolysis techniques, which will be the focus of this chapter.

With cost reductions inherent with the use of NPMCs in comparison with Pt/C, the primary considerations are ORR activity, catalyst utilization, and operational stability. Increasing the loading of NPMC at the PEMFC cathode would not provide an economic burden, and by extension, due to the relatively thicker NPMC layers utilized in comparison to Pt/C, ORR activity is generally evaluated on a volumetric basis (A cm^{-3}). By 2017, the United States Department of Energy has set NPMC performance targets of 300 A cm^{-3} at 0.8 V (iR-corrected) and minimal performance loss occurring after 5,000 h of MEA operation [12]. In order to realize these goals and perpetuate the NPMC research and development efforts, practical improvements are required for (1) volumetric activity, dependent on the active site density and turnover frequency; (2) NPMC utilization, related to the mass transport and reactant access throughout the bulk of the catalyst layer; and (3) NPMC stability under potentiodynamic and acidic operating conditions encountered at the PEMFC cathode. This chapter does not provide a comprehensive overview on the entire field of NPMC research, and for this, readers are referred to several in-depth review papers published recently [13–15]. The primary focus herein will be on pyrolyzed carbon-supported transition metal-nitrogen complexes, with the transition metal comprising iron and/or cobalt. Significant research efforts and technological advancements have been made toward this class of NPMC development, and the recent progress and research trends over the past 3–4 years will form the basis of this chapter.

9.2 Non-precious Metal Catalyst Volumetric Activity

With the cost of NPMCs paling in comparison with platinum-based catalysts, the use of significantly higher catalyst loadings is economically feasible. With these higher catalyst loadings, the catalyst layers will be up to ten times thicker than conventional Pt/C catalyst layer thickness [16], and thus, ORR activity metrics are generally evaluated on a volumetric basis at a cell potential of 0.8 V [12]. Under complete ORR kinetic control (no mass transfer limitations), NPMC volumetric activity can be considered a product of the active site density and the average ORR kinetics occurring on a single active site. The active site density is simply the number of sites available to facilitate the ORR per unit volume of NPMC (a product of the catalyst layer thickness and electrode surface area). The NPMC synthesis techniques utilized will have a direct impact on active site densities which depend on active site size, dispersion, and catalyst morphologies. The average single site kinetic activity is commonly referred to as the turnover frequency, or put simply, the number of electrons transferred per site, per unit time. Turnover frequency is site specific, depending on the exact nature and surrounding environment of the active site structures present in the NPMC. Overall, efforts to increase the volumetric activity of NPMC materials have primarily focused on improving active site densities using unique synthesis and processing strategies. This approach has garnered dramatic NPMC activity improvements over recent years that has perpetuated this class of catalyst from a fundamental research and development phase to the point where it can be considered extremely promising for application in future generation PEMFC systems [17]. Fundamental progress has also been made toward identification of the specific active site structures present in NPMC, along with understanding on the impact of catalyst structural and electronic properties on ORR turnover frequencies. This allows for guided efforts directed at tailoring the physical properties of NPMCs in an attempt to modulate and improve their volumetric activities. Progress made on this front over the past several years will be discussed in this section along with potential strategies proposed for moving forward.

9.2.1 Active Site Densities

The pioneering work of Jasinski [18] demonstrating the potential of using metal-nitrogen macrocyclic compounds to facilitate the ORR in alkaline conditions initiated a field of NPMC research that has realized significant progress and fundamental progress over the past several decades. Supporting these bulky macrocycle complexes on high surface area carbons could bestow promising ORR activity in acidic electrolytes; however, poor stability was the ultimate downfall of this strategy [19]. It was later discovered that a heat treatment (400–1,000 °C) under inert atmospheres could overcome these stability limitations while also markedly increasing the ORR activity of the macrocycle complexes due to enhanced interactions with the carbon support and thermally modified ligand structures [20, 21]. Apart from the thermal modifications of the active site structures, heat treatments could cause migration of active sites [22]. Based on this model, random, well-dispersed active site structures will aid in active site density improvements, mitigating aggregation and carbon support pore blockages which are pertinent concerns when using bulky macrocycle precursor complexes. Using synthesis techniques capable of establishing NPMCs with high surface areas and well-dispersed active sites in a monolayer configuration would undoubtedly serve to increase the overall active site density of these materials. On this front, it was later established that the use of bulky and expensive macrocycle complexes was unnecessary and that pyrolysis of simple nitrogen, transition metal, and carbon-containing species could produce NPMCs with promising ORR activity and stability [23]. Not only did this technique present an economical advantage allowing the use of simplistic, inexpensive precursor materials but also enabled researchers to have increased capabilities and flexibility for the design and fabrication of NPMC with high active site densities owing to the small size of the precursor materials, coupled with high catalyst surface areas. These preliminary investigations formed the foundation for recent progress made toward the improvement of M-Nx/C active site densities, coupled with fundamental investigations in order to further aid in the design and development of these materials.

Based on years of research, Dodelet's group at the INRS developed a unique strategy for NPMC synthesis by mixing a carbon support with iron-containing precursor and then subjecting the materials to a heat treatment in ammonia as the source of nitrogen [24–26]. These researchers determined that the ORR activity of this class of NPMC was influenced by the formation of micropores occurring during ammonia treatment, resulting from ammonia etching of the carbonaceous materials with a preference for the disordered carbon phase. They observed at a weight loss of approximately 35 % [24] ORR activity was optimized, owing to the maximum number of active sites formed, hosted in the micropores of the carbon support in a configuration similar to Fig. 9.1. Clearly, there is a marked benefit of having a higher number of micropores with uniform dispersion throughout the entirety of the NPMC catalyst particles in order to increase and maximize the active site density for this class of catalyst.

Advancing on these fundamentally significant findings, Dodelet's research team opted to use a pore filler method using highly microporous Black Pearls 2000 (BP) carbon support as the starting substrate for NPMC synthesis [28]. The pores of the BP support were filled by ball milling with organic 1,10-phenanthroline and iron acetate as the source of nitrogen and iron, respectively. This pore-filled composite was then subjected to pyrolysis in argon at 900 °C, inducing carbonization of the organic complexes to a disordered carbon phase, most likely accompanied by the formation of the proposed micropore-hosted active site structures entrapped within

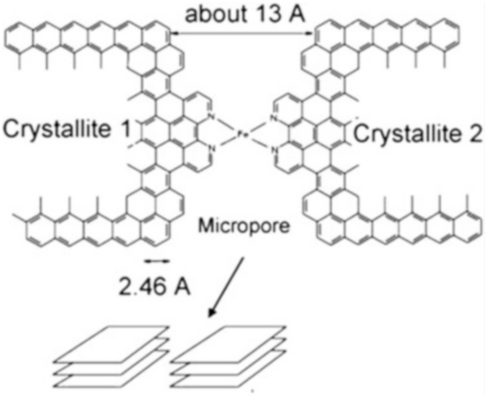

Fig. 9.1 Schematic illustration of the micropore-hosted active site structure present in ammonia-treated NPMCs prepared by the Dodelet group, consisting of an Fe ion bridged between two adjacent nitrogen-doped graphitic crystallites (reprinted from [27], with permission from Elsevier)

this phase. A second heat treatment in ammonia was then employed, where preferential etching of this disordered carbon phase occurred along with simultaneous nitrogen doping. Figure 9.2 provides a schematic illustration of the process occurring during active site formation. This catalyst was found to possess unprecedented NPMC activity, approaching that of platinum catalyst at near open circuit potential and providing a volumetric activity of 99 A cm^{-3} at an iR-corrected cell voltage of 0.8 V, approaching the DOE's 2010 target of 130 A cm^{-3} (article published in 2009). Clearly, capitalizing on the inherent high microporosity of BP carbon supported allowed the development of NPMC with a large active site densities and dispersion.

Zelenay's group at the Los Alamos National Laboratory utilized a different approach to the development of highly active NPMC [29]. Aniline precursor was used and polymerized in the presence of transition metal species (Fe and/or Co) and a high surface area graphitic Ketjenblack support (alternatively they also used an ethylenediamine/Co impregnated carbon support). The authors claimed that the structural similarities between polyaniline (PANI) and the graphitic carbon support (Fig. 9.3) could enhance the interaction between the two species and effectively facilitate the formation of active site structures on the support surface during high-temperature heat treatment (between 400 and 1,000 °C) in an inert environment. Moreover, enhanced active site densities could be obtained due to the high nitrogen content of PANI which is a prerequisite for ORR active site formation. The ordered structure of PANI further ensures the uniform distribution of nitrogen throughout the catalyst precursors and can allow for improved active site dispersion throughout the entire NPMC surface area. Following heat treatment, these catalysts were acid leached in 0.5 M H_2SO_4 at 80 °C for 8 h, followed by another heat treatment under inert environment. This posttreatment procedure is utilized in order to leach surface inactive species, such as metal and/or metal oxide nanoparticles that can block ORR active moieties. Similar posttreatment acid leaching and pyrolysis techniques have been deemed effective for improving the performance of NPMCs [30, 31], indicative of the importance of increasing active site exposure. By half-cell ORR kinetic

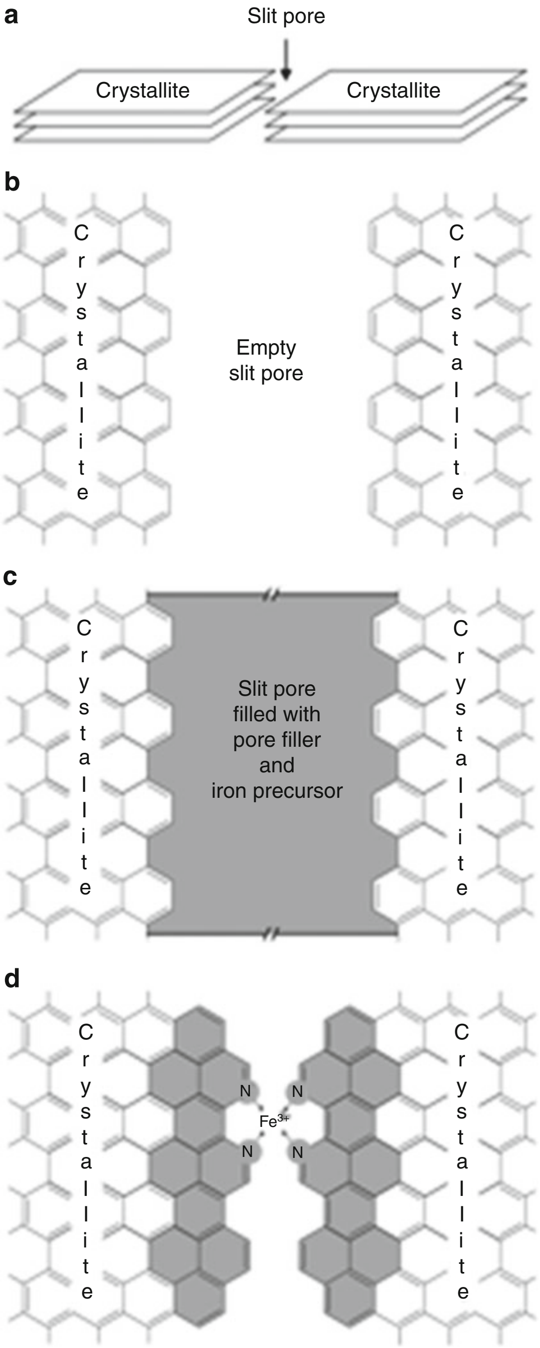

Fig. 9.2 Schematic illustration of the micropore filling technique and active site formation during NPMC synthesis. (**a**) Two adjacent graphitic crystallites hosting a slit micropore in the BP carbon support, (**b**) cross section view of the empty micropore, (**c**) micropore after being filled with 1,10-phenanthroline and iron acetate precursors, and (**d**) active site formation and nitrogen-doped graphitic carbon deposition after subsequent heat treatments in argon and ammonia (from [28] with permission from AAAS)

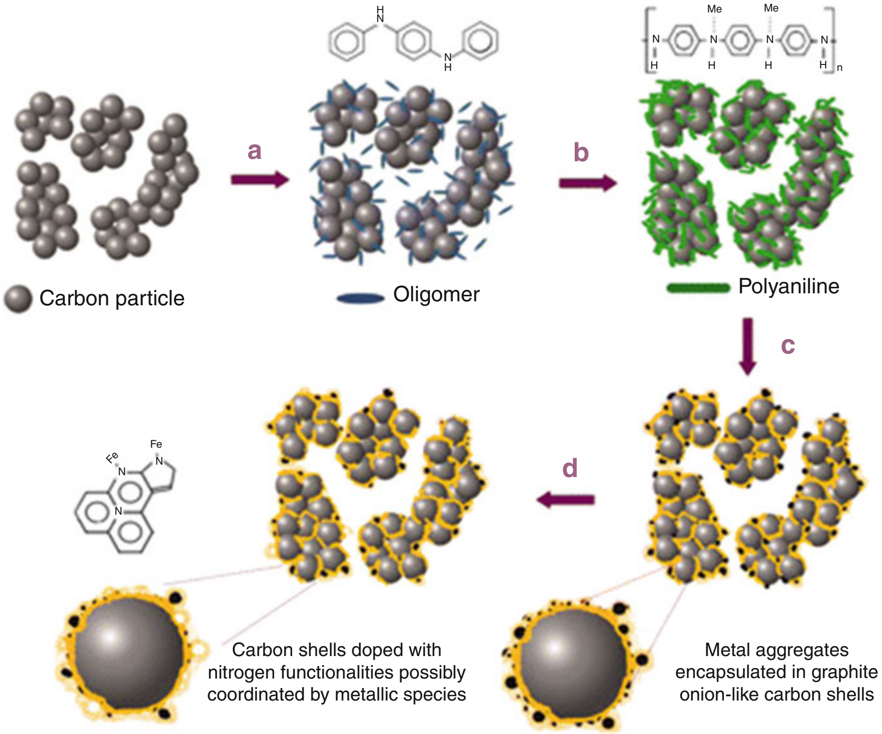

Fig. 9.3 Schematic illustration of the fabrication of highly active PANI-based NPMCs. (a) Mixing carbon support particles with aniline monomer and transition metal precursors, (b) polymerization of aniline with ammonium persulfate, (c) heat treatment in nitrogen, and (d) acid leaching and second heat treatment (from [29] with permission from AAAS)

investigations of the best reported PANI-based materials [29], a half-wave potential only ca. 59 mV below a commercial Pt/C catalyst-coated electrode with a Pt loading of 60 μg cm^{-2} was achieved. Moreover, through MEA testing, a maximum MEA power density of 0.55 W cm^{-2} was obtained, coupled with promising operational stability demonstrated through half-cell and MEA degradation protocols. In this study, appropriate selection of precursor materials and careful control and optimization of the fabrication techniques resulted in a high density of active site formation. This provides substantial progress in the field of NPMC developments and indicates the promise of investigating different combinations of precursor materials in order to facilitate the formation of a large number of active sites with good dispersion, along with techniques (i.e., acid washing and subsequent heat treatment) to increase their exposure.

Li et al. [32] recognized that carbon nanotube (CNT)-based catalysts traditionally had very limited ORR activity under the acidic conditions of PEMFCs, attributed to the low surface areas and formation density of active sites on the

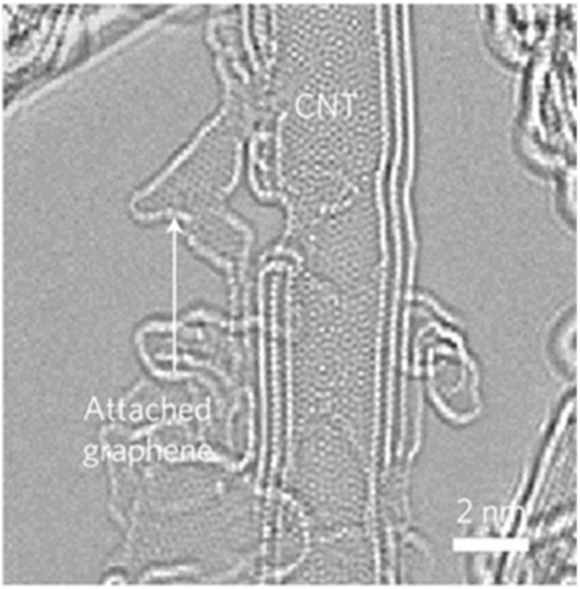

Fig. 9.4 Aberration-corrected transmission electron microscopy image of partially unzipped outer walls of CNTs forming graphene–CNT complex catalyst with a high degree of edge exposure (reprinted with permission from Macmillan Publishers Ltd [32], copyright 2012)

planar graphitic walls of CNTs. To overcome this inherent limitation, they exposed CNTs to an oxidative treatment using $KMnO_4$ and H_2SO_4 in a process similar to the Hummer's method for the preparation of graphene oxide. The result was partially unzipped outer walls of the intact CNTs (Fig. 9.4) with an abundance of defect and edge plane sites that could successfully facilitate active site formation. Upon treatment at 900 °C under a 10 % NH_3 in Ar environment for 30 min, this developed catalyst was found to provide excellent ORR activity evaluated by half-cell testing in 0.1 M $HClO_4$, demonstrating an onset and half-wave potential ca. 100 mV lower than that of commercial 20 wt. % Pt/C. Although fuel cell performance was not evaluated, this work opens up an interesting pathway to the generation of a high density of surface active sites due to the generation of defective graphene sheets attached to the CNTs, which by atomic scale imaging were found to host active site species consisting of nitrogen and Fe remaining in the form of impurities from CNT growth. These results can be linked to numerous other reports that have highlighted the importance of edge plane sites and surface defects for hosting ORR active site structures [33–35]. This illustrates the positive impact of generating NPMCs that have a high degree of edge plane exposure, with different strategies investigated over recent years with variable amounts of success. For example, Choi et al. [35] found that simultaneously doping NPMCs with phosphorus dramatically increased the amount of graphitic buckling and edge exposure in the nanostructured carbon, owing to the larger atomic size of phosphorus and its preferential sp3 bonding configuration. This technique was found to result in ORR activity enhancements of over 100 %, evaluated in terms of mass-based current densities at 0.6 V versus RHE through half-cell investigations using 1 M $HClO_4$ electrolyte. Structural modifications of this nature, using techniques such as heteroatomic doping and oxidative treatment techniques or by employing unique synthesis procedures, offer the potential to improve active site densities and NPMC performance, and their further investigation using a broad range of catalyst materials would be beneficial.

Clearly, there are several effective strategies that can be employed in order to increase the concentration of exposed ORR active site structures on the surface of synthesized NPMCs. These strategies provide beneficial activity enhancements toward the ORR and provide increased understanding for researchers regarding the specific parameters governing NPMC performance. Modification to these techniques, along with the development of unique catalyst synthesis approaches, will provide further understanding of the factors governing active site formation, density, and catalyst morphologies. Further investigations of alternative synthesis strategies will provide guidance to researchers and serve to perpetuate this field of NPMC research and development.

9.2.2 Average Active Site Turnover Frequency

With recent developments toward improving active site densities previously highlighted and discussed, it is imperative to consider the concept of active site turnover frequencies and the progress made on this front. Each specific active site structure, present in different amounts, will have a certain turnover frequency (dependent on potential) associated with it. Developing strategies to effectively modulate the turnover frequency of the ORR active sites or increase the preferential formation of active site structures with high turnover frequencies will allow researchers the capability to further improve the activity and performance of NPMC to practical levels approaching or even potentially 1 day surpassing commercial platinum-based catalysts. The physicochemical properties of the NPMC, along with the exact structure and identity of the active sites, will have a significant impact on the turnover frequency. Despite significant debate in the scientific community on the exact nature of the active site structures associated with NPMCs [15], progress made in recent years toward understanding the overall impact of catalyst properties and fabrication techniques in order to deliberately modulate the turnover frequencies will be discussed in this section.

Primarily, the uncertainty with heat-treated NPMCs lies in elucidation of the exact identity of the sites responsible for ORR activity. Several authors claim that transition metal centers are not the locale for ORR activity and that performance is governed by catalytically active nitrogen–carbon species [31, 33, 36–39]. Of these species, graphitic nitrogen, pyridinic nitrogen, or edge plane exposure sites arising due to nitrogen incorporation have been claimed to provide the most activity out of available species. While they may provide catalytic activity in varying amounts, there are no detailed reports available that elucidate the differences in ORR turnover frequencies for each of these species. Detailed studies of this nature will aid in the development of improved NPMCs, where it will be possible to develop unique synthesis strategies that allow for the preferential formation of only the most active nitrogen–carbon moieties with optimal structural configurations.

Conversely, numerous authors claim that metal-centered structures comprise the locale for catalytic activity [28, 40–44], such as in the case of non-pyrolyzed transition metal macrocycles. For these cases, the impact of the metal type, redox behavior, electronic properties, and ligand effects will be influential toward the inherent ORR activity or turnover frequency of each active site structure. During high-temperature heat treatments, it is extremely difficult to predict, control, and probe the atomic reconfigurations occurring, so several researchers have turned to studies on non-pyrolyzed macrocycle NPMCs for fundamental insight into the factors governing catalytic activity. The drastically varying ORR activity of macrocycle complexes consisting of different transition metal species (i.e., Fe, Co, Cu, Ni) highlights the impact of metal type, with Fe- and/or Co-based catalysts providing the highest turnover frequencies among several transition metal macrocycles investigated [45] and providing reasonable explanation for their almost exclusive use in NPMC studies over recent years. The nature of the environment surrounding the active site metal center will also have a direct impact on catalytic turnover frequencies, elucidated by the difference in activity observed between various macrocycle structures (i.e., phthalocyanine of porphyrin). Furthermore, substituent groups are capable of tailoring the physicochemical properties of the metal-centered active site structures. For example, Baker et al. [46] investigated several substituted iron phthalocyanine structures (Fig. 9.5) and suggested that the presence of substituent groups could influence the electron density of the active metal centers, ultimately governing their turnover frequencies. While studies of this nature (non-pyrolyzed) provide a good foundation for the design and development of future generation NPMC, reliable techniques of transferring over the concepts to pyrolyzed NPMC are necessary.

Recently, investigations have shifted to focus on how the physicochemical properties and surrounding environments of the metal-centered active site structures in NPMCs can positively impact ORR turnover frequencies. Using carbon black-supported Fe macrocycles as a starting point, Kramm et al. [42] utilized X-ray photoelectron spectroscopy coupled with Mossbauer spectroscopy to probe the electronic properties of coordinated Fe-nitrogen active site structures remaining after high-temperature pyrolysis. The authors observed that increasing pyrolysis temperatures would lead to an increase in the electron density of the metal ion center, ultimately leading to improved ORR kinetics observed for these samples. These results can be linked to the fundamental investigations on non-pyrolyzed NPMCs, whereby heat treatment at different temperatures will enhance interactions between the macrocycle complex and the carbon support, modifying the active site surrounding environment and tuning the ligand–metal center interactions. This can potentially exert electron-donating behavior to the Fe ion centers and improve the overall turnover frequency of each individual active site structure. This investigation provides fundamental significance because it exclusively demonstrated the possibility of modulating the turnover frequencies of metal-centered active sites in pyrolyzed NPMCs by tuning the specific electronic

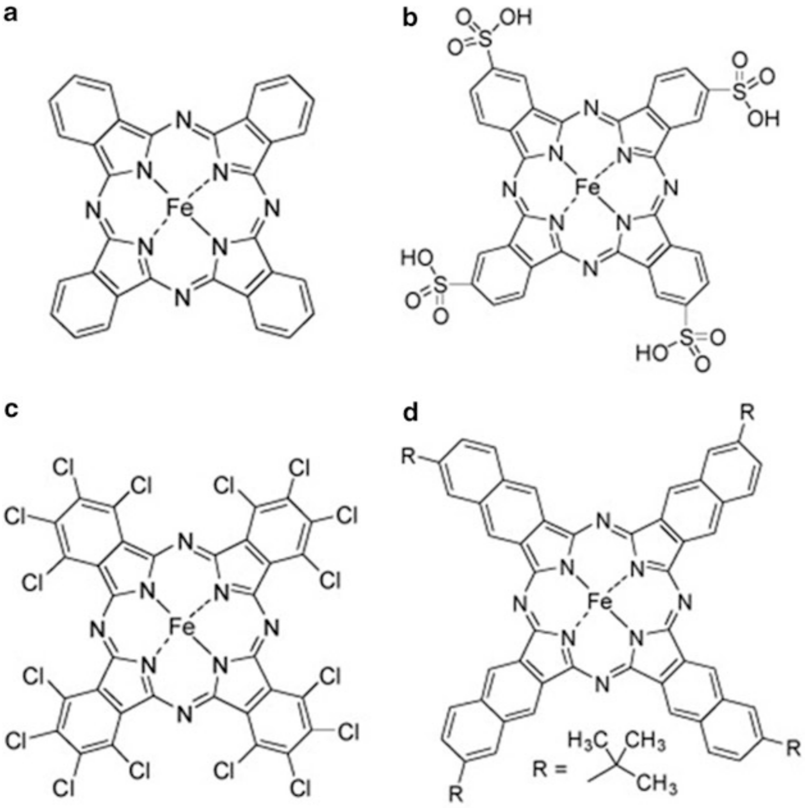

Fig. 9.5 Molecular structure of (**a**) iron phthalocyanine and (**b**–**d**) iron phthalocyanine with various substituent groups (reprinted from [46], with permission from Elsevier)

and structural properties of the surrounding environments. Zagal et al. [47] provided a similar report on a series of non-pyrolyzed and pyrolyzed NPMCs that associated differences in the catalytic activity to variations in the redox potential of the metal centers. Using different precursor materials, synthesis techniques, and pyrolysis temperatures can lead to these variations, and developing effective strategies to deliberately control the electrochemical properties of the metal centers should be a focus of future investigations.

Fundamental active site investigations using Mossbauer spectroscopy was recently applied to the class of NPMCs prepared by impregnation of a carbon support with iron acetate, followed by heat treatment in ammonia [48]. Five different Fe species were observed in the developed catalysts, three of which consisting of the Fe–N_4 moieties traditionally believed by these researchers to be the locale of ORR activity. In this work, the impact of the active site surrounding environment and ligand contributions was exclusively elucidated, with only two of these Fe–N_4 species deemed active toward the ORR, albeit possessing drastically

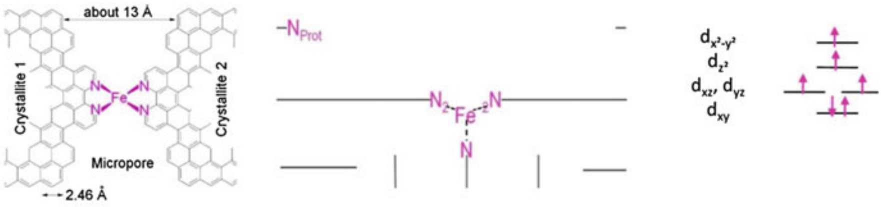

Fig. 9.6 (*Left*) Side view, (*middle*) top view, and (*right*) molecular orbitals of the five nitrogen-coordinated Fe-centered sites providing the highest turnover frequency for this class of ammonia-treated NPMC [48] (reproduced by permission of the PCCP Owner Societies)

varying magnitudes of activity. The structure the authors concluded as most active for the ORR is illustrated in Fig. 9.6, surprisingly comprising a fifth coordinating nitrogen, along with the presence of a basic nitrogen group in close proximity to the active metal center. The turnover frequency of this specific active site structure was calculated to be 11.4 electrons transferred per site every second, at a half-cell electrode potential of 0.8 V versus RHE. They further proposed a mechanism for the formation of various Fe species in this class of ammonia-treated catalyst that can aid further investigations toward the development of NPMC, where deliberate control strategies can be applied in order to preferentially form active site structures with optimal surrounding environments and improved turnover frequencies.

While it is undoubtedly difficult to predict and control the structural, electronic, and compositional changes occurring during high-temperature treatment of NPMC, emerging strategies can offer the potential to modulate active site turnover frequencies in NPMC based on deliberate control of the synthesis techniques and catalyst precursors. Drawing on the fundamental insight and progress discussed in this section, researchers are provided the opportunity to expand these investigations in order to provide further insight into the exact factors governing NPMC turnover frequencies and establish reliable optimization techniques.

9.3 Non-precious Metal Catalyst Utilization

Recent and extremely promising advances in NPMC development have rendered materials with activities approaching ORR activity levels that are practical for application in PEMFC systems. Using NPMCs with extremely low cost in comparison to platinum-based catalysts allows for the economic viability of using significantly higher catalyst loadings. However, when using catalyst layers of ca. 100 μm, almost ten times thicker than state-of-the-art Pt/C-based electrodes, mass transport hindrance and poor catalyst utilization present a pertinent technical challenge for fuel cells requiring higher operating current and power densities. Important considerations include the transport of ORR-related species throughout both the entirety of the catalyst layer and the individual NPMC catalyst particles, in order to provide utilization of all active site structures. Reactant access (oxygen and protons) and H_2O product removal must simultaneously be facilitated in order to provide power density outputs practical for many modern applications. The importance of porosity (micro, meso, and macro), and impact of ionomer content and distribution, has been elucidated for carbon-supported platinum-based catalyst layers [49, 50]; however, owing to the just recent emergence of NPMCs with practical activity for PEMFC application, studies of this nature for thicker NPMC catalyst layers are nonexistent. Despite the necessity for such studies, NPMC morphologies must be designed appropriately in order to facilitate adequate mass transport and improve upon traditionally limited maximum power densities of NPMC cathodes reported in the literature. This can be accomplished by developing unique catalyst fabrication strategies to control catalyst particle porosity and surface properties, along with the development and investigation of improved catalyst layer architectures.

In a recent study published by Dodelet et al. [44], these authors opted to use PEMFC performance at a voltage of 0.6 V as a practical gauge for NPMC cathode performance, combining the effects of fuel cell efficiency (activity) and power density (catalyst layer utilization). Recognizing that even the best NPMCs reported in the literature obtained power densities of only one-third to half of those reported for state-of-the-art platinum catalysts [29, 30, 51–53], these researchers recognized the need to adapt these catalyst technologies in order to obtain power densities practical for commercialization. With the importance of microporosity formation for ORR activity highlighted in their previous work [25, 28], strategies were investigated in order to couple high NPMC microporosity with the introduction of a large number of meso- and macropores into the catalyst structures to properly facilitate mass transport processes during fuel cell operation. In order to accomplish this, they used a microporous Zn(II) zeolitic metal-organic framework impregnated by ball milling with 1,10-phenanthroline and iron acetate precursors [44]. This composite was subjected to an initial high-temperature (1,050 °C) pyrolysis in argon, followed by a 15-min heat treatment in ammonia at 950 °C. This technique was not only able to accomplish a high density of micropore-hosted active site structures but was also capable of facilitating effective mass transport throughout the bulk of the NPMC layer (ca. 90–120 μm thickness). This enhanced reactant access and product removal was attributed to high mesopore content, consisting of interconnected alveolar-like nanostructures with ca. 50-nm-diameter pores clearly observable from SEM topological imaging. For comparison, NPMC was fabricated using the same technique, albeit with Black Pearls 2000 carbon support in place of the metal-organic framework similar to their previously reported highest performing catalyst [28]. The NPMC developed using the metal-organic framework was found to result in significantly improved MEA polarization curves (Fig. 9.7) and a peak power density of 0.91 W cm^{-2}, performance approaching that of state-of-the-art platinum catalyst, and over double the performance of the Black Pearls 2000-based catalyst. This effectively elucidated the importance of using catalyst synthesis techniques that can couple high active site densities with improved meso- and macroporosity in order to facilitate the transport of ORR active species.

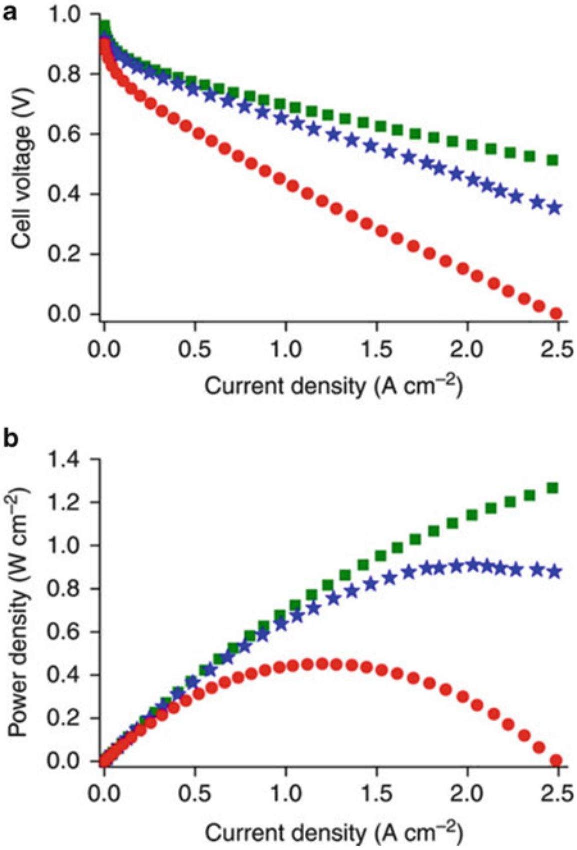

Fig. 9.7 (**a**) MEA polarization and (**b**) power density curves for (*squares*) state-of-the-art Pt/C catalyst, (*stars*) NPMC based on metal-organic framework, and (*circles*) NPMC based on Black Pearls 2000 carbon support (reprinted with permission from Macmillan Publishers Ltd [44], copyright 2011)

Several other templating techniques have been utilized in order to render NPMC materials with high porosity to aid in mass transfer and active site exposure. Silica is a commonly used template that can be impregnated by carbon, nitrogen, and iron precursors, followed by a high-temperature pyrolysis in order to induce active site formation [31, 53–57]. This technique is promising as it allows deliberate control of the resultant catalyst morphology based on the morphology of the silica template utilized; however, it often relies upon complex synthesis techniques and requires the removal of silica with HF or other etchants, leading to obvious health and safety considerations. Many of the silica template NPMC studies, however, did not investigate the impact of morphology on MEA performance or demonstrated performance well below the results reported by Dodelet et al. [44]. Other interesting approaches to prepare high surface area NMPCs with a large degree of porosity are by using soft-template techniques [58] or by the inclusion of transition metal oxalate precursor as a structure-forming agent [59]. For the latter, the impact of increased mesoporous surface areas on the ORR overpotential was demonstrated (Fig. 9.8); however, MEA testing was not reported.

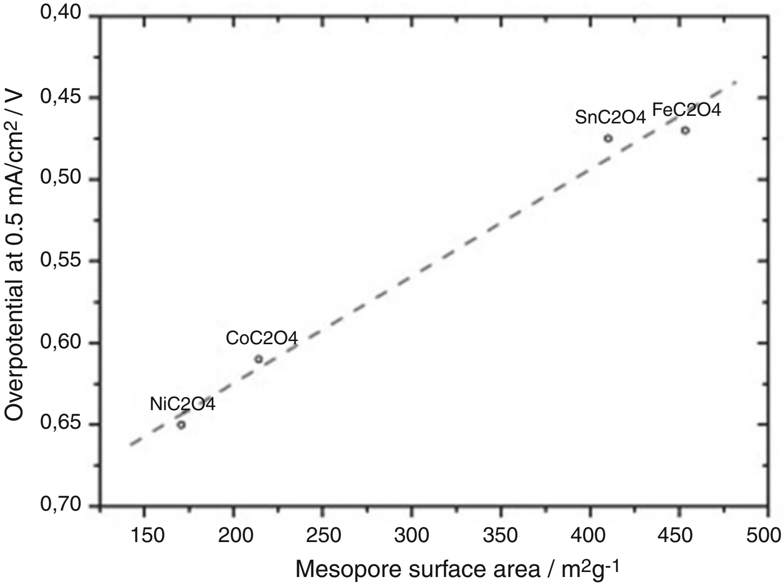

Fig. 9.8 Half-cell investigated ORR overpotential at a current density of 0.5 mA cm^{-2} plotted versus mesopore surface areas of catalyst synthesized from different transition metal oxalate structure-forming agents (reprinted from [59], with permission from Elsevier)

Clearly, there is a gap in understanding on the impact of pore sizes, size distributions, and pore structure/interconnectivity on the practical performance of these thicker NPMC electrodes. Scientists have the capability to tailor pore sizes and structures based on the use of templating or other techniques; however, this must be accomplished without sacrificing catalyst active site densities. Furthermore, at the current state of NPMC technology, scientists are provided minimal guidance regarding optimal pore sizes and size distributions for effective mass transport facilitation. The ionomer content of the electrode and distribution will have an impact on the porosity, catalyst particle aggregate structure, and mass transport characteristics of the catalyst layer which is well documented for Pt/C catalysts [49, 50, 60, 61]. Furthering the fundamental understanding on how these factors can impact fuel cell performance and power density output for thicker NPMC catalyst layers will aid in the design and development of future generation catalyst technologies that can effectively couple high active site densities with exemplary mass transport considerations. The optimization of the catalyst layer (consisting of NPMC and ionomer) architectures and compositions offers the potential to further improve upon the progress made recently in this field research. Detailed experimental investigations coupled with computational transport studies can perpetuate the development of NPMC catalyst layers with increased utilization and performance over the practical operating range of PEMFCs.

9.4 Non-precious Metal Catalyst Stability

At the current state of NPMC development, catalyst and electrode instabilities are now considered the most pertinent technical challenges facing their practical application in PEMFC cathodes. Heat treatment of ORR active transition metal macrocycles was initially found to dramatically improve the stability of these materials, attributed primarily to thermal modification of the ligand and surrounding environments in which the most reactive components react and are no longer susceptible to degradation during ORR. The impact of the active metal center surrounding environment was illustrated recently by Li et al. [62], demonstrating that attaching diphenylphenthioether electron-donating groups to iron phthalocyanine could significantly alleviate the instability of iron phthalocyanine in acidic environments. This enhanced stability was attributed to the electron-donating behavior of the substituent groups that could significantly reduce the lifetime of highly oxidizing species that can deactivate the catalyst structures. Despite fundamental studies of this nature, when dealing with pyrolyzed NPMC materials, there is a large amount of uncertainty surrounding the exact nature of performance instability. The most prevalent hypothesis will be discussed in this section, along with progress in this field made in recent years.

The ORR can proceed either by an overall four-electron reduction mechanism to form water or by a two-electron mechanism forming hydrogen peroxide (H_2O_2) species. Apart from reducing the efficiency of the fuel cell, H_2O_2 can act as an oxidizing agent or highly reactive radical species, either of which can be responsible for catalyst deactivation or decomposition. Furthermore, upon release from the catalyst layer, these species can cause instability issues with the polymer electrolyte membrane or other fuel cell components due to their highly oxidizing nature [63]. Designing catalysts with a higher selectivity would be necessary to alleviate these issues or by inclusion of a material that can facilitate the further reduction or decomposition of peroxide species. Olson et al. [43] recently proposed that this could be accomplished in the case of pyrolyzed Co-based catalysts, with Co-nitrogen-coordinated sites being responsible for the initial two-electron reduction of oxygen to H_2O_2, and Co/Co-oxide particle species responsible for the further reduction of H_2O_2 to water products. This could offer a potential explanation for the improved stabilities of Fe-based NPMC upon addition of Co species [29, 64, 65]. Interestingly, however, while some researchers illustrated marked NPMC performance loss upon H_2O_2 exposure [65, 66], others demonstrated a negligible impact of these species [67]. This provides indication that the impact of H_2O_2 species on NPMC stability is material dependent, and there must be other underlying factors influencing catalyst stability.

Increasing the degree of graphitization in NPMCs has been positively linked to improvements in operational stability [65, 68]. This could be due to the enhanced resistance to corrosion of highly coordinated graphitic structures or to the reduced number of structural defects that are hydrophilic in nature, leading to active site and catalyst layer flooding over longer periods of fuel cell operation. Researchers from

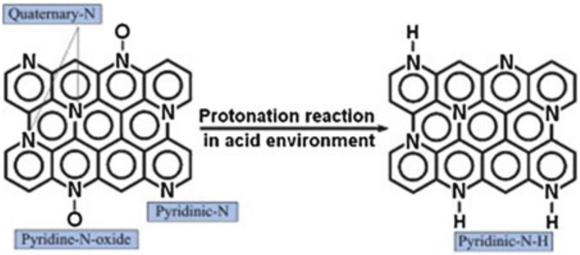

Fig. 9.9 Schematic illustration of the ORR active pyridinic species protonation occurring in acidic environments such as those encountered during PEMFC operation (reprinted from [53], with permission from Elsevier)

the Los Alamos National Laboratory [29, 65] reported that by using polyaniline precursors with an aromatic structure could enhance the precursor-graphitic carbon support interactions, allowing for the formation of well-ordered carbon structures following pyrolysis that can provide stability enhancements. Negligible performance loss of their polyaniline-based NPMC after 700 h of operation at a constant fuel cell voltage of 0.4 V was reported. It is also possible to improve NPMC stability using highly graphitized support materials such as carbon nanotubes [65, 69, 70] or graphene materials [71, 72]. Further investigation of similar, highly graphitized support materials along with elucidation of the specific factors influencing their stability (i.e., functional groups, hydrophilicity/hydrophobicity, and degree of defects) will provide beneficial insight for further NPMC stability improvements. The exact nature of the surface species and active site structures will also have a significant impact on catalyst stability and specific degradation mechanisms. For example, Popov's group attributes ORR activity to the presence of nitrogen–carbon functional groups, with pyridinic nitrogen providing high catalytic performance. The authors propose that ORR activity losses of NPMC arise due to protonation of the pyridinic sites upon exposure to acid, forming catalytically inactive pyridinic-H^+ sites [31, 53] as depicted in Fig. 9.9.

Some of the most active NPMCs reported to date have been prepared by thermal treatment of catalyst precursors with ammonia [28, 44, 58]; however, it has been demonstrated that even using small amounts of ammonia during catalyst synthesis will result in significant stability loss [73]. This raises the question as to what the sources of these instabilities are in order to develop mitigation strategies to improve the operational durability of this class of NPMC to levels practical for fuel cell integration. Herranz et al. [74] recently reported that for this class of catalyst, surface nitrogen species in proximity but not part of the active site structures are the source of the loss of catalytic activity during fuel cell operation. Based on acid washing of their developed NPMC (0.1 M H_2SO_4 for 24 h), the authors observed that ORR activity would be significantly reduced. This was followed by a reheat treatment in argon (>300 °C) where a significant portion of catalyst activity would be recovered. The authors claimed that the performance loss following acid washing was due to protonation of the aforementioned surface nitrogen species, followed by anion binding as depicted schematically in Fig. 9.10. The former would not negatively impact ORR turnover frequencies of the active site structures; however, once anion binding occurred, the majority of ORR activity would be lost. In an

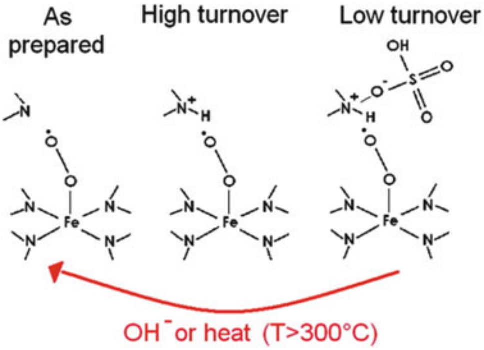

Fig. 9.10 Schematic depicting (*left*) metal-centered active site structure in proximity to a surface nitrogen species, (*center*) protonation of the surface nitrogen species with the active site having a high turnover frequency, and (*right*) anion binding to protonated surface nitrogen species dramatically reducing active site turnover frequency (reprinted with permission from [74], copyright 2011 American Chemical Society)

aqueous acidic solution such as that utilized in the reported investigation, the rate of anion binding is very rapid, whereas in a PEMFC, the rate of anion supply from the polymer electrolyte or ionomer species is much slower, albeit prevalent over longer periods of operation. While the authors observed that a significant portion of the ORR activity could be recovered by thermal or hydroxide chemical treatment, the pertinent issue is how to prevent this occurrence during PEMFC operation where these treatments would not be practical. Modifications to the polymer electrolyte membrane or catalyst layer ionomer may provide improvements to the NPMC stability. Other options include modifying or functionalizing the NPMC surface in order to prevent anion penetration and loss of activity.

The majority of NPMC stability investigations either involve repeated half-cell electrode cycling, or operating MEA setups at low operating voltages or current densities. These durability testing protocols can provide indication of NPMC stability; however, they do not adequately simulate the potentiodynamic conditions of the cathode during practical PEMFC operation, especially in the case of transportation applications. Furthermore, the impact of operating conditions, including reactant feed humidity, flow rates, backpressure, and operation temperature, will all have an impact on NPMC performance and durability, albeit with currently unknown magnitudes of impact. With NPMC activity and performance approaching levels for practical integration in fuel cell technologies, improvements to the operational stability are a necessity and must be demonstrated by testing protocols established specifically for NPMCs. Development and application of these testing protocols should be a primary focus of future investigations, along with detailed diagnostic studies in order to determine the primary mechanistic pathways of NPMC performance degradation during PEMFC operation. This will provide valuable insight to researchers in order to improve the stability of NPMC technologies to practical levels.

9.5 Conclusions

The development of NPMC that can combine high ORR activity, mass transport capabilities, and operational stability will provide the necessary breakthrough for the widespread commercialization of cost-effective PEMFC technologies, alleviating the current economic hindrance of platinum-based catalyst technologies. Steady progress has been made over the past several decades on the development of practical NPMC technologies, and the most pertinent technological advances made over the past 3–4 years are outlined in this chapter.

Scientists have successfully developed NPMC with high activity using innovative fabrication techniques that can combine excellent ORR active site densities and turnover frequencies. Further improvements are required in order to ensure high utilization of the relatively thick (ca. 100 μm) NPMC-based catalyst layers in order to provide high-power output at increased current densities. Mass transport limitations are the primary factor governing catalyst utilization and can be improved by incorporating a high degree of meso- and macroporosity into current NPMC technologies. In order to provide further improvements and optimization of mass transport considerations, fundamental investigations are required in order to elucidate the exact impact of pore sizes and distribution, along with the impact of ionomer content and distribution throughout the catalyst layer.

Currently, the primary limiting factor facing the successful deployment of NPMCs for PEMFC applications is the poor operational stability of these materials. Reliable degradation testing protocols must be developed and detailed diagnostic investigations carried out in order to identify and understand the degradation mechanisms occurring in this class of catalyst materials. This will allow the appropriate design and implementation of degradation mitigation strategies for the development of NPMCs that can combine activity, performance, and long-term stability, providing immense economic advantages to current PEMFC markets.

References

1. James D, Kalinoski J (2010) Mass production cost estimation for direct H_2 PEM fuel cell systems for automotive applications: 2010 update. http://www1.eere.energy.gov/hydrogenandfuelcells/pdfs/dti_80kwW_fc_system_cost_analysis_report_2010.pdf
2. Qu L, Liu Y, Baek J-B, Dai L (2010) Nitrogen-doped graphene as efficient metal-free electrocatalyst for oxygen reduction in fuel cells. ACS Nano 4(3):1321–1326
3. Higgins D, Chen Z, Chen Z (2011) Nitrogen doped carbon nanotubes synthesized from aliphatic diamines for oxygen reduction reaction. Electrochim Acta 56:1570–1575
4. Gong K, Du F, Xia Z, Durstock M, Dai L (2009) Nitrogen-doped carbon nanotube arrays with high electrocatalytic activity for oxygen reduction. Science 323(5915):760–764
5. Chen Z, Higgins D, Tao H, Hsu R, Chen Z (2009) Highly active nitrogen-doped carbon nanotubes for oxygen reduction reaction in fuel cell applications. J Phys Chem C 113 (49):21008–21013

6. Bashyam R, Zelenay P (2006) A class of non-precious metal composite catalysts for fuel cells. Nature 443(7107):63–66
7. Sulub R, Martinez-Millan W, Smit MA (2009) Study of the catalytic activity for oxygen reduction of polythiophene modified with cobalt or nickel. Int J Electrochem Sci 4 (7):1015–1027
8. Feng YJ, He T, Alonso-Vante N (2009) Oxygen reduction reaction on carbon-supported $CoSe_2$ nanoparticles in an acidic medium. Electrochim Acta 54(22):5252–5256
9. Feng YJ, He T, Alonso-Vante N (2010) Carbon-supported $CoSe_2$ nanoparticles for oxygen reduction reaction in acid medium. Fuel Cells 10(1):77–83
10. Lee K, Zhang L, Zhang JJ (2007) Ternary non-noble metal chalcogenide (W-Co-Se) as electrocatalyst for oxygen reduction reaction. Electrochem Commun 9(7):1704–1708
11. Ishihara A, Ohgi Y, Matsuzawa K, Mitsushima S, Ota K (2010) Progress in non-precious metal oxide-based cathode for polymer electrolyte fuel cells. Electrochim Acta 55(27):8005–8012
12. DOE (2011) Technical plan – fuel cells. http://www1.eere.energy.gov/hydrogenandfuelcells/mypp/pdfs/fuel_cells.pdf
13. Othman R, Dicks AL, Zhu Z (2012) Non precious metal catalysts for the PEM fuel cell cathode. Int J Hydrogen Energy 37(1):357–372
14. Jaouen F, Proietti E, Lefèvre M, Chenitz R, Dodelet JP, Wu G, Chung HT, Johnston CM, Zelenay P (2010) Recent advances in non-precious metal catalysis for oxygen-reduction reaction in polymer electrolyte fuel cells. Energy Environ Sci 4:114–130
15. Chen Z, Higgins D, Yu A, Zhang L, Zhang J (2011) A review on non-precious metal electrocatalysts for PEM fuel cells. Energy Environ Sci 4(9):3167–3192
16. Gasteiger HA, Kocha SS, Sompalli B, Wagner FT (2005) Activity benchmarks and requirements for Pt, Pt-alloy, and non-Pt oxygen reduction catalysts for PEMFCs. Appl Catal B Environ 56(1–2):9–35
17. Gasteiger HA, Markovic NM (2009) Just a dream – or future reality? Science 324(5923):48–49
18. Jasinski R (1964) New fuel cell cathode catalyst. Nature 201(492):1212–1213
19. Alt H, Binder H, Sandsted G (1973) Mechanism of electrocatalytic reduction of oxygen on metal-chelates. J Catal 28(1):8–19
20. Gruenig G, Wiesener K, Gamburzev S, Iliev I, Kaisheva A (1983) Investigations of catalysts from the pyrolyzates of cobalt-containing and metal-free dibenzotetraazaannulenes on active-carbon for oxygen electrodes in an acid-medium. J Electroanal Chem 159(1):155–162
21. Franke R, Ohms D, Wiesener K (1989) Investigation of the influence of thermal-treatment on the properties of carbon materials modified by N-4-chelates for the reduction of oxygen in acidic media. J Electroanal Chem 260(1):63–73
22. van der Putten A, Elzing A, Visscher W, Barendrecht E (1986) Oxygen reduction on pyrolyzed carbon-supported transition-metal chelates. J Electroanal Chem 205(1–2):233–244
23. Gupta S, Tryk D, Bae I, Aldred W, Yeager E (1989) Heat-treated polyacrylonitrile-based catalysts for oxygen electroreduction. J Appl Electrochem 19(1):19–27
24. Jaouen F, Dodelet JP (2007) Non-noble electrocatalysts for O_2 reduction: how does heat treatment affect their activity and structure? Part I. Model for carbon black gasification by NH3: parametric calibration and electrochemical validation. J Phys Chem C 111 (16):5963–5970
25. Jaouen F, Lefevre M, Dodelet JP, Cai M (2006) Heat-treated Fe/N/C catalysts for O_2 electroreduction: are active sites hosted in micropores? J Phys Chem B 110(11):5553–5558
26. Jaouen F, Serventi AM, Lefevre M, Dodelet JP, Bertrand P (2007) Non-noble electrocatalysts for O_2 reduction: how does heat treatment affect their activity and structure? Part II. Structural changes observed by electron microscopy, Raman, and mass spectroscopy. J Phys Chem C 111 (16):5971–5976
27. Charreteur F, Jaouen F, Ruggeri S, Dodelet JP (2008) Fe/N/C non-precious catalysts for PEM fuel cells: influence of the structural parameters of pristine commercial carbon blacks on their activity for oxygen reduction. Electrochim Acta 53(6):2925–2938

28. Lefevre M, Proietti E, Jaouen F, Dodelet JP (2009) Iron-based catalysts with improved oxygen reduction activity in polymer electrolyte fuel cells. Science 324(5923):71–74
29. Wu G, More KL, Johnston CM, Zelenay P (2011) High-performance electrocatalysts for oxygen reduction derived from polyaniline, iron, and cobalt. Science 332(6028):443
30. Wu L, Nabae Y, Moriya S, Matsubayashi K, Islam NM, Kuroki S, Kakimoto M, Ozaki J, Miyata S (2010) Pt-free cathode catalysts prepared via multi-step pyrolysis of Fe phthalocyanine and phenolic resin for fuel cells. Chem Commun (Camb) 46(34):6377–6379
31. Liu G, Li XG, Ganesan P, Popov BN (2009) Development of non-precious metal oxygen-reduction catalysts for PEM fuel cells based on N-doped ordered porous carbon. Appl Catal B Environ 93(1–2):156–165
32. Li Y, Zhou W, Wang H, Xie L, Liang Y, Wei F, Idrobo J-C, Pennycook SJ, Dai H (2012) An oxygen reduction electrocatalyst based on carbon nanotube-graphene complexes. Nat Nanotechnol 7(6):394–400
33. Matter PH, Zhang L, Ozkan US (2006) The role of nanostructure in nitrogen-containing carbon catalysts for the oxygen reduction reaction. J Catal 239(1):83–96
34. Ikeda T, Boero M, Huang S-F, Terakura K, Oshima M, Ozaki J-i (2008) Carbon alloy catalysts: active sites for oxygen reduction reaction. J Phys Chem C 112(38):14706–14709
35. Choi CH, Park SH, Woo SI (2012) Binary and ternary doping of nitrogen, boron, and phosphorus into carbon for enhancing electrochemical oxygen reduction activity. ACS Nano. doi:10.1021/nn3021234
36. Nabae Y, Moriya S, Matsubayashi K, Lyth SM, Malon M, Wu LB, Islam NM, Koshigoe Y, Kuroki S, Kakimoto MA, Miyata S, Ozaki J (2010) The role of Fe species in the pyrolysis of Fe phthalocyanine and phenolic resin for preparation of carbon-based cathode catalysts. Carbon 48(9):2613–2624
37. Ozaki J, Tanifuji S, Furuichi A, Yabutsuka K (2010) Enhancement of oxygen reduction activity of nanoshell carbons by introducing nitrogen atoms from metal phthalocyanines. Electrochim Acta 55(6):1864–1871
38. Matter PH, Wang E, Millet JMM, Ozkan US (2007) Characterization of the iron phase in CNx-based oxygen reduction reaction catalysts. J Phys Chem C 111(3):1444–1450
39. Li XG, Liu G, Popov BN (2010) Activity and stability of non-precious metal catalysts for oxygen reduction in acid and alkaline electrolytes. J Power Sources 195(19):6373–6378
40. Bouwkamp-Wijnoltz AL, Visscher W, van Veen JAR, Boellaard E, van der Kraan AM, Tang SC (2002) On active-site heterogeneity in pyrolyzed carbon-supported iron porphyrin catalysts for the electrochemical reduction of oxygen: an in situ Mossbauer study. J Phys Chem B 106(50):12993–13001
41. Tributsch H, Koslowski UI, Dorbandt I (2008) Experimental and theoretical modeling of Fe-, Co-, Cu-, Mn-based electrocatalysts for oxygen reduction. Electrochim Acta 53(5):2198–2209
42. Kramm U, Abs-Wurmbach I, Herrmann-Geppert I, Radnik J, Fiechter S, Bogdanoff P (2011) Influence of the electron-density of FeN-centers towards the catalytic activity of pyrolyzed FeTMPPCl-based ORR-electrocatalysts. J Electrochem Soc 158:B69–B78
43. Olson TS, Pylypenko S, Fulghum JE, Atanassov P (2010) Bifunctional oxygen reduction reaction mechanism on non-platinum catalysts derived from pyrolyzed porphyrins. J Electrochem Soc 157:B54–B63
44. Proietti E, Jaouen F, Lefèvre M, Larouche N, Tian J, Herranz J, Dodelet J-P (2011) Iron-based cathode catalyst with enhanced power density in polymer electrolyte membrane fuel cells. Nat Commun 2:416–425
45. Zagal JH (1992) Metallophthalocyanines as catalysts in electrochemical reactions. Coord Chem Rev 119:89–136
46. Baker R, Wilkinson DP, Zhang JJ (2008) Electrocatalytic activity and stability of substituted iron phthalocyanines towards oxygen reduction evaluated at different temperatures. Electrochim Acta 53(23):6906–6919
47. Zagal JH, Ponce I, Baez D, Venegas R, Pavez J, Paez M, Gulppi M (2012) A possible interpretation for the high catalytic activity of heat-treated non-precious metal Nx/C catalysts

for O2 reduction in terms of their formal potentials. Electrochem Solid State Lett 15(6): B90–B92

48. Kramm U, Herranz J, Larouche N, Arruda T, Lefevre M, Jaouen F, Bogdanoff P, Fiechter S, Abs-Wurmbach I, Mukerjee S, Dodelet JP (2012) Structure of the catalytic sites in Fe/N/C-catalysts for O2-reduction in PEM fuel cells. Phys Chem Chem Phys. doi:10.1039/c1030xx00000x
49. Soboleva T, Zhao X, Malek K, Xie Z, Navessin T, Holdcroft S (2010) On the micro-, meso-, and macroporous structures of polymer electrolyte membrane fuel cell catalyst layers. ACS Appl Mater Interfaces 2(2):375–384
50. Ignaszak A, Ye S, Gyenge E (2008) A study of the catalytic interface for O2 electroreduction on Pt: the interaction between carbon support meso/microstructure and ionomer (Nafion) distribution. J Phys Chem C 113(1):298–307
51. Choi J, Hsu R, Chen Z (2010) Highly active porous carbon-supported nonprecious metal-N electrocatalyst for oxygen reduction reaction in PEM fuel cells. J Phys Chem C 114 (17):8048–8053
52. Huang H-C, Shown I, Chang S-T, Hsu H-C, Du H-Y, Kuo M-C, Wong K-T, Wang S-F, Wang C-H, Chen L-C, Chen K-H (2012) Pyrolyzed cobalt corrole as a potential non-precious catalyst for fuel cells. Adv Funct Mater. doi:10.1002/adfm.201200264
53. Liu G, Li XG, Ganesan P, Popov BN (2010) Studies of oxygen reduction reaction active sites and stability of nitrogen-modified carbon composite catalysts for PEM fuel cells. Electrochim Acta 55(8):2853–2858
54. Garsuch A, Dahn T, Klepel O, Garsuch RR, Dahn JR (2008) Oxygen reduction behavior of highly porous non-noble metal catalysts prepared by a template-assisted synthesis route. J Electrochem Soc 155:B236–B243
55. Garsuch A, MacIntyre K, Michaud X, Stevens DA, Dahn JR (2008) Fuel cell studies on a non-noble metal catalyst prepared by a template-assisted synthesis route. J Electrochem Soc 155 (9):B953–B957
56. Liu HS, Shi Z, Zhang JL, Zhang L, Zhang JJ (2009) Ultrasonic spray pyrolyzed iron-polypyrrole mesoporous spheres for fuel cell oxygen reduction electrocatalysts. J Mater Chem 19(4):468–470
57. Serov A, Robson MH, Smolnik M, Atanassov P (2012) Templated bi-metallic non-PGM catalysts for oxygen reduction. Electrochim Acta. doi:10.1016/j.electacta.2012.1007.1008
58. Wang XQ, Lee JS, Zhu Q, Liu J, Wang Y, Dai S (2010) Ammonia-treated ordered mesoporous carbons as catalytic materials for oxygen reduction reaction. Chem Mater 22(7):2178–2180
59. Herrmann I, Kramm U, Fiechter S, Bogdanoff P (2009) Oxalate supported pyrolysis of CoTMPP as electrocatalysts for the oxygen reduction reaction. Electrochim Acta 54 (18):4275–4287
60. Xie J, Xu F, Wood Iii DL, More KL, Zawodzinski TA, Smith WH (2010) Influence of ionomer content on the structure and performance of PEFC membrane electrode assemblies. Electrochim Acta 55(24):7404–7412
61. Liu Y, Ji C, Gu W, Baker DR, Jorne J, Gasteiger HA (2010) Proton conduction in PEM fuel cell cathodes: effects of electrode thickness and ionomer equivalent weight. J Electrochem Soc 157(8):B1154–B1162
62. Li W, Yu A, Higgins DC, Llanos BG, Chen Z (2010) Biologically inspired highly durable iron phthalocyanine catalysts for oxygen reduction reaction in polymer electrolyte membrane fuel cells. J Am Chem Soc 132:17056–17058
63. Borup R, Meyers J, Pivovar B, Kim YS, Mukundan R, Garland N, Myers D, Wilson M, Garzon F, Wood D, Zelenay P, More K, Stroh K, Zawodzinski T, Boncella J, McGrath JE, Inaba M, Miyatake K, Hori M, Ota K, Ogumi Z, Miyata S, Nishikata A, Siroma Z, Uchimoto Y, Yasuda K, Kimijima KI, Iwashita N (2007) Scientific aspects of polymer electrolyte fuel cell durability and degradation. Chem Rev 107(10):3904–3951

64. Li S, Zhang L, Kim J, Pan M, Shi Z, Zhang J (2010) Synthesis of carbon-supported binary FeCo-N non-noble metal electrocatalysts for the oxygen reduction reaction. Electrochim Acta 55(24):7346–7353
65. Wu G, Artyushkova K, Ferrandon M, Kropf AJ, Myers D, Zelenay P (2009) Performance durability of polyaniline-derived non-precious cathode catalysts. ECS Trans 25(1):1299–1311
66. Lefevre M, Dodelet JP (2003) Fe-based catalysts for the reduction of oxygen in polymer electrolyte membrane fuel cell conditions: determination of the amount of peroxide released during electroreduction and its influence on the stability of the catalysts. Electrochim Acta 48 (19):2749–2760
67. Koslowski UI, Abs-Wurmbach I, Fiechter S, Bogdanoff P (2008) Nature of the catalytic centers of porphyrin-based electrocatalysts for the ORR: a correlation of kinetic current density with the site density of Fe-N-4 Centers. J Phys Chem C 112(39):15356–15366
68. Charreteur F, Jaouen F, Dodelet JP (2009) Iron porphyrin-based cathode catalysts for PEM fuel cells: influence of pyrolysis gas on activity and stability. Electrochim Acta 54 (26):6622–6630
69. Schilling T, Bron M (2008) Oxygen reduction at Fe–N-modified multi-walled carbon nanotubes in acidic electrolyte. Electrochim Acta 53(16):5379–5385
70. Byon HR, Suntivich J, Crumlin EJ, Shao-Horn Y (2011) Fe-N-modified multi-walled carbon nanotubes for oxygen reduction reaction in acid. Phys Chem Chem Phys 13(48):21437–21445
71. Choi JY, Higgins D, Chen Z (2012) Highly durable graphene nanosheet supported iron catalyst for oxygen reduction reaction in PEM fuel cells. J Electrochem Soc 159:B87–B90
72. Byon HR, Suntivich J, Shao-Horn Y (2011) Graphene-based non-noble-metal catalysts for oxygen reduction reaction in acid. Chem Mater 23(15):3421–3428
73. Meng H, Larouche N, Lefèvre M, Jaouen F, Stansfield B, Dodelet J (2010) Iron porphyrin-based cathode catalysts for polymer electrolyte membrane fuel cells: effect of NH3 and Ar mixtures as pyrolysis gases on catalytic activity and stability. Electrochim Acta 55 (22):6450–6461
74. Herranz J, Jaouen F, Lefèvre M, Kramm UI, Proietti E, Dodelet J-P, Bogdanoff P, Fiechter S, Abs-Wurmbach I, Bertrand P, Arruda TM, Mukerjee S (2011) Unveiling N-protonation and anion-binding effects on Fe/N/C catalysts for O2 reduction in proton-exchange-membrane fuel cells. J Phys Chem C 115(32):16087–16097

Chapter 10
The Controversial Role of the Metal in Fe- or Co-Based Electrocatalysts for the Oxygen Reduction Reaction in Acid Medium

Jean-Pol Dodelet

Abstract Despite decades of research on Fe (or Co)-based electrocatalysts for the oxygen reduction reaction (ORR) in acidic medium, such as that in PEM fuel cells, the role of the metal is still one that raises a great deal of controversy. Consequently, the nature of the catalytic site in these non-noble metal ORR catalysts is still a topic of debate. One camp within the scientific community believes that the metal is an integral and electrochemically active part of the catalytic site, while the other believes that the metal is merely a chemical catalyst for the formation of special oxygen-reducing N-doped carbon structures. After presenting the case for the importance of non-noble catalysts at the cathode of PEM fuel cells, we introduce the three models of active sites that were advocated during the 1980s by van Veen, Yeager, and Wiesener and discuss how they have evolved, especially that of Yeager. Wiesener's model is analyzed in detail through the work of several research groups that have been staunch supporters. The oxygen reduction mechanism on Fe-based and N-doped carbon catalytic sites is also reviewed. It is concluded that all the active sites proposed by van Veen, Yeager, and Wiesener in the 1980s, while different, are in fact simultaneously present in Fe (or Co)-based catalysts active for ORR in acidic medium, except that their activity and relative population in these catalysts are different, depending on the choice of the metal precursor, nitrogen precursor, structural properties of the carbon support, and the synthesis procedure.

10.1 Introduction

It is a well-known fact that fossil fuels like coal, oil, and gas are the energy sources that account for about 90 % of all the energy consumed by the developed world. With a global consumption of 85 million barrels per day (1 barrel = 160 L), oil is

---

J.-P. Dodelet (✉)
INRS-Énergie Matériaux et Télécommunications, 1650 blvd Lionel Boulet, Varennes, QC, Canada J3X 1S2
e-mail: dodelet@emt.inrs.ca

M. Shao (ed.), *Electrocatalysis in Fuel Cells*, Lecture Notes in Energy 9,
DOI 10.1007/978-1-4471-4911-8_10,

the energy source of choice for transportation [1]. This sector represents more than one third of today's total energy consumption per capita [2]. Despite a projected increase of oil consumption in the next few decades, known oil reserves are not overly abundant and may represent only about 40 years' worth of energy at the present consumption rate. The projected life of natural gas reserves is of about 60 years, while it is about 250 years for coal [3]. In the not-so-distant future, we will therefore likely need an alternative energy source to fossil fuels. The latter may be more valuable and important as a source of carbon in the petrochemical, chemical, and pharmaceutical industries for future generations.

Among the possible sustainable replacements for fossil fuels are two key prospects: methanol and hydrogen. A methanol-based society, like the one advocated by G. Olah, would use the half-cycle of the oxidation of methanol to CO_2 to produce energy and the other half-cycle to return CO_2 back to methanol in a sustainable way [4]. Similarly, a hydrogen-based society would oxidize H_2 to H_2O to produce energy and reduce H_2O back to H_2 in a sustainable way. The advantage of using H_2 as a fuel is that, unlike methanol, it is easily oxidizable electrochemically by O_2 (Air), even at the low temperatures (around 80 °C) in polymer H_2/O_2 (Air) electrolyte membrane (PEM) fuel cells. The latter are very efficient electrical power generators that are especially well adapted for transportation applications, but also for smaller portable applications. Using (compressed) pure H_2 as a fuel, PEM fuel cells would only produce H_2O as a reaction product. Then, in an electrolyzer, water can be efficiently split back into H_2 and O_2 using stationary renewable electrical energy sources like solar, wind, and hydroelectricity.

In order to generate acceptable power levels, however, low-temperature PEM fuel cells need catalyzed electrodes. Thus far, the electrocatalysts used in PEM fuel cells have been exclusively Pt based. However, Pt is an industrial metal, mainly mined in South Africa (with about 75 % of the world production) and Russia (about 15 % of the world production). Today, 50 ± 10 % of Pt production of the 200,000 kg/year is used as chemical catalyst in catalytic converters for internal combustion engine vehicles. A mere glance at Fig. 10.1 immediately emphasizes the link between the cost of Pt, that of crude oil, and the health of the economy. *In other words, one cannot hope for a strong economy and for Pt price to stay low at the same time.*

Since Pt is a scarce and expensive metal, in 2002, the US Department of Energy (DOE) set targets for the maximum quantity of Pt to be used in H_2/O_2 (Air) PEM fuel cells. Initially, the 2015 target was set to 0.2 g Pt/kWe (with kWe for the rated electric power) for total anode and cathode Pt content combined. However, due to the considerable rise in Pt price, a new target—0.125 g Pt/kWe—was recently set for 2017 [5]. At around $1,700–1,800 per Pt Troy ounce (31.1 g), 0.125 g Pt/kWe would represent a Pt raw material cost of around $7 Pt/kWe. Meanwhile, the DOE also sets the cost target for the entire membrane electrode assembly to $9/kWe! There is, therefore, a strong case for replacing Pt with a lower cost non-noble metal-based electrocatalyst (or a metal-free electrocatalyst).

In the acid medium of PEM fuel cells (around pH 1), the oxidation of H_2 on Pt is a much easier electrochemical reaction than the oxygen reduction reaction (ORR) on Pt. The latter reaction is notoriously slow. Consequently, about 5–10 times more

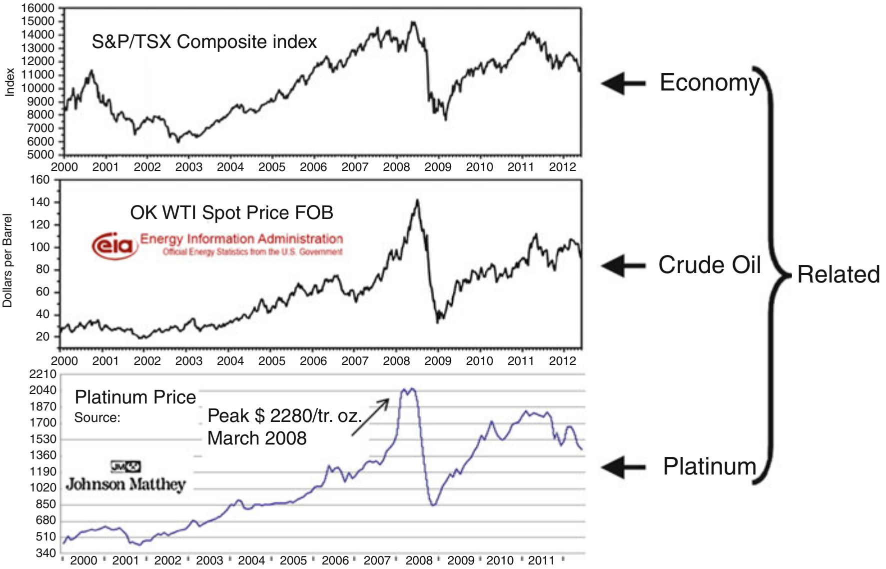

Fig. 10.1 Relationship between the costs of Pt, crude oil, and the health of the economy since the year 2000

Pt is needed at the cathode of PEM fuel cells than at their anode [6]. Therefore, a much greater cost reduction can be achieved by replacing Pt with a lower cost non-noble metal-based catalyst at the cathode of PEM fuel cells.

It is not possible to simply replace Pt with a non-noble metal as these metals (in their metallic state) will quickly corrode at the cathode of a PEM fuel cell. Oxides also have a strong tendency to dissolve in such an acidic environment. Some oxides, however, are acid resistant, but despite important advances recently reported in performing ORR in acid medium on these catalysts, they are still insufficiently active to replace Pt in fuel cells [7]. A detailed review on this topic can be found in Chap. 13. Promising contenders for the substitution of Pt-based catalysts for the cathode are Fe (or Co)-based electrocatalysts since they were recently reported to exhibit relatively high activity, stability, and high power in the potential range useful for transport and portable applications of PEM fuel cells [8–10].

The DOE has also set targets for non-platinum group metal (non-PGM) electrocatalysts. These targets are, of course, different from the DOE targets set for Pt-based catalysts because the nature of their catalytic sites is different from those of Pt nanoparticles or Pt layers on a carbon or inorganic support. Pt-based electrocatalysts are evaluated for their mass and specific activities at 900 mV iR-free in PEM fuel cells under operating conditions defined in ref. [6]. The 2015 target set by the DOE for non-PGM-based electrocatalysts for the cathode of H_2/O_2 (Air) PEM fuel cells was first set at a volumetric activity of 300 A/cm^3 measured at 800 $mV_{iR\text{-}free}$ and has remained so for the 2017 target [5]. The fuel cell operating conditions are the same as for Pt-based electrocatalysts. Today (2012), the highest volumetric activity reported was 230 A/cm^3, achieved with a Fe-based electrocatalyst [10]. This is already quite close to and within grasp of the 2017 DOE target value of 300 A/cm^3 for non-PGM catalysts. Note that it should be better now, that non-PGM catalysts have non-negligible volumetric activities at 900 mV$_{\text{iR-free}}$, to set their DOE target at that potential rather than at 800 mV$_{\text{iR-free}}$ in order to avoid extended extrapolations to obtain their kinetic activity free of mass transport limitations.

It may seem unusual to measure and compare the catalytic activity in terms of the volume of the electrode (A/cm^3), but contrary to Pt-based catalysts, which have a much higher raw material cost and are generally used with high Pt loadings on a conductive support in electrodes having a thickness lower than 10 μm, the lower-cost non-noble metal electrocatalysts may be used in much thicker cathodes (up to about 100 μm thick) before being subject to significant mass transport limitations. In an electrode using a non-noble metal electrocatalyst for ORR, the kinetically controlled current per unit of volume is given by Eq. (10.1):

$$\text{Current }(E) = \text{SD} \times \text{TOF}(E) \times \text{e}^- \tag{10.1}$$

where Current (E), in A/cm^3, is a function of the applied potential E; SD is the number of catalytic sites/cm^3; TOF (E), in electron per site and per second, is the average turnover frequency of the catalytic site(s) and is also a function of E; and e^- is the charge of the electron in Coulombs. To increase the current per unit of volume at a specific potential, one needs to increase either (1) SD, (2) TOF (E), or (3) both SD and TOF (E). The turnover frequency for ORR of a catalytic site is an intrinsic property of this site. It is probably difficult to change it, let alone to increase it. It is much easier to increase the number of catalytic sites by modifying the synthesis of the catalyst. In order to do so, it is useful to have at least a basic understanding about the nature of the various catalytic site(s) at work in the catalyst.

Despite decades of research, the nature of the catalytic sites in non-noble metal ORR catalysts is still a topic of healthy debate and is the subject of this chapter. There are indeed two very different schools of thought regarding the nature of these catalytic sites: the metal in the non-noble metal electrocatalyst is either an active participant in the ORR or it is not. In the remainder of this chapter, a brief history of the various structures of the catalytic sites proposed in the early days will be presented. This will be followed by the contribution of our group and others to elucidate what we believe is the nature of the catalytic site(s) in these catalysts and why we (and others) believe that the metal is at the heart of the catalytic sites for ORR in these most active catalysts. This will be followed by a presentation of the arguments of the other schools of thought, which advocate that the metal is not electrocatalytically active, but instead only serves as a chemical catalyst for producing special carbon structures, which are the actual active site for ORR. The chapter continues with a discussion about these differing views regarding the nature of the catalytic site(s) and the mechanism for ORR on these catalytic sites to end up with concluding remarks.

10.2 The First Three Models of Catalytic Sites for ORR

Me–N_4 macrocyclic complexes (with N_4-macrocycles being, for instance, tetraazaannulene [TAA], tetramethoxyphenyl-porphyrin [TMPP], phthalocyanine [Pc]), and Me = Co or Fe were the first to be used as precursors of the catalytic sites. In particular, unsupported Co–N_4 chelates (CoTAA, CoTMPP, and CoPc) or Co–N_4 chelates adsorbed on a carbon support were used in the 1970s as ORR electrocatalysts [11]. However, both unsupported and carbon-supported Co–N_4 chelate electrocatalysts underwent a rapid decline in the activity. An important discovery in these early years was that catalyst stability as well as activity toward ORR could be improved by subjecting Co–N_4 chelate/carbon samples to thermal treatment in an inert gas like N_2 or Ar [12].

The question then was the following: what happens to the Me–N_4 catalytic site of the chelate after the heat treatment? This topic was strongly debated in the early days and is still not completely understood today. Essentially, three models of the catalytic site for ORR were presented, one each by van Veen, Yeager, and Wiesener, and their respective collaborators.

- For van Veen, the thermal treatment at temperatures at which catalytic activity is maximum (500–600 °C) does not lead to the complete destruction of the macrocycles, but rather to a ligand modification which keeps the Me–N_4 moiety intact (see Fig. 10.2) [13, 14].
- Yeager and coworkers, who were mainly working at higher pyrolysis temperatures (800–850 °C), disagreed. They proposed that the decomposition of Me–N_4 macrocycles starts at about 400–500 °C. At 800 °C, most of the metal becomes a mixture of oxides and metal, the latter spontaneously oxidizing when exposed to air at room temperature. Upon contact with an electrolyte solution, oxide species undergo dissolution. Metallic ions subsequently adsorb or coordinate to thermally formed sites on the carbon surface, most likely involving one or more nitrogen atoms bound to the carbon surface, but of a type different from the macrocycle-derived Me–N_4 centers proposed by van Veen and coworkers. The resulting structure, C–N_x–Me, was believed to be the true catalytic site for oxygen reduction [15–17].
- A third model was proposed by Wiesener. In his view, the Co or Fe ions of the adsorbed N_4 chelates promoted the decomposition of the chelate upon thermal heat treatment followed by the formation, at high temperature, of CNx, a special form of carbon, bearing nitrogen atoms that would be the true catalyst [18, 19]. In this scenario, the metal is believed to be only an intermediate and has no role in the electroreduction of oxygen.

In 1989, Yeager and coworkers reported the preparation and characterization of a novel catalyst active for oxygen reduction in acid medium that was made from the heat treatment at 800 °C of polyacrylonitrile (PAN) and a Co^{II} or Fe^{II} salt dissolved in dimethylformamide and impregnated on a carbon support [20]. This novel preparation procedure allowed for the generalization of the ingredients necessary

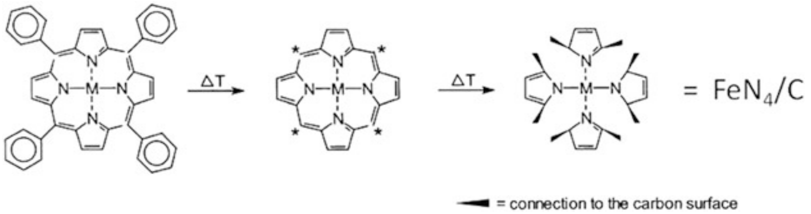

Fig. 10.2 Reaction steps of porphyrin with the carbon support during heat treatment (according to Fig. 9 in ref. [13]; reproduced with permission of the American Chemical Society)

to obtain an ORR electrocatalyst in acid medium: (1) a Co or Fe precursor, (2) a nitrogen precursor, and (3) a carbon support for the adsorption or impregnation of the metal and nitrogen precursors. The resulting material had to be pyrolyzed at relatively high temperature, which, according to Yeager, was necessary to incorporate nitrogen functionalities onto the carbon support and to reduce the metal ions. The previous procedure using Me–N_4 chelates was only a coincidental case in which the nitrogen and metal precursors were present in the same molecule, the N_4-metal chelate. The possibility to use two separate precursors, one for the metal and the other for nitrogen, offered much more flexibility in the preparation of the catalysts and led to the use of much cheaper molecular precursors than the Me–N_4 chelates. According to Yeager [20], the active site resulting from the novel procedure was the same as that previously proposed for the catalysts made from Me–N_4 chelates. Once again, the catalytic site was C–N_x–Me and was self-assembled when in contact with the electrolyte which dissolved the metal particles generated during pyrolysis. Here, however, as PAN was used, the nitrile nitrogen of PAN was converted to pyridinic nitrogen during the heat treatment and were believed to provide binding sites for the transition metal ions.

In the years following 1989, many groups including ours prepared catalysts for ORR using various Me–N_4 chelates as well as new nitrogen and metal precursors. The overall work reported during these years is reviewed in ref. [21]. One work in particular stands out. It is a work by van Veen and collaborators [22], who used several pyrrole derivatives, as nitrogen precursors, which were loaded onto Vulcan and Norit BRX with Co acetate, as the metal precursor. The Co loading was 1.5 wt% for Vulcan and 4.5 wt% Co for Norit. The heat-treatment temperature was 700 °C in inert atmosphere. The best catalyst was obtained for a Co:N ratio of 1:10 with 2,5-dimethylpyrrole adsorbed on Vulcan. This catalyst was found to be equivalent to that obtained with CoTMPP loaded at 7 wt% chelate (0.6 wt% Co) on Vulcan and also heat treated at 700 °C. After EXAFS analysis of their catalysts, van Veen and coworkers concluded that a Co–N_4 complex identical to that obtained with CoTMPP was, once again, the active catalytic site in their two catalysts. They also realized that the nitrogen precursor (2,5-dimethylpyrrole) had a structure that closely resembled one of the four metal-ligating groups in the proposed catalytic site (Fig. 10.2).

It is clear that, as far as the catalytic site is concerned, both Yeager and van Veen maintained their early positions. They did share a common point, however, which was that a metallic Fe or Co ion was at the heart of their proposed respective catalytic sites: Me–N_4 bound to carbon for van Veen and C–N_x–Me for Yeager. While van Veen and Yeager's models for ORR catalytic sites were popular in the 1990s, the third model, proposed by Wiesener, had very few supporters during this same period. The most important work, invoking a metal-less catalytic site based on nitrogen, oxygen, and carbon atoms and on various oxidation states of the nitrogen atom, was that of Savy and coworkers [23]. Their catalyst was obtained by adsorbing CoTAA on Norit SX Ultra at a loading of 2.3 wt% Co and then heat treated up to 900 °C in inert atmosphere. Because no more Co was detectable by XPS after longevity testing in 0.5 M H_2SO_4 solution, while the catalyst was still active, they concluded that the catalytic site had to be metal-less. A sequence of reactions for the reduction of oxygen on a metal-less catalytic site is given in their paper. This is, however, a rare case where Savy invoked a metal-less catalytic site, because in most of his other work, he mainly agreed with the model proposed by van Veen. Wiesener's CNx model of the catalytic site for ORR would, however, gain some interest after 2000 and rally many vocal supporters, as will be discussed later.

Using high non-noble metal loadings on carbon supports (following the example of Pt/C catalysts highly loaded in Pt) was characteristic of non-noble metal catalyst research in the 1990s, including for work done by our group (see ref. [21] for details). However, doing so resulted in high levels of inactive material being formed in the non-noble metal catalysts. The latter predominated the characterization of these catalysts and prevented any conclusions from being drawn about the identity or nature of the catalytic site(s). By the end of the 1990s, our group radically modified the procedure for synthesizing non-noble catalysts for ORR by using very low loadings (either as Fe or Co acetate or as Co- or ClFeTMPP) and replacing CH_3–CN, used as nitrogen precursor, with NH_3 gas during pyrolysis (in a mixture with H_2 and Ar). We also used a synthetic carbon precursor, pyrolyzed perylene tetracarboxylic dianhydride (PTCDA) (see insert in Fig. 10.3), to create our own metal-free carbon supports. PTCDA (a dye) loses its carboxylic moiety upon heat treatment above 520 °C, a temperature at which PTCDA begins to polymerize into carbon fibers [25]. The reasons for using a carbon precursor like PTCDA were twofold. The first was that it was possible to fully purify the as-delivered PTCDA of most of its metallic impurities [26]. The second reason was that pyrolyzed PTCDA gave a carbon support with little background signal in ToF-SIMS, a surface analytical technique that we used to obtain important information about the catalytic site.

Figure 10.3 shows that, when iron acetate is used as the Fe precursor, the catalytic activity increases very quickly with Fe loading between 0 and 2,500 ppm and then levels off at loadings of 5,000 ppm (0.5 wt%) Fe and higher. Larger Fe loadings (up to about 2 wt%) could be reached before a leveling off of the catalytic activity when the Fe precursor was chloro-iron tetramethoxy phenyl porphyrin (ClFeTMPP). However, the maximum activity reached with ClFeTMPP

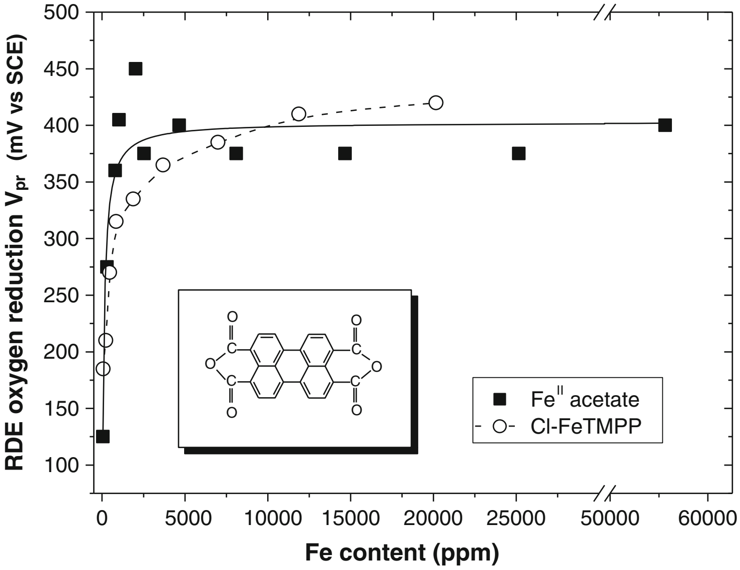

Fig. 10.3 The catalytic activity for O_2 reduction (in O_2-saturated H_2SO_4 solution at pH 1) vs. the Fe content for catalysts prepared by adsorbing either iron acetate or ClFeTMPP on PTCDA and pyrolyzing the material at 900 °C in H_2:Ar:NH_3 (1:1:2) (according to Fig. 2 in ref. [24]; reproduced with permission of the American Chemical Society). *Note*: 5,000 ppm = 0.5 wt%

and iron acetate as iron precursors was the same [24]. All catalysts in Fig. 10.3 were prepared via the impregnation of the Fe precursor on PTCDA. The resulting material was then pyrolyzed at 900 °C in H_2:Ar:NH_3. The difference between iron acetate and porphyrin precursors was interpreted in terms of a better interaction of the PTCDA with the Fe-porphyrin than with iron acetate, leading to a better dispersion of the iron ions on the carbon precursor. Given that similar activity results were obtained from catalysts made with iron acetate and the iron porphyrin, we mostly concentrated our efforts on the iron acetate as iron precursor in the preparation of these catalysts. Unless otherwise specified, all the results from our group that are described throughout the remainder of this chapter were obtained with iron acetate as the iron precursor.

The XPS spectra of the catalysts prepared with iron acetate were quite instructive [27]. Narrow-scan spectra of Fe $2p_{3/2}$ and $2p_{1/2}$ revealed that Fe was always found in the ionic form for all Fe loadings, but that a reduced form of Fe (either Fe^0 or an iron carbide) was also detected above 8,100 ppm (0.81 wt%) Fe, in agreement with the leveling off of the catalytic activity observed in Fig. 10.3. Narrow-scan spectra of N1s of the same catalysts revealed that only the low-binding energy peak mainly assigned to pyridinic nitrogen [28, 29] (see Fig. 10.4 for the meaning of pyridinic nitrogen) was shifting toward higher binding energies for higher Fe loadings. A saturation of this effect at 0.3 eV appeared above 4,660 ppm Fe, again in agreement with the leveling off of the catalytic activity observed in Fig. 10.3. This shift has been interpreted in terms of a preferential interaction of

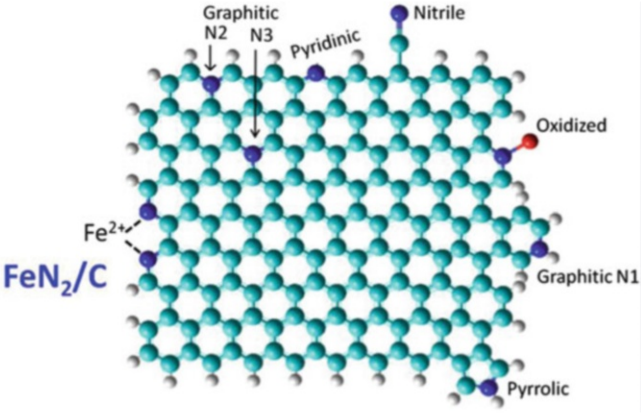

Fig. 10.4 Proposed moiety of the catalytic site referred to as FeN_2/C consisting of two pyridinic N atoms in a 1,10-phenanthroline-type structure coordinating a Fe^{2+} ion [30]. The complete structure of this site was still undetermined in 2002; also shown are the various types of nitrogen atoms in a typical graphene plane

Fe ion with pyridinic nitrogen atoms in the catalytic site. These nitrogen atoms are located at the edge of a graphene layer and contribute one electron to the π orbitals of the layer. Pyridinic nitrogen atoms also have an orbital in the plane of the graphene layer containing two nonbonding electrons, which are available to coordinate a metal ion such as iron.

ToF-SIMS experiments performed on similar catalysts also prepared with iron acetate revealed (1) that the catalytic site contained at least two pyridinic nitrogen atoms and (2) that these nitrogen atoms were in a 1,10-phenanthroline-type structure like the one reproduced in Fig. 10.4 and proposed by our group in 2002 as part of the catalytic site in these catalysts [30]. This conclusion was reached because one ion—$FeN_2C_4^+$—came to the fore out of all ions detected by ToF-SIMS when the catalysts were prepared at various temperatures. The change in the relative intensity (abundance) of the latter is compared in Fig. 10.5 [24] with the evolution of the catalytic activity for the same Fe-based catalysts vs. the pyrolysis temperature. The coincidence of the two patterns indicated that $FeN_2C_4^+$ is the ToF-SIMS signature of the main catalytic site found in such catalysts. We refer to this site as FeN_2/C. The full coordination of the catalytic site proposed in Fig. 10.4 was unknown at that time. More about the coordination will be revealed later.

Besides $FeN_2C_4^+$, other ions of the type $FeN_xC_y^+$ were also detected in the ToF-SIMS spectra of the catalysts prepared with iron acetate as Fe precursor (see Fig. 10.6). They were of much lower relative abundance than $FeN_2C_4^+$ and could be divided into four families, each one having a different number of nitrogen atoms (from 1 to 4) bound to various numbers of carbon atoms. For instance, another ion—$FeN_4C_8^+$—was of relatively high abundance (up to 8 % at 500 °C, compared with the abundance of about 80 % for $FeN_2C_4^+$ at 800 °C). It was assigned to a Fe ion coordinated to four nitrogen atoms, each nitrogen atom being itself bound to two carbon atoms (see Fig. 10.6). This ion is typical of the fragmentation of

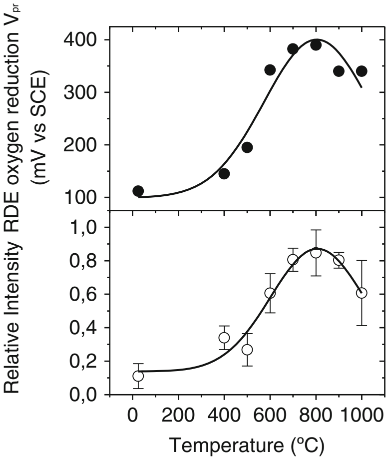

Fig. 10.5 Comparison of the catalyst activity for ORR in O_2 saturated H_2SO_4 solution at pH 1 (*top panel*) and the relative intensity of $FeN_2C_4^+$ (*bottom panel*) vs. pyrolysis temperature for catalysts obtained by adsorbing iron acetate (0.2 wt% Fe) on pre-pyrolyzed PTCDA followed by heat treatment in inert atmosphere at various temperatures, ranging from 400 to 1,000 °C. Pre-pyrolyzed PTCDA is obtained by heat-treating PTCDA at 900 °C in H_2:Ar:NH_3 (1:1:2) (according to Fig. 8 in ref. [24]; reproduced with permission of the American Chemical Society)

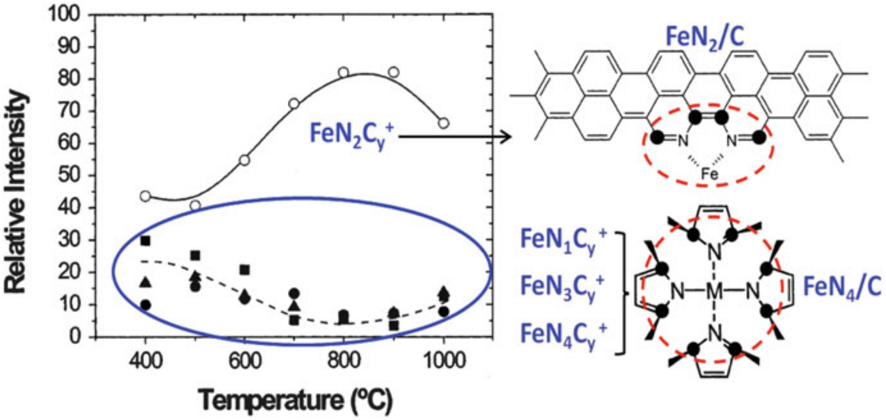

Fig. 10.6 Relative intensity for all $FeN_xC_y^+$ ions of the $FeN_2C_y^+$ family (*open circles*), $FeN_1C_y^+$ family (*dark squares*), $FeN_3C_y^+$ family (*dark triangles*), and $FeN_4C_y^+$ family (*dark circles*) as a function of the pyrolysis temperature for catalysts analyzed by ToF-SIMS. The catalysts were obtained by adsorbing iron acetate (0.2 wt% Fe) on pre-pyrolyzed PTCDA and heat-treating in inert atmosphere at various temperatures ranging from 400 to 1,000 °C. Pre-pyrolyzed PTCDA was obtained by heat-treating PTCDA at 900 °C in H_2:Ar:NH_3 (1:1:2) (according to Fig. 4 in ref. [30]: reproduced with permission of the American Chemical Society). $FeN_2C_y^+$, which is mainly composed of $FeN_2C_4^+$, is the signature for the proposed FeN_2/C structure for the major catalytic site in these catalysts. $FeN_4C_y^+$, which is mainly composed of $FeN_4C_8^+$, and $FeN_1C_y^+$ and $FeN_3C_y^+$, which are fragments of ionic products of $FeN_4C_y^+$, are all the signatures of the proposed FeN_4/C structure for the minor catalytic site in these catalysts

ClFeTMPP$^+$ and is characteristic of the Fe–N_4 moiety of the porphyrins [30]. *It was, however, found in catalysts prepared with iron acetate*! As $FeN_4C_8^+$ is also reminiscent of the structure of the catalytic site proposed by van Veen and collaborators, which is illustrated in Fig. 10.2, the typical catalytic site referred to as FeN_4/C.

In a refined analysis of the ToF-SIMS spectra of catalysts prepared with iron acetate as the Fe precursor, it was assumed that all the ions having the same number of N atoms, originated from the same catalytic site(s). Figure 10.6 shows the relative intensity of each family of ions vs. the pyrolysis temperature. From Fig. 10.6, we observe two different behaviors. On the one hand, the family of ions of the type $FeN_2C_y^+$ increases in relative abundance with the pyrolysis temperature, then goes through a maximum at 800–900 °C, and decreases at 1,000 °C. On the other hand, the relative intensity of the three other families of ions behaves similarly, but with a maximum abundance at a low pyrolysis temperature. From this behavior, one may conclude that the ions belonging to the N_1, N_3, and N_4 families have the same origin: FeN_4/C (N_1 and N_3 ions would all originate from the fragmentation of N_4 containing ions). On the other hand, the origin of the ions of the N_2 family is FeN_2/C, whose structure is presented in Fig. 10.4. *Both FeN_4/C and FeN_2/C were therefore found simultaneously, but in various proportions based on the pyrolysis temperature, in catalysts obtained with iron acetate as the Fe precursor*.

The simultaneous presence of the same two FeN_2/C and FeN_4/C catalytic sites was also observed when ToF-SIMS experiments were performed on catalysts made with an Fe-porphyrin (ClFeTMPP) with the same Fe loading as that of iron acetate (0.2 wt% Fe, nominal) and prepared under the same experimental conditions as those used for the catalysts made with iron acetate. In this case, however, the relative intensity of ions from the FeN_4/C sites was always greater than that of the ions released by the FeN_2/C sites. Four families of N-containing ions were again found, with the N_2 family behaving differently from the N_1, N_3, and N_4 families of ions. Two types of catalytic sites emerged once again from this analysis. *As a general conclusion from these experiments, it appears that irrespective of the iron or nitrogen precursor used to obtain a catalyst for ORR, the resulting catalyst material always contains two types of catalytic sites referred to as Fe–N_2/C and Fe–N_4/C, the relative proportions of which depend on the pyrolysis temperature and the particular iron and nitrogen precursors used.*

FeN_4/C corresponds to the catalytic site proposed by van Veen. One may wonder, however, if FeN_2/C corresponds to the catalytic site (C–N_x–Me) proposed by Yeager. The answer to this question is no! Remember that, according to Yeager, C–N_x–Me is not obtained during pyrolysis, but after contact of the pyrolyzed material with the acid electrolyte in which iron oxides and iron metal produced during pyrolysis are dissolved and re-coordinated to C–N_x functionalities of the carbon to produce C–N_x–Me sites for ORR. A recent experiment confirmed, however, that C–N_x–Fe is only the precursor of the FeN_2/C catalytic site [31]. In this experiment, when a commercial N234 carbon black was first pyrolyzed in NH_3 at 950 °C, its N content increased from 0 to 2.2 at.%. When this N-enriched carbon

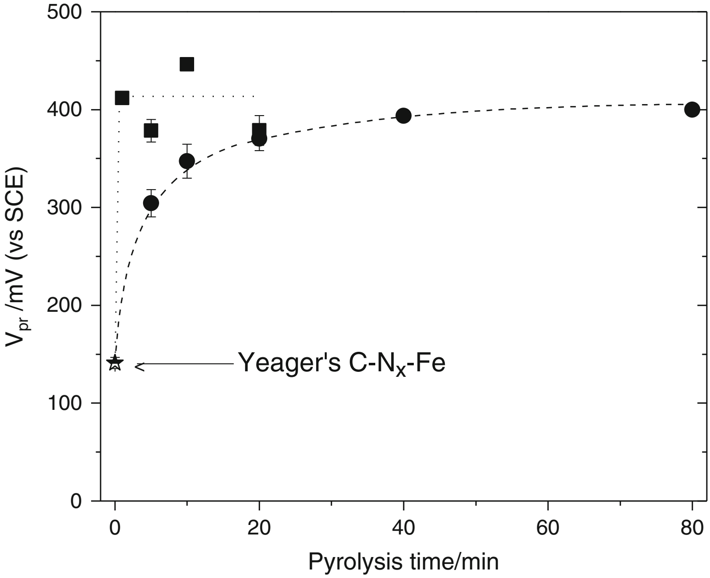

Fig. 10.7 Catalytic activity in O_2 saturated H_2SO_4 solution at pH 1 vs. pyrolysis time for N234 pristine carbon black that was first etched in NH_3 at 950 °C and then impregnated with 0.2 wt% Fe (as iron acetate) (*half-shaded star*). A second pyrolysis of this material performed at 950 °C in pure NH_3 (*black squares*) or in Ar (*black circles*) resulted in a sharp increase in the catalytic activity (according to Fig. 5 in ref. [31]; reproduced with permission of the American Chemical Society)

was then impregnated with 0.2 wt% Fe (as iron acetate), a very poor catalyst for ORR was obtained. This is illustrated by the half-shaded star in Fig. 10.7. A second pyrolysis step in pure NH_3 of this Fe-impregnated material, performed again at 950 °C, resulted in a sharp increase in its catalytic activity even after a second pyrolysis lasting only 1 min (black squares in Fig. 10.7). If the second pyrolysis was instead performed in Ar at the same temperature (black circles in Fig. 10.7), it took at least 40 min to reach the same activity as that reached with a pyrolysis in NH_3. These experiments revealed the importance of the second heat-treatment step (and the nature of the gas used during the second pyrolysis) for producing catalytic sites under these conditions. In other words, the C–N_x–Me structure proposed as a catalytic site by Yeager and collaborators was only the precursor of the actual catalytic site as C–N_x–Me needed to be thermally activated at high temperature to become the actual catalytic site referred to as FeN_2/C.

10.3 Influence of the Carbon Support

In the previous section, we learned that two catalytic sites, referred to as FeN_4/C and FeN_2/C, were simultaneously produced when pyrolyzing a carbon support on which 0.2 wt% (nominal) Fe was loaded as iron acetate. We also learned that

FeN_4/C is the catalytic site proposed by van Veen, while the C–N_x–Me structure proposed by Yeager is the precursor of FeN_2/C catalytic sites. The nitrogen atoms chelating the iron ion in FeN_4/C are of pyrrolic character, while they are of pyridinic character in FeN_2/C. FeN_4/C is also a fully coordinated catalytic site, while FeN_2/C is only the moiety of a more complex catalytic site for ORR. From these conclusions, it became clear that N-bearing functionalities on the carbon support are crucial because they are needed for ligating the iron ion of the catalytic site to the carbon support. Consequently, it seemed logical that increasing the number of N-bearing functionalities (either pyrrolic for FeN_4/C or pyridinic for FeN_2/C) on the carbon support would lead to more catalytic sites on this support. It was therefore of paramount importance to determine if N-bearing functionalities were the only factor or if other characteristics of carbon blacks were also important to maximize the ORR catalytic activity obtained with these carbon supports.

Starting in 2000 or so, few studies focused on the role of the carbon support and its influence on the activity of the electrocatalysts. In 2002, Bron and his colleagues compared the activity of catalysts made by the adsorption of Fe-phenanthroline on three different supports: Vulcan (254 m^2/g), Printex (900 m^2/g), and Black Pearls (1,500 m^2/g) [32]. The Fe loading was 1.14 wt% for the three carbon supports, and all catalysts were obtained after pyrolysis at 900 °C in Ar. They found a difference of about one order of magnitude in the current densities measured at the same potentials for these catalysts on different carbon supports, with the catalyst on Black Pearls having the highest activity for ORR. This difference was attributed to the larger specific surface area of Black Pearls compared with that of Vulcan, which allowed for a larger density of catalytic sites. Our group also performed several studies on catalysts made with various carbon supports. In the first study [33] published in 2003, we used (1) six commercial carbons (Printex XE-2, Norit SX Ultra, Ketjenblack EC-600JD, acetylene black, Vulcan XC-72R, and Black Pearls 2000), (2) three developmental carbons (HS 300 from Lonza, RC1, and RC2 from Sid Richardson Carbon Corporation; RC1 was enriched in nitrogen, while RC2 was not), (3) the same nine previous supports pre-pyrolyzed at 900 °C in an atmosphere containing NH_3 to increase their N content, and (4) a synthetic carbon made by pyrolyzing perylene tetracarboxylic dianhydride at 900 °C in an atmosphere containing NH_3. The same Fe precursor, iron acetate, with a nominal loading of 0.2 wt% Fe, was impregnated on all these carbon supports, and the resulting materials were heat treated at 900 °C in an atmosphere containing NH_3. The variation of activity measured in RDE or in fuel cell for these catalysts, all performed under the same experimental conditions, except for the carbon support, was significant. On the one hand, no correlation between the specific surface area and catalytic activity was found. On the other hand, there was a definite correlation between the catalytic activity and their surface nitrogen concentration measured by XPS.

In order to understand why different carbon supports had varying abilities in gaining N-bearing functionalities during pyrolysis in NH_3, further studies were conducted on various commercially available furnace blacks as carbon supports. These materials were made of aggregates of sphere-like particles having a diameter varying between 23 and 375 nm with their ASTM grade. References to the properties of furnace blacks (which are used primarily in the rubber/tire industry) may be found in a book by Kinoshita [34] or by Donnet et al. [35].

The main reaction which occurs when a carbon support is pyrolyzed in NH_3 at temperatures between 850 and 1,400 °C is the gasification of carbon by ammonia gas as given by Eq. (10.2) [36–38]:

$$C + NH_3 \rightarrow HCN + H_2 \tag{10.2}$$

In order to better understand the consequences of carbon gasification by reaction (10.2), this reaction was modeled for furnace carbon black particles [39, 40]. The premises of the model were that the particles of a pristine furnace black are composed of two solid phases: (1) an ordered phase containing graphitic crystallites and (2) a disordered phase resulting from the fast and out-of-equilibrium production of carbon black from oil feedstock. The assumed initial microstructure of a particle is represented in Fig. 10.8a where the gray area represents disordered carbon and the black rectangles graphitic crystallites. Before reacting with ammonia, the furnace black spherical particles have very little or no micro- or mesopores and their total surface area is about that of the combined exterior surface area of the carbon spheres. The model computed, as a function of the reaction time with NH_3, how much mass of the graphitic and disordered carbon phase was left at various depths inside the particle. The model parameters were estimated from experimental data of the chosen specific carbon black as (1) the evolution, during heat treatment with NH_3, of its specific surface area (available by BET measurements) and weight loss percentage; (2) the average initial diameter of the pristine carbon black particles (available by HRTEM or BET of pristine carbon black); and (3) the initial in-plane size of the graphitic crystallites of the pristine carbon black (available by Raman spectroscopy or Rietveld refinement of the XRD diffractogram).

One of the important findings of the modeled gasification was that the disordered carbon in the particular carbon black studied reacts (or gasifies) about ten times faster with NH_3 than the graphitic crystallites in the same carbon black. This leads to the creation of pores in the pristine nonporous spherical carbon black particles via the fast progressive gasification of disordered carbon by reaction with NH_3, while the graphitic crystallites in the same particle are etched much more slowly. Furthermore, the reaction of NH_3 with the disordered carbon content of these supports leaves nitrogen-bearing functionalities at the surface of the resulting carbon.

An estimate of the disordered carbon content in a pristine carbon may be obtained from its Raman spectrum. An example of the Raman spectrum of pristine carbon black of grade N120 is given in Fig. 10.8b [41]. This spectrum has been deconvoluted into five components [42]. The component of interest for disordered carbon content is peak D (the "defect band"). In polycrystalline carbonaceous materials consisting of a large number of small graphitic crystallites, like in pristine carbon black, it has been suggested that carbon atoms at the edge of a graphene layer are considered as the most probable origin of the D band [43]. Graphene

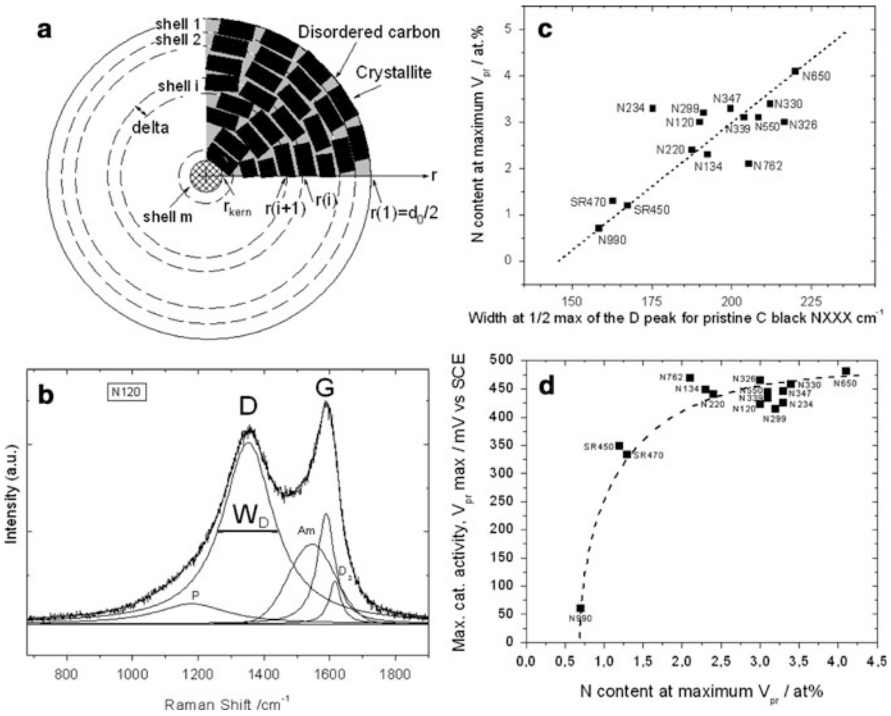

Fig. 10.8 (**a**) Schematic representation of the initial nonporous pristine carbon particle with its structure partitioned into m shells. Disordered phases (*gray zone*) and graphitic crystallites (*black rectangles*, not drawn to scale) (according to Fig. 1A in ref. [39]; reproduced with permission of the American Chemical Society). (**b**) Raman spectrum of the pristine carbon black N120 showing the deconvolution into five bands: P, D, Am, G, and D2 (according to Fig. 2A in ref. [41]; reproduced with permission of Elsevier). (**c**) N content, determined by XPS at the surface of the catalysts made with various pristine carbon blacks of Nxxx grade, vs. the width at half maximum W_D of the Raman D peak. (**d**) Maximum catalytic activity for each series of catalysts based on carbon blacks of Nxxx grade vs. the N content determined by XPS at the surface of the catalysts

layers in formation in a disordered carbon phase are therefore strong contributors to the D peak. It was found that W_D, the full width at half maximum of the D band, measured experimentally in Raman, is a very good parameter to estimate the relative amount of disordered carbon phase in a carbon black [40]. Figure 10.8c shows the linear correlation found between the maximum nitrogen content in the catalysts vs. W_D for the various pristine carbon blacks used to obtain these catalysts. The larger is W_D (or the relative amount of disorder carbon phase in a specific carbon black), the larger is the nitrogen content measured at the surface of the catalyst prepared with this specific carbon black. Here, each carbon black was first loaded with 0.2 wt% of Fe as iron acetate then pyrolyzed in NH_3 at 950 °C until an optimal weight loss corresponding to a maximum activity, as shown in Fig. 10.9a (right *Y* axis), was reached for each carbon black [41]. This optimum weight loss is reached when the thickness of the porous layer etched by NH_3 in the pristine

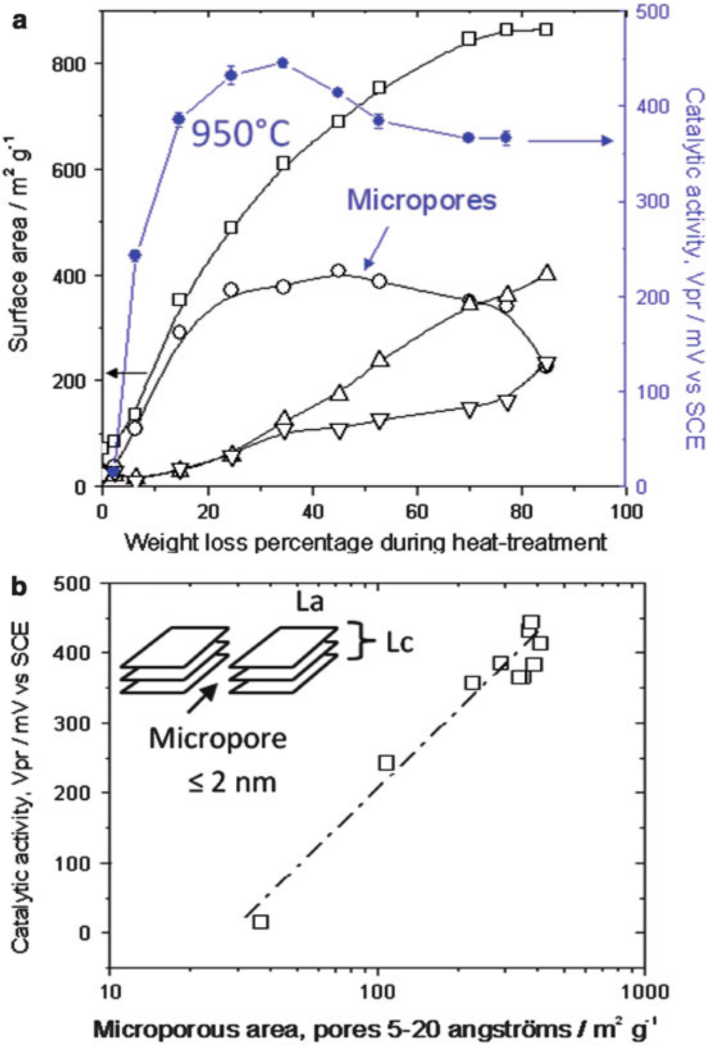

Fig. 10.9 (**a**-*right axis*) ORR activity in O_2 saturated H_2SO_4 solution at pH 1 of catalysts made in pure NH_3 at 950 °C (*filled circles*) vs. the percentage weight loss by the catalyst during the heat treatment. All catalysts were made by impregnation of 0.2 wt% Fe as iron acetate (according to Fig. S5B in the supplementary information of [44]; reproduced with permission of The American Chemical Society). (**a**-*left axis*) Surface area of three types of pores and total specific area vs. weight loss percentage of carbon during the heat treatment in NH_3 at 950 °C. Total surface area (*open squares*), surface area of micropores (width $\leq$ 2 nm; *open circles*), mesopores (*up triangles*), macropores (*down triangles*) (according to Fig. 5 in ref. [44]; reproduced with permission of The American Chemical Society). (**b**) Catalytic activity for O_2 reduction in O_2-saturated H_2SO_4 solution at pH 1 against microporous surface area of the catalysts of **a**, right axis (according to Fig. 6 in ref. [44]; reproduced with permission of The American Chemical society). The *insert* in **b** is a schematic representation of a slit-shaped micropore between two graphitic crystallites having La and Lc dimensions

spherical carbon particle of Fig. 10.8a is maximum [39]. Further etching will lead to a decrease of the spherical particle diameter and a decrease of the catalytic activity for ORR. Figure 10.8d shows the correlation between the maximum catalytic activity obtained with specific pristine carbon blacks and the nitrogen content measured at the surface of these catalysts. It indicates that the catalytic activity first increases rapidly when the nitrogen content is small, but the effect saturates when the nitrogen content at the surface of the catalyst reaches about 2 at.%.

Besides the reaction of NH_3 with the disordered content of a carbon black leaving nitrogen-bearing functionalities at the surface of the etched carbon, there is another important consequence of the reaction of NH_3 with carbon. As disordered carbon is mainly gasified, leaving behind a more crystalline structure of the carbon black, the occurrence of porosities in the carbon black follows the reaction front. Therefore, the total surface area of the carbon black greatly increases with the loss of carbon mass resulting from reaction (10.2). This is illustrated in Fig. 10.9a (left Y axis). The new porosities may be categorized as micropores ($\leq$2 nm), mesopores (between 2 and 50 nm), and macropores ($\geq$50 nm). Figure 10.9a (left Y axis) also shows the change in the surface areas assigned to the micropores, mesopores, and macropores versus the weight loss percentage. By comparing the trend of the catalytic activity in Fig. 10.9a (right Y axes) with the trends for the surface area of the various pore sizes, we can see that there is a direct correlation between the catalytic activity and the micropore surface area of the catalyst. This is illustrated more clearly in Fig. 10.9b. From Fig. 10.9b, and other results obtained with catalysts made with a wide range of commercial pristine carbons [41], *we concluded that the most active catalytic sites that were previously referred to as* FeN_2/C *are hosted in the micropores of the carbon support*. These micropores were etched in the pristine nonporous carbon blacks by their reaction with NH_3. For the catalyst presented in Fig. 10.9a, we also found that, at maximum catalytic activity, the nitrogen content of the catalyst was around 4 at.%, a value within the saturation region of Fig. 10.8d. In other words, the N content in this case was not a limiting factor to the catalytic activity. The latter was only limited by the availability of micropores for hosting the catalytic sites. A schematic structure of a slit-shaped micropore usually found in carbon blacks [45] is illustrated in the insert of Fig. 10.9b. This interstice between two graphitic crystallites was previously filled with disordered carbon. These graphitic crystallites consist of a few graphene layers characterized by La, the in-plane dimension of the graphene layers (between 2 and 3.5 nm), and a Lc, the height of the graphene stack (between 1 and 1.8 nm) for carbon black particles with diameters between 23 and 375 nm, respectively [41].

Following the discovery of the two important factors (the N and micropore contents) that govern the activity of catalysts made by the impregnation of a carbon black with 0.2 wt% Fe as iron acetate and its pyrolysis in NH_3 at high temperature, in 2008, we proposed a structure that would replace FeN_2/C, the incomplete catalytic site structure depicted in Fig. 10.4 that was previously introduced as a possible part of the most active type of catalytic site.

This new structure was referred to as FeN_{2+2}/C and is depicted in Fig. 10.10. The label FeN_{2+2}/C was chosen to distinguish this catalytic site from the van Veen

Fig. 10.10 FeN_{2+2}/C is a possible structure of the major catalytic sites in Fe/N/C catalysts. This structure is derived from the previous partial FeN_2/C structure illustrated in Fig. 10.4 (according to Fig. 15 in ref. [41]; reproduced with permission of Elsevier)

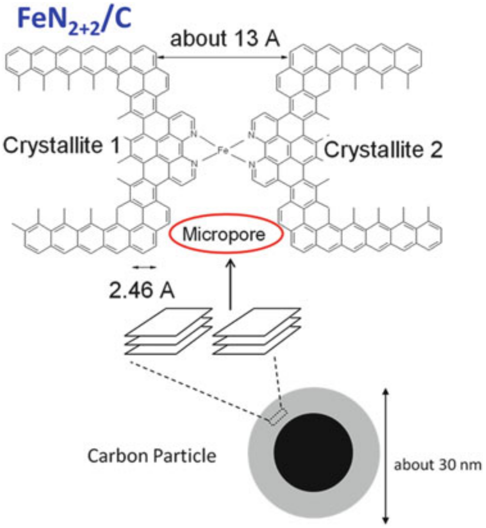

type of site—FeN_4/C (Fig. 10.2)—that was shown to be simultaneously present with FeN_2/C (now FeN_{2+2}/C) in Fe/N/C catalysts [30]. Here, however, the four nitrogen atoms chelating the iron ion in FeN_{2+2}/C are of pyridinic character, while they are of pyrrolic character in the van Veen type FeN_4/C site. The depicted structure of FeN_{2+2}/C is based on several experimental findings, namely, (1) the previously found importance of pyridinic (and even phenanthrolic) nitrogen atoms in FeN_2/C [27, 30], (2) the fact that these FeN_{2+2}/C catalytic sites are hosted in micropores [44] which are slit shaped in carbon black [45] and that the width of the slit-shaped micropore hosting the catalytic site are between 1 and 2 nm wide [46], and (3) most EXAFS and Mössbauer experiments performed so far on Fe/N/C (and Co/N/C catalysts) always concluded that the metal ion of the catalytic sites was surrounded by four nitrogen atoms [22, 32, 47–50].

10.4 The Revival of the Wiesener Model

10.4.1 Stevenson and His Collaborators

In 2004, Maldonado and Stevenson published a paper about the electrocatalytic behavior of carbon nanofibers (CNFs) toward oxygen reduction obtained via the pyrolysis of $iron^{II}$ phthalocyanine [51]. They suggested that the disorder in the graphitic fibers, i.e., the presence of exposed edge phase defects, and the nitrogen functionalities were important factors influencing the adsorption of reactive intermediates generated during the reduction of oxygen. The enhancement of the ORR electrocatalysis on these materials was attributed to all of these factors. Their carbon nanofibers were obtained at 1,000 °C in a reducing atmosphere (Ar–H_2) on a Ni mesh. The growth of the CNFs was catalyzed by a diffusion-controlled mechanism where iron particles that were left over from the pyrolysis of the phthalocyanine served as nucleation sites for the carbon fibers. Iron nanoparticles still present with the CNF were indeed observed by TEM and were predominantly encapsulated within graphitic envelopes. TEM also revealed that the nanofibers had a bamboo-like structure resulting from the substitution of N atoms into the graphene structure of the nanofibers. The possibility of N substitution in the CNFs was attributed to the formation of pentagonal-like defects, which were most likely responsible for the compartmentalized morphology of the carbon nanostructure. About 1 at.% of nitrogen atoms was detected by XPS as pyridinic, pyrrolic, and quaternary nitrogen at the surface of these catalysts, while the amount of Fe at the surface of CNFs was measured at about 0.1 at.% by the same analysis technique. From Raman spectroscopy of the N-doped CNFs, it was also deduced that significant edge plane sites were present in the catalyst.

All electrochemical measurements in the latter work were performed at pH 7, showing that oxygen reduction on N-containing carbon nanofibers was shifted by about 0.25 V toward more positive potentials compared with a glassy carbon electrode immersed in the same 1 mM O_2-saturated solution of 1 M KNO_3. The number of electrons transferred during ORR was determined to be 2. Maldonado and Stevenson concluded that it appeared highly unlikely that O_2 reduction at their N-doped CNFs proceeded via a Fe-redox mediation-type mechanism typical for most intact iron macrocycle supported on a carbon electrode. They believed that the increased catalytic activity and more positive O_2 reduction potential observed for their N-doped CNF electrode was predominantly the result of enhanced adsorption at nitrogen functional groups that accelerated ORR by a 2e process and improved the decomposition of peroxide. They also speculated that Fe predominantly acted to promote and stabilize nitrogen incorporation into the graphene sheets of CNFs rather than of being at the heart of the catalytic sites for oxygen reduction.

This paper was followed by another in 2005 [52] where the N-doped CNFs were prepared by a chemical vapor deposition at 800 °C using ferrocene and pyridine this time. Undoped CNFs were also prepared similarly with ferrocene and xylene. The residual bulk iron percentages for N-doped CNFs were obtained by TGA. It was 9 ± 1 wt% Fe for N-doped CNFs and 7 ± 1 wt% Fe for the undoped fibers. XPS surface analysis of the same fibers gave 1.1 and 1.2 at.% Fe, respectively, which corresponds to about 4.5 wt% Fe. The electrochemical properties of the two types of fibers were measured at pH 7 (1 M KNO_3) and at pH 14 (1 M KOH), see Fig. 10.11a, b, respectively. From these figures, one may conclude that N-doped CNFs are better catalysts for ORR than the undoped ones. However, the potential difference between the two nanostructures decreases as the pH increases! Again, in this paper, they concluded that the activity of N-doped carbon nanofibers toward oxygen reduction and hydroperoxide decomposition is a direct result of nitrogen doping and is not related to the residual iron content. They added that they saw no evidence for the presence of iron-chelated surface sites (like FeN_2/C or FeN_4/C), but if these sites were indeed present on the surface of the N-doped CNFs, they

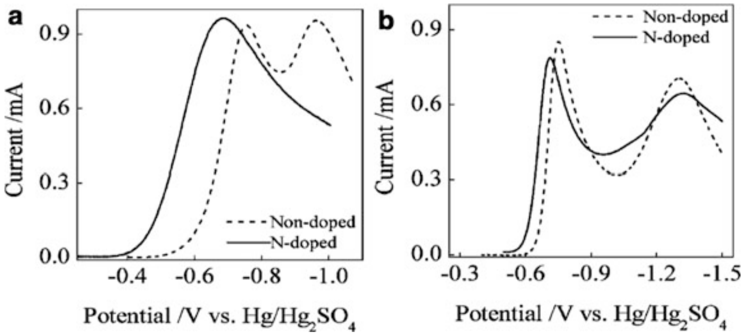

Fig. 10.11 (**a**) Voltammetric responses for the oxygen reduction reaction of a non-doped carbon nanofiber electrode (*dashed line*) and a N-doped carbon nanofiber electrode (*solid line*) immersed in an O_2 saturated 1 M KNO_3 solution (according to Fig. 6 in ref. [52]; reproduced with permission of the American Chemical Society). (**b**) Same as in (**a**), except the electrolyte used is an O_2-saturated 1 M KOH solution (according to Fig. 10.7 in ref. [53]; reproduced with permission of Elsevier)

should be easily poisoned by the presence of CO due to the strong irreversible binding of CO to the active iron site. Furthermore, nitrogen incorporation produced activated carbons with increased stability toward the fiber oxidation.

In an accompanying paper [53], the same N-doped carbon nanofibers were grown with ferrocene and pyridine, but this time, NH_3 was added in addition to pyridine in order to increase their N content from 4 at.%, when no NH_3 was added, up to 12 at.% with addition of NH_3. At the same time, the residual Fe content increased from 9 wt% to about 20 wt%! Typically, most of the iron particles were encapsulated with layers of graphene. While both the amount of pyridinic and pyrrolic/graphitic nitrogen atoms increased with the Fe content, the pyridinic N peak showed a twofold greater increase in abundance compared to the pyrrolic/graphitic peaks. Raman spectra also indicated that the ratio of the D/G bands of CNFs also increased with an increase of the total N content in the fiber, suggesting an increase of the edge plane density with the N content as well. The prevalence of pyridinic functionalities in N-doped CNFs confers an alkaline character to these fibers with a pH_{pzc} (pKa) of 9.3 for 4 at.% nitrogen in N-doped carbon nanofibers. These nitrogen atoms, located on the edge of graphitic planes, exhibit an extra lone pair of electrons which increase the electron density and electron-donating character of graphitic edge planes. It is reasonable to expect that these edge planes, which are commonly known to be reactive sites, will show an increased reactivity for ORR due to the electron density generated from the incorporation of nitrogen in pyridinic-like coordination. The reducing capability of these materials was indeed verified by iodimetric titration.

In subsequent years, Stevenson's group continued the investigation of N-doped CNFs and carbon nanotubes (CNT) grown from ferrocene and pyridine [54, 55]. From these experiments, they concluded that O_2 reduction at neutral pH was not catalyzed by surface-bound $Fe^{II/III}$ species. In their last paper [56], they used the electroreducing properties of N-doped CNTs to reduce O_2 at near neutral pH (pH 6.4) and generate hydroperoxide anions (HO_2^-) that may further react with toxic CN^- anions and oxidize them into OCN^- nontoxic anionic species.

It is worth noting, after a thorough review of the publications by Stevenson and his collaborators, that they have always used N-doped carbon nanostructures as ORR electrocatalysts in neutral or in alkaline solutions, where the oxygen reduction reaction is facilitated and achievable even with carbon alone. The fundamental kinetic advantage in the alkaline medium arises primarily from the improved stabilization of the peroxide intermediates on the catalyst surface [57]. It is our opinion that it is not in studying non-noble electrocatalysts in alkaline or even in neutral media that it is possible to resolve the long-debated question about the controversial role of Fe (or Co) in the active site for ORR. The specific role of Fe (if any) can only be confirmed (or infirmed) from studies conducted in relatively strong acid medium, in which carbon is largely inactive for ORR [58]. This point is illustrated in Fig. 10.11 which demonstrates the decreased influence of nitrogen doping on the ORR activity for carbon nanofibers when measured at pH 14 vs. pH 7. On the contrary, when comparing the ORR activity of one metal-free, two Fe-based catalysts, and a Pt/C catalyst in pH 13 and pH 1, as illustrated in Fig. 10.12A (pH 13) and Fig. 10.12B (pH 1), the catalytic activities behave differently. In these figures, the curves labeled “d” are for an N-doped Black Pearls catalyst containing 0 wt% Fe (or a Fe content below the detection limit of 50 ppm for Fe in Neutron Activation Analysis), while curves “b” and “a” are for two Fe-based catalysts obtained with a nominal Fe loading of 0.2 wt% [41, 44] and 1 wt% [8], respectively. Curve “c” is for a 46 wt% Pt/C catalyst [60]. The blue arrows in Fig. 10.12A, B is an indication of the onset potential (V_{onset}) of the catalysts, which will be defined in the next section. It is clear from Fig. 10.12A (at pH 13) that V_{onset} is 0.85 V vs. RHE for curve “d,” which represents the metal-free N-doped Black Pearls, is practically the same as the V_{onset} of 0.87 V vs. RHE for curve “b,” which represents the least active Fe/N/C catalyst in the same figure. On the other hand, in Fig. 10.12B (at pH 1), V_{onset} is 0.63 V vs. RHE for curve “d” (metal-free N-doped Black Pearls), while it is 0.83 V vs. RHE for the least active Fe/N/C catalyst. Here we have a difference of 0.20 V between the two V_{onset} values. With a Tafel slope of about 0.10 V per decade at pH 1(at 0.8 V vs. RHE) for the metal-free N-doped black Pearls [61], a factor of about $10^{0.20/0.10}$ (or 100) is therefore expected at the same potential, between the mass activity (in A/g catalyst) of metal-free N-doped Black Pearls and that of the least active Fe/N/C catalyst in this acid medium!

10.4.2 Ozkan and Her Collaborators

The view that the role of Fe is merely a chemical catalyst for the formation of ORR-active CNx structures, first proposed by Wiesener and collaborators in 1986 [18], and again by Stevenson and collaborators in 2004, from their experiments on carbon nanostructures in neutral and alkaline media, was also held by Ozkan and

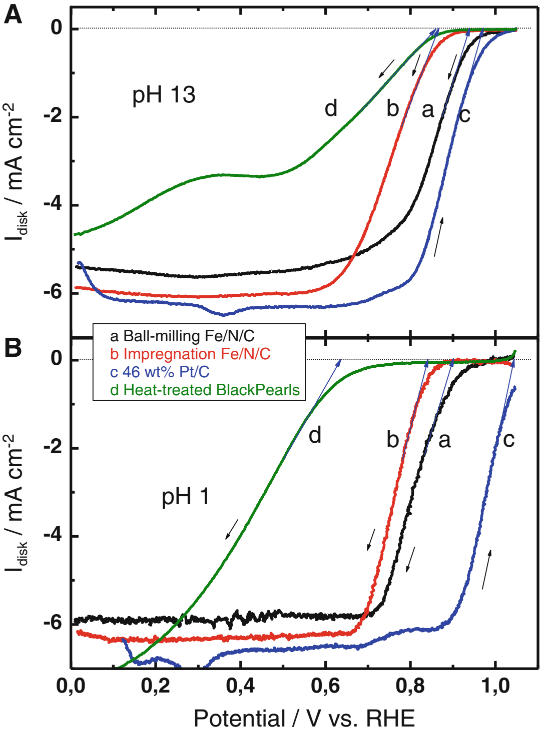

Fig. 10.12 (**A**) Disk currents at 1,600 rpm and 10 mV/s from RRDE measurements in O_2-saturated KOH solution at pH 13 for the ball-milled Fe/N/C catalyst (curve a), the Fe/N/C catalyst made by impregnation (curve b), 46 wt% Pt/C (curve c), and heat-treated Black Pearls (curve d). Fe/N/C and Black Pearls were all heat treated in pure NH_3 at 950 °C during the synthesis of the catalysts. *Black arrows* indicate the scan direction. *Blue arrows* pointing toward the axis of potentials give the V_{onset} values (vs. RHE) for each catalyst (see also Fig. 10.13 for V_{onset} definition). V_{onset} are 0.85 V for curve d, 0.87 V for curve b, 0.93 V for curve a, and 0.97 V for curve c (according to Fig. 3b in ref. [60]; reproduced with permission of Elsevier). (**B**) Same as (**A**) except that RRDE measurements are performed in O_2 saturated $HClO_4$ solution at pH 1. The values of V_{onset} vs. RHE for each catalyst are given by the *blue arrows* pointing to the axis of potentials. They are 0.63 V for curve d, 0.83 V for curve b, 0.90 V for curve a, and 1.03 V for curve c (according to Fig. 1b in ref. [60]; reproduced with permission of Elsevier)

collaborators in 2006 [62], but this time for ORR experiments in the acid medium (0.5 M H_2SO_4). Their first publication [62] has since been followed by many others who have arrived at the same conclusion: that the role of Fe is limited to catalyzing the growth of ORR-active CNx structures. To properly assess and compare reported ORR activity for catalysts measured in so many different conditions in many publications, we will require a tool or convention. This can be done by defining a consistent way to read the V_{onset} for ORR of all these catalysts, as most researchers working in acid medium report at least the initial part of the ORR cyclic voltammogram (CV) starting at OCV and measured with a rotating disk electrode.

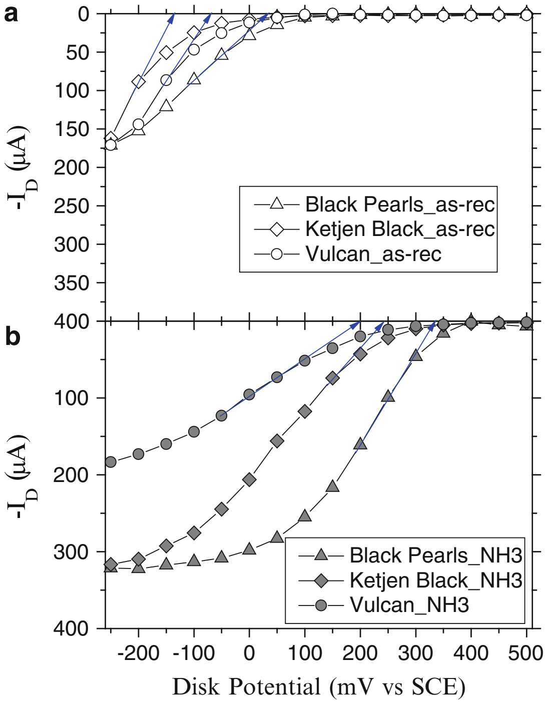

Fig. 10.13 (**a**) Disk currents at 200 rpm and 10 mV/s from RRDE measurements in O_2 saturated H_2SO_4 solution at pH 1 for as-received Ketjen Black, Vulcan, and Black Pearls. V_{onset} values are obtained from a line tangent to the inflection point of the CV curve (when possible) and extrapolated to zero disk current. It is the potential at the tip of the *arrow*. V_{onset} (vs. RHE) is 0.16 V for Ketjen Black, 0.23 V for Vulcan, and 0.34 V for Black Pearls (according to Figs. 1A, 2A, and 3A in ref. [59]; reproduced with permission of Elsevier). (**b**) Same as (**a**) except that all carbon blacks were heat treated at 900 °C in NH_3:H_2:Ar (2:1:2; in vol.). V_{onset} (vs. RHE) is 0.50 V for Vulcan_NH_3, 0.54 V for Ketjen Black_NH_3, and 0.63 V for Black Pearls_NH_3 (according to Figs. 1B, 2B, and 3B in ref. [59]; reproduced with permission of Elsevier)

Figure 10.13 shows how these V_{onset} values will be read on the reported CVs. Here straight lines (arrows) are drawn tangent to the inflection point (when possible) of the CV curves and extrapolated to zero disk current. For the purpose of this chapter, V_{onset} shall therefore be defined as the potential at the arrow point. It will be expressed vs. RHE in order to compare experiments performed by different researchers in O_2-saturated solutions of different acid concentrations [from 1 M to 0.005 M H_2SO_4 (or $HClO_4$)]. V_{onset} is not a perfect indicator of catalytic activity, but it is the only one which allows for a fair and meaningful comparison of the reported cyclic voltammograms of electrodes loaded with various catalyst loadings, as well as being recorded at various rotations and scan rates.

Figure 10.13 was obtained by combining the CV curves measured at pH 1 that were published in 2004 by our group [59] for the ORR on three as-received carbon supports (Vulcan_as rec; Ketjen Black_as-rec; Black Pearls_as-rec, open symbols in Fig. 10.13a) and the same carbon supports after a heat treatment at 900 °C in Ar: H_2:NH_3 (Vulcan_NH3; Ketjen Black NH3; Black Pearls_NH3, gray symbols in Fig. 10.13b). The latter are all metal-free and N-doped carbons (Vulcan_NH3: 1.1 at.% N; Ketjen Black NH3: 0.8 at.% N; Black Pearls_NH3: 0.6 at.% N) [33]. The conversion from the potential vs. SCE reference electrode (0.24 V vs NHE) to vs RHE was done by adding 0.30 V at pH 1. So, for instance, $V_{\text{onset}} = -0.07$ V vs. SCE for Vulcan_as-rec became 0.23 V vs. RHE and $V_{\text{onset}} = 0.20$ V vs. SCE of Vulcan_NH3 became 0.50 V vs. RHE. All V_{onset} values vs. RHE of Fig. 10.13a, b are given in their respective captions. V_{onset} values were extrapolated similarly for both Fig. 10.12A, B. They are also given in their respective captions. Figure 10.13b shows that our group was already well aware of the beneficial role of N doping of metal-free carbon supports in 2004, but we were most interested in the much higher activities that could be achieved in the acid medium (pH 1) by adding a Fe (or Co) precursor to the synthesis of Fe-based catalysts for ORR as illustrated in Fig. 10.12B. Contrary to Wiesener and followers, we attributed this enhancement of activity to the presence of Fe-containing catalytic sites. Let us now go back to the catalysts obtained by Ozkan and collaborators.

The catalysts synthesized by Ozkan and her collaborators [62–77] were carbon nanostructures like multiwalled carbon nanotubes or carbon nanofibers with a herringbone structure, stacked platelets, or stacked cups. Onion-type carbon nanostructures were also obtained. They were always prepared by impregnating a metal acetate (usually iron or nickel acetate) onto an oxide support (alumina, silica, magnesia) or on Vulcan. The nominal metal loading on the support was always 2 wt%. This catalyst precursor was then pyrolyzed at 900 °C in acetonitrile (CH_3–CN) vapors. Then the oxide support was removed by its dissolution in KOH, HF, or HCl, depending on the nature of the support. Finally, the resulting material was washed in HCl to remove the exposed metal and to obtain the CNx catalyst. The latter were labeled: CNx-Fe/Vulcan or CNx-Fe/Al_2O_3, or CNx-Ni/MgO to identify each type of catalyst based on of their synthesis procedure. Metal-free CNx catalysts were also prepared. In that case, the catalyst precursor contained no metal. All other steps of the above-described procedure remained the same. All these catalysts had a large distribution of N-doped nanostructures. For instance, CNx-Fe/Al_2O_3 was composed of 57 % stacked cups, 3 % fibers, and 40 % multiwalled carbon nanotubes, while CNx-Ni/Al_2O_3 was composed of 6 % stacked cups, 17 % fibers, 17 % multiwalled carbon nanotubes, and 60 % broken multiwalled carbon nanotubes [65, 71].

The carbon nanostructures were characterized using several techniques: BET (for the determination of their surface area), thermogravimetry and differential scanning calorimetry (to determine their stability toward oxidation), X-ray diffraction (to detect metallic and carbon phases), X-ray photoelectron spectroscopy (to obtain their surface nitrogen content), and transmission electronic microscopy (to identify the carbon nanostructures and observe the presence of remaining metal particles). All catalysts were also evaluated for their activity toward ORR in 0.5 M H_2SO_4 solutions at 1,000 rpm. Inks prepared by mixing the catalysts with Nafion were then deposited on the surface of a glassy carbon electrode for RDE characterization. Typical electrochemical results for ORR are shown in Fig. 10.14a, b.

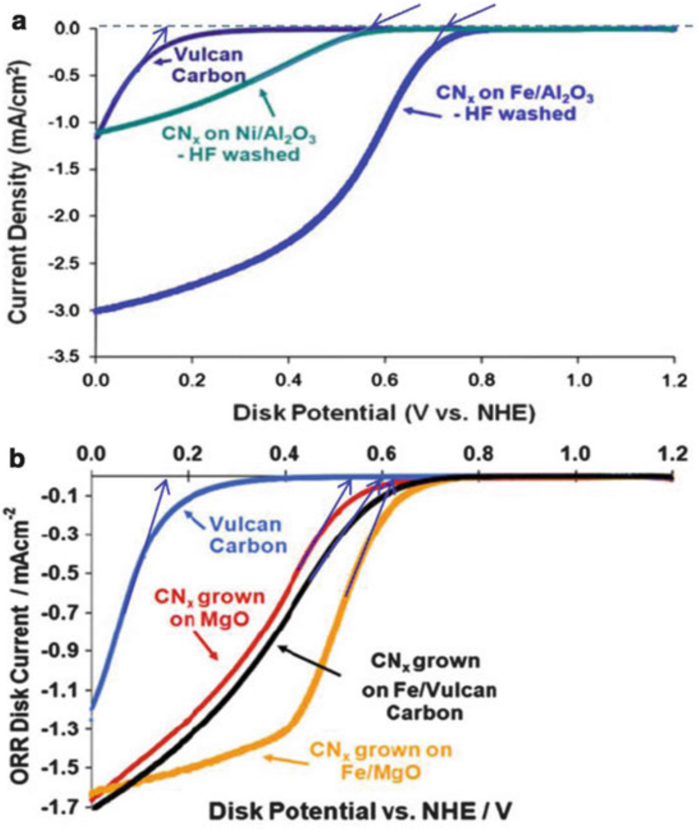

Fig. 10.14 (**a**) Disk currents at 1,000 rpm from cyclic voltammetry experiments in O_2-saturated 0.5 M H_2SO_4 solution for as-received Vulcan ($V_{onset} = 0.14$ V vs. RHE), HF-washed CNx grown on Ni/Al_2O_3 ($V_{onset} = 0.56$ V vs. RHE), and HF-washed CNx grown on Fe/Al_2O_3 ($V_{onset} = 0.72$ V vs. RHE) (according to Fig. 1 in ref. [71]; reproduced with the permission of Springer). (**b**) Disk currents at 1,000 rpm and 10 mV/s from cyclic voltammetry experiments in O_2 saturated 0.5 M H_2SO_4 solution for as-received Vulcan ($V_{onset} = 0.16$ V vs. RHE), HCl-washed metal-free CNx grown on MgO ($V_{onset} = 0.53$ V vs. RHE), CNx grown on Fe/Vulcan ($V_{onset} = 0.60$ V vs. RHE), and HCl-washed CNx grown on Fe/MgO ($V_{onset} = 0.63$ V vs. RHE) (according to Fig. 2b of [75]; reproduced with permission of Springer)

The three curves in Fig. 10.14a [71] are those of the oxygen reduction reaction on as-received Vulcan ($V_{onset} = 0.14$ V vs. RHE), CNx-Ni/Al_2O_3 ($V_{onset} = 0.56$ V vs. RHE), and CNx-Fe/Al_2O_3 ($V_{onset} = 0.72$ V vs. RHE). The four curves in Fig. 10.14b [75] are those of the oxygen reduction reaction on as-received Vulcan ($V_{onset} = 0.16$ V vs. RHE), metal-free CNx/MgO ($V_{onset} = 0.53$ V vs. RHE), CNx-Fe/Vulcan ($V_{onset} = 0.60$ V vs. RHE), and CNx-Fe/MgO ($V_{onset} = 0.63$ V vs. RHE).

In all their reports, Ozkan and collaborators found that N-doped carbon nanostructures made with Ni were always less active than those made with Fe. Their explanation of this behavior was that, depending on the metal and the support used, carbon nanostructures were found to vary significantly developing into different nano-geometries. Depending on the obtained geometry, the exposed graphitic crystal planes and the nitrogen functional groups on the surface also varied significantly. *A correlation was found between the edge plane exposure of the graphitic crystallites*, *the pyridinic nitrogen content of the catalysts*, *and the ORR activity*. As CNx structures grown on Fe-containing supports were characterized by high amounts of edge plane exposure and high pyridinic nitrogen content, these CNx structures tended to be the most active ones for ORR. Their mean V_{onset} value (when all results for Fe-containing catalysts published by Ozkan and collaborators are averaged) is 0.67 V vs. RHE. This is followed by CNx grown on metal-free supports, which are characterized by a mean value of their V_{onset} of 0.61 V vs. RHE. Next are the CNx structures grown on Ni-containing supports with a mean V_{onset} value of 0.52 V vs. RHE. While the mean value of V_{onset} for all catalysts grown on Fe-containing support is 0.67 V vs. RHE, individual reports vary from a low $V_{\mathrm{onset}} = 0.55$ V [76] to a high $V_{\mathrm{onset}} = 0.77$ V vs. RHE [65]. There is less variation in the V_{onset} (but also fewer samples) for the catalysts obtained without metal (from 0.53 [75] to 0.67 vs. RHE [65]) for a mean value of 0.61 V vs. RHE. The same is also true for the catalysts grown on Ni supports (from 0.46 [65] to 0.56 vs. RHE [71]) for a mean value of 0.52 V vs. RHE. The lowest, average, and highest V_{onset} values from the paper by Ozkan and collaborators are illustrated in Fig. 10.15. The same figure also shows V_{onset} values obtained from the publications of other groups.

It should be noted that in Fig. 10.15, the metal-free CNx nanostructures grown by Ozkan and collaborators by pyrolyzing CH_3–CN at 900 °C on Al_2O_3 and those obtained by Dodelet and collaborators by pyrolyzing carbon blacks in NH_3 at 900 °C have practically the same V_{onset}, despite the large difference in their total nitrogen content (5.2 at.% N for metal-free CNx/Al_2O_3 and between 0.6 and 1.1 at.% N [33] for all the metal-free catalysts of Fig. 10.13b). As a matter of fact, the N-doped Black Pearls in Figs. 10.13b and 10.12B are also both characterized by the same V_{onset}: 0.63 V vs. RHE, despite the large difference in their total N contents. Indeed, the N-doped Black Pearls in Fig. 10.13b has a total N content of 0.6 at.%, while it is about 4 at.% for the N-doped Black Pearls in Fig. 10.12B [44]. The difference arises from the procedure used for their preparation: a pyrolysis step at 900 °C in a mixture of Ar:H_2:NH_3 for the former, while it was a pyrolysis step at 900 °C in pure NH_3 for the latter. Furthermore, the percentage of their total N content that was pyridinic was always around 30 %, a value often obtained by Ozkan and collaborators. No improvement of the catalytic activity for ORR was therefore observed by our group when the total N content (or its pyridinic fraction) was increased from 0.6 to 4 at.% N (or from 0.2 to 1.3 at.% pyridinic N) for N-doped Black Pearls.

While the improvement of the catalytic activity observed by Ozkan and collaborators when their CNx nanostructures were grown on Fe-impregnated supports was interpreted in terms of an increased formation of graphitic edges stabilized by pyridinic nitrogen atoms (and perhaps also by graphitic nitrogen atoms), an alternative explanation to their ORR activity improvement may be the

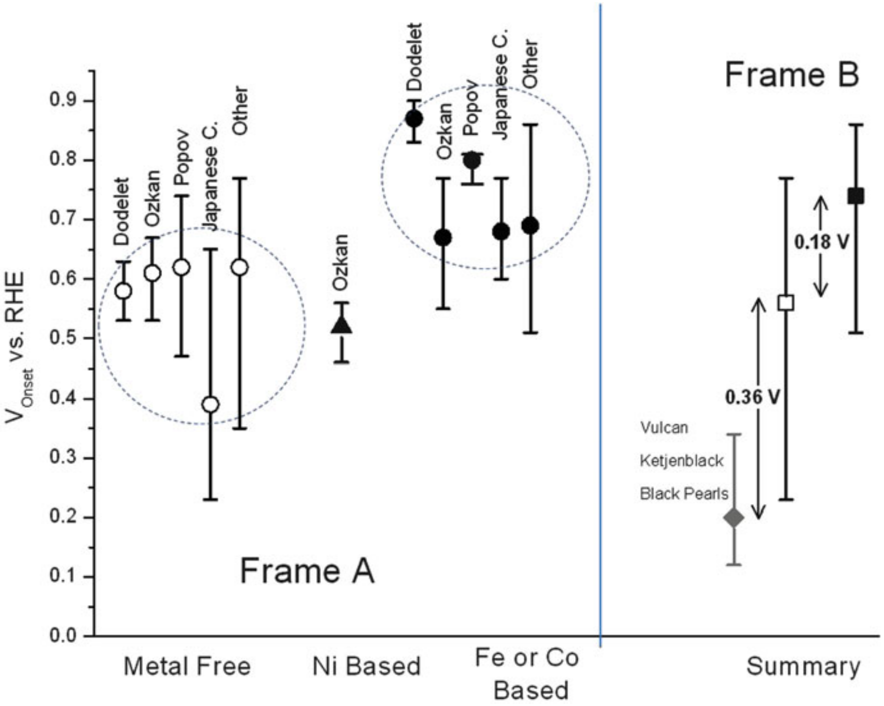

Fig. 10.15 Frame A—lowest, average (*symbol*), and highest V_{onset} values (vs. RHE) reported by various groups for the oxygen reduction reaction in acid medium. The N-doped catalysts were either metal-free (*open circles*), grown on Ni/support (*black triangle*), Fe/support (*black circles*), or Co/support (*black circles*). Frame B—summary of the lowest, average (*symbol*), and highest V_{onset} values (vs. RHE) reported for various groups for the oxygen reduction reaction in acid medium. Here, the *open square* represents the overall average of the *open symbols* in Frame A, while the *black square* represents the overall average of the *black circles* in Frame A. The *gray diamond* is the average value reported by various groups for all as-received carbon black supports

contribution of a few catalytic sites involving a Fe ion active for the ORR. For Ozkan and collaborators, the numerous metal particles observed by TEM in their materials only served to catalyze the formation of this special carbon and its stabilization by N doping, with N contents up to 9.3 at.% [70]. They used a similar argument for the lower catalytic activity of CNx nanostructures grown on Ni-impregnated supports. In this case, according to them, much less catalytic edges were formed and were also stabilized by a lower number of N atoms (down to 4.1 at.%) [71]. Our alternative explanation for this behavior would be that, even if sites involving Ni ions were obtained, all materials made with Ni as metal precursor have always been found to be inactive toward ORR [26] and these catalysts should therefore show an activity similar to that of metal-free CNx.

Besides doping their carbon nanostructures with nitrogen, Ozkan and collaborators also tried to increase their nitrogen doping of the graphitic edges in their catalysts with additional phosphorous atoms [72, 74] or with additional sulfur atoms [70]. CNx-Fe/MgO catalysts doped with a P/Fe = 1 ratio were prepared by pyrolysis at 900 °C in CH_3–CN vapors. Both catalysts did not show much difference in their V_{onset} (0.65 V without P and 0.67 V vs. RHE with P/Fe = 1). Here, P was introduced by adding triphenylphosphine to acetonitrile vapors in the reactor. The same conclusion was reached when *S* was added as thiophene to acetonitrile. In this case, V_{onset} increased from 0.65 V vs. RHE for $S = 0$–0.68 V vs. RHE for 8.9 % thiophene in acetonitrile. Attempts to poison any Fe/N/C sites still present in purified CNx-Fe/MgO using a subsequent heat-treatment step at 350 °C in a mixture of 1,050 ppm H_2S in H_2 were unsuccessful [77]. As Fe/N/C sites were expected by Ozkan and her collaborators to be poisoned in these conditions, they concluded that no residual iron that might be catalytic for ORR was accessible for ORR in their material. This poisoning presumption of Fe/N/C by H_2S has not, however, been verified with known structures, like unpyrolyzed iron phthalocyanine or porphyrins that contain a catalytic iron ion indeed able to reduce oxygen in acid medium. A similar poisoning presumption of Fe/N/C was made for CO to demonstrate that there was no iron active for ORR in these catalytic sites [52], until it was shown that CO, in fact, does not poison Fe sites in iron phthalocyanine [78]. Instead of H_2S "poisoning" of their CNx catalysts, Ozkan and collaborators actually reported an improvement of their ORR catalytic after heat-treating their catalyst in the gas mixture containing H_2S and H_2! The V_{onset} of the latter increased from 0.64 V vs. RHE before H_2S heat treatment to 0.72 V vs. RHE after heat-treating CNx-Fe/MgO with H_2S in H_2. A similar improvement was also found by heat-treating CNx-Fe/MgO in 5.7 % H_2 in N_2. They suggested that the catalyst improvement was the result of its heat treatment in a reducing atmosphere. This may be so, but still does not explain why heat-treating a catalyst in a reducing atmosphere improves its activity for ORR. Further studies are necessary to rationalize this interesting observation.

10.4.3 Popov and His Collaborators

The view that the role of Fe (or Co) is limited to merely acting as chemical catalyst for the formation of active CNx structures for ORR in the acid medium is also shared by Popov and his collaborators. After a first publication in 2007 [79] about carbon-based metal-free catalysts that offered no details about their synthesis procedure, they published, in 2008, an interesting paper about the modification of carbon by Te as catalysts for ORR [80]. This catalyst was obtained by mixing Ketjenblack with telluric acid (H_2TeO_4) and then reducing the oxidized tellurium to Te with hydrazine. The resulting material was finally pyrolyzed in Ar to obtain Te/C. They showed by XRD that no Te particles existed above 600 °C and, by XPS, that above 600 °C Te formed C–Te species with catalytic activity toward ORR. The best activity was obtained after a pyrolysis at 1,000 °C. The V_{onset} of this metal-free catalyst was 0.67 V vs. RHE. It was measured by RRDE at 900 rpm in 0.5 M H_2SO_4. The same catalyst produced only 0.6 % H_2O_2 at 0.6 V vs. RHE.

After this publication on Te/C, Popov and collaborators focused on producing N-doped carbons for ORR in the acid medium. In a 2008 publication [81], they reported the synthesis of several metal-free catalysts using the following procedure: Ketjenblack was first treated in HCl to remove metallic impurities before being oxidized in HNO_3. The oxidized carbon black was then used as a support for several resins obtained by the polymerization of formaldehyde with (1) melamine, (2) urea, (3) thiourea, or (4) selenourea. The oxidized carbon covered with each of the polymerized resins was then pyrolyzed in N_2 at various temperatures to obtain catalysts for ORR. The best catalyst was obtained with selenourea pyrolyzed at 800 °C (SeUF/C-800). Its V_{onset} in 0.5 M H_2SO_4 (900 rpm) was 0.65–0.70 V vs. RHE, while a V_{onset} of 0.69 V vs. RHE was obtained for the catalyst made with urea (UF/C-800; only composed of C and N). V_{onset} was 0.22 V vs. RHE for unoxidized Ketjenblack. UF/C-800 showed only carbon diffraction peaks in XRD. The total N content of that catalyst was determined by XPS to be 2.2 wt% (~8.8 at.% N) with pyridinic, pyrrolic, and quaternary (graphitic) types of nitrogen atoms. In another publication [82], more details about the same catalyst were revealed. Here, the V_{onset} of UF/C-800 was 0.67 V vs. RHE, with a %H_2O_2 of 3 % released at 0.5 V vs. RHE. The catalyst had a surface area of 321 m^2/g. The Fe and Co contents of UF/C-800 were 0.4 and 0.3 ppm, respectively. As there was no Fe or Co in that catalyst, *the origin of the measured activity was definitively attributed to pyridinic and quaternary nitrogen atoms substituting for C in the CNx structure. The strong Lewis basicity of carbon doped with pyridinic and quaternary nitrogen atoms facilitated the reductive adsorption reaction of* O_2 *without the irreversible formation of oxygen functionalities.*

The next publication [83] represents a turning point in the publications of Popov's group because this time they added Co and/or Fe to their synthesis procedure in order to improve the activity of CNx catalysts, while at the same time denying any direct metal participation toward ORR for these catalysts. In this paper, carbon metal-free catalysts were first prepared according to the procedure described previously [82], except for the pyrolysis temperature which was now 900 °C instead of 800 °C. V_{onset} values of 0.28 V vs. RHE were obtained for Ketjenblack, 0.36 V vs. RHE for oxidized Ketjenblack, and 0.74 V vs. RHE for UF/C-900. A Ketjenblack treated with NH_3 (preparation procedure not reported) with a V_{onset} of 0.53 V vs. RHE was also synthesized. A peroxide yield of 3 % measured at 0.5 V vs. RHE was reported for UF/C-900. Carbon composite catalysts were also prepared. In the latter case, UF/C-900 was used as a carbon support on which a mixture of Co nitrate and Fe sulfate complexed with ethylene diamine was impregnated. The resulting material was pyrolyzed at 900 °C in Ar. Then it was washed with H_2SO_4 to remove excess metal. The best catalysts obtained with an equal amount of Co and Fe (labeled Co–Fe on metal-free/C-900) was characterized in 0.5 M H_2SO_4. Its V_{onset} was 0.79 V vs. RHE, while the metal-free/C-900 catalyst had a V_{onset} of 0.70 V vs. RHE. Co-Fe metal on metal-free/C-900 and metal-free/C-900 catalysts yielded 0.9 and 1.2 % H_2O_2 at 0.5 V vs. RHE, respectively.

These catalysts were characterized by the following techniques: (1) EXAFS on unleached Co metal-free/C-900 (no Co–N bonds were detected at temperatures

≥800 °C); (2) TEM and XRD on leached Co–Fe on metal-free/C-900 (Co, Fe, and Co_xFe_y phases were detected as well as Fe_3C, but the metal-containing phases were covered with graphitic layers); (3) ICP-MS and XPS on leached Co-Fe on metal-free/C-900 (9.6 wt% Co and 1.4 wt% Fe were measured by ICP-MS in the bulk of the catalyst, but no metal was detected by XPS at its surface); and (4) the N content of the leached Co–Fe on metal-free/C-900 was measured by XPS and found to be 1.9 wt% N (~7.6 at.% N). Only pyridinic and quaternary N1s peaks appeared in the XPS spectrum. From these observations, they concluded that:

1. *Despite of their presence at several wt% in the leached Co–Fe on metal-free/C, neither Co nor Fe metal was involved in the active catalytic sites for ORR*
2. *The only catalytic species were pyridinic and quaternary nitrogen atoms*. A similar publication [84] reached the same conclusions but also mentioned that, in fuel cell, catalysts predominated by pyridinic-type nitrogen atoms showed higher activity, but lower stability than catalysts predominated by quaternary nitrogen atoms, which showed lower activity but higher stability

The next publication [85] which is the most detailed one, offers all the necessary information to discuss Popov and collaborators' position concerning the origin of the catalytic activity of these catalysts prepared with relatively high Co and/or Fe contents. In ref. [85], only Fe was used and the following catalysts were synthesized and characterized electrochemically for ORR in 0.5 M H_2SO_4 (see Fig. 10.16a), as well as by XPS for their N content:

1. Silica was first impregnated with acrylonitrile (AN) and then polymerized as PAN and pyrolyzed in Ar at 900 °C. The resulting material was washed in NaOH to remove SiO_2 leaving CNx-900 as metal-free catalyst. The V_{onset} of CNx-900 was 0.47 vs. RHE with a total N content of 6.88 at.%, broken down as 1.85 at.% pyridinic, 2.06 at.% graphitic, 1.69 at.% pyrrolic, and 1.28 at.% $N^+–O^-$.
2. CNx was also impregnated with 1.2 wt% Fe as iron^{II} acetate and then pyrolyzed at 1,000 °C. The V_{onset} of 1.2 wt% Fe-CNx-1000 was 0.80 V vs. RHE with a total N content of 3.51 at.%, broken down as 0.96 at.% pyridinic, 1.49 at.% graphitic, and 1.06 at.% $N^+–O^-$.
3. A sample similar to (2) but with 0 wt% Fe was also prepared for comparison. The V_{onset} of 0 wt% Fe-CNx-1000 was 0.54 V vs. RHE with a total N content of 3.64 at.%, broken down as 0.78 at.% pyridinic, 1.52 at.% quadratic, and 1.34 at.% $N^+–O^-$.
4. Sample (2) was then leached (L) to remove excess metal. The V_{onset} of 1.2 wt% Fe-CNx-1000L was 0.74 V vs. RHE, while its total N content was 3.44 at.%, broken down as 0.84 pyridinic, 1.97 quadratic, and 0.63 $N^+–O^-$.
5. Sample (4) was then reheat treated (H) at 1,000 °C. The V_{onset} of 1.2 wt%Fe-CNx-1000LH was 0.80 V vs. RHE with a total N content of 3.47 at.%, broken down as 0.68 at.% pyridinic, 2.26 quadratic, and 0.53 $N^+–O^-$.

Figure 10.16a shows the ORR behavior of these five samples. Here again, based on the data presented previously [83, 84], Popov and collaborators concluded that "*it seems reasonable to suggest that pyridinic N and quadratic N may be the active*

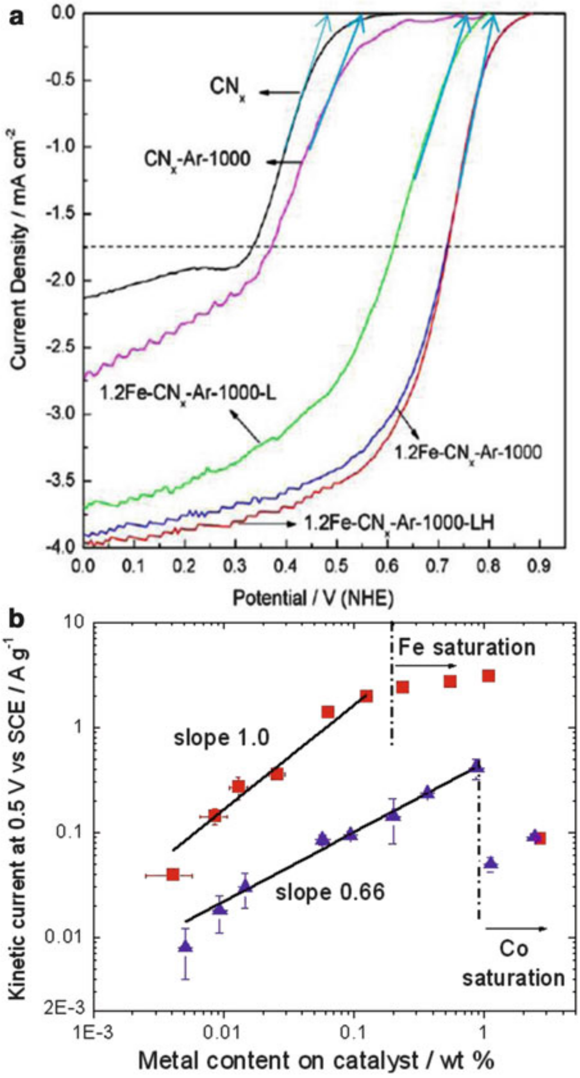

Fig. 10.16 (**a**) Disk currents at 900 rpm and 5 mV/s from cyclic voltammetry experiments in O_2-saturated 0.5 M H_2SO_4 solution for: (1) a metal-free CNx grown on SiO_2 at 900 °C ($V_{\text{onset}} = 0.47$ V vs. RHE); (2) 1.2 Fe-CNx-Ar-1000 obtained by the impregnation of 1.2 wt% Fe as iron$^{\text{II}}$ acetate on CNx and then pyrolyzed at 1,000 °C in Ar ($V_{\text{onset}} = 0.80$ V vs. RHE); (3) CNx-Ar-1000 obtained by the pyrolysis of CNx at 1,000 °C in Ar ($V_{\text{onset}} = 0.54$ V vs. RHE); (4) 1.2 Fe-CNx-Ar-1000L is sample (2) leached in H_2SO_4 ($V_{\text{onset}} = 0.74$ V vs. RHE); and (5) 1.2 Fe-CNx-Ar-1000LH is sample (4) reheat treated at 1,000 °C in Ar ($V_{\text{onset}} = 0.80$ V vs. RHE) (according to Fig. 6 in ref. [85]; reproduced with the permission of Elsevier). (**b**) Mass activity, for the reduction of oxygen in an O_2-saturated H_2SO_4 solution at pH 1 on Fe/N/C and Co/N/C catalysts, vs. the metal content of the catalysts. Fe/N/C and Co/N/C were obtained by impregnation of either iron$^{\text{II}}$ or cobalt$^{\text{II}}$ acetates onto a nonporous carbon black followed by the pyrolysis of these materials at 950 °C in pure NH_3 (according to Fig. 3 in ref. [86]; reproduced with the permission of Elsevier)

sites for ORR." On this basis, one would therefore expect that a sample with the highest content of pyridinic and quadratic atoms would also be the sample with the highest catalytic activity. This is not what is observed in Fig. 10.16a! Indeed, with its highest content of 1.85 at.% of pyridinic and 2.06 at.% of quadratic nitrogen atoms for a total content of **3.91** at.% N active for ORR, CNx-900 is the sample with the lowest activity. Furthermore, its apparent number of electron transfer during ORR was only 2, while a sample like 1.2 wt% Fe-CNx-1000, which was the best performing catalyst in Fig. 10.16a, was characterized by a lower content of 0.96 at.% of pyridinic and 1.49 at.% of quadratic nitrogen atoms for a total content of **2.45** at.% N active for ORR. Its apparent number of electron transfer during ORR was 4! Even if we compare samples 3 and 2, prepared at the same pyrolysis temperature of 1,000 °C, but with 0 and 1.2 wt% Fe, respectively, sample 3 was characterized by a content of 0.78 at.% of pyridinic and 1.52 at.% of quadratic nitrogen atoms for a total N content of 2.30 at.% active for ORR, while sample 2 was characterized by a content of 0.96 at.% of pyridinic and 1.49 at.% of quadratic nitrogen atoms for a total content of 2.45 N active for ORR. These two values of total ORR-active N content only differ by 0.15 at.%, while their V_{onset} differs by $0.80-0.54 = 0.26$ V as seen in Fig. 10.16a! Furthermore, sample 3 with 0 at.% Fe reduces O_2 with an apparent number of transferred electrons close to 2, while it is 4 for sample 2!

According to Popov and collaborators, "*encapsulated Fe species in carbon substrate may exert some electron effect on N-modified active sites and facilitate ORR*, *but they are not active sites*!" An alternative explanation would be that some Fe–Nx species are also generated upon pyrolysis of 1.2 wt% Fe-CNx-1000 and those Fe–Nx species are greatly increasing the activity toward ORR for these catalysts. Indeed, we show in Fig. 10.16b [86] that even small Fe loadings were enough to obtain a definite effect on the ORR activity of catalysts made by impregnation of iron$^{\text{II}}$ acetate onto a nonporous carbon black, followed by pyrolysis at 950 °C. The catalytic mass activity increases linearly with the Fe content from 0.005 to 0.10 wt%, where it reaches about 50 % of its maximum activity. The ORR activity of the catalysts presented in Fig. 10.16b are very similar to that presented in Fig. 10.12B, curve "b," which is characterized by a V_{onset} of 0.83 V vs. RHE, a value close to that attributed to 1.2 wt% Fe-CNx-1000 (0.80 V vs. RHE) in Fig. 10.16a. Because the actual content of 0.1 wt% Fe (measured by NAA) in Fig. 10.16b is only 8 % of the nominal Fe loading of 1.2 wt% Fe-CNx-1000 (Fig. 10.16a), any physical characterization of 1.2 wt% Fe-CNx-1000 will be predominated by the high content of Fe not involved in Fe–Nx bonds. It is also important to remember that 0.1 wt% Fe is only 0.025 at.% Fe, a level that is not easily detectable by most XPS spectrometers. An average value of V_{onset} for metal-free catalysts and metal-containing catalysts from all the publications of Popov and collaborators is shown in Fig. 10.15, where it is compared with average V_{onset} values obtained by other groups.

From the following publications [84–87] and from the recent minireview [88] published in 2011, we also learn that *the catalysts rich in pyridinic nitrogen displayed higher activity but lower stability*. This was attributed to the protonation of the basic pyridinic N. According to Popov and collaborators, *the protonated pyridinium species* (*NH^+*) *is no longer active because the interaction of NH^+ with O_2 would be prevented in such a case*. The protonation of all the pyridinic nitrogen atoms was followed by recording the N1s XPS spectrum before and after stability experiments of the catalysts in 0.5 M H_2SO_4. Before protonation, the XPS spectrum displayed three components: pyridinic, quadratic, and N^+–O^-, while after stability experiments, only one peak was visible. This lone peak was attributed to the simultaneous presence of NH^+ and quadratic N, which are both characterized by similar binding energies. Quadratic nitrogen atoms are not affected by their contact with an acid solution. It is for this reason that their catalytic behavior is quite stable [87–89].

10.4.4 The Japanese Consortium

A Japanese consortium following Wiesener's view on CNx catalytic sites is also worthy of discussion. It started with a 2006 publication by Ozaki and collaborators who reported on the synthesis of metal-free catalysts for ORR in acid medium [90]. The catalysts were prepared by mixing a furan resin with various phthalocyanines (H_2Pc, Li_2Pc, MgPc) as nitrogen precursors and then pyrolyzing the resulting material at 1,000 °C in N_2. The respective N/C loadings were 0.04, 0.05, and 0.04 for H_2Pc, Li_2Pc, and MgPc with a V_{onset} in 1 M H_2SO_4 of 0.23, 0.33, and 0.23 V vs. RHE, respectively. All catalysts were amorphous carbons and *the enhancement of ORR activity* vs. that of the pyrolyzed furan resin alone ($V_{\text{onset}}=$ 0.15 V vs. RHE) *was attributed to the introduction of edge-site nitrogen atoms on the surface of these amorphous carbons*. In a second publication [91], the catalysts were prepared by pyrolyzing at 1,000 °C a mixture of polyfurfuryl alcohol and melamine. Two catalysts with different N dopings were obtained by varying the melamine content in the mixture. Their respective N/C loading was 0.011 and 0.032, and their V_{onset} in 0.5 M H_2SO_4 were 0.26 V vs. RHE for the lowest N loading and 0.30 V vs. RHE for the highest one. *The catalytic activity was attributed to the presence of N atoms at the edge of graphene planes* obtained after pyrolyzing the precursors of carbon and nitrogen. Later on, in collaboration with other authors, they compared the catalysts synthesized with melamine in the previous publication with catalysts obtained by other synthesis procedures, in particular that of a nitrogen-doped carbon black reacted with NH_3 for which they reported a N doping of 1.3 at.% and a V_{onset} of 0.33 V vs. RHE [92]. A series of N-containing rod polymers—polyimides (PI), polyamides (PA), and polyazoles (AZ)—were also prepared as nitrogen and carbon precursors. Catalysts were obtained from these materials after their carbonization at 900 °C in N_2 [93]. Their ORR properties were evaluated in 0.5 M H_2SO_4 and $V_{\text{onset}} = 0.48$ V vs. RHE was measured for carbonized PI, while it was 0.52 and 0.62 V vs. RHE for carbonized PA and AZ, respectively. Relatively high N contents were measured by XPS in these catalysts (4.83 and 5.31 at.% N for catalysts obtained with PA and AZ).

The XPS spectra were deconvoluted in several components and *the catalytic activity was attributed to the presence of pyridinic and graphitic types of nitrogen atoms in the carbonized materials*. For all of the studied materials, the graphitic nitrogen content was always higher than the pyridinic nitrogen one.

In parallel with these syntheses of metal-free catalysts, the Japanese consortium also prepared catalysts using either cobalt- or iron-containing precursors in their syntheses but denied the existence of metal-containing ORR catalytic sites in these catalysts. For instance, in 2009 [94], a Co complex (Co-[poly(4-vinylpyridine)]) was first loaded on Ketjenblack and pyrolyzed in N_2 at 1,000 °C. The resulting material was acid washed to remove excess Co species. The same procedure was repeated with Ketjenblack alone for comparison. The V_{onset} of the carbonized Co complex on Ketjenblack was measured in 0.5 M H_2SO_4 at 0.70 V vs. RHE, a potential much higher than for Ketjenblack alone ($V_{\text{onset}} = 0.26$ V vs. RHE). As no Co was detected by XPS in the catalyst made with the Co complex, *the drastic improvement in ORR activity* for that catalyst vs. the ORR activity of Ketjenblack alone *was explained in terms of nitrogen doping of the catalyst made with the Co complex*. Similar catalysts were also prepared, but this time without carbon support, using either cobalt phthalocyanine (CoPc) or iron phthalocyanine (FePc) mixed with N-containing polymers or with phenolic resins that were carbonized at various temperatures, and then eventually washed with acids to remove the metal in excess. In a first publication [92], the mixture of CoPc and N-containing polymer were pyrolyzed at 900 °C. Again, the XPS of that catalyst did not show any Co 2p signal after acid washing and its V_{onset} in 0.5 M H_2SO_4 was 0.60 V vs. RHE. *Despite its relatively low N content* (*0.8 at.%*), *its catalytic activity was mostly attributed to the presence in this material of graphitic nitrogen atoms*. It is important to note that 0.1 at.% metal is usually considered to be the detection limit for Co (or Fe) by XPS and that the detection of Co (or Fe) contents below this limit is not trivial and requires at least a very large number of scans to ascertain the presence (or absence) of the metal. It will be seen later in this section that even cobalt contents below 0.1 at.% Co (or ~0.4 wt% Co in these carbon-based catalysts) may indeed be responsible for an important ORR activity that can be attributed to Co–Nx active sites.

In 2010 [95], Ozaki and collaborators mixed a furan resin with iron, cobalt, or nickel acetylacetonates and carbonized the mixture in N_2 at 600 to 1,000 °C. The resulting material was ball milled and then acid washed to remove excess metal. The best catalyst was obtained with the Co complex carbonized at 800 °C. Its V_{onset} in 0.5 M H_2SO_4 was 0.62 V vs. RHE. The catalyst had a specific surface area of 211 m^2/g and its N/C ratio was 0.035. *Its ORR activity was explained by the formation of carbon nanoshells*, *but also by N doping of the catalyst carbonaceous material*.

In two following publications [96, 97], a catalyst similar to that previously described in ref. [92] and obtained by the carbonization at 1,000 °C of a mixture of CoPc and phenolic resin followed by acid washing was studied in greater detail. Its nominal Co content was 3 wt%. The V_{onset} of the latter, measured in 0.5 M H_2SO_4, was 0.68 V vs. RHE. Its N content was 0.37 at.%. The latter was determined

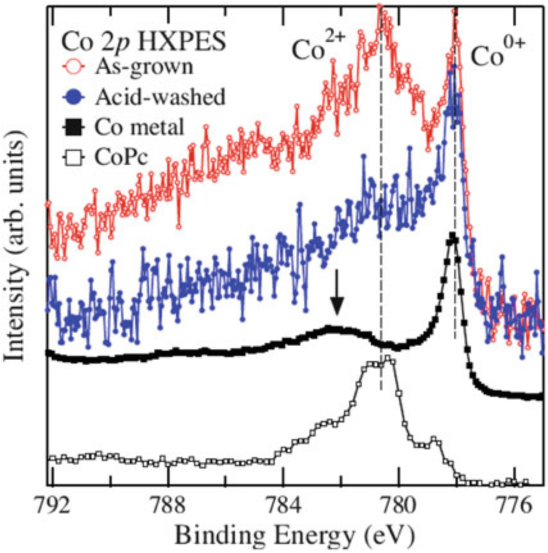

Fig. 10.17 Co 2p HXPES spectra of as-grown (*open circles*) and acid-washed (*filled circles*) CoPc-PhRs1000 catalysts. As-grown CoPc-PhRs1000 was obtained by the carbonization at 1,000 °C of a mixture of CoPc and phenolic resin. The intensities are normalized to the total photon flux to enable comparison of Co contents between the as-grown and the acid-washed samples. *Dashed lines* are guides. As reference, Co 2p HXPES spectra of Co metal (*black squares*) and CoPc (*open squares*) are also shown. The *arrow* denotes oxidized Co components on the surface of the Co metal (according to Fig. 4 in ref. [97]; reproduced with the permission of Elsevier)

by hard X-ray photoemission spectroscopy (HXPES), a surface analytic technique probing the first 10 nm of an analyzed material. Washing the catalyst with HCl did not change its V_{onset} or its nitrogen content, which remained the same at 0.68 V vs. RHE and 0.37 at.% N, respectively, but somewhat decreased the Co detected by HXPES from 0.05 at.% in the as-synthesized catalyst to 0.03 at.% after acid washing. Also, the surface area of the as-synthesized catalyst, which was 287 m^2/g, decreased to 242 m^2/g after HCl washing. Most of the cobalt in these two catalysts formed clusters surrounded with a carbon shell structure made of an average number of eight graphene layers producing Co-containing nanostructures. XANES and EXAFS spectra at the Co edge indicated that, in both catalysts, Co was mainly in the metallic state with only a small amount of oxidized cobalt. The detection of a small amount of oxidized cobalt by XANES and EXAFS spectroscopies, both able to probe several micrometers, and the detection of the same oxidized cobalt by HXPES, characterized by a depth probed of about 10 nm, inferred that this oxidized cobalt was at the surface of the catalyst or accessible to HXPES in cobalt nanostructures encapsulated with only one or two graphitic layers. The Co 2p HXPES spectra of the as-synthesized and acid-washed catalysts are presented in Fig. 10.17. According to the authors, it is likely that such a low oxidized cobalt content (0.05 at.% detected by HXPES in the as-synthesized catalyst and 0.03 at.% after acid washing) cannot be responsible for *the ORR activity of these catalysts*. The latter *was mainly attributed to carbon atoms that are the first neighbors of a quadratic nitrogen atom at the zigzag edge of graphene planes*. These first carbon neighbors at favorable –C–N–C– sites had a density of 0.29 at.% in both catalysts. A theoretical study [98] of these sites concluded that their number may be increased by controlling the degree of hydrogenation of edge carbons by introducing some H_2 gas in the reactor during the carbonization process. According to the authors, the presence of CoPc during the synthesis of these N-doped carbons will only catalyze the formation of the favored –C–N–C– sites, but neither metallic nor oxidized Co played any role in the ORR properties of these materials because their concentration, as detected by HXPES, was extremely low.

This conclusion seems to rule out the eventual presence of Co–Nx ORR-active sites in these catalysts. However, it can be seen in Fig. 10.16b [86] that oxidized Co contents in the 0.03–0.05 at.% range (and even below) may indeed exhibit a clear ORR activity in Co/N/C catalysts. When this Co content, expressed in at.%, is translated into Co wt%, it becomes 0.12–0.20 wt% Co. In Fig. 10.16b, it is shown that a maximum ORR mass activity of 0.40 A/g was measured at 0.8 V vs. RHE for Co/N/C catalysts containing 1 wt% Co (measured by neutron activation analysis). At 0.20 wt% Co, the mass activity was 0.16 A/g and it was 0.12 A/g at 0.12 wt% Co. This is 40 and 30 % of the maximum measured mass activity, respectively, and is not at all negligible. As a matter of fact, Co–Nx sites are detected in the HXPES spectrum of the as-synthesized catalyst presented in Fig. 10.17. Indeed, there is an obvious peak at 781–782 eV (see the vertical dashed line) that is at the same binding energy as that of oxidized cobalt in CoPc (bottom curve in Fig. 10.17). This peak is less obvious in the acid-washed catalyst, but is still there because, otherwise, a dip would be observed in the spectrum at the same binding energy as that shown by the curve for Co metal in Fig. 10.17. In conclusion, even if a fraction of all the Co atoms detected in Fig. 10.17 in these catalysts were in oxidized form, metal-containing Co–Nx sites, which are active for ORR, may actually contribute to part of their ORR activity!

The same remark also holds true for the following two publications. The same authors also used FePc (instead of CoPc) to improve the ORR activity of their catalysts [99, 100]. Here, Fe was loaded at 3 wt% as FePc with the phenolic resin and pyrolyzed at various temperatures, the best one being 600 °C. This material had a large number of metal-containing particles detected by TEM and a graphitic nanoshell morphology similar to that detected with CoPc. The metal-containing particles were mainly Fe_3C (cementite) as concluded from XRD measurements. There was less than 0.5 at.% Fe in the catalyst. A comparison was made with materials produced with H_2Pc instead of FePc. A large difference was observed in their V_{onset}, measured in 0.5 M H_2SO_4: 0.70 V vs. RHE for the catalyst made with FePc, but only 0.46 V vs. RHE for the material made with H_2Pc. Specific surface area and N contents were also measured. They were 400–500 m^2/g and 3.7 wt% N for the catalyst made with FePc, while 500–600 m^2/g and 2 wt% N were measured for the catalyst made with H_2Pc. Pyridine and quaternary nitrogen atoms were the major nitrogen species in both catalysts. In the same publication [99], the authors also describe a model explaining the differences between both catalysts during carbonization: the decomposition of the phenolic resin in the mixture begins at 200–450 °C, while that of H_2Pc and FePc starts around 400–600 °C. H_2Pc and FePc decompose in phthalonitrile, but less phthalonitrile is lost, and more nitrogen atoms remain in the resulting carbonized material when FePc is present. The presence of iron enhances the growth of nanoshell structures and the N doping of the resulting graphitic material. *It was assumed that quaternary nitrogen atoms increase the occurrence of zigzag edge graphene and edge exposure*, *therefore improving the ORR activity*. It is also worth noting that the same catalyst and several catalysts, derived from the pyrolysis at 600 °C in N_2 of the mixture of FePc with phenolic resins and then further activated in NH_3 at 800 and 1,000 °C, resulted in catalysts that showed very good performance and/or stability when tested in fuel cells [100].

Finally, the same Japanese consortium also reported the synthesis and characterization of carbon nitride made without iron, as catalysts for ORR in acid medium (0.5 M H_2SO_4). In a seminal work [101], the synthesis of C_3N_4 was performed at 220 °C from the reaction of sodium azide with cyanuric chloride $(3NaN_3 + C_3N_3Cl_3 \rightarrow g\text{-}C_3N_4 + NaCl + 4N_2)$, where g-$C_3N_4$ is the planar phase of the nitride made up of condensed tri-*s*-triazine (melem) subunits. This material had a nitrogen content of 23 at.%. It was not pyrolyzed at higher temperature, but mixed with Vulcan to increase the electrical conductivity of the mixture. Its V_{onset} was 0.30 V vs. RHE, while the V_{onset} of Vulcan alone was 0.13 V vs. RHE. In a second and more detailed publication [102], the same synthesis procedure was used, but this time, carbon black was added in the reaction chamber as a high surface area catalyst support. Furthermore, the resulting g-C_3N_4 was pyrolyzed at 1,000 °C. The resulting material had a nitrogen content of 1.8 at.%. Its XPS spectrum was deconvoluted into 55 % pyridinic, 40 % graphitic, and 5 % amine nitrogen atoms.

V_{onset} measured in 0.5 M H_2SO_4 was 0.76 V vs. RHE, as shown in Fig. 10.18a, with an apparent number of electrons of $n = 3.55$ transferred during ORR. *The authors suggested that quaternary nitrogen atoms are responsible for the oxygen reduction in this carbon nitride catalyst via a* $4e^-$ *process*.

Curiously, some iron contaminated this otherwise "metal-free" g-C_3N_4 catalyst. This contamination was traced to the stainless steel high-pressure reactor used for the synthesis of the material. In order to produce g-C_3N_4 free of iron contamination, the synthesis was again performed, but this time without carbon black support and in a Teflon melting pot, using the same experimental conditions as the ones described previously. The V_{onset} measured for this true iron-free catalyst (and according to the procedure described in Fig. 10.13) is 0.65 V vs. RHE (see Fig. 10.18b), and the apparent number of electrons transferred during ORR was now 3.4. This again illustrates the obvious influence that even small amounts of iron impurity may have on the V_{onset} of these catalysts active for ORR in acid medium.

The mean values of metal-free catalysts prepared by the Japanese consortium with and without Co- or Fe-containing precursors are reported in Fig. 10.15.

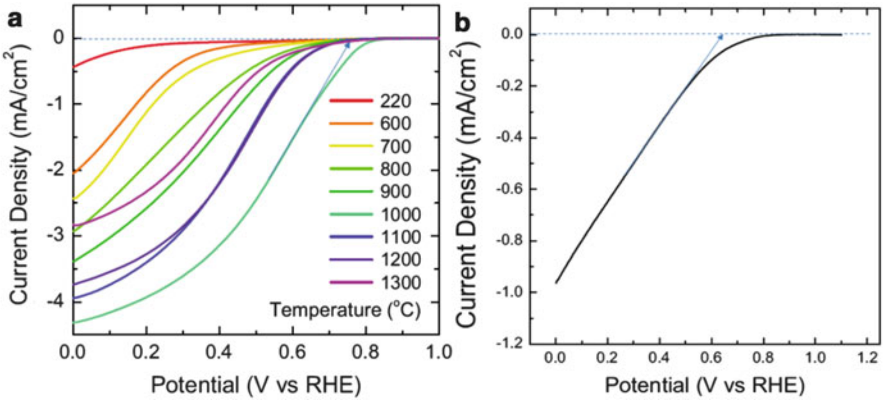

Fig. 10.18 Disk currents at 1,500 rpm and 0.1 V/s from cyclic voltammetry experiments in O_2-saturated 0.5 M H_2SO_4 solution for the following: (**a**) Carbon nitride (g-C_3N_4) supported on carbon black, synthesized in a stainless steel high-pressure reactor and pyrolyzed at various temperatures. The best catalyst is obtained at 1,000 °C with a $V_{\text{onset}} = 0.76$ V vs. RHE. (**b**) Fe-free unsupported carbon nitride (g-C_3N_4) synthesized in a Teflon melting pot and pyrolyzed at 1,000 °C. $V_{\text{onset}} = 0.65$ V vs. RHE (according to Fig. 6 in ref. [102] for (**a**) and Fig. 8 in the same reference for (**b**); reproduced with permission of The Electrochemical Society)

10.4.5 Other Authors

Besides the work of Ozkan and Popov's groups and the work of the Japanese consortium, other authors also defended the same view as Wiesener: that of a CNx catalytic site for ORR. Their results will now be summarized. It should be stressed that among these authors, some have made a particular effort to avoid any metal trace in the synthesis of their catalysts in order to determine the true ORR activity of the nitrogen-doped carbon materials. Their results will be presented first, followed by the results of authors using either Fe- or Co-containing molecules in the synthesis of their N-doped carbon catalysts.

10.4.5.1 ORR Catalysts Made *Without* Any Fe or Co

In 2009 [103] and 2010 [104], Takasu and his collaborators used carbonized silk to perform ORR in acid medium (0.5 M H_2SO_4). The catalysts were derived from a *Bombix mori* silk fibroin containing 18 different amino acids. The silk was first carbonized at 500 °C in N_2 and then ball milled and heat treated in N_2 at various temperatures between 500 and 1,500 °C. The resulting materials were finally steam activated at 850 °C. The best results were obtained for a heat treatment of the carbonized silk at 900 °C in N_2. This catalyst had a surface area of 588 m^2/g and an N content of 6 at.% with 29 % of pyridinic and 59 % of graphitic nitrogen atoms. Its V_{onset} was 0.69 V vs. RHE [103] or 0.73 V vs. RHE [104]. By comparison, the V_{onset} for Vulcan was 0.20 V vs. RHE. The catalyst was also characterized, for potentials below 0.5 V vs. RHE, of an apparent number of electron transfer of $n = 3.5$ which could be pushed up to $n = 3.9$ by adding ZrO_2 in the catalytic layer. *Its ORR activity was mostly attributed to quadratic N doping*. This was the only type of nitrogen atom left in the N1s XPS spectrum of the catalyst obtained after a heat treatment at 1,200 °C, while some pyridinic nitrogen atoms were also detected in the catalyst heat treated at 900 °C. A single MEA fuel cell was performed with the best catalyst. It yielded a maximum of 150 mW cm^2 at 80 °C in H_2/O_2 (0.2 MPa at both electrodes).

In 2012, the group of Rao and Ishikawa produced vertically aligned carbon nanotubes (with and without N doping) without metal impurities by coating various polymers with different nitrogen contents in the pores of an alumina membrane [105]. This was followed by the carbonization at 900 °C of the material and by a KOH treatment to remove alumina. The nitrogen-free polymer was poly (phenylacetylene). In 0.5 M H_2SO_4, it was characterized by a V_{onset} of 0.23 V vs. RHE. The four other polymers, from poly(4-vinylpyridine) to poly(*p*-pyridazine-3,6-diyl) had an increasing N content that yielded V_{onset} values of 0.36 V vs. RHE (N = 4.3 at.%), 0.47 V vs. RHE ($N = 5.6$ at.%), 0.56 V vs. RHE ($N = 8.4$ at.%) and 0.60 V vs. RHE ($N = 10.7$ at.%). *The increase of ORR activity was closely correlated with the total content of pyridinic and quadratic nitrogen in the catalysts* ($N_{\text{pyr}} + N_{\text{quad}} = 3.9$, 5.3, 8.0, 10 at.%, respectively).

In 2010, Liming Dai and his collaborators also synthesized, on a Si substrate and from SiO_2 nanoparticles catalyst, absolutely metal-free carbon nanotubes by chemical vapor deposition at 900 °C from a mixture of CH_4 and H_2 [106]. The tubes were doped by adding NH_3 in the gas mixture. The nanotubes were then transferred onto a glassy carbon electrode in order to test their ORR activity in 0.5 M H_2SO_4. A V_{onset} of 0.53 V vs. RHE was measured for the tubes containing 3.6 at.% N. In this case, there was no graphitic nitrogen atom in the total nitrogen content, as only pyridinic (83 %) and pyrrolic (17 %) nitrogen atoms were detected by XPS in that material. The same year [107], metal-free N-doped carbons were also produced by impregnation of a mesoporous silica template (SBA-15) with pyrrole, which was then polymerized. The resulting material was heat treated at 800 °C. After removal of the silica template by KOH, the ORR activity of the metal-free catalyst was measured in 0.5 M H_2SO_4. Its V_{onset} was 0.35 V vs. RHE. Its total surface area was 544 m^2/g and a N/C ratio of 0.12 was measured, with 36 % pyridinic and 25 % graphitic nitrogen atoms.

The following results obtained by Sheng Dai and his collaborators deserve a special mention as these authors obtained the highest activity reported so far with truly N-doped metal-free carbon materials [108]. These catalysts were obtained by heat-treating at high temperature (950–1,050 °C) and with NH_3 a 2D hexagonal-ordered mesoporous carbon having a total surface area of 658 m^2/g before its reaction with NH_3. When the latter material was measured in 0.05 M H_2SO_4 for its ORR activity, a V_{onset} of 0.34 V vs. RHE was obtained. The V_{onset} jumped to 0.72, 0.76, and 0.77 V vs. RHE after a heat treatment in NH_3 at 950, 1,000, and 1,050 °C, respectively. This is illustrated in Fig. 10.19.

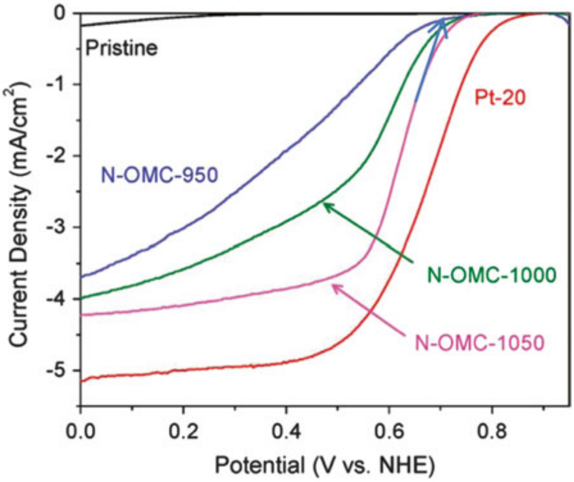

Fig. 10.19 Disk currents at 1,600 rpm and 10 mV/s from cyclic voltammetry experiments in O_2-saturated 0.05 M H_2SO_4 solution of an N-doped metal-free carbon catalyst heat treated in NH_3 between 950 and 1,050 °C. The best catalyst is obtained at 1,050 °C. It has a V_{onset} of 0.77 V vs. RHE (according to Fig. 2 in ref. [108]; reproduced with permission of The American Chemical Society)

The heat treatment greatly increased the total surface area of the three N-doped catalysts which reached 1,681, 2,121, and 1,923 m^2/g, respectively, with a total N content of 6.0, 3.6, and 4.6 at.%, respectively. Their Fe content was also measured (by inductively coupled plasma spectrometry) and found to be below 100 ppm. The only particularity of these catalysts is their very high specific surface area which for the best catalyst (the one obtained at 1,050 °C) was nearly 2,000 m^2/g. On the other hand, their total nitrogen content is not particularly high at 4.6 at.% N for the best catalyst with 46.9 and 10.0 % of pyridinic and graphitic nitrogen atoms, respectively. *It is possible here that both the nitrogen content and the particular textured properties of the very high specific surface area of these materials are acting together to drastically improve the ORR activity of these materials*. A comparative study of various carbon electrodes has previously shown that carbon substrates with a large number of edge plane sites have higher activity toward ORR [58]. In 0.1 M H_2SO_4, there is indeed a difference of 0.34 V for ORR on basal plane pyrolytic graphite and edge plane pyrolytic graphite substrates. When the V_{onset} values of all N-doped metal-free carbon catalyst of this section are considered, an average V_{onset} of 0.62 V vs. RHE is obtained with a minimum and maximum V_{onset} of 0.35 and 0.78 V vs. RHE. This is plotted as OTHER in Fig. 10.15. This average V_{onset} value of 0.62 V vs. RHE is however significantly boosted by the high V_{onset} from the last series of catalysts reported by Sheng Dai and collaborators.

10.4.5.2 ORR Catalysts Made with Fe or Co

Similarly to Ozkan, Popov, and the Japanese consortium, other authors also obtained their ORR catalysts using Fe- or Co-containing precursors to improve their catalytic activity without attributing at least part of this activity to Fe–Nx or Co–Nx catalytic sites. In 2009 [109], Muhler and collaborators grew N-containing carbon nanotubes from acetonitrile over Co metal used as catalyst on a silica support. Two growth temperatures were used: 550 and 750 °C. The N-containing carbon nanotubes (N-CNT) were refluxed in KOH to remove the silica support and HCl to dissolve the metal in excess. The Co surface content, measured by XPS after sample purification, was 0.4 at.% for N-CNT550 and 0.2 at.% for N-CNT750. Some of this cobalt was fully covered by a carbon layer. Oxidized cobalt was also seen in the XPS spectrum of N-CNT550 and N-CNT750. The nitrogen content, also measured by XPS, was 6.3 at.% in N-CNT550 and was broken down as 43 % pyridinic and 28 % graphitic nitrogen atoms, while a nitrogen content of 7.5 at.% broken down as 20 % pyridinic and 46 % graphitic nitrogen atoms was found for N-CNT750. The ORR activity of these catalysts was measured in 0.5 M H_2SO_4 at 900 rpm. N-CNT550 was found to be more active, with a V_{onset} of 0.70 V vs. RHE, than N-CNT750 with a V_{onset} of 0.55 V vs. RHE. *The higher activity of N-CNT550 was explained in terms of a higher edge plane exposure and a higher pyridinic content for the catalyst grown at lower temperature*. The apparent number of electrons transferred during ORR was also $n = 3.92$ for N-CNT550, but only $n = 2.48$ for N-CNT750.

In 2010, Liming Dai and collaborators [110] grew on a silica/Si support, vertically aligned N-doped carbon nanotubes (N-CNT) at 850 °C and from a mixture of Ar, H_2, and NH_3 in the presence of iron phthalocyanine (FePc). The N-CNTs were removed from the SiO_2/Si support and measured on a glassy carbon electrode. The V_{onset} determined at pH 3 for this catalyst was 0.86 V vs. RHE. Its total N content was 4 at.%. This experiment was anterior to the one reported by this group and already commented in Sect. 10.4.5.1 [106]. In the latter experiment, similar N-doped carbon nanotubes were grown without FePc. The N content of that catalyst was 3.6 at.% and its V_{onset} was only 0.53 V vs. RHE. The comparison between the two types of vertically grown N-doped carbon nanotubes clearly illustrates the important role played by FePc in the sharp rise in ORR activity when Fe-containing compounds are present in the reactor during the growth of the N-doped nanotubes!

In 2011, Woo and collaborators prepared ORR catalysts from the pyrolysis at 700, 800, and 900 °C of a mixture of iron oxide supported on Vulcan and dicyandiamide ($C_2H_4N_4$; a dimer of cyanamide) [111]. TEM of the catalysts revealed that at 700 °C metal particles were encapsulated with a carbon layer, while they were mostly in carbon tubes at 900 °C. The total N content was 2.2, 3.5, and 6.6 at.% for the catalysts heat treated at 700, 800, and 900 °C, respectively. This N content was broken down as 54 % pyridinic and 0 % graphitic nitrogen atoms at 700 °C, while it was 61.4 % pyridinic and 10.7 % graphitic at 900 °C. The Fe content was also measured in these catalysts and also for Fe_2O_3/C, the catalyst iron precursor. It was 1.7, 1.4, and 0.5 at.% after heat treatments at 700, 800, and 900 °C, while it was 1.8 at.% Fe for FeO_3/C. The V_{onset}, measured in 1 M $HClO_4$ at 2,000 rpm, was 0.78, 0.73 and 0.78 V vs. RHE for the three catalysts made at 700, 800, and 900 °C, respectively, but Fe_2O_3/C had a negligible catalytic activity for ORR. Since the Fe content in Fe_2O_3/C and in the catalyst heat treated at 700 °C were about the same (1.8 vs. 1.7 at.% Fe), but the activity increased dramatically after the heat treatment of Fe_2O_3/C mixed with dicyandiamide, *it was concluded that* (*1*) *Fe-containing catalytic sites were not involved in this catalyst and* (*2*) *that the catalytic activity was the result of N doping* (*especially by pyridinic nitrogen atoms*) *of the carbon material.*

In 2011, Sun and collaborators also prepared N-doped carbon nanotubes by the CVD at 950 °C of a mixture of Ar and CH_4 on a ferrocene and melamine catalyst [112]. The N content in these N-CNT materials was varied from 0 to 7.7 at.%, while the Fe content was always between 0.3 ± 0.1 at.% in the same materials. The ORR activity of the N-CNT doped with 7.7 at.% was measured in 0.5 M H_2SO_4 at 900 rpm. Its V_{onset} was 0.51 V vs. RHE.

The same year, Kim and collaborators [113] published results about catalysts made on three carbon supports: Ketjenblack (an amorphous carbon), platelet carbon nanofibers (P-CNF with many edges of graphene planes appearing at the surface of the support), and carbon nanotubes (CNT without edges along the surface of the tube). Urea and formaldehyde were first polymerized on these three carbon supports. This was followed by the impregnation on the polymerized material of a complex made by the reaction of cobalt nitrate with ethylene diamine. Finally, the three materials were pyrolyzed at 800 °C and then washed in acid to remove excess cobalt. The total N content increased from 0.7 wt% for the catalyst made on the CNT support, to 1.5 wt% for the catalyst made on Ketjenblack, and finally to 3.8 wt% for the catalyst obtained on the platelet carbon nanofibers. Their surface areas were 450, 906, and 45 m^2/g, respectively. The V_{onset} of the catalysts followed their N content with 0.53, 0.66, and 0.74 V vs. RHE. *The ORR activity was attributed to the nitrogen content*, *the type of nitrogen* (*mostly pyridinic*), *and to the number of edges available on the carbon support*. There was no mention of a possible role of Co–Nx sites in these catalysts, and the remaining Co content was not determined. These catalysts were also measured in fuel cell at 75 °C, with 2 atm. H_2/2 atm. O_2. The best catalyst provided a power density of 0.320 W/cm^2 at 0.35 V. This is a power density typical of many catalysts containing Co or Fe precursors.

In a following publication [114], the same group polymerized pyrrole around carbon nanofibers and then impregnated this material with the complex made from cobalt nitrate and ethylene diamine before pyrolyzing the resulting material at 800 °C in Ar to obtain a catalyst for ORR. The final material was washed in acid to remove the metal in excess. The total N content of the catalyst was 4.5 wt% broken down as 49 % pyridinic, 22 % pyrrolic, and 30 % quadratic nitrogen atoms. The Co particles in the catalyst were protected from dissolution by a carbon layer formed during the heat treatment. The Co content of the leached catalyst was 2.7 wt%. Only fuel cell measurements at 75 °C, 2 atm. H_2/2 atm. O_2 were made with this catalyst, which yielded a maximum power density of 0.34 W/cm^2 at 0.3 V, similar again to what was already obtained with the previous catalyst. Despite the possible contribution of Co–Nx sites to the activity, *these authors attribute the ORR activity of their catalyst to pyridinic and quadratic nitrogen atoms*, *even suggesting a possible synergetic effect on increasing the N content and therefore the activity of the catalyst to the simultaneous presence of polypyrrole and ethylenediamine.*

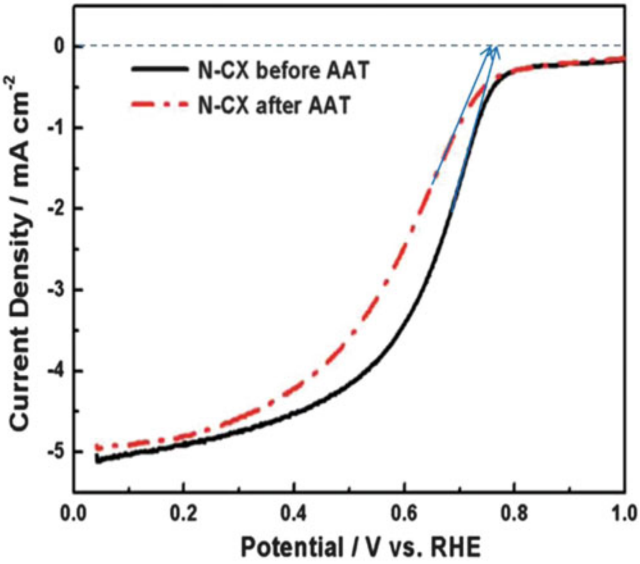

Fig. 10.20 Disk currents at 1,600 rpm and 5 mV/s from cyclic voltammetry experiments in O_2-saturated 0.5 M H_2SO_4 solution of an acid leached nitrogen-doped xerogel (N-CX) made from a mixture of resorcinol formaldehyde and cobalt nitrate. The material was pyrolyzed at 800 °C in NH_3. The disk current for the same catalyst is also shown after accelerating aging tests (AAT). V_{onset} for N-CX before AAT is 0.77 V vs. RHE. It is 0.75 V vs. RHE after AAT (according to Fig. 7a in ref. [115]; reproduced with permission of The Royal Society of Chemistry)

The last publication examined in this section will again give us the opportunity to illustrate that minute amounts of metal content (either Fe or Co) in N-doped carbons are capable of having a significant effect on their ORR activity in acid medium. In this publication by Zhang and collaborators [115], a nitrogen-doped carbon xerogel was made from a mixture of resorcinol formaldehyde and cobalt nitrate, where cobalt nitrate was considered an N-doping catalyst. The material was pyrolyzed at 800 °C in NH_3, which was considered as the nitrogen source. The resulting material was leached in H_2SO_4 to remove all soluble species and yielded the catalyst labeled N-CX. When the activity of N-CX was measured for ORR in 0.5 M H_2SO_4 at 1,600 rpm, a V_{onset} of 0.77 V vs. RHE was obtained. This is shown in Fig. 10.20. In these conditions, the catalyst reduced O_2 with an apparent number $n = 3.5–3.7$ of electrons. In fuel cell at 80 °C, 0.2 MPa H_2/0.2 MPa O_2, it yielded a maximum power density of 0.36 W/cm^2 at 0.35 V, a value similar to the two previous catalysts measured in fuel cell in this section. Curiously, the total N content is not reported, but a XPS spectrum at the N1s edge is shown and deconvoluted into pyridinic, quaternary, and oxidized nitrogen atoms with the quaternary peak predominating the spectrum. *The ORR activity of this catalyst is substantially attributed to quaternary nitrogen atoms*, *which are doped in the carbon aerogel. The same quaternary nitrogen atoms also play an important role in the stability of the catalyst*. This is also shown in Fig. 10.20 for N-CX after accelerated aging test (AAT) based on a continuous cycling of the potential for 1,000 cycles at room temperature from 0 to 1.2 V vs. RHE. The Co content in this catalyst is quite low and was measured at 0.07 wt%. This metal content is considered by the authors to be too low to have any effect on the catalyst activity. However, as it is shown in Fig. 10.16b, a Co content of 0.07 wt% may be responsible for 20 % of the maximum mass activity obtained with a catalyst made by the impregnation of 1 wt% of cobalt acetate on nonporous carbon black, followed by the pyrolysis of this material in NH_3 at 950 °C. A value of 20 % of the maximum mass activity is obviously not negligible and Co–Nx catalytic sites may be contributing to the ORR activity of this catalyst. The average value of V_{onset} for all the catalysts produced in the presence of Fe- or Co-containing molecules in this section is plotted as OTHERS in Fig. 10.15.

10.5 Discussion

A summary of the ORR activity, in terms of V_{onset} in strong acid medium, is presented graphically in Fig. 10.15 for all catalysts prepared by the various research groups and discussed in this chapter. Figure 10.13 demonstrates how these V_{onset} values were extrapolated from the various cyclic voltammograms reported in the literature. Figure 10.15 Frame A shows a cluster of the average V_{onset} values (open circles) attributed to the catalysts based on N-doped carbon produced by various research groups. These catalysts were produced without any strategic metals, like Fe or Co, either in the precursor molecules used in their synthesis, or as chemical catalysts to generate their carbon nanostructures. Also shown in Frame A is a cluster of the average V_{onset} values attributed to the catalysts produced by various research groups with strategic metals (Fe or Co), either in the precursor molecules used in their synthesis (dark circles) or as chemical catalysts to generate their carbon nanostructures (dark circles for Fe or Co and dark triangle for Ni). Each symbol includes a vertical line whose limits represent the highest and lowest individual V_{onset} values reported for each group.

In Fig. 10.15a, the cluster of the average V_{onset} values represented by the open circles is discernibly lower than the cluster of the average V_{onset} values represented by dark circles. We may further simplify the presentation of the activity results for all these catalysts by calculating overall average values for each of these clusters. The overall average V_{onset} value for all N-doped carbon catalysts prepared without strategic metal (Fe or Co) represented by open circles in Frame A is presented as an open square in Fig. 10.15b and has a value of 0.56 V vs. RHE. The overall average V_{onset} value for the N-doped carbon catalysts prepared with strategic metal (Fe or Co) is presented as a dark square in Fig. 10.15b and has a value of 0.74 V vs. RHE. Each overall average V_{onset} in Frame B includes a vertical line whose limits represent the highest and lowest individual V_{onset} values reported for each cluster, respectively. In addition, Fig. 10.15b also includes the overall average, minimum, and maximum V_{onset} values for ORR of all carbon blacks (Vulcan, Ketjenblack,

Black Pearls, etc.) having RDE data in the publications reviewed in this chapter. The latter is presented as a gray diamond with a value of 0.20 V vs. RHE.

From Fig. 10.15b, we see a large potential difference (0.36 V) between the overall average onset potential of oxygen reduction on carbon (gray diamond) and on N-doped carbon obtained without any strategic metal (Fe or Co). According to the authors cited in this chapter, doping carbon with two types of nitrogen atoms (pyridinic and quadratic [also referred to as graphitic]) is an important factor for increasing the ORR catalytic activity. The presence of graphene plane edges in the catalyst is another important factor because carbon atoms at graphene plane edges are believed to have a better interaction with O_2 than carbon atoms located in graphene basal planes. Since pyridinic-type nitrogen atoms are located on the edge of graphitic planes (see Fig. 10.4), it is difficult to attribute with certainty the observed positive effect on the catalytic activity for N-doped carbons to either the nitrogen atoms or to the graphene edges. The only case encountered in this chapter where graphene edges were the dominant factor in increasing the ORR activity was that of the catalyst presented in Fig. 10.19, for which a specific surface area of about 2,000 m^2/g was measured. This very high surface area likely implied that O_2 had access to a large number of graphene edges, while the total N content of the same catalyst was relatively low (4.6 at.%) compared to other N-doped catalysts discussed in this chapter. Furthermore, the iron content of the latter catalyst was only 100 ppm. Consequently, this catalyst is among the best examples of an N-doped carbon obtained without any strategic metal. The likely origin of its high ORR activity ($V_{\mathrm{onset}} = 0.77$ V vs. RHE) is therefore related to its large number of graphene edges available for O_2 interaction and its reduction.

From the observation of Figs. 10.15a, b, one may also conclude that there is practically no difference between the average V_{onset} value of 0.52 V vs. RHE for the reduction of O_2 on N-doped carbon catalysts produced with Ni (dark triangle in Fig. 10.15a) and that of the overall average V_{onset} value of 0.56 V vs. RHE of N-doped catalysts prepared without strategic metal. Since Ni is a strategic metal capable of chemically catalyzing the growth of carbon nanostructures, as shown by Ozkan and collaborators [65, 66, 68, 71], these authors have explained that the carbon nanostructures produced with Ni were mainly devoid of graphene plane edges. Therefore, these N-doped carbon materials were poorly interacting with O_2. Our interpretation of the same results was based on the possible occurrence of Ni–Nx sites that were previously found to have some, but very low, ORR activity [26, 116]. According to our alternative explanation, these N-doped carbon nanostructures would therefore have an ORR activity similar to that of N-doped carbon catalysts made without any strategic metal like Fe or Co.

A third conclusion that may be deduced from Fig. 10.15b is that there is a difference of 0.18 V between the overall average V_{onset} for the N-doped carbons catalysts prepared with Fe or Co in their synthesis (dark square) and the N-doped carbons obtained without either Fe or Co (open square). The latter may not seem large, but in fact means that a N-doped carbon made with a strategic metal will be able to generate (at about 0.8 V vs. RHE) $10^{0.18/0.10} = 63$ times more current density per unit mass compared to a N-doped catalyst made without a strategic metal. This calculation is based on a Tafel slope of 100 mV/decade (0.10 V/decade) at the same potential [61]. An experimental ratio of ORR activity at 0.8 V vs. RHE of about 60 was found between the mass activity (in A/g of catalyst) measured by RDE in H_2SO_4 at pH 1 for a Fe/N/C catalyst containing 0.27 wt% Fe (similar to that shown in Fig. 10.12B curve “b”) and a N-containing (but Fe-free) carbon prepared by pyrolysis in NH_3 (see Fig. S7 in ref. [117]).

The reason for this factor of about 60 in ORR activity between the two types of N-doped carbon catalysts, i.e., N-doped carbons made with strategic metals like Fe or Co and those made without any strategic metal, is what divides the scientific community. One camp believes the presence of Fe–Nx or Co–Nx catalytic sites explains the drastic improvement while the other defends the hypothesis that a larger number of N atoms (pyridinic or graphitic) or a larger number of graphene edges catalyzed by Fe or Co is what explains the difference.

We have shown several examples in this chapter where residual strategic metals contents ≤ 0.2 wt% (Fe or Co) in N-doped catalysts, considered negligible by some researchers, can in fact result in non-negligible catalytic activity for ORR in acid medium, given that this activity increases quickly with the Fe or Co content in N-doped catalysts (see Figs. 10.3 and 10.16b). We also believe that the existence of Fe–Nx sites in Fe/N/C catalysts have now been proven with little or no doubt by ToF-SIMS, Mössbauer spectroscopy, STEM imaging and EELS analysis, and by some carefully performed poisoning experiments. These four types of proofs are now discussed.

10.5.1 ToF-SIMS

In Figs. 10.3 and 10.16b, the increase in catalytic activity with metal content in the Fe/N/C catalysts was attributed to the presence of Fe–Nx (or Co–Nx) catalytic sites capable of interacting with oxygen and reducing it to water. This assertion was based on the detection by ToF-SIMS in these Fe/N/C catalysts of several $FeN_xC_y^+$ ions (see Fig. 10.6) ejected from the top molecular surface layer of the probed catalyst. A strong correlation was found (see Fig. 10.5) between the relative intensity of the $FeN_2C_4^+$ type ions detected by ToF-SIMS and the ORR catalytic activity for Fe/N/C catalysts prepared at various heat-treatment temperatures. This finding led us to propose the involvement of a FeN_2/C catalytic site (see Fig. 10.4) as the most active site in these Fe/N/C catalysts, while also acknowledging that this proposed moiety was only part of the complete molecular site.

10.5.2 Mössbauer Spectroscopy

The second proof of the presence of Fe–Nx catalytic sites and their involvement in ORR in Fe/N/C catalysts comes from recent experiments performed by Mössbauer

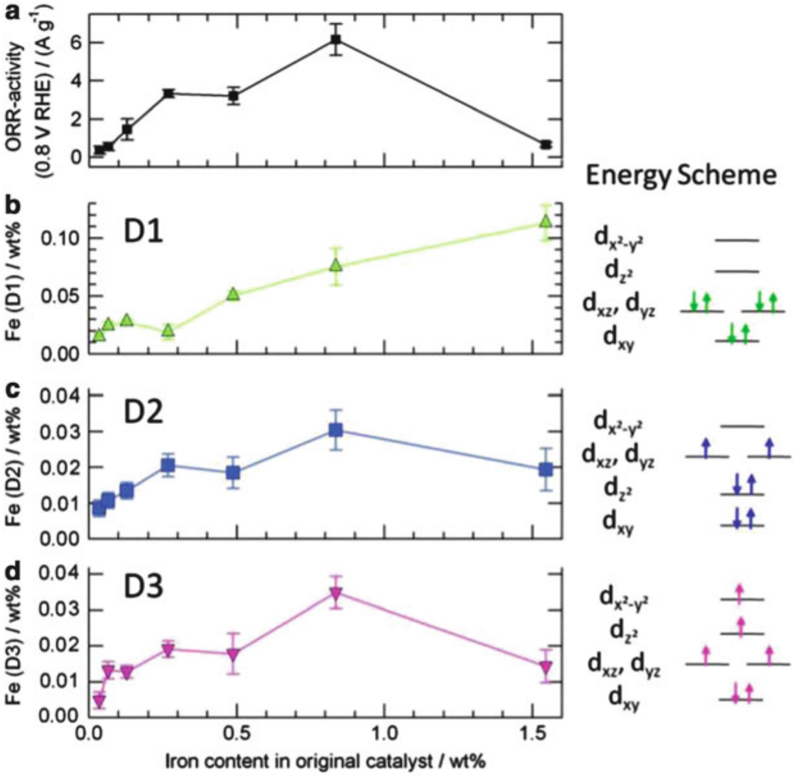

Fig. 10.21 ORR activity and the relative composition of each Fe species vs. the bulk iron content. Also shown are the Energy Schemes of D1, D2, and D3, as well as the filling of the molecular orbitals for the iron^{II} ion in the structure proposed for each site according to its proposed spin state: low in D1, intermediate in D2, and high in D3 [118] (according to Fig. 4 in ref. [117] for the *left frame* and to Fig. 2 in ref. [117] for the *right frame*; reproduced with permission of The Royal Society of Chemistry)

spectroscopy on these catalysts. The latter were obtained by adsorbing increasing amounts of iron acetate on a nonporous carbon black and heat-treating these materials in NH_3 at 950 °C [117]. The change in the catalytic activity with the iron loading is presented in Fig. 10.21a. Figure 10.22 shows that several Fe-containing species were detected by Mössbauer spectroscopy in each of these catalysts. Three broad doublets, D1, D2, and D3, as well as two narrow doublets (D4 and D5) were found in all catalysts. Based on their Mössbauer parameters, D1, D2, and D3 have been assigned to three different FeN_4-like species whose possible structures are illustrated in Fig. 10.23. D4 and D5 have both been attributed to iron nitride nanoparticles. The latter are also seen by high-resolution TEM. A last Fe species characterized by a broad singlet in the Mössbauer spectrum only appears when the actual Fe content in the catalyst reaches at least 0.27 wt% (see Fig. 10.22). This singlet has been assigned to incomplete FeN_4-like sites that are irreversibly

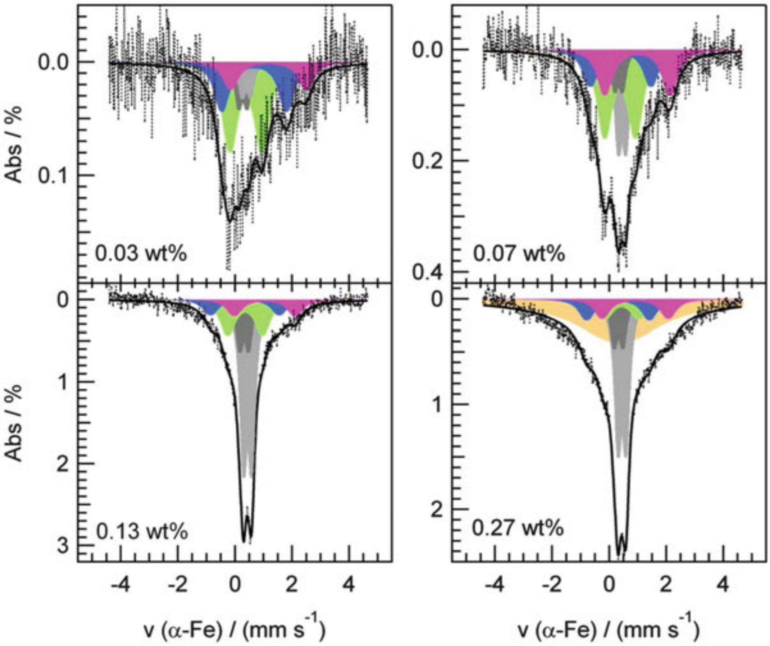

Fig. 10.22 Deconvoluted Mössbauer spectra of the Fe/N/C catalysts. The iron content of the original catalyst is specified in each frame (according to Fig. 1 in ref. [117]; reproduced with permission of The Royal Society of Chemistry)

lost when the Fe/N/C catalyst becomes in contact with an acidic solution of H_2SO_4 at pH 1.

Among the four different Fe species left after acid washing, only D1 and D3 have been found to be active for the ORR, the most active one being D3 as shown by the similarity between the ORR activity of the catalysts illustrated in Fig. 10.21a, d. Here, Fig. 10.21d represents the changes in the amount of iron ions (in wt%) assigned to D3 species vs. the total iron content in the Fe/N/C in the original catalyst (before acid washing). Although D2 in Fig. 10.21c shows the same trend as D3, it is not ORR active because the $3dz^2$ orbital of its iron^{II} ion (the orbital interacting with O_2 [119]) is already filled. This is illustrated in D2's Energy Scheme in Fig. 10.21. On the other hand, the $3dz^2$ orbitals of the iron^{II} ion in D3, with a population of only one electron, and that of the iron^{II} ion in D1 with no electron, may both interact with O_2 and therefore result in active sites for the reduction of oxygen. The similarity between Fig. 10.21c for D2 and Fig. 10.21d for D3 indicates that the two FeN_4-like species are structurally related as shown in Fig. 10.23. Indeed, both D2 and D3 represent FeN_4-like sites hosted in carbon micropores. The difference between D2 and D3 is that, according to the Mössbauer parameters of D3, a fifth coordinating nitrogen was postulated below the FeN_4 plane pulling the Fe ion toward it. This modifies the sequence of the iron^{II} ion energy levels [118] as shown in Fig. 10.21 and changes the spin of the FeN_4-like

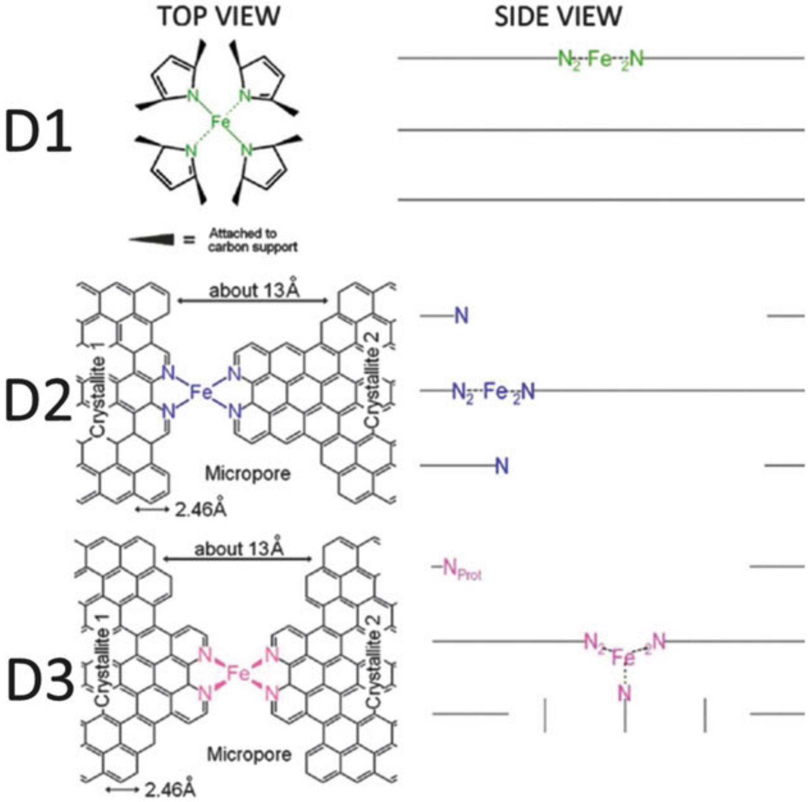

Fig. 10.23 Top and side views of the proposed structures of the FeN_4/C catalytic site in heat-treated, macrocycle-based catalysts assigned to Mössbauer doublet D1, the FeN_{2+2}-like micropore-hosted site found in the catalyst prepared with iron acetate and heat treated in ammonia assigned to doublet D2, and the N-FeN_{2+2}-like composite site, where N-FeN_{2+2} is assigned to doublet D3. In all side views, graphene planes are drawn as *lines*. For D2, the distance between the two nitrogen atoms belonging to the graphene planes above and below the FeN_{2+2}-plane is similar to that in crystalline iron phthalocyanine, thus similarly influencing the lattice contribution to the quadrupole splitting. For D3, the iron^{II} ion in N-FeN_{2+2} is coordinated by five pyridinic nitrogen atoms, one of them belonging to a plane located vertically below the N_4-plane. This axial nitrogen coordination moves the iron^{II} ion out of the N_4-plane towards the fifth coordinating nitrogen atom. D3 may exists as N-FeN_{2+2}/C or as a composite site N-FeN_{2+2} … N_{prot}/C, where N_{prot} is a protonable pyridinic nitrogen atom appearing at the edge of the upper plane in the side view of D3 [128]. N_{prot} is too far from N-FeN_{2+2} to have an influence on the Mössbauer spectrum of D3, but it is close enough to drastically improve the turnover frequency of the proposed composite site N-FeN_{2+2} … N_{prot}/C. According to Fig. 2 in ref. [117]; reproduced with permission of The Royal Society of Chemistry

site assigned to D3. The iron^{II} in the site proposed for D3 is in a high spin state ($S = 2$), while it is in medium spin state ($S = 1$) for D2 and in low spin state for D1. These spin states affect the Mössbauer parameters of the FeN_4-like doublets assigned to these sites as it is detailed in the literature [120–127].

From Fig. 10.23, the catalytic site illustrated in Fig. 10.2 has a D1 Mössbauer signature, while both D2 and D3 signatures represent sites whose incomplete structure was initially proposed as FeN_2/C (Fig. 10.4), and later completed as FeN_{2+2}/C (Fig. 10.10) and is now present either as an ORR inactive site, having the D2 signature, or as an ORR-active site ($N–FeN_{2+2}/C$) having the D3 signature. Moreover, we have shown [128] that if there is a basic (pyridinic) nitrogen in the vicinity of an $N–FeN_{2+2}/C$ active site which is protonable, it may possibly act as a relay for quickly transferring protons to the iron ion of the $N–FeN_{2+2}/C$ catalytic site during ORR. The synergy between $N–FeN_{2+2}/C$ and the neighboring protonated pyridinic nitrogen drastically increases the turnover frequency of what is now the composite site: $N–FeN_{2+2}\cdots NH^+/C$. A value of 11.4 electrons per site per second has been measured for the turnover frequency of $N–FeN_{2+2}\cdots NH^+/C$ [117]. This is only 2.2 times lower than the turnover frequency measured for Pt [6]. The high turnover frequency of $N–FeN_{2+2}\cdots NH^+/C$ is drastically reduced when the protonated NH^+ in the composite site is neutralized by an anion. This was found to be the main mechanism affecting the ORR activity of the composite $N–FeN_{2+2}\cdots NH^+/C$ site in H_2SO_4 solution. The same phenomenon also occurs in fuel cell, where the neutralization of $N–FeN_{2+2}\cdots NH^+/C$ involves the sulfonate group (SO_3^-) of the proton-conducting ionomer. This neutralization has been identified as the main problem leading to an apparent instability of these catalysts in fuel cells. “Apparent” is used to emphasize the fact that, in this neutralization reaction, the structure of the active site does not change, but the site is simply deactivated. Here, it should be noted that our interpretation of the apparent instability of these catalysts in fuel cells is at odds with that proposed by Popov and collaborators [88] as in their case, it is claimed that the protonation of the pyridinic nitrogen atoms of their N-doped catalysts leads to a decay of activity, while in our case, it is when $N–FeN_{2+2}\cdots NH^+/C$ is in its protonated form that the catalytic site is the most active.

Thus, to summarize the results obtained by Mössbauer spectroscopy, it is clear from the similarity between the changes in ORR activity of these Fe/N/C catalysts illustrated in Fig. 10.21a and the changes in the amount of $N–FeN_{2+2}\cdots NH^+/C$ highly active sites illustrated in Fig. 10.21d in the same catalysts that Fe–Nx catalytic sites are indeed active toward ORR in these Fe/N/C catalysts.

10.5.3 STEM Imaging and EELS Analysis

In a recent publication [129], Hongjie Dai and his collaborators reported the preparation of few-walled carbon nanotubes, with a high percentage of double-walled nanotubes and a small percentage of triple-walled nanotubes, grown from MgO-supported iron seeds by chemical vapor deposition. The outer walls of these few-walled carbon nanotubes were then partially opened by controlled oxidation, producing disordered graphene layers still partially attached to what was left of the carbon nanotube. When this material was subjected to a pyrolysis step in NH_3 at 900 °C, N functionalities were generated at the defect sites in the tube and in the

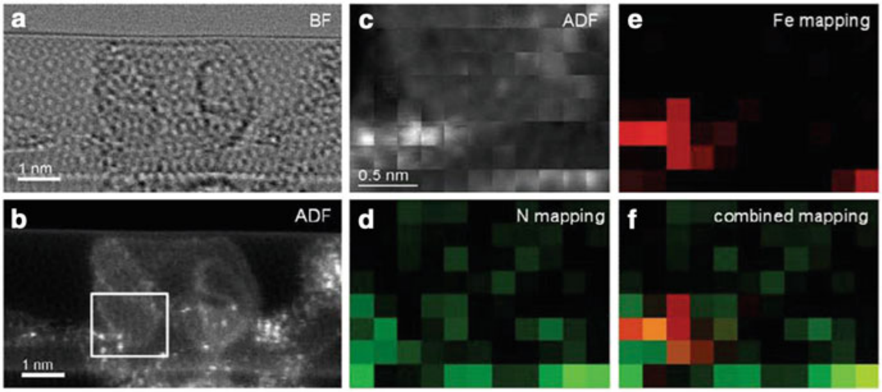

Fig. 10.24 Distribution of Fe and N atoms in the NT-G ORR catalyst. (**a**) Bright field STEM and (**b**) corresponding ADF images of NT-G. The area indicated by a *white square* in (**b**) is further characterized by (**c**) ADF intensity mapping, (**d**) N EELS mapping, (**e**) Fe EELS mapping, and (**f**) overlaid Fe and N EELS maps. The ADF and EELS maps were recorded simultaneously (according to Fig. S8 in ref. [129]; reproduced with permission of Nature)

disordered graphene layers, and this, in conjunction with "iron impurities" left over from the nanotube growing process, produced Fe–Nx-type centers that were active for the oxygen reduction reaction in basic and acid solution. This catalyst was labeled NT-G (or NT-NG in the supplementary information).

Scanning transmission electron microscopy (STEM) imaging and simultaneous elemental analysis by electron energy loss spectroscopy (EELS) supplemented by annular dark field (ADF) imaging were performed on these catalysts. They indicated that Fe and N species were important to the high ORR electrocatalytic activity observed for NT-G and that this catalyst falls within the category of metal-nitrogen catalysts since its activity for ORR decreased when the "impurity" Fe content was lowered from 1 wt% to 0.1 wt%! Fig. 10.24 presents an example of bright field STEM images and their corresponding elemental analysis for a catalyst showing individual Fe and N atoms in close proximity as they should be in Fe–Nx catalytic sites. Note that each square in the elemental mapping represents a surface area of about 2 Å × 2 Å.

10.5.4 Poisoning Experiments

The most conclusive evidence to demonstrate the presence of Fe–Nx active sites for ORR in Fe/N/C catalysts would be to show the possibility of poisoning these sites with a strong ligand to the iron ion of Fe–Nx in contact with an O_2 saturated electrolytic solution. In such a case, the poisoning ligand would prevent access of the site to O_2 and hence suppress its subsequent reduction. CO would seem to be a good poison candidate since it is well known to poison hemoglobin in neutral pH. However, it has been shown that CO does not poison Fe-based catalysts in acid medium [78] (or even in neutral or basic media [unpublished results]). CO does not poison the oxygen reduction reaction on unpyrolyzed iron phthalocyanine (FePc) adsorbed on carbon in which the FeN_4 moiety is known to have ORR activity [119].

Recent experiments by Gewirth and collaborators [130] have shown that the oxygen reduction activity of carbon-supported FePc or pyrolyzed (800 °C) carbon-supported FePc remain practically unaffected in pH 6 phosphate buffer containing NaF, KSCN, or ethane thiol (C_2H_5 SH). Only KCN is able to strongly decrease the oxygen reduction activity of the same catalysts in O_2 saturated 0.1 M NaOH solution. Potassium cyanide is known to form very strong complexes with iron and poison the ORR at iron centers [131–133]. These results are consistent with those originally obtained by Yeager and collaborators on an unpyrolyzed FePc derivative showing a poisoning effect with cyanide in basic medium [131]. Rinsing cyanide-poisoned FePc and pyrolyzed FePc electrodes with water resulted in almost complete recovery of the ORR activity in fresh electrolyte without cyanide. This indicates that cyanide ions compete with O_2 for access to the iron ion in the active site, but do not permanently bind to this site or alter it. Therefore, these results demonstrate that the active sites in these materials are Fe-centered both before and after pyrolysis. Similar poisoning experiments cannot, of course, be performed in an acidic medium, but if Fe–Nx active sites exist in basic medium, there is a strong presumption that they should also exist in acid medium.

10.6 Mechanism of O_2 Reduction

10.6.1 O_2 Reduction on Fe–Nx Active Sites

Given the fact that iron exists in several oxidation states and is the main transition metal found in many oxidoreductases (enzymes responsible for electron exchange in biological reactions) [134], including in the Fe-porphyrin-containing catalytic site of cytochrome c oxidase, the enzyme responsible for the oxygen reduction in the mammalian respiratory electron transfer chain embedded in the mitochondrial membrane [135], it is relatively easy to understand why iron in Fe/N/C catalysts should also be at the heart of the active sites that reduce O_2 to H_2O or O_2 to H_2O_2 in acidic medium. A plausible mechanism for the electrochemical reduction of O_2 on Fe/N/C catalysts may be similar to the one proposed by Boulatov for the catalyzed reduction of O_2 on porphyrins [135]. This mechanism is illustrated in Fig. 10.25. In this figure, the solid lines on either side of the iron ion represent the porphyrin plane (that we will also refer to as L_4 in this chapter, as it was also used in the theoretical work by Anderson and Sidik on the reduction of oxygen on L_4Fe catalysts [136]; see below) with its four N atoms coordinating the iron ion. It is also proposed, in our case, that the fifth coordinating atom represented by X under the iron ion in L_4Fe in Fig. 10.25 is a basic pyridinic nitrogen atom, as illustrated for D3 in Fig. 10.23.

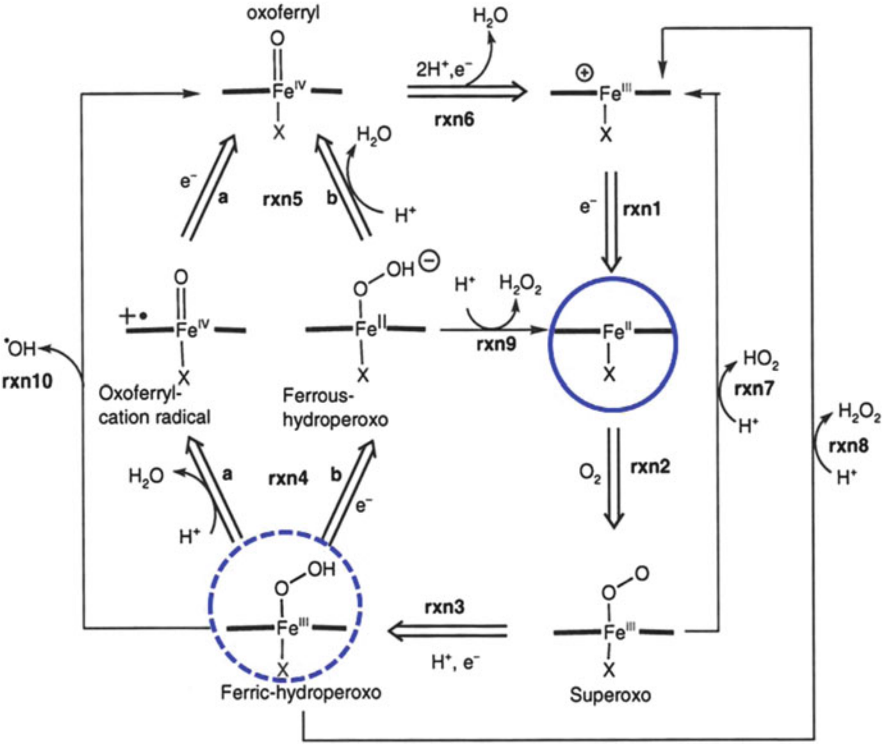

Fig. 10.25 A plausible mechanism for electrochemical reduction of O_2 catalyzed by Fe-porphyrins (according to Fig. 12 in ref. [135]; reproduced with the permission of Springer Science + Business Media)

The oxygen reduction reaction starts when the iron ion is in the ferrous state (the L_4Fe^{II} state indicated by a solid circle in Fig. 10.25). According to the calculations of Anderson and Sidik for oxygen reduction on iron-coordinated N_4-chelates [136], L_4Fe^{II} is most probably hydrated as L_4Fe^{II}–OH_2. The same calculations show that O_2, in acid solution, is capable of displacing H_2O from L_4Fe^{II}–OH_2 to form the ferric hydroperoxo species according to Eq. (10.3):

$$L_4Fe^{II}-OH_2 + O_2 + H^+ + e^- \rightarrow L_4Fe^{III}-O-OH + H_2O \qquad (10.3)$$

L_4Fe^{III}–O–OH, which is indicated by a dashed circle in Fig. 10.25, is a branching point, where one option (left arrow) is that the reduction reaction may release H_2O and form an oxoferryl cation radical, then an oxoferryl species, then a ferric species, and finally back to the original ferrous species, ready to repeat the cycle. The following equations are involved in this long turnover cycle:

$$L_4Fe^{III}-O-OH + H^+ + e^- \rightarrow L_4Fe^{IV}=O + H_2O \qquad (10.4)$$

$$L_4Fe^{IV}=O + H^+ + e^- \rightarrow L_4Fe^{III}-OH \qquad (10.5)$$

$$L_4Fe^{III}{-}OH + H^+ + e^- \rightarrow L_4Fe^{II}{-}OH_2 \tag{10.6}$$

On the other hand (right arrow), L_4Fe^{III}–O–OH in Fig. 10.25 may release H_2O_2 and returning to the starting point, according to

$$L_4Fe^{III}{-}O{-}OH + H^+ + e^- \rightarrow L_4Fe^{II} + H_2O_2 \tag{10.7}$$

$$L_4Fe^{II} + H_2O \rightarrow L_4Fe^{II}{-}OH_2 \tag{10.8}$$

Following the left arrow option therefore leads to the reduction of O_2 to H_2O with the transfer of $4e^-$ and $4H^+$. It requires, however, going through the highly oxidized state of Fe^{IV} in the catalytic site. On the other hand, following the right arrow leads to the reduction of O_2 to H_2O_2 with the transfer of $2e^-$ and $2H^+$. For van Veen and his collaborators [137], the ability for the transition metal center to stabilize $L_4Fe^{IV}{=}O$ gives these catalysts the possibility, at high applied potential, to reduce oxygen to water by a direct $4e^-$ reaction. According to them, it may explain why, for most Co–N_4 chelates, no direct water formation was observed, other than the apparent formation caused by H_2O_2 decomposition. Anderson and Sidik [136] did not agree with the obliged passage of the Fe-centered site through $L_4Fe^{IV}{=}O$, but instead suggested the replacement of Eqs. (10.3)–(10.6) with Eqs. (10.9)–(10.12):

$$L_4Fe^{II}{-}OH_2 + O_2 + H^+ + e^- \rightarrow L_4Fe^{III}{-}O{-}OH + H_2O \tag{10.9}$$

$$L_4Fe^{III}{-}O{-}OH + H^+ + e^- \rightarrow L_4Fe^{II}(OH{-}OH) \tag{10.10}$$

$$L_4Fe^{II}(OH{-}OH) + H^+ + e^- \rightarrow L_4Fe^{III}{-}OH + H_2O \tag{10.11}$$

$$L_4Fe^{III}{-}OH + H^+ + e^- \rightarrow L_4Fe^{II}{-}OH_2 \tag{10.12}$$

Here, Eq. (10.9) is the same as Eq. (10.3), ending with the ferric hydroperoxo species as indicated by the dashed circle in Fig. 10.25. Equations (10.10–10.12) describe a reduction reaction path which does not appear on Fig. 10.25, where L_4Fe^{II} (OH–OH) represents H_2O_2 bound to the L_4Fe^{II} catalytic site. According to our experimental results on the oxygen reduction properties in acid medium of Fe/N/C catalysts [116], we have shown that those obtained after high-temperature pyrolysis in NH_3 of iron^{II} acetate adsorbed on nonporous carbon black were practically unable to reduce H_2O_2 electrochemically in H_2SO_4 solution at pH 1. Therefore, we do not believe that the catalytic sites in Fe/N/C would follow the oxygen reducing path described by Eqs. (10.9)–(10.12), but rather a path described by Eqs. (10.3)–(10.6), which is also illustrated by the turnover along the left arrow in Fig. 10.25. Essentially, the same conclusions about the oxygen reduction path were reached by Chlistunoff for a pyrolyzed Fe/PANI catalyst (where PANI =

polyaniline), with the exception that he also claimed that his results indicated that a relatively strong interaction between O_2 and a ferric site may be possible, adding another starting point for ORR, besides the already known ferrous site indicated by a solid circle in Fig. 10.25 [138].

Although there are some disagreements between various groups about the exact reaction path during ORR, all groups agree on the fact that the first electron transfer (Eqs. 10.3 or 10.9) is the rate-limiting step in the O_2 reduction reaction in acidic medium [136, 137, 139]. As such, the first reduction step of O_2 on L_4Fe^{II} site is responsible for the observed Tafel slopes of about 60 mV/decade (at 25 °C) or about 70 mV/decade (at 80 °C) which are usually observed for O_2 reduction on Pt (see for instance Table 3.4 in ref. [21] and also the slope of 61 mV/decade determined over a current range of nearly three decades in Fig. 3 of [8]).

10.6.2 O_2 Reduction on N-Doped Carbons

While it may be relatively easy to understand the interaction between O_2 (a diradical in its fundamental state) and the $3dz^2$ orbital of the L_4Fe^{II} catalytic site (see the Energy Scheme in Fig. 10.21), it is not so easy to understand the interaction mechanism and reaction path followed during the reduction reaction of O_2 on N-doped carbons in acid medium. Several calculations were performed by various groups to determine the precise origin of the reduction capabilities and the oxygen reduction mechanism on these N-based catalysts. They will now be reviewed.

In their first quantum calculations of the ORR properties of N-doped graphite [140], Anderson and his collaborators found that carbon radical sites were formed adjacent to substitutional N in graphite and were active for O_2 electroreduction to H_2O_2 via an adsorbed OOH intermediate. They also found that substitutional N atoms that were at a distance from graphite sheet edges (graphitic N of type N_3 in Fig. 10.4) led to more ORR activity than those closer to the edge (graphitic N of type N_2 in Fig. 10.4). In a subsequent publication [141], they focused on the properties of pyridinic nitrogen atoms at the graphite edge and found that, at potentials greater than 0.3 V (when N atoms were not hydrogenated), they were not active toward ORR because their OOH bonds were too weak. At potentials below 0.3 V, the hydrogenation of these pyridinic N made them radical centers. Because the latter bonded too strongly to OOH, they were not active either.

Later, in studying the properties of two pyridinic N atoms substituting for adjacent edge CH groups (–N–C–N–) [142], Anderson and his colleagues discovered that, at potentials below 1.70 V, one of these N atoms would be in NH form and that the adsorption of possible oxygen intermediates on these edge pyridinic nitrogen atoms would be blocked after an initial reduction leading to O bonded to one N and H bonded to the other one (–NO–C–NH–). However, this edge structure, with its unpaired electron, can bond OOH to the carbon bridging the pyridinic N atoms, with a bond strength that led to a two-electron reduction to H_2O_2. This overall reaction took place according to the following equations:

$$O_2 + (-NO-C-NH-) + H^+ + e^- \rightarrow (-NO-C[OOH]-NH-) \text{ at } U^0 = 0.73\ V \tag{10.13}$$

$$(-NO-C[OOH]-NH-) + H^+ + e^- \rightarrow (-NO-C-NH-) + H_2O_2 \text{ at } U^0 = 0.66\ V \tag{10.14}$$

If two carbon atoms in a graphene layer were each substituted with a nitrogen atom, the latter would be of the pyridinic type because their substitution for the carbon on the graphene edge is energetically favorable. However, it is more likely to find these pyridinic N atoms far apart from each other because the (–N–C–N–) configuration is not energetically favorable [143]. The latter (–N–C–N–) configuration described by Anderson and his colleagues is therefore unlikely and leaves us once again with pyridinic-type nitrogen without ORR activity. However, Ikeda and his colleagues [144] confirmed that graphitic N of type 2 in Fig. 10.4 are capable of reducing oxygen as long as they are on a zigzag edge of the graphene plane. If the analogous (–C–N–C–) configuration is realized in an armchair edge, O_2 adsorption does not give rise to stable structures.

Thus far, all N-doped carbons appear to only be able to reduce oxygen on graphitic-type nitrogen atoms, and this reduction only leads to the production of H_2O_2. However, experimentally, it is known that metal-free N-doped carbons are capable of reducing O_2 to water with an apparent transfer of $4e^-$, as reported by various research groups covered in this chapter. It is also clear from Fig. 3 in ref. [116], for instance, that similar limiting current densities are reached at the same rotation rate (from 100 to 1,600 rpm) for ORR on a metal-free N-doped carbon, a Fe/N/C or a Pt/C electrocatalyst.

The first report of the reduction of oxygen to water on a graphene layer doped with nitrogen of the pyridinic type was published in 2011 [145]. Here the N-containing graphene sheet is modeled as $C_{45}NH_{20}$ as shown in Fig. 10.26a. Each atom is numbered and a spin density (upper number) and atomic charge (lower number) were calculated for each atom. All carbon or nitrogen atoms on the edge are terminated by hydrogen atoms. The ORR process was simulated beginning with a first electron transfer. In acidic environment, O_2 can adsorb H^+ to form H^+–O–O [146] and this intermediate can be reduced at the electrode according to Eq. (10.15):

$$H^+-O-O + e^- \rightarrow H-O-O \tag{10.15}$$

In the next step, OOH adsorbs on a carbon near the pyridinic N atom on the graphene sheet. The adsorbed OOH species is represented as *OOH. There are two possible reaction paths described as follows:

Reaction path 1

$$^*OOH + H^+ + e^- \rightarrow {}^*OH\ (\text{adsorbed 1}) + {}^*OH\ (\text{adsorbed 2}) \tag{10.16}$$

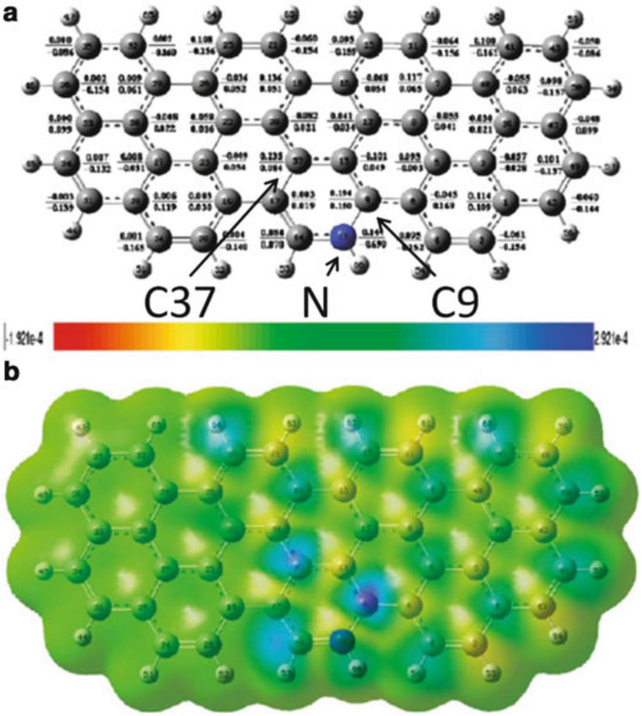

Fig. 10.26 (**a**) Charge distribution and spin density distribution on the N-graphene with pyridine structure (C45NH20). Each atom is identified by a number. The fractions next to each atom represents the spin density value (*numerator*) and charge density value (*denominator*); (**b**) Spin density distribution on the electron density isovalue plane; the most negative values are in *red*, the most positive in *blue*. Spin and charge density values for C37 are (0.235/0.084), N (0.144/−0.690), and C9 (0.194/0.150) (according to Fig. 4 in ref. [145]; reprinted with permission of The American Chemical Society)

$$^{*}\mathrm{OH}\ (\mathrm{adsorbed}\ 1) + \mathrm{H}^{+} + \mathrm{e}^{-} \rightarrow \mathrm{H_2O} \tag{10.17}$$

$$^{*}\mathrm{OH}\ (\mathrm{adsorbed}\ 2) + \mathrm{H}^{+} + \mathrm{e}^{-} \rightarrow \mathrm{H_2O} \tag{10.18}$$

Reaction path 2

$$^{*}\mathrm{OOH} + \mathrm{H}^{+} + \mathrm{e}^{-} \rightarrow {}^{*}\mathrm{O} + \mathrm{H_2O} \tag{10.19}$$

$$^{*}\mathrm{O} + \mathrm{H}^{+} + \mathrm{e}^{-} \rightarrow {}^{*}\mathrm{OH} \tag{10.20}$$

$$^{*}\mathrm{OH} + \mathrm{H}^{+} + \mathrm{e}^{-} \rightarrow \mathrm{H_2O} \tag{10.21}$$

Energetically, it was found that reaction path 1 was more favorable than reaction path 2.

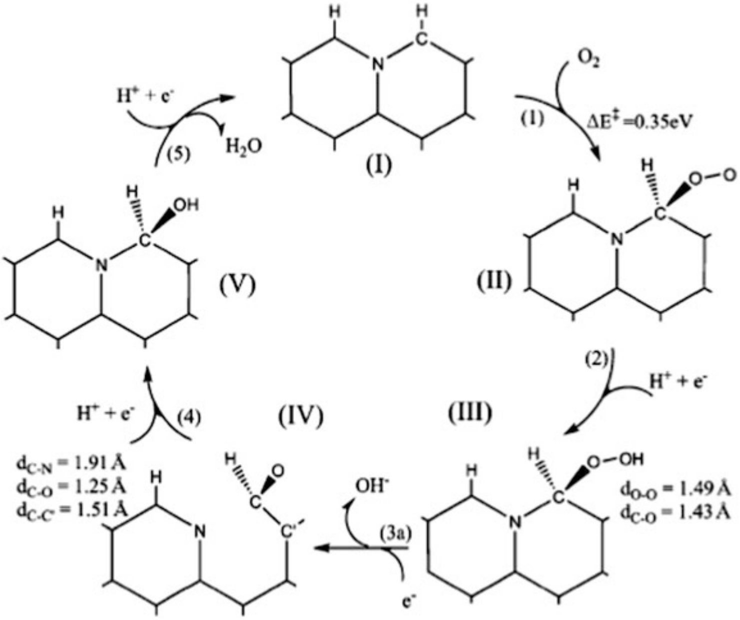

Fig. 10.27 Proposed mechanism for a $4e^-$ reduction of O_2 on a graphitic nitrogen of type N_2 along the zigzag edge (see Fig. 10.4) (according to Fig. 3 in ref. [147]; reproduced with permission of The Royal Society of Chemistry)

The above reaction does not happen on graphene; only on N-doped graphene. One of the reasons is that HOMO-LUMO gap decreases by a factor of two compared to pure graphene (2.7 eV), after nitrogen atom substitution. Hence, the chemical reactivity of N-doped graphene is significantly improved because the electrons are more easily excited from valence band to conduction band when the band gap is smaller. The other reason is that nitrogen doping introduces an unpaired electron which causes spin and charge densities to appear in the N-doped graphene model as shown in Fig. 10.26a. Figure 10.26b illustrates the change in spin density introduced on individual atoms in the graphene layer. As spin densities are the largest on C37 and C9, these atoms predominantly bond OOH as *OOH in the equations of reaction path 1. Therefore, the occurrence of a large spin density on these carbon atoms transforms them into catalytic sites for ORR.

Another recent work [147] proposes an interesting mechanism for a $4e^-$ reduction of O_2 on N-doped graphite of type 2 along the zigzag edge (see Fig. 10.4). This mechanism is illustrated in Fig. 10.27. A notable feature in this mechanism is state III with *OOH on the catalytic site. In this state, due to the higher strength of the C–O vs. the O–O bond, *OOH is easily dissociated into *O and OH^-. The remaining *O becoming a carbonyl group, cleaves the C–N bond in step 3a to form a stable CHO group and the broken-bonded nitrogen atom becomes pyridinic in IV. According to Jung and his colleagues [147], this new type of active site that switches between pyridinic and graphitic types of nitrogen atoms may reconcile the experimental controversy as to whether the pyridinic, graphitic, or both types of nitrogen atoms are the ORR-active sites for N-doped graphene materials.

10.7 Conclusions

Despite decades of research on Fe- or Co-based electrocatalysts for the oxygen reduction reaction (ORR) in acidic medium, such as that in PEM fuel cells, the role of the metal is still one that raises a great deal of controversy. Consequently, the nature of the catalytic site in these non-noble metal ORR catalysts is still a topic of debate. One camp within the scientific community believes that the metal is an integral and electrochemically active part of the catalytic site, while the other believes that the metal is merely a chemical catalyst for the formation of special oxygen-reducing N-doped carbon structures.

From this work, we conclude that the three models for the nature of the active ORR sites in non-noble metal catalysts, proposed and advocated by van Veen, Yeager, and Wiesener during the 1980s, all have merit because there appears to be more than a single type of active ORR site in Fe/N/C (or Co/N/C) catalysts in acidic medium. Indeed, FeN_4/C active sites, proposed by van Veen and having a D1 Mössbauer signature, are present in Fe/N/C catalysts. Other sites, referred to as N–FeN_{2+2}/C, having a D3 Mössbauer signature, are also present in the same catalysts. The latter is derived from C–N_x–Me, the model proposed by Yeager for the catalytic site, in which the transition metal ion M (Fe or Co) bonds to the carbon support by coordination through pyridinic nitrogen substituting for carbon in the support.

Our group has shown that C–N_x–Fe is only the precursor of the true catalytic site, which is formed after a high-temperature pyrolysis step. We initially referred to this catalytic site as FeN_2/C. Complementary experiments relating to the influence of the carbon support on the activity of Fe/N/C catalysts led us to conclude that (1) FeN_2/C, whose structure was obviously incomplete, was in fact FeN_{2+2}/C and (2) this site is hosted in the slit-shaped micropores of the carbon support. Our most recent Mössbauer experiments revealed yet more details about the exact structure. It appears that FeN_{2+2}/C may exist either with or without an axial coordination of the iron ion in the site to a supplementary pyridinic-type nitrogen atom located below the FeN_{2+2}/C site. This supplementary coordination pulls the iron ion out of its FeN_{2+2} coordination plane and changes its Fe^{II} spin from $S = 1$ to $S = 2$, modifying the relative energy level of the 3d orbitals of Fe^{II} and the electronic population of its $3dz^2$ orbital, which binds to O_2 in the first step of the oxygen reduction reaction. N–FeN_{2+2}/C with its $S = 2$ spin is ORR active, while FeN_{2+2}/C with its $S = 1$ spin is inactive. Finally, it is also very likely that the CNx sites proposed by Wiesener are also present in Fe/N/C catalysts since their total nitrogen content always significantly outnumbers the active-site-related Fe ion content.

In Fe/N/C catalysts obtained from iron acetate as the iron precursor, we have shown that (1) the catalytic activity follows the relative concentration of N–FeN_{2+2}/C-type catalytic sites, as measured by Mössbauer spectroscopy and neutron activation analysis of the Fe content, and (2) the catalytic activity also follows of the relative intensity of the $FeN_2C_4^+$ ions as measured by ToF-SIMS experiments. From these two observations, and the fact that (3) individual iron atoms can be detected in these catalysts surrounded by nitrogen atoms and (4) the Fe-containing site can be poisoned by KCN in alkaline medium, it was deduced that iron is indeed active in these sites and that among the three types of catalytic sites present in these catalysts (N–FeN_{2+2}/C, FeN_4/C, and CNx), N–FeN_{2+2}/C are the most active (when they are coupled with a neighboring protonated nitrogen atom). Iron-based active sites are also acid resistant.

ToF-SIMS results obtained for catalysts made with ClFeTMPP as the iron precursor in similarly made catalysts show that FeN_4/C is the major type of catalytic site present. However, the two other active sites are also present in these catalysts, N–FeN_{2+2}/C being here in smaller proportion. The opposite is true when the iron precursor is iron acetate.

As far as CNx sites are concerned, they may indeed be the only type of site in the catalyst when the latter is obtained from a nitrogen precursor and carbon support only, i.e., without involving any strategic metal like Fe or Co in the synthesis procedure. The ORR mass activity of these CNx catalysts is about 50–100 times lower, at 0.8 V vs. RHE in the kinetic region of the ORR current-potential curve, than that of catalysts produced in the presence of a strategic metal like Fe or Co. When at least one of these metals is present during the synthesis, it appears highly probable that the supplementary activity imparted to these catalysts may well be explained by the presence of some Fe–Nx (or Co–Nx) active sites, given that even very small contents of Fe (or Co), i.e., well below 0.1 wt% (1,000 ppm), in the catalysts precursor may significantly increase the catalytic activity. Such small strategic metal contents are often considered negligible by many researcher groups who use several wt% Fe (and/or Co) in their synthesis but deny any active role of the metal in the ORR properties of these catalysts.

Finally, it is relatively easy to understand how iron ions may be involved in every step of the oxygen reduction reaction in acidic medium because its $3dz^2$ orbital is able to accept one electron of the oxygen diradical molecule. On the other hand, it is not so easy to understand, without performing quantum calculations, how O_2 interacts with N-doped carbon. According to the sequence of reactions published in the literature about the activity of CNx catalytic sites, it appears that doping carbon with nitrogen atoms by substitution for carbon in a graphene layer modifies the electronic charge and the spin of each neighboring carbon atom, enabling some of these carbon atoms to interact with O_2. However, it is still not completely clear what type of nitrogen atom substitution, i.e., pyridinic or graphitic type, in graphene layers results in the best CNx-based catalysts for ORR.

Acknowledgments I am very grateful to NSERC, General Motors of Canada, and MDEIE (Gouvernement du Québec) for providing research funds in support of my work on non-noble metal catalysts for ORR in PEM fuel cells at INRS for more than 20 years. I would like to thank the numerous students, postdoctoral fellows, and research associates that have worked in my group in this field. In particular, I wish to thank Eric Proietti and Regis Chenitz for their help in the editing and final presentation of this chapter as well as Ulrike Kramm and Frédéric Jaouen for providing comments.

References

1. Kerr RA (2011) Peak oil production may already be here. Science 331(6024):1510–1511
2. Chow J, Kopp RJ, Portney PR (2003) Energy resources and global development. Science 302 (5650):1528–1531
3. Cho A (2010) Energy's tricky tradeoffs. Science 329(5993):786–787
4. Olah G, Prakash GKS, Goeppert A (2011) Anthropogenic chemical carbon cycle for a sustainable future. J Am Chem Soc 133:12881–12898
5. http://www1.eere.energy.gov/hydrogenandfuelcells/mypp/pdfs/fuel_cells.pdf
6. Gasteiger H, Kocha SS, Sompalli B, Wagner FT (2005) Activity benchmarks and requirements for Pt, Pt-alloy, and non-Pt oxygen reduction catalysts for PEMFCs. Appl Catal B Environ 56:9–35
7. Ishihara A, Ohgi Y, Matsuzawa K, Mitsushima S, Ota KI (2010) Progress in non-precious metal oxide-based cathode for polymer electrolyte fuel cells. Electrochim Acta 55:8005–8012
8. Lefèvre M, Proietti E, Jaouen F, Dodelet JP (2009) Iron-based catalysts with improved oxygen reduction activity in polymer electrolyte fuel cells. Science 324(5923):71–74
9. Wu G, More KL, Johnston CM, Zelenay P (2011) High-performance electrocatalysts for oxygen reduction derived from polyaniline, iron and cobalt. Science 332(6027):443–447
10. Proietti E, Jaouen F, Lefèvre M, Larouche N, Tian J, Herranz J, Dodelet JP (2011) Iron-based cathode catalyst with enhanced power density in polymer electrolyte membrane fuel cells. Nat Commun 2:416
11. Jahnke H, Schönborn M, Zimmermann G (1976) Organic dyestuffs as catalysts for fuel cells. Top Curr Chem 61:133–181
12. Bagotzky VS, Tarasevich MR, Radyushkina KA, Levina OE, Andrusyova SI (1977) Electrocatalysis of the oxygen reduction process on metal chelates in acid electrolyte. J Power Sources 2:233–240
13. Bouwkamp-Wijnoltz AL, Visscher W, van Veen JAR, Boellaard E, Van der Kraan AM, Tang SC (2002) On active-site heterogeneity in pyrolyzed carbon supported iron porphyrin catalysts for the electrochemical reduction of oxygen: an in-situ Mössbauer study. J Phys Chem B 106:12993–13001
14. van Veen JAR, Colijn HA, Van Baar JF (1988) On the effect of heat-treatment on the structure of carbon-supported metalloporphyrins and phthalocyanines. Electrochim Acta 33:801–804
15. Yeager E (1984) Electrocatalysis for O_2 reduction. Electrochim Acta 1984(29):1527–1537
16. Scherson DA, Tanaka A, Gupta SL, Tryk D, Fierro C, Holze R, Yeager EB (1986) Transition metal macrocycles supported on high area carbon: pyrolysis-mass spectrometry studies. Electrochim Acta 31:1247–1258
17. Tanaka A, Gupta SL, Tryk D, Fierro C, Yeager EB, Scherson, DA (1992) Electrochemical and spectroscopic aspects of heat-treated transition metal macrocycles as electrocatalysts for oxygen reduction. In: Scherson D, Tryk D, Daroux M, Xing X (eds) Proceedings of the symposium "on structural effects in electrocatalysis and oxygen electrochemistry", The Electrochemical Society, Pennington, NJ, pp 555–572
18. Wiesener K (1986) N_4-chelates as electrocatalysts for cathodic oxygen reduction. Electrochim Acta 31:1073–1078

19. Franke R, Ohms D, Wiesener KJ (1989) Investigation of the influence of thermal treatment on the properties of carbon materials modified by N_4-chelates for the reduction of oxygen in acidic media. J Electroanal Chem 260:63–73
20. Gupta S, Tryk D, Bae I, Aldred W, Yeager E (1989) Heat-treated polyacrylonitrile-based catalysts for oxygen electroreduction. J Appl Electrochem 19:19–27
21. Dodelet JP (2006) Oxygen reduction in PEM fuel cell conditions: heat-treated non-precious metal-N_4 macrocycles and beyond. In: Zagal JH, Bedioui F, Dodelet JP (eds) N_4-macrocyclic metal complexes. Springer, New York, pp 83–147, Chapter 3
22. Bouwkamp-Wijnoltz AL, Visscher W, vanVeen JAR, Tang SC (1999) Electrochemical reduction of oxygen: an alternative method to prepare active CON_4 catalysts. Electrochim Acta 45:379–386
23. Gouerec P, Biloul A, Contamin O, Scarbeck G, Savy M, Riga J, Weng LT, Bertrand P (1997) Oxygen reduction in acid media catalyzed by heat-treated cobalt tetraazaannulene supported on an active charcoal: correlation between the performance after longevity tests and the active site configuration as seen by XPS and ToF-SIMS. J Electroanal Chem 422:61–75
24. Lefèvre M, Dodelet JP, Bertrand P (2000) O_2 reduction in PEM fuel cells: activity and active site structural information for catalysts obtained by the pyrolysis at high temperature of Fe precursors. J Phys Chem B 104:11238–11247
25. Murakami M, Iijima S, Yoshimura S (1986) Morphology and structure of a one dimensional graphite polymer, poly-per-naphthalene. J Appl Phys 60:3856–3863
26. He P, Lefèvre M, Faubert G, Dodelet JP (1999) Oxygen reduction catalysts for polymer electrolyte fuel cells from the pyrolysis of various transition metal acetates adsorbed on 3,4,9,10-perylenetetracarboxylic dianhydride. J New Mater Electrochem Syst 2:243–251
27. Faubert G, Côté R, Dodelet JP, Lefèvre M, Bertrand P (1999) Oxygen reduction catalysts for polymer electrolyte fuel cells from the pyrolysis of Fe^{II} acetate adsorbed on 3,4,9,10-perylenetetracarboxylic dianhydride. Electrochim Acta 44:2589–2603
28. Casanovas J, Manelicart J, Rubio J, Illas F, Jiménez Mateos JM (1996) Origin of the large N1s binding energy in X-ray photoelectron spectra of calcined carbonaceous materials. J Am Chem Soc 118:8071–8076
29. Jiménez-Mateos J, Fierro JLG (1996) X-ray photoelectron spectroscopic study of petroleum fuel cokes. Surf Interface Anal 24:223–236
30. Lefèvre M, Dodelet JP, Bertrand P (2002) Molecular oxygen reduction in PEM fuel cells: evidence for the simultaneous presence of two active sites in Fe-based catalysts. J Phys Chem B 106:8705–8713
31. Herranz J, Lefèvre M, Larouche N, Stansfield B, Dodelet JP (2007) Step-by-step synthesis of non-noble electrocatalysts for O_2 reduction under proton exchange membrane fuel cell conditions. J Phys Chem C 111:19033–19042
32. Bron M, Radnik J, Fieber-Herdmann M, Bogdanoff P, Fiechter SJ (2002) EXAFS, XPS and electrochemical studies on oxygen reduction catalysts obtained by heat-treatment of iron phenanthroline complexes supported on high surface area carbon black. J Electroanal Chem 535:113–119
33. Jaouen F, Marcotte S, Dodelet JP, Lindberg G (2003) Oxygen reduction catalysts for polymer electrolyte fuel cells from the pyrolysis of iron acetate adsorbed on various carbon supports. J Phys Chem B 107:1376–1386
34. Kinoshita K (1988) Carbon, electrochemical and physicochemical properties. Wiley, New York, pp 3–12
35. Hess WH, Herd CR (1993) Microstructure, morphology and general physical properties. In: Donnet JB, Bansal RC, Wang MJ (eds) Carbon black, 2nd edn. Dekker, New York, pp 89–173, Chapter 3
36. Johnson GE, Decker WA, Forney AJ, Field JH (1968) Hydrogen cyanide produced from coal and ammonia. Ind Eng Chem Process Des Dev 7:137–143
37. Sherwood TK, Gilligand ER, Ing SW (1960) Hydrogen cyanide: synthesis from its elements and from ammonia and carbon. Ind Eng Chem 52:601–604

38. Griffiths DM, Standing HA (1966) Thermodynamic aspects of the reactions of carbon and coal at high temperatures. In: Given PH (ed) Coal science. American Chemical Society, Washington, DC, pp 666–676, Chapter 42
39. Jaouen F, Dodelet JP (2007) Non-noble electrocatalysts for O_2 reduction: how does heat-treatment affect their activity and structure? Part I. Model for carbon black gasification by NH_3: parametric calibration and electrochemical validation. J Phys Chem C 111:5963–5970
40. Jaouen F, Serventi AM, Lefèvre M, Dodelet JP, Bertrand P (2007) Non-noble electrocatalysts for O_2 reduction: how does heat-treatment affect their activity and structure? Part II. Structural changes observed by electron microscopy, Raman, and mass spectroscopy. J Phys Chem C 111:5971–5976
41. Charreteur F, Jaouen F, Ruggeri S, Dodelet JP (2008) Fe/N/C non-precious catalysts for PEM fuel cells: influence of the structural parameters of pristine commercial carbon blacks on their activity for oxygen reduction. Electrochim Acta 53:2925–2938
42. Sadezky A, Muckenhuber H, Grothe H, Niessner R, Pöschl U (2005) Raman microscopy of soot and related carbonaceous materials: spectral analysis and structural information. Carbon 43:1731–1742
43. Katagiri G, Ishida H, Ishitani H (1988) Raman spectra of graphite edge planes. Carbon 26:565–571
44. Jaouen F, Lefèvre M, Dodelet JP, Cai M (2006) Heat-treated Fe/N/C catalysts for O_2 electroreduction: are active sites hosted in micropores? J Phys Chem B 110:5553–5558
45. Ravikovitch PI, Vishnyakov A, Russo R, Neimark AV (2000) Unified approach to pore size characterization of microporous carbonaceous materials from N_2, Ar, and CO_2 adsorption isotherms. Langmuir 16:2311–2320
46. Jaouen F, Herranz J, Lefèvre M, Dodelet JP, Kramm UI, Herrman I, Bogdanoff P, Maruyama J, Nagaoka T, Garsuch A, Dahn J, Olson T, Pylypenko S, Atanassov P, Ustinov EA (2009) Cross-laboratory experimental study of non-noble metal electrocatalysts for the oxygen reduction reaction. Appl Mater Interfaces 1:1623–1639
47. Yuasa M, Yamaguchi A, Itsuki H, Tanaka K, Yamamoto M, Oyaizu K (2005) Modifying carbon particles with polypyrrole for adsorption of cobalt ions as electrocatalytic site for oxygen reduction. Chem Mater 17:4278–4281
48. Maruyama J, Abe I (2007) Fuel cell cathode catalyst with Heme-like structure formed from nitrogen of glycine and iron. J Electrochem Soc 154:B297–B304
49. Bron M, Fiechter S, Bogdanoff P, Tributsch H (2002) Thermogravimetry/spectrometry investigations on the formation of oxygen reduction catalysts for PEM fuel cells on the basis of heat-treated iron phenanthroline complexes. Fuel Cells 2:127–142
50. Schulenburg H, Stankov S, Schünemann V, Radnik J, Dorbrandt I, Fiechter S, Bogdanoff P, Tributsch HJ (2003) Catalysts for the oxygen reduction from heat-treated iron (III) tetramethoxyphenylporphyrin chloride: structure and stability of active sites. J Phys Chem B 107:9034–9041
51. Maldonado S, Stevenson KJ (2004) Direct preparation of carbon nanofiber electrodes via pyrolysis of iron(II) phthalocyanine: electrocatalytic aspects of oxygen reduction. J Phys Chem B 108:11375–11383
52. Maldonado S, Stevenson KJ (2005) Influence of nitrogen doping on oxygen reduction electrocatalysis at carbon nanofiber electrodes. J Phys Chem B 109:4707–4716
53. Maldonado S, Morin S, Stevenson KJ (2006) Structure, composition, and chemical reactivity of carbon nanotubes by selective nitrogen doping. Carbon 44:1429–1437
54. Lyon JL, Stevenson KJ (2007) Anomalous electrochemical dissolution and passivation of iron growth catalysts in carbon nanotubes. Langmuir 23:11311–11318
55. Wiggins-Camacho JD, Stevenson KJ (2009) Effect of nitrogen concentration on capacitance, density of states, electronic, conductivity, and morphology of N-doped carbon nanotube electrodes. J Phys Chem C 113:19082–19090
56. Wiggins-Camacho JD, Stevenson KJ (2011) Indirect electrocatalytic degradation of cyanide at nitrogen-doped carbon nanotube electrodes. Environ Sci Technol 45:3650–3656

57. Ramaswamy N, Mukerjee S (2011) Influence of inner-and outer-sphere electron transfer mechanisms during electrocatalysis of oxygen reduction in alkaline media. J Phys Chem C 115:18015–18026
58. Gara M, Compton RG (2011) Activity of carbon electrodes towards oxygen reduction in acid: a comparative study. New J Chem 35:2647–2652
59. Marcotte S, Villers S, Guillet N, Roué L, Dodelet JP (2004) Electroreduction of oxygen on Co-based catalysts: determination of the parameters affecting the two-electron transfer reaction in an acid medium. Electrochim Acta 50:179–188
60. Meng H, Jaouen F, Proietti E, Lefèvre M, Dodelet JP (2009) pH effect on oxygen reduction activity of Fe-based electrocatalysts. Electrochem Commun 11:1986–1989
61. Herranz J, Jaouen F, Dodelet JP (2009) Electrochemical evidence of two types of active sites for oxygen reduction in Fe-based catalysts. ECS Trans 25:117–128
62. Matter PH, Zhang L, Ozkan U (2006) The role of nanostructure in nitrogen-containing carbon catalysts for the oxygen reduction reaction. J Catal 239:83–96
63. Matter PH, Ozkan U (2006) Non-metal catalysts for dioxygen reduction in an acid electrolyte. Catal Lett 109:115–123
64. Matter PH, Wang E, Arias M, Biddinger EJ, Ozkan U (2006) Oxygen reduction reaction catalysts prepared from acetonitrile pyrolysis over alumina-supported metal particles. J Phys Chem B 110:18374–18384
65. Matter PH, Wang E, Ozkan U (2006) Preparation of nanostructured nitrogen-containing carbon catalysts for the oxygen reduction reaction from SiO_2- and MgO-supported metal particles. J Catal 243:395–403
66. Matter PH, Wang E, Arias M, Biddinger EJ, Ozkan U (2007) Oxygen reduction reaction activity and surface properties of nanostructures nitrogen-containing carbon. J Mol Catal A Chem 264:73–81
67. Matter PH, Wang E, Millet JMM, Ozkan U (2007) Characterization of the iron phase in CNx-based oxygen reduction reaction catalysts. J Phys Chem C 111:1444–1450
68. Biddinger E, Ozkan U (2007) Methanol tolerance of CNx oxygen reduction catalysts. Top Catal 46:339–348
69. Biddinger E, von Deak D, Ozkan US (2009) Nitrogen-containing carbon nanostructures as oxygen reduction catalysts. Top Catal 52:1566–1574
70. Biddinger EJ, Knapke DS, von Deak D, Ozkan US (2010) Effect of sulfur as a growth promoter for CNx nanostructures as PEM and DMFC ORR catalysts. Appl Catal B Environ 96:72–82
71. Woods MP, Biddinger EJ, Matter PH, Mirkelamoglu B, Ozkan US (2010) Correlation between oxygen reduction reaction and oxidative dehydrogenation activities over nanostructures carbon catalysts. Catal Lett 136:1–8
72. von Deak D, Biddinger EJ, Luthman KA, Ozkan US (2010) The effect of phosphorus in nitrogen-containing carbon nanostructures on oxygen reduction in PEM fuel cells. Carbon 48:3635–3658
73. Biddinger EJ, Ozkan US (2010) Role of graphitic edge plane exposure in carbon nanostructures for oxygen reduction reaction. J Phys Chem C 114:15306–15314
74. Bao X, von Deak D, Biddinger EJ, Ozkan US, Haddad CM (2010) A computational exploration of the oxygen reduction reaction over a carbon catalyst containing a phosphinate functional group. Chem Commun 46:8621–8623
75. von Deak D, Biddinger EJ, Ozkan U (2011) Carbon corrosion characteristics of CNx nanostructures in acidic media and implications for ORR performance. J Appl Electrochem 41:757–763
76. Biddinger EJ, von Deak D, Singh D, Marsh H, Tan B, Knapke DS, Ozkan US (2011) Examination of catalyst loading effect on the selectivity of CNx and Pt/VC ORR catalysts using RRDE. J Electrochem Soc 158:B402–B409

77. von Deak D, Singh D, Biddinger EJ, King JC, Bayram B, Miller JT, Ozkan US (2012) Investigation of sulfur poisoning of CNx oxygen reduction catalysts for PEM fuel cells. J Catal 285:145–151
78. Birry L, Zagal JH, Dodelet JP (2010) Does CO poison Fe-based catalysts for ORR? Electrochem Commun 12:628–631
79. Nallathambi V, Wu G, Subramanian NP, Kumaraguru SP, Lee JW, Popov BN (2007) Highly active carbon composite electrocatalysts for PEM fuel cells. ECS Trans 11:241–247
80. Li X, Liu L, Lee JW, Popov BN (2008) Development of tellurium-modified carbon catalysts for oxygen reduction reaction in PEM fuel cells. J Power Sources 182:18–23
81. Nallathambi V, Li X, Lee JW, Popov BN (2008) Development of nitrogen-modified carbon-based catalysts for oxygen reduction in PEM fuel cells. ECS Trans 16:405–417
82. Subramanian NP, Li X, Nallathambi V, Kumaraguru SP, Mercado HC, Wu G, Lee JW, Popov BN (2009) Nitrogen-modified carbon-based catalysts for oxygen reduction reaction in polymer electrolyte membrane fuel cells. J Power Sources 188:38–44
83. Nallathambi V, Lee JW, Kumaraguru SP, Wu G, Popov BN (2008) Development of high performance carbon composite catalysts for oxygen reduction in PEM proton exchange membrane fuel cells. J Power Sources 183:34–42
84. Liu G, Li X, Popov BN (2009) Stability study of nitrogen-modified carbon composite catalysts for oxygen reduction reaction in polymer electrolyte membrane fuel cells. ECS Trans 25:1251–1259
85. Liu G, Li X, Ganesan P, Popov BN (2009) Development of non-precious metal oxygen-reduction catalysts for PEM fuel cells based on N-doped ordered porous carbon. Appl Catal B Environ 93:156–165
86. Jaouen F, Dodelet JP (2007) Average turn-over frequency of O_2 electro-reduction for Fe/N/C and Co/N/C catalysts in PEFCs. Electrochim Acta 52:5975–5984
87. Liu G, Li X, Ganesan P, Popov BN (2010) Studies of oxygen reduction reaction active sites and stability of nitrogen-modified carbon composite catalysts for PEM fuel cells. Electrochim Acta 55:2853–2858
88. Liu G, Li X, Lee JW, Popov BN (2011) A review of the development of nitrogen-modified carbon catalysts for oxygen reduction at USC. Catal Sci Technol 1:207–217
89. Li G, Liu G, Popov BN (2010) Activity and stability of non-precious metal catalysts for oxygen reduction in acid and alkaline electrolytes. J Power Sources 195:6373–6378
90. Ozaki JI, Tanifuji SI, Kimura N, Furuichi A, Oya A (2006) Enhancement of oxygen reduction activity by carbonization of furan resin in the presence of phthalocyanines. Carbon 44:1298–1352
91. Ozaki JI, Kimura N, Tomonori A, Oya A (2007) Preparation and oxygen reduction activity of BN-doped carbons. Carbon 45:1847–1853
92. Niwa H, Horiba K, Harada Y, Oshima M, Ikeda T, Terakura K, Ozaki JI, Miyata S (2009) X-ray absorption analysis of nitrogen contribution to oxygen reduction reaction in carbon alloy cathode catalysts for polymer electrolyte fuel cells. J Power Sources 187:93–97
93. Chokai M, Taniguchi M, Moriya S, Matsubayashi K, Shinoda T, Nabae Y, Kuroki S, Hayakawa T, Kakimoto MA, Ozaki JI, Miyata S (2010) Preparation of carbon alloy catalysts for polymer electrolyte fuel cell from nitrogen-containing rigid-rod polymers. J Power Sources 195:5947–5951
94. Kobayashi R, Ozaki JI (2009) Novel N-doped carbon cathode catalyst for polymer electrolyte membrane fuel cells formed on carbon black. Chem Lett 38:396–397
95. Ozaki JI, Tanifuji SI, Furuichi A, Yabutsuka K (2010) Enhancement of oxygen reduction activity of nanoshell carbons by introducing nitrogen atoms from metal phthalocyanines. Electrochim Acta 55:1864–1871
96. Niwa H, Kobayashi M, Horiba K, Harada Y, Oshima M, Terakura K, Ikeda T, Koshigoe Y, Ozaki JI, Miyata S, Ueda S, Yamashita Y, Yoshikawa H, Kobayashi K (2011) X-ray photoemission spectroscopy analysis of N-containing carbon-based cathode catalysts for polymer electrolyte fuel cells. J Power Sources 196:1006–1011

97. Kobayashi M, Niwa H, Harada Y, Horiba K, Oshima M, Ofuchi H, Terakura K, Ikeda T, Koshigoe Y, Ozaki JI, Miyata S, Ueda S, Yamashita Y, Yosikawa H, Kobayashi K (2011) Role of residual transition metal atoms in oxygen reduction reaction in cobalt phthalocyanine-based carbon cathode catalysts for polymer electrolyte fuel cell. J Power Sources 196:8346–8351
98. Wang X, Hou Z, Ikeda T, Huang SF, Terakura K, Boero M, Oshima M, Kakimoto MA, Miyata S (2011) Selective nitrogen doping in graphene: enhanced catalytic activity for the oxygen reduction reaction. Phys Rev B 84:245434-1–245434-7
99. Nabae Y, Moriya S, Matsubayashi K, Lyth SM, Malon M, Wu L, Islam NM, Koshigoe Y, Kuroki S, Kakimoto MA, Miyata S, Ozaki JI (2010) The role of Fe species in the pyrolysis of Fe phthalocyanine and phenolic resin for preparation of carbon-based cathode catalysts. Carbon 48:2613–2624
100. Wu L, Nabae Y, Moriya S, Matsubayashi K, Islam NM, Kuroki S, Kakimoto MA, Ozaki JI, Miyata S (2010) Pt-free cathode catalysts prepared via multi-step pyrolysis of Fe phthalocyanine and phenolic resin for fuel cells. Chem Commun 46:6377–6379
101. Lyth SM, Nabae Y, Moriya S, Kuroki S, Kakimoto MA, Ozaki JI, Miyata S (2009) Carbon nitride as a nonprecious catalyst for electrochemical oxygen reduction. J Phys Chem C 113:20148–20151
102. Lyth SM, Nabae Y, Islam NM, Kuroki S, Kakimoto M, Miyata S (2011) Electrochemical oxygen reduction activity of carbon nitride supported on carbon black. J Electrochem Soc 158:B194–B201
103. Iwazaki T, Obinata R, Sugimoto W, Takasu Y (2009) High oxygen reduction activity of silk derived activated carbon. Electrochem Commun 11:376–378
104. Iwasaki T, Yang H, Obinata R, Sugimoto W, Takasu Y (2010) Oxygen-reduction activity of silk-derived carbons. J Power Sources 195:5840–5847
105. Rao CV, Cabrera CR, Ishikawa Y (2010) In search of the active site in nitrogen-doped carbon nanotube electrodes for the oxygen reduction reaction. J Phys Chem Lett 1:2622–2627
106. Yu D, Zhang Q, Dai L (2010) Highly efficient metal-free growth of nitrogen-doped single-walled carbon nanotubes on plasma-etched substrates for oxygen reduction. J Am Chem Soc 132:15127–15129
107. Shrestha S, Mustain WE (2010) Properties of nitrogen-functionalized ordered mesoporous carbon prepared using polypyrrole precursor. J Electrochem Soc 157:B1665–B1672
108. Wang X, Lee JS, Zhu Q, Liu J, Wang Y, Dai S (2010) Ammonia-treated ordered mesoporous carbons as catalytic materials for oxygen reduction reaction. Chem Mater 22:2178–2180
109. Kundu S, Nagaiah TC, Xia W, Wang Y, Van Dommele S, Bitter JH, Santa M, Grundmeier G, Bron M, Schuhmann W, Muhler M (2009) Electrocatalytic activity and stability of nitrogen-containing nanotubes in the oxygen reduction reaction. J Phys Chem C 113:14302–14310
110. Xiong W, Du F, Liu Y, Perez A, Supp M, Ramakrishnan S, Dai L, Jiang L (2010) 3-D carbon nanotube structures used as high performance catalyst for oxygen reduction reaction. J Am Chem Soc 132:15839–15841
111. Choi CH, Lee SY, Park SH, Woo SI (2011) Highly active N-doped-CNT grafted on Fe/C prepared by pyrolysis of dicyandiamide on Fe_2O_3/C for electrochemical oxygen reduction reaction. Appl Catal B Environ 103:362–368
112. Geng D, Liu H, Chen Y, Li R, Sun X, Ye S, Knights S (2011) Non-noble metal oxygen reduction electrocatalysts based on carbon nanotubes with controlled nitrogen contents. J Power Sources 196:1795–1801
113. Oh HS, Oh JG, Lee WH, Kim HJ, Kim H (2011) The influence of the structural properties of carbon on the oxygen reduction reaction of nitrogen modified carbon based catalysts. Int J Hydrogen Energy 36:8181–8186
114. Oh HS, Oh JG, Roh B, Hwang I, Kim H (2011) Development of highly active and stable non-precious oxygen reduction catalysts for PEM fuel cells using polypyrrole and chelating agent. Electrochem Commun 13:879–881

115. Jin H, Zhang H, Zhong H, Zhang J (2011) Nitrogen-doped carbon xerogel: a novel carbon-based electrocatalyst for oxygen reduction reaction in proton exchange membrane (PEM) fuel cells. Energy Environ Sci 4:3389–3394
116. Jaouen F, Dodelet JP (2009) O_2 reduction mechanism on non-noble metal catalysts for PEM fuel cells. Part I: Experimental rates for O_2 electroreduction, H_2O_2 electroreduction, and H_2O_2 disproportionation. J Phys Chem C 113:15422–15432
117. Kramm U, Herranz J, Larouche N, Arruda TM, Lefèvre M, Jaouen F, Bogdanoff P, Fiechter S, Abs-Wurmbach I, Mukerjee S, Dodelet JP (2012) Structure of the catalytic sites in Fe/N/C-catalysts for O_2-reduction in PEM fuel cells. Phys Chem Chem Phys 14:11673–11688
118. Walker FA, Simonis U (2006) Iron porphyrin chemistry. In: Scott RA (ed) Encyclopedia of inorganic chemistry. Wiley Online Library. doi: 10.1002/0470862106.ia111
119. Zagal JH, Paez MA, Silva JF (2006) Fundamental aspects on the catalytic activity of metallomacrocyclics for the electrochemical reduction of O_2. In: Zagal JH, Bedioui F, Dodelet JP (eds) N_4-macrocyclic metal complexes. Springer, New York, pp 41–82, Chapter 2
120. Koslowski UI, Abs-Wurmbach I, Fiechter S, Bogdanoff P (2008) Nature of the catalytic centers of porphyrin-based electrocatalysts for ORR: a correlation of kinetic current density with the site density of Fe-N_4 centers. J Phys Chem C 112:15356–15366
121. Kramm UI, Abs-Wurmbach I, Herrmann-Geppert I, Radnik J, Fiechter S, Bogdanoff P (2011) Influence of the electron-density of FeN4-centers towards the catalytic activity of pyrolyzed FeTMPPCl-based ORR-electrocatalysts. J Electrochem Soc 158:B69–B78
122. Melendres CA (1980) Mössbauer and Raman spectra of carbon-supported iron phthalocyanine. J Phys Chem 84:1936–1939
123. Kuzmann E, Nath A, Chechersky V, Li S, Wei Y, Chen X, Li J, Homonnay Z, Gal M, Garg VK, Klencsar Z, Vertes A (2002) Mössbauer study of oxygenated iron-phthalocyanines, a precursor of magnetic storage material. Hyperfine Interact 139/140:631–639
124. Schulz CE, Hu C, Scheidt WR (2006) On spin Hamiltonian fits for Mössbauer spectra of high-spin Fe(II) porphyrinate systems. Hyperfine Interact 170:55–60
125. Sams JR, Tsin TB (1979) Mössbauer spectroscopy of iron porphyrins. In: Dolphin D (ed) The porphyrins. Volume IV. Physical chemistry, part B. Academic, New York, pp 425–478, Chapter 9
126. Collman JP, Gagne R, Reed CA, Halbert TR, Lang G, Robinson WT (1975) “Picket fence porphyrins” synthetic model for oxygen binding hemoproteins. J Am Chem Soc 97:1427–1439
127. Collman JP, Hoard JL, Kim N, Lang G, Reed CA (1975) Synthesis, stereochemistry, and structure-related properties of α, β, γ, δ-tetraphenylporphinatoiron (II). J Am Chem Soc 97:2676–2681
128. Herranz J, Jaouen F, Lefèvre M, Kramm UI, Proietti E, Dodelet JP, Bogdanoff P, Fiechter S, Abs-Wurmbach I, Bertrand P, Arruda TM, Mukerjee S (2011) Unveiling N-protonation and anion-binding effects on Fe/N/C catalysts for O_2 reduction in proton exchange-membrane fuel cells. J Phys Chem C 115:16087–16097
129. Li Y, Zhou W, Wang H, Xie L, Liang Y, Wei F, Idrobo JC, Pennycook J, Dai H (2012) An oxygen reduction electrocatalyst based on carbon nanotube-graphene complexes. Nat Nanotechnol 7:394–400
130. Thorum M, Hankett JM, Gewirth AA (2011) Poisoning the oxygen reduction reaction on carbon-supported Fe and Cu electrocatalysts: evidence for metal-centered activity. J Phys Chem Lett 2:295–298
131. Gupta S, Fierro C, Yeager E (1991) The effect of cyanide on the electrochemical properties of transition metal macrocycles for oxygen reduction in alkaline solutions. J Electroanal Chem 306:239–250
132. Burgess J, Twigg MV (2006) Iron: inorganic & coordination chemistry. In: King RB (ed) Encyclopedia of inorganic chemistry. Wiley, New York

133. Li W, Yu A, Higgins DC, Llanos BG, Chen Z (2010) Biologically inspired highly durable iron phthalocyanine catalysts for oxygen reduction reaction in polymer electrolyte membrane fuel cells. J Am Chem Soc 132:17056–17058
134. Waldron K, Rutherford JC, Ford D, Robinson NJ (2009) Metalloproteins and metal sensing. Nature 460:823–830
135. Boulatov R (2006) Billion-year old oxygen cathode that actually works: respiratory oxygen reduction and its biomimetic analogs. In: Zagal JH, Bedioui F, Dodelet JP (eds) N_4-macrocyclic metal complexes. Springer, New York, pp 41–82, Chapter 1
136. Anderson AB, Sidik RA (2004) Oxygen reduction on Fe^{II} and Fe^{III} coordinated to N_4 chelates. Reversible potentials for the intermediate steps from quantum theory. J Phys Chem B 108:5031–5035
137. Bouwkamp-Wijnoltz AL, Visscher W, Van Veen JAR (1998) The selectivity of oxygen reduction by pyrolyzed iron porphyrin supported on carbon. Electrochim Acta 43:3141–3152
138. Chlistunoff J (2011) RRDE and voltammetric study of ORR on pyrolyzed Fe/polyaniline catalysts. On the origin of variable Tafel slopes. J Phys Chem C 115:6496–6507
139. Van Veen JAR, Van Baar JF, Kroese CJ, Coolegem JGF, De Wit N, Colijn HA (1981) Oxygen reduction on transition metal porphyrins in acid electrolyte: I. Activity. Ber Bunsenges Phys Chem 85:693–700
140. Sidik RA, Anderson AB, Subramanian NP, Kumaraguru SP, Popov BN (2006) O_2 reduction on graphite and nitrogen-doped graphite: experiment and theory. J Phys Chem B 110:1787–1793
141. Vayner E, Anderson AB (2007) Theoretical predictions concerning oxygen reduction in nitride graphite edges and a cobalt center bonded to them. J Phys Chem C 111:9330–9336
142. Kurak KA, Anderson AB (2009) Nitrogen-treated graphite and oxygen reduction on pyridinic edge sites. J Phys Chem C 113:6730–6734
143. Huang SF, Terakura K, Ozaki T, Ikeda T, Boero M, Oshima M, Ozaki JI, Miyata S (2009) First-principles calculations of the electronic properties of graphene clusters doped with nitrogen and boron: analysis of catalytic activity for the oxygen reduction reaction. Phys Rev B 80:235410-1–235410-4
144. Ikeda T, Boero M, Huang SF, Terakura K, Oshima M, Ozaki JI (2008) Carbon alloy catalysts: active sites for oxygen reduction reaction. J Phys Chem C 112:14706–14709
145. Zhang L, Xia Z (2011) Mechanism of oxygen reduction reaction on nitrogen-doped graphene for fuel cells. J Phys Chem C 115:11170–11176
146. Wang Y, Balbuena PB (2005) Ab initio molecular dynamics simulations of the oxygen reduction reaction on a Pt(111) surface in the presence of hydrated hydronium $(H_3O)^+(H_2O)_2$: direct or series pathway? J Phys Chem B 109:14896–14907
147. Kim H, Lee K, Woo SI, Jung Y (2011) On the mechanism of enhanced oxygen reduction reaction in nitrogen-doped graphene nanoribbons. Phys Chem Chem Phys 13:17505–17510

Chapter 11
Theoretical Study of Oxygen Reduction Reaction Catalysts: From Pt to Non-precious Metal Catalysts

Xin Chen, Dingguo Xia, Zheng Shi, and Jiujun Zhang

Abstract Fuel cells are regarded as one of the most promising candidates for stationary and mobile power generation due to their high energy yield and low environmental impact of hydrogen oxidation. The oxygen reduction reaction (ORR) at cathode is a very complex process and plays a crucial role during operation of the PEM fuel cells. However, its mechanism and the nature of intermediates involved remain vague. This chapter focuses on the recent theoretical modeling studies of ORR catalysts for PEMFC. Recent theoretical investigations on oxygen reduction electrocatalysts, such as Pt-based catalysts, non-Pt metal catalysts (Pd, Ir, CuCl), and non-precious metal catalysts (transitional metal macrocyclic complexes, conductive polymer materials, and carbon-based materials), are reviewed. The oxygen reduction mechanisms catalyzed by these catalysts are discussed based on the results.

X. Chen
College of Environmental and Energy Engineering, Beijing University of Technology,
Xidawang Road, Chaoyang District, Beijing 100124, P. R. China

D. Xia (✉)
College of Engineering, Peking University, No.5 Yiheyuan Road, Haidian District,
Beijing 100871, P. R. China
e-mail: dgxia@pku.edu.cn

Z. Shi
NRC-Institute for Fuel Cell Innovation, 4250 Wesbrook Mall, Vancouver,
British Columbia, Canada

J. Zhang (✉)
NRC Energy, Mining & Environment Portfolio, National Research Council Canada,
4250 Wesbrook Mall, Vancouver, BC, CanadaV6T 1W5
e-mail: jiujun.zhang@nrc.gc.ca

M. Shao (ed.), *Electrocatalysis in Fuel Cells*, Lecture Notes in Energy 9,
DOI 10.1007/978-1-4471-4911-8_11, © Springer-Verlag London 2013

11.1 Introduction

Fuel cells are electrochemical devices that directly convert the chemical energy of a fuel into electrical energy by electrochemical reactions. Since their invention in the middle of the nineteenth century, fuel cells have been identified as the most promising energy conversion technology and have been successfully used in many specific areas, including space exploration. Fuel cells offer many advantages such as high efficiency and reliability, minimum impact to environment, unique operating characteristics, and so on.

There exist a variety of fuel cells. For practical reasons, fuel cells are classified by the type of electrolyte employed. The following names and abbreviations are frequently used in publications: alkaline fuel cells (AFC), molten carbonate fuel cells (MCFC), phosphoric acid fuel cells (PAFC), solid oxide fuel cells (SOFC), and proton exchange membrane fuel cells (PEMFC). Among different types of fuel cells under development today, the PEMFC, also called polymer electrolyte membrane fuel cells (PEFC), is considered as a potential future power source due to its unique characteristics [1–3]. The PEMFC consists of an anode where hydrogen oxidation takes place, a cathode where oxygen reduction occurs, and an electrolyte membrane that permits the transfer of protons from anode to cathode. PEMFC operates at low temperature that allows rapid start-up. Furthermore, with the absence of corrosive cell constituents, the use of the exotic materials required in other fuel cell types is not required [4].

Although PEMFC has many advantages compared with other kinds of fuel cells, there are several barriers challenging PEMFC's commercialization. These barriers are performance, cost, and durability. PEMFCs are sensitive to poisoning by trace levels of contaminants including CO, sulfur species, and ammonia. The high overpotential from oxygen reduction at cathode contributes significantly to performance losses [5]. Under PEMFC's operating environment, platinum can react with water and oxygen forming a surface oxide layer that inhibits the catalysis of the oxygen reduction reaction (ORR) especially at high potential [6, 7]. Thus development of more efficient ORR electrocatalysts and reducing their cost are the major focuses for advancing PEMFC technology.

ORR is a very complex process. It involves multi-electrons, various intermediates, and many possible pathways [8–10]. Different experimental characterization methods have been employed to study the ORR mechanism, such as ultraviolet photoemission spectroscopy (UPS) [11], X-ray photoemission spectroscopy (XPS) [12, 13], electron energy loss spectroscopy (EELS) [14], near-edge X-ray absorption spectroscopy (NEXAFS), and Auger spectroscopy (AES) [15, 16]. Despite all these studies, the nature of intermediates involved in the reduction steps remains vague. First-principle theoretical modeling is a good tool complementing state-of-the-art experimental techniques [17]. It provides important insights regarding electronic structure, geometries of reaction intermediates, and adsorption energies at metal/gas or metal/liquid interfaces. Theoretical modeling is becoming an indispensible tool in electrochemical study [18].

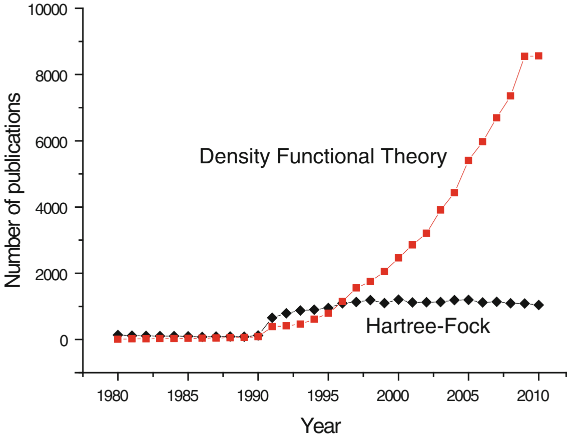

Fig. 11.1 Number of publications that employ DFT each year (from 1980 to September 23, 2011) based on search from Web of Science database (http://apps.webofknowledge.com) using "density," "functional," and "theory" as the keywords. This is compared with a similar search for keywords "Hartree" and "Fock," using Web of Science database

This chapter focuses on the theoretical modeling studies of ORR catalysts for PEMFC. Theoretical methods, such as density functional theory (DFT) and ab initio molecular dynamics (AIMD) simulation, are presented. Current understanding of ORR mechanism in acidic medium is briefly discussed. Recent theoretical investigations on oxygen reduction electrocatalysts, such as Pt-based catalysts, non-Pt metal catalysts (Pd, Ir, CuCl), and non-precious metal catalysts (transitional metal macrocyclic complexes, conductive polymer materials, and carbon-based materials), are reviewed. The oxygen reduction mechanisms catalyzed by these catalysts are discussed based on the results.

11.2 Computational Methods

11.2.1 Density Functional Theory Methods

DFT has become increasingly the method of choice for the solution of large systems, not only because of its sufficiently high accuracy but also of its computational simplicity. DFT reduces the calculation of system of many interacting particles to the solution of single-particle Hartree-type equations. Figure 11.1 shows the usage of DFT method from the year of 1980, as compared with the application of Hartree–Fock method.

In DFT, a many-electron (N) system is considered as a fictitious system of N noninteracting electrons which is described by a single determinant wave function with N "orbitals" φ_i. The electron density of this fictitious state can be obtained exactly by solving a set of one-electron Schrödinger equations (Kohn–Sham orbital) [19]. The Kohn–Sham self-consistent equation can be described as

$$\left[-\frac{1}{2}\nabla^2 + V_{\mathrm{eff}}(r)\right]\varphi_i = \varepsilon_i \varphi_i \tag{11.1}$$

The effective external potential, $V_{\mathrm{eff}}(r)$, is described as

$$V_{\mathrm{eff}}(r) = V(r) + \int \frac{\rho(r')}{|r - r'|}\mathrm{d}r' + V_{\mathrm{XC}}(r) \tag{11.2}$$

where $V(r)$ is the external potential, $\int \frac{\rho(r')}{|r-r'|}\mathrm{d}r'$ is Hartree potential, and $V_{\mathrm{XC}}(r)$ is the exchange–correlation potential. The ground-state energy is given by

$$E = \sum_i^N \varepsilon_i - \frac{1}{2}\int\int \frac{\rho(r)\rho(r')}{|r - r'|}\mathrm{d}r\mathrm{d}r' + E_{\mathrm{XC}}[\rho] - \int V_{\mathrm{XC}}(r)\rho(r)\mathrm{d}r \tag{11.3}$$

In spite of the appearance of simplicity, the Kohn–Sham equation is in principle "exact" provided that the exact exchange–correlation energy E_{XC} is used. In other words, the only error in Eq. (11.3) is due to the approximate nature of E_{XC}.

Since the exact exchange–correlation term is unknown, several different schemes have been developed to obtain approximation of the E_{XC}. There are several types of approximate functionals such as local density approximation (LDA) and generalized gradient approximation (GGA) [20]. The LDA is very successful for many systems of interest, especially those with uniform electronic density distributions such as those in bulk metals, but LDA fails in systems where weak molecular bonds exist [21]. To account for the inhomogeneity of the electron density, a nonlocal correlation is often added to the exchange energy; this is the so-called generalized gradient approximation (GGA). There are several exchange–correlation functionals such as P86 [22], PW91 [23, 24], BPW91 [25], LYP [26], BLYP [20, 26], B3LYP [25–27], and PBE [28]. In general, as the exchange–correlation functional contains both exchange and Coulomb correlation terms, the DFT methods provide better results than that of a single determinant Hartree–Fock (HF) methods which do not have Coulomb correlation term [5].

The selection of functional directly controls the accuracy of the DFT methods. A study of ORR by hybrid density functional (HDFT) method and MP2 method has been reported by Albu et al. [29, 30]. They evaluated a large number of HDFT methods toward calculation of potential-dependent activation energies for uncatalyzed and Pt-catalyzed oxygen reduction and hydroperoxyl oxidation reactions. In the HDFT methods, the one-parameter hybrid Fock–Kohn–Sham operator is written as

$$F = F^{\mathrm{H}} + \left(\frac{X}{100}\right)F^{\mathrm{HFE}} + \left[1 - \left(\frac{X}{100}\right)\right]\left(F^{\mathrm{SE}} + F^{\mathrm{GCE}}\right) + F^{\mathrm{C}} \tag{11.4}$$

where F^{H} is the Hartree operator (i.e., the non-exchange part of the Hartree–Fock operator), F^{HFE} is the Hartree–Fock (HF) exchange operator, X is the fraction of Hartree–Fock exchange, F^{SE} is the Dirac–Slater local density functional for exchange, F^{GCE} is the gradient correction for the exchange functional, and F^{C} is the total correlation functional including both local and gradient-corrected parts.

Table 11.1 lists results obtained from MP2/6-31G(d,p) and various HDFT methods for uncatalyzed ORR. Table 11.2 contains results obtained with MP2/6-31G(d,p) and a subset of HDFT methods for Pt-catalyzed ORRs. In the tables, HDFT methods are named by the gradient-correlated exchanged functional used, followed by 1 (indicating a one-parameter method), followed by the correlation functional used, and finally by the value of X separated by a dash. For example, mPW1B95-50 represents a one-parameter hybrid DFT method based on the modified Perdew–Wang (mPW) gradient-corrected exchange functional [31] and B95 gradient-corrected correlation functional [32], and with a Hartree–Fock exchange contribution of 50 % ($X = 50$).

The results indicate that the inclusion of diffuse functions for oxygen by using the 6-31+G(d,p) basis set is unnecessary and gives inferior results. The HDFT methods with low HF exchange contributions show typically larger errors in comparison with the results obtained with the MP2 method. These errors are a consequence of a systematic underestimation of the transition-state energy for oxygen reduction to hydroperoxyl and hence its reverse hydroperoxyl oxidation reaction. Among the 25 HDFT methods investigated, the best results were obtained using the HDFT method based on Becke's exchange functional, B95 correlation functional, and a Hartree–Fock exchange contribution of 50 % in conjunction with the 6-31G(d,p) basis set [B1B95-50/6-31G(d,p)]. Results with similar accuracy were obtained using the HDFT method based on Becke's exchange functional, PW91 correlation functional, and a Hartree–Fock exchange contribution of 50 % in conjunction with the 6-31G(d,p) basis set [B1PW91-50/6-31G(d,p)]. Both of these methods also give very accurate gas-phase bond energies for the oxygenated species. Based on the calculated results, these two methods are recommended for study of electrochemical ORR.

11.2.2 Ab Initio Molecular Dynamics Method

Recently, ab initio or the first-principle molecular dynamics (AIMD), which is based on Car and Parrinello's technique [33], has become a valuable method for study condensed matter structure and dynamics, in particular liquids, surfaces, and clusters. The basic idea underlying AIMD method is to compute the forces acting on the nuclei from electronic structure that are calculated "on the fly" as the molecular dynamics trajectory is generated [34]. In this way, the electronic variables are not integrated out beforehand, but are considered as active degrees of freedom. Thus, the Car and Parrinello (CP) algorithm overcomes limitations of standard empirical-potential approaches employed in classical molecular dynamics and

Table 11.1 Comparison of calculated reversible potential for $O_2 + 4H^+ + 4e^- \rightarrow 2H_2O$ reaction, electrochemical potentials (V) and activation energies (eV) for $O_2 + H_3O^+ + e^- \rightarrow OOH + H_2O$ reaction, and the average relative error to the MP2/6-31G(d,p) results [29]

Basis set/HDFT method	X^a	$U°$(V)	$(U)E_a^{red} = 0$	$\left(E_a^{oxi}\right)U_{red} = 0$	$(U)E_a^{oxi} = 0$	$\left(E_a^{red}\right)U_{oxi} = 0$	Error
MP2/6-31G(d,p)		1.12	−1.867	2.278	3.513	3.102	0.00
6-31G(d,p)							
B3PW91	20	1.12	−0.998	1.907	3.221	2.312	0.89
B3LYP	20	1.20	−0.837	1.816	3.301	2.322	0.97
BH&HLYP	50	1.24	−1.293	2.233	3.865	2.925	0.48
PBE1PBE	25	1.03	−1.084	1.910	3.213	2.387	0.82
mPW1PW91	25	1.10	−1.069	1.958	3.296	2.406	0.80
MPW1K	42.8	1.22	−1.240	2.193	3.708	2.755	0.52
mPW1PW91-60	60	1.32	−1.318	2.345	4.010	2.983	0.53
B1B95	28	1.06	−1.225	1.984	3.211	2.452	0.71
BB1K	42	1.17	−1.395	2.216	3.614	2.793	0.40
B1B95-50	50	1.22	−1.436	2.289	3.778	2.924	0.38
B1B95-60	60	1.28	−1.464	2.363	3.950	3.051	0.43
mPW1B95	31	1.08	−1.233	2.023	3.345	2.554	0.63
MPWB1K	44	1.16	−1.351	2.188	3.643	2.806	0.42
mPW1B95-50	50	1.20	−1.387	2.247	3.764	2.904	0.40
6-31G+(d,p)							
B3PW91	20	1.92	−0.448	1.913	3.787	2.323	1.15
B3LYP	20	2.08	−0.207	1.828	3.952	2.331	1.30
BH&HLYP	50	2.00	−0.695	2.178	4.361	2.878	1.03
PBE1PBE	25	1.83	−0.500	1.891	3.783	2.392	1.09
mPW1PW91	25	1.89	−0.506	1.948	3.852	2.410	1.09
MPW1K	42.8	1.91	−0.715	2.152	4.166	2.729	0.96
mPW1PW91-60	60	1.94	−0.833	2.283	4.377	2.927	0.96
B1B95	28	1.87	−0.650	1.981	3.791	2.461	0.98
BB1K	42	1.90	−0.845	2.178	4.111	2.778	0.85
mPW1B95	31	1.89	−0.637	2.002	3.920	2.555	0.97
MPWB1K	44	1.90	−0.782	2.144	4.147	2.786	0.90

[a] Hartree–Fock exchange contribution X

Table 11.2 Electrochemical potentials and activation energies (eV) for Pt–O_2 + H_3O^+ + e^- → Pt–OOH + H_2O reaction and the average relative error to the MP2/6-31G(d,p) results [29]

HDFT method	$(U)E_{\mathrm{a}}^{\mathrm{red}} = 0$	$\left(E_{\mathrm{a}}^{\mathrm{oxi}}\right)U_{\mathrm{red}} = 0$	$(U)E_{\mathrm{a}}^{\mathrm{oxi}} = 0$	$\left(E_{\mathrm{a}}^{\mathrm{red}}\right)U_{\mathrm{oxi}} = 0$	Error
MP2/6-31G(d,p)[a]	0.382	1.330	2.681	0.969	0.00
B3PW91/6-31G(d,p)	0.929	0.529	2.280	0.822	0.70
BH&HLYP/6-31G(d,p)	0.493	0.846	2.651	1.312	0.42
MPW1K/6-31G(d,p)	0.633	0.762	2.651	1.256	0.45
mPW1PW91-60/6-31G(d,p)	0.470	0.904	2.709	1.335	0.40
B1B95-50/6-31G(d,p)	0.451	0.877	2.636	1.307	0.40
mPW1B95-50/6-31G(d,p)	0.475	0.862	2.661	1.324	0.42

The electrochemical potentials are in V, and the activation energies are in eV
[a] The basis set used for platinum is LANL2DZ

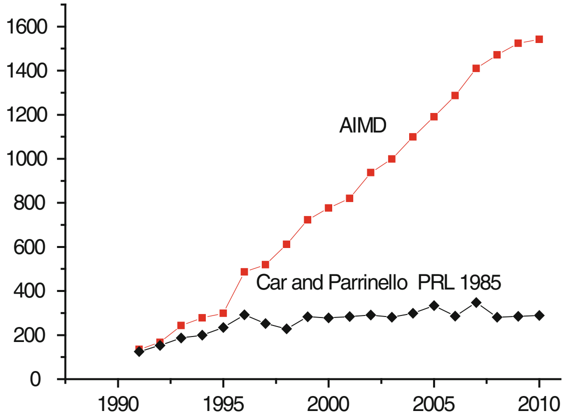

Fig. 11.2 Publication and citation analysis. *Squares*: number of publications with usage of AIMD each year from 1991 to September 28, 2011, which is based on Web of Science database (http://apps.webofknowledge.com) using "ab initio" and "molecular dynamics" (or synonym such as "first-principle MD" and "Car–Parrinello simulations") as the keywords. *Diamonds*: number of publications which cite the 1985 paper by Car and Parrinello [33]

provides direct information about the electronic structure. Figure 11.2 depictures the number of publications related to AIMD method.

The CP method makes use of the following classical Lagrangian

$$L_{\mathrm{CP}} = \sum_i \frac{1}{2}\mu_i \langle \psi_i | \psi_i \rangle + \frac{1}{2}\sum_I M_I \dot{R}_I^2 - E(\psi_0,\ \vec{R}) + \text{constraints} \tag{11.5}$$

to generate trajectories for the nuclear and electronic degrees of freedom via the coupled set of equations of motion:

$$M_I \ddot{R}_I(t) = -\frac{\partial}{\partial R_I}\langle \psi_0 | H | \psi_0 \rangle + \frac{\partial}{\partial R_I}\{\text{constraints}\} \tag{11.6}$$

$$\mu_i \ddot{\psi}_i(t) = -\frac{\partial}{\partial \psi_i^*}\langle \psi_0 | H | \psi_0 \rangle + \frac{\partial}{\partial \psi_i^*}\{\text{constraints}\} \tag{11.7}$$

where $|\psi_0\rangle = \det\{\psi_i\}$ is the total wave function; M_I and R_I are atom I's nuclear mass and position, respectively; μ_i are the "fictitious electron masses" or inertia parameters assigned to the orbital degrees of freedom; and E is the energy functional of the system. For a given nuclear geometry, the ground-state electronic wave function can be obtained by standard techniques such as steepest descent or other higher order methods:

$$\dot{\psi}_i(t) = -\frac{1}{2}\frac{\delta E}{\delta \psi} + \sum_j \Lambda_{ij}\psi(t) = -\frac{1}{2}H\psi_i(t) + \sum_j \Lambda_{ij}\psi(t) \tag{11.8}$$

where Λ_{ij} are Lagrange multipliers which impose orthonormality constraints on the electronic orbitals. Thus, once the ground-state wave function has been determined, the dynamical behavior of a system can be studied at a given time; the force acting on the nuclei is given by Eq. (11.6). In the dynamical simulation, both the electronic and nuclear (ionic) degrees of freedom can propagate concurrently [35].

Compared to ordinary quantum chemical approaches, the AIMD free-energy calculations have significant advantage as entropic effects and anharmonicity are explicitly included in the calculation. In contrast, a normal static DFT procedure requires that the vibrational entropy be added via harmonic frequency calculations and the computational demands may be quite substantial for large molecular systems. Furthermore, the harmonic approximation may not even be valid in situations where weak interactions are dominant.

11.3 ORR in Acidic Medium

The ORR is a multi-electron reaction that includes a number of elementary reactions. Yeager proposed two pathways for the ORR in acidic medium [36]: (1) a "direct" four-electron pathway where O_2 is reduced directly to water without involvement of hydrogen peroxide (H_2O_2), $O_2 + 4H^+ + 4e^- \rightarrow 2H_2O$ and (2) a "series" pathway in which O_2 is reduced to H_2O_2, $O_2 + 2H^+ + 2e^- \rightarrow H_2O_2$, followed by its further reduction to H_2O, $H_2O_2 + 2H^+ + 2e^- \rightarrow 2H_2O$. Adzic et al. proposed a parallel pathway, with the direct and series mechanisms occur simultaneously, with the direct pathway as the dominant one [37].

For transition metal catalysts, two-electron reduction was reported for less active metals such as Au and Hg. For the most active catalyst, Pt and Pt-based alloys, four-electron reduction steps are generally believed. However, the detailed mechanism and reduction pathways are not clear and much debate remains. Even for the first electron transfer step, different views still exist [38–40]. Examples of plausible first steps include the following: (1) splitting of the O–O bond upon oxygen adsorption on two Pt sites (S) in a bridge configuration, $O_2 + 2S \rightarrow O^* + O^*$; (2) formation of

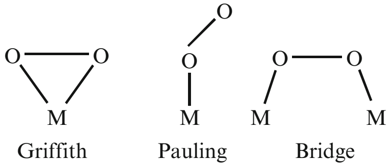

Fig. 11.3 Models of O_2 adsorption on electrode surfaces

the superoxide anion, $O_2 + 2S + e^- \rightarrow O_2^-$; and (3) simultaneous electron and proton transfer, $O_2 + 2S + (H^+ + e^-) \rightarrow OOH$.

O_2 reduction pathways were affected to a great extent by the O_2 adsorption modes on catalyst surfaces. There are three adsorption models for molecular oxygen adsorption (Fig. 11.3):

1. O_2 interacts with a single substrate atom (Griffith model) [41] forming a bond between its σ-orbitals and the empty d_{z^2} orbitals of the metal surface atom and by forming a σ-backbond from the partially filled d_{xy} or d_{yz} metal orbitals to the antibonding π^* orbitals of O_2.
2. End-on adsorption through a single σ-type bond (Pauling model), in which the σ-orbital of O_2 donates electron to the d_{z^2} orbital on the metal.
3. Bridge model, with O_2 bonds with two sites, which was proposed by Yeager [42] principally for the reaction on platinum group metals.

In order to study the oxygen reduction mechanism, it is crucial to know the nature and coverage of adsorbed reaction intermediates. However, there is no simple adequate spectroscopic method for identifying adsorbed intermediates. Computational studies can provide insights regarding intermediates, their geometries, and energies. Anderson and Albu [30] carried out ab initio studies of reversible potentials and activation energies for uncatalyzed oxygen reduction to water and the reverse oxidation reaction. The electrode was modeled by a noninteracting electron-donor molecule with a chosen ionization potential (IP). When the reactant reached a point on the reaction path where its electron affinity (EA) matched the donor's IP, an electron transfer was assumed occurring, and the donor's IP or reactant's EA was identified with the electrode potential. To locate transition state, potential surface scan is deployed [43]. Once the transition state is located, the energy difference between the transition-state structure and reactants energy is taken as the activation energy. They calculated the activation energy of the following one-electron transfer steps:

$$O_2(g) + H^+(aq) + e^-(U) \rightarrow HO_2^\bullet(aq) \tag{11.9}$$

$$HO_2^\bullet(aq) + H^+(aq) + e^-(U) \rightarrow H_2O_2(aq) \tag{11.10}$$

$$H_2O_2(aq) + H^+(aq) + e^-(U) \rightarrow HO^\bullet(g) + H_2O(aq) \tag{11.11}$$

$$HO^\bullet(g) + H^+(aq) + e^-(U) \rightarrow H_2O(aq) \tag{11.12}$$

The MP2/6-31G** method is used. The H^+(aq) was modeled with $H_3O^+(H_2O)_2$ cluster. The electron transfer was assumed to occur when the electron affinity of the reaction complex equaled the ionization potential, IP, of the electrode.

They studied activation energies for the four-electron transfer steps at potentials range between 0 and 2 V (vs. standard hydrogen electrode, SHE). The results showed that as the electrode potential increases, the activation barriers increase as well. The third electron and proton transfer step (Eq. 11.11), i.e., the H_2O_2 reduction, has the highest activation energy. Over the potential range they considered, activation energies for the reduction reactions decrease in the sequence: third step (Eq. 11.11) > first step (Eq. 11.9) > second step (Eq. 11.10) > fourth step (Eq. 11.12). From the calculation results, it is evident that an efficient four-electron reduction catalyst must not liberate hydrogen peroxide and it must activate the first and third reduction steps without deactivating the other two steps. Complete dissociation of HOOH on the electrode surface should lead to good activity, based on the low activation energy calculated for $HO^{\bullet}$ reduction.

In a subsequent study, Anderson and Albu [44] employed a similar method to study the catalytic effect of Pt on ORR. A single Pt atom is used to model the system. They calculated activation energies of the following four reduction steps:

$$\mathrm{Pt-O_2 + H^+(aq) + e^-}(U) \rightarrow \mathrm{Pt-OOH} \tag{11.13}$$

$$\mathrm{Pt-OOH + H^+(aq) + e^-}(U) \rightarrow \mathrm{Pt-OHOH} \tag{11.14}$$

$$\mathrm{Pt-OHOH + H^+(aq) + e^-}(U) \rightarrow \mathrm{Pt-OH + H_2O} \tag{11.15}$$

$$\mathrm{Pt-OH + H^+(aq) + e^-}(U) \rightarrow \mathrm{Pt-OH_2} \tag{11.16}$$

It is evident that the Pt atom has a significant catalytic effect on the most difficult step of the ORR, i.e., $H_2O_2 \rightarrow HO^{\bullet} + H_2O$. Activation energies drop about 1 eV over the 0–2 V potential range studied. Activation energies for the other reduction steps are also substantially reduced. The activation energies for $HO^{\bullet}$ reduction to H_2O increase when $HO^{\bullet}$ is bonded to the Pt atom and bonding to Pt decreases the activation energies for $OOH^{\bullet}$ reduction to H_2O_2. In all cases, the activation energies are predicted to increase with increasing potential (Fig. 11.4).

Sidik and Anderson further studied the O_2 electroreduction when bonded to Pt dual sites [45]. A Pt dimmer, Pt_2, with the bulk distance of 2.775 Å, was used to provide one- and twofold bonding sites for coordinating O_2, O, OOH, and OH. The results suggest that the O_2 on dual sites does not dissociate before the first electron transfer and the product for this step, OOH, easily dissociates with a small 0.06 eV activation barrier to form O and OH. The first electron transfer step has the highest activation barrier (0.60 eV at 1.23 V), which is close to the experimental value, and is predicted to be the rate-determining step.

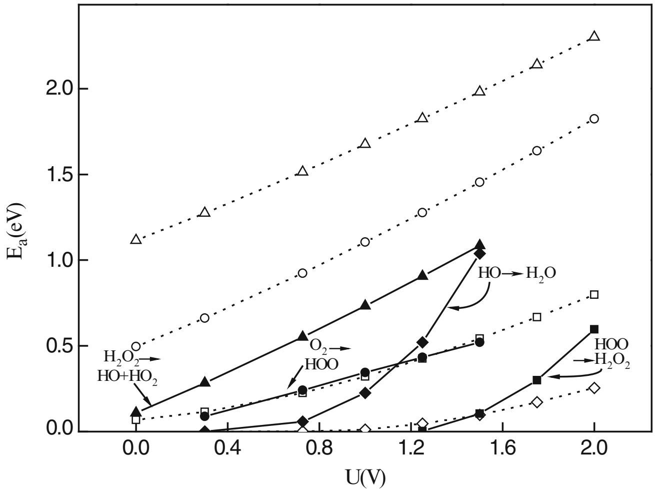

Fig. 11.4 Activation energy for the four steps of oxygen reduction to water as a function of electrode potential, *U*. *Heavy lines* connect points with species undergoing reduction bonded to a Pt atom. *Dotted lines* connect points with no bonding to the Pt. The same key applies to both sets of curves [44]

Li and Balbuena [46] used DFT method with B3PW91 functional, LANL2DZ effective core pseudopotentials for Pt, and 6-311G(d) basis set for O and H to study the first electron transfer step:

$$Pt_5 - O_2 + H^+(aq) + e^- \rightarrow Pt_5 - OOH \qquad (11.17)$$

The solvent influence on the reaction is considered with $H_3O^+(H_2O)_2$ ion cluster model. It is found that the electron transfer process takes place gradually as the hydronium ion gets close to the adsorbed oxygen. The activation energies show a strong dependence on the $O_{ads}\cdots H\cdots O_{water}$ distance between the adsorbed oxygen and the proton water. The proton transfer reaction is not involved in the rate-determining step if the $O_{ads}\cdots H\cdots O_{water}$ distance is smaller than a certain threshold, which depends on the degree of proton solvation. Negatively charging the cluster/adsorbate complex causes a sharp decrease in the activation barrier.

Jinnouchi and Okazaki [47] performed AIMD studies of the first electron transfer reaction with one oxygen molecule, 1 hydronium ion, 9 water molecules, and 12 Pt atoms at 350 K. They proposed that the first reaction step would be rapid oxygen adsorption on the catalyst induced from the strong attractive force between the oxygen molecule and the platinum surface. The adsorbed water molecules and the hydronium ion hydrated the adsorbed oxygen atoms, and proton transfer through the constructed hydrogen bonds frequently occurred. When the conformation of these species satisfied certain conditions, the oxygen dissociation with the proton transfer reaction was induced, and three OH were generated on the platinum surface. The authors suggested that the generation of ordered cluster structure that provides the effective path for ions and water molecules is the most important guiding principle for designing high ion conductive electrolytes.

11.4 ORR Catalyzed by Metal Catalysts

11.4.1 Platinum

Platinum has long been known as the best electrocatalyst for oxygen reduction in acidic medium [48]. The first step of catalyzing oxygen reduction involves chemisorption of oxygen molecule on the electrocatalyst surface. The adsorbate's structure, bonding type, and energy are key elements in understanding the effects of adsorption on the reaction kinetics. Theoretical studies of chemisorption of oxygen molecule can provide information about the nature of bonding at the surface, bond strength, geometry, and site preferences of adsorbates. Furthermore, theoretical calculations have advantage that the study can be performed for situations not realizable experimentally and can eliminate concerns about the effects of contaminants or other unknown variables.

Li and Balbuena [49] performed DFT calculation to study the interactions of oxygen with platinum clusters. They firstly calculated the ground-state structures of Pt_n clusters ($n = 4$–6). The results indicated that the structures for Pt_n clusters are nonplanar and most of them exhibit Jahn–Teller distortions. For atomic oxygen, a bridge-site adsorption is found as the most stable structure for Pt_3O. The adsorption energy for atomic oxygen shows a strong dependence on the metal cluster size and geometry. The bridge site is found to be the most favorable site for the adsorption of O_2 on Pt_n. In the dimer complexes Pt_2O_2, they found that the electron transferred from the Pt's *s* orbitals to the oxygen *p* orbitals, whereas in Pt_nO_2 ($n > 2$), the electron transferred from the Pt's *d* and *p* orbitals. The potential energy surface for the adsorption of oxygen shows a double well feature. The first potential energy minimum occurs at adsorption distances relatively far from the metal cluster. As the molecule gets closer to the cluster, the second minimum, which is more stable than the first one, appears corresponding to adsorbed state. A bond-order conservation approximation analysis illustrates that the dissociation activation energies depend on the Pt cluster size. The activation energies are reduced as the cluster's ionization potential (IP) decreases, which facilitates the charge transfer to the adsorbate. A similar effect on dissociation is observed upon application of an electric field along the direction of increase of the dipole moment of the adsorbate–cluster complex.

Similarly, Wang et al. [50] used B3LYP functional to study the adsorption and decomposition of the radical OOH and H_2O_2 on Pt clusters (Pt_3, Pt_4, Pt_6, and Pt_{10}). The potential energy surface for the complete reduction of oxygen in acidic medium has been calculated (Fig. 11.5). They found that the OOH radical has a very strong adsorption on Pt clusters. Both thermodynamics and kinetics indicate

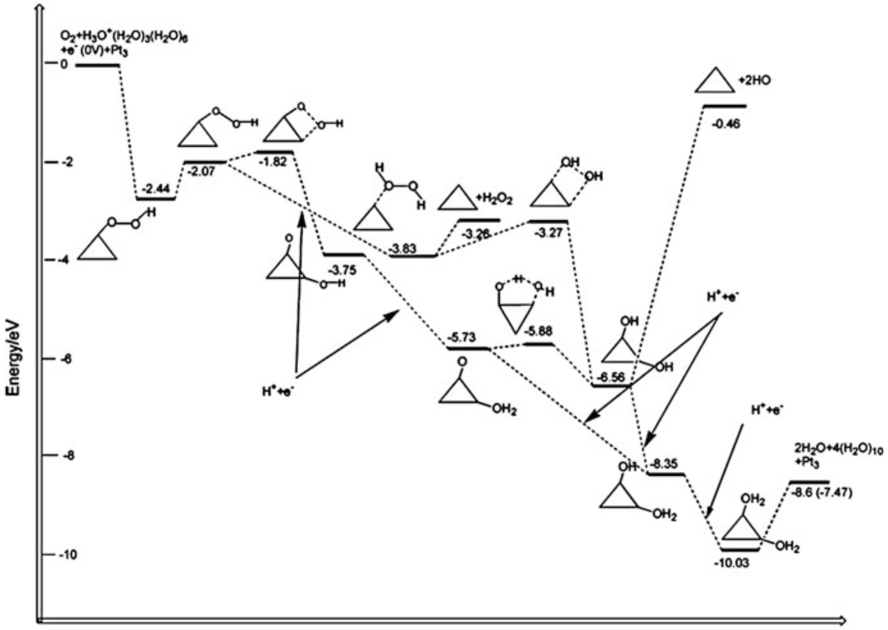

Fig. 11.5 Potential energy surface profile for the oxygen reduction reaction at the standard hydrogen electrode potential scale: the proton was modeled by two shells of water molecules, $H^{+}OH_2(H_2O)_3(H_2O)_6$, and the data in parentheses are Gibbs free energies [50]

that OOH readily decomposes into O and OH before a second electron transfer takes place. Thus, although a one-end adsorbed hydrogen peroxide H_2O_2, arising from the reduction of adsorbed OOH, has been located on Pt_3 and Pt_{10}, a favorable pathway for the second electron transfer should occur on the coadsorbed O and OH species, suggesting that O_2 reduction on a Pt surface may proceed via a *parallel* pathway: the *direct* (no H_2O_2 generated as intermediate) and *series* (H_2O_2 generated) occurring simultaneously, with the *direct* as the dominant step.

As discussed above, the oxygen adsorption and reduction processes are often simulated either on small Pt clusters or flat surfaces. However, both experimental measurements [51, 52] and computational calculations [53, 54] indicate that nanosized electrocatalysts show a considerably different catalytic activity from extended flat surfaces. These investigations would suggest that effects observed with particle size reduction go well beyond the increase in surface area and involve fundamental physical and chemical changes in the reaction steps. Han and his coworkers [55] studied explicitly Pt nanoparticles with 1 and 2 nm sizes and compared their chemical adsorption properties to those of an extended flat Pt (111) surface. As atomic oxygen (O) and hydroxyl group (OH) are two species of considerable importance [56], they focused on effect of particle size and Pt coordination on the chemisorption energies of O and OH.

Based on their calculations, the chemisorption energies of O and OH on the Pt (111) surface vary considerably from on that of 1 and 2 nm particles. With only sites near the center of the (111) facet on the 2 nm particle display similar adsorption energies to that of the Pt(111) bulk surface. While they find that on the bulk surface the fcc site is the most stable adsorption site, in agreement with previous work [57–59], oxygen adsorption is strongest at bridge sites on the edges of the 2 and 1 nm particles. For both particles, the maximal adsorption energy is larger than on the bulk surface. Depending on the location of sites, the adsorption energies at the fcc and hcp sites of the nanoparticles can be larger or small than that of the bulk surface value, with adsorption getting stronger as the site location getting closer to the edge of the surface.

While, in general, the adsorption energy on the 1 nm particle on equivalent sites is higher than on the 2 nm particle, this trend is reversed for the fcc (111) site. This peculiarity is attributed to the significant curvature on the surface of 1 nm particle in order to reduce the total surface area of the particle. This causes the distance between nearest neighbor Pt atoms to be longer on the surface of the 1 nm particle (2.85 Å) than on the 2 nm particle (2.7 Å). This bond elongation prevents the effective interaction between oxygen and the three Pt atoms defining the site.

The effect of particle size on adsorption energy and catalytic activity is complex. It depends on the precise role that the adsorbed species play in the catalytic process and on the change in adsorption of other relevant species. Watanabe et al. [60] argued that particle size has no effect on the rate of the ORR; however, the mean particle spacing on the support is the more relevant variable though his findings have been disputed by Giordanoa et al. [61] and Takasu et al. [62]. Similarly, Yano et al. [63] studied the ORR catalytic activity and the ratio of peroxide (H_2O_2) formation on Pt particles with 1.6, 2.6, and 4.8 nm in diameter. By NMR analysis of ^{195}Pt located at surfaces of the Pt nanoparticles, they found that the electronic structure of Pt does not change with particle size, from which they concluded that the ORR activity does not change with Pt particle size. Mayrhofer et al. [64], on the other hand, argued that the rate of the ORR decreases with decreasing in particle size as stronger OH adsorption blocks oxygen adsorption sites. Based on the analysis above, the authors concluded that there might be no general relationship between the particle size and the catalytic activity. Nevertheless, clever engineering of nanostructure of catalyst materials to optimize the adsorption strength and increase number of adsorption sites for the intermediate species involved could, in principle, be used to fabricate better electrocatalysts. Certainly such an approach would require a better understanding of reaction mechanism and effect of nanostructure on adsorption of various intermediate species.

11.4.2 Platinum-Based Metal Catalysts

The polarization in a PEMFC comes mainly from the slow cathodic ORR. Reducing the Pt loading (particularly in the cathode catalyst layer) without compromising fuel cell performance is a strategy to meet the cost reduction requirements for PEMFC commercialization [65, 66]. In other words, the design of novel catalysts requires not only reducing the amount of Pt used but also enhancing catalytic activity and stability [67]. Several approaches have been developed to address reduction of Pt loading, including (1) improving nanostructures to increase the surface-to-volume ratio of catalyst materials [68]; (2) using an alloying technique to incorporate non-precious metals into the nanostructures; and (3) texturing nanostructures, e.g., replacing the core atoms in Pt nanoparticles with a non-precious metal, resulting in a Pt-skin [69, 70] or Pt monolayer catalysts [71–73].

Several Pt-based bimetallic systems have been reported showing good ORR activity. For instance, alloying Pt with transition metals such as Co [74, 75], Ni [76–78], Fe [79], Mn [79], Cr [80–82], and V [83] is highlighted as a promising approach toward improving ORR electrocatalysis in acidic solutions. A number of explanations have been proposed for the observed improvement in activity by the addition of a less noble metal to Pt [84]. These include the lower oxidation state of the Pt which can suppress Pt oxide formation, a shortening of Pt–Pt interatomic distance and therefore a more favorable adsorption of O_2 (geometric effect), an increased *5d*-orbital vacancies (electronic effect), and formation of a thin Pt skin on the surface of the alloy [85] which has unusual electronic properties. Using the conventional Pt/C catalyst as the baseline, the ORR activities of PtM alloys ($M = Ni$, V, Co, and Fe) follow the order: Pt/C $<$ PtNi/C $<$ PtV/C $<$ PtCo/C $<$ PtFe/C [86–88].

Wang et al. [89] carried out first-principle DFT calculations to investigate how a subsurface transition metal M ($M = Ni$, Co, or Fe) affects the energetics and mechanisms of ORR on the outermost mono-surface layer of Pt/M(111). With the calculation, they illustrated that the subsurface Ni, Co, and Fe could downshift the *d*-band center of the Pt surface and thus weaken the binding of chemical species to the Pt/M(111) surface. Moreover, the subsurface Ni, Co, and Fe could modify the heat of reaction and activation energy of various elementary reactions of ORR. The results revealed that, due to the influence of the subsurface Ni, Co, or Fe, ORR would adopt a hydrogen peroxide dissociation pathway. The activation energy for the rate-determining O_2 protonation reaction is 0.15, 0.17, and 0.16 eV on Pt/Ni (111), Pt/Co(111), and Pt/Fe(111), respectively. In contrast, the activation energy for the same reaction on a pure Pt(111) surface is 0.79 eV. The theoretical study explained why the subsurface Ni, Co, and Fe could lead to multifold enhancement in catalytic activity of ORR on the Pt/M(111) catalysts.

Xu et al. [57] performed self-consistent periodic DFT calculations (GGA–PW91) to study the adsorption of O and O_2 and the dissociation of O_2 on the (111) facets of ordered Pt_3Co and Pt_3Fe alloys and on monolayer Pt skins covering these two alloys. They also investigated explicitly the strain effect by a 2 % compression of Pt(111). They discovered that the Co atoms on the $Pt_3Co(111)$ surface allow O_2 to dissociate more easily than on Pt(111) [the lowest activation energy on $Pt_3Co(111)$ is 0.24 eV/O_2, compared to 0.77 eV/O_2 on Pt(111)] and also bind O and O_2 more strongly (-4.29 eV/O vs. -3.88 eV/O, -0.92 eV/O_2 vs. -0.62 eV/O_2). While for monolayer Pt-skin catalysts, the authors showed that

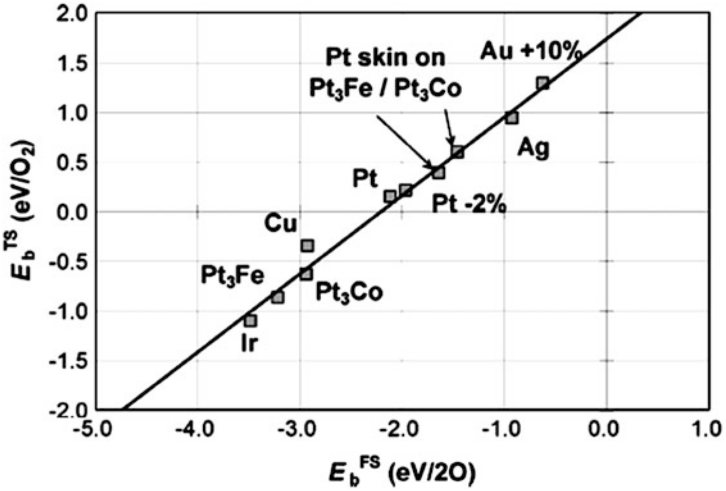

Fig. 11.6 Binding energies of the transition states of O_2 dissociation (E_b^{TS}) vs. binding energies of the atomic final states with respect to gas-phase O_2 (E_b^{FS}) on the (111) facets of several fcc transition metals and alloys [57]

although these catalysts are less reactive than pure Pt for O_2 dissociation, they are more active toward the ORR because they are less poisoned by O and facilitate the activation of O and O-containing intermediates in bond-making elementary reaction steps in the ORR.

The authors also revealed that there is a linear relationship between atomic oxygen binding energy and the oxygen dissociation barrier of the transition metals and alloys (Fig. 11.6). The more strongly a material binds atomic oxygen, the more effective it will be in dissociating molecular oxygen. So instead of conducting a complicated and expensive transition-state study, a more affordable atomic binding study can be used to screen and design better oxygen reduction catalysts.

Mavrikakis et al. [90] performed spin-polarized DFT calculations to study the ORR catalytic activity of platinum monolayers supported on close-packed transition metal surfaces [(Au(111), Pt(111), Pd(111), and Ir(111)]. To estimate the relative activity of these catalysts at two different cell potentials (1.23 and 0.80 V), both the free-energy changes and activation energy barriers for elementary reactions are calculated. They observed that OH removal is the rate-limiting step for ORR at the potential of 1.23 V. At a cell potential of 0.80 V, the proton/electron transfer steps become easier, and Pt*/Pd shows the highest activity among the surfaces examined, even higher than that of pure Pt(111). The activity of the other two surfaces, namely, Pt*/Au and Pt*/Ir, is lower due to the difficulty in OH removal and in O–O bond scission, respectively. Their findings provide additional insights into the ORR mechanism for these supported platinum monolayer surfaces.

11.4.3 Other Metal Catalysts

Palladium-alloy materials have been recently introduced as a promising ORR cathode electrocatalyst for replacing Pt [91–98]. Pd alloys are considerably less expensive than Pt. Besides, experimental studies indicate that they have high methanol tolerance for direct methanol fuel cells (DMFCs) in which the methanol crossover to the cathode significantly decreases the cell's efficiency [99, 100].

Shao et al. [101] measured the ORR activity of Pd monolayers supported on Ru (0001), Rh(111), Ir(111), Pt(111), and Au(111) using the rotating disk electrode technique and correlated the findings with the *d*-band center of Pd calculated from DFT method. They observed the activity of Pd monolayers supported on Ru(0001), Rh(111), Ir(111), Pt(111), and Au(111) increased in the following order: Pd/Ru (0001) $<$ Pd/Ir(111) $<$ Pd/Rh(111) $<$ Pd/Au(111) $<$ Pd/Pt(111). A volcano-type dependence of activity on the energy of the *d*-band center of Pd monolayers was found, with Pd/Pt(111) at the top of the curve. They also synthesized a Pd_2Co/C alloy, and the results showed that the non-Pt alloy's ORR activity is comparable to that of commercial Pt-based catalysts. The kinetics of the ORR catalyzed by this electrocatalyst predominantly involves a four-electron reduction with the first electron transfer being the rate-determining step. The downshift of the *d*-band center of the Pd "skin," which constitutes the alloy surface due to the strong surface segregation of Pd at elevated temperatures, contributed to its high ORR activity. Additionally, the catalyst showed very high methanol tolerance, retaining very high catalytic activity for the ORR at high concentrations of methanol.

Very recently, Erikat et al. [102] used periodic self-consistent DFT calculations to study the adsorption and the reaction barrier for the dissociation of O_2 on Ir(100) surface. Dissociative adsorption is found to be energetically more favorable than molecular adsorption. Among all the cases studied, parallel approaches (*Prl*1 and *Prl*2) on a hollow site, with the same adsorption energy of -3.93 eV, are found to be the most energetically preferred sites of adsorptions. Hybridization between *p*-O_2 and *d*-metal orbitals is responsible for the dissociative adsorption. By using the nudge elastic band method (NEB), they found that the dissociation occurs immediately and very early along the dissociation path with a small activation barrier (0.26 eV).

Through DFT slab calculations, the adsorption and dissociation of O_2 on CuCl (111) surface have been systematically studied by Zhang et al. [103]. Different modes of atomic O and molecular O_2 adsorption on CuCl(111) surface and possible dissociation pathways are examined; vibrational frequency and Mulliken charge are also calculated. Their results showed that the favorable adsorption occurs at hollow site for O atom and molecular O_2 lying flatly on the surface with one O atom on top of Cu atom is the most stable adsorption configuration. The O–O stretching vibrational frequencies are significantly red-shifted, and the charges are transferred from CuCl to oxygen. Upon O_2 adsorption, adsorbed species on CuCl(111) surface exhibit the characteristic of the superoxo (O_2^-), which contributes to improving the catalytic activity of CuCl. Meanwhile, O_2 dissociation into atomic O could also occur; however, it needs to overcome a very large activation barrier.

11.5 Non-precious Metal Catalysts

At the current technology stage, Pt-based electrocatalysts are the most practical materials in terms of both activity and stability, although their performance is still insufficient and needs further improvement. The major drawback of these Pt-based catalysts is the limited availability and high cost, contributing to the excessive production costs of fuel cell systems.

The search for inexpensive, high-performance electrocatalysts has taken two different approaches. The first approach is to reduce catalyst usage through increasing Pt utilization in the catalyst layers. This can be achieved by alloying Pt with inexpensive metals (Co, Fe, etc.) and/or by utilizing unique support materials for thin-layer Pt nanoparticle deposition. In the last two decades, the required Pt loading has been reduced significantly to approximately 0.4 mg cm^{-2} [104]. Unfortunately, the increasing of Pt price during the same time has totally offset the Pt loading reduction, rendering the efforts toward Pt loading reduction ineffective. Therefore, this approach may not be a viable solution for cost reduction of PEMFC. The other approach is to develop non-precious metal-based electrocatalysts. Although the performance of the non-precious metal catalysts (carbon-supported Fe– and/or Co–N catalysts) is still inferior to Pt-based catalysts in terms of both activity and stability, in the last few years, significant progress has been made in the development of non-precious metal catalysts making it one of the most active and promising research areas [105].

Non-precious metal catalyst research covers a broad range of materials. The most promising catalysts investigated thus far are carbon-supported $M–N_x/C$ materials ($M = Co, Fe, Ni, Mn$, etc.) formed by pyrolysis of a variety of metal, nitrogen, and carbon precursor materials [106]. Other non-precious metal electrocatalyst materials investigated include non-pyrolyzed transition metal macrocycles [107–122], conductive polymer-based complexes (pyrolyzed and non-pyrolyzed) [123–140], transition metal chalcogenides [141–148], metal oxide/carbide/nitride materials [149–166], as well as carbon-based materials [167–179]. The advances of these types of materials can be found in Chaps. 7–10 and 12–15 of this book.

To meet the need of PEMFC, increasing volumetric density of non-precious metal catalysts is required; however, without knowledge of active-site structure, it is very challenging to increase the active-site density. There are many challenges in determining the active-site structures. There is lack of adequate material characterization techniques. The active sites may be scarce. Furthermore, different active sites may contribute to the catalytic activity of the materials [180]. There are different reviews regarding the nature of active sites. One school believes that metal is at the active sites, while the other believes that metal merely catalyzes the formation of active sites from carbon, nitrogen, and perhaps oxygen atoms [181–184]. Some researchers believe that the ORR activity is originated from the formation of graphitic nitrogen and/or pyridinic nitrogen functional groups. This claim has been supported in the literature with ORR activity of metal-free N/C catalyst materials [185, 186]. This further demonstrates the convoluted understanding regarding the exact nature of the catalytically active moieties with respect to ORR. First-principle modeling is a valuable tool in exploring active-site structures and providing insights into the reaction mechanism.

11.5.1 Transition Metal Macrocycle Catalysts

Transition metal macrocycle compounds have been employed as ORR catalysts since the first study by Jasinski in 1964 [187]. The activity of these complexes has been found to be directly related to the metal ion center and encompassing ligand structure [105]. Simple cobalt-based complexes (i.e., cobalt phthalocyanines or cobalt porphyrins) have catalytic activity toward the reduction of oxygen by a two-electron process to produce H_2O_2, whereas a four-electron reduction process forming H_2O is commonly observed for Fe-based complexes. Although the activity of unpyrolyzed transition metal macrocycle catalysts is inferior to its pyrolyzed counterpart, the major benefit of studying non-pyrolyzed macrocyclic catalyst is for fundamental understanding, as the active sites of these catalysts are well known, which allows a direct link between the catalyst structure and its ORR activity. Thus, theoretical studies have been conducted to understand the relationship between the transition metal macrocyclic complex structures and their electrocatalytic properties.

Sun et al. [188] performed DFT calculation to study the electrochemical reduction mechanism of oxygen on four metal macrocyclic complexes, iron phthalocyanines (FePc), iron porphyrin (FeP), cobalt phthalocyanine (CoPc), and cobalt porphyrin (CoP). Based on their calculation results, for the four metal macrocyclic complexes, O_2 will not directly be cleaved without the cooperation of hydrogen. In the reduction process, with FePc or FeP as catalyst, O_2 is reduced to H_2O ($4e^-$ transfer) without the formation of intermediate H_2O_2, while on CoPc or CoP, O_2 is reduced to H_2O_2 ($2e^-$ transfer). The authors attributed the four-electron reduction capability of Fe complexes to their high-lying HOMO of these complexes (see Fig. 11.7), which make the electron donation to oxygen easier; as a result, more electron are transferred to O–O antibonding orbital, and O–O bond is readily broke.

Shi and Zhang [189] carried out DFT calculations to study the dioxygen-binding abilities on the following iron and cobalt systems: CoPc (cobalt phthalocyanine), $CoF_{16}Pc$ (cobalt hexadecafluorophthalocyanine), CoMeOPc (cobalt octamethoxyphthalocyanine), CoTSPc (cobalt tetrasulfophthalocyanine), CoTNPPc (cobalt tetraneopentoxyphthalocyanine), CoP (cobalt porphyrin), CoTPP (cobalt tetraphenylporphyrin), CoTPFPP (cobalt tetrakis(pentafluorophenyl)porphyrin), FePc, $FeF_{16}Pc$, FeMeOPc, FeTSPc, FeTPyPz (iron-2,3-pyridinoporphyrazine) FeP, FeTPP, and FeTPFPP. The ionization potential of the above metal macrocyclic complexes was also calculated.

Their calculations demonstrated that dioxygen-binding abilities of the transition metal macrocyclic complexes are determined by central metal, ligand, and substituents. For cobalt phthalocyanine systems, electron-donating substituents increase

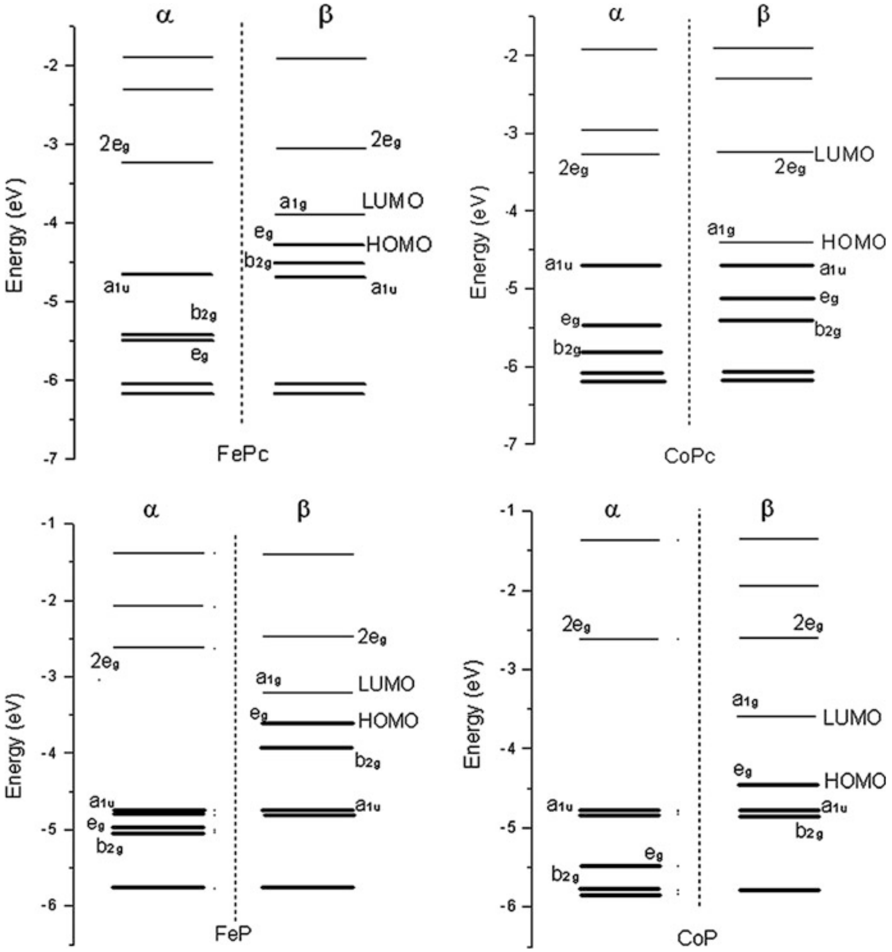

Fig. 11.7 Energy levels of MPc and MP (M = Fe, Co, α = spin-down orbital, β = spin-up orbital) [188]

its dioxygen-binding ability, and electron-withdrawing substituents decrease the dioxygen-binding ability of the systems. In general, the transition metal macrocyclic systems' ORR catalytic activity is related to its ionization potential and dioxygen-binding ability. Higher ionization potential and larger dioxygen-binding energy are associated with better catalytic activity. For porphyrin systems, cobalt derivatives have higher ionization potential and higher reactivity. For phthalocyanine systems, iron derivatives have good ionization potential and large oxygen-binding energy.

Similarly, Li et al. [190] investigated the interaction between dioxygen and various iron macrocyclic complexes (Fig. 11.8) by means of first-principle calculations. Their results indicated that the macrocyclic ligands without aromaticity were better electron-donor ligands, facilitating the backbonding from iron to O_2

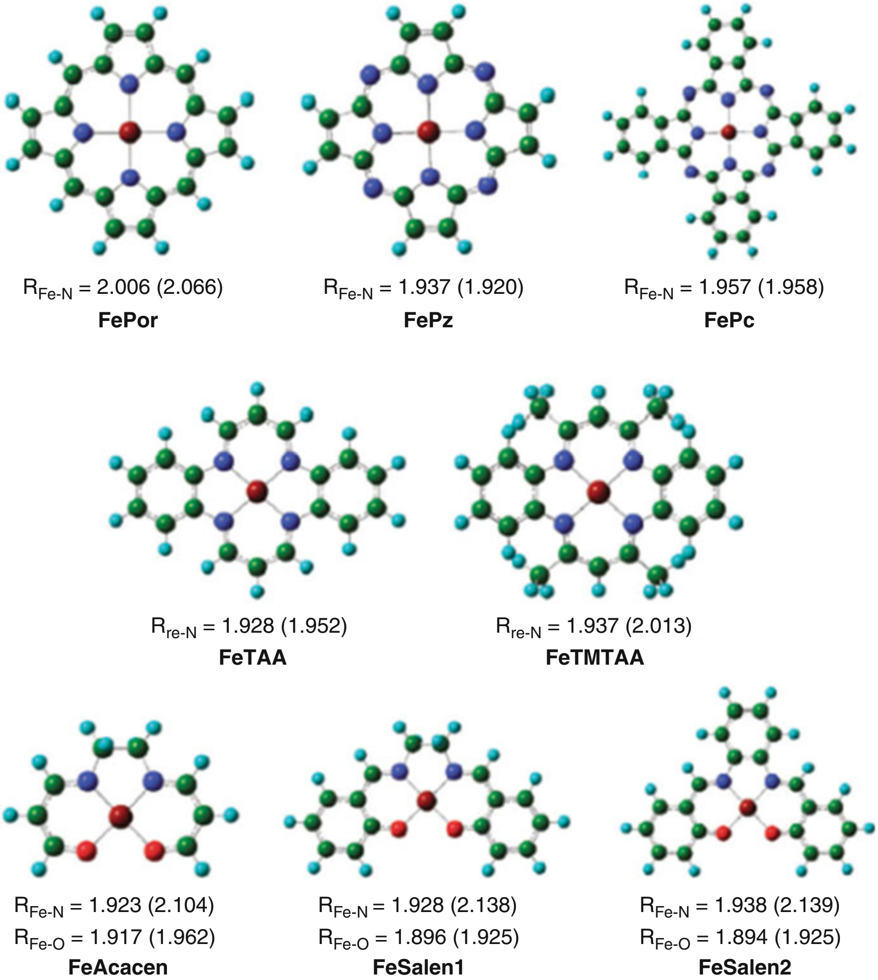

$R_{Fe\text{-}N}$ = 2.006 (2.066)
FePor

$R_{Fe\text{-}N}$ = 1.937 (1.920)
FePz

$R_{Fe\text{-}N}$ = 1.957 (1.958)
FePc

$R_{re\text{-}N}$ = 1.928 (1.952)
FeTAA

$R_{re\text{-}N}$ = 1.937 (2.013)
FeTMTAA

$R_{Fe\text{-}N}$ = 1.923 (2.104)
$R_{Fe\text{-}O}$ = 1.917 (1.962)
FeAcacen

$R_{Fe\text{-}N}$ = 1.928 (2.138)
$R_{Fe\text{-}O}$ = 1.896 (1.925)
FeSalen1

$R_{Fe\text{-}N}$ = 1.938 (2.139)
$R_{Fe\text{-}O}$ = 1.894 (1.925)
FeSalen2

Fig. 11.8 The structures for the deoxy-systems (FeX) under study. The *maroon balls* are iron atoms, the *blue balls* are nitrogen atoms, the *red balls* are oxygen atoms, the *green-black balls* are carbon atoms, and the *turquoise balls* are hydrogen atoms. $R_{\text{Fe–N}}$ is the distance (Å) between the Fe and the coordinated nitrogen atom, and $R_{\text{Fe–O}}$ is the distance between the Fe and the coordinated oxygen atom. Data out of the parentheses are for the triplets, in the parentheses for the quintets [190]

and activated O_2 more significantly. Furthermore, the activation of O_2 was closely related to the energy of the HOMO of iron macrocyclic complexes. The smaller the energy gap between the HOMO of iron macrocyclic complexes and the LUMO of dioxygen, the more reactive the adsorbed O_2 became, with a longer O–O bond distance and a shorter Fe–O bond length. Based on their study, the authors proposed that FeTMTAA is a potential catalyst in oxidation reactions using O_2 as oxidant. FeAcacen, FeSalen1, and FeSalen2 are also promising catalysts for oxidation

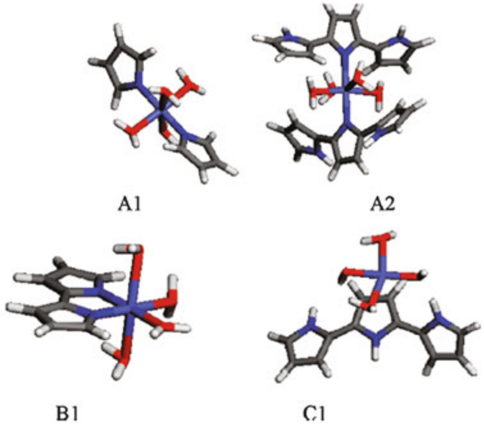

Fig. 11.9 Optimized structures of four proposed active sites [193]. *Blue*: Co, *dark blue*: N, *gray*: C, *white*: H, *red*: O

reactions. Furthermore, by modifying the structure of iron macrocyclic complexes through substituent groups and axial ligand, the ORR catalytic efficiency could be tuned.

11.5.2 Conductive Polymer-Based Complex Catalysts

Conductive polymers such as polypyrrole (PPy), polyaniline (PAni), and polythiophen (PTh) have been the subject of much research owing to their wide applications in biosensors, electrochemistry, and electrocatalysis [191, 192]. Recently, conductive polymers have been also investigated as ORR electrocatalysis in three different ways: (1) utilizing conductive polymers as ORR electrocatalysts on their own, (2) incorporating non-precious metal complexes into the conductive polymer matrix, and (3) employing conductive polymers as a nitrogen/carbon precursor material for pyrolyzed M–N_x/C catalysts [105].

Shi et al. [193] employed DFT and experimental characterization to investigate active-site structures of unpyrolyzed cobalt–polypyrrole (Co–PPy) composites. They specifically examined four types of the active-site structures and studied the stability of each structure. They also examined oxygen adsorption on these structures with both end-on and side-on configurations and calculated the redox potential of each structure (Fig. 11.9). The theoretical simulations indicated that various active-site structures could contribute to the ORR activity of non-heat-treated Co–PPy catalysts and both Co(III) and Co(II) could play the role of an active center. The active site's oxygen binding strength (end-on or side-on) dictates its dominant reaction pathway ($2e^-$ or $4e^-$). With calculated redox potential of each active site and its oxygen binding strength, each active site's contribution to $2e^-$ or $4e^-$ pathway at a defined potential can be deduced. Base on their results, the studied active sites contributed more to $2e^-$ pathway at low potential (0.3 V vs. RHE) than that at high potential (0.6 V vs. RHE), which is consistent with experimental observed change of hydrogen peroxide formation at different potentials. The calculations illustrated that more than one type of active sites contribute to the ORR activity observed with untreated cobalt–polypyrrole catalysts. Type A structures give similar potential dependence hydroperoxide formation trend as that observed from experiment. They postulated that for untreated Co–PPy composites, the presence of the type A structures is likely.

Another insight provided by their study is that the side-on oxygen adsorption requires more space than the end-on adsorption configuration. This may be one of the reasons why cobalt porphyrin and phthalocyanine systems cannot form stable side-on adducts which generally lead to $4e^{-}$ transfer products. The destruction of the ordered structure of such a macrocyclic catalyst during the heat treatment is likely to increase the number of sites that facilitate the side-on oxygen adsorption, and this leads to an increase in the number of electrons transferred in the ORR.

Similarly, the interaction between the oxygen molecule and Co–(n)pyrrole model clusters ($n = 4, 6$) was recently studied by Dipojono et al. [194, 195]. The stable adsorption site of the O_2 molecule on Co–(4)pyrrole is found to be in a side-on configuration, while for the case of Co–(6)pyrrole cluster, the O_2 molecule is slightly deviated from the side-on configuration. The O–O bonds of the O_2/Co–(4)pyrrole and the O2/Co–(6)pyrrole systems have elongated by 11.84 and 9.86 %, respectively. The elongation mechanism of O_2 on Co–(n)pyrrole is induced by the interaction between the cobalt d-orbitals and the O_2 antibonding π^* orbital, which results in a charge transfer from the cobalt atom toward the O_2 molecule. In Co–(4)pyrrole, the elongation of the O_2 bond is larger than that of Co–(6)pyrrole since a complete side-on configuration has more symmetric overlapping between the cobalt d-orbitals and the O_2 antibonding orbital. Furthermore, the dissociation energy is affected by the amount of the charge transferred from Co–(n)pyrrole clusters to the O_2 molecule in the transition state.

11.5.3 Carbon-Based Materials

Carbon-based materials with large surface area such as carbon nanotubes, nanofibers, and graphene have recently received attention as potential metal-free catalyst materials for ORR [167–179]. In particular, nitrogen (N)-doped carbon materials have been shown to yield high ORR activity with four-electron transfer mechanism [167, 169]. Matter et al. [173] reported that the N-doped carbon nanofibers have high ORR catalytic activity and the N-doped nanotubes and graphene [170] were also recently reported to have high activity for ORR in the absence of transition metal atoms. The pyridinic N site (nitrogen atoms with lone pair electrons) has been generally considered as catalytic active site for ORR due to delocalizing of π electrons to pyridinic N, and existence of a large amount of pyridinic nitrogen is usually observed with highly active carbon materials [169, 170, 172]. On the contrary, a recent experiment suggested that the graphitic N (nitrogen bonded to three sp^2 carbon atoms) was the key for ORR activity rather

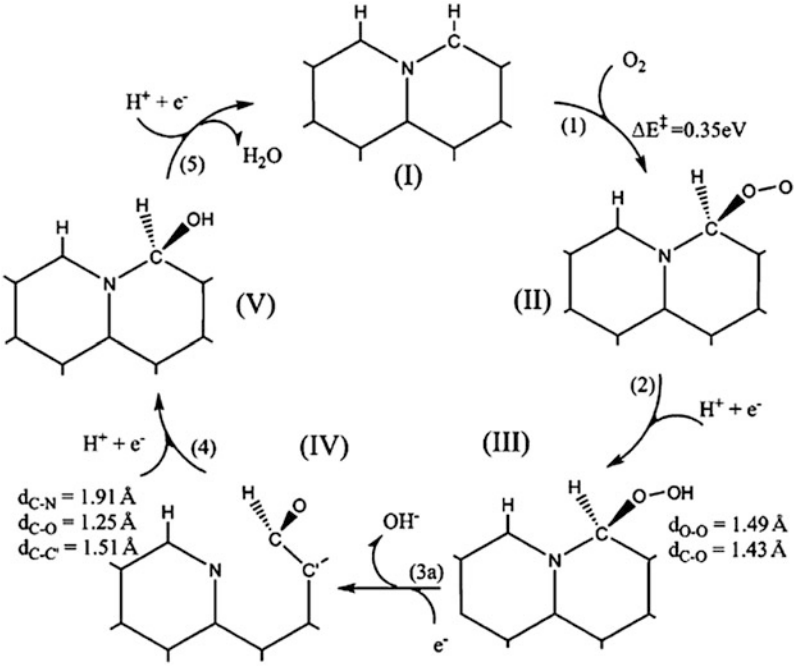

Fig. 11.10 The proposed ORR catalytic cycle [198]

than pyridinic N [196]. It is, in fact, difficult to distinguish the edge vs. pyridinic N experimentally [197], as graphitic N at edge can become a pyridinic N.

In order to elucidate the active sites for N-doped graphene materials, Jung et al. [198] performed the spin-polarized DFT calculations of graphene nanoribbon edges. They observed that the nitrogen doping increases the activity of graphene edges by enhancing the first electron transfer and giving dominate four-electron reduction products, which are the two most important aspects for improving ORR selectivity and performance. The outermost graphitic nitrogen site among others yields the lowest barrier for the rate-limiting first electron transfer as well as the highest selectivity toward the four-electron reduction pathway and hence is proposed to be the primary active site. Furthermore, the proposed catalytic cycle (Fig. 11.10) involves a ring opening of the cyclic C–N bond at the edge of graphene which converts the graphitic N to pyridinic N. This interconversion of graphitic to pyridinic N may reconcile the controversy regarding pyridinic or graphitic nitrogen as the ORR active sites for N-doped graphene materials.

Functionalized graphitic materials with late transition metals were recently studied by Rossmeisl et al. [199]. They showed that graphitic materials with active sites composed of four nitrogen atoms and transition metal atoms belonging to groups 7–9 in the periodic table are active toward ORR. Spin analyses suggested that the oxidation state of those elements in the active sites is, in general, +2. Moreover, their results showed that transition metals do not have intrinsic catalytic activities, since their adsorption behavior can be severely altered by changes in the local geometry of the active site, the chemical nature of the nearest neighbors, and the oxidation states. Furthermore, the catalytic performance of ORR can be improved by stabilizing the adsorption of OOH with respect to that of OH, which can be achieved by carefully engineering the active sites.

Yu et al. [200] performed periodic DFT calculations to study the ORR catalyzed by N-graphene. The study took the solvent, surface adsorbates, and surface coverage into consideration. They observed that it is essential to include water effect in constructing a reliable free-energy reaction profile, especially for O_2 adsorption which is significantly enhanced by the polarization of O_2 in the presence of water due to hydrogen bond formation. Without water, O_2 cannot be adsorbed on the N-graphene surface. The formation of OOH^- is found to be energetically unfavored compared with the dissociation reaction $OOH_{(ads)} \rightarrow O_{(ads)} + OH^-$. The result suggests that O_2 is mainly reduced via a "$4e^-$ reduction" pathway on N-doped graphene. The rate-determining step is the removal of $O_{(ads)}$ from the N-graphene surface. Thus, they suggested that a catalyst with a high efficiency in $O_{(ads)}$ removing should have a high activity.

11.6 Conclusions

Past few years or so have witnessed a big increase of theoretical modeling studies in electrocatalyst materials. These studies are enabled by better computational algorithms and fast computational facilities and fueled by the demand of environmental friendly and sustainable energy resources. Theoretical modeling complementing experimental study has shed light on detailed surface phenomena, formation of intermediates, and the activation energies related to elementary reaction steps and provided better understanding of ORR mechanisms. Methodologies that employ structure activity relationship such as adsorption energy, activation energies, and *d*-band centers have shown encourage results in identifying better electrocatalysts. They are invaluable tools to screen for better electrocatalysts. On the other hand, due to its limitation with simple model and small-sized systems, first-principle methods have difficulty in providing quantitative numbers for detailed reaction steps. The major issue with theoretical study of ORR in PEMFC is how to model the interface effectively. Better models and methodologies need to be developed to study electrochemical systems. More theoretical studies are needed to provide better understanding of ORR and to help design novel electrocatalysts.

References

1. Jacobson MZ, Colella WG, Golden DM (2005) Cleaning the air and improving health with hydrogen fuel-cell vehicles. Science 308(5730):1901–1905
2. Dusastre V (2001) Materials for clean energy. Nature 414(6861):331

3. Bashyam R, Zelenay P (2006) A class of non-precious metal composite catalysts for fuel cells. Nature 443(7107):63–66
4. EG&G Technical Services Inc (2004) Fuel cell handbook. 7th ed. Morgantown, West Virginia: National Energy Technology Lab, US Department of Energy
5. Shi Z, Zhang J, Liu ZS, Wang H, Wilkinson DP (2006) Current status of ab initio quantum chemistry study for oxygen electroreduction on fuel cell catalysts. Electrochim Acta 51(10): 1905–1916
6. Xu H, Kunz R, Fenton JM (2007) Investigation of platinum oxidation in PEM fuel cells at various relative humidities. Electrochem Solid State Lett 10(1):B1–B5
7. Holby EF, Greeley J, Morgan D (2012) Thermodynamics and hysteresis of oxide formation and removal on platinum (111) surfaces. J Phys Chem C 116(18):9942–9946
8. Appleby AJ (1993) Electrocatalysis of aqueous dioxygen reduction. J Electroanal Chem 357(1–2):117–179
9. Markovic NM, Ross PN Jr (2002) Surface science studies of model fuel cell electrocatalysts. Surf Sci 45(4–6):117–229
10. Schmickler W (1999) Recent progress in theoretical electrochemistry. Annu Rep Prog Chem Sect C Phys Chem 95:117–162, Chapter 5
11. Grimbolt J, Luntz AC, Fowler DE (1990) Low temperature adsorption of O_2 on Pt (111). J Electron Spectrosc Relat Phenom 52:161–174
12. Luntz AC, Williams MD, Bethune DS (1988) The sticking of O_2 on a Pt(111) surface. J Chem Phys 89(7):4381–4395
13. Stohr J, Gland JL, Eberhard W, Outka D, Madix RJ, Sette F, Koestner RJ, Doebler U (1983) Bonding and bond lengths of chemisorbed molecules from near-edge X-ray-absorption fine-structure studies. Phys Rev Lett 51(26):2414–2417
14. Sexton BA (1981) Identification of adsorbed species at metal-surfaces by electron-energy loss spectroscopy (EELS). Appl Phys A 26(1):1–18
15. Wurth W, Stohr J, Feulner P, Pan X, Bauchspiess KR, Baba Y, Hudel E, Rocker G, Menzel D (1990) Bonding, structure, and magnetism of physisorbed and chemisorbed O_2 on Pt (111). Phys Rev Lett 65(19):2426–2429
16. Puglia C, Nilsson A, Hernnas B, Karis O, Bennich P, Martensson N (1995) Physisorbed, chemisorbed and dissociated O_2 on Pt(111) studied by different core level spectroscopy methods. Surf Sci 342(1–3):119–133
17. Keith JA, Jacob T (2010) Computational simulations on the oxygen reduction reaction in electrochemical. In: Balbuena PB, Subramanian VR (eds) Theory and experiment in electrocatalysis. Springer, New York, pp 89–132
18. Koper MTM (2003) Ab initio quantum-chemical calculations in electrochemistry. In: Vayenas CG, Conway BE, White RE (eds) Modern aspects of electrochemistry, vol 36. Kluwer/Plenum, New York, Chapter 2
19. Kohn W, Sham LJ (1965) Self-consistent equations including exchange and correlation effects. Phys Rev 140(4A):A1133–A1138
20. Becke AD (1988) Density-functional exchange-energy approximation with correct asymptotic behavior. Phys Rev A 38(6):3098–3100
21. Kohanoff J, Gidopoulos NI (2003) Density functional theory: basics, new trends and applications. In: Wilson S (ed) Handbook of molecular physics and quantum chemistry, vol 2. Wiley, Chichester, pp 532–568, Part 5, Chapter 26
22. Perdew JP (1986) Density-functional approximation for the correlation-energy of the inhomogeneous electron-gas. Phys Rev B 33(12):8822–8824
23. Perdew JP, Chevary JA, Vosko SH, Jackson KA, Pederson MR, Singh DJ, Fiolhais C (1992) Atoms, molecules, solids, and surfaces-applications of the generalized gradient approximation for exchange and correlation. Phys Rev B 46(11):6671–6687
24. Perdew JP, Wang Y (1992) Accurate and simple analytic representation of the electron-gas correlation-energy. Phys Rev B 45(23):13244–13249
25. Becke AD (1993) Density-functional thermochemistry. III. The role of exact exchange. J Chem Phys 98(7):5648–5652

26. Lee C, Yang W, Parr RG (1988) Development of the colle-salvetti correlation-energy formula into a functional of the electron-density. Phys Rev B 37(2):785–789
27. Becke AD (1993) A new mixing of Hartree-Fock and local density-functional theories. J Chem Phys 98(2):1372–1377
28. Perdew JP, Burke K, Ernzerhof M (1996) Generalized gradient approximation made simple. Phys Rev Lett 77(18):3865–3868
29. Albu TV, Mikel SE (2007) Performance of hybrid density functional theory methods toward oxygen electroreduction over platinum. Electrochim Acta 52(9):3149–3159
30. Anderson AB, Albu TV (1999) Ab initio determination of reversible potentials and activation energies for outer-sphere oxygen reduction to water and the reverse oxidation reaction. J Am Chem Soc 121(50):11855–11863
31. Adamo C, Barone V (1998) Exchange functionals with improved long-range behavior and adiabatic connection methods without adjustable parameters: the mPW and mPW1PW models. J Chem Phys 108(2):664–675
32. Becke AD (1996) Density-functional thermochemistry. IV. A new dynamical correlation functional and implications for exact-exchange mixing. J Chem Phys 104(3):1040–1046
33. Car R, Parrinello M (1985) Unified approach for molecular-dynamics and density-functional theory. Phys Rev Lett 55(22):2471–2474
34. Grotendorst J, Blügel S, Marx D (eds) (2006) Computational nanoscience: do it yourself! vol 31, NIC Series. John von Neumann Institute for Computing, Jülich, pp 195–244
35. Tse JS (2002) Ab initio molecular dynamics with density functional theory. Annu Rev Phys Chem 53:249–290
36. Yeager E (1984) Electrocatalysts for O_2 reduction. Electrochim Acta 29(11):1527–1537
37. Adzic RR, Wang JX (1998) Configuration and site of O_2 adsorption on the Pt(111) electrode surface. J Phys Chem B 102(45):8988–8993
38. Damjanovic A, Brusic V (1967) Electrode kinetics of oxygen reduction on oxide-free platinum electrodes. Electrochim Acta 12(6):615–628
39. Yeager E, Razaq M, Gervasio D, Razaq A, Tryk D (1992) The electrolyte factor in O_2 reduction electrocatalysis. In: Scheerson D, Tryk D, Daroux M, Xing X (eds) Structural effects in electrocatalysis and oxygen electrochemistry. Proc vol 92–11. The Electrochemical Society, Pennington NJ, p 440
40. Shao MH, Liu P, Adzic RR (2006) Superoxide anion is the intermediate in the oxygen reduction reaction on platinum electrodes. J Am Chem Soc 128(23):7408–7409
41. Griffith JS (1956) On the magnetic properties of some haemoglobin complexes. Proc R Soc Lond A 235(1200):23–36
42. Yeager E (1981) Recent advances in the science of the electrocatalysis. J Electrochem Soc 128(4):160C–171C
43. Marcus RA (1997) Electron transfer reactions in chemistry. Theory and experiment. J Electroanal Chem 438(1–2):251–259
44. Anderson AB, Albu TV (2000) Catalytic effect of platinum on oxygen reduction: an ab initio model including electrode potential dependence. J Electrochem Soc 147(11):4229–4238
45. Sidik RA, Anderson AB (2002) Density functional theory study of O_2 electroreduction when bonded to a Pt dual site. J Electroanal Chem 528(1–2):69–76
46. Li T, Balbuena PB (2003) Oxygen reduction on a platinum cluster. Chem Phys Lett 367(3–4): 439–447
47. Jinnouchi R, Okazaki K (2003) New insight into microscale transport phenomena in PEFC by quantum MD. Microscale Thermophys Eng 7(1):15–31
48. Hyman MP, Medlin JW (2007) Effects of electronic structure modifications on the adsorption of oxygen reduction reaction intermediates on model Pt(111)-alloy surfaces. J Phys Chem C 111(45):17052–17060
49. Li T, Balbuena PB (2001) Computational studies of the interactions of oxygen with platinum clusters. J Phys Chem B 105(41):9943–9952

50. Wang Y, Balbuena PB (2005) Potential energy surface profile of the oxygen reduction reaction on a Pt cluster: adsorption and decomposition of OOH and H_2O_2. J Chem Theory Comput 1(5):935–943
51. Valden M, Lai X, Goodman DW (1998) Onset of catalytic activity of gold clusters on titania with the appearance of nonmetallic properties. Science 281(5383):1647–1650
52. Meier J, Friedrich KA, Stimming U (2002) Novel method for the investigation of single nanoparticle reactivity. Faraday Discuss 121:365–372
53. Lopez N, Nørskov JK (2002) Catalytic CO oxidation by a gold nanoparticle: a density functional study. J Am Chem Soc 124(38):11262–11263
54. Maillard F, Eikerling M, Cherstiouk OV, Schreier S, Savinova E, Stimming U (2004) Size effects on reactivity of Pt nanoparticles in CO monolayer oxidation: the role of surface mobility. Faraday Discuss 125:357–377
55. Han BC, Miranda CR, Ceder G (2008) Effect of particle size and surface structure on adsorption of O and OH on platinum nanoparticles: a first-principles study. Phys Rev B 77(7):075410
56. Han BC, Ceder G (2006) Effect of coadsorption and Ru alloying on the adsorption of CO on Pt. Phys Rev B 74(20):205418
57. Xu Y, Ruban AV, Mavrikakis M (2004) Adsorption and dissociation of O_2 on Pt–Co and Pt–Fe alloys. J Am Chem Soc 126(14):4717–4725
58. Starke U, Materer N, Barbieri A, Döll R, Heinz K, Van Hove MA, Somorjai GA (1993) A low-energy-electron diffraction study of oxygen, water and ice adsorption on Pt(111). Surf Sci 287–288:432–437
59. Gland JL, Sexton BA, Fisher GB (1980) Oxygen interactions with the Pt(111) surface. Surf Sci 95(2–3):587–602
60. Watanabe M, Saegusa S, Stonehart P (1988) Electro-catalytic activity on supported platinum crystallites for oxygen reduction in sulphuric acid. Chem Lett 17(9):1487–1490
61. Giordano N, Passalacqua E, Pino L, Arico AS, Antonucci V, Vivaldi M, Kinoshita K (1991) Analysis of platinum particle size and oxygen reduction in phosphoric acid. Electrochim Acta 36(13):1979–1984
62. Takasu Y, Ohashi N, Zhang XG, Murakami Y, Minagawa H, Sato S, Yahikozawa K (1996) Size effects of platinum particles on the electroreduction of oxygen. Electrochim Acta 41(16): 2595–2600
63. Yano H, Inukai J, Uchida H, Watanabe M, Babu PK, Kobayashi T, Chung JH, Oldfield E, Wieckowski A (2006) Particle-size effect of nanoscale platinum catalysts in oxygen reduction reaction: an electrochemical and ^{195}Pt EC-NMR study. Phys Chem Chem Phys 8(42): 4932–4939
64. Mayrhofer KJJ, Blizanac BB, Arenz M, Stamenkovic VR, Ross PN, Markovic NM (2005) The impact of geometric and surface electronic properties of Pt-catalysts on the particle size effect in electrocatalysis. J Phys Chem B 109(30):14433–14440
65. Li X, Chen G, Xie J, Zhang L, Xia D, Wu Z (2010) An electrocatalyst for methanol oxidation in DMFC: PtBi/XC-72 with Pt solid-solution structure. J Electrochem Soc 157(4): B580–B584
66. Aricoo AS, Bruce P, Scrosati B, Tarascon JM, van Schalkwijk W (2005) Nanostructured materials for advanced energy conversion and storage devices. Nat Mater 4(5):366–377
67. Bing Y, Liu H, Zhang L, Ghosh D, Zhang J (2010) Nanostructured Pt-alloy electrocatalysts for PEM fuel cell oxygen reduction reaction. Chem Soc Rev 39(6):2184–2202
68. Antolini E (2003) Formation, microstructural characteristics and stability of carbon supported platinum catalysts for low temperature fuel cells. J Mater Sci 38(14):2995–3005
69. Stamenkovic VR, Fowler B, Mun BS, Wang G, Ross PN, Lucas CA, Markovic NM (2007) Improved oxygen reduction activity on $Pt_3Ni(111)$ via increased surface site availability. Science 315(5811):493–497

70. Stamenkovic V, Schmidt TJ, Ross PN, Markovic NM (2002) Surface composition effects in electrocatalysis: kinetics of oxygen reduction on well-defined Pt_3Ni and Pt_3Co alloy surfaces. J Phys Chem B 106(46):11970–11979
71. Zhang J, Mo Y, Vukmirovic MB, Klie R, Sasaki K, Adzic RR (2004) Platinum monolayer electrocatalysts for O_2 reduction: Pt monolayer on Pd(111) and on carbon-supported Pd nanoparticles. J Phys Chem B 108(30):10955–10964
72. Koh S, Strasser P (2007) Electrocatalysis on bimetallic surfaces: modifying catalytic reactivity for oxygen reduction by voltammetric surface dealloying. J Am Chem Soc 129(42): 12624–12625
73. Srivastava R, Mani P, Hahn N, Strasser P (2007) Efficient oxygen reduction fuel cell electrocatalysis on voltammetrically dealloyed Pt–Cu–Co nanoparticles. Angew Chem Int Ed 46(47):8988–8991
74. Mukerjee S, Srinivasan S, Soriaga MP, McBreen J (1995) Effect of preparation conditions of Pt alloys on their electronic, structural, and electrocatalytic activities for oxygen reduction-XRD, XAS, and electrochemical studies. J Phys Chem 99(13):4577–4589
75. Arico AS, Shukla AK, Kim H, Park S, Min M, Antonucci V (2001) An XPS study on oxidation states of Pt and its alloys with Co and Cr and its relevance to electroreduction of oxygen. Appl Surf Sci 172(1–2):33–40
76. Paulus UA, Wokaun A, Scherer GG, Schmidt TJ, Stamenkovic V, Radmilovic V, Markovic NM, Ross PN (2002) Oxygen reduction on carbon-supported Pt-Ni and Pt-Co alloy catalysts. J Phys Chem B 106(16):4181–4191
77. Markovic NM, Schmidt TJ, Stamenkovic V, Ross PN (2001) Oxygen reduction reaction on Pt and Pt bimetallic surfaces: a selective review. Fuel Cell 1(2):105–116
78. Drillet JF, Ee A, Friedemann J, Kotz R, Schnyder B, Schmidt V (2002) Oxygen reduction at Pt and $Pt_{70}Ni_{30}$ in H_2SO_4/CH_3OH solution. Electrochim Acta 47(12):1983–1988
79. Mukerjee S, Srinivasan S, Soriaga MP, McBreen J (1995) Role of structural and electronic properties of Pt and Pt alloys on electrocatalysis of oxygen reduction: an in situ XANES and EXAFS investigation. J Electrochem Soc 142(5):1409–1422
80. Min M, Cho J, Cho K, Kim H (2000) Particle size and alloying effects of Pt-based alloy catalysts for fuel cell applications. Electrochim Acta 45(25–26):4211–4217
81. Neergat M, Shukla AK, Gandhi KS (2001) Platinum-based alloys as oxygen-reduction catalysts for solid-polymer-electrolyte direct methanol fuel cells. J Appl Electrochem 31(4):373–378
82. Paffett MT, Barry JG, Gottesfeld S (1988) Oxygen reduction at $Pt_{0.65}Cr_{0.35}$, $Pt_{0.2}Cr_{0.8}$ and roughened platinum. J Electrochem Soc 135(6):1431–1436
83. Antolini E, Passos RR, Ticianelli EA (2002) Electrocatalysis of oxygen reduction on a carbon supported platinum–vanadium alloy in polymer electrolyte fuel cells. Electrochim Acta 48(3):263–270
84. Lai FJ, Chou HL, Sarma LS, Wang DY, Lin YC, Lee JF, Hwang BJ, Chen CC (2010) Tunable properties of Pt_xFe_{1-x} electrocatalysts and their catalytic activity towards the oxygen reduction reaction. Nanoscale 2(4):573–581
85. Toda T, Igarashi H, Uchida H, Watanabe M (1999) Enhancement of the electroreduction of oxygen on Pt alloys with Fe, Ni, and Co. J Electrochem Soc 146(10):3750–3756
86. Mukerjee S, Srinivasan S (1993) Enhanced electrocatalysis of oxygen reduction on platinum alloys in proton exchange membrane fuel cells. J Electroanal Chem 357(1–2):201–224
87. Antolini E, Salgado JRC, Gonzalez ER (2006) The stability of Pt–M (M = first row transition metal) alloy catalysts and its effect on the activity in low temperature fuel cells: a literature review and tests on a Pt–Co catalyst. J Power Sources 160(2):957–968
88. Colon-Mercado HR, Popov BN (2006) Stability of platinum based alloy cathode catalysts in PEM fuel cells. J Power Sources 155(2):253–263
89. Duan Z, Wang G (2011) A first principles study of oxygen reduction reaction on a Pt(111) surface modified by a subsurface transition metal M (M = Ni, Co, or Fe). Phys Chem Chem Phys 13(45):20178–20187

90. Nilekar AU, Mavrikakis M (2008) Improved oxygen reduction reactivity of platinum monolayers on transition metal surfaces. Surf Sci 602(14):L89–L94
91. Shao MH, Sasaki K, Adzic RR (2006) Pd−Fe nanoparticles as electrocatalysts for oxygen reduction. J Am Chem Soc 128(11):3526–3527
92. Fernandez JL, Raghuveer V, Manthiram A, Bard AJ (2005) Pd–Ti and Pd–Co–Au electrocatalysts as a replacement for platinum for oxygen reduction in proton exchange membrane fuel cells. J Am Chem Soc 127(38):13100–13101
93. Fernandez JL, Walsh DA, Bard AJ (2005) Thermodynamic guidelines for the design of bimetallic catalysts for oxygen electroreduction and rapid screening by scanning electrochemical microscopy. M–Co (M: Pd, Ag, Au). J Am Chem Soc 127(1):357–365
94. Savadogo O, Lee K, Oishi K, Mitsushimas S, Kamiya N, Ota KI (2004) New palladium alloys catalyst for the oxygen reduction reaction in an acid medium. Electrochem Commun 6(2):105–109
95. Savadogo O, Lee K, Mitsushima S, Kamiya N, Ota KI (2004) Investigation of some new palladium alloys catalysts for the oxygen reduction reaction in an acid medium. J New Mater Electrochem Syst 7(2):77–83
96. Raghuveer V, Manthiram A, Bard AJ (2005) Pd–Co–Mo electrocatalyst for the oxygen reduction reaction in proton exchange membrane fuel cells. J Phys Chem B 109(48): 22909–22912
97. Tarasevich MR, Zhutaeva GV, Bogdanovskaya VA, Radina MV, Ehrenburg MR, Chalykh AE (2007) Oxygen kinetics and mechanism at electrocatalysts on the base of palladium–iron system. Electrochim Acta 52(15):5108–5118
98. Opalka SM, Huang W, Wang D, Flanagan TB, Lovvik OM, Emerson SC, She Y, Vanderspurt TH (2007) Hydrogen interactions with the PdCu ordered B2 alloy. J Alloys Compd 446–447:583–587
99. Bittins-Cattaneo B, Wasmus S, Lopez-Mishima B, Vielstich W (1993) Reduction of oxygen in an acidic methanol/oxygen (air) fuel cell: an online MS study. J Appl Electrochem 23(6): 625–630
100. Gurau B, Smotkin ES (2003) Methanol crossover in direct methanol fuel cells: a link between power and energy density. J Power Sources 112(2):339–352
101. Shao MH, Huang T, Liu P, Zhang J, Sasaki K, Vukmirovic MB, Adzic RR (2006) Palladium monolayer and palladium alloy electrocatalysts for oxygen reduction. Langmuir 22(25): 10409–10415
102. Erikat IA, Hamad BA, Khalifeh JM (2011) A density functional study on adsorption and dissociation of O_2 on Ir(100) surface. Chem Phys 385(1–3):35–40
103. Zhang R, Liu H, Wang B, Ren J, Li Z (2011) Adsorption and dissociation of O_2 on CuCl(111) surface: a density functional theory study. Appl Surf Sci 258(1):408–413
104. Gasteiger HA, Kocha SS, Sompalli B, Wagner FT (2005) Activity benchmarks and requirements for Pt, Pt-alloy, and non-Pt oxygen reduction catalysts for PEMFCs. Appl Catal B 56(1–2):9–35
105. Chen Z, Higgins D, Yu A, Zhang L, Zhang J (2011) A review on non-precious metal electrocatalysts for PEM fuel cells. Energy Environ Sci 4(9):3167–3192
106. Bezerra CWB, Zhang L, Lee KC, Liu HS, Marques ALB, Marques EP, Wang HJ, Zhang JJ (2008) A review of Fe–N/C and Co–N/C catalysts for the oxygen reduction reaction. Electrochim Acta 53(15):4937–4951
107. van Veen J, Visser C (1979) Oxygen reduction on monomeric transition-metal phthalocyanines in acid electrolyte. Electrochim Acta 24(9):921–928
108. Wiesener K, Ohms D, Neumann V, Franke R (1989) N_4 macrocycles as electrocatalysts for the cathodic reduction of oxygen. Mater Chem Phys 22(3–4):457–475
109. Baranton S, Coutanceau C, Garnier E, Leger JM (2006) How does alpha-FePc catalysts dispersed onto high specific surface carbon support work towards oxygen reduction reaction (orr)? J Electroanal Chem 590(1):100–110

110. Baranton S, Coutanceau C, Roux C, Hahn F, Leger JM (2005) Oxygen reduction reaction in acid medium at iron phthalocyanine dispersed on high surface area carbon substrate: tolerance to methanol, stability and kinetics. J Electroanal Chem 577(2):223–234
111. Shi CN, Anson FC (1990) Catalytic pathways for the electroreduction of oxygen by iron tetrakis(4-N-methylpyridyl)porphyrin or iron tetraphenylporphyrin adsorbed on edge plane pyrolytic graphite electrodes. Inorg Chem 29(21):4298–4305
112. Cardenas-Jiron GI (2002) Substituent effect in the chemical reactivity and selectivity of substituted cobalt phthalocyanines. J Phys Chem A 106(13):3202–3206
113. Song EH, Shi CN, Anson FC (1998) Comparison of the behavior of several cobalt porphyrins as electrocatalysts for the reduction of O_2 at graphite electrodes. Langmuir 14(15):4315–4321
114. Vasudevan P, Mann SN, Tyagi S (1990) Transition metal complexes of porphyrins and phthalocyanines as electrocatalysts for dioxygen reduction. Transit Met Chem 15(2):81–90
115. Zhang L, Song CJ, Zhang JJ, Wang HJ, Wilkinson DP (2005) Temperature and pH dependence of oxygen reduction catalyzed by iron fluoroporphyrin adsorbed on a graphite electrode. J Electrochem Soc 152(12):A2421–A2426
116. Kadish KM, Fremond L, Ou ZP, Shao JG, Shi CN, Anson FC, Burdet F, Gros CP, Barbe JM, Guilard R (2005) Cobalt(III) corroles as electrocatalysts for the reduction of dioxygen: reactivity of a monocorrole, biscorroles, and porphyrin-corrole dyads. J Am Chem Soc 127(15): 5625–5631
117. Kobayashi N, Janda P, Lever ABP (1992) Cathodic reduction of oxygen and hydrogen peroxide at cobalt and iron crowned phthalocyanines adsorbed on highly oriented pyrolytic graphite electrodes. Inorg Chem 31(25):5172–5177
118. Shi C, Steiger B, Yuasa M, Anson FC (1997) Electroreduction of O_2 to H_2O at unusually positive potentials catalyzed by the simplest of the cobalt porphyrins. Inorg Chem 36(20): 4294–4295
119. Song C, Zhang L, Zhang J, Wilkinson DP, Baker R (2007) Temperature dependence of oxygen reduction catalyzed by cobalt fluoro-phthalocyanine adsorbed on a graphite electrode. Fuel Cells 7(1):9–15
120. Steiger B, Anson FC (1997) [5,10,15,20-tetrakis(4-((pentaammineruthenio)-cyano)phenyl) porphyrinato] cobalt(II) immobilized on graphite electrodes catalyzes the electroreduction of O_2 to H2O, but the corresponding 4-cyano-2,6-dimethylphenyl derivative catalyzes the reduction only to H_2O_2. Inorg Chem 36(18):4138–4140
121. Baker R, Wilkinson DP, Zhang JJ (2008) Electrocatalytic activity and stability of substituted iron phthalocyanines towards oxygen reduction evaluated at different temperatures. Electrochim Acta 53(23):6906–6919
122. Liu HS, Zhang L, Zhang JJ, Ghosh D, Jung J, Downing BW, Whittemore E (2006) Electrocatalytic reduction of O_2 and H_2O_2 by adsorbed cobalt tetramethoxyphenyl porphyrin and its application for fuel cell cathodes. J Power Sources 161(2):743–752
123. Wu G, Chen Z, Artyushkova K, Garzon FH, Zelenay P (2008) Polyaniline-derived non-precious catalyst for the polymer electrolyte fuel cell cathode. ECS Trans 16(2):159–170
124. Wu G, Artyushkova K, Ferrandon M, Kropf AJ, Myers D, Zelenay P (2009) Performance durability of polyaniline-derived non-precious cathode catalysts. ECS Trans 25(1): 1299–1311
125. Wu G, More KL, Johnston CM, Zelenay P (2011) High-performance electrocatalysts for oxygen reduction derived from polyaniline, iron, and cobalt. Science 332(6028):443–447
126. Sulub R, Martinez-Millan W, Smit MA (2009) Study of the catalytic activity for oxygen reduction of polythiophene modified with cobalt or nickel. Int J Electrochem Sci 4(7): 1015–1027
127. Khomenko VG, Barsukov VZ, Katashinskii AS (2005) The catalytic activity of conducting polymers toward oxygen reduction. Electrochim Acta 50(7–8):1675–1683
128. Martinez-Millan W, Smit MA (2009) Study of electrocatalysts for oxygen reduction based on electroconducting polymer and nickel. J Appl Polym Sci 112(5):2959–2967

129. Qin HY, Liu ZX, Yin WX, Zhu JK, Li ZP (2008) A cobalt polypyrrole composite catalyzed cathode for the direct borohydride fuel cell. J Power Sources 185(2):909–912
130. Chen J, Zhang WM, Officer D, Swiegers GF, Wallace GG (2007) A readily-prepared, convergent, oxygen reduction electrocatalyst. Chem Commun 32:3353–3355
131. Cong HN, El Abbassi K, Gautier JL, Chartier P (2005) Oxygen reduction on oxide/polypyrrole composite electrodes: effect of doping anions. Electrochim Acta 50(6):1369–1376
132. Coutanceau C, Elhourch A, Crouigneau P, Leger JM, Lamy C (1995) Conducting polymer electrodes modified by metal tetrasulfonated phthalocyanines: preparation and electrocatalytic behaviour towards dioxygen reduction in acid medium. Electrochim Acta 40(17):2739–2748
133. Hirayama T, Manako T, Imai H (2008) A metal coordination polymer for fuel cell applications: nanostructure control toward high performance electrocatalysis. e J Surf Sci Nanotechnol 6:237–240
134. Reddy ALM, Rajalakshmi N, Ramaprabhu S (2008) Cobalt-polypyrrole-multiwalled carbon nanotube catalysts for H_2 and alcohol fuel cells. Carbon 46(1):2–11
135. Shao Y, Cong HN (2007) Oxygen reduction on high-area carbon cloth-supported oxide nanoparticles/polypyrrole composite electrodes. Solid State Ionics 178(23–24):1385–1389
136. Zhang WM, Chen J, Wagner P, Swiegers GF, Wallace GG (2008) Polypyrrole/Co-tetraphenylporphyrin modified carbon fibre paper as a fuel cell electrocatalyst of oxygen reduction. Electrochem Commun 10(4):519–522
137. Zhou Q, Li CM, Li J, Lu JT (2008) Electrocatalysis of template-electrosynthesized cobalt−porphyrin/polyaniline nanocomposite for oxygen reduction. J Phys Chem C 112(47):18578–18583
138. Lee K, Zhang L, Lui H, Hui R, Shi Z, Zhang JJ (2009) Oxygen reduction reaction (ORR) catalyzed by carbon-supported cobalt polypyrrole (Co–PPy/C) electrocatalysts. Electrochim Acta 54(20):4704–4711
139. Yuan XX, Zeng X, Zhang HJ, Ma ZF, Wang CY (2010) Improved performance of proton exchange membrane fuel cells with p-toluenesulfonic acid-doped Co–PPy/C as cathode electrocatalyst. J Am Chem Soc 132(6):1754–1755
140. Yuasa M, Yamaguchi A, Itsuki H, Tanaka K, Yamamoto M, Oyaizu K (2005) Modifying carbon particles with polypyrrole for adsorption of cobalt ions as electrocatatytic site for oxygen reduction. Chem Mater 17(17):4278–4281
141. Alonso-Vante N, Tributsch H, Solorza-Feria O (1995) Kinetics studies of oxygen reduction in acid medium on novel semiconducting transition metal chalcogenides. Electrochim Acta 40(5):567–576
142. Cao DX, Wieckowski A, Inukai J, Alonso-Vante N (2006) Oxygen reduction reaction on ruthenium and rhodium nanoparticles modified with selenium and sulfur. J Electrochem Soc 153(5):A869–A874
143. Delacote C, Bonakdarpour A, Johnston CM, Zelenay P, Wieckowski A (2009) Aqueous-based synthesis of ruthenium–selenium catalyst for oxygen reduction reaction. Faraday Discuss 140:269–281
144. Fischer C, Alonsovante N, Fiechter S, Tributsch H (1995) Electrocatalytic properties of mixed transition metal tellurides (Chevrel-phases) for oxygen reduction. J Appl Electrochem 25(11):1004–1008
145. Lee K, Zhang L, Zhang JJ (2007) A novel methanol-tolerant Ir-Se chalcogenide electrocatalyst for oxygen reduction. J Power Sources 165(1):108–113
146. Lewera A, Inukai J, Zhou WP, Cao D, Duong HT, Alonso-Vante N, Wieckowski A (2007) Chalcogenide oxygen reduction reaction catalysis: X-ray photoelectron spectroscopy with Ru, Ru/Se and Ru/S samples emersed from aqueous media. Electrochim Acta 52(18):5759–5765
147. Alonso-Vante N, Jaegermann W, Tributsch H, Honle W, Yvon K (1987) Electrocatalysis of oxygen reduction by chalcogenides containing mixed transition metal clusters. J Am Chem Soc 109(11):3251–3257

148. Alonso-Vante N, Tributsch H (1986) Energy conversion catalysis using semiconducting transition metal cluster compounds. Nature 323(6087):431–432
149. Doi S, Ishihara A, Mitsushima S, Kamiya N, Ota KI (2007) Zirconium-based compounds for cathode of polymer electrolyte fuel cell. J Electrochem Soc 154(3):B362–B369
150. Ishihara A, Lee K, Doi S, Mitsushima S, Kamiya N, Hara M, Domen K, Fukuda K, Ota K (2005) Tantalum oxynitride for a novel cathode of PEFC. Electrochem Solid State Lett 8(4): A201–A203
151. Liu Y, Ishihara A, Mitsushima S, Kamiya N, Ota K (2005) Zirconium oxide for PEFCs cathode. Electrochem Solid State Lett 8(8):A400–A402
152. Armstrong RD, Douglas AF, Williams DE (1971) A study of the sodium tungsten bronzes for use as electrocatalysts in acid electrolyte fuel cells. Energy Convers 11(1):7–10
153. Bockris JO, Mchardy J (1973) Electrocatalysis of oxygen reduction by sodium tungsten bronze: II. The influence of traces of platinum. J Electrochem Soc 120(1):61–66
154. Mchardy J, Bockris JO (1973) Electrocatalysis of oxygen reduction by sodium tungsten bronze: I. Surface characteristics of a bronze electrode. J Electrochem Soc 120(1):53–60
155. Houston JE, Laramore GE, Park RL (1974) Surface electronic properties of tungsten, tungsten carbide, and platinum. Science 185(4147):258–260
156. Levy RB, Boudart M (1973) Platinum-like behavior of tungsten carbide in surface catalyst. Science 181(4099):547–549
157. Binder H, Kohling A, Kuhn W, Lindner W, Sandsted G (1969) Tungsten carbide electrodes for fuel cells with acid electrolyte. Nature 224:1299–1300
158. Izhar S, Yoshida M, Nagai M (2009) Characterization and performances of cobalt–tungsten and molybdenum–tungsten carbides as anode catalyst for PEFC. Electrochim Acta 54(4): 1255–1262
159. Nikolov I, Vitanov T (1980) The effect of method of preparation on the corrosion resistance and catalytic activity during corrosion of tungsten carbide I. Corrosion resistance of tungsten carbide in sulfuric acid. J Power Sources 5(3):273–281
160. Palanker VS, Sokolsky DV, Mazulevsky EA, Baybatyrov EN (1976) Highly dispersed tungsten carbide for fuel cells with an acidic electrolyte. J Power Sources 1(2):169–176
161. Rees EJ, Essaki K, Brady CDA, Burstein GT (2009) Hydrogen electrocatalysts from microwave-synthesised nanoparticulate carbides. J Power Sources 188(1):75–81
162. Yang XG, Wang CY (2005) Nanostructured tungsten carbide catalysts for polymer electrolyte fuel cells. Appl Phys Lett 86(22):224104
163. Zhong HX, Zhang HM, Liu G, Liang YM, Hu JW, Yi BL (2006) A novel non-noble electrocatalyst for PEM fuel cell based on molybdenum nitride. Electrochem Commun 8(5): 707–712
164. Xia DG, Liu SZ, Wang ZY, Chen G, Zhang LJ, Zhang L, Hui SQ, Zhang JJ (2008) Methanol-tolerant MoN electrocatalyst synthesized through heat treatment of molybdenum tetraphenylporphyrin for four-electron oxygen reduction reaction. J Power Sources 177(2):296–302
165. Takagaki A, Takahashi Y, Yin FX, Takanabe K, Kubota J, Domen K (2009) Highly dispersed niobium catalyst on carbon black by polymerized complex method as PEFC cathode catalyst fuel cells and energy conversion. J Electrochem Soc 156(7):B811–B815
166. Yin FX, Takanabe K, Kubota J, Domen K (2010) Polymerized complex synthesis of niobium- and zirconium-based electrocatalysts for PEFC cathodes. J Electrochem Soc 157(2): B240–B244
167. Biddinger EJ, Deak D, Ozkan US (2009) Nitrogen-containing carbon nanostructures as oxygen-reduction catalysts. Top Catal 52(11):1566–1574
168. Gong K, Du F, Xia Z, Durstock M, Dai L (2009) Nitrogen-doped carbon nanotube arrays with high electrocatalytic activity for oxygen reduction. Science 323(5915):760–764
169. Kundu S, Nagaiah TC, Xia W, Wang Y, Dommele SV, Bitter JH, Santa M, Grundmeier G, Bron M, Schuhmann W, Muhler M (2009) Electrocatalytic activity and stability of nitrogen-containing carbon nanotubes in the oxygen reduction reaction. J Phys Chem C 113(32): 14302–14310

170. Lee KR, Lee KU, Lee JW, Ahn BT, Woo SI (2010) Electrochemical oxygen reduction on nitrogen doped graphene sheets in acid media. Electrochem Commun 12(8):1052–1055
171. Maldonado S, Stevenson KJ (2005) Influence of nitrogen doping on oxygen reduction electrocatalysis at carbon nanofiber electrodes. J Phys Chem B 109(10):4707–4716
172. Zhang L, Xia Z (2011) Mechanisms of oxygen reduction reaction on nitrogen-doped graphene for fuel cells. J Phys Chem C 115(22):11170–11176
173. Matter PH, Wang E, Arias M, Biddinger EJ, Ozkan US (2007) Oxygen reduction reaction activity and surface properties of nanostructured nitrogen-containing carbon. J Mol Catal A Chem 264(1–2):73–81
174. Qu L, Liu Y, Baek JB, Dai L (2010) Nitrogen-doped graphene as efficient metal-free electrocatalyst for oxygen reduction in fuel cells. ACS Nano 4(3):1321–1326
175. Imran Jafri R, Rajalakshmi N, Ramaprabhu S (2010) Nitrogen doped graphene nanoplatelets as catalyst support for oxygen reduction reaction in proton exchange membrane fuel cell. J Mater Chem 20(34):7114–7117
176. Titov A, Zapol P, Kral P, Liu DJ, Iddir H, Baishya K, Curtiss LA (2009) Catalytic Fe-xN sites in carbon nanotubes. J Phys Chem C 113(52):21629–21634
177. Kurak KA, Anderson AB (2009) Nitrogen-treated graphite and oxygen electroreduction on pyridinic edge sites. J Phys Chem C 113(16):6730–6734
178. Okamoto Y (2009) First-principles molecular dynamics simulation of O_2 reduction on nitrogen-doped carbon. Appl Surf Sci 256(1):335–341
179. Geng D, Chen Y, Chen Y, Li Y, Li R, Sun X, Ye S, Knights S (2011) High oxygen-reduction activity and durability of nitrogen-doped graphene. Energy Environ Sci 4(3):760–764
180. Chlistunoff J (2011) RRDE and voltammetric study of ORR on pyrolyzed Fe/polyaniline catalyst. On the origins of variable tafel slopes. J Phys Chem C 115(14):6496–6507
181. Ikeda T, Boero M, Huang SF, Terakura K, Oshima M, Ozaki J (2008) Carbon alloy catalysts: active sites for oxygen reduction reaction. J Phys Chem C 112(38):14706–14709
182. Matter PH, Zhang L, Ozkan US (2006) The role of nanostructure in nitrogen-containing carbon catalysts for the oxygen reduction reaction. J Catal 239(1):83–96
183. Maldonado S, Morin S, Stevenson KJ (2006) Structure, composition, and chemical reactivity of carbon nanotubes by selective nitrogen doping. Carbon 44(8):1429–1437
184. Subramanian NP, Li X, Nallathambi V, Kumaraguru SP, Colon-Mercado H, Wu G, Lee JW, Popov BN (2009) Nitrogen-modified carbon-based catalysts for oxygen reduction reaction in polymer electrolyte membrane fuel cells. J Power Sources 188(1):38–44
185. Rao CV, Cabrera CR, Ishikawa Y (2010) In search of the active site in nitrogen-doped carbon nanotube electrodes for the oxygen reduction reaction. J Phys Chem Lett 1(18):2622–2627
186. Wang XQ, Lee JS, Zhu Q, Liu J, Wang Y, Dai S (2010) Ammonia-treated ordered mesoporous carbons as catalytic materials for oxygen reduction reaction. Chem Mater 22(7):2178–2180
187. Jasinski R (1964) A new fuel cell cathode catalyst. Nature 201(4925):1212–1213
188. Sun S, Jiang N, Xia D (2011) Density functional theory study of the oxygen reduction reaction on metalloporphyrins and metallophthalocyanines. J Phys Chem C 115(19): 9511–9517
189. Shi Z, Zhang J (2007) Density functional theory study of transitional metal macrocyclic complexes' dioxygen-binding abilities and their catalytic activities toward oxygen reduction reaction. J Phys Chem C 111(19):7084–7090
190. Sun Y, Chen K, Jia L, Li H (2011) Toward understanding macrocycle specificity of iron on the dioxygen-binding ability: a theoretical study. Phys Chem Chem Phys 13(30): 13800–13808
191. Lu W, Fadeev AG, Qi B, Smela E, Mattes BR, Ding J, Spinks GM, Mazurkiewicz J, Zhou D, Wallace GG, Macfarlane DR, Forsyth SA, Forsyth M (2002) Use of ionic liquids for π-conjugated polymer electrochemical devices. Science 297(5583):983–987
192. Hepel M, Chen YM, Stephenson RJ (1996) Effect of the composition of polypyrrole substrate on the electrode position of copper and nickel. Electrochem Soc 143(2):498–505

193. Shi Z, Liu H, Lee K, Dy E, Chlistunoff J, Blair M, Zelenay P, Zhang J, Liu ZS (2011) Theoretical study of possible active site structures in cobalt–polypyrrole catalysts for oxygen reduction reaction. J Phys Chem C 115(33):16672–16680
194. Dipojono HK, Saputro AG, Aspera SM, Kasai H (2011) Density functional theory study on the interaction of O_2 molecule with cobalt–(6)pyrrole clusters. Jpn J Appl Phys 50(5):055702
195. Dipojono HK, Saputro AG, Belkada R, Nakanishi H, Kasai H, David M, Dy ES (2009) Adsorption of O_2 on cobalt–(*n*)pyrrole molecules. J Phys Soc Jpn 78(9):094710
196. Niwa H, Horiba K, Harada Y, Oshima M, Ikeda T, Terakura K, Ozaki J, Miyata S (2009) X-ray absorption analysis of nitrogen contribution to oxygen reduction reaction in carbon alloy cathode catalysts for polymer electrolyte fuel cells. J Power Sources 187(1):93–97
197. Biddinger EJ, Ozkan US (2010) Role of graphitic edge plane exposure in carbon nanostructures for oxygen reduction reaction. J Phys Chem C 114(36):15306–15314
198. Kim H, Lee K, Woo SI, Jung Y (2011) On the mechanism of enhanced oxygen reduction reaction in nitrogen-doped graphene nanoribbons. Phys Chem Chem Phys 13(39): 17505–17510
199. Calle-Vallejo F, Martínez JI, Rossmeisl J (2011) Density functional studies of functionalized graphitic materials with late transition metals for oxygen reduction reactions. Phys Chem Chem Phys 13(34):15639–15643
200. Yu L, Pan X, Cao X, Hu P, Bao X (2011) Oxygen reduction reaction mechanism on nitrogen-doped graphene: a density functional theory study. J Catal 282(1):183–190

Chapter 12
Metal-Free Electrocatalysts for Oxygen Reduction

Sheng Zhang, Kuanping Gong, and Liming Dai

Abstract Polymer electrolyte membrane (PEM) fuel cells are attracting much attention as promising clean alternative power sources to conventional power sources, including internal combustion engines and secondary batteries. Electrocatalysts for the oxygen reduction reaction (ORR) are a key component of PEM fuel cells, which convert chemical energy directly into electricity by coupling the ORR with the oxidation of fuel molecules at the other electrode via the diffusion of ions through the membrane. Although Pt-based ORR catalysts are given high priority in formulating electrodes for PEM fuel cells, they still suffer from multiple competitive disadvantages, including their high cost, susceptibility to CO gas poisoning, and fuel crossover effect. Due to their unique electrical and thermal properties, wide availability, environmental acceptability, corrosion resistance, and large surface area, certain carbon nanomaterials have recently been studied as metal-free ORR electrocatalysts to circumvent those issues associated with the Pt catalyst. Much effort has been devoted to developing metal-free ORR catalysts for fuel cells, which led to great advances in both fundamental and applied research. In this chapter, we present an overview on recent progresses in the development of metal-free ORR electrocatalysts for fuel cells.

S. Zhang • L. Dai (✉)
Department of Macromolecular Science and Engineering, Case School of Engineering,
Case Western Reserve University, 10900 Euclid Avenue, Cleveland, OH 44106, USA
e-mail: liming.dai@case.edu

K. Gong
San Jose Lab, Corporate Research Institute, Samsung Cheil Industries Inc., San Jose,
95131, California

M. Shao (ed.), *Electrocatalysis in Fuel Cells*, Lecture Notes in Energy 9,
DOI 10.1007/978-1-4471-4911-8_12,

12.1 Introduction

Polymer electrolyte membrane (PEM) fuel cells start up fast and operate at a low temperature (<100 °C) and are being developed as a clean electrical energy device for powering vehicles and other stationary and portable applications [1–5]. Instead of burning fuel to create heat, fuel cells convert chemical energy directly into electricity through an electrochemical process involving the anode, cathode, and electrolyte [6]. At anode, hydrogen is oxidized into its constituent electrons and protons. While the protons diffuse through the separate membrane toward the cathode, the electrons flow out of the anode to provide electrical power. Electrons and protons both end up at the cathode to combine with reduced oxygen to form water [7]. The oxygen reduction reaction (ORR) at the cathode can proceed either through a four-electron process to directly combine oxygen with electrons and protons into water as the end product or a less efficient two-step, two-electron pathway involving the formation of hydrogen peroxide ions as an intermediate. Compared to the anodic hydrogen oxidation reaction (HOR), the cathodic ORR suffers more from potential drop because of its relatively sluggish kinetics, so dictating the output of a PEM fuel cell. Platinum nanoparticles have long been regarded as the best catalyst for the ORR, though the Pt-based electrode suffers from its susceptibility to time-dependent drift. Moreover, the scarcity and high cost of platinum pose one of the major concerns that have precluded fuel cells from commercial applications [8]. Therefore, it is highly desirable to develop low-cost, high-performance ORR catalysts.

In order to reduce Pt usage, nanostructured alloys comprising Pt and a transition metal were constructed and explored as an alternative to the all-Pt ORR electrocatalyst [9]. Although the required Pt loading has been reduced by replacing it with inexpensive metals, either partially or entirely [10], the significantly increasing Pt price during the past decade has largely offset this effort [11]. In addition, the ORR catalysts of this kind often have very poor durability because the second metal is susceptible to de-alloying under practical conditions, viz., a longstanding problem that can paralyze a fuel cell stack by dysfunctioning the ion exchange membrane. Another alternative approach to non-precious metal electrocatalysts is based on the active center MNx (M = Fe, Co, Ni; N = nitrogen; X = 2, 4) that was built in conductive carbon nanostructures [3, 4, 12]. However, constructed cathode electrodes and/or whole fuel cells, even with the best optimized surface state of the ORR catalysts of this kind, performed less efficiently than its Pt-based counterparts so far. The recent progress of non-precious metal electrocatalysts can be found in Chaps. 7–11 of this book.

Recently, the research on exploring the use of carbon nanomaterials as metal-free catalysts has been one of the major subjects for the fuel cell research. Owing to their wide availability, environmental acceptability, corrosion resistance, and unique surface and bulk properties, carbon nanomaterials are ideal candidates for metal-free ORR catalysts. In this context, we have demonstrated that vertically aligned nitrogen-doped carbon nanotube (VA-NCNTs) array exhibited three times higher ORR electrocatalytic activity and better long-term operation durability without the CO-poisoning effect, compared with commercial platinum-based catalyst, in alkaline fuel cells [5]. In parallel, a large array of stratagems have been developed to create heteroatom-doped carbon nanomaterials that are free from metals yet perform well in ORR, promising in devising future fuel cells. This chapter is aimed to provide an overview on the recent advances in formulating metal-free ORR electrocatalysts, with emphasis on correlating their structural and chemical properties to the ORR performance.

12.2 State-of-the-Art Metal-Free ORR Catalysts

12.2.1 Carbon Nanotubes

Carbon materials with ordered graphitic structure are expected to expedite the electron transfer rate and exhibit high electrochemical stability, which are very important for improving both catalytic activity and durability of fuel cell electrocatalysts [13–16]. In particular, nitrogen-doped carbon nanotubes [17–21] have been reported to exhibit excellent ORR electrocatalytic activity. Stevenson et al. [22] demonstrated that N-doped carbon nanofiber prepared by a floating catalyst CVD of ferrocene in either xylene or pyridine exhibited electrocatalytic activities for ORR via a two-step, two-electron pathway with an over 100 times increase in catalytic activity for H_2O_2 decomposition in both neutral and alkaline conditions. A strong correlation between the ORR peak potential positions and nitrogen doping contents was established [23]: ORR peaks shift about +30 mV per 1 at. % nitrogen incorporated.

More recently, Gong et al. [5] have found for the first time that vertically aligned nitrogen-doped carbon nanotubes (VA-NCNTs, as shown in Fig. 12.1a, b) could act as extremely efficient metal-free ORR electrocatalysts. Our quantum mechanical calculations [5] indicated that carbon atoms adjacent to nitrogen dopants in the VA-NCNTs possess a substantially high positive charge density to balance the strong electron affinity of the nitrogen atom (Fig. 12.1c). The nitrogen-induced charge transfer could change the chemisorption mode of O_2 from the usual end-on adsorption (Pauling model) at the conventional CNT surface to a side-on adsorption (Yeager model) at the NCNT surface (Fig. 12.1d). The parallel diatomic adsorption could effectively weaken the O–O bonding, which facilitated the oxygen reduction process at the NCNT cathode. Meanwhile, doping CNTs with nitrogen heteroatoms could also efficiently create the metal-free active sites for electrochemical reduction of O_2. Experimentally, the metal-free VA-NCNTs were demonstrated to catalyze a four-electron ORR process with a lower overpotential, higher electrocatalytic activity (Fig. 12.1e), weaker crossover effect, and better long-term operation stability compared with commercially available Pt/C catalysts.

Later, Star et al. [24] compared the ORR activity of nitrogen-doped carbon nanotube cups (NCNCs) to that of commercial Pt-decorated multiwalled carbon

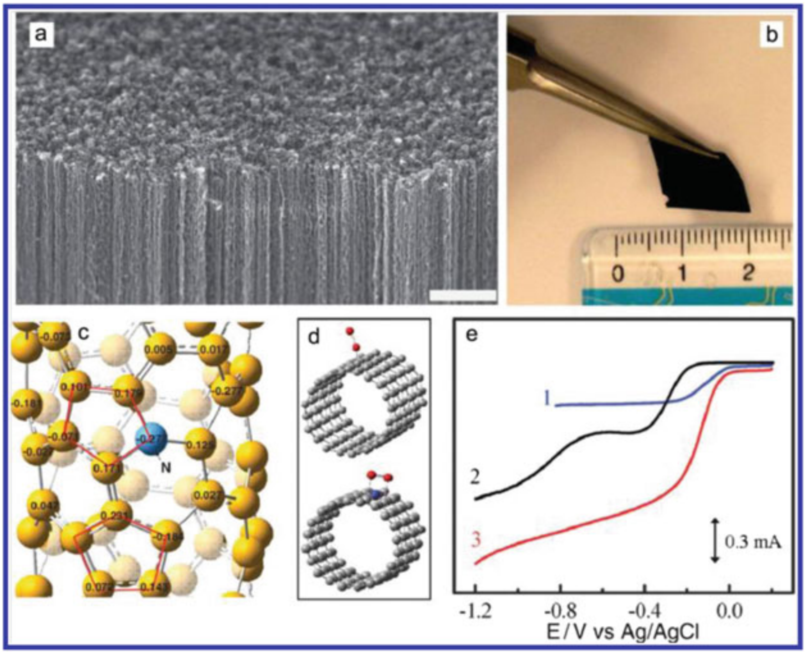

Fig. 12.1 Typical SEM image (**a**) of as-synthesized vertically aligned nitrogen-doped carbon nanotubes (VA-NCNTs) prepared by pyrolysis of iron phthalocyanine on a quartz substrate (*scale bars*, 2 μm); digital photograph (**b**) of the transferred VA-NCNTs array; calculated charge density distribution (**c**) for the NCNTs; schematic representations (**d**) of possible modes of oxygen adsorption at the CCNTs (*top*) and NCNTs (*bottom*); steady-state voltammograms (**e**) for oxygen reduction in air-saturated 0.1 M KOH at the Pt–C (curve 1), VA-CCNT (curve 2), and VA-NCNT (curve 3) electrodes (reproduced with permission [5])

nanotubes (Pt/CNTs). These NCNCs were composed of individual nanocups stacked together to form long nanofiber with a nitrogen content of 2–7 wt. % and diameters in the range of 12–40 nm. It was found that NCNCs and Pt/CNTs had similar ORR peak shapes, intensities, and positions, indicating that NCNCs have a comparable ORR electrocatalytic activity to that of Pt/CNTs in alkaline medium.

As the CVD growth processes for the VA-NCNTs and NCNCs involve metal catalysts (e.g., Fe, Ni), considerable care has been taken during the electrode preparation to completely remove the catalyst residue. Even though VA-NCNT electrode was purified by electrochemical oxidation in a phosphate buffer solution, possible effects of metal contaminates on the observed superb ORR performance could still be a matter of controversy unless nitrogen-doped carbon nanomaterials with excellent ORR electrocatalytic activities can be produced by a metal-free preparation procedure. To address this issue, Yu et al. [25] developed a simple, but very effective, plasma-etching approach to metal-free growth of undoped and nitrogen-doped single-walled carbon nanotubes (CNTs). In contrast to undoped CNTs, the metal-free nitrogen-containing CNTs thus synthesized were demonstrated to show high electrocatalytic activity and long-term stability toward ORR in an acidic medium.

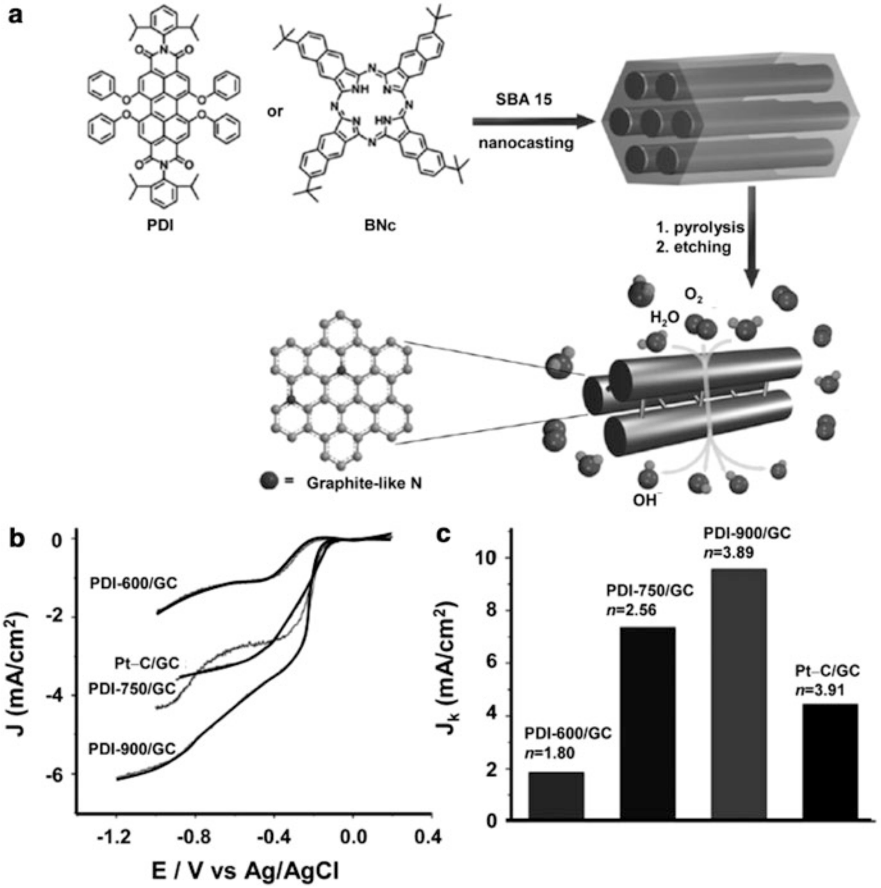

Fig. 12.2 (**a**) Preparation of NOMGAs as metal-free catalysts for the ORR. (**b**) RDE voltammograms of the series of PDI-NOGMAs and Pt–C supported on GC electrodes at a rotation rate of 1,600 rpm. (**c**) Electrochemical activity given as the kinetic-limiting current density (J_K) at 0.35 V for the PDI-NOGMAs supported on GC electrodes in comparison with that of a commercial Pt–C electrode (reproduced with permission [26])

Using a metal-free nanocasting approach, Liu et al. [26] have also reported a superior ORR electrocatalytic performance to platinum for nitrogen-doped ordered mesoporous graphitic arrays (NOMGAs, Fig. 12.2). Due to the metal-free preparation procedure, the reported electrocatalytic activity can be exclusively attributed to the incorporation of nitrogen in NOMGAs. Metal-free N-doped MWCNTs or ordered mesoporous carbons (OMCs) have also been prepared through carbonization of a MWCNT-supported polyaniline (PANI) coating [21] or via NH_3 activation to show high ORR activities in acidic medium [27].

Since doped nitrogen plays an essential role in forming the active sites for oxygen reduction catalysts, it is necessary to understand the influence of nitrogen content and its chemical nature on the ORR activity. Chen et al. [28] produced NCNTs with varying nitrogen contents through a single-step CVD process and found that NCNTs with higher nitrogen content and more defects exhibited better ORR performance in acidic medium. Kundu et al. [29] prepared NCNTs via pyrolysis of acetonitrile at different temperatures in the presence of cobalt catalysts. The NCNTs synthesized at 550 °C exhibited a higher amount of pyridinic groups and a higher ORR electrocatalytic activity than its counterpart prepared at 750 °C. However, recent studies suggest that more graphitic nitrogen atoms rather than the pyridinic ones are important for the ORR. Therefore, the exact catalytic role for each of the nitrogen forms in nanocarbon ORR catalysts is still controversial. It is a challenge to determine the exact locations of nitrogen atoms in the carbon materials, chemical nature of the catalytic sites, and electrochemical kinetics of the N-doped carbon materials.

In addition to nitrogen doping, boron doping and phosphorus doping can also facilitate the oxygen reduction process on the CNT surface. In this regard, Hu et al. [30] used benzene, triphenylborane (TPB), and ferrocene as precursors and catalyst to synthesize the B-doped carbon nanotubes (BCNTs) with a tunable boron content of 0–2.24 at. % by using different TPB concentrations. The ORR onset and peak potentials shifted positively, and the current density increased noticeably with increasing boron content, indicating a strong dependence of the ORR performance on boron content. Theoretical calculations indicated that boron doping enhanced the O_2 chemisorption on BCNTs. The electrocatalytic ability of BCNTs for ORR stemmed from the electron accumulation in the vacant $2p_z$ orbital of boron dopant from the π^* electrons of the conjugated system; thereafter, the electron transfer readily occurred to the chemisorbed O_2 molecules with boron as a bridge. The transferred charge weakens the O–O bonds and facilitates the ORR on BCNTs. Peng et al. [31] synthesized the phosphorus-doped carbon nanotubes by the thermolysis of carbon nanotubes. The phosphorus doping significantly improved the electrocatalytic activity of carbon nanotubes for the ORR in alkaline media. Carbon nanotubes doped with small amounts of phosphorus exhibited higher electrocatalytic activity and stability than the Pt/C catalyst.

12.2.2 *Graphene*

Graphene, a one-atom thick sheet of sp^2-bonded carbon, has attracted considerable interests since its discovery in 2004 [32–36]. Of particular interest, the CVD growth of N-graphene nanosheets in the presence of ammonia has recently been demonstrated to show a super ORR performance similar to that of VA-NCNTs with the same nitrogen content in alkaline medium. Qu et al. [37] prepared N-graphene films (Fig. 12.3) using a nitrogen-containing reaction gas mixture and a Ni-coated SiO_2/Si substrate. The resultant N-graphene film could be readily etched off from the substrate by dissolving Ni catalyst layer in an aqueous solution of HCl, allowing the freestanding N-graphene sheets to be transferred onto substrates suitable for electrochemical investigation.

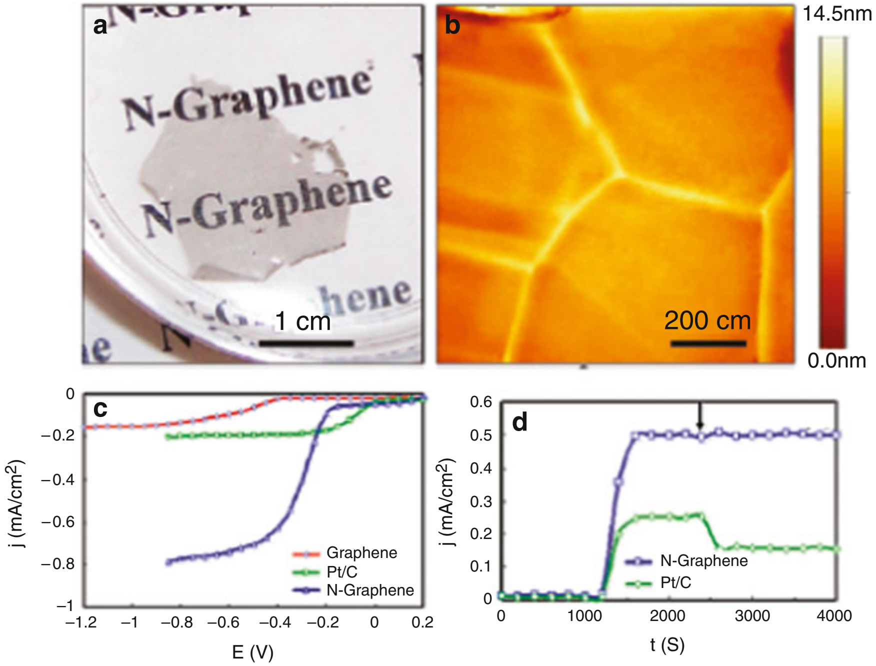

Fig. 12.3 Digital photo image (**a**) of a transparent N-graphene film floating on water after removal of the nickel layer by dissolving in an aqueous acid solution; atomic force microscopic image (**b**) of the N-graphene film; linear sweep voltammetry (**c**) curves for the ORR in air-saturated 0.1 M KOH at the graphene electrode (*red line*), Pt–C electrode (*green line*), and N-graphene electrode (*blue line*). Electrode rotating rate, 1,000 rpm. Scan rate, 0.01 V s^{-1}; current density vs. time chronoamperometric responses (**d**) obtained at the Pt–C (*circle line*) and N-graphene (*square line*) electrodes at 0.4 V in air-saturated 0.1 M KOH. The *arrow* indicates the addition of 2 % (w/w) methanol into the air-saturated electrochemical cell (reproduced with permission [37])

It was flexible and transparent, consisting of only single or a few layers of graphene nanosheets. More importantly, this N-graphene was demonstrated to act as a metal-free electrode with a much better electrocatalytic activity, long-term operation stability, and tolerance to crossover effect than platinum for oxygen reduction via a four-electron pathway in alkaline fuel cells. In addition, Shao et al. [38] also synthesized nitrogen-doped graphene (N-graphene) by exposing graphene to nitrogen plasma. It was found that N-graphene exhibited higher ORR activity than Pt/C without the methanol crossover effect, which indicated the possibility of replacing expensive Pt with low-cost N-graphene. On the other hand, Baek et al. [39] have recently developed a scalable synthetic method for producing high-quality N-graphene films via solution processing of edge-selectively functionalized graphite (EFG), followed by thermal treatment. Typically, EFG was prepared from the reaction between 4-aminobenzoic acid and the "pristine" graphite (P-graphite) to afford 4-aminobenzoyl functionalized graphite. The resultant EFG was readily dispersible in *N*-methyl-2-pyrrolidone (NMP). The 4-aminobenzoyl moieties (4-H_2N-Ph-CO-) at the edges of EFG could act as the in situ feedstock of carbon and nitrogen sources for simultaneous “C welding” and “N doping.” Solution casting of EFG and subsequent heat treatment led to the formation of large-area N-graphene film, which was demonstrated to be efficient metal-free catalysts for ORR in fuel cells.

In addition to nitrogen-doped graphene, sulfur-, iodine-, and phosphorus-doped graphene can also be used as efficient metal-free oxygen reduction electrocatalysts. Yang et al. [40] synthesized sulfur-doped graphene by directly annealing graphene oxide (GO) and benzyl disulfide (BDS) in argon. The sulfur-doped graphene (S-graphene) exhibited excellent ORR catalytic activity, long-term stability, and high methanol tolerance in alkaline medium. Graphene doped with another element of a similar electronegativity as carbon (e.g., selenium; electronegativity, 2.55) showed also a similarly high ORR catalytic activity as S-graphene. Given that sulfur has a close electronegativity to carbon and that the C–S bonds are predominately at the edge or the defect sites, the change of atomic charge distribution for the S-graphene is relatively small with respect to N (B or P)-doped carbon materials. As such, the charge transfer alone cannot explain the observed high ORR electrocatalytic activities for S-/Se-graphene. Nevertheless, the density functional theory (DFT) calculation performed by Zhang et al. [41] indicated that the spin density also plays an important role in determining the ORR catalytic activity, in addition to the charge transfer. Therefore, the spin density was considered to be the dominant factor to regulate the observed ORR activity in the S-/Se-graphene. Yao et al. [42] prepared iodine-doped graphene by annealing graphene oxide and iodine in argon, which exhibited better catalytic activity and long-term stability than a commercial Pt/C catalyst. Phosphorus-doped graphite of a high ORR electrocatalytic activity, long-term stability, and excellent tolerance to crossover effect of methanol in an alkaline medium has also been prepared by pyrolysis of toluene and triphenylphosphine (TPP) [43].

12.2.3 Carbon Nitride

Carbon nitride, a class of carbonaceous material with a very high nitrogen content, is promising for developing metal-free catalyst for ORR. Indeed, Lyth et al. [44] found that carbon nitride materials exhibited a higher ORR catalytic activity in acidic media than their N-free counterparts, though their current density for oxygen reduction was still low. Through uniform incorporation of carbon nitride into a mesoporous carbon to enhance the electron transfer efficiency of carbon nitride, Zheng et al. [45] prepared metal-free carbon nitride@carbon composites that showed a significantly improved oxygen reduction current density for a four-electron ORR process (Fig. 12.4).

Owing to its excellent electrical properties, the 2D graphene sheets are ideal support for carbon nitride. In this context, Feng et al. [46] synthesized graphene-based carbon nitride (G-CN) nanosheets using graphene-based mesoporous silica nanosheets (GM-silica) as a template and ethylenediamine and carbon tetrachloride

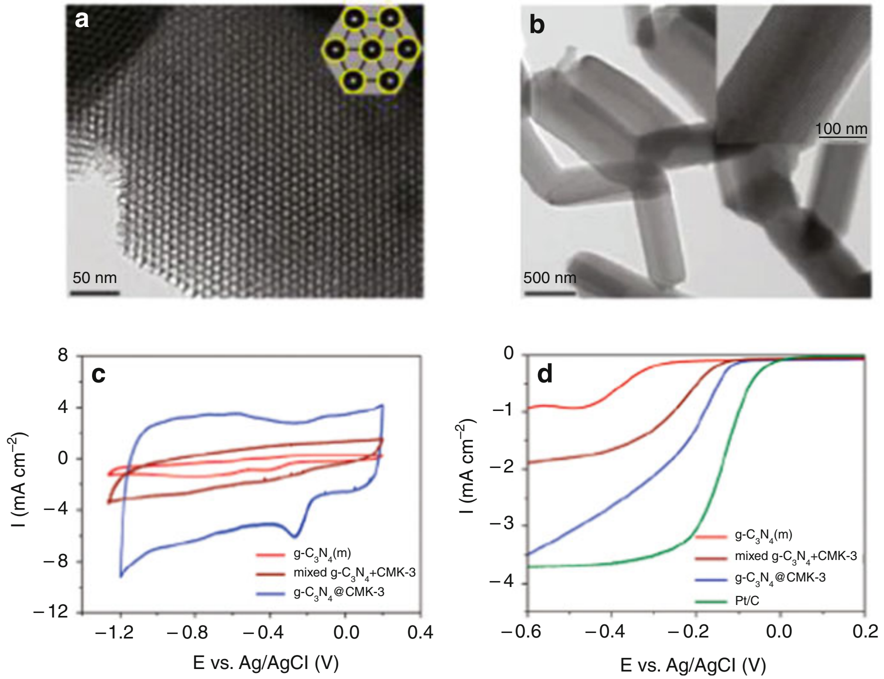

Fig. 12.4 Typical HRTEM images (**a**, **b**) of ordered mesoporous g-C_3N_4@CMK-3 nanorods. Inset in panel (**a**) represents a schematic illustration (*yellow*, g-C_3N_4; *black*, carbon); *inset* in panel (**b**) reveals the ordered mesoporous channels; cyclic voltammograms (**c**) of ORR on various electrocatalysts in O_2-saturated 0.1 M KOH solution; LSV (**d**) of various electrocatalysts on RDE at 1,500 rpm in O_2-saturated 0.1 M KOH solution (reproduced with permission [45])

as CN precursors. The resultant G-CN nanosheets possessed a high nitrogen content, thin thickness, high surface area, and large aspect ratio. Superior to those for pure CN sheets without graphene, the G-CN nanosheets exhibited an excellent ORR electrocatalytic performance, including a high electrocatalytic activity, long-term durability, and high selectivity. Sun et al. [47] also immobilized carbon nitride onto graphene sheets to form carbon nitride/graphene composites in a liquid-phase solution. The composite exhibited an enhanced electrocatalytic activity for ORR and CO tolerance comparable to that of 23 wt. % Pt nanoparticles supported on graphene sheets. These authors attributed the observed high ORR activity of the carbon–nitrogen system to the high electron affinity of nitrogen atoms, which induced a high positive charge density on the adjoining carbon atoms. Theoretical calculations showed that the barrier to oxygen reduction on a carbon atom can be reduced in the presence of an adjacent nitrogen atom. The porosity of the catalytic layer in fuel cells is also critical for maximizing the accessibility of catalysts to proton exchange ionomers, enhancing the transport of reactants, thereby mitigating diffusion polarization. So, a well-defined porous structure would offer a straightforward pathway for transporting reactants and products, respectively, to and out of the catalytic center. Recently, Liang et al. [48] prepared macroporous carbon nitride/C with three-dimensionally ordered interconnected structures using silica microspheres as hard templates. The catalytic activity of carbon nitride/C for ORR was evaluated by comparing with commercial Pt/C. It was found that the carbon nitride/C with ordered pores of about 150 nm showed the highest ORR performance, which was comparable to Pt/C in both the limit current and the commencing potential. This carbon nitride/C also exhibited a high tolerance against fuel crossover and excellent durability.

12.3 Oxygen Reduction Mechanism on Metal-Free Catalysts

Recent research results carried out in many laboratories have confirmed that the doping-induced charge transfer plays a key role in the new metal-free catalytic materials for fuel cell and many other applications [6]. As mentioned above, quantum mechanical calculations performed by Gong et al. [5] have indicated that N doping of CNTs could induce a relatively high positive charge density onto adjacent carbon atoms to weaken the O–O bonding by changing the chemisorption mode of O_2 (Fig. 12.1c), leading to an efficient four-electron ORR process. On this basis, Yang et al. [30] recently extended the doping atoms to include boron with a lower electronegativity than that of carbon and found that the doping-induced charge redistribution, regardless whether the dopants had a higher (as N) or lower (as B) electronegativity than that of carbon, could create charged sites (C^+ or B^+) favorable for O_2 adsorption to facilitate the ORR process. This work suggested further exploration of the metal-free electrocatalysts based on carbon nanotubes doped by atoms (other than N and B) with electronegativities different from that of carbon atom. By extension, Wang et al. [49, 50] have successfully prepared vertically aligned BCN (VA-BCN) nanotubes and BCN graphene containing both nitrogen and boron heteroatoms. Due to a synergetic effect arising from the co-doping of carbon nanotubes with boron and nitrogen, the resultant VA-BCN nanotubes and BCN graphene exhibited higher electrocatalytic activity for ORR in alkaline media than VA-CNTs and graphene doped with either boron or nitrogen only. The observed superior ORR performance with a good methanol and CO tolerance and excellent durability for the VA-BCN nanotube and BCN graphene electrode than the commercial Pt/C electrode opens up avenues for the development of novel efficient metal-free ORR catalysts by co-doping carbon nanotubes with more than one heteroatom of electronegativities different from that of carbon atom.

In addition to the intramolecular charge transfer that imparts ORR electrocatalytic activities to heteroatom-doped carbon nanotubes, graphene, and graphite described above, Wang et al. [51, 52] have recently demonstrated that certain polyelectrolyte (e.g., poly(diallyldimethylammonium chloride) PDDA) adsorbed pure carbon CNTs or graphene (Fig. 12.5) could also act as metal-free electrocatalysts for ORR through the intermolecular charge transfer from the all-carbon CNTs or graphene to the adsorbed PDDA. It is notable that the PDDA

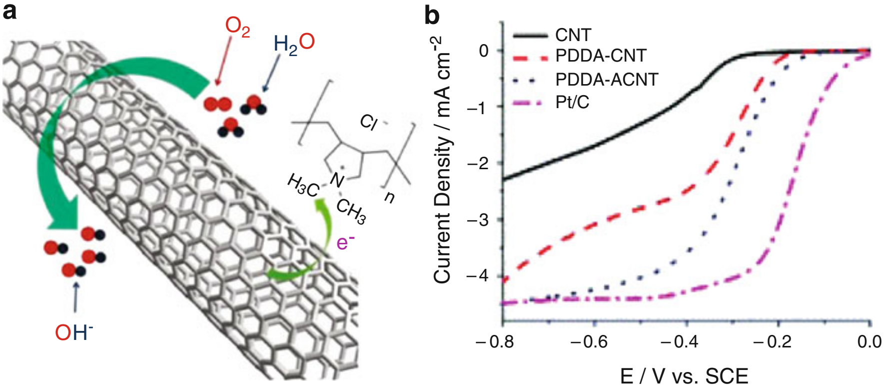

Fig. 12.5 (**a**) Illustration of charge transfer process and oxygen reduction reaction on PDDA-CNT; (**b**) LSV curves of ORR in an O_2-saturated 0.1 M KOH solution at a scan rate of 10 mV s^{-1}. The rotation rate is 1,600 rpm (reproduced with permission [51])

adsorbed vertically aligned CNT electrode possesses remarkable electrocatalytic properties for ORR, comparable to that of commercially available Pt/C electrode. These results clearly indicate that the important role of intermolecular charge transfer to ORR can be applied to carbon nanomaterials in general for the development of various other metal-free efficient ORR catalysts for fuel cell applications, even new catalytic materials for applications beyond fuel cells. However, further study on the catalytic mechanism and kinetics is still needed in order to design and develop polyelectrolyte adsorbed carbon-based catalysts with a desirable activity and durability.

Apart from the aforementioned charge transfer, electron spin is also an important factor influencing oxygen reduction process on metal-free electrocatalysts. Xia et al. [41] concluded that dopant-induced redistribution of spin density and charge density on the graphene strongly affect the formation of the intermediate molecules in ORR, including OOH, or O_2 adsorption, O–O bond break, and water formation. Anderson et al. [53] have also demonstrated that the adsorption bond strengths of adsorbate radicals, H and OOH, exhibit a correlation with the spin density. So, spin density may be regarded as a factor determining positional selectivity of radical adsorption, while charge density determines the attractive force between charged atoms.

12.4 Conclusions

In summary, platinum has been considered as the state-of-the-art catalyst for oxygen reduction in fuel cells. However, its high cost is a barrier to larger-scale production of fuel cells for commercial applications. Doped carbon nanomaterials have been demonstrated to be promising metal-free ORR catalysts to overcome these challenges. Heteroatom doping of carbon nanomaterials to induce the intramolecular charge transfer has been shown to be a promising approach to the development of metal-free, carbon-based catalysts with even higher electrocatalytic activity and better long-term operation stability than that of commercially available platinum-based electrodes for oxygen reduction in fuel cells. Furthermore, intermolecular charge transfer and electron spin density have also been demonstrated to have an effect on the ORR activities of carbon nanomaterials. These findings suggest considerable room for cost-effective preparation of efficient metal-free catalysts for oxygen reduction in fuel cells and even new catalytic materials for applications beyond fuel cells.

Acknowledgments The author is grateful for the financial support from NSF, NSF-NSFC, AFOSR, DoD-MURI, DoD-Army, DOE, AFOSR-Korea NBIT, and UNIST-WCU and would also like to thank colleagues and collaborators for their work cited in this article.

References

1. Borup R, Meyers J, Pivovar B, Kim YS, Mukundan R, Garland N, Myers D, Wilson M, Garzon F, Wood D, Zelenay P, More K, Stroh K, Zawodzinski T, Boncella J, McGrath JE, Inaba M, Miyatake K, Hori M, Ota K, Ogumi Z, Miyata S, Nishikata A, Siroma Z, Uchimoto Y, Yasuda K, Kimijima KI, Iwashita N (2007) Scientific aspects of polymer electrolyte fuel cell durability and degradation. Chem Rev 107(10):3904–3951
2. Zhang S, Shao YY, Yin GP, Lin YH (2010) Electrostatic self-assembly of a Pt-around-Au nanocomposite with high activity towards formic acid oxidation. Angew Chem Int Ed 49(12): 2211–2214
3. Wu G, More KL, Johnston CM, Zelenay P (2011) High-performance electrocatalysts for oxygen reduction derived from polyaniline, iron, and cobalt. Science 332(6028):443–447
4. Lefevre M, Proietti E, Jaouen F, Dodelet JP (2009) Iron-based catalysts with improved oxygen reduction activity in polymer electrolyte fuel cells. Science 324(5923):71–74
5. Gong KP, Du F, Xia ZH, Durstock M, Dai LM (2009) Nitrogen-doped carbon nanotube arrays with high electrocatalytic activity for oxygen reduction. Science 323(5915):760–764
6. Yu D, Nagelli E, Du F, Dai L (2010) Metal-free carbon nanomaterials become more active than metal catalysts and last longer. J Phys Chem Lett 1(14):2165–2173
7. Dai L, Chang DW, Baek J-B, Lu W (2012) Carbon nanomaterials for advanced energy conversion and storage. Small 8(8):1130–1166
8. Zhang S, Shao YY, Yin GP, Lin YH (2009) Stabilization of platinum nanoparticle electrocatalysts for oxygen reduction using poly(diallyldimethylammonium chloride). J Mater Chem 19(42):7995–8001
9. Stamenkovic VR, Fowler B, Mun BS, Wang GF, Ross PN, Lucas CA, Markovic NM (2007) Improved oxygen reduction activity on Pt3Ni(111) via increased surface site availability. Science 315(5811):493–497
10. Chen Z, Higgins D, Yu A, Zhang L, Zhang J (2011) A review on non-precious metal electrocatalysts for PEM fuel cells. Energy Environ Sci 4(9):3167–3192
11. Zhang S, Shao YY, Yin GP, Lin YH (2010) Carbon nanotubes decorated with Pt nanoparticles via electrostatic self-assembly: a highly active oxygen reduction electrocatalyst. J Mater Chem 20(14):2826–2830
12. Liang Y, Li Y, Wang H, Zhou J, Wang J, Regier T, Dai H (2011) Co_3O_4 nanocrystals on graphene as a synergistic catalyst for oxygen reduction reaction. Nat Mater 10(10):780–786

13. Zhang S, Shao Y, Yin G, Lin Y (2011) Self-assembly of Pt nanoparticles on highly graphitized carbon nanotubes as an excellent oxygen-reduction catalyst. Appl Catal B Environ 102(3–4): 372–377
14. Shao YY, Yin GP, Wang HH, Gao YZ, Shi PF (2006) Multi-walled carbon nanotubes based Pt electrodes prepared with in situ ion exchange method for oxygen reduction. J Power Sources 161(1):47–53
15. Wang C, Waje M, Wang X, Tang JM, Haddon RC, Yan YS (2004) Proton exchange membrane fuel cells with carbon nanotube based electrodes. Nano Lett 4(2):345–348
16. Zhang S, Shao YY, Li XH, Nie ZM, Wang Y, Liu J, Yin GP, Lin YH (2010) Low-cost and durable catalyst support for fuel cells: graphite submicronparticles. J Power Sources 195(2): 457–460
17. Geng D, Liu H, Chen Y, Li R, Sun X, Ye S, Knights S (2011) Non-noble metal oxygen reduction electrocatalysts based on carbon nanotubes with controlled nitrogen contents. J Power Sources 196(4):1795–1801
18. Wang Z, Jia R, Zheng J, Zhao J, Li L, Song J, Zhu Z (2011) Nitrogen-promoted self-assembly of N-doped carbon nanotubes and their intrinsic catalysis for oxygen reduction in fuel cells. ACS Nano 5(3):1677–1684
19. Xu X, Jiang S, Hu Z, Liu S (2010) Nitrogen-doped carbon nanotubes: high electrocatalytic activity toward the oxidation of hydrogen peroxide and its application for biosensing. ACS Nano 4(7):4292–4298
20. Shao Y, Sui J, Yin G, Gao Y (2008) Nitrogen-doped carbon nanostructures and their composites as catalytic materials for proton exchange membrane fuel cell. Appl Catal B Environ 79(1):89–99
21. Jin C, Nagaiah TC, Xia W, Spliethoff B, Wang S, Bron M, Schuhmann W, Muhler M (2010) Metal-free and electrocatalytically active nitrogen-doped carbon nanotubes synthesized by coating with polyaniline. Nanoscale 2(6):981–987
22. Maldonado S, Stevenson KJ (2005) Influence of nitrogen doping on oxygen reduction electrocatalysis at carbon nanofiber electrodes. J Phys Chem B 109(10):4707–4716
23. Yang J, Liu D-J, Kariuki NN, Chen LX (2008) Aligned carbon nanotubes with built-in FeN4 active sites for electrocatalytic reduction of oxygen. Chem Commun 3:329–331
24. Tang Y, Allen BL, Kauffman DR, Star A (2009) Electrocatalytic activity of nitrogen-doped carbon nanotube cups. J Am Chem Soc 131(37):13200–13201
25. Yu D, Zhang Q, Dai L (2010) Highly efficient metal-free growth of nitrogen-doped single-walled carbon nanotubes on plasma-etched substrates for oxygen reduction. J Am Chem Soc 132(43):15127–15129
26. Liu RL, Wu DQ, Feng XL, Mullen K (2010) Nitrogen-doped ordered mesoporous graphitic arrays with high electrocatalytic activity for oxygen reduction. Angew Chem Int Ed 49(14): 2565–2569
27. Wang X, Lee JS, Zhu Q, Liu J, Wang Y, Dai S (2010) Ammonia-treated ordered mesoporous carbons as catalytic materials for oxygen reduction reaction. Chem Mater 22(7):2178–2180
28. Chen Z, Higgins D, Tao H, Hsu RS, Chen Z (2009) Highly active nitrogen-doped carbon nanotubes for oxygen reduction reaction in fuel cell applications. J Phys Chem C 113(49):21008–21013
29. Kundu S, Nagaiah TC, Xia W, Wang Y, Dommele SV, Bitter JH, Santa M, Grundmeier G, Bron M, Schuhmann W, Muhler M (2009) Electrocatalytic activity and stability of nitrogen-containing carbon nanotubes in the oxygen reduction reaction. J Phys Chem C 113(32): 14302–14310
30. Yang L, Jiang S, Zhao Y, Zhu L, Chen S, Wang X, Wu Q, Ma J, Ma Y, Hu Z (2011) Boron-doped carbon nanotubes as metal-free electrocatalysts for the oxygen reduction reaction. Angew Chem Int Ed 50(31):7132–7135
31. Liu Z, Peng F, Wang H, Yu H, Tan J, Zhu L (2011) Novel phosphorus-doped multiwalled nanotubes with high electrocatalytic activity for O_2 reduction in alkaline medium. Catal Commun 16(1):35–38

32. Novoselov KS, Geim AK, Morozov SV, Jiang D, Zhang Y, Dubonos SV, Grigorieva IV, Firsov AA (2004) Electric field effect in atomically thin carbon films. Science 306(5696): 666–669
33. Li XL, Wang XR, Zhang L, Lee SW, Dai HJ (2008) Chemically derived, ultrasmooth graphene nanoribbon semiconductors. Science 319(5867):1229–1232
34. Zhang S, Shao Y, Liao H, Engelhard MH, Yin G, Lin Y (2011) Polyelectrolyte-induced reduction of exfoliated graphite oxide: a facile route to synthesis of soluble graphene nanosheets. ACS Nano 5(3):1785–1791
35. Kou R, Shao YY, Wang DH, Engelhard MH, Kwak JH, Wang J, Viswanathan VV, Wang CM, Lin YH, Wang Y, Aksay IA, Liu J (2009) Enhanced activity and stability of Pt catalysts on functionalized graphene sheets for electrocatalytic oxygen reduction. Electrochem Commun 11(5):954–957
36. Zhang S, Shao Y, Liao H-G, Liu J, Aksay IA, Yin G, Lin Y (2011) Graphene decorated with PtAu alloy nanoparticles: facile synthesis and promising application for formic acid oxidation. Chem Mater 23(5):1079–1081
37. Qu LT, Liu Y, Baek JB, Dai LM (2010) Nitrogen-doped graphene as efficient metal-free electrocatalyst for oxygen reduction in fuel cells. ACS Nano 4(3):1321–1326
38. Shao YY, Zhang S, Engelhard MH, Li GS, Shao GC, Wang Y, Liu J, Aksay IA, Lin YH (2010) Nitrogen-doped graphene and its electrochemical applications. J Mater Chem 20:7491–7496
39. Choi E-K, Jeon I-Y, Bae S-Y, Lee H-J, Shin HS, Dai L, Baek J-B (2010) High-yield exfoliation of three-dimensional graphite into two-dimensional graphene-like sheets. Chem Commun 46(34):6320–6322
40. Yang Z, Yao Z, Li G, Fang G, Nie H, Liu Z, Zhou X, Chen X, Huang S (2011) Sulfur-doped graphene as an efficient metal-free cathode catalyst for oxygen reduction. ACS Nano 6(1): 205–211
41. Zhang L, Xia Z (2011) Mechanisms of oxygen reduction reaction on nitrogen-doped graphene for fuel cells. J Phys Chem C 115(22):11170–11176
42. Yao Z, Nie H, Yang Z, Zhou X, Liu Z, Huang S (2012) Catalyst-free synthesis of iodine-doped graphene via a facile thermal annealing process and its use for electrocatalytic oxygen reduction in an alkaline medium. Chem Commun 48(7):1027–1029
43. Liu Z-W, Peng F, Wang H-J, Yu H, Zheng W-X, Yang J (2011) Phosphorus-doped graphite layers with high electrocatalytic activity for the O_2 reduction in an alkaline medium. Angew Chem Int Ed 50(14):3257–3261
44. Lyth SM, Nabae Y, Moriya S, Kuroki S, Kakimoto M-a, Ozaki J-i, Miyata S (2009) Carbon nitride as a nonprecious catalyst for electrochemical oxygen reduction. J Phys Chem C 113(47):20148–20151
45. Zheng Y, Jiao Y, Chen J, Liu J, Liang J, Du A, Zhang W, Zhu Z, Smith SC, Jaroniec M, Lu GQ, Qiao SZ (2011) Nanoporous graphitic-C3N4@carbon metal-free electrocatalysts for highly efficient oxygen reduction. J Am Chem Soc 133(50):20116–20119
46. Yang S, Feng X, Wang X, Müllen K (2011) Graphene-based carbon nitride nanosheets as efficient metal-free electrocatalysts for oxygen reduction reactions. Angew Chem Int Ed 50(23):5339–5343
47. Sun Y, Li C, Xu Y, Bai H, Yao Z, Shi G (2010) Chemically converted graphene as substrate for immobilizing and enhancing the activity of a polymeric catalyst. Chem Commun 46(26): 4740–4742
48. Liang J, Zheng Y, Chen J, Liu J, Hulicova-Jurcakova D, Jaroniec M, Qiao SZ (2012) Facile oxygen reduction on a three-dimensionally ordered macroporous graphitic C3N4/carbon composite electrocatalyst. Angew Chem Int Ed 51(16):3892–3896
49. Wang S, Iyyamperumal E, Roy A, Xue Y, Yu D, Dai L (2011) Vertically aligned BCN nanotubes as efficient metal-free electrocatalysts for the oxygen reduction reaction: a synergetic effect by Co-doping with boron and nitrogen. Angew Chem Int Ed 50(49):11756–11760

50. Wang S, Zhang L, Xia Z, Roy A, Chang DW, Baek J-B, Dai L (2012) BCN graphene as efficient metal-free electrocatalyst for the oxygen reduction reaction. Angew Chem Int Ed 51(17):4209–4212
51. Wang S, Yu D, Dai L (2011) Polyelectrolyte functionalized carbon nanotubes as efficient metal-free electrocatalysts for oxygen reduction. J Am Chem Soc 133(14):5182–5185
52. Wang S, Yu D, Dai L, Chang DW, Baek J-B (2011) Polyelectrolyte-functionalized graphene as metal-free electrocatalysts for oxygen reduction. ACS Nano 5(8):6202–6209
53. Sidik RA, Anderson AB, Subramanian NP, Kumaraguru SP, Popov BN (2006) O_2 reduction on graphite and nitrogen-doped graphite: experiment and theory. J Phys Chem B 110(4): 1787–1793

Chapter 13
Metal Oxide-Based Compounds as Electrocatalysts for Oxygen Reduction Reaction

Ken-ichiro Ota and Akimitsu Ishihara

Abstract The cathode catalysts for polymer electrolyte fuel cells should have high stability as well as excellent catalytic activity for oxygen reduction reaction (ORR). Group 4 and 5 metal oxide-based compounds have been evaluated as a cathode from the viewpoint of their high catalytic activity and high stability. Although group 4 and 5 metal oxides have high stability even in acidic and oxidative atmosphere, they are almost insulator and have poor ORR activity because they have large bandgaps. It is necessary to modify the surface of the oxides to improve the ORR activity. We have tried the surface modification methods of oxides into four methods: (1) formation of complex oxide layer containing active sites, (2) substitutional doping of nitrogen, (3) creation of oxygen defects without using carbon and nitrogen, and (4) partial oxidation of compounds which include carbon and nitrogen. These modifications were effective to improve the ORR activity of the oxides. The solubility of the oxide-based catalysts in 0.1 M H_2SO_4 at 30°C under atmospheric condition was mostly smaller than that of platinum black, indicating that the oxide-based catalysts had sufficient stability compared to the platinum. The onset potential of various oxide-based cathodes for the ORR in 0.1 M H_2SO_4 at 30°C achieved over 0.97 V vs. a reversible hydrogen electrode. This high onset potential suggests that the quality of the active sites of the oxide-based catalysts is mostly equivalent to that of platinum.

K.-i. Ota (✉) • A. Ishihara
Green Hydrogen Research Center, Yokohama National University, 79-5 Tokiwadai,
Hodogaya-ku, Yokohama 240-8501, Japan
e-mail: ken-ota@ynu.ac.jp; a-ishi@ynu.ac.jp

M. Shao (ed.), *Electrocatalysis in Fuel Cells*, Lecture Notes in Energy 9,
DOI 10.1007/978-1-4471-4911-8_13, © Springer-Verlag London 2013

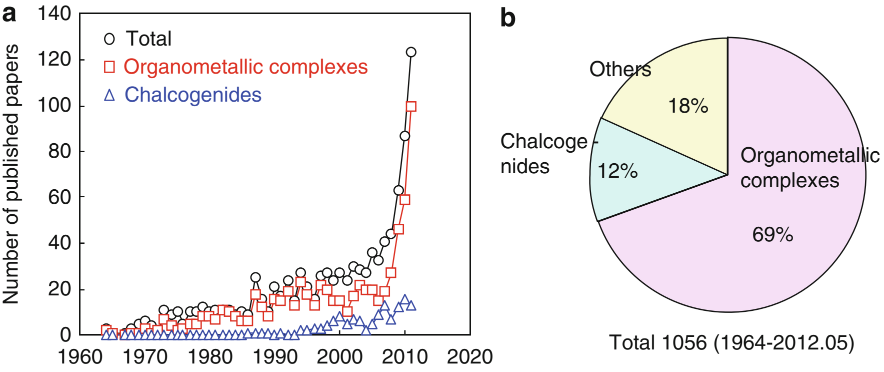

Fig. 13.1 (**a**) Trend of number of the research paper deals with the non-platinum cathode catalysts from 1964. (**b**) Percentage of the paper about the non-precious metal oxygen reduction catalyst in an acid electrolyte

13.1 Introduction

Polymer electrolyte fuel cells (PEFCs) are expected as power sources for residential and transport applications due to their high theoretical efficiency of energy conversion, high power density, and low operating temperature. However, PEFCs have some serious problems to be solved before wide commercialization. In particular, a large overpotential of oxygen reduction reaction (ORR) must be reduced in order to obtain high energy efficiency. Although Pt is generally used as a cathode catalyst in the present PEFCs, its catalytic activity for the ORR is insufficient to obtain a high efficiency [1, 2]. Main issues regarding the Pt usage are its high cost and limited resources. Considering an application to fuel cell vehicles, the natural resource of Pt is insufficient. Therefore, many attempts, such as a higher dispersion of Pt particles and/or an alloying with transition metals, have been made to reduce the Pt usage. However, because the dissolution of Pt particles became a great barrier for long-time operation in recent years, a drastic reduction of the Pt utilization seemed to be difficult. The development of a stable non-platinum catalyst is strongly required [3, 4].

Many studies have been performed to develop non-platinum cathode catalysts for low-temperature fuel cells. Figure 13.1 shows that the trend of number of the research papers deal with the non-platinum cathode catalysts from 1964. Platinum group metals such as Ir, Ru, Pd, Os, and Rh were excluded from the total. However, chalcogenides included some precious metals, that is, RuMoSe, MoRhS, and so on, as reviewed in Chap. 14. Organometallic complexes [5–8] and chalcogenides [9–13] were popular candidates for an alternative Pt catalyst. Nitrogen-doped carbon catalysts were included in organometallic complexes. In particular, the number of papers about organometallic complexes drastically increased after 2008. Chapters 7–12 reviewed the recent development of organometallic complexes as oxygen reduction catalysts. Approximately 100 papers about organometallic complexes were published in 2011. One thousand and fifty-six papers that

Papers of 1056 dealed with non-Pt catalysts were found from 1964 to 2011. The amount of papers which treated organometallic complexes was 69 % and that of chalcogenides is 12 %. However, we think that these catalysts have neither enough electrocatalytic activity for the ORR nor long-term stability.

We believe that high stability is an essential requirement for a cathode of PEFCs because the cathode catalysts are exposed to an acidic and oxidative atmosphere, that is, a strong corrosive environment. Transition metal nitrides and carbonitrides are used as anticorrosion and coating materials [14–16]. For PEFCs, titanium nitrides and chromium nitrides have been tried to apply to the coating materials of metallic bipolar plates [17, 18]. In addition, some researchers have studied transition metal carbonitrides and nitrides as non-precious cathodes [19–21]. However, the transition metal nitrides and carbonitrides are essentially unstable because oxides are thermochemically stable under O_2 atmosphere. Oxide-based compounds might be superior candidates of platinum substitute from the viewpoint of their stability. In particular, group 4 and 5 metal oxides, which are well known as valve metals, are expected to have high stability even in acid electrolyte. Although group 4 and 5 metal oxides had high stability in acid electrolyte, these oxides were almost insulators. It is difficult to apply the insulators to electrocatalysts, because electrocatalysts must have a sufficient electrical conductivity. In addition, oxygen molecules hardly adsorb on a surface of the perfect oxides. Therefore, group 4 and 5 metal oxides were necessary to be modified to have a definite catalytic activity for the ORR.

On the other hand, because it is not very long since we have started our study on non-precious metal oxide-based cathode, the systematic methodology and strategy of the catalyst design have not been established yet. We have paid attention mostly to the method of the surface modification of the oxides. We classified the surface modifications, which were performed individually, into four: (1) formation of complex oxide layer containing active sites, (2) substitutional doping of nitrogen, (3) creation of oxygen defects without using carbon and nitrogen, and (4) partial oxidation of compounds including carbon and nitrogen.

In this chapter, first we summarized the investigations about nitrides and carbonitrides as cathode catalysts. Second, the stability of nitrides, carbonitrides, and oxides in acid electrolyte was discussed and introduced the applicability of oxides to support of platinum particles. Then, the necessity of modifications of oxides was described. As mentioned above, the modifications of oxides were classified into four ways, and development of oxide-based cathodes was summarized.

13.2 Transition Metal Nitrides and Carbonitrides as Cathode Catalysts

Azuma et al. have studied the electrochemical properties of transition metal nitrides prepared by a reactive radio-frequency sputtering method such as ZrN [22], NbN [23], CoN [24], TiN, and VN [23]. Electrochemical reduction of oxygen was

Fig. 13.2 Dependence of onset potential of the Fe–C–N and Co–C–N for the ORR on the nitrogen content of the films

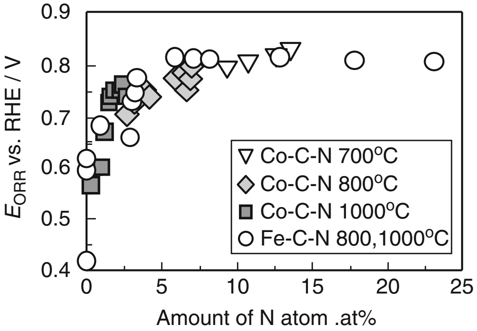

carried out on amorphous cobalt-nitride thin film electrode prepared by the reactive RF sputtering [24]. However, their results were obtained in a neutral solution, not in an acid. Deng et al. showed thin films of amorphous Co–C–N mixture which were co-sputtered in vacuum had good catalyst properties for oxygen reduction in alkaline solution [25, 26].

Yang and coworkers have regularly investigated the applicability of transition metal carbonitrides as cathodes of PEFCs [19, 27, 28]. Their investigations were derived from the research of transition metal complexes [29]. Fe–C–N and Co–C–N thin films prepared by sputtering with metal and carbon target under N_2 were mainly investigated because Fe and Co were thought to act as active sites in macrocyclic complexes. These films were subsequently annealed at higher temperature. Figure 13.2 shows the dependence of onset potential of the Fe–C–N and Co–C–N for the ORR on the nitrogen content of the films. Co–C–N in this figure showed a nanoscale mixture of N-containing graphitic carbon and β-Co. Temperatures in the figure exhibit annealing temperature. In both Fe–C–N and Co–C–N, a sharp increase in the onset potential up to 0.81 V vs. reversible hydrogen electrode (RHE) was observed in 0.1 M $HClO_4$ at room temperature when N content was increased from 0 to 3 atom%. Although N played an important role in the ORR activity, the ORR activity saturated above N content of 3 atom%. The stability of the Fe–C–N films was examined by the acid exposure test. Although Fe dissolved out of Fe–C–N, the activity remained after the acid exposure. Therefore, the dissolved Fe might come from Fe_3C, which did not participate in the ORR activity.

We have examined Cr–C–N and Ta–C–N prepared by the reactive sputtering with heat treatment during the film formation [20, 30]. We found that the Cr–C–N and Ta–C–N with a heat treatment had high stability and the heat treatment during the film formation was effective to enhance the ORR activity. In both cases, the ORR activity increased with the increasing crystallinity of the films. The maximum onset potentials of Cr–C–N and Ta–C–N in 0.1 M H_2SO_4 at 30°C were 0.72 and 0.73 V vs. RHE, respectively. In case of Cr–C–N, both C and N were essential to have an ORR activity. A long-term stability was not examined for these materials.

Zhong et al. prepared molybdenum nitride (Mo_2N) nanoparticles supported on carbon powder. They exhibited the onset potential for ORR of ca. 0.7 V vs. standard

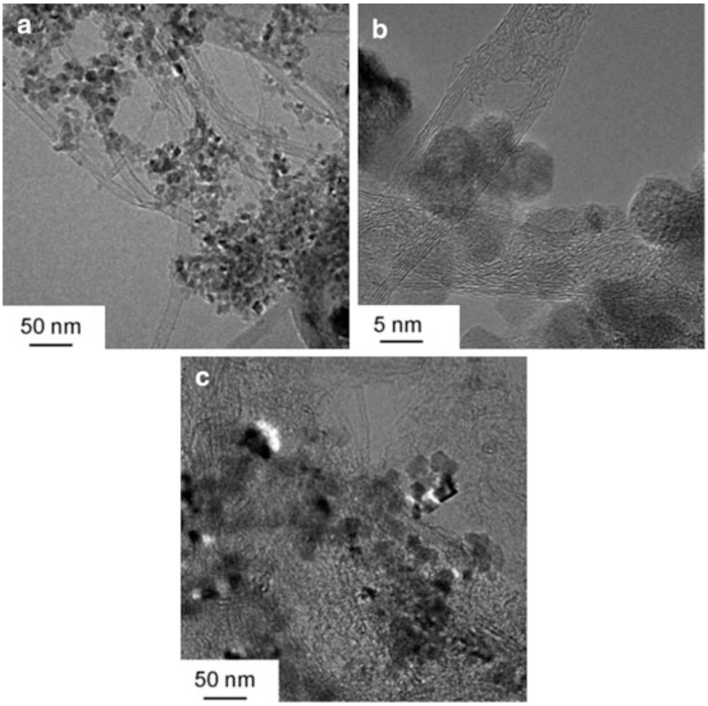

Fig. 13.3 (**a**, **b**) Transmission electron micrographs of a composite of nano-TiN/FWCNT with a TiN/FWCNT weight ratio of 50:1 and (**c**) 2.5:1 (reproduced from [32])

hydrogen electrode (SHE) in 0.5 M H_2SO_4 at room temperature. A single cell test using the Mo_2N/C cathode was performed, and no remarkable deterioration in performance was observed throughout the cell test of 60 h [21]. Xia et al. prepared MoN/C prepared by heat-treating carbon-supported molybdenum tetraphenylporphyrin in a flow of NH_3 [31]. Results of X-ray diffraction (XRD), X-ray photoelectron spectroscopy (XPS), transmission electron microscope (TEM), and energy dispersive X-ray spectroscopy (EDX) showed that the catalytic activity would be attributed to the hexagonal MoN phase with an average particle size of approximately 4 nm. The ORR onset potential was about 0.58 V vs. SHE in 0.5 M H_2SO_4 at room temperature.

Domen et al. successfully demonstrated the direct synthesis of titanium nitride nanoparticles (nano-TiN) on a carbon support using a composite of mesoporous graphitic-C_3N_4 as a rigid template and carbon nanotube [32]. Cyanamide, few-walled carbon nanotubes (FWCNTs), and colloidal nano-silica were mixed, and the mixture was heated at 823 K under flowing N_2. The heat-treated mixture was immersed in 4 M NH_4HF_2 to remove the colloidal silica to prepare the composite of mesoporous graphitic-C_3N_4 and FWCNTs. Then, the composite was mixed with $TiCl_4$ and anhydrous ethanol. And the mixture was heated under flowing N_2 at 1,073 K to obtain the composite of TiN nanoparticles and FWCNTs. Figure 13.3a, b

Table 13.1 Standard Gibbs energy of oxidation reaction of group 4 and 5 metal carbides and nitrides (0.1 MPa, 298.15 K)

Reaction	$\Delta G°$ (kJ mol^{-1})
$TiC(s) + O_2(g) = TiO_2(s) + CO_2(g)$	−1,103
$ZrC(s) + O_2(g) = ZrO_2(s) + CO_2(g)$	−1,241
$2NbC(s) + 9/2O_2(g) = Nb_2O_5 + 2CO_2(g)$	−2,281
$2TaC(s) + 9/2O_2(g) = Ta_2O_5(s) + 2CO_2(g)$	−2,414
$TiN(s) + O_2(g) = TiO_2(s) + 1/2\ N_2(g)$	−580
$ZrN(s) + O_2(g) = ZrO_2(s) + 1/2O_2(g)$	−703
$2NbN(s) + 5/2O_2(g) = Nb_2O_5(s) + N_2(g)$	−1,354
$2TaN(s) + 5/2O_2(g) = Ta_2O_5(s) + N_2(g)$	−1,458

shows the transmission electron micrographs of a composite of nano-TiN/FWCNT with a TiN/FWCNT weight ratio of 50:1 and (c) 2.5:1. The nano-TiN/FWCNT composite with a TiN/FWCNT ratio of 50:1 contains nano-TiN particles of 6 nm in diameter, and FWCNTs were composed of about five walls, 6–10 nm in diameter. The particle size of nano-TiN reflected the original pore size of the mpg-C_3N_4 template (ca. 12 nm). This confirms that it is possible to synthesize nano-TiN particles with a uniform size distribution using the regular confinement of mpg-C_3N_4 pores. The nano-TiN/FWCNT composites showed a high ORR activity with an onset potential of about 0.85 V vs. RHE. This result showed that nano-TiN nanoparticles served as active centers for the ORR. However, nano-TiN itself showed a small ORR current, which can be attributed to the low electrical conductivity between nano-TiN particles. The presence of FWCNTs was essential to achieve an excellent electrocatalytic performance in this synthetic method.

13.3 Stability of Oxides in Acid Electrolyte

Although transition metal carbonitrides have been studied for alternative materials of platinum, these compounds were thermochemically unstable in acid electrolyte under O_2. Table 13.1 shows the standard Gibbs energies of oxidation reactions of group 4 and 5 metal carbides and nitrides [33]. Due to a large decrease in the standard Gibbs energy, transition metal oxides were theoretically more stable than carbonitrides and nitrides [34–36]. Since these transition metal oxides have high theoretical stability, these oxides have been tried to apply to a new high oxidation-resistant support of platinum particles. In the present PEFCs, carbon-supported Pt or Pt-alloy electrocatalysts are widely used. Carbon supports such as carbon blacks have a relatively high electronic conductivity, a chemical stability in an acidic medium, and a high surface area which is suitable for dispersing nanosized catalyst particles. However, recent investigations have revealed that degradation of the electrocatalysts including carbon supports under the cathode condition led to loss of cell performance during a long-time operation [37]. The carbon corrosion due to oxidation under the cathode condition causes a serious degradation of the electrocatalysts. Metal oxides such as Ti_4O_7 [38], indium tin oxide (ITO) [39], tantalum oxide [40], tungsten oxide [41], SnO_2 [42], and silica nanoparticle [43]

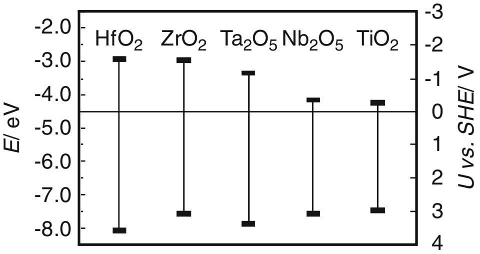

Fig. 13.4 Band structure of group 4 and 5 metal oxides (extracted from [45])

were proposed as high oxidation-resistant supports. For example, a high-potential holding test (1 h holding at 1.0–1.5 V vs. anode) demonstrated that the Pt/Ti_4O_7 catalyst was quite stable against high potential up to 1.5 V [38]. However, few reports have been tried the direct application of these oxides to catalysts.

Oxides of group 4 and 5 elements which are well known as valve metals are highly stable even in an acid media. Although the oxides of group 4 elements such as titanium, zirconium, and hafnium are thermochemically unstable in acid electrolyte [44], they are sufficiently stable kinetically. Figure 13.4 shows the band structure of group 4 and 5 oxides [45]. Since these perfect oxides have wide bandgap as shown in Fig. 13.4, they are almost insulators. Even if they have sufficient stability in acid electrolyte, the materials without ORR activity cannot be applied to a cathode catalyst. The rate of a redox reaction depends on the product of the density of state of electrons in the electrode and that of electrons in the reductant and oxidant particles near Fermi level [46]. For example, because the upper energy level of the valence band in Ta_2O_5 is far from the Fermi level of Ta_2O_5, ca. 0 V vs. SHE [47], the ORR might hardly proceed on Ta_2O_5. The density of state of electrons in the Ta_2O_5 is necessary to be changed. An addition of other elements and/or an introduction of some surface defects affects the density of state of electrons. In this review, the way of changing the electronic structure of oxides was classified into the following four: (1) formation of complex oxide layer containing active sites, (2) substitutional doping of nitrogen, (3) creation of oxygen defects without using carbon and nitrogen, and (4) partial oxidation of compounds including carbon and nitrogen. Almost all the researches on oxide-based cathodes would be classified into these four ways.

13.4 Non-precious Metal Oxide-Based Cathode Catalysts

13.4.1 Stability of Group 4 and 5 Metal Oxide-Based Catalysts

Before the discussion on the catalytic activity for the ORR, the stability of the oxide-based catalysts should be considered. Table 13.2 shows the solubility of oxide-based catalysts prepared by various methods in 0.1 M H_2SO_4 at 30 °C under atmospheric condition [48–50]. The solubility of the platinum black powder

Table 13.2 Solubility of oxide-based catalysts prepared by various methods in 0.1 mol dm^{-3} H_2SO_4 at 30 °C under atmospheric condition

Catalysts	Preparation method	Solubility (μmol dm^{-3})
TaO_xN_y (powder)	Nitridation of Ta_2O_5 with NH_3	0.33
TaO_xN_y (thin film)	Reactive sputtering	0.20
ZrO_xN_y (thin film)	Reactive sputtering	0.041
TiO_{2-x} (plate)	Heat treatment	0.36 (50°C)
Pt black (powder)	Thermal decomposition	0.56

under the same condition was also included for comparison [51]. The solubility of the oxide-based catalysts was smaller than that of platinum black. Therefore, these oxide-based catalysts were chemically stable in acid electrolyte under atmospheric condition. In addition, cyclic voltammograms of these compounds in 0.1 M H_2SO_4 in inert atmosphere under the potential range of PEFC operation reached steady state immediately, and the anodic charge was corresponded to the cathodic one [48–50]. These results show that there is no significant one-sided reaction in this potential range. In addition, no specific oxidation or reduction current peak was observed in the CVs. Group 4 and 5 metal oxide-based compounds would have a sufficient electrochemical stability as well as chemical stability in an acidic media.

13.4.2 Formation of Complex Oxide Layer Containing Active Sites

Tungsten carbide and molybdenum carbide have the platinum-like electronic structure [52] and exhibit platinum-like behavior for hydrogen chemisorption and isomerization of 2, 2-dimethypropane [53]. For this reason, the tungsten carbide and molybdenum carbide have been studied for a fuel cell anode [54–56]. The electrochemical behaviors of transition metal carbides (tungsten carbide and its alloys [57, 58], tantalum carbide [58, 59], titanium carbide [58, 60], and molybdenum carbide [59]) have been reported. These results showed that tungsten and other carbides were unstable at the high-potential region in an acid solution. There might be limited applications of tungsten and other carbides to oxygen reduction catalysts in an acid solution [61, 62].

In recent years, tungsten carbide was reported as a Pt support for PEFC cathode [63, 64]. Nie et al. prepared Pt on a tungsten carbide nanocrystalline support (Pt-WC/C) by the direct reduction of a platinum salt precursor combined with intermittent microwave heating [64]. The Pt-WC/C catalyst showed the onset potential for the ORR of 1.05 V vs. SHE, which was over 150 mV more positive compared to that of a commercial Pt/C. Zhu and coworkers also synthesized tungsten carbide-modified mesoporous carbon with uniform dispersion of Pt nanoparticles [63]. Both an enhanced thermal stability and a good electrochemical stability were observed. It might be necessary to pay attention to the stability of these materials. More details can be found in Chap. 24.

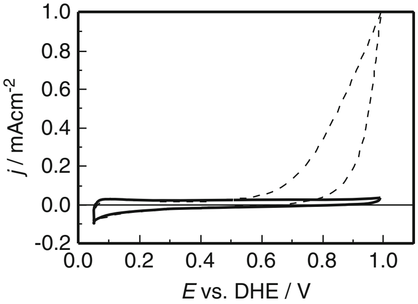

Fig. 13.5 Cyclic voltammograms of pure tungsten carbide and tungsten carbide with tantalum addition thin film catalysts on polymer electrolyte membrane under N_2 atmosphere (reproduced from [65])

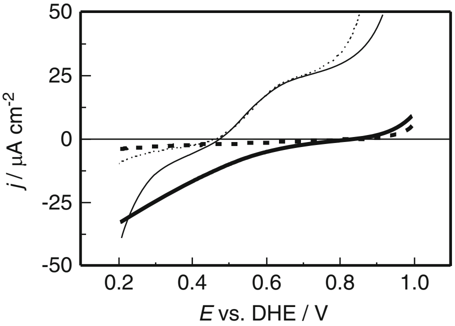

Fig. 13.6 Slow scan voltammograms for tantalum addition to tungsten carbide and pure WC catalysts on polymer electrolyte membrane with a scan rate of 5 mV s^{-1} in N_2 or O_2 atmosphere at 30 °C. *Solid line*, under O_2; *dashed line*, under N_2 (reproduced from [65])

We examined the effect of addition of tantalum to tungsten carbide using thin films prepared by sputtering [65, 66]. Figure 13.5 shows cyclic voltammograms of pure tungsten carbide and tungsten carbide with tantalum addition on a polymer electrolyte under N_2 or O_2 atmosphere. The pure WC catalyst showed a significant anodic current above 0.5 V vs. DHE (dynamic hydrogen electrode). The tungsten in the WC was oxidized to tungsten oxide (WO_3) with the evolution of CO_2. The anodic current was responsible for the formation of WO_3 and CO_2. However, the tantalum addition to tungsten carbide catalyst showed no large anodic current up to 1.0 V vs. DHE. Tungsten and tantalum formed complex hydroxide films, which had high corrosion resistance [67]. The surface of the film was covered by complex hydroxide film. Figure 13.6 shows the slow scan voltammograms for a tantalum-added tungsten carbide and pure tungsten carbide catalysts with a scan rate of 5 mV s^{-1} in N_2 and O_2 atmosphere at 30 °C. Pure WC showed the anodic current even under N_2, suggesting that WC corroded at high-potential region. On the other hand, the WC with Ta addition was stable, and the onset potential for the ORR was observed at about 0.8 V vs. DHE. XPS suggested that the surface of the WC with Ta addition was mainly consisted of complex hydroxide and there existed WC near the surface. Because the thin hydroxide film of W and Ta was formed on WC, the catalytic activity was remained and the stability increased.

Burstein and coworkers reported the electrocatalytic properties of a unique combination of nickel, tantalum, and carbon prepared by DC magnetron sputtering [68]. Amorphous films of mean composition $Ni_{0.33}Ta_{0.41}C_{0.26}$ showed low corrosion rate due to the rapid formation of passive film, which mainly consisted of Ta-oxide. Fortunately, this passive film might be an electron conductor, because the ORR proceeded fluently in 1.5 M H_2SO_4, suggesting that the electron transfer reaction occurred through the passive film. They suggested that any nickel present in the surface must be trapped within the oxide matrix and electrocatalytic nature of the surface was provided by the nickel component. Dahn et al. also investigated sputtered Ta–Ni–C for the ORR activity [69]. Heat treatment after the film formation was effective to enhance the ORR activity. They also suggested that the Ni component played an important role in the electrocatalytic activity of Ta–Ni–C system. However, the onset potential of their best catalysts ($Ta_{0.26}Ni_{0.73}C_{0.01}$ and $Ta_{0.01}Ni_{0.16}C_{0.83}$) was about 0.45 V vs. RHE. They concluded that Ta–Ni–C ternary system prepared by the DC magnetron sputtering method was not a good system for the ORR catalyst. It seemed that the carbon was also important although Burstein and Dahn did not emphasize the effect of the carbon. In addition, long-term durability should be investigated.

13.4.3 Substitutional Doping of Nitrogen

In order to obtain a narrower bandgap of these oxides, the substitutional doping of N might be effective since its *p* states contribute to the bandgap narrowing by mixing with O 2*p* states [70]. The density functional theory calculations show that the valence band is composed mainly of the anion 2*p* orbitals hybridized with metal *d* states. In case of TaON, the upper energy level of the valence band is dominated by N 2*p* states [71].

We have reported that tantalum oxynitride ($TaO_{0.92}N_{1.05}$) powder had some catalytic activity for the ORR [72]. Ta_3N_5 and $TaO_{0.92}N_{1.05}$ were prepared by heating Ta_2O_5 powder in alumina tube reactor under a flow of ammonia gas at 1,123 K for several hours. Figure 13.7a, b shows the potential–current curves of Ta_3N_5 and $TaO_{0.92}N_{1.05}$ under N_2 or O_2 in 0.1 M H_2SO_4 at a scan rate of 5 mV s^{-1}. Ta_3N_5 had poor catalytic activity for the ORR because the ORR current was observed below 0.4 V vs. RHE. On the other hand, the ORR current with $TaO_{0.92}N_{1.05}$ started to flow at 0.8 V vs. RHE. This result indicated that $TaO_{0.92}N_{1.05}$ had definite catalytic activity for the ORR. TaON had been studied for use as visible light-driven photocatalysts [73]. But no trial had been performed to apply to new catalysts for the ORR. We have started the development of the oxide-based catalysts from this research.

Domen et al. evaluated highly dispersed niobium compounds synthesized by a polymerized complex method, followed by nitridation under flowing ammonia [74, 75]. They revealed that the onset potential for the ORR depended on the crystallinity of the powders and Nb^{5+} content on the surface. An addition of barium suppressed the formation of Nb^{4+} on the surface, resulting in a higher density of the highest oxidation state of Nb^{5+}. Therefore, the addition of barium was effective to increase the ORR activity. The onset potential of Ba–Nb–O–N achieved

Fig. 13.7 Potential–current curves of (**a**) Ta_3N_5 and (**b**) $TaO_{0.92}N_{1.05}$ in N_2 or O_2 atmospheres in 0.1 mol dm^{-3} sulfuric acid. Potential was scanned from 1.2 V vs. RHE to 0.2 V with a scan rate of 5 mV s^{-1} (reproduced from [72])

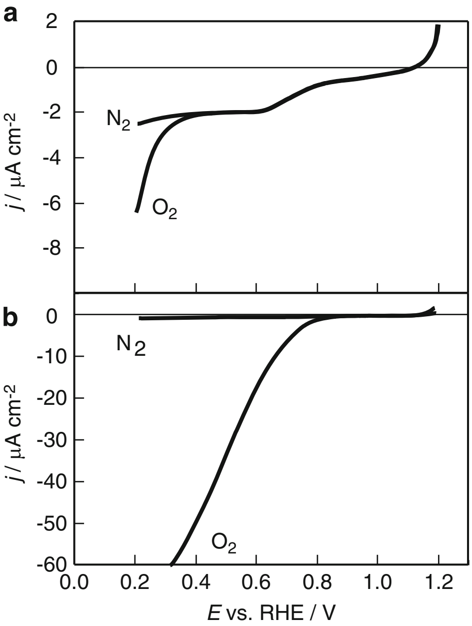

0.77 V vs. SHE in 0.1 mol dm^{-3} H_2SO_4 at room temperature [74]. The effect of the addition of zirconium was also investigated to enhance the ORR activity [76]. The Ba–Nb–Zr–O–N/CB showed higher ORR activity with the ORR onset potential of ca. 0.93 V. The ORR proceeded primarily via a four-electron transfer reaction to water, and the maximum proportion of the hydrogen peroxide formation was less than 12 %. The incorporation of Ba and Nb into Zr^{4+} matrix may have affected the surface structure and/or state of the catalyst, possibly causing the high ORR activity.

They also investigated the effect of the introduction of nitrogen on the ORR activity using vacuum method [77]. Figure 13.8 shows the ORR voltammogram in 0.1 M H_2SO_4 at 303 K for Nb–O/CB and Nb–O–N/CB prepared by arc plasma method. Both Nb–O/CB and Nb–O–N/CB catalysts exhibited ORR activity, with onset potentials for the ORR of 0.78 and 0.86 V vs. RHE, respectively. In addition, the apparent current density was drastically improved by the introduction of nitrogen. XPS measurements suggested that the surface of niobium on the Nb–O–N/CB catalysts was mainly perfectly oxidized (Nb^{5+} species). However, they estimated that the nitrogen incorporation into the oxide matrix might form new active sites for oxygen adsorption and reduction, such as oxygen defects and/or reduced sites.

Zirconium compounds prepared by reactive sputtering under Ar + O_2 + N_2 atmosphere also had some catalytic activity for the ORR in acid electrolyte [49, 78]. We investigated the effect of the gaseous atmosphere during the sputtering on the ORR activity [78]. The thin film XRD and Rutherford backscattering

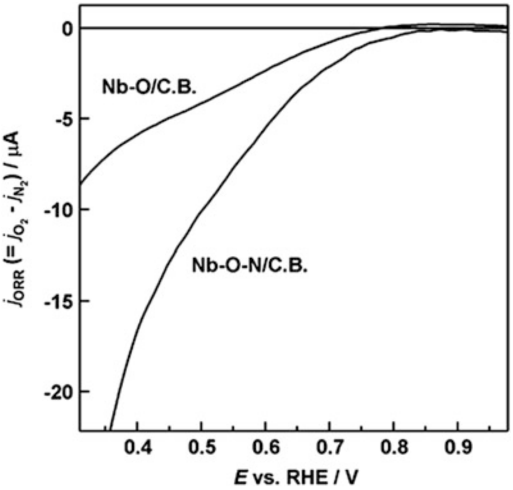

Fig. 13.8 ORR voltammograms in 0.1 M H_2SO_4 for (a) Nb–O/CB and (b) Nb–O–N/CB (10,000 pulses). Sweep rate −5 mV s^{-1} (reproduced from [77])

spectrometry (RBS) showed that the ZrO_xN_y with the highest catalytic activity for the ORR contained a Zr_2ON_2 crystalline structure. The onset potential for the ORR had a maximum of 0.8 V vs. RHE in 0.1 M H_2SO_4 at 30°C.

These results indicate that group 4 and 5 metal oxynitrides such as TaON, Nb–O–N, and Zr_2ON_2 have some catalytic activity for the ORR. Because these pure oxynitrides have wide bandgap, it is predicted that pure oxynitrides might have poor catalytic activity. In case of ZrO_xN_y, the ionization potential of the zirconium compounds with a high ORR activity (5.06 eV) was lower than that of pure oxynitrides (>5.6 eV). TaON prepared by reactive sputtering showed the same behavior [79]. These results indicate that the surface of the films might have some defects which create the donor levels close to the edge level of the conduction band, that is, close to the Fermi level. The electrons in the donor level due to the surface defects probably participate in the ORR. Therefore, not only substitutional doping of N but also creating surface defects was required to enhance the catalytic activity for the ORR. Recently, we also showed that the addition of carbon to TaON was effective to increase the ORR current [80]. The role of surface defects, nitrogen, and carbon in the ORR is necessary to investigate in relation to the active sites of the oxynitrides.

Liu et al. prepared carbon-supported zirconium oxynitride (ZrO_xN_y/C) by ammonolysis of carbon-supported zirconia (ZrO_2/C) at 950°C [81]. The onset potential of the ZrO_xN_y/C for the ORR was 0.7 V vs. RHE, and the four-electron pathway for the ORR was achieved on the surface of the ZrO_xN_y/C. The maximum power density of the single cell using the ZrO_xN_y/C as a cathode at 80°C was 50 mW cm^{-2}, which was much lower than that of a single cell using commercial Pt/C as a cathode. The enhancement of the catalytic activity is required to obtain a superior single cell performance.

Chisaka et al. synthesized carbon-supported hafnium oxynitrides (HfO_xN_y-C) by heating carbon-supported hafnium oxide under NH_3 gas [82]. They revealed that

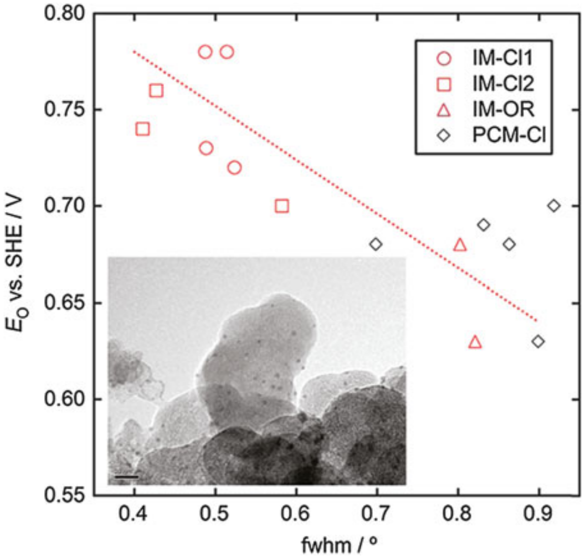

Fig. 13.9 Onset potential vs. full width at half-maximum (E_O—fwhm) curves of HfO_xN_y-C catalysts (reproduced from [82])

the ORR activity of the HfO_xN_y-C catalysts depended on the crystallinity of the Hf_2ON_2. Figure 13.9 shows the onset potential of the ORR vs. full width at half-maximum curves of the HfO_xN_y-C catalysts. The onset potential of the ORR increased with the increasing crystallinity of the Hf_2ON_2 phase in the HfO_xN_y particles. Catalysts prepared via an impregnation method using hydrolysis of hafnium tetrachloride in the dispersion, consisting of nitric acid-refluxed C powders and water, showed (a) the most uniform and smallest HfO_xN_y particle sizes, in the order of a few nanometers, (b) the highest crystallinity, and (c) the highest ORR current and activity levels.

13.4.4 *Creation of Oxygen Defects Without Using Carbon and Nitrogen*

Adsorption of oxygen molecules on the surface was required as the first step to proceed the ORR. Many researches reveal that the presence of surface defect sites is required to adsorb the oxygen molecules on the surface of the oxides such as TiO_2 (110) [83], ZnO [84], NiO (100) [85], $Ce_xZr_{(1-x)}O_2$ [86], V_2O_5 [87], and MoO_3 [88].

Zirconium oxide (ZrO_2), having the highest oxidation state, had a wide bandgap of 4.6 eV, and the upper energy level of the valence band is 3.0 V vs. SHE [45]. In case of stabilized zirconia, the Fermi level was ca. −0.1 V vs. SHE [89], and the Fermi level of the ZrO_2 probably had almost the same value. The ORR hardly proceeds on the ZrO_2 theoretically, just like the Ta_2O_5. An introduction of some surface defects might be necessary to make the adsorption sites of oxygen molecules.

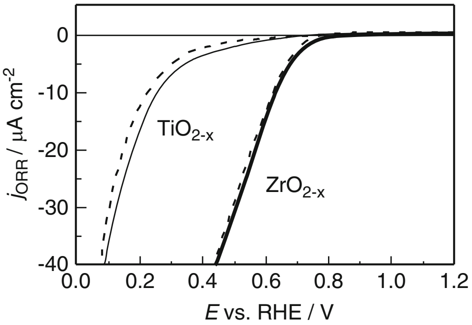

Fig. 13.10 Potential–current curves of ZrO_{2-x} and TiO_{2-x} for ORR in 0.1 mol dm^{-3} H_2SO_4 without 0.1 mol dm^{-3} methanol (*solid line*) and with 0.1 mol dm^{-3} methanol (*dashed line*) (reproduced from [91])

We revealed that ZrO_{2-x} prepared by sputtering with ZrO_2 target under Ar atmosphere had a clear catalytic activity for the ORR [90–91]. The oxygen reduction current of the sputtered ZrO_{2-x} was observed below 0.9 V vs. RHE in 0.1 mol dm^{-3} H_2SO_4 at 30°C. Other metal oxides such as Co_3O_{4-x}, TiO_{2-x}, SnO_{2-x}, and Nb_2O_{5-x} prepared by sputtering also showed ORR activity to some extent. The oxygen reduction activity of the metal oxides was the following order: $ZrO_{2-x} > Co_3O_{4-x} > TiO_{2-x} > SnO_{2-x} > Nb_2O_{5-x}$. In addition, these oxides were inactive for methanol oxidation. Figure 13.10 shows the potential–current curves of ZrO_{2-x} and TiO_{2-x} in 0.1 M H_2SO_4 under O_2 with or without 0.1 M methanol [91]. The presence of methanol did not affect the ORR activity of the oxides. Therefore, these oxides could be a possible candidate substituting the platinum cathode for direct methanol fuel cells.

Okamoto reported the first-principles molecular dynamics simulation of O_2 reduction on ZrO_2 (1 1 1) surface [92]. Density functional calculations suggested that the surface of ZrO_2 was poisoned by OH, which formed through three paths: dissociative adsorption of H_2O, H termination of O atom in ZrO_2 by a proton, and O_2 reduction intermediate. The OH poison indicated the ZrO_2 (1 1 1) surface was inactive for the ORR. However, as the author claimed in the chapter, defects such as O vacancies on the surface may participate in ORR and contribute to a sustainable catalytic cycle. A simulation based on this reaction model might be necessary.

Titanium oxide prepared by the heat treatment of titanium sheets under nitrogen gas including a trace of oxygen had also some catalytic activity for the ORR [50]. It was found that the catalytic activity for ORR on the Ti oxide catalysts increased with the increase of the specific crystalline structure, such as the TiO_2 (rutile) (1 1 0) plane. XPS spectra suggested that the surface of the heat-treated titanium sheets was closed to TiO_2.

An important finding from these studies is that the surface of the oxides with high ORR activity was almost completely oxidized although these oxides were expected to have the defects on the surface. Namely, a metal element should have highest oxidation state to get a high ORR activity [50, 93]. Oxides composed of low oxidation state such as NbO and NbO_2 had lower catalytic activity for the ORR [93], and these oxides were unstable in acidic and oxidative atmosphere. It may be important to form the defects as the oxygen adsorption sites on a surface while the metal is basically maintained by the highest oxidation state.

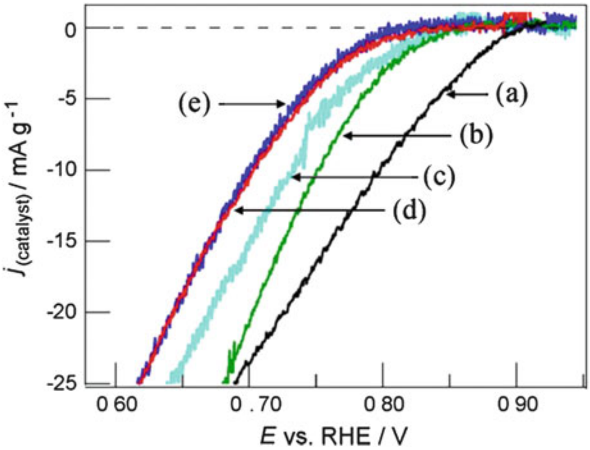

Fig. 13.11 ORR current curves of the TiO_x/Ti, ZrO_x/Ti, TaO_x/Ti, Ti–Zr–O/Ti, and Ti–Ta–O/Ti binary electrodes prepared by dip-coating method at 450°C. The ORR current curves were drawn by deducting the voltammograms in the deaerated $HClO_4$ solution from those of the O_2-saturated solution. Electrode: (a) TiO_x/Ti, (b) $Ti_{0.7}Zr_{0.3}O_x$/Ti, (c) $Ti_{0.3}Ta_{0.7}O_x$/Ti, (d) ZrO_x/Ti, and (e) TaO_x/Ti (reproduced from [97])

Takasu et al. examined RuO_2/Ti, IrO_2/Ti, and IrM (M: Ru, Mo, W, V)O_x/Ti binary oxide electrodes prepared by using a dip-coating method on a Ti substrate [94–96]. $Ir_{0.6}V_{0.4}O_2$/Ti prepared at 450°C had maximum onset potential for the ORR of 0.86–0.90 V vs. RHE. The valency of the iridium ion at the onset potential of ORR was estimated to be 3.78, suggesting that there existed some oxygen vacancies on the surface. They also prepared iridium oxide nanoparticles by the Adams fusion method and concluded that IrO_2, but neither metallic Ir nor the hydrated IrO_2, behaved as an active catalyst for the ORR.

They also prepared non-precious metal oxide catalysts such as titanium oxide, zirconium oxide, tantalum oxide, and some of the corresponding binary oxides using a Ti plate substrate prepared by the dip-coated method at a temperature between 400 and 500°C [97]. Figure 13.11 shows the ORR current curves of the (a) TiO_x/Ti, (b) $Ti_{0.7}Zr_{0.3}O_x$/Ti, (c) $Ti_{0.3}Ta_{0.7}O_x$/Ti, (d) ZrO_x/Ti, and (e) TaO_x/Ti prepared by dip-coating method at 450°C. The ORR activity was presented as mass–current density. Although the TiO_x/Ti electrode gave the highest mass activity among these oxide-coated electrodes, the catalytic activity depended on the surface area of the oxides. Table 13.3 presented the electrochemical characteristics of various oxide-coated electrodes. As presented in Table 13.3, the addition of TiO_x to ZrO_x resulted in an increase in pseudocapacitance, while its addition to TaO_x resulted in a slight decrease in capacitance. The pseudocapacitance of the oxides probably had linear relation with the surface area. A current density for the ORR at 0.7 V vs. RHE divided by the pseudocapacitance of the electrodes, $j_{SA,0.7}$, could be regarded as the surface-specific activity. An evident increase in both $j_{SA,0.7}$ and E_{ORR} by the formation of binary oxide was observed at the$Ti_{0.7}Zr_{0.3}O_x$/Ti electrode. In addition, they prepared tantalum oxide powder containing no nitrogen or carbon by dip-coating method. The tantalum oxide powder (TaO_x) was prepared from the dip-coating solution of the butanolic solution of $TaCl_5$ with heat treatment at 450°C in air. According to XPS measurement, the $Ta4f_{7/2}$ peak from this powder sample appeared at 26.0 eV, suggesting that the valency of the tantalum ions of this oxide

Table 13.3 Electrochemical characteristics of various oxide-coated electrodes

Electrode	E_{ORR} vs. RHE(V)	C_{pc} μF cm^{-2} (geometric)	$j_{\mathrm{geo,0.7}}$ μA cm^{-2} (geometric)	$j_{\mathrm{SA,0.7}}$ mA F^{-1} (oxide)	$j_{\mathrm{m,0.7}}$ mA g^{-1} (oxide)
TiO_x/Ti	0.91	478	3.9	8.2	24
ZrO_x/Ti	0.81	274	2.0	7.3	11
TaO_x/Ti	0.82	284	1.8	6.3	10
$Ti_{0.7}Zr_{0.3}O_x$/Ti	0.86	287	3.6	12.5	21
$Ti_{0.5}Zr_{0.5}O_x$/Ti	0.85	297	1.7	5.7	10
$Ti_{0.3}Zr_{0.7}O_x$/Ti	0.76	373	1.0	2.7	5.6
$Ti_{0.7}Ta_{0.3}O_x$/Ti	0.90	415	2.1	5.1	12
$Ti_{0.5}Ta_{0.5}O_x$/Ti	0.81	196	2.3	11.7	13
$Ti_{0.3}Ta_{0.7}O_x$/Ti	0.84	279	2.7	9.7	17

E_{ORR}, onset potential for the ORR at the cathodic potential sweep; C_{pc}, pseudocapacitance; $j_{\mathrm{geo,0.7}}$, current density for the ORR at 0.7 V vs. RHE per geometric surface area of the electrodes; $j_{\mathrm{SA,0.7}}$, current density for the ORR at 0.7 V vs. RHE divided by the pseudocapacitance of the electrodes; $j_{\mathrm{m,0.7}}$, current density of the oxide-coated electrodes for the ORR at 0.7 V vs. RHE per mass of the oxide loaded on each Ti substrates

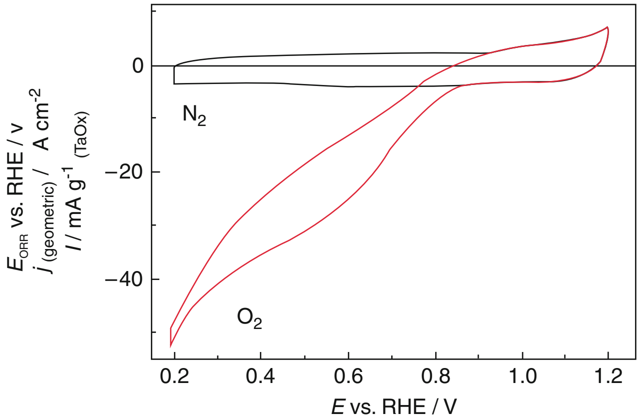

Fig. 13.12 Hydrodynamic voltammograms of the (TaO_x particles + carbon black) electrode rotated at 2,000 rpm with the RDE equipment. Electrode: TaO_x (95 mass%) mixed with carbon black (Vulcan XC-72R; 5 mass%). TaO_x powder was prepared by calcination of the dried dip-coating solution at 450°C for 30 min. Loading amount of TaO_x on the GC (glassy carbon) surface of the working electrode of the RDE, 1 mg cm^{-2}. 0.1 M $HClO_4$, 30°C, 5mV s^{-1}, 2,000 rpm (reproduced from [97])

was lower than that of Ta^{5+} (26.5 eV). Figure 13.12 shows the hydrodynamic voltammogram of the (TaO_x particles; 95 mass% + carbon black; 5 mass%) electrode rotated at 2,000 rpm with the RDE equipment. The TaO_x powder provided high ORR current density; the ORR onset potential and the ORR mass activity at 0.7 V vs. RHE were 0.90 V and 12 mA g^{-1} at 30°C, respectively. These oxides catalysts were prepared at lower temperature such as 400–500°C; therefore, the crystallite size was small and probably contained a large number of lattice defects of oxide ion. A detailed examination on the characteristics of these oxides is necessary to clarify the active site and its stability.

13.4.5 Partial Oxidation of Compounds Including Carbon and Nitrogen

The surface oxidation state would be changed by the control of a partial oxidation of non-oxides. We used carbonitrides of group 4 and 5 elements as starting materials for a partial oxidation [99–104]. We have mainly investigated partially oxidized tantalum carbonitride [98, 101–103]. Tantalum carbonitride consists of TaC and TaN. Both TaC and TaN have the same crystalline structure (rock-salt type) and form a complete solid solution to compose TaC_xN_y. TaC and TaN have a high electrical conductivity at room temperature: TaC 4×10^4 S cm^{-1} and TaN 4–7×10^3 S m^{-1}. The band structure of TaC is characterized by overlapping C 2*p* and Ta 5*d* bands. The Fermi level lies slightly above the minimum of the density of states of the band, indicating that TaC shows metallic behavior. In the case of TaN, the band structure is fundamentally similar to that of TaC. Therefore, the electronic structure of TaC_xN_y changes consecutively with the substitution of C atoms for N atoms. A partial oxidation, that is, the substitution for O atoms, brings an increase in ionic components among the chemical bonding, because the energy difference between the Ta 5*d* and O 2*p* orbitals is higher than that between Ta 5*d* and C or N 2*p*. The electronic state might be controlled by the control of the degree of the oxidation. This partial oxidation method might produce the oxygen defects, which formed the release point of C and/or N, and/or remaining C or N on the surface. Although it is not clear to get high catalytic activity for the ORR, this method was found to be very powerful to prepare powder catalysts with a high ORR activity.

$TaC_{0.58}N_{0.42}$ was heat treated under a trace amount of oxygen gas at 1,000°C. The XRD patterns of the heat-treated specimens showed both Ta_2O_5 and TaC_xN_y peaks. In order to quantify the degree of oxidation of the $TaC_{0.58}N_{0.42}$, the peak intensity at $2\theta = 35°$ of TaC_xN_y (1 0 0), which was expressed as I (TaC_xN_y), and the peak intensity at $2\theta = 28.3°$ of Ta_2O_5 orthorhombic (1 11 0), which was expressed as I (Ta_2O_5), were utilized to calculate the ratio, I (Ta_2O_5)/[I (TaC_xN_y) + I (Ta_2O_5)]. The ratio was designated as the degree of oxidation of the TaC_xN_y and is expressed as DOO (degree of oxidation). Figure 13.13 shows the cross-sectional TEM images of the (a) TaC_xN_y (DOO = 0), (b) DOO = 0.55, (c) DOO = 0.98, and (d) commercial Ta_2O_5 (DOO = 1) [101]. The partially oxidized $TaC_{0.58}N_{0.42}$ powders had a porous structure at the inner part and a fine crystal structure at the outer layer. It was noted that the mixture of the carbon black such as Ketjenblack as

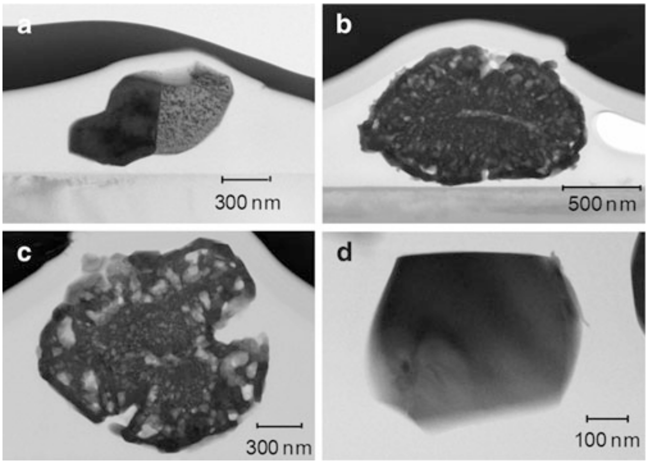

Fig. 13.13 Cross-sectional TEM images of (**a**) $TaC_{0.58}N_{0.42}$ (DOO = 0), (**b**) DOO = 0.55, (**c**) DOO = 0.98, and (**d**) commercial Ta_2O_5 (DOO = 1) (reproduced from [101])

Fig. 13.14 Relationship between DOO and E_{ORR} in 0.1 mol dm^{-3} H_2SO_4 at 30 °C (reproduced from [102])

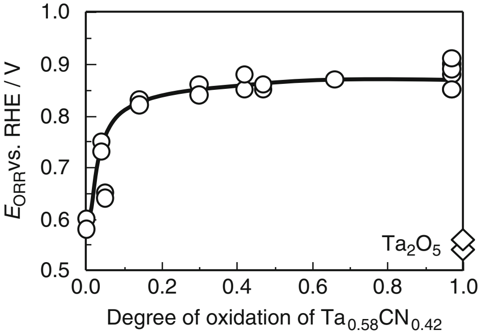

a current collector was required to obtain a sufficient electrical conductivity because the surface of the partially oxidized specimens considerably oxidized and had poor electrical conductivity. Figure 13.14 shows the relationship between the DOO and the onset potential for the ORR (E_{ORR}) in 0.1 M H_2SO_4 at 30 °C [102]. All partially oxidized powders were mixed with 7 wt% of Ketjenblack EC300J. The E_{ORR} abruptly increased with the increasing DOO up to 0.2. The E_{ORR} had high value over 0.85 V vs. RHE above the DOO of 0.3. The maximum of the E_{ORR} is approximately 0.9 V vs. RHE. The starting material (DOO = 0) and the completely oxidized Ta_2O_5 (DOO = 1) had a poor catalytic activity. This result indicated that the active surface immediately formed by a slight partial oxidation and the active surface did not change even the partial oxidation proceeded. An XPS analysis revealed that the surface with a high ORR activity was identified mostly as Ta_2O_5.

Imai et al. analyzed the local structure of the surface Ta-oxide phase of TaC_xN_y/Ta_2O_5 core-shell particles that have a high oxygen reduction activity by

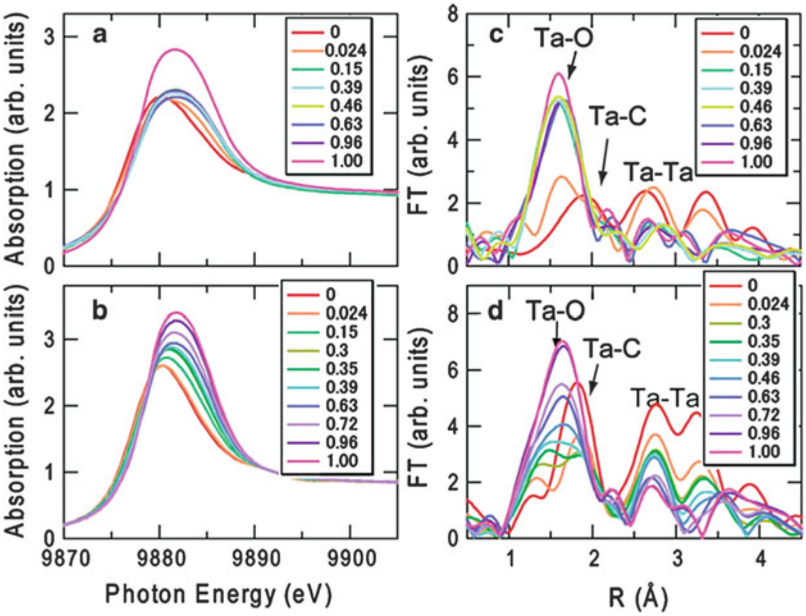

Fig. 13.15 XAS spectra for TaCN/Ta_2O_5 particles. (**a**) CEY-XAS XANES spectra. (**b**) XANES spectra taken in transmission mode. (**c**) Fourier transforms of Ta L3 EXAFS (CEY mode). (**d**) Fourier transforms of Ta L_3 EXAFS (transmission mode). The FT amplitude for CEY-XAS for below DOO = 0.15 is rather small due to the presence of the Ta–C or Ta–N bonds, while in the DOO range from 0.15 to 0.96, the radial structure functions have a Ta_2O_5-like characteristic with a peak near 1.6 Å corresponding to the Ta–O bonds. However, the maximum amplitude is slightly smaller than those of DOO = 1 (stoichiometric Ta_2O_5) (reproduced from [103])

using surface-sensitive conversion-electron-yield X-ray absorption spectroscopy (CEY-XAS), suppressing the contribution from the TaC_xN_y cores [103]. The active Ta–CNO particles were synthesized by slightly oxidizing the TaC_xN_y (approximately 1,000 nm) under a low oxygen pressure of 10^{-5} Pa at 1,273 K, which results in a core-shell structure consisting of a TaC_xN_y core and a Ta_2O_5 shell. Figure 13.15 shows the XAS spectra for TaC_xN_y/Ta_2O_5 particles: (a) CEY-XAS XANES spectra, (b) XANES spectra taken in transmission mode, (c) Fourier transforms of Ta L_3 EXAFS (CEY mode), and (d) Fourier transforms of Ta L_3 EXAFS (transmission mode). The FT amplitude for CEY-XAS for below DOO = 0.15 is rather small due to the presence of the Ta–C or Ta–N bonds, while in the DOO range from 0.15 to 0.96, the radial structure functions have a Ta_2O_5-like characteristic with a peak near 1.6 Å corresponding to the Ta–O bonds. However, the maximum amplitude is slightly smaller than those of DOO = 1 (stoichiometric Ta_2O_5). These results indicate that, below DOO = 0.15, the TaC_xN_y phase remains within ~30 nm (probing depth) below the surface, and thus, the CEY-XAS spectra includes a contribution from the TaC_xN_y cores. Above DOO = 0.15, however, the surface oxide phase grows to a thickness that is larger than the probing depth, and

Table 13.4 Coordination numbers and bond lengths for Ta–O first shells of partially oxidized $TaC_{0.52}N_{0.48}$ and commercial Ta_2O_5

R	*N* (DOO = 1)	*N* (DOO = 0.96)
1.912	2.8	2.4
1.923	0.5	0.5
1.944	1.0	1.0
1.976	0.5	0.5
2.008	0.5	0.5
2.359	1.0	1.0

consequently, CEY-XAS can selectively detect the surface information with the exclusion of any contribution from the cores. Since both the XANES spectra and the radial structure functions (thus, the structural and electronic properties) are identical in the intermediate ORR range ($0.15 < \text{DOO} < 0.96$) regardless of DOO, the electronic and structural differences between such intermediate DOOs (from 0.15 to 0.96) and DOO = 1 might be responsible for the emergence of the ORR activity. Table 13.4 shows coordination numbers and bond lengths for Ta–O first shells. The fitting of the radial structure function for DOO = 0.96 was carried out and reasonably completed by reducing the coordination number for the shortest Ta–O bonds (1.912 Å) from 2.8 to 2.4 with the other parameters left unchanged. This suggests that oxygen vacancies are introduced at an O site at a Ta–O length of approximately 1.912 Å, causing slight lattice expansions (a slight shift in radial structure functions). CEY-XAS analysis revealed that the ORR active Ta-oxide contains oxygen-vacancy sites, most likely at the in-plane threefold sites, providing both oxygen adsorption sites and electron conduction paths. It is interesting that nearly insulating materials, which are usually considered unsuitable for electrocatalysts, could work if they have defects on their surfaces.

The partially oxidized ZrC_xN_y also had superior catalytic activity for the ORR [104]. The onset potential of the appropriate oxidized ZrC_xN_y reached 0.97 V vs. RHE in 0.1 M H_2SO_4 at 30°C. In particular, resource of zirconium oxide, 51×10^3 kton, is three orders of magnitude greater than that of platinum, 39 kton. Therefore, zirconium oxides might be a good candidate for the non-precious metal cathode of PEFCs, considering both its stability and amount of resources.

We have developed the oxide-based non-Pt cathode catalysts [20, 30, 48–50, 65, 66, 72, 78–80, 90, 91, 99–104]. Figure 13.16 shows the annual trend of the onset potential for the ORR of the oxide-based non-Pt cathode catalysts prepared by the Yokohama National University research group. The onset potential increased year by year.

Four modification methods were effective to give the catalytic activity. However, the most important information, that is, the active sites of the catalysts, has not been clarified yet. In order to obtain the oxide-based non-precious cathodes with the same or superior performance as platinum, it is necessary to both enhance the quality of the active sites and increase the quantity of the active sites. Because the oxide-based catalysts had a high stability in acid electrolyte,

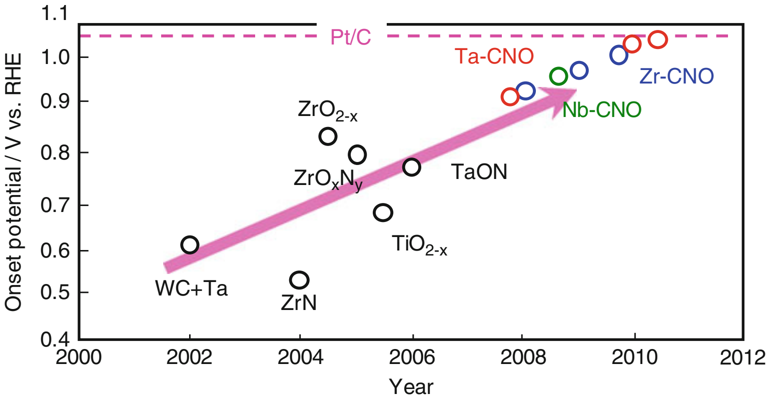

Fig. 13.16 Annual change of onset potential for ORR of oxide-based non-Pt cathode catalysts prepared by Yokohama National University group. Ta–CNO, Nb-CNO, and Zr–CNO exhibit partially oxidized TaC_xN_y, NbC_xN_y, and ZrC_xN_y, respectively

they might be promising substitutes for platinum. More fundamental research is necessary in order to understand the origin of the catalytic activity for the ORR.

13.5 Conclusions

In this chapter we have summarized development of non-precious metal oxide-based cathode for polymer electrolyte fuel cell. Among non-precious metal oxides, group 4 and 5 metal oxides have a high stability even in acid electrolyte. However, group 4 and 5 metal oxides have a large bandgap and are almost insulators. Therefore, it is necessary to modify the surface of the oxides. We classified the surface modification methods, which had been performed individually, into four methods: (1) formation of complex oxide layer containing active sites, (2) substitutional doping of nitrogen, (3) creation of oxygen defects without using carbon and nitrogen, and (4) partial oxidation of compounds including carbon and nitrogen. These modifications were effective to improve the catalytic activity to the oxides with a high stability. The solubility of the group 4 and 5 metal oxide-based catalysts in 0.1 mol dm^{-3} at 30 °C under atmospheric condition was mostly smaller than that of platinum black. This means that our catalysts might be more stable than platinum in acid media. The onset potential of various oxide-based cathodes for the ORR in 0.1 M H_2SO_4 at 30 °C achieved approximately 0.97 V vs. RHE. It is expected that the onset potential increases over 1.0 V by the optimization of the modification. However, the active sites of those catalysts have not been elucidated yet. More fundamental research is necessary in order to understand the origin of the catalytic activity for the ORR and to develop new strategies to get both the quality and quantity of active sites. Because group 4 and 5 metal oxide-based catalysts had a high stability in an acid electrolyte and the ORR activity was enhanced by a surface modification, they might be promising substitutes of platinum for PEFC cathode.

Acknowledgments The authors thank the financial support of the New Energy and Industrial Technology Development Organization (NEDO) for the development of oxide-based non-precious metal cathode for PEFCs.

References

1. Ishihara A, Mitsushima S, Kamiya N, Ota K (2004) Exergy analysis of polymer electrolyte fuel cell systems using methanol. J Power Sources 126:34–40
2. Bernardi DM, Verbrugge MW (1992) A mathematical model of the solid-polymer-electrolyte fuel cell. J Electrochem Soc 139:2477–2491
3. Metal Economics Research Institute (2005) Japan, Report on trends for the supply and demand of platinum group metals for fuel cell systems. p 38 and 351 (in Japanese)
4. Japan Automobile Manufacturers Association, INC. (2005) The Motor Industry of Japan: 42
5. Jasinski R (1964) A New fuel cell cathode catalyst. Nature (London) 201:1212–1213
6. Jahnke H, Schönborn M (1969) Zur Kathodischen reduktion von Sauerstoff an Phthalocyanin-Kohle-Katalysatoren, Comptes Rendus. Troisièmes Journées Internationales d'Etude des Piles à Combustible. Presses Académiques Européennes, Bruxelles, pp 60–65
7. Bezerra CWB, Zhang L, Lee K, Liu H, Marques ALB, Marques EP, Wang H, Zhang J (2008) A review of Fe–N/C and Co–N/C catalysts for the oxygen reduction reaction. Electrochim Acta 53:4937–4951
8. Zagal JH (2003) Chap. 37 Macrocycles, In: Vielstich W, Lamm A, Gasteiger HA (eds) Handbook of fuel cells – fundamentals technology and applications, vol 2. Wiley, West Sussex, pp 545–554
9. Bashyam R, Zelenay P (2006) A class of non-precious metal composite catalysts for fuel cells. Nature (London) 443:63–66
10. Lefevre M, Proietti E, Jaouen F, Dodelet JP (2009) Iron-based catalysts with improved oxygen reduction activity in polymer electrolyte fuel cells. Science 324(5923):71–74
11. Alonso Vante N, Tributsch H (1986) Energy conversion catalysis using semiconducting transition metal cluster compounds. Nature (London) 323(2):431–432
12. Lewera A, Inukai J, Zhou WP, Cao D, Duong HT, Alonso-Vante N, Wieckowski A (2007) Chalcogenide oxygen reduction reaction catalysis: X-ray photoelectron spectroscopy with Ru, Ru/Se and Ru/S samples emersed from aqueous media. Electrochim Acta 52(18): 5759–5765
13. Alonso-Vante N (2003) Chap. 36 Chevrel phases and chalcogenides, In: Vielstich W, Lamm A, Gasteiger HA (eds) Handbook of fuel cells – fundamentals, technology and applications, vol 2. Wiley, West Sussex, pp 534–543
14. Aromaa J, Ronkainen H, Mahiout A, Hannula SP (1999) Identification of factors affecting the aqueous corrosion properties of (Ti, Al) N-coated steel. Surf Coating Technol 49:353–358
15. Chou WJ, Yu GP, Huang JH (2003) Corrosion resistance of ZrN films on AISI 304 stainless steel substrate. Surf Coating Technol 167:59–67
16. Souto RM, Alanyali H (2000) Electrochemical characteristics of steel coated with TiN and TiAlN coatings. Corros Sci 42:2201–2211
17. Surviliene S, Bellozor S, Kurtinaitiene M, Safonov VA (2004) Protective properties of the chromium–titanium carbonitride composite coatings. Surf Coating Technol 176:193–201
18. Tawfik H, Hung Y, Mahajan D (2007) Metal bipolar plates for PEM fuel cell – a review. J Power Sources 163:755–767

19. Yang R, Bonakdarpour A, Bradley Easton E, Stoffyn-Egli P, Dahn JR (2007) Co–C–N oxygen reduction catalysts prepared by combinatorial magnetron sputter deposition. J Electrochem Soc 154:A275–A282
20. Kim JH, Ishihara A, Mitsushima S, Kamiya N, Ota K (2007) Oxygen reduction reaction of Ta-C-N prepared by reactive sputtering with heat treatment. Electrochemistry 75(2):166–168
21. Zhong H, Zhang H, Liu G, Liang Y, Hu J, Yi B (2006) A novel non-noble electrocatalyst for PEM fuel cell based on molybdenum nitride. Electrochem Commun 8:707–712
22. Azuma M, Nakato Y, Tsubomura H (1987) Efficient and stable oxygen evolution of zirconium nitride thin film electrodes prepared by the reactive RF sputtering technique. J Electroanal Chem 220:369–372
23. Azuma M, Nakato Y, Tsubomura H (1988) Oxygen and chlorine evolution on niobium-, zirconium- and other metal-nitride amorphous thin film electrodes prepared by the reactive RF sputtering technique. J Electroanal Chem 255:179–198
24. Azuma M, Kashihara M, Nakato Y, Tsubomura H (1988) Reduction of oxygen to water on cobalt-nitride thin film electrodes prepared by the reactive RF sputtering technique. J Electroanal Chem 250:73–82
25. Deng CZ, Dignam MJ (1998) Sputtered cobalt-carbon-nitrogen thin films as oxygen reduction electrocatalysts. J Electrochem Soc 145:3507–3512
26. Deng CZ, Dignam MJ (1998) Sputtered cobalt-carbon-nitrogen thin films as oxygen reduction electrocatalysts. J Electrochem Soc 145:3513–3520
27. Easton EB, Bonakdarpour A, Yang R, Stevens DA, Dahn JR (2008) Magnetron sputtered Fe–C–N, Fe–C, and C–N based oxygen reduction electrocatalysts. J Electrochem Soc 155: B547–B577
28. Yang R, Stevens K, Dahn JR (2008) Investigation of activity of sputtered transition-metal (TM)–C–N (TM = V, Cr, Mn, Co, Ni) catalysts for oxygen reduction reaction. J Electrochem Soc 155:B79–B91
29. Bonakdarpour A, Lefevre M, Yang R, Jaouen F, Dahn T, Dodelet JP, Dahn JR (2008) Impact of loading in RRDE experiments on Fe–N–C catalysts: two- or four-electron oxygen reduction? Electrochem Solid State Lett 11:B105–B108
30. Kim JH, Ishihara A, Mitsushima S, Kamiya N, Ota K (2007) Oxygen reduction reaction of Cr-C-N prepared using reactive sputtering with heat treatment. Chem Lett 36(4):514–515
31. Xia D, Liu S, Wang Z, Chena G, Zhang L, Zhang L, (Rob) Hui S, Zhang J (2008) Methanol-tolerant MoN electrocatalyst synthesized through heat treatment of molybdenum tetraphenylporphyrin for four-electron oxygen reduction reaction. J Power Sources 177:296–302
32. Isogai S, Ohnishi R, Katayama M, Kubota J, Kim DY, Noda S, Cha D, Takanabe K, Domen K (2012) Composite of TiN nanoparticles and few-walled carbon nanotubes and its application to the electrocatalytic oxygen reduction reaction. Chem Asian J 7:286–289
33. Barin I, Knacke O, Kubaschewski O (1977) Thermochemical properties of inorganic substances: supplement. Springer, Berlin
34. Wiame H, Centeno MA, Picard S, Bastians P, Grange P (1998) Thermal oxidation under oxygen of zirconium nitride studied by XPS, DRIFTS, TG-MS. J Eur Ceram Soc 18:1293–1299
35. Shimada S (2001) Interfacial reaction on oxidation of carbides with formation of carbon. Solid State Ionics 141–142:99–104
36. Shimada S, Johnsson M, Urbonaite S (2004) Thermoanalytical study on oxidation of $TaC_{1-x}N_x$ powders by simultaneous TG-DTA-MS technique. Thermochim Acta 419:143–148
37. Tada T (2003) Chap. 38 High dispersion catalysts including novel carbon supports, In: Vielstich W, Lamm A, Gasteiger HA (eds) Handbook of fuel cells: fundamentals, technology, and applications, vol 3. Wiley, New York, p 481
38. Ioroi T, Senoh H, Samazaki S, Siroma Z, Fujiwara N, Yasuda K (2008) Stability of corrosion-resistant magnéli-phase Ti_4O_7-supported PEMFC catalysts at high potentials. J Electrochem Soc 155:B321–B326
39. Chhina H, Campbell S, Kesler O (2006) An oxidation-resistant indium tin oxide catalyst support for proton exchange membrane fuel cells. J Power Sources 161:893–900

40. Baturina OA, Garsany Y, Zega T, Stroud R, Schull E, Swider-Lyonsa KE (2008) Oxygen reduction reaction on platinum/tantalum oxide electrocatalysts for PEM fuel cells. J Electrochem Soc 155:B1314–B1321
41. Chhina H, Campbell S, Keslerc O (2007) Ex situ evaluation of tungsten oxide as a catalyst support for PEMFCs. J Electrochem Soc 154:B533–B539
42. Sudan Saha M, Li R, Cai M, Suna X (2007) High electrocatalytic activity of platinum nanoparticles on SnO_2 nanowire-based electrodes. Electrochem Solid State Lett 10:B130–B133
43. Seger B, Kongkanand A, Vinodgopal K, Kamat PV (2008) Platinum dispersed on silica nanoparticle as electrocatalyst for PEM fuel cell. J Electroanal Chem 621:198–204
44. Pourbaix M (1974) Atlas of electrochemical equilibria in aqueous solutions (trans: Franklin JA). National Association of Corrosion Engineers, Houston, TX
45. Schmickler W, Schultze JW (1986) Electron Transfer Reactions on Oxide-Covered Metal Electrodes, In: Bockris JO'M, Conway BE, White RE (eds) Modern aspects of electrochemistry, vol 17. Plenum, New York, p 357
46. Sato N (1998) Electrochemistry at metal and semiconductor electrodes. Elsevier, Amsterdam, Chap. 8
47. Chun WJ, Ishikawa A, Fujisawa H, Takata T, Kondo JN, Hara M, Kawai M, Matsumoto Y, Domen K (2003) Conduction and valence band positions of Ta_2O_5, TaON, and Ta_3N_5 by UPS and electrochemical methods. J Phys Chem B 107(8):1798–1803
48. Ishihara A, Doi S, Liu Y, Mitsushima S, Kamiya N, Ota K (2007) Development of zirconium based non-platinum cathode. Mater Sci Forum 539–543:1379–1384
49. Doi S, Ishihara A, Mitsushima S, Kamiya N, Ota K (2007) Zirconium based compounds for new cathode of polymer electrolyte fuel cell. J Electrochem Soc 154(3):B362–B369
50. Kim JH, Ishihara A, Mitsushima S, Kamiya N, Ota K (2007) Catalytic activity of titanium oxide for oxygen reduction reaction as a non-platinum catalyst for PEFC. Electrochim Acta 52(7):2492–2497
51. Mitsushima S, Koizumi Y, Uzuka S, Ota K (2008) Dissolution of platinum in acidic media. Electrochim Acta 54:455–460
52. Houston JE, Laramore GE, Park RL (1974) Surface electronic properties of tungsten, tungsten carbide, and platinum. Science 185:258–260
53. Levy RB, Boudart M (1973) Platinum-like behavior of tungsten carbide in surface catalysis. Science 181:547–549
54. Binder H, Köhling A, Kuhn W, Lindner W, Sandstede G (1969) Tungsten carbide electrodes for fuel cells with acid electrolyte. Nature 224:1299–1300
55. Kawamura G, Okamoto H, Ishikawa A, Kudo T (1987) Tungsten molybdenum carbide for electrocatalytic oxidation of methanol. J Electrochem Soc 134:1653–1658
56. Izhar S, Yoshida M, Nagai M (2009) Characterization and performances of cobalt–tungsten and molybdenum–tungsten carbides as anode catalyst for PEFC. Electrochim Acta 54:1255–1262
57. Yoneyama H, Kaneda M, Tamura H (1973) Electrochemical properties of tungsten carbide in aqueous solutions. Denki Kagaku 41:719–723
58. Bianchi VG, Mazza F, Trasatti S (1964) Anodisches Verhalten und Passivitat einiger interstitieller Verbindungen von Niobium, Tantal, Titan und Wolfram. Z Phys Chem 226:40–58
59. Armstrong RD, Douglas AF (1972) The anodic oxidation of the binary compounds of the transition elements in sulphuric acid. J Appl Electrochem 2:143–149
60. Cowling RD, Hintermann HE (1970) The corrosion of titanium carbide. J Electrochem Soc 117:1447–1449
61. Mazza F, Trasatti S (1963) Tungsten, titanium, and tantalum carbides and titanium nitrides as electrodes in redox systems. J Electrochem Soc 110:847–849
62. Voïnov M, Bühler D, Tannenberger H (1971) Oxygen reduction on tungsten carbide. J Electrochem Soc 118:1137–1138
63. Zhu Q, Zhou S, Wang X, Dai S (2009) Controlled synthesis of mesoporous carbon modified by tungsten carbides as an improved electrocatalyst support for the oxygen reduction reaction. J Power Sources 193:495–500

64. Nie M, Shen PK, Wu M, Wei Z, Meng H (2006) A study of oxygen reduction on improved Pt-WC/C electrocatalysts. J Power Sources 162:173–176
65. Lee K, Ishihara A, Mitsushima S, Kamiya N, Ota K (2004) Stability and electrocatalytic activity for oxygen reduction in WC+Ta catalyst. Electrochim Acta 49(21):3479–3485
66. Ota K, Ishihara A, Mitsushima S, Lee K, Suzuki Y, Horibe N, Nakagawa T, Kamiya N (2005) Improvement of cathode materials for polymer electrolyte fuel cell. J New Mater Electrochem Syst 8:25–35
67. Bhattarai J, Akiyama E, Habazaki H, Kawashima A, Asami K, Hashimoto K (1998) The passivation behavior of sputter-deposited W-Ta alloys in 12M HCl. Corros Sci 40:757–779
68. McIntyre DR, Vossen A, Wilde JR, Burstein GT (2002) Electrocatalytic properties of a nickel–tantalum–carbon alloy in an acidic electrolyte. J Power Sources 108:1–7
69. Yang R, Bonakdarpour A, Dahn JR (2007) Investigation of sputtered Ta-Ni-C as an electrocatalyst for the oxygen reduction reaction. J Electrochem Soc 154:B1–B7
70. Asahi R, Morikawa T, Ohwaki T, Aoki K, Taga Y (2001) Visible-light photocatalysis in nitrogen-doped titanium oxides. Science 293:269–271
71. Fang CM, Orhan E, de Wijs GA, Hintzen HT, de Groot RA, Marchand R, Saillard JY, de With G (2001) The electronic structure of tantalum (oxy)nitrides TaON and Ta_3N_5. J Mater Chem 11:1248–1252
72. Ishihara A, Lee K, Doi S, Mitsushima S, Kamiya N, Hara M, Domen K, Fukuda K, Ota K (2005) Tantalum oxynitride for a novel cathode of PEFC. Electrochem Solid State Lett 8(4):A201–A203
73. Hara M, Hitoki G, Takata T, Kondo JN, Kobayashi H, Domen K (2003) TaON and Ta_3N_5 as new visible light driven photocatalysts. Catal Today 78:555–560
74. Takagaki A, Takahashi Y, Yin F, Takanabe K, Kubota J, Domen K (2009) Highly dispersed niobium catalyst on carbon black by polymerized complex method as PEFC cathode catalyst. J Electrochem Soc 156:B811–B815
75. Chen J, Takanabe K, Ohnishi R, Li D, Okada S, Hatasawa H, Morioka H, Antonietti M, Kubota J, Domen K (2010) Nano-sized TiN on carbon black as an efficient electrocatalyst for the oxygen reduction reaction prepared using an mpg-C_3N_4 template. Chem Commun 46:7492–7494
76. Yin F, Takanabe K, Kubota J, Domen K (2010) Polymerized complex synthesis of niobium and zirconium based electrocatalysts for PEFC cathodes. J Electrochem Soc 157:B240–B244
77. Ohnishi R, Katayama M, Takanabe K, Kubota J, Domen K (2010) Niobium-based catalysts prepared by reactive radio-frequency magnetron sputtering and arc plasma methods as non-noble metal cathode catalysts for polymer electrolyte fuel cells. Electrochim Acta 55:5393–5400
78. Maekawa Y, Ishihara A, Mitsushima S, Ota K (2008) Catalytic activity of zirconium oxynitride prepared by reactive sputtering for ORR in sulfuric acid. Electrochem Solid State Lett 11(7):B109–B112
79. Ishihara A, Doi S, Mitsushima S, Ota K (2008) Tantalum (oxy)nitrides prepared using reactive sputtering for new cathodes of polymer electrolyte fuel cell. Electrochim Acta 53 (16):5442–5450
80. Kikuchi A, Ishihara A, Matsuzawa K, Mitsushima S, Ota K (2009) Tantalum-based compounds prepared by reactive sputtering as a new non-platinum cathode for PEFC. Chem Lett 38(12):1184–1185
81. Liu G, Zhang HM, Wang MR, Zhong HX, Chen J (2007) Preparation, characterization of ZrO_xN_y/C and its application in PEMFC as an electrocatalyst for oxygen reduction. J Power Sources 172:503–510
82. Chisaka M, Suzuki Y, Iijima T, Sakurai Y (2011) Effect of synthesis route on oxygen reduction reaction activity of carbon-supported hafnium oxynitride in acid media. J Phys Chem C 115:20610
83. Pan JM, Maschhoff BL, Diebold U, Madey TE (1992) Interaction of water, oxygen, and hydrogen with $TiO_2(110)$ surfaces having different defect densities. J Vac Sci Technol A 10:2470–2476

84. Lisebigler AL, Lu G, Yates JT Jr (1995) Photocatalysis on TiO_2 surfaces: principles, mechanisms, and selected results. Chem Rev 95:735–758
85. Descorme C, Madier Y, Duprez D (2000) Infrared study of oxygen adsorption and activation on cerium–zirconium mixed oxides. J Catal 196:167–173
86. Blaisdell JM, Kunz AB (1984) Theoretical study of O chemisorption on NiO. Perfect surfaces and cation vacancies. Phys Rev B 29:988–995
87. Göpel W (1978) Reactions of oxygen with ZnO-1010-surfaces. J Vac Sci Technol 15:1298–1310
88. Witko M, Tokarz-Sobieraj R (2004) Surface oxygen in catalysts based on transition metal oxides: what can we learn from cluster DFT calculations. Catal Today 91–92:171–176
89. Vohrer U, Wiemhöfer HD, Göpel W, Van Hassel BA, Burggraaf AJ (1993) Electronic properties of ion-implanted yttria-stabilized zirconia. Solid State Ionics 59:141–149
90. Liu Y, Ishihara A, Mitsushima S, Kamiya N, Ota K (2005) Zirconium oxide for PEFC cathodes. Electrochem Solid State Lett 8(8):A400–A402
91. Liu Y, Ishihara A, Mitsushima S, Kamiya N, Ota K (2007) Transition metal oxides as DMFC cathodes without platinum. J Electrochem Soc 154(7):B664–B669
92. Okamoto Y (2008) First-principles molecular dynamics simulation of O_2 reduction on ZrO_2 (111) surface. Appl Surf Sci 255:3434–3441
93. Ohnishi R, Takahashi Y, Takagaki A, Kubota J, Domen K (2008) Niobium oxides as cathode electrocatalysts for platinum-free polymer electrolyte fuel cells. Chem Lett 37:838–839
94. Takasu Y, Yoshinaga N, Sugumoto W (2008) Oxygen reduction behavior of RuO_2/Ti, IrO_2/Ti and IrM (M: Ru, Mo, W, V) O_x/Ti binary oxide electrodes in a sulfuric acid solution. Electrochem Commun 10:668–672
95. Yoshinaga N, Sugimoto W, Takasu Y (2008) Oxygen reduction behavior of rutile-type iridium oxide in sulfuric acid solution. Electrochim Acta 54:566–573
96. Takasu Y, Oohori K, Yoshinaga N, Sugimoto W (2009) An examination of the oxygen reduction reaction on RuO_2-based oxide coatings formed on titanium substrates. Catal Today 146:248–252
97. Takasu Y, Suzuki M, Yang H, Ohashi T, Sugimoto W (2010) Oxygen reduction characteristics of several valve metal oxide electrodes in $HClO_4$ solution. Electrochim Acta 55:8220–8229
98. Ishihara A, Shibata Y, Mitsushima S, Ota K (2008) Partially oxidized tantalum carbonitrides as a new nonplatinum cathode for PEFC–1–. J Electrochem Soc 155(4):B400–B406
99. Ohgi Y, Ishihara A, Shibata Y, Mitsushima S, Ota K (2008) Catalytic activity of partially oxidized transition metal carbonitrides for oxygen reduction reaction in sulfuric acid. Chem Lett 37(6):608–609
100. Nam KD, Ishihara A, Matsuzawa K, Mitsushima S, Matsumoto M, Imai H, Ota K (2010) Partially oxidized niobium carbonitride as non-platinum cathode for PEFC. Electrochim Acta 55:7290–7297
101. Ishihara A, Tamura M, Matsuzawa K, Mitsushima S, Ota K (2010) Tantalum oxide-based compounds as new non-noble cathodes for polymer electrolyte fuel cell. Electrochim Acta 55 (26):7581–7589
102. Ishihara A, Tamura M, Matsuzawa K, Mitsushima S, Ota K (2011) Partially oxidized tantalum carbonitride as new cathodes without platinum group metals for polymer electrolyte fuel cell. J Fuel Cell Sci Technol 8:031005
103. Imai H, Matsumoto M, Miyazaki T, Fujieda S, Ishihara A, Tamura M, Ota K (2010) Structural defects working as active oxygen-reduction sites in partially oxidized Ta-carbonitride core-shell particles probed by using surface-sensitive conversion-electron-yield x-ray absorption spectroscopy. Appl Phys Lett 96:191905
104. Ohgi Y, Ishihara A, Matsuzawa K, Mitsushima S, Ota K (2010) Zirconium oxide-based compound as new cathode without platinum group metals for PEFC. J Electrochem Soc 157: B885–B891

Chapter 14
Transition Metal Chalcogenides for Oxygen Reduction

Nicolas Alonso-Vante

Abstract Transition metal chalcogenide materials represent nowadays a new family of alternative materials for the cathode oxygen reduction reaction (ORR). During the last decade, the efforts have been concentrated in developing this kind of materials due to their capacity to remain selective and tolerant in the presence of small organics in acid as well as in alkaline media. This is a good advantage regarding their potential use in low power systems working in mixed reactant conditions. Recent efforts have focused on the discovery and/or modification of sensitive catalytic centers. This chapter adds new challenges for the development of such "sophisticated" materials that become popular in recent years, giving a panorama of the state of the art particularly of nanodivided materials.

14.1 Introduction

In the quest of novel materials to be synthesized for the oxygen reduction reaction (ORR), the family of transition metal chalcogenides, first introduced some years ago, represents nowadays a non-negligible activity in groups working on electrochemical energy conversion systems worldwide, as judged by the number of publications shown in Fig. 14.1. The figure clearly shows an important and significant linear evolution in three decades. The catalysts used in the studies depicted in this histogram contain precious and non-precious metal centers partially embedded in/or bonded to chalcogen atoms forming metastable or thermodynamically stable phases. However, the trend analyzed by the author recently [1] clearly shows that materials based on a precious metal such as platinum constitute the hot topic. In a similar plot, studies using platinum-based materials show in fact an exponential increase for the same period of time. This is not the case of chalcogenide materials,

---

N. Alonso-Vante (✉)
IC2MP UMR-CNRS 7285, University of Poitiers, 4 rue Michel Brunet, 86022 Poitiers, France
e-mail: nicolas.alonso.vante@univ-poitiers.fr

M. Shao (ed.), *Electrocatalysis in Fuel Cells*, Lecture Notes in Energy 9,
DOI 10.1007/978-1-4471-4911-8_14,

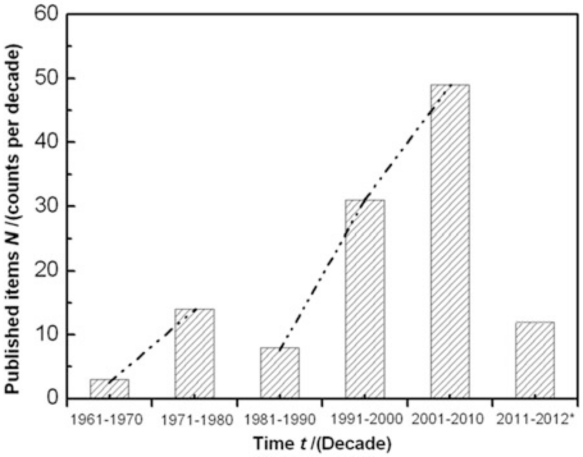

Fig. 14.1 Number of publications devoted to the oxygen reduction on chalcogenides between 1961 and present date (April 10, 2012) based on SciFinder database using oxygen reduction as the keyword

since we observe a gap at the end of the 1980s. Pioneering work was undertaken by Baresel et al. in the 1970s [2] using materials based on cobalt–sulfur and cobalt–nickel–sulfur in a massive form. Nonetheless, the starting point of this line of research can be considered to be the use of a new kind of cluster material, the so-called Chevrel phase [3]. Its basic structure is given by T_6X_8, where T is a transition metal, e.g., essentially Mo, although rhenium has also been identified to form part of a cluster in a semiconductor compound, $Re_6X_8Br_2$ [4], and X a chalcogen: S, Se, or Te. The basic cluster structure, Mo_6Se_8, already showed that the electronic modification of the Mo by selenium in the cluster unit favored the ORR kinetics, in acid medium as compared to pure Mo, which can be considered as a huge cluster. The ORR overpotential in acid medium of the Mo_6Se_8 cluster was very important, ca. 0.9 V [5, 6]. Thereafter, it was found that this electrochemical parameter was also a function of the nature of the embedding chalcogen and the number of valence electrons in the cluster going from 20 to 24 e^- per cluster unit, stressing again the concept of electronic atom modification of the catalytic active site—ligand effect. In other words, the more the ORR overpotential losses reduce to form water, the higher the number of delocalized electrons within the cluster. We can thus consider that Chevrel phase in the specific case of a pseudo-ternary compound, $Mo_4Ru_2Se_8$ [5–7], where the cluster contains 24 electrons [6] constitutes a nice model that bridges the gap between electronic modification of the catalytic center and the design of novel materials using chalcogen atoms to enhance essentially the ORR activity and selectivity in presence of organics.

As aforementioned (see, e.g., [5–9]), the Chevrel phase cluster compounds paved, on one hand, the way to tailor a new chemical route of synthesis in mild conditions using nonaqueous organic solvents [10–13] as well as in aqueous medium [14], and on the other hand, it provided the necessary ingredients to understand the electronic interaction between the chalcogen and the catalytic metal site [15–18]. Since some recent reviews on the topic of chalcogenides have been done by the author in the last 10 years [6, 8, 9, 19, 20], the present chapter will provide an overview of recent

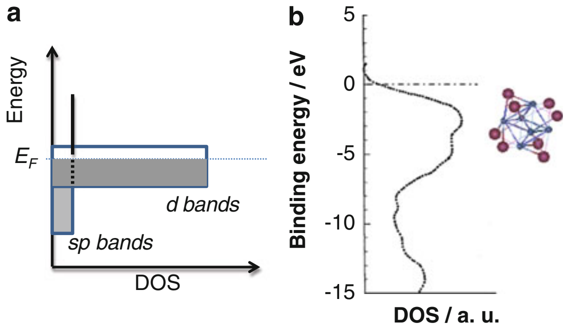

Fig. 14.2 (**a**) Schematics showing the broad sp-band and the narrow d-bands filled up to the Fermi level, E_F. (**b**) The valence band distribution of electrons near the Fermi level of the $Mo_4Ru_2Se_8$ cluster shows the coupling of the sp-bands (Se) with the d-bands (Mo, Ru). An octahedral mixed-metal cluster is shown in the *inset* (figure adapted from ref. [21])

advances on chalcogenides materials, essentially in the nanodivided form (2–5 nm) devoted to the oxygen reduction reaction in acid and in alkaline medium, giving account, nevertheless, of some conceptions that induced the process of physical–chemical concepts which allowed the development of these materials.

14.2 ORR Catalyzed by Transition Metal Chalcogenides

14.2.1 d-Metal-Centered Pathway for ORR

It is believed that the catalytic activity on transition metal chalcogenides takes place through the interaction of the molecular oxygen with the transition metal d-states. The bands are filled with valence electrons of the atoms up to the Fermi level as shown for $Mo_4Ru_2Se_8$ cluster compounds (Fig. 14.2) [21].

It was identified via in situ electrochemical-EXAFS measurements and analysis that the catalytic center in $Mo_4Ru_2Se_8$ was centered at ruthenium atoms [22]. Indeed, the density of states at the Fermi level is higher on ruthenium than on molybdenum clusters: Mo_6Se_8 [23]. Therefore, it was reasonable to imagine that the electron transfer between the cluster, serving as electron reservoir, and adsorbed O_2 is favored to form water via a four-electron charge transfer process. The other idea which was brought up was the fact that during the charge transfer process a change in the cluster volume, ca. 15 %, takes place favoring the bond breaking of the adsorbed oxygen molecule. The interfacial dynamics with the applied electrode potential such as the change of bond distances during the charge transfer exist [22], and it was later further confirmed using nanodivided chalcogenides materials [17, 24, 25].

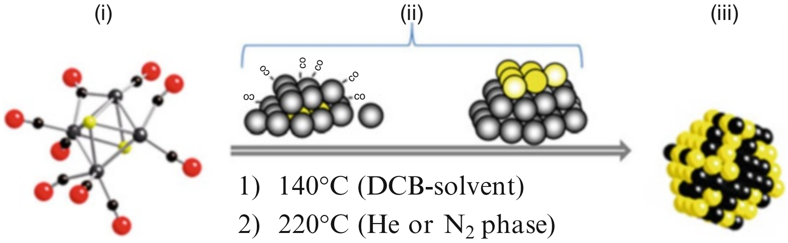

Fig. 14.3 Steps (i) to (iii) leading to the Ru–Se cluster-like nanoparticles by the pyrolysis of $Ru_4Se_2(CO)_3(CO)_8$ in either an organic medium containing 1,2 dichlorobenzene (DCB) or in gas phase in presence of helium or nitrogen. The possible structural change during pyrolysis is schematized by step (ii) in order to obtain a ruthenium core in step (iii)

14.2.2 Materials Design

Based on the knowledge acquired via the Chevrel phase clusters as electron reservoirs, the carbonyl chemical route was developed to design a transition metal chalcogenide. The natural choice was the selection of ruthenium as the metal center and selenium as a chalcogen [10, 26]. After the first synthesis, it took a decade to understand that the novel chalcogenide nanoobject was essentially a metallic core center whose surface was coordinated by a fraction of a monolayer of selenium atoms [27]. The departure from a heterocomplex cluster compound [12] to the nanoparticle is schematized in Fig. 14.3. This synthesis route paved the way to other possibilities of synthesis of these Ru–Se chalcogenides using friendly solvents such as water and less complex chemical precursors such as metallic salts' reduction and thereafter selenization [14, 28] or simply by the modification of ruthenium black nanoparticles [29, 30].

From a theoretical point of view, the understanding of chalcogenide nanoparticles, particularly that of Ru_xSe_y, whose stoichiometry, from the solvent synthesis, always led to $x \approx 2$ and Se ≈ 1, requires (semi-) infinitely extended surfaces and a thermodynamic equilibrium. This length and time scale allowed obtaining some interesting information about the particle environmental conditions using DFT calculations [31]. Indeed, under the condition $\mu_{\mathrm{RuSe2}} > \mu_{\mathrm{Ru}} + 2\mu_{\mathrm{Se}}$, the formation of $RuSe_2$ (pyrite structure) is not favorable, and it can be assumed that all Se atoms will be at or near the surface of the Ru core. This corresponds to the area in which $\Delta\mu_{\mathrm{Ru}} < 0$ (Fig. 14.4). The pyrite structure also favors, under this condition, a Se-rich surface, as shown by the horizontal lines in Fig. 14.4.

Therefore, we can conclude that Ru_xSe_y is a nanostructure that contains Ru *hcp* core clusters whose surface is coordinated to selenium atoms. This statement was later assessed by other workers using various synthetic chemical routes [32–35]. We recall that this kind of surface structure presents a promising activity to enhance the ORR process rate, the tolerance, e.g., for methanol, and to obtain a small fraction of hydrogen peroxide via the four-electron charge transfer to water. The understanding of selenium surface coverage is necessary to get an insight into the energy of the

Fig. 14.4 Surface-free energy diagram (γ) of $RuSe_2$ versus the chemical energy (μ) of Ru, involving low-index surfaces (conf.1 to conf.5). The *darker region* is the existence of Ru_xSe_y cluster-like nanoparticles, given by $\Delta\mu_{Ru} < 0$ (figure adapted from ref. [31])

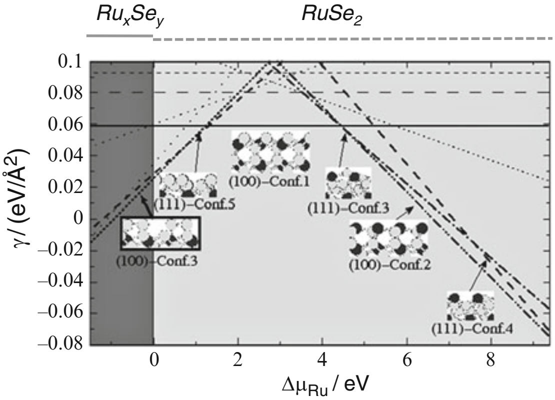

ORR on such nanoobjects, since it is known that the reactivity of transition metal surfaces can be modulated by changes of the local density of electronic states. The strength of covalent O–M bonds is determined by the hybridization of the occupied and non-occupied oxygen and metal states. This depends on the density of *d*-states at the Fermi level. The density of states (DOS) at the Fermi level decreases (shift of the band center position [36]), indicating the weakening of the oxygen–metal bond or other species, such as selenium, as calculated by Stolbov [37] (Fig. 14.5, cf. Fig. 14.2). Another ingredient that induces a surface chemistry of the chalcogen atoms coordinating to ruthenium atoms is the charge transfer of Ru to Se that causes a reduction of the binding energies of O and OH species, in other words chemically stabilized against oxidation. The outcome is that selenium becomes metallic [15].

14.2.3 ORR Trend on Transition Metal Chalcogenides

The reduction of molecular oxygen in acid medium, $O_2 + 4(H^+ + e^-) \rightarrow H_2O$, proceeds only if this molecule adsorbs on the active catalyst surface $\bullet - O_{2ads}$. The fate of this process is further described in terms of intermediate generation, as depicted by the series of reactions (14.2)–(14.5):

$$\bullet + O_2 \rightarrow \bullet - O_{2ads} \tag{14.1}$$

$$\bullet - O_{2ads} + (H^+ + e^-) \rightarrow \bullet - OOH_{ads} \tag{14.2}$$

$$\bullet - OOH_{ads} + (H^+ + e^-) \rightarrow \bullet - O_{ads} + H_2O \tag{14.3}$$

$$\bullet - O_{ads} + (H^+ + e^-) \rightarrow \bullet - OH_{ads} \tag{14.4}$$

$$\bullet - OH_{ads} + (H^+ + e^-) \rightarrow \bullet + H_2O \tag{14.5}$$

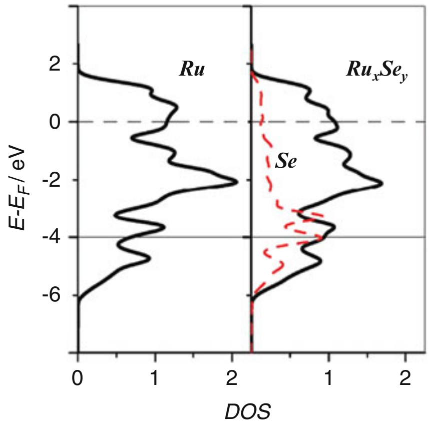

Fig. 14.5 Calculated density of states for Ru (0001) and for a top layer of Ru_xSe_y ($x = 1$; $y = 1/3$), where selenium interacts onto Ru (0001) surface. Selenium is a semiconductor ($E_g = 1.74$ eV). The selenium atoms interacting with the metal center atoms surface becomes metallic [15] (figure adapted from ref. [37])

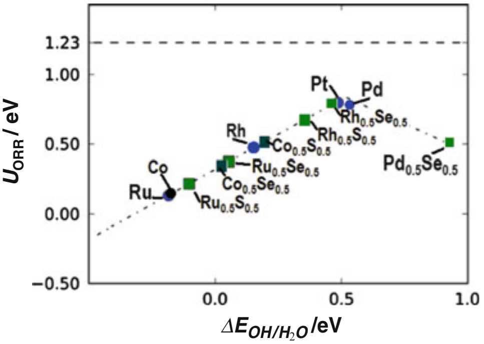

Fig. 14.6 The ORR activity on Ru, Rh, and Co modified by selenium and sulfur (*square symbols*). Pure metals are indicated in *circles*. The Pt represents here the one-metal center of the highest ORR activity. The figure was adapted from ref. [38] to show the trend of the overpotential at similar chalcogen coverage on transition metal centers

For the ORR activity of chalcogenide-modified surfaces, it was identified that in reaction (Eq. 14.5) the transfer of ($H^+ + e^-$) to adsorbed OH is the rate-determining step, and thus the calculated energy $\Delta E_{OH/H2O}$ was used as descriptor for electrocatalytic activity. This is the basis of a recent theoretical work by Tritsaris et al. [38] in rationalizing the electrocatalytic trend of chalcogenide materials (Fig. 14.6). In addition to Ru, other metal centers such as Rh, Ir, Pd, and Co with Se have been synthesized and studied for the ORR [30, 39–48]. The reason for such surface "modification" is to enhance the selectivity of the metal center which otherwise is poisoned by the presence of small organics, such as carbon monoxide, methanol, ethanol, or formic acid. Sulfur has also been reported to modify platinum [49], rhodium [50], and Ru [51, 52]. The rationalization of all the chalcogenide materials up to date synthesized and investigated for the ORR process deserves some analysis.

This figure illustrates, in the first place, that the chalcogens (Se or S) modifying metal center surfaces, on the left side of the volcano diagram, produce an increase in the ORR activity, and the trend is clearly addressed towards the activity of the best catalysts, Pt. On the other hand, and for the same chalcogen coverage, the interaction of the chalcogen seems to depend on the nature of the transition surface atoms, cf. cobalt. This observation deserves further theoretical investigation on

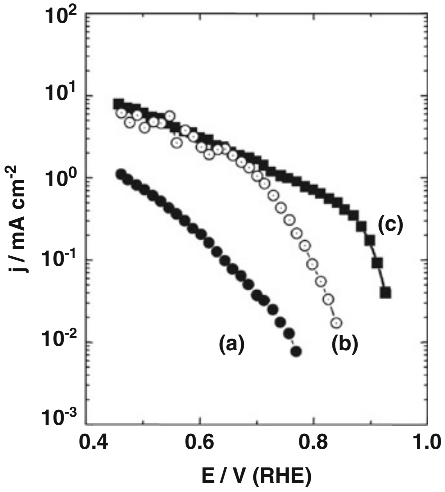

Fig. 14.7 ORR-Tafel plots on Ru_xX_y electrocatalysts in 0.5 M H_2SO_4. (a) Ru_xS_y, (b) Ru_xTe_y, and (c) Ru_xSe_y (figure adapted from ref. [24])

non-precious metals centers; the volcano plot must be extended to other recently developed chalcogenide materials for the same ORR process, such as Pt. In this connection, we notice that a “negative” effect appears on palladium, as seen on the right part of the volcano diagram. This is also expected for the platinum center.

Prior to these theoretical studies, the ruthenium cluster surface modification by chalcogens was done using Se, S, and Te via the carbonyl chemical process in xylene solvent [24].

The electrochemical ORR was performed under constant stirring conditions in sulfuric acid, and data are contrasted in the Tafel plots in Fig. 14.7 on samples deposited in thin layers. It is clearly observed that within the chalcogen series Ru_xSe_y is the most catalytically active compound for oxygen reduction followed by Ru_xTe_y and Ru_xS_y which is the least active. This observation is in agreement with the theoretical results shown in Fig. 14.6. It is noteworthy to mention that the Ru/X ratio is ca. one for Ru_xSe_y and Ru_xS_y and 20 for Ru_xTe_y, meaning that this latter catalyst is essentially a metallic ruthenium cluster coordinated to a small fraction of Te atoms. Summing up, the effect of binding chalcogen clearly shows a link between the reactivity of the nanoparticulate catalyst and its electronic structure [53]. This effect is even more evident when tailoring the surface chemical state of nanoparticulate oxide precursors of ruthenium. The example is illustrated in Fig. 14.8, which undoubtedly encompasses the electronic effect induced by adsorbates onto or on the catalytic center.

Indeed, the oxidized state of ruthenium nanoparticles, curve (a), deposited onto a composite of oxide (TiO_2)-carbon shows a scanty activity. This latter is enhanced by reducing the oxide species (Ru_xO_y), but the kinetics is still limited (curve b), since the same metal center as prepared onto carbon solely shows a significant shift of the half-wave potential towards the positive potential. This experimental evidence shows the reducing effect of ruthenium nanoparticles, which are prone to be easily oxidized when deposited onto the oxides sites of the oxide–carbon composite. This latter sample, when reduced, shows a slight improvement

Fig. 14.8 Oxygen reduction (ORR) curves at 900 rpm on (a) 15 wt % Ru/5 wt % TiO_2/C (as prepared), (b) 15 wt % Ru/5 wt % TiO_2/C (reduced form), (c) 15 wt % Ru/C (as prepared), (d) 15 wt % Ru/C (reduced form), (e) 15 wt % Ru_xSe_y/C, and (f) 15 wt % Ru_xSe_y/5 wt % TiO_2/C in oxygen-saturated 0.5 M H_2SO_4 at 25 °C. Scan rate of 5 mV s^{-1}

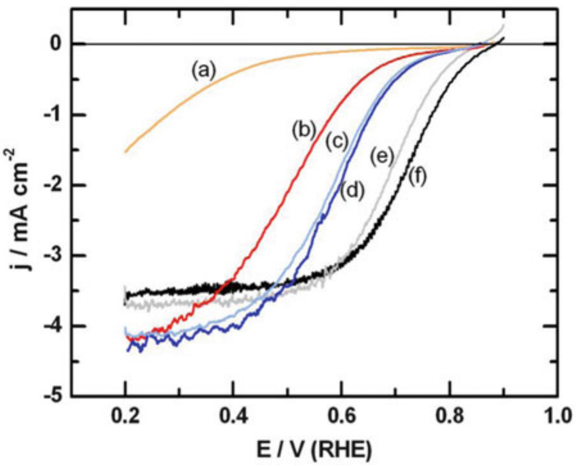

Fig. 14.9 ORR current–potential curves obtained on RDE in O_2-saturated 0.5 M H_2SO_4 solution at 2,500 rpm. (a) $CoSe_2$/C (20 wt %; 44 µg cm^{-2}), (b) Ru_xSe_y/C (20 wt %; 56 µg cm^{-2}), and (c) Pt/C (10 wt %; 56 µg cm^{-2}). Scan rate 5 mV s^{-1}

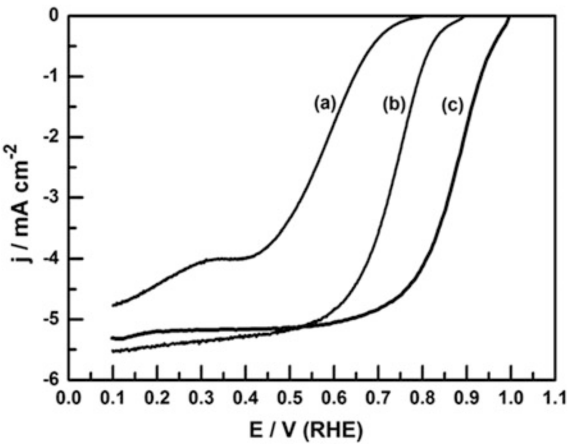

(curve d), testifying of the reducing character of the carbon substrate. Now the role of the selenium becomes evident when comparing curve (e) with (d). The potential shift in the half-wave potential between curves (d) and (e) recalls the electronic change induced by coordinating selenium to ruthenium surface atoms, assessing the activity ORR trend (cf. Fig. 14.6). The phenomenon interesting to stress is the fact that the oxide environment given by the presence of TiO_2 can shift the half-wave potential further to positive values, curve (f). Such a phenomenon has been named a strong metal–support interaction (SMSI) [54]. Unfortunately, the limitation here is the electrochemical oxidation of selenium at potentials higher than 0.9 V/RHE. This phenomenon makes these electrocatalysts, compared to platinum centers, show a further ORR overpotential of -100 mV (Fig. 14.9). Besides the beneficial effect of the chalcogenide coordinating atoms, the nature of the metal center, i.e., Co and Ru, also plays a role in the kinetics enhancement.

Indeed, metallic cobalt atoms show a corrosion potential of -0.277 V/SHE ($Co \rightleftarrows Co^{2+} + 2e^-$) [55]. This negative potential and chemical instability vis-à-vis platinum confers an intrinsic limitation of non-precious metal centers as such to replace precious metal centers. However, recent studies on cobalt diselenide ($CoSe_2$) in orthorhombic and cubic phase (pyrite structure) nanoparticles supported onto carbon [44, 56, 57] showed a remarkable ORR activity and selectivity in acid medium. One typical response is depicted in Fig. 14.9a. Unlike ruthenium, rhodium, platinum, or palladium, cobalt atoms react chemically with selenium to form stable phases: orthorhombic and cubic. The cubic phase showed the highest activity in acid medium [46, 57]. We may outline that the trend on selenides of Co and Ru follows the theoretical calculation depicted in Fig. 14.6.

With respect to the stability and the concomitant increase of the activity of metal centers via the ligand effect modification of such centers, various strategies have been devised; namely, one of them is the substrate effect, which is an important issue on the ORR activity and the durability of catalysts for fuel cells [58–61] (cf. Fig. 14.8, curve f). Within this line of research, various groups [62–64] modified carbon-supported Ru–Se catalysts using WO_3 and observed the enhancement of the catalytic activity towards the ORR because WO_3 can accelerate the decomposition of hydrogen peroxide. Moreover, the ORR multi-electron charge transfer path leading to water formation still remains uncertain. In spite of the fact that two possible mechanisms are proposed: the indirect (via the hydrogen peroxide formation) and the direct one (water formation). However, as discussed by the author in 2010 [65], the ORR actually proceeds via the indirect pathway. An analysis of various systems using nanoparticles supported or arranged in arrays led to the conclusion that the pathway depends on the density and size of the catalytic nanoparticles. The hydrogen production obtained by the rotating ring-disk electrode (RRDE) on various catalysts (chalcogenide or not) as a function of loading confirms this expectation (see Fig. 14.10). It is interesting to recall that, up to date, no spectroscopic method has been developed for an in situ identification of ORR intermediates, Eqs. (14.2)–(14.4). This is one of the main reasons that reaction schemes, based on general kinetics and thermodynamics, have been derived from indirect experimental findings obtained in a majority of the cases with the RDE (Koutecky–Levich analysis) and/or RRDE techniques [66–69]. An analysis of the mol percentage of hydrogen peroxide production via the RRDE technique of various systems is contrasted in Fig. 14.10. This figure shows that the increase of the mass of catalyst per unit surface leads to an increase in the molecular oxygen reduction current with a concomitant decrease in hydrogen peroxide production according to the reaction (Eq. 14.6):

$$H_2O_2 + 2H^+ + 2e^- \rightarrow 2H_2O \tag{14.6}$$

From ring I_R and disk I_D currents' data at a defined electrode potential, the mol % of hydrogen peroxide can be calculated by Eq. (14.7), where N is the collection efficiency.

$$\text{mol}\,\%\,H_2O_2 = \frac{200 \times \, I_R/N}{I_D + \, I_R/N} \tag{14.7}$$

Fig. 14.10 Calculated mol % of H_2O_2 as a function of the specific mass loading at the same ratio of catalyst to carbon at a defined electrode potential. For the ruthenium–selenide system, the data (*filled circles*) were extracted from ref. [70], for o-$CoSe_2$/C (*filled squares*) from ref. [45], for c-$CoSe_2$/C (*half-filled squares*) from ref. [56], and data shown in the *inset* for Fe–C–N (*filled triangles*) from ref. [71]

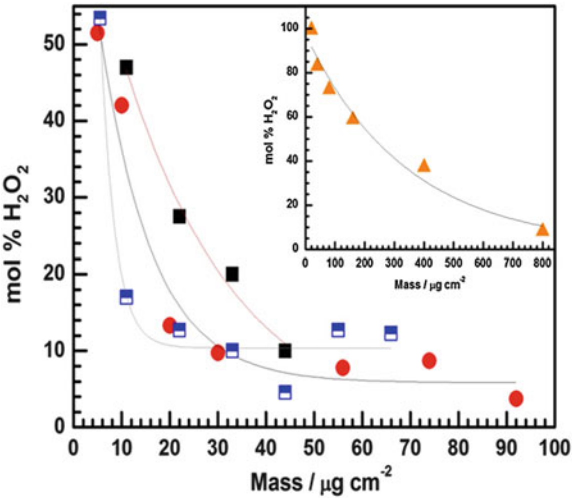

The data depicted in Fig. 14.10 summarize the RRDE results of ORR generated in acid medium on 20 wt % catalyst loading of Ru_xSe_y [70], o-$CoSe_2$ [45], and Fe–C–N [71] and in alkaline medium for c-$CoSe_2$ [56]. It seems clear that keeping the same catalyst/carbon ratio makes the layer thickness through consequent deposition of catalyst thicker. We have to assume that an increase in the number of catalytic sites (or mass surface density) is necessary to produce the higher reaction rate equation (14.6). The amount of hydrogen peroxide production levels off below 10 mol % for the chalcogenide materials either in acid or in alkaline media. This corresponds to a mass loading between 30 and 40 µg cm^{-2}. Within the non-precious metal centers, like $CoSe_2$, Fe–C–N requires a mass loading at least ten times larger than the former one to produce the same amount of hydrogen peroxide (see inset in Fig. 14.10). A similar trend, although with a factor of 5 less for the production of hydrogen peroxide, as compared to chalcogenides, was found from analyzing the literature data of platinum material and summarized in ref. [65]. This variation of the catalytic site density in the release rate of H_2O_2 into the electrolyte has to be taken into account for practical systems, since mass-transport limitations are related to electrode thickness [72].

14.3 The ORR in Alkaline Medium

Materials that are not stable in acid medium have been tested in alkaline media. As examples we can cite the metal macrocycles [73, 74] and transition metal oxides, such as perovskite [75, 76] and spinels [77–79]. This family of materials pertains to inexpensive alternatives, but the remaining stability issues make this kind of objects less appropriate for practical purposes. As exposed above, alternative and

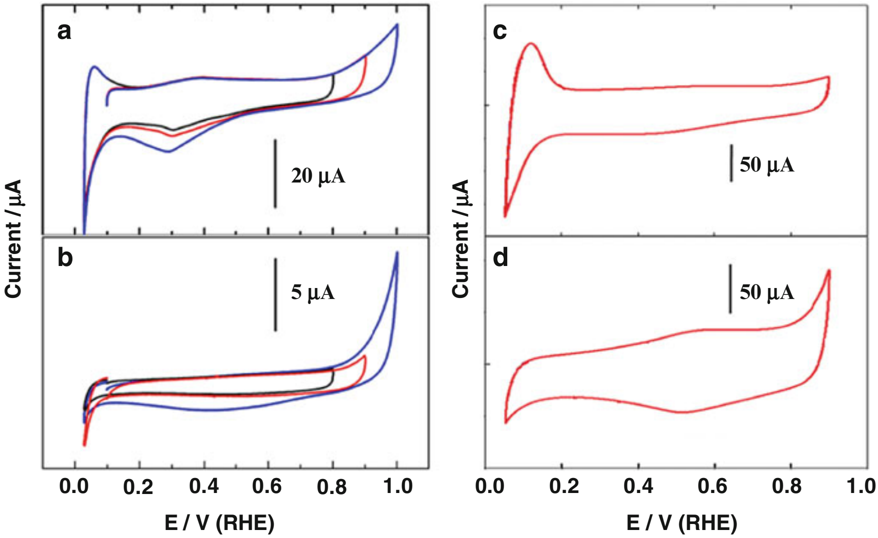

Fig. 14.11 Cyclic voltammetries in deoxygenated electrolytes at 25 °C. *Left* (acid): with variable anodic limits for Ru/C (**a**) and $RuSe_{0.15}/C$ (**b**), scan rate 5 mV s^{-1} in 0.1 M H_2SO_4. Catalyst loading (30 μg) was deposited on Au support. *Right* (alkaline): Ru/C (**c**) and $RuSe_{0.6}/C$ (**d**), scan rate 20 mV s^{-1}in 0.1 M NaOH. Catalyst loading (51 μg cm^{-2}) was deposited on glassy carbon support. Results in alkaline solutions were adapted from ref. [18]

promising ORR cathodes together with fuel crossover tolerance (see Sect. 14.3.3) are the transition metal chalcogenide materials.

14.3.1 The Ruthenium Chalcogenide: Ru_xSe_y

Most studies reported on ruthenium chalcogenides containing Se, S, and Te relate, so far, to the acid medium. It is, however, interesting to compare some features from the cyclic voltammetry results generated in acid as well as in alkaline media for the metal core as well as the selenium coordinated to the metallic core (Fig. 14.11).

The electrochemical signature in acid medium of ruthenium nanoparticles supported onto carbon shown in Fig. 14.11a resembles that of ruthenium's well-defined surface (0001) [80]. Indeed, surface oxide formation starts at ca. 0.2 V/RHE. The cathodic scan shows a broad peak between 0.2 and 0.4 V attributed to the surface oxide reduction. The irreversibility of this peak is enhanced when a more positive anodic potential is explored. In the alkaline counterpart (pH 13) (Fig. 14.11c), this material clearly shows a well-resolved hydrogen desorption peak centered at 0.1 V. Here, one can observe the interaction of OH^- species with the ruthenium surface atoms in the region of 0.3 V/RHE. The reverse scan also reveals the reduction of the ruthenium oxide species centered at ca. 0.4 V. Hence, the signature of Ru nanoparticles looks similar in both media. However, comparison of parts (a) and

(c) with (b), and (d) of Fig. 14.11 shows that modifications of the surface of ruthenium nanoparticles with selenium atoms outcome in drastic changes in the CVs shape in an acid as well as in an alkaline medium. These changes are the following: (1) the double layer shrinks indicating the decrease of the interfacial capacitance, (2) the peaks attributed to OH adsorption/desorption disappear, (3) the anodic peak attributed to the buildup of the Ru surface oxide disappears, and (4) the cathodic peak attributed to the oxide reduction diminishes and shifts to more positive potentials. One can also notice that the anodic limit to avoid coordinated selenium oxidation in acid is about 0.9 V, whereas in alkaline medium this limit seems to be reduced to 0.8 V/RHE. This limit is shifted to a more positive potential by a heat treatment at 500 °C, under argon as reported by Ramaswamy et al. [18]. Nonetheless, the CVs changes observed in both acid and alkaline media for Ru–Se obviously confirm again the surface electronic modification of ruthenium surface atoms discussed in Sect. 14.2.2.

Some differences in the ORR activity in alkaline medium, compared to the acid one, exist. This behavior is contrasted in Fig. 14.12. Even though the figure compares results generated on quite similar electrocatalysts of two laboratories, one can clearly deduce that the ORR kinetics is more facile in alkaline than in acid medium. The features are a shift towards the positive potential, of ca. 50 mV, and the hydrogen peroxide production (upper panel of Fig. 14.12) showing two waves. The wave centered at 0.72 V/RHE is absent in the acid medium [11]. In spite of the amount of generated hydrogen peroxide in alkaline medium, the authors [18] conclude that the number of electrons transferred is higher than 3.6. Up to now the analysis as to the effect of the catalyst mass loading has not been made so far in this alkaline medium for Ru–Se materials, cf. Fig. 14.10. This leaves open the question if an indirect reaction via HO_2^- species to water formation is possible. This depends on the number of the catalyst site density. It is very well known that the alkaline medium facilitates the ORR reaction almost on any electronic conducting material. The reason for this phenomenon must be related to the way the active species interact with the catalytic surface, i.e., putting into play the inner- versus outer-sphere reaction. Certainly, in alkaline media, hydroxyl species adsorb specifically mediating an outer-sphere electron charge transfer to solvated molecular oxygen in order to form the superoxide radical anion, Eq. (14.8), with a release of hydrogen peroxide, Eq. (14.9), as detected by the RRDE technique (cf. Fig. 14.12).

$$\bullet - \mathrm{OH}_{\mathrm{ads}} + \mathrm{O}_2 + 2\mathrm{e}^- \rightarrow \bullet - \mathrm{HO}^-_{2\mathrm{ads}} \tag{14.8}$$

$$\bullet - \mathrm{HO}^-_{2\mathrm{ads}} \rightarrow \mathrm{HO}^-_{2,\mathrm{aq}} \tag{14.9}$$

The reduction of the overpotential in alkaline on chalcogenide ruthenium metal centers is certainly the result of the generation of HO_2^- species, via the outer-sphere reaction mechanism, phenomenon that also occurs on oxide-covered surfaces. This is apparently the rational of the kinetics facility in alkaline media in comparison to the acid medium.

Fig. 14.12 ORR on $RuSe_{0.6}/C$ in oxygen-saturated alkaline electrolyte at 20 mV s^{-1}. Figure adapted from ref. [18]. For comparison the ORR activity of 15 wt % Ru_xSe_y and saturated 0.5 M H_2SO_4 is done at 5 mV s^{-1}. These data were extracted from Fig. 14.8, curve (e). Both sets of data were generated at 900 rpm. The *upper panel* shows the hydrogen peroxide production in alkaline medium

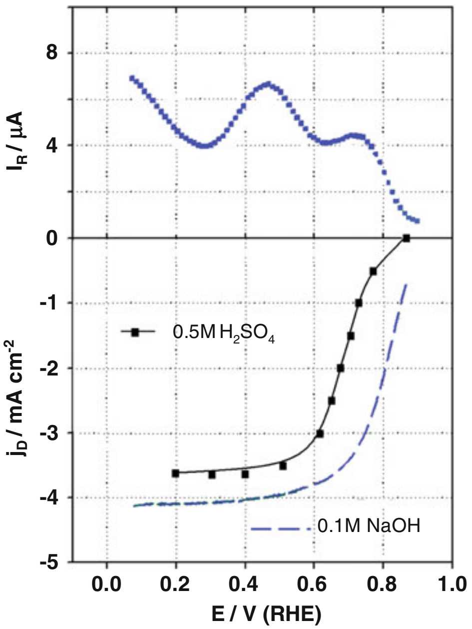

14.3.2 Non-precious Metal Chalcogenide: $CoSe_2$

Our group reviewed the preparation methods of non-precious transition metal (NPTM) chalcogenides based on, e.g., Ni, Co, W, and Fe metal centers [19]. Ruthenium pertains to the platinum group metals (PGM), i.e., high cost and low abundance. Chalcogenide with NPTM can be generated in such a way as to generate smaller particles with a reasonably good particle size distribution in mild conditions. At difference with metal core coordinated chalcogen atoms, such as Ru_xSe_y or Rh_xS_y, NPTM tends to form stable structural phases, e.g., for Co and S: CoS_2, Co_3S_4, and Co_9S_8. We have developed via the carbonyl method cobalt diselenide $CoSe_2$ [44, 46, 57]. This material can indeed be obtained in orthorhombic and cubic phase. The phase structure conversion from orthorhombic to cubic phase takes place after a heat treatment of 400 °C. The cubic (pyrite) phase showed higher ORR activity than the orthorhombic one in acid medium. With a defined catalyst mass loading and structure, the ORR activity was also investigated in alkaline medium, as depicted in Fig. 14.13. One can also clearly deduce that the ORR kinetics is more facile in alkaline than in acid medium. A shift towards the positive potential of ca. 50 mV at $j = 0$ mA cm^{-2} is obtained.

The data represented in Fig. 14.13 show the ORR activity corresponding to an identical number of catalytic sites. As testified by the RRDE results and summarized in Fig. 14.10, the amount of hydrogen peroxide decreases in both media. The number of electrons transferred approaches four. Moreover, since the kinetics in alkaline medium is again facile on the cobalt center of $CoSe_2$, we must

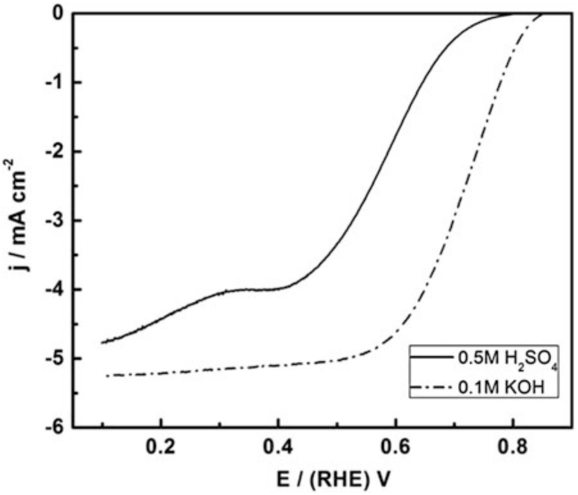

Fig. 14.13 ORR on c-$CoSe_2$/C in oxygen-saturated alkaline electrolyte and in sulfuric acid at 5 mV s^{-1}. Catalyst loading (20 wt %; 44 µg cm^{-2}) was deposited on glassy carbon disks. Both sets of data were generated at 2,500 rpm

arrive at the conclusion that a similar mechanism is taking place as that on Ru_xSe_y material. In other words, whatever the electrolyte medium is, the path for water formation follows a two + two electrons reaction pathway; therefore, reaction (Eq. 14.10) must work in parallel to reaction (Eq. 14.9).

$$\bullet - HO^-_{2ads} + H_2O + 2e^- \rightarrow \bullet + 3OH^- \tag{14.10}$$

The difference between acid and alkaline media is apparently dictated by the inner- versus outer-sphere reaction mechanism for the rate-determining step and therefore influencing the ORR kinetics. In view of the present results on Ru and Co chalcogenides, the advantage that offers using alkaline media seems significant, but it requires materials stability. A test of stability using c-$CoSe_2$ shows a promising expectation [56].

14.3.3 Tolerance to Small Organics

The operation in a “less-clean” environment requires anode or cathode materials with the capacity of being selective to the reaction and tolerant in presence of other species. For example, for a cathode, the conditions are subjected to the presence of gases other than oxygen in the atmosphere, i.e., CO, CO_2, NO_x or SO_x, and O_3 species [81–83]. On the other hand, when the need to use other fuels than hydrogen is necessary, liquid fuels such as methanol, ethanol, and formic acid seem to be good alternatives, though they possess a reasonable energy density, more easily handled, transported, and stored [84–93]. Among PMG, Pt–M alloy catalysts show higher tolerance to the crossover effect of methanol [94], but these non-platinum 3*d* metals (M) in the alloy compositions have less stability under fuel cell operating conditions [95]. On the other hand, S- and Se-modified Pt–metal nanoparticles [49, 96] also display significant improvement of tolerance to methanol and less reduction of ORR activity. However, chalcogenide-modified non-platinum catalysts, Ru_xSe_y [5, 30, 97] and $CoSe_2$ [45, 56, 98], have "complete" tolerance to methanol although these catalysts have a lower ORR activity.

14.4 Concluding Remarks

The intent of this chapter is to give readers a flavor of research into the ORR performed during three decades on transition metal chalcogenide materials. Although not discussed in this chapter, it is likely that the ORR arena is nowadays dominated by the platinum-based catalysts. But the issue of stability and activity as well as tolerance requirements for large-scale fuel cell application is still a matter that requires efforts of materials scientists, and therefore, it remains still a challenging aspect in ORR electrocatalysis.

The activity towards the ORR on chalcogenides compared with the performance of platinum-based materials has still a long way to go since they still present lower activity, although their tolerance to organics is rather impressive. Novel routes of synthesis have been developed that allow a deeper insight into the understanding of the generated materials as well as their reactivity and/or selectivity in presence of small organics. Nonetheless, the various contributions of laboratories all over the world translate efforts in the search of non-precious metal centers that are labile to the corrosion process, but whose centers can be stabilized. One approach to obtain such stabilization was demonstrated herein using chalcogen atoms.

Acknowledgments The author warmly thanks the various contributions made during the years from his students and collaborators.

References

1. Alonso-Vante N (2011) Structure and reactivity of transition metal chalcogenides toward the molecular oxygen reduction reaction. In: Vayenas CG (ed) Interfacial phenomena in electrocatalysis, vol 51, Modern aspects of electrochemistry. Springer, New York, pp 255–300
2. Baresel D, Sarholz W, Scharner P, Schmitz J (1974) Transition metal chalcogenides as oxygen catalysts for fuel cells. Ber Bunsen-Ges 78(6):608–611
3. Alonso-Vante N, Tributsch H (1986) Energy conversion catalysis using semiconducting transition metal cluster compounds. Nature 323(6087):431–432
4. Fischer C, Alonso-Vante N, Fiechter S, Tributsch H, Reck G, Schulz W (1992) Structure and photoelectrochemical properties of semiconducting rhenium cluster chalcogenides: $Re_6X_8Br_2$ ($X = S, Se$). J Alloys Compd 178(1–2):305–314
5. Alonso-Vante N, Schubert B, Tributsch H (1989) Transition metal cluster materials for multi-electron transfer catalysis. Mater Chem Phys 22(3–4):281–307

6. Alonso-Vante N (2003) Chevrel phase and cluster-like chalcogenide materials. In: Vielstich W, Lamm A, Gasteiger H (eds) Handbook of fuel cells, vol 2. Wiley, Chichester, pp 534–543
7. Alonso-Vante N, Tributsch H (1994) Electrode materials and strategies for (photo)electrochemistry. In: Lipkowski J, Ross P (eds) Electrochemistry of novel materials, vol III. VCH, New York, pp 1–63
8. Alonso-Vante N (2003) Novel nanostructured materials based on transition-metal compounds for electrocatalysis. In: Wieckowski A, Savinova ER, Vayenas CG (eds) Catalysis and electrocatalysis at nanoparticle surfaces. Marcel Dekker, New York, pp 931–958
9. Feng Y, Alonso-Vante N (2008) Nonprecious metal catalysts for the molecular oxygen-reduction reaction. Phys Stat Sol (b) 245(9):1792–1806
10. Alonso-Vante N, Giersig M, Tributsch H (1991) Thin layer semiconducting cluster electrocatalysts for oxygen reduction. J Electrochem Soc 138(2):639–640
11. Alonso-Vante N, Tributsch H, Solorza-Feria O (1995) Kinetics studies of oxygen reduction in acid medium on novel semiconducting transition metal chalcogenides. Electrochim Acta 40(5):567–576
12. Le Rhun V, Alonso-Vante N (2000) Tailoring of nanodivided electrocatalyst materials based on transition metal. J New Mater Electrochem Syst 3(4):331–336
13. Alonso-Vante N (1998) Inert for selective oxygen reduction of oxygen and method for the production thereof. Germany Patent WO1997DE02453 19971016; DE19961044628 19961017
14. Campbell SA (2004) Non-noble metal catalysts for the oxygen reduction reaction. US Patent 7,125,820
15. Babu PK, Lewera A, Jong HC, Hunger R, Jaegermann W, Alonso-Vante N, Wieckowski A, Oldfield E (2007) Selenium becomes metallic in Ru-Se fuel cell catalysts: an EC-NMR and XPS investigation. J Am Chem Soc 129(49):15140–15141
16. Lewera A, Inukai J, Zhou WP, Cao D, Duong HT, Alonso-Vante N, Wieckowski A (2007) Chalcogenide oxygen reduction reaction catalysis: X-ray photoelectron spectroscopy with Ru, Ru/Se and Ru/S samples emersed from aqueous media. Electrochim Acta 52(18):5759–5765
17. Malakhov IV, Nikitenko SG, Savinova ER, Kochubey DI, Alonso-Vante N (2002) In situ EXAFS study to probe active centers of Ru chalcogenide electrocatalysts during oxygen reduction reaction. J Phys Chem B 106(7):1670–1676
18. Ramaswamy N, Allen RJ, Mukerjee S (2011) Electrochemical kinetics and X-ray absorption spectroscopic investigations of oxygen reduction on chalcogen-modified ruthenium catalysts in alkaline media. J Phys Chem C 115(25):12650–12664.
19. Feng Y, Gago A, Timperman L, Alonso-Vante N (2010) Chalcogenide metal centers for oxygen reduction reaction: activity and tolerance. Electrochim Acta 56(3):1009–1022
20. Alonso-Vante N (2003) Physico-chemical properties of novel nanocrystalline ruthenium based chalcogenide materials. In: Kokorin AI, Bahnemann DW (eds) Chemical physics of nanostructured semiconductors. VSP Brill Academic, Zeist, pp 135–152
21. Alonso-Vante N, Jaegermann W, Tributsch H, Hönle W, Yvon K (1987) Electrocatalysis of oxygen reduction by chalcogenides containing mixed transition metal clusters. J Am Chem Soc 109(11):3251–3257
22. Alonso-Vante N, Fieber-Erdmann M, Rossner H, Holub-Krappe E, Giorgetti C, Tadjeddine A, Dartyge E, Fontaine A, Frahm R (1997) The catalytic centre of transition metal chalcogenides vis-à-vis the oxygen reduction reaction: an in situ electrochemical EXAFS study. J Phys IV 7(2 Part 2):887–889
23. Jaegermann W, Pettenkofer C, Alonso-Vante N, Schwarzlose T, Tributsch H (1990) Chevrel phase type compounds: electronic, chemical and structural factors in oxygen reduction electrocatalysis. Ber Bunsen-Ges Phys Chem 94:513–520
24. Alonso-Vante N, Malakhov IV, Nikitenko SG, Savinova ER, Kochubey DI (2002) The structure analysis of the active centers of Ru-containing electrocatalysts for the oxygen reduction. An in situ EXAFS study. Electrochim Acta 47(22–23):3807–3814
25. Alonso-Vante N, Borthen P, Fieber-Erdmann M, Strehblow HH, Holub-Krappe E (2000) In situ grazing incidence X-ray absorption study of ultra thin Ru_xSe_y cluster-like electrocatalyst layers. Electrochim Acta 45(25–26):4227–4236

26. Solorza-Feria O, Ellmer K, Giersig M, Alonso-Vante N (1994) Novel low-temperature synthesis of semiconducting transition metal chalcogenide electrocatalyst for multielectron charge transfer: molecular oxygen reduction. Electrochim Acta 39(11–12):1647–1653
27. Vogel W, Le Rhun V, Garnier E, Alonso-Vante N (2001) Ru clusters synthesized chemically from dissolved carbonyl: in situ study of a novel electrocatalyst in the gas phase and in electrochemical environment. J Phys Chem B 105(22):5238–5243
28. Zaikovskii VI, Nagabhushana KS, Kriventsov VV, Loponov KN, Cherepanova SV, Kvon RI, Bonnemann H, Kochubey DI, Savinova ER (2006) Synthesis and structural characterization of se-modified carbon-supported Ru nanoparticles for the oxygen reduction reaction. J Phys Chem B 110(13):6881–6890
29. Alonso-Vante N, Zelenay P, Choi JH, Wieckowski A, Cao D (2009) Chalcogen catalysts for polymer electrolyte fuel cell. US Patent 7,588,857
30. Cao D, Wieckowski A, Inukai J, Alonso-Vante N (2006) Oxygen reduction reaction on ruthenium and rhodium nanoparticles modified with selenium and sulfur. J Electrochem Soc 153(5):A869–A874
31. Vogel W, Kaghazchi P, Jacob T, Alonso-Vante N (2007) Genesis of Ru_xSe_y nanoparticles by pyrolysis of $Ru_4Se_2(CO)_{11}$: a combined X-ray in situ and DFT study. J Phys Chem C 111:3908–3913
32. Liu G, Zhang H, Hu JW (2007) Novel synthesis of a highly active carbon-supported Ru85Se15 chalcogenide catalyst for the oxygen reduction reaction. Electrochem Commun 9 (11):2643–2648
33. Zehl G, Schmithals G, Hoell A, Haas S, Hartnig C, Dorbandt I, Bogdanoff P, Fiechter S (2007) On the structure of carbon-supported selenium-modified ruthenium nanoparticles as electrocatalysts for oxygen reduction in fuel cells. Angew Chem Int Ed 46(38):7311–7314
34. Delacote C, Bonakdarpour A, Johnston CM, Zelenay P, Wieckowski A (2009) Aqueous-based synthesis of ruthenium-selenium catalyst for oxygen reduction reaction. Faraday Discuss 140:269–281
35. Colmenares L, Jusys Z, Behm RJ (2007) Activity, selectivity, and methanol tolerance of Se-modified Ru/C cathode catalysts. J Phys Chem C 111(3):1273–1283
36. Mavrikakis M, Hammer B, Nørskov JK (1998) Effect of strain on the reactivity of metal surfaces. Phys Rev Lett 81 (13):2819–2822
37. Stolbov S (2012) Nature of the selenium submonolayer effect on the oxygen electroreduction reaction activity of ru(0001). J Phys Chem C 116 (12):7173–7179.
38. Tritsaris GA, Nørskov JK, Rossmeisl J (2011) Trends in oxygen reduction and methanol activation on transition metal chalcogenides. Electrochim Acta 56(27):9783–9788
39. Liu G, Zhang H (2008) Facile synthesis of carbon-supported Ir_xSe_y chalcogenide nanoparticles and their electrocatalytic activity for the oxygen reduction reaction. J Phys Chem C 112 (6):2058–2065
40. Lee K, Zhang L, Zhang JJ (2007) A novel methanol-tolerant Ir-Se chalcogenide electrocatalyst for oxygen reduction. J Power Sources 165(1):108–113
41. Serov AA, Cho S-Y, Han S, Min M, Chai G, Nam KH, Kwak C (2007) Modification of palladium-based catalysts by chalcogenes for direct methanol fuel cells. Electrochem Commun 9(8):2041–2044
42. Madhu, Singh RN (2011) Palladium selenides as active methanol tolerant cathode materials for direct methanol fuel cell. Int J Hydrogen Energy 36(16):10006–10012
43. Lee K, Zhang L, Zhang JJ (2007) Ternary non-noble metal chalcogenide (W-Co-Se) as electrocatalyst for oxygen reduction reaction. Electrochem Commun 9(7):1704–1708
44. Feng Y, He T, Alonso-Vante N (2008) In situ free-surfactant synthesis and ORR- electrochemistry of carbon-supported Co_3S_4 and $CoSe_2$ nanoparticles. Chem Mater 20(1):26–28
45. Feng Y, He T, Alonso-Vante N (2009) Oxygen reduction reaction on carbon-supported $CoSe_2$ nanoparticles in an acidic medium. Electrochim Acta 54(22):5252–5256
46. Alonso-Vante N, Feng Y, He T (2010) Carbon-supported $CoSe_2$ nanoparticles for oxygen reduction and hydrogen evolution in acid environments. USA Patent Application 20100233070

47. Nekooi P, Akbari M, Amini MK (2010) CoSe nanoparticles prepared by the microwave-assisted polyol method as an alcohol and formic acid tolerant oxygen reduction catalyst. Int J Hydrogen Energy 35(12):6392–6398
48. Zhu L, Teo M, Wong PC, Wong KC, Narita I, Ernst F, Mitchell KAR, Campbell SA (2010) Synthesis, characterization of a $CoSe_2$ catalyst for the oxygen reduction reaction. Appl Catal A Gen 386(1–2):157–165
49. Gochi-Ponce Y, Alonso-Nunez G, Alonso-Vante N (2006) Synthesis and electrochemical characterization of a novel platinum chalcogenide electrocatalyst with an enhanced tolerance to methanol in the oxygen reduction reaction. Electrochem Commun 8(9):1487–1491
50. Papageorgopoulos DC, Liu F, Conrad O (2007) A study of Rh_xS_y/C and $RuSe_x$/C as methanol-tolerant oxygen reduction catalysts for mixed-reactant fuel cell applications. Electrochim Acta 52(15):4982–4986
51. Ziegelbauer JM, Gulla AF, O'Laoire C, Urgeghe C, Allen RJ, Mukerjee S (2007) Chalcogenide electrocatalysts for oxygen-depolarized aqueous hydrochloric acid electrolysis. Electrochim Acta 52(21):6282–6294
52. Ziegelbauer JM, Murthi VS, O'Laoire C, Gullá AF, Mukerjee S (2008) Electrochemical kinetics and X-ray absorption spectroscopy investigations of select chalcogenide electrocatalysts for oxygen reduction reaction applications. Electrochim Acta 53(17):5587–5596
53. Abild-Pedersen F, Greeley J, Studt F, Rossmeisl J, Munter TR, Moses PG, Skúlason E, Bligaard T, Nørskov JK (2007) Scaling properties of adsorption energies for hydrogen-containing molecules on transition-metal surfaces. Phys Rev Lett 99(1):016105
54. Tauster SJ, Fung SC, Garten RL (1978) Strong metal-support interactions. Group 8 noble metals supported on TiO_2. J Am Chem Soc 100(1):170–175
55. Bard AJ, Faulkner LR (2002) Electrochemical methods: fundamentals and applications, 2nd edn. Wiley, New York
56. Feng Y, Alonso-Vante N (2012) Carbon-supported Cubic $CoSe_2$ catalysts for oxygen reduction reaction in alkaline medium. Electrochim Acta. 72(6):129–133
57. Feng YJ, He T, Alonso-Vante N (2010) Carbon-supported $CoSe_2$ nanoparticles for oxygen reduction reaction in acid medium. Fuel Cells 10(1):77–83
58. Timperman L, Gago AS, Alonso-Vante N (2011) Oxygen reduction reaction increased tolerance and fuel cell performance of Pt and Ru_xSe_y onto oxide-carbon composites. J Power Sources 196(9):4290–4297
59. Nekooi P, Amini MK (2010) Effect of support type and synthesis conditions on the oxygen reduction activity of Ru_xSe_y catalyst prepared by the microwave polyol method. Electrochim Acta 55(9):3286–3294
60. Timperman L, Feng YJ, Vogel W, Alonso-Vante N (2010) Substrate effect on oxygen reduction electrocatalysis. Electrochim Acta 55(26):7558–7563
61. de Tacconi NR, Chenthamarakshan CR, Yogeeswaran G, Watcharenwong A, de Zoysa RS, Basit NA, Rajeshwar K (2006) Nanoporous TiO_2 and WO_3 films by anodization of titanium and tungsten substrates: influence of process variables on morphology and photoelectrochemical response. J Phys Chem B 110(50):25347–25355
62. Kulesza PJ, Grzybowska B, Malik MA, Galkowski MT (1997) Tungsten oxides as active supports for highly dispersed platinum microcenters: electrocatalytic reactivity toward reduction of hydrogen peroxide and oxygen. J Electrochem Soc 144(6):1911–1917
63. Kulesza PJ, Miecznikowski K, Baranowska B, Skunik M, Fiechter S, Bogdanoff P, Dorbandt I (2006) Tungsten oxide as active matrix for dispersed carbon-supported $RuSe_x$ nanoparticles: enhancement of the electrocatalytic oxygen reduction. Electrochem Commun 8(5):904–908
64. Barczuk PJ, Tsuchiya H, Macak JM, Schmuki P, Szymanska D, Makowski O, Miecznikowski K, Kulesza PJ (2006) Enhancement of the electrocatalytic oxidation of methanol at Pt/Ru nanoparticles immobilized in different WO_3 matrices. Electrochem Solid State Lett 9(6): E13–E16
65. Alonso-Vante N (2010) Platinum and non-platinum nanomaterials for the molecular oxygen reduction reaction. Chemphyschem 11(13):2732–2744

66. Damjanovic A, Genshaw MA, Bockris JOM (1967) The role of hydrogen peroxide in oxygen reduction at platinum in H_2SO_4 solution. J Electrochem Soc 114(5):466–472
67. Damjanovic A, Genshaw MA, Bockris JOM (1967) The mechanism of oxygen reduction at platinum in alkaline solutions with special reference to H_2O_2. J Electrochem Soc 114 (11):1107–1112
68. Damjanovic A, Genshaw MA, O'M Bockris J (1966) Distinction between intermediates produced in main and side electrodic reactions. J Chem Phys 45(11):4057–4059
69. Hsueh KL, Gonzalez ER, Srinivasan S (1983) Electrolyte effects on oxygen reduction kinetics at platinum: a rotating ring-disc electrode analysis. Electrochim Acta 28(5):691–697
70. Bonakdarpour A, Delacote C, Yang R, Wieckowski A, Dahn JR (2008) Loading of Se/Ru/C electrocatalyst on a rotating ring-disk electrode and the loading impact on a H_2O_2 release during oxygen reduction reaction. Electrochem Commun 10(4):611–615
71. Bonakdarpour A, Lefevre M, Yang R, Jaouen F, Dahn T, Dodelet J-P, Dahn JR (2008) Impact of loading in RRDE experiments on Fe–N–C catalysts: two- or four-electron oxygen reduction? Electrochem Solid State Lett 11(6):B105–B108
72. Lefevre M, Proietti E, Jaouen F, Dodelet J-P (2009) Iron-based catalysts with improved oxygen reduction activity in polymer electrolyte fuel cells. Science 324(5923):71–74
73. Song C, Zhang L, Zhang J, Wilkinson DP, Baker R (2007) Temperature dependence of oxygen reduction catalyzed by cobalt fluoro-phthalocyanine adsorbed on a graphite electrode. Fuel Cells 7(1):9–15
74. Tarasevich MR, Sadkowski A, Yeager E (1983) Oxygen electrochemistry. In: Bockris JOM, Conway BE, Yeager E, Khan SUM, White RE (eds) Comprehensive treatise in electrochemistry, vol 7. Plenum, New York, pp 301–398
75. Bursell M, Pirjamali M, Kiros Y (2002) $La_{0.6}Ca_{0.4}CoO_3$, $La_{0.1}Ca_{0.9}MnO_3$ and $LaNiO_3$ as bifunctional oxygen electrodes. Electrochim Acta 47(10):1651–1660
76. Singh RN, Malviya M, Anindita, Sinha ASK, Chartier P (2007) Polypyrrole and $La_{1-x}Sr_xMnO_3$ ($0 \leq x \leq 0.4$) composite electrodes for electroreduction of oxygen in alkaline medium. Electrochim Acta 52(12):4264–4271
77. Ponce J, Rehspringer JL, Poillerat G, Gautier JL (2001) Electrochemical study of nickel–aluminium–manganese spinel $Ni_xAl_{1-x}Mn_2O_4$. Electrocatalytical properties for the oxygen evolution reaction and oxygen reduction reaction in alkaline media. Electrochim Acta 46(22):3373–3380
78. Ríos E, Abarca S, Daccarett P, Nguyen Cong H, Martel D, Marco JF, Gancedo JR, Gautier JL (2008) Electrocatalysis of oxygen reduction on $Cu_xMn_{3-x}O_4$ ($1.0 \leq x \leq 1.4$) spinel particles/polypyrrole composite electrodes. Int J Hydrogen Energy 33(19):4945–4954
79. Restovic A, Ríos E, Barbato S, Ortiz J, Gautier JL (2002) Oxygen reduction in alkaline medium at thin $Mn_xCo_{3-x}O_4$ ($0 \leq x \leq 1$) spinel films prepared by spray pyrolysis. Effect of oxide cation composition on the reaction kinetics. J Electroanal Chem 522(2):141–151
80. Zei MS, Ertl G (2000) Structural changes of a Ru(0001) surface under the influence of electrochemical reactions. Phys Chem Chem Phys 2(17):3855–3859
81. Stephens-Romero S, Carreras-Sospedra M, Brouwer J, Dabdub D, Samuelsen S (2009) Determining air quality and greenhouse gas impacts of hydrogen infrastructure and fuel cell vehicles. Environ Sci Technol 43(23):9022–9029
82. Trasatti S (1995) Electrochemistry and environment: the role of electrocatalysis. Int J Hydrogen Energy 20(10):835–844
83. McIntyre DR, Burstein GT, Vossen A (2002) Effect of carbon monoxide on the electrooxidation of hydrogen by tungsten carbide. J Power Sources 107(1):67–73
84. Spendelow JS, Wieckowski A (2007) Electrocatalysis of oxygen reduction and small alcohol oxidation in alkaline media. Phys Chem Chem Phys 9(21):2654–2675
85. Wasmus S, Küver A (1999) Methanol oxidation and direct methanol fuel cells: a selective review. J Electroanal Chem 461(1–2):14–31
86. Scott K, Shukla AK, Jackson CL, Meuleman WRA (2004) A mixed-reactants solid-polymer-electrolyte direct methanol fuel cell. J Power Sources 126(1–2):67–75

87. Antolini E (2007) Catalysts for direct ethanol fuel cells. J Power Sources 170(1):1–12
88. Gago AS, Morales-Acosta D, Arriaga LG, Alonso-Vante N (2011) Carbon supported ruthenium chalcogenide as cathode catalyst in a microfluidic formic acid fuel cell. J Power Sources 196(3):1324–1328
89. Gago AS, Arriaga LG, Gochi-Ponce Y, Feng YJ, Alonso-Vante N (2010) Oxygen reduction reaction selectivity of Ru_xSe_y in formic acid solutions. J Electroanal Chem 648(1):78–84
90. Yu X, Pickup PG (2008) Recent advances in direct formic acid fuel cells (DFAFC). J Power Sources 182(1):124–132
91. Kim J, Jung C, Rhee CK, T-h L (2007) Electrocatalytic oxidation of formic acid and methanol on Pt deposits on Au(111). Langmuir 23(21):10831–10836
92. Rice C, Ha RI, Masel RI, Waszczuk P, Wieckowski A, Barnard T (2002) Direct formic acid fuel cells. J Power Sources 111(1):83–89
93. Gasteiger HA, Markovic N, Ross PN, Cairns EJ (1994) Electrooxidation of small organic-molecules on well-characterized Pt-Ru alloys. Electrochim Acta 39(11–12):1825–1832
94. Antolini E, Lopes T, Gonzalez ER (2008) An overview of platinum-based catalysts as methanol-resistant oxygen reduction materials for direct methanol fuel cells. J Alloys Compd 461(1–2):253–262
95. Colón-Mercado HR, Popov BN (2006) Stability of platinum based alloy cathode catalysts in PEM fuel cells. J Power Sources 155(2):253–263
96. Wang R-F, Liao S-J, Liu H-Y, Meng H (2007) Synthesis and characterization of Pt-Se/C electrocatalyst for oxygen reduction and its tolerance to methanol. J Power Sources 171 (2):471–476
97. Cheng H, Yuan W, Scott K, Browning DJ, Lakeman JB (2007) The catalytic activity and methanol tolerance of transition metal modified-ruthenium-selenium catalysts. Appl Catal B Environ 75(3–4):221–228
98. Gao M-R, Gao Q, Jiang J, Cui C-H, Yao W-T, Yu S-H (2011) A methanol-tolerant Pt/$CoSe_2$ nanobelt cathode catalyst for direct methanol fuel cells. Angew Chem Int Ed 50 (21):4905–4908

Chapter 15
Non-Pt Cathode Electrocatalysts for Anion-Exchange-Membrane Fuel Cells

Rongrong Chen, Junsong Guo, and Andrew Hsu

Abstract This chapter provides an overview of the recent advancement in the development of non-Pt electrocatalysts for oxygen reduction reactions (ORRs) in alkaline media; catalyst materials discussed include carbon-supported transition metals (Pt/C, Pd/C, Ag/C), transition-metal macrocycles (M–N–C), and multifunctional materials (e.g., metallic alloys, metallic MnO_2, macrocycle-treated metals). The important factors affecting ORR kinetics are identified through combined theoretical simulations and experimental measurements. The inconsistencies between the ORR activities observed in fuel cell tests and those observed in rotating disk electrodes, as reported by several research groups, were analyzed in details, and plausible theoretical explanations were proposed. Several promising bifunctional catalysts and their potentials as replacements for Pt in anion-exchange-membrane fuel cell (AEMFC) applications are discussed. For the AEMFC technology to mature as a low-cost high-performance energy device, further improvement of the performance and durability of the catalysts is essential; we believe that the necessary improvements can be achieved through intelligent design of multifunctional catalysts.

15.1 Introduction

Fuel cells as clean and efficient energy devices convert chemical energy in a fuel directly into electricity via electrochemical reactions. Several types of fuel cells, such as phosphoric acid (PAFC), proton exchange membrane (PEMFC), molten carbonate (MCFC), solid oxide (SOFC), and alkaline fuel cells (AFCs), have been

---

R. Chen (✉) • J. Guo
Indiana University Purdue University Indianapolis, 799 W. Michigan St., ET 201A, Indianapolis, IN 46202, USA
e-mail: rochen@iupui.edu

A. Hsu
Charles W. Davidson College of Engineering, San José State University, One Washington Square, San José, CA 95192, USA

M. Shao (ed.), *Electrocatalysis in Fuel Cells*, Lecture Notes in Energy 9,
DOI 10.1007/978-1-4471-4911-8_15,

developed for various applications and achieved energy efficiencies from 25 to 60 %, depending on the types of fuel cell [1, 2]. During the last three decades, PEMFC has attracted the most attention due to features such as high power density, no electrolyte leakage, and suitability for vehicular applications; however, current PEMFC still faces major challenges for commercialization due to the need of expensive Pt-based catalysts in a highly oxidative acidic environment.

AFCs that use liquid electrolytes have been well developed from 1960s to 1980s, and were successfully applied in space programs. They are the best performing of all known fuel cell types operable below 150 °C owing to their facile kinetics at the cathode and anode [1–3]. Compared to the harsher acidic environment, AFCs not only offer advantages in cathode and anode kinetics but also improved material stability. Many less expensive non-Pt electrocatalysts, such as Pd, Ag, and Ni, have been successfully applied in AFCs [4–8]. However, the fundamental difficulty with the AFCs is that the aqueous KOH electrolyte reacts with CO_2 from the air to form carbonate species that lower the AFC performance and reduce the lifetime of the cell through the formation of carbonate precipitates on the electrodes.

Anion-exchange-membrane fuel cells (AEMFCs) are a relatively recent development. This type of fuel cells not only inherits advantages of the AFCs but also overcomes the problems associated with carbonate precipitates in AFCs by using polymeric electrolytes that do not contain mobile alkaline cations [9–24]. Additionally, there are more flexible fuel choices for AEMFCs since alcohol (methanol, ethanol, or ethylene glycol) oxidation rates are significantly faster in an alkaline media than in an acid media [8, 25, 26]. The working principle of an AEMFC using hydrogen as the anode fuel is shown in Fig. 15.1 and described in the following equations:

$$\text{Anode}: \mathrm{H_2} + 4\mathrm{OH^-} \rightarrow 4\mathrm{H_2O} + 4\mathrm{e^-}, \quad E_{0,\mathrm{a}} = 0.83\ \mathrm{V}\ \text{versus SHE}, \tag{15.1}$$

$$\text{Cathode}: \mathrm{O_2} + 2\mathrm{H_2O} + 4\mathrm{e^-} \rightarrow 4\mathrm{OH^-}, \quad E_{0,\mathrm{c}} = 0.40\ \mathrm{V}\ \text{versus SHE}, \tag{15.2}$$

$$\text{Overall}: 2\mathrm{H_2} + \mathrm{O_2} \rightarrow 2\mathrm{H_2O}, \quad E_{0,\mathrm{cell}} = 1.23\ \mathrm{V}\ \text{versus SHE}. \tag{15.3}$$

Although recent developments in OH^--conducting ionomers and anion-exchange membranes have resulted in significant improvements in the performance of AEMFCs [9–23], their performances are still considerably lower than the PEMFCs. While improving performance and stability of anion-exchange polymeric electrolytes is a top priority in AEMFC development, reducing the polarizations of oxygen electrodes and hydrogen or alcohol electrodes in alkaline media are also the major challenges that need to be addressed, especially when non-Pt catalysts are used.

Extensive research related to electrocatalysis of oxygen reduction reactions (ORRs) and hydrogen or methanol or ethanol oxidation reactions (HORs, MORs, or EORs) in alkaline media have been conducted worldwide in the last five decades. Spendelow and Wieckowski have provided an in-depth review of electrocatalysis for O_2 reduction on Pt-group and Ag metal and alloys, for methanol oxidation on

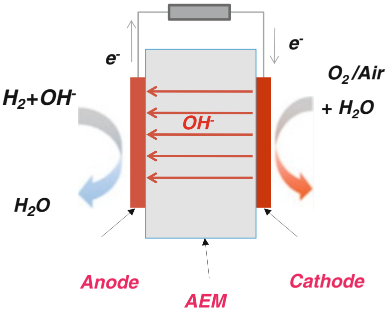

Fig. 15.1 Schematic illustration of a H_2/O_2 AEMFC

Pt-based anode catalysts, and for ethanol oxidation on Ni–Fe–Co alloy electrodes in alkaline media [8]. Antolini and Gonzalez gave a comprehensive overview of catalysts and membranes for alkaline direct alcohol fuel cells (ADAFCs) [26]. Recent progresses of ADAFCs can also be found in Chaps. 5 and 6 of this book. In this chapter, we intend to focus on the application aspects of various non-Pt electrocatalysts for ORRs in AEMFCs. ORR activity on various cathode catalysts, including carbon-supported transition metals (Pt/C, Pd/C, Ag/C), transition-metal macrocycles (M–N–C), metal oxides (MnO_2/C), and multifunctional materials (e.g., metallic alloys, metallic MnO_2, macrocycle-treated metals), in both liquid electrolytes and AEMFCs is presented. Fundamental issues related to the design of low-cost, high-performance electrocatalysts for AEMFCs are discussed.

15.2 ORR on Carbon-Supported Pure Metallic Nanocatalysts

Electrochemical reduction of O_2 is a multielectron reaction that has two main possible pathways: one involving the transfer of two electrons ($2e^-$) to produce H_2O_2 and the other, a direct four-electron ($4e^-$) pathway to produce water. In alkaline media, the $2e^-$ pathway can be written [27] as:

$$O_2 + H_2O + 2e^- \rightarrow HO_2^- + OH^-, \quad E_0 = -0.065 \text{ V versus SHE}, \qquad (15.4)$$

And the direct $4e^-$ pathway can be written as:

$$O_2 + 2H_2O + 4e^- \rightarrow 4OH^-, \quad E_0 = 0.40 \text{ V versus SHE}. \qquad (15.5)$$

To achieve the maximum energy capacity, it is desirable to select catalysts that reduce O_2 with minimal overpotentials via the $4e^-$ pathway.

Cyclic voltammetry (CV), rotating disk electrode (RDE), and rotating ring-disk electrode (RRDE) in a traditional tri-electrode cell are often employed in the study of the ORR kinetics and mechanisms on various catalysts in liquid electrolytes [27, 28]. As shown in Fig. 15.2, a tri-electrode cell contains a working electrode (WE), a reference electrode (RE), and a counter electrode (CE). The CE has much

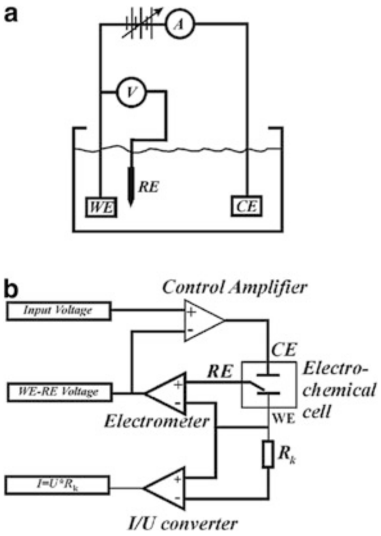

Fig. 15.2 (**a**) The simplest experimental setup for performing electrochemical experiments. (**b**) A schematic representation of a three-electrode potentiostat

larger surface area than the WE and is placed a few centimeters apart from the WE. The WE is either a disk electrode or a disk electrode surrounded by a ring electrode. The WE potentials are controlled against the RE by a potentiostat or bipotentiostat, while the electric current between the WE and CE is recorded as a function of the varying potential. For the O_2 reduction reaction in alkaline solutions, the currents flow from the CE to the WE. Since all three electrodes (WE, RE, and CE) are often immersed in the same electrolyte solution, the potential of the CE can be more positive than the potential of a WE during the O_2 reduction reaction. By contrast, the cathode in an AEMFC is less than 10–50 μm apart from the anode depending on the thickness of anion-exchange membrane. The potential of the cathode is always more positive than that of the anode, which could result in a strong positive electrical field for the anion adsorption at the cathode, especially at the high cell voltages. Therefore, in order to successfully develop electrocatalysts for practical fuel cell applications, it is essential to study the catalysts not just in aqueous electrolytes using tri-electrode cells but also in practical fuel cell test environments.

In this section, we review progress made in the study of the carbon-supported various pure metallic nanocatalysts, both in terms of experimental observations and theoretical studies, as an effort to provide current understanding of ORR in alkaline media. Particularly, as have been observed and pointed out by many researchers, ORR catalytic activities observed in traditional experimental setups such as RDE and RRDE may not be consistent with those observed in fuel cell testing. To explore this difference and provide a better understanding, we summarize RDE and RRDE studies and the fuel cell results on ORR separately in Sects. 2.1 and 2.2. Theoretical and fundamental studies aimed at explaining and bridging the differences between RDE and fuel cell results are provided in Sect. 2.3.

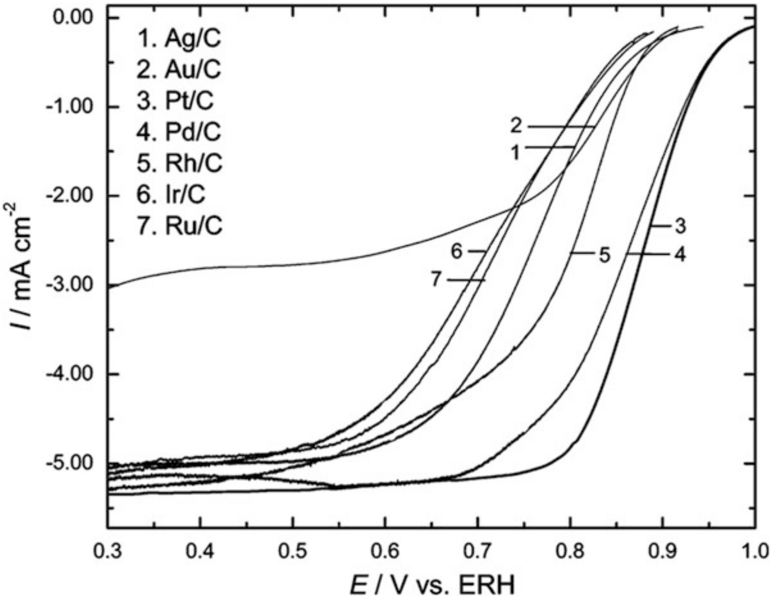

Fig. 15.3 Polarization curves obtained using a rotating disk electrode for O_2 reduction on different carbon dispersed metal nanoparticles in a 0.1 M NaOH solution. Rotation rate 1,600 rpm; sweep rate 5 mV s^{-1} [29]

15.2.1 ORR Activity Obtained with RDE or RRDE in Alkaline Solutions

The ORR activities on various metallic catalysts have been widely studied by RDE or RRDE in alkaline media [28–48], as briefly summarized here. Several precious metals and their alloys are known to promote the $4e^-$ ORR pathway. The kinetics of ORR on the surfaces of nanoparticles of various metals dispersed on high-surface area carbon determined by the RDE technique in 0.1 M NaOH solutions are shown in Fig. 15.3 [29]. Among the tested metallic catalysts, Pd/C seems to be the most promising alternative to Pt/C. Detailed comparisons of the ORR activity of Pd/C and Pt/C catalysts in alkaline solutions revealed that the activation energy for the ORR on Pd/C was slightly lower than that on Pt/C (39 vs. 48 kJ mol^{-1} at an overpotential of 300 mV) [30]. The $4e^-$ pathway was dominant on both the Pt/C and the Pd/C catalysts. As shown in Fig. 15.4, ORR was more favorable on a clean Pd surface than on a clean Pt surface; however, Pd was more easily oxidized at fuel cell cathode working potentials (Fig. 15.5). One of the merits of the Pd/C catalyst is that it is less sensitive to ethanol presented in the electrolyte as compared to the Pt/C [30]. To use the Pd, a realistic fuel cell cathode catalyst in the alkaline media, the problem of Pd oxidization at fuel cell cathode working potentials needs to be resolved.

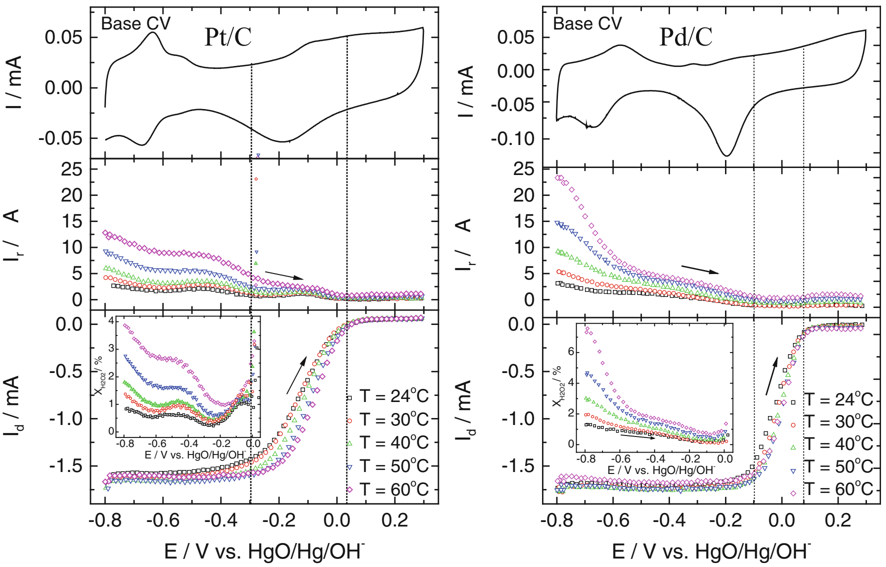

Fig. 15.4 RRDE measurements of ORR on the Pt/C and Pd/C electrodes with a rotation rate of 2,500 rpm in a 0.1 M NaOH solution during positive scanning. Collection efficiency $N = 0.40$; ring potential $E_r = 0.5$ V versus HgO/Hg/OH$^-$. Scan rate 10 mV s^{-1} [30]

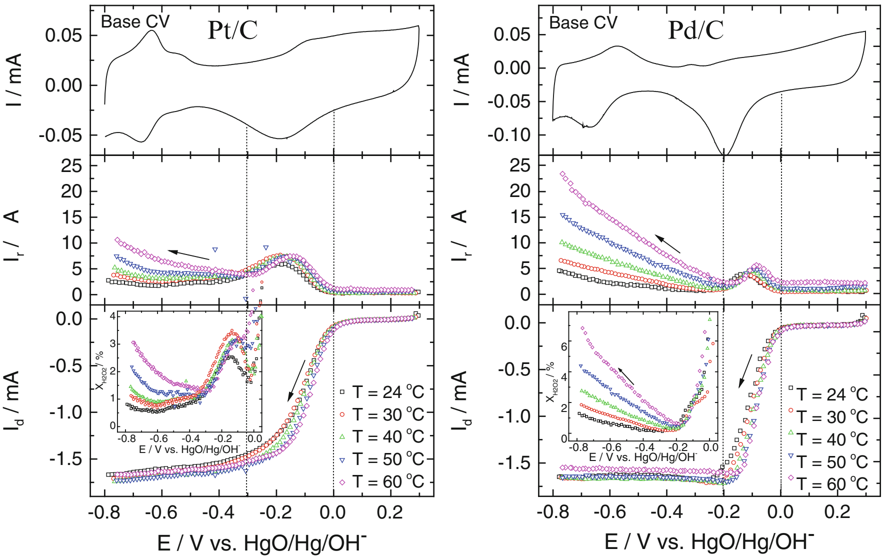

Fig. 15.5 RRDE measurements of ORR on the Pt/C and Pd/C electrodes with a rotation rate of 2,500 rpm in a 0.1 M NaOH solution during negative scanning. Collection efficiency $N = 0.40$; ring potential $E_r = 0.5$ V versus HgO/Hg/OH$^-$. Scan rate 10 mV s^{-1} [30]

Another potential replacement of Pt/C as an ORR cathode catalyst is Ag/C, which has a reasonably high ORR activity and lower cost (~1/60 of the cost of Pt and 1/20 of that of Pd). The ORRs on Ag/C catalysts can proceed mainly via the $4e^-$ pathway [8, 26, 29, 31–38] but generally have 50–100 mV larger overpotentials than those observed on the Pt catalysts. It was reported [36] that on 20 weight percent (wt.%) of Ag/C with 174 nm mean Ag particle size, ORR via the $4e^-$ pathway was observed, while the finer catalysts with 4.1 nm mean particles size appeared to facilitate the $2e^-$ pathway. Lima [32] reported a 2.3-electron ORR reaction on 20 wt.% Ag/C with relatively large 47.7 nm silver particle size, while the result of Demarconnay et al. showed a 3.6-electron ORR reaction on 20 wt.% Ag/C with a particle size close to 15 nm [33]. Countanceau et al. [34] investigated the influence of metal loading on Ag/C catalyst activity in a half-cell and found that the optimum loading of silver was around 20 wt.%.

Recently, we studied ORR activities on Ag/C catalysts with four different metal loadings but similar particle sizes (~15 nm) [37]. As shown in Fig. 15.6, the ORRs on Ag/C catalysts were found to proceed mainly through a $4e^-$ pathway. Ag/C catalytic activities for the ORRs greatly depended on the formation of a surface monolayer of Ag_2O films, which was a key parameter to correlate ORR activities on the Ag/C catalysts. By increasing Ag loading onto the carbon supports, the formation of Ag_2O films increased linearly, and the ORR onset potential shifted positively about 62 mV with Ag loading increasing from 10 to 60 wt.%, as the Ag loading increased to 0.02, 0.04, 0.08, and 0.12 mg cm^{-2}, respectively. Silicate was identified as a poisoning species that greatly inhibits the ORR activity on Ag/C catalysts, while carbonate was not demonstrated to be a poisonous species for ORRs on Ag/C catalysts.

Singh and Buttry compared ORR on silver nanoparticles (Ag-NPs) and polycrystalline silver electrodes in 0.1 M NaOH solution using CV and RDE methods [38]. An exchange electron number between 3 and 4 was reported, depending on the electrode potentials and the morphology of the Ag catalysts. A higher n-value under some conditions was observed for the Ag-NPs than for bare Ag polycrystalline. Based on the observations of the presence of a substantial $2e^-$ pathway at more negative potentials for the bulk Ag and Ag NP surfaces, it was argued that OH_{ads} may exist at relatively high-surface coverage over a wide potential range on the bulk Ag and Ag NP surfaces, in contrast to the behavior proposed for the single crystal surfaces [35].

In summary, the RDE results indicate that ORR kinetics obtained on Pd/C and Ag/C catalysts were comparable to that on Pt/C, with reactions primarily through a $4e^-$ ORR pathway but with 50–100 mV larger overpotentials. However, Pd oxidization at fuel cell cathode working potentials can be a hindrance for its practical application in AEMFCs. Balancing cost, performance, and durability, Ag/C catalysts have been identified by several research groups as the preferred cathode catalysts to replace Pt/C for AEMFC applications. The performance of Ag/C catalysts as compared with Pt/C catalysts in AEMFCs is presented here.

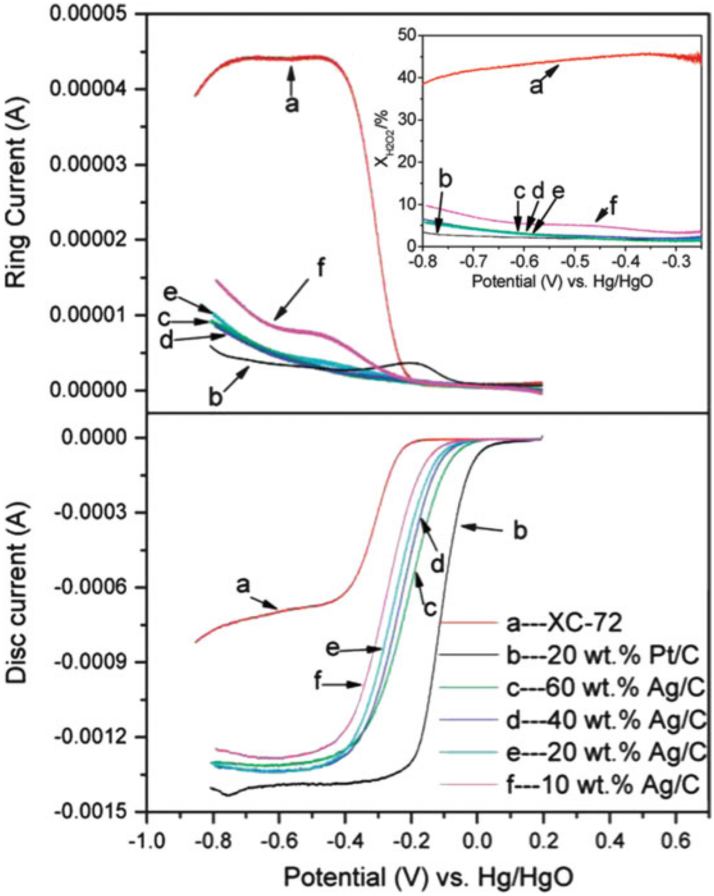

Fig. 15.6 RRDE measurements of oxygen reduction reactions on four Ag/C catalysts with different metal loadings, Vulcan XC-72, and 20 wt.% Pt/C (BASF) with a rotation rate of 2,500 rpm in oxygen-purged 0.1 M NaOH. Collection efficiency $N = 0.23$; ring potential $E_r = 0.3$ V versus Hg/HgO; scan rate 20 mV s^{-1} [37]

15.2.2 ORR Activity Observed in AEMFCs

The performance of H_2/O_2 AEMFCs on commercial Pt/C, Au/C, and Ag/C cathodes was first reported by Varcoe and his coworkers [39, 40]. Figure 15.7a shows the steady-state cell voltage (V_{cell}) versus current density (i) plots for the AEM-MEAs containing three different metal/C (Pt/C, Au/C, and Ag/C) cathodes. Pt/C was found to outperform the Ag/C and Au/C catalysts, with a peak power density of 62 mW cm^{-2} at a current density of 140 mA cm^{-2} [40]. The performance of the catalysts decreased in order of Pt/C > Au/C > Ag/C. The iR-corrected V_{cell} in Fig. 15.7b shows that the three MEAs had similar overpotential trends within the

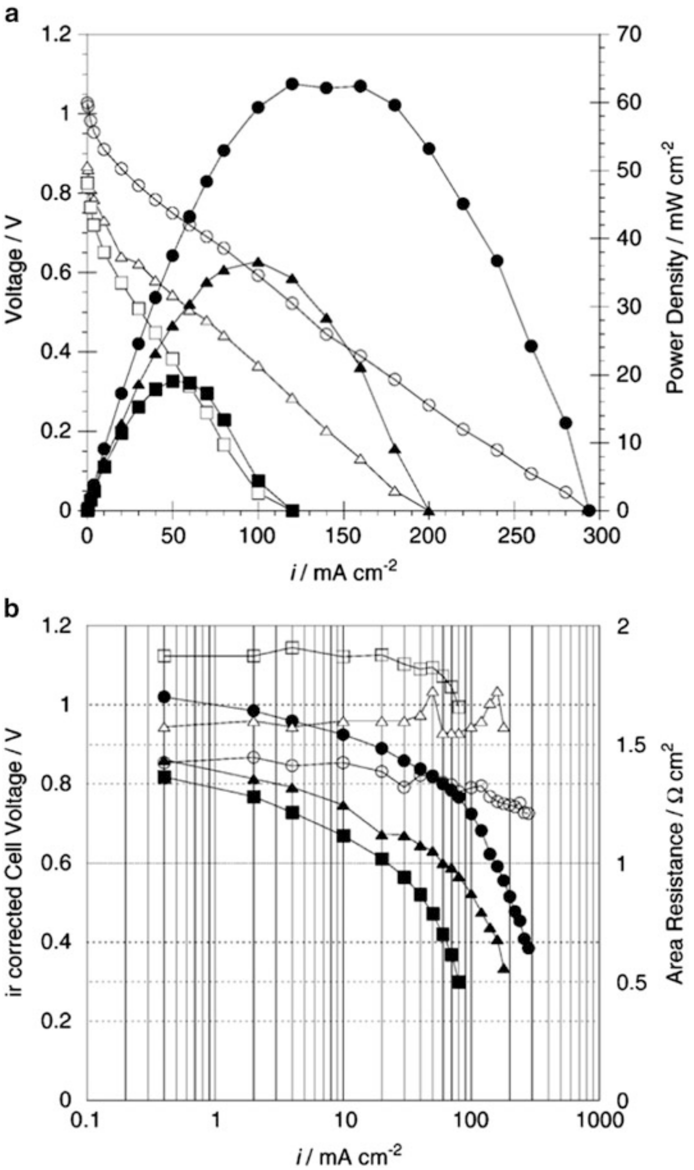

Fig. 15.7 (**a**) Fuel cell performance at 50 °C, anode: 0.5 mg cm^{-2} Pt prefabricated carbon cloth electrode; cathode: 0.5 mg cm^{-2} transition-metal carbon paper electrode. With (*filled circle*) Pt/C; (*filled triangle*) Au/C and (*filled square*) Ag/C. The *open symbols* represent the V_{cell} versus *i* plot, and the *filled symbols* represent the P_{cell} versus *i* plot. (**b**) iR-corrected V_{cell} and area resistance plots against log *i* for (*filled circle*) Pt/C, (*filled triangle*) Au/C, and (*filled square*) Ag/C measured using EIS during fuel cell test with H_2/O_2 at 50 °C. *Filled symbol* represents iR-corrected V_{cell}, and *open symbols* represent area resistance data [40]

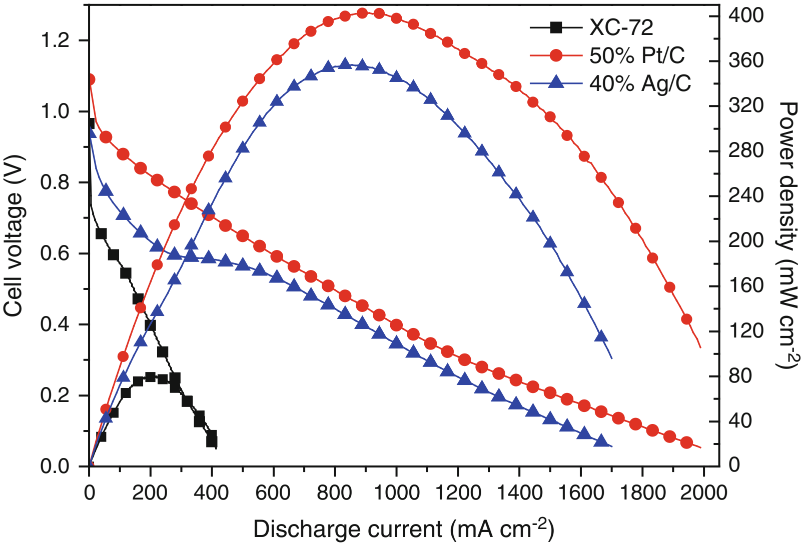

Fig. 15.8 Fuel cell performance at 50 °C, 20 psi back pressure for both H_2 and O_2, anode: 1.25 mg cm^{-2} Pt/C; cathode: 2.5 mg cm^{-2} catalyst loading. With (*red filled circles*) Pt/C; (*blue filled triangles*) Ag/C and (*black filled squares*) XC-72 [32]

ohmic and mass-transport regions, but the electrokinetic influence showed substantial initial losses, especially for the Ag/C and Au/C catalysts. Area resistances of the three catalysts varied substantially and in the order expected from the power densities, decreasing in the order Ag/C > Au/C > Pt/C. It was not clear to the original authors at the time of their research why much larger overpotentials were observed in AEMFCs than those in RDE measurements. Lu et al. reported the performance of a H_2/O_2 AEMFC using an OH^- conductive polymer membrane, a Ni-catalyzed anode, and an Ag-catalyzed cathode [41]. The operating temperature was 60 °C; the Ni loading in anode was 5 mg cm^{-2}, whereas the Ag loading in cathode was 1 mg cm^{-2}. Anode and cathode gases were humidified at 60 °C, and the back pressure of gases was ~20 psi at both sides of the cell. A peak power density of 50 mW cm^{-2} at a current density of 100 mA cm^{-2} was achieved.

Based on the ORR activity observed on Ag/C with various metal loadings in 0.1 M NaOH solution (Fig. 15.6), we selected 40 wt.% Ag/C as the cathode catalysts for making AEM-MEAs and tested in H_2/O_2 AMEFCs [32]. Figure 15.8 shows the polarization and power curves of AEM-MEAs containing three different cathode catalysts, including Pt/C (50 wt.%), Ag/C (40 wt.%), and XC-72 carbon. Both cathode and anode catalyst loadings were maintained at 2.5 mg cm^{-2}, which resulted in a Pt loading of 1.25 mg cm^{-2} and an Ag loading of 1.00 mg cm^{-2}. Commercially available anion-exchange membranes (Tokuyama A901) and ionomers (Tokuyama A4) were used for preparing the MEAs. Compared with what was reported in the literatures [40, 41], significantly improved performances were obtained with the AEM-MEAs using catalysts prepared in our lab and the commercial membranes and ionomers. Even carbon catalysts in the AEM-MEAs displayed reasonable ORR activity. Similar to earlier reported results [40, 41], substantial initial cell voltage losses ($>$150 mV) were observed on C and Ag/C cathode catalysts as compared with the Pt/C catalysts. For the Ag/C MEA, there were two distinct discharge regions observed in its polarization curve. When the cell voltage was above 0.590 V, the cell voltages fell sharply with increasing discharge currents. But after the cell voltage dropping to below 0.530 V, the cell voltages fell much slowly with increasing discharge current. A peak power density of 356 mW cm^{-2} at a current density of 855 mA cm^{-2} was demonstrated on Ag/C catalysts, while a peak power density of 402 mW cm^{-2} was achieved on the Pt/C cathode catalysts. The combination of rather high ORR activity and low price makes the Ag/C catalyst an attractive alternative to replace Pt/C as the cathode catalyst for AEMFC applications. Fundamental understandings of limiting factors of ORR kinetics on Ag/C surfaces would help further improving ORR activities on Ag-based catalysts in alkaline media.

15.2.3 Fundamental Aspects of ORRs on Ag/C Versus Pt/C Catalysts

In the previous two sections, we discussed the experimental observations of ORRs on various carbon-supported metallic nanoparticle catalysts through RDE, RRDE, and fuel cell testing. This section provides a summary of some fundamental studies that aim at a better understanding of the RDE and AEMFC observations, which may then lead to the design of better catalysts for AEMFCs.

By using density functional theory (DFT) calculations, Nørskov and others investigated the electrochemically stable surface structures as a function of pH for Pt(111), Ag(111), and Ni(111)[43]. According to the DFT calculation results, Pourbaix diagrams for a Pt(111) and Ag(111) were constructed [43], which showed that Ag dissolution is a much larger problem in acidic than in alkaline electrolytes. At $\mathrm{pH} = 0$, dissolution of Ag is spontaneous at potentials above 0.80 V, so ORR on this surface is not likely. But Ag becomes more stable relative to RHE as pH increased. The pH-dependent stability offers an explanation for the success of using Ag in AFCs or AEMFCs as an ORR catalyst, but not in PEMFCs.

According to the DFT calculation and RDE measurement results [29], it has been proposed that among the various pure metallic electrocatalysts, Pt provides the highest ORR activity due to its optimum oxygen adsorption strength (neither too weak nor too strong), while oxygen adsorption on Ag is relatively weak that the O–O bond cannot be broken as efficiently as on Pt. It has been recognized that the optimal ORR catalyst should exhibit a balance between O–O bond-breaking and the electroreduction of the oxygenated intermediates. One of the key differences for the ORR in an AEMFC and a PEMFC is the ORR products: OH^- species are produced at the cathodes of the AEMFC, but water is formed at the cathode of the PEMFC. Removing water from the cathode to prevent cathode flooding is one of the major technical challenges in developing PEMFCs.

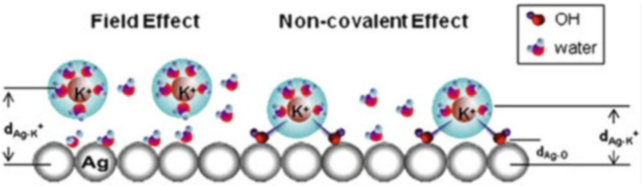

Fig. 15.9 A schematic illustration of the interface structure at the negatively charged (*left*) and positively charged (*right*) surface. The layer separations obtained from the crystal truncation rod (CTR) measurements are indicated [46]

Similarly, removing OH^- species efficiently from the catalyst surface is essential for AEMFC to prevent the active sites of the catalysts being blocked by the OH^- species, which could hinder O_2 adsorption.

At the cathode operation potentials of an AEMFC, the metallic electrode surfaces (such as Pt, Au, Pd, or Ag) tend to be covered by bonded OH^- groups due to the electrode potentials for the ORR are often more positive than the potential of zero charge (pzc) of the metallic electrodes. The OH^- binding on the cathode catalysts is likely one of the major factors causing large cell voltage losses in AEMFCs as comparing with the polarization curves observed with the PEMFC under similar test conditions. Additionally, the presence of the hydrated cation layer was postulated by Strmcnik et al. [44] who reported that the ORR reactivity on Pt(111) electrodes was dependent on the particular cation present in the electrolyte solution. They proposed a model in which hydrated alkali metal cations form a non-covalent bond with adsorbed OH_{ad} species on the surface and thus influence the ORR electrocatalytic reactivity. The influence of non-covalent interactions on the electrochemical interface of a metallic electrode in an alkaline electrolyte depended on the nature of the metal and the cation. For example, the impact of the cation on the ORR on Au electrodes was negligible, but the ORR activity on Pt electrodes was significantly affected by the type of the cations in the electrolyte solution [44, 45].

Lucas et al. studied the structure of the electrochemical double layer at the interface between a Ag(111) electrode and 0.1 M KOH electrolyte using in situ surface X-ray scattering (SXS) and proposed an interface structure, at the negatively charged and positively charged surface, as shown in Fig. 15.9. At negative potential ($E = -1.0$ V vs. SCE), the presence of an hydrated K^+ cation layer at a distance of 4.1 ± 0.3 Å from the Ag surface was detected, and at a more positive potential ($E = -0.2$ V), the presence of OH_{ad} stabilized the hydrated K^+ cations through a non-covalent interaction forming a compact double-layer structure in which the Ag–K^+ distance was reduced to 3.6 ± 0.2 Å, which (the compact double layer) hindered the O_2 adsorption for ORR. Since the strong electric field favorable for OH^- adsorption on the cathode presents in AEMFCs, especially at high cell voltages [42], we believe that the OH_{ads} on the catalyst surface as a function of the electrode potential could play important roles in determining the ORR activity.

The OH^- binding effects on ORR on Ag(hkl) surfaces were studied by Markovic et al. [46, 47]. Similar to that on Pt surfaces, the rate-determining step (rds) for the

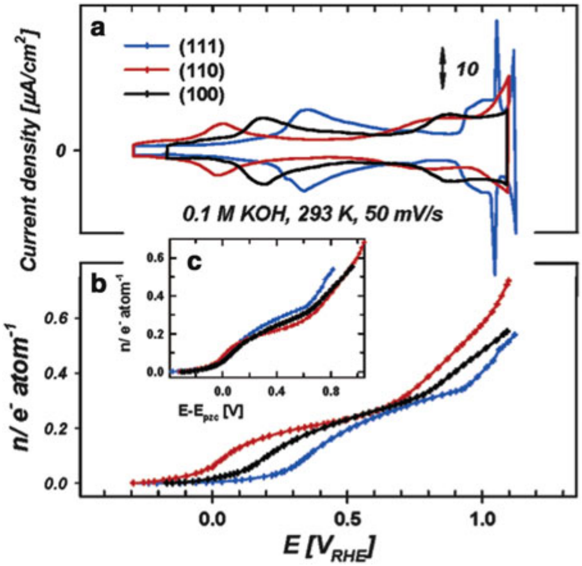

Fig. 15.10 (**a**) CV curves in Ar-purged 0.1 M KOH on Ag (hkl) surfaces. All CVs were obtained at room temperature with a sweep rate of 50 mV s^{-1}. (**b**) Fractional charge per atom, obtained by integrating the anodic sweep direction of CV (from **a**) after accounting for the different surface atom density of different Ag(hkl) orientations. (**c**) Fractional charge per atom expressed on the rational potential scale (RPS) [47]

ORR on Ag single crystal surfaces was assumed to be the first charge-transfer step [47] and described as:

$$O_{2,ad} + e^{-} \rightarrow {}^{\bullet}O_{2,ad}{}^{-}, \tag{15.6}$$

The rate of the ORR on an Ag surface can be expressed as [46]

$$i = nFkC_{O2}(1 - \theta_{ad})^{x} \exp^{((-\beta FE)/RT)} \exp^{((-\gamma r^{\theta}_{ad})/RT}. \tag{15.7}$$

where n is the number of electrons; k is the chemical rate constant; C_{O2} is the concentration of O_2 in the alkaline media; θ is the degree of the total surface coverage by all adsorbed species; x is either 1 or 2, depending on the sites of requirements of the adsorbates; β and γ are the symmetry factors; r is the parameter for the rate of change of the free energy of the adsorption of the reacting intermediates with the surface coverage by the adsorbed species; and E is the applied potential. In either a 0.1 M NaOH solution or under the AEMFC test conditions, the OH_{ad} species can be considered as the dominating adsorbates on the Ag surface that determine the value of θ_{ad}.

The OH adsorption isotherm on various Ag (hkl) surfaces as a function of the electrode potential was reported by Blizanac et al. [47], as shown in Fig. 15.10. It is seen that the OH coverage (θ_{OH}) was quite low at a cell voltage of about 0.1 V versus RHE and increased with increasing electrode potentials (0.2–0.4 V vs. RHE). Then, a θ_{OH} plateau was observed at potentials of 0.4–0.7 V versus RHE, and a new steep increase in θ_{OH} was observed when the electrode potential was higher than 0.7 V versus RHE. This OH adsorption isotherm as a function of the electrode potentials can explain why there were two distinct discharge regions in the polarization curves observed on the Ag/C MEAs in the H_2/O_2 AEMFCs (Fig. 15.8). When the cell voltage was above 0.55 V, the cell voltages on the Ag/C MEA fell sharply with the increasing discharge current. But when the cell voltages fall below 0.5 V, the electrode polarizations with increasing discharge current seem to become less. Referring to the OH adsorption isotherms [47], the OH coverage on the Ag catalyst surfaces at the cell voltages above 0.7 V in H_2/O_2 AEMFCs could be rather high (30–50 %), which would lead to lower ORR kinetic currents on the Ag/C catalysts according to Eq. (15.7). Corresponding to the θ_{OH} plateau in Fig. 15.10, a cell voltage plateau (0.60–0.50 V) was observed in the steady-state polarization curves on the Ag/C MEA in the H_2/O_2 AEMFC performed at 50 °C. When the cell voltages continued to fall to 0.1 V, the θ_{OH} on Ag/C electrode continued to drop, causing the discharge current to increase substantially; these observations also agree well with the prediction of OH adsorption on Ag(111) surface by DFT calculations [43]. Therefore, one can conclude that when the cell voltages fall below 0.5 V, the ORR kinetics on the Ag/C MEAs were significantly improved due to the reduction in OH coverage (θ_{OH}) on the Ag surface at the lower cell voltages. To further improve the performance of Ag/C catalysts in AEMFCs, it is essential to reduce the θ_{OH} on the Ag surface in AEMFCs, especially at the high cell voltages. Macrocyclic molecules can be used to modify Ag/C electrodes [42, 48] and have been demonstrated by the present authors to reduce OH^- coverage on Ag/C surfaces in AEMFCs; the results for macrocycle-modified Ag/C electrodes will be presented in the last section of this chapter.

15.3 ORR on Carbon-Supported Transition-Metal Macrocycles ($M/N_4/C$)

Inspired by biological catalysts such as myoglobin and hemoglobin, many $M–N_4$-macrocycles have been investigated extensively as promising catalysts for the ORR in alkaline and acid media for several decades; such macrocycles include transition-metal porphyrins (MPs) and phthalocyanines (MPcs), and nitrogen-coordinated iron or cobalt in a carbon matrix (Fe/N/C or Co/N/C) [27, 49–88]. It has been established that (1) the type of the central metal atom is the determining factor on catalytic activity; (2) the majority of mononuclear Co-macrocycles catalyze the ORR via a $2e^-$ pathway to produce peroxide (H_2O_2), while iron complexes tend to promote the $4e^-$ pathway to form water; (3) the polymeric or heat-treated $M–N_4$ or $M–N_2$ forms could lead to better chemical and thermal stabilities, higher electronic conductivities, and higher O_2 activities than their monomeric species; and (4) the pH values of electrolytes can affect the activity and stability of the catalysts. A breakthrough in the synthesis of Fe/N/C or Co/N/C catalysts was achieved by Yeager et al. who reported that the MPc or MP macrocycles can be replaced by the catalyst materials derived from separate metal (Co(II) and Fe(II) containing salts) and nitrogen (polyacrylonitrile) [62]. Following this approach, several synthesis methods to prepare various pyrolysis Fe/N/C or Co/N/C catalysts have been reported [64–78]. Recently, Lefèvre et al. reported their best Fe–N–C catalysts could match the initial performance of state-of-the-art Pt/C catalysts in PEMFCs, but were less stable [75–79]. Zelenay et al. reported non-precious metal catalysts derived from polyaniline, iron, and cobalt having ORR at potentials within ~60 mV of that delivered by state-of-the-art Pt/C, remarkable performance stability (700 h at a fuel cell voltage of 0.4 V), and excellent four-electron ORR activity (hydrogen peroxide yield <1.0 %) [80]. Recent advances of these types of catalysts in an acidic medium can be found in Chaps. 7–11 of this book.

A collaborative work from five different laboratories was reported [75] that non-noble-metal catalysts (NNMCs) prepared by various synthesis methods, including wet impregnation, planetary ball milling, a foaming agent technique, or a templating method, were investigated for the catalysis of ORRs in an acidic medium. All catalyst precursors were heat-treated at 700–1,050 °C in an inert or reactive atmosphere. These catalysts were tested with an identical set of electrochemical characterizations, including RDE and PEMFC tests and voltammetry under N_2. The RDE and PEMFC test results are shown in Figs. 15.11 and 15.12, respectively. Although different synthesis methods were used, the observed ORR activity on these NNMC catalysts was 150–200 mV below that of Pt/C. The most interesting results from this work are shown in Fig. 15.13, in which the ORR mass activity of the NNMCs was found to be higher in the fuel cell than in RDE, up to a multiplication factor >20 for the samples M786 and DAL900C. It was also found that Pt-based catalysts did not show such an effect. To explain this difference by RDE and PEMFC tests with various NNMCs, the authors suggested new comprehensive studies of the effect of the temperature on the mass activity of NNMC and the optimization of the catalyst ink with respect to the Nafion ionomer and catalyst ratio for a correct measurement of the mass activity both in a RDE and a fuel cell.

Mukerjee et al. [81] studied Fe/N/C catalysts prepared by an impregnation method then heat-treated at 950 °C under a flow of NH_3 for the ORR activity in acid media. They found that N-protonation and anion-binding effects on the Fe/N/C catalyst resulted in ORR activity decay. The bound anions could be removed thermally or chemically, which restored the activity of the acid-resistant FeN_4 sites. They proposed that protonation of basic N-groups occurs immediately in RDE or fully humidified PEMFC environment but that anion binding is delayed in PEMFC due to restricted mobility of the sulfonate groups, which was considered to explain the difference of ORR activity on the Fe/N/C catalysts by RDE and PEMFC measurements. By analyzing the electrical fields presented in a RDE and a PEMFC, we recognize that unlike in an AEMFC, the potentials on the counter electrodes in acidic solutions are more positive than the RDE to provide the currents for the ORR at the RDE, while the potentials at the cathode of a PEMFC are always more positive than the potentials at the anode. The electrical field in the RDE could cause the N-protonation on the Fe/N/C catalyst occurred more favorably than that in PEMFCs. Depending on the nature of the M/N/C catalysts, the strength of N-protonation and

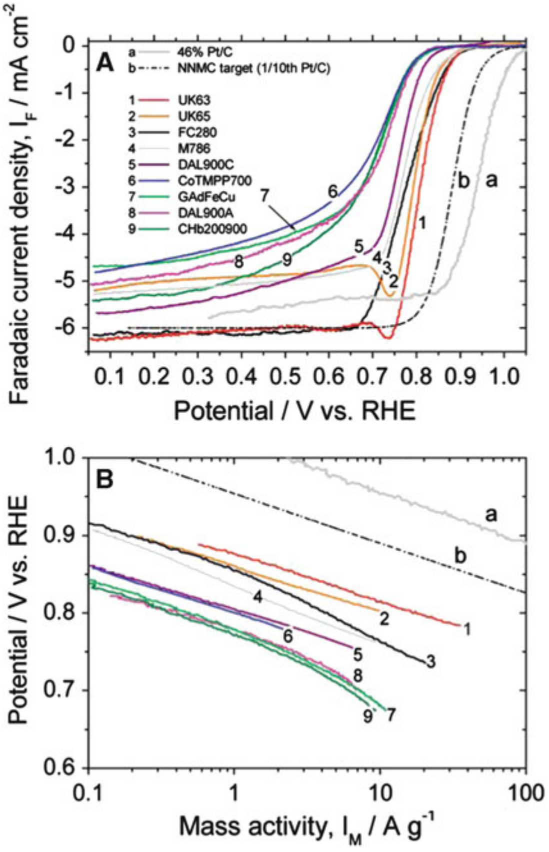

Fig. 15.11 (**A**) Polarization curves in RDE at 1,500 rpm. O_2-saturated electrolyte of pH 1 at 20 °C. NNMC loading of 800 μg cm^{-2} except UK63–65 (460 μg cm^{-2}) and CoTMPP700 (306 μg cm^{-2}). Curve a: Pt/C, 302 μg of Pt cm^{-2} (355 μg of C cm^{-2}). Curve b: NNMC target for year 2010 for a loading of 460 μg cm^{-2}. Other curve labels are 1 (UK63), 2 (UK65), 3 (FC 280), 4 (M786), 5 (DAL900C), 6 (CoTMPP700), 7 (GAdFeCu), 8 (DAL900A), and 9 (CHb200900). (**B**) Tafel plots (*E* vs. log *I*) in RDE. Same conditions as those in part **A**. Curve a: 46 % Pt/C. Curve b: NNMC target by US DOE for year 2010 [75]

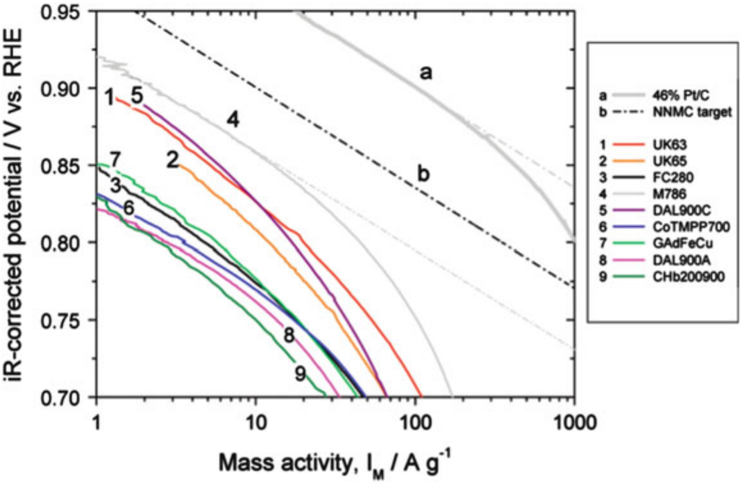

Fig. 15.12 Tafel plots of the various NNMC cathodes in a PEMFC. NNMC loading 1 mg cm^{-2}. Naf/Cat = 2. Curve a: 46 % Pt/C; 0.33 mg of Pt cm^{-2}; Naf/Cat = 2. Curve b: estimated target activity for NNMC for year 2010 [75]

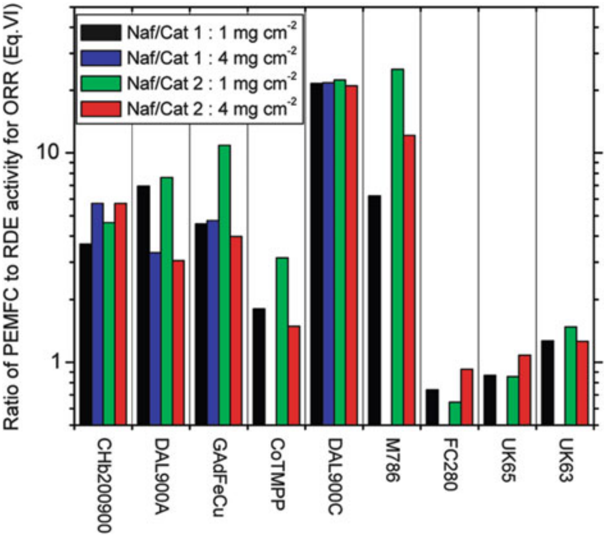

Fig. 15.13 ORR mass activity normalized by mass capacitance: effect of a switch from the RDE system (20 °C) to the PEMFC system (80 °C) [75]

anion-binding effects on the catalysts can be different, which would reflect in the variations of ORR mass activities of the NNMCs observed in the fuel cell and in RDE, respectively.

Olson and his coworkers studied the ORR on a family of electrocatalysts derived from a Co-containing precursor and a polypyrrole/C composite material (PPy/C) in alkaline media [82]. Based on structural evaluations and electrochemical studies, it was revealed that pyrolysis leads to the formation of a composite catalyst material, featuring Co nanoparticles coated with Co oxides and Co^{2+} species associated with N–C moieties that originate from the polypyrrole structures. Based on the structure-to-property correlations, they proposed a dual-site mechanism: O_2 is initially reduced at a Co^{2+}-containing N–C type site in a $2e^-$ process to form HO_2^-; then, the HO_2^- species can undergo either further electrochemical reduction to form OH^- species or chemical disprotonation to form OH^- species and molecular O_2 at the decorating Co_xO_y/Co surface nanoparticle phase. The importance of developing bifunctional catalyst materials for the ORR in alkaline media is recognized as essential for their potential applications in AEMFC systems; these types of studies are also reported by several groups [42, 48, 83, 84] and will be discussed in more details in the last section.

Since extensive research has been carried out in the last five decades to understand ORR mechanisms on various N_4-macrocyclic metal complexes with and without heat treatment in both acid and alkaline solutions, here we will not repeat what has been reviewed by other experts in the field but only focus on the application aspects of carbon-supported N_4-macrocyclic metal complexes (M–N_4/C) in alkaline conditions and for AEMFCs. Here, the ORR activity on M–N_4/C catalysts measured in RDE and AEMFCs is presented and compared. Key fundamental aspects of the ORR activity and stability of M–N_4/C catalysts for practical AEMFC applications are discussed.

15.3.1 ORR Activity Obtained by RDE or RRDE

The RDE or RRDE in an electrochemical cell (Fig. 15.2) is widely used to study ORR kinetics on M–N_4/C complexes in electrolyte solutions. Co and Fe macrocycles have been studied extensively as catalysts for oxygen reduction [27, 49–93]. Co-phthalocyanine (CoPc) and Co-tetrasufonated phthalocyanine (CoTsPc) adsorbed on carbon surfaces have been found to catalyze 2e reduction of O_2 to form H_2O_2 in both alkaline and acid solutions, while Fe-phthalocyanine (FePc) and Fe-tetrasufonated phthalocyanine (FeTsPc) catalyze the overall 4e reduction in alkaline solutions [83–86]. In an acid solution, certain face-to-face Co-porphyrins, which can form a dioxygen bridge between two Co-centers on graphite surface, have been shown to catalyze 4e reduction [58–60].

The central metal atoms in phthalocyanines have dominant influences on the ORR catalytic activities of the MPc molecules. Kazarinov et al. [89] reported that regardless of pH, the ORR activity of MPcs varies in the order: Fe(II, III) $>$ Co(II), Mn(II) $\gg$ Ni(II) $>$ Cu(II) $>$ hydrogen. Shukla et al. [90] also found a similar trend in the order of electrocatalytic activity with the exception of MnPc, i.e., FePc $>$ CoPc ~ CoTPP $>$ NiPc $\ggg$ MnPc where TPP is tetraphenylporphyrin. Guo et al. tested the ORR activity on XC-72 carbon and various MPc/C (M = Mn, Fe, Co, and Ni) catalysts on a RRDE in O_2-saturated 0.1 M NaOH solutions with the identical experimental setup and test procedures. The RRDE polarization curves for O_2 reduction on these catalysts at a rotation rate of 2,500 rpm are shown in Fig. 15.14a [92], which indicate that O_2 undergoes a $4e^-$ reduction pathway to produce OH^- on FePc and MnPc, respectively, but the ORR occurs on CoPc or NiPc complexes via a 2e pathway to produce H_2O_2. The results agree well with those reported by others [87–90]. The mass-corrected Tafel plots of log I_k (mA cm^{-2}) at a rotation rate of 2,500 rpm are shown in Fig. 15.14b. The Tafel slope for the FePc/C catalyst can be divided into two parts, i.e., about 40 mV dec^{-1} in the lower overpotential region ($E > 0$ V vs. Hg/HgO) and about 120 mV dec^{-1} in the higher overpotential region ($E < -100$ mV vs. Hg/HgO). The Tafel slope of the CoPc/C catalyst was around 140 mV dec^{-1} in the higher overpotential region ($E < -150$ mV vs. Hg/HgO). At a typical alkaline fuel cell cathode working potential (−0.05 V vs. Hg/HgO, equivalent to an overpotential of 0.280 V), the ORR kinetic current on the FePc/C is 10 mA cm^{-2}, which is about three times higher than that of the Pt/C electrode (3.1 mA cm^{-2}) [93]. The ORR activities measured from RDE are in the following order: FePc/C $>$ CoPc/C $>$ NiPc/C ~ MnPc/C ~ C. Among the five tested MPc/C catalysts, FePc/C displayed the highest ORR activity in a RDE in an O_2-saturated 0.1 M NaOH electrolyte environment. However, as shown in Fig. 15.15a, compared with CoPc, the FePc pre-coated on a RDE displayed a more significant reduction in its ORR current density with each cycle [93]. After 30 cycles, the ORR catalytic activity on the FePc electrode dropped dramatically. At the end of the 30th cycle, the FePc electrode was left in the same

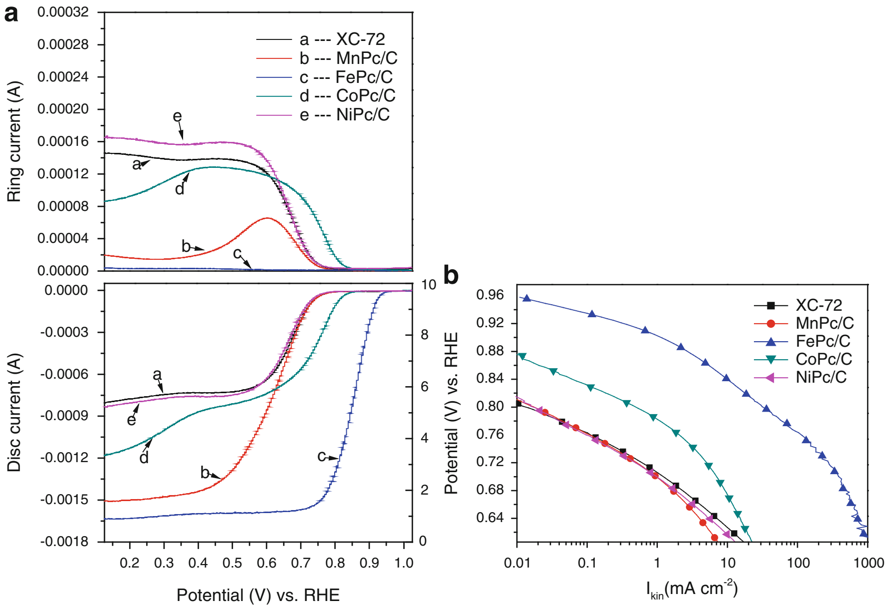

Fig. 15.14 (**a**) RRDE measurements of ORRs on XC-72, MnPc/C, FePc/C, CoPc/C, and NiPc/C catalysts with a rotation rate of 2,500 rpm in oxygen-saturated 0.1 M NaOH solutions. Collection efficiency $N = 0.41$; ring potential $E_r = 0.3$ V versus Hg/HgO; scan rate 20 mV s^{-1}. (**b**) Tafel plots of the ORRs on the XC-72, MnPc/C, FePc/C, CoPc/C, and NiPc/C catalysts [92]

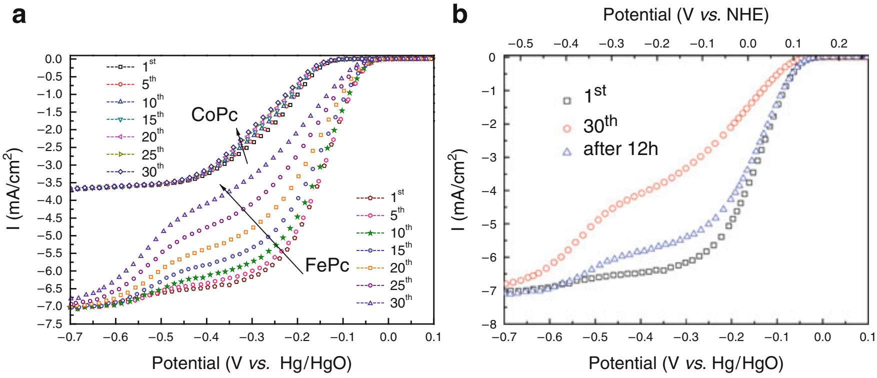

Fig. 15.15 (**a**) The stability test for FePc and CoPc pre-adsorbed on a RDE in an O_2-saturated 0.1 M NaOH with a scanning rate 10 mV s^{-1}; a rotating rate of 2,500 rpm; room temperature. (**b**) The performance recovery test for the FePc RDE in the O_2-satureated 0.1 M NaOH solution [93]

NaOH solution for 12 h, then put under the ORR activity test again. As shown in Fig. 15.15b, a noticeable recovery in the ORR catalytic activity of the FePc catalyst was observed, which suggested that the instability of FePc in electrocatalyzing O_2 reduction in alkaline media is not mainly caused by irreversible demetalation, which was considered to be responsible for the degradation of FePc in acid system [70, 94].

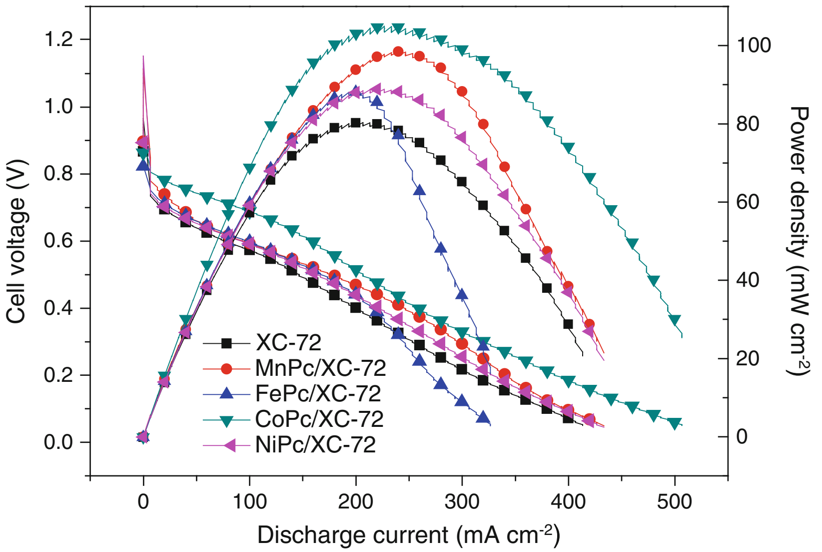

Fig. 15.16 Polarization and power density curves of AEMFCs using XC-72, MnPc/C, FePc/C, CoPc/C, and NiPc/C as cathode catalysts, respectively. Anode: 50 wt.% Pt/C, flow rate 200 sccm H2, 100 % humidity. Cathode: 2.0 mg catalyst cm^{-2}, flow rate: 200 sccm O_2, 100 % humidity. Test temperature: 50 °C; back pressure: 20 psi [92]

15.3.2 ORR in AEMFC

The performance of XC-72 carbon, MnPc/C, FePc/C, CoPc/C, and NiPc/C, as described in the previous section, was also tested in AEMFCs, which were assembled with the same anode (50 wt.% Pt/C), anion-exchange membranes (A901 from Tokuyama), but various cathode catalysts [92]. The loadings of the cathode catalysts in the MEAs were 2 mg cm^{-2} for all the test cells. The polarization and power density curves obtained with XC-72 carbon, MnPc/C, FePc/C, CoPc/C, and NiPc/C MEAs are shown in Fig. 15.16 [92]. Unlike the non-noble-metal catalysts (NNMCs) that displayed the higher ORR activity in the PEMFC than in RDE (Fig. 15.13), the FePc/C showed much better ORR activity in RDE than in the AEMFC, while CoPc, NiPc, and MnPc showed similar ORR activity in RDE as in AEMFCs. Based on DFT calculations and electrochemical impedance measurements [93], the strong OH^- binding effect on FePc catalysts in the AEMFC test environment was considered to be responsible for the discrepancy of ORR activity in RDE and AEMFCs on FePc/C catalysts, which are discussed in more details later.

As shown in Fig. 15.17, Kim et al. studied various cathode catalysts for oxygen reduction in microbial fuel cells that contained culture media prepared with 1 g L^{-1} sodium acetate solution in 50 mM phosphate buffer containing 12.5 mL L^{-1} mineral solution and 5 mL L^{-1} vitamin solution [95]. Carbon-supported FePc showed similar ORR activity as the carbon powder, which had more than

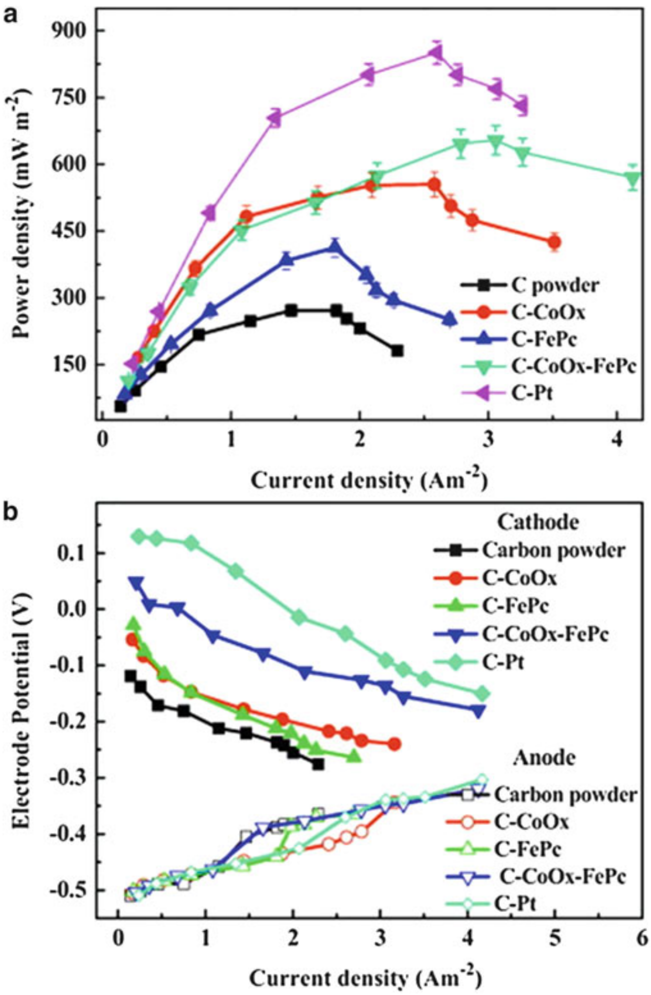

Fig. 15.17 Power density versus current density curves with various cathodes (**a**) and electrode potentials (vs. SCE) as a function of different cathodes (**b**) [95]

200 mV larger overpotentials and delivered less than half of power capacity in microbial fuel cells. Mamlouk et al. reported ORR activities on FePc/KJB carbon and Pt/C in RDE and AEMFC [96], as well as Co-based catalysts (named as GP2 and GP4) in RDE and AEMFC [97]. In 1.0 M KOH solution, the FePc/KJB C displayed slightly better ORR activity than Pt/C, which agrees well with our work [93]. The performance of FePc/KJB in AEMFCs was much lower than what was observed in RDE, especially for the FePc/KJB electrodes prepared with an anion-exchange polymeric electrolyte as the ionomer. The authors believed that the poor performance of the FePc/KJB electrodes was due to the dissolution of FePc from the carbon (Ketjen Black) support during the amination process leaving

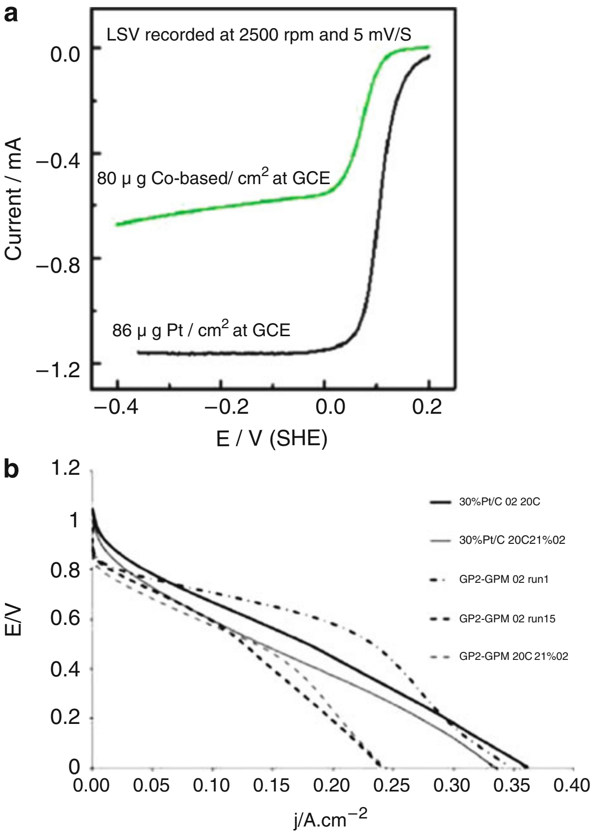

Fig. 15.18 (**a**) LSV response recorded at 5 mV s^{-1} scan rate for Co-based/C (GP2) and Pt/C in O_2-saturated 1 M KOH solution at 2,500 rpm rotation rate. (**b**) AEMFC performance comparison between MEAs utilizing platinum and Co-based as cathode catalyst for ORR in AAEM at 20 °C with oxygen and air (atm) [97]

mainly the carbon support as the acting catalyst. However, using the similar electrode preparation procedures, the Co-based catalysts displayed similar ORR activity in both the liquid KOH solution and AEMFCs [97]. Comparing the polarization curves of the Co-based catalyst in Fig. 15.18b with that on the CoPc/C in Fig. 15.16 and Pt/C in Fig. 15.17, one can see that the cell voltages of these Co-based MEAs from different research groups had similar polarization behaviors: cell voltages dropped quickly to ~0.80 V at the beginning of discharge with 150–200 mV higher overpotentials than that on the Pt/C MEAs. These results indicate that, for Co-based or Pt/C catalysts, the ORR activities in RDE and AEMFCs are fairly comparable, regardless what polymeric electrolytes and catalyst inks were used in preparing the MEAs, while the ORR activities observed in RDE on Fe-based catalysts were significantly higher than those in AEMFCs.

15.3.3 Fundamental Aspects

For Pt and other metallic catalysts, DFT calculations have been successfully applied to elucidate the origin of the overpotential of the ORR [98], the mechanism of the

ORR in acids [99], and the alloying effect on the catalytic activity for the ORR [100]. However, similar studies for M–N_4-macrocycles are relatively few. Liao et al. [101] reported the influence of some peripheral ligands [-porphyrin (P), -porphyrazine (Pz), and -phthalocyanine (Pc)] on the electronic structure of a series of M–N_4 complexes (here, M = Fe, Co, Ni, Cu, and Zn). They found that replacing the CH-groups in the MP molecules by N atoms led to the stabilization of all valence molecular orbitals in the MPz molecules, while introducing the benzo rings into the MPz molecules to form the MPc molecules destabilized the occupied valence molecular orbitals [101]. They also studied how varying the central transition atom (here, M = Fe, Co, Ni, Cu, Zn, Mg) would affect the electronic structures of the MPc molecules [102]. It was concluded that the highest occupied molecular orbital (HOMO) of the FePc, CoPc, and CuPc molecules resembled the 3d orbital of the metals, while the HOMO of the NiPc and ZnPc molecules localized on the phthalocyanine ring [102]. Shi and Zhang [103] applied the DFT calculations to determine the adsorption structures of O_2 molecule on various MP and MPc complexes. They found that the central metal, ligand, and substituents were major factors in affecting the oxygen adsorption on these MP and MPc molecules. We also conducted DFT calculations to study the molecular and electronic structures of O_2, H_2O, OH, and H_2O_2 molecules adsorbed on various MPc molecules (M = Fe, Co, Ni, and Mn) [92, 93, 104, 105]. The DFT calculation results can be used to better explain ORR activities (on various MPc/C catalysts) observed in the RDE and AEMFCs tests [92, 93].

Based on Eqs. (15.4) and (15.5), for the ORR in an alkaline media, O_2 and H_2O are the reactants, while OH^- is the final reaction product. The strength of the interactions between the O_2 or OH^- species and the M–N_4 molecules is expected to profoundly influence the rate of ORR on the molecular catalysts. In the DFT calculations, adsorption energy (E_{ad}), which is defined as the energy difference between the adsorption assembly and the isolated systems of the adsorbate and molecular catalyst, is used to gauge the binding strength between the adsorbate and the molecular catalyst [93, 104]. Negative adsorption energy indicates that the adsorbate is energetically favorable to be adducted to the surface of the molecular catalyst. Consequently, the negative adsorption energy of the O_2 molecule on the catalyst surfaces is a requirement for the catalyst to promote the ORR.

There are two possible ways for O_2 to be adsorbed on M–N_4 molecules: the end-on configuration and the side-on configuration. In the end-on configuration (see Fig. 15.19a, b), one oxygen atom lies right above the central metal atom over the catalyst molecule plane, and the other oxygen atom is farther away from the metal atom. In the side-on configuration (see Fig. 15.19c, d), the adsorbed O_2 molecule lies parallel to the catalyst molecule plane, and the two oxygen atoms are in equal distance from the central metal atom. It was found that all four structures shown in Fig. 15.19 are stable for the O_2 on FePc, while only the end-on configurations are energetically stable for O_2 on CoPc molecule. By using in situ ambient-pressure X-ray photoelectron spectroscopy and X-ray absorption spectroscopy under hydrogen and oxygen atmospheres, Miedema et al. [106] studied the electronic structure of the CoPc and FePc. Their experimental results

Fig. 15.19 Optimized structural configurations for O_2 molecule adsorbed on FePc and CoPc molecules. (**a**) and (**b**) are two end-on configurations; (**c**) and (**d**) are two side-on configurations. The *central yellow ball* represents metal Fe or Co atom, the *central two red balls* represent the adsorbed O_2 molecule, *blue balls* represent N atoms, *gray balls* represent C atoms, and *light white balls* represent H atoms [104]

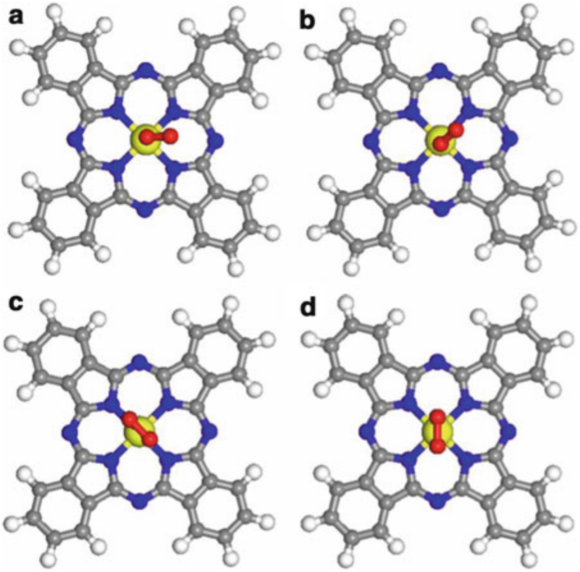

showed that when oxygen was introduced, the iron changed oxidation state, while the cobalt did not, and support our DFT calculation results that oxygen binds in an end-on configuration in CoPc, while for FePc side-on binding is most likely [104].

The latest DFT calculation results of O_2 adsorbed on ten different M–N_4 complexes indicate that the adsorption energies of O_2 on the Fe macrocyclic complexes were lower than those on the Co macrocyclic complexes [105]. Moreover, the distance ($D_{\text{TM-O1}}$) between the central metal atom and the adjacent O atom of O_2 on the Fe macrocyclic complexes was considerably shorter than the corresponding value of O_2 on the Co macrocyclic complexes [105]. The DFT results indicate that the adsorbed O_2 molecule would form stronger bonding with the Fe macrocyclic complexes than with the Co macrocyclic complexes. Yeager et al. [107] had postulated many years ago that the affinity of Fe(II)Pc for O_2 may be very high compared to that for the reaction intermediates, products, or other solution-phase components and suggested that this strong interaction with O_2 compared to that with other species can be of critical importance to the electrocatalytic activity involving a single type of iron site. Our finding in DFT calculations and RDE results [93] supports the postulation that O_2 adsorption plays a key role in the activation and reduction of oxygen: the lower the O_2 adsorption energy, the higher the kinetics of the ORR on the MPC molecular catalysts.

Although FePc/C catalysts possess high ORR activities in alkaline media, they were found to degrade rapidly on a RDE in alkaline solutions [92] and showed poorer ORR activity than the carbon supports in AEMFCs [93, 96]. In contrast, the ORR activity on CoPc/C catalysts was rather stable in both the RDE and AEMFCs [93, 97]. We could use DFT results to explain these experimental observations:

Table 15.1 Calculated adsorption energy (in units of eV) of reactant (O_2 and H_2O), product (OH), and reaction intermediate (HOOH and H_2OO) molecules adsorbed on FePc, CoPc, NiPc, and MnPc catalyst molecules using the first-principle DFT method

	O_2	H_2O	OH	HOOH	H_2OO
FePc	−1.16	−1.05	−3.41	−1.05	−1.03
CoPc	−0.40	−0.32	−2.36	−0.24	−0.47
NiPc	−0.31	−0.05	−1.33	−0.10	−0.49
MnPc	−0.96	−0.28	−2.93	−2.76	−0.30

Table 15.1 lists the DFT calculation results of the adsorption energy of O_2, H_2O, H_2O_2, and OH on various MPc molecules [92]. It can be seen clearly that the energy for OH adsorption on various MPc molecules was significantly lower than the energy for O_2, H_2O, or H_2O_2 adsorption on the same molecules, following the order of FePc $>$ MnPc $>$ CoPc $>$ NiPc. Based on the DFT calculation results and the ORR activities on various MPc molecules in RDE and AEMFCs, it can be deduced that OH adsorption on the catalysts is an important factor that determines the ORR activity and stability of the MPc catalysts [92, 93]. The OH adsorption is more energetically favorable than O_2 adsorption on MPc (M = Fe, Co, Ni, and Mn) catalyst molecules. This would cause the produced OH molecule to occupy the active sites of the catalysts and hamper further progress (O_2 adsorption) of ORR. The DFT results indicate that this degradation process due to the OH^- adsorption should be more severe for FePc than other MPc (M = Co, Ni, and Mn) molecules due to its larger energy for adsorbing OH. Consistent with the DFT calculation results, the RDE stability tests showed clearly that the FePc/C catalyst lost its performance much more quickly than the CoPc/C catalyst and that the performance of FePc/C in H_2/O_2 AEMFCs was poorer than its carbon supports due to the strong electric field that favors strong OH^- adsorption on FePc molecules [92].

In the previous sections, we have pointed out the fact that the strong electric field presented in a MEA could have major effects on protonation and OH adsorption and causing inconsistencies between RDE and fuel cell testing results on ORR activities. For RDE tests in acid solutions and for PEMFCs, the electric field is more favorable for protonation in RDE than in PEMFCs; consequently, the N-protonation effects on the Fe/N/C catalyst could occur more favorably in RDE than in PEMFCs and resulted in poorer ORR activity observed in RDE than in PEMFC on various M/N/C catalysts (Fig. 15.13). On the other hand, the electric field in an alkaline condition is such that the OH^- binding effects on FePc/C catalysts were more severe in AEMFCs than in RDE; the FePc/C catalysts tended to lose their ORR activity in AEMFCs rapidly. A balance of O_2 and OH^- adsorption strength is important for achieving high ORR activity and for catalytic stability in AEMFCs. Among the four tested MPc/C (M = Fe, Co, Ni, and Mn) catalysts, the CoPc/C catalysts displayed the highest ORR activity in AEMFCs (Fig. 15.16), but still much lower than the Pt/C catalysts (Fig. 15.8).

The RDE and RRDE measurements of various MPc/C catalysts in O_2-saturated alkaline solutions lead to the conclusion that O_2 undergoes a $4e^-$ reduction

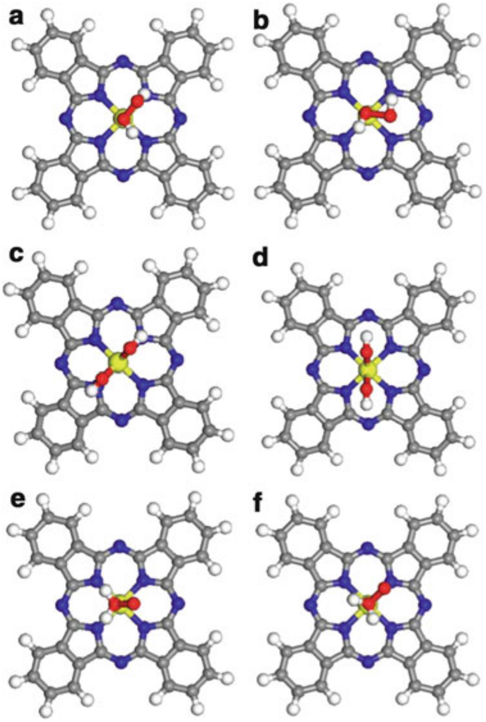

Fig. 15.20 Optimized structural configurations for HOOH (**a**–**d**) and H_2OO (**e** and **f**) molecules adsorbed on FePc/CoPc molecules. The *central yellow ball* represents the metal Fe/Co atom, the *two red balls* represent O atoms, *blue balls* represent N atoms, *gray balls* represent C atoms, and *light white balls* represent H atoms [93]

pathway to produce OH^- on either FePc or MnPc catalysts, but a $2e^-$ reduction to produce H_2O_2 on CoPc or NiPc complexes. H_2O_2 is a product of the $2e^-$ ORR and might be an intermediate molecule in the $4e^-$ route of ORR. As shown in Fig. 15.14a, either no H_2O_2 or very small amounts of H_2O_2 were detected on the FePc/C electrodes, but significant amounts of H_2O_2 were observed on the CoPc/C, NiPc electrodes. The DFT calculations could be used to provide an explanation as to the above observation. The H_2O_2 molecule has two isomers: HOOH (hydrogen peroxide) and H_2OO (oxywater). Figure 15.20 shows the possible structures of HOOH and H_2OO molecules adsorbed on the catalyst molecules (according to DFT). On FePc molecules at the lowest energy state, H_2O_2 has a geometric structure as shown in Fig. 15.20c. DFT calculation predicts that the two O atoms in an H_2O_2 molecule bind to the common central Fe atom with a distance of 1.820 Å, bind to individual H atoms with a distance of 0.972 Å, but are separated from each other by a distance of 2.368 Å. In an isolated HOOH molecule, the O–O bond length is calculated to be 1.487 Å. Hence, O–O bond breaking, which is a prerequisite for $4e^-$ ORRs, will occur during the process of H_2O_2 adsorption on FePc molecules. In contrast, Fig. 15.20c shows an unfavorite adsorption configuration for HOOH on CoPc molecules. Instead, the H_2O_2 molecule prefers to have the configuration of Fig. 15.20e when adsorbed on CoPc. In that optimized configuration, the two O atoms in the H_2O_2 molecule are only 1.536 Å apart, which is very close to the equilibrium O–O bond length of 1.501 Å in an isolated H_2OO molecule. One can therefore deduce that O–O bond breaking does not happen during the process of H_2O_2 adsorption on CoPc molecules. The DFT calculations of the adsorption of HOOH and H_2OO on NiPc and MnPc molecules were also performed [100]. As shown in Table 15.1, the energies for H_2O_2 adsorption on the FePc and MnPc molecules were significantly lower than those on the CoPc and NiPc molecules. On the MnPc molecule, O–O bond breaking was shown to be the most stable configuration during the process of H_2O_2 adsorption, while the H_2O_2 molecule preferred to have the configurations of Fig. 15.20d when adsorbed on the NiPc molecule. The above described DFT results on H_2O_2 adsorption suggest that the ability to break the O–O bond accounts for the $4e^-$ ORR on the FePc or MnPc catalyst molecules, while the lack of this ability leads to the $2e^-$ ORR on the CoPc or NiPc catalysts.

15.3.4 Summary of ORR on M/N_4/C Catalysts

By performing detailed DFT simulations of the adsorption of O_2, H_2O, OH, and H_2O_2 molecules on various “model” M/N_4/C molecular catalysts, several principles for selecting M/N_4/C molecules as cathode catalysts for AEMFCs can be established (1) the lower the O_2 adsorption energy, the higher the kinetics of the ORR on the M/N_4/C can be expected; (2) the breaking of the O–O bond during H_2O_2 adsorption is essential for the $4e^-$ ORR on M/N_4/C catalysts, while the lack of the O–O bond breaking process leads to the $2e^-$ ORR; (3) OH adsorption on the catalysts is an important factor to determine the stability of the M/N_4/C molecular catalysts, especially in AEMFCs. The M/N_4/C catalysts must not bind OH^- species too strongly in order for OH^- to be removed quickly. Based on the DFT calculation results and ORR activities observed in RDEs and AEMFCs, one may conclude that a balance between the O_2 and OH adsorption strengths on M/N_4/C catalysts is essential to high-performance cathode catalysts for practical AEMFC applications. None of the single “known” M/N_4/C catalysts seems to have the desired balance of O_2 and OH adsorption strengths, e.g., FeN_4 complexes show a too strong OH adsorption strength, while CoN_4 complexes have a rather weak O_2 adsorption [105]. An ideal catalyst for achieving the highest activity should possess the combined properties of (1) strong O_2 adsorption, (2) the ability of O–O bond breaking, and (3) weak OH^- adsorption to avoid OH^- accumulation at the cathode. Our systematic DFT calculations have predicted that the O_2 adsorption on M/N_4 molecules is about 1 eV weaker than the OH adsorption [105], which can become a major challenge for the application of M/N_4/C molecular catalysts in AEMFCs since the OH^- binding effects on these catalysts may reduce the number of active sites for O_2 reduction, especially at the high cell voltages of an AEMFC. Consequently, none of the M/N_4/C catalysts seems to be able to achieve an ORR activity comparable to the benchmark Pt/C catalysts in AEMFCs, regardless of whether they exhibit better ORR activities than Pt/C in RDE.

15.4 Bifunctional Non-Pt Catalysts for ORRs in Alkaline Media

By examining the ORR activities observed on various catalyst materials in AEMFCs as shown in Figs. 15.6, 15.7, 15.16, and 15.17, the Ag/C catalyst is identified as the most promising one to replace Pt/C for AEMFC applications. However, the initial cell voltage losses were found to be 150 mV larger on the Ag/C than on Pt/C catalysts in AEMFCs. To reduce the ORR overpotentials on the Ag/C catalysts, new approaches to form bifunctional catalysts have been investigated by either alloying Ag with other transition metals or metal oxides [108–112] or by modifying Ag with MPc molecules [42, 48]. The ORR activities on various bifunctional catalyst materials in RDE and AEMFC are presented as in this section.

15.4.1 Ag-Alloys for ORRs in Alkaline Media

Pt-bimetallic (PtM) materials have been extensively investigated as catalysts for ORR in acid and alkaline media [113–120]. The enhanced ORR kinetics on PtM catalysts depend on the structural and electronic features of the Pt atoms in the PtM electrocatalysts, e.g., the Pt–Pt bond distance, the number of nearest neighbors to a Pt atom, the electron density in the Pt-5d band, and the presence of surface oxide layers. When the electronic structures of Pt are modified by alloying it with other metals, the adsorption of species from the electrolyte and the binding energies of key reaction intermediates can be altered accordingly, and thus improve the ORR reaction kinetics [32, 113–115]. Adzic et al. showed enhanced ORR activity on electrocatalysts that were prepared by placing a Pt monolayer on nanoparticle substrates [117]. Based on DFT calculations and electrochemical measurement results, the concept of activity-d-band center volcano dependences was proposed [29, 118]. It was found that the formation of a surface metal-metal bond significantly changed the electronic properties of the metal overlayer, leading to pronounced differences in the ORR reactivity of some transition-metal monolayers on various substrates [29]. The mechanism of the enhanced ORR activity on the PtM catalysts was ascribed to the reduced adsorption of oxygenated spectator species (e.g., OH^-) by modified electronic properties of Pt in the nano-segregated near-surface region [115, 116].

Compared to the publications in the literature related to PtM catalysts for the ORR, the investigations of Ag-alloy catalyst for the ORR are rather scarce. Carbon-supported Ag–Co alloys were found to have higher ORR activity in alkaline media than pure Ag, a result attributed to modification of the Ag electronic structure by Co, leading to a stronger interaction between Ag and O containing species [8, 112]. By coating carbon-supported silver nanoparticles (60 wt.% Ag/C, ~15 nm) with Pd (Pd@Ag/C) via a galvanic displacement method, Jiang et al. studied the activity and stability of Pd@Ag/C catalysts for ORR in alkaline media [108]. The XRD and CVs results indicated that Pd was deposited on Ag nanoparticles. As shown in

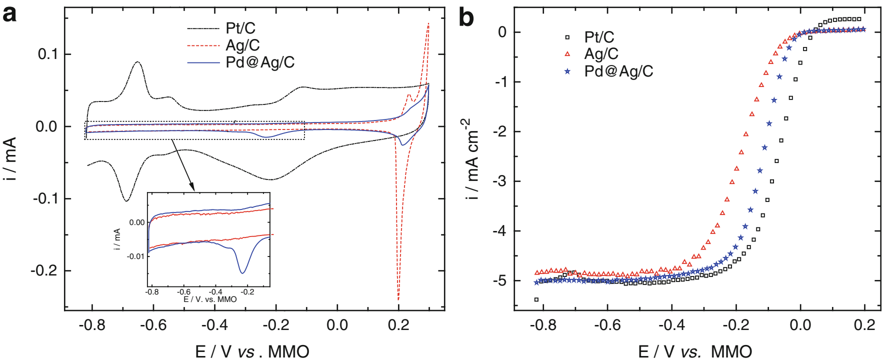

Fig. 15.21 (**a**) CV curves of the Pt/C, Ag/C, and Pd@Ag/C in Ar-saturated 0.1 M NaOH solutions. The *inset* is the enlargement of Fig. 15.1 from −0.82 to −0.1 V. Scanning rate: 10 m Vs^{-1}. Comparison of polarization curves for the ORR on the Pt/C, Ag/C, and Pd@Ag/C. Rotating speed: 1,600 rpm, scanning rate: 10 m Vs^{-1} [108]

Fig. 15.21a, the reduction peak of silver oxide on the Pd@Ag/C electrode was weakened during the anodic scan, indicating that the oxidation of silver could be inhibited due to the Pd covering of the silver surface. RDE measurement results (Fig. 15.21b) showed that the half-wave potential of the ORR on Pd@Ag/C was shifted ~70 mV more positively than that on the Ag/C electrode but was still 50 mV lower than that on the Pt/C electrode [108]. Slanac et al. reported Ag-rich AgPd alloy nanoparticles (∼5 nm) with high activities for the ORR in alkaline media [111]. As shown in Fig. 15.22, the diffusion-limited current density for the alloy corresponds to a four-electron process, higher than either pure Ag (3.4) or pure Pd (3.4). The ORR mass activity at −0.05 V versus NHE in oxygen-saturated 0.1 M KOH solutions was ~598 mA mg^{-1} of the total metal weight, which was almost an order of magnitude higher than that observed on the pure Ag/C catalysts (60 mA mg^{-1} of Ag). The enhanced ORR activity on AgPd alloy catalysts was believed to be caused by a combination of modified electronic structure and ensemble effects, which could facilitate the oxygen bond breaking and desorption for the ORR [111]. Alloying alters the electronic structure of the metals (Ag and Pd), as can be observed from the binding energy shifts in XPS. However, because of the fact that the electronic ligand effect plays a minor role next to the ensemble effects in AgPd films toward CO adsorption and oxidation [121], it was believed that the ligand effects alone are not responsible for the observed ORR activity synergy for the AgPd alloys [111]. An ensemble effect, whereby a suitable geometric arrangement of Ag next to Pd surface atoms catalyzes ORR, was believed to be also responsible for the improved ORR activity. It was proposed that, on an AgPd alloy surface, the Pd atoms may facilitate the initial oxygen binding, whereas the Ag may help to desorb the reaction products such as OH^-, evidenced by the smaller double-layer capacitances for the AgPd alloys versus Pd/VC [111]. Although the high catalytic activity of AgPd alloys for the ORR has not been verified in AEMFC applications, the concept of alloying Ag with extremely low concentrations of a highly active, precious metal for high ORR activity is applicable to a wide variety of nano-alloys.

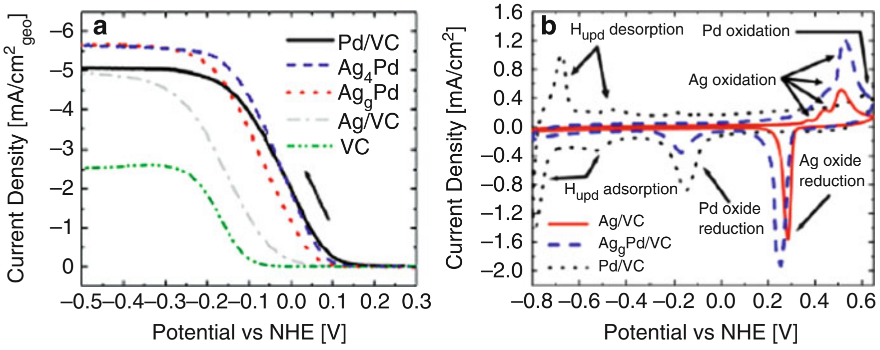

Fig. 15.22 (**a**) Linear sweep voltammograms from a RDE measurement in O_2-saturated 0.1 M KOH. The diffusion-limited current density for the alloy corresponds to a 4-electron process, higher than either pure Ag or Pd (3.4). (**b**) CV curves showing the characteristic redox peaks for the alloy and pure metal catalysts supported on Vulcan XC72 carbon. The presence of both Ag and Pd oxide reduction peaks shows that the surface is composed of both metals. However, the lack of H_{upd} for the alloy suggests that the Pd is dispersed primarily as single atomic sites. The silver oxidation peaks from 0.3 to 0.6 V shift slightly positive for the alloy catalyst, suggesting some resistance to oxidation due to the small amount of Pd. The large reduction peak of silver oxide is shifted negative, suggesting slightly more stable oxide formation [111]

15.4.2 MPc-Modified Ag/C Catalysts for ORRs in Alkaline Media

Adsorbed organic compounds on metallic substrates have attracted considerable attention with respect to the controlled functionalization of surfaces in nanoscale [121–123]. Electronic and geometric properties of Co-tetraphenylporphyrin (CoTPP) layers on Ag (111) were studied by Auwarter et al. using photoelectron diffraction (PED), near-edge X-ray absorption fine-structure (NEXAFS) measurements, and DFT calculations [124]. This fundamental work indicates that (1) the central Co atom of the CoTPP resides predominantly above the fcc and hcp hollow sites of the Ag (111) substrate, and (2) the interaction of the CoTPP with the Ag (111) substrate can induce modifications of the CoTPP molecular configuration, such as a distorted macrocycle with a shifted position of the Co metal center. By using similar experimental techniques and DFT calculations, Baran et al. investigated the interaction between a number of phthalocyanine molecules (SnPc, PbPc, and CoPc) and the Ag (111) surface [125]. Each of the phthalocyanine molecules (SnPc, PbPc, and CoPc) was found to donate a charge to the silver surface, and back-donation from Ag to the metal atom (Co, Sn, or Pb) in the macrocycle was only significant for CoPc. The adsorbed MP or MPcs molecules were found to induce a local restructuring process of the metallic Ag substrate, which could alter Ag's functionality and the morphology of the adsorbed MP or MPc molecules.

Recently, we reported a new bifunctional catalyst system of CoPc or the fully fluorinated cobalt phthalocyanine ($CoPcF_{16}$) adsorbed on Ag/C catalysts (CoPc@Ag/C or $CoPcF_{16}$@Ag/C) for ORR in alkaline media [48]. As shown in Fig. 15.23, the CoPc@Ag/C or $CoPcF_{16}$@Ag/C had lower overpotentials and higher

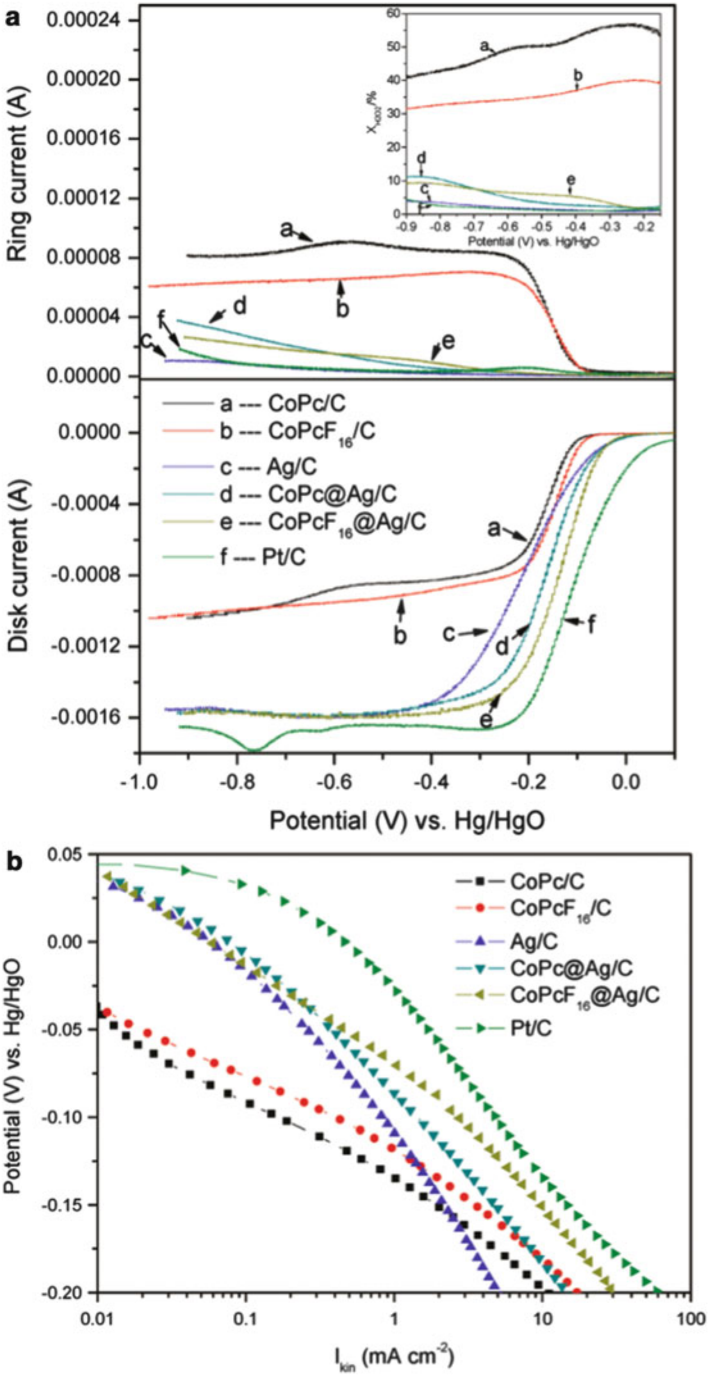

Fig. 15.23 (**a**) RRDE measurements of ORR with a rotation rate of 2,500 rpm in oxygen-purged 0.1 M NaOH. Collection efficiency $N = 0.41$; ring potential $E_r = 0.3$ V versus Hg/HgO; scan rate 20 mV s^{-1}. (**b**) Tafel plots of the ORRs derived from RDE measurement results obtained on the Ag/C, CoPc@Ag/C, $CoPcF_{16}$@Ag/C, CoPc/C, $CoPcF_{16}$/C, and Pt/C catalysts [48]

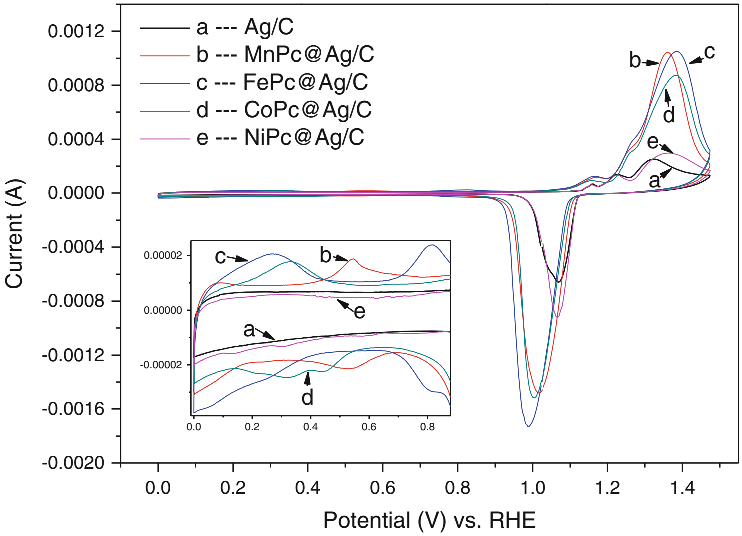

Fig. 15.24 Cyclic voltammetric curves obtained on various catalysts in an Ar-saturated 0.1 M NaOH solution [42]

ORR kinetic currents at a given potential than those on the individual components, namely, CoPc/C, CoPcF$_{16}$/C, or Ag/C. The RDE and RRDE measurements indicate that the ORR on these new catalysts occurs almost entirely via a four-electron pathway and shows 50 mV lower overpotentials for CoPc@Ag/C and 82 mV for CoPcF$_{16}$@Ag/C as compared to that found on Ag/C catalyst. The current densities are higher, and Tafel slopes are lower for ORR on CoPc@Ag/C and CoPcF$_{16}$@Ag/C than on Ag/C catalysts in the high overpotential region.

Further studies of various MPc (M = Fe, Co, Ni, and Mn) on Ag/C in RDE and AEMFCs indicate that the benefits of MPc molecules for enhanced ORR activity on Ag/C catalysts depend not only on their interactions with the Ag surface but also their bonding strength with the OH$^-$ species [42]. The basic CV curves obtained on the Ag/C and various MPc-modified Ag/C catalysts are shown in Fig. 15.24. The peak currents on the FePc@Ag/C, MnPc@Ag/C, and CoPc@Ag/C catalysts were significantly higher than those on the NiPc@Ag/C or Ag/C catalysts, which implies that there may be more active sites available for oxidization on the silver nanoparticles when the silver surface was modified with MnPc, FePc, or CoPc molecules. The anodic peaks of silver on the NiPc@Ag/C catalyst were very similar to those observed on the Ag/C catalyst. Based on the enhancement of the Ag anode peak currents, the interaction strength between the silver nanoparticles and the MPc molecules was found to follow this trend: FePc/Ag > MnPc/Ag > CoPc/Ag $\gg$ NiPc/Ag, which seems to agree reasonably with the DFT calculation results listed in Table 15.2 [48].

The ORR polarization curves obtained on a RDE coated with various catalysts at a rotation rate of 2,500 rpm in O$_2$-saturated 0.1 M NaOH solutions are shown in Fig. 15.25.

Table 15.2 Calculated adsorption energy (in units of eV) of different MPc molecules on Ag (111) by DFT [42]

	MnPc	FePc	CoPc	NiPc
Ag(111)	−2.09	−1.72	−1.35	−0.63

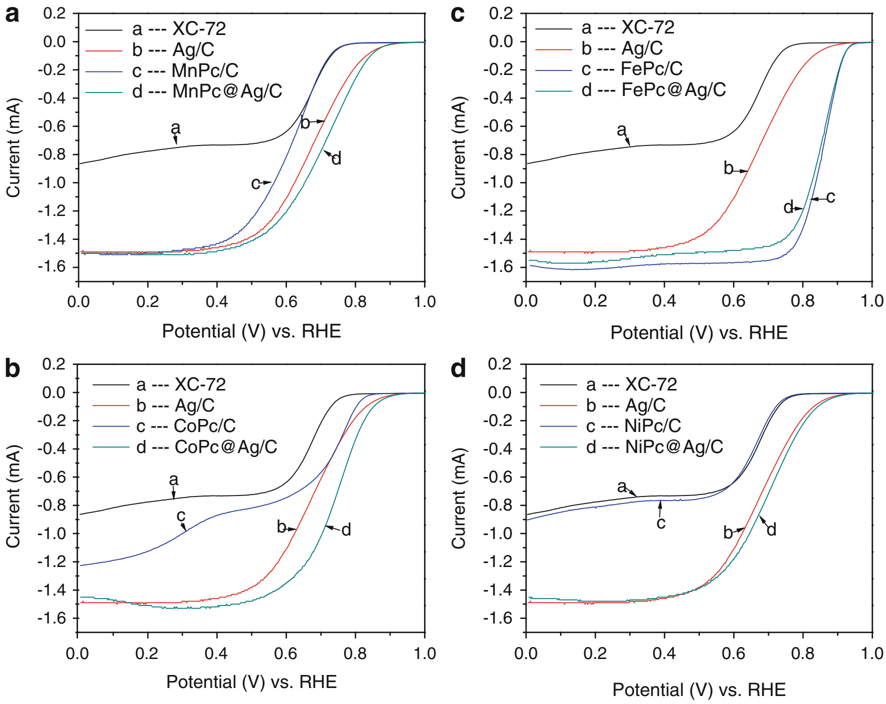

Fig. 15.25 Comparison of oxygen reduction polarization curves on (**a**) MnPc/C and MnPc@Ag/C, (**b**) FePc/C and FePc@Ag/C, (**c**) CoPc/C and CoPc@Ag/C, and (**d**) NiPc/C and NiPc@Ag/C with Ag/C and XC-72 catalysts at 2,500 rpm in O_2-purged 0.1 M NaOH solutions. Scan rate: 20 mV s^{-1}

Compared with the Ag/C catalysts, the half-wave potentials for the ORR on the FePc@Ag/C, CoPc@Ag/C, MnPc@Ag/C, and NiPc@Ag/C catalysts shifted positively about 178, 64, 32, and 24 mV, respectively. The kinetic currents obtained on the FePc@Ag/C, CoPc@Ag/C, MnPc@Ag/C, and NiPc@Ag/C catalysts were about 67.85, 3.09, 1.53, and 1.37 times higher than what was observed on the Ag/C catalyst at 0.68 V (vs. RHE), respectively. The MPc@Ag/C catalysts are more active toward the ORR than the Ag/C catalyst with a trend of FePc@Ag/C > CoPc@Ag/C > MnPc@Ag/C > NiPc@Ag/C. Based on the observed limiting disk currents and ring currents on the RDE or RRDE, the ORRs on various MPc@Ag/C catalysts were found to occur via a 4e ORR pathway, which suggests that the active sites for the O_2 reduction on the MPc@Ag/C catalysts are mainly on the Ag/C catalysts. The improved ORR activities on the MnPc@Ag/C, CoPc@Ag/C, and NiPc@Ag/C catalysts over that on the Ag/C catalyst authentically reflect the promotional effect by the MnPc, CoPc, or NiPc molecules. Ag nanoparticles modified with FePc molecules behave differently from those with CoPc, NiPc, or MnPc molecules. The ORR onset potentials and half-wave potentials overlapped for both the FePc/C and the FePc@Ag/C catalysts and were ~200 mV more positive than those on the Ag/C catalyst. Varying the MPc molecules could result in various degrees of improvements in ORR activity on the Ag/C catalysts. In 0.1 M NaOH solutions, the ORR activity on a RDE coated with various Ag-based catalysts follows the order of FePc@Ag/C > CoPc@Ag/C > MnPc@Ag/C > NiPc@Ag/C > Ag/C.

The performance of Ag/C, MnPc@Ag/C, FePc@Ag/C, CoPc@Ag/C, and NiPc@Ag/C as the cathode catalysts in AEMFCs is shown in Fig. 15.26. The AEMFCs were assembled with the same anodes, the same membranes (Tokuyama A901) and A4 ionomers, and varying cathode catalysts containing the same Ag loadings. For comparison, the polarization curves obtained with the XC-72 carbon and the MnPc/C, FePc/C, CoPc/C, and NiPc/C MEAs were also included in Fig. 15.26. The results show that in AEMFCs, the ORR activities of the MPc@Ag/C catalysts are significantly higher than that of the MPc/C catalyst, especially at the high current density region. Among the four MPc@Ag/C catalysts, the CoPc@Ag/C cathode catalyst shows the best performance with a peak power density of 537 mW cm^{-2} at 1260 mA cm^{-2}, which is better than the benchmark Pt/C cathode catalysts (Fig. 15.8). The performances of the MnPc@Ag/C and NiPc@Ag/C MEAs were found to be identical with that of the Ag/C MEA. However, for the FePc/C MEAs in the AEMFCs, the current dropped sharply when the cell voltage was below 0.5 V. Again, the RDE results for the FePc@Ag/C catalysts cannot be reproduced in the AEMFC test. As shown in Fig. 15.26b, the performance of either FePc/C or FePc@Ag/C catalysts in the AEMFCs was found to be similar to that on the carbon or Ag/C catalysts at high cell voltages (>0.6 V) but much poorer at low cell voltages.

Based on DFT calculations and electrochemical impedance spectra (EIS) analysis results, it was concluded that the strong electric field presented in an AEMFC at high cell voltages induces the strong OH$^-$ adsorption on the FePc molecules, resulting in the loss of the active sites of the FePc molecules regardless of whether they are adsorbed on the carbon supports or Ag/C catalysts [42, 100]. Due to the loss of active sites on the FePc molecules, the ORR kinetics on the FePc@Ag/C MEAs at high cell voltages occurred mainly on the Ag/C catalyst, but not on the FePc molecules. At low voltages (<0.5 V), the high OH$^-$ transport resistances were observed by EIS on the FePc@Ag/C electrodes [42], which is similar to what was observed on the FePc/C electrodes [92]. Therefore, both the FePc/C and FePc@Ag/C catalysts performed poorly compared to the other catalysts due to the strong OH$^-$ binding effects on the FePc molecules in H_2/O_2 AEMFCs.

From the ORR activity obtained in RDEs and AEMFCs on various MPc@Ag/C catalysts, DFT calculation results of interactions between MPc molecules and the Ag (111) surface, and EIS recorded at various cell voltages during AEMFC operation, one can clearly see that MPc molecules play an important role in tuning the electrochemical interface of Ag electrodes in alkaline media [42]. For the ORRs

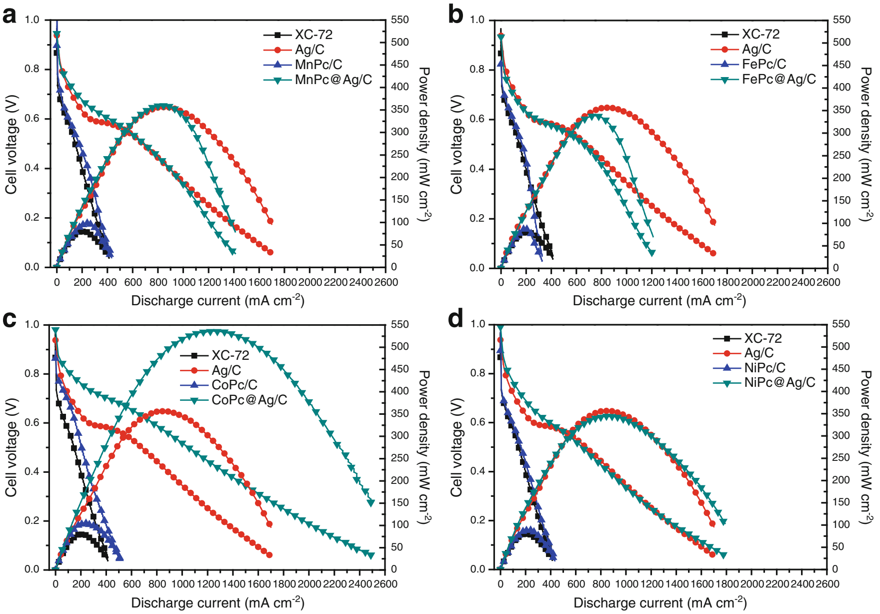

Fig. 15.26 Comparison of polarization and power density curves of anion-exchange membrane fuel cells using (**a**) MnPc/C and MnPc@Ag/C, (**b**) FePc/C and FePc@Ag/C, (**c**) CoPc/C and CoPc@Ag/C, and (**d**) NiPc/C and NiPc@Ag/C with Ag/C and XC-72 as cathode catalysts, respectively. Anode: 50 wt.% Pt/C, flow rate 200 sccm H_2, 100 % humidity. Cathode: 2.0 mg catalyst cm^{-2}, flow rate: 200 sccm O_2, 100 % humidity. Test temperature: 50 °C; back pressure: 20 psi [42]

on MPc@Ag/C catalysts, the electrochemical active sites for the initial O_2 binding were found mainly on the Ag surfaces except for FePc@Ag/C catalysts. Depending on the nature of the adsorbed MPc molecules, the Ag surfaces could become more active toward O_2 binding through electronic properties altered by the interactions between the MPc molecules and the Ag atoms, while MPc molecules tend to be energetically favorable to the adsorption of OH^-, which is a reaction product that needs to be removed quickly from the Ag atoms to maintain the O_2 adsorption ability of the catalyst [111]. The effects of the various MPc molecules for increasing active sites of the Ag/C catalysts follow the order of FePc@Ag/C > MnPc@Ag/C > CoPc@Ag/C > NiPc@Ag/C, which resembles the MPc-OH binding strength predicted by the DFT calculations. To achieve high ORR activities on MPc@Ag/C catalysts in AEMFCs, it is essential for the MPc molecules to have optimum OH^- binding effects, because if OH^- binding strength is either too strong (e.g., FePc) or too weak (e.g., NiPc), the MPc molecules could lose their ability to modify the Ag/C catalysts under AEMFC operation conditions.

Both carbon-supported Ag-alloys and MPc-modified Ag catalysts can be considered as the bifunctional catalyst materials for the ORR, in which one of the compositions serves as the active sites for the initial O_2 adsorption and reduction, while the other compositions help to remove the intermediate and final products from the primary active sites to promote the 4e ORR pathway and to free active sites for the further O_2 adsorption. Some of the bifunctional catalyst materials have been demonstrated to achieve much higher ORR activity than their sole materials in both the RDE and AEMFCs. By a combination of theoretical simulations and a wide range of experimental measurements, multifunctional catalysts for further improved ORR activity and stability are expected to be designed and demonstrated for practical AEMFC applications.

15.4.3 Other Bifunctional Catalysts

Other bifunctional catalyst systems, such as $Pd/MnO_2/C$ [109] or $Ag/MnO_2/C$, were also reported for ORRs in alkaline media [110]. Shown in Fig. 15.27, Pd nanoparticles were deposited on β-MnO_2 nanorods with diameters 40–50 nm and lengths of 500–1,000 nm [109]. As shown in Fig. 15.28, significantly improved ORR activities were observed on the $Pd@MnO_2/C$ catalysts in both RDE and AEMFCs, as compared to that on MnO_2/C [109]. However, the ORR activity of the $Pd@MnO_2/C$ is not as good as what was observed on Ag-based catalysts. Slanac reported the synthesis and characterization of a catalyst composed of Ag particles (3 nm) in contact with thin (∼1 nm) MnO_x domains on Vulcan carbon (C), as shown in Fig. 15.29 [110]. A threefold increase in mass activity was observed for Ag–MnO_x/C (125 $mA/mg_{Ag + MnOx}$) over the linear combination of pure component activities by RDE measurements. The Ag–MnO_x/C mass activity was reported to be comparable to commercial Pd/C (111 mA mg^{-1} Pd) and Pt/C (136 mA mg^{-1} Pt). Although the ORR activity on commercial Pd/C was significantly lower than 799 mA mg^{-1} Pd reported by the same authors in another paper [111], the benefits of Ag coating on MnO_x were apparent. A bifunctional mechanism for ORR on Ag–MnO_x/C catalysts was proposed by the same authors [110], in which Ag and MnO_x domains facilitate the formation and disproportionation of HO_2^-, respectively.

The heat-treated M/N/C composite materials, such as CoPPy/C, can also be considered as multifunctional catalysts, featuring Co nanoparticles coated with Co oxides and Co^{2+} species associated with N–C moieties that originate from the polypyrrole structures [82]. An illustration of the CoPPy/C catalyst surface and the ORR processes is shown in Fig. 15.30. The Co–N_x type site (shown as a Co–N_4 complex) supports the initial adsorption of the O_2 molecule and conversion of O_2 to the intermediate reaction product, HO_2^-, by a $2e^-$ reduction reaction. The HO_2^- species can further react at a decorating Co_xO_y/Co nanoparticle phase. Chu et al. [126] found that the mixture of the heat-treated Co- and Fe-tetraphenylporphyrins (CoTPP/FeTPP) had better catalytic performance for ORRs in acid media than that of the respective heat-treated single components. All of the above cited research results point to the fact that carefully designed bifunctional or multifunctional catalysts can be much more active for ORR than their single components.

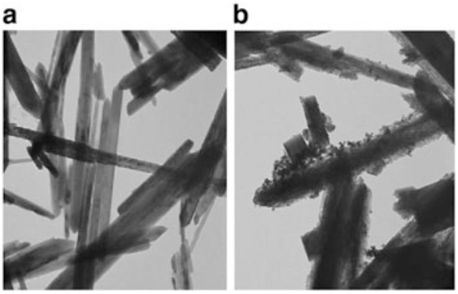

Fig. 15.27 TEM images of synthesized β-MnO_2 (**a**) and Pd@MnO_2 catalysts with Pd 4.6 wt.% (**b**)

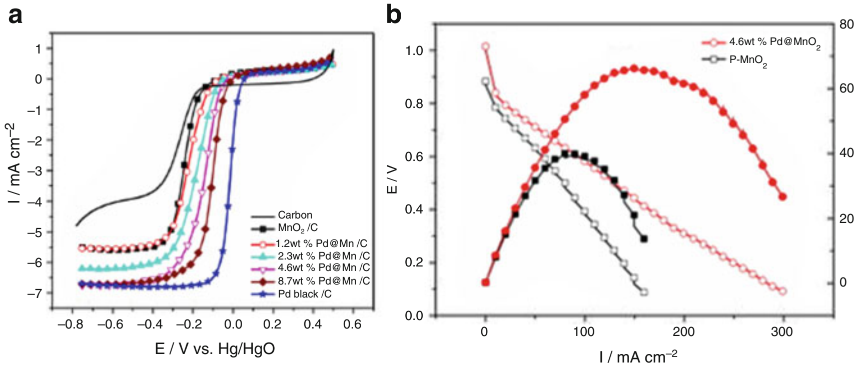

Fig. 15.28 (**a**) Polarization curves of the Pd@MnO_2/C catalysts on a RDE in a 0.1 M KOH solution saturated with oxygen at room temperature. Scan rate 10 m Vs^{-1}. Rotating speed 2,500 rpm. (**b**) Performance of the alkaline fuel cell using 4.6 wt.% Pd@MnO_2/C catalyst and uncoated β-MnO_2 in the cathode, at 60 °C temperature, and 10 psi backpressure

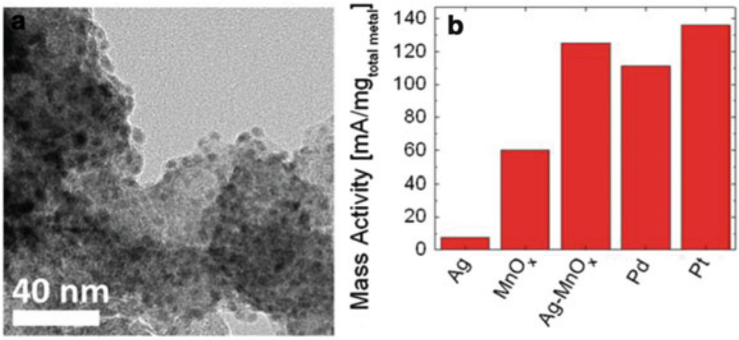

Fig. 15.29 (**a**) Low magnification TEM for 20 % Ag–35 % MnO_x on VC shows Ag particles uniformly distributed over the support (*left*). (**b**) Mass OR activity obtained in RDE on various catalysts [110]

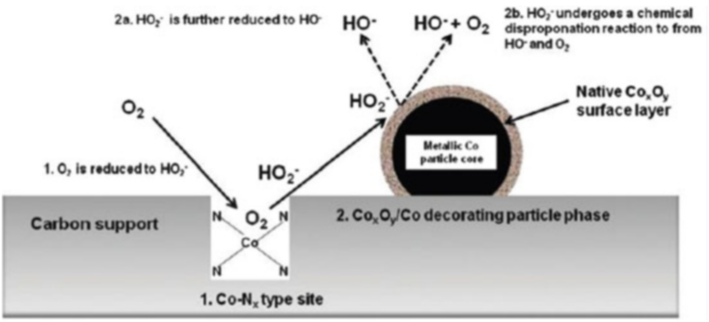

Fig. 15.30 Model of the active pyrolyzed CoPPy/C catalyst surface [82]

15.5 Conclusions

Great progress has made during recent years on non-Pt cathode electrocatalysts, including carbon-supported metallic nanoparticles (M/C), macrocycles catalysts ($M/N_4/C$), and bifunctional catalysts, for anion-exchange-membrane fuel cells. Based on our own data and those from other research groups, and based on an analysis of the electric field in the various experiments, we proposed in this chapter a theoretical explanation for the discrepancy between the ORR activities observed on $M/N_4/C$ catalysts with an RDE in a standard three-electrode cell and ORR activities observed in a PEMFC or an AEMFC. Due to the strong OH^- binding effects in AEMFCs, the high ORR activities observed on $Fe/N_4/C$-macrocycles in a RDE could not be duplicated in H_2/O_2 AEMFCs. In contrast, higher ORR activities on the $Fe/N_4/C$-macrocycles were observed in the PEMFC than in the RDE due to the N-protonation effects on the Fe/N/C catalyst occurred more favorably in the RDE than that in PEMFCs. A combination of theoretical simulation and comprehensive experimental measurements proves to be very useful in developing catalysts for fuel cell applications. Ag-based bifunctional catalysts are shown to be promising replacement for Pt/C catalysts in AEMFC applications. A novel design strategy for developing multifunctional catalysts for ORR in alkaline media has been proposed; an optimal catalyst would have the following characteristics (1) maximal electrochemical active sites for strong O_2 adsorption, (2) optimal composition and structure for promoting a four-electron ORR pathway through either directly breaking $O{-}O$ bonds or converting H_2O_2 into OH^- electrochemically, (3) the ability to remove OH^- species quickly from the catalyst active sites, and (4) good electron conductors. Successfully developing multifunctional catalysts for ORR in alkaline media will assure further improvement of the performance and durability of AEMFCs.

References

1. Cifrain M, Kordesch K (2003) Fundamentals and survey of systems. In: Vielstich W, Lamm A, Gasteiger HA (eds) Handbook of fuel cells, vol 1. Wiley, Milan, pp 267–280
2. McLean GF, Niet T, Richard SP, Djilali N (2002) An assessment of alkaline fuel cell technology. Int J Hydrogen Energy 27:507–526
3. Kinoshita K (1992) Electrochemical oxygen technology. Wiley, New York
4. Gamburzev S, Petrov K (2002) Silver-carbon electrocatalyst for air cathodes in alkaline fuel cells. J Appl Electrochem 32(7):805–809
5. Schulze M, Gulzow E (2004) Degradation of nickel anodes in alkaline fuel cells. J Power Sources 127(1–2):252–263
6. Wagner N, Shulze M, Gulzow E (2004) Long term investigation of silver cathodes for alkaline fuel cells. J Power Sources 127(1–2):264–272
7. Choban ER, Spendelow JS, Gancs L, Wieckowski A, Kenis PJA (2005) Membraneless laminar flow-based micro fuel cells operating in alkaline, acidic, and acidic/alkaline media. Electrochim Acta 50(27):5390–5398
8. Spendelow JS, Wieckowski A (2007) Electrocatalysis of oxygen reduction and small alcohol oxidation in alkaline media. Phys Chem Chem Phys 9:2654–2675
9. Varcoe JR, Slade RCT (2005) Prospects for alkaline anion-exchange membranes in low temperature. Fuel Cells 5:187–200
10. Yu EH, Scott K (2005) Direct methanol alkaline fuel cells with catalysed anion exchange membrane electrodes. J Appl Electrochem 35:91–96
11. Matsuoka K, Iriyama Y, Abe T, Matsuoka M, Ogumi Z (2005) Alkaline direct alcohol fuel cells using an anion exchange membrane. J Power Sources 150(4):27–31
12. Varcoe JR, Slade RCT, Yee ELH (2006) An alkaline polymer electrochemical interface: a breakthrough in application of alkaline anion-exchange membranes in fuel cells. Chem Commun 13:1428–1429
13. Yang CC, Chiu SJ, Chien WC (2006) Development of alkaline direct methanol fuel cells based on crosslinked PVA polymer membranes. J Power Sources 162(1):21–29
14. Varcoe JR, Slade RCT (2006) An electron-beam-grafted ETFE alkaline anion-exchange membrane in metal-cation-free solid-state alkaline fuel cells. Electrochem Commun 8(5):839–843
15. Lin BYS, Kirk DW, Thorpe SJ (2006) Performance of alkaline fuel cells: a possible future energy system. J Power Sources 161(1):474–483
16. Tamain C, Poynton SD, Slade RCT, Carroll B, Varcoe JR (2007) Development of cathode architectures customized for H_2/O_2 metal-cation-free alkaline membrane fuel cells. J Phys Chem C 111(49):18423–18430
17. Park JS, Park SH, Yim SD, Yoon YG, Lee WY, Kim CS (2008) Performance of solid alkaline fuel cells employing anion-exchange membranes. J Power Sources 178:620–626
18. Unlu M, Zhou J, Kohl P (2009) Anion exchange membrane fuel cells: experimental comparison of hydroxide and carbonate conductive ions fuel cells and energy conversion. Electrochem Solid State Lett 12(3):B27–B30
19. Gu S, Cai R, Luo T, Chen ZW, Sun MW, Liu Y, He GH, Yan YS (2009) A soluble and highly conductive ionomer for high-performance hydroxide exchange membrane fuel cells. Angew Chem Int Ed 48(35):6499–6502
20. Switzer EE, Olson TS, Datye AK, Atanassov P, Hibbs MR, Fujimoto CY, Cornelius CJ (2010) Novel KOH-free anion-exchange membrane fuel cell: performance comparison of alternative anion-exchange ionomers in catalyst ink. Electrochim Acta 55(9):3404–3408
21. Piana M, Boccia M, Filpi A, Flammia E, Miller HA, Orsini M, Salusti F, Santiccioli S, Ciardelli F, Pucci A (2010) H_2/air alkaline membrane fuel cell performance and durability, using novel ionomer and non-platinum group metal cathode catalyst. J Power Sources 195(18):5875–5881

22. Fukuta K, Inoue H, Chikashige Y, Yanagi H (2010) Improved maximum power density of alkaline fuel cells (AMFCs) by the optimization of mea construction. ECS Trans 28(30):221–225
23. Sun L, Guo J, Zhou J, Xu Q, Chu D, Chen R (2012) Novel nanostructured high-performance anion exchange ionomers for anion exchange membrane fuel cells. J Power Sources 202:70–77
24. Bidault F, Brett DJL, Middletonc PH, Brandon NP (2009) Review of gas diffusion cathodes for alkaline fuel cells. J Power Sources 187:39–48
25. Jiang L, Hsu A, Chu D, Chen R (2010) Ethanol electro-oxidation on Pt/C and PtSn/C catalysts in alkaline and acid solutions. Int J Hydrogen Energy 35(1):365–372
26. Antolini E, Gonzalez ER (2010) Alkaline direct alcohol fuel cells. J Power Sources 195(11):3431–3450
27. Jagal JH (2006) N4-macrocyclic metal complexes, 1st edn. Springer, New York, pp 41–82
28. Adzic R (1998) Recent advances in the kinetics of oxygen reduction. In: Lipkowski J, Ross PN (eds) Elecrocatalysis, Frontier in science. Wiley, New York, pp 197–242
29. Lima FHB, Zhang J, Shao MH, Sasaki K, Vukmirovic MB, Ticianelli EA, Adzic R (2007) Catalytic activity-d-band center correlation for the O_2 reduction reaction on platinum in alkaline solutions. J Phys Chem C 111:404–410
30. Jiang L, Hsu A, Chu D, Chen R (2009) Oxygen reduction reaction on carbon supported pt and pd in alkaline solution. J Electrochem Soc 156(3):B370–B376
31. Hurlen T, Sandler YL, Pantier EA (1966) Reactions of oxygen and hydrogen peroxide at silver electrodes in alkaline solutions. Electrochim Acta 11:1463–1473
32. Lima FHB, Sanches CD, Ticianelli EA (2005) Physical characterization and electrochemical activity of bimetallic platinum-silver particles for oxygen reduction in alkaline electrolyte. J Electrochem Soc 152(7):A1466–A1473
33. Demarconnay L, Coutanceau C, Leger JM (2004) Electroreduction of dioxygen (ORR) in alkaline medium on Ag/C and Pt/C nanostructured catalysts – effect of the presence of methanol. Electrochim Acta 49:4513–4521
34. Coutanceau C, Demarconnay L, Lamy C, Leger JM (2006) Development of electrocatalysts for solid alkaline fuel cell (SAFC). J Power Sources 156(1):14–19
35. Blizanac BB, Ross PN, Markovic NM (2006) Oxygen reduction on silver low-index single-crystal surfaces in alkaline solution: rotating ring disk Ag(hkl) studies. J Phys Chem B 110(10):4735–4741
36. Han JJ, Li N, Zhang TY (2009) Ag/C nanoparticles as an cathode catalyst for a zinc-air battery with a flowing alkaline electrolyte. J Power Sources 193(2):885–889
37. Guo J, Hsu A, Chu D, Chen R (2010) Improving oxygen reduction reaction activities on carbon-supported ag nanoparticles in alkaline solutions. J Phys Chem C 114(10):4324–4330
38. Singh P, Buttry DA (2012) Comparison of oxygen reduction reaction at silver nanoparticles and polycrystalline silver electrodes in alkaline solution. J Phys Chem C 116(19):10656–10663
39. Varcoe JR, Slade RCT, Wright GL, Chen Y (2006) Steady-state dc and impedance investigations of H_2/O_2 alkaline membrane fuel cells with commercial Pt/C, Ag/C, and Au/C cathodes. J Phys Chem B 110(42):21041–21049
40. Poynton SD, Kizewski JP, Slade RCT, Varcoe JR (2010) Novel electrolyte membranes and non-Pt catalysts for low temperature fuel cells. Solid State Ionics 181(3–4):219–222
41. Lu S, Pan J, Huang A, Zhuang L, Lu J (2008) Alkaline polymer electrolyte fuel cells completely free from noble metal catalysts. Proc Natl Acad Sci USA 105(52):20611–20614
42. Guo J, Zhou J, Chu D, Chen R (2013) Tuning the electrochemical interface of Ag/C electrodes in alkaline media with metallophthalocyanine molecules. J Phys Chem C. doi:10.1021/jp310655y
43. Hansen H, Rossmeisl J, Nørskov JK (2008) Surface Pourbaix diagrams and oxygen reduction activity of Pt, Ag and Ni(111) surfaces studied by DFT. Phys Chem Chem Phys 10:3722–3730
44. Strmcnik D, Kodama K, Vliet DVD, Greeley J, Stamenkovic VR, Markovic NM (2009) The role of non-covalent interactions in electrocatalytic fuel-cell reactions on platinum. Nat Chem 1:466–472

45. Strmcnik D, Vliet DFVD, Chang KC, Komanicky V, Kodama K, You H, Stamenkovic VR, Markovic NM (2011) Effects of Li^+, K^+, and Ba^{2+} cations on the ORR at model and high surface area Pt and Au surfaces in alkaline solutions. J Phys Chem Lett 2(21):2733–2736
46. Lucas CA, Thompson P, Grunder Y, Markovic NM (2011) The structure of the electrochemical double layer: Ag(111) in alkaline electrolyte. Electrochem Commun 13(11):1205–1208
47. Blizanac BB, Ross PN, Markovic NM (2006) Oxygen reduction on silver low-index single-crystal surfaces in alkaline solution: rotating ring disk Ag(hkl) studies. J Phys Chem B 110(10):4735–4741
48. Guo J, Li H, He H, Chu D, Chen R (2011) CoPc- and $CoPcF_{16}$-modified Ag nanoparticles as novel catalysts with tunable oxygen reduction activity in alkaline media. J Phys Chem C 115(17):8494–8502
49. Jasinski R (1964) A new fuel cell cathode catalyst. Nature 201:1212–12113
50. Alt H, Binder H, Sandstede G (1973) Mechanism of the electrocatalytic reduction of oxygen on metal chelates. J Catal 28(1):8–19
51. Veen JARV, Baar JFV, Kroese CJ, Coolegem JGF, Wit NE, Colijn HA (1981) Oxygen reduction on transition-metal porphyrins in acid electrolyte I. Activity. Phys Chem 85:693–700
52. Scherson DA, Gupta SL, Fierro C, Yeager E, Kordesch M, Eldridge J, Hoffman R (1983) Cobalt tetramethoxyphenyl porphyrin – emission Mossbauer spectroscopy and O_2 reduction electrochemical studies. Electrochim Acta 28(9):1205–1209
53. Zagal J, Bindra P, Yeager E (1980) A mechanistic study of O_2 reduction on water soluble phthalocyanines adsorbed on graphite electrodes. J Electrochem Soc 127:1506–1517
54. Scherson D, Tanaka AA, Gupta SL, Tryk D, Fierro C, Holze R, Yeager EB, Lattimer RP (1986) Transition metal macrocycles supported on high area carbon: pyrolysis – mass spectrometry studies. Electrochim Acta 31(10):1247–1258
55. Zagal J, Sen R, Yeager E (1977) Oxygen reduction by Co(II) tetrasulfonatephthalocyanine irreversibly adsorbed on a stress-annealed pyrolytic graphite electrode surface. J Electroanal Chem 83(1):207–213
56. Yeager E (1984) Electrocatalysts for O_2 reduction. Electrochim Acta 29(11):1527–1537
57. Putten AVD, Elzing A, Visscher W, Barendrecht E (1986) Oxygen reduction on vacuum-deposited and absorbed transition-metal phthalocyanine films. J Electroanal Chem 214(1–2):523–533
58. Collman JP, Marrocco M, Denisovich P, Koval C, Anson FC (1979) Potent catalysis of the electroreduction of oxygen to water by dicobalt porphyrin dimers adsorbed on graphite electrodes. J Electroanal Chem 101(1):117–122
59. Collman J, Danisovich P, Yutaka K, Marrocco M, Koval C, Anson F (1980) Electrode catalysis of the four-electron reduction of oxygen to water by dicobalt face-to-face porphyrins. J Am Chem Soc 102(19):6027–6036
60. Liu H, Weaver M, Wang C, Chang C (1983) Dependence of electrocatalysis for oxygen reduction by adsorbed dicobalt cofacial porphyrins upon catalyst structure. J Electroanal Chem 145(2):439–447
61. Yeager E (1986) Dioxygen electrocatalysis: mechanisms in relation to catalyst structure. J Mol Catal 38(1–2):5–25
62. Gupta S, Tryk D, Bae I, Aldred W, Yeager E (1989) Heat-treated polycrylonitrile-based catalysts for oxygen electroreduction. J Appl Electrochem 19(1):19–27
63. Tse Y, Janda P, Lam H, Zhang J, Pietro W, Lever ABP (1997) Monomeric and polymeric tetra-aminophthalocyanatocobalt(II) modified electrodes: electrocatalytic reduction of oxygen. J Porphyr Phthalocyanines 1(1):3–16
64. Ramirez G, Trollund E, Isaacs M, Armijo F, Zagal J, Costamagna J, Aguirre M (2002) Electroreduction of molecular oxygen on poly-iron-tetraaminophthalocyanine modified electrodes. J Electroanal 14:540–545

65. Jaouen F, Marcotte S, Dodelet JP, Lindbergh G (2003) Oxygen reduction catalysts for polymer electrolyte fuel cells from the pyrolysis of iron acetate adsorbed on various carbon supports. J Phys Chem B 107(6):1376–1386
66. Lefevre M, Dodelet JP (2003) Fe-based catalysts for the reduction of oxygen in polymer electrolyte membrane fuel cell conditions: determination of the amount of peroxide released during electroreduction and its influence on the stability of the catalysts. Electrochim Acta 48(19):2749–2760
67. Schulenburg H, Stankov S, Schnemann V, Radnik J, Dorbandt I, Fiechter S, Bogdanoff P, Tributsch H (2003) Catalysts for the oxygen reduction from heat-treated iron(III) tetramethoxyphenylporphyrin chloride: structure and stability of active sites. J Phys Chem B 107(34):9034–9041
68. Villers D, Jacques-Bedard X, Dodelet JP (2004) Fe-based catalysts for oxygen reduction in PEM fuel cells: pretreatment of the carbon support. J Electrochem Soc 151(9):A1507–A1515
69. Marcotte S, Villers D, Guillet N, Roue L, Dodelet JP (2004) Electroreduction of oxygen on Co-based catalysts: determination of the parameters affecting the two-electron transfer reaction in an acid medium. Electrochim Acta 50(1):179–188
70. Barnanton S, Couranceau C, Roux C, Hahn F, Leger JM (2005) Oxygen reduction reaction in acid medium at iron phthalocyanine dispersed on high surface area carbon substrate: tolerance to methanol, stability and kinetics. J Electroanal Chem 577(2):223–234
71. Lefevre M, Dodelet JP, Bertrand P (2005) Molecular oxygen reduction in PEM fuel cell conditions: ToF-SIMS analysis of co-based electrocatalysts. J Phys Chem B 109 (35):16718–16724
72. Jaouen F, Lefevre M, Dodelet JP, Cai M (2006) Heat-treated Fe/N/C catalysts for O_2 electroreduction: are active sites hosted in micropores? J Phys Chem B 110(11):5553–5558
73. Guillet N, Roue L, Marcotte S, Villers D, Dodelet JP, Chhim N, Trevin S (2006) Electrogeneration of hydrogen peroxide in acid medium using pyrolyzed cobalt-based catalysts: influence of the cobalt content on the electrode performance. J Appl Electrochem 36(8):863–870
74. Baker R, Wilkinson D, Zhang J (2008) Electrocatalytic activity and stability of substituted iron phthalocyanines towards oxygen reduction evaluated at different temperatures. Electrochim Acta 53(23):6906–6919
75. Jaouen F, Herranz J, Lefevre M, Dodelet JP, Kramm UI, Herrmann I, Bogdanoff P, Maruyama J, Nagaoka T, Garsuch A, Dahn JR, Olson T, Pylypenko S, Atanassov P, Ustinov EA (2009) Cross-laboratory experimental study of non-noble-metal electrocatalysts for the oxygen reduction reaction. ACS Appl Mater Interfaces 1(8):1623–1639
76. Jaouen F, Dodelet JP (2009) O_2 reduction mechanism on non-noble metal catalysts for pem fuel cells. Part I: Experimental rates of O_2 electroreduction, H_2O_2 electroreduction, and H_2O_2 disproportionation. J Phys Chem C 113(34):15422–15432
77. Lefevre M, Proietti E, Jaouen F, Dodelet JP (2009) Iron-based catalysts with improved oxygen reduction activity in polymer electrolyte fuel cells. Science 324:71–74
78. Gasteiger H, Markovic NM (2009) Just a dream-or future reality. Science 324:48–49
79. Proietti E, Jaouen F, Lefèvre M, Larouche N, Tian J, Herranz J, Dodelet JP (2011) Iron-based cathode catalyst with enhanced power density in polymer electrolyte membrane fuel cells. Nat Commun 2:416. doi:10.1038/ncomms1427
80. Wu G, More KL, Johnston CM, Zelenay P (2011) High-performance electrocatalysts for oxygen reduction derived from polyaniline, iron, and cobalt. Science 332:443–447
81. Herranz J, Jaouen F, Lefevre M, Kramm UI, Proietti E, Dodelet JP, Bogdanoff P, Fiechter S, Abs-Wurmbach I, Bertrand P, Arruda TM, Mukerjee S (2011) Unveiling N-protonation and anion-binding effects on Fe/N/C catalysts for O_2 reduction in proton-exchange-membrane fuel cells. J Phys Chem C 115(32):16087–16097
82. Olson TS, Pylypenko S, Atanassov P, Asazawa K, Yamada K, Tanaka H (2010) Anion-exchange membrane fuel cells: dual-site mechanism of oxygen reduction reaction in alkaline media on cobalt–polypyrrole electrocatalysts. J Phys Chem C 114(11):5049–5059

83. Jahnke H, Schonborn M, Zimmermann G (1976) Organic dyestuffs as catalysts for fuel cells. Top Curr Chem 61:133–181
84. Zagal J, Sen R, Yeager E (1977) Oxygen reduction by Co(II) tetrasulfonatephthalocyanine irreversibly adsorbed on a stress-annealed pyrolytic graphite electrode surface. J Electroanal Chem 83(1):207–213
85. Yeager E (1984) Electrocatalysts for O_2 reduction. Electrochim Acta 29(11):1527–1537
86. Putten AVD, Elzing A, Visscher W, Barendrecht E (1986) Oxygen reduction on vacuum-deposited and absorbed transition-metal phthalocyanine films. J Electroanal Chem 214(1–2):523–533
87. Vasudevan P, Mann SN, Tyagi S (1990) Transition metal complexes of porphyrins and phthalocyanines as electrocatalysts for dioxygen reduction. Transit Met Chem 15(2):81–90
88. Zagal JH (1992) Metallophthalocyanines as catalysts in electrochemical reactions. Coord Chem Rev 119:89–136
89. Kazarinov VE, Tarasevich MR, Radyushkina KA, Andreev VN (1979) Some specific features of the metalloporphyrin/electrolyte interface and the kinetics of oxygen electroreduction. J Electroanal Chem 100(1–2):225–232
90. Shukla A, Manoharan R, Paliteiro C, Hamnett A, Goodenough J (1984) High efficiency cathodes for alkaline air electrodes. J Appl Electrochem 15(5):774–777
91. Zagal J, Paez M, Tanaka A, Santos J, Linkous C (1992) Electrocatalytic activity of metal phthalocyanines for oxygen reduction. J Electroanal Chem 339(1–2):13–30
92. Guo J, He H, Chu D, Chen R (2012) OH^- -Binding effects on metallophthalocyanine catalysts for O_2 reduction reaction in anion exchange membrane fuel cells. Electrocatalysis. 3:252–264
93. Chen R, Li H, Chu D, Wang G (2009) Unraveling oxygen reduction reaction mechanisms on carbon-supported Fe-phthalocyanine and Co-phthalocyanine catalysts in alkaline solutions. J Phys Chem C 113(48):20689–20697
94. Gouerec P, Biloul A, Contamin O, Scarbeck G, Savy M, Riga J, Weng LT, Bertrand P (1997) Oxygen reduction in acid media catalyzed by heat treated cobalt tetraazaannulene supported on an active charcoal: correlations between the performances after longevity tests and the active site configuration as seen by XPS and ToF-SIMS. J Electroanal Chem 422(1–2):61–75
95. Ahmed J, Yuan Y, Zhou L, Kim S (2012) Carbon supported cobalt oxide nanoparticles–iron phthalocyanine as alternative cathode catalyst for oxygen reduction in microbial fuel cells. J Power Sources 208:170–175
96. Mamlouk M, Wang X, Scott K, Horsfall J, Williams C (2011) Characterization and application of anion exchange polymer membranes with non-platinum group metals for fuel cells. Proc Inst Mech Eng A J Power Energy 225(2):152–160
97. Mamlouk M, Kumar SM, Gouerec P, Scott K (2011) Electrochemical and fuel cell evaluation of Co based catalyst for oxygen reduction in anion exchange polymer membrane fuel cells. J Power Sources 196:7594–7600
98. Nørskov JK, Rossmeisl J, Logadottir A, Lindqvist L, Kitchin JR, Bligaard T, Jonsson H (2004) Origin of the overpotential for oxygen reduction at a fuel-cell cathode. J Phys Chem B 108(46):17886–17892
99. Nilekar AU, Mavrikakis M (2008) Improved oxygen reduction reactivity of platinum monolayers on transition metal surfaces. Surf Sci 602(14):L89–L94
100. Roques J, Anderson AB (2004) Electrode potential-dependent stages in OH_{ads} formation on the Pt_3Cr alloy (111) surface. J Electrochem Soc 151(11):E340–E347
101. Liao M, Scheiner S (2002) Comparative study of metal-porphyrins, -porphyrazines, and -phthalocyanines. J Comput Chem 23(15):1391–1403
102. Liao M, Scheiner S (2001) Electronic structure and bonding in metal phthalocyanines, metal=Fe, Co, Ni, Cu, Zn, Mg. J Chem Phys 114(22):9780–9791
103. Shi Z, Zhang J (2007) Density functional theory study of transitional metal macrocyclic complexes' dioxygen-binding abilities and their catalytic activities toward oxygen reduction reaction. J Phys Chem C 111(19):7084–7090

104. Wang G, Ramesh N, Hsu A, Chu D, Chen R (2008) Density functional theory study of the adsorption of oxygen molecule on iron phthalocyanine and cobalt phthalocyanine. Mol Simulat 34:1051–1056
105. He H, Lei Y, Xiao C, Chu D, Chen R, Wang G (2012) Molecular and electronic structures of transition-metal macrocyclic complexes as related to catalyzing oxygen reduction reactions: a density functional theory study. J Phys Chem C 116(30):16038–16046
106. Miedema PS, Schooneveld M, Bogerd R, Rocha T, Havecker M, Gericke A, Groot F (2011) Oxygen binding to cobalt and iron phthalocyanines as determined from in situ X-ray absorption spectroscopy. J Phys Chem C 115(51):25422–25428
107. Tanaka A, Fierro C, Scherson D, Yeager E (1987) Electrocatalytic aspects of iron phthalocyanine and its μ-oxo derivatives dispersed on high surface area carbon. J Phys Chem 91(14):3799–3807
108. Jiang L, Hsu A, Chu D, Chen R (2010) A highly active Pd coated Ag electrocatalyst for oxygen reduction reactions in alkaline media. Electrochim Acta 55(15):4506–4511
109. Sun W, Hsu A, Chen R (2011) Palladium-coated manganese dioxide catalysts for oxygen reduction reaction in alkaline media. J Power Sources 196:4491–4498
110. Slanac DA, Lie A, Paulson JA, Stevenson KJ, Johnston KP (2012) Bifunctional catalysts for alkaline oxygen reduction reaction via promotion of ligand and ensemble effects at Ag/MnO_x nanodomains. J Phys Chem C 116(20):11032–11039
111. Slanac DA, Hardin WG, Johnston KP, Stevenson KJ (2012) Atomic ensemble and electronic effects in Ag-rich AgPd nanoalloy catalysts for oxygen reduction in alkaline media. J Am Chem Soc 134(23):9812–9819
112. Lima FHB, Castro JFR, Ticianelli E (2006) Silver-cobalt bimetallic particles for oxygen reduction in alkaline media. J Power Sources 161(2):806–812
113. Lima FHB, Calegaro ML, Ticianelli EA (2007) Electrocatalytic Activity of Dispersed Platinum and Silver Alloys and Manganese Oxides for the Oxygen Reduction in Alkaline Electrolyte. Russian Journal of Electrochemistry 42:1283–1290.
114. Gasteiger HA, Kocha S, Sompalli B, Wagner FT (2005) Activity benchmarks and requirements for Pt, Pt-alloy, and non-Pt oxygen reduction catalysts for PEMFCs. Appl Catal Environ 56(1–2):9–35
115. Stamenkovic VR, Fowler B, Mun BS, Wang GF, Ross PN, Lucas CA, Markovic NM (2007) Improved oxygen reduction activity on Pt3Ni(111) via increased surface site availability. Science 315:493–497
116. Stamenkovic VR, Mun BS, Arenz M, Mayrhofer KJJ, Lucas CA, Wang GF, Ross PN, Markovic NM (2007) Trends in electrocatalysis on extended and nanoscale Pt-bimetallic alloy surfaces. Nat Mater 6:241–247
117. Zhang J, Mo Y, Vukimirovic MB, Klie R, Sasaki K, Adzic RR (2004) Platinum monolayer electrocatalysts for O2 reduction: Pt monolayer on Pd(111) and on carbon-supported Pd nanoparticles. J Phys Chem B 108(20):10955–10964
118. Greeley J, Stephens IEL, Bondarenko AS, Johansson TP, Hansen HA, Jaramillo TF, Rossmeis J, Chorkendorff I, Nørskov JK (2009) Alloys of platinum and early transition metals as oxygen reduction electrocatalysts. Nat Chem 1:552–556
119. Wang C, Wang G, Vliet D, Chang K, Markovica NM, Stamenkovic VR (2010) Monodisperse Pt_3Co nanoparticles as electrocatalyst: the effects of particle size and pretreatment on electrocatalytic reduction of oxygen. Phys Chem Chem Phys 12:6933–6939
120. Wang C, Chi M, Wang G, Vliet D, Li D, More K, Wang H, Schlueter JA, Markovic NM, Stamenkovic VR (2011) Nanoparticles: correlation between surface chemistry and electrocatalytic properties of monodisperse Pt_xNi_{1-x} nanoparticles. Adv Funct Mater 21:147–152
121. Barth JV (2007) Molecular architectonic on metal surface. Annu Rev Phys Chem 58:375–407
122. Lin N, Stepanow S, Ruben M, Barth JV (2009) Surface-confined supramolecular coordination chemistry. Top Curr Chem 287:1–44
123. Bai Y, Buchner F, Kellner I, Schmid M, Vollnhals F, Steinruck H, Marbach H, Gottfried JM (2009) Adsorption of cobalt (II) octaethylporphyrin and 2H-octaethylporphyrin on Ag(111): new insight into the surface coordinative bond. New J Phys 11:125004

124. Auwarter W, Seufert K, Klappenberger F, Reichert J, Weber-Bargioni A, Verdini A, Cvetko D, Dell'Angela M, Floreano L, Cossaro A, Bavdek G, Morgante A, Seitsonen AP, Barth JV (2010) Site-specific electronic and geometric interface structure of Co-tetraphenyl-porphyrin layers on Ag(111). Phys Rev B 81:245403
125. Baran JD, Larsson J, Woolley R, Cong Y, Moriarty P, Cafolla A, Schulte K, Dhanak V (2010) Theoretical and experimental comparison of SnPc, PbPc, and CoPc adsorption on Ag(111). Phys Rev B 81:075413
126. Chu D, Jiang R (2002) Novel electrocatalysts for direct methanol fuel cells. Solid State Ionics 148:591–599

Chapter 16
Au Electrocatalysis for Oxygen Reduction

Francisco J. Vidal-Iglesias, José Solla-Gullón, Enrique Herrero, and Juan M. Feliu

Abstract This chapter reviews the recent advances on the study of the oxygen reduction reaction (ORR) on gold electrodes. The initial part is devoted to the study of the reaction on single-crystal electrodes to determine the effect of the surface structure on the reactivity of gold electrodes for this reaction. The best reactivity is found for the Au(100) electrode in alkaline medium. For the nanoparticle electrodes, the reactivity for this reaction depends on two different effects: size and surface structure effects. Regarding the size effects, the different studies found in the literature do not agree on whether the size of the nanoparticles has a significant impact on the reactivity for the ORR. This disagreement between different authors is probably due to the lack of control of the surface structure of the nanoparticles. On the other hand, significant effects are found when the surface of the nanoparticle is changed. In general, the reactivity in alkaline media increases as the fraction of {100} domains on the surface increases. In some cases, the reactivity of gold in alkaline medium is similar to that measured for platinum electrodes.

16.1 Introduction

It is clear that the oxygen reduction reaction (ORR) is one of the most important electrochemical reactions since it has multiple applications. The potential fields range from the energy conversion to corrosion science. For this reason, it has been the subject of numerous works throughout the years. In the complete reduction of oxygen to water, there are four electrons exchanged. This high number of electrons

---

F.J. Vidal-Iglesias • J. Solla-Gullón • E. Herrero (✉) • J.M. Feliu (✉)
Instituto de Electroquímica, Universidad de Alicante, Apdo. 99, 03080 Alicante, Spain
e-mail: herrero@ua.es; juan.feliu@ua.es

M. Shao (ed.), *Electrocatalysis in Fuel Cells*, Lecture Notes in Energy 9,
DOI 10.1007/978-1-4471-4911-8_16,

exchanged necessarily implies existence of several intermediates. Since the reaction is sensitive to the nature of the electrode, at least one of the intermediates (if not all) should be adsorbed on the electrode surface. Thus, nature and surface structure of the electrode is a fundamental aspect to consider when the ORR is studied. Among pure metals, platinum is recognized as the electrode with the highest electrocatalytic activity [1].

The substrate not only affects the electrocatalytic activity but also the final product of the reaction and the mechanism. The general mechanism for oxygen reduction consists in two interconnected parallel pathways: the first leading to the formation of water (OH^- in basic media) with hydrogen peroxide (HO_2^- in basic media) as intermediate species and the second path yielding water (OH^- in basic media) directly [2, 3]. Depending on the metal, the final product can be water (OH^-) or hydrogen peroxide. In these latter cases, the further reduction of hydrogen peroxide is highly inhibited.

In the case of gold electrodes, the general mechanism for the ORR [1] can be simplified as follows for the reactions in acid medium:

$$O_2 + 4H^+ + 4e \rightleftharpoons 2H_2O$$

$$\begin{tikzcd}
O_{2,b} \arrow[r, "dif"] & \boxed{O_{2,a} \xrightarrow[H^+]{1e^-} HO_{2,a}} \arrow[r, leftrightarrow, "1e^-", "H^+"'] & H_2O_{2,a} \arrow[r, leftrightarrow, "1e^-", "H^+"'] \arrow[d, leftrightarrow] & OH_a + H_2O \arrow[r, leftrightarrow, "1e^-", "H^+"'] & 2H_2O \\
& & H_2O_{2,b} & &
\end{tikzcd}$$

where the subscript "a" denotes an adsorbed species and "b" a bulk species. When the reaction occurs in alkaline medium, the mechanism is transformed into

$$O_2 + 2H^+ + 4e \rightleftharpoons 2OH^-$$

$$\begin{tikzcd}
O_{2,b} \arrow[r, "dif"] & \boxed{O_{2,a} \xrightarrow{1e} O^-_{2,a}} \arrow[r, leftrightarrow, "1e", "H^+"'] & HO^-_{2,a} \arrow[r, leftrightarrow, "1e"] \arrow[d, leftrightarrow] & O^-_a + OH^- \arrow[r, leftrightarrow, "1e", "H^+"'] & 2OH^- \\
& & HO^-_{2,b} & &
\end{tikzcd}$$

In this chapter, recent results on the oxygen reduction reaction will be covered. We will focus on the results obtained with gold nanoparticles. However, some results obtained with single-crystal electrodes will be presented since they are necessary to understand the results found for the nanoparticle electrodes. Although the mean electrocatalytic activity of the gold electrode is lower than that of platinum, Au(100) electrode in alkaline medium has a similar activity for the ORR than platinum, and for that reason, it has been studied systematically and abundantly.

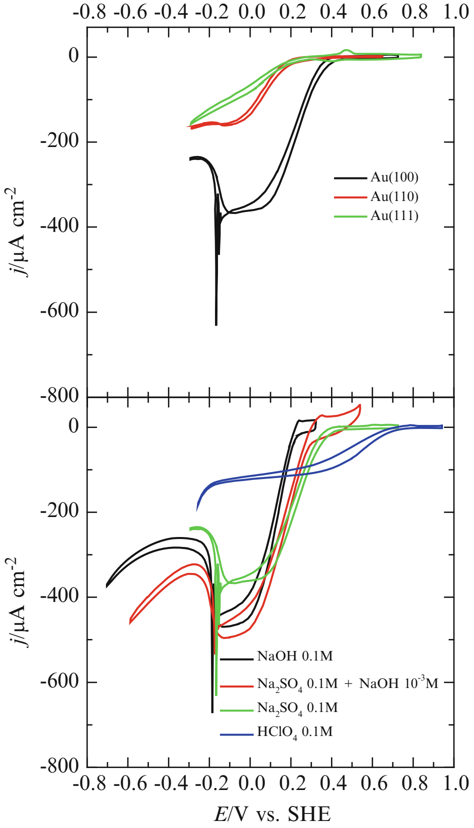

Fig. 16.1 *Top panel*. Current densities measured for oxygen reduction in the impinging jet system in 0.1 M Na_2SO_4 (pH = 6) for the Au (100), Au(111), and Au(110) electrodes. *Bottom panel*. Effect of the pH in the oxygen reduction in the impinging jet system for the Au(100) electrode

16.2 ORR in Gold Single Crystals

The electrocatalytic activity of gold electrodes for the ORR is not very high. The first studies carried out in acid medium with Au single crystals showed that the reaction was structure sensitive, but the onset for the ORR was ca. 400 mV more negative than those measured in equivalent conditions for platinum [4, 5]. Additionally, the number of electrons transferred in the reaction was two, indicating that the final product was hydrogen peroxide. In fact, the reduction of hydrogen peroxide was highly inhibited and only took place at potentials close to hydrogen evolution.

When the same experiments were carried out in neutral and alkaline media, the voltammetric behavior showed significant differences for some electrodes. The Au(111) and Au(110) electrodes exhibited a similar behavior to that observed in acid medium. However, the onset for the ORR on the Au(100) electrode was displaced significantly to more positive potentials, with an electrocatalytic activity similar to that of platinum (Fig. 16.1) [6–13]. Additionally, four electrons were exchanged at high potentials, whereas a change in mechanism took place at lower potential and only hydrogen peroxide was formed. In parallel with this behavior, the Au(100) electrode exhibited a significant activity for the reduction of hydrogen peroxide in the same region where the four-electron mechanism is operative [6, 9]. In the transition between the two- and four-electron mechanisms, oscillations can be observed [9, 13]. The oscillations are linked to the appearance of the inhibition of the reaction at lower potentials, which corresponds to a negative resistance in the equivalent that compensates the solution resistance [14].

The studies with stepped surfaces revealed that the enhanced electrocatalytic activity for the ORR in alkaline solutions is exclusively linked to the presence of $\{100\}$ bidimensional domains [10, 12, 15, 16]. However, the origin of the high catalytic activity of these domains for the ORR is still not clear. Adzic and col. attributed the differences to the different OH adsorption properties of the domains [15]. In summary, it has been proposed that adsorbed OH catalyzes the cleavage of the O–O bond in the peroxide and leads to the transfer of four electrons [10, 17]. However, the voltammetric profiles of the different electrodes show similar OH adsorption properties in the region where the oxygen reduction takes place [13]. Thus, it was proposed that different behavior for the ORR should be related to structural differences. Additionally, the transition between the two- and four-electron mechanism takes place at a constant potential, which also suggests that OH adsorption is not responsible for the catalytic enhancement of the ORR on the Au(100) electrode [13]. Some experiments have suggested the presence of adsorbed HO_2^- in alkaline medium on gold electrodes and attributed a very important role in the mechanism to this species [18]. Also DFT studies indicate that adsorbed OOH, rather than O_2, is the most important intermediate which determines the final outcome of the reduction process [19]. Other studies propose that the Au(100)–O_2 interaction and the number of sites available for the reduction of oxygen controls the reaction rate [20].

The previous discussion/introduction summarizes the knowledge of electrocatalytic properties of Au single crystals toward ORR. Nevertheless, it is well known that for practical purposes, the use of the catalysts in the form of nanoparticles of dimensions as small as possible is required. In these nanoparticles the surface over volume ratio is maximized and consequently the amount of catalyst is minimized, thus reducing costs associated with their use in large-size/scale applications. In addition, it is well established that the electrocatalytic properties of a nanoparticle are mainly determined by the electronic properties of the surface atoms which in turn depend on a set of physical parameters that include chemical composition (at surface and bulk), particle size, and particle shape/surface structure. In principle, one could tailor their properties by controlling any of those parameters to optimize the activity of the catalyst for a particular reaction. Thus, and because the aim of this chapter is to review the electrocatalysis of gold toward ORR, the chemical composition of the nanoparticles is defined (gold), and therefore in the following sections, we will summarize and discuss the most relevant contributions related to the effect of the particle size and particle shape/surface structure for gold nanostructures toward ORR.

16.3 Effect of Particle Size

The electrocatalytic properties defined as the current density per active area measured at given potential should be in principle independent of the size of the nanoparticles. However, the diminution of size could lead to changes in the reactivity due to two main factors: (1) if the number of atoms in the nanoparticle is too small, the band structure of the metal is not completely developed and the electronic properties may differ significantly from that observed for bulk gold and (2) the ratio of atoms with low-coordination number in the surface, which are regarded generally as more reactive, increases with the diminution of the size. For that reason, below a certain size (ca. 4–7 nm), different electrocatalytic activities can be found for the nanoparticles. Thus, the effect of the nanoparticle size has been extensively studied.

One of the first contributions related to the effect of the particle size for oxygen reduction on gold was reported by Sarapuu et al. [21]. They investigated the influence of the loading of evaporated gold on the kinetics of the ORR at thin-film gold electrodes in acid electrolyte (0.5 M H_2SO_4) and compared their behavior with bulk gold with the main objective of evaluating the influence of the particle size in the ORR. They observed that the kinetics of O_2 reduction on the electrodes, including specific activity, Tafel slope, and n (number of transferred electrons) value, were almost independent of the film thickness (thickness between 0.25 and 50 nm) and similar to those observed with a bulk gold electrode, thus suggesting the absence of a particle size dependence. However, subsequent contributions by El-Deab and Ohsaka [22] and Zhang et al. [23] observed remarkably high electrocatalytic activities toward oxygen reduction in acidic solutions with electrochemically deposited Au nanoparticles on polycrystalline Au and boron-doped diamond (BDD) electrodes, respectively. El-Deab and Ohsaka [22] reported that for gold nanoparticles electrodeposited on gold electrodes, the ORR in 0.5 M H_2SO_4 solution showed two well-defined reduction peaks at +50 and −250 mV versus Ag/AgCl. This behavior was remarkably different from that observed with the bare gold electrode in which only a reduction peak was observed at −200 mV. They attributed these two reduction peaks at the gold nanoparticles as a two-step four-electron reduction pathway of O_2 in which the peak at more positive potential was due to the two-electron reduction of O_2 to H_2O_2, whereas that at lower potentials was assigned to the further reduction of H_2O_2 to H_2O. This behavior was clearly different from that found with the bulk gold electrode, at which only the two-electron reduction peak of O_2 to H_2O_2 was observed. The proposed mechanism was verified by performing similar ORR experiments in presence of 2.3 mM H_2O_2 solution resulting in an evident increase in the reduction peak current related to the reduction of H_2O_2 to H_2O, while the reduction peak current associated with the reduction of O_2 to H_2O_2 remained almost unaltered. Interestingly, they also observed that the increase of the particle size resulted in a clear loss of the activity of the two-electron reduction of O_2 to H_2O_2 (Fig. 16.2).

Fig. 16.2 CVs obtained for the O_2 reduction at Au nanoparticle-deposited Au electrodes in O_2-saturated 0.5 M H_2SO_4. A potential step from 1.1 to 0 V was used for the electrodeposition of Au particles from 0.5 M H_2SO_4 solution containing 0.11 mM $Na[AuCl]_4$ with deposition time of (a) 5 s and (b) 10 s. Potential scan rate = 100 mV s^{-1} (extracted from [22])

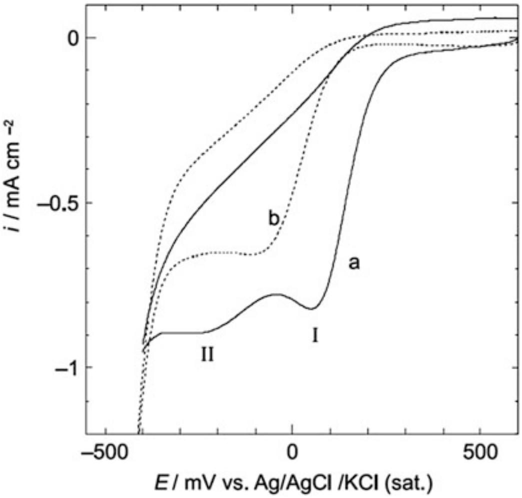

In a later work, and using the RDE, they also observed [24] that the number of electrons involved in the electrochemical reduction of O_2 was about 4 for the Au nanoparticle-electrodeposited electrode and 3 for bulk Au electrode at the same potential (−350 mV vs. Ag/AgCl/KCl(sat.)) (Fig. 16.3), thus indicating a higher reduction and decomposition of H_2O_2 at the gold nanoparticles. In addition, the reported Tafel slopes for both systems (the nanoparticles and bulk gold electrode) were similar, suggesting that the O_2 reduction at both electrodes proceeds by a similar mechanism. However, they also observed that the kinetic current of the gold nanoparticles was higher than that of the bulk Au electrode at the same potential.

Similarly, Zhang et al. [23] reported that the O_2 reduction rate on the Au nanoparticles (~60 nm) deposited on BDD was 20 times higher than that of bulk Au electrode. In addition, they also observed that the reaction mechanism of oxygen reduction was modified from a two-electron reduction to a four-electron reduction in the potential range of −200 to −400 mV versus SCE at the Au nanoparticle-deposited BDD. However, when similar experiments were performed in alkaline (0.1 M KOH) or in neutral (0.1 M phosphate buffer solution ~ pH 7.2) solutions, such enhanced activity toward ORR was not clearly observed [25, 26].

When the electrocatalysis of the ORR was studied on gold nanoclusters deposited by vacuum evaporation on a BDD electrode in 50 mM H_2SO_4 solution, Yagi et al. observed that the ORR activity was again influenced by the particle size [27]. Thus, the electrode with 3 nm nanoparticles was the most active. Unfortunately, as authors stated, the size dispersions of the samples were quite broad and the optimum particle size for oxygen reduction could not be determined. However, the activity of the samples was significantly higher than that at a polycrystalline gold electrode, and a clear positive shift of the O_2 reduction peak toward positive potentials and an increase in the current efficiency consumed for the four-electron reduction were observed. In addition, a two-step four-electron reduction pathway of

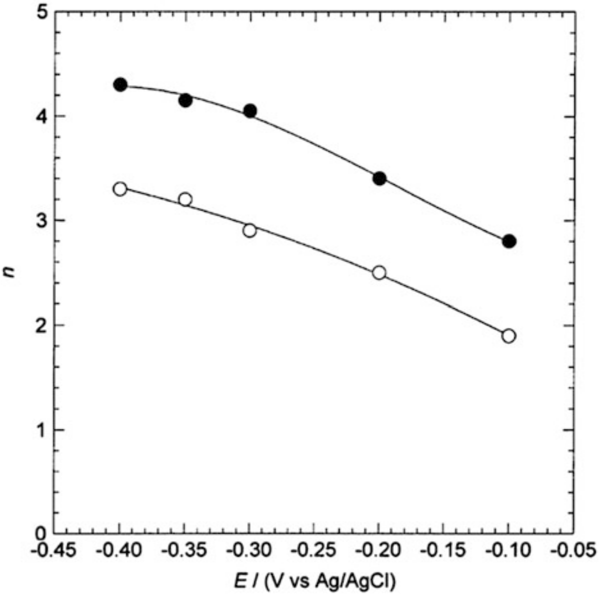

Fig. 16.3 Dependence of *n* on the potential for O_2 reduction at (*open circles*) bulk and (*filled circles*) Au nanoparticle-electrodeposited Au electrodes (extracted from [24])

O_2 to H_2O at the Au nanoparticles was directly proved by a four-electrode configuration. Also, they observed that after a heat treatment (600 °C under H_2 atmosphere) of the samples, the electrocatalytic activity improved, which was attributed to a modification of the particle shape and consequently with a modification of the crystallographic orientations exposed at the surface of the nanoparticles.

In good agreement with Yagi et al., Guerin et al. observed that for gold nanoparticles supported on substoichiometric titanium dioxide (TiO_x) and on carbon, the activity decreased for diameters <3 nm with decreasing particle size, independently of the supporting material [28]. Nevertheless, unlike the aforementioned studies, the catalytic activity was clearly independent of particle size above this critical size (Fig. 16.4).

In contrast with some of the previous observations, Bron observed that the ORR in acidic electrolyte solution at various Au/C catalysts with different support materials (VULCAN XC72 and Black Pearls) and different gold particle sizes between 2.7 and 42 nm [29] was neither dependent on the particle size nor on the supporting material. In addition, he found Tafel slopes around 105 mV and an average number of electrons transferred per oxygen molecule between 2 and 3, finding also that both parameters were independent on the gold particle size. From these results, he concluded that the oxygen reduction on carbon-supported gold catalysts is structure insensitive for particle sizes up to 2.7 nm.

In the same way, Sarapuu et al. [30] extended their previous works studying the ORR on nanostructured gold electrodes both in acidic (0.5 M H_2SO_4) and alkaline

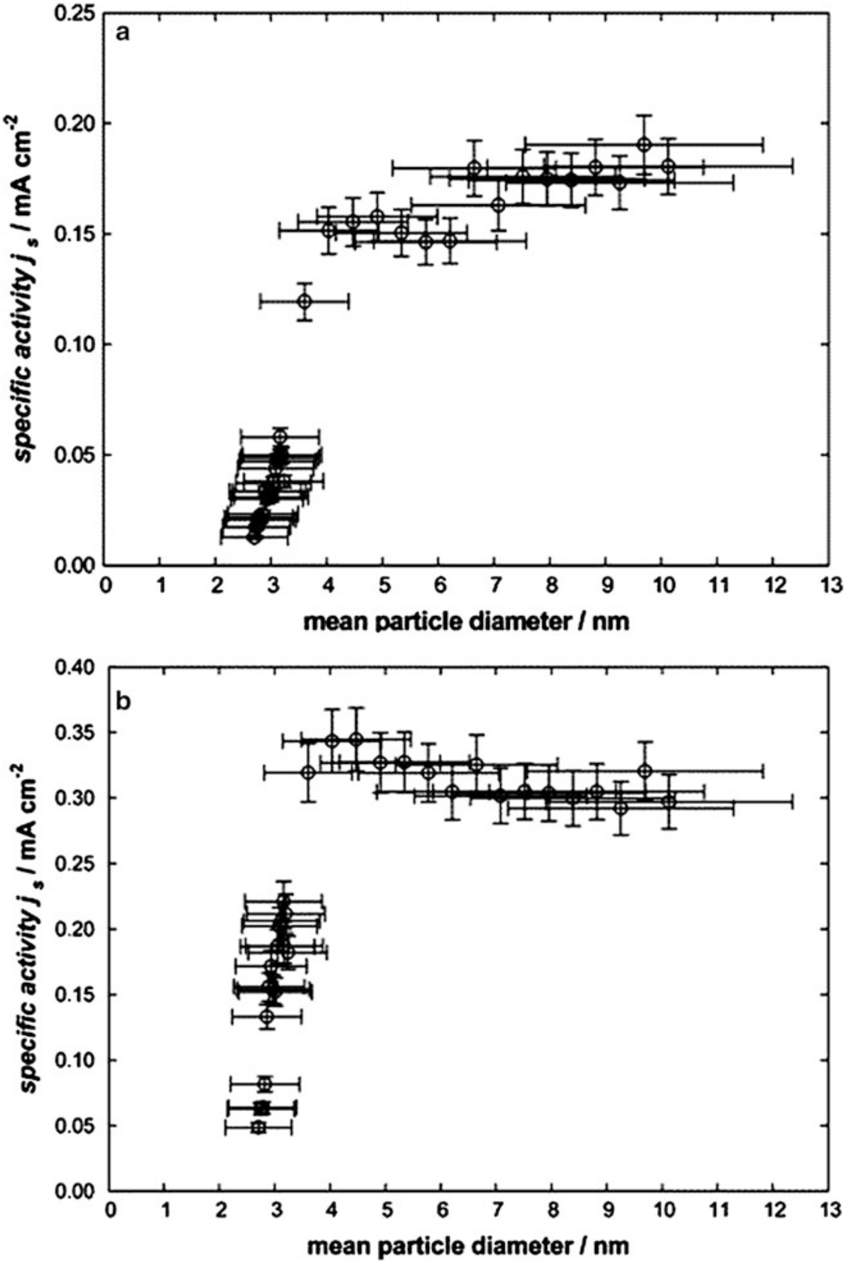

Fig. 16.4 Specific oxygen reduction activity of carbon-supported gold particles at (**a**) 0.40 V and (**b**) 0.30 V versus RHE measured on the (10 × 10) array of electrodes. The *error bars* along the particle size axis indicate the range of particle size (in fact, the standard deviation of the particle size) observed by TEM. The *error bars* on the specific activity axis reflect the standard deviation of the currents measured at the 10 electrodes on the array with a mean particle size (extracted from [28])

(0.1 M KOH) media. Thin films of gold surfaces, with a nominal thickness of 0.25–20 nm, were prepared by vacuum evaporation onto glassy carbon (GC) electrodes and coated with a Nafion film. The Au particle size was clearly dependent on the loading of gold and varied from 2.7 ± 1.0 nm for a nominal thickness of 0.25 nm to 16 ± 6 nm corresponding to 20 nm nominal thickness. In agreement with their previous findings, they again observed that the Tafel slopes were close to -120 mV for all electrodes in both solutions, indicating that the O_2 reduction mechanism is the same for thin film as for bulk Au electrodes. In addition, the specific O_2 reduction activity (SA) of the nanostructured Au electrodes in 0.5 M H_2SO_4 was almost constant over the range of Au thicknesses studied, whereas in 0.1 M KOH, the SA slightly decreased with decreasing film thickness. However, it is important to point out that the average SA values were approximately three times lower (0.14 ± 0.03 mA cm^{-2}) than those obtained with Au films in the absence of Nafion (SA $= 0.43 \pm 0.05$ mA cm^{-2}) [21]. This evidence was attributed to a decrease in the number of reaction sites by Nafion, as proposed by Maruyama et al. who studied the effect of fluorinated alcohols on the kinetics of the ORR on bulk Au electrodes [31, 32]. A similar decrease of the kinetic current was also reported on Nafion-coated GC electrodes as compared to bare GC which was related to the lower pH at Nafion-coated GC and/or to blocking by the side chains of the Nafion polymer.

Subsequent studies by Tang et al. [33] suggested a strong size effect. They analyzed the dependence of the kinetics of the ORR in alkaline solution (0.5 M KOH) with the particle size of gold nanoparticles (3 and 7 nm) supported on carbon (Fig. 16.5). They observed that the ORR activity (kinetic current density, j_k) of the 3 nm gold nanoparticles was 2.5 times higher than that obtained with the 7 nm gold nanoparticles (3.5 vs. 1.5 mA cm^{-2} measured at -0.6 V vs. Ag/AgCl). In addition, a two-electron reduction was obtained with the 7 nm, whereas in case of the 3 nm, a four-electron reduction was observed. This unusual four-electron transfer obtained with the 3 nm Au nanoparticles was speculatively explained due to the high density of low-coordination sites on the 3 nm nanoparticles that may increase the activation of the peroxide intermediate, facilitating further reduction to water. Very interestingly, from experiments at different temperatures, they estimated the apparent activation energy for the 3 nm particles that was found to be half that of the 7 nm particles (0.1 and 0.2 eV, respectively). They proposed that the presence of a high fraction of surface sites with low-coordination atoms together with the decreased electrophilicity of the 3 nm Au nanoparticles results in an increase in the O–Au bond energy with a corresponding decrease in the activation energy of the critical step of molecular oxygen dissociative chemisorption, thus accelerating the rate-limiting step for oxygen reduction.

Likewise, Inasaki and Kobayashi [34] studied the influence of the particle size of Au nanoparticles on the kinetics of ORR in acidic solution (0.5 M H_2SO_4) and found a size effect. They prepared carbon-supported Au nanoparticles with different particle size (1.7 ± 0.5, 4.8 ± 2 and 13.2 ± 2 nm) and evaluated their electrocatalytic activity toward ORR together with that of a bulk Au electrode (Fig. 16.6). The results obtained showed a clear dependence of the ORR activity

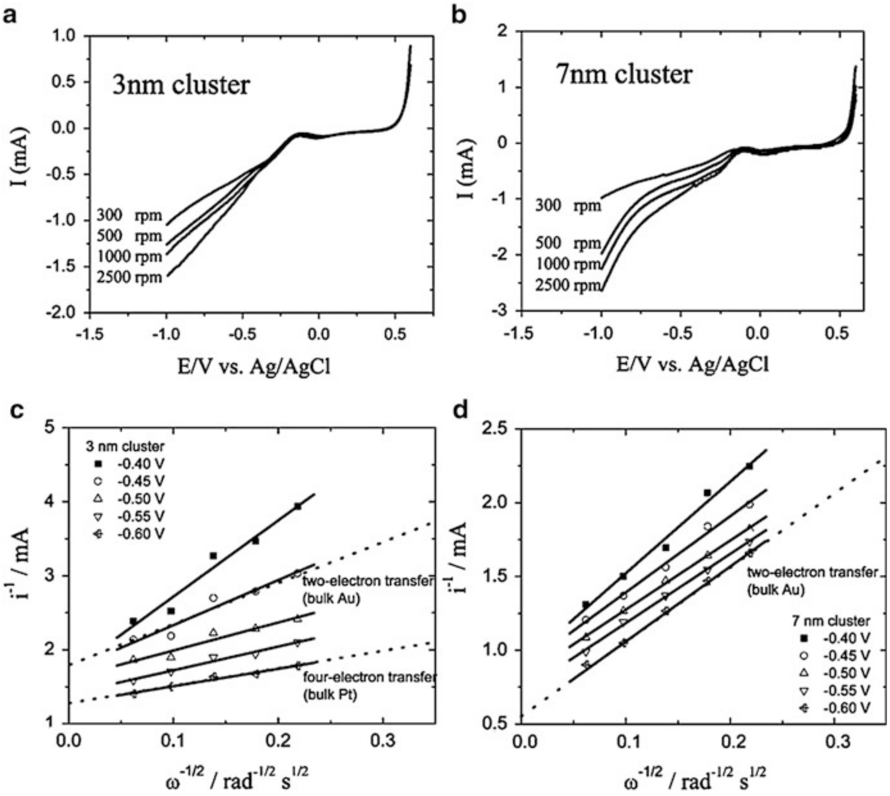

Fig. 16.5 Oxygen electroreduction on 3 and 7 nm Au nanoclusters in oxygen-saturated 0.5 M KOH. Cyclic voltammograms (sweep rate 10 mV s^{-1}) of Au nanoparticles on carbon rotating disk electrodes at several rotation speeds: (**a**) 3 and (**b**) 7 nm clusters. Levich plots of the voltammogram data (the currents at −0.6 V were used): (**c**) 3 and (**d**) 7 nm clusters (extracted from [33])

with the particle size. In detail, they reported that whereas for bulk gold, the number of electrons involved in the ORR was 2 and nearly constant at potentials above −0.2 V, for the nanoparticles, the n values increased as the potential became more negative and reached values of 2.3, 2.6, and 3.0 at −0.2 V versus Ag/AgCl for particles sizes of 1.7, 4.8, and 13 nm, respectively. These findings suggested that for smaller particle size, a two-step four-electron reduction or the direct four-electron reduction of O_2 to H_2O was favored.

Erikson et al. [35] also reported ORR results obtained with carbon-supported Au nanoparticles in 0.5 M H_2SO_4 and 0.1 M KOH solutions. They used commercial Au catalysts with different metal loading, 20 and 30 wt%, which also resulted in a different particle size, 11.0 ± 1.7 nm for 20 wt% catalyst and 14.0 ± 1.7 nm for 30 wt% catalyst. Nevertheless, in agreement with some of their previous studies, they concluded that the oxygen reduction activity of both carbon-supported Au

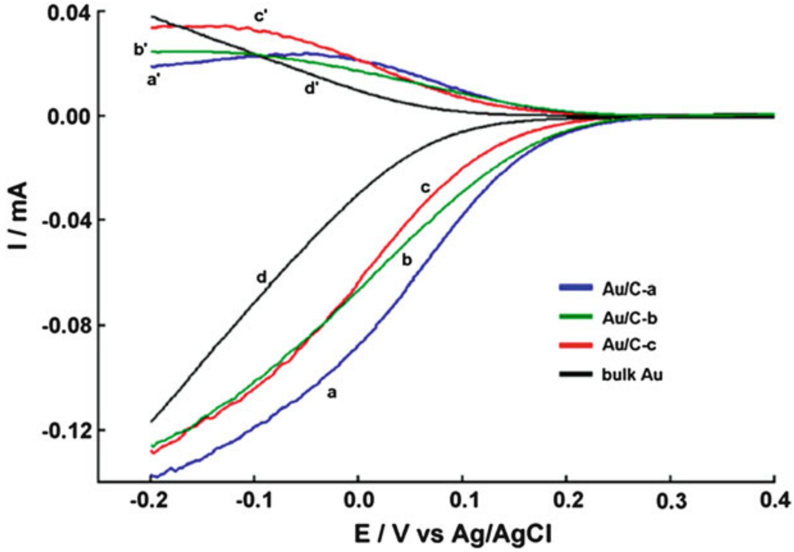

Fig. 16.6 RRDE voltammograms for the oxygen reduction in O_2-saturated 0.5 M H_2SO_4, at (a) (1.7 nm), (b) (4.8 nm), and (c) (13.2 nm) Au/C-modified GC electrodes and (d) bulk Au electrode at a rotation rate of 500 rpm. Curves a′–d′ represent the corresponding Pt-ring currents (polarized at 1.0 V). For the Au/C-modified electrodes, loading of Au metal on a GC electrode was fixed at 0.45 μg/electrode. $\nu = 10$ mV s^{-1} (extracted from [34])

nanoparticles was similar to the activity of bulk Au, both in acid and alkaline solutions. In addition, they also observed that the specific activity of Au was independent of the thickness of the catalyst layers, between 1.5 and 10 μm, indicating that the diffusion of O_2 within the layer was not affecting the results. In addition, they reported that the number of electrons involved in the reaction and the Tafel slopes were similar to those of bulk polycrystalline gold, which implies that the mechanism of O_2 reduction is not affected by the particle size.

The activity of very small nanoparticles has also been studied. Chen and Chen [36] prepared a series of Au nanoclusters with 11–140 gold atoms in the cores, corresponding to 0.8–1.7 nm in diameter, and performed ORR studies in alkaline medium to evaluate the size effect on the ORR electrocatalytic activity. Clear size dependence was observed in (1) the limiting current densities, increasing with decreasing core size; (2) the onset potential for ORR shifted to negative potential values with increasing Au cluster size; and (3) the kinetic current density increased with decreasing particle cores. Also, the oxygen reduction reaction was found to proceed by the efficient four-electron reaction pathway with the smaller clusters (Au_{11}, Au_{25}, and Au_{55}), whereas incomplete reduction occurred with the largest one (Au_{140}), for which the two-electron reaction route was favored.

In all these studies regarding the size effect in the ORR on gold electrodes, a general problem is the size distribution. The electrochemical response is always a macroscopic property which depends on the individual contributions of the different

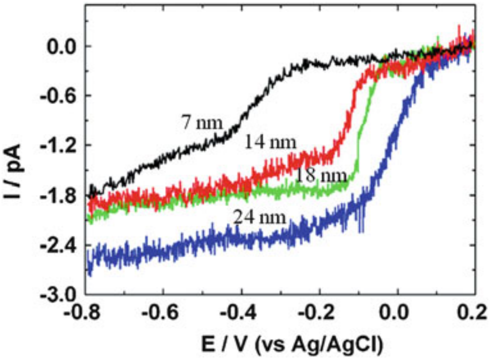

Fig. 16.7 Voltammetric responses of an oxygen-saturated 0.10 M KOH solution using a bare 7 nm diameter Pt nanoelectrode, a 14 nm Au SNPE, an 18 nm Au SNPE, and a 24 nm Au SNPE. The scan rate was 10 mV s (extracted from [37])

nanoparticles in the sample. In order to understand the effects of the size in the reaction, it would be important to address the reactivity of a single nanoparticle, as has been done using innovative methods by Li et al. [37]. In this study, they were able to immobilize a single Au nanoparticle at a SiO_2-encapsulated Pt disk nanoelectrode, previously oxidized and silanized. In such a system, the ORR in alkaline medium (0.1 M KOH solution) was studied. The Au single-nanoparticle electrode (SNPE) provided a larger diffusion-limited steady-state current than the one obtained with the bare Pt nanoelectrode. The Au nanoparticle exhibited a one-step process instead of a two-step pathway, similarly to the behavior of the bare Pt nanoelectrode for the ORR in alkaline medium. Moreover, the half-wave potential for the ORR at the Au SNPE was shifted toward higher potentials. The electrocatalytic activity for the ORR was also compared with Au nanoparticles of different sizes (14, 18, and 24 nm) and shown in Fig. 16.7. The steady-state limiting current increased with increasing the size of the Au nanoparticles, being 1.0, 1.7, and 2.0 pA for the 14, 18, and 24 nm Au nanoparticles, respectively. In addition, the half-wave potential at larger Au nanoparticles was also shifted to higher potentials, indicating higher catalytic activity. The half-wave potentials shifted from −365 mV versus Ag/AgCl at the bare Pt nanoelectrode to −130, −75, and −35 mV at the 14, 18, and 24 nm samples, respectively. These results clearly evidence a good Au size-dependent electrocatalytic activity toward ORR.

In some studies, the higher activity for the nanoparticle samples was credited to a lower contamination of the surface and/or the presence of higher number of low-coordinated atoms. Thus, Lee et al. [38] obtained the electrocatalytic properties for ORR in alkaline medium (0.5 M KOH solution) of carbon-supported Au nanoparticles with controlled particle size (3, 6, and 8 nm). The activity of these samples was compared with that obtained with commercial 5 and 10 nm Au nanoparticles. In all cases, the activity of the samples was higher than that of the commercial ones, which was attributed to the effectively cleaning and to the higher degree of disorder on the surfaces. However, the most active Au samples were those having 8 nm particle size, even when the currents were normalized by the weight of Au NPs, which is, from our point of view, quite unexpected.

Also, the surface structure effects were found in the study by Alexeyeva et al. [39]. They reported the analysis of the ORR on Au nanoparticles deposited on multiwalled carbon nanotubes (MWCNTs). The carbon nanotubes were decorated with Au nanoparticles using a magnetron-sputtering technique. The sample was heat-treated and they found that by varying the annealing temperature it was possible to modify the morphology of Au nanoparticles thus allowing correlating their morphology with their electrocatalytic activity toward the ORR in acidic solution (0.5 M H_2SO_4). They showed an optimal temperature of 300 °C which was proved to be beneficial to ensure a larger active surface area and increased electrocatalytic activity. This sample consisted of regularly shaped rounded Au nanoparticles with a mean particle size of 11 nm. However, a high Tafel slope value was observed at low overpotentials (−200 mV), far from the typical slope value for O_2 reduction on gold in acid solution (−120 mV), corresponding to the slow transfer of the first electron to O_2 molecule. The reasons for this high Tafel slope remain still unclear.

In the same way, Jirkovsky et al. [40] used carbon-supported Au nanoparticles of mean size between 4.2 and 9.5 nm and studied the dependence of the ORR on nanoparticle size. Their findings suggested particle size dependence and showed a maximum electrocatalytic activity at a particle size of 5.7 nm from which the activity significantly decreased with particle size. In addition, the number of electrons exchanged per O_2 molecule increased from a value close to 2–3.4 as the potential was made more negative. They proposed different possible reasons to explain the effect of the particle size, including changes in the stability of surface oxygen species on Au particles of different sizes as a consequence of the different abundance of atoms on edges with respect to those on crystal planes [41], the decrease in number density of {100} surface atoms at these sizes [41], or the stronger adsorption of OH groups on the surface [42].

More recently, Brülle et al. [43] prepared gold nanoparticles with a narrow size distribution deposited on HOPG and single-crystalline boron-doped diamond surfaces using a potentiostatic double-pulse technique. The particle size ranged between 5 and 30 nm on HOPG and between <1 and 15 nm on boron-doped diamond surfaces while keeping the particle density constant. The ORR activity of both samples was studied in 0.1 M H_2SO_4 (Fig. 16.8). Independently of the particle size as well as of the substrate, the specific current densities were always higher than that obtained for a bulk Au electrode. On the other hand, a clear size-dependent ORR activity was observed, increasing the ORR activity with decreasing particle sizes.

This clear size dependence on ORR activity was in agreement with previous observation by Chen and Chen [36]. However, contrarily, Bron [29] reported no size effect for particle sizes in the range between 2.7 and 42 nm supported on carbon black in acidic solutions, whereas Guerin et al. [28] observed that the activity decreased for diameters <3 nm with decreasing particle size. From these previous discussions, it is evident that the effect of Au particle size on the kinetics of O_2 reduction on Au nanoparticles, both in acidic and alkaline media, is a matter of controversy and very different trends can be observed in the literature. In addition, to have a full picture of the situation, it is important to note that theoretical studies predicted an increase in ORR activity with decreasing Au particle size [44]. In our opinion, and in agreement with some of the conclusions reported by Brülle et al. [43],

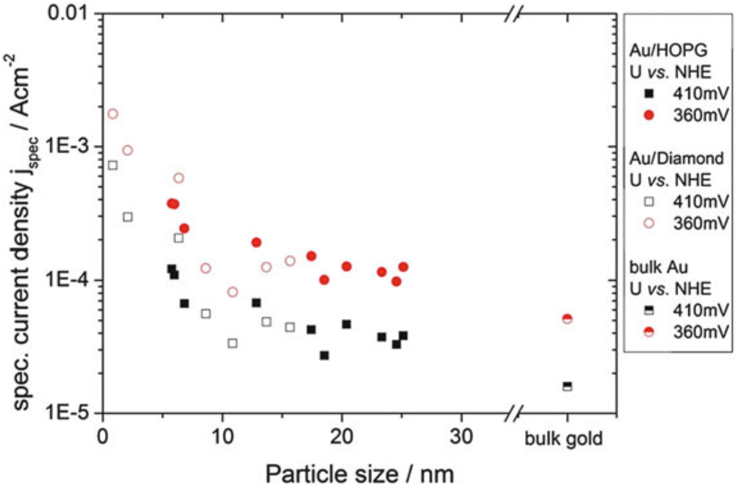

Fig. 16.8 Comparison of the ORR-specific current density for Au/HOPG (*filled symbols*) and Au/diamond (*open symbols*). The current densities versus particle sizes are comparable for the two substrates. The data for an extended gold surface was added as a reference (extracted from [43])

we believe that these discrepancies on particle size trends may be attributed to the strong dependence of the reaction on the surface structure of the nanoparticles. In this regard, it is relevant to point out that in one of the first contributions of our group in this topic [45], we evidenced that gold nanoparticles with a similar particle size (~4 nm) showed different electrocatalytic properties toward ORR as a consequence of their different surface structure and in particular to their different fraction of {100} surface sites. Consequently, as previously demonstrated with Au single-crystal studies, it is of outstanding importance to evaluate the effect of the surface structure of the Au nanoparticles and then correlate it with their electrocatalytic properties. In this context, the correlation between the shape of the nanoparticle and its preferential surface structure is now well established. Thus, as a first approximation, shape will determine which surface structure facets will comprise the surface of the nanoparticle. By controlling their shape, both the reactivity and selectivity of a catalyst can be tailored because the exposed surfaces of the nanoparticle have different surface structures depending on its particular morphology/shape. Very relevant contributions can be already found in the literature about the correlation between the shape/surface structure of different nanoparticles and their electrocatalytic properties [46–55].

16.4 Effect of Shape/Surface Structure

As previously demonstrated from single-crystal studies, Au(100) was the most active catalyst in basic media. Moreover, the overpotential on Au(100) in 0.1 M NaOH is 0.34 V [56] even lower than that on Pt surfaces in 0.1 M $HClO_4$, which is 0.48 V [57]. One of the main strategies to increase the electrocatalytic activity for

ORR has been the preparation of gold nanoparticles containing a high fraction of these {100} surface sites. Therefore, from a crystallographic point of view, the use of cubic Au nanoparticles in which the amount of {100} surface sites is maximized should be a clear goal. Nevertheless, it is very important to note that the critical point determining the electrocatalytic properties is the particular surface structure of the samples and not the shape. Thus, it is of paramount importance to probe the correlation between shape and surface structure on a particular sample. Regarding this issue, one question arises: how can the surface structure of the Au nanoparticles be evaluated and then correlated with their electrocatalytic properties? From transmission electron microscopy (TEM) images, it is relatively easy to determine the preferential shape of the samples. However, the measurement of the different types of sites present on the surface of the nanoparticles by TEM is not simple and requires more specific instrumentation. In this sense, for instance, Gontard et al. [58] showed that spherical-aberration-corrected transmission electron microscopy can be used to provide atomic-resolution information about the local topologies of active sites on commercial nanoparticles with greatly improved sensitivity, as shown in Fig. 16.9. Unfortunately, this kind of analysis is still rather unusual due to the highly sophisticated techniques and time-consuming analyses that are required.

One option could be the analysis of the oxide formation region which, as previously reported by Hamelin et al. [59, 60] with Au single-crystal electrodes, showed different contributions as a function of the specific surface structure. Unfortunately, the inclusion in such high-potential limits would compromise the surface stability of the Au nanoparticles, thus resulting in a surface disordering.

Another possibility to qualitatively measure the amount of the different facets is using surface structure-sensitive reactions which may serve as an indirect technique to estimate the response dependence on the surface geometry of the sample. In this sense, electrodeposition of a monolayer of a given metal on a different substrate at a potential more positive to that of the metal bulk deposition which is known as underpotential deposition (UPD) is generally regarded as a reaction very sensitive to the surface structure of the electrodes [61], since it depends on the specific interaction between the surface atoms of the supporting metal and the depositing atoms of the foreign metal. Lead UPD and its desorption on Au has shown to be a structure-sensitive process [45, 62–65], and the three basal planes give well-defined voltammetric peaks in different potential ranges as shown in Fig. 16.10.

For Au(111) the deposition peak appears at 0.38 V and the dissolution peak at 0.435 V with an overlapping shoulder in the ascending branch. In the case of Au(100), two different contributions appear for both deposition (0.38 and 0.43 V) and dissolution (0.385 and 0.475 V) being those at higher potentials for each process the main peaks. For the Au(110) electrode, the contributions are much broader due to the fact that the process is quite slow. Peaks are centered at 0.50 and 0.56 V for the deposition and dissolution processes. Interestingly, the dissolution peaks for the three basal planes appear at potentials where the other two basal planes have small contributions. Therefore, these contributions at the

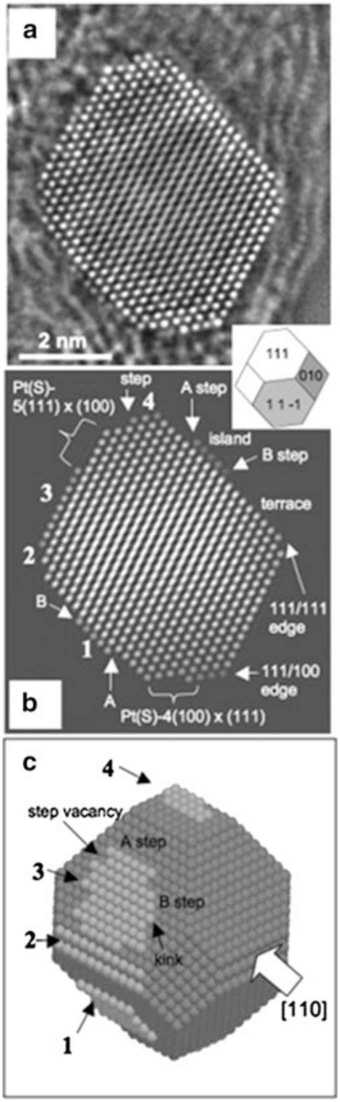

Fig. 16.9 (**a**) Restored phase of a 6 nm Pt particle obtained by applying spherical-aberration correction and through-focus exit wave function restoration to a defocus series of 20 images acquired at 200 kV with the coefficient of spherical aberration, CS, adjusted to −30 µm. (**b**) Best-fitting simulated phase. (**c**) Three-dimensional atomic model used to calculate the best-fitting phase in part (**b**). The *large white arrow* indicates the direction of the electron beam. The *inset* overlapping parts (**a**, **b**) shows the crystallographic details of the particle. In parts (**b**, **c**), 1–4 correspond to the same features on the surface of the particle. The notation $\mathrm{Pt(S)} - n(x, y, z) \times (u, v, w)$ refers to the microfacets, on which n is the number of atoms in the terrace, (x, y, z) is the Miller index of the terrace, and (u, v, w) is the Miller index of the step (extracted from [58])

aforementioned potentials can be used as indicators of the presence of a particular structure at the surface of a gold electrode.

Surface characterization using Pb UPD of a polycrystalline gold electrode, which is expected to contain all surface sites, shows three main peaks for the dissolution processes at the same potentials that the main dissolution peaks recorded for the three Au basal planes. The only significant difference is that the peak corresponding to the {111} facets is split. Moreover, other small peaks are observed in the voltammetric

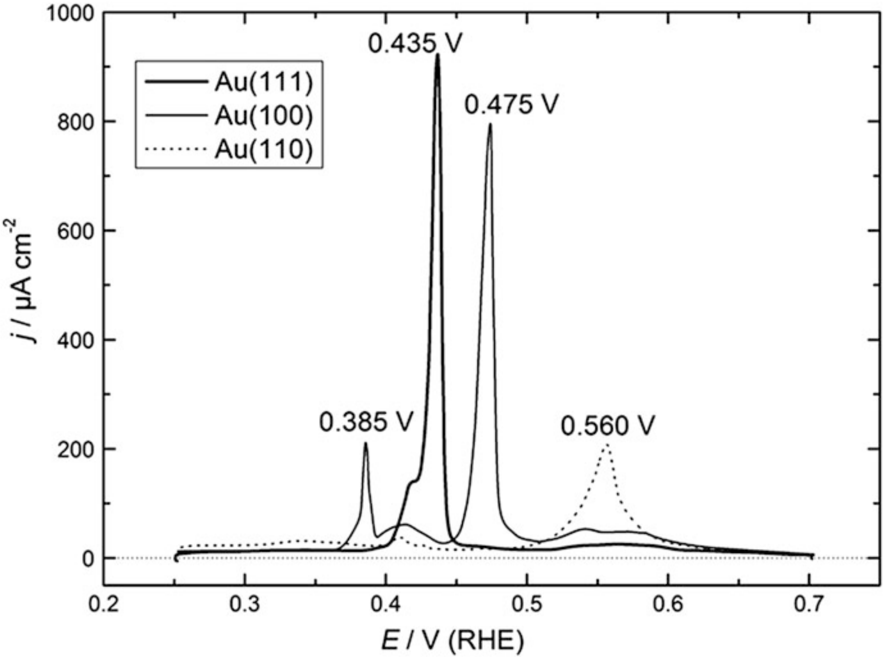

Fig. 16.10 Comparison of the stripping voltammograms for the Pb UPD on the Au(111), Au(100), and Au(110) electrodes in 0.1 M NaOH + 10^{-3} M $Pb(NO_3)_2$. Scan rate = 50 mV s^{-1}

profile, which are ascribed to the dissolution of lead from steps or kinks in the polyoriented surface (especially at potentials below 0.40 V vs. RHE) [45]. The charge of the peaks can be used to qualitatively estimate the relative amount of {100}, {110}, and {111} domains in a polyoriented electrode such as gold nanoparticles. Nevertheless, as it has been observed with stepped surfaces, when domains become smaller, the Pb UPD contributions may take place at different potentials, as observed for Au(775) [45], but the peak shift is small, even for narrow domains, making it positive for nanoparticle electrode characterization, for which domains are expected to be small.

Moreover, Pb UPD can be used to calculate the real area of the electrode from the recorded charge between 0.25 and 0.75 V and assuming a charge density of 420 μC cm^{-2} (measured for a polyoriented surface) [45]. Pb UPD can be also employed to clean the nanoparticles from the organics used during their syntheses by forming an electrochemical PbO_2 film deposited on the gold surface [45, 46, 66–70]. When Pb UPD is performed in basic media (and oxygen reduction is normally studied in these media), the characterization and ORR can be performed in the same medium.

Another interesting option to estimate the fraction of the different surface sites present at the surface of a nanoparticle is the reductive desorption of thiol compounds such as cysteine, mercaptoacetic acid, or cystamine. El-Deab et al., following previous observations by Porter et al. [71, 72] with polyoriented Au electrodes, used this approach to evaluate the fraction of the surface sites in different types of gold nanostructures [73–75].

One of the first papers in this sense, if not the first, was published by Hernández et al. where gold nanoparticles were synthesized in a water-in-oil microemulsion [45]. In order to modify the surface structure of the Au nanoparticles, iodide and sulfide were added as additives to the water phase of the microemulsion before the chemical reduction with $NaBH_4$. Pb UPD analysis confirmed that those nanoparticles synthesized in the presence of iodide showed a higher ratio of {100} and {111} facets. On the other hand, for those in the presence of sulfide, the two previously mentioned facets were almost missing. Rotating ring-disk experiments for ORR were performed in 0.1 M NaOH with these nanoparticles and the results were compared with additive-free spherical nanoparticles prepared with the same methodology. As expected from single-crystal studies, the gold nanoparticles prepared in the presence of iodide and containing a higher ratio of {100} facets had the highest catalytic activity. As a result, for a surface structure-sensitive reaction as is ORR, a good relationship was obtained between the ratio of {100} facets and the electrocatalytic activity. As previously stated, the evaluation of the amount of the different sites was carried out with Pb UPD and an estimation of the size of the different facets present in the nanoparticles was made by comparing the Pb UPD profile of the nanoparticles with those obtained for the gold single-crystal basal planes.

A similar strategy using additives was used by El-Deab et al. [76] where Au nanoparticles were prepared by adding cysteine or iodide in the electrodeposition bath. Two effects were observed: (1) those nanoparticles prepared in the presence of iodide had a lower particle size (10–40 nm), whereas those prepared with cysteine showed an enhancement of the coalescence of neighboring particles and thus particle sizes of 50–300 nm were observed, and (2) an enrichment of the {100} + {110} facet domains at the expense of the {111} facets was observed in the case of cysteine, while iodide ions enriched the {111} facets of the Au nanoparticles, contrasting with the higher ratio of {111} but also {100} facets shown by Hernández et al. [45], although using different synthesis methods. Therefore, the cysteine-prepared Au nanoparticles exhibited a high catalytic activity for the ORR as previously reported for Au(100) accomplishing a four-electron reduction of oxygen to water at a reasonably low cathodic overpotential in O_2-saturated 0.5 M KOH. These findings were more deeply studied by the same group in different publications [74, 77–79]. In one of these papers, the effect of the support was also evaluated [79]. Interestingly, when HOPG was used, an electrooxidative pretreatment of the support led to more active cysteine-prepared Au nanoparticles in comparison with untreated HOPG. On the other hand, no improvement was observed in the case of using iodide as additive.

Another strategy was to synthesize nanoparticles with shapes that would have a preferential surface structure. Concerning this idea, oxygen reduction reaction on some shape-controlled gold nanoparticles was reviewed in 2009 [46]. In this sense Hernández et al. studied the ORR with gold nanorods [67]. Their surface structure

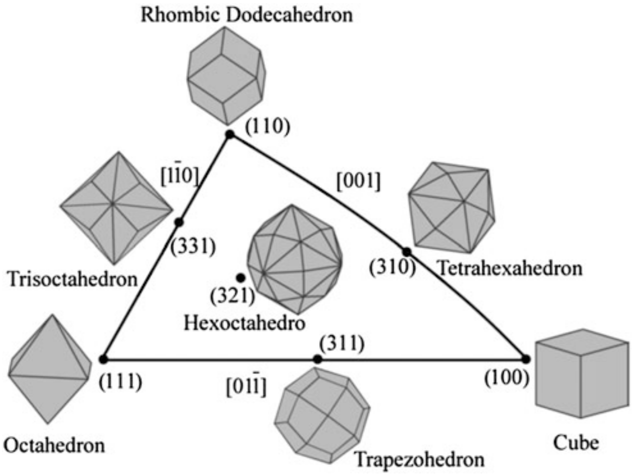

Fig. 16.11 Unit stereographic triangle of polyhedral nanocrystals bounded by different crystal planes (extracted from [83])

was analyzed with Pb UPD, revealing that their nanorods were composed by {111} and {110} domains, while {100} domains were practically absent. Hydrogen peroxide was the final product in the whole potential range confirming the absence of {100} sites as obtained from the Pb UPD analysis. This conclusion was in agreement with HRTEM images which indicated that the side faces of the nanorods were {110} faces [80] and with selective area electron diffraction (SAED) experiments, which indicated that the nanorods were capped at both ends by five {111} faces [81]. Nevertheless, Gao et al. observed a higher activity of Au nanorods in comparison with spherical nanoparticles but their synthesis conditions were different [82]. In this case the authors used an electrodeposition method in the presence of cysteine, which as mentioned before produced an enrichment of the {100} + {110} facet domains at the expense of the {111} facets [76]. For the nanorods the authors explained the behavior of a continuous unidirectional growth of the crystal along the {111} orientation, leading to a pin-like morphology of the crystals.

In analogy with the stereographic triangle where the three basal planes are located at the vertices, an intrinsic triangle can be made which coordinates the crystal surface index and the shape of fcc metal nanocrystals as shown in Fig. 16.11 [83, 84]. The three vertices represent the coordinates of polyhedral nanocrystals bounded by basal facets, i.e., cube covered by {100}, octahedron by {111}, and rhombic dodecahedron by {110} faces.

Nevertheless, as previously stated, it is important to recall that the main issue is the final arrangement of the atoms at the surface, which may not be that expected from the nanoparticle shape. This fact highlights the importance of characterization tools such as Pb UPD. Going back to the analogy with the stereographic triangle, if from single-crystal knowledge it is known that Au(100) is the most active catalyst in alkaline medium, it seems interesting to study the ORR with gold nanocubes. Hernández et al. prepared this type of gold nanoparticles for this purpose [69]. Deliberately, the authors synthesized large cubic Au nanoparticles (average size 40 nm) using a seed-mediated method in the presence of cetyltrimethylammonium bromide. SAED patterns confirmed that the cubic nanoparticles were single crystals. Although lead UPD confirmed the presence of a large amount of {100} domains, the majority of the surface sites had a {111} or {110} symmetry, suggesting that surface faceting or ripening had taken place. Nevertheless, due to the large amount of {100} sites, this type of nanoparticles showed a very high catalytic activity for the four-electron oxygen reduction paths in alkaline medium. As a result, water was obtained as the final product of the reaction in the whole potential range, except in the lower potential range where hydrogen peroxide was obtained, in a similar way as reported for Au(100). Moreover, the authors studied the stability of the surface of the cubic nanoparticles during the electrocatalytic experiments performing Pb UPD experiments after the ORR. Although the reactivity was maintained, the amount of {100} domains decreased, concluding that the transport-controlled reaction of interest is less sensitive to the surface order.

The electrocatalytic activity of the different samples can be addressed using the scanning electrochemical microscopy (SECM). Thus several samples can be probed simultaneously, allowing a direct comparison. The activity for the ORR of different shape-controlled gold nanoparticles and nanorods was studied by Sánchez-Sánchez et al. [70]. The different shaped nanoparticles were characterized by TEM and Pb UPD, providing information on the shape and surface structure of the different nanoparticles (spherical and cubic) and short nanorods. Cubic gold nanoparticles were the most active toward ORR in alkaline medium followed by the spherical nanoparticles and being the short nanorods the least active, as shown in Fig. 16.12. These results are expected taking into account single-crystal results and from the fact that a nanocube is ideally enclosed by six {100} faces. These results were also in agreement with previous works from the same research group [45, 67, 69].

Nanopyramidal, nanorod-like, and spherical gold nanostructures were also used to study the ORR in 0.5 M KOH [85]. They were synthesized on polycrystalline gold substrates through electrochemical overpotential deposition by manipulating the deposited potentials and concentrations of $HAuCl_4$. X-ray diffraction and electrochemical experiments showed that the pyramidal structures were dominated by {111} facets, and therefore due to the lowest amount of {100} sites, the activity toward ORR was the lowest. The reduction peak current increased and the peak potential shifted positively in the following order: nanopyramids $<$ nanorods $<$ nanospheres.

El-Deab studied the influence of the electrodeposition time on the crystallographic orientation of Au nanoparticles electrodeposited on glassy carbon prepared by potential step electrolysis and on their electrocatalytic properties toward ORR in alkaline medium (0.5 M KOH) [73]. He observed that particles prepared in short time (5–60 s) had smaller size (10–50 nm) and showed a higher particle density (number of particles per unit area), as revealed by SEM images, than those prepared

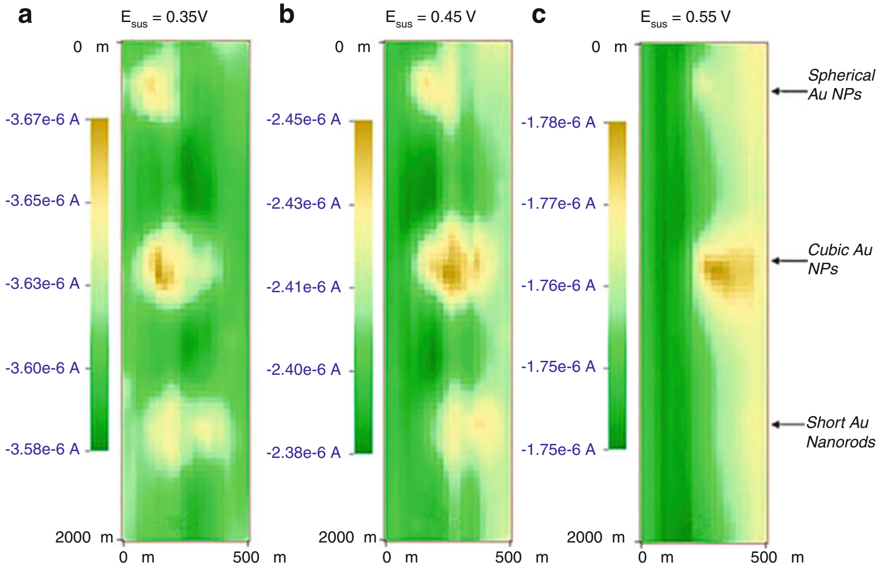

Fig. 16.12 SECM TG-SC images displaying the substrate current for ORR of an array composed by 3 different types of shape-controlled gold particles supported on a glassy carbon plate. Substrate potential held constant at (**a**) 0.35 V, (**b**) 0.45 V, and (**c**) 0.55 V versus RHE in an oxygen-free 0.1 M NaOH solution. Tip-substrate distance = 25 μm. Oxygen flux generated at the tip at a constant current of 150 nA. Scan rate = 125 μm s^{-1} (extracted from [70])

by longer electrolysis time. On the other hand, Au deposits prepared for times higher than 60 s were larger (>100 nm). SEM, XRD, and electron backscatter diffraction (EBSD) techniques were used to characterize both the size and preferential facet orientation of the nanoparticles. Interestingly from the EBSD patterns, the author estimated the fraction for the {100} {110}, and {111} orientations corresponding to the Au samples being the total fraction of a specific facet, the percentage of a specific orientation relative to the total area of the analyzed region of the surface [86]. From EBSD analysis the author found that increasing the deposition time resulted in an increase in the total fraction of {100} and {110} facets, while for short deposition times the deposit was rich in {111} facets. ORR was studied with gold nanoparticles prepared after 60, 300, and 900 s and showed to be influenced by the surface structure as shown in Fig. 16.13. The sample enriched with {111} domains (60 s) had a much lower activity than those containing a lower fraction of {111} surface domains (300 and 900 s), being the peak current density about 1.7 times higher than those prepared after 60 s. This difference was ascribed to the increase of the number of exchanged electrons as a consequence of their polycrystalline surface structure instead of a {111} enriched. In fact the behavior was very similar for the polycrystalline bulk Au electrode and those nanoparticles prepared after longtime deposits. In addition, a possible particle size effect was ruled out because the diffusion layer thickness ($\delta \approx 0.021$ cm) was much larger than the average distance between Au nanoparticles (≈50–200 nm).

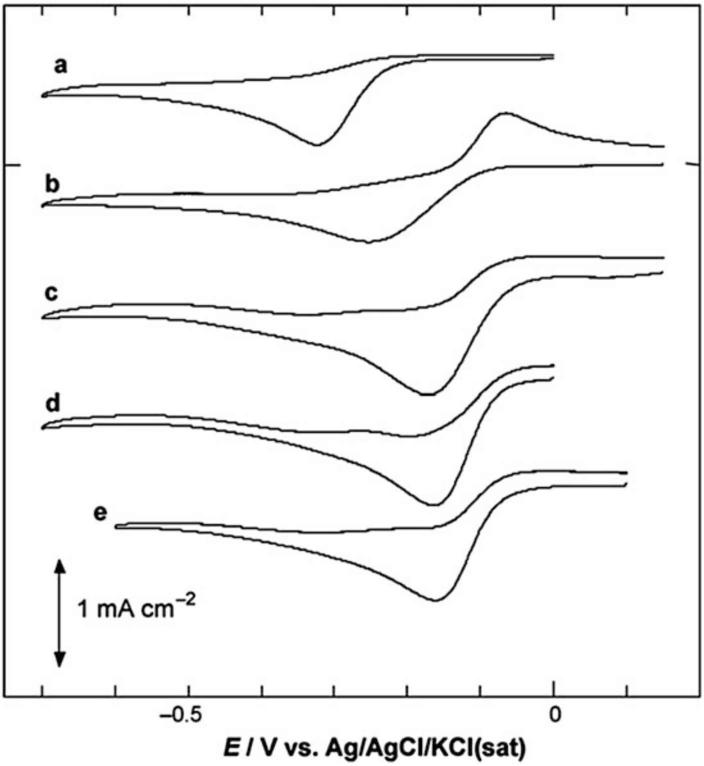

Fig. 16.13 CVs measured at 100 mV s^{-1} for the oxygen reduction at (a) bare GC, (b) 60 s nano-Au/GC, (c) 300 s nano-Au/GC, (d) 900 s nano-Au/GC, and (e) bare polycrystalline Au electrodes in O_2-saturated 0.5 M KOH (extracted from [73])

Several strategies have been used to maximize the electrocatalytic activity of the gold nanoparticles by tailoring the shape. Xu et al. [87] studied the ORR with indium tin oxide (ITO)-supported dendritic gold nanostructures prepared with a “green” templateless, surfactantless, simple electrochemical route. The samples were characterized by scanning electron microscopy (SEM), TEM, energy-dispersive X-ray spectroscopy (EDX), X-ray diffraction (XRD), and X-ray photoelectron spectroscopy (XPS). The dendritic gold nanostructures showed an improved behavior toward ORR in comparison to a bulk gold electrode in neutral O_2-saturated KCl solution as the peak position shifted about 0.2 V positively and the peak current increased significantly. In the voltammogram for the oxygen reduction with the dendritic gold nanostructure, two different reduction peaks were observed, the first one corresponding to oxygen reduction to H_2O_2 and the second peak corresponding to the reduction of H_2O_2 to H_2O, which was confirmed by adding H_2O_2 to the solution. Similar results were obtained by Jena and Raj [88], who synthesized branched flowerlike gold nanocrystals using *N*-2-hydroxyethylpiperazine-*N*-2-ethanesulphonic acid as reducing/stabilizing agent. These nanomaterials were self-assembled on a solgel-derived silicate network, which was preassembled on a polycrystalline Au electrode, and they retained their morphology on the silicate network. Their electrocatalytic activity toward ORR was higher than that of citrate-stabilized Au nanoparticles, being the reduction of oxygen to hydrogen peroxide and its oxidation to water in neutral pH (phosphate buffer) observed at more positive potentials. The same authors also studied this reaction using triangular gold nanoprisms (70–110 nm) and nanoperiwinkles (150–230 nm), also self-assembled on a three-dimensional silicate network [89]. The samples were prepared using 5-hydroxytryptamine as a reducing/stabilizing agent at room temperature. Although the X-ray diffraction profiles of both samples revealed that they were composed mainly of a Au(111) lattice plane, both structures showed higher electrocatalytic activity than spherical gold nanoparticles.

Kuai et al. prepared icosahedral Au nanoparticles through a facile, one-pot, seedless, water-based method and studied ORR with them [90]. The growth mechanism indicated that the icosahedral nanoparticles were formed from multiple-twinned seeds and PVP was used both as reducing agent and surfactant. In spite of the fact that icosahedra are enclosed by {111} facets, the authors found higher electrocatalytic activities than sphere-like nanoparticles for ORR in alkaline medium. In fact, the reduction peak for oxygen reduction was positively shifted 0.05 V for icosahedra and also their peak current was 1.6-fold higher than that of spherical nanoparticles. Moreover, the gold icosahedra displayed even lower overpotential than a commercial Pt/C electrocatalyst.

The electrocatalytic activity of gold nanoplates toward ORR in 0.1 M NaOH was also evaluated. Seo et al. prepared this type of nanomaterials by reducing $KAu(CN)_2$ in a Na_2CO_3 solution at a constant potential [91]. The prepared nanoplates were rich in {110} and {100} domains (studied by Pb UPD) and exhibited higher electrocatalytic activity than bare gold for ORR. Both the peak potential for oxygen reduction shifted positively (about 70–80 mV) and the current density increased (about three times) for the nanoplates in comparison with bare Au. In addition, to get information about the reduction mechanism, the authors also performed RDE experiments and found that the number of electrons associated with the oxygen reduction was 4 for the nanoplate electrode, while on bare Au was 2, thus indicating the effective four-electron reduction of oxygen to water in alkaline medium for the Au nanoplates.

Das and Raj observed also an enhancement in the electrocatalytic activity toward ORR with penta-twined Au nanostructures (average size 52 nm) in neutral medium [92]. These nanomaterials were prepared using piperazine derivatives in the absence of seeds or surfactants and were characterized by TEM (average size 52 nm) and X-ray diffraction, which revealed the existence of face-centered cubic nanocrystalline Au. The penta-twined nanostructures were reported to catalyze the reduction of oxygen in neutral solution to water through the formation of hydrogen peroxide. Two well-defined peaks corresponding to the reduction of oxygen to hydrogen peroxide and the further reduction of electrogenerated hydrogen peroxide to water were obtained. A significant increase in the peak current (1.6 times) and a decrease in the overpotential for the ORR were observed in comparison with spherical nanoparticles. In fact, the reduction peak potential for the spherical nanoparticles was considerably more negative (~120 mV) than that of the penta-twined nanoparticles. Moreover, the onset potential for the penta-twined nanoparticles was 80–90 mV more positive than for the spherical nanoparticles.

Plowman et al. reported a very interesting contribution determining what the surface active sites responsible of the activity of different nanostructured gold electrodes are [93]. In this work they studied anisotropic Au, well-dispersed hierarchical Au, and continuous porous honeycomb Au structures. The analysis was carried out under acidic and alkaline conditions using electrochemical techniques such as cyclic voltammetry and a large-amplitude Fourier transformed alternating current (FT-ac) method which can effectively discriminate between capacitive and faradaic processes occurring at an electrode surface. Interestingly, it was observed that the response of these electrodes is similar to that observed for activated gold electrodes whose surfaces have been treated by cathodic polarization in the hydrogen evolution region. According to the authors, this activation results in the disruption of the outer layers of the metal to create an active surface. These active sites, which are believed to consist of low-coordinated active gold sites, or clusters of atoms, are more readily oxidized than the bulk Au electrodes. This more facile oxidation of active gold results in significant electrochemical responses recorded in the double-layer region. In particular, they reported the reduction of oxygen both in acid and alkaline media with the porous honeycomb Au structures. The results obtained indicated that the ORR commences at potentials where the surface active sites responses were observed.

Finally, some electrochemical treatments have been also used to change the surface structure of the gold nanoparticles, so that higher activity for the ORR is obtained. Shim et al. also studied the effect of an electrochemical pretreatment in a 0.05 M phosphate buffer solution (pH ~7.4) on bulk Au and Au nanoparticles (~10 nm diameter) toward the ORR [94]. Both samples were electrochemically pretreated by repetitive potential cycling between −0.2 and 1 V (vs. SCE) for 200 cycles at a scan rate of 50 mV s^{-1}. The RDE voltammetric experiments showed that after the pretreatment, the ORR activity was enhanced in both samples. The number of electrons for both pretreated samples became close to 4, the onset potential became more positive, and the currents became higher. Moreover, nanoparticles' performance was better than that of bulk Au. The authors attributed the enhanced catalytic activity to the formation of a thick Au oxide layer, which was corroborated with a thermally pretreated Au microwire electrode. Moreover, the authors claimed that the Au oxide layer was able to adsorb O_2 more favorably than the initial Au surface. In addition, the pretreated bulk and nanoparticles also showed higher activity toward the oxidation of hydrogen peroxide than the corresponding untreated ones.

Chen et al. [95], very recently, prepared Au thin-film electrodes made by electroless deposition for in situ electrochemical attenuated total-reflection surface-enhanced infrared adsorption spectroscopy (ATR-SEIRAS) which consisted of ~46 nm Au nanoparticles deposited on a Si infrared window. Very interestingly, they observed that a square-wave treatment of the Au film led to a much enhanced ORR activity (O_2-saturated 0.1 M $HClO_4$) as a consequence of the surface reconstruction of the nanoparticle film. Thus, whereas the ORR activity of the initial Au film electrode was similar to that obtained with a polycrystalline Au in acid solution, after the square-wave potential treatment, a remarkable shift to positive potential of about 0.14 V on the ORR half-wave potential was observed. In addition, the Tafel slope changed from 119 to 90 mV, indicating a modification in the rate-determining step. From SEM images, they observed that the square-wave treatment caused a significant surface reconstruction by "melting" the Au nanoparticles, thus leading to a more continuous Au electrode surface. However, from the analysis of the voltammetric curves in the Au oxide region, they observed that the {100} surface sites remained almost intact or even increased slightly in this reconstructed surface, whereas the characteristic signal of the {111} and {110} sites decreased. Nevertheless, the enhanced ORR activity was not attributed to the {100} orientation of the reconstructed film but to the formation of a new type of surface sites whose oxide reduction peak was observed at 0.4 V versus Ag/AgCl once the upper potential limit was more positive than 1 V. The experimental evidences indicated that this new type of surface sites was responsible of the ORR activity enhancement, and they suggested that these new sites could stabilize better the adsorbed ORR intermediates, thus facilitating the subsequent reaction step(s). More work is still needed to understand the nature and electrochemical properties of this type of surface sites.

16.5 Conclusions

The results presented in this chapter clearly indicate that the reactivity of gold for the ORR is mainly controlled by the surface structure. In alkaline medium, the Au(100) electrode shows a high activity transferring four electrons at high potentials, whereas a much lower activity with the transfer of only two electrons is observed for the Au(111) and Au(110) electrodes. The strong surface structure sensitivity results in a significant effect of the shape of the nanoparticles in the reactivity for this reaction. Thus, for nanoparticles with similar size, the reactivity depends mainly on the fraction of {100} domains on the surface.

Acknowledgments This work has been financially supported by the MICINN (Spain) (project CTQ2010-16271) and Generalitat Valenciana (project PROMETEO/2009/045, FEDER).

References

1. Adzic RR (1998) Recent advances in the kinetics of oxygen reduction. In: Lipkowski J, Ross PN (eds) Electrocatalysis. Wiley, New York, pp 197–242
2. Anastasijević NA, Vesović V, Adžić RR (1987) Determination of the kinetic parameters of the oxygen reduction reaction using the rotating ring-disk electrode: Part I. Theory. J Electroanal Chem 229(1–2):305–316
3. Anastasijević NA, Vesović V, Adžić RR (1987) Determination of the kinetic parameters of the oxygen reduction reaction using the rotating ring-disk electrode: Part II. Applications. J Electroanal Chem 229(1–2):317–325

4. Alvarez-Rizatti M, Jüttner K (1983) Electrocatalysis of oxygen reduction by UPD of lead on gold single-crystal surfaces. J Electroanal Chem 144(1–2):351–363
5. Sayed SM, Jüttner K (1983) Electrocatalysis of oxygen and hydrogen peroxide reduction by UPD of bismuth on poly- and mono-crystalline gold electrodes in acid solutions. Electrochim Acta 28(11):1635–1641
6. Adžić RR, Marković NM (1982) Structural effects in electrocatalysis: oxygen and hydrogen peroxide reduction on single crystal gold electrodes and the effects of lead ad-atoms. J Electroanal Chem 138(2):443–447
7. Markovic NM, Adzic RR, Vesovic VB (1984) Structural effects in electrocatalysis Oxygen reduction on the gold single crystal electrodes with (110) and (111) orientations. J Electroanal Chem 165:121–133
8. Adžić RR, Marković NM, Vesović VB (1984) Structural effects in electrocatalysis. Oxygen reduction on the Au (100) single crystal electrode. J Electroanal Chem 165(1–2):105–120
9. Štrbac S, Adžić RR (1992) Oscillatory phenomena in oxygen and hydrogen peroxide reduction on the Au(100) electrode surface in alkaline solutions. J Electroanal Chem 337(1–2):355–364
10. Štrbac S, Anastasijević NA, Adžić RR (1992) Oxygen reduction on Au (100) and vicinal Au (910) and Au (11, 1, 1) faces in alkaline solution: a rotating disc-ring study. J Electroanal Chem 323(1–2):179–195
11. Polewska W, Vitus CM, Ocko BM, Adzic RR (1994) Direct observation of the Au(100) reconstruction during the course of O2 reduction in alkaline solution. J Electroanal Chem 364(1–2):265–269
12. Štrbac S, Anastasijević NA, Adžić RR (1994) Oxygen reduction on Au(111) and vicinal Au (332) faces: a rotating disc and disc-ring study. Electrochim Acta 39(7):983–990
13. Prieto A, Hernández J, Herrero E, Feliu JM (2003) The role of anions in oxygen reduction in neutral and basic media on gold single-crystal electrodes. J Solid State Electrochem 7(9):599–606
14. Koper MTM (1998) Non-linear phenomena in electrochemical systems. J Chem Soc Faraday Trans 94(10):1369–1378
15. Štrbac S, Adžić RR (1996) The influence of OH- chemisorption on the catalytic properties of gold single crystal surfaces for oxygen reduction in alkaline solutions. J Electroanal Chem 403 (1–2):169–181
16. Anastasijević NA, Štrbac S, Adžić RR (1988) Oxygen reduction on the Au (311) electrode surface in alkaline electrolyte. J Electroanal Chem 240(1–2):239–252
17. Strbac S, Adzic RR (1996) The influence of pH on reaction pathways for O-2 reduction on the Au(1 00) face. Electrochim Acta 41(18):2903–2908
18. Wu B-l, Lei H-w, Cha C-s, Chen Y-y (1994) Investigation of the intermediates of the O_2 reduction reaction on Au electrodes in alkaline solution. J Electroanal Chem 377 (1–2):227–230
19. Vassilev P, Koper MTM (2007) Electrochemical reduction of oxygen on gold surfaces: a density functional theory study of intermediates and reaction paths. J Phys Chem C 111(6):2607–2613
20. Blizanac BB, Lucas CA, Gallagher ME, Arenz M, Ross PN, Marković NM (2003) Anion adsorption, CO oxidation, and oxygen reduction reaction on a Au(100) surface: the pH effect. J Phys Chem B 108(2):625–634
21. Sarapuu A, Tammeveski K, Tenno TT, Sammelselg V, Kontturi K, Schiffrin DJ (2001) Electrochemical reduction of oxygen on thin-film Au electrodes in acid solution. Electrochem Commun 3(8):446–450
22. El-Deab MS, Ohsaka T (2002) An extraordinary electrocatalytic reduction of oxygen on gold nanoparticles-electrodeposited gold electrodes. Electrochem Commun 4(4):288–292
23. Zhang Y, Asahina S, Yoshihara S, Shirakashi T (2003) Oxygen reduction on Au nanoparticle deposited boron-doped diamond films. Electrochim Acta 48(6):741–747
24. El-Deab MS, Ohsaka T (2002) Hydrodynamic voltammetric studies of the oxygen reduction at gold nanoparticles-electrodeposited gold electrodes. Electrochim Acta 47(26):4255–4261

25. El-Deab MS, Ohsaka T (2003) Electrocatalysis by nanoparticles: oxygen reduction on gold nanoparticles-electrodeposited platinum electrodes. J Electroanal Chem 553(suppl):107–115
26. El-Deab MS, Okajima T, Ohsaka T (2003) Electrochemical reduction of oxygen on gold nanoparticle-electrodeposited glassy carbon electrodes. J Electrochem Soc 150(7): A851–A857
27. Yagi I, Ishida T, Uosaki K (2004) Electrocatalytic reduction of oxygen to water at Au nanoclusters vacuum-evaporated on boron-doped diamond in acidic solution. Electrochem Commun 6(8):773–779
28. Guerin S, Hayden BE, Pletcher D, Rendall ME, Suchsland JP (2006) A combinatorial approach to the study of particle size effects on supported electrocatalysts: oxygen reduction on gold. J Comb Chem 8(5):679–686
29. Bron M (2008) Carbon black supported gold nanoparticles for oxygen electroreduction in acidic electrolyte solution. J Electroanal Chem 624(1–2):64–68
30. Sarapuu A, Nurmik M, Mandar H, Rosental A, Laaksonen T, Kontturi K, Schiffrin DJ, Tammeveski K (2008) Electrochemical reduction of oxygen on nanostructured gold electrodes. J Electroanal Chem 612(1):78–86
31. Maruyama J, Inaba M, Ogumi Z (1999) Effect of fluorinated alcohol on the kinetics of cathodic oxygen reduction at gold electrodes. Electrochim Acta 45(3):415–422
32. Maruyama J, Inaba M, Morita T, Ogumi Z (2001) Effects of the molecular structure of fluorinated additives on the kinetics of cathodic oxygen reduction. J Electroanal Chem 504(2):208–216
33. Tang W, Lin H, Kleiman-Shwarsctein A, Stucky GD, McFarland EW (2008) Size-dependent activity of gold nanoparticles for oxygen electroreduction in alkaline electrolyte. J Phys Chem C 112(28):10515–10519
34. Inasaki T, Kobayashi S (2009) Particle size effects of gold on the kinetics of the oxygen reduction at chemically prepared Au/C catalysts. Electrochim Acta 54(21):4893–4897
35. Erikson H, Jürmann G, Sarapuu A, Potter RJ, Tammeveski K (2009) Electroreduction of oxygen on carbon-supported gold catalysts. Electrochim Acta 54(28):7483–7489
36. Chen W, Chen S (2009) Oxygen electroreduction catalyzed by gold nanoclusters: strong core size effects. Angew Chem Int Ed 48(24):4386–4389
37. Li Y, Cox JT, Zhang B (2010) Electrochemical responses and electrocatalysis at single Au nanoparticles. J Am Chem Soc 132(9):3047–3054
38. Lee Y, Loew A, Sun S (2009) Surface- and structure-dependent catalytic activity of Au nanoparticles for oxygen reduction reaction. Chem Mater 22(3):755–761
39. Alexeyeva N, Matisen L, Saar A, Laaksonen P, Kontturi K, Tammeveski K (2010) Kinetics of oxygen reduction on gold nanoparticle/multi-walled carbon nanotube hybrid electrodes in acid media. J Electroanal Chem 642(1):6–12
40. Jirkovsky JS, Halasa M, Schiffrin DJ (2010) Kinetics of electrocatalytic reduction of oxygen and hydrogen peroxide on dispersed gold nanoparticles. Phys Chem Chem Phys 12(28):8042–8052
41. Kinoshita K (1990) Particle size effects for oxygen reduction on highly dispersed platinum in acid electrolytes. J Electrochem Soc 137(3):845–848
42. Mayrhofer KJJ, Blizanac BB, Arenz M, Stamenkovic VR, Ross PN, Markovic NM (2005) The impact of geometric and surface electronic properties of Pt-catalysts on the particle size effect in electrocatalysis. J Phys Chem B 109(30):14433–14440
43. Brülle T, Ju W, Niedermayr P, Denisenko A, Paschos O, Schneider O, Stimming U (2011) Size-dependent electrocatalytic activity of gold nanoparticles on HOPG and highly boron-doped diamond surfaces. Molecules 16(12):10059–10077
44. Greeley J, Rossmeisl J, Hellman A, Nørskov JK (2007) Theoretical trends in particle size effects for the oxygen reduction reaction. Z Phys Chem 221(9–10):1209–1220
45. Hernández J, Solla-Gullón J, Herrero E (2004) Gold nanoparticles synthesized in a water-in-oil microemulsion: electrochemical characterization and effect of the surface structure on the oxygen reduction reaction. J Electroanal Chem 574(1):185–196

46. Hernández J, Solla-Gullón J, Herrero E, Feliu JM, Aldaz A (2009) In situ surface characterization and oxygen reduction reaction on shape-controlled gold nanoparticles. J Nanosci Nanotechnol 9(4):2256–2273
47. Solla-Gullon J, Vidal-Iglesias FJ, Feliu JM (2011) Shape dependent electrocatalysis. Annu Rep Prog Chem C Phys Chem 107:263–297
48. Koper MTM (2011) Structure sensitivity and nanoscale effects in electrocatalysis. Nanoscale 3(5):2054–2073
49. Cheng Q, Jiang Y-X, Tian N, Zhou Z-Y, Sun S-G (2010) Electrocatalytic reduction of nitric oxide on Pt nanocrystals of different shape in sulfuric acid solutions. Electrochim Acta 55(27):8273–8279
50. Vidal-Iglesias FJ, Solla-Gullón J, Rodríguez P, Herrero E, Montiel V, Feliu JM, Aldaz A (2004) Shape-dependent electrocatalysis: ammonia oxidation on platinum nanoparticles with preferential (100) surfaces. Electrochem Commun 6(10):1080–1084
51. Solla-Gullón J, Vidal-Iglesias FJ, Rodríguez P, Herrero E, Feliu JM, Aldaz A (2006) Shape-dependent electrocatalysis: CO monolayer oxidation at platinum nanoparticles. In: Brisard GM, Adzic R, Birss V, Vieckowski A (eds) Proceedings – Electrochemical Society 2005–11 (Electrocatalysis). The Electrochemical Society, Pennington, NJ, pp 1–11
52. Solla-Gullón J, Vidal-Iglesias FJ, Herrero E, Feliu JM, Aldaz A (2006) CO monolayer oxidation on semi-spherical and preferentially oriented (100) and (111) platinum nanoparticles. Electrochem Commun 8(1):189–194
53. Solla-Gullón J, Vidal-Iglesias FJ, López-Cudero A, Garnier E, Feliu JM, Aldaz A (2008) Shape-dependent electrocatalysis: methanol and formic acid electrooxidation on preferentially oriented Pt nanoparticles. Phys Chem Chem Phys 10(25):3689–3698
54. Sanchez-Sanchez CM, Solla-Gullon J, Vidal-Iglesias FJ, Aldaz A, Montiel V, Herrero E (2010) Imaging structure sensitive catalysis on different shape-controlled platinum nanoparticles. J Am Chem Soc 132(16):5622–5624
55. Erikson H, Sarapuu A, Tammeveski K, Solla-Gullón J, Feliu JM (2011) Enhanced electrocatalytic activity of cubic Pd nanoparticles towards the oxygen reduction reaction in acid media. Electrochem Commun 13(7):734–737
56. Adžić RR, Strbac S, Anastasijević N (1989) Electrocatalysis of oxygen on single crystal gold electrodes. Mater Chem Phys 22(3–4):349–375
57. Marković NM, Adžić RR, Cahan BD, Yeager EB (1994) Structural effects in electrocatalysis: oxygen reduction on platinum low index single-crystal surfaces in perchloric acid solutions. J Electroanal Chem 377(1–2):249–259
58. Gontard LC, Chang LY, Hetherington CJD, Kirkland AI, Ozkaya D, Dunin-Borkowski RE (2007) Aberration-corrected imaging of active sites on industrial catalyst nanoparticles. Angew Chem Int Ed 46(20):3683–3685
59. Hamelin A (1996) Cyclic voltammetry at gold single-crystal surfaces. 2. Behaviour of high-index faces. J Electroanal Chem 407(1–2):13–21
60. Hamelin A (1996) Cyclic voltammetry at gold single-crystal surfaces. 1. Behaviour at low-index faces. J Electroanal Chem 407(1–2):1–11
61. Herrero E, Buller LJ, Abruna HD (2001) Underpotential deposition at single crystal surfaces of Au, Pt, Ag and other materials. Chem Rev 101(7):1897–1930
62. Hamelin A (1979) Lead adsorption on gold single crystal stepped surfaces. J Electroanal Chem 101(2):285–290
63. Hamelin A, Katayama A (1981) Lead underpotential deposition on gold single-crystal surfaces: the (100) face and its vicinal faces. J Electroanal Chem 117(2):221–232
64. Hamelin A (1984) Underpotential deposition of lead on single crystal faces of gold. Part I. The influence of crystallographic orientation of the substrate. J Electroanal Chem 165(1–2):167–180
65. Hamelin A, Lipkowski J (1984) Underpotential deposition of lead on gold single crystal faces. Part II. General discussion. J Electroanal Chem 171(1–2):317–330

66. Hernández J, Herrero E, Solla-Gullón J, Vidal-Iglesias FJ, Feliu JM, Aldaz A (2006) Shape-dependent electrocatalysis: oxygen reduction on gold nanoparticles. In: Brisard GM, Adzic R, Birss V, Vieckowski A (eds) Proceedings – Electrochemical Society 2005–11 (Electrocatalysis). The Electrochemical Society, Pennington, NJ, pp 200–212
67. Hernández J, Solla-Gullón J, Herrero E, Aldaz A, Feliu JM (2005) Characterization of the surface structure of gold nanoparticles and nanorods using structure sensitive reactions. J Phys Chem B 109(26):12651–12654
68. Hernández J, Solla-Gullón J, Herrero E, Aldaz A, Feliu JM (2006) Methanol oxidation on gold nanoparticles in alkaline media: unusual electrocatalytic activity. Electrochim Acta 52(4):1662–1669
69. Hernández J, Solla-Gullón J, Herrero E, Aldaz A, Feliu JM (2007) Electrochemistry of shape-controlled catalysts: oxygen reduction reaction on cubic gold nanoparticles. J Phys Chem C 111(38):14078–14083
70. Sanchez-Sanchez CM, Vidal-Iglesias FJ, Solla-Gullon J, Montiel V, Aldaz A, Feliu JM, Herrero E (2010) Scanning electrochemical microscopy for studying electrocatalysis on shape-controlled gold nanoparticles and nanorods. Electrochim Acta 55(27):8252–8257
71. Walczak MM, Alves CA, Lamp BD, Porter MD (1995) Electrochemical and X-ray photoelectron spectroscopic evidence for differences in the binding sites of alkanethiolate monolayers chemisorbed at gold. J Electroanal Chem 396(1–2):103–114
72. Zhong CJ, Zak J, Porter MD (1997) Voltammetric reductive desorption characteristics of alkanethiolate monolayers at single crystal Au(111) and (110) electrode surfaces. J Electroanal Chem 421(1–2):9–13
73. El-Deab MS (2009) On the preferential crystallographic orientation of Au nanoparticles: effect of electrodeposition time. Electrochim Acta 54(14):3720–3725
74. El-Deab MS, Sotomura T, Ohsaka T (2005) Size and crystallographic orientation controls of gold nanoparticles electrodeposited on GC electrodes. J Electrochem Soc 152(1):C1–C6
75. El-Deab MS, Arihara K, Ohsaka T (2004) Fabrication of Au(111)-like polycrystalline gold electrodes and their applications to oxygen reduction. J Electrochem Soc 151(6):E213–E218
76. El-Deab MS, Sotomura T, Ohsaka T (2005) Oxygen reduction at electrochemically deposited crystallographically oriented Au(1 0 0)-like gold nanoparticles. Electrochem Commun 7(1):29–34
77. El-Deab MS, Sotomura T, Ohsaka T (2005) Morphological selection of gold nanoparticles electrodeposited on various substrates. J Electrochem Soc 152(11):C730–C737
78. Gao F, El-Deab MS, Okajima T, Ohsaka T (2005) Electrochemical preparation of a Au crystal with peculiar morphology and unique growth orientation and its catalysis for oxygen reduction. J Electrochem Soc 152(6):A1226–A1232
79. El-Deab MS, Sotomura T, Ohsaka T (2006) Oxygen reduction at Au nanoparticles electrodeposited on different carbon substrates. Electrochim Acta 52(4):1792–1798
80. Gai PL, Harmer MA (2002) Surface atomic defect structures and growth of gold nanorods. Nano Lett 2(7):771–774
81. Johnson CJ, Dujardin E, Davis SA, Murphy CJ, Mann S (2002) Growth and form of gold nanorods prepared by seed-mediated, surfactant-directed synthesis. J Mater Chem 12(6):1765–1770
82. Gao F, El-Deab MS, Ohsaka T (2005) Electrodeposition of gold nanorods with a unidirectional crystal growth and lower Au(111) facets area. Indian J Chem A 44(5):932–937
83. Zhou Z-Y, Tian N, Huang Z-Z, Chen D-J, Sun S-G (2009) Nanoparticle catalysts with high energy surfaces and enhanced activity synthesized by electrochemical method. Faraday Discuss 140:81–92
84. Tian N, Zhou ZY, Sun SG (2008) Platinum metal catalysts of high-index surfaces: from single-crystal planes to electrochemically shape-controlled nanoparticles. J Phys Chem C 112(50):19801–19817
85. Tian Y, Liu H, Zhao G, Tatsuma T (2006) Shape-controlled electrodeposition of gold nanostructures. J Phys Chem B 110(46):23478–23481

86. Koblischka-Veneva A, Koblischka MR (2008) Analysis of twin boundaries using the electron backscatter diffraction (EBSD) technique. Mater Sci Eng B Solid State Mater Adv Technol 151(1):60–64
87. Xu X, Jia J, Yang X, Dong S (2010) A templateless, surfactantless, simple electrochemical route to a dendritic gold nanostructure and its application to oxygen reduction. Langmuir 26(10):7627–7631
88. Jena BK, Raj CR (2007) Synthesis of flower-like gold nanoparticles and their electrocatalytic activity towards the oxidation of methanol and the reduction of oxygen. Langmuir 23(7):4064–4070
89. Jena BK, Raj CR (2007) Shape-controlled synthesis of gold nanoprism and nanoperiwinkles with pronounced electrocatalytic activity. J Phys Chem C 111(42):15146–15153
90. Kuai L, Geng B, Wang S, Zhao Y, Luo Y, Jiang H (2011) Silver and gold icosahedra: one-pot water-based synthesis and their superior performance in the electrocatalysis for oxygen reduction reactions in alkaline media. Chemistry 17(12):3482–3489
91. Seo B, Choi S, Kim J (2011) Simple electrochemical deposition of Au nanoplates from Au(I) cyanide complexes and their electrocatalytic activities. ACS Appl Mater Interfaces 3(2):441–446
92. Das AK, Raj CR (2011) Rapid room temperature synthesis of electrocatalytically active Au nanostructures. J Colloid Interface Sci 353(2):506–511
93. Plowman BJ, O’Mullane AP, Bhargava SK (2011) The active site behaviour of electrochemically synthesised gold nanomaterials. Faraday Discuss 152:43–62
94. Shim JH, Kim J, Lee C, Lee Y (2010) Electrocatalytic activity of gold and gold nanoparticles Improved by electrochemical pretreatment. J Phys Chem C 115(1):305–309
95. Chen D-J, Xu B, Sun S-G, Tong YJ (2012) Electroless deposition of ultrathin Au film for surface enhanced in situ spectroelectrochemistry and reaction-driven surface reconstruction for oxygen reduction reaction. Catal Today 182(1):46–53

Chapter 17
Palladium-Based Electrocatalysts for Oxygen Reduction Reaction

Minhua Shao

Abstract Fuel cells are clean energy devices that are expected to help address the energy and environmental problems in our society. Platinum-based nanomaterials are usually used as the electrocatalysts for both the anode (hydrogen oxidation) and cathode (oxygen reduction) reactions. The high cost and limited resources of this precious metal hinder the commercialization of fuel cells. Recent efforts have focused on the discovery of palladium-based electrocatalysts with little or no platinum for oxygen reduction reaction (ORR). This chapter overviews the recent progress of electrocatalysis of palladium-based materials including both extended surfaces and nanostructured ones for ORR.

17.1 Introduction

In a low-temperature fuel cell, hydrogen gas is oxidized into protons, electrons, and other by-products when other fuels are used at the anode. At the cathode of the fuel cell, the oxygen is reduced, leading to formation of water. Both the anodic and cathodic reactions require electrocatalysts to reduce the overpotentials and increase reaction rates. In the state-of-the-art low-temperature fuel cells, Pt-based materials are used as the electrocatalysts for both the reactions; however, the high cost and limited resources of this precious metal are hindering the commercialization of fuel cells. Recent efforts have focused on the discovery of electrocatalysts with little or no Pt for oxygen reduction reaction (ORR) [1–3].

The electrocatalytic activity of Pd is the second highest among the pure metals for ORR, only behind Pt. This, combined with the fact that the cost of Pd is lower than that of Pt, makes it an attractive alternative to Pt. Figure 17.1 compares the prices per troy ounce of Pd and Pt in the last 10 years [4]. The cost of Pd is roughly

---

M. Shao (✉)
UTC Power, 195 Governor's Highway, South Windsor, CT 06074, USA
e-mail: minhua@gmail.com

M. Shao (ed.), *Electrocatalysis in Fuel Cells*, Lecture Notes in Energy 9,
DOI 10.1007/978-1-4471-4911-8_17,

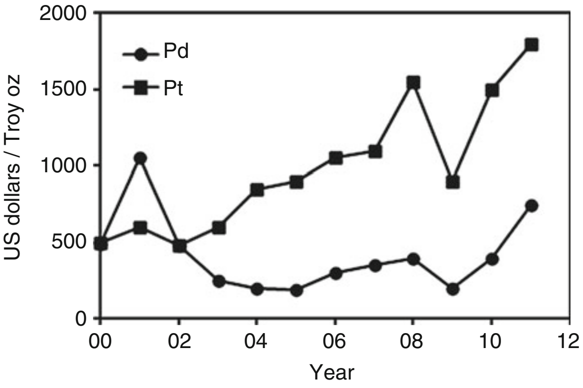

Fig. 17.1 Comparison of the cost of Pd and Pt per troy ounce in the period of 2000–2011

one quarter of Pt except in the period of 2000–2002 when it spiked to \$1,100 per troy oz due to insufficient supply in the market. Similar to Pt, most Pd today is used in the automotive industry for catalytic converters to reduce the toxicity of emissions from a combustion engine.

While Pd is less expensive than Pt, the electrocatalytic activity of bulk polycrystalline Pd for ORR is at least five times lower than that of Pt, which prevents it from being used directly in fuel cells. Great efforts have been dedicated to improve the activity of Pd by surface modification and alloying. This chapter attempts to summarize the recent progress of electrocatalysts containing Pd for ORR. The development of Pd electrocatalysts for electrooxidation of hydrogen and small organic molecules is not discussed in this chapter but has been adequately covered in Chaps. 5 and 6 and recent reviews [5–7].

17.2 ORR in Acid Solutions

17.2.1 ORR on Bulk Surfaces

Due to its complexity, the ORR mechanisms on noble metal surfaces are not fully understood despite five decades' extensive studies [8–10]. On Pt surfaces, it is generally accepted that the first electron transfer or oxygen adsorption together with an electron and proton transfer forming superoxide (Eq. 17.1) is the slow step determining the overall reaction rate of oxygen reduction:

$$O_2 + H^+ + e^- \rightarrow OOH_{ads}. \tag{17.1}$$

It is reasonable to assign (Eq. 17.1) to the rate-determining step of ORR since it requires a significant energy to form a bond between Pt and oxygen before the O–O can break. This assignment has been supported by recent experimental and theoretical work. One may agree that a reactive surface facilitates the reaction (Eq. 17.1), i.e., the more reactive the surface, the stronger the oxygen bond. The O–O bond dissociation generates adsorbed OH species, which need to be further reduced to complete the four-electron reaction according to

$$\mathrm{OH_{ads}} + \mathrm{H}^+ + \mathrm{e}^- \rightarrow \mathrm{H_2O}. \tag{17.2}$$

Unlike Eq. (17.1), the strong adsorption of OH on catalyst surfaces hinders its reduction and hence slows down the ORR rate. In addition, the buildup coverage of oxygen-containing species decreases the availability of active surface sites. Thus, a good ORR catalyst is one that forms a moderate bond with the adsorbates to balance the kinetics of O–O bond breaking and removal of oxygen-containing species generated from the former step. Density functional theory (DFT) calculations demonstrated that the oxygen binding energy (BEo) on Pt(111) is a little bit too strong and Eq. (17.2) is the bottleneck of the ORR. If slightly weakened, such as found for a surface of Pt monolayer on Pd(111) (denoted as Pt/Pd(111)) [11] and for a Pt skin on various Pt alloys [12–14], the ORR activity can be enhanced remarkably.

Pd is a more reactive metal than Pt and binds oxygen more strongly. It oxidizes at more negative potentials than Pt and is expected to be less active for ORR [15]. The study of ORR on Pd bulk electrodes in acidic media has received less attention than on Pt due to the lower activity and stability of the former. The first direct comparison of ORR activity between polycrystalline Pd and Pt was attempted by Damjanovic and Brusic [16], who found that the exchange current densities for a polycrystalline Pd and Pt electrode were 2×10^{-11} and 10^{-10} A cm^{-2}, respectively, in a $\mathrm{HClO_4}$ solution. In other words, the bulk Pt is five times more active than Pd in this study. It has been well known that the ORR kinetics strongly depends on the electrolyte used in the experiment and on the crystallographic orientation of the electrodes. For instance, the ORR activity of low index planes of Pt follows the order of Pt(111) < Pt(110) < Pt(100) in $\mathrm{H_2SO_4}$ solutions. While in $\mathrm{HClO_4}$ solutions, it follows the order of Pt(100) < Pt(111) $\leq$ Pt(110) [17]. The main reason for the lower activity of Pt(111) than Pt(100) in $\mathrm{H_2SO_4}$ solutions is the much stronger adsorption of $\mathrm{SO_4}^{2-}$ and $\mathrm{HSO_4}^{-}$ on the former. On the other hand, there is no anion strongly adsorbed on either surface in the $\mathrm{HClO_4}$ solutions. In such electrolytes, the discrepancy of the activity on the different surfaces originates primarily from the structural and electronic properties of the surfaces rather than from the poisoning effect from specific adsorption of the anions.

Due to the difficulty of preparing Pd single crystals and their poor stability, the facet-dependent ORR activities of the Pd single crystals have not been available until very recently. Kondo et al. [18] measured the ORR activities of low index planes of Pd single crystals in $\mathrm{HClO_4}$ solution and found that the activity increased following the order of Pd(110) < Pd(111) $\ll$ Pd(100). This order is completely opposite to that on Pt(hkl) in the same solution. The comparison of the kinetic activities on different Pd and Pt facets is shown in Fig. 17.2. Surprisingly, the

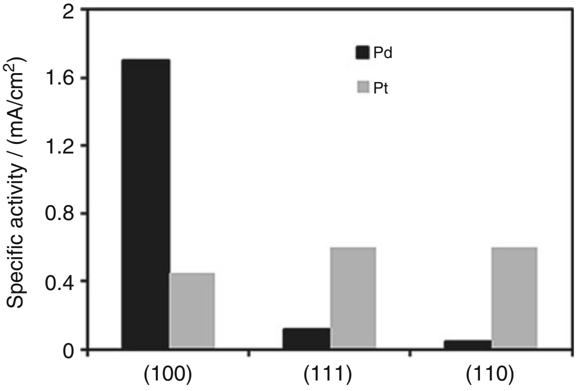

Fig. 17.2 Comparison of specific activity of oxygen reduction on low index facets of Pd and Pt single crystals at 0.9 V [18]

activity of Pd(100) is 14 times as high as that of Pd(111). It is also worth noting that Pd(100) is even more active than Pt(111). The kinetic current densities of ORR correlate well with the terrace atom density on *n*(100)-(111) and *n*(100)-(110) series of Pd suggesting that (100) atoms are the most active sites for ORR on Pd electrodes. Further fundamental studies are needed to understand the mechanisms of facet dependence of ORR activity on Pd(hkl). Recent DFT study revealed a dramatic difference in reactivity between the Pd(111) and (100) surfaces. The Pd–O bond on Pd(100) surface is weaker than that on Pd(111) by 0.04 eV. As discussed above, the Pd(111) binds to the oxygen intermediates too strongly resulting in a low ORR activity. A weaker Pd–O bond on (100) may explain its superior ORR activity.

According to d-band center theory, one way to improve the ORR kinetics of Pd surfaces is to reduce the BEo by lowering its d-band center. The DFT calculations reported by Shao et al. [19] revealed that the Pd monolayer on Pt(111) has a lower d-band center than a bare Pd(111) surface and hence a lower BEo, making Pd/Pt (111) a better catalyst than Pd(111) for ORR. This argument was supported by their experimental work, which showed that Pd/Pt(111) had a higher ORR activity than Pd(111), but somewhat lower than Pt(111) [19].

17.2.2 ORR on Pd-Based Nanocatalysts

By alloying Pt with transition metals M (M = V, Cr, Co, Ni, Fe, Ti, etc.), the ORR activity can be enhanced remarkably in both phosphoric acid fuel cell (PAFC) and PEMFC [20–22]. The activity enhancement mechanisms have been an open question for more than three decades and ascribed to decreased Pt–Pt bond distance [23], enhanced surface roughness [24], increased Pt d-band vacancy [25–27], weakened OH adsorption [28, 29], and downshifted d-band center [30–35]. Nørskov and Mavrikakis et al. combined the structural and electronic effects by introducing a d-band model that correlates changes in the energy center of the valence d-band density of states at the surface sites with their ability to form chemisorption bonds.

According to their model, the binding energy of oxygen-containing species on Pt skin formed during selective leaching of non-noble metals or annealing at high temperatures was weaker than on a pure Pt surface due to the compressive strain and electron transfer from the transition metal on the subsurface layer. Similar to Pt, the activity of Pd can be enhanced by alloying with transition metals.

17.2.2.1 Binary Pd Alloy Catalysts

Savadogo's group was the first to discover the enhanced ORR activities on Pd alloys [36]. It was found that Pd–Co, Ni, and Cr bulk alloys prepared by sputtering had higher activity than Pt prepared in a same way in acidic solutions. Since their groundbreaking results, many groups have reported the oxygen reduction behaviors of various Pd alloys. Bard's group [37–39] identified a series of Pd-based catalysts, including binary systems Pd–Co, Mn, V, and Ti, that showed higher ORR activity than pure Pd. For Pd–Co/C, the maximum activity was observed with a Co atomic ratio in the range of 10–20 %, but the high activity was lost quickly during electrochemical testing, maybe due to the fast dissolution of Co atoms [38]. One would expect that the dissolution rate of Co in Pd–Co alloy is much faster than that in Pt–Co.

The compositions of Pd alloys play an important role in ORR activity. Depending on the synthesis methods and annealing temperatures, different optimum Pd:M ratios for ORR were reported. Shao et al. [19] found that Pd_2Co/C synthesized by the impregnation method and annealed at 900 °C exhibited the highest ORR activity. The same optimum ratio was also observed by Wang et al. [40], who co-reduced Pd and Co salts in ethylene glycol and annealed the dried product at 500 °C. The highest ORR activity for Pd–Co catalysts (30–40 at.% Co), formed by co-reducing Pd and Co salts in aqueous solutions, was obtained by Zhang et al. [41]. Particle size, as well as the activity, increased with increasing annealing temperature, and the highest activity was observed at the lowest annealing temperature (300 °C). For the Pd–Fe systems, an optimized composition of Pd:Fe = 3:1 was found by several groups [42–45]. The ORR activity of Pd_3Fe/C was comparable to or higher than that of Pt/C. The activity was found to correlate well with the Pd–Pd bond distance and the Fe content in the alloy (Fig. 17.3) [42, 46]. The highest ORR activity was obtained for Pd_3Fe, which has a Pd–Pd bond distance of 0.273 nm, smaller than that of Pd by 2.3 %. Similar results were obtained for the Pd–Co alloys [40], suggesting the compressed lattice plays a role in the activity enhancement. The activity of Pd_3Fe was found to be further enhanced by adding a small amount of Ir in it [43]. The enhancement mechanism is unknown. For Pd–W alloys annealed at 800 °C, only 5 % W is needed to maximize the activity [47].

Oxygen reduction activities of some Pd–nonmetallic element alloys (Pd–Se, S, and P) were also studied, but no significant improvements have been observed [48, 49]. Pd–Pt alloys, however, showed higher ORR activity than Pt with a small amount of Pd in the alloys. For instance, Li et al. found that Pt–Pd/C exhibited a slightly higher ORR activity than Pt/C [50]. Guerin et al. found that the Pd–Pt alloys showed higher

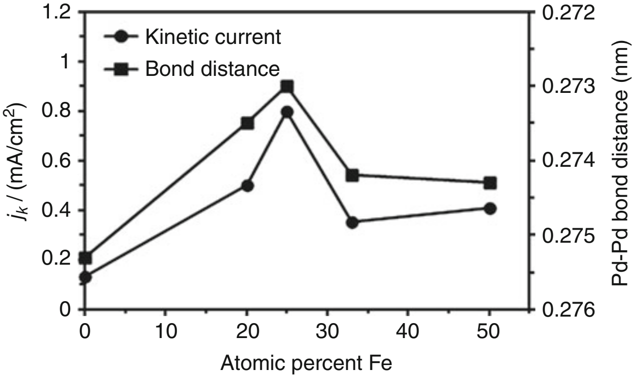

Fig. 17.3 Specific activity and Pd–Pd bond distance calculated from XRD data against the concentration of Fe in Pd–Fe/C electrocatalysts. All samples were treated at 500 °C [42]

activity than Pt in a composition range of 70–90 % Pt [51]. The high activity was also observed on dendrimer-encapsulated Pd–Pt nanoparticles containing 180 atoms with a Pt:Pd ratio of 5:1 [52]. The enhanced activity may be explained by a shorter Pt–Pt bond distance.

17.2.2.2 Ternary Pd Alloy Catalysts

Most of the binary alloys have limited durability. By incorporating a more corrosion-resistant metal, like Au, Mo, and Mn, the stability of the alloy was enhanced significantly [37, 53]. For example, Pd–Co–Mo catalysts with a Pd:Co:Mo atomic ratio of 70:20:10 exhibited not only higher activity than Pt/C but with excellent chemical stability during fuel cell testing [53]. Other Pd–Co–M (M = Pt, Au, Ag) ternary catalysts have been investigated by Mathiyarasu and Phani [54]. As expected, the Pd–Co–Pt combination showed the highest activity which was higher than Pt/C, but Pd–Co and Pd–Co–Au exhibited very low activity, which is contrast to other reports [19, 37].

17.2.2.3 Synthesis and Particle Size Effect

The activity discrepancy for Pd-based catalysts with similar compositions has been seen in the literature. One of the main reasons is that the properties of the Pd alloys highly depend on the synthesis method and posttreatment. A good example is the Pd–Cu system. Wang et al. [55, 56] found that $PdCu_3$ catalysts synthesized by a colloidal method showed a higher activity than those made by thermodecomposition, benefiting from the more uniform alloying and much smaller particle size in the former method. Raghuveer et al. [57] also concluded that the activity of Pd–Co–Au synthesized by the microemulsion method was higher than that prepared by the conventional sodium borohydride reduction method due to the smaller particle size and higher degree of alloying.

The effects of particle size and degree of alloying were studied by Liu and Manthiram in the $Pd_{70}Co_{30}/C$ catalysts [58]. Upon increasing the annealing temperature from 350 to 500 °C, the catalytic activity decreased due to increasing the alloying degree and particle size. Further increasing the annealing temperature resulted in further activity decreases, though this was attributed solely to the increase in particle size. An interesting trend is that the activity of Pd–Co alloy decreased with increasing the degree of alloying in the case of the same particle size. It seems that high Co content is not necessary for activity improvement. Further study is needed to understand the role of alloying degree and transition metal contents by controlling the particle size and compositions. Due to the high surface energy of Pd, it is very difficult to synthesize monodispersed Pd–M (M = transition metals) nanoparticles with small particle size. Such study requires novel synthesis method of Pd alloys.

17.2.2.4 Structural Effect

The ORR activity of Pd-based catalysts depends on the shape and morphology of the materials. Pd(100) exhibited the highest ORR activity among the low index facets [18]. Several studies reported the shape-dependent ORR activities in nanoscale materials. The specific activity of Pd nanorods prepared by Xiao et al. [59] was ten times higher than that of Pd nanoparticles and comparable to that of bulk Pt. The authors attributed the high activity to the contribution from (110) sites according to their DFT calculations, which is in contrast to what was observed in the single-crystal work [18]. Li et al. [60] synthesized PdFe nanorods with a diameter of 3 nm and length of 10–50 nm, which can be controlled by the amount and type of surfactants. The PdFe nanorods demonstrated a higher PEMFC performance than commercial Pt/C in the practical working voltage region (0.80–0.65 V). The electrocatalytic activities of other shape-controlled Pd-based nanomaterials (cubic, octahedral, nanowires, etc.) are also of interest.

Erikson et al. demonstrated that cubic Pd particles enriched with {100} facets with an average size of ~27 nm had a higher ORR activity than spherical Pd particles (2.8 nm) [62]. A systematic study on the structural dependence of electrochemical behavior of Pd nanocrystals with a much smaller particle size (5–6 nm) was reported by Shao et al. [63]. As shown in Fig. 17.4a, the hydrogen adsorption peaks were observed at 0.16 and 0.21 V for the Pd cubes and octahedra, respectively [61]. The peak for the Pd cubes was sharper than that for the Pd octahedra. The differences in position and shape of hydrogen peaks may be caused by a weaker adsorption of hydrogen on Pd(100) than that on Pd(111). The differencebetween Pd cubes and octahedral was also confirmed by their Cu underpotential deposition (UPD) curves (Fig. 17.4b) [61]. For Pd octahedra, a sharp current peak was observed at 0.51 V due to UPD of Cu on {111} facets. On the other hand, a broader

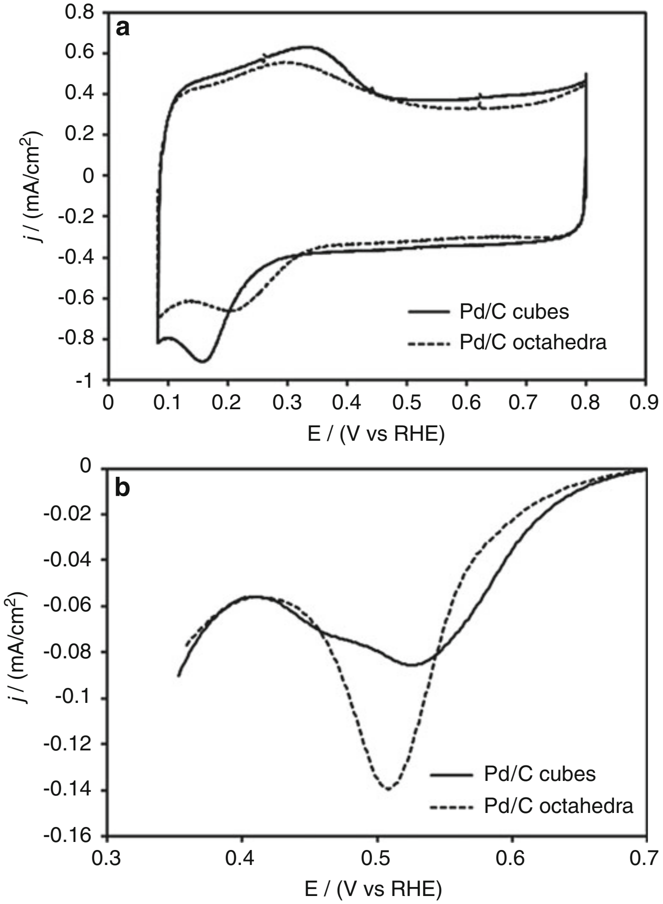

Fig. 17.4 Cyclic voltammetry curves of carbon-supported Pd nanocrystals. (**a**) In a nitrogen-saturated 0.1 M $HClO_4$ solution. Scanning rate = 50 mV s^{-1}. (**b**) In a nitrogen-saturated 0.05 M H_2SO_4 + 0.05 M $CuSO_4$ solution. Scanning rate = 5 mV s^{-1}. The double-layer currents were subtracted from the Cu UPD curves [61]

peak appeared at ca. 0.54 V for Pd cubes due to UPD of Cu on {100} facets. The higher Cu UPD potential on {100} than on {111} facets is due to a larger difference in work function between Pd(100) and Cu(100) than that between Pd (111) and Cu(111) and is consistent with the results obtained from bulk single crystals [64].

The oxygen polarization curve of Pd/C cubes is much more positive compared to those of octahedral and conventional Pd/C (Fig. 17.5a). This indicates that the Pd/C cubes were much more active for oxygen reduction. The specific ORR activities of Pd atoms in different samples were compared in the inset of Fig. 17.5a. The specific activities of cubic, octahedral, and conventional Pd/C were 0.31, 0.033, and 0.055 mA cm^{-2}, respectively. The activity enhancement of Pd cubes was about

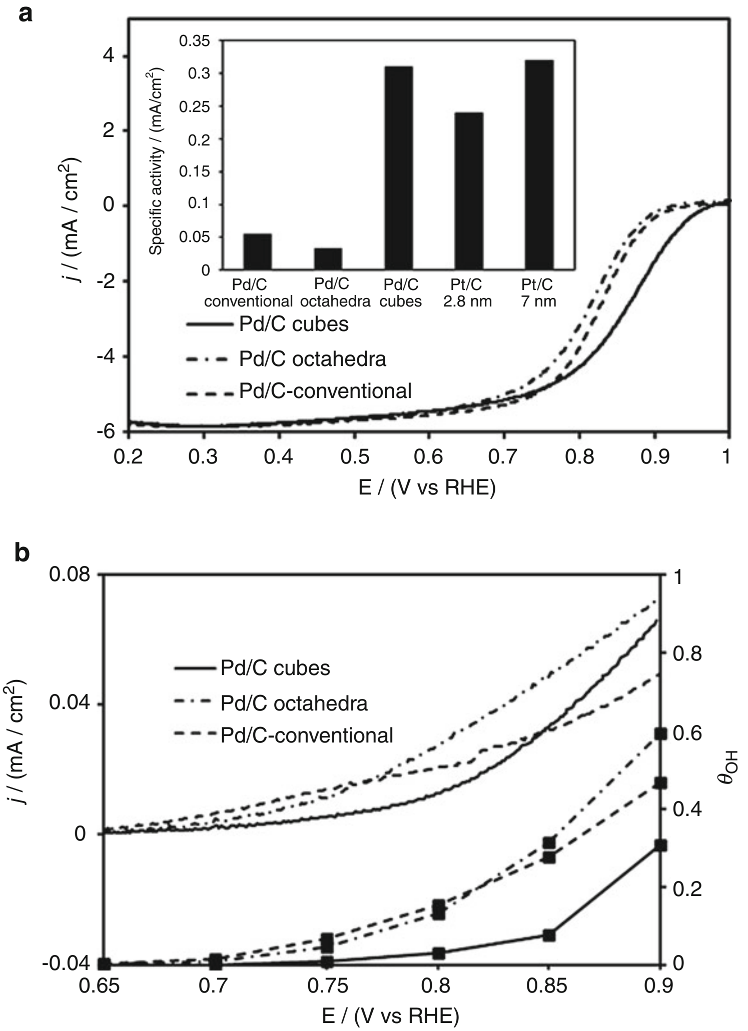

Fig. 17.5 (**a**) Anodic polarization curves for the ORR on Pd cubes and octahedra supported on carbon black in 0.1 M $HClO_4$. The data of conventional Pd/C is also included for comparison. Sweep rate = 10 mV s^{-1}; rotating speed = 1,600 rpm; and room temperature. The currents were normalized to the geometric area of the rotating disk electrode. The electrochemically active areas of Pd/C cubes, Pd/C octahedra, and Pd/C-HT were 1.27, 1.4, and 0.98 cm^2, respectively. *Inset*: comparison of specific activities for Pd/C cubes, Pd/C octahedra, conventional Pd/C, Pt/C (2.8 nm), and Pt/C (7 nm) at 0.9 V. (**b**) Anodic polarization curves in 0.1 M $HClO_4$ and coverage of OH of Pd/C cubes, Pd/C octahedra, and conventional Pd/C after subtracting the double-layer current density. The currents were normalized to the electrochemical active area. The coverage of OH was calculated by integrating the charge associate with OH_{ad} formation and normalized to half of the charge of Cu UPD [63]

ten and six times over Pd/C octahedra and conventional Pd/C, respectively. The Pd/C cubes were even more active than the state-of-the-art Pt/C catalysts with an average particle size of 2.8 nm and comparable to Pt/C with a similar particle size. This result demonstrated that Pd(100) sites are much more active than Pd(111) at the nanoscale, consistent with the extended surface study.

The ORR kinetics is controlled by the amount of available active sites on the catalyst's surface and the interaction between the surface and oxygen-containing species (e.g., O_2, O, OH, and OOH). The chemisorbed OH (OH_{ad}) acts as a poison species in the potential range where oxygen reduction is under combined kinetic–diffusion control, since it blocks the surface sites for O_2 adsorption. Shao et al. [63] compared the anodic branches of the voltammetry curves (0.65–0.9 V) for cubic, octahedral, and conventional Pd/C after subtracting the double-layer currents (Fig. 17.5b). The onset potential of OH_{ad} formation for both octahedral and conventional Pd was more than 50 mV lower than Pd cubes. Consequently, the coverage of OH_{ad} (Θ_{OH}) on Pd cubes was much lower than other surfaces in the potential range > 0.7 V. Thus, the higher ORR activity on Pd cubes can be attributed to its lower OH_{ad} coverage and consequently more available reaction sites.

17.3 ORR in Alkaline

17.3.1 ORR on Bulk Surfaces

The development of alkaline fuel cells promotes the studies of ORR on Pd-based materials in alkaline medium. A four-electron transfer reaction is expected on Pd surfaces:

$$O_2 + 2H_2O + 4e^- \rightarrow 4OH^-. \tag{17.3}$$

Lima et al. studied the ORR activities of different noble metals with a {111} facet in a 0.1 M NaOH solution [65]. The results showed that Pd(111) was more active in an alkaline solution than in an acidic solution, with an ORR activity very close to that of Pt(111) in the former solution.

Arenz et al. found that Pd/Pt(111) has a higher ORR activity than Pt(111) in alkaline solution, which is different from that in acid solution [66]. In alkaline solution, where only OH anions are present, the inhibition effect from the strong anion adsorption is much smaller than in acidic solution, resulting in a high ORR activity. Pd overlayers on Au(100) and Au(111) also showed significant activity improvement with respect to an unmodified Au substrate in the alkaline solutions [67–69]. The very high activity of Pd in alkaline solutions is surprising and deserves further attention.

17.3.2 ORR on Pd-Based Nanocatalysts

Pd exhibits a higher ORR activity in alkaline than in acidic solutions due to a decrease in the anion poisoning effect in alkaline solutions. Indeed, many studies have shown that the ORR activity of Pd/C in alkaline solutions is comparable to that of Pt/C [70, 71]. Similar to that of Pt/C, the ORR activity of Pd/C is dependent on the particle size of the metal. Jiang et al. [71] demonstrated that the specific activity increased monotonically by a factor of about 3 with the particle size increasing from 3 to 16.7 nm, while the mass activity first increased when the Pd particle size increased from 3 to 5 nm and then decreased with further Pd particle size increases. The increase of the specific activity is contributed to the increase of the fraction of the facet atoms with increasing the particle size.

The ORR activities of Pd–M alloys (M = Fe, Ni, Au, Sn) [70, 72–74] have also been studied in alkaline solutions. The Pd_3Fe/C was twofold more active than pure Pd/C [70]. Similar activity enhancement was also observed on Pd–Sn alloys [72]. For Pd–Ni/C catalyst, the ORR activity depends on the composition of the alloys. The highest activity was observed on PdNi/C and Pd_3Ni/C, which was not superior to Pd/C or Pt/C [73]. A synergistic effect from WC on ORR activity has been observed by Ni et al. [74]. The Pd nanoparticles supported on WC/C synthesized by an intermittent microwave heating method showed an enhanced ORR activity in comparison to Pd/C and Pt/C. By alloying with Au, the activity of Pd was significantly enhanced, but the exact enhancement mechanism is not clear. The strong interaction between the supports and metal nanoparticles and its effect on ORR activity may be an interesting topic to study. The development of Pd-based ORR catalysts for alkaline fuel cells is of interest to replace costly Pt materials. The ORR activity and stability of Pd-based catalysts, however, has to be compared to that of less expensive non-precious metal electrocatalysts [75, 76].

17.4 Methanol Tolerance

One of the main issues in the direct alcohol fuel cells (DAFCs) is that the fuel can easily permeate into the cathode through the proton exchange membrane, which causes dramatic performance loss since the currently used Pt-containing cathode catalysts have no or little methanol tolerance. One of the advantages of Pd–M alloys over Pt in DAFCs is their high methanol and ethanol tolerance in acid. In particular, methanol tolerance was demonstrated for Pd–Fe, Pd–Co, Pd–Cr, Pd–Ni, and Pd–Pt alloys [19, 41, 53, 77–80].

Shao et al. found no evidence of methanol oxidation on Pd_2Co/C in nitrogen-saturated $HClO_4$ solution containing 0.1 M methanol (Fig. 17.6) [19]. For the ORR, the half-wave potential drops ca. 20 mV with 0.1 M methanol in solution, compared to the same electrocatalyst without methanol. The loss of 20 mV might reflect the blocking of some active sites for oxygen reduction by the adsorbed methanol or its intermediates from oxidation. Similar methanol tolerance properties of Pd–M

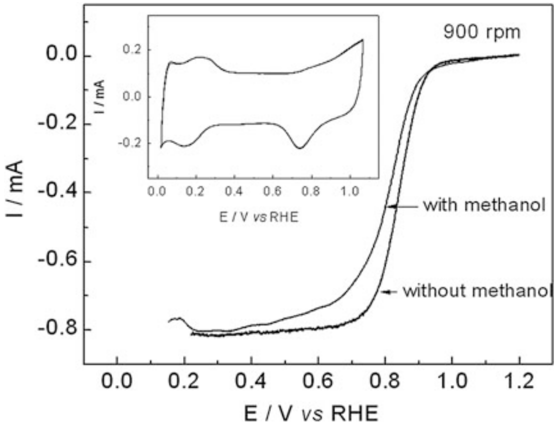

Fig. 17.6 Comparison of polarization curves for ORR on Pd_2Co/C in oxygen-saturated 0.1 M $HClO_4$ solution with and without 0.1 M methanol; rotation rate 900 rpm; sweep rate 10 mV s^{-1}. The *inset* is the cyclic voltammetry of Pd_2Co/C nanoparticles in nitrogen-saturated 0.1 M $HClO_4$ + 0.1 M methanol solutions; sweep rates 20 mV s^{-1} [19]

alloys have been reported by numerous groups [41, 77, 80–82]. All the results confirmed the excellent methanol tolerance of Pd-based alloys due to the low methanol oxidation on these electrocatalysts. By alloying with Pd, the methanol tolerance of Pt-based catalysts can be improved by diluting the Pt–Pt bonds, which are required for dissociative adsorption of methanol and ethanol on the surface of the catalyst. Accordingly, both Pd–M and Pd–Pt catalysts might be good candidates for resolving the problem of methanol crossover in DMFCs.

17.5 Mechanism of ORR Activity Enhancement

An understanding of the origin of the high activities of Pd–M alloys may help us in designing inexpensive and more active catalysts. Some thermodynamic guidelines were proposed to understand the enhancement effect from the alloying with transition metals. Bard and coworkers [38, 39] suggested that for Pd–M alloys the reactive metal M constitutes the site for breaking the O–O bonds, forming O_{ads} that would migrate to the hollow sites dominated by Pd atoms, where it would be readily reduced to water. Based on this mechanism, the alloy surface should consist of a relatively reactive metal such as Co, and the atomic ratio of this metal should be 10–20 % so that there are sufficient sites for reactions of O–O bond breaking on M and O_{ads} reduction at hollow sites formed by Pd atoms. The DFT calculations [39] indicated that one of the O atoms diffused to the Pd hollow site while the other still adsorbed on the hollow site near Co after the dissociative adsorption of the O_2 molecule. The second O_2 could dissociate on Co with an O atom prebound on the hollow site near it. Balbuena et al. [83] and Savadogo et al. [84] proposed a similar thermodynamic guideline for designing Pd alloy catalysts. For Pd with fully occupied valence d-orbitals, alloying with transition metals, such as Co with unoccupied valence d-orbitals, significantly reduces the Gibbs free energy both for the first charge-transfer step and for the steps involving the reduction of intermediates.

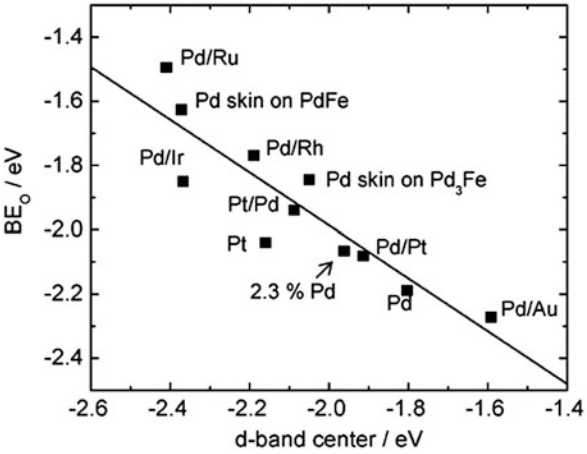

Fig. 17.7 Calculated oxygen binding energies on Pd and Pt overlayers on various substrates as a function of the Pd d-band center (relative to the Fermi level). The energies plotted correspond to the most stable configuration for O adsorption at the Pd or Pt hollow sites on each surface [89]

A Pd-enriched surface or called Pd skin can be formed either by annealing at elevated temperatures [85–87] or potential cycling before ORR activity evaluation. DFT calculations show that, like the Pt_3Co alloy surfaces, the electronic structure of the Pd skin is modified by the compressive strain (the transition metals used in the Pd alloys usually have a smaller atomic radius than that of Pd) and the underlying alloy, which in turn modifies the reactivity of the surface [88, 89]. As shown in Fig. 17.7, compressive strain alone accounts for a 0.1 eV destabilization of the Pd–O bond. A $Pd_3Fe(111)$ substrate contributes a further destabilization of O by ca. 0.25 eV, whereas a PdFe(111) substrate contributes a further destabilization of O by ca. 0.35 eV. The Pd skin on $Pd_3Fe(111)$ is very similar to Pt(111) in terms of both the d-band center position and the oxygen binding energy, and should have a high ORR activity. The high activity of this alloy was confirmed by using a $Pd_3Fe(111)$ single crystal by Zhou et al. [90].

17.6 Durability of Pd-Based Electrocatalysts

The durability of low-temperature fuel cell is one of the essential topics in the fuel cell development. The fuel cell performance gradually decreases due to the degradation of the Pt-based catalyst l under the harsh operating conditions including high potential, low pH, high temperature, and frequent start–stop cycling [2, 91]. The thermodynamic behavior of bulk Pt is described by the potential–pH diagrams (Pourbaix diagrams) [92]. The main pathways for Pt dissolution involve either the direct dissolution of metal,

$$\mathrm{Pt} \rightarrow \mathrm{Pt}^{2+} + 2\mathrm{e}^- \quad E_0 = 1.19 + 0.029 \log\left[\mathrm{Pt}^{2+}\right], \tag{17.4}$$

or an oxide film formation and a subsequent chemical reaction,

$$\mathrm{Pt} + \mathrm{H_2O} \rightarrow \mathrm{PtO} + 2\mathrm{H}^+ + 2\mathrm{e}^- \quad E_0 = 0.98 - 0.59\,\mathrm{pH}, \tag{17.5}$$

$$\mathrm{PtO} + 2\mathrm{H}^+ \rightarrow \mathrm{Pt}^{2+} + \mathrm{H_2O} \quad \log[\mathrm{Pt}^+] = -7.06 - 2\,\mathrm{pH}. \tag{17.6}$$

The dissolution through Pt oxides is expected to be slow due to the self-passivation effect. Similar to Pt, Pd can dissolve in acid solution via [92]

$$\mathrm{Pd} \rightarrow \mathrm{Pd}^{2+} + 2\mathrm{e}^- \quad E_0 = 0.99 + 0.029\,\log\left[\mathrm{Pd}^{2+}\right], \tag{17.7}$$

or

$$\mathrm{Pd} + \mathrm{H_2O} \rightarrow \mathrm{PdO} + 2\mathrm{H}^+ + 2\mathrm{e}^- \quad E_0 = 0.90 - 0.59\,\mathrm{pH}, \tag{17.8}$$

$$\mathrm{PdO} + 2\mathrm{H}^+ \rightarrow \mathrm{Pd}^{2+} + \mathrm{H_2O} \quad \log[\mathrm{Pd}^+] = -2.35 - 2\,\mathrm{pH}. \tag{17.9}$$

In the direct dissolution pathway, the equilibrium potential of Pd dissolution is 0.2 V lower than that of Pt. In the chemical dissolution pathway, the Pd^{2+} equilibrium concentration is ~5 orders of magnitude higher than Pt^{2+}. Thus, Pd should have a much higher dissolution rate at the same operation potential and thus much less stable than Pt in the fuel cell environment. Consequently, Pd is not expected to meet the durability requirement of the PEMFC, especially for those in the automotive application due to intensive start–stop driving cycles. The very low stability of Pd/C during potential cycling was confirmed recently [93]. The stability of Pd in alkaline medium may not be a problem; however, no such study is available in the literature.

Considerable efforts have been taken to improve the stability of Pd-based catalysts in the acidic medium. One way is to alloy with certain elements. Pd ternary alloys, including Pd–Co–Au [38, 39] and Pd–Co–Mo [53], have been developed to improve the stability of the catalysts. By adding 10 % Au to the Pd–Mo mixture, its stability can be improved significantly. However, the long-term durability of these catalysts has not been addressed yet.

Another promising way to improve the activity and durability of Pd-based nanocatalysts is to deposit a Pt layer on them. Recently, Pd/C and PdM/C catalysts modified by a Pt monolayer were found to possess higher activity than that of Pt/C due to the strain and electronic effects from the Pd-based cores, and the durability of the catalysts is improved significantly and comparable to Pt/C [70, 93–95]. The Pd-based core materials are expected to be partially dissolved under the fuel cell operation conditions due to some defects in the Pt monolayer. In the meantime, the diffusion of Pt atoms on the surface results in a more compact shell. Thus, further dissolution of Pd-based core is greatly reduced.

17.7 Conclusions

Pd-based electrocatalysts have shown comparable ORR activity to state-of-the-art Pt/C. It may play a role to replace or partially replace costly Pt catalysts in the cathode of low-temperature fuel cells.

As expected, the oxygen reduction rate strongly depends on the orientations of the Pd surface with Pd(100) having a much higher ORR activity than any other facets in acid. This trend has been confirmed both in the studies of bulk single crystals and nanocrystals of Pd. Synthesis and characterization of shape-controlled Pd and Pd alloy nanomaterials are of importance to design next generation Pd-based electrocatalysts.

The long-term stability of Pd-based electrocatalysts is one of the unavoidable issues for PEM fuel cell applications. Pd–Pt-based ORR catalysts are more stable than Pd-transition metal alloys under harsh fuel cell conditions, but may still not meet the long-term fuel cell operation requirement due to the Pd leaching out. Future research may focus on improving the durability of Pd-based catalysts by surface modification and composition optimization. Core–shell type of catalyst with Pd-based materials as the core and Pt as the shell may be one of the most promising candidates to be used in the automotive fuel cell due to its low Pt content and high activity and stability.

References

1. Adzic RR, Zhang J, Sasaki K, Vukmirovic MB, Shao M, Wang JX, Nilekar AU, Mavrikakis M, Valerio JA, Uribe F (2007) Platinum monolayer fuel cell electrocatalysts. Top Catal 46(3–4): 249–262
2. Gasteiger HA, Kocha SS, Sompalli B, Wagner FT (2005) Activity benchmarks and requirements for Pt, Pt-alloy, and non-Pt Oxygen reduction catalysts for PEMFCs. Appl Catal B Environ 56(1–2):9–35
3. Lefevre M, Proietti E, Jaouen F, Dodelet JP (2009) Iron-based catalysts with improved oxygen reduction activity in polymer electrolyte fuel cells. Science 324(5923):71–74
4. www.monex.com
5. Antolini E (2009) Palladium in fuel cell catalysis. Energy Environ Sci 2(9):915–931
6. Bianchini C, Shen PK (2009) Palladium-based electrocatalysts for alcohol oxidation in half cells and in direct alcohol fuel cells. Chem Rev 109(9):4183–4206
7. Shao M (2011) Palladium-based electrocatalysts for hydrogen oxidation and oxygen reduction reactions. J Power Sources 196(5):2433–2444
8. Adzic RR (1998) Electrocatalysis. In: Lipkowski J, Ross PN (eds) Frontiers in electrochemistry, vol 5. Wiley, New York, p 197
9. Shao MH, Liu P, Adzic RR (2006) Superoxide is the intermediate in the oxygen reduction reaction on platinum electrode. J Am Chem Soc 128:7408–7409
10. Tarasevich MR, Sadkowski A, Yeager E (1983) Oxygen electrochemistry. In: Conway BE, Bockris JO, Yeager E, Khan SUM, White RE (eds) Comprehensive treatise of electrochemistry, vol 7. Plenum, New York, p 301

11. Zhang J, Vukmirovic MB, Xu Y, Mavrikakis M, Adzic RR (2005) Controlling the catalytic activity of platinum-monolayer electrocatalysts for oxygen reduction with different substrates. Angew Chem Int Ed 44:2132–2135
12. Xu Y, Greeley J, Mavrikakis M (2005) Effect of subsurface oxygen on the reactivity of the Ag(111) surface. J Am Chem Soc 127(37):12823–12827
13. Stamenkovic V, Mun BS, Mayrhofer KJJ, Ross PN, Markovic NM, Rossmeisl J, Greeley J, Nørskov JK (2006) Changing the activity of electrocatalysts for oxygen reduction by tuning the surface electronic structure. Angew Chem Int Ed 45(18):2897–2901
14. Stamenkovic VR, Fowler B, Mun BS, Wang G, Ross PN, Lucas CA, Markovic NM (2007) Improved oxygen reduction activity on $Pt_3Ni(111)$ via increased surface site availability. Science 315:493
15. Norskov JK, Rossmeisl J, Logadottir A, Lindqvist L, Kitchin JR, Bligaard T, Jonsson H (2004) Origin of the overpotential for oxygen reduction at a fuel-cell cathode. J Phys Chem B 108: 17886–17892
16. Damjanovic A, Brusic V (1967) Oxygen reduction at Pt-Au and Pd-Au alloy electrodes in acid solution. Electrochim Acta 12(9):1171–1184
17. Markovic NM, Adzic RR, Cahan BD, Yeager EB (1994) Structural effects in electrocatalysis – oxygen reduction on platinum low-index single-crystal surfaces in perchloric-acid solutions. J Electroanal Chem 377(1–2):249–259
18. Kondo S, Nakamura M, Maki N, Hoshi N (2009) Active sites for the oxygen reduction reaction on the low and high index planes of palladium. J Phys Chem C 113(29):12625–12628
19. Shao MH, Huang T, Liu P, Zhang J, Sasaki K, Vukmirovic MB, Adzic RR (2006) Palladium monolayer and palladium alloy electrocatalysts for oxygen reduction. Langmuir 22(25): 10409–10415
20. Jalan VM, Luczak FJ, Lee J (1980) US Patent 4192967
21. Landsman DA, Luczak FJ (1982) US Patent 4316944
22. Landsman DA, Luczak FJ (2003) Catalyst studies and coating technologies. In: Vielstich W, Gasteiger H, Lamm A (eds) Handbook of fuel cells, vol 4. Wiley, p 811
23. Jalan V, Taylor EJ (1983) Importance of interatomic spacing in catalytic reduction of oxygen in phosphoric acid. J Electrochem Soc 130:2299
24. Paffett MT, Beery JG, Gottesfeld S (1988) Oxygen reduction at $Pt_{0.65}Cr_{0.35}$, $Pt_{0.2}Cr_{0.8}$ and roughened platinum. J Electrochem Soc 135(6):1431
25. Mukerjee S, Srinivasan S, Soriaga M, McBreen J (1995) Role of structural and electronic properties of Pt and Pt alloys on electrocatalysis of oxygen reduction. J Electrochem Soc 142(5):1409
26. Toda T, Igarashi H, Uchida H, Watanabe M (1999) Enhancement of the electroreduction of oxygen on Pt alloys with Fe, Ni, and Co. J Electrochem Soc 146(10):3750
27. Toda T, Igarashi H, Watanabe M (1998) Role of electronic property of Pt and Pt alloys on electrocatalytic reduction of oxygen. J Electrochem Soc 145(12):4185
28. Paulus UA, Wokaun A, Scherer GG, Schmidt TJ, Stamenkovic V, Markovic NM, Ross PN (2002) Oxygen reduction on high surface area Pt-based alloy catalysts in comparison to well defined smooth bulk alloy electrodes. Electrochim Acta 47(22–23):3787–3798
29. Paulus UA, Wokaun A, Scherer GG, Schmidt TJ, Stamenkovic V, Radmilovic V, Markovic NM, Ross PN (2002) Oxygen reduction on carbon-supported Pt-Ni and Pt-Co alloy catalysts. J Phys Chem B 106:4181
30. Hammer B, Nørskov JK (1995) Electronic factors determining the reactivity of metal surfaces. Surf Sci 343:211
31. Hammer B, Nørskov JK (2000) Theoretical surface science and catalysis calculations and concepts. Adv Catal 45:71
32. Kitchin JR, Nørskov JK, Barteau MA, Chen JG (2004) Role of strain and ligand effects in the modification of the electronic and chemical properties of bimetallic surfaces. Phys Rev Lett 93(15):156801

33. Kitchin JR, Nørskov JK, Barteau MA, Chen JG (2004) Modification of the surface electronic and chemical properties of Pt(111) by subsurface 3d transition metals. J Chem Phys 120(21): 10240
34. Greeley J, Nørskov JK, Mavrikakis M (2002) Electronic structure and catalysis on metal surfaces. Annu Rev Phys Chem 53:319–348
35. Xu Y, Ruban AV, Mavrikakis M (2004) Adsorption and dissociation of O_2 on Pt- Co and Pt-Fe alloys. J Am Chem Soc 126:4714
36. Savadogo O, Lee K, Oishi K, Mitsushima S, Kamiya N, Ota KI (2004) New palladium alloys catalyst for the oxygen reduction reaction in an acid medium. Electrochem Commun 6(2): 105–109
37. Fernandez JL, Raghuveer V, Manthiram A, Bard AJ (2005) Pd-Ti and Pd-Co-Au electrocatalysts as a replacement for platinum for oxygen reduction in proton exchange membrane fuel cells. J Am Chem Soc 127:13100–13101
38. Fernandez JL, Walsh DA, Bard AJ (2005) Thermodynamic guidelines for the design of bimetallic catalysts for oxygen electroreduction and rapid screening by scanning electrochemical microscopy. J Am Chem Soc 127:357–365
39. Fernandez JL, White JM, Sun YM, Tang WJ, Henkelman G, Bard AJ (2006) Characterization and theory of electrocatalysts based on scanning electrochemical microscopy screening methods. Langmuir 22(25):10426–10431
40. Wang W, Zheng D, Du C, Zou Z, Zhang X, Xia B, Yang H, Akins DL (2007) Carbon-supported Pd-Co bimetallic nanoparticles as electrocatalysts for the oxygen reduction reaction. J Power Sources 167(2):243–249
41. Zhang L, Lee K, Zhang JJ (2007) The effect of heat treatment on nanoparticle size and ORR activity for carbon-supported Pd-Co alloy electrocatalysts. Electrochim Acta 52(9):3088–3094
42. Shao MH, Sasaki K, Adzic RR (2006) Pd-Fe nanoparticles as electrocatalysts for oxygen reduction. J Am Chem Soc 128(11):3526
43. Wang RF, Liao SJ, Fu ZY, Ji S (2008) Platinum free ternary electrocatalysts prepared via organic colloidal method for oxygen reduction. Electrochem Commun 10(4):523–526
44. Tarasevich MR, Zhutaeva GV, Bogdanovskaya VA, Radina MV, Ehrenburg MR, Chalykh AE (2007) Oxygen kinetics and mechanism at electrocatalysts on the base of palladium-iron system. Electrochim Acta 52(15):5108–5118
45. Song SQ, Wang Y, Tsiakaras P, Shen PK (2008) Direct alcohol fuel cells: a novel non-platinum and alcohol inert ORR electrocatalyst. Appl Catal B Environ 78(3–4):381–387
46. Xu Y, Shao MH, Mavrikakis M, Adzic RR (2009) Recent developments in the electrocatalysis of the O_2 reduction reaction. In: Koper MTM (ed) Fuel cell catalysis: a surface science approach. Wiley, Hoboken, pp 271–316
47. Sarkar A, Murugan AV, Manthiram A (2009) Low cost Pd-W nanoalloy electrocatalysts for oxygen reduction reaction in fuel cells. J Mater Chem 19:159–165
48. Serov AA, Cho S-Y, Han S, Min M, Chai G, Nam KH, Kwak C (2007) Modification of palladium-based catalysts by chalcogenes for direct methanol fuel cells. Electrochem Commun 9(8):2041–2044
49. Cheng L, Zhang Z, Niu W, Xu G, Zhu L (2008) Carbon-supported Pd nanocatalyst modified by non-metal phosphorus for the oxygen reduction reaction. J Power Sources 182(1):91–94
50. Li H, Sun G, Li N, Sun S, Su D, Xin Q (2007) Design and preparation of highly active Pt-Pd/C catalyst for the oxygen reduction reaction. J Phys Chem C 111(15):5605–5617
51. Guerin S, Hayden BE, Lee CE, Mormiche C, Russell AE (2006) High-throughput synthesis and screening of ternary metal alloys for electrocatalysis. J Phys Chem B 110(29): 14355–14362
52. Ye HC, Crooks RM (2007) Effect of elemental composition of PtPd bimetallic nanoparticles containing an average of 180 atoms on the kinetics of the electrochemical oxygen reduction reaction. J Am Chem Soc 129(12):3627–3633

53. Raghuveer V, Manthiram A, Bard AJ (2005) Pd-Co-Mo electrocatalyst for the oxygen reduction reaction in proton exchange membrane fuel cells. J Phys Chem B 109(48): 22909–22912
54. Mathiyarasuz J, Phani KLN (2007) Carbon-supported palladium-cobalt-noble metal (Au, Ag, Pt) nanocatalysts as methanol tolerant oxygen-reduction cathode materials in DMFCs. J Electrochem Soc 154:B1100–B1105
55. Wang XP, Kariuki N, Vaughey JT, Goodpaster J, Kumar R, Myers DJ (2008) Bimetallic Pd-Cu oxygen reduction electrocatalysts. J Electrochem Soc 155(6):B602–B609
56. Myers DJ (2008) In: DOE hydrogen and fuel cell review meeting, Arlington, VA
57. Raghuveer V, Ferreira PJ, Manthiram A (2006) Comparison of Pd-Co-Au electrocatalysts prepared by conventional borohydride and microemulsion methods for oxygen reduction in fuel cells. Electrochem Commun 8(5):807–814
58. Liu H, Manthiram A (2008) Tuning the electrocatalytic activity and durability of low cost $Pd_{70}Co_{30}$ nanoalloy for oxygen reduction reaction in fuel cells. Electrochem Commun 10(5): 740–744
59. Xiao L, Zhuang L, Liu Y, Lu J, Abruna HD (2008) Activating Pd by morphology tailoring for oxygen reduction. J Am Chem Soc 131(2):602–608
60. Li WZ, Haldar P (2009) Supportless PdFe nanorods as highly active electrocatalyst for proton exchange membrane fuel cell. Electrochem Commun 11(6):1195–1198
61. Shao MH Unpublished data
62. Erikson H, Sarapuu A, Tammeveski K, Solla-Gullon J, Feliu JM (2011) Enhanced electrocatalytic activity of cubic Pd nanoparticles towards the oxygen reduction reaction in acid media. Electrochem Commun 13(7):734–737
63. Shao M, Yu T, Odell JH, Jin M, Xia Y (2011) Structural dependence of oxygen reduction reaction on palladium nanocrystals. Chem Commun 47(23):6566–6568
64. Chierchie T, Mayer C (1988) Voltammetric study of the underpotential deposition of copper on polycrystalline and single crystal palladium surfaces. Electrochim Acta 33(3):341–345
65. Lima FHB, Zhang J, Shao M, Sasaki K, Vukmirovic B, Ticianelli EA, Adzic RR (2007) Catalytic activity-d-band center correlation for the O_2 reduction on Pt in alkaline solutions. J Phys Chem C 111:404–410
66. Arenz M, Schmidt TJ, Wandelt K, Ross PN, Markovic NM (2003) The oxygen reduction reaction on thin palladium films supported on a Pt(111) electrode. J Phys Chem B 107(36): 9813–9819
67. Naohara H, Ye S, Uosaki K (2000) Electrocatalytic reactivity for oxygen reduction at epitaxially grown Pd thin layers of various thickness on Au(111) and Au(100). Electrochim Acta 45(20): 3305–3309
68. Schmidt TJ, Stamenkovic V, Arenz M, Markovic NM, Ross PN (2002) Oxygen electrocatalysis in alkaline electrolyte: Pt(hkl), Au(hkl) and the effect of Pd-modification. Electrochim Acta 47(22–23): 3765–3776
69. Dursun Z, Ulubay Ş, Gelmez B, Ertaş F (2009) Electrocatalytic reduction of oxygen on a Pd ad-layer modified Au(111) electrode in alkaline solution. Catal Lett 132(1):127–132
70. Shao M, Sasaki K, Liu P, Adzic RR (2007) Pd_3Fe and Pt monolayer-modified Pd_3Fe electrocatalysts for oxygen reduction. Z Phys Chem 221:1175–1190
71. Jiang L, Hsu A, Chu D, Chen R (2009) Size-dependent activity of palladium nanoparticles for oxygen electroreduction in alkaline solutions. J Electrochem Soc 156(5):B643–B649
72. Kim J, Park JE, Momma T, Osaka T (2009) Synthesis of Pd-Sn nanoparticles by ultrasonic irradiation and their electrocatalytic activity for oxygen reduction. Electrochim Acta 54(12): 3412–3418
73. Li B, Prakash J (2009) Oxygen reduction reaction on carbon supported palladium-nickel alloys in alkaline media. Electrochem Commun 11(6):1162–1165
74. Nie M, Shen PK, Wei ZD (2007) Nanocrystalline tungsten carbide supported Au-Pd electrocatalyst for oxygen reduction. J Power Sources 167:69–73

75. Lu S, Pan J, Huang A, Zhuang L, Lu J (2008) Alkaline polymer electrolyte fuel cells completely free from noble metal catalysts. Nat Acad Sci Proc 105(52):20611–20614
76. Catanorchi S, Piana M, Gasteiger HA (2008) Kinetics of non-platinum group metal catalysts for the oxygen reduction reaction in alkaline medium. ECS Trans 16(2):2045–2055
77. Mustain WE, Kepler K, Prakash J (2007) CoPdx oxygen reduction electrocatalysts for polymer electrolyte membrane and direct methanol fuel cells. Electrochim Acta 52(5):2102–2108
78. Li HQ, Xin Q, Li WZ, Zhou ZH, Jiang LH, Yang SH, Sun GQ (2004) An improved palladium-based DMFCs cathode catalyst. Chem Commun 23:2776–2777
79. Lopes T, Antolini E, Gonzalez ER (2008) Carbon supported Pt-Pd alloy as an ethanol tolerant oxygen reduction electrocatalyst for direct ethanol fuel cells. Int J Hydrogen Energy 33(20): 5563–5570
80. Lee K, Savadogo O, Ishihara A, Mitsushima S, Kamiya N, Ota K (2006) Methanol-tolerant oxygen reduction electrocatalysts based on Pd-3D transition metal alloys for direct methanol fuel cells. J Electrochem Soc 153(1):A20–A24
81. Mustain WE, Kepler K, Prakash J (2006) Investigations of carbon-supported $CoPd_3$ catalysts as oxygen cathodes in PEM fuel cells. Electrochem Commun 8(3):406–410
82. Tarasevich M, Bogdanovskaya V, Kuznetsova L, Modestov A, Efremov B, Chalykh A, Chirkov Y, Kapustina N, Ehrenburg M (2007) Development of platinum-free catalyst and catalyst with low platinum content for cathodic oxygen reduction in acidic electrolytes. J Appl Electrochem 37(12):1503–1513
83. Wang YX, Balbuena PB (2005) Design of oxygen reduction bimetallic catalysts: ab-initio-derived thermodynamic guidelines. J Phys Chem B 109:18902–18906
84. Fouda-Onana F, Bah S, Savadogo O (2009) Palladium-copper alloys as catalysts for the oxygen reduction reaction in an acidic media I: Correlation between the ORR kinetic parameters and intrinsic physical properties of the alloys. J Electroanal Chem 636(1–2):1–9
85. Rousset JL, Bertolini JC, Miegge P (1996) Theory of segregation using the equivalent-medium approximation and bond-strength modifications at surfaces: application to fcc Pd-X alloys. Phys Rev B 53(8):4947
86. Ruban AV, Skriver HL, Nørskov JK (1999) Surface segregation energies in transition-metal alloys. Phys Rev B 59(24):15990
87. Bozzolo G, Noebe RD, Khalil J, Morse J (2003) Atomistic analysis of surface segregation in Ni-Pd alloys. Appl Surf Sci 219(1–2):149–157
88. Suo YG, Zhuang L, Lu JT (2007) First-principles considerations in the design of Pd-alloy catalysts for oxygen reduction. Angew Chem Int Ed 46(16):2862–2864
89. Shao M, Liu P, Zhang J, Adzic RR (2007) Origin of enhanced activity in palladium alloy electrocatalysts for oxygen reduction reaction. J Phys Chem B 111:6772–6775
90. Zhou W-P, Yang X, Vukmirovic MB, Koel BE, Jiao J, Peng G, Mavrikakis M, Adzic RR (2009) Improving electrocatalysts for O_2 reduction by fine-tuning the Pt-support interaction: Pt monolayer on the surfaces of a $Pd_3Fe(111)$ single-crystal alloy. J Am Chem Soc 131(35): 12755–12762
91. Sasaki K, Shao MH, Adzic RR (2009) Dissolution and stabilization of platinum in oxygen cathodes. In: Buchi FN, Inaba M, Schmidt T (eds) Proton exchange membrane fuel cell durability. Springer, New York, pp 7–28
92. Pourbaix M (1974) Atlas of electrochemical equilibria, 2nd edn. NACE, Houston
93. Wells PP, Crabb EM, King CR, Wiltshire R, Billsborrow B, Thompsett D, Russell AE (2009) Preparation, structure and stability of Pt and Pd monolayer modified Pd and Pt electrocatalysts. Phys Chem Chem Phys 11:5773–5781
94. Zhang J, Vukmirovic MB, Sasaki K, Uribe F, Adzic RR (2005) Platinum monolayer electrocatalysts for oxygen reduction: effect of substrates, and long-term stability. J Serb Chem Soc 70(3):513–525
95. Shao MH, Shoemaker K, Peles A, Kaneko K, Protsailo L (2010) Pt monolayer on porous Pd-Cu alloys as oxygen reduction electrocatalysts. J Am Chem Soc 132(27):9253–9255

Chapter 18
Dealloyed Pt-Based Core–Shell Catalysts for Oxygen Reduction

Lin Gan and Peter Strasser

Abstract In this chapter, we review recent works of dealloyed Pt core–shell catalysts, which are synthesized by selective removal of transition metals from a transition-metal-rich Pt alloys (e.g., PtM_3). The resulted dealloyed Pt catalysts represent very active materials for the oxygen reduction reaction (ORR) catalysis in terms of noble-metal-mass-normalized activity as well as their intrinsic area-specific activity. The mechanistic origin of the catalytic activity enhancement and the stability of dealloyed Pt catalysts are also discussed.

18.1 Introduction

As a highly efficient and clean energy conversion technology, polymer electrolyte membrane fuel cells (PEMFCs) have attracted substantial interests over the past few decades [1–4]. Prototype vehicles powered by fuel cells with impressive performance have been released by several manufactures, but it is still difficult to move to practical technique that can be mass-produced cost-effectively. One of the main obstacles is the slow rate of the cathodic oxygen reduction reaction (ORR), which currently relies on noble-metal Pt as the electrocatalysts. The high cost and limit resource of Pt force the urgent development of low-/non-Pt catalysts. Ideally, non-noble-metal catalyst is the best and ultimate goal. Unfortunately, although significant progress has been made in terms of the activities of noble-metal-free catalysts in recent years, their stability as well as the mass transport still needs further breakthroughs [5–8]. As a compromise, low-Pt catalyst appears to be a feasible way for the medium-term development of PEMFCs. In this direction, the United States Department of Energy (DOE) sets up a 2017 target on the total platinum group

---

L. Gan • P. Strasser (✉)
The Electrochemical Energy, Catalysis, and Materials Science Laboratory, Department of Chemistry, Chemical Engineering Division, Technical University Berlin, 10623 Berlin, Germany
e-mail: pstrasser@tu-berlin.de

M. Shao (ed.), *Electrocatalysis in Fuel Cells*, Lecture Notes in Energy 9,
DOI 10.1007/978-1-4471-4911-8_18,

metals (PGM) loading of 0.125 mg cm^{-2} on MEAs to achieve a power density of 8 kW $g^{-1}{}_{Pt}$. This corresponds to the use of 8 g of PGM per vehicle, which is comparable to what has been used in an internal combustion engine today [4]. To realize this target, the new ORR electrocatalyst must show a stable Pt-normalized mass activity of at least fourfold improvement compared with the state-of-the-art Pt catalyst.

Rational catalyst development to meet the activity target needs a comprehensive understanding of the ORR kinetics. This is why the ORR has been extensively studied for several decades. Regardless the mechanistic detail, it is proposed that the intermediate oxygenated species (such as $–OH_{ad}$) adsorbs on the Pt surface too strongly to be removed and results in high coverage ratio of the oxygenated species on the Pt surface, which become the main reason for the slow kinetics of ORR on Pt. It is therefore expected that a slightly weakened binding energy between the oxygenated species and Pt surface could result in a higher ORR activity. This could be realized by tailoring the electronic structure of Pt surface (particularly the d-band center), as predicted by density functional calculations [9–11].

From the late 1990s, Pt alloys containing a late 3d-transition metal "M" (M = Fe, Co, Ni, etc.) were found to be more catalytically active than pure Pt on ORR [1, 12–17]. The Pt alloys, mostly close to a stoichiometric ratio of Pt_3M, showed around twofold enhancement in the Pt-mass activity. Although their activities were far away from the DOE target, these pioneer studies provide important insights on the possible activity-enhancement mechanisms: (1) ligand effects, due to proximity of transition metals with different electron negativity and thus direct electron interaction, typically operative over one to three atomic layers, and (2) geometric effects associated with shortened nearest-neighboring Pt–Pt interatomic distances in the Pt alloys. Both of the two effects could induce the change of electronic structure of Pt surface and therefore weakened adsorption of intermediate oxygenated species.

Based on these guidelines, great progress on the structural design of Pt-based bimetallic/trimetallic catalysts has been made in past 10 years, as highlighted by several recent reviews [2–4]. For instance, the "Pt-monolayer catalysts" reported by Adzic and coworkers, which consist of a single Pt monolayer supported on non-Pt metal substrate (e.g., Pd) [11, 18–23], exhibited significant ORR activity enhancement based on Pt mass. Meanwhile, Stamenkovic et al. reported a class of highly active "Pt-skin catalysts," which were formed by surface segregation in Pt_3M alloys upon thermal annealing, resulting in a Pt monolayer on top of an M-enriched second layer [9, 24–26]. A common structural feature of the two classes of highly active catalysts is that a single Pt monolayer supported on the second layer containing a heteroatom, which could not only result in direct electron interaction with Pt but also a strain effect on the Pt monolayer caused by lattice mismatch. As a result, both ligand effect and geometric effect could contribute to their enhanced ORR activities.

In this chapter, we review dealloyed core–shell nanoparticle catalysts, which were synthesized by selective dissolution of transition metals from the surface of a transition-metal-rich Pt alloys (e.g., PtM_3). Figure 18.1 shows an illustration of the

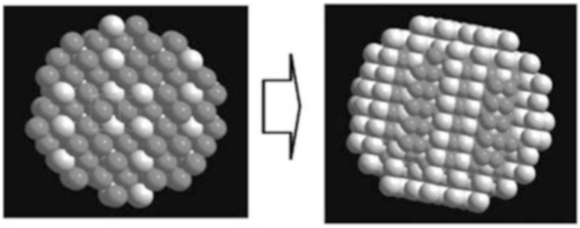

Fig. 18.1 Dealloying of $PtCu_3$ nanoparticles formed Cu-rich alloy core and Pt-rich shell (*gray*: Cu; *white*: Pt) (reprint with permission from ref. [27])

dealloyed core–shell nanoparticle concept, indicating the formation of a transition-metal-rich core and Pt-rich shell. We will show that the dealloyed core–shell nanoparticles represent very active materials for the ORR catalysis in terms of their noble-metal-mass-based ORR activity as well as their intrinsic specific activity. In contrast to the "Pt-skin" and the "Pt-monolayer" catalysts, the thickness of the Pt-enriched shell of the dealloyed catalysts is thicker than a single monolayer, which results in a dominate lattice-strain-controlled ORR activities of the dealloyed surfaces. The activities as well as the stability of the family of dealloyed Pt-based catalysts would be discussed in detail. Finally, we will discuss recent advances on the atomic-scale structural studies of the dealloyed core–shell nanoparticles, providing a deeper insight on their structure–activity–stability relationship.

18.2 A Historical View of Dealloying: From Bulk Materials to Nanoparticles

Dealloying, also called selective leaching, is a process where the less-noble metals are selectively dissolved out of an alloy and has been historically used in technologically important alloys in the context of corrosion area [28]. A most common example is the selective leaching of zinc from brass alloys (15 at% Zn) in the presence of oxygen and moisture, resulting in a copper-rich sponge with poor mechanical properties. In this situation, the dealloying process caused undesired performance decline and thus needs to be avoided, which continues to be a main task in corrosion area. Despite its negative effect in the corrosion area, dealloying can be useful in some certain areas regarding its ability to create porous structure. A well-known instance is the Raney nickel developed by Murray Raney more than 80 years ago [29], which was produced from a block of Ni–Al alloy treated with concentrated alkaline, dissolving most of Al out of the alloy and leaving behind a porous structure. The size of these pores was already in the nanoscale region, even though the concept of "nanotechnology" arises several decades later. The resulted nanoporous nickel-rich structure showed a high specific surface area, making it quite useful as heterogeneous catalysts in a variety of organic synthesis (e.g., hydrogenation reactions).

Inspired by the successful application of Raney nickel and also the arising of nanotechnology, there are increasing interests in synthesizing nanoporous materials

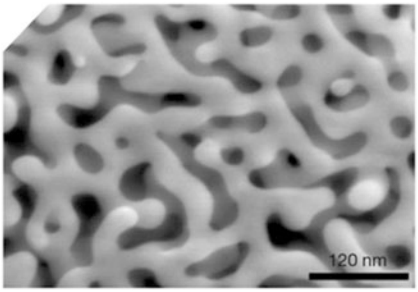

Fig. 18.2 Nanoporosity formed by dealloying of a bulk Ag–Au alloy (reprint with permission from ref. [30])

using dealloying protocol for applications in catalysis and sensors in recent years [30–35]. For example, nanoporous gold (Fig. 18.2) was synthesized by electrochemical dealloying of silver–gold alloy. Other nanoporous materials, such as Pt and Pd, were also synthesized.

The dynamic process of dealloying was discussed using Monte Carlo simulations [30, 36, 37]. The dissolution of the less-noble atoms from the topmost surface resulted in steps and kinks, where the coordinated numbers of noble atoms increased. This induced a surface diffusion of noble atoms. The competition between the dissolution rate of less-noble metals and the surface diffusion of noble metals is considered to be a key factor that controls the morphology of the dealloyed product. In bulk alloys, surface diffusion rate of the noble atoms is slow across the extended surface, which causes a Rayleigh surface instability [37] and leads to the formation of nanoporosity.

Until recently, all dealloying processes are studied in bulk alloy materials with the aim to produce nanoporosity. From 2007 on, we applied and studied the dealloying process in real engineered fuel cell Pt–M alloy nanoparticle catalysts. Unlike macro bulk materials, dealloying of alloy nanoparticles with small enough particle size produces solid core–shell nanoparticles. This may be due to the fact that the residual Pt atoms on the nanoparticles exhibited lower average coordination and hence experienced a much faster surface diffusion compared to those on the bulk surface. We will show that, using transition-metal-rich Pt alloy precursors, the dealloyed nanoparticle catalyst can produce up to eightfold enhancement in the Pt-mass-normalized ORR activity due to an enhanced lattice-strain effect.

18.3 Dealloyed Pt-Bimetallic Nanoparticle Catalysts

18.3.1 Dealloyed $PtCu_3$ Catalysts: Synthesis and Activities

The synthesis of dealloyed $PtCu_3$ catalyst involved the preparation of $PtCu_3$ precursor alloys at the first step, which was followed by electrochemical dissolution of Cu (dealloying). $PtCu_3$ alloy precursors were prepared by a conventional

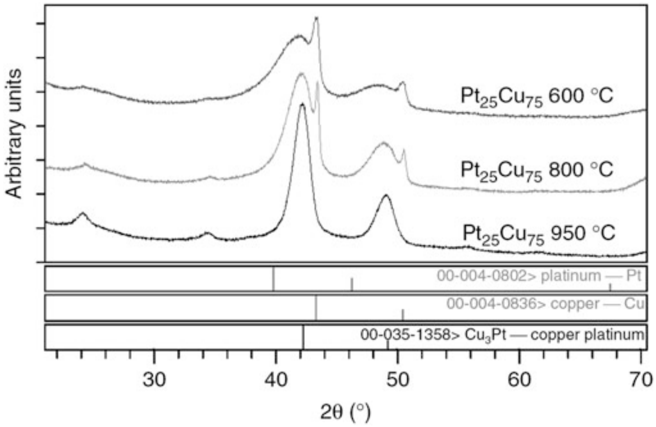

Fig. 18.3 XRD patterns of $Pt_{25}Cu_{75}$ precursor alloys annealed at different temperatures (reprint with permission from ref. [27])

impregnation-reductive annealing method. Normally, a carbon-supported Pt catalyst was impregnated with Cu salt at a desired atomic ratio between Pt and Cu firstly, which was further annealed by H_2 at elevated temperatures to reduce Cu and promote the alloying of Cu with Pt.

Figure 18.3 shows the XRD patterns of $PtCu_3$ catalyst annealed at 600, 800, and 950 °C and also the standard diffraction peaks of pure Pt and Cu for comparison [27]. The {111} diffraction peak position is located between the Pt {111} peak and Cu {111} peak, indicating a smaller lattice parameter of the alloy compared to pure Pt. The higher annealing temperature resulted in a more uniform alloy from multiphase (Pt-rich and Cu-rich alloys) to single phase, while the average crystal size evaluated from the full width at half maximum (FWHM) increased due to particle sintering at higher temperatures. The maximum annealing temperature essentially controlled the Cu content of the resulting disordered Pt–Cu lattices, while increasing annealing times, in contrast, leads primarily to particle growth [38, 39]. Correlation of annealing control parameters, such as heating rate, temperature, and time, with microscopic alloy structure, composition, and particle size has also been studied in situ by using high-temperature XRD [39].

The subsequent dissolution (dealloying) of Cu is the key process to form the active catalyst. Briefly, the dealloying can be performed by chemical leaching in acid solution (HNO_3 for Cu) or in an electrochemical way. One benefit of the electrochemical dealloying is its ability to in situ monitoring the dissolution of Cu. Figure 18.4a shows the initial three cyclic voltammograms (CV) of the dealloying of $PtCu_3$ catalyst annealed at 600 °C. Normally, there is a characteristic underpotential adsorption/desorption peak of H (H_{upd}) on a Pt electrode between 0.05 and 0.4 V/RHE as demonstrated on the commercial Pt catalyst in Fig. 18.4a. However, in the very first Pt–Cu dealloying CV, no H_{upd} peak could be found, consistent with complete Cu surface segregation in Cu-rich Pt alloys. Sweeping

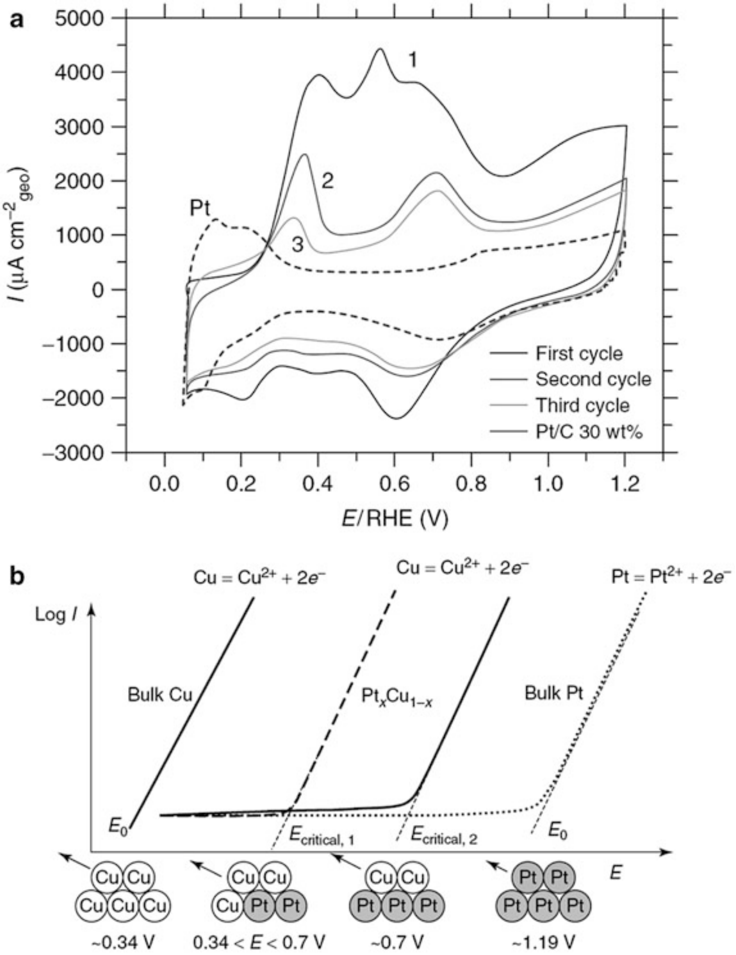

Fig. 18.4 (**a**) Initial three CVs of the PtCu$_3$ catalyst annealed at 600 °C during electrochemical dealloying compared to the CV of a commercial Pt catalyst (reprint with permission from ref. [27]). (**b**) Diagrammatic illustration of how the critical dissolution potential of a Cu monolayer depends on the composition of its subsurface layer (reprint with permission from ref. [40])

anodically, a broad peak from 0.3 to 0.85 V arises corresponding to the Cu dissolution, in which several fine sub-peaks can be resolved. A detailed description of these fine peaks was performed by density functional calculations, suggesting the dissolution of Cu at different surface sites, as shown in Fig. 18.4b [40]. On the second and the third cycle, additional anodic Cu dissolution peaks can be still seen but decreased gradually in intensity, while the H$_{upd}$ features gradually emerged, indicating exposure of Pt atoms on the surface.

After 200 cycles of electrochemical dealloying, the Cu dissolution vanished completely and the CV for all the dealloyed PtCu$_3$ catalysts exhibited stable Pt-like

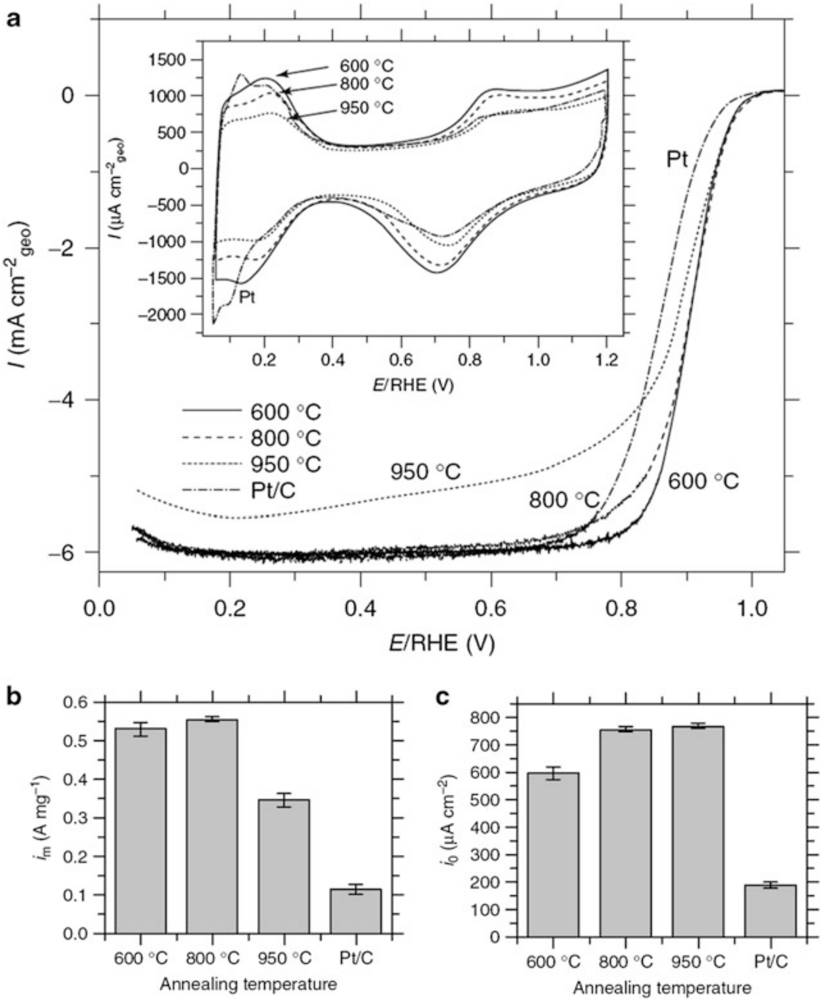

Fig. 18.5 (**a**) ORR voltammetry in O_2-saturated 0.1 M $HClO_4$ of dealloyed PtCu3 catalysts using the alloy precursors annealed at 600, 800, and 950 compared to a commercial Pt catalyst. (*Inset*) CV curves of the dealloyed PtCu3 catalysts in N_2 saturated 0.1 M $HClO_4$. (**b**) Comparison of Pt-mass activities at 0.9 V/RHE. (**c**) Comparison of Pt-area-specific activities at 0.9 V/RHE (reprint with permission from ref. [27])

feature (as shown in the inset of Fig. 18.5a). The resulted dealloyed "$PtCu_3$" catalysts showed very high catalytic activities in the ORR measurements (Fig. 18.5a), producing previously unachieved 3–5-fold improvement on the Pt-mass activity (Fig. 18.5b) and 3–4-fold on the Pt-area-specific activity (Fig. 18.5c) over pure Pt at 0.9 V vs. RHE. The highest Pt-mass activity (0.56 A $mg^{-1}{}_{Pt}$) was achieved on the dealloyed $PtCu_3$ catalyst using the precursor annealed at 800 °C, which obviously exceeded the DOE 2017 activity target (0.44 $mg^{-1}{}_{Pt}$). This fivefold activity enhancement would

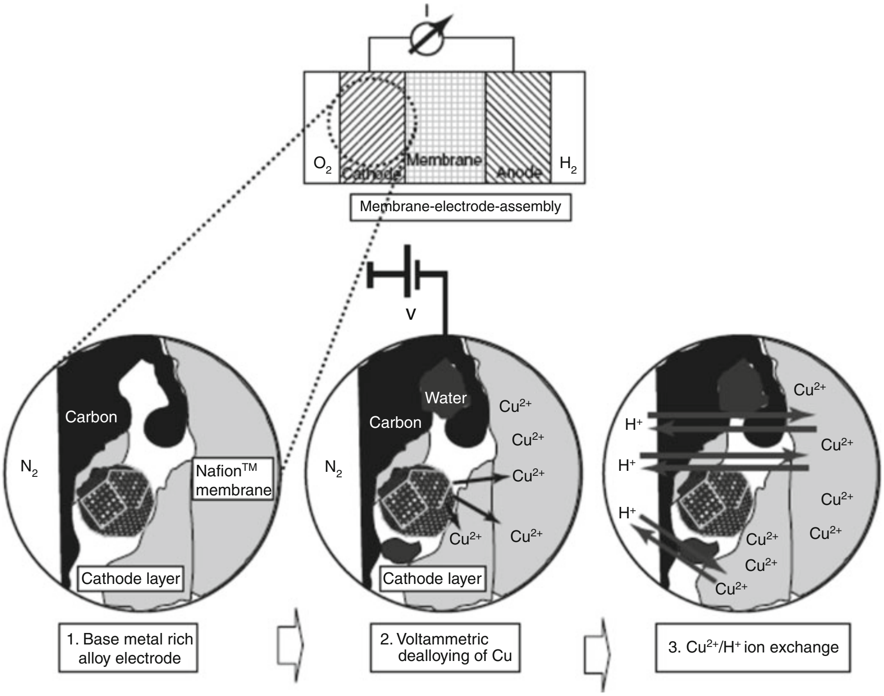

Fig. 18.6 A novel three-step method for in situ electrochemical dealloying of transition-metal-rich Pt alloy catalyst inside MEA (reprint with permission from ref. [41])

correspond to 80 % reduction on the Pt usage, thus providing a promising route for the development of low-Pt fuel cell catalysts. This study demonstrates that electrochemical dealloying of non-noble base metals from base-metal-rich Pt-bimetallic alloys significantly alters the catalytic rates of the resulting Pt shells.

The practical usefulness of a novel ORR electrocatalyst depends on the feasibility to incorporate it into a realistic MEA and a single fuel cell. For this purpose, we developed a novel three-step method to implement in situ electrochemically dealloyed $PtCu_3$ ORR catalysts inside the MEA [38, 41], as schematically illustrated by Fig. 18.6. In step 1, the Cu-rich alloy precursor is incorporated in the cathode of a fuel cell. During step 2, a CV treatment is applied to the fuel cell, which results in the in situ dissolution of Cu atoms from the alloy particle surface. The dissolved Cu ions would diffuse into the Nafion polyelectrolyte and get trapped at negatively charged sulfonic acid groups of the latter, which is detrimental to the ion conductivity and result in decreased fuel cell performance. As a result, an ion-exchange step (step 3) is needed, where the MEA is treated with an inorganic acid to completely exchange the trapped Cu ions with protons from the liquid acid. After the three steps, the catalyst has been converted into its active state and is ready for use.

18.3.2 Mechanism of Activity Enhancement: Lattice-Strain Effect

Unlike Pt-monolayer catalysts and Pt-skin catalysts, the dealloyed $PtCu_3$ catalysts consist of a pure Pt shell with several atomic layers. The near-surface content of Cu was very low. The thickness of the Pt shell can be clearly imaged by scanning transmission electron microscopy (STEM) and energy-dispersive X-ray spectroscopy (EDX) line profiles (Fig. 18.7a, b). In the Z-contrast STEM image, the dealloyed particles show a brighter shell relative to a darker core, indicating the formation of Pt-rich shell. From the EDX line profiles, the thickness of the Pt-rich shell can be determined to be around 0.6 nm (corresponding to ca. 3 atomic layers). This result is consistent with the anomalous small-angle X-ray scattering (ASAXS) studies, which revealed a minimum Pt-shell thickness of 0.5 nm [42]. Across the Pt shell with a thickness of three atomic layers, a significant electronic interaction between the Cu atoms at the core and the outmost Pt surface is unlikely. Instead, the structural arrangement of Pt atoms on the surface with its shorter than normal Pt–Pt distance is creating a compressive-strain effect. This arises because of a lattice mismatch between the Pt shell and the Cu-rich alloy core. The compressive lattice strain changes the electronic properties of Pt and the adsorption on oxygenated species and thus accounts for the observed enhanced ORR activity.

To investigate the possible lattice-strain mechanism on the enhanced ORR activities, we synthesized two sets of dealloyed $Pt_{1-x}Cu_x$ catalysts from a wide range of alloy precursor compositions (Pt_3Cu, PtCu, and $PtCu_3$); one set was annealed at 800 °C and the other set annealed at 950 °C [43]. The idea is that the composition of the alloy core determines the upper limit of the strain on the Pt shell and thus enables a lattice-strain control, which is crucial for the study of strain–activity relationships.

The lattice strain in the Pt shell can be quantitatively estimated by anomalous X-ray diffraction (AXRD) analysis using a simple two-phase model (Fig. 18.7c), i.e., a Pt–Cu alloy core and a uniformly strained Pt shell. Figure 18.7d shows the measured average lattice parameters of the Pt shells (a_{shell}) as a function of precursor composition and preparation temperature. As expected, for all the dealloyed catalysts, a_{shell} is smaller than that of pure Pt (dotted line, Fig. 18.7d), indicating a compressive strain in the Pt shells. Increasing Cu in the alloy precursor or with a higher preparation temperature resulted in a decreased a_{shell} and hence a larger magnitude of the compressive strain. This can be well understood based on the core–shell model. That is, the lattice mismatch between the Pt shell and the Pt–Cu core causes a reduced Pt–Pt distance in the shell; the richer in Cu the particle core is, the smaller the lattice parameter and hence the higher the compressive strain induced in the shell. Similarly, in the high-temperature material, the bimetallic precursor phase is alloyed more uniformly with less residual, unalloyed Cu, which effectively makes the alloy phase richer in Cu.

To mimic the structural and electronic environment of the Pt layers surrounding a particle core with smaller lattice parameters in the dealloyed Pt–Cu catalysts, we extended and applied these ideas to bimetallic single-crystal model surfaces that consist of Pt overlayers with various thicknesses grown on a Cu(111) substrate.

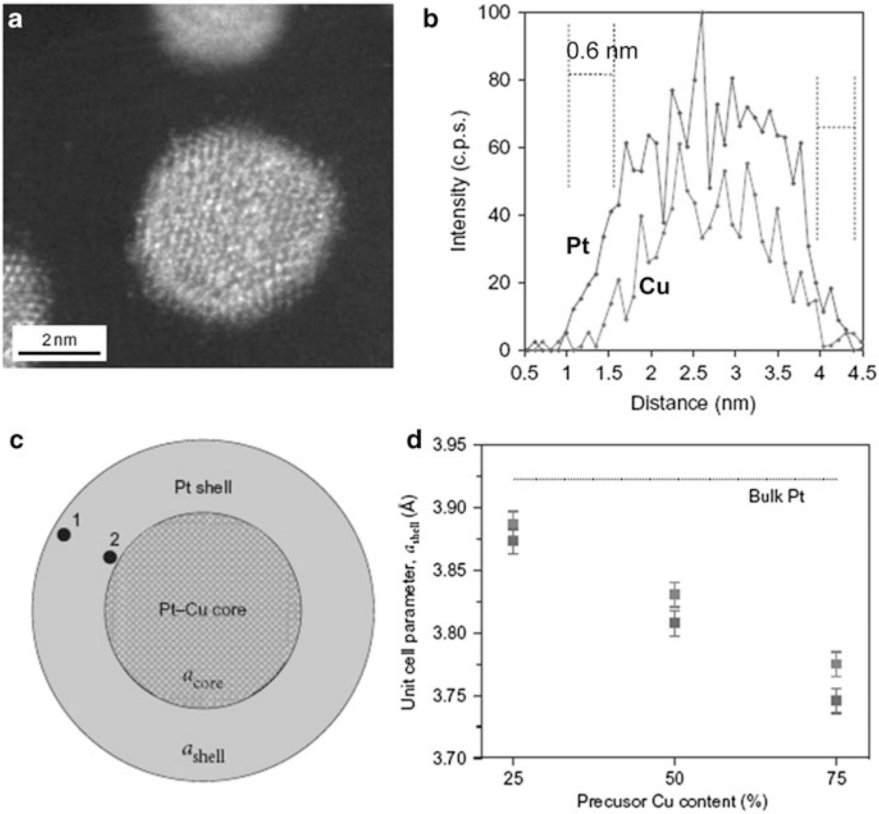

Fig. 18.7 (**a**) HAADF-STEM image of the dealloyed PtCu3 nanoparticle, showing an outer Pt-enriched shell (which images *brightly*) and a Cu-rich alloy core (which images *less brightly* than the shell). Contrast variations in the HAADF-STEM images relate to the atomic number (Z) difference between Pt and Cu, i.e., the so-called Z-contrast imaging. (**b**) EDX line profile across an individual dealloyed PtCu$_3$ nanoparticle acquired using a probe-corrected STEM with a probe size of ~0.2 nm. The thickness of the Pt-enriched shell was determined to be ~0.6 nm as shown by the *dash lines*. (**c**) A simple structural two-phase core–shell model for the dealloyed nanoparticle, i.e., pure Pt layers, surrounds an alloy particle core, where a_{shell} and a_{core} represent the average lattice parameters in shell and core, respectively. (**d**) Determination of a_{shell} as a function of the Cu content in the precursors annealed at 950 °C (*bottom*) and 800 °C (*top*). All alloys show Pt shells with lattice parameters below that of pure bulk Pt (*dotted line*) (reprint with permission from ref. [43])

The strain in the deposited platinum layers was measured by low-energy electron diffraction (LEED), as shown in Fig. 18.8a. An increase of the thickness of Pt layers resulted in decreased strain, indicating that the strain was relaxing in the Pt layers. Meanwhile, we have used X-ray emission spectroscopy (XES) and X-ray adsorption spectroscopy (XAS) to probe the occupied and unoccupied portion of the Pt-projected d bands, as illustrated in Fig. 18.8b. The sketch of Fig. 18.8c on left

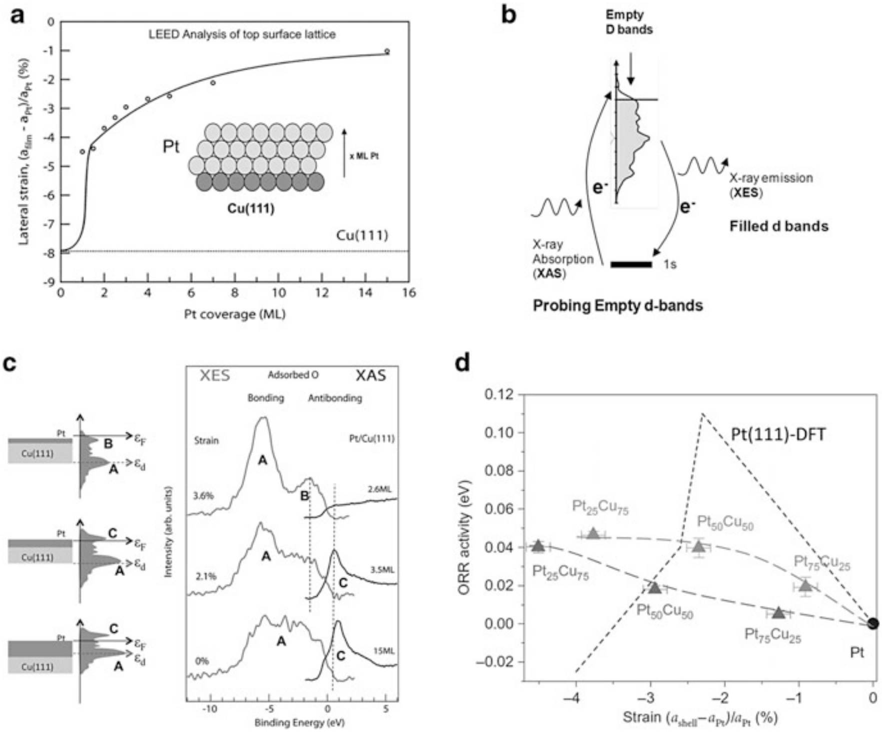

Fig. 18.8 (**a**) Compressive strains in Pt overlayers deposited on Cu (111), deduced from LEED patterns as a function of film thickness. (**b**) An illustration of probing the occupied and unoccupied portion of the Pt-projected d bands by using XES and XAS, respectively. (**c**) In-plane polarized oxygen K-edge XAS and normal emission oxygen K-edge XES of 0.2 ML of oxygen chemisorbed on Pt layers on Cu(111) with different thickness. (**d**) Experimental and predicted relationships between ORR activity and lattice strain in units of $kT \cdot \ln(j_{s,alloy}/j_{s,Pt})$, $T = 298$ K. The experimental ORR activities of the two families of dealloyed Pt–Cu nanoparticles (precursors prepared at 850 °C (*top*) and 900 °C (*bottom*)) are plotted as a function of strain in the particle shell (*dash lines* are to guide the eye). The *short dashed line* is the DFT-predicted volcano-shaped trend of the ORR activity for a Pt(111) single-crystal slab under isotropic strain. Moderate compressive lattice strain is predicted to enhance the rate of ORR catalysis (reprint with permission from ref. [43])

indicates three different thicknesses of the Pt overlayer (shell) on the Cu substrate (core). The sketches of the d bands on left stem from density functional calculation (DFT) predictions. The experimental XES and XAS results show that as the shell becomes thinner (top case), unoccupied states (still visible in XAS in bottom experiment) become occupied (top experiment) and thus show up in the XES curve rather than in the XAS curve, leading to a downward shift of the Pt d-band center.

Nørskov and coworkers have successfully developed a d-band theory in relating the adsorption properties of rate-limiting intermediates in catalytic process to electronic structure of catalyst surfaces [44, 45]. According to this theory, the valence p-level of the ORR intermediate adsorbate (O/OH) forms bonding and antibonding states with the Pt d-band. Population of any antibonding state would lead to Pauli repulsion, and the Pt–O bond strength would be thereby weakened. A downward shift of the Pt d-band pulls more of the antibonding states below the Fermi level, which results in increasing occupation and weaker adsorbate bonding [9]. To understand the relationship between surface strain, Pt–O binding energy, and the catalytic ORR reactivity, we further carried out DFT calculations for a strained Pt(111) model surface (the dashed line in Fig. 18.8d). The DFT calculations derived a "volcano" relation between the predicted ORR rate and the strain, implying that compressive strain first enhances the overall ORR activity by reducing the binding energy of intermediate oxygenated adsorbate and, thereby, lowers the activation barriers for proton- and electron-transfer processes. Beyond a critical strain, however, the binding becomes too weak, and the catalytic activity is predicted to decrease because of an increased activation barrier for either oxygen dissociation or the formation of oxygenated intermediate.

Correlating the experimental synthesis–strain–activity data of the two sets of dealloyed core–shell nanoparticles (Fig. 18.8d), we provide the experimental evidence that the deviation of the Pt-shell lattice parameter from that of bulk Pt, i.e., the lattice strain in the shell, is the controlling factor in the catalytic enhancement of dealloyed Pt nanoparticles. In each set of dealloyed Pt–Cu catalysts, it is unambiguously confirmed that a moderate increase of the compressive strain in the Pt shell resulted in a higher ORR activities, which correlates well with our DFT predictions. Nevertheless, we did not observe a decrease in the experimental activity values on the left side of the volcano curve, as predicted by the DFT calculations. This is related to compressive-strain relaxation in the Pt shells, which prevent the buildup of high strain energy. Pt atoms adjacent to the Pt–Cu cores (Fig. 18.7c, point 2) adopt a lattice parameter closer to that of the cores, but outer Pt-shell atoms (Fig. 18.7c, point 1) relax toward the lattice constant of bulk Pt. Hence, the real surface strain is less than a_{shell}, which is an average strain in the Pt shell; if the real surface strain was plotted in Fig. 18.8d, we would expect a shift of all experimental data points to the right. Figure 18.8d also reveals that the set of dealloyed nanoparticle catalysts prepared at the higher annealing temperature exhibits reduced activity at comparable lattice strain in the particle shells, presumably because of differences in the mean particle size. Hence, our strain-related conclusion generally refers to particles of comparable size.

18.3.3 Extension to Other Dealloyed Transition-Metal-Rich Pt-Bimetallic Catalysts

The dealloyed core–shell nanoparticle concept revealed in the dealloyed Pt–Cu catalysts can be generalized in a broad range of transition-metal-rich Pt-bimetallic catalysts such as Pt–Co, Pt–Ni, and Pt–Fe alloys. As suitable candidates for the ORR catalysts, these Pt-bimetallic alloys have been extensively investigated during the past years, and most of these studies were focused on a stoichiometry of around Pt_3M [1, 12–14, 46].

Mani et al. [47] reported a comparative study of different dealloyed Pt binary PtM_3 (M = Cu, Co, and Ni) catalysts for use in PEMFC cathode. All the catalysts were prepared by impregnation and followed annealing protocol, after which they were implemented in single fuel cell MEA and activated by in situ electrochemical dealloying. The dealloyed binary PtM_3 catalysts showed more than a threefold improvement for M = Co, Cu and close to a threefold improvement for M = Ni in terms of Pt-mass activity of the single fuel cell compared to a 45 wt% Pt/C reference cathode catalyst. An overview of the Pt-mass ORR activities reported in further reports suggests an order of dealloyed $PtCu_3$ > dealloyed $PtCo_3$ > dealloyed $PtNi_3$ [47–50]. Nevertheless, the synthesis based on the impregnation and annealing used here generally resulted in nanoparticles with a broad size distribution and different alloy degrees, which make direct result explanation difficult. Further studies in preparing homogenous nanoparticles are therefore needed to clarify the effect of different transition metals (Fig. 18.9).

The enhanced ORR activities of the dealloyed Pt binary catalysts could be related to a similar lattice-strain effect as revealed in the dealloyed $PtCu_3$ catalysts. However, it is still unclear what the origin of the different activities of different dealloyed PtM_3 catalysts is. Regarding their comparable atomic radius, the alloy elements Co, Ni, and Cu are assumed to induce a similar extent of lattice strain. Nevertheless, due to different redox chemistry of the transition metals, different extent of metal dissolution may exist [47], which might result in different core–shell fine structures and hence different activities.

The advantage of using transition-metal-rich alloys was further demonstrated by composition-dependent activity studies. In a series of Pt_3Co, PtCo, and $PtCo_3$, a maximum Pt-mass activity was observed in dealloyed $PtCo_3$ catalyst in O_2-saturated $HClO_4$ solution [51]. By preparation of monodisperse single-phase $Pt_{1-x}Ni_x$ catalysts, a ORR activity maximum was also uncovered at initial Ni content in the range of 70–75 at% [52, 53]. These results are consistent with the reports in dealloyed thin-film catalysts by researchers at 3M company, where a maximum ORR activity was observed in dealloyed $Pt_{1-x}Co_x$ catalyst with $x = 0.66$–0.67 and in dealloyed $Pt_{1-x}Ni_x$ catalyst with $x = 0.69$ [54, 55]. Nevertheless, there is discrepancy on the optimized initial composition in several other reports, where the highest ORR mass activity was found to be at a lower transition-metal content around 50 at% (e.g., $Pt_{50}Ni_{50}$ in both $Pt_{1-x}Ni_x$ nanoparticles [56] and $Pt_{1-x}Ni_x$ thin-film catalysts [57]). This discrepancy may possibly originate from different structure of precursor alloy catalyst (such as particle size and alloying degree) and also different dealloying protocols.

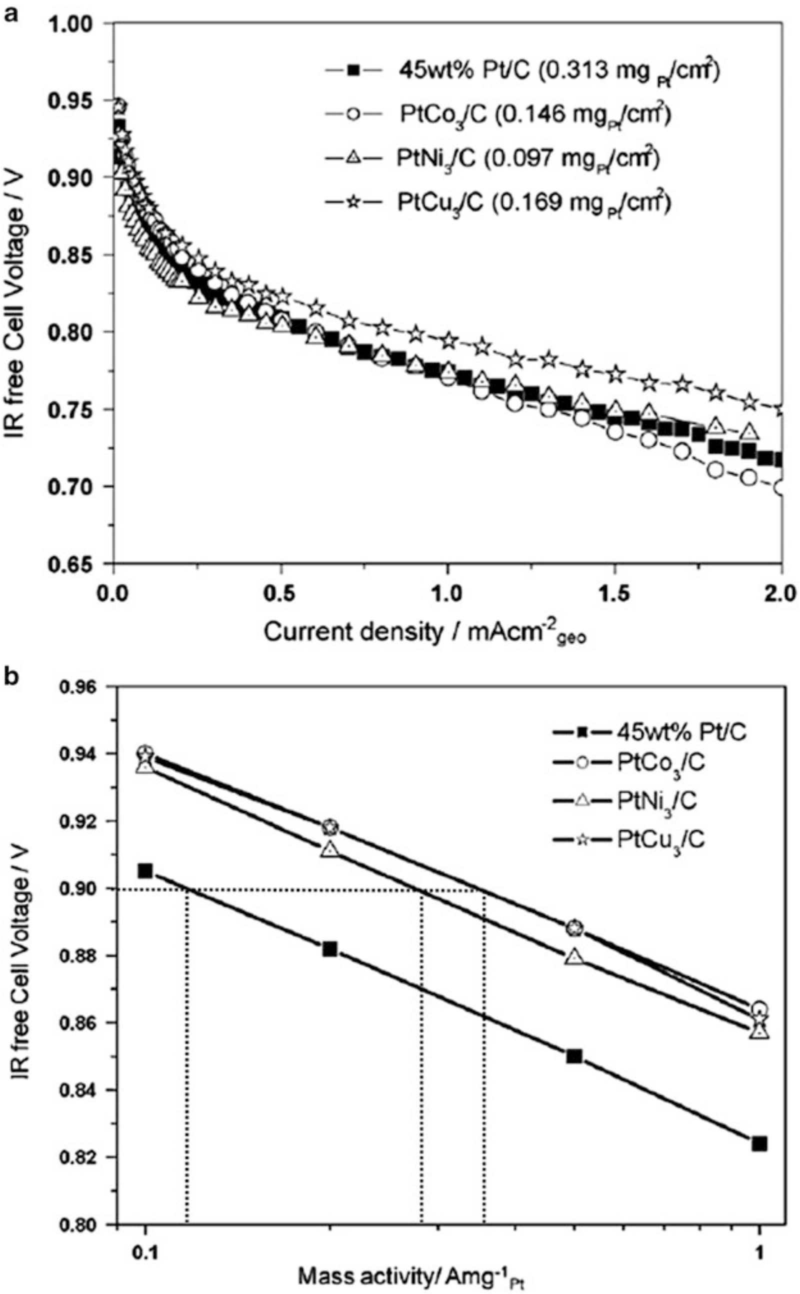

Fig. 18.9 (**a**) Current–voltage characteristics of 10 cm^2 single H_2/O_2 fuel cells using dealloyed $PtCu_3$, dealloyed $PtNi_3$, and dealloyed $PtCo_3$ cathode catalyst, in comparison with standard Pt cathode catalysts. (**b**) Pt-mass activities at 0.9 V of the dealloyed Pt-bimetallic cathode catalysts (reprint with permission from ref. [47])

18.4 Dealloyed Pt-Based Ternary Nanoparticle Catalysts

By introducing a third kind of transition-metal element, Pt ternary alloy catalysts attract considerable interests since the possibility of fine-tuning the geometric/electronic structures for further improved catalytic activity [58, 59]. Here, we show that the dealloying concept can be further applied in Pt ternary alloy catalysts, demonstrating a powerful approach to optimize the structure and activities of Pt alloy catalysts.

Figure 18.10 shows the ORR activities of dealloyed Pt–Cu–Co ternary catalysts with different Cu/Co compositions measured on a single 10 cm^2 single H_2/O_2 fuel cell [41]. The polarization curves for all the ternary catalysts shifted to more positive potentials compared to Pt catalyst, indicating lower overpotentials and hence higher catalytic activities. The dealloyed $Pt_{20}Cu_{20}Co_{60}$ exhibited unprecedented ORR activities of up to 0.5 A $mg^{-1}{}_{Pt}$, substantially surpassing the technological Pt-mass activity target in fuel cells (0.44 A $mg^{-1}{}_{Pt}$). The synergy between Co and Cu can be revealed by improved mass activity of dealloyed $Pt_{20}Cu_{20}Co_{60}$ compared to both dealloyed $PtCo_3$ and dealloyed $PtCu_3$ in the fuel cell test [41, 47]. Similar activity improvements were also reported in dealloyed $Pt_{20}Ni_{60}Cu_{20}$, $Pt_{20}Ni_{60}Fe_{20}$ and $Pt_{20}Ni_{60}Co_{20}$ catalyst compared to dealloyed $PtNi_3$ catalysts [47].

In principle, a similar compressive lattice-strain effect as revealed in the dealloyed Pt binary catalysts could also account for the higher activity of dealloyed Pt ternary catalysts compared with the pure Pt catalysts. Nevertheless, the origin of the activity enhancement for dealloyed ternary catalyst compared to the dealloyed Pt binary catalysts is still far from well understood. Exactly what kind of roles that the third element plays needs further studies.

18.5 Stability of Dealloyed Pt-Based Nanoparticle Catalysts

Stability is a critical criterion with the same importance as activity for the viability of an ORR catalyst in practical fuel cells. Since the ORR potential at the cathode of PEMFCs is up to 1.2 V, a carbon-supported Pt nanoparticle catalyst can exhibit several degradation mechanisms: (1) Ostwald ripening associated with Pt dissolution/redeposition, (2) particle migration and coalescence, and (3) carbon corrosion [60]. For Pt alloy catalysts, dissolution of non-noble element at high potentials becomes an additional mechanism for the catalyst instability. Dealloyed core–shell nanoparticles with protective Pt shells are assumed to be stable against further degradation associated with the dissolution of non-noble element. However, Mayrhofer and coworkers found that there was a surface segregation of the oxophilic non-noble metals initiated by the adsorption of oxygenated species (such as OH_{ad}) under the reactive conditions [61]. Such adsorption-induced surface segregation

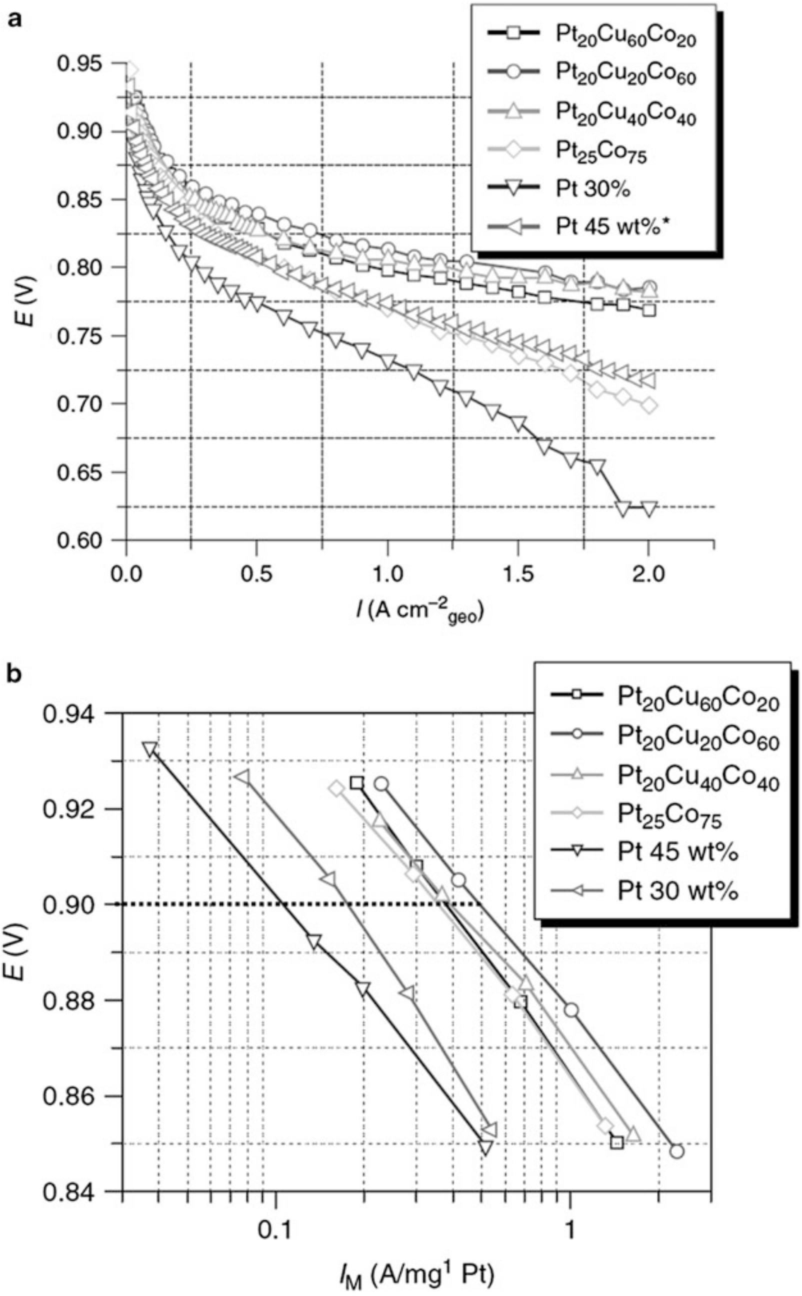

Fig. 18.10 (**a**) Current–voltage characteristics of 10 cm^2 single H_2/O_2 fuel cells using dealloyed Pt–Co–Cu cathode catalyst, in comparison with dealloyed $PtCo_3$ cathode catalyst and standard Pt cathode catalysts. (**b**) Pt-mass activities at 0.9 V of the dealloyed Pt–Co–Cu cathode catalysts (reprint with permission from ref. [41])

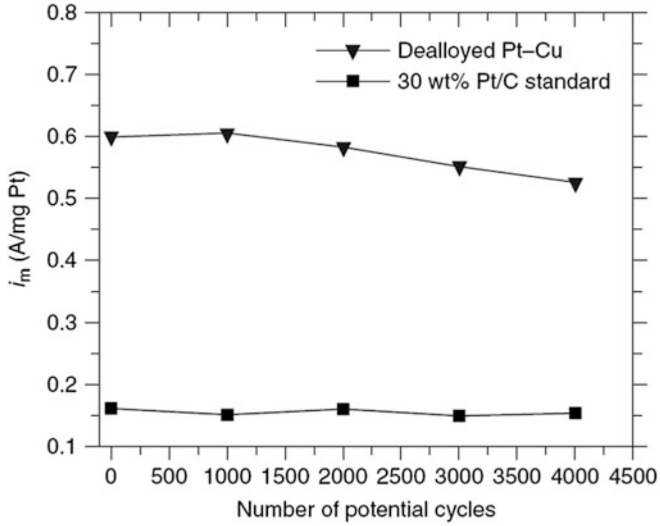

Fig. 18.11 Stability test of a dealloyed $PtCu_3$ catalyst prepared at 600 °C by potential cycles between 0.6 and 1 V/RHE in oxygen-saturated 0.1 M $HClO_4$ (100 mV s^{-1}) (reprint with permission from ref. [27])

would result in continued dissolution of the non-noble metals, which is detrimental to the stability of the particle-core composition and hence the lattice-strain-controlled ORR activities of the dealloyed Pt catalysts.

Figure 18.11 presents the evolution of the mass activity of a dealloyed $PtCu_3$ catalyst during 4,000 potential cycles between 0.6 and 1.0 V/RHE at 100 mV s^{-1}, indicating that it is able to maintain the activity enhancement over the Pt benchmark for a long period [27]. Nevertheless, continued degradation of the catalytic activity of dealloyed $PtCu_3$ is clearly shown.

The influence of different non-noble alloy component (e.g., Cu, Co, Ni, Fe) on the catalyst stability has not been well addressed until now. In a recent study, the specific activity of dealloyed $PtCu_3$ decreased 24 % after 10,000 cycles between 0.5 and 1.0 V while that decreased 42 % for dealloyed $PtCo_3$ [48]. The loss of Cu/Co in the catalysts was confirmed by compositional analysis using EDX. In comparison, dealloyed $PtNi_3$ showed 50 % decrease in the specific activity after the same test protocol [50]. It therefore seems that the stability of the different catalysts is in the order of dealloyed $PtCu_3$ > dealloyed $PtCo_3$ > dealloyed $PtNi_3$ [50]. This difference is likely due to the different redox chemistry or different Pt–M interactions of different alloy elements, but further systematic studies are needed to verify this hypothesis.

We also investigated the stability of dealloyed $Pt_{25}Cu_{75}$ and dealloyed $Pt_{20}Cu_{20}Co_{60}$ catalysts in a realistic fuel cell MEA operated at 80 °C by voltage cycling from 0.5 to 1.0 V at 100 mV s^{-1} (Fig. 18.12) [62]. After 30,000 voltage cycles, both dealloyed $Pt_{25}Cu_{75}$ and dealloyed $Pt_{20}Cu_{20}Co_{60}$ were able to retain their mass and specific activity advantage relative to Pt/C. The mass activity of the

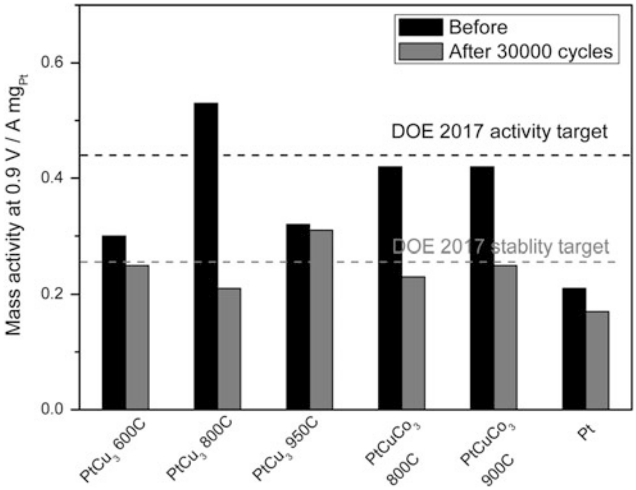

Fig. 18.12 Stability measurement of various dealloyed $PtCu_3$ and dealloyed $PtCuCo_3$ catalyst compared to pure Pt standard cathode catalysts in single fuel cell MEAs. The Pt-mass activities at 0.9 V are plotted before and after 30,000 voltage cycles (0.5–1.0 V, $100 mV s^{-1}$). Cell conditions: anode H_2/cathode N_2, 100 % relative humidity, 80 °C (reprint with permission from ref. [62])

dealloyed $Pt_{25}Cu_{75}$ prepared at 950 °C was even almost unchanged. Attractively, dealloyed $PtCuCo_3$ almost fulfilled both the DOE activity and stability target of 2017 (the dash lines in Fig. 18.12), which again highlights the benefit of dealloyed ternary catalysts compared to binary catalysts. Nevertheless, there is a disadvantage for Cu-containing catalysts that, once Cu was leached out, it can diffuse to and redeposit on the anode side, which would cause continuous performance loss of the anode side during long-term operation. Further optimization of the composition and structure of a wide range of ternary catalysts is currently underway.

18.6 Core–Shell Fine Structures: Understanding the Structure–Activity–Durability Relationships at Nano-/Atomic Scale

So far, we have presented several types of dealloyed Pt binary and ternary nanoparticle catalysts, which showed substantially enhanced ORR activities compared with pure Pt. The activity enhancement originated from a lattice-strain-controlled mechanism. However, it is still unclear why different transition metals resulted in different activities and stabilities and how particle structural characteristics such as size, shape, and composition would come into play. To understand these issues, it is important to achieve an atomic-scale understanding of the core–shell fine structures of the dealloyed nanoparticles, i.e., Pt-shell thickness as well as compositional profile across the particle core, which play a critical role in the lattice-strain-controlled ORR activities.

The core–shell structure character of dealloyed Pt catalysts has been disclosed by various techniques such as anomalous X-ray diffraction [43], small-angle X-ray scattering [42], X-ray photoelectron spectroscopy [27, 43], and TEM/STEM [43, 63–69]. Among them, TEM/STEM is an indispensable tool for characterization at nano-/atomic scale in real space. In particular, the recently developed aberration-corrected TEM [70, 71] provides significantly improved spatial resolution down to sub-Ångstrom scale. Due to much decreased contrast delocalization and hence high accuracy on surface atomic structures, direct evidence of a gradient compressive strain on the Pt-rich shell was provided using aberration-corrected high-resolution TEM [67]. Meanwhile, combined with spectroscopic techniques such as energy-dispersive X-ray spectra (EDX) and electron energy loss spectroscopy (EELS), the convergent electron beam in the probe-corrected STEM becomes a powerful tool in revealing the compositional distribution in individual nanoparticles at atomic scale. Thanks to this advance, core–shell fine structures of the dealloyed nanoparticles were revealed at atomic scale, enabling a comprehensive understanding of the structure–activity relationships [23, 53, 63–66, 68, 69, 72, 73].

18.6.1 Size-Dependent Core–Shell Fine Structures

Particle size is an important parameter that strongly influences the activity of catalyst nanoparticles. There are extensive studies on the particle size effect of Pt particles on the ORR catalysis, showing that the area-specific activity increased as the particle size increases due to a lower portion of low-coordinated Pt atoms on the edges and corners [13, 74–77]. Taking the surface area into account, this leads to a maximum mass activity at particle size of around 3–5 nm. Similar trends were also reported in Pt_3M alloy catalysts [13, 78, 79]. For dealloyed nanoparticles, situation becomes more complex as the morphologies and core–shell structures were found to be dependent on the particle size, being an additional contribution to the overall size effect.

Oezaslan et al. found that there were three distinctly different size-dependent morphology regimes in dealloyed $PtCu_3$ and $PtCo_3$ particles, as illustrated in Fig. 18.13 [69]. When smaller than 10 nm, the dealloyed particles generally showed a simple core–shell structure. When the size was between 10 and 20 nm, the dealloyed particles showed more complex core/shell structure, where the Co-/Cu-rich regions split into multiple separate core regions, indicating a near-surface enrichment of Co/Cu. At even larger sizes (greater than 30 nm), surface pits and nanopores coexisting with multiple cores were formed. The appearance of porous dealloyed $PtCu_3$/$PtCo_3$ nanoparticle at larger particle size is also shown in other reports, although the detailed critical sizes may be different [65]. The uncovered size-dependent morphology seems to be general in a wide range of dealloyed

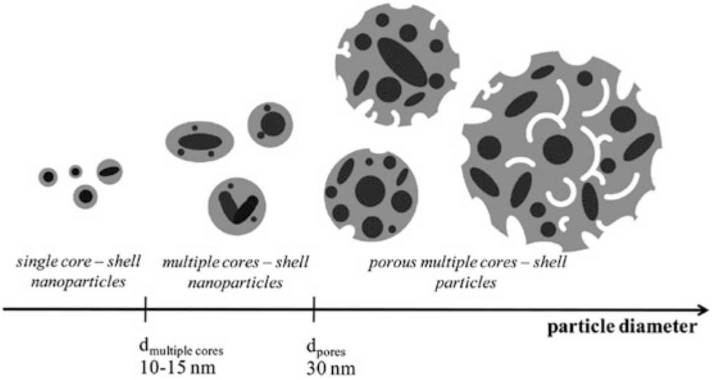

Fig. 18.13 Illustration of the evolution of size-dependent morphology and core–shell fine structures of dealloyed $PtCu_3$ and $PtCo_3$ nanoparticle catalysts (reprint with permission from ref. [69])

Pt nanoparticles. In monodisperse dealloyed $PtNi_3$ nanoparticles, Snyder et al. found that particles with a size greater than approximately 15 nm tended to form nanoporous structure, while particles smaller than 15 nm generally showed nonporous structure [80].

The observed size-dependent morphology of the dealloyed nanoparticle provides an important insight into the existing material gap between dealloyed nanoparticles and highly porous bulk-like bimetallic particles in corrosion science as we previously discussed. The occurrence of porous particles at larger sizes can be explained well from an atomic-scale description of the dealloying process [30, 36, 37]. In larger particles or even bulk bimetallic alloys, diffusion of residual more noble atoms along the extended surface is relatively slow, which results in Rayleigh surface instabilities promoting the formation of nanoporosity. In contrast, in small enough alloy nanoparticles, the lower average coordination of the noble-metal atoms on the surface increases their surface diffusion rate, suppressing the formation of porosity and leading to solid core–shell nanoparticles.

It is still unclear that which kind of core–shell structure contributes the most to the macroscopic overall catalytic activities of the dealloyed catalyst particle ensemble. Researchers at General Motors found that the single-core–shell nanoparticles provided most of the activity for dealloyed $PtCu_3$ catalyst [3], while Snyder et al. found that nanoporous dealloyed $PtNi_3$ particles exhibited higher mass activity and specific activity compared to the dealloyed solid nanoparticles $PtNi_3$ with smaller sizes [80]. Further studies are needed to clarify this issue.

18.6.2 Composition-Dependent Core–Shell Fine Structures

As previously shown in Sect. 18.3.2, the initial compositions of the precursor alloy nanoparticles have a great influence on the activities of the dealloyed nanoparticles.

A higher initial content of the transition metals is expected to result in a higher extent of compressive strain over the formed Pt shell and hence possibly higher ORR activity.

Recently, atomic-scale STEM analysis revealed more complex effects of the initial composition on the core–shell fine structures of dealloyed nanoparticles. By STEM/EDX analysis of a series of $Pt_{1-x}Ni_x$ nanoparticles (Pt_3Ni to $PtNi_3$), Wang et al. found that a higher initial Ni composition resulted in a higher extent of dissolution of Ni atoms, which resulted in a larger Pt-shell thickness [56] (Fig. 18.14). As the strain energy cost would increase with the Pt-shell thickness, there must be a strain relaxation over the shell-thickness direction, leading to a lower extent of the compressive strain on the outmost Pt surface and thus lower ORR activities. Very recently, STEM/EELS studies found that at further larger initial composition, the Pt-shell thickness decreased again [53]. Apart from the different Pt-shell thickness, an unusual Ni-enriched inner shell at subsurface layers was also uncovered in the dealloyed Pt_xNi_{1-x} nanoparticles with higher initial Ni compositions. The composition and the location of the Ni-enriched inner shells are strongly dependent on the initial composition, which further controls the degree of the surface lattice strain and hence the ORR activity of the Pt shell. Therefore, the composition-dependent activity is controlled by a combined effect of Pt-shell thickness and compositional distributions from the subsurface layers to the particle core.

18.6.3 Atomic-Scale Mechanisms of Catalyst Instability

As described in Sect. 18.5, dealloyed Pt catalysts suffered from activity degradation during long-term potential cycling. Both particle growth and dissolution of less-noble transition metals after the potential cycling were confirmed by TEM and EDX analysis. The particle growth was likely caused by a similar instability mechanism as that for Pt, i.e., Ostwald ripening and coalescence, which would lead to a lower surface area. The dissolution of the transition metals would lower down the lattice-strain effect and hence the specific activity. The extent of the dissolution can be dependent on the nature of the transition metals. For instance, dealloyed $PtCu_3$ catalyst exhibited higher Cu content ($Pt_{66}Cu_{34}$) after 10,000 potential cycles compared to dealloyed $PtCo_3$, which changed to $Pt_{83}Co_{17}$ [48]. The higher residual content of Cu can help maintain the lattice strain on the Pt shell and hence results in higher stability. This result suggests that a rational selection of the transition metals is important to achieve high catalyst stability.

Using aberration-corrected STEM and EELS mapping, Xin et al. performed a statistical analysis of elemental distributions in hundreds of Pt_3Co nanoparticles across different stages of catalyst aging in PEMFCs, revealing a surprising coupling among different instability mechanisms (Co leaching, Ostwald ripening, and particle coalescence) [68]. The Pt_3Co catalyst was chemically leached from a PtCo

Fig. 18.14 Aberration-corrected STEM and EDX line scan analysis of the core–shell fine structures of dealloyed $Pt_{1-x}Ni_x$ nanoparticles (reprint with permission from ref. [56])

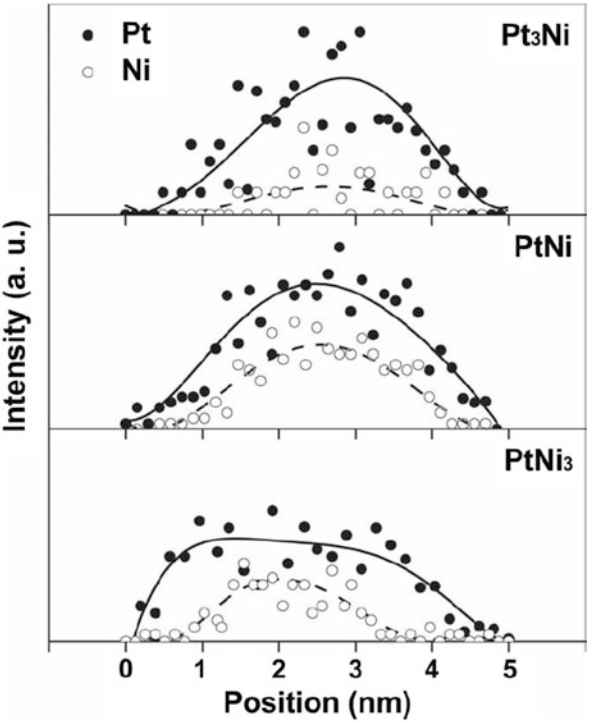

precursor alloy and exhibited single-core–shell structure with a uniform Pt-shell thickness of around 0.7 nm (~3 monolayers). After 30,000 cycles between 0.6 and 1.0 V in a fuel cell MEA, core–shell features were clearly disclosed besides the apparent particle coarsening: firstly, unlike single-core–shell particles before stability test, multiple alloy cores were found in many particles with more complex shape after long-term potential cycling, showing a signature of significant particle coalescence. Such particle coalescence was further clearly visualized by 3-D electron tomography [72]. Secondly, much thicker Pt shells were found, and the larger the particles, the larger the Pt-shell thickness. Interestingly, the increased Pt-shell thickness was found to originate from Pt redeposition through Ostwald ripening instead of Co dissolution. The Co dissolution was suspected to be from smaller particles that had dissolved completely. This is consistent with the Ostwald ripening mechanism, that is, the preferential dissolution of Pt atoms in smaller particles exposed subsurface Co to be co-dissolved, while redeposition of Pt atoms on larger particles protected their Co-containing cores and resulted in thicker Pt shell. Finally, the coalescent multi-core particles exhibited not only larger particle size but also much larger Pt-shell thickness compared to single-core nanoparticles. This may be because there were more Pt redeposition on the irregular coalescent particles to minimum the surface curvature, suggesting a complex interplay between coalescence and Ostwald ripening mechanism. The thickening of Pt shell especially at larger particles after long-term potential cycling was further confirmed by Carlton et al. [66].

The increased Pt-shell thickness associated with Pt redeposition due to the Ostwald ripening provides a new insight on the instability mechanisms for dealloyed Pt-bimetallic catalyst. Apart from the particle growth that leads to a lowered specific surface area during the Ostwald ripening, the increased Pt-shell thickness gradually relaxed the lattice strain and is a critical reason for the activity degradation. The uncovered Pt-shell thickening due to Ostwald ripening suggests that durability of the catalysts can be further improved through advance in the synthesis of monodisperse nanoparticles. Further studies are also needed to investigate the relative contribution of Pt redeposition and transition-metal dissolution to the increased Pt-shell thickness.

18.7 Conclusion

We have reviewed the family of dealloyed Pt-based nanoparticle electrocatalysts for the electroreduction of oxygen at PEMFC cathodes, which were synthesized by selective dissolution of less-noble atoms from Pt alloy nanoparticle precursors. The dealloyed $PtCu_3$ catalyst showed a promising improvement factor of 4–6 times on the Pt-mass ORR activity compared to a state-of-the-art Pt catalyst. The highly active dealloyed Pt catalysts can be implemented inside a realistic MEA of PEMFCs, where an in situ voltammetric dealloying procedure was used to constructed catalytically active nanoparticles. The core-shell structural character of the dealloyed nanoparticles was confirmed by advanced STEM and elemental line profile analysis. The lattice-contracted transition-metal-rich core resulted in a compressive lattice strain in the Pt-rich shell, which, in turn, favorably modified the chemisorption energies and resulted in improved ORR kinetics.

The dealloyed core–shell nanoparticle concept was successfully extended to a wide range of transition-metal-rich Pt bimetallics ($PtCo_3$ and $PtNi_3$) and Pt trimetallics (Pt–Co–Cu, Pt–Ni–Cu, Pt–Ni–Co, etc.), demonstrating a general strategy to modify the surface catalytic properties of noble metals. Stability tests showed that dealloyed Pt catalysts could in principle maintain their high ORR activities over extended period. However, long-term stability is still a critical challenge. To solve this problem, developing dealloyed Pt-ternary catalysts shows to be a promising way.

Thanks to the advanced characterization techniques such as aberration-corrected electron microscopy and spectroscopy, more complex core–shell fine structures of the dealloyed nanoparticles can be studied at atomic scale [53, 73], enabling a comprehensive understanding on the structure–activity–stability relationship. To achieve both high activity and stability, future works will concentrate on understanding and optimizing the core–shell fine structures of dealloyed nanoparticles through the control of particle size, composition and shape, the dealloying conditions, etc.

Acknowledgments We thank Dr. Marc Heggen for continuing support in advanced electron microscopy. We also thank the Zentraleinrichtung für Elektronenmikroskopie (Zelmi) of the Technical University Berlin for their support with TEM and EDS techniques. LG thanks Dr. Rong Yu and Prof. Jing Zhu for their previous instructions. PS thanks Dr. Shirlaine Koh, Dr. Chengfei Yu, Dr. Ratndeep Srivastava, Dr. Prasanna Mani, Dr. Zengcai Liu, and Dr. Mehtap Oezaslan for their support over the past years. PS acknowledges financial support through the Cluster of Excellence in Catalysis (UniCat) funded by DFG and managed by TU Berlin.

References

1. Gasteiger HA, Kocha SS, Sompalli B, Wagner FT (2005) Activity benchmarks and requirements for pt, pt-alloy, and non-pt oxygen reduction catalysts for PEMFCs. Appl Catal B Environ 56(1–2):9–35
2. Gasteiger HA, Markovic NM (2009) Just a dream-or future reality? Science 324(5923):48–49
3. Wagner FT, Lakshmanan B, Mathias MF (2010) Electrochemistry and the future of the automobile. J Phys Chem Lett 1(14):2204–2219
4. Debe MK (2012) Electrocatalyst approaches and challenges for automotive fuel cells. Nature 486(7401):43–51
5. Bashyam R, Zelenay P (2006) A class of non-precious metal composite catalysts for fuel cells. Nature 443(7107):63–66
6. Lefevre M, Proietti E, Jaouen F, Dodelet JP (2009) Iron-based catalysts with improved oxygen reduction activity in polymer electrolyte fuel cells. Science 324(5923):71–74
7. Wu G, More KL, Johnston CM, Zelenay P (2011) High-performance electrocatalysts for oxygen reduction derived from polyaniline, iron, and cobalt. Science 332(6028):443–447
8. Li Y, Zhou W, Wang H, Xie L, Liang Y, Wei F, Idrobo J-C, Pennycook SJ, Dai H (2012) An oxygen reduction electrocatalyst based on carbon nanotube-graphene complexes. Nat Nanotechnol 7(6):394–400
9. Stamenkovic V, Mun BS, Mayrhofer KJJ, Ross PN, Markovic NM, Rossmeisl J, Greeley J, Norskov JK (2006) Changing the activity of electrocatalysts for oxygen reduction by tuning the surface electronic structure. Angew Chem Int Ed 45(18):2897–2901
10. Greeley J, Stephens IEL, Bondarenko AS, Johansson TP, Hansen HA, Jaramillo TF, Rossmeisl J, Chorkendorff I, Norskov JK (2009) Alloys of platinum and early transition metals as oxygen reduction electrocatalysts. Nat Chem 1(7):552–556
11. Zhang JL, Vukmirovic MB, Xu Y, Mavrikakis M, Adzic RR (2005) Controlling the catalytic activity of platinum-monolayer electrocatalysts for oxygen reduction with different substrates. Angew Chem Int Ed 44(14):2132–2135
12. Toda T, Igarashi H, Uchida H, Watanabe M (1999) Enhancement of the electroreduction of oxygen on pt alloys with Fe, Ni, and Co. J Electrochem Soc 146(10):3750–3756
13. M-k M, Cho J, Cho K, Kim H (2000) Particle size and alloying effects of Pt-based alloy catalysts for fuel cell applications. Electrochim Acta 45(25–26):4211–4217
14. Paulus UA, Wokaun A, Scherer GG, Schmidt TJ, Stamenkovic V, Radmilovic V, Markovic NM, Ross PN (2002) Oxygen reduction on carbon-supported Pt-Ni and Pt-Co alloy catalysts. J Phys Chem B 106(16):4181–4191
15. Salgado JRC, Antolini E, Gonzalez ER (2004) Structure and activity of carbon-supported Pt-Co electrocatalysts for oxygen reduction. J Phys Chem B 108(46):17767–17774
16. Yang H, Alonso-Vante N, Leger JM, Lamy C (2004) Tailoring, structure, and activity of carbon-supported nanosized Pt-Cr alloy electrocatalysts for oxygen reduction in pure and methanol-containing electrolytes. J Phys Chem B 108(6):1938–1947

17. Yang H, Vogel W, Lamy C, Alonso-Vante N (2004) Structure and electrocatalytic activity of carbon-supported Pt-Ni alloy nanoparticles toward the oxygen reduction reaction. J Phys Chem B 108(30):11024–11034
18. Zhang J, Mo Y, Vukmirovic MB, Klie R, Sasaki K, Adzic RR (2004) Platinum monolayer electrocatalysts for O_2 reduction: Pt monolayer on Pd(111) and on carbon-supported Pd nanoparticles. J Phys Chem B 108(30):10955–10964
19. Zhang J, Lima FHB, Shao MH, Sasaki K, Wang JX, Hanson J, Adzic RR (2005) Platinum monolayer on nonnoble metal-noble metal core-shell nanoparticle electrocatalysts for O_2 reduction. J Phys Chem B 109(48):22701–22704
20. Zhang JL, Vukmirovic MB, Sasaki K, Nilekar AU, Mavrikakis M, Adzic RR (2005) Mixed-metal Pt monolayer electrocatalysts for enhanced oxygen reduction kinetics. J Am Chem Soc 127(36):12480–12481
21. Adzic RR, Zhang J, Sasaki K, Vukmirovic MB, Shao M, Wang JX, Nilekar AU, Mavrikakis M, Valerio JA, Uribe F (2007) Platinum monolayer fuel cell electrocatalysts. Top Catal 46 (3–4):249–262
22. Zhang J, Sasaki K, Sutter E, Adzic RR (2007) Stabilization of platinum oxygen-reduction electrocatalysts using gold clusters. Science 315(5809):220–222
23. Wang JX, Inada H, Wu LJ, Zhu YM, Choi YM, Liu P, Zhou WP, Adzic RR (2009) Oxygen reduction on well-defined core-shell nanocatalysts: particle size, facet, and pt shell thickness effects. J Am Chem Soc 131(47):17298–17302
24. Stamenkovic VR, Mun BS, Mayrhofer KJJ, Ross PN, Markovic NM (2006) Effect of surface composition on electronic structure, stability, and electrocatalytic properties of pt-transition metal alloys: Pt-skin versus Pt-skeleton surfaces. J Am Chem Soc 128(27):8813–8819
25. Stamenkovic VR, Fowler B, Mun BS, Wang GF, Ross PN, Lucas CA, Markovic NM (2007) Improved oxygen reduction activity on $Pt_3Ni(111)$ via increased surface site availability. Science 315(5811):493–497
26. Stamenkovic VR, Mun BS, Arenz M, Mayrhofer KJJ, Lucas CA, Wang GF, Ross PN, Markovic NM (2007) Trends in electrocatalysis on extended and nanoscale Pt-bimetallic alloy surfaces. Nat Mater 6(3):241–247
27. Koh S, Strasser P (2007) Electrocatalysis on bimetallic surfaces: modifying catalytic reactivity for oxygen reduction by voltammetric surface dealloying. J Am Chem Soc 129(42):12624–12625
28. Bardal E (2004) Corrosion and protection. Springer, London
29. Raney M (1927) Method of producing finely divided nickel. US Patent 1,628,190
30. Erlebacher J, Aziz MJ, Karma A, Dimitrov N, Sieradzki K (2001) Evolution of nanoporosity in dealloying. Nature 410(6827):450–453
31. Ding Y, Erlebacher J (2003) Nanoporous metals with controlled multimodal pore size distribution. J Am Chem Soc 125(26):7772–7773
32. Ding Y, Chen MW, Erlebacher J (2004) Metallic mesoporous nanocomposites for electrocatalysis. J Am Chem Soc 126(22):6876–6877
33. Ding Y, Kim YJ, Erlebacher J (2004) Nanoporous gold leaf: “ancient technology”/advanced material. Adv Mater 16(21):1897–1900
34. Snyder J, Asanithi P, Dalton AB, Erlebacher J (2008) Stabilized nanoporous metals by dealloying ternary alloy precursors. Adv Mater 20(24):4883–4886
35. Snyder J, Fujita T, Chen MW, Erlebacher J (2010) Oxygen reduction in nanoporous metal-ionic liquid composite electrocatalysts. Nat Mater 9(11):904–907
36. Erlebacher J (2004) An atomistic description of dealloying – porosity evolution, the critical potential, and rate-limiting behavior. J Electrochem Soc 151(10):C614–C626
37. Erlebacher J (2011) Mechanism of coarsening and bubble formation in high-genus nanoporous metals. Phys Rev Lett 106(22):225504
38. Mani P, Srivastava R, Strasser P (2008) Dealloyed Pt-Cu core-shell nanoparticle electrocatalysts for use in PEM fuel cell cathodes. J Phys Chem C 112(7):2770–2778
39. Oezaslan M, Hasche F, Strasser P (2011) In situ observation of bimetallic alloy nanoparticle formation and growth using high-temperature XRD. Chem Mater 23(8):2159–2165

40. Strasser P, Koha S, Greeley J (2008) Voltammetric surface dealloying of Pt bimetallic nanoparticles: an experimental and DFT computational analysis. Phys Chem Chem Phys 10(25):3670–3683
41. Srivastava R, Mani P, Hahn N, Strasser P (2007) Efficient oxygen reduction fuel cell electrocatalysis on voltammetrically dealloyed Pt-Cu-Co nanoparticles. Angew Chem Int Ed 46(47):8988–8991
42. Yu CF, Koh S, Leisch JE, Toney MF, Strasser P (2008) Size and composition distribution dynamics of alloy nanoparticle electrocatalysts probed by anomalous small angle X-ray scattering (ASAXS). Faraday Discuss 140:283–296
43. Strasser P, Koh S, Anniyev T, Greeley J, More K, Yu CF, Liu ZC, Kaya S, Nordlund D, Ogasawara H, Toney MF, Nilsson A (2010) Lattice-strain control of the activity in dealloyed core-shell fuel cell catalysts. Nat Chem 2(6):454–460
44. Hammer B, Norskov JK (1995) Why gold is the noblest of all the metals. Nature 376 (6537):238–240
45. Mavrikakis M, Hammer B, Norskov JK (1998) Effect of strain on the reactivity of metal surfaces. Phys Rev Lett 81(13):2819–2822
46. Wang C, Chi MF, Li DG, van der Vliet D, Wang GF, Lin QY, Mitchell JF, More KL, Markovic NM, Stamenkovic VR (2011) Synthesis of homogeneous pt-bimetallic nanoparticles as highly efficient electrocatalysts. ACS Catal 1(10):1355–1359
47. Mani P, Srivastava R, Strasser P (2011) Dealloyed binary PtM_3 (M = Cu, Co, Ni) and ternary $PtNi_3M$ (M = Cu, Co, Fe, Cr) electrocatalysts for the oxygen reduction reaction: performance in polymer electrolyte membrane fuel cells. J Power Sources 196(2):666–673
48. Hasché F, Oezaslan M, Strasser P (2011) Activity, stability, and degradation mechanisms of dealloyed $PtCu_3$ and $PtCo_3$ nanoparticle fuel cell catalysts. ChemCatChem 3(11):1805–1813
49. Oezaslan M, Strasser P (2011) Activity of dealloyed $PtCo_3$ and $PtCu_3$ nanoparticle electrocatalyst for oxygen reduction reaction in polymer electrolyte membrane fuel cell. J Power Sources 196(12):5240–5249
50. Hasche F, Oezaslan M, Strasser P (2012) Activity, structure and degradation of dealloyed $PtNi_3$/nanoparticle electrocatalyst for the oxygen reduction reaction in PEMFC. J Electrochem Soc 159(1):B25–B34
51. Oezaslan M, Hasche F, Strasser P (2012) Oxygen electroreduction on $PtCo_3$, PtCo and Pt_3Co alloy nanoparticles for alkaline and acidic PEM fuel cells. J Electrochem Soc 159(4): B394–B405
52. Rudi S, Tuaev X, Strasser P (2012) Electrocatalytic oxygen reduction on dealloyed $Pt_{1-x}Ni_x$ alloy nanoparticle electrocatalysts. Electrocatalysis. doi:10.1007/s12678-12012-10098-x
53. Gan L, Heggen M, Rudi S, Strasser P (2012) Core-shell compositional fine structures of dealloyed Pt_xNi_{1-x} nanoparticles and their impact on oxygen reduction catalysis. Nano Lett 12(10):5423–5430
54. Debe MK, Steinbach AJ, Vernstrom GD, Hendricks SM, Kurkowski MJ, Atanasoski RT, Kadera P, Stevens DA, Sanderson RJ, Marvel E, Dahn JR (2011) Extraordinary oxygen reduction activity of Pt_3Ni_7. J Electrochem Soc 158(8):B910–B918
55. Stevens DA, Wang S, Sanderson RJ, Liu GCK, Vernstrom GD, Atanasoski RT, Debe MK, Dahn JR (2011) A combined rotating disk electrode/x-ray diffraction study of co dissolution from $Pt_{1-x}Co_x$ alloys. J Electrochem Soc 158(8):B899–B904
56. Wang C, Chi MF, Wang GF, van der Vliet D, Li DG, More K, Wang HH, Schlueter JA, Markovic NM, Stamenkovic VR (2011) Correlation between surface chemistry and electrocatalytic properties of monodisperse Pt_xNi_{1-x} nanoparticles. Adv Funct Mater 21(1):147–152
57. Liu Y, Hangarter CM, Bertocci U, Moffat TP (2012) Oxygen reduction reaction on electrodeposited $Pt_{100-x}Ni_x$: influence of alloy composition and dealloying. J Phys Chem C 116(14):7848–7862

58. Wanjala BN, Fang B, Luo J, Chen YS, Yin J, Engehard MH, Loukrakpam R, Zhong CJ (2011) Correlation between atomic coordination structure and enhanced electrocatalytic activity for trimetallic alloy catalysts. J Am Chem Soc 133(32):12714–12727
59. Wang C, Li D, Chi M, Pearson J, Rankin RB, Greeley J, Duan Z, Wang G, van der Vliet D, More KL, Markovic NM, Stamenkovic VR (2012) Rational development of ternary alloy electrocatalysts. J Phys Chem Lett 3(12):1668–1673
60. Shao-Horn Y, Sheng W, Chen S, Ferreira P, Holby E, Morgan D (2007) Instability of supported platinum nanoparticles in low-temperature fuel cells. Top Catal 46(3):285–305
61. Mayrhofer KJJ, Hartl K, Juhart V, Arenz M (2009) Degradation of carbon-supported Pt bimetallic nanoparticles by surface segregation. J Am Chem Soc 131(45):16348–16349
62. Neyerlin KC, Srivastava R, Yu CF, Strasser P (2009) Electrochemical activity and stability of dealloyed Pt-Cu and Pt-Cu-Co electrocatalysts for the oxygen reduction reaction (ORR). J Power Sources 186(2):261–267
63. Chen S, Ferreira PJ, Sheng WC, Yabuuchi N, Allard LF, Shao-Horn Y (2008) Enhanced activity for oxygen reduction reaction on "Pt_3Co" nanoparticles: direct evidence of percolated and sandwich-segregation structures. J Am Chem Soc 130(42):13818–13819
64. Chen S, Sheng WC, Yabuuchi N, Ferreira PJ, Allard LF, Shao-Horn Y (2009) Origin of oxygen reduction reaction activity on "Pt_3Co" nanoparticles: atomically resolved chemical compositions and structures. J Phys Chem C 113(3):1109–1125
65. Dutta I, Carpenter MK, Balogh MP, Ziegelbauer JM, Moylan TE, Atwan MH, Irish NP (2010) Electrochemical and structural study of a chemically dealloyed PtCu oxygen reduction catalyst. J Phys Chem C 114(39):16309–16320
66. Carlton CE, Chen S, Ferreira PJ, Allard LF, Shao-Horn Y (2012) Sub-nanometer-resolution elemental mapping of "Pt_3Co" nanoparticle catalyst degradation in proton-exchange membrane fuel cells. J Phys Chem Lett 3(2):161–166
67. Gan L, Yu R, Luo J, Cheng ZY, Zhu J (2012) Lattice strain distributions in individual dealloyed Pt-Fe catalyst nanoparticles. J Phys Chem Lett 3(7):934–938
68. Xin HL, Mundy JA, Liu ZY, Cabezas R, Hovden R, Kourkoutis LF, Zhang JL, Subramanian NP, Makharia R, Wagner FT, Muller DA (2012) Atomic-resolution spectroscopic imaging of ensembles of nanocatalyst particles across the life of a fuel cell. Nano Lett 12(1):490–497
69. Oezaslan M, Heggen M, Strasser P (2012) Size-dependent morphology of dealloyed bimetallic catalysts: linking the nano to the macro scale. J Am Chem Soc 134(1):514–524
70. Haider M, Uhlemann S, Schwan E, Rose H, Kabius B, Urban K (1998) Electron microscopy image enhanced. Nature 392(6678):768–769
71. Urban KW (2008) Studying atomic structures by aberration-corrected transmission electron microscopy. Science 321(5888):506–510
72. Yu Y, Xin HL, Hovden R, Wang D, Rus ED, Mundy JA, Muller DA, Abruña HD (2012) Three-dimensional tracking and visualization of hundreds of Pt−Co fuel cell nanocatalysts during electrochemical aging. Nano Lett 12(9):4417–4423
73. Heggen M, Oezaslan M, Houben L, Strasser P (2012) Formation and analysis of core–shell fine structures in Pt bimetallic nanoparticle fuel cell electrocatalysts. J Phys Chem C 116(36): 19073–19083
74. Yamamoto K, Imaoka T, Chun WJ, Enoki O, Katoh H, Takenaga M, Sonoi A (2009) Size-specific catalytic activity of platinum clusters enhances oxygen reduction reactions. Nat Chem 1(5):397–402
75. Nesselberger M, Ashton S, Meier JC, Katsounaros I, Mayrhofer KJJ, Arenz M (2011) The particle size effect on the oxygen reduction reaction activity of pt catalysts: influence of electrolyte and relation to single crystal models. J Am Chem Soc 133(43):17428–17433
76. Shao MH, Peles A, Shoemaker K (2011) Electrocatalysis on platinum nanoparticles: particle size effect on oxygen reduction reaction activity. Nano Lett 11(9):3714–3719
77. Perez-Alonso FJ, McCarthy DN, Nierhoff A, Hernandez-Fernandez P, Strebel C, Stephens IEL, Nielsen JH, Chorkendorff I (2012) The effect of size on the oxygen electroreduction activity of mass-selected platinum nanoparticles. Angew Chem Int Ed 51(19):4641–4643

78. Wang C, van der Vilet D, Chang KC, You HD, Strmcnik D, Schlueter JA, Markovic NM, Stamenkovic VR (2009) Monodisperse Pt_3Co nanoparticles as a catalyst for the oxygen reduction reaction: size-dependent activity. J Phys Chem C 113(45):19365–19368
79. Wang C, Wang GF, van der Vliet D, Chang KC, Markovic NM, Stamenkovic VR (2010) Monodisperse Pt_3Co nanoparticles as electrocatalyst: the effects of particle size and pretreatment on electrocatalytic reduction of oxygen. Phys Chem Chem Phys 12(26):6933–6939
80. Snyder J, McCue I, Livi K, Erlebacher J (2012) Structure/processing/properties relationships in nanoporous nanoparticles as applied to catalysis of the cathodic oxygen reduction reaction. J Am Chem Soc 134:8633–8645

Chapter 19
Core–Shell Catalysts in PEMFC Cathode Environments

Sarah Ball

Abstract A wide variety of core–shell electrocatalysts have been investigated in recent years, showing benefits for the oxygen reduction reaction (ORR) in acid electrolytes. Particularly high values of activity per gram of Pt are often measured for core–shell systems in rotating disc electrode (RDE) measurements; however, fewer systems have been tested for performance and durability in membrane electrode assemblies (MEAs) under realistic proton exchange membrane fuel cell (PEMFC) conditions. This chapter discusses the various approaches, both electrochemical and chemical, used to prepare core–shell materials at both small and gram scales and highlights some of the methods used to assess the uniformity of the Pt shell and activity and durability. Available data from MEA testing is reviewed along with some of the implications on overall cost of the use of precious metals within the core. So far, a limited number of core–shell materials have been tested in MEAs, and these data tend to show a lower activity compared to testing at microgram scale under more idealized conditions, due to the combination of catalyst scale-up issues and differences in testing protocols, test conditions (temperature, pH), and catalyst instability. Thus, an increasing focus on the validation of the core–shell approach under realistic MEA test conditions is necessary, to demonstrate their true benefits as cost-effective cathode catalysts for PEMFCs.

19.1 Introduction

At present, the commercial large-scale use of PEM fuel cell technology, particularly in automotive applications, is limited by the relatively high cost and insufficient durability of the currently available electrocatalyst materials used for the oxygen

---

S. Ball (✉)
Johnson Matthey Technology Centre, Blount's Court, Sonning Common, Reading,
Berkshire RG49NH, UK
e-mail: ballsc@matthey.com

M. Shao (ed.), *Electrocatalysis in Fuel Cells*, Lecture Notes in Energy 9,
DOI 10.1007/978-1-4471-4911-8_19,

reduction reaction (ORR) at the cathode [1–3]. The core–shell electrocatalyst approach deliberately deposits the high-cost, high-activity precious metal component (usually Pt) as a thin layer on the surface of a lower-cost substrate/nanoparticle core, as only atoms at the nanoparticle surface actively participate in the electrochemical reactions. This approach can provide significant benefits in precious metal thrifting, depending on the choice of core type, compared with Pt nanoparticle catalysts, as precious metal within the center of the nanoparticle (core) is replaced with lower-cost elements. To date a wide range of different types of core have been investigated including Pd, Pd alloys, Ir, Ir alloys, Au, Ag, and various first-row transition metals and their oxides [4–7]. In addition to cost reduction achieved by reducing/removing precious metal content within the particle core, the geometric and electronic effects induced by the underlying substrate core can enhance the activity of the Pt overlayer for the oxygen reduction reaction, leading to greater activity per mass of Pt than that expected based on thrifting alone.

Pt-based mass activities from 0.5 to over 2 A/mgPt at 900 mV [8–10], significantly exceeding the US Department of Energy Targets of 0.44 A/mgPt for automotive fuel cell applications, have been reported for a wide variety of core–shell electrocatalyst systems in measurements of oxygen reduction activity using the rotating disc electrode (RDE) setup, at room temperature in liquid electrolytes. These high activities also significantly exceed the typical mass activity of commercial carbon-supported Pt nanoparticles of around 0.15 A/mgPt [1]. However, these very high activities reported for core–shell materials are yet to be translated to such high performances in membrane electrode assemblies (MEAs), with the highest Pt-based mass activity reported in MEAs using US DoE-recommended protocols remaining a much more modest 0.3–0.4 A/mgPt [11, 12]. The discrepancies between the oxygen reduction activity observed in MEAs compared with that under more ideal conditions may be caused by a range of factors, such as differences in catalyst layer preparation and utilization, test protocol, temperature, and electrolyte type [13]. However, these discrepancies often appear larger in the case of core–shell catalyst materials compared to pure Pt and Pt alloy nanoparticles on carbon [14]. Electrochemical cycles and oxidizing conditions are expected to segregate core atoms toward the surface of the nanoparticles, disrupting the uniformity and stability of the Pt overlayer [15], and such processes may be more aggressive in the MEA environment. In addition, the highest activity values reported for core–shell material are, for example, prepared by electrochemical Pt deposition in situ on the RDE tip, while the preparation of sufficient material for MEA testing often requires adjustments to the methods used and tends to give lower activities both in MEA and RDE test environments, presumably as a consequence of poorer shell uniformity in the scaled-up samples [9, 16]. Therefore, multiple factors can influence the performance and durability of core–shell catalyst materials within the MEA environment, and these will be discussed in the subsequent sections of this chapter.

This chapter will focus mainly on core–shell materials prepared by the addition of a Pt monolayer (PtML) to a preformed core, by various approaches (chemical and electrochemical), and consider the uniformity, stability, and activity of materials of this structure. Chapter 18 in this book describes alternative methods used to produce a core–shell or surface-segregated structures, such as annealing treatments and dealloying/electrochemical cycling of base-metal-rich Pt alloy particles to produce a Pt-rich surface, so these approaches will not be discussed in detail here. As many reported core–shell electrocatalysts use alloys of alternative precious metals to Pt within the core, such as Pd, Au, and Ir, the implications of core type on catalyst cost reduction will also be considered.

19.2 Background

The preparation of core–shell catalysts for the ORR was pioneered by Adzic et al. Initially, this group investigated the preparation and behavior of Pt monolayers deposited on a range of different single crystal surfaces, prepared by galvanic displacement of a copper monolayer that had been deposited by Cu under potential deposition (Cu UPD). The effects of different underlying metal substrates on the O_2 dissociation and OH formation energies on the Pt overlayer [17] and correlation with the oxygen reduction activity of these different surfaces were observed. This balance between ease of O_2 dissociation and ease of OH_{ads} formation (required to react further with H^+ and generate water) produces a typical volcano plot, illustrated in Fig. 19.1. The slight contraction in the Pt overlayer on a Pd substrate results in enhanced ORR activity for PtML/Pd(111) over Pt only, while PtML/Au (111) binds O_{ads} too strongly and PtML/Ir(111) binds O_{ads} too weakly for these examples to give enhanced activity.

Both geometric and electronic effects from the underlying substrate create shifts in the d-band center of the core–shell electrocatalyst compared to Pt only, which influence the activity for the ORR. The Pt monolayer deposition via Cu UPD displacement is described in the next section in comparison with other core–shell preparation methods.

This approach was then applied to produce Pt monolayer catalysts on Pd nanoparticles [18] and a wide range of different nanoparticle cores supported on carbon, as well as other single crystal surfaces. Various Pd alloy cores have been investigated, aiming to fine-tune the strength of the Pt–O bond in PtML/$Pd_yX_{(1-y)}$ ($X = $ Co, Fe, Cu, Cr) and further enhance the activity for the ORR by progressing toward the peak of the activity volcano [8, 14]. The effects of mixing other elements such as Ir and Re into the Pt overlayer and the use of full and partial interlayers of Pd, Ir, and Au between the main part of the core and Pt overlayer have also been explored [6, 19, 20] and shown to influence both the activity and stability of the core–shell electrocatalysts.

Various electroless preparation methods have also been investigated, and the different synthetic approaches will be reviewed in the next section. Synthesis of shaped core particles such as tetrahedra, cubes, and nanowires has also been attempted to increase the fraction of the particle surface that is present as particularly active crystal facets, such as (111).

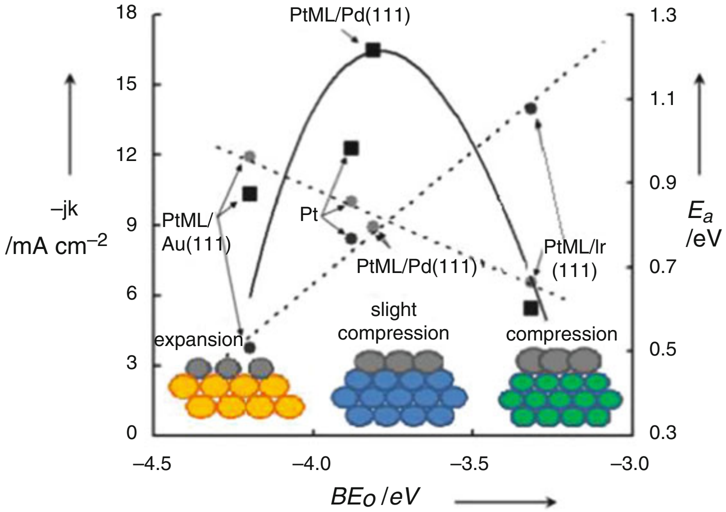

Fig. 19.1 Models of pseudomorphic monolayers of Pt on three different substrates inducing compressive strain (Ir(111) and Pd(111)) and expansive strain (Au(111)) and activation energies for O_2 dissociation and OH formation on different PtML/X surfaces as a function of oxygen binding energy. Figure redrawn by the author with permission based on a diagram provided by R. Adzic, based on diagrams in [17]

19.3 Overview of Core–Shell Preparation Methods, Characterization, and Factors Affecting Shell Uniformity

19.3.1 Pt Shell Deposition Methods: Electrochemical

The deposition of a Pt monolayer via the galvanic displacement of an under potentially deposited (UPD) Cu monolayer has been widely used to deposit Pt shells onto various substrate cores. Figure 19.2 illustrates a schematic of this process for the deposition of Cu onto a Pd@Co core followed by displacement of the Cu layer with Pt [21].

The precursor core material, Pd or Pd alloy nanoparticles supported on carbon, for example, is dispersed in solvent + Nafion ionomer solution and coated onto a glassy carbon RDE and dried. The electrode is then immersed in a 50 mM H_2SO_4 + 50 mM $CuSO_4$ solution and held at or cycled to potentials positive of the bulk Cu deposition potential of 0.36 V vs. RHE to achieve Cu monolayer deposition. Initial descriptions of this procedure describe removal and washing of the electrode before transferring to a 1.0 mM K_2PtCl_4 + 50 mM H_2SO_4 for the Pt galvanic displacement step [21] where Cu^0 is spontaneously oxidized by Pt^{2+} to leave Pt on the nanoparticle surface and the removal of Cu. However, more recent reports use a slow injection of K_2PtCl_4 at lower concentrations and repeated cycles between 0.37 and 0.67 V in the presence of both the Cu and Pt salts. This is thought to lead to an increased uniformity of the Pt

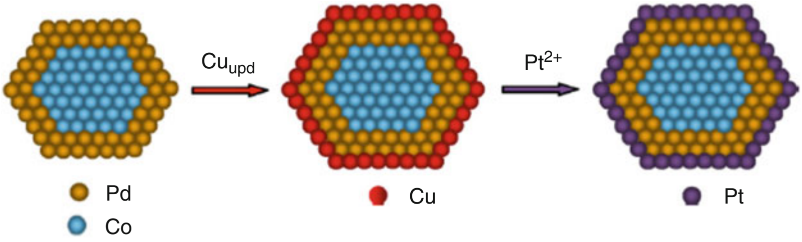

Fig. 19.2 Schematic illustrating the process of Cu under potential deposition followed by galvanic displacement by Pt for a PdCo nanoparticle core [21]

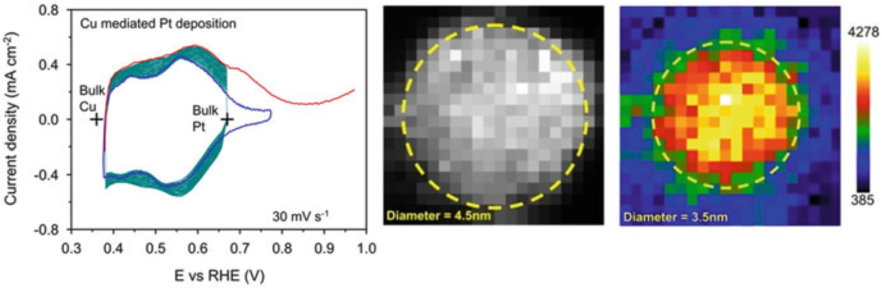

Fig. 19.3 *LHS* diagram illustrates the cyclic voltammetry changes during repeated cycles of Cu-mediated Pt deposition onto Pd cores, while central diagram shows HAADF for a single particle and the *RHS* Pd EELS for the same particle, indicating difference in radius between entire particle and Pd-rich center [22]

overlayer, as the repeated Cu UPD and stripping cycles slow the rate of Pt deposition and allow time for the surface diffusion of Pt adatoms so smooth layers may be formed [22]. A final sweep to 1 V is used to completely remove Cu. A combination of high-angle annular dark-field (HAADF) imaging and Pd electron energy loss spectroscopy (EELS) used to map the nanoparticles and presence of Pd within them suggested a 0.5 nm difference in radius consistent with the formation of a two-layer-thick Pt shell [22] (Fig. 19.3).

In addition to the preparation of microgram samples on the RDE tip, this approach has been modified to scale up to gram-size quantities using an electrochemical cell where core nanoparticles are dispersed as powder in the electrolyte and a RuO_2-coated Ti cylinder acts as the working electrode (WE) [9].

The uniformity of the Pt overlayer is of great importance in determining the activity and stability of the final catalyst material. While original studies were performed using uniform single crystal surfaces, small nanoparticles contain a range of particle sizes and coordination sites/surface facets. As described above, high-resolution TEM (HAADF) and EELS may be combined to map the structure of individual particles in some core–shell systems, but such analysis is limited by the small fraction of the total number of particles studied (and the EELS signal associated with core atoms). X-ray absorption spectroscopy (XAS) and X-ray diffraction (XRD) measurements provide information on the average coordination of different elements within the structure, giving a more global view of the electrocatalyst structure.

Recently XAS investigations were used to explore the Cu UPD process as a function of applied potential on carbon-supported Au nanoparticles [23]. Analysis of both the Cu and Au extended X-ray absorption fine structure (EXAFS) indicated only partial monolayer coverage at potentials where a complete Cu monolayer is predicted for single crystals. The structure of deposited Cu was found to be more consistent with Cu cluster formation at defects in the Au surface than the presence of a smooth monolayer due to lower than expected numbers of Au–Cu neighbors and Cu–Cu neighbors fitted in EXAFS analysis. The absence of a uniform monolayer of Cu on the nanoparticles implies that subsequent displacement of Cu by Pt is unlikely to result in the formation of a uniform Pt shell [23].

The presence of Pt nanoparticles/clusters compared to the desired uniform shell has also been inferred from changes to synchrotron XRD patterns under He and H_2 for PtML/Pd core–shell samples via Cu UPD at gram scales [24]. The similar lattice constants of Pt (0.389 Å) and Pd (0.391 Å) result in XRD peak at similar positions; however, Pd nanoparticles absorb H_2 resulting in an increase in lattice constant causing the XRD peak to shift to lower 2θ values. While a thin Pt monolayer on the Pd nanoparticle surface would be expected to also expand in the presence of H_2, isolated Pt clusters on the Pd surface/detached Pt nanoparticles will be uninfluenced by the change to an H_2 atmosphere. This technique has been used as a diagnostic to observe the benefits of modifications to a preparation procedure [24, 25]. The effect of reducing potentials and H absorption into the Pd core lattice have also been explored via EXAFS on PtML/Pd/C core–shell samples of varying Pt shell thickness prepared by a chemical deposition procedure [26]; these results are discussed in Sect. 19.3.2.

The Cu UPD approach has recently been applied to produce Pt–Pd core–shell nanowire catalysts [27]. Ultrathin Pd nanowires with diameters of ~2 nm were prepared and deposited onto XC-72R carbon, followed by surfactant removal by either acetic acid wash or a novel UV–ozone process, then selective CO adsorption to remove undesirable organic residue. Pt was then deposited via a Cu UPD galvanic displacement step using a sample of the treated Pd nanowires deposited on an RDE tip. At 900 mV, high mass activities for the ORR reaction of 1.83 A/mgPt and 1.47 A/mgPt were achieved for the ozone-treated and acid-treated samples, respectively. Pt monolayers have also been prepared on Pd tetrahedra using the Cu UPD galvanic displacement approach [28].

In addition to analysis by HAADF and elemental line scans, changes to the X-ray absorption near edge structure (XANES) may be investigated as a function of potential to investigate the structure of core–shell materials. Figure 19.4 shows results of these types of analysis for PtML/IrNi/C core–shell particles, where smaller changes in the XANES spectra vs. reference spectra at 0.41 V [plotted as $(\Delta\mu - \Delta\mu_{0.41})/\Delta\mu_{0.41}$ y axis, Fig. 19.4c] are observed for the core–shell compared to a Pt/C reference catalyst material. These data may be interpreted as a smaller change in Pt surface oxidation for the core–shell system, indicative of lower OH

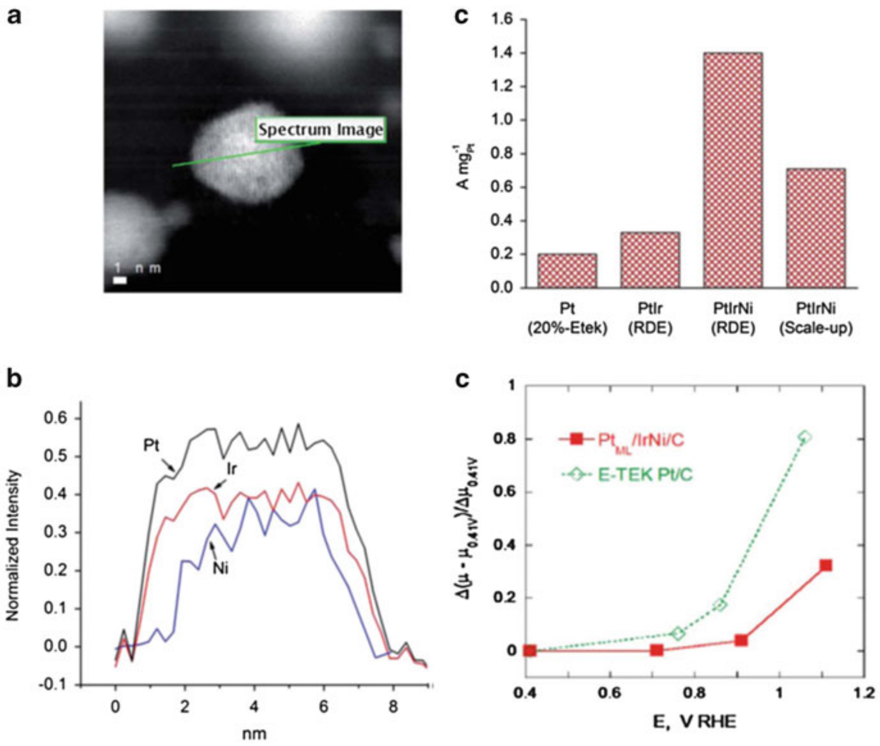

Fig. 19.4 (**a**) and (**b**) *Dark-field* TEM line scan and elemental mapping of PtML/IrNi core–shell particle, (**c**) variation in mass activity in RDE testing for RDE and g-scale Cu UPD scale up, and (**d**) $\Delta\mu$ XANES of PtML/IrNi compared with Pt-only nanoparticles [29]

coverage and O binding energy, correlating with a higher activity for ORR vs. Pt only (Fig. 19.4d) [29].

Pt deposition via galvanic displacement of a Cu UPD layer has been achieved for a variety of nanoparticle cores/substrates such as Nb$_2$O$_5$ nanoparticles, Au nanoparticles, Ir and Ir alloy [29], and Pd and Pd alloys [11, 30]. The activity of some of these systems is summarized in Table 19.1 in Sect. 19.4 of this chapter. Direct deposition of Pt onto lower-cost transition metal cores such as Co and Ni is challenging, due to the highly oxidizable nature of these cores and the presence of a more noble metal as an interlayer, or preparation of a surface-segregated alloy core, have been explored. Voltage cycling of the core in the presence of Br– anions has been used to remove low coordination sites in Pd$_3$Co cores and increase Pt shell uniformity and activity; however, Co is still leached from the core under operational conditions [31]. The use of Pd$_9$Au alloy cores has been shown to significantly enhance the durability in MEA potential cycling tests (see Sect. 19.4) compared to PtML/Pd/C where substantial Pd dissolution was observed [11]. The same group has also reported similar benefits for a hydrogen adsorption/desorption core–shell preparation method (although full details are yet to be published) [12].

In all cases where direct comparisons are reported, the scale-up of Cu UPD-based preparations from RDE tip to gram scale results in an associated drop in measured activity [29, 30] (as illustrated in Fig. 19.4d) for the PtML/IrNi/C system and summarized in the table at the end of Sect. 19.4. Successful scale-up of electrochemical Pt overlayer deposition to the tens to hundreds of grams required for commercial MEA production remains a challenge with various groups investigating different electrochemical cell designs, additives, and procedures to improve shell uniformity in large batches of material. Japan-based company N.E. Chemcat recently licensed BNL core–shell catalyst scale-up technology including apparatus used in gram-scale manufacture [32].

19.3.2 Pt Shell Deposition Methods: Chemical

Core–shell catalyst materials may also be prepared by non-electrochemical routes. Core–shell nanoparticles may be produced in solution using colloidal methods, by sequential deposition of the core and shell components [33], or Pt layers may be deposited chemically or via displacement reactions onto preprepared core nanoparticles, but in contrast to approaches described in Sect. 19.3.1, no applied potential is required; typically core particles or colloidal core–shell particles are deposited onto carbon supports.

In colloidal preparation routes using various metal salts, either aqueous or organic solvents, a surfactant and a reducing agent can be used to produce nanoparticles and core–shell materials of varying types. A recent review by Peng covers many of these approaches and discusses how the choice of metal salt, solvent, surfactant, reducing agent, and reaction conditions may be used to control the size, shape, and metal shell growth mode [34] of various types of nanoparticles. Where surfactants are used to control electrocatalyst shape, size, and morphology, the steps required to later remove these organic species from the catalyst surface should also be considered, as such species may act to poison the surface sites.

An example of such a core–shell preparation is the synthesis of PtML/PdPt core–shell nanoparticles using an organic colloidal method. The PtPd cores were prepared by premixing palladium chloride (precursor metal salt) with sodium citrate (surfactant) and ethylene glycol (both solvent and reducing agent), followed by addition of hexachloroplatinate, pH adjustment, and heating at 160 °C in an autoclave for 8 h; then further Pt salt was added via a similar procedure to produce the Pt shell [33]. PtML/Pd_3Fe/C [35] and PtML/Au/C core–shells [36, 37] have been prepared using similar types of approaches. The nanoparticles may be added to a carbon support after synthesis, or in some case, the carbon support is present during the autoclave/reflux step. The concentration and choice of surfactant used influence both the size and shape of the nanoparticles formed [34].

A chemical preparation route was also used to prepare Pt on Ag nanoparticles, where silver trifluoroacetate was mixed with oleylamine in isoamyl ether to synthesize Ag nanoparticles which were isolated, washed, then further reacted with

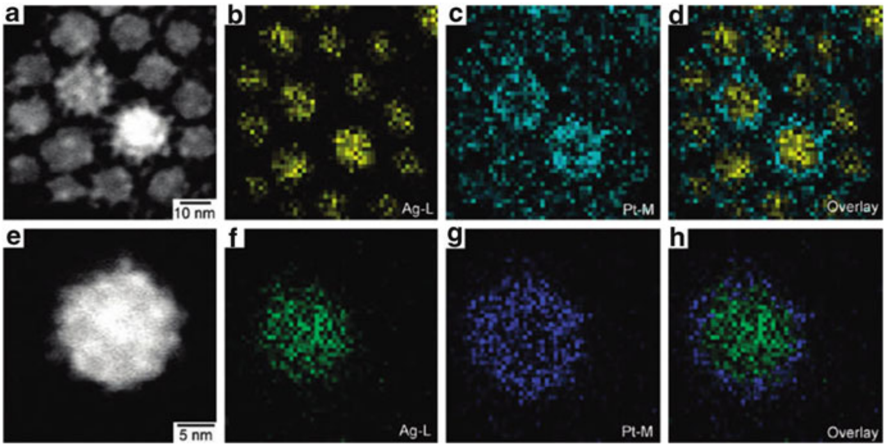

Fig. 19.5 Representative HAADF-STEM images and their corresponding elemental maps of Pt-on-Ag nanoparticles at (**a**–**d**) low and (**e**–**h**) high magnifications [38]

Pt(acac)$_2$ [38]. UV–vis spectroscopy was used to monitor the growth of Pt onto the Ag nanoparticle, with a gradual decrease in the intensity of the Ag plasmon band indicating increasing coverage by Pt nanoparticles. HAADF-STEM and elemental mapping were used to confirm the presence of an Ag core almost completely covered with multiple 3 nm Pt nanoparticle rather than a continuous Pt overlayer (Fig. 19.5). Two types of treatment were investigated to remove the surface-capping agents on the Pt–Ag nanoparticles: (1) reaction with acetic acid where the Pt–Ag nanoparticle structure remained intact and (2) heat treatment in air to 300 °C followed by exposure to a reducing atmosphere where XRD evidence suggests mixing to form an alloy had occurred; the effect of electrochemical leaching of Ag to generate hollow Pt spheres was also explored—see Sect. 19.3.3 [38].

Pt–Pd bimetallic nanodendrites produced by a chemical route exhibit a somewhat similar morphology to the Pt–Ag samples described above; however, in the case of the Pt–Pd nanodendrites, Pt branches appear to grow epitaxially on faceted Pd nanocrystal seeds. Reduction of Na_2PdCl_4 with L-ascorbic acid in aqueous solution was used to generate these truncated octahedral Pd nanocrystals, followed by addition of K_2PtCl_4, nucleation of Pt on the Pd facets, and further growth of Pt on these nuclei to form the nanodendrites [39]. These systems showed ORR mass activity of 0.241 A/mgPt at 900 mV in RDE tests.

A series of PtML/Pd/C core–shell samples with varying nominal Pt shell thickness have also been prepared via a proprietary chemical method and explored using XAS and electrochemical techniques [26]. Analysis of EXAFS at the Pd K and Pt L_3 edges for catalyst pellet samples revealed the expected increase in Pt–Pt and decrease in Pd–Pt and Pt–Pd neighbors with increasing nominal Pt coverage from 0.5 to 2 monolayers of Pt (calculated based on catalyst surface area of the Pd/C cores). Further EXAFS measurements under electrochemical control in liquid electrolytes revealed an increase in average Pd–Pd bond distance to 2.780 Å at 0.0 V for the 0.5 of

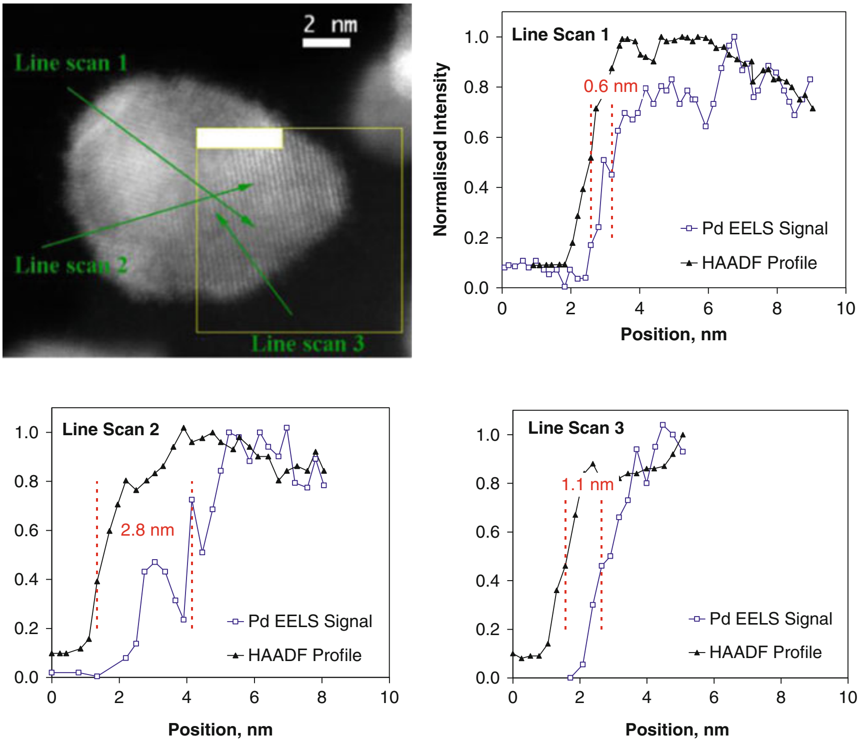

Fig. 19.6 STEM micrograph of 10 nm PtML/Pd_3Co/C particle and Pd EELS and HAADF signals from line scans, providing structural evidence for the formation of a Pt shell [41]

a monolayer nominal coverage compared to 2.740 Å at 0.525 V (vs. RHE) associated with absorption of H atoms into the Pd lattice with low potentials. This effect was particularly pronounced for the 0.5 monolayer coverage sample but still present in a catalyst with nominal coverage of two monolayers of Pt, although to a lesser degree, implying higher Pt coverage creates a barrier or constraint to H adsorption into the Pd core [26].

Preparation of core–shell nanoparticles of PtML/Pd core on carbon has also been attempted via an electroless Cu deposition intermediate step, where preformed carbon-supported Pd nanoparticles are suspended in a solution containing $CuSO_4$ and ethylenediaminetetraacetic acid (EDTA) to deposit Cu, then Pt salt added to galvanically displace the Cu. XPS and HAADF-STEM of the intermediate Cu/Pd nanoparticles confirmed the successful deposition of Cu via electroless deposition. The Pt and Pd distributions in the final sample tracked one another in TEM elemental analysis, and ~2.5 times Pt mass activity improvement was observed in RDE tests [40].

The behavior of PtML/Pd_3Co nanoparticles on carbon prepared by (1) electrochemical (Cu UPD) and (2) chemically deposited (proprietary) methods has been compared using the same precursor core batch [41, 42]. Figure 19.6 shows STEM of a single particle and Pd EELS and HAADF signals from line scans in different directions for a scaled catalyst prepared by a chemical route, providing structural evidence for the formation of a Pt shell. Variations in the apparent thickness of the Pt shell may relate to thinning at the Pd_3Co–carbon interface and thickening of the Pt shell on the opposing side of the particle. In addition, certain faces or defects on the Pd_3Co nanoparticle core may be preferred sites for Pt deposition. Similar variations in Pt shell thickness from 0.5 to 1.2 nm are also reported for gram-scale PtML/Pd_2Co/C samples prepared by Cu UPD (Pd:Co 2:1 atomic ratio cores). A comparison of activity for ORR in the RDE activity comparison of samples prepared on the RDE tip, gram-scale Cu UPD preparations, and gram-scale chemical route preparations shows ~1 A/mgPt for microgram-scale RDE tip preparations, falling to 0.7 A/mgPt for both scaled preparation routes, again highlighting the difficulties of effective core–shell catalyst scale-up using either electrochemical or chemical routes.

Preparation of Pt shells on Co cores has also been explored via a redox-transmetalation process, where Pt^{2+} in $Pt(hfac)_2$ is reduced to Pt, while surface Co atoms on the Co core are oxidized via migration of the hfac ligand; repeated cycles of the reaction are required to generate the Pt shell [43] (hfac = hexafluoroacetylacetonate).

19.3.3 Other Approaches: Surface Segregation and Dealloying

Core–shell structures may also be achieved via annealing of alloy particles under particular atmospheres or dealloying of the more oxidizable elements from alloy nanoparticles. Electrochemical dealloying approaches are generally used to generate a Pt-rich shell and base-metal-rich core and are reviewed in detail in Chap. 18.

Annealing has been used to segregate particular elements to the surfaces of nanoparticle alloys, where relative atomic size, energies of formation, and the choice of gas environment influence which of the component elements segregates to the surface. Annealing of alloy catalyst powders in the gas phase in certain gas environments may be used to increase the Pt surface content for PtCo and other Pt-containing alloys. Annealing of PtCo alloy particles in CO gas results in segregation of Pt to the surface as a consequence of the increased absorption enthalpy of CO on Pt compared to Co [44]. These approaches have also been used to produce surface-segregated alloy core particles for subsequent Pt deposition via the electrochemical and chemical described in Sects. 19.3.1 and 19.3.2. Annealing in H_2/Ar atmospheres is used to produce Ir-rich shells on IrFe [45] and IrNi [46] cores used to prepare PtML/IrX core–shell systems, with greater uniformity of Pt deposition observed on the Ir-rich surface. Electrochemical annealing in CO-saturated electrolyte has been shown to segregate Pt to the particle surface and enhance activity for the ORR reaction [44].

Electrochemical dealloying of Pt–Ag [38] and other Pt-metal core–shell systems has been used to produce hollow Pt spheres. This is a manifestation of the nanoscale Kirkendall effect whereby less stable core metal atoms are lost from the center of

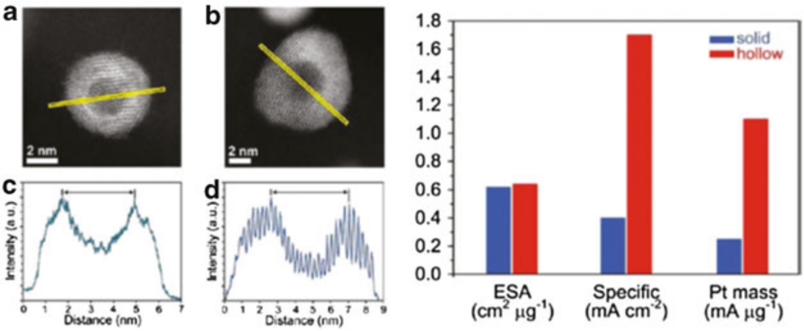

Fig. 19.7 (*LHS*) (**a** and **b**) High-resolution STEM images of Pt hollow spheres and (**c** and **d**) line scans parallel and perpendicular to the lattice planes (*RHS*) comparison of the ESA of solid and hollow Pt spheres based on hydrogen desorption charges and ORR-specific and Pt mass activities measured at 0.9 V in RDE measurements [47]

the particle via vacancy-mediated diffusion. Although this effect essentially dooms all core–shell structures to the gradual loss of the activity-enhancing elements from the core, hollow Pt sphere catalyst particles may be generated that retain a lattice contraction and enhanced activity over standard Pt electrocatalysts, as illustrated in Fig. 19.7 [47].

Porous/hollow Pd–Cu nanoparticles have also been prepared on the RDE tip by selectively dealloying Cu from $PdCu_6/C$, and subsequent Pt electrochemical deposition via Cu UPD used to create highly active surfaces for the ORR. Very high oxygen mass activities of ~2.8 A/mgPt were reported, and HAADF-TEM imaging confirms much lower Cu content in porous particle compared with the uncycled precursor [10].

Physical processes may also be used to deposit Pt onto various types of supports. An example of this type of approach is the preparation of Pt-metal monolayers supported on low-cost transition metal carbides, prepared by magnetron sputtering of Pt onto thin films of W and Mo carbides. While Pt monolayers were achieved on the thin-film electrode geometry used in this study, uniform deposition of Pt onto high surface area particulate materials or mesoporous structures by these methods remains challenging [48].

19.4 Performance and Stability of Core–Shell Catalysts

19.4.1 Performance of Core–Shell Materials in Membrane Electrode Assemblies and Comparison with Rotating Disc Electrode

It has been repeatedly observed by various researchers that the very high oxygen reduction activities reported for core–shell catalyst materials measured with the

RDE setup are not reproduced within the MEA operating environment. While very high Pt-based mass activities in the range from 0.5 to 1.5 A/mgPt at 900 mV may be observed under rotating disc operating conditions depending on the core–shell type, the highest Pt-based mass activity reported in MEAs using US DoE-recommended protocols remains a much more modest 0.3–0.4 A/mgPt. A range of factors can contribute to this so-called RDE-MEA gap, and these will now be discussed.

Table 19.1 summarizes some of the available published data for oxygen mass activity values at 900 mV iR-free under RDE and MEA test conditions and where possible also shows the effect of catalyst scale-up vs. preparation on the RDE tip on the mass activity. The reported activities for carbon-supported conventional Pt and PtCo alloy catalysts are shown for comparison purposes. Many core–shell systems also exhibit high specific activities (activity corrected per active catalyst surface area typically reported as $\mu A/cm^2$ Pt) when compared to state of the art Pt/C. Increasing catalyst particle size has been shown to enhance specific activity for carbon-supported Pt and Pt alloys, as larger particles have a lower proportion of edge and corner sites, fewer defects, and more faceted surfaces, leading to greater intrinsic activity (the particle size effect). However, as the mass activity [A/mgPt or A/mgPGM (PGM = platinum group metal)] is of greater importance in determining the usefulness of the core–shell approach in MEAs as a cost reduction measure, specific activity improvements are not discussed further here. Specific activity values for many of the core–shell systems can be found in the references cited in Table 19.1 and elsewhere in this chapter.

As alluded to in Sect. 19.3, the scale-up of electrochemically prepared core–shell catalyst materials from preparations on the RDE tip to gram-scale batches results in a decrease in the mass activity, from over 1 A/mgPt to ~0.5–0.7 A/mgPt for PtML/PdxCo and PtML/IrNi systems where comparative data is available. While no detailed information on the reasons for this discrepancy is provided, variations in the uniformity and Pt shell thickness between RDE and gram-scale preparations are likely to be responsible. In addition, activity values are subject to reasonably large error bars due to the small amounts of Pt present. While gram-scale preparations allow an accurate determination of the Pt assay of the final product via ICP-MS, the exact Pt content of samples prepared on the RDE tip may be less accurately known if calculated from cyclic voltammetry Cu stripping charges [22]. In some cases, activity is quoted per g of PGM as well as per g of Pt, and these values should scale by the same factor for samples prepared by the different methods, if the same precursor cores are used and the same Pt thickness (Pt to core atom ratio) is achieved. However, Pt/IrNi/C cores prepared on the RDE tip show activity of 1.4 A/mgPt and 0.78 A/mgPGM, while versions from the gram-scale preparations show 0.77 A/mgPt and 0.22 A/mgPGM, indicating some variations in overall composition between the RDE and gram-scale-prepared samples [16].

$PtML/Pd_3Co/C$ systems show similar RDE activity values for gram-scale samples prepared by either electrochemical or chemical routes, but samples prepared by both of these methods are lower in activity (0.7 A/mgPt at 900 mV) compared with the sample prepared on the RDE tip [41]. On transfer to the MEA, $PtML/Pd_3Co/C$ catalysts (prepared either electrochemically or chemically) show

Table 19.1 Comparison of mass activity values obtained from RDE (on-tip and g-scale catalyst preparations) and MEA testing; where mass activity is reported at 0.85 V (some RDE samples) or under alternative MEA test conditions, the improvement factor over Pt only is quoted

	Mass activity 0.9 V RDE A/mgPt Data in ( ) show A/mgPGM was provided		Mass activity 0.9 V MEA A/mgPt Data in ( ) show A/mgPGM was provided
Sample details	Cu UPD RDE prep	g-scale prep	
	~0.15–0.2 A/mgPt [1]		0.16 A/mgPt [1]
Pt_3Co (TKK)	0.3–0.35 A/mgPt [56]		0.28 A/mgPt [1, 57]
PtML/Pd	5–8× Pt activity/mgPt (2× Pt based on A/mgPGM) [18]	0.57 A/mgPt (0.21 A/mgPGM) [9]	0.3 A/mgPt (not quoted per PGM) [11] 0.55 A/mgPt (0.12 A/mgPGM) [52] (cabot scaled)
PtIrML/Pd	–	0.66 A/mgPt (0.24 A/mgPGM) [9, 52]	–
PtML/Pd_9Au	–		0.3 A/mgPt (not quoted per PGM) [11]
PtML/IrNi	1.4 A/mgPt (0.78 A/mgPGM) [29]	0.71 A/mgPt (0.22 A/mgPGM) [29]	–
PtML/IrFe	1.1 A/mgPt (0.36 A/mgPGM) [45]	–	–
PtML/Pd_2Co	1.02 A/mgPt (not quoted per PGM) [30]	0.7 A/mgPt (not quoted per PGM) [30]	–
PtML/Pd_3Co	1.0 A/mgPt (0.36 A/mgPGM) [41]	0.72 (Cu UPD scaled) 0.7 (chemical route) (~0.25 A/mgPGM) [41]	0.14 A/mgPt 2× Pt activity at 0.85 V (not quoted per PGM) [42]
PtML/Nb_2O_5	0.21 A/mgPt [7]	–	–
PtML/$AuNi_5$	~0.89 A/mgPt (0.45 A/mgPGM) [52]	–	3.3× Pt (30 psig test conds) [52]
PtML/Pd3Fe	5× Pt only (0.8 A/mgPGM) [8]	–	–

PtML/Au	1.2 A/mgPt (not quoted per PGM) [54]	–	–
PtML/AuNi$_{0.5}$Fe	1.38 A/mgPt (0.18 A/mgPGM) [53]	–	–
PtML/PdCu (dealloyed)	2.8 A/mgPt (not quoted per PGM) [10]	–	–
PtML/IrCo	0.15 A/mgPt (0.036 A/mgPGM) [55]	–	–
PtML/Pd interlayer/IrCo	1.18 A/mgPt (0.16 A/mg PGM) [55]	–	–
Pt hollow spheres (from dealloying PtML/Ag)	0.32 A/mgPt (not quoted per PGM) [38]	–	–
Pd–Pt bimetallic nanodendrites	0.241 A/mgPt (0.204 A/mgPGM) [39]	–	–
Pt–Pd core–shell nanowires*	1.83 A/mgPt (ozone treated) 1.47 A/mgPt (acid treated) (not quoted per PGM) [27]	–	–
PtML/Pd tetrahedra	0.82 A/mgPt (not quoted per PGM) [28]	–	–

substantially lower activity than in the RDE environment (falling from 0.7 A/mgPt to ~0.15 A/mgPt) [42], and PtML/Pd/C (electrochemically prepared) samples showed a more modest halving of activity from 0.6 A/mgPt [9] to 0.3 A/mgPt [11]. During tests in liquid electrolytes, PtML/Pd_3Co/C catalysts, both electrochemically and chemically prepared versions, showed at least 25 % Pd loss on exposure to 1 M H_2SO_4 at 80 °C (analogous to the MEA environment) via ICP-MS measurements on the electrolyte. However, no Pd loss was observed in 0.1 M $HClO_4$ at RT (equivalent to RDE conditions) [14].

PtML/Pd/C also clearly shows loss of Pd in the MEA environment, via the formation of a Pd band within the membrane following voltage cycles (Sect. 19.4) [11]. The increased temperature and more aggressive environment within the MEA are therefore thought to contribute to the lower activities observed (compared to the RDE environment) as a consequence of the propensity of the less noble elements to dissolve from the core.

The variation in RDE and MEA activity is also partially due to the different testing protocols used. ORR activity measurements in the MEA often use the protocols defined by the US DOE, involving a polarization curve using pure oxygen, 150 kPa_{abs}, 100 % RH at 80 °C, running the measurement from low to high current with 15 min holds at each measurement point [2]. Cell voltage is then corrected for ohmic resistance and current values corrected for the cathode Pt load, such that mass activity at 900 mV may be determined. In contrast, values quoted from RDE measurements are typically measured in O_2-saturated 0.1 M $HClO_4$ at RT, based on data measured during a sweep from low to high voltage at ~10 mV/s. Data are then corrected using the Koutechy–Levich equation and corrected for Pt mass and in some cases ohmic resistance and capacitative effects, to yield a mass activity at 900 mV [49, 50]. Aside from the obvious differences in temperature, pressure, and electrolyte, the difference in the direction of the potential sweep and time at each potential appear to alter the observed electrocatalyst activity, presumable due to variations in the degree of O_{ads}/ spectator species present on the catalyst surface.

Figure 19.8 illustrates the effect of hold time at each current density point in MEA tests using different nanostructured thin film (NSTF) MEAs, showing increased MEA mass activity at 900 mV using 5 s holds (matching RDE values more closely) compared with lower MEA mass activity using 1,050 s holds at each point in the polarization curve [13]; similar variations in activity between the MEA and RDE techniques may also be expected for core–shell catalyst materials.

Typically MEA performances for core–shell cathode catalysts report mass activity at 900 mV on oxygen, rather than the full polarization data, and minimal information is available on the performance of such systems using air at the cathode. Low absolute voltages are generally achieved at high current densities using pure oxygen [51], and even lower values might therefore be expected when using air, due to mass transport effects. Figure 19.9 illustrates the H_2/air performance of a PtML/Pd/C core–shell system (scaled up using a spray pyrolysis approach by Cabot) in 50 cm^2 MEAs [52] albeit at 30 psig (~200 kPa back pressure) rather than the lower operating pressure of 50 kPag recommended by the US DOE. Oxygen mass activity of 0.55 A/mgPt at 900 mV is reported in this testing.

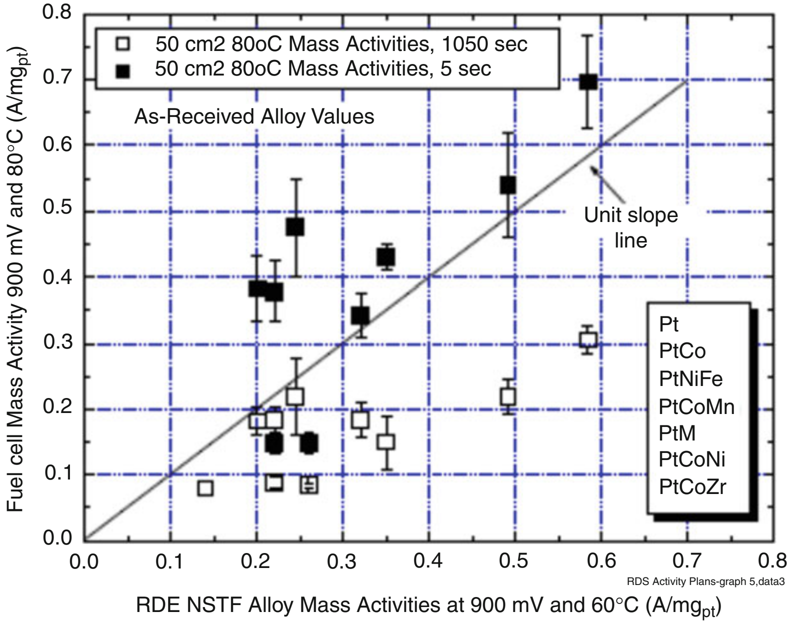

Fig. 19.8 Plot of RDE mass activity at 900 mV and 60 °C for nanostructured thin film (NSTF) catalysts (3 M) vs. fuel cell mass activity at 900 mV and 80 °C using (1) 5 s holds (*black-filled squares*) and (2) 1,050 s holds (*unfilled squares*) in MEA polarization curves [13]

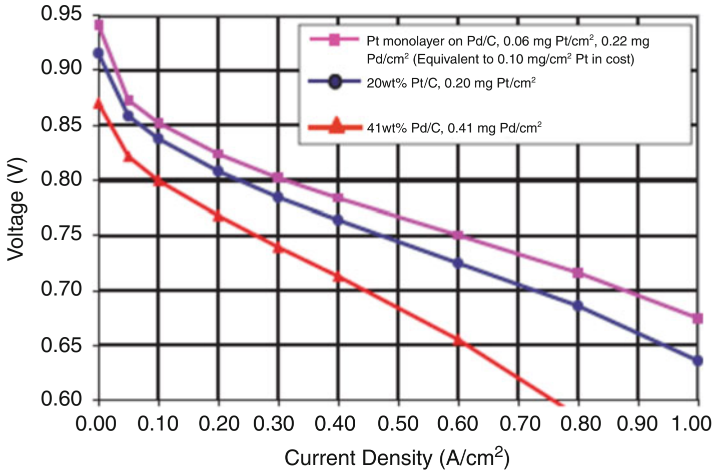

Fig. 19.9 Fuel cell testing of PtML/Pd/C catalyst from scale-up synthesis by Cabot, 50 cm^2 MEAs, 80 °C, 100 % RH, 30 psig back pressure, and 10 min/point [52]

To the author's knowledge, these data, along with the high activity achieved using PtML/$AuNi_5$/C (same high-pressure test conditions) and MEA mass activities for PtML/Pd/C and PtML/Pd_9Au/C, represent the best performances achieved so far in MEA testing of core–shell samples. These systems all show 2–3.5 times activity enhancement over Pt/C comparative samples in MEA tests.

Thus, a wide variety of core–shell systems have been reported as showing high ORR activity when prepared and tested in the RDE setup, including those already discussed and others such as PtML/$AuNi_{0.5}Fe$/C [53], PtML/Pd_3Fe/C [8], PtML/Au/C [54], PtML/Pd/Au/C [11], and PtML/Pd/IrCo/C [55] shown in Table 19.1 (PtML/Pd/core/C denotes the use of Pd interlayer). (Table 19.1 also shows activity values for Pt_3Co/C in the RDE [56] and Pt_3Co/C in MEAs [57] and data for Pt/C for reference purposes.) However, of these systems, only PtML/Pd/C, PtML/Pd_9Au/C, and PtML/$AuNi_5$/C have been successfully scaled up and translated to MEAs, and all show a reduction in activity compared to samples prepared at small scale. So for many published core–shell systems (Table 19.1), successful catalyst scale-up and the translation of high performances to the MEA environment are yet to be achieved. Further optimization is therefore required to translate the high oxygen mass activities observed in the RDE setup for other types of core–shell systems to the high mass activity and performance required under realistic conditions in MEAs.

19.4.2 Stability of Core–Shell Materials: MEA and RDE Environments

Although the stability of many core–shell electrocatalysts have been investigated via the RDE using multiple rapid voltage cycles at room temperature in 0.1 M $HClO_4$, only a few systems have been assessed in MEAs at the cathode, by using voltage cycling to simulate extended operation in an automotive environment. Data reported by Sasaki et al. show the best durability reported in MEA voltage cycling to date using PtML/Pd/C and PtML/Pd_9Au/C core–shell materials [11, 12]. Figure 19.10 shows results from these tests, illustrating the changes in mass activity at 900 mV, O_2, 50 kPa_{abs}, 100 % RH using the DoE protocol, at different stages of a cycling test, using cycles from 0.7 to 0.9 V square wave (DOE protocol). Figure 19.10a illustrates results from 2010 [12, 58], while Fig. 19.10b shows more recent data extending testing to an increased number of cycles (100,000) and improvements to activity and stability for PtML(H)Pd/C, an improvement to the core–shell catalyst preparation procedure yet to be disclosed [12].

All these core–shell electrocatalysts show an improved Pt-based mass activity over Pt only which is maintained throughout the cycling test. However, the mass activities/g total PGM are not disclosed; therefore, the overall cost reduction that might be expected from the use of these core–shell materials in MEAs is not clear.

Postmortem analysis of MEA samples using PtML/Pd/C after 100,000 potential cycles showed a Pd band precipitated within the membrane, a clear indication of Pd

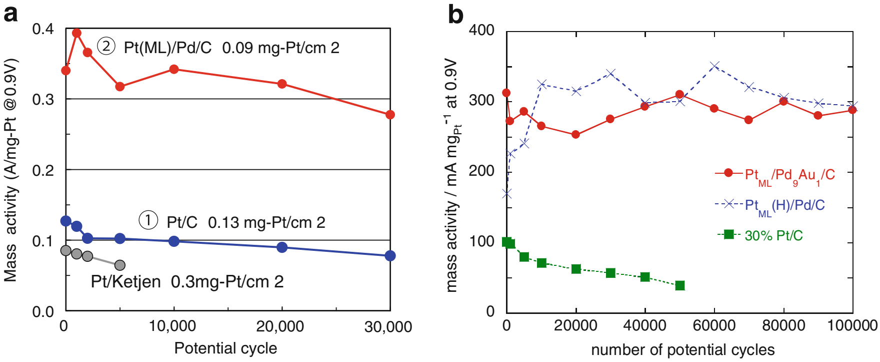

Fig. 19.10 Change in Pt mass activity in MEAs with cycles from 0.7 to 0.9 V, 30 s square wave, 80 °C, 100 % RH, for Pt/C compared to (**a**) PtML/Pd/C [12] and (**b**) PtML/Pd$_9$Au/C and PtML(H) Pd/C [58]

dissolution from the cores of the nanoparticles during operation [11]. This phenomenon had not been previously reported for core–shell electrocatalysts but is well documented for cycled MEAs containing Pt/C cathodes, resulting from Pt dissolution during voltage cycles and re-precipitation within the membrane on encountering hydrogen diffusing from the anode. In the case of PtML/Pd/C, the loss of Pd from the core is described as a means of protecting the Pt shell via sacrificial dissolution, and this observation is consistent with the higher diffusivity of less stable species from the core, a nanoscale Kirkendall effect [47]. Segregation of Pd and other less noble metals to the surface of a core–shell material in the presence of O_{ads} is also consistent with findings of the modeling studies by Balbuena et al. [15].

The use of a PtML/Pd$_9$Au core–shell system resolved these stability issues, with no Pd band observed within the membrane and hence minimal dissolution of Pd. Alloying of Pd with Au is thought to stabilize Pd by causing a positive shift of the Pd oxidation potential, with less Pd–OH formation observed in cyclic voltammetry and EXAFS spectra of the Pd$_9$Au/C cores compared to Pd/C [11]. Excellent stability of the Pt-based mass activity was achieved with a mass activity in MEAs of 0.2 A/mgPt remaining after 200,000 voltage cycles in MEAs; however, mass activity per g PGM is not quoted, so the possible effect of the additional PGM used on the overall catalyst cost is not clear.

So far limited durability data exists on core–shell catalysts within MEAs, and often cycling tests in the RDE setup are used to investigate catalyst stability. Recent RDE testing on PtML/IrFe and PtML/IrNi shows minimal change in ORR activity following 30,000 and 50,000 cycles, respectively, 0.6–1.0 V at 50 mV/s, RT, 0.1 M $HClO_4$ electrolyte [29, 45]. HAADF-STEM line scans of PtML/IrNi after 50,000 cycles also show that Ni is retained within the core of the particles after cycling, providing good evidence of the stability of the core under the RDE test conditions, attributed to the use of precursor cores with a Ni-rich center and Ir-rich outer region [29] (Fig. 19.11).

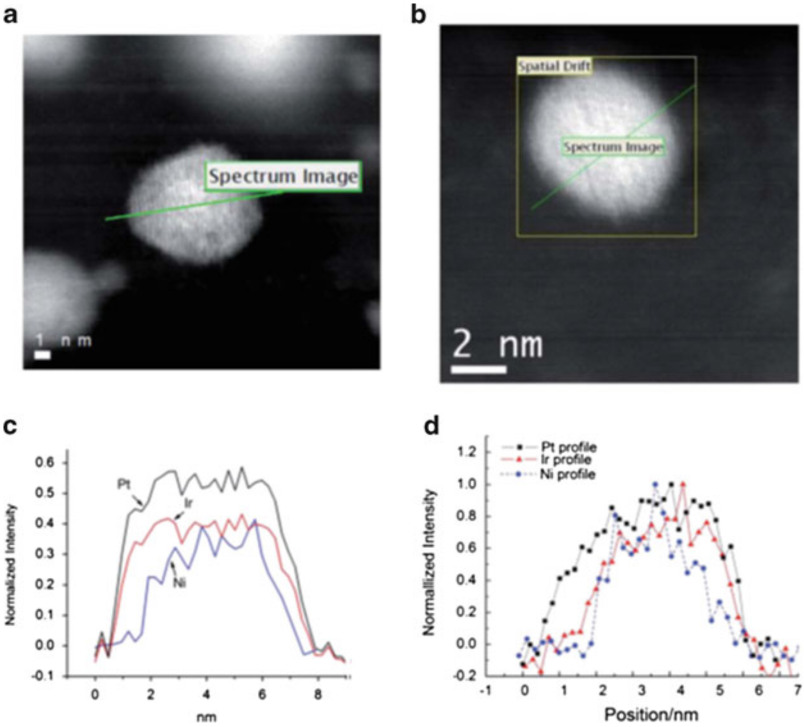

Fig. 19.11 HAADF-STEM and Pt, Ir, and Ni line scans for PtML/IrNi core–shell catalyst before testing (**a** and **c**) and after 50,000 cycles (**b** and **d**) 0.6–1.0 V at 50 mV/s, RT, 0.1 M $HClO_4$ electrolyte [29]

RDE testing of PtML/Pd_3Co catalysts has shown varying degrees of stability depending on the preparation route used. Adzic et al. observed improved stability after applying a bromide treatment to remove low coordination sites on the Pd_3Co core before Pt deposition. No change in ORR and surface area was observed after 25,000 cycles between 0.6 and 1.0 V using Br^- treated cores compared to a substantial shift in half wave potential after only 30 mV after 5,000 cycles on untreated examples. Other testing using treated PtML/Pd_3Co/C (no Br^- treatment) catalyst [41, 42]-coated gas diffusion electrodes in liquid electrolytes was performed under two different test conditions, (1) 0.1 M $HClO_4$, RT, and (2) 80 °C 1 M H_2SO_4, using 0.4–0.95 V square wave, 10 s per potential in both cases [14, 59]. Under the RDE-type test conditions, only minimal dissolution of Pd into the electrolyte (~10 % Pd loss) was observed, and HAADF-TEM measurements showed that the core–shell structure remained intact (bright outer regions were observed around the core due to heavier Pt atoms). However, under the test conditions in (1) 80 °C, 1 M H_2SO_4, substantial Pd dissolution (around 75 % removed after 1,000 cycles) occurred and TEM showed the formation of hollow spheres and some alloy, showing greater disruption to the structure in test

(2) thought to be closer to MEA test conditions [59]. Significant loss of Co occurred under both test conditions, and similar ECA change and metal loss with cycles were observed using PtML/Pd_3Co catalysts prepared by either the Cu UPD route or via a chemical method [14].

The substantial Co loss and disruption of the core–shell structure in more aggressive environment are consistent with expectations that less noble elements are prone to leaching when used in the core. Furthermore, the significant differences in Pd dissolution found between the RDE- and MEA-type test conditions imply that some caution may be required when extrapolating the stability of core–shell systems from the RDE to MEA. Therefore, more MEA activity and stability testing of the various types of core–shell systems is required to probe their true stability under realistic test conditions.

19.5 Use of Core–Shell Approach to Reduce Catalyst's Precious Metal Content and Cost

Many of the core–shell systems discussed so far in this chapter use precious metals such as Pd, Au, and Ir within the core or as interlayers within the structure. Clearly, where alternative metals (Au, Ag, or PGMs such as Pd or Ir) are used to replace some of the Pt within electrocatalysts used for the ORR, the impact of this on the overall catalyst cost should also be considered. The activity targets for PEMFC cathodes of 0.44 A/mgPt at 900 mV are based around the requirement for a 0.2 gPt/kW linked to a target cost per kW for large-scale automotive MEA production. Various studies have shown that the world platinum resources are sufficient to support the large-scale use of fuel cell electric vehicles, provided the targets relating to the Pt content in fuel cell stacks are achieved and PGM producers have sufficient visibility of the increase in demand [60]. Studies by TIAX concluded sufficient Pt availability for long-term demands of automotive fuel cells, assuming a gradual increase in the number of vehicles over several decades, a 95 % efficient recycling of PGM, and an achievement of a 0.2 gPt/kW by 2025 in their calculations [61]. However, as a large number of reported core–shell systems achieve reductions in Pt content by including alternative precious metals within the core, the impact of this on the overall catalyst, MEA, and automotive fuel cell stack should also be taken into consideration.

Where Pt is replaced by alternative precious metals, activity values have often been quoted as A/mgPGM as well as A/mgPt; however, this type of analysis does not reflect any cost differences between the different precious metals. The factors affecting metal prices in the market are complex, with supply and demand varying due to the interplay of the various technological and industrial uses (particularly vehicle emission control catalysts in the case of Pt and Pd), purchasing for investment purposes, use in jewelry, etc., against the availability and abundance of the different metals from primary refining of ore and also from recycling. The precious metals Pd, Ir, Ru, and Rh are produced as by-products of Pt mining. Figure 19.12

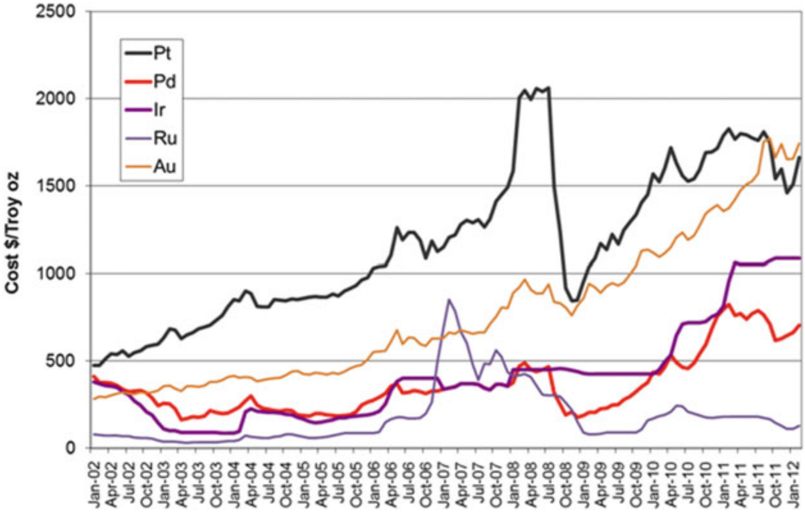

Fig. 19.12 Average monthly price of Pt, Pd, Ir, Ru, and Au precious metals since Jan 2002. Data from http://www.platinum.matthey.com/pgm-prices/ and http://www.kitco.com. One Troy oz = 31.1035 g of metal [62, 63]

shows the relative costs of Pt, Pd, Ir, Ru [62], and Au [63] precious metals over the last 10 years. A plot of the Rh price is not included in Fig. 19.12, as plotting Rh price on the same axes limits the visibility of subtle changes in the costs of the other precious metals, due to the significantly higher cost of Rh (ranging from two to five times that of Pt depending on the time scale viewed). Also significant use of Rh in ORR core–shell catalysts has not been reported to date, so discussion of the implications of Rh use is less relevant here.

Figure 19.12 shows some significant trends. Firstly, an overall general increase in price is observed for all the metals with time, in line with rising industrial demand and increasing GDP (gross domestic product), broken by a sharp drop in July 2008 linked to the global recession. The global downturn had a significant effect on the prices of Pt and Pd due to the drop in industrial metals' usage, particularly a drop in automotive manufacturing, reducing demand for Pt and Pd used in catalysts for vehicle exhaust cleanup and hence impacting the price. Over the time period shown, changes in Pd price tend to track those of Pt but with Pd prices typically around 70 % lower. Au prices remained robust during the recession, as a result of purchasing for investment purposes [64].

The factors affecting the costs of Ru and Ir are more subtle. Ru is used in the electronics industry in chip resistors, flat screen displays, and the hard disc manufacturing process. In 2006–2007, an increase in Ru demand from the electronics industry due to changes in the technology in hard disc drives resulted in a price spike, but only for a limited period. Once purchased or leased, a large proportion of Ru metal used in hard disc manufacturing is subsequently recycled, and minimal amounts are actually present in the consumer products, so increased

Table 19.2 Relative costs of Pd, Ir, Ru, Rh, and Au with respect to Pt cost over the last 5- and 10-year periods [62, 63]

PGM	Pd	Ir	Ru	Rh	Au
Fraction of Pt cost—1-year average	0.42	0.64	0.09	1.07	0.97
Fraction of Pt cost—5-year average	0.31	0.40	0.17	2.35	0.73
Fraction of Pt cost—10-year average	0.31	0.36	0.15	2.33	0.66

demand was only temporary and prices have therefore decreased again in subsequent years. Ir is used in catalysts used for acetic acid manufacture and electrochemical use in the chlor-alkali process and to make crucibles for producing high-quality sapphire single crystals used in the manufacture of LED televisions. Increased demand for Ir as a consequence of consumer demand for LED televisions and refitting of the Chinese chlor-alkali industry have both influenced the substantial increase in Ir price over the last 2 years [64].

While Pd prices have tended to retain a relative value of ~30 % with respect to the price of Pt over the time period shown in Fig. 19.9, the relative prices of other precious metals with respect to Pt are more variable. Table 19.2 shows the costs of various precious metals with respect to Pt over the last 1-, 5-, and 10-year periods calculated from the data in Fig. 19.12 and prices for Rh over the same time period.

In addition to the A/mgPt and A/mgPGM typically quoted, the relative precious metal cost values can be used to determine an activity per relative PGM cost for different core–shell materials. While Pd cost remains around 0.3 or 0.4 times that of Pt, use of Pd within the core of core–shell catalysts appears viable, depending on the performance achieved and the metal amount used. Pd is produced as a by-product of Pt mining in South Africa and Ni mining in Russia [64]. Newer mined deposits in South Africa in the UG2 reef in the Eastern Bushveld contain a higher proportion of Pd:Pt compared to previously exploited Merensky Reef ores which are higher in Pt content [65]. However, in the past (1999–2001) Pd prices have maintained parity or exceeded those of Pt, as a consequence of Pd supply issues and changes in the technology used in car exhaust catalysts to use more Pd. Also in recent years, Pd prices have been influenced by Russian state stocks being supplied into the markets, and these stocks are becoming depleted. So it is likely that Pd demand will exceed supply in coming years leading to increasing Pd prices. So although the MEA mass activities of ~0.3 A/mgPt achieved using PtML/Pd and PtML/Pd_9Au[11] are promising, once Pd and Au content/cost are included and considered, these become more similar in activity/PGM cost to conventional PEMFC catalysts.

In contrast to Pd and Pt, there is a lower natural abundance of Ir in metal ores [66], so using a substantial amount of Ir within the core of a core–shell catalyst would be likely to increase Ir cost and make such a catalyst inappropriate as a long-term use in automotive PEMFC systems. The effect of Ir content on likely cost of both alloy and core–shell catalysts should therefore be scrutinized as well as the activity per mgPt.

Although the complex interplay of various factors in the precious metal market does not allow simple predictions of future costs based on abundance alone, the price increase in Ir in recent years due to increased use in LED manufacturing for flat screen televisions illustrates the likely outcome of increased Ir demand on the metal price; the Ru price spike in 2006–2007 associated with increased use in hard disc manufacture is another example. Increasing demand for Pd would also lead to increasing price, affecting the long-term viability of using Pd as a core for core–shell catalyst materials. Overall, minimizing the amount of total PGM used within core–shell materials and achieving a true reduction in overall precious metal content appear to be the best way forward in the long term. However, alternative nonprecious metal lower-cost core constituents are typically of lower stability in the electrochemical environment.

19.6 Outlook

A wide variety of core–shell systems have been explored for use at the PEMFC cathode, and many systems show great promise in the form of high activity when measured in the RDE environment (see Table 19.1). Often these high activity values relate to samples made at small scales or in situ on the RDE tip, and only a few groups have generated data using scaled materials tested in the MEA environment. Notable efforts by Sasaki and colleagues to scale the Cu UPD galvanic displacement method for core–shell preparation and perform long-term MEA testing have shown promising results using PtML/Pd/C and PtML/Pd_9Au/C. Otherwise there is so far a conspicuous lack of other reliable MEA test data on these systems. Differences in activity are observed between small-scale core–shell catalyst preparations and the larger-scale batches necessary for MEA testing (Table 19.1) highlighting the difficulties associated with catalyst scale-up. The long-term effect on overall catalyst cost of using significant amounts of alternative precious metals such as Pd, Ir, or Au within the cores of core–shell catalysts must also be considered. Also, MEA activity and durability testing may reveal different performance and aging of catalyst materials compared to tests under more ideal, milder conditions. Thus, further development of scalable materials and evaluation in MEAs are needed to demonstrate the full promise of core–shell systems for use in the PEMFC environment.

References

1. Gasteiger HA, Kocha SS, Sompalli B, Wagner FT (2005) Activity benchmarks and requirements for Pt, Pt-alloy and non-Pt oxygen reduction catalysts for PEMFCs. Appl Catal B 46:9–35
2. http://www1.eere.energy.gov/hydrogenandfuelcells/fuelcells/
3. Borup R et al (2007) Scientific aspects of polymer electrolyte membrane fuel cell durability and degradation. Chem Rev 107:3904–3951
4. Adzic RR, Zhang J, Sasaki K, Vukmirovic MB, Shao M, Wang JX, Nilekar AU, Mavrikakis M, Valerio JA, Uribe F (2007) Platinum monolayer fuel cell electrocatalysts. Top Catal 46:249–262

5. Adzic RR, Lima FHB (2009) Platinum monolayer oxygen reduction electrocatalysts, Chapter 1. In: Vielstich W, Yokokawa H, Gasteiger HA (eds) Handbook of fuel cells, fundamentals, technology and applications, Advances in electrocatalysis, materials diagnostics and durability, vol 5, part 1. Wiley, West Sussex
6. Cai Y, Adzic RR (2011) Platinum monolayer electrocatalysts for the oxygen reduction reaction; improvements induced by surface and subsurface modification of cores. Adv Phys Chem 11:16. doi:10.1155/2011/530397, Article ID 530397
7. Sasaki K, Zhang L, Adzic RR (2008) Niobium oxide-supported platinum ultra-low amount electrocatalysts for oxygen reduction. Phys Chem Chem Phys 10:159–167
8. Shao M, Sasaki K, Liu P, Adzic RR (2007) Pd_3Fe and Pt monolayer-modified Pd_3Fe electrocatalysts for oxygen reduction. Z Phys Chem 221:1175–1190
9. Sasaki K, Wang JX, Naohara H, Marinkovic N, More K, Inada H, Adzic RR (2010) Recent advances in platinum monolayer electrocatalysts for the oxygen reduction reaction: scale-up synthesis, structure and activity of Pt shells on Pd cores. Electrochim Acta 55:2645–2652
10. Shao M, Shoemaker K, Peles A, Kaneko K, Protsailo L (2010) Pt monolayer on porous Pd-Cu alloys as oxygen reduction electrocatalysts. J Am Chem Soc 132:9253–9255
11. Sasaki K, Naohara H, Cai Y, Choi YM, Liu P, Vukmirovic MB, Wang JX, Adzic RR (2010) Core-protected platinum monolayer shell high stability electrocatalysts for fuel-cell cathodes. Angew Chem Int Ed 49:1–7
12. Sasaki K, Naohara H, Choi YM, Cai Y, Chen WF, Marinkovic N, Liu P, Adzic RR (2011) Enhanced stability of platinum monolayer on palladium-gold nanoparticle electrocatalysts in long-term fuel cell tests. In: Abs 1056 220th meeting of the Electrochemical Society
13. Debe M (2009) Advanced cathode catalysts and supports for PEM fuel cells, DoE Hydrogen Program Review Project FC_17
14. Murthi V (2010) Highly dispersed alloy catalysts for durability, DoE Hydrogen Program Reviews FC-002
15. Ramirez-Caballero GE, Ma Y, Callejas-Tovar R, Balbeuna P (2010) Surface segregation and stability of core-shell alloy catalysts for oxygen reduction in acid medium. Phys Chem Chem Phys 12:2209–2218
16. Kuttiyeil K, Sasaki K, Adzic RR (2010) Bimetallic Ni-Ir core platinum monolayer shell electrocatalysts for the O_2 reduction reaction. In: Abs 744, 218th meeting of the Electrochemical Society
17. Zhang J, Vukmirovic MB, Xu Y, Mavrikakis M, Adzic RR (2005) Controlling the catalytic activity of platinum monolayer electrocatalysts for oxygen reduction with different substrates. Angew Chem Int Ed 44:2132–2135
18. Zhang J, Mo Y, Vukmirovic MB, Klie R, Sasaki K, Adzic RR (2004) Platinum monolayer electrocatalysts for O_2 reduction: Pt monolayer on Pd(111) and on carbon-supported Pd nanoparticles. J Phys Chem B 108:10955–10964
19. Zhang J, Shao MH, Sasaki K, Vukmirovic MB, Uribe F, Adzic RR (2006) Platinum and mixed platinum metal monolayer fuel cell electrocatalysts: design, activity and long-term performance stability. ECS Trans 3(1):31–36
20. Xing Y, Cai Y, Vukmirovic MB, Zhou W-P, Karan H, Wang JX, Adzic RR (2010) enhancing oxygen reduction reaction activity via Pd-Au alloy sublayer mediation of the Pt monolayer electrocatalysts. J Phys Chem Lett 1:3238–3242
21. Shao M, Sasaki K, Marinkovic NS, Zhang L, Adzic RR (2007) Synthesis and characterisation of platinum monolayer oxygen-reduction electrocatalysts with Co-Pd core-shell nanoparticle supports. Electrochem Commun 9:2848–2853
22. Wang JX, Inada H, Wu L, Zhu Z, Choi Y, Liu P, Zhou W-P, Adzic RR (2009) Oxygen reduction on well-defined core-shell nanocatalysts: particle size, facet and Pt shell thickness effects. J Am Chem Soc 131:17298–17302
23. Price SWT, Speed JD, Kannan P, Russell AE (2011) Exploring the first steps in core-shell electrocatalyst preparation: in situ characterisation of the underpotential deposition of Cu on supported Au nanoparticles. J Am Chem Soc 133:19448–19458

24. Shao M, Humbert M, Smith B (2011) Synthesis and characterisation of core-shell electrocatalysts for fuel cells. In: Abs 941, 220th meeting of the Electrochemical Society
25. Humbert M, Smith B, Wang Q, Ehrlich S, Shao M (2012) Synthesis and characterization of palladium–platinum core–shell electrocatalysts for oxygen reduction. Electrocatalysis 3:298–303
26. Russell AE, Tessier BC, Wise AM, Rose A, Price SWT, Richardson PW, Ball SC, Theobald B, Thompsett D, Crabb EM (2011) In situ XAS studies of core-shell PEM fuel cell catalysts: the opportunities and challenges. ECS Trans 41(1):55–67
27. Koenigsmann C, Santulli AC, Gong K, Vukmirovic MB, Zhou W-P, Sutter E, Wong SS, Adzic RR (2011) Enhanced electrocatalytic performance of processed, ultrathin supported Pd-Pt core-shell nanowire catalysts for the oxygen reduction reaction. J Am Chem Soc 133:9783–9795
28. Gong K, Sasaki K, Vukmirovic MB, Adzic RR (2011) Tetrahedral palladium nanocrystals – a new support of platinum monolayer electrocatalysts having improving activity and stability in oxygen reduction reaction. In: Abs 1941, 219th meeting of the Electrochemical Society
29. Kuttiyeil K, Sasaki K, Choi Y, Su D, Liu P, Adzic RR (2012) Bimetallic IrNi core platinum monolayer shell electrocatalysts for the oxygen reduction reaction. Energy Environ Sci 5:5297–5304
30. Zhou W-P, Sasaki K, Su D, Zhu Y, Wang JX, Adzic RR (2010) Gram-scale-synthesised Pd_2Co-supported Pt monolayer electrocatalysts for oxygen reduction reaction. J Phys Chem C 114:8950–8957
31. Cai Y, Ma C, Zhu Y, Wang JX, Adzic RR (2011) Low coordination sites in oxygen-reduction electrocatalysis: their roles and removal. Langmuir 27(13):8540–8547
32. http://www.greencarcongress.com/2012/01/chemcat-20120103.html
33. Wu Y-N, Liao S-J, Liang Z-X, Yang L-J, Wang RF (2009) High performance core-shell PdPt@Pt/C catalysts via decorating PdPt alloy cores with Pt. J Power Sources 194(2):805–810
34. Peng Z, Yang H (2009) Designer platinum nanoparticles: control of shape, composition in alloy, nanostructure and electrocatalytic property. Nano Today 4:143–164
35. Wang H, Ji S, Wang W, Linkov V, Pasupathi S, Wang R (2012) Pt decorated PdFe/C: extremely high electrocatalytic activity for methanol oxidation. Int J Electrochem Sci 7:3390–3398
36. Peng Z, Yang H (2009) PtAu bimetallic heteronanostructures made by post-synthesis modification of Pt-on-Au nanoparticles. Nano Res 2:406–415
37. Kristian N, Wang X (2008) Pt_{shell}-Au_{core}/C electrocatalyst with a controlled shell thickness and improved Pt utilisation for fuel cell reactions. Electrochem Commun 10:12–15
38. Peng Z, Wu J, Yang H (2010) Synthesis and oxygen reduction electrocatalytic property of platinum hollow and platinum-on silver nanoparticles. Chem Mater 22:1098–1106
39. Lim B, Jiang M, Camargo PHC, Cho EC, Tao J, Lu X, Zhu Y, Xia Y (2009) Pt-Pd bimetallic nanodendrites with a high activity for oxygen reduction. Science 5:1302–1305
40. Choi I, Ahn SH, Kim JJ, Kwon OJ (2011) Preparation of Pt_{shell}-$Pd_{\ core}$ nanoparticle with electroless deposition of copper for polymer electrolyte membrane fuel cell. Appl Catal B Environ 102:608–613
41. Ball S, Burton SL, Fisher J, O'Malley R, Tessier B, Theobald BRC, Thompsett D, Zhou WP, Su D, Zhu Y, Adzic RR (2009) Structure and activity of novel Pt-core-shell catalysts for the oxygen reduction reaction. ECS Trans 25(1):1023–1036
42. Ball S, Burton SL, Christian E, Davies A, Fisher J, O'Malley R, Passot S, Tessier B, Theobald BRC, Thompsett D (2009) Activity and stability of Pt monolayer core-shell catalysts. ECS Trans 25(1):1011–1022
43. Park J, Kim MG, Jun Y, Lee JS, Lee W, Cheon J (2004) Characterisation of superparamagnetic "core-shell" nanoparticles and monitoring of their anisotropic phase transition to ferromagnetic "solid-solution" nanoalloys. J Am Chem Soc 126(29):9072–9078
44. Mayrhofer KJJ, Hanzlik M, Arenz M (2009) The influence of electrochemical annealing in CO saturated solution on the catalytic activity of Pt nanoparticles. Electrochim Acta 54(22):5018–5022

45. Sasaki K, Kuttiyiel KA, Su D, Adzic RR (2011) Platinum monolayer IrFe core-shell nanoparticle electrocatalysts for the oxygen reduction reaction. Electrocatalysis 2:134–140
46. Sasaki K, Kuttiyiel KA, Barrio L, Su D, Frenkel AI, Marinkovic N, Mahajan D, Adzic RR (2011) Carbon-supported IrNi core-shell nanoparticles: synthesis, characterisation and catalytic activity. J Phys Chem C 115:9894–9902
47. Wang JX, Ma C, Choi Y-M, Su D, Zhu Z, Liu P, Si R, Vukmirovic MB, Zhang Y, Adzic RR (2011) Kirkendall effect and lattice contraction in nanocatalysts: a new strategy to enhance sustainable activity. J Am Chem Soc 133:13551–13557
48. Esposito D, Hunt ST, Kimmel YC, Chen JG (2011) A new class of electrocatalyst for hydrogen production from water electrolysis: metal monolayers supported on low-cost transition metal carbides. J Am Chem Soc 134:3025–3033
49. Paulus UA, Schmidt TJ, Gasteiger HA, Behm RJ (2001) Oxygen reduction on a high-surface area Pt:Vulcan carbon catalyst: a thin-film rotating ring-disk electrode study. J Electroanal Chem 495:134–145
50. van der Vliet D, Strmcnik DS, Wang C, Stamenkovic V, Markovic NM, Koper MTM (2010) On the importance of correcting for the uncompensated ohmic resistance in model experiments of the oxygen reduction reaction. J Electroanal Chem 647:29–34
51. Zelenay P (2008) Advanced cathode catalysts, DoE Hydrogen Program Review Project FC_003
52. Zelenay P (2009) Advanced cathode catalysts, DoE Hydrogen Program Review Annual Project Progress Report V.E.5
53. Gong K, Su D, Adzic RR (2010) Platinum-monolayer shell on $AuNi_{0.5}Fe$ nanoparticle core electrocatalyst with high activity and stability for the oxygen reduction. J Am Chem Soc 132(41):14364–14366
54. Shao M, Peles A, Shoemaker K, Gumalla M, Njoki PN, Luo J, Zhong C-J (2010) Enhanced oxygen reduction activity of platinum monolayer on gold nanoparticles. J Phys Chem Lett 2:67–72
55. Gong K, Chen W-F, Sasaki K, Su D, Vukmirovic MB, Zhou W, Izzo E, Perez-Acosta C, Hirunsit P, Balbuena P, Adzic RR (2009) Platinum-monolayer electrocatalysts: palladium interlayer on IrCo alloy core improves activity in oxygen reduction reaction. J Electroanal Chem 649(1–2):232–237
56. Chen S, Sheng W, Yabuuchi N, Ferereira PJ, Allard LF, Shao-Horn Y (2009) Origin of oxygen reduction reaction activity on “PtCo” nanoparticles: atomically resolved chemical compositions and structures. J Phys Chem C 133:1109–1125
57. Matsutani K, Hayakawa K, Tada T (2010) Effect of particle size of platinum and platinum-cobalt catalysts on stability against load cycling. Platinum Met Rev 4:223–232
58. Naohara H, Sasaki K, Adzic RR (2010) Fuel cell performance and long term stability of platinum monolayer electrocatalysts. In: 216th ECS meeting, Abs 980
59. Ozkaya D, Ball S, Davies A, Fisher J, O’Malley R, Theobald BRC (2010) Unpublished work
60. Jaffray C, Hards G (2003) Precious metal supply requirements. In: Vielstich W, Gasteiger HA, Lamm A (eds) Hand book of fuel cells – fundamentals, technology and applications, Fuel cell technology and applications. Wiley, New York
61. Tiax (2003) Platinum availability and economics for PEMFC commercialisation, Report to US Department of Energy, http://www1.eere.energy.gov/hydrogenandfuelcells/pdfs/tiax_platinum.pdf
62. Pt, Pd, Ru, Ir and Rh prices taken from http://www.platinum.matthey.com/pgm-prices/
63. Au prices taken from http://www.kitco.com
64. PGM market reviews, from 1999 to present, http://www.platinum.matthey.com/publications/pgm-market-reviews/
65. Cawthorn RG (2010) The platinum group element deposits of the Bushveld Complex in South Africa. Platinum Met Rev 54(4):205–215
66. African Rainbow Minerals (2006) Annual report (showing values of PGM split in the two rivers platinum mine). http://www.arm.co.za/im/files/annual/2006/ar_2006.pdf, p 23

Chapter 20
Understanding Activity and Durability of Core/Shell Nanocatalysts for Fuel Cells

Rafael Callejas-Tovar and Perla B. Balbuena

Abstract We review recent analyses of the various aspects related to the performance of core/shell nanocatalyst particles used as electrodes in proton exchange membrane fuel cells. These nanoparticles usually consist of a thin layer of pure Pt in the shell and a core alloy made of a combination of metal elements that are targeted to meet two main objectives: reducing the catalyst price and enhancing the activity of the surface layer with respect to an equivalent particle made of pure Pt. Even though both objectives have been shown to be met, a huge challenge remains that is related to the long-term durability of the particle. This is because the less noble components are prone to relatively easy dissolution in the harsh acid conditions in which low-temperature fuel cells operate. The catalytic behavior of the nanoparticle towards the oxygen reduction reaction (ORR) and the evolution of the catalytic particle under this complex environment require a combination of experimental modern surface science and electrochemical techniques but also the formulation of models that allow a better understanding and a rational catalyst design. In this chapter, we review the state-of-the-art modeling of core/shell catalysts for the ORR. This involves various aspects that are intrinsic to the core/shell structure: surface segregation, metal dissolution, and catalytic activity. A number of methods ranging from ab initio density functional theory to classical molecular dynamics and Kinetic Monte Carlo are included in our discussion.

R. Callejas-Tovar
Artie McFerrin Department of Chemical Engineering, Texas A&M University, College Station,
TX 77843, USA

P.B. Balbuena (✉)
Artie McFerrin Department of Chemical Engineering, Texas A&M University, College Station,
TX 77843, USA

Materials Science and Engineering Program, Texas A&M University, College Station,
TX 77843, USA
e-mail: balbuena@tamu.edu

M. Shao (ed.), *Electrocatalysis in Fuel Cells*, Lecture Notes in Energy 9,
DOI 10.1007/978-1-4471-4911-8_20,

20.1 Introduction

Proton exchange membrane fuel cells (PEMFCs) are promising green alternatives to replace fossil fuels in transportation applications. However, the high cost and poor catalytic efficiency of the electrocatalyst where the oxygen reduction reaction takes place are crucial challenges that need to be overcome in order to exploit this technology. The ORR is a kinetically slow reaction in which molecular oxygen is reduced and combines with protons producing water. Platinum has been widely used as electrocatalyst for the ORR in fuel cells, but its prohibitive cost and relatively sluggish ORR kinetics[1] have motivated the development of catalysts with improved efficiency and low cost. The use of nanoparticles to carry out the electrocatalysis of the ORR minimizes the required amount of precious material that is able to maximize the catalytic performance. By employing Pt-based alloy catalytic nanoparticles containing less expensive 3d metals [2–9], the required amount of platinum is further reduced; some of these alloys have shown enhanced ORR activity compared to pure Pt catalysts[3, 5, 8, 10–12]. Recently, in addition to alloying platinum with non-precious metals, novel nanoparticle configurations with remarkable activity have been proposed such as the core–shell catalysts consisting of a Pt monolayer shell over cores made of a metal core constituted by a less noble metal or a less expensive alternative alloy. Among these, some interesting ORR activities have been detected on nanoparticles having porous/hollow Pd–Cu alloy cores [13], acid-treated Pt_3Co alloys [5, 14, 15], or dealloyed $PtCu_3$ [16, 17]. The role of theoretical studies in the search for enhanced ORR catalyst has been crucial, from screening of new materials to fundamental understanding of the processes involved in the activity and durability of the catalyst at a molecular level. In this chapter we review the efforts towards the development of enhanced ORR catalysts using theoretical and molecular simulation techniques.

20.2 Activity for Oxygen Reduction Reaction Studies

In previous years, platinum has been widely used as electrocatalyst for the ORR because it is the most efficient pure catalyst material. However, its scarcity and associated high cost motivated the development of alloy materials to reduce the load of Pt. Moreover, the ORR kinetics is slow on pure Pt catalysts, requiring a high overpotential due to the presence of oxygen and hydroxyl strongly bonded to the surface as it was determined by electronic structure calculations [18]. Therefore, there is a need for catalysts with low cost and enhanced ORR activity to replace pure Pt.

Near-surface alloys (NSAs) are alloys wherein a solute metal is present near the surface of a host metal in concentrations different from the bulk (e.g., Pt monolayers on base metals). The understanding and development of NSAs is a promising area of research in catalyst design [11, 19–22]. For example, it has been shown that NSAs of Pt enhance the catalytic properties of pure Pt for H_2 activation kinetics, whereas at the same time they bind adsorbates much weaker than pure Pt [19, 20, 22]. These features make NSAs promising catalysts for the ORR reducing the binding energy of intermediate species making the reaction mechanism more efficient. Core/shell alloy nanoparticles are NSAs that represent an alternative configuration where minimum amounts of Pt are required to obtain a remarkable ORR activity. Core–shell structures may be formed naturally as a consequence of a surface segregation process induced by adsorbates, the presence of an electric field such as that existing when the nanocatalyst is operating as a fuel cell electrode, or it could be originated by a dealloying process during synthesis or under operation conditions. However, this novel core/shell configuration causes surface phenomena that affect the catalytic performance and durability due to differences in size and electronic structure among the alloy components and differences in crystal structure due to different compositions. Provided that core–shell structures have been obtained during synthesis, the next question is how stable is the core. In this section we focus on the theoretical approaches to understand the surface segregation of alloy atoms especially in core–shell nanocatalysts, and then we review the studies that analyze the reasons for activity enhancement of novel ORR catalysts.

20.2.1 The Surface Segregation Phenomenon

It has been reported that the catalytic activity of alloys depends dramatically on how the atoms arrange in the outmost layers of the catalyst surface [23–25], and it is influenced by the surface segregation phenomenon in which atoms migrate from the core to the surface layer causing changes in the structure and local composition that affect the physicochemical properties of the material. For this reason, surface segregation is important to the design and performance of novel materials, drawing the attention of numerous experimental [4, 5, 7, 9, 13, 26–42] and theoretical investigations [43–61].

Remarkable catalytic activity can be attained as a result of surface segregation as in the case of the acid-treated Pt_3Co alloy [5, 11, 14, 15] in which the enhanced activity is partially attributed to the formation of a "Pt-skin" structure produced by an exchange of Pt and Co in the first two layers [11]; this and other reports [4, 11, 62] are evidence of the key role of surface segregation in the ORR activity. Therefore, it is important to characterize the surface atomic distribution of catalytic alloys and to elucidate the effect of segregation on the catalytic properties, in order to design materials with enhanced performance. Although for some of the previously mentioned Pt-based alloys the surface and subsurface structures have been clearly identified, the details of their inherent surface segregation are not yet completely understood. Since information at atomic level is required, theoretical studies are ideal to elucidate the driving force and the tendency of this phenomenon. Several theoretical investigations of surface segregation have used different approaches such as thermodynamic [43], tight-binding [44, 45], embedding atom

(EAM) [46, 47], Monte Carlo [48–51], and first-principles methods [52–54], mainly density functional theory (DFT). The thermodynamic method is based on Gibbs free energy models for mixtures whose parameters are determined using experimental information. Semiempirical atomistic approaches are used by tight-binding, classical molecular dynamics, and Monte Carlo techniques. The last two techniques use many body force fields such as EAM to describe metal–metal interactions. An important problem arises with the description of phase behavior in nanoparticles, which may dramatically differ from bulk. This is an area which is largely unexplored. We have recently analyzed the phase stability of Cu–Ag core–shell nanoparticles [63] based on their thermodynamic mixing properties for both randomly mixed and core–shell clusters as functions of nanoparticle size, temperature, and composition, using classical molecular dynamics (MD) simulations. We found that at room temperature, the alloying of Cu and Ag is thermodynamically feasible only for a nanocluster size range, excluding very small (<1.8 nm) and large clusters ($>$ ~4 nm), in the size range of favorable alloy formation; Cu–Ag core/shell structures are more stable than random configurations; and the same conclusion holds for most of the composition range at fixed cluster size. The effect of temperature was evaluated for nanoclusters of fixed size and composition; it was found that core/shell structures are preferred up to the melting temperature of the nanoparticle. In addition, an analytical model was proposed to predict the thermodynamic properties of mixing of nanoalloys using bulk enthalpies of mixing of the pure components and those of the corresponding bulk alloy. The enthalpies and Gibbs free energies of mixing obtained from the analytical model qualitatively agree with those obtained from MD simulations, especially when the nanoparticle size increases above 2.8 nm. Adding the shape effect to those of size and composition, Qi et al. [64] formulated a new model and calculated phase diagrams and alloying phenomena in nanoparticles in a wide range of compositions. A shape factor is introduced in the model as the ratio of the surface area of nonspherical to that of spherical particles. It was found that as the particle size decreases, alloying takes place at dilute solute compositions then extends to higher concentrations and finally all mixtures can be alloyed. However, in spite of these and other initial theoretical investigations [63–67], the thermodynamics and kinetics of alloy formation in nanoparticles is a topic that has not been yet fully addressed, so the synthesis in most cases is guided by trial and error experimentation [68–70].

First-principles theoretical and computational studies have also been employed to determine the thermodynamics of surface segregation by calculating the segregation energy, which is typically defined in DFT studies as the difference of the corresponding energies of the structure showing segregation and the original one [57]. Using this approach, researchers have studied the most relevant factors responsible of changing the segregation trends: the effect of the identity of the alloy atoms, presence of adsorbed ORR intermediates, surface configuration, and morphology on the surface segregation of alloy ORR catalysts [55–61, 71]. It has been concluded that the driving force for surface segregation is not only the difference in size of the alloy constituents, surface energies, and heats of formation of alloys but a very important role is given by the presence of adsorbates such as atomic oxygen [60]. DFT studies addressing the effect of this factor on the surface segregation of $Pt_3M(111)$ ($M = Fe$, Co, and Ni) alloys revealed that the segregation trend is substantially modified by the adsorbed oxygen. Under 0.25 monolayer of O coverage, both the Pt-segregated and M-segregated surfaces are less stable than the nonsegregated one. Moreover, the segregation energy under the presence of adsorbates can be expressed as the sum of the segregation energy under vacuum conditions and the adsorption energy difference of the segregated and nonsegregated alloy systems. Hence, the surface segregation trend under adsorption conditions is directly correlated to the surface–adsorbate binding strength [55, 60]. The complex effects driven by the affinity of metal elements with adsorbates on the surface have attracted the attention of several theoretical studies. Recently, DFT calculations were carried out to investigate the effect of surface segregation on the trends for dissolution of Pt surface atoms in acid medium and oxygen reduction reaction activity of core/shell materials, consisting of a monolayer of Pt over a monometallic or bimetallic core [72]. Two groups of cores were investigated: Pt/X with $X = Ir$, Au; Pd, Rh, Ag; Co, Ni, Cu; and Pt/Pd_3X, with $X = Co$, Fe, Cr, V, Ti, Ir, Re. Considering clean and oxygenated surfaces, it was found that all the 4d and 5d pure cores may serve as stable cores, and their beneficial effect on the Pt monolayer may be further tuned by alloying the core to another element, chosen from 3d or 5d groups. The analyses of pure cores revealed that elements such as Ir with larger surface energies and larger cohesive energies than pure Pt have strong antisegregation energies. On the other hand elements such as Au (larger size, lower surface energy, and lower cohesive energy) would be expected to segregate, and although the calculated energy to take one atom from the bulk core to the Pt surface is negligible, the segregation trend increases significantly as the surface concentration of Au atoms increases [72]. Gold is very stable in the core under adsorbed oxygen, when its antisegregation trends are dramatically enhanced. Both electronic and geometric effects make the Pt/Ir very different than the Pt/Au systems; although Pt/Au is the most reactive system according to its electronic parameters, the OH adsorption is weaker than in Pt/Ir due to geometric effects that determine a change of the surface Pt–Pt distance. Similar discussions have been presented for cores made of 4d elements (Ag, Rh, Pd). On the other hand, 3d elements (Cu, Co, Ni) behave very differently and they are all unstable cores. Their common characteristics are smaller sizes, lower cohesive energies, and high oxophilicity compared to pure Pt [72, 73]. Natural combinations for core–shell systems would be cores composed of 4d or 5d metals combined with those of the 3d group. Figure 20.1 illustrates the segregation energy properties on Pt/Pd_3X clean surfaces and under 0.25 ML of O, where $X = Co$, Fe, Cr, V, Ti, Ir, and Re. The segregation behavior of both Pd and X elements was investigated. Note that negative values correspond to favorable segregation trends, whereas positive energies indicate antisegregation trends. The energies are correlated with the charge on the segregated atom X. On clean surfaces, some segregation of Pd is observed, but the other elements show strong antisegregation trends. In contrast, under oxygen, the antisegregation trend of X reverts in all cases. Thus, Fig. 20.1b immediately warns about the strong effect of oxygen as a driving force for surface segregation (usually followed by metal dissolution) in all the selected core elements.

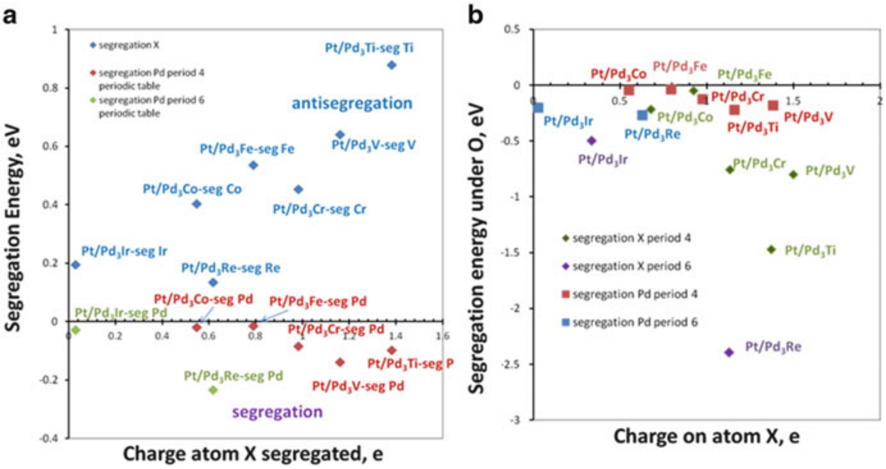

Fig. 20.1 (**a**) Segregation energy of X (*blue diamonds*) and segregation energy of Pd (*red diamonds* for X belonging to period 4 and *green diamonds* for X belonging to period 6 of the periodic table) from the core to the surface of clean core–shell Pt/Pd$_3$X alloys, in vacuum. (**b**) Segregation energy of X (*green diamonds* for X belonging to period 4 and *purple diamonds* for X belonging to period 6 of the periodic table) and segregation energy of Pd (*red squares* for X belonging to period 4 and *blue squares* for X belonging to period 6 of the periodic table) from the core to the surface of core–shell Pt/Pd$_3$X alloys covered by 0.25 ML of O (adapted from [72])

Thus, the high affinity of the Pd$_3$X cores to oxygen may cause surface poisoning with oxygenated species, surface reconstruction, and metal dissolution in acid medium. High coverage of oxygen adsorption and absorption may take place at high potentials during fuel cell operation resulting in surface roughening, migration of oxygen into the subsurface, and formation of surface oxides, as discussed in a later section. Another important factor affecting surface segregation is the morphology of the surface since nanoparticles (in the order of 1–10 nm) have a low fraction of low-coordinated sites present in step sites of the catalyst which have an effect on the segregation trend when oxygen is adsorbed [56]. All the previously discussed factors affecting surface segregation, in addition to others such as pH and temperature, are present in a fuel cell under operating conditions; their coupling yields to a number of complex scenarios which make difficult to propose a general model that describes the behavior of all the alloy systems under reaction conditions. However, with the advances in computer hardware and software, we expect that complete models based on ab initio and other first-principles-based models may become a reality [74].

As already mentioned, core–shell structures generally show excellent catalytic activity, and theoretical studies have investigated the origin of such enhancement as discussed in the next subsection. In addition, unfortunately surface segregation may induce the degradation of Pt bimetallic nanoparticles [41, 42] by promoting metal dissolution as it will be discussed in the following sections.

20.2.2 Novel Catalysts with Enhanced Oxygen Reduction Reaction Activity

Theoretical studies have helped to develop enhanced alloy catalysts by screening several materials and compositions, identifying promising candidates with desired properties. Specifically, recent advances in DFT allow the accurate description of surface reactions to determine the performance of a catalyst; this approach has proven to be a powerful tool which has been applied to different types of reactions of economic interest, and it has been linked to reactor design [75–78]. However, in order to efficiently screen catalytic materials through simulations, it is required to find appropriate descriptors to estimate the performance of the catalyst that is being tested. Nørskov et al. [75] demonstrated through an extensive set of DFT calculations that there is a universal relationship between the activation energy and the adsorption energy of the reaction intermediates. This concept applied to the ORR results in DFT evaluations of the adsorption energy of stable intermediate species, such as O and OH, which are used to estimate the catalytic activity of alloy systems. Moreover, this concept has been extended to determine the ORR mechanism and the effect of the electrochemical potential on the rate-limiting step [79]. Other ideas have been formulated based on the recognition that when discussing bimetallic systems, an immediate connection may be done to enzymatic reactions [80]. Figure 20.2 shows the similarity between the ORR mechanism expected in a bimetallic surface and that found in a metalloenzyme such as cytochrome-c oxidase (CcO) also having two active metal sites. The similarity is based on the ability of one of the metal atoms (Fe^{II} in the case of CcO) being active for the dissociation of molecular oxygen and in presence of a proton for formation of the OOH intermediate, whereas the other metal (Cu^{I} in CcO) promotes the reduction of O and OH to water. In previous work we had reported a thermodynamic analysis to explain the ORR mechanism in bimetallic systems. In that analysis, we used the following equations:

$$O_2 + M_A + H^+ + e^- \rightarrow HOO - M_A \tag{20.1}$$

$$HOO - M_A + M_B \rightarrow O - M_A + HO - M_B \tag{20.2}$$

$$O - M_A + HO - M_B + 3H^+ + 3e^- \rightarrow 2H_2O + M_A + M_B \tag{20.3}$$

Equation (20.1) represents the formation of the OOH intermediate on one of the metal sites, which is unstable and dissociates as indicated by Eq. (20.2), and the products (adsorbed O and OH) are further reduced as shown by Eq. (20.3) [81].

On the basis of Eqs. (20.1)–(20.3), we had suggested [81] a set of thermodynamic rules for a prescreening evaluation of appropriate metals that could be alloyed to Pt. According to these rules, the relative Gibbs free energies, $\Delta\Delta G_n$ ($n = 1$ and 3), are defined taking Pt as a reference:

$$\Delta\Delta G_n = \Delta G_n(\mathrm{M}) - \Delta G_n(\mathrm{Pt}) \tag{20.4}$$

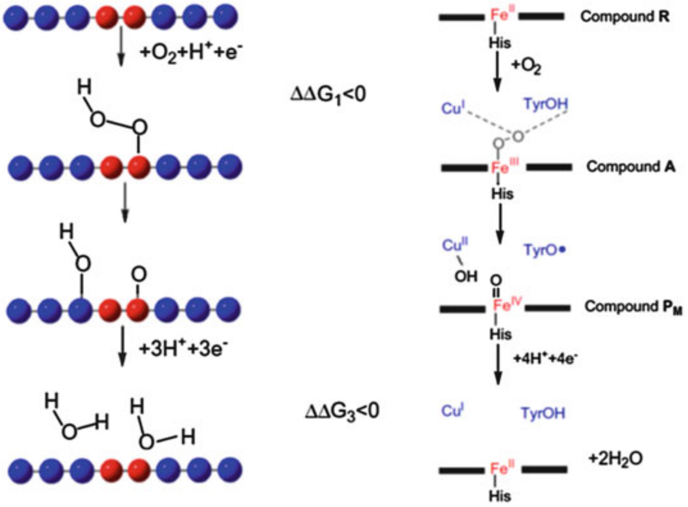

Fig. 20.2 *Left*: proposed ORR mechanism on bimetallic surfaces, where M_A atoms (*red*) favor OOH formation, and M_B atoms (*blue*) favor O and OH reduction. *Right*: simplified model of the ORR on the heme/Cu site of cytochrome-c oxidase metalloenzyme (adapted from [80])

where ΔG_1 and ΔG_3 refer to standard Gibbs free energies of Eqs. (20.1) and (20.3), respectively. Note that a good alloy catalyst should have negative values of both $\Delta\Delta G_1$ and $\Delta\Delta G_3$, so O and OH are not that strongly adsorbed that could not be further reduced, but the metal is able to dissociate molecular oxygen forming a sufficiently unstable OOH species. Figure 20.3 shows the results of $\Delta\Delta G_1$ and $\Delta\Delta G_3$ calculated for several neutral and ionic metals [80]. The results indicate that many cations satisfy the criteria; $\Delta\Delta G_3$ is more negative for each cation than for their corresponding neutral atoms. Thus, as expected, the reductions of HO–M and O–M are more favorable for cations because the positive charge weakens the M–O bond strength. In addition, the more negative values of $\Delta\Delta G_1$ for most cations suggest that most of them are thermodynamically more suitable for the formation of HOO–M [80]. Thus, the simple model is able to provide a thermodynamic explanation to the question why reduced transition-metal ions are ideal catalysts for O_2 reduction. This topic is also interesting in connection to fuel cells working in alkaline media and to other non-Pt materials based on pyridine-like organic molecules that have shown good ORR catalytic activity and discussed in other chapters of this book.

In addition to the adsorption energy of intermediate species, another descriptor of the ORR activity which can be obtained from electronic structure calculations is the position of the d-band center with respect to the Fermi level of the surface atoms of the alloy [5, 8, 24, 61, 82–85]. The calculation of these descriptors as meaningful representations of the catalytic surface is feasible in terms of computational time and, provided the appropriate resources, have shown to be useful in a high-throughput screening of catalytic materials[86]. Recently, Greeley and Nørskov

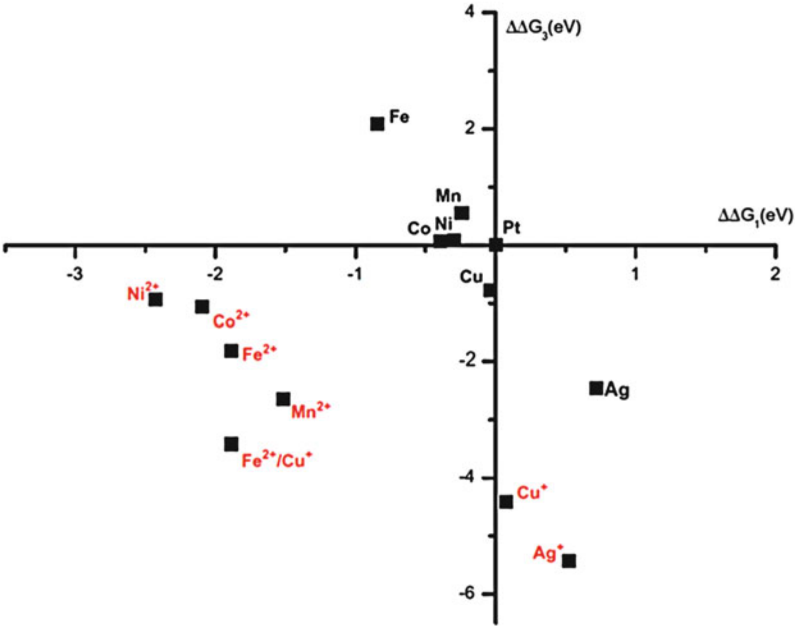

Fig. 20.3 Calculated relative Gibbs free energies (eV), $\Delta\Delta G_3$ vs. $\Delta\Delta G_1$, for metal cations and their corresponding neutral atoms (adapted from [80])

[87] used a combinatorial DFT-based approach to screen binary alloy catalysts for the ORR with enhanced stability. The studied alloys consisted of a solute metal alloyed into the surface layer of a homogeneous host metal (Pt, Cu, Ni, Ru, Re, Co, Fe, Cd, As, Sb, Ir, Ag, Pd, Rh, and Bi). In a first stage, the alloys with promising activity were screened using the binding energy of atomic oxygen as a descriptor. Approximately 750 alloy systems were studied, many of which showed enhanced ORR activity; these promising alloys were tested in a second stage with a rigorous potential-dependent stability approach. Unfortunately it was determined that nearly all of the alloy candidates will be thermodynamically unstable at the high potentials associated with the ORR; therefore, additional ways to stabilize binary surface alloys are required since they are not durable ORR catalysts. This study and many others emphasize the need of developing not only highly active but also durable ORR catalysts. The theoretical approach of the durability problem is discussed in the next section.

In core–shell catalysts, the Pt surface is deposited over an alloy core that strongly modifies its geometric and electronic properties. An important aspect is given by the charge transfer between the core and the shell which sometimes results in the development of a negative charge on the top layer [72]. Such effect is the result of a strong electrostatic interaction between the top surface and the sub-surface layers. For the Pt/Pd_3X systems shown in Fig. 20.1, we have calculated that the binding energy of the Pt monolayer to the core increases in the order

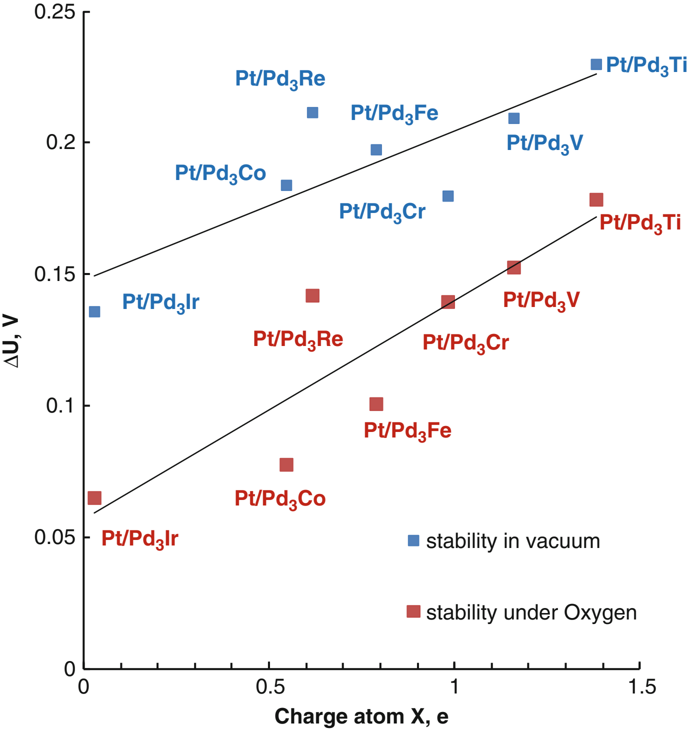

Fig. 20.4 Calculated electrochemical potential shift (ΔU, in V) for dissolution of Pt atoms from the surface of the core–shell system compared to those in pure Pt (adapted from [72])

Ir $<$ Co $<$ Fe $<$ Re $<$ V $<$ Ti $<$ Cr; this order approximately agrees with the trend observed for the surface stability shown in Fig. 20.4. The results in Fig. 20.4 display the calculated electrochemical potential shift corresponding to dissolution of the surface Pt atoms from a core–shell system, relative to those in a pure Pt one. The strongest the heterometallic bond, the most stable the top Pt layer.

Calculations of electrochemical potential shift were first reported by Roques et al. [88], and alternative schemes were introduced later [58, 89]. The calculated property is a good stability indicator and has been extensively used to investigate dissolution properties [90, 91]. In relation to Fig. 20.4 it is important to remark that the calculated stability refers only to the surface Pt atoms. However, the core atoms may migrate to the surface (as suggested by their segregation energies shown in Fig. 20.1) and induce a degradation process on the catalyst surface that will be discussed in the next sections.

Recent developments in catalysis for ORR in fuel cells are showing that enhanced activity may be attained using a Pt monolayer on porous or hollow cores [5, 14, 15, 92] which can even not contain platinum [13]. The latter configurations are especially attractive because, in addition to their high ORR activity, they minimize the required amount of Pt. It has been shown that it is

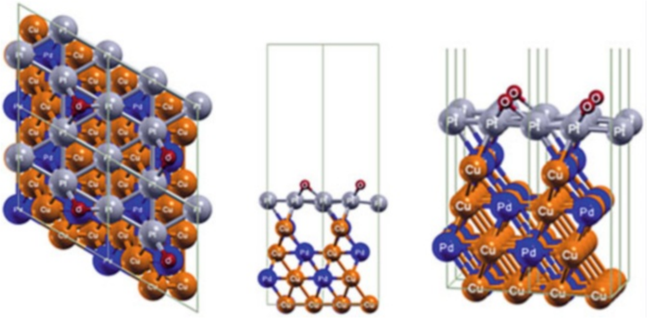

Fig. 20.5 Top, side, and perspective views of a Pt/PdCu$_3$-optimized slab under 0.25 ML of O and 0.50 ML of surface vacancies

possible to synthesize Pt hollow nanoparticles with enhanced Pt mass activity for ORR nanocrystals [92] and the synthesis process is explained on the basis of the Kirkendall effect [93]. This effect caused by the difference in diffusivities of the alloy metals has been used to fabricate hollow nanocrystals as high-efficiency catalysts or drug-delivery agents [94]. DFT calculations [92], using a simplified model of the highly active hollow ORR catalyst, suggest that the enhanced activity may be caused by a lattice contraction induced by the hollows. Although there is a consensus that the enhanced ORR activity of these porous structures may be partially attributed to a contraction in the Pt–Pt distance of the shell [13, 14, 62, 92], the role of the porosity is not yet clear. Recently, we studied the effect of metal porosity on the ORR activity of core/shell Pt-based alloys composed by a monolayer of Pt on top of an alloy core for bimetallic Pt/PtM/Pt$_3$M (M = Co, Pd, Ir, Cu) and trimetallic Pt/M1$_3$M2 (M1, M2 = Pd, Cu; M1 $\neq$ M2) using DFT [95].

It was found that subsurface vacancies (Fig. 20.5) induce relatively weaker binding energies of O and especially of OH, and reduced Pt–Pt surface distances, which can explain the experimentally observed activity enhancement. We remark that in addition to explaining the interesting ORR activity enhancement on these novel porous/hollow nanoparticles, further studies regarding their oxidation and their stability to potential cycling are still required.

20.3 Catalyst Durability Under Operating Conditions

The ORR typically takes place in acid medium which causes a continuous decay on the activity and durability of the metal nanocatalyst. Atomic oxygen resultant from O_2 dissociation has been identified as a predominant intermediate species of the ORR on the surface of the catalyst; its interaction with the surface atoms mainly determines the catalytic activity, and it has been found experimentally to have an effect in the durability of the catalyst [96–99]. There is a direct relationship between the degree of surface oxidation and the extent of metal dissolution, and they both correlate with the electrochemical potential [98]. Determining the structure of the oxide that is formed on the surface is a key issue to explain the metal dissolution mechanism causing durability problems in PEMFC catalysts. This is because depending on the extent of oxidation, the surface oxide may enhance dissolution or may act as a passivation layer. The effect of adsorbed oxygen and other adsorbates on the surface and subsurface of fuel cell catalysts has been previously studied by several theoretical reports [100–108]. Several computational studies have investigated potential energy surfaces and surface reconstruction effects due to oxygen adsorption and absorption [100–103, 106]. Hawkins et al. [100] examined the initial stages of oxidation of the Pt(111) surface at total coverages of 0.25–1.0 ML using DFT calculations, finding a strong preference for the formation and growth of one-dimensional Pt oxide chains; specifically at coverages above 0.50 ML, additional oxygen atoms tend to aggregate inducing a large buckling of ~1.8 Å and oxidizing the surface Pt atoms, as reflected in their positive charges. Other work showed the most stable configurations of oxygen absorbed in Pt(111) and Pt(100) surfaces based on DFT calculations [97, 101, 106]. Moreover, it was shown that increasing the on-surface oxygen or OH coverages can energetically and kinetically stabilize subsurface atomic oxygen [102]. Recently, the influence of oxygen on the dissolution of Pt from carbon-supported platinum nanoparticles (Pt/C), bulk polycrystalline Pt electrodes, and Pt(111) single crystals was studied [99]. An enhancement of the catalyst degradation caused by the presence of oxygen even in the lower potential regions was found, the Pt(111) single crystals being the most sensitive to the potential cycling under O_2. Moreover, a surface roughening caused by the exposure to oxygen was found, suggesting a relationship between the change in the structure of the surface oxide and the metal dissolution. Recent work on Jacob's group [109, 110] has used ab initio thermodynamics techniques [111, 112] to determine the most stable oxide surfaces on transition metals exposed to highly oxidative conditions. This information should be very useful to understand the reaction kinetics on highly oxidized surfaces.

In order to design materials resistant to corrosion, theoretical studies provide fundamental information about the surface oxidation on alloys [113–115]. Specifically, for ORR catalysts, such studies are focused on the effect of oxygen on the local composition of the surface which has an important role in its performance. Since dealloying may be used to modify the surface electrocatalytic reactivity of Pt bimetallic nanoparticles for the ORR, bimetallic Pt–Cu alloys were modeled using DFT calculations to obtain trends in the thermodynamics of surface Cu dissolution potentials from highly stepped and kinked Pt(854) single crystal surfaces[116]. It is found that there is a dependence of the electrochemical Cu dissolution potentials on the coordination number and nature of coordinating atoms of the bimetallic Pt–Cu surfaces. However, the specific energetics of each metal is required to explain the detailed dealloying behavior of bimetallic surfaces. A thermodynamic formalism combined with DFT calculations determined periodic trends in the reversible deposition/dissolution potentials of admetals on a variety of transition-metal substrates [90]. It was demonstrated that structural effects are a strong function of the local coordination number of the metal atoms, and periodic trends for the potential shifts are observed. Other work focused on electrode dissolution on Pt and Pt–Co alloys using a thermodynamic approach and DFT calculations to evaluate the Gibbs free energy and adsorption energies of O, OH, and H_2O [108]. It was found that the reversible potential for Co–OH formation from oxidation of H_2O on the $Pt_3Co(111)$ surface was significantly lower than the one for Pt–OH formation on the Pt(111) surface. Hence, Co will dissolve at lower potential than Pt in the alloy surface forming a Pt surface skin, and edge atoms are shown to be removed before terrace sites.

Molecular simulation is an ideal tool to elucidate the complex surface dynamics of the oxidized catalyst causing its degradation. We suggested that a multi-scale simulation approach would be appropriate to tackle this problem due to the diverse time and length scales needed to properly describe the oxidation phenomenon. Probably the simplest multi-scale approach may couple DFT calculations and classical molecular dynamics (MD) simulations in two stages to identify changes at a molecular level on the structure of the catalyst caused by oxidation of Pt and Pt/PtCo/Pt_3Co catalysts [95, 117–120] and then follow the time evolution of the structures when the main surface sites carry the oxidation/reduction charges. Within this scheme, classical MD simulations are used to model the catalyst that is exposed to increasing amounts of atomic oxygen and water. The MD model considers electrostatic interactions between the adsorbates, atomic oxygen and water, and the two topmost layers of the catalyst, where the atoms in the first and second surface layers are charged with average values obtained from DFT calculations. The effect of the electrode potential (or the degree of surface oxidation, which is an equivalent variable) is represented in the model by increasing charges (more positive for the surface atoms and more negative for the adsorbed oxygen), as resultant from the DFT evaluations. In our work water dissociation was taken into account using the CF1 central force model, where water is assumed to behave as a molten salt made of OH anions and H cations that under normal pH conditions reproduces the physicochemical behavior of liquid water [121]. In addition, the model includes the effect of low pH [117] incorporating acid-like molecules able to dissociate in water and to induce water dissociation as well. Initial simulations were done with an extended surface exposed to the acid electrolyte, and then a supported nanoparticle [120] was introduced thus achieving a realistic representation of the ORR occurring in a fuel cell. The MD simulations of Pt and Pt/PtCo/Pt_3Co nanoparticles supported over carbon revealed that water dissociation occurs only in presence of acid molecules which do not modify the relaxed structure of the nanoparticles. However, the dissociated cations and anions from the acid enhance water dissociation into OH^- and H^+ due to strong electrostatic interactions. The Pt/PtCo/Pt_3Co nanoparticle is more active than that of pure Pt in terms of water dissociation, but it shows a greater area loss after ten cycles of reduction and oxidation. The metal dissolution mechanism after reduction–oxidation cycles in the alloy nanoparticle involves (1) adsorption of oxygen, (2) surface segregation of non-noble alloy atoms, (3) oxygen absorption in the subsurface, (4) destabilization of the nascent surface oxide phase due to electrostatic interactions with ions in the solvent, and (5) detachment of single metal atoms bonded to oxygen atoms Fig. 20.6.

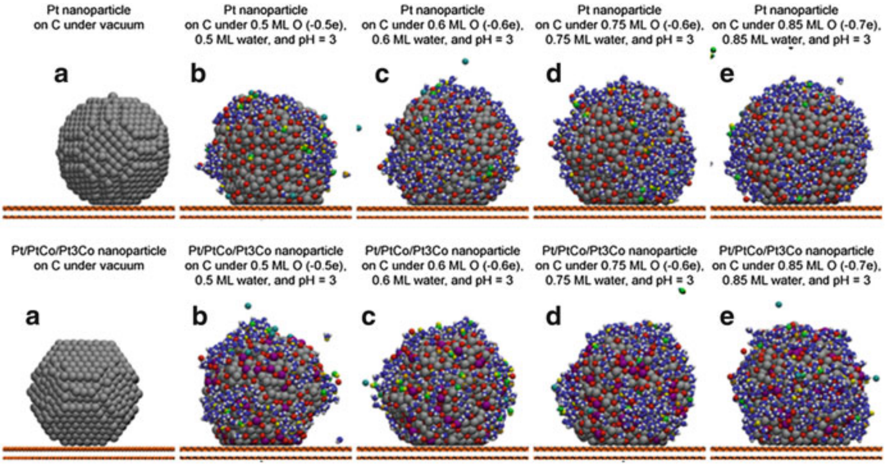

Fig. 20.6 Snapshots from molecular dynamics simulations showing the evolution of nanoparticles exposed to high O contents, water, and acid molecules. *Top row* shows pure Pt particles and *bottom row* displays Pt/PtCo/Pt_3Co particles: (**a**) under vacuum, (**b**) under 0.5 ML of O and 0.5 ML of water, (**c**) under 0.6 ML of O and 0.6 ML of water, (**d**) under 0.75 ML of O and 0.75 ML of water, and (**e**) under 0.85 ML of O and 0.85 ML of water. In all cases acid molecules were added to the systems in an amount equivalent to have a pH of 3 (adapted from [120])

We note that our model could be improved by introducing a reactive force field also for the metal phase, where the formation of an oxide phase with the correct stoichiometry may be induced. This is because a reactive force field may allow changes of the charges on O and the metal atoms as the oxide reaction is taking place. However, our simulation is a very good approximation that captures many of the qualitative features observed on the surface at the onset of surface oxidation formation.

In order to emulate a cyclic voltammetry experiment, we exposed the supported nanoparticle to simulated cycles of reduction and oxidation, in which the charges of the oxygen and metal atoms forming the outmost layers of the nanoparticle under 0.85 ML of oxygen were gradually decreased (reduction steps). Once neutrality was attained, the charges were steadily increased until recovering their original values (oxidation steps). The radial R-density profiles and snapshots of the surface of both studied systems after one and ten cycles are shown in Fig. 20.7 and Fig. 20.8, respectively. The R-density profiles provide the distribution of the number of atoms of the species as a function of the distance to the center of mass of the nanoparticle. The R-density profiles in Fig. 20.7 indicate that oxygen absorbs deeper in the subsurface as the cycling process occurs in the pure platinum nanoparticle, whereas in the alloy nanoparticle, simultaneous to the migration of O to the subsurface, Co atoms segregate from the subsurface to the outmost layers. After ten cycles of reduction and oxidation, metal dissolution of atoms forming the outer layers in both systems (Fig. 20.7) is observed; the estimated decrease in surface area compared to the area of the nanoparticle under vacuum is presented in Tables 20.1 and 20.2.

Comparison of the results in Tables 20.1 and 20.2 illustrates that there is a greater loss in surface area of the alloy nanoparticle compared to the one found in

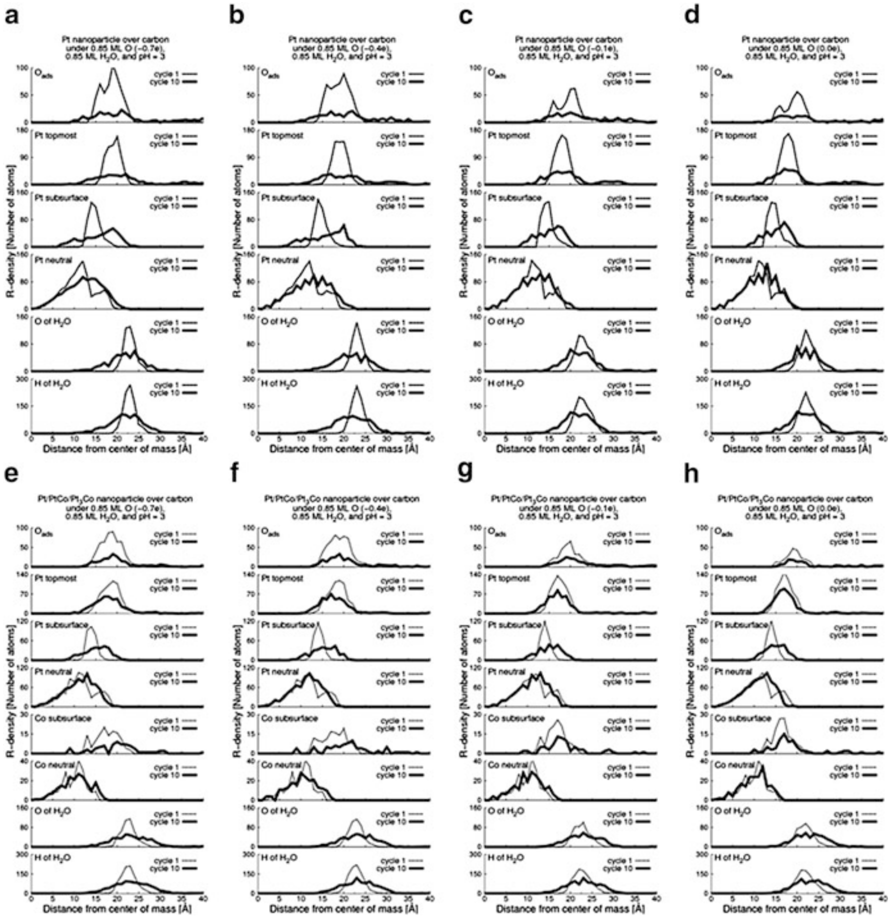

Fig. 20.7 *R*-density profiles of Pt (**a**–**d**) and Pt/PtCo/Pt_3Co (**e**–**h**) supported nanoparticles over C under 0.85 ML of oxygen and water, and pH = 3 after 1 and 10 reduction–oxidation cycles (adapted from [120])

the pure Pt system. After the first cycle the ratio of Co atoms to Pt atoms that are detached is approximately 2:1. However, after ten cycles such ratio reverses to 1:4; this implies that the segregated Co atoms dissolve before the Pt atoms which detach after most of the Co atoms near to the surface are dissolved. These findings are in agreement with several experimental reports showing the instability towards dissolution of Pt_3Co nanoparticles after operating cycles [122–124]. The dissolution process occurs mainly when the magnitude of the charge of the oxygen atoms is higher than −0.4e (in the reduction branch); the detached metal atoms agglomerate far from the nanoparticle. Interestingly, we found that the dissolution process takes place only when acid molecules are present. The role of the dissociated ions is destabilizing the metal oxide layers due to electrostatic interactions causing the

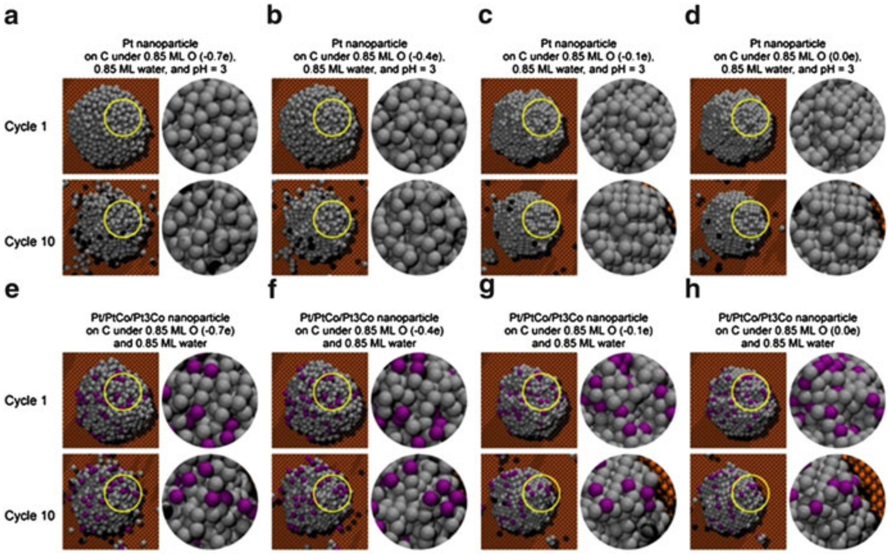

Fig. 20.8 Snapshots of the supported Pt (**a**–**d**) and Pt/PtCo/Pt_3Co (**e**–**h**) nanoparticles on C under 0.85 ML of oxygen and water, and pH = 3 taken at the end of the simulation after 1 and 10 reduction–oxidation cycles. All the adsorbates are hidden. Color key: platinum (*gray*), cobalt (*purple*), carbon (*orange*) (adapted from [120])

Table 20.1 Detached Pt atoms and estimated surface area of the supported Pt nanoparticle after reduction–oxidation cycles (taken from [120])

	Cycle 1	Cycle 10
Detached Pt atoms	4	36
Area/area vacuum	99.02 %	90.44 %

Table 20.2 Detached metal atoms and estimated surface area of the supported Pt/PtCo/Pt_3Co nanoparticle after reduction–oxidation cycles (taken from [120])

	Cycle 1	Cycle 10
Detached Pt atoms	4	36
Detached Co atoms	8	10
Area/area vacuum	94.26 %	86.87 %

detachment of single metal atoms bonded typically to one or two oxygen atoms. The facets of the nanoparticle are partially recovered when the charge of oxygen atoms is 0.0e, although steps and kinks in the outmost layers are permanent. Water molecules agglomerate in defined regions of the nanoparticle. This behavior is more evident after ten cycles of reduction and oxidation.

Further information can be obtained using coarse-grained methods such as Kinetic Monte Carlo (KMC) [125]. These simulations which can include much larger systems and the results evaluated in much longer times could be particularly useful to investigate degradation processes such as those discussed in this chapter.

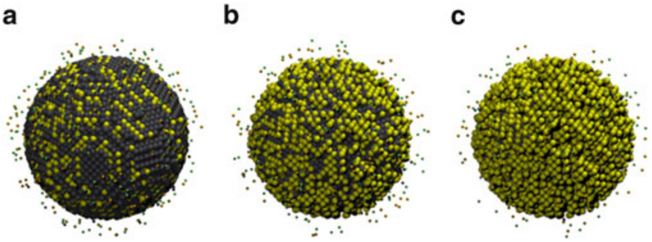

Fig. 20.9 KMC simulation of a dealloying process. A PtCo alloy nanoparticle of approximately 8 nm diameter is exposed to an acidic solution (represented by the *small spheres* surrounding the surface of the nanoparticle). (**a**), (**b**), and (**c**) represent snapshots taken at increasing times. Co segregates to the surface and dissolves. The lowest coordination sites are the first to dissolve causing a dramatic increase of the surface roughness (Callejas-Tovar and Balbuena, unpublished results)

As an example of the application of KMC simulations, Fig. 20.9 displays the evolution of a dissolution process of a nanoparticle exposed to an acidic solution. The KMC approach can provide extremely useful information about degradation processes during fuel cell operation but also about nanoparticle synthesis processes such as dealloying to produce hollow particles discussed in Sect. 20.2.

20.4 Conclusions

The complex design of PEMFCs nanocatalysts targeted to accomplish the requirements for automobile applications needs, in addition to experimental studies, the fundamental insight at atomistic level that molecular simulations provide. With recent advances in theoretical methods, in computational implementations, and in the required computational resources, it is possible to design improved catalysts guided by meaningful simulations. Theoretical studies are present in every aspect of the ORR catalyst design, from the identification of highly active alloys to the elucidation of the mechanisms of degradation. The progress in the area has been remarkable, and it continues towards a more accurate representation of the catalytic conditions providing firm guidelines to the design of better catalysts.

Acknowledgments This work is supported by the Department of Energy, grant DE-FG02-05ER15729. The authors acknowledge the following institutions for providing computing resources that were essential in the research reported in this chapter: Texas A&M University Brazos HPC cluster, Texas A&M University Supercomputing Facility, Texas Advanced Computing Center (UT-Austin), Argonne National Laboratory, National Energy Research Scientific Computing Center (supported by the Office of Science of the US Department of Energy under Contract No. DE-AC03-76SF00098), and Army Research Laboratory (ARL).

References

1. Wang B (2005) Recent development of no n-platinum catalysts for oxygen reduction reaction. J Power Sources 152:1–15
2. Mukerjee S, Srinivasan S, Soriaga MP, McBreen J (1995) Effect of preparation conditions of Pt alloys on their electronic, structural, and electrocatalytic activities for oxygen reduction. XRD, XAS, and electrochemical studies. J Phys Chem 99(13):4577–4589
3. Paulus UA, Wokaun A, Scherer GG, Schmidt TJ, Stamenkovic V, Radmilovic V, Markovic NM, Ross PN (2002) Oxygen reduction on carbon-supported Pt-Ni and Pt-Co alloy catalysts. J Phys Chem B 106(16):4181–4191
4. Stamenkovic V, Schmidt TJ, Ross PN, Markovic NM (2003) Surface segregation effects in electrocatalysis: kinetics of oxygen reduction reaction on polycrystalline Pt3Ni alloy surfaces. J Electroanal Chem 554–555:191–199
5. Stamenkovic VR, Mun BS, Mayrhofer KJJ, Ross PN, Markovic NM (2006) Effect of surface composition on electronic structure, stability, and electrocatalytic properties of Pt-transition metal alloys: Pt-skin versus Pt-skeleton surfaces. J Am Chem Soc 128(27):8813–8819
6. Stamenkovic V, Mun BS, Mayrhofer KJJ, Ross PN, Markovic NM, Rossmeisl J, Greeley J, Nørskov JK (2006) Changing the activity of electrocatalysts for oxygen reduction by tuning the surface electronic structure. Angew Chem Int Ed 45(18):2897–2901
7. Shao MH, Sasaki K, Adzic RR (2006) Pd-Fe nanoparticles as electrocatalysts for oxygen reduction. J Am Chem Soc 128(11):3526–3527
8. Stamenkovic VR, Fowler B, Mun BS, Wang G, Ross PN, Lucas CA, Marković NM (2007) Improved oxygen reduction activity on Pt3Ni(111) via increased surface site availability. Science 315(5811):493–497
9. Shao M, Liu P, Zhang J, Adzic R (2007) Origin of enhanced activity in palladium alloy electrocatalysts for oxygen reduction reaction. J Phys Chem B 111(24):6772–6775
10. Mukerjee S, Srinivasan S (1993) Enhanced electrocatalysis of oxygen reduction on platinum alloys in proton exchange membrane fuel cells. J Electroanal Chem 357(1–2):201–224
11. Stamenkovic V, Schmidt TJ, Ross PN, Markovic NM (2002) Surface composition effects in electrocatalysis: kinetics of oxygen reduction on well-defined Pt_3Ni and Pt_3Co alloy surfaces. J Phys Chem B 106(46):11970–11979
12. Duong HT, Rigsby MA, Zhou W-P, Wieckowski A (2007) Oxygen reduction catalysis of the Pt_3Co alloy in alkaline and acidic media studied by X-ray photoelectron spectroscopy and electrochemical methods. J Phys Chem C 111(36):13460–13465
13. Shao M, Shoemaker K, Peles A, Kaneko K, Protsailo L (2010) Pt monolayer on porous Pd−Cu alloys as oxygen reduction electrocatalysts. J Am Chem Soc 132(27):9253–9255
14. Chen S, Ferreira PJ, Sheng W, Yabuuchi N, Allard LF, Shao-Horn Y (2008) Enhanced activity for oxygen reduction reaction on “Pt3Co” nanoparticles: direct evidence of percolated and sandwich-segregation structures. J Am Chem Soc 130(42):13818–13819
15. Chen S, Sheng W, Yabuuchi N, Ferreira PJ, Allard LF, Shao-Horn Y (2008) Origin of oxygen reduction reaction activity on “Pt3Co” nanoparticles: atomically resolved chemical compositions and structures. J Phys Chem C 113(3):1109–1125
16. Yang R, Leisch J, Strasser P, Toney MF (2010) Structure of dealloyed $PtCu_3$ thin films and catalytic activity for oxygen reduction. Chem Mater 22(16):4712–4720
17. Dutta I, Carpenter MK, Balogh MP, Ziegelbauer JM, Moylan TE, Atwan MH, Irish NP (2010) Electrochemical and structural study of a chemically dealloyed PtCu oxygen reduction catalyst. J Phys Chem C 114(39):16309–16320
18. Nørskov JK, Rossmeisl J, Logadottir A, Lindqvist L, Kitchin JR, Bligaard T, Jónsson H (2004) Origin of the overpotential for oxygen reduction at a fuel-cell cathode. J Phys Chem B 108(46):17886–17892
19. Greeley J, Mavrikakis M (2004) Alloy catalysts designed from first principles. Nat Mater 3(11):810–815

20. Greeley J, Mavrikakis M (2006) Near-surface alloys for hydrogen fuel cell applications. Catal Today 111(1–2):52–58
21. Knudsen J, Nilekar AU, Vang RT, Schnadt J, Kunkes EL, Dumesic JA, Mavrikakis M, Besenbacher F (2007) A Cu/Pt near-surface alloy for water-gas shift catalysis. J Am Chem Soc 129(20):6485–6490
22. Alayoglu S, Nilekar AU, Mavrikakis M, Eichhorn B (2008) Ru-Pt core-shell nanoparticles for preferential oxidation of carbon monoxide in hydrogen. Nat Mater 7(4):333–338
23. Calvo SR, Balbuena PB (2007) Theoretical analysis of reactivity on Pt(111) and Pt–Pd(111) alloys. Surf Sci 601(21):4786–4792
24. Lamas EJ, Balbuena PB (2006) Oxygen reduction on $Pd_{0.75}Co_{0.25}$ and $Pt_{0.75}Co_{0.25}$ surfaces: an ab initio comparative study. J Chem Theory Comput 2:1388–1394
25. Sotelo JC, Seminario JM (2007) Biatomic substrates for bulk-molecule interfaces: the PtCo-oxygen interface. J Chem Phys 127(24):244706
26. Mun BS, Lee C, Stamenkovic V, Markovic NM, Ross PN Jr (2005) Electronic structure of Pd thin films on Re(0001) studied by high-resolution core-level and valence-band photoemission. Phys Rev B Condens Matter Mater Phys 71(11):115420
27. Van Den Oetelaar LCA, Nooij OW, Oerlemans S, Denier Van Der Gon AW, Brongersma HH, Lefferts L, Roosenbrand AG, Van Veen JAR (1998) Surface segregation in supported Pd-Pt nanoclusters and alloys. J Phys Chem B 102(18):3445–3455
28. Gauthier Y, Joly Y, Baudoing R, Rundgren J (1985) Surface-sandwich segregation on nondilute bimetallic alloys: $Pt_{50}Ni_{50}$ and $Pt_{78}Ni_{22}$ probed by low-energy electron diffraction. Phys Rev B 31(10):6216–6218
29. Deckers S, Habraken FHPM, Van Der Weg WF, Denier Van Der Gon AW, Pluis B, Van Der Veen JF, Baudoing R (1990) Segregation at the $Pt_{0.5}Ni_{0.5}$(111) surface studied by medium-energy ion scattering. Phys Rev B 42(6):3253–3259
30. Burton JJ, Polizzotti RS (1977) Surface segregation in alloys: dilute solid solutions of Cr, Fe and Ni in Pt. Surf Sci 66(1):1–13
31. Gauthier Y, Senhaji A, Legrand B, Tréglia G, Becker C, Wandelt K (2003) An unusual composition profile: a LEED-TBIM study of $Pt_{25}Cu_{75}$(1 1 1). Surf Sci 527(1–3):71–79
32. Gauthier Y, Baudoing-Savois R, Bugnard JM, Hebenstreit W, Schmid M, Varga P (2000) Segregation and chemical ordering in the surface layers of $Pt_{25}Co_{75}$(111): a LEED/STM study. Surf Sci 466(1–3):155–166
33. Gauthier Y, Baudoing-Savois R, Rosink JJWM, Sotto M (1993) LEED study of $Pt_{25}Co_{75}$(111). Surf Sci 297(2):193–201
34. Visser RF, Roux JP (1991) Segregation and oxidation studies on Cr, Cr_5Pt and $Cr_{15}Pt$. Appl Surf Sci 51(3–4):115–124
35. Creemers C, Deurinck P (1997) Platinum segregation to the (111) surface of ordered $Pt_{80}Fe_{20}$: LEIS results and model simulations. Surf Interface Anal 25(3):177–190
36. Hansen PL, Molenbroek AM, Ruban AV (1997) Alloy formation and surface segregation in zeolite-supported Pt-Pd bimetallic catalysts. J Phys Chem B 101(10):1861–1868
37. Chen W, Severin L, Göthelid M, Hammar M, Cameron S, Paul J (1994) Electronic and geometric structure of clean Pt3Ti(111). Phys Rev B 50(8):5620–5627
38. Brown D, Quinn PD, Woodruff DP, Noakes TCQ, Bailey P (2002) Surface and sub-surface segregation at the $Pt_{25}Rh_{75}$(111) surface: a medium energy ion scattering study. Surf Sci 497(1–3):1–12
39. Tsong TT, Ren DM, Ahmad M (1988) Atomic-layer by atomic-layer compositional depth profiling: surface segregation and impurity cosegregation of Pt-Rh and Pt-Ru alloys. Phys Rev B 38(11):7428–7435
40. Gasteiger HA, Ross PN Jr, Cairns EJ (1993) LEIS and AES on sputtered and annealed polycrystalline Pt-Ru bulk alloys. Surf Sci 293(1–2):67–80
41. Mayrhofer KJJ, Hartl K, Juhart V, Arenz M (2009) Degradation of carbon-supported Pt bimetallic nanoparticles by surface segregation. J Am Chem Soc 131(45):16348–16349

42. Mayrhofer KJJ, Juhart V, Hartl K, Hanzlik M, Arenz M (2009) Adsorbate-induced surface segregation for core–shell nanocatalysts. Angew Chem Int Ed 48(19):3529–3531
43. Williams FL, Nason D (1974) Binary alloy surface compositions from bulk alloy thermodynamic data. Surf Sci 45(2):377–408
44. Tréglia G, Legrand B (1987) Surface-sandwich segregation in Pt-Ni and Ag-Ni alloys: two different physical origins for the same phenomenon. Phys Rev B 35(9):4338–4344
45. Teraoka Y (1990) Surface relaxation effects on surface segregation and order-disorder transition temperatures of binary alloys. Surf Sci 238(1–3):L453–L456
46. Daw MS, Baskes MI (1984) Embedded-atom method: derivation and application to impurities, surfaces, and other defects in metals. Phys Rev B 29(12):6443–6453
47. Foiles SM, Baskes MI, Daw MS (1986) Embedded-atom-method functions for the fcc metals Cu, Ag, Au, Ni, Pd, Pt, and their alloys. Phys Rev B 33(12):7983–7991
48. Deng H, Hu W, Shu X, Zhao L, Zhang B (2002) Monte Carlo simulation of the surface segregation of Pt-Pd and Pt-Ir alloys with an analytic embedded-atom method. Surf Sci 517(1–3):177–185
49. Joubert HD, Swart HC, Terblans JJ (2004) Monte-Carlo program for simulating segregation and diffusion utilizing chemical potential calculations. Surf Interface Anal 36(11):1441–1448
50. Wang G, Van Hove MA, Ross PN, Baskes MI (2004) Monte Carlo simulations of segregation in Pt-Re catalyst nanoparticles. J Chem Phys 121(11):5410–5422
51. Wang G, Van Hove MA, Ross PN, Baskes MI (2005) Monte Carlo simulations of segregation in Pt-Ni catalyst nanoparticles. J Chem Phys 122(2):024706
52. Ruban AV, Skriver HL, Nørskov JK (1999) Surface segregation energies in transition-metal alloys. Phys Rev B 59(24):15990–16000
53. Løvvik OM (2005) Surface segregation in palladium based alloys from density-functional calculations. Surf Sci 583(1):100–106
54. Chepulskii RV, Butler WH, van de Walle A, Curtarolo S (2010) Surface segregation in nanoparticles from first principles: the case of FePt. Scr Mater 62(4):179–182
55. Ramirez-Caballero GE, Balbuena PB (2008) Surface segregation of core atoms in core-shell structures. Chem Phys Lett 456(1–3):64–67
56. Callejas-Tovar R, Balbuena PB (2008) Oxygen adsorption and surface segregation in (211) surfaces of Pt(shell)/M(core) and Pt_3M (M=Co, Ir) alloys. Surf Sci 602(22):3531–3539
57. Ma Y, Balbuena PB (2008) Pt surface segregation in bimetallic Pt_3M alloys: a density functional theory study. Surf Sci 602(1):107–113
58. Ma Y, Balbuena PB (2008) Surface properties and dissolution trends of Pt_3M alloys in the presence of adsorbates. J Phys Chem C 112(37):14520–14528
59. Ma Y, Balbuena PB (2008) Kinetic model of surface segregation in Pt-based alloys. J Chem Theory Comput 4(12):1991–1995
60. Ma Y, Balbuena PB (2009) Surface segregation in bimetallic Pt_3M (M = Fe, Co, Ni) alloys with adsorbed oxygen. Surf Sci 603(2):349–353
61. Hirunsit P, Balbuena PB (2009) Surface atomic distribution and water adsorption on Pt-Co alloys. Surf Sci 603(6):912–920
62. Adzic R, Zhang J, Sasaki K, Vukmirovic M, Shao M, Wang J, Nilekar A, Mavrikakis M, Valerio J, Uribe F (2007) Platinum monolayer fuel cell electrocatalysts. Top Catal 46 (3):249–262
63. Martinez De La Hoz JM, Callejas Tovar R, Balbuena PB (2009) Size effect on the stability of Cu-Ag nanoalloys. Mol Simulat 35(10–11):785–794
64. Xiong SY, Qi WH, Huang BY, Wang MP (2011) Size-, shape- and composition-dependent alloying ability of bimetallic nanoparticles. Chemphyschem 12(7):1317–1324
65. Ferrando R, Jellinek J, Johnston RL (2008) Nanoalloys: from theory to applications of alloy clusters and nanoparticles. Chem Rev 108(3):845–910
66. Baletto F, Ferrando R (2005) Structural properties of nanoclusters: energetic, thermodynamic, and kinetic effects. Rev Mod Phys 77(1):371–423

67. Delogu F (2010) Free energy differences between Ag-Cu nanophases with different chemical order. J Phys Chem C 114(47):19946–19951
68. Manikam VR, Cheong KY, Razak KA (2011) Chemical reduction methods for synthesizing Ag and Al nanoparticles and their respective nanoalloys. Mater Sci Eng B Adv Funct Solid State Mater 176(3):187–203
69. Cable RE, Schaak RE (2006) Reacting the unreactive: a toolbox of low-temperature solution-mediated reactions for the facile interconversion of nanocrystalline intermetallic compounds. J Am Chem Soc 128:9588–9589
70. Ewers TD, Sra AK, Norris BC, Cable RE, Cheng C-H, Shantz DF, Schaak RE (2005) Spontaneous hierarchical assembly of rhodium nanoparticles into spherical aggregates and superlattices. Chem Mater 17(3):514–520
71. Menning CA, Chen JG (2009) General trend for adsorbate-induced segregation of subsurface metal atoms in bimetallic surfaces. J Chem Phys 130(17):174709
72. Ramirez-Caballero GE, Ma Y, Callejas-Tovar R, Balbuena PB (2010) Surface segregation and stability of core-shell alloy catalysts for oxygen reduction in acid medium. Phys Chem Chem Phys 12:2209–2218
73. Balbuena PB, Callejas-Tovar R, Hirunsit P, de la Hoz JMM, Ma Y, Ramirez-Caballero GE (2012) Evolution of Pt and Pt-alloy catalytic surfaces under oxygen reduction reaction in acid medium. Top Catal 55(5–6):322–335
74. de Morais RF, Sautet P, Loffreda D, Franco AA (2011) A multiscale theoretical methodology for the calculation of electrochemical observables from ab initio data: application to the oxygen reduction reaction in a Pt(111)-based polymer electrolyte membrane fuel cell. Electrochim Acta 56(28):10842–10856
75. Nørskov JK, Bligaard T, Logadottir A, Bahn S, Hansen LB, Bollinger M, Bengaard H, Hammer B, Sljivancanin Z, Mavrikakis M, Xu Y, Dahl S, Jacobsen CJH (2002) Universality in heterogeneous catalysis. J Catal 209(2):275–278
76. Norskov JK, Scheffler M, Toulhoat H (2006) Density functional theory in surface science and heterogeneous catalysis. MRS Bull 31(9):669–674
77. Norskov JK, Bligaard T, Rossmeisl J, Christensen CH (2009) Towards the computational design of solid catalysts. Nat Chem 1(1):37–46
78. Greeley J, Norskov JK (2007) Large-scale, density functional theory-based screening of alloys for hydrogen evolution. Surf Sci 601(6):1590–1598
79. Hansen HA, Rossmeisl J, Norskov JK (2008) Surface Pourbaix diagrams and oxygen reduction activity of Pt, Ag and Ni(111) surfaces studied by DFT. Phys Chem Chem Phys 10(25):3722–3730
80. Ma Y, Balbuena PB (2007) Designing oxygen reduction catalysts: insights from metalloenzymes. Chem Phys Lett 440:130–133
81. Wang Y, Balbuena PB (2005) Design of oxygen reduction bimetallic catalysts: ab-initio derived thermodynamic guidelines. J Phys Chem B 109(40):18902–18906
82. Hammer B, Nørskov JK (1995) Electronic factors determining the reactivity of metal surfaces. Surf Sci 343(3):211–220
83. Santos E, Schmickler W (2006) d-Band catalysis in electrochemistry. Chemphyschem 7 (11):2282–2285
84. Xu Y, Greeley J, Mavrikakis M (2005) Effect of subsurface oxygen on the reactivity of the Ag(111) surface. J Am Chem Soc 127(37):12823–12827
85. Xu Y, Ruban AV, Mavrikakis M (2004) Adsorption and dissociation of O_2 on Pt-Co and Pt-Fe alloys. J Am Chem Soc 126(14):4717–4725
86. Greeley J, Jaramillo TF, Bonde J, Chorkendorff I, Norskov JK (2006) Computational high-throughput screening of electrocatalytic materials for hydrogen evolution. Nat Mater 5 (11):909–913
87. Greeley J, Nørskov JK (2009) Combinatorial density functional theory-based screening of surface alloys for the oxygen reduction reaction. J Phys Chem C 113(12):4932–4939

88. Roques J, Anderson AB, Murthi VS, Mukerjee S (2005) Potential shift for OH(ads) formation on the Pt skin on Pt[sub 3]Co(111) electrodes in acid. J Electrochem Soc 152(6):E193–E199
89. Greeley J, Norskov JK (2007) Electrochemical dissolution of surface alloys in acids: thermodynamics trends from first principles calculations. Electrochim Acta 52:5829–5836
90. Greeley J (2010) Structural effects on trends in the deposition and dissolution of metal-supported metal adstructures. Electrochim Acta 55(20):5545–5550
91. Ma YG, Balbuena PB (2010) Role of iridium in Pt-based alloy catalysts for the ORR: surface adsorption and stabilization studies. J Electrochem Soc 157(6):B959–B963
92. Wang JX, Ma C, Choi Y, Su D, Zhu Y, Liu P, Si R, Vukmirovic MB, Zhang Y, Adzic RR (2011) Kirkendall effect and lattice contraction in nanocatalysts: a new strategy to enhance sustainable activity. J Am Chem Soc 133(34):13551–13557
93. Yin Y, Rioux RM, Erdonmez CK, Hughes S, Somorjai GA, Alivisatos AP (2004) Formation of hollow nanocrystals through the nanoscale Kirkendall effect. Science 304(5671):711–714
94. Jin fan H, Knez M, Scholz R, Nielsch K, Pippel E, Hesse D, Zacharias M, Gosele U (2006) Monocrystalline spinel nanotube fabrication based on the Kirkendall effect. Nat Mater 5(8):627–631
95. Callejas-Tovar R, Balbuena PB (2012) Effect of metal porosity on oxygen reduction reaction activity. J Phys Chem C 116(27):14414–14422
96. Borup R, Meyers J, Pivovar B, Kim YS, Mukundan R, Garland N, Myers D, Wilson M, Garzon F, Wood D, Zelenay P, More K, Stroh K, Zawodzinski T, Boncella J, McGrath JE, Inaba M, Miyatake K, Hori M, Ota K, Ogumi Z, Miyata S, Nishikata A, Siroma Z, Uchimoto Y, Yasuda K, Kimijima K-i, Iwashita N (2007) Scientific aspects of polymer electrolyte fuel cell durability and degradation. Chem Rev 107(10):3904–3951
97. Darling RM, Meyers JP (2003) Kinetic model of platinum dissolution in PEMFCs. J Electrochem Soc 150(11):A1523–A1527
98. Wang X, Kumar R, Myers DJ (2006) Effect of voltage on platinum dissolution. Electrochem Solid State Lett 9(5):A225–A227
99. Matsumoto M, Miyazaki T, Imai H (2011) Oxygen-enhanced dissolution of platinum in acidic electrochemical environments. J Phys Chem C 115(22):11163–11169
100. Hawkins JM, Weaver JF, Asthagiri A (2009) Density functional theory study of the initial oxidation of the Pt(111) surface. Phys Rev B 79(12):13
101. Gu Z, Balbuena PB (2007) Absorption of atomic oxygen into subsurfaces of Pt(100) and Pt(111): density functional theory study. J Phys Chem C 111(27):9877–9883
102. Gu Z, Balbuena PB (2007) Chemical environment effects on the atomic oxygen absorption into Pt(111) subsurfaces. J Phys Chem C 111(46):17388–17396
103. Gu Z, Balbuena PB (2008) Atomic oxygen absorption into Pt-based alloy subsurfaces. J Phys Chem C 112:5057–5065
104. Martínez de la Hoz JM, León-Quintero DF, Hirunsit P, Balbuena PB (2010) Evolution of a Pt (1 1 1) surface at high oxygen coverage in acid medium. Chem Phys Lett 498(4–6):328–333
105. Balbuena PB, Calvo SR, Callejas-Tovar R, Gu Z, Ramirez-Caballero GE, Hirunsit P, Ma Y (2010) Challenges in the design of active and durable alloy nanocatalysts for fuel cells. In: Balbuena PB, Subramanian VR (eds) Theory and experiment in electrocatalysis, vol 50, Modern aspects of electrochemistry. Springer, New York
106. Getman RB, Xu Y, Schneider WF (2008) Thermodynamics of environment-dependent oxygen chemisorption on Pt(111). J Phys Chem C 112(26):9559–9572. doi:10.1021/jp800905a
107. Hirunsit P, Balbuena PB (2010) Stability of Pt monolayers on Ir-Co cores with and without a Pd interlayer. J Phys Chem C 114(30):13055–13060
108. Tian F, Anderson AB (2011) Effective reversible potential, energy loss, and overpotential on platinum fuel cell cathodes. J Phys Chem C 115(10):4076–4088
109. Bandlow J, Kaghazchi P, Jacob T, Papp C, Trankenschuh B, Streber R, Lorenz MPA, Fuhrmann T, Denecke R, Steinruck HP (2011) Oxidation of stepped Pt(111) studied by x-ray photoelectron spectroscopy and density functional theory. Phys Rev B 83(17):174107

110. Jacob T (2007) Theoretical investigations on the potential-induced formation of Pt-oxide surfaces. J Electroanal Chem 607(1–2):158–166
111. Kitchin JR, Reuter K, Scheffler M (2008) Alloy surface segregation in reactive environments: first principles atomistic thermodynamics study of $Ag_3Pd(111)$ in oxygen atmospheres. Phys Rev B 77:075437
112. Reuter K, Scheffler M (2003) Composition and structure of the $RuO_2(110)$ surface in an O_2 and CO environment: implications for the catalytic formation of CO_2. Phys Rev B 68:045407
113. Tsuchiya M, Sankaranarayanan SKRS, Ramanathan S (2009) Photon-assisted oxidation and oxide thin film synthesis: a review. Prog Mater Sci 54(7):981–1057
114. Sankaranarayanan SKRS, Ramanathan S (2008) Molecular dynamics simulation study of nanoscale passive oxide growth on Ni-Al alloy surfaces at low temperatures. Phys Rev B 78(8):085420
115. Edvin L, Anders M, Jesper NA, Georg K, Michael S, Peter V (2006) Surface oxides on close-packed surfaces of late transition metals. J Phys Condens Matter 18(30):R481
116. Strasser P, Koh S, Anniyev T, Greeley J, More K, Yu CF, Liu ZC, Kaya S, Nordlund D, Ogasawara H, Toney MF, Nilsson A (2010) Lattice-strain control of the activity in dealloyed core-shell fuel cell catalysts. Nat Chem 2(6):454–460
117. Callejas-Tovar R, Balbuena PB (2011) Molecular dynamics simulations of surface oxide-water interactions on Pt(111) and Pt/PtCo/Pt3Co(111). Phys Chem Chem Phys 13 (45):20461–20470
118. Callejas-Tovar R, Liao W, Martinez de la Hoz JM, Balbuena PB (2011) Molecular dynamics simulations of surface oxidation on Pt(111) and Pt/PtCo/Pt3Co(111). J Phys Chem C 115 (10):4104–4113
119. Callejas-Tovar R, Liao W, Martinez JM, Balbuena PB (2012) Modeling oxidation of Pt-based alloy surfaces for fuel cell cathode electrocatalysts. In: Spivey JJ, Gupta M (eds) Royal Society of Chemistry Catalysis Series, vol 24. Royal Society of Chemistry, Cambridge, pp 323–357
120. Callejas-Tovar R, Liao W, Mera H, Balbuena PB (2011) Molecular dynamics simulations of surface oxidation on Pt and $Pt/PtCo/Pt_3Co$ nanoparticles supported over carbon. J Phys Chem C 115:23768–23777
121. Duh DM, Perera DN, Haymet ADJ (1995) Structure and properties of the CF1 central force model of water – integral-equation theory. J Chem Phys 102(9):3736–3746
122. Chen S, Gasteiger HA, Hayakawa K, Tada T, Shao-Horn Y (2010) Platinum-alloy cathode catalyst degradation in proton exchange membrane fuel cells: nanometer-scale compositional and morphological changes. J Electrochem Soc 157(1):A82–A97
123. Maillard F, Dubau L, Durst J, Chatenet M, André J, Rossinot E (2010) Durability of Pt3Co/C nanoparticles in a proton-exchange membrane fuel cell: direct evidence of bulk Co segregation to the surface. Electrochem Commun 12(9):1161–1164
124. Dubau L, Maillard F, Chatenet M, André J, Rossinot E (2010) Nanoscale compositional changes and modification of the surface reactivity of Pt_3Co/C nanoparticles during proton-exchange membrane fuel cell operation. Electrochim Acta 56(2):776–783
125. Gillespie DT (1977) Exact stochastic simulation of coupled chemical reactions. J Phys Chem 81(25):2340–2361

Chapter 21

Nanostructured Electrocatalysts for Oxygen Reduction Reaction: First-Principles Computational Insights

Amra Peles

Abstract The goal of catalyst development is to be able to adjust the structure and composition of catalytic materials to obtain the optimal electronic properties for desired chemical reactivity. Key features of the electronic structure that influence the reactivity of nanostructured catalysts are reviewed. Conclusions derived from the DFT electronic structure and the surface reactivity computations, with emphasis on the catalyst property intrinsically governed by the local, site-specific interactions, for nanostructured catalysts are presented.

21.1 Introduction

Proton exchange membrane fuel cells (PEMFC) are an efficient, carbon-neutral energy conversion device and a much-needed alternative to conventional combustion engine devices. Unparalleled, theoretically achievable thermodynamic efficiency and the high energy density of PEMFC set this technology apart as a viable solution to the global energy problem [1]. Despite significant technical progress in the large-scale deployment of PEMFC, the fundamental problem of high cost per power output hinders worldwide commercialization [1]. Efficient electrochemical energy conversion on both electrodes of current state-of-the-art PEMFC depends on the availability of precious metal catalysts that in large part contribute to the high cost of this technology [2]. Recent research efforts have focused on advanced catalyst concepts that either minimize utilization of precious metal or explore alternative catalysts consisting of earth-abundant elements [3–6]. In particular, high catalyst loadings are required at the cathodes of fuel cells, where oxygen reduction reactions (ORR) proceed, reducing the oxygen to the water by continuous supply of electrons and protons:

A. Peles (✉)
United Technologies Research Center, East Hartford, CT 06118, USA
e-mail: pelesa@utrc.utc.com

M. Shao (ed.), *Electrocatalysis in Fuel Cells*, Lecture Notes in Energy 9,
DOI 10.1007/978-1-4471-4911-8_21, © Springer-Verlag London 2013

$$O_2 + 4e^- + 4H^+ \rightarrow 2H_2O \quad (21.1)$$

Significant cost reduction has been made over the past few decades by improving the catalytic activity per mass of Pt, replacing bulk-like crystals with finely dispersed particles [1–3]. However, a sharp drop in specific catalytic activity has been observed going from Pt bulk surfaces to Pt nanoparticles [3, 7]. The understanding of the effect of particle sizes on the catalytic activities has been studied extensively and remains a fundamental objective of heterogeneous catalysis [8–12]. Influence of particle size on the intrinsic ORR activity in the size range that maximizes Pt utilization (1–5 nm) is still debated [11–33]. Some investigators have observed essentially no effect of particle size on ORR activity [25–28]. It has been argued that interparticle distances, rather than particle size, affect specific activity. According to this hypothesis, specific activity increases with reduction of particle size, provided certain particle separation remains [21–27]. The size-independent specific activity in 1–5 nm Pt particles has been further attributed to similar surface electronic structures of different particles based on ^{195}Pt electrochemical magnetic resonance results [28]. A majority of investigators have observed decreases in specific activity as the particle size is decreased [3, 13–21, 23, 34, 35]. The mechanisms of such decreases, however, are not been fully understood, and different explanations have been proposed, including a lower ratio of preferable crystal facets [13, 18, 36], stronger interaction between oxygen-containing species and Pt atoms [15, 37, 38], and lower potential of total point zero charge (PZC) [23, 24].The overall activity of a given catalyst is traditionally understood in terms of the Sabatier principle, an empirical law correlating the catalyst performance with the reactivity of the catalyst surface [39, 40]. According to this principle, the reaction rate is maximized when the interactions between the catalyst and the reaction intermediates are neither too strong nor too weak. Consequently, the best catalysts balance opposing tendencies to either bind reaction intermediates too strongly, thereby impeding formation or desorption of products, or exhibit inertness toward the transforming reactants to products due to an inability to break and transform their chemical bonds. Pt metal nanoparticles dispersed on high surface area carbon supports are the current state-of-the-art ORR catalysts in PEMFC. This catalyst is very selective toward the desirable four-electron reduction shown in Eq. (21.1). The onset of ORR at high overpotential and observed low exchange current densities indicate sluggish reaction kinetics, in addition to the less than optimal thermodynamic driving force [1]. The removal of the adsorbed ORR intermediates has been suggested as a rate-limiting step, because Pt surfaces have somewhat stronger surface reactivity than would be optimum suggested by Sabatier principle [24]. The design of new catalysts with improved catalytic activity and more effective precious metal utilization presents a milestone for current research. The fundamental understanding of reaction mechanisms and inherent material properties governing the kinetics of ORR at the atomic scale is recognized as critical in guiding the selection of materials for catalysts and may result in the rational design of better catalysts [41–43]. Significant progress in understanding the correlation of extended surface reactivity and the electronic structure property of metallic catalysts has been made by introducing the d-band center model by Hammer and Norskov [44, 45]. This model captures essential features of the experimental observations on well-defined surfaces of single crystals and polycrystalline samples [7, 24, 46–49]. The first-principles-based numerical methods are a powerful tool to investigate material properties. The advantage of these methods is that they do not rely on simplifying assumptions or empirical inputs, and the design of various models is closely related to exact theoretical principles and also experience, as in the case of real experimental setup. Advances in computational methods, algorithms, and availability of computational resources allow elucidation of the role that particular particle surface features play in determining the particle size effects [35]. Specific aspects presented here include insights and conclusions derived from the DFT electronic structure and surface reactivity computations for nanostructured and advanced catalyst concepts.

21.2 Theoretical Concepts

21.2.1 Density Functional Theory and Computational Methods

First-principles calculations based on the density functional theory (DFT) present a standard approach for calculating the electronic structure and the various physical and chemical properties of materials. Unlike Hartree–Fock-based theory, which starts with an ansatz about many-electron wave function, DFT is based upon two basic theorems which establish electron density as the fundamental quantity of interest and replaces the computationally intractable many-electron problem with a soluble set of one-particle equations [50–53]. In contrast to computational intensity of wave-function-based quantum chemistry methods which implementation becomes formidable for large systems, DFT methods present a fine compromise between computational intensity and accuracy to study nano-size models. DFT is based on an exact quantum mechanical treatment of the interacting electrons in order to find the ground-state total energy of a system. The starting point in the electronic structure calculations is the time-independent Schrödinger equation for the interacting many-electron and many-nuclei systems:

$$H\Psi(\mathbf{r}_1,\ \mathbf{r}_2,\ldots,\mathbf{r}_N;\mathbf{R}_1,\mathbf{R}_2,\ldots,\mathbf{R}_M) = E\Psi(\mathbf{r}_1,\ \mathbf{r}_2,\ldots,\mathbf{r}_N;\mathbf{R}_1,\mathbf{R}_2,\ldots,\mathbf{R}_M) \tag{21.2}$$

where H is the Hamiltonian that includes all interactions among and between electrons and atomic nuclei, E is the total energy of the system, and Ψ is the many-body wave function that depends on the positions and spins of all electrons and nuclei. The motion of heavy nuclei is instantaneously followed by the motion of much lighter electrons, which allows, to a good approximation, a separate treatment of the nuclei and electrons known as the Born–Oppenheimer approximation [54]. The decoupling of electrons and nuclei motion yields the Hamiltonian that consists of the kinetic energy of electrons, T; the electron–electron Coulomb repulsion energy, U; and the interactions of electrons with the external potential, which includes the electrostatic interaction with the fixed nuclei, V, that is, in atomic system of units:

$$H = T + U + V = \sum_{i}^{N} \frac{-1}{2}\nabla_i^2 + \sum_{j}^{N}\sum_{i \neq j}^{N} \frac{1}{r_{ij}} + \sum_{i}^{N} V_{\text{ext}}(\mathbf{r}_i) \tag{21.3}$$

Hohenberg and Kohn [52, 55–57] have shown that the external potential V is the unique functional of the spatial distribution of electron density $n(\mathbf{r})$ in the ground state, and consequently, $n(\mathbf{r})$ uniquely determines the ground-state properties of the system. In particular, the total energy functional, $E[n(\mathbf{r})] = T[n(\mathbf{r})] + U[n(\mathbf{r})] + V[n(\mathbf{r})]$, attains its minimum value, the ground-state energy, for the correct ground-state density when varied over all functions $n(\mathbf{r})$. This theory is exact and allows application to any system. However, neither the kinetic energy functional, $T[n(\mathbf{r})]$, nor the electron–electron interaction energy functional, $U[n(\mathbf{r})]$, is known explicitly for the inhomogeneous electron systems. Kohn and Sham [53] have decomposed the energy functional by explicitly separating the known kinetic energy contribution of a fictitious system of independent non-interacting electrons $T_{\text{n}}\,[n(\mathbf{r})]$ in the external potential $V[n(\mathbf{r})]$ and the classical electrostatic Coulomb interaction energy $U_{\text{H}}\,[n(\mathbf{r})]$ as follows:

$$E[n(\mathbf{r})] = T_{\text{n}}[n(\mathbf{r})] + U_{\text{H}}[n(\mathbf{r})] + E_{\text{xc}}[n(\mathbf{r})] + \int V_{\text{ext}}(\mathbf{r})n(\mathbf{r})\mathrm{d}\mathbf{r} \tag{21.4}$$

The $E_{\text{xc}}\,[n(\mathbf{r})]$ term is called the exchange correlation functional and contains all nonclassical Coulomb effects and all non-independent electron kinetic energy effects that preserve $E[n(\mathbf{r})]$ exact. This decomposition transforms exact theory into the practical tool for accurate computations by introducing the set of equations referred to as the Kohn–Sham equations:

$$\left[-\frac{1}{2}\nabla^2 + \int \frac{n(\boldsymbol{r}')}{|\boldsymbol{r}-\boldsymbol{r}'|}\mathrm{d}\boldsymbol{r}' + \frac{\partial E_{\text{xc}}(\boldsymbol{r})}{\partial n(\boldsymbol{r})} + V_{\text{ext}}(\boldsymbol{r})\right]\phi_i(\boldsymbol{r}) = \varepsilon_i \boldsymbol{\phi_i}(\boldsymbol{r}) \tag{21.5}$$

The first term is the kinetic energy of non-interacting electrons and the remaining terms are classical Coulomb repulsion, exchange correlations, and external potential, respectively. $\phi_i(\mathbf{r})$ are Kohn–Sham orbitals whose density

$$n(\mathbf{r}) = \sum_i f_i |\phi_i(\mathbf{r})|^2 \tag{21.6}$$

is identical to the density of the real electron assembly and the fundamental quantity of interest [52, 53]. The equations (Eq. 21.5) are solved self-consistently for the fixed positions of nuclei. The energy of the electronic ground state, obtained as a function of nuclear positions, can serve as a potential energy for the motion of nuclei. The force on the atoms can be computed and minimized using the Hellmann–Feynman theorem [58, 59]. This feature of the DFT approach is central to the structural optimization and for obtaining the true ground-state geometry.

Although the Kohn–Sham equations solve the problem exactly, they require knowledge of the exchange-correlation energy, E_{xc}, which contains all explicitly unknown terms. Thus, for the modeling of real systems, the exchange-correlation part of the total energy must be approximated. There are many approximations for the unknown functional. In the simplest, local density approximation, (LDA) the exchange-correlation functional:

$$E_{\mathrm{xc}}(n(\mathbf{r})) = \int V_{\mathrm{xc}}^{\mathrm{LDA}}[n(\mathbf{r})]\mathrm{d}\mathbf{r} \tag{21.7}$$

is approximated by the exchange-correlation potential, $V_{\mathrm{xc}}^{\mathrm{LDA}}$, of a homogeneous electron gas with density $n(\mathbf{r})$ [60]. The more effective generalized gradient approximation (GGA) functional, which includes the gradient of electronic density to account for the non-homogeneity of the electron density in the real systems, has been also developed [61, 62]. GGA provides for much better accuracy that is especially suitable for applications in chemistry [63]. Hybrid functional approaches further improve accuracy by replacing the fraction of the GGA exchange energy with exact Hartree–Fock exchange energy; however, improved accuracy comes at the expense of computation time [64]. In general, computational effort with DFT is directly linked to the number of atoms, or more precisely, the number of electrons that are considered in the model. Because most material properties are determined by the valence electrons, it allows for the Kohn–Sham equations to be solved for the valence electrons only. The core electrons are then treated in the frozen-core approximations using pseudo-potential methods [65, 66]. Furthermore, the projector-augmented wave (PAW) approach developed by Blöchl goes beyond the pseudo-potential approach and retains information about the all-electron calculation without significant addition to the computational time [67]. In most DFT applications, the Kohn–Sham orbitals are expanded with respect to either the plane-wave basis or a localized linear combination of atomic orbitals (LCAO) basis. DFT method is regarded as nonempirical, first principles, since once the density functional is adopted, the only remaining input required for the calculations of the ground-state properties is the atomic number of the elements in the structure to be studied. Thanks to developments of DFT-based algorithms, as well as increases in computer power, the first-principles calculations have reached practical levels of accuracy in treating increasingly larger systems at the atomistic level [68, 69]. The theoretical modeling of chemisorption on nanoparticles requires the description of hundreds of atoms at a quantum mechanical level of theory. The results discussed here were determined using the DFT method, with the plane-wave expansion of electronic wave functions, the GGA approximation to exchange correlations, and the periodic boundary conditions as implemented in the Vienna Ab-Initio Simulation Package (VASP) [68, 69]. The standard super cell approach was used with vacuum layers in all three spatial directions, ensuring that the spurious interactions of the nanoparticle with periodically repeated images are minimized. All atom positions in particles, together with adsorbate coordinates, were fully relaxed. The relaxation allowed reduction of the stress and minimization of the elastic energy at the particle surface due to the presence of under-coordinated surface atoms. Consequently, the change in the electronic structure due to the geometric relaxation at surfaces was treated inherently in the presented approach. The parameters specific to the GGA functional, Brillouin zone sampling, plane-wave cutoff energy, and PAW method can be found in the original literature [35].

21.2.2 Surface Reactivity and the d-Band Model

Most fundamental properties of materials can be traced back to the underlying features of their electronic structure. Types of chemical bonding, particularly relevant to applications in catalysis, are direct consequences of the electronic structure properties. Chemisorption occurs when adsorbates interact with the surfaces, forming chemical bonds. This interaction results in a redistribution of electronic density and to a large extent depends on the coupling strength between the adsorbate states and the surface valence band. In chemisorptions theory [70], the shape of the valence band interacting with a one-electron state in an adsorbate molecule governs the intensity of bonding. Two limiting cases can be distinguished: (1) interaction of the adsorbate with a broad valence band that merely broadens the adsorbate state, resulting in weak chemisorption, and (2) interaction with the narrow valence band that splits the adsorbate state into two states, often termed as bonding and antibonding states, resulting in strong chemisorption [45, 70–73].

Chemisorption strength as a measure of the surface reactivity toward adsorbed species on a given surface adsorption site can be obtained directly from first-principles computations:

$$E_{\mathrm{b}} = E_{\mathrm{sur\,+\,ads}} - \left(E_{\mathrm{sur}} + E_{\mathrm{ads}}\right) \tag{21.8}$$

where E_{b} is the adsorbate binding energy and $E_{\mathrm{surf\,+\,ads}}$, E_{surf}, and E_{ads} are the total electronic energies for system consisting of adsorbate on the surface, isolated surface, and isolated adsorbate, respectively. For transition metals, in which catalytic properties are dominated by the d-electrons, a simple model was proposed by Hamer and Norskov to describe the reactivity of transition metal surfaces [44, 45]. The d-band center model builds on the Newns–Anderson model of chemisorption [70]. Consequently, the reactivity of a metal surface is governed by the coupling of adsorbate states with a metal *d* state. Adsorbate reaction with a wide *sp* band is considered the same across transition metal series. The model correlates the *d*-band center, ε_d; the adsorbate energy level, ε_a; the fractional electron occupation of the *d*-band, f_d; and the coupling matrix element, V_{ad}, that gives the coupling strength between adsorbate state *a* and the metal *d* state.

$$\Delta\mathrm{BE} \sim f_d \frac{V_{ad}^2}{(\varepsilon_a - \varepsilon_d)^2} \Delta\varepsilon_d \tag{21.9}$$

For similar adsorbates, the d-band occupation and the coupling matrix element are assumed to differ only slightly; thus, change in the chemisorption strength is directly proportional to the change or shift in the d-band center in the transition metal surface. The modifications in the electronic structure that result in shifts of the d-band center closer to the Fermi level increase chemisorption strength, while shifts away from the Fermi level result in decreased chemisorption energy. These modifications are observed across the transition metal series and may also take place by ligand or strain effects induced by composition modifications or change in catalyst size and shape. The d-band center can be obtained directly from computation of the electronic density of states N (E) as a first moment of density distribution:

$$\mu^{(1)} = \int_{-\infty}^{\infty} EN(E)\mathrm{d}E = \varepsilon_d; \qquad \int_{-\infty}^{\infty} N(E)\mathrm{d}E = 1 \tag{21.10}$$

The d-band center model has been used extensively to describe experimentally measured catalytic activities, as a descriptor of catalyst behavior. Most computations have been performed on flat surfaces or surfaces with steps and kinks [7, 24, 46–49]. The electronic structure of nanoparticles is expected to be deeply affected by the characteristic particle size and morphology. Particle size is therefore a critical parameter. The surface science studies that involve the reactions on a uniform single crystal surfaces and introduce the complexity characteristic to real nanoparticles by involving the defects, kinks, and steps in the models may not be sufficient to model the catalytic behavior at nanoscale. Such model does not take into account an inherent particle property sensitively dependent on structural parameters such as the particle size, strain, and local surface morphology.

21.2.3 Electronic Structure at Reduced Dimensions

Profound changes in the electronic structure of materials have been observed when their size changes from bulk to nanometer dimensions [74]. The electronic structure of a large ensemble of atoms as in a single crystal is accurately described by continuous bands [75]. In contrast, atoms and molecule have discrete atomic and molecular orbitals. Nanoparticles represent a state of matter in the transition region between bulk crystals and single molecule. As a consequence, their physical and chemical properties may be expected to gradually change from the solid state to the molecular behavior with decreasing spatial dimension and particle size. A quantitatively accurate description of electronic structure changes with reduction of spatial dimension can be obtained from the electron density of states, a number of states per unit of energy at an atomic site, and its projections to the angular momentum components, a so-called partial density of states. The impact of reducing the size and dimensionality of a catalyst on its electronic structure properties is shown in Fig. 21.1, where the d momentum-projected density of states for Pt bulk, i.e., macroscopic amount of material, the (111) extended surface, and nanoparticles of 1.65 and 0.83 nm diameter are shown.

To gain better understanding of the electronic structure and factors that govern the surface reactivity at systems with reduced dimensions, such as nanoparticles, it is useful to consider the second moment of d density of states distribution:

$$\mu^{(2)} = \int_{-\infty}^{\infty} E^2 N(E)\mathrm{d}E = \varepsilon_d^2 + W_d \tag{21.11}$$

where W_d denotes the width of d-band. The W_d is proportional to the number of nearest neighbor bonds, the atom coordination number, Z [76, 77].

$$W_d = Z\sqrt{\sum_{i \neq j} \beta(r_{ij})^2} \tag{21.12}$$

β represents the average hopping integral that determines the hopping probability of a d-electron from one atom to another, assuming only the nearest neighbor hopping. The bandwidth dependence on the coordination number plays a particularly important role in nanoparticles, where a great number of atoms are situated on the surface. These atoms are missing the part of the neighbors they have in the bulk. Narrowing of the d-band on the surfaces has great consequences on the surface reactivity [70]. The estimate of the d-bandwidth on the surface atom with coordination number Z_S due to the change in the bulk characteristic coordination number Z_B can be made from Eq. (21.11):

$$W_d^\mathrm{S} \sim W_d^\mathrm{B}\sqrt{\frac{Z_\mathrm{S}}{Z_\mathrm{B}}} \tag{21.13}$$

At the (111) surface of Pt, this narrows the d-band by approximately 13.5 % compared to the bandwidth on the bulk Pt atom. The computed density of states shown in Fig. 21.1a, b agrees well with this prediction. Consequent shift in the d-band center closer to the Fermi level is observed. However, narrowing of the d-band due to a lower coordination on the surface of particles is not the only factor that should be considered. In addition to the bulk-like smooth d-band profile, the new electronic states localized at the vicinity of the surface exist due to the spatial electron confinement perpendicular to the surface [75]. In large crystals, an overall contribution of these states is proportional to the number of surface atoms, and it becomes negligible for macroscopic crystals. When spatial dimension is further reduced, as in

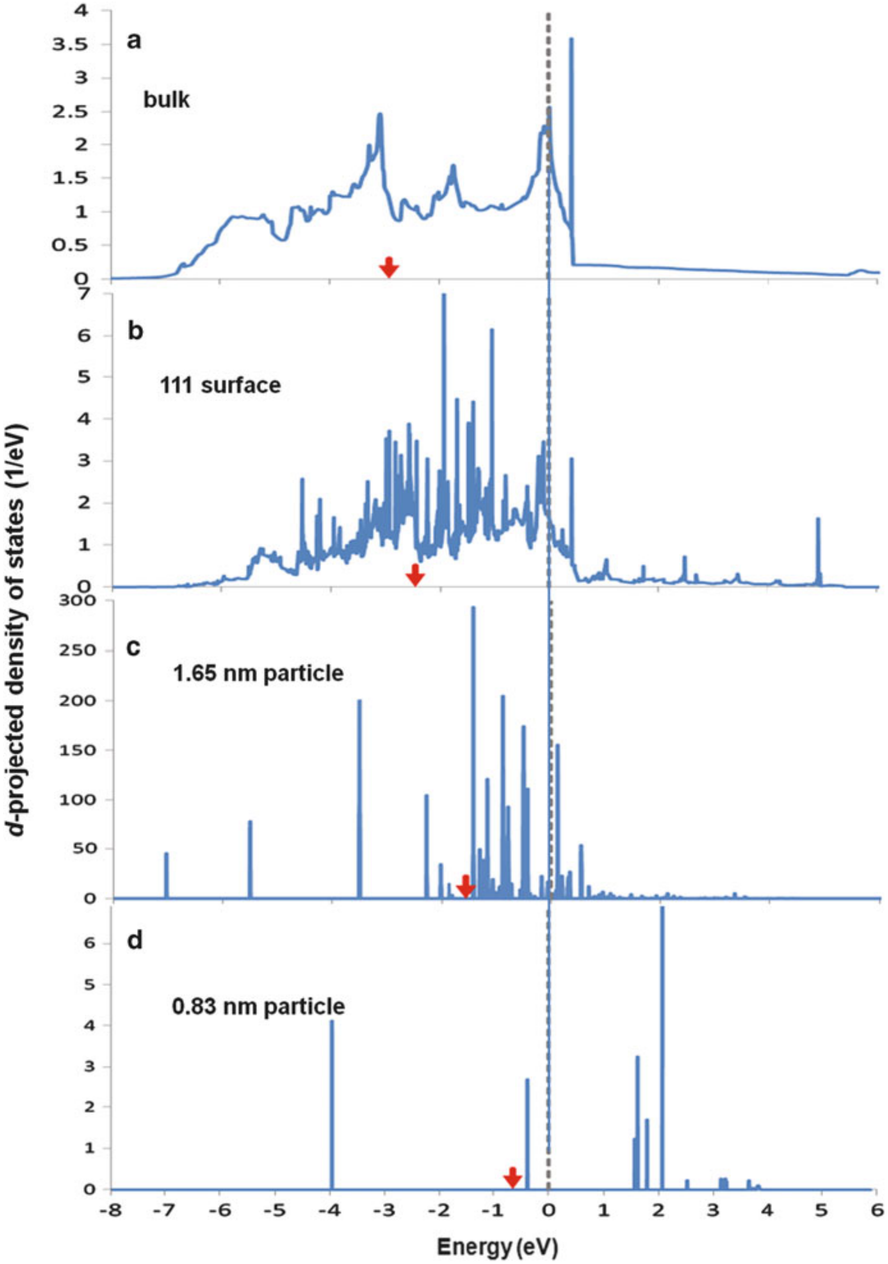

Fig. 21.1 Pt d-projected density of states for (**a**) 12-fold coordinated bulk atom (**b**) 9-fold coordinated surface atom on extended (111) surface (**c**) 7-fold coordinated surface atom on 1.65 nm particle (**d**) 6-fold coordinated surface atom in 0.83 nm nanoparticles. Position of average center of d-electron energies is marked by *arrows*. Fermi energy is set to zero

thin films or particles of nanometer dimensions, the importance of these localized states becomes more important. Figure 21.1c, d illustrates the point for the Pt nanoparticles. The *d*-band electronic structure is altered in the nanoparticles through reduction of volume in which electrons (electron wave functions) can exist. The confinement results in the bound electron states and alters the positions of energy levels. Because of the wavelike nature of conduction electrons confined in the nanometer spatial dimensions, electrons can have only discrete kinetic energies or wavelengths. This property unambiguously shows in the 0.83 nm Pt particle in Fig. 21.1d where all three dimensions are reduced to the nanoscale. The density of states of a larger, 1.65 nm, particle, illustrated in Fig. 21.1c, exhibits the discrete type of features superimposed on the continuum narrowed d-bands. The inspection of electronic level energies that make up discrete particle levels shows that the ratio between energy spacing and room temperature thermal energy is at least an order of magnitude less than one, indicating the quantum mechanics driven properties in the 0.83 nm particle. The position of the average center of *d*-electron energies is marked in Fig. 21.1; note that the *d*-band center loses its meaning for the discrete density of states. The center shifts toward the Fermi level on surfaces and in the particles. The amount of shift correlates with the atom coordination number and qualitative correlation to the surface reactivity is expected. In addition, the modification of electronic structure can be caused by the strain in the surfaces through the changes in the overlap integrals of d-electrons on neighboring atoms. The example is a pseudomorphic Pt monolayer on a substrate with somewhat larger of smaller lattice parameter, resulting in tensile or compressive strain in the monolayer [78, 79]. The strain yields to the change in the bandwidth. The compressive (tensile) strain results in the narrower (wider) bandwidth [78].

21.3 First-Principles Insights in ORR Catalysis for PEMFC

21.3.1 Oxygen Reduction Reaction Mechanism

The overall ORR is a multi-electron complex reaction that may involve numerous elementary steps and many reaction intermediates. Reaction mechanism details predominantly depend on the nature of electrode material, catalyst, and electrolyte. In aqueous solution, ORR occurs mainly by two pathways: the direct four-electron reduction pathway from O_2 to H_2O and the series two-electron reduction pathway from O_2 to H_2O_2 and from H_2O_2 to H_2O [34, 80, 81]. Obtaining the insights to the ORR mechanism from the experimental kinetics data is a very demanding task and often precluded with existing experimental techniques [49, 82]. First-principles computations have provided the fundamental understanding of underlying reaction mechanism at molecular level and at the different levels of model complexity [48, 83–96].

Norskov et al. examined the mechanistic steps for the ORR and the stability of reaction intermediates including the effect of applied electrode voltage and reported on the origin of experimentally observed overpotential for ORR on Pt catalyst [91]. General method for calculating the free energy of the intermediate steps of the ORR was introduced. It was shown that for Pt (111), adsorbed oxygen tends to be too stable at high potentials such that the proton and electron transfer becomes impossible. Lowering of the potential was found to be needed to destabilize oxygen and allows for proton and electron transfer to proceed. The potential difference between maximum potential needed to destabilize oxygen and theoretical thermodynamic potential for fuel cell agreed well with experimental observations of the overpotential value. The endothermicity of the electron/proton transfer to adsorbed oxygen at high potentials is proposed to be the origin of the overpotential for Pt catalyst. In addition, the oxygen binding energy strength has been correlated with the computed maximal activity based on micro-kinetic model for ORR for the selected d-block metals. The trends in the theoretical activity with the reactivity of the most stable surfaces in terms of O or OH binding energy have shown the volcano-type behavior, distinguishing metals such as Au and Ag which are expected to have dissociation of O–O bond as rate-determining step (RDS), from the rest of group (Pt, Pd, Ir, Cu, Rh, Ni, Ru, Co, Fe, Mo, W) where the electron/ proton transfer have high activation barrier due to strong bonding of oxygen. This theoretical examination has shown that more active catalyst is possible, the catalyst which would have somewhat lower reactivity than Pt, but not as low to preclude O–O bond cleavage steps. In addition to the effect of the potential, the complexity of the electrolyte-surface interface and local electric field effects have been considered [92, 93, 95]. The study of ORR on Pt (111) in a half-dissociated water layer at the 0.9 V potential has revealed lower and local environment-dependent energy barrier for cleavage of O–O bond than in study that did not take the effect of water layer into account [91, 92]. An additional insight in the reaction pathways for the ORR on Pt (111) in the presence of hydrated proton has been examined by the first-principles molecular dynamics study by Wang and Balbuena [93]. Both studies have theoretically validated that direct four-electron pathway in the O_2 reduction on Pt surface is dominant reaction pathway.

21.3.2 Advanced Catalyst Concepts

DFT approach is consistently used to resolve electronic structure features of various advanced catalyst concepts including core-shell catalyst, nanostructured shape-selective catalysts, Pt monolayer catalyst, and selectively dealloyed catalysts [7, 24, 43, 46, 84, 91, 97–99, 119].

Pt monolayer catalyst introduced by the Adzic group, is a particularly promising concept that allows ultra low Pt content [49]. The correlation between the position of *d*-band center relative to the Fermi energy and measured kinetic current density has been reported by Zhang et al. for the Pt monolayer catalyst supported on single crystal substrates of Ru, Ir, Rh, Au, and Pd [48]. Pt monolayer supported on Pd has been found to have superior kinetic current to that of Pt alone, consistent with the change in d-band center and surface reactivity. The pseudomorphic Pt monolayers are subject to the strain due to the lattice mismatch between Pt and support metal. The correlation between the strain in metal surfaces and the position of d-band center has been reported by Mavrikakis et al. [78]. The compressive strain tends to shift d-band center of Pt to lower energy, while tensile strain has opposite effect. In addition to the strain, the electronic interaction between the Pt monolayer and substrate metal plays an important role for the changes in the position of d-band center, a so-called ligand effect [99]. The shift in d-band center of Pd, in Pd over layer catalyst on Pd–Fe alloys, has been found as origin of enhanced activity for Pd-based core-shell catalyst [47]. In addition to the periodic surface models, a semispherical model for core-shell particles consisting of Pd core and Pt shell has been examined by DFT for the effect of particle size, crystallographic facets, and Pt-shell thickness on the ORR and catalyst performance. The observed enhancement in specific activity is attributed to the size and facet-dependent compressive strain, computed by DFT [100]. Near-surface alloys (NSA) in which stoichiometry in near surface of alloy catalyst is different from that in the bulk, have been studied extensively as cathode catalysts in PEMFC [7, 24, 43, 46, 84, 97]. In order to change the activity of electrocatalysts, Stamenkovic et al. [7, 24] have considered tuning the surface electronic structure by alloying Pt with 3d metals. A thermal treatment of these alloys in ultrahigh vacuum (UHV) has resulted in surface enrichment with Pt atoms as a result of surface segregation phenomena [101–103]. The kinetic model was developed that gave volcano-type dependence for computed ORR rates at 0.9 V in relation to single descriptor, oxygen binding energy, for the series of Pt_3M alloys (M = Ti, Ni, Co, Fe). In addition, the oxygen binding energy has been correlated with the d-band center, measured for the alloys by the high-resolution photoemission spectroscopy. The comparison of computed and measured NSA catalyst activities and their relation to the d-band center have shown remarkably similar trends. Similar changes in d-band center have been observed in computations by Kitchin et al. for Pt (111) surface with 3d metals embedded in the surface sublayer [99].

21.3.3 Catalyst Chemical Stability

In addition to the convincing success of first-principles computations in predicting more active catalyst compositions and morphologies, the important challenge associated with the chemical stability in the reaction environment of the catalyst has been pointed out [7, 24, 104]. ORR occurs in aqueous electrochemical environment and at high potentials where both metal dissolution and surface oxidation of catalyst may become favorable. The thermodynamic trends for electrochemical dissolution of surface alloys in acids from first-principles calculation have been reported by Greeley and Norskov [105]. The dissolution potentials for solute metal atoms in the surface layer of host metal are calculated. Correlation between the trends in dissolution potential and trends in surface segregation energy, an energy cost to bring solute atom from bulk to the surface, was reported [105]. Greeley and Norskov have performed potential-dependent computational stability throughput screening for binary transition metal surface alloys considering the surface segregation, surface island formation, surface oxidation, and metal dissolution as stability criteria [104]. The vast majority of high-activity catalyst candidates have been found thermodynamically unstable with respect to dissolution in the acidic electrochemical environment. It has been suggested that kinetic or other thermodynamic mechanism is necessary to stabilize bimetallic catalysts for ORR in PEMFC. DFT calculations for the semispherical particle model of Pt monolayer on Pd and Pd–Au core have offer the possible mechanism for stabilization of Pt monolayer catalyst. The computed, particle size-dependent, shift of the dissolution potential of Pt in monolayer suggested higher stability to dissolution in larger particles. In addition, a partial dissolution of Pd was found to lead to the stabilization of Pt monolayer, arguably by relative shift of Pt dissolution potential to higher values [106]. The effect of electrostatic potential and pH factor of aqueous environment for Pt (111), Ni (111), and Ag (111) has been computed by constructing the surface Pourbaix diagrams revealing the pH factor-dependent stability of these surfaces. The underlying reasons for the lack of the performance of Ni (111) with respect to ORR in acid-based environment were discussed in terms of the dramatic change in the highly reactive Ni (111) surface due to oxidation [107].

21.4 Catalyst Properties at Nanoscale

21.4.1 Geometry Aspects of Nanoparticles

An important aspect of nanostructured catalysts is their surface area. When compared to the same mass of material in bulk or polycrystalline form, nanostructured catalysts have a considerably larger surface area, dependent on the size and shape of the nanostructured particles. In PEMFC, optimized utilization of precious metals as catalysts is critical for enabling technology commercialization. It is critical to achieve the largest active surface area for the given mass of a catalyst. In order to quantify the utilization of precious metals in the form of nanoparticles, we consider the number of accessible atoms on the surfaces of particles, the morphology of accessible sites, their coordination with other atoms, and the relative contribution of each atom type to the overall surface. A commonly observed cubo-octahedral particle shape is illustrated in Fig. 21.2a. The surface of the illustrated particle consists of {111} and {100} face-centered cubic facets; at the intersection of these facets are edges and vertices. Atoms comprising these surfaces can be differentiated by their number of nearest neighbor atoms, the coordination number. The coordination number of atoms on {111}, {100}, edges, and vertices are nine, eight, seven, and six, respectively. Only atoms on the surface of particles are

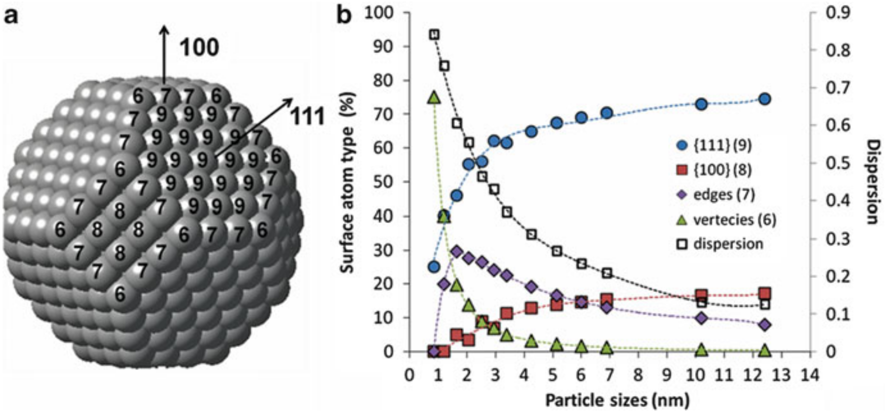

Fig. 21.2 (**a**) Cubo-octahedral geometry of 2.6 nm Pt particle showing the {111} and {100} facets and coordination numbers of atoms comprising these facets, particle edges, and vertices. (**b**) Size dependence of dispersion and surface percentage of atoms on {111}, {100} facets, and on the edges and vertices between the facets [35]

accessible to the reaction intermediates, while atoms buried in the core of particle are not utilized. Figure 21.2b shows the dispersion, computed as a ratio of the number of surface atoms to the total number of atoms in the particles, and its dependence on particle sizes. Dramatic increase in the number of surface atoms with decreased particle sizes is evident—an indication that loading of precious metals on fuel cell electrodes could be reduced by decreasing the catalyst particle size. However, this is possible only if a specific catalyst activity of the sites of the particle surface remains comparable and close to that of the sites on dominant extended surfaces in the single crystals. Distribution of surface atom types, characterized by their coordination number, with change in particle sizes is also shown in Fig. 21.2b. For particle sizes with low dispersion, less than 0.3, the predominant contribution to the surface comes from highly coordinated atoms on {111} and {100} facets. With an increase in dispersion and the reduction in particle size, a dramatic drop in the {111} and {100} highly coordinated atoms is compensated for by the low coordinated edge and vertex sites. Particularly interesting is the region below ~4 nm, where changes in the surface atom type are the most pronounced. The reactivity is probed by the adsorption strength of atomic oxygen.

21.4.2 Size-Dependent Particle Surface Reactivity

Diverse surface morphologies on a particle dictates that surface reactivity at distinct sites be systematically examined. These sites include hollow, bridge, and top sites on {111} and {100} facets, edges, and vertices among atoms with the same or different coordination number. Figure 21.3 shows the relationship between oxygen

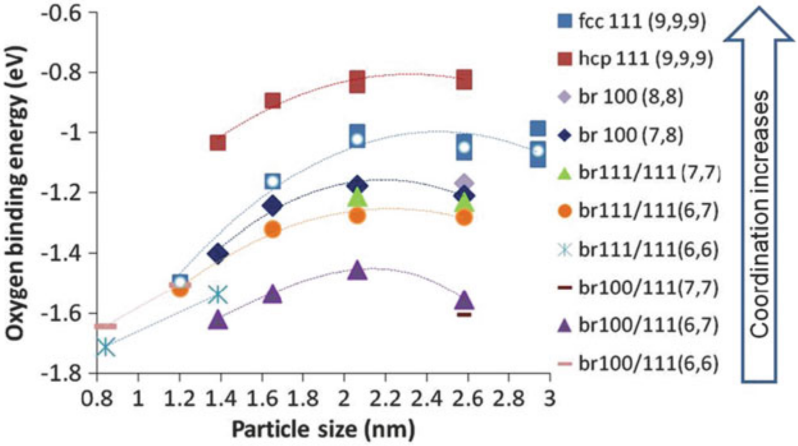

Fig. 21.3 Calculated oxygen binding energy as a function of the particle size for the most stable adsorption sites which include hollow fcc and hcp on {111} facets, bridge site on {100} facets, and bridge sites on edges between different facets. Besides site notation, coordination numbers for atoms making sites are given in brackets [35]

binding energy for possible adsorption sites on particles with sizes between 0.8 and 3 nm. For the 3 nm particle, only fcc sites were considered due to the increased computational intensity. The reactivity of the surface sites show dependence on both the particle sizes and the coordination numbers of atoms making up the site, reflected by the different oxygen binding energies. As particle size increases, the site-dependent binding energy decreases considerably up to ~2.1 nm, remaining similar to the binding energy of 2.1 nm particle as sizes increase further. At the same particle sizes, the binding energy is correlated to the coordination number of atoms making up the adsorption site, showing significant decrease with increase in coordination. Furthermore, in addition to the coordination number, coordination geometry and symmetry of sites with the same coordination reflect on the binding energy. It is a well-known difference between binding strength on face-centered cubic (fcc) and hexagonal closed-packed (hcp) sites on 111 extended Pt surfaces related to the "*d*-electron frustration" [108]. Similar difference in binding strength is observed between 111/111 and 100/111 bridge sites with the same (6, 6) coordination. This difference stems from the different overall geometry and symmetry of these sites; notably 100/111 edges have lower coordination to the neighboring surface atoms (5) than 111/111 (6) edge sites. These changes toward stronger binding with decrease of the coordination number can be understood through the profound changes in the electronic structure, in particular the energy of d-electrons of Pt shown in Fig. 21.1. The reactivity of particles is intrinsically governed by the local, site-specific interactions and the qualitative correlation between oxygen binding energy and the shifts in the d-band center.

21.4.3 Stability Effects and Comparison with Experiments

In general, comparison of experiments is complicated by many factors. Literature reports of specific activity measurements of the catalysts present an averaged activity value over the range of different particle sizes. This leads to the uncertainty in the activity value, which is assigned to the particle size with the highest distribution of weight and can mask the particle-size effect all together, especially in the region of sizes with similar adsorption site distribution shown in Fig. 21.3. In addition, comparison is complicated by significant electrolyte-dependent specific activities that have been observed in experiments [109]. Another important factor to consider when comparing experiments is the true particle morphology and shape. Equilibrium particle shapes depend on the particle sizes and also the chemical environment for measurements; the adsorbate-induced surface reconstruction and changes in particle morphology have been reported [37, 110, 111].

Particle size-dependent instabilities have been correlated to the loss in the electrochemical active surface area (ECA) [112, 113]. The main loss of ECA comes from the sintering of small particles into larger particles by either the diffusion of intact particles followed by the coalescence or the mechanism of Ostwald ripening. In Ostwald ripening, individual atoms on the particle surface get dissolved in the form of chemical complex that leaves the metal particle and diffuses away to join another particle, ultimately resulting in increase in particle diameters [113–116]. The driving force for sintering is the difference in chemical potential of atoms in a particle of radius R and bulk as described by a basic Gibbs–Thompson relation:

$$\mu(R) - \mu(\infty) = \frac{2\gamma V}{R} \tag{21.14}$$

where γ represents surface free energy of the metal and V represents the bulk metal volume per atom. Due to the increase in the chemical potential with the decreased particle radius, sintering is promoted and this leads to the change in the particle-size distribution during the cycling measurements. Most reported activity measurements on Pt particles have been on catalysts with particle sizes greater than 3 nm; this is known as a scalable interval, the measured activity scale with the inverse of particle diameter [3, 117]. Interestingly, most stunning changes in materials properties have been observed in the so-called non-scalable interval. Quite remarkable size-dependent specific activity in this interval has been measured for layer-by-layer synthesized Pt particles, allowing the careful control of particle sizes [35]. The measurements showed dramatic drop in the specific activity in this range (<2.5 nm) correlated with the computed nanoparticles reactivities, shown in Fig. 21.3 [35]. The results of this study firmly support the structural sensitivity of ORR.

Fig. 21.4 Particle-size-dependent surface strain for Pt, Au, and Pd nanoparticles on different facets and edges of cubo-octahedral particles. The particles' {111} and {100} facets and edges (in *gray*) are illustrated in the *inset* in the *upper left corner* [122]

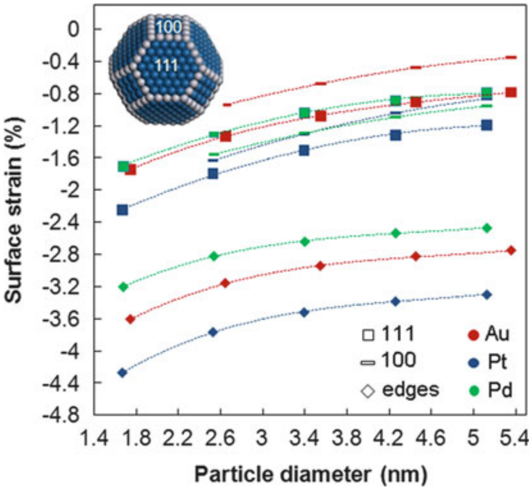

21.4.4 *Strain in Metallic Nanoparticles*

It has been previously shown that strain can have significant effect on the binding energies of adsorbates and on the activation energy barriers for bond-making and bond-breaking events on transition metal surfaces [41, 48, 78, 118, 119]. The lattice parameter or bond-length changes influence the electronic structure and, as a result, the catalyst reactivity [78, 79, 99]. The particle-size-dependent lattice contraction relative to the bulk values has been reported in the fcc metals [79, 120–122].

In order to gain insight into the geometric features for particles larger than 3 nm, structural optimization can be performed using the embedded atom method (EAM) potentials and the classical molecular dynamics approach as implemented in the LAMMPS code [123]. The computed average surface strains with respect to bulk lattice interatomic distances are plotted in Fig. 21.4 for ninefold coordinated atoms on {111} facets, eightfold coordinated atoms on the {100} facets, and six- and sevenfold coordinated atoms at edges and vertices for Pt, Pd, and Au nanoparticles with various particle sizes. The amount of strain clearly depends on the location of the atoms, with the largest strain at the edges and vertices of the particles, while the strains in {111} and {100} facets are approximately twofold smaller than in under-coordinated sites. This is consistent with the report of a linear correlation between the bond length and coordination number [124]. Nanoparticles of these metals show compressive strains that increase as the particle size decreases.

21.5 Conclusions

The insights from the first-principles approaches are particularly useful to uncover the effects of structural features of particle surfaces on the catalytic activity. The surface reactivity in nanoparticles is site specific and thus is significantly different from that of flat bulk surfaces. The reactivity results from studies of extended bulk surface and surfaces with defects while showing some common qualitative features appear less pertinent to nanoparticles catalysis, especially in the limit of small particles. The d-electron properties dominate the trends in surface reactivity. Decreasing the number of atoms per particle has large impact on the electronic structure of d-electrons. As the spatial dimensions decrease from the macroscopic limit toward the surfaces and particles, electronic structure of d-electrons shows continuous evolution toward the narrower d-band related to the growing importance of the dominant surface atoms and spatial confinement of electrons perpendicular to the surfaces. Two basic phenomena are reviewed:

- The coordination number-dependent narrowing of d-band on the surfaces. The effect becomes more and more pronounced as surface-to-volume ratio increases, owing to the increase in the number of low coordinated surface atoms.
- The reduction in volume in small nanoparticles that result in the quantum confinement, as consequence of which the quasi-continuous density of states, in the valence and conduction bands splits into discrete electronic levels.

The underlying reasons for the structural sensitivity of ORR have been related to the changes in the reactivity which is both particle size dependent and adsorption site specific. The adsorption site specificity is unambiguously related to the coordination to the nearest neighbors of atoms forming the adsorption site and the site symmetry. Overall adsorption energies increase as the particle size decreases; this trend projects the high drop of ORR-specific activity in the particle sizes below ~2.5 nm, where scaling of activity with inverse diameter of particles do not apply anymore. The increased reactivity within this region represents a theoretical limitation to the particle dispersion and sets limit to the precious metal utilization. However, informed engineering of both the composition and the shape and size of nanostructured catalysts, in the way of optimizing the adsorption strength and number of adsorption sites for the relevant reaction intermediates, sets a path to better catalyst design.

References

1. Vielstich W, Lamm A, Gasteiger HA (2009) Handbook of fuel cells, vol 1–6. Wiley, Chichester
2. Stone H (2005) Economic analysis of stationary PEMFC systems DOE hydrogen program FY 2005 progress report 961. Battelle Memorial Institute, Columbus, OH
3. Gasteiger HA, Kocha SS, Sompalli B, Wagner FT (2005) Activity benchmarks and requirements for Pt, Pt-alloy, and non-Pt Oxygen reduction catalysts for PEMFCs. Appl Catal B Environ 56(1–2):9–35
4. Adzic RR, Zhang J, Sasaki K, Vukmirovic MB, Shao M, Wang JX, Nilekar AU, Mavrikakis M, Valerio JA, Uribe F (2007) Platinum monolayer fuel cell electrocatalysts. Top Catal 46 (3–4):249–262
5. Lefevre M, Proietti E, Jaouen F, Dodelet JP (2009) Iron-based catalysts with improved oxygen reduction activity in polymer electrolyte fuel cells. Science 324(5923):71–74

6. Bashyam R, Zelenay P (2006) A class of non-precious metal composite catalysts for fuel cells. Nature 443:63–66
7. Stamenkovic VR, Fowler B, Mun BS, Wang G, Ross PN, Lucas CA, Markovic NM (2007) Improved oxygen reduction activity on $Pt_3Ni(111)$ via increased surface site availability. Science 315:493
8. Somorjar GA (1993) Introduction to surface chemistry and catalysis. Wiley, New York
9. Henry CR (1998) Surface studies of supported model catalysts. Surf Sci Rep 31:231–325
10. Yoo SJ, Jeon T-Y, Lee K-S, Park K-W, Sung Y-E (2010) Effects of particle size on surface electronic and electrocatalytic properties of Pt/TiO_2 nanocatalysts. Chem Commun 46 (5):794–796
11. Hayden BE, Suchsland J-P (2009) Support and particle size effects in electrocatalysis. In: Koper MTM (ed) Fuel cell catalysis: a surface science approach. Wiley, Hoboken, NJ, pp 567–592
12. Maillard F, Pronkin S, Savinova ER (2009) Size effects in electro catalysis of fuel cell reactions on supported metal nanoparticles. In: Koper MTM (ed) Fuel cell catalysis: a surface science approach. Wiley, Hoboken, NJ, pp 507–566
13. Kinoshita K (1990) Particle size effects for oxygen reduction on highly dispersed platinum in acid electrolytes. J Electrochem Soc 137:845–848
14. Bregoli LJ (1978) The influence of platinum crystallite size on the electrochemical reduction of oxygen in phosphoric acid. Electrochim Acta 23:489–492
15. Sattler ML, Ross PN (1986) The surface structure of Pt crystallites supported on carbon black. Ultramicroscopy 20:21–28
16. Peuckert M, Yoneda T, Dalla Betta RA, Boudart M (1986) Oxygen reduction on small supported platinum particles. J Electrochem Soc 133:944–947
17. Giordano N, Antonucci PL, Passalacqua E, Pino L, Arico AS, Kinoshita K (1991) Relationship between physicochemical properties and electrooxidation behaviour of carbon materials. Electrochim Acta 36:1931–1935
18. Takasu Y, Ohashi N, Zhang XG, Murakami Y, Minagawa H, Sato S, Yahikozawa K (1996) Size effects of platinum particles on the electroreduction of oxygen. Electrochim Acta 41:2595–2600
19. Gamez A, Richard D, Gallezot P, Gloaguen F, Faure R, Durand R (1996) Oxygen reduction on well-defined platinum nanoparticles inside recast ionomer. Electrochim Acta 41:307–314
20. Genies L, Faure R, Durand R (1998) Electrochemical reduction of oxygen on platinum nanoparticles in alkaline media. Electrochim Acta 44:1317–1327
21. Min M, Cho J, Cho K, Kim H (2000) Particle size and alloying effects of Pt-based alloy catalysts for fuel cell applications. Electrochim Acta 45:4211–4217
22. Maillard F, Martin M, Gloaguen F, Leger JM (2002) Oxygen electroreduction on carbon-supported platinum catalysts. Particle-size effect on the tolerance to methanol competition. Electrochim Acta 47:3431–3440
23. Maryrhofer KJJ, Blizanac BB, Arenz M, Stamenkovic VR, Ross PN, Markovic NM (2005) The impact of geometric and surface electronic properties of Pt-catalysts on the particle size effect in electrocatalysis. J Phys Chem B 109:14433–14440
24. Stamenkovic V, Mun BS, Mayrhofer KJJ, Ross PN, Markovic NM, Rossmeisl J, Greeley J, Nørskov JK (2006) Changing the activity of electrocatalysts for oxygen reduction by tuning the surface electronic structure. Angew Chem Int Ed 45(18):2897–2901
25. Bett J, Lundquist J, Washington E, Stonehart P (1973) Platinum crystallite size considerations for electrocatalytic oxygen reduction. Electrochim Acta 18:343–348
26. Watanabe M, Saegusa S, Stonehart P (1988) Electro-catalytic activity on supported platinum crystallites for oxygen reduction in sulphuric acid. Chem Lett Jpn 9:1487–1490
27. Watanabe M, Sei H, Stonehart P (1989) The influence of platinum crystallite size on the electroreduction of oxygen. J Electroanal Chem 261:375–387
28. Yano H, Inukai J, Uchida H, Watanabe M, Babu PK, Kobayashi T, Chung JH, Oldfield E, Wieckowski A (2006) Particle-size effect of nanoscale platinum catalysts in oxygen

reduction reaction: an electrochemical and ^{195}Pt EC-NMR study. Phys Chem Chem Phys 8 (42):4932–4939

29. Yamamoto K, Imaoka T, Chun W-J, Enoki O, Katoh H, Takenaga M, Sonoi A (2009) Size-specific catalytic activity of platinum clusters enhances oxygen reduction reactions. Nat Chem 1:397–402
30. Leontyev IN, Belenov SV, Guterman VE, Haghi-Ashtiani P, Shaganov AP, Dkhil B (2011) Catalytic activity of carbon-supported Pt nanoelectrocatalysts. Why reducing the size of Pt nanoparticles is not always beneficial. J Phys Chem C 115(13):5429–5434
31. St. John S, Dutta IP, Angelopoulos A (2010) Synthesis and characterization of electrocatalytically active platinum atom clusters and monodisperse single crystals. J Phys Chem C 114 (32):13515–13525
32. Tammeveski K, Tenno T, Claret J, Ferrater C (1997) Electrochemical reduction of oxygen on thin-film Pt electrodes in 0.1 M KOH. Electrochim Acta 42:893–897
33. Sarapuu A, Kasikov A, Laaksonen T, Kontturi K, Tammeveski K (2008) Electrochemical reduction of oxygen on thin-film Pt electrodes in acid solutions. Electrochim Acta 53:5873–5880
34. Kinoshita K (1992) Electrochemical oxygen technology. Wiley, New York
35. Shao M, Peles A, Shoemaker K (2011) Electrocatalysis on platinum nanoparticles: particle size effect on oxygen reduction reaction activity. Nano Lett 11(9):3714–3719
36. Markovic NM, Gasteiger HA, Ross PN (1997) Kinetics of oxygen reduction on Pt(hkl) electrodes: implications for the crystallite size effect with supported Pt electrocatalysts. J Electrochem Soc 144:1591–1597
37. Mukerjee S, McBreen J (1998) Effect of particle size on the electrocatalysis by carbon-supported Pt electrocatalysts: an in situ XAS investigation. J Electroanal Chem 448:163–171
38. Greeley J, Rossmeisl J, Hellman A, Norskov JK (2007) Theoretical trends in particle size effects for the oxygen reduction reaction. Z Phys Chem 221:1209–1220
39. Balandin A (1969) Modern state of the multiplet theory of heterogeneous catalysis. Adv Catal Rel Subj 19:1–210
40. Sabatier P (1911) Hydrogénations et déshydrogénations par catalyse. Ber Dtsch Chem Ges 44:1984–2001
41. Nørskov JK, Abild-Pedersen F, Studt F, Bligaard T (2011) Density functional theory in surface chemistry and catalysis. Proc Natl Acad Sci USA 108:937–943
42. Nørskov JK, Bligaard T, Rossmeisl J, Christensen CH (2009) Towards the computational design of solid catalysts. Nat Chem 1:37–46
43. Greeley J, Mavrikakis M (2004) Alloy catalysts designed from first principles. Nat Mat 3:810–815
44. Hammer B, Nørskov JK (1995) Electronic factors determining the reactivity of metal surfaces. Surf Sci 343:211–220
45. Hammer B, Nørskov JK (2000) Theoretical surface science and catalysis calculations and concepts. Adv Catal 45:71–129
46. Stamenkovic VR, Mun BS, Arenz M, Mayrhofer KJJ, Lucas CA, Wang G, Ross PN, Markovic NM (2007) Trends in electrocatalysis on extended and nanoscale Pt-bimetallic alloy surfaces. Nat Mat 6:241–247
47. Shao M, Liu P, Zhang J, Adzic RR (2007) Origin of enhanced activity in palladium alloy electrocatalysts for oxygen reduction reaction. J Phys Chem B 111:6772–6775
48. Zhang J, Vukmirovic MB, Xu Y, Mavrikakis M, Adzic RR (2005) Controlling the catalytic activity of platinum-monolayer electrocatalysts for oxygen reduction with different substrates. Angew Chem Int Ed 44:2132–2135
49. Adzic RR (1998) Recent advances in the kinetics of oxygen reduction. In: Lipkowski J, Ross PN (eds) Electrocatalysis. Wiley, New York, pp 197–242
50. Szabó A, Ostlund NS (1989) Modern quantum chemistry: introduction to advanced electronic structure theory. McGraw-Hill, New York
51. Pople JA (1999) Nobel lecture: quantum chemical models. Rev Mod Phys 71:1267–1274

52. Hohenberg P, Kohn W (1964) Inhomogeneous electron gas. Phys Rev 136:B864–B871
53. Kohn W, Sham L (1965) Self-consistent equations including exchange and correlation effects. Phys Rev 140:A1133–A1138
54. Born M, Oppenheimer JR (1927) On the quantum theory of molecules. Ann Phys 84:457–484
55. Levy M (1976) Universal variational functionals of electron densities, first-order density matrices, and natural spin-orbitals and solution of the v-representability problem. Proc Nat Acad Sci USA 76(12):6062–6065
56. Levy M (1982) Electron densities in search of Hamiltonians. Phys Rev A 26:1200–1208
57. Lieb EH (1985) Density Functionals for Coulomb Systems. In: Dreizler RM and da Providencia J (eds) Density functional methods in physics. Plenum, New York, pp 31–80
58. Hellmann H (1937) Einfuhrung in die Quantumchemie. Franz Deutsche, Leipzig, pp 285
59. Feynman RP (1939) Forces in molecules. Phys Rev 56(4):340–343
60. Ceperley DM, Alder BJ (1980) Ground state of the electron gas by a stochastic method. Phys Rev Lett 45(7):566–569
61. Perdew JP, Burke K, Ernzerhof M (1996) Generalized gradient approximation made simple. Phys Rev Lett 77:3865–3868
62. Perdew JP, Wang Y (1992) Accurate and simple analytic representation of the electron-gas correlation energy. Phys Rev B 45:13244–13249
63. Johnson BJ, Gill PMW, Pople JA (1993) The performance of a family of density functional methods. J Chem Phys 98:5612–5627
64. Becke AD (1988) Density-functional exchange-energy approximation with correct asymptotic behavior. Phys Rev A 38:3098–3100
65. Fuchs M, Scheffler M (1999) Ab initio pseudopotentials for electronic structure calculations of poly-atomic systems using density-functional theory. Comp Phys Comm 119:67–98
66. Vanderbilt D (1990) Soft self-consistent pseudopotentials in a generalized eigenvalue formalism. Phys Rev B 41:7892–7895
67. Blöchl PE (1994) Projector augmented-wave method. Phys Rev B 50:17953–17979
68. Kresse G, Furthmüller J (1996) Efficient iterative schemes for ab initio total-energy calculations using a plane-wave basis set. Phys Rev B 54:11169–11186
69. Kresse G, Hafner J (1993) Ab initio molecular dynamics for liquid metals. Phys Rev B 47: R558–R561
70. Newns DM (1969) Self-consistent model of hydrogen chemisorption. Phys Rev 178:1123–1135
71. Grimley TB (1971) Electronic structure of adsorbed atoms and molecules. J Vac Sci Technol 8:31–38
72. Schrieffer JR (1972) Theory of chemisorption. J Vac Sci Technol 9:56
73. Lundqvist BI, Gunnarsson O, Hjelmberg H, Nørskov JK (1979) Theoretical description of molecule-metal interaction and surface reactions. Surf Sci 89:196–225
74. Halperin WP (1986) Quantum size effects in metal particles. Rev Mod Phys 58:533–606
75. Ashcroft NW, Mermin ND (1981) Solid state physics. Saunders College Publishing, Philadelphia, PA
76. Friedel J (1969) The ordinary transport properties of metals. In: Ziman JM (ed) The physics of metals. Cambridge University Press, London, pp 250–281
77. Sutton AP (1996) Electronic Structure of Materials, Oxford University Press
78. Mavrikakis M, Hammer B, Nørskov JK (1998) Effect of strain on the reactivity of metal surfaces. Phys Rev Lett 81:2819–2822
79. Huang WJ, Sun R, Tao J, Menard LD, Nuzzo RG, Zuo JM (2008) Coordination-dependent surface atomic contraction in nanocrystals revealed by coherent diffraction. Nat Mater 7:308–313
80. Yaeger E (1984) Electrocatalysts for O_2 reduction. Electrochim Acta 29:1527–1537
81. Wroblowa HS, Pan Y-C, Razumney G (1976) Electroreduction of oxygen: a new mechanistic criterion. J Electroanal Chem 75:1465–1469

82. Wang JX, Markovic NM, Adzic RR (2004) Kinetic analysis of oxygen reduction on Pt(111) in acid solutions: intrinsic kinetic parameters and anion adsorption effects. J Phys Chem B 108(13):4127–4133
83. Greeley J, Nørskov JK (2005) A general scheme for the estimation of oxygen binding energies on binary transition metal surface alloys. Surf Sci 592:104–111
84. Zhang J, Vukmirovic MB, Sasaki K, Nilekar AU, Mavrikakis M, Adzic RR (2005) Mixed-metal Pt monolayer electrocatalysts for enhanced oxygen reduction kinetics. J Am Chem Soc 127(36):12480–12481
85. Jacob T (2006) The mechanism of forming H_2O from H_2 and O_2 over a Pt catalyst via direct oxygen reduction. Fuel Cells 3–4:159–181
86. Jacob T, Goddard WA III (2006) Water formation on Pt and Pt-based alloys: a theoretical description of a catalytic reaction. Chem Phys Chem 7(5):992–1005
87. Jacob T, Muller RP, Goddard WA III (2003) Chemisorption of atomic oxygen on Pt(111) from DFT studies of Pt-clusters. J Phys Chem B 107:9465–9476
88. Anderson AB (2003) Theory at the electrochemical interface: reversible potentials and potential-dependent activation energies. Electrochim Acta 48:3743–3749
89. Li T, Balbuena PB (2003) Oxygen reduction on a platinum cluster. Chem Phys Lett 367:439–447
90. Hyman MP, Medlin JW (2006) Mechanistic study of the electrochemical oxygen reduction reaction on Pt(111) using density functional theory. J Phys Chem B 110:15338–15344
91. Norskov JK, Rossmeisl J, Logadotir A, Lindqvist L, Kitchin JR, Bligaard T (2004) Origin of the overpotential for oxygen reduction at a fuel cell cathode. J Phys Chem B 108:17886–17892
92. Tripkovic V, Skúlasona E, Siahrostamia S, Nørskova JK, Rossmeisla J (2010) The oxygen reduction reaction mechanism on Pt(1 1 1) from density functional theory calculations. Electrochim Acta 55:7975–7981
93. Wang Y, Balbuena PB (2005) Ab initio molecular dynamics simulations of the oxygen reduction reaction on a Pt(111) surface in the presence of hydrated hedonism (H3O) +(H2O)2: direct or series pathway? J Phys Chem B 109:14896–14907
94. Nilekar AU, Mavrikakis M (2008) Improved oxygen reduction reactivity of platinum monolayer's on transition metal surfaces. Surf Sci 602:L89–L94
95. Janice MJ, Taylor CD, Enrick M (2009) First-principles analysis of the initial electroreduction steps of oxygen over Pt(111). J Electrochem Soc 156:B126–B135
96. Sha Y, Yu TH, Merinov BV, Goddard WA III (2012) Prediction of the dependence of the fuel cell oxygen reduction reactions on operating voltage from DFT calculations. J Phys Chem C 116:6166–6173
97. Marković NM, Ross PN Jr (2002) Surface science studies of model fuel cell electrocatalysts. Surf Sci Rep 45:117–229
98. Bligaard T, Nørskov JK (2007) Ligand effects in heterogeneous catalysis and electrochemistry. Electrochim Acta 51:5512–5516
99. Kitchin JR, Nørskov JK, Barteau MA, Chen JG (2004) Modification of the surface electronic and chemical properties of Pt(111) by subsurface 3d transition metals. J Chem Phys 120 (21):10240–10246
100. Wang JX, Inada H, Wu L, Zhu Y, Choi YM, Liu P, Zhou W-P, Adzic RR (2009) Oxygen reduction on well-defined core−shell nanocatalysts: particle size, facet, and Pt shell thickness effects. J Am Chem Soc 131(47):17298–17302
101. Han BC, Van der Ven A, Ceder G, Hwang B-J (2005) Surface segregation and ordering of alloy surfaces in the presence of adsorbates. Phys Rev B 72:205409–205418
102. Ramirez-Caballero G, Balbuena PB (2008) Surface segregation of core atoms in core-shell structures. Chem Phys Lett 456:64–67
103. Nilekar AU, Ruban AV, Mavrikakis M (2009) Surface segregation energy in low-index open surfaces of bimetallic transition metal alloys. Surf Sci 603:91–96
104. Greeley J, Nørskov JK (2009) Combinatorial density functional theory-based screening of surface alloys for the oxygen reduction reaction. J Phys Chem C 113(12):4932–4939

105. Greeley J, Norskov JK (2007) Electrochemical dissolution of surface alloys in acids: thermodynamic trends from first principles calculations. Electrochim Acta 52(19):5829–5836
106. Sasaki K, Naohara H, Cai Y, Choi YM, Liu P, Vukmirovic MB, Wang JX, Adzic RR (2010) Core-protected platinum monolayer shell high-stability electrocatalysts for fuel-cell cathodes. Angew Chem Int Ed 49(46):8602–8607
107. Hansen HA, Rossmeisl J, Norskov JK (2008) Surface Pourbaix diagrams and oxygen reduction activity of Pt, Ag and Ni (111) surfaces studied by DFT. Phys Chem Chem Phys 10(25):3722–3730
108. Feibelman PJ (1997) d-electron frustration and the large fcc versus hcp binding preference in O adsorption on Pt(111). Phys Rev B 56:10532–10537
109. Hsueh K-L, Gonzalez ER, Srinivasan S (1983) Electrolyte effects on oxygen reduction kinetics at platinum: a rotating ring-disc electrode analysis. Electrochim Acta 28:691–697
110. Frenkel AI, Hills CW, Nuzzo RG (2001) View from the inside: complexity of the atomic scale ordering in metal nanoparticles. J Phys Chem B 105:12689–12703
111. Henry CR (2003) Adsorption and reaction at supported metal catalyst. In: Wiecowski A, Savinova ER, Vayenas CG (eds) Catalysis and electrocatalysis at nanoparticle surfaces. CRC Press, pp 239–280
112. Bi W, Gray GE, Fuller TF (2007) PEM fuel cell Pt/C dissolution and deposition in Nafion electrolyte. Electrochem Solid State Lett 10:B101–B104
113. Ferreira PJ, La O' GJ, Shao-Horn Y, Morgan D, Makharia R, Kocha S, Gasteiger HA (2005) Instability of Pt/C electrocatalysts in proton exchange membrane fuel cells. J Electrochem Soc 152:A2256–A2271
114. Campbell CT (1997) Ultrathin metal films and particles on oxide surfaces: structural, electronic and chemisorptive properties. Surf Sci Rep 227:1–111
115. Valden M, Lai X, Goodman DW (1998) Onset of catalytic activity of gold clusters on Titania with the appearance of nonmetallic properties. Science 281:1647–1650
116. Lai X, Goodman DW (2000) Structure–reactivity correlations for oxide-supported metal catalysts: new perspectives from STM. J Mol Catal A 162:33–50
117. Roduner E (2006) Nanoscopic materials: size-dependent phenomena. Royal Society of Chemistry, Cambridge
118. Zhang J, Mo Y, Vukmirovic MB, Klie R, Sasaki K, Adzic RR (2004) Platinum monolayer electrocatalysts for O2 reduction: Pt monolayer on Pd(111) and on carbon-supported Pd nanoparticles. J Phys Chem 108:10955–10964
119. Shao MH, Shoemaker K, Peles A, Kaneko K, Protsailo L (2010) Pt monolayer on porous Pd-Cu alloys as oxygen reduction electrocatalysts. J Am Chem Soc 132:9253–9255
120. Mays CW, Vermaak JS, Kuhlmann-Wilsdorf D (1968) On surface stress and surface tension: II. Determination of the surface stress of gold. Surf Sci 12:134–140
121. Wasserman HJ, Vermaak JS (1972) On the determination of the surface stress of copper and platinum. Surf Sci 32:168–174
122. Shao M, Peles A, Shoemaker K, Gummalla M, Njoki PN, Luo J, Zhong CJ (2011) Enhanced oxygen reduction activity of platinum monolayer on gold nanoparticles. J Phys Chem Lett 2:67–72
123. Foils SM, Baskes MI, Daw MS (1986) Embedded-atom-method functions for the fcc metals Cu, Ag, Au, Ni, Pd, Pt, and their alloys. Phys Rev B 33:7983–7991
124. Krueger S, Vent S, Roesch N (1997) Size dependence of bond length and binding energy in palladium and gold clusters. Berichte der Bunsengesellschaft für physikalische Chemie 101:1640–1643

Chapter 22
Efficient Oxygen Evolution Reaction Catalysts for Cell Reversal and Start/Stop Tolerance

Radoslav T. Atanasoski, Ljiljana L. Atanasoska, and David A. Cullen

Abstract Minute amounts of ruthenium and iridium on platinum nanostructured thin films have been evaluated in an effort to reduce carbon corrosion and Pt dissolution during transient conditions in proton exchange membrane fuel cells. Electrochemical tests showed the catalysts had a remarkable oxygen evolution reaction (OER) activity, even greater than that of bulk, metallic thin films. Stability tests within a fuel cell environment showed that rapid Ru dissolution could be managed with the addition of Ir. Membrane electrode assemblies containing a Ru to Ir atomic ratio of 1:9 were evaluated under start-up/shutdown and cell reversal conditions for OER catalyst loadings ranging from 1 to 10 μg/cm^2. These tests affirmed that electrode potentials can be controlled through the addition of OER catalysts without impacting the oxygen reduction reaction on the cathode or the hydrogen oxidation reaction on the anode. The morphology and chemical structure of the thin OER layers were characterized by scanning transmission electron microscopy and X-ray photoelectron spectroscopy in an effort to establish a correlation between interfacial properties and electrochemical behavior.

22.1 Introduction

The motivation for studying the oxygen evolution reaction (OER) on minute amounts of platinum group metal (PGM) catalysts stems from the necessity to add robustness to the fuel cell (FC) catalysts during the so-called transient

---

R.T. Atanasoski (✉)
Fuel Cell Components Program, 3M Company, St. Paul, MN 55144, USA
e-mail: rtatanasoski@mmm.com

L.L. Atanasoska
Corporate Research Analytical Laboratory, 3M Company, St. Paul, MN 55144, USA

D.A. Cullen
Materials Science and Technology Division, Oak Ridge National Lab, Oak Ridge, TN 37831, USA

M. Shao (ed.), *Electrocatalysis in Fuel Cells*, Lecture Notes in Energy 9,
DOI 10.1007/978-1-4471-4911-8_22,

conditions. One of the key FC durability issues is failure of the catalyst and the other thermodynamically unstable membrane electrode assembly (MEA) components during start-up/shutdown (SU/SD) and local fuel starvation events at the anode that can lead to cell reversal (CR). If left unchecked, during these periods the electrodes can reach potentials up to 2 V.

The SU/SD phenomena were described by the General Motors (GM) and United Technologies Corporation (UTC) groups some time ago [1, 2] and have been a topic of intense research ever since. After a prolonged period of rest, the hydrogen in the anode is replaced by air. Upon start-up, a hydrogen/air front moves across the anode. The part of the fuel cell in which air is replaced by the arriving hydrogen exhibits the typical open circuit voltage (OCV), ordinarily around 1 V. Being on the same bipolar plate and gas diffusion layer (GDL), the potential of the part of the anode with air still remaining in the anode compartment is forced to be close to 0 V. As a result, the remaining oxygen at the anode will be reduced. However, the completion of the oxygen reduction reaction (ORR) in the part of the anode still under air requires a source of protons. The transport of protons laterally along the membrane is limited only to the immediate vicinity of the approaching hydrogen front [3]. Therefore, since the driving force for this reaction is very large, ~1 V, the protons could be coerced from the cathode. There, the protons can come from two sources: the oxidation of water or the oxidation of carbon:

$$H_2O \rightarrow {}^1\!/_2 O_2 + 2H^+ + 2e^-, \quad E^0 = 1.229\ \text{V}, \tag{22.1}$$

$$C + 2H_2O \rightarrow CO_2 + 4H^+ + 4e^-, \quad E^0 = 0.207\ \text{V}. \tag{22.2}$$

Although the kinetics of carbon oxidation are sluggish, exposure to high potentials even for short periods of time might be sufficient to oxidize the surface layers of carbon, thus altering its hydrophobicity and consequently the MEA's water transport properties. In electrochemical terms, the SU/SD events last until an equivalent of 5–10 mC/cm^2 of the remnant oxygen is reacted [4, 5]. Depending of the flow rate of the hydrogen, the effect passes in ~1–3 s [6]. Therefore, such an event would require current densities of no more than 10 mA/cm^2.

Even more severe positive potentials can be experienced by the anode during cell reversal. This situation arises when there is a substantial lack of hydrogen at the anode on one of the cells in the stack. This can occur at cold temperatures when icicles plug the hydrogen inlet. Since the same current must pass through each cell, in the absence of hydrogen on the anode, the next reactant to oxidize will be either water or carbon. These reactions require the anode to reach a more positive potential than the cathode, thus the term cell reversal (CR). Qualitatively, the anode is in the same situation as is the cathode during SU/SD. However, the current densities imposed on the anode are 1–2 orders of magnitude higher than during the SU/SD events and range in the hundreds of mA/cm^2.

There are a variety of system-related strategies for avoiding the undesirable effects of SU/SD and CR, such as gas purging and cell voltage sensors (for reviews, see [7, 8]). Unlike these methods, a materials-based approach provides protection from within the MEA and is therefore always "ON." One promising materials-based approach is to develop/implement catalysts with high activity towards the OER from water. This concept consists of modifying both the anode and the cathode catalysts to favor the oxidation of water and to maintain the potentials close to the onset for water oxidation [9–11]. Due to FC performance requirements as well as the strict United States Department of Energy (DOE) PGM loading restrictions, the OER catalysts must be added in minute amounts, mostly in the range below 10 μg/cm^2, while still providing adequate protection during damaging fuel starvation conditions throughout the lifetime of the stack.

In order to be able to properly examine the inherent activity of minute amounts of OER catalysts, one needs a substrate with minimal interference, extremely slow OER kinetics of its own and extraordinary stability at high positive electrode potentials. The unique features of 3M's Pt–NSTF (nanostructured thin film) catalyst [12] such as superior durability, electrochemical inertness at high potentials, and the absence of corrosion interference due to exposed carbon, made it a logical choice as a support [13, 14]. It is well known that pure platinum has a high overpotential for OER. For instance, at a current density of 1 mA/cm^2, the OER on platinum proceeds at a potential that is 0.47 V higher than on single crystal ruthenium oxide [15]. Thus, the OER partial current density on the Pt–NSTF substrate will be orders of magnitudes lower than on ruthenium, iridium, and other similar OER-active materials.

The NSTF fabrication process of physical vapor deposition via sputtering in vacuum allows for a wide range of OER-active materials in a variety of compositions to be easily synthesized [16]. The requirements for using minimal amounts of PGM for the OER is accomplished by sputter depositing the OER catalyst as a separate, discontinuous nanostructured phase onto the base of the NSTF anode or cathode catalyst-coated whiskers [9, 17]. In this form, the number of available ORR/hydrogen oxidation reaction (HOR) active sites will be maximized, allowing the electrode reactions to proceed normally during usual, non-transitional operating conditions.

Ruthenium and iridium in both metallic and oxide states are known to have the best catalytic properties for OER in aqueous solutions [18]. In this review, the properties of the pure elements, Ru and Ir, in the MEA environment will be reviewed first. In the second part, the applied aspects of the combination of the two catalysts in SU/SD and CR testing will be covered. In order to fulfill properly its function, a balance must be struck between OER activity, which allows minimum PGM to be used, and durability, which allows the OER catalysts to accomplish its function many times over during the lifetime of a FC stack.

The OER on metallic Ru and Ir and especially on their oxides has been extensively studied during the last 50 years. The area has been reviewed in numerous articles, and a good starting point for this topic would be the brief overview by Trasatti [19]. We will only refer to and compare data with publications which have a more direct relevance to this work, in particular those which deal with metallic Ru and Ir. In this way, due attention will be given to the fundamentals of the *extraordinary activity* of extremely small amounts of Ru and Ir in an MEA environment.

This review is limited to and covers the research which has been carried out in our labs over a period of the last 2 years. The majority of this work has been reported to DOE and is available on the DOE hydrogen program web site [20].

22.2 OER Catalyst Characterization by STEM and XPS

Small amounts of Ru or Ir were sputter-deposited on Pt–NSTF substrate to determine their stability and OER activity in a fuel cell environment. Ex situ characterization of as-grown material was first performed in order to characterize the morphology and surface state of each OER catalyst. Scanning transmission electron microscopy (STEM) and X-ray photoelectron spectroscopy (XPS) were employed to complete this task. Two different OER catalyst loadings were studied, 2 and 10 μg/cm^2, in order to explore the impact of layer thickness on the catalyst morphology and composition.

22.2.1 STEM of As-Grown OER Catalysts

Aberration-corrected STEM coupled with energy dispersive X-ray spectroscopy (EDS) was used to resolve the structure of the OER catalysts on the Pt–NSTF whisker surfaces with atomic resolution [21–25]. High-angle annular dark-field (HAADF) and bright-field (BF) images were recorded simultaneously and provided complementary information. For high-resolution imaging, BF images provided the clearest view of the whisker surfaces. However, since Pt, Ir, and Ru all have a similar lattice spacing, the three constituents could not be readily distinguished by way of lattice measurements in BF images. The contrast in HAADF imaging, on the other hand, is sensitive to atomic number and therefore could be used to distinguish different elements at the whisker surfaces. However, the heavy Pt grains and thickness variations at the whisker surfaces complicated the interpretation of HAADF images, especially in the case of the Ir OER catalysts. Thus, EDS mapping of individual whiskers played an important role in determining the OER layer thickness and continuity.

The results from the Ru-coated samples are summarized in Fig. 22.1. Unlike Ir, Ru is much lighter than Pt, and thus, sufficient contrast exists in the HAADF images to distinguish the two elements. This can be clearly observed by direct inspection of the HAADF image in Fig. 22.1d of a Pt whisker with a Ru loading of 10 μg/cm^2. The EDS map of this whisker confirmed the presence of Ru on the whisker surfaces. For this loading, EDS maps showed a nearly continuous thin layer of Ru, but only intermittent coverage of Ru at the lower 2 μg/cm^2 loading. High-resolution BF images showed a strong crystalline component in the 10 μg/cm^2 Ru overlayer, which was indexed as metallic Ru. The layer was slightly more structured than the thicker Pt catalyst, and consisted of thin, interconnected particles of Ru, many of

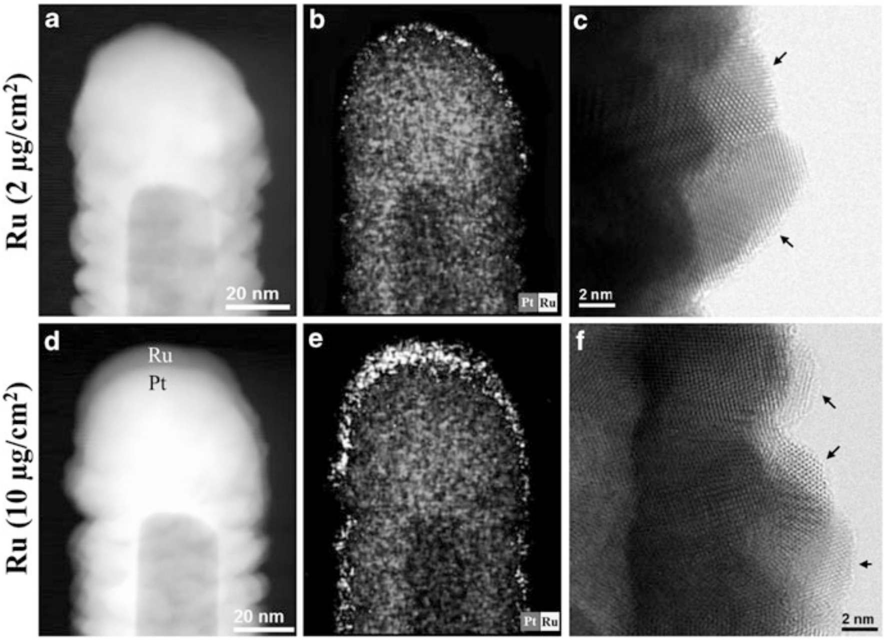

Fig. 22.1 (**a**, **d**) HAADF images with accompanying (**b**, **e**) EDS maps and (**c**, **f**) high-resolution BF images of Ru-coated whiskers at the low and high loadings. The *arrows* in the BF images mark the location of the Ru layer on the Pt grains [17]

which grew epitaxially on the underlying Pt. At the lower loading, the presence of Ru on the whisker surfaces was not as obvious, and electron energy loss spectroscopy (EELS) mapping (not shown) was necessary to show the presence of a thin, intermittent Ru layer epitaxially coating the Pt grains.

STEM analysis of the Ir overlayer is shown in Fig. 22.2. It was not possible to distinguish Ir from Pt in HAADF images. Instead, EDS mapping was used to visualize the Ir layer on the Pt–NSTF. The Ir, like Ru, was present at a higher concentration at the tips, but unlike Ru, the Ir layer appeared to be discontinuous for both the high and low loadings. At the lower loading, the thin Ir layer on the whisker sidewalls was barely detectable by EDS. Even at the higher loading, the Ir overlayer appeared discontinuous, suggesting exposed Pt surfaces were available for the ORR at both loadings. The BF images of the whiskers with the lower loading suggest that Ir deposits as a thin, epitaxial layer on the Pt surface (Fig. 22.2c). At a higher loading, small clusters of Ir began to emerge on the whisker surfaces (Fig. 22.2f), suggesting a slight difference in catalyst morphology between the two loadings.

The STEM analysis suggests a change in catalyst morphology with loading for both Ru and Ir. As the surface layer thickness increased, the structure of the OER catalysts became more particle-like. The potential impact on the ORR activity by blockage of Pt surface sites appeared to be marginal except for the 10 μg/cm^2 Ru sample, where a large percentage of the whisker surface appeared to be covered.

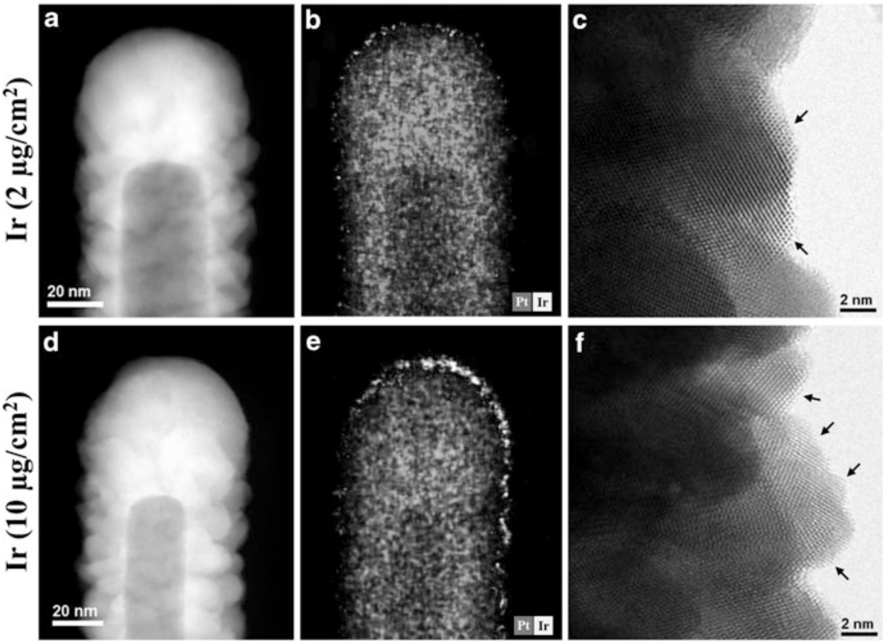

Fig. 22.2 (**a**, **d**) HAADF images with accompanying (**b**, **e**) EDS maps and (**c**, **f**) high-resolution BF images of Ir-coated whiskers at the low and high loadings. The *arrows* in the BF images mark the location of Ir on the Pt grains [17]

Differences in the surface morphology between the Ru and Ir catalysts for a given loading were more subtle. However, as the following section will show, morphology is only one of many variables impacting catalyst activity and stability.

22.2.2 Surface Characterization by XPS

While STEM methods were valuable in investigating the morphology and the structure of OER catalysts, they lacked the ability to discriminate between different valence states of Ir and Ru overlayers or altered chemical environments at the interface with Pt–NSTF whiskers. Therefore, the interfacial region, which plays a critical role in catalyst performance and durability, was also characterized by XPS [17, 26].

In the case of Ru overlayers, the differences in interfacial chemistry of 2 and 10 μg/cm^2 Ru loadings were evident from the line shape of their C 1s-Ru 3d core level spectra (Fig. 22.3a) even before subjecting the data to more elaborate curve fitting analysis. Both ruthenium and carbon XPS data strongly suggested that the interaction occurs at the interface of Pt–NSTF with the 2 μg/cm^2 Ru. Firstly, the thinner 2 μg/cm^2 coating had much broader Ru 3d$_{5/2}$ peak, which implies the

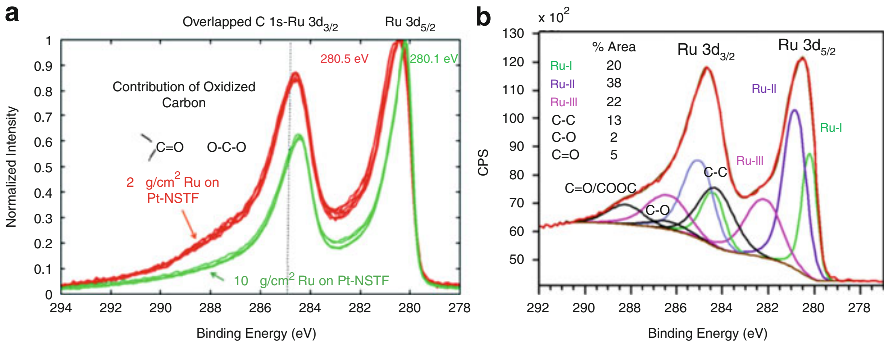

Fig. 22.3 (**a**) Comparison of Ru 3d-C 1s core level spectra for 2 and 10 μg Ru loadings per geometric surface area of Pt–NSTF in cm^2, normalized view for multiple randomly selected analysis locations, and (**b**) curve fitting analysis of Ru 3d-C 1s core level spectra for a 2 μg/cm^2 Ru loading on Pt–NSTF: metallic ruthenium Ru^0 photoemission contributes to the resolved Ru-I peak, while reacted ruthenium Ru^{x+} photoemissions contribute to the resolved Ru-II and Ru-III peaks [17, 27, 28]

presence of multiple Ru valence states. Secondly, the Ru 3d$_{5/2}$ peak of the thinner coating was shifted by ~0.4 eV towards higher binding energies (BE) with respect to the 10 μg/cm^2 peak location. Although small, this shift hinted to a ruthenium transition from its metallic zero valence into a reacted $x+$ state. The difference in the contribution of oxidized (ether and carbonyl) carbon between 2 and 10 μg/cm^2 Ru loadings is also strikingly apparent from the C 1s-Ru 3d line shapes. The visible dominance of ether (C–O) bonds in the thin 2 μg/cm^2 Ru coating and subsequent attenuation of oxidized carbon by the higher ruthenium loading of 10 μg/cm^2 was an implication that ruthenium preferentially covers and interacts with the available carbonyl bonds of perylene red sites. The O, C, and Ru stoichiometry balance derived from the curve fitting analysis (Fig. 22.3b) suggested that the chemical interaction of perylene red with ruthenium results mainly in the formation of organometallic-type bonds such as Ru(OC)x or Ru(CO)x along with low levels of ruthenium oxide (Table 22.1).

The ruthenium interaction with the perylene red carbonyl groups is not unexpected, as this type of interaction has been reported for other metals and molecules with structures comparable to perylene red [29–31]. Nonetheless, it was surprising to find that ruthenium interacts with the perylene red, due to the fact that the whiskers are covered with a relatively thick layer of Pt (15–20 nm; see Fig. 22.1). It was even more surprising to observe the extent to which this interaction occurs, as presented in Table 22.1. Our initial assumption was that the Ru–perylene interaction takes place through the discontinuities in the Pt layer. However, if taking place only at the Pt–perylene interface, the size and density of the discontinuities would have to be much higher than that observed in STEM images.

In order to better understand the interaction between Ru and perylene red, a subsequent study was conducted on ruthenium overlayers deposited directly on the bare perylene red whiskers with a systematic range of loadings [32]. The intention

Table 22.1 Interface soichiometry for 2 μg/cm^2 Ru on Pt-NSTF

	Oxygen			Carbon			Ruthenium	
Total content (at.%)	22			41			12	
Functional groups	Ether	Carbonyl	Oxide	Aliphatic	Ether	Carbonyl	Ru^0	Ru^{x+}
% Contribution to O 1s, C 1s and Ru 3d photoemission	25	46	29	65	10	25	25	75
Concentration (at.%)	6	10	6	27	4	10	3	9

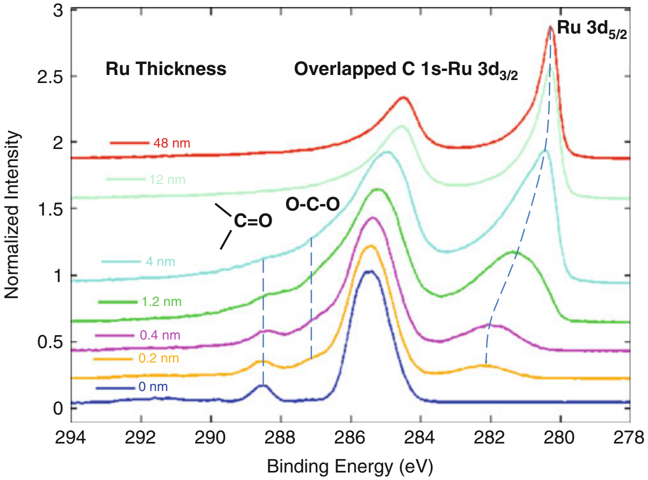

Fig. 22.4 C 1s-Ru 3d core level spectra as a function of Ru thickness on perylene red whiskers

of these experiments was to verify methodically that the Ru–O–C bonds do indeed form at the Ru interface with perylene red, since these bonds might play a role in the stability of Ru-containing OER catalysts. The C 1s core level spectra for bare perylene red substrate and the C 1s-Ru 3d core level photoemission for Ru deposits ranging from 0.2 to 48 nm are plotted together in Fig. 22.4.

As expected, the C 1s core level spectrum of bare perylene red substrate (Ru thickness of 0 nm in Fig. 22.4) has only carbon peaks associated with the carbonyl and aromatic/aliphatic carbons; there is no peak at 287 eV related to the ether (C–O) bonds. However, the C 1s-Ru 3d core level spectra for ultrathin Ru loadings do clearly show the emergence of the new carbon peak at 287 eV, along with the BE shift and broadening of Ru 3d$_{5/2}$ photoemission. The obtained XPS data confirm the occurrence of a Ru interaction with perylene red and formation of multiple ruthenium oxidation states. The formation of Ru(CO)x- or Ru(OC)x-type bonds was further confirmed by the stoichiometry derived from curve fitting analysis.

The difference in the interfacial chemistry between 2 and 10 μg/cm^2 Ir loadings on Pt–NSTF was not as obvious from the raw Ir 4f core level line shapes, as in the case of Ru overlayers [17, 26]. The curve fitting analysis of Ir 4f core level spectra

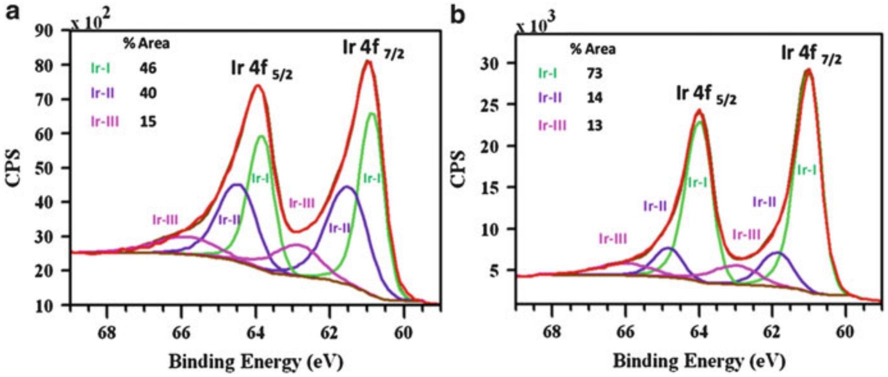

Fig. 22.5 Curve fitting analysis of Ir 4f core level spectra for (**a**) 2 and (**b**) 10 μg/cm^2 Ir loadings on Pt–NSTF: metallic iridium Ir^0 photoemission contributes to the resolved Ir-I peak while reacted iridium Ir^{x+} photoemissions contribute to the resolved Ir-II and Ir-III peaks[33, 34]

Table 22.2 Interface soichiometry for 2 μg/cm^2 Ir on Pt-NSTF

	Oxygen			Carbon			Iridium	
Total content (at.%)	24			22			10	
Functional groups	Ether	Hydroxide + carbonyl	Oxide	Aliphatic	Ether	Carbonyl	Ir^0	Ir^{x+}
% Contribution to O 1s, C 1s and Ir 4f photoemission	28	51	21	75	14	11	45	55
Concentrations (at.%)	7	12	5	16.5	3	2.5	4.5	5.5

for the thin 2 μg/cm^2 Ir coating (Fig. 22.5a, Table 22.2) shows that the interaction of Ir with perylene red whiskers is less pronounced when compared to the ruthenium layer of the same thickness. Only ~50 % of the total Ir 4f photoemission comes from the reacted iridium (Table 22.2), while, in the case of ruthenium, reacted Ru accounted for up to ~75 % of the total Ru 3d photoemission (Table 22.1). Subsequent attenuation of the reacted iridium by the higher 10 μg/cm^2 iridium loading is also true for this interface (Fig. 22.5b). Only Ir–O bonds are present at the iridium interface with Pt–NSTF as confirmed by the O:Ir ratio calculated after subtracting oxygen bound to carbon and taking into account the reacted iridium only. The O (oxide + hydroxide):Ir^{x+} ratio of ~2.5 in Table 22.2 suggests the presence of iridium in both 3+ and 4+ valence states. There is no indication of organometallic bond formation at the interface of iridium with Pt-coated perylene red whiskers.

In order to explain the observed differences in the ruthenium and iridium behavior at the interface with Pt–NSTF, the iridium overlayers were also grown on the bare perylene red whiskers by systematically increasing their thickness in the range from 0.1 to 34.8 nm [32].

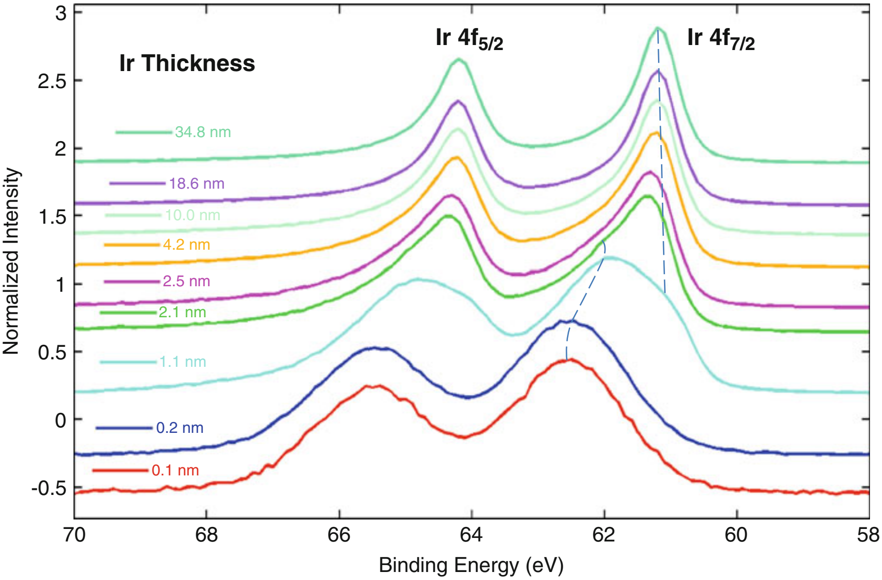

Fig. 22.6 Ir 4f core level spectra as a function of Ir thickness on perylene red whiskers

The changes in BE and line shapes of Ir 4f core level photoemission with increasing Ir coverage on perylene red whiskers clearly demonstrate the existence of reacted Ir^{x+} valence state at low Ir coverage (Fig. 22.6). The Ir 4f and Ru 3d core level curve fitting analysis reveals that the contribution of metallic state is higher for iridium, which indicates its much weaker chemical interaction at the interface with perylene red. Unreacted ruthenium was not even present at low coverage up to ~1 nm (Fig. 22.7).

The XPS data indicates clearly an interaction of both Ru and Ir with the perylene red whiskers. However, the nature and the extent of these interactions with the perylene red were found to be fundamentally different. The impact of these differences on the catalysts' stability and durability needs to be studied further.

22.3 Electrochemical Evaluation of OER Catalysts in MEA

The activity and the stability of the added OER catalysts were evaluated via quasi-steady state polarization measurements. Slow scan cyclic voltammetry (CV) was performed from 0.7 V to the upper voltage limit which was sequentially increased in increments of 0.05 V from 1.45 to 1.65 V. Three consecutive scans for each upper potential limit were recorded. In Fig. 22.8, some of the characteristic polarization scans that best illustrate the OER on Ru and Ir overcoated on Pt–NSTF are presented. Up to the first voltage limit of 1.45 V, only the added Ru produced a substantial

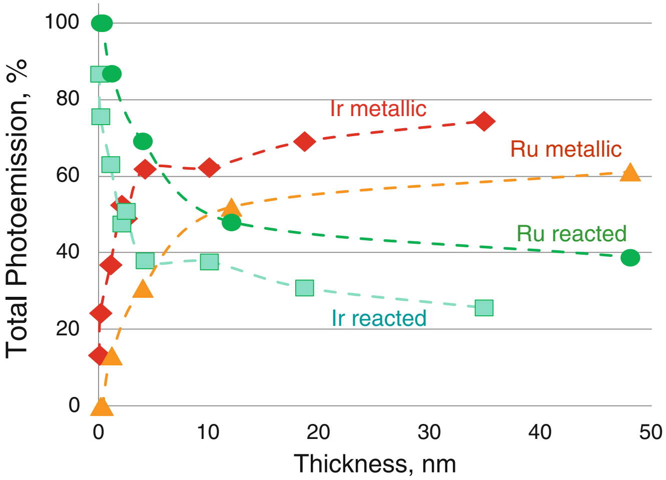

Fig. 22.7 Comparison of metallic Ru and Ir contributions at the interface with perylene red

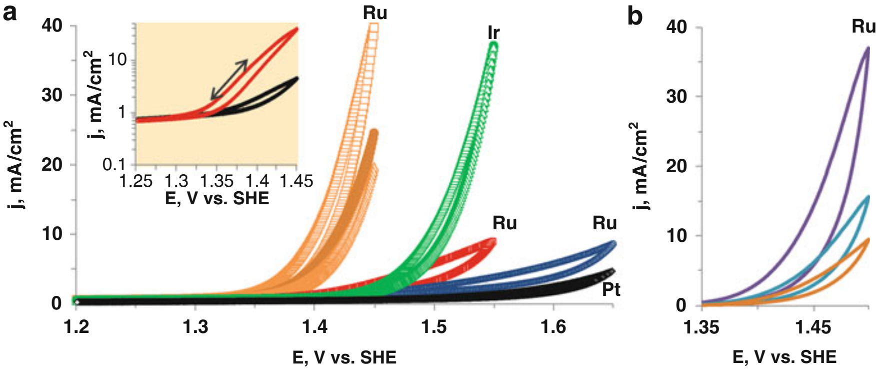

Fig. 22.8 Polarization curves for oxygen evolution on 10 μg/cm^2 Ru and Ir sputter-deposited on Pt–NSTF. OER curve on Pt–NSTF substrate also included. (**a**) Ruthenium: all three consecutive polarization curves for end voltage of 1.45 V and only the first of the three for 1.55 and 1.65 V are presented. Iridium: all three consecutive polarization curves for end voltage of 1.55 V are presented; note that the three curves overlap. *Inset*: comparison of the first polarization curves for 10 μg/cm^2 (*upper*) and 2 μg/cm^2 Ru (*lower*); the *line* with *arrows* indicates the linear, Tafel region of the polarization curve. (**b**) The three consecutive polarizations curves for Ru up to 1.5 V. All polarization curves recorded at 2 mV/s in 50-cm^2 MEA under nitrogen/1 % hydrogen, 70 °C, fully saturated. Electrode potentials expressed vs. SHE

current—39 mA/cm^2. This value is almost a factor of 20 higher than the current on Ir at the same potential. Further, the onset of OER, defined as 1 mA/cm^2 current density after the subtraction of the background current, on Ru occurs at 1.37 V, while on Ir it occurs at 1.45 V. Figure 22.8 presents a wealth of information concerning OER stability and activity, which will be analyzed in detail in the following subsections.

22.3.1 Ru and Ir Stability

Ru is highly unstable at these high potentials, which is illustrated by the lower current of the repeated scans to 1.45 V. Following the first scan, the current drops by 38 % and then by 50 % on the third scan. This drop in the activity implies a substantial loss of Ru during the polarization scans. As large as the Ru loss is, relative to the literature data, Ru on Pt–NSTF is appreciably more stable.

A widely accepted mechanism for Ru dissolution is via formation of Ru^{8+} [18]. Hence, a complete dissolution of the 10 μg/cm^2 Ru would require a charge of 76.4 mC. This charge is only ~2.3 % of the total charge during the first three scans to 1.45 V (the charge of the third scan in the negative going potential was not included in the calculation). Therefore, we can conclude that the current during the polarization scans is mainly due to OER. The dissolution of Ru continues at a faster rate during the next three scans to 1.5 V (Fig. 22.8b). The current densities reached at 1.5 V are 37, 15.6, and 9.2 mA/cm^2. If expressed as relative loss with respect to the first potential sweep, the loss in activity is 58 % for the second and 75 % for the third sweep. Additionally, the hysteresis between the positive vs. the negative going potential sweeps is much larger than for the sweeps up to 1.45 V, indicating again a rapid dissolution rate of Ru at this more positive voltage.

At 1.5 V, a direct comparison of the Ru stability with published data is possible. While some OER activity is still detected on the potential scans upon the increase of the voltage limit to 1.55 V (see Ru curve in Fig. 22.8), for simplicity, we will assume that all the Ru has been dissolved by the third scan at 1.5 V. The total charge during the six polarization scans, three to 1.45 V and three to 1.5 V, integrated from 1.3 V to the upper potential limit, was ~8,000 mC/cm^2. Therefore, the charge needed to dissolve all of the 10 μg/cm^2 Ru—76.4 mC—is only ~1 % of the average current density during the potential sweeps. In other words, the average dissolution rate of Ru accounts for only 1 % of the average current during the six scans. The total charge collected was ~13 mA/cm^2, which brings the average Ru dissolution current to 0.13 mA/cm^2. This dissolution rate of Ru on Pt–NSTF of 1 % is extremely low when compared with the dissolution rate reported by Kötz and Stucki of 31 and 57 % [35]. The latter was measured on a sputter-deposited 200-nm-thick film of Ru in the same voltage range in sulfuric acid. A corrosion rate of 10 %, at constant current in a similar voltage range, has been reported elsewhere (see refs. [2, 8, 9 in 35]).

The onset potential of Ru dissolution can also be a measure of the Ru stability. A rough estimate of this value for Ru on Pt–NSTF can be inferred by comparing the negative going potential scan with the subsequent positive going scan. The two overlap up to 1.40–1.42 V, after which the current during the positive going scan starts to fall behind. The other indicator of Ru stability is the Tafel region on the positive going scans (see inset in Fig. 22.8a). The Tafel relationship holds for only a narrow potential range between ~1.35 and 1.39 V, suggesting the Ru remains reasonably stable up to 1.39 V, a value close to the already estimated stability limit of 1.40–1.42 V. Kötz and Stucki were able to detect products of Ru dissolution

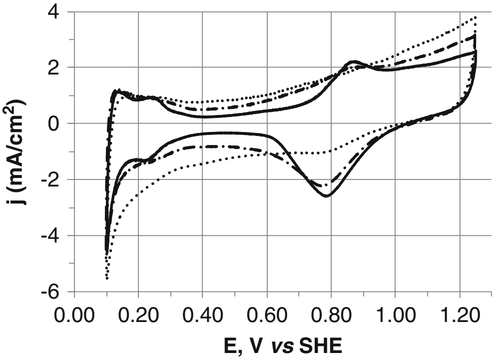

Fig. 22.9 Cyclic voltammograms for 10 µg/cm^2 Ru at beginning of test (*dotted curve*) and after exposure to 1.45 V (*dash-dotted curve*) and to 1.50 V (*solid curve*). CVs scan rate at 100 mV/s. Test conditions same as in Fig. 22.8

only at potentials higher than 1.45 V. Thus, our estimate of the onset potential of Ru dissolution in an MEA environment is slightly lower. In spite of this, the stability of Ru on Pt–NSTF is much higher, as implied by our dissolution rate, than that reported by Kötz and Stucki [35].

The impact of the exposure to high potentials on Ru stability can also be followed via CVs recorded after each set of three polarization curves in the voltage range between hydrogen evolution and the onset of the OER. This provides diagnostics of the changes of the overcoated Ru catalyst (Fig. 22.9). The "as received" sample is dominated by the pseudo-capacitive properties of Ru which overshadow the underlying Pt–NSTF substrate in the H_{upd}, the double layer, and the Pt oxidation region. Following the three polarization scans to 1.45 V, the CV begins to resemble that of pure Pt, especially in the double layer region. The CV becomes almost Pt-like after the increase of the polarization limit to 1.5 V. Further increase of the polarization limit up to the final upper voltage of 1.65 V had no detectable effect on the CVs.

The presence of 10 µg/cm^2 of Ru on the FC performance is also indicative of the initial state of Ru on Pt–NSTF and its stability during the exposure to high positive potentials (Fig. 22.10). Before the OER test, i.e. before the exposure of Ru to higher potentials, Ru covers most of the underlying Pt, as shown by STEM–EDS mapping (see Fig. 22.1), thus inhibiting substantially the ORR on the cathode. After the Ru dissolves at higher potentials, the CVs of the cathode become Pt-like (Fig. 22.9), and the ORR proceeds uninhibited as it does on pure Pt. Note that 2 µg/cm^2 of Ru did not obstruct the FC performance nor were Ru-like features observed in the CVs. The same is true for both 2 and 10 µg/cm^2 of Ir.

STEM–EDS measurements were unable to detect Ru on the whiskers after testing, corroborating the conclusions from CV measurements that Ru rapidly dissolves from the whisker surfaces at higher potentials. However, Ru nanoparticles were found in the microporous layer (MPL) next to the electrode.

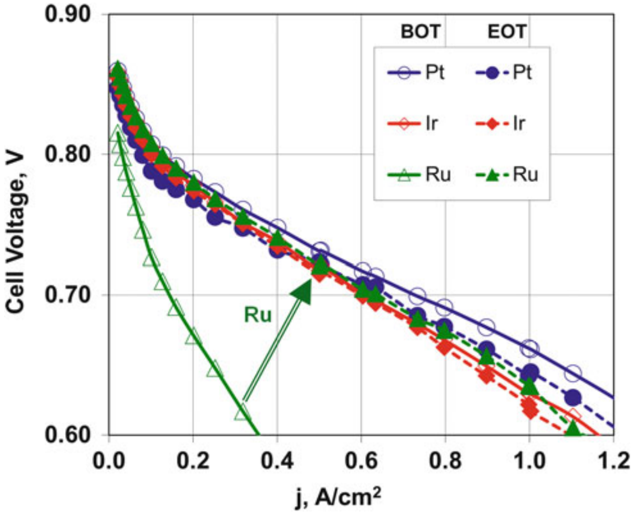

Fig. 22.10 Fuel cell polarization curves before (BOT) and after (EOT) OER testing for 10 μg/cm^2 of Ir and Ru on 0.15 mg/cm^2 Pt–NSTF. Uncoated Pt–NSTF presented for comparison. Test conditions: Galvano-dynamic scans at 80 °C; H_2/air, constant stoich 2.0/2.5, 68 °C/68 °C, and dew point, 50/50 kPa

It should also be noted that the sensitivity of EDS is limited to approximately 1 at. %, and a small, but electrochemically noticeable amount of Ru may still remain on the whisker surfaces. This is observed in Fig. 22.8a, where the higher OER activity at 1.65 V of the Ru sample (~8 mA/cm^2) compared with the Pt–NSTF substrate (~3.5 mA/cm^2) could be explained by the presence of trace amounts of Ru on the electrode at the end of test. Indeed, complementary high-resolution XPS measurements were able to detect some Ru in the tested catalyst-coated membrane (CCM), via a weak Ru $3d_{5/2}$ peak in the C 1s-Ru 3d region and the very visible Ru 3p doublet (Fig. 22.11a). No Ru was detected on the counter electrode. By comparison, the XPS spectra for Ir (Fig. 22.11b) have a much stronger peak intensity, indicating again that Ru has dissolved during the test, while Ir is much more stable.

In contrast to Ru, Ir proved to be quite stable in the fuel cell environment. As presented in Fig. 22.8, the three consecutive scans to 1.55 V practically overlapped, and, as a result, the OER activity of Ir at 1.55 V was 18 times higher than that of Ru, albeit that Ru had a much higher initial OER activity. Kötz and Stucki estimated the Ir dissolution rate proceeded at only 1 % of the total current during the OER test [35]. Unlike for Ru, we have not observed any quantitative changes in the electrochemical performance for Ir. The electrode potential limit for Ir stability beyond 1.65 V will be presented later (see Sect. 22.4).

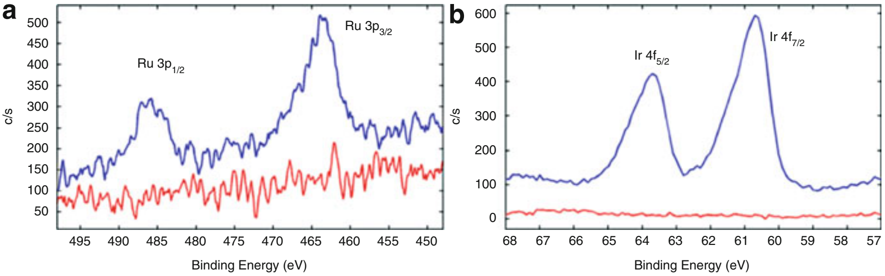

Fig. 22.11 XPS core level spectra of tested CCM with 10 μg/cm^2 of Ru (**a**) and Ir (**b**). Working electrode side: Ru 3p and Ir 4f, peaks (upper spectra). Counter electrode side (lower spectra) indicating that no Ru nor Ir peaks are detected in the same BE region on the counter electrode (uncoated Pt–NSTF)

22.3.2 Ru and Ir OER Activity

In order to put the OER activity for both Ru and Ir in perspective, we will express them in terms of mass activity, OER current per unit weight, inherent/specific activity, and the current per catalyst surface area and compare these values with data from the open literature. The evaluation of the OER inherent activity was calculated from the kinetic region, where the smaller current densities eliminate the need for IR corrections.

The activities of the OER catalysts were determined from the initial scans up to 1.45 V for 10 and 2 μg/cm^2 of Ru (see inset in Fig. 22.8). These scans are perhaps the best indicator of the intrinsic OER activity, since no substantial Ru dissolution has yet occurred. On the first scan to 1.45 V, the mass activity for the 10 μg/cm^2 Ru overlayer was 4 A/mg and for the 2 μg/cm^2 Ru overlayer was 2 A/mg. This activity is over an order of magnitude higher than the generally reported value of around 0.1 A/mg [36], and as such requires a detailed comparison with data published elsewhere. To the best of our knowledge, the highest activity of metallic Ru for OER has been reported by Miles et al. [18]. In their systematic study of the three metals in this report, Pt, Ir, and Ru, as well as their binary alloys, they found that the activity for OER follows this order: Ru $>$ Ru–Ir alloy ~ Ir $\gg$ Ir–Pt alloy $>$ Ru–Pt alloy $>$ Pt. This chapter is of interest to the present study because of the mostly metallic nature (see Tables 22.1 and 22.2) of our 10 μg/cm^2 deposit and (partly) the extended nature of the Ru and Ir deposited on Pt–NSTF substrate (see Figs. 22.1 and 22.2) which, in principle, could be considered analogous to the flat metal samples used by Miles et al. At 20 mA/cm^2 they reported a potential of 1.46 V (80 °C, in H_2SO_4). At 70 °C, we measured a value of 1.42 V. In comparing the Tafel slopes, 65 mV in this work and 41 mV in Miles et al., the 40-mV difference can be interpreted as the 10 μg/cm^2 Ru overlayer being more active by a factor of 4–10. Further interpretation leading to estimates of the specific activity of the two catalysts requires data of the real surface area of the catalyst on which the OER takes place. Miles et al. report a surface roughness factor of their catalyst of 30.

We can only estimate that the maximum surface area of Ru on Pt–NSTF, if deposited conforming to the underlying platinum on NSTF, is approximately 10 m^2/m^2 (see CVs in Fig. 22.9). On the other hand, as shown in Fig. 22.1f, the Ru layer does not perfectly conform to the Pt surfaces. Within the confine of the uncertainties in the surface area which participates in the OER, it still seems plausible that the inherent activity of the Ru deposits on Pt–NSTF is greater than those measured on bulk Ru metal. Much work will be needed to understand the origin of the high inherent activity of the thin Ru deposits on Pt–NSTF beyond its real surface area, most notably, its interaction with the Pt substrate.

Most of the more recent literature on Ru and Ir and their oxides is related to the areas of proton exchange membrane (PEM) electrolyzers and reversible FC. Due to its instability in the operational voltage range of these devices, metallic Ru has not attracted much interest. Song et al. have shown that in a PEM environment, metallic Ru particles (BET surface area 20.9 m^2/g) are more active than RuO_2, IrO_2, and metallic Ir [37]. At 1.45 V, the mass activity of their Ru is approximately 110 A/g, or 1½ orders of magnitude lower than ours.

From the vast literature on RuO_2, we have chosen the report by Lee et al. because of the claim that they have produced stable 6-nm particles of rutile RuO_2 and IrO_2 [38]. They reported an OER mass activity of 10 A/g for RuO_2 at 1.48 V and a specific activity of 0.01 mA/cm^2. These values, again, are much lower than the mass activity of over 4,000 A/g for 10 $\mu g/cm^2$ Ru on Pt–NSTF. Similarly, the specific activity of Ru on Pt–NSTF, assuming a roughness factor of 10, is 4 mA/cm^2, a factor of 400 higher than that reported by Lee et al. These comparisons, on the one hand, establish the exceptional activities of minute amounts of Ru catalyst for OER, while, on the other, corroborate the assumption in Miles et al. that the oxide film formed in situ on metallic Ru has the highest inherent activity [18].

In view of the previous statement that oxide films formed on metallic Ru are the most inherently active material, we can explain the fact that the 2 $\mu g/cm^2$ overlayer of Ru has a mass activity only half that of the 10 $\mu g/cm^2$ Ru overlayer. Namely, the XPS data indicated that much of the Ru in the thinner 2 $\mu g/cm^2$ overlayer is in the oxidized state, and hence, there is much less metallic Ru, only 0.5 $\mu g/cm^2$, on which oxide film can be formed (see Table 22.1).

Finally, the finding that the Ru overcoating achieves an OER current density of 1 mA/cm^2 at 1.37 V qualifies this material as one of the most active OER catalysts. According to Trasatti, oxygen evolution scarcely starts below 1.4 V [19]. The Tafel slope for the higher loading (65 mV) lies in the middle of the usual range of 30–120 mV for OER as reported in the literature, while the 130 mV Tafel slope for the lower Ru loading is slightly above the upper end of that range. The Tafel slope for Ir, 170 mV, could be interpreted as being due to a "double barrier," consisting of the OER and formation of the oxide at the Ir metal–oxide interface [19].

The activity of *Ir at 10* $\mu g/cm^2$ loading can be more readily compared with published data due to the wider use of Ir for water electrolysis in PEM environment. Because their study was done on Ir metal, we start the comparison with Miles et al. [18]. At 20 mA/cm^2, they report an electrode potential of 1.61 V vs. our Ir sample at 1.48 V. One might try to explain this difference strictly in terms of the higher surface area of our catalyst. To comply with the Tafel slope between 85 mV, as reported by Miles et al., and 170 mV, as determined for Ir on Pt–NSTF, a roughness factor of approximately 10 is required for our catalyst. However, since Miles et al. do not provide a roughness factor for their Ir catalyst, a comparison of the inherent activity of the two catalysts cannot be made.

Another comparison can be made with the OER activity of Ir dispersed on TiC [39]. TiC is a stable substitute for traditionally used carbon supports. Based on their data, the derived mass activity for 0.02 mg/cm^2 of Ir on TiC at 1.55 V is 615 A/g as compared to our value at 3,900 A/g Ir.

The comparison of our catalyst with the stable 6-nm nanoparticles of rutile-phase IrO_2 [38], which was reported as having a mass activity of 3 A/g of Ir oxide (~3.5 A/g Ir metal), shows that the mass activity of our Ir at the same voltage is higher by a factor of ~570.

An interesting comparison can also be made with sputter-deposited IrOx. After equilibration for 60 s at 1.5 V, we calculated a mass activity of 1,200 A/g. Obtained at 70 °C, this value for the Ir overlayer on Pt–NSTF compares favorably with the sputter-deposited IrOx with a 0.2 mg/cm^2 Ir loading and mass activity of approximately 240 A/g at 60 °C and 640 A/g at 80 °C [40]. At 1.55 V, we have obtained a mass activity of 3,900 A/g, which, again, compares favorably with an earlier reported value of 1,500 A/g at 80 °C [41].

On a fundamental level, these results demonstrate the behavior of extremely small amounts of Ir and Ru at very positive potentials in a PEM environment. The nature of these extraordinary OER activities needs further elucidation both from a practical and fundamental point of view. The thin film morphology could be one of the main factors affecting activity, first of all through the favorable surface to mass ratio and further due to the discontinuous nature of the thinner coatings. Finally, the observed interactions with the substrate and the NSTF perylene core could have an effect both on the activity and stability of the OER catalyst.

On a practical level, the initial evaluation of Ru and Ir overlayers provided a direction for the future development of the OER catalysts for fuel cell applications. One would like to use Ir both for its stability at high positive potentials and lack of inhibition of the ORR. Adding a small amount of Ru will probably improve the OER activity of Ir, while the appropriate amount of Ir will in turn protect Ru from extremely fast dissolution. In optimizing the Ir to Ru ratio, one has to bear in mind the short time duration of the transient conditions, typically 1–3 s for SU/SD and 15 s for cell reversal [6].

22.4 Combined Ru–Ir Catalysts

As pointed out in the introduction, the activity for OER is a necessary property of the added/modified existing anode or cathode FC catalyst. However, the high OER activity, such as exhibited by the added Ru on Pt, must be able to withstand numerous high positive potential excursions during the lifetime of a FC stack in

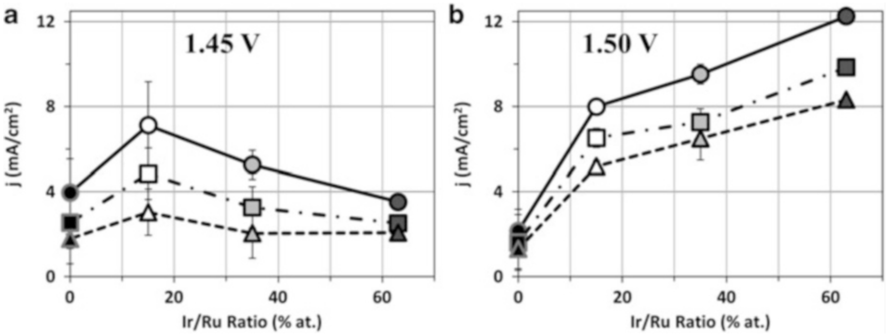

Fig. 22.12 OER currents at the end of the three consecutive potential scans to 1.45 V (**a**) and 1.5 V (**b**) of sputter-deposited Ir on Ru with total amount of the two elements at 2 μg/cm^2. Order of lines from the top: 1st, 2nd, 3rd potential scans. Test procedure and conditions same as in Fig. 22.8

automotive applications. The addition of Ir as a path to achieve this goal has exhibited some interesting properties. The stabilization effect by sputter-deposited Ir on Ru is presented in Fig. 22.12. The total amount of the two elements was kept constant at 2 μg/cm^2. First, it is interesting to observe that the OER activity during the first potential sweep to 1.45 V was lower than that for pure Ru only when ¾ (1.5 μg/cm^2) of the Ru was substituted by Ir. At ½ and ¼ Ru substituted by Ir, the OER activity was expressly higher than for pure Ru. While this observation may be explained by greater Ru retention by the time the electrode reaches 1.45 V, it is plausible that a synergistic effect exists between Ru and Ir. From a utilitarian point of view, by the third excursion to 1.45 V, the catalyst with the highest Ir content retains the most activity, ~57 %, while the others, including pure Ru, retain only 39–45 %. The retention of the OER activity of the high content Ir catalysts becomes more obvious when the upper voltage limits is increased by 0.05 V, from 1.45 V to 1.5 V. At 1.5 V, the OER activity behaves as expected, namely, the highest maintained OER activity arose from the catalyst with the highest Ir loading (75 %). The OER activity retention is also the highest, 68 % from cycle #1 to cycle #3. At 1.5 V, one has to consider that Ir has more OER activity on its own; therefore, it is difficult to speculate on the contribution of the retained Ru catalyst towards the total OER current.

Kötz and Stucki studied the OER activity and stability of 200-nm-thick Ru–Ir metallic alloys sputter-deposited on glass [42]. In sulfuric acid, they found that 14 % at. Ir already had produced a substantial stabilization effect on Ru which is similar to our data for 15 % at. Ir (Fig. 22.12). Based on XPS measurements before and after the electrochemical testing, they concluded that the stabilization is due to the formation of a protective oxide layer with increased Ir content. However, unlike our findings, they saw a steady decrease in the OER current with an increase of Ir content. In addition, our Ru–Ir catalyst, estimated to be only 2 nm thick, has at least an order of magnitude higher OER activity. This obviously points to differences in the structure and the morphology between the two films which could be due to the preparation procedures as well as the substrates.

We can also compare our measurements on Pt–NSTF-supported Ru–Ir with the work of Fuentes et al. using metallic Ru–Ir deposited on anatase TiO_2 as a support [43]. Tested in acid aqueous environment, they reported a mass activity of 100 A/g Ru–Ir. As presented in Fig. 22.12, our 2 μg/cm^2 Ru–Ir at the same potential of 1.5 V has a mass activity of between 5,600 and 6,200 A/g.

Qualitatively, the behavior of our Ru–Ir is also in agreement with the behavior of thermally produced mixed RuO_2 and IrO_2 tested in aqueous systems (Matos et al. [44]). The range of the Ru:Ir ratios for the best activity (70 % at. Ru in Matos et al.) and the best stability (50–90 % at. Ir) is very similar. However, the oxides of Matos et al. exhibit huge differences in inherent activity when compared with our metal catalysts. At 1 mA/cm^2, a current density where Ru is presumed stable and the IR corrections are negligible, the electrode potential range of all the compositions containing Ru (excluding pure IrO_2) in Matos et al. are within 1.42 and 1.47 V. At the same current density, our samples are in the range of 1.38–1.40 V. What makes this difference significant is the fact that the Matos et al.' samples are 2 μm thick, with a loading of ~2 mg/cm^2, which is a factor of 1,000 more than ours. If evenly distributed over the real surface area of the Pt–NSTF substrate, a Ru + Ir loading of 2 μg/cm^2 would result in a layer thickness of less than 2 nm.

The "thickness" consideration can shed some light on the enhanced catalytic effect of the mixed samples with 1.5 and 1.0 μg/cm^2 of Ru over the sample with pure 2 μg/cm^2 of Ru. Mattos et al. ascribed the enhanced activity of the mixed Ru + Ir samples to "a combination of catalytic and roughness effect." In the case of our samples, the catalyst is so thin that we cannot speak of any kind of layer and consequently we can disregard the roughness factor as a contributor to the enhanced activity. This leaves the enhanced inherent activity as the predominant reason for the increased activity.

22.5 Ir–Ru Catalysts for Practical Applications

While the addition of Ir improved substantially the retained OER activity, for numerous SU/SD and CR events, a much more stable behavior is still required. The trend of higher stability with increasing Ir content (see Fig. 22.12) indicates that a higher Ir:Ru ratio than 63:37 (% at.) is needed. As pointed out in Matos et al., 90 % at. Ir exhibits the highest stability [44]. For that reason, the choice was made to go with an Ir:Ru atomic ratio of 90:10 for practical applications involving SU/SD and CR testing. In order to evaluate the effect of loading on OER activity and stability, different loadings of Ir–Ru catalyst between 1 and 10 μg/cm^2 were deposited on NSTF decals with a fixed Pt loading. The MEAs with different OER catalyst loadings were evaluated via generic, electrochemical test procedures mimicking the real events experienced by a fuel cell during SU/SD or CR.

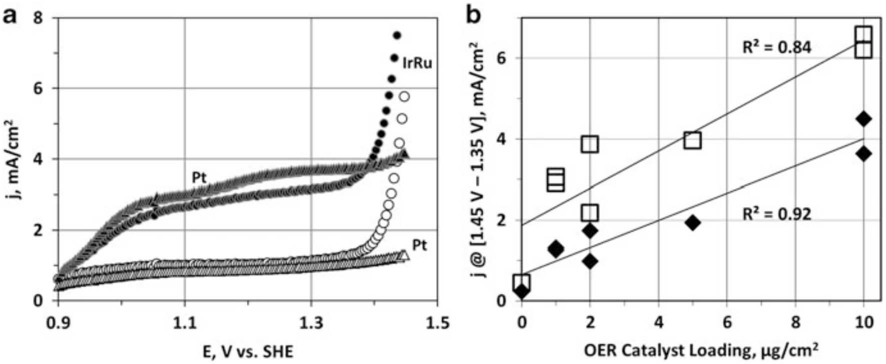

Fig. 22.13 Characteristic graphs during the evaluation of OER catalyst in MEA by electrochemical test mimicking the SU/SD. (**a**) Current responses from 0.9 to 1.45 V for 10 μg/cm^2 of Ir–Ru on Pt–NSTF and for the Pt–NSTF substrate, 250 mV/s. *Two upper curves*: the first cycle after the catalyst was held at 0.7 V, *two lower curves*: at cycle 50. (**b**) OER peak current dependence on the Ir–Ru loading at pulse1 (*open square*) and pulse 50 (*solid diamond*), current values at 1.45 V

22.5.1 Start-up/Shutdown

Start-up/shutdown tests consisted of numerous triangular potential ramps from the typical FC OCV (~0.9 V) to an upper voltage between 1.4 and 1.6 V. To mimic the depletion of oxygen from the anode, the potential was held at the upper limit until a fixed amount of charge was passed, estimated to be 5–10 mC/cm^2. In order to assure that the OER-added catalyst maintains sufficient activity, an additional requirement was imposed such that the test was terminated if the current during the hold fell below a certain level, initially set at 1 mA/cm^2. At regular intervals, the electrode potential was brought down to 0.65–0.7 V, which is the usual cathode potential during normal FC operation. During this period, the oxides of Pt and of the OER catalysts are reduced. After every 1,000 cycles, the Pt surface area was evaluated via cyclic voltammetry in the H_{upd} region.

Typical results illustrating the behavior of the OER catalyst and the final outcome of the testing after 10,000 start-up equivalent cycles are presented in Figs. 22.13 and 22.14. In Fig. 22.13a, typical current responses from 0.9 to 1.45 V are presented for 10 μg/cm^2 of Ir–Ru on Pt–NSTF and for the Pt–NSTF substrate. The two upper curves were recorded during the first cycle after the catalyst was held at 0.7 V, while the two lower were recorded at cycle 50. In both cases the current traces run almost identical to each other until the potential reaches ~1.35 V, at which point the current for the catalyst with the added Ir–Ru takes off due to the onset of oxygen evolution. The higher current before the OER onset potential in the cycle 1 curves is due to the oxidation of platinum which immediately before the potential ramp was at 0.7 V and therefore reduced. During subsequent cycles, the potential does not drop below 0.9 V, the Pt oxide does not

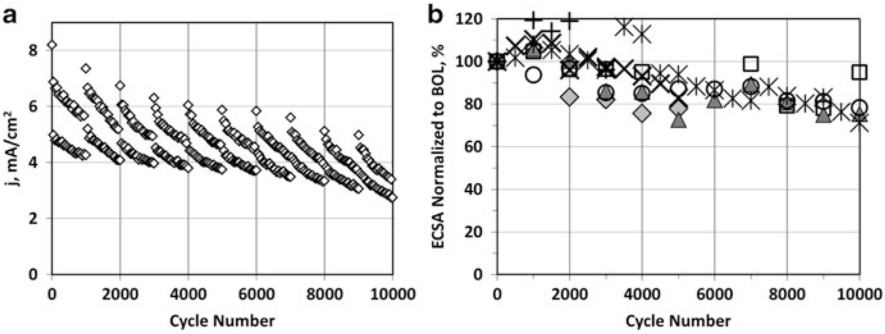

Fig. 22.14 (**a**) Currents at 1.45 V of the characteristic cycles (every 50 and every 51) throughout the 10,000 cycles. (**b**) Pt surface at every 1,000 cycles for six MEAs, two with 2 μg/cm^2 and four with 10 μg/cm^2 of Ir–Ru. Test conditions same as in Fig. 22.8. Electrode potentials expressed vs. SHE

get reduced, and consequently the current on the following upward potential ramps to 1.45 V is practically zero.

The difference from the onset of the OER current at 1.35 V and at the peak voltage of 1.45 V is a good measure of the activity of the OER catalyst. In Fig. 22.13b the dependence of this current difference on the amount of the Ir–Ru catalyst is presented for the two characteristic cycles, the one immediately after (reduced surface) and the other just before (oxidized surface) the catalyst is held at 0.7 V. A linear relationship is observed in both cases. However, the linearity has a slope of only 1/3, which suggests that only 1/3 of the deposited Ir–Ru contributes to the electrochemically active surface area.

In Fig. 22.14a, the changes in the currents at 1.45 V of the characteristic cycles throughout the 10,000 cycles are presented. The first observation is that the activity of the OER catalysts steadily decays at the rate of 3 % per 1,000 cycles. The second is that the OER currents form three distinctive "bands." The upper band contains only ten points, the first point of each of the ten scans immediately following the evaluation of the surface area. During these measurements the electrode potential is close to 0 V, and therefore, the electrode surface is fully reduced, i.e., regenerated. The middle band contains the partially regenerated surfaces, after the voltage is dropped to 0.7 V (see the example in Fig. 22.13b). There are 20 of these points per 1,000 cycles. The third band represents the currents recorded on the most oxidized catalyst surface, i.e., immediately before the voltage is dropped to 0.7 V.

Finally, the effectiveness of the OER catalyst to slow down Pt dissolution is demonstrated in Fig. 22.14b. There, the changes in Pt surface area, measured at every 1,000 cycles for six different MEAs, two with 2 μg/cm^2 and four with 10 μg/cm^2 of Ir–Ru, are presented. On average, the rate of the surface area Pt loss was at only 2 % per 1,000 cycles, which is acceptable for the lifetime of automotive stacks. One obvious reason for the Pt retention is the ability of the OER catalyst to keep the voltage down. However, an additional effect, applicable in an MEA environment only, was recently offered as a possible explanation of the suppressed carbon

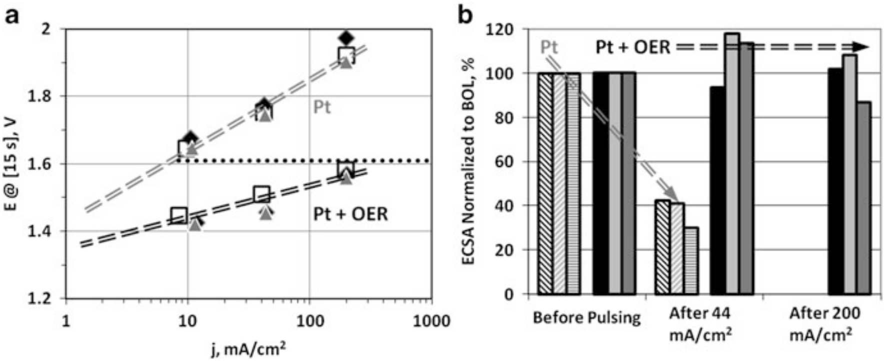

Fig. 22.15 The impact of Pt loading on the OER polarization. (**a**) *Upper line*: Pt–NSTF substrate with 0.05, 0.10 and 0.15 mg/cm^2 Pt. *Lower line*: same Pt–NSTF substrates with 10 μg/cm^2 of Ir–Ru voltage recorded 15 s after constant current pulse from −1 mA/cm^2 to 12, 44, and 200 mA/cm^2. (**b**) Relative electrochemical surface area changes of Pt with (*solid bars*) and without (*patterned bars*) the OER catalyst before any current pulses, after 20 × 44 mA/cm^2 and after 200 × 200 mA/cm^2 (Ir–Ru on Pt–NSTF only)

corrosion in the presence of IrO_2 [45]. Namely, during the oxidation of water, the local environment around the catalytic sites gets deprived of water molecules. Since water is a reactant in the corrosion process, water deprivation will have a positive effect in the corrosion retardation. Water certainly plays a role in the dissolution of platinum and this could be an additional benefit of the presence of the OER catalyst. Nonetheless, as we will see in the next subsection, high positive potentials are the main cause for the degradation of Pt.

22.5.2 Cell Reversal

As we pointed out in the introduction, cell reversal requires the OER to proceed at much higher current densities. In addition, the OER proceeds at the anode during CR, where the Pt loading is much lower relative to the cathode. Thus, the impact of Pt loading, with and without the added Ir–Ru catalyst, on the peak anode voltage was explored, as presented in Fig. 22.15. The most obvious observation drawn from Fig. 22.15a is the large difference in the polarization between the bare Pt and the Ir–Ru overcoated Pt. All the data points for bare Pt are above 1.6 V, while, even for the highest current density, the Ir–Ru samples are below that value. As we will see, this demarcation can be related to the stability of the catalysts. Secondly, within the reproducibility of the tested MEAs, the Pt loading does not appear to have much of an impact on anode potential. Further, the Tafel slope for bare Pt is ~200 mV while for Ir–Ru it is ~100 mV, both in line with literature data and the data presented previously in Sect. 22.3.2 for the behavior of Ru and Ir overlayers on Pt–NSTF. The impact of the current pulses on the Pt surface area is rather striking (Fig. 22.15b).

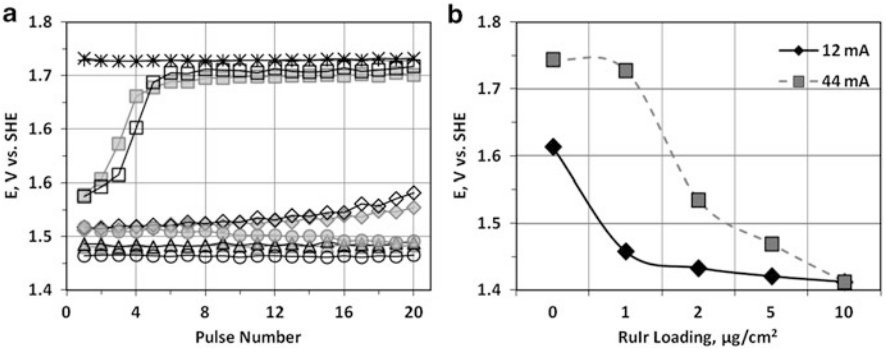

Fig. 22.16 The impact of Ir–Ru loading on the OER activity and the catalyst stability. Pt–NSTF loading 0.05 mg/cm^2, Ir–Ru loading 1–10 μg/cm^2. (**a**) End voltage after 30 s at 44 mA/cm^2; two MEAs tested for each Ir–Ru loading. The *lines* follow the Ir–Ru loading, uncoated Pt–NSTF at the *top* and 10 μg/cm^2 at the *bottom*. (**b**) The end voltage at 20th current pulse at 12 mA/cm^2 (*upper curve*) and 44 mA/cm^2 (*lower curve*)

After the 44 mA/cm^2, the surface area of Pt–NSTF is less than half of the original value, while the samples with overcoated Ir–Ru hardly lost any Pt surface area even after 200 pulses at 200 mA/cm^2.

In Fig. 22.16, the impact of Ir–Ru loading in the range of 0–10 μg/cm^2 is presented. The purpose of the test is to determine the minimum amount of Ir–Ru that will satisfy the cell reversal requirements. In addition, some interesting observations about the OER activity and the stability of Ir–Ru at high current densities can also be made. Similar to what was presented in Fig. 22.13b, for low current densities, the OER potential is higher at lower Ir–Ru loadings, the highest being on uncoated Pt–NSTF. Even more informative are the findings about the durability of the Ir–Ru. At the smallest loading, 1 μg/cm^2, the potential rises rapidly with the repeating pulses and, at pulse #7, approaches the polarization of Pt. This can be interpreted as a clear indication of the dissolution of the catalyst. Even after dissolution occurs, the 1 μg/cm^2 Ir–Ru samples still level off at a potential ~20 mV lower than pure Pt. In that aspect, the effect of the OER coating is similar to the effect of pure Ru on Pt–NSTF pointed out in Fig. 22.8. The summary of the loading effect is presented in Fig. 22.16b, where, except for the highest Ir–Ru loading, 10 μg/cm^2, all OER catalyst loadings showed some deterioration in the OER activity after testing, which was more pronounced with decreasing Ir–Ru loading.

The requirement for practical transportation applications is that the OER catalysts endure 200 current pulses of 200 mA/cm^2, with a pulse duration of 15 s each, without reaching a cell voltage of 2 V. To mimic the normal FC operation, the potential between the 200 mA/cm^2 pulses was brought down to 0 V for 1 min. Practically all samples with 10 μg/cm^2 of Ir–Ru fulfilled this requirement with the voltage at the end of the 200th pulse at ~1.6 V. In order to further pursue the limits of the durability of the Ir–Ru, following the 200 pulses, a constant current of 200 mA/cm^2 was applied until the voltage reached 2 V. In Fig. 22.17, the cell voltage vs. time is presented for four replicates of the nominally same MEA.

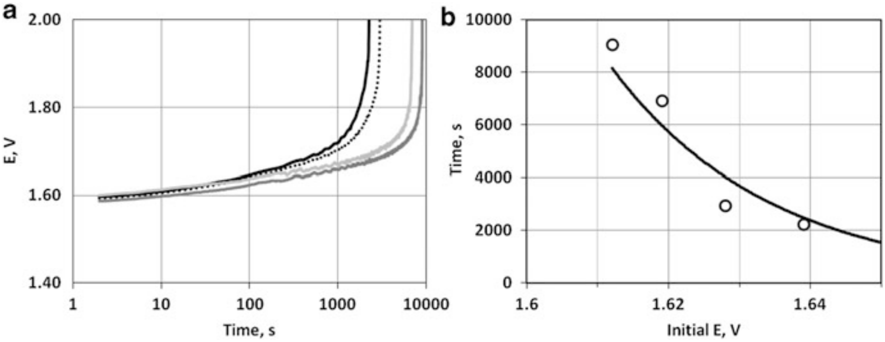

Fig. 22.17 (**a**) Time to failure (2 V) at constant current of 200 mA/cm^2 after the 200th 15 s pulse of the same current density. Four MEA replicates of the nominally same 10 μg/cm2 of Ir–Ru presented. (**b**) Time to failure as function of the initial voltage at beginning of test

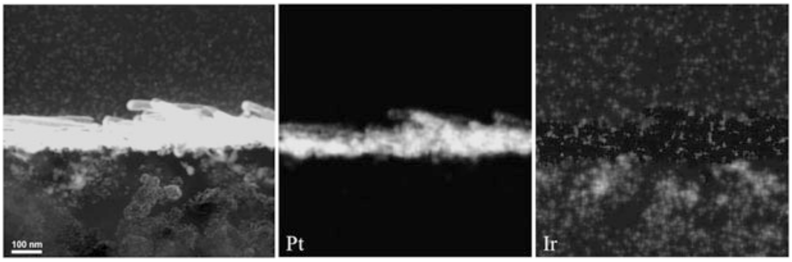

Fig. 22.18 HAADF-STEM image with EDS Pt and Ir maps of NSTF electrode subjected to cell reversal conditions. EDS mapping showed that significant amounts of Ir precipitated within the MPL. Agglomerates of Ir/Pt particles were found in the membrane, while pure Ir particles were found in the MPL [47]

The starting voltage of these replicates is within a narrow range of ~40 mV. Yet, as is presented in the inset, the time to reach 2 V varies by a factor of five, between 1,800 and 9,000 s. The variations in the last phase, the end-of-life testing, exacerbates all the imperfections and variations in all the stages of the catalyst testing, from the catalyst fabrication, through the MEA assembly and through the FC test conditions. Note that the catalyst durability is inversely related to the starting voltage, an interesting observation that can serve as an additional criterion to predict the catalyst durability.

From a fundamental point of view, a more interesting event occurs around 1.75 V. It appears that this is the voltage limit of the Ir–Ru catalysts, since beyond this voltage a rapid increase in cell voltage takes place. STEM studies were performed on the end-of-life MEAs for each loading and indicated that little to no Ru or Ir remains on the whisker surfaces once the critical 2 V limit was reached. Thus, dissolution is the key deactivation mechanism. Some Ir was found with Pt in the membrane near the NSTF electrodes, while most was present within the MPL as small, pure metallic nanoparticles (Fig. 22.18).

While outside the scope of this chapter, we would like to complete this review by pointing out that real, rather than electrochemical, testing of the OER-modified catalyst was also carried out. Some formulations of the practical catalyst were extensively evaluated by a major stack developer [3, 46]. The evaluation was done in subscale as well in a full-sized architecture. The extremely favorable outcome of the protective properties of the Ir–Ru on Pt–NSTF for both CR and SU/SD tests confirmed the laboratory testing results.

22.6 Conclusions

Minute amounts of Ru and Ir deposited on Pt–NSTF have shown surprisingly high activity towards OER and can be utilized for controlling electrode potentials during transient events such as start-up/shutdown and cell reversal. STEM–EDS and XPS complemented electrochemical tests in characterizing the fundamental nature of these materials and their potential impact on fuel cell technology.

The large activity of Ru was successfully coupled with the superior stability of Ir to create an OER overcoating able to withstand the extreme conditions experienced during SU/SD and CR while at the same time promoting Pt stability by reducing the overall potentials seen by the electrodes. Careful XPS studies showed that the OER catalysts become increasingly metallic with higher loadings. Interesting interactions between Ru and perylene were uncovered and will be the topic of future investigations. Evaluation of the Pt surface area coupled with STEM imaging and EDS mapping showed that the OER catalysts could be successfully integrated without impacting the ORR activity. STEM imaging also revealed that OER overlayers took on more of a discontinuous film-like structure, which may explain why the measured activities were more similar to those measured on bulk thin films than nanoparticles.

Future efforts should seek to answer several key questions, the most important of which is why the intrinsic OER activity of Ru and Ru–Ir overcoated Pt–NSTF is so high and remains enhanced even after complete dissolution.

References

1. Yu PT, Kocha S, Paine L, Gu W, Wagner FT (2004) The effects of air purge on the degradation of PEM fuel cells during startup and shutdown procedures. In: AIChE annual meeting, New Orleans, LA
2. Reiser CA, Bregoli L, Patterson TW, Yi JS, Yang JD, Perry ML, Jarvi TD (2005) A reverse-current decay mechanism for fuel cells. Electrochem Solid State Lett 8(6):A273–A276
3. Gu W, Carter RN, Yu PT, Gasteiger HA (2007) Start/stop and local H_2 starvation mechanisms of carbon corrosion: model vs. experiment. ECS Trans 11(1):963–973
4. Atanasoski RT (2011) DOE Hydrogen Program Review. Washington, DC. Available online at: http://www.hydrogen.energy.gov/pdfs/review11/fc006_atanasoski_2011_o.pdf

5. Atanasoski RT (2011) DOE Annual Progress Report. Washington, DC. Available online at: http://www.hydrogen.energy.gov/pdfs/progress11/v_d_3_atanasoski_2011.pdf
6. Ohma A, Shinohara K, Iiyama A, Yoshida T, Daimaru A (2011) Membrane and catalyst performance targets for automotive fuel cells by FCCJ membrane, catalyst, MEA WG. ECS Trans 41(1):775–784
7. Yu Y, Li H, Wang HJ, Yuana XZ, Wang GJ, Pan M (2012) A review on performance degradation of proton exchange membrane fuel cells during startup and shutdown processes: causes, consequences, and mitigation strategies. J Power Sources 205:10–23
8. Ye S (2008) Reversal-tolerant catalyst layers. In: Zhang J (ed) PEM fuel cell electrocatalysts and catalyst layers: fundamentals and application. Springer, London
9. Atanasoski RT (2009) Kickoff meeting for new DOE fuel cell projects. Washington, DC. Available online at: http://www1.eere.energy.gov/hydrogenandfuelcells/pdfs/atanasoski_kickoff.pdf
10. Atanasoski RT (2010) DOE Hydrogen Program Review. Washington, DC. Available online at: http://www.hydrogen.energy.gov/pdfs/review10/fc006_atanasoski_2010_o_web.pdf
11. Atanasoski RT (2010) DOE annual progress report. Available online at: http://www.hydrogen.energy.gov/pdfs/progress10/v_e_6_atanasoski.pdf
12. Debe MK (2012) Nanostructured thin film electrocatalysts for PEM fuel cells – a tutorial on the fundamental characteristics and practical properties of NSTF catalysts. ECS Trans 45(2): 47–68
13. Debe MK, Hendricks SM, Schmoeckel AK, Atanasoski RT, Vernstrom GD, Haugen GM (2006) Durability aspects of nanostructured thin film catalysts for PEM fuel cells. ECS Trans 1(8):51–66
14. Debe MK, Schmoeckel AK, Vernstrom GD, Atanasoski RT (2006) High voltage stability of nanostructured thin film catalysts for PEM fuel cells. J Power Sources 161(2):1002–1011
15. Trasatti S (1991) Physical electrochemistry of ceramic oxides. Electrochim Acta 36(2): 225–241
16. Debe MK (2003) Novel catalysts, catalyst supports and catalyst coated membrane methods. In: Vielstich W, Lamm A, Gasteiger HA (eds) Handbook of fuel cells – fundamentals, technology and applications. Wiley, Weinheim
17. Atanasoski RT, Atanasoska LL, Cullen DA, Haugen GM, More KL, Vernstrom GD (2012) Fuel cells catalyst for start-up and shutdown conditions: electrochemical, XPS, and STEM evaluation of sputter-deposited Ru, Ir, and Ti on Pt-coated nanostructured thin film supports. Electrocatalysis. Electrocatal 3:284–297
18. Miles MH, Klaus EA, Gunn BP, Locker J, Serafin WE, Srinivasan S (1978) The oxygen evolution reaction on platinum, iridium, ruthenium and their alloys at 80°C in acid solutions. Electrochim Acta 23(6):521–526
19. Trasatti S (2009) Oxygen evolution. In: Garche J, Dyer C, Moseley P, Ogumi Z, Rand D, Scrosati B (eds) Encyclopedia of electrochemical power sources, vol 1. Elsevier, Amsterdam
20. http://www.hydrogen.energy.gov/library.html
21. Wu G, More KL, Johnston CM, Zelenay P (2011) High-performance electrocatalysts for oxygen reduction derived from polyaniline, iron, and cobalt. Science 332(6028):443–447
22. Wang C, Chi MF, Li DG, van der Vliet D, Wang GF, Lin QY, Mitchell JF, More KL, Markovic NM, Stamekovic VR (2011) Synthesis of homogeneous Pt-bimetallic nanoparticles as highly efficient electrocatalysts. ACS Catal 1(10):1355–1359
23. Chen S, Sheng W, Yabuuchi N, Ferreira PJ, Allard LF, Shao-Horn Y (2009) Origin of oxygen reduction reaction activity on "Pt_3Co" nanoparticles: atomically resolved chemical compositions and structures. J Phys Chem C 113(3):1109–1125
24. Kongkanand A, Liu Z, Dutta I, Wagner FT (2011) Electrochemical and microstructural evaluation of aged nanostructured thin film fuel cell electrocatalyst. J Electrochem Soc 158(11): B1286–B1291
25. Cullen DA, More KL, Reeves KS, Vernstrom GD, Atanasoska LL, Haugen GM, Atanasoski RT (2011) Characterization of durable nanostructured thin film catalysts tested under transient conditions using analytical aberration-corrected electron microscopy. ECS Trans 41(1): 1099–1103

26. Atanasoska LL, Vernstrom GD, Haugen GM, Atanasoski RT (2011) Catalyst durability for fuel cells under start-up and shutdown conditions: evaluation of Ru and Ir sputter-deposited films on platinum in PEM environment. ECS Trans 41(1):785–795
27. Atanasoska LL, O'Grady WE, Atanasoski RT, Pollak FH (1988) The surface structure of RuO_2: a LEED, auger and XPS study of the (110) and (100) faces. Surf Sci 202:142–166
28. Atanasoska LL, Atanasoski RT, Pollak FH, O'Grady WE (1990) Single crystal RuO_2/Ti and RuO_2/TiO_2 interface: LEED, auger and XPS study. Surf Sci 230:95–112
29. Atanasoska LL, Anderson SG, Meyer HM, Lin Z, Weaver JH (1987) Aluminum/polyimide interface formation: an X-ray photoelectron spectroscopy study of selective chemical bonding. J Vac Sci Technol A 5(6):3325–3333
30. Atanasoska LL, Meyer HM, Anderson SG, Weaver JH (1988) Semiconductor/polyimide interface formation: an X-ray photoelectron spectroscopy study of germanium chemical bonding. J Vac Sci Technol A 6(4):2175–2181
31. Atanasoska LL, Anderson SG, Meyer HM, Lin Z, Weaver JH (1990) XPS study of chemical bonding at polyimide interfaces with metal and semiconductors overlayers. Vacuum 40:85–90
32. Atanasoska LL, Cullen DA, Hester A, Atanasoski RT (2012) XPS and STEM of the interface formation between ultra-thin Ru, Ir and Pt layers and perylene red catalyst support whiskers. In: PRiME 2012, Honolulu, HI
33. Atanasoska LL, Atanasoski R, Trasatti S (1990) XPS and AES study of mixed layers of IrO_2 and RuO_2. Vacuum 40:91–94
34. Atanasoska LL, Gupta P, Deng C, Thompson J (2009) XPS, AES, and electrochemical study of iridium oxide coating materials for cardiovascular stent application. ECS Trans 16(38):37–48
35. Kotz R, Stucki S, Scherson D, Kolb DM (1984) In-situ identification of RuO4 as the corrosion product during oxygen evolution on ruthenium in acid media. J Electroanal Chem 172(1): 211–219
36. Forgie R, Bugosh G, Neyerlin KC, Liu Z, Strasser P (2010) Bimetallic Ru electrocatalysts for the OER and electrolytic water splitting in acidic media. Electrochem Solid State Lett 13(4): D36–D39
37. Song SD, Zhang HM, Ma XP, Shao ZG, Baker RT, Yi BL (2008) Electrochemical investigation of electrocatalysts for the oxygen evolution reaction in PEM water electrolyzers. Int J Hydrogen Energy 33(19):4955–4961
38. Lee Y, Suntivich J, May KJ, Perry EE, Shao-Horn Y (2012) Synthesis and activities of rutile IrO2 and RuO2 nanoparticles for oxygen evolution in acid and alkaline solutions. J Phys Chem Lett 3(3):399–404
39. Ma LR, Sui S, Zhai YC (2008) Preparation and characterization of Ir/TiC catalyst for oxygen evolution. J Power Sources 177(2):470–477
40. Slavcheva E, Radev I, Bliznakov S, Topalov G, Andreev P, Budevski E (2007) Sputtered iridium oxide films as electrocatalysts for water splitting via PEM electrolysis. Electrochim Acta 52(12):3889–3894
41. Slavcheva E, Schnackenberg U, Mokwa W (2006) Deposition of sputtered iridium oxide – influence of oxygen flow in the reactor on the film properties. Appl Surf Sci 253(4):1964–1969
42. Kotz R, Stucki S (1985) Oxygen evolution on ruthenium-iridium alloys. J Electrochem Soc 132(1):103–107
43. Fuentes RE, Farell J, Weidner JW (2011) Multimetallic electrocatalysts of Pt, Ru, and Ir supported on anatase and rutile TiO2 for oxygen evolution in an acid environment. Electrochem Solid State Lett 14(3):E5–E7
44. Mattos-Costa FI, de Lima-Neto P, Machadoa SAS, Avaca LA (1998) Characterization of surfaces modified by sol–gel derived RuxIr11-x O_2 coatings for oxygen evolution in acid medium. Electrochim Acta 44(8):1515–1523
45. Jang SE, Kim H (2010) Effect of water electrolysis catalysts on carbon corrosion in polymer electrolyte membrane fuel cells. J Am Chem Soc 132(42):14700–14701
46. Atanasoski RT (2012) DOE Hydrogen Program Review. Washington, DC. Available online at: http://www.hydrogen.energy.gov/pdfs/review12/fc006_atanasoski_2012_o.pdf
47. Cullen DA, More KL, Atanasoski RT (2012) Towards quantifying catalyst losses from fuel cell electrodes: an electron microscopy study. Microsc Microanal 17(S2):64544

Chapter 23
Metal Carbides in Fuel Cell Cathode

**Belabbes Merzougui, Ahsanulhaq Qurashi, Oki Muraza,
and Mohammad Qamar**

Abstract Moderate-temperature fuel cells are clean power generators for both stationary and mobile applications. In particular, polymer electrolyte membrane fuel cells (PEMCs) have attracted much attention due to their high gravimetric and volumetric power densities. However, due to their acidic environment, platinum-based nanocatalysts are the only feasible electrocatalyts for such systems. High cost and limited resources of this precious metal hinder the commercialization of PEMFCs. As a result, tremendous efforts are being exerted to either reduce Pt loading or substitute Pt metal with other non-noble metals. In this context, metal carbides have been extensively investigated due to their bifunctional mechanism as a catalyst as well as a catalyst support. Hence, the aim of using metal carbides is to replace carbon support since carbon suffers from corrosion problem and at the same time to reduce a substantial amount of Pt in fuel cell cathode. In this chapter, we have given an overview on metal carbides and their benefits as catalyst support for fuel cell cathode reactions.

B. Merzougui (✉)
Center of Excellence in Nanotechnology (CENT) & Department of Chemistry, King Fahd University of Petroleum and Minerals (KFUPM), Dhahran 31261, Saudi Arabia
e-mail: Belabbes@kfupm.edu.sa

A. Qurashi
Center of Excellence in Nanotechnology (CENT) and Department of Chemistry, King Fahd University of Petroleum and Minerals (KFUPM), Dhahran 31261, Saudi Arabia

O. Muraza
Center of Excellence in Nanotechnology (CENT) and Department of Chemical Engineering, King Fahd University of Petroleum and Minerals (KFUPM), Dhahran 31261, Saudi Arabia

M. Qamar
Center of Excellence in Nanotechnology (CENT), King Fahd University of Petroleum and Minerals (KFUPM), Dhahran 31261, Saudi Arabia

M. Shao (ed.), *Electrocatalysis in Fuel Cells*, Lecture Notes in Energy 9,
DOI 10.1007/978-1-4471-4911-8_23, © Springer-Verlag London 2013

23.1 Introduction

The growing pressure on clean fuels and reduction in emission of carbon dioxide has rendered fuel cell technology as one of the alternative green power devices for next generation of cars. However, fuel cell technology is still encountering a number of issues which are related in particular to cost and durability. In the moderate-temperature fuel cells, such PEMFCs and phosphoric acid fuel cells (PAFCs), operating below 200 °C, the state-of-the-art catalyst is generally based on Pt and Pt alloys [1]. Even though these systems use noble metals, they still suffer from performance loss during the course of operation as a result of catalyst degradation and, in particular, corrosion of carbon supports [2–5]. Carbon is well known by its unique properties, such as conductivity, porosity, water and gas manageability, and the ease to disperse in a sort of ink for thin layer coatings of catalyst, either on gas diffusion electrode or directly onto membranes. Unfortunately, carbon suffers dramatically from corrosion leading to an irreversible loss in electrode performance, notably at the cathode side of fuel cells. Kinetically, corrosion rate of carbon black at potentials lower than 0.9 V/RHE is reasonably slow at temperature between 60 and 80 °C. However, long-term operations can cause a decrease in carbon content in the catalyst layers [3]. Moreover, during start–stop cycling and fuel starvation, the cathode can experience high potential excursion reaching 1.5 V/RHE [6–8]. Under these conditions, severe carbon corrosion causes agglomeration of catalyst particles and an increase in ohmic resistance in catalyst layer due to collapse of the porous structure. Hence, stable catalyst and support materials are strongly needed to improve the durability of PEMFCs cathode [4].

On the other hand, according to Department of Energy (DOE), cost of catalyst (Pt) presents over 1/3 of the total cost of a fuel cell stack. Many approaches have been seriously considered in order to reduce the catalyst cost, especially by reducing Pt loadings on both electrodes in fuel cell systems, namely, using metal carbides [9], metal oxide–CNT composites [10], metal phosphides [11], transition metal–carbon composites [12], metal chalcogenides [13], Pt monolayers [14], and iron-based catalyst (called, nowadays, Pt-free catalysts) [15–17].

This chapter is devoted, in particular, to metal carbides in fuel cell cathode as potential alternative materials to conventional carbon support owing to their bifunctional capability, catalysts and catalyst supports.

23.2 History of Metal Carbides in Fuel Cells

In early 1960s, some of the metal carbides such as silicone carbide (SiC) and boron carbide (BC) were tested for the first time in fuel cell environment. For example, BC was used as catalyst support in both phosphoric and alkaline fuel cells by GE in the USA [18]. Since then, it took 20 years for other carbides to be evaluated in fuel cells, in particular phosphoric acid fuel cell (PAFC). United Technologies Corporation

(UTC) has been using SiC for 50 years as an electrolyte matrix in PAFC because of its extreme stability in hot phosphoric acid. The system could not be used in fuel cell electrodes due to its poor catalytic activity and electrical conductivity. However, SiC has been evaluated as a catalyst support with addition of carbon black to enhance conductivity in the catalyst layer. The approach included the deposition of Pt particles on SiC by chemical route followed by mixing with carbon to formulate catalyst. Authors claimed that a higher Pt loading has led to improved electrode performance even with large particles of Pt. This indicated that electrode performance depends not only on surface area of Pt but also on the interaction nature between support and metal catalyst [19].

On the other hand, TiC has been also studied for fuel cell applications since the system is electrically conductive and can be prepared with high surface area. In hot phosphoric acid, TiC carbide performed well as catalyst support, presumably due to formation of oxide layer or oxocarbide layer as shell [20]. Since then, metal carbides, especially tungsten monocarbide (WC), have been proposed as catalyst support due to their stability, electrical conductivity, and strong metal–support interaction property [21–29]. Chhina et al. [25] compared the stability of Pt-supported tungsten carbide to that of supported on Vulcan XC-72 and found that the former could retain the surface area and activity better during the corrosion testing in acid. The high stability of tungsten carbides in the electrochemical testing was attributed to a core–shell-type structure that was formed when the surface of tungsten carbide oxidizes to oxide layer, WOx or WOCx. This passive shell encapsulates and protects the carbide core from severe corrosion. Such data agreed well with the data reported for TiC [20].

It is important to note, however, that the stability of tungsten carbides also depends on the structure, phase and shape. For instance, it has been reported that single-phase WC is more stable than W_2C in the acidic medium [23, 30]. In addition to the high stability, tungsten carbides are also expected to enhance the catalytic activity of Pt nanoparticles due to the strong metal–support interaction (SMSI) [31]. Shen's group reported that oxygen reduction reaction (ORR) activities of Pt- and Pd-based catalysts were enhanced significantly on tungsten carbide-modified carbon support [9, 32–34]. The possible reason for activity enhancement includes more uniform catalyst distribution on modified carbon and the synergistic interaction between metal particles and tungsten carbides. Such interaction may cause some change in the electronic environment of Pt leading to low oxide formation on the surface of Pt, which is believed to be one of the causes for Pt dissolution and sluggish kinetics of oxygen reduction reaction [2].

In terms of catalytic activity, the early studies reported on metal carbides, especially on WC, have shown a good catalytic activity toward hydrogen and hydrazine oxidation [35, 36]. Since then, research interest on metal carbides has tremendously increased and indicated that these materials can replace a substantial amount of Pt in fuel cell electrodes. The work reported by Bennett et al. [37] has clearly demonstrated the evidence of WC activity by establishing a close relationship between the catalytic activity and the density of *d*-like states at Fermi level. The density of states at Fermi level of WC is intermediate in character between that of W and Pt. However, authors mentioned that such observation of Pt-like in WC does not provide a complete explanation for its catalytic behavior. Moreover, it was claimed that a higher density of state at Fermi level is necessary, but not sufficient as criteria to obtain a higher catalytic activity. Therefore, based on Fermi level energy alone, one can expect a higher catalytic activity for metals, such as vanadium and tantalum. Yet, these metals are not active for both hydrogen oxidation and oxygen reduction reactions. So, one possibility to explain metal carbides activity might be related to ferromagnetic property, which is generally characteristic of heavier metals, like Pt.

Alloying metal carbides with other metals (for instant alloying WC with Mo or Ta) can also affect the catalytic property, which indicates that the origin of WC activity might be associated with surface change, such as formation of hydrogen tungsten bronze as results of oxide layer encapsulating bulk carbide [38].

23.3 Synthesis Methods

23.3.1 Hydrothermal Synthesis

Hydrothermal synthesis is simple and convenient method for nanomaterial synthesis. Hydrothermal technique can be precisely defined as the use of water or an organic solvent as reaction medium in a proper sealed container at elevated temperature (100–300 °C). In hydrothermal conditions, the pressure of the container dramatically increases due to increase of temperature. The increase of pressure also depends on other reaction parameters like filling level of the container and dissolved metal salts. There are a few important advantages of hydrothermal synthesis like elevated temperature and pressure enhancing the reactivity of inorganic solids, providing solubility of various compounds, and initiating reactivity in slow reactions. These hydrothermal conditions tailor nucleation and subsequent crystal growth. As an example, Pie et al. synthesized silicon carbide (SiC) nanotubes using supercritical hydrothermal conditions [39]. The synthesis of silicon carbide nanotubes was performed in stainless-steel ($Cr_1Ni_{18}Ti_9$) kettle. The maximal pressure inside the vessel was 8.0 MPa, temperature around 470 °C. In this synthesis method, high purity of SiC (particle size < 50 nm) and SiO_2 (particle size 30 ± 5 nm) were used as starting materials. The SiC nanotubes were composed of β crystalline structure along with some residual carbon. The nanotubes were formed in high aspect ratio. On the other hand, Hu et al. prepared 5–15 nm cubic vanadium carbide (VC) nanoparticles dispersed on carbon matrix following hydrothermal method [40]. The synthesis was carried out in Teflon-lined stainless-steel autoclave at 150 °C. These nanocrystalline cubes V_8C_7 were used as oxygen reduction electrocatalyst support to enhance the mass activity of Pt nanoparticles. The mass activity of Pt/VC was increased significantly compared to conventional catalyst, Pt/C.

23.3.2 Sol–Gel Synthesis

Sol–gel is a wet chemistry technique and is widely used for the synthesis of metal oxide and sulfide nanostructured materials. Sol–gel method generally involves the formation of sol pursued by the formation of gel using metal precursors as starting materials [41]. Hydrolysis and condensation reactions result into various interesting shapes of these metal oxide and sulfide nanostructures. In this method the nature of metal precursor, type of solvent, reaction pH, temperature, support, and time are vital parameters which predominantly affect the morphology, size, and porosity of the resulting nanostructured materials. Elevated temperature calcination is used to remove the organic framework, and metal oxide/sulfide/carbide nanostructures can be obtained. Sol–gel chemistry also enables to produce cheap and sustainable metal carbide nanostructures. Recently Hudson et al. synthesized metal carbide (WC) nanoparticles using the sol–gel method [42]. Tungsten carbide nanoparticles synthesized by the gel precipitation of tungstic acid in the presence of an organic gelling agent (10 % ammonium poly(acrylic acid)] in water and HCl saturated hexanol, followed by washing, drying, and subsequent pyrolysis under Ar at 900 °C and then under CO_2 at similar temperature. XRD clearly showed the formation of tungsten carbide with lattice fringes in the crystal are oriented in (111) plane with spacing of 0.25 nm. The size of WC nanoparticles was in the range of 40–75 nm. Yao et al. also prepared highly uniform metal carbide nanocrystals [43]. In this work, they prepared concentrated solution of metal precursor in ethanol using various metal precursors, such as $TiCl_4$, $MoCl_5$, WCl_4, and $NbCl_5$. The metal precursor was reacted with ethanol vigorously to release the HCl and to form metal orthoesters, followed by formation of metal/urea precursor in gel phase. Finally the gel was placed in an oven and treated under nitrogen at 800 °C. This sol–gel synthesis method is very interesting and convenient and also it can be applied to a various types of metals to generate well-defined and highly crystalline carbides [44].

23.3.3 Temperature-Programmed Reaction

Temperature-programmed reactions (TPR), developed by Volpe and co-workers, are efficiently used for the synthesis of metal carbides [45]. This method is prominent for the synthesis of metal carbides and other inorganic nanomaterials of desired shape and properties. Metal oxides are essentially heated at high temperature in the presence of hydrocarbon. In this synthesis method, the reactant gases of optimized ratio of CH_4/H_2 or C_2H_6/H_2 are passed over the metal oxides. After the reaction, samples need to be quenched in the presence of argon at room temperature. However, before exposing the sample to the atmosphere, the carbide generally needs to be partly passivated in the presence of trace of oxygen, O_2/Ar (1–2 %). The shape of the nanostructured carbides depends upon the temperature, metal oxide precursors, and ratio of gases.

Shao et al. produced high-surface-area-modified tungsten carbide (WC) by TPR without significant loss of carbon support [46]. This method can also be used for scale up synthesis of kilogram metal carbide nanoparticles with particle size in the range of 10–50 nm. The Pt catalyst supported on tungsten carbide on Ketjenblack (KB) showed a better oxygen reduction reaction activity compared to conventional catalyst, Pt/KB.

23.3.4 Microwave Synthesis Method

Microwave chemical synthesis method has become very important due to its remarkable advantages for the synthesis of organic and inorganic nanomaterials. This method allows synthesis to be done in a faster and cleaner way with reduced solvent consumption as a "greener" process. Shen et al. synthesized platinum-loaded tungsten carbide nanoparticles by microwave synthesis [47]. In this method, metal salt dissolved in distilled water and alcohol under magnetic stirring to obtain homogenous mixture. Carbon as the supporting material was added to the mixture and continuously stirred to obtain the dispersed ink. The ink was dried at 80 °C and finally transferred to a homemade program-controlled microwave oven (2,000 W, 2.45 GHz) for further heating at different times. This experiment was carried out in ambient air. The average particle size of WC was ~21.5 nm under optimized conditions. TEM micrograph showed highly uniform dispersed Pt nanoparticles on the surface of WC. Pt supported and unsupported on nanosized WC was used as electrocatalyst for alcohol oxidation and oxygen reduction reaction. High performance for alcohol oxidation was obtained with Pt supported on WC.

Zhang et al. also prepared titanium carbide (TiC) nanoparticles at 1,200 °C by combining sol–gel and microwave carbothermal reduction using tetrabutyl titanate and sucrose as the starting materials [48]. The obtained TiC nanoparticles were in the range of 100–500 nm.

23.3.5 Vapor Transport Method

Vapor transport is a novel method for the synthesis of one-dimensional nanostructures. Nanomaterials prepared by vapor transport show excellent structural properties with tailored shapes. In this method, shape, morphology and properties of materials strongly depend on the temperature, pressure, nature of metal source, flow of gases, and nature of the substrate (support). Among the carbides, silicon carbide (SiC) nanostructures are most commonly synthesized by this method. Seong et al. prepared silicon carbide nanowires, SiC NWs, in a horizontal hot-wall chemical vapor deposition (CVD) furnace [49]. Oxidized silicon was used as substrate to grow SiC NWs. The substrate was coated by 2 nm nickel layer by sputtering method to direct the vapor liquid solid (VLS) growth. The substrate was kept in the uniform temperature region in an inner quartz tube reactor surrounded by an outer alumina tube. Methyltrichlorosilane (MTS, CH_3SiCl_3) was chosen as a source precursor since it has an equal amount of Si to C. This precursor decomposes at a relatively low temperature. The average diameter of nanowires was less than 100 nm and their length was up to several microns. These SiC nanowires were single crystalline in nature and grown along (111) orientation.

Sunderasan et al. prepared SiC nanowires by catalyst-assisted microwave heating-assisted physical vapor transport from a "source" 4H-SiC wafer [50]. The diameter of nanowires was in the range of 15–300 nm and their length in several microns. These SiC nanowires are grown through VLS mechanism at 1,650–1,750 °C.

23.3.6 Sputtering Method

Sputtering is a physical vapor deposition method commonly used for the growth of thin films with tunable grain size and porosity. Sputtering is highly reproducible, and various types of materials with controlled thickness can be produced. In this method, target material is ejected from the target and then deposited onto the substrate in the form of thin films, nanoparticles [51]. Film thickness, morphology, grain size, uniformity, and porosity depend on the nature of the target, substrate, gases, and pressure of the chamber. Xu et al. developed multiple target radio frequency (RF)/direct magnetron (DC) sputtering system [52]. This system was employed for the growth of SiC nanoparticle films. The growth was carried out on silicon (100) substrate. In a typical experiment, aluminum nitride (AlN) buffer layer was created on the silicon substrate by using aluminum target and nitrogen and argon–hydrogen plasma. Finally SiC nanoparticles were grown by using SiC target in the presence of nitrogen–argon and hydrogen in the ratio of 6.4:35.2:9.6 sccm, respectively. The particle sizes of produced SiC were in the range of 10–50 nm.

In general, WC has been formed from different sources, such as its oxides, nitrides, and sulfides, as starting materials and found that the crystalline phase depends strongly on reaction condition and synthetic methods [53]. If a mixture of C_2H_6 and H_2 is used, the formed WC from W-oxide was found having a hexagonal close-packed shape. However, for WC that is formed from W_2N precursor acquires a face-centered cubic shape. Hara et al. have investigated the formation of WC by different methods attempting to produce subcarbides by carburization [54]. It was noticed that high content of sub-WC can be obtained using precursor like WCl_4 instead of W-oxides. As carburization time goes on, phase transformation of WC was noticeable following the evolution of the ratio of sub-WC using XRD. It is important to mention that the net activity of WC prepared via nitrides and sulfides was much better than that obtained with WC prepared from oxide precursors. To understand such difference in catalytic properties of WC, Ross at al. have relied on XPS data and found that the low activity for WC formed from oxides is mainly due to free carbon covering active sites of WC [55]. Also, Delannoy et al. found that the increase in binding energy of WC prepared from oxide is due to formation of

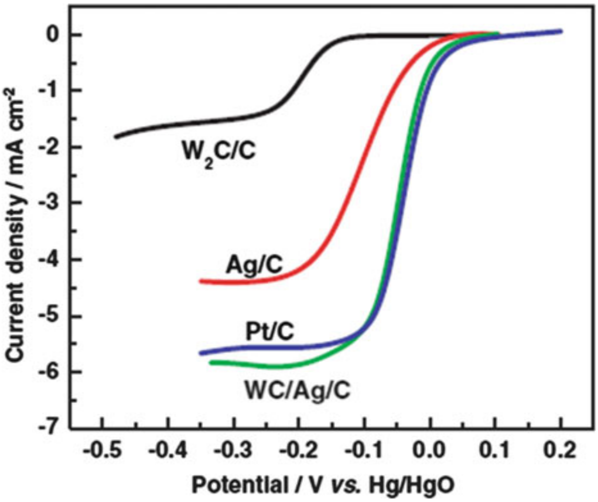

Fig. 23.1 RDE response of ORR on W_2C/C, Ag/C, Ag/W_2C/C, and Pt/C on glass-carbon rotating disk electrodes in O_2 saturated 1 M KOH solution at 25 °C; scan rate, 5 mV/s; rotation speed: 2,500 rpm. Loadings: W2C/C (11.43 μg of W_2C), Ag/C (11.43 μg of Ag), Ag/W_2C/C (11.43 μg of W_2C and 11.43 μg of Ag), and Pt/C (22.86 μg Pt) [9]

graphite like carbon [56]. This latter clearly confirms the highest activity of WC, observed by Hara et al., must have a direct relationship with low carbon coverage on WC when W_2N and WS_2 are used as precursors.

23.4 Metal Carbides as Catalyst and Catalyst Support

Metal carbides attracted much attention because they can have a dual function, as catalyst and catalyst support. In particular, WC is being extensively explored as potential catalyst support in fuel cells. It has been reported that ORR test for Pt/WC in alkaline medium did show a significant improvement in activity; at fixed current density, the shift in potential was more pronounced for Pt/WC, almost ten times higher than that of conventional catalyst, Pt/C. Authors elaborated on the mechanism based on the evidence that metal carbides are good catalysts for hydrogen, formic, and monoxide oxidation reactions [34]. The same group reported elsewhere on the effect of WC on ORR by using Pt-free metal like Ag. WC nanocrystals promoted Ag as novel catalyst was prepared using microwave heating method and tested for ORR. The activity of Ag/WC catalyst was found to be almost similar to that of Pt supported on carbon (Pt/C). Also, the studies by AC impedance spectroscopy techniques have shown small charge transfer impedance for Ag/WC/C as compared to that of Ag/C in alkaline medium, proving fast kinetics process for ORR on Ag/WC/C (see Fig. 23.1 above). Furthermore, the composite Ag/WC/C

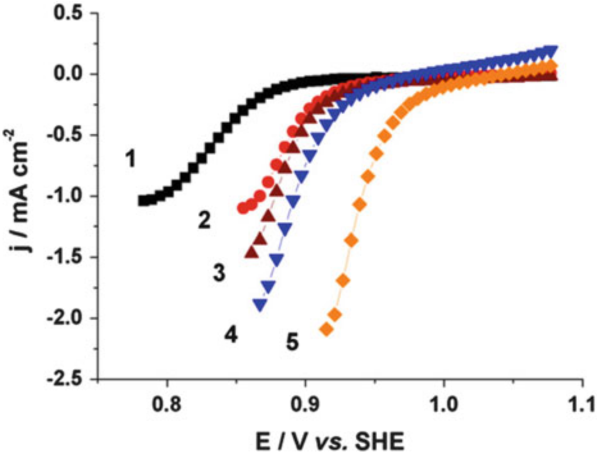

Fig. 23.2 Linear sweep curves of oxygen reduction on different electrodes in O_2 saturated 1 M KOH solution at 25 °C. The metal loadings in electrodes are as follows: for curve 1, 20 μg Au; curve 2, 20 μg Pt; curve 3, 20 μg Pd; curve 4, 20 μg Pd + 20 μg WC/C; and for curve 5, 6.7 μg Au + 6.7 μg Pd + 6.7 μg WC/C; sweep rate: 2 mV/s [33]

was considered as unique system since it has a good catalytic selectivity toward ORR in the presence of alcohols. As result, such a low-cost catalyst could have potential applications in the fuel cell including direct methanol fuel cell [9].

Although metal carbides (for instance, WC) provide some ORR activity as seen in Fig. 23.1, most studies reported in the scientific literature have shown that metal carbides when used as catalyst support offer certain synergy effect that can boost the catalyst catalytic activity further. Nie et al. [33] prepared WC to support Au–Pd alloy; preparation method was based on dissolution of W metal with hydrogen peroxide and alcohol. Vulcan carbon was added to form a sort of ink by ultrasonication. The dried ink was then heat treated in a microwave oven to produce WC. ORR test on produced catalyst Au–Pd/WC was performed in both acidic and alkaline mediums. The electrode response, as illustrated in Fig. 23.2, shows an exceptional activity, much higher than that of Pt/C. In the kinetic region, a shift in ORR potential could be estimated as high as 70 mV more positive than that recorded for conventional catalyst, Pt/C, even though the loading of Pt/C on electrode was much higher than the combined loading of Au and Pd on WC. This clearly proves the benefits of a support that has affinity to interact electronically with metal catalyst. One can assume that such improvement in ORR activity may be due to faster kinetics in alkaline medium, rather than the effect introduced by WC. In this regard, the test in acidic affirmed that the catalytic behavior was maintained. However, the shift in ORR potential was less compared to that in alkaline medium.

Moreover, Yin et al. [57] developed WC on carbon surface by intermittent microwave heating method to support other Pt-free catalyst, such as Pd–Fe (catalyst noted as Pd–Fe/WC/C). According to TEM images, a good dispersion was obtained with particle sizes in the range of 4 nm for Pd–Fe/WC/C and 2.8 nm for the

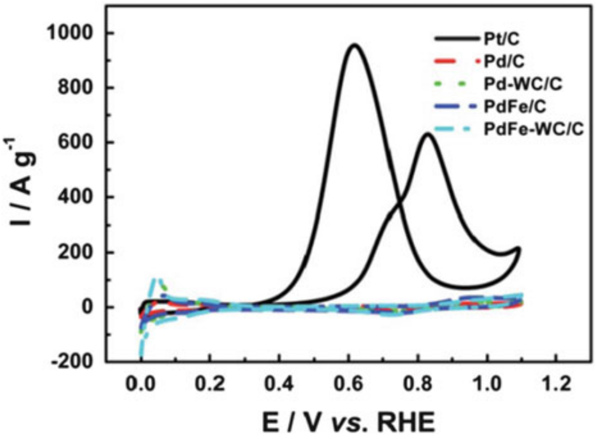

Fig. 23.3 Cyclic voltammogram of Pd–Fe/WC/C and other electrocatalysts in 0.5 M H_2SO_4 containing 1 M CH_3OH at 25 °C. Scan rate, 50 mV/s [57]

benchmark catalyst Pt/C (Vulcan), in a good agreement with XRD data. This new catalyst was tested against ORR in 0.5 M H_2SO_4 and showed almost the same performance like the one obtained with conventional catalyst, Pt/C, especially in the kinetics region, putting in evidence the synergy effect exhibited by WC on Pd–Fe alloys. However, a small drop in ORR limiting current was noticeable for the system Pd–Fe/WC/C as compared to Pt/C. Such decrease in limiting current could be associated with three possible scenarios: (1) low catalyst coverage on glassy carbon electrode; (2) film thickness, which affects the mass transport reaction; and (3) hydrogen peroxide formation as result of uncompleted ORR. Nevertheless, a huge improvement was observed in ORR for Pd–Fe/WC/C compared to Pd/C, which clearly proved the direct role of surface change induced by either Fe, which acts as oxygen storage component, or by the electronic effect of Pd atoms leading to strong bonding between Pd and Fe. In addition, there is a synergy effect coming from WC, which can facilitate the reaction of oxygen dissociation due to the layer of hydrogen tungsten bronze, commonly known for WC and WOx in acidic environment.

Yet, the most interesting results for ORR on Fe–Pd/WC catalyst are those obtained in the presence of alcohol. The electrode response for Fe–Pd/WC system in oxygen saturated acid has not been affected even at high concentrations of methanol, whereas the ORR on conventional catalyst Pt/C was completely restrained since the dominant reaction was basically methanol oxidation only. Such results suggested that Pd–Fe/WC/C could be an excellent candidate for direct methanol fuel cell (DMFC) cathode because of its inert activity toward methanol oxidation as seen in Fig. 23.3. The utilization of a completely inert catalyst to methanol oxidation is one of the important criteria for DMFCs to operate at higher power densities since the issue of methanol crossover is unavoidable and can cause dramatic loss in cell performance, especially with common catalysts that are active

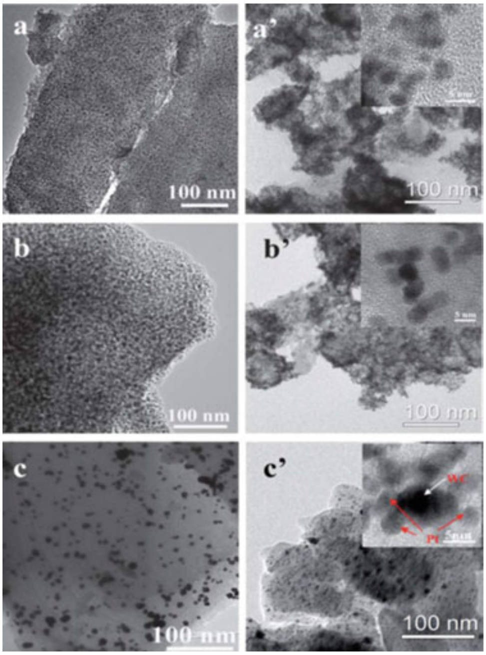

Fig. 23.4 TEM images of the carbides (**a**) V_8C_7/CF, (**b**) MoC/CF, (**c**) WC/CF, (**a′**) Pt-V_8C_7/CF, (**b′**) Pt–MoC/CF, and (**c′**) Pt–WC/CF (reproduced from [58])

toward methanol oxidation such as Pt and Pt alloys. Limited availability of scientific literature suggest that further investigation on this type of catalysts is needed to verify its stability against potential cycling and high temperature, in order to assess its applicability in PEMFC systems.

In another attempt, He et al. [58] reported a new method to develop highly dispersed metal carbides based on different elements, such as W, Mo, and V on carbon surface. Essentially, the method relies on the utilization of an ion-exchange resin to complex metal precursors prior to heat treatment. Starting with a macroporous acrylic-type resin to incorporate anions, such as (VO_3^-), ($MO_7O_{24}^{-6}$), and ($H_2W_{12}O_{40}^{-6}$). After carburization at high temperature, 1,000 °C, in N_2 atmosphere, the metal carbides along with carbon foam (CF) were formed as composites with a surface area ranged between 88 and 120 m^2/g. These composites were loaded with Pt and tested as ORR catalysts. As TEM shows in Fig. 23.4, composites with and without Pt seem to have good dispersion and low particle size, which make them suitable for highly performing cathode.

In general, all aforementioned metal carbide composites and Pt-supported catalyst showed much better ORR activity as compared to the conventional catalyst Pt/C in 0.1 M HClO4 medium. Among these carbides, the highest ORR mass activity was obtained with the catalyst noted as Pt/V_8C_7/C, which has the largest surface area. However, when performing studies on hydrogen peroxide detection, it was noticed that the lowest peroxide formation took place with the system of Pt/WC/CF, not with Pt/V_8C_7/CF. These findings agreed well with those reported in literature because metal carbides, in particular WC, form oxide layer shell which acts as a

Table 23.1 DFT estimated binding energy for atomic oxygen

Surface	Binding energy for atomic oxygen (K cal/mol)
WC (0001)	−173.2 [63]
Pt (111)	−91.7 [63]
1 ML Pt on WC (0001)	−92.9 [63]

sink for decomposition of H_2O_2 [59, 60]. Since catalysts activity is generally evaluated in the electrode kinetic region, higher mass activity for the catalyst, Pt/V_8C_7/C does not mean that hydrogen peroxide would not be formed because the decomposition of the latter strongly depends on solution pH and electrode potential.

The same group reported a new type of vanadium carbide in cubic shape via hydrothermal method at 160 °C using glucose and NH_4VO_3 as carbon and V sources, respectively. Synthesized cubic VC nanostructure was used as a support for Pt catalyst in order to boost the catalytic activity of Pt. At 0.9 V/RHE, mass activity measured by a rotating disk electrode in oxygen-saturated 0.1 M $HClO_4$ was found to be 230 mA/mg_{Pt} for Pt/VC/C and 97 mA/mg_{Pt} for Pt/C; two-fold enhancement in ORR activity was observed. This significant improvement in activity was explained in terms of interaction between nanostructured VC (support) and Pt particles [61]. In comparison with previous studies, it appeared that VC as support has a better synergy effect than WC. Presumably, the redox chemistry of V plays an important role in determining the interaction between Pt and VC and making the system more catalytically favorable for oxygen reduction reaction. It is worth noting, however, that the cubic nanostructured VC was having a range of particle size between 5 and 15 nm that was uniformly dispersed on carbon matrix with a composition of V_8C_7.

To further increase the gravimetric catalytic activity of a catalyst with metal carbides support, Esposito and Chen investigated a new approach where Pt can be deposited in atomic monolayer fashion [62].

23.5 Pt Monolayer (Pt_{ML}) on WC as Low-Cost Catalyst for ORR

Chen group has intensively investigated the electronic properties of WC in order to have better understanding of its catalytic activity. Using density functional theory (DFT) calculation, the binding energy of reactants relevant to electrochemical application was quantified since it is considered as a crucial property that reflects the electronic behavior of each surface in correlation with the evaluated catalytic activity. As an example, binding energy of oxygen on different surfaces was estimated, as listed in Table 23.1.

For a catalyst to be highly active, it is well understood that the desirable situation is to bond with reactive intermediates in moderate strength. The electronic structure of the catalyst surface as described by d-band density of states (DOS) plays a key

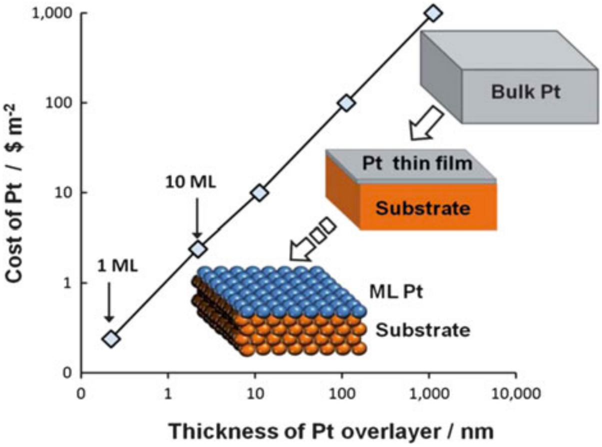

Fig. 23.5 Relationship between Pt cost and its overlayer loading for a planar surface configuration [62]

role in determining the catalytic behavior vis-a-vis an adsorbed atom or molecule [64]. Such a relationship between electronic structure and binding energy can indeed predict the corresponding catalytic activity. As shown in Table 23.1, the system, Pt_{ML}/WC, seems to have almost an identical value of oxygen atom binding energy compared to that of Pt, indicating the synergetic impact of WC as support for Pt layer. Such system may lead to a significant reduction in Pt loading and subsequently low cost of catalyst. Figure 23.5 illustrates the cost reduction of Pt as a function of its thickness on planar surface. Presumably, without compromising cell performance, such a large reduction in Pt loading may overcome the obstacle encountered in fuel cell commercialization [62].

Employing RDE electrode technique, Pt_{ML}/WC was tested for ORR in 0.5 M H_2SO_4, and the results showed that obtained activity was not comparable to that of Pt bulk. Authors believed that the poor activity for Pt_{ML}/WC may be due to the instability of WC underneath as result of high cathode potential, which is always close to 1 V/RHE. At this potential, WC can be oxidized to form oxides layer. Also, the possibility of partial dissolution of Pt in acid cannot be ruled out. However, Pt_{ML} dissolution is most likely evidenced from the electrode response in the limiting current regime, which indicates catalyst low coverage on glassy carbon substrate. Moreover, the hypothesis of surface oxidation of WC was verified by XPS analysis. After cycling the electrode in oxygen saturated 0.5 M H_2SO_4 between 0 and 1 V/RHE, two peaks appeared at 35.9 and 38 eV in XPS spectrum which correspond to the formation of WO_3 for both samples, WC and Pt_{ML}/WC as well [65].

In our view, deposition of Pt_{ML} on metal carbides is an excellent and cost-effective approach. Yet, the challenge for this concept to succeed is to make it more stable in fuel cell conditions. One practical approach to circumvent this issue is to further decorate Pt_{ML} with atomic fraction of gold (e.g., 20–60 atomic percentage) in order to improve the stability without affecting the ORR activity as reported elsewhere [66].

For practical applications, development of Pt_{ML}/WC catalyst with high surface area that can generate sufficient power densities is highly desired. In addition, materials should possess mesoporous structures to facilitate mass transport reactions. The other challenges such as uniformity of Pt_{ML} on WC particles and the development of single-phase WC in powder forms should also be taken into account.

With regard to Pt_{ML}, there are several techniques besides the physical vapor deposition that have been used for 3D structures deposition including atomic layer deposition (ALD). In the form of thin films, uniformity of Pt overlayers can be achieved easily and successfully on materials containing oxides or phosphates due to strong attraction between the components. Therefore, for WC as a core, it is likely that Pt_{ML} would adhere well since WC has a good tendency to form oxide or oxycarbide layers.

Nevertheless, currently the development of Pt_{ML} on WC with good Pt uniformity remains a big challenge. To overcome this issue, one can look for a method by which Pt_{ML} can be deposited chemically on high surface area metal carbides in order to mass produce Pt_{ML}/WC catalyst in a cost-effective manner.

23.6 Electrochemical Stability of Metal Carbides

Metal carbides have gained much attention in fuel cell technology due to their potential use as catalyst and catalyst support. WC in particular has been known to promote the ORR activity. However, electrochemical stability of WC is crucial in PEM fuel cells since the cathode is always subjected to high voltage that can reach 1.5 V/RHE in some cases, especially during start-up and anode starvation. Generally, tungsten carbide exists in two forms: the monocarbide (noted as WC) and the subcarbide (W_2C). It was reported by Zellner and Chen that the former is more stable when exposed to an oxidizing environment and high potential [30]. However, it is worth noting that electrochemical stability of metal carbides depends on their composition and their surface area. For instance, TiC seems to be more corrosion resistant than WC in acid medium and at potential up to 1.3 V/RHE, which makes the system very useful as a catalyst support for fuel cells and electrolysers [67].

Despite the low stability of tungsten carbides, the material attracted much attention as catalyst support for fuel cells. Zhang et al. have compared both activity and stability of carbon and W_xC_y modified with Pt under real cell conditions. The test showed that the cell performance with Pt/C electrode was initially higher than that of the cell with Pt/W_xC_y. But, when cells were subjected to durability tests, the degradation was much severe for the cell with Pt/C than that of Pt/W_xC_y. This proves that stability of Pt/W_xC_y is much higher than that of Pt/C and the reason was attributed to the effect of W_xC_y support [68]. Such results are expected because of the tendency of W_xC_y to form an oxide layer that acts as protector to carbon and also enhances the stability of Pt particles by generating strong interaction. Chhina et al. [25] also investigated the stability of platinized tungsten carbide in comparison with Pt/C. In order to have a realistic comparison, authors have deposited Pt on carbon and on WC by taking the density of materials into account. The results of electrochemical stability test were very interesting; after 100 cycles in an accelerated mode, the activity of Pt/WC remained unchanged, while the activity of Pt/C was completely lost after only 20 cycles. These results were in good agreement with those reported earlier by Zhang et al. [68]. Noting that activity measurement for both catalysts, Pt/C and Pt/WC, was simply taken from the charge corresponding to hydrogen adsorption/desorption on Pt and this may not be the right approach to evaluate the catalyst activity, especially with metal carbides that have tendency to form oxides, which involve hydrogen absorption under spillover mechanism in the presence of Pt. In a similar study, Ion et al. [69] found that the charge of hydrogen adsorption/desorption for Pt/WOx system was almost six times higher than that of Pt/C as results of contribution from hydrogen–tungsten–bronze compound, well known to form on WOx surface.

However, the important criteria for WC to be implemented in fuel cells are its surface area, phase, and porosity. Ganesan and Lee reported that WC with a surface area of 170 m^2/g was obtained by thermal method, but the product tuned to be containing more sub-tungsten carbide (W_2C) [70]. The latter was used to support Pt catalyst for methanol oxidation reaction. No test was done for ORR. Nevertheless, authors believed that oxide layer formed on carbide support is the key player in promoting alcohol oxidation by providing oxygen species as indicated by the decrease in desorption temperature of CO. In a different study carried out by the same group, mesoporous WC was synthesized and used as a support for Pt [71]. The mesoporosity was introduced by addition of surfactant like cetyltrimethylammonium bromide (CTABr). Catalyst performance was evaluated under identical conditions as previously stated; however, no statement has been reported on ORR activity and electrochemical stability in both cases [70, 71].

On the other hand, Chhina et al. [21] used a higher surface area carbon as a template for high dispersion of W, and DC magnetron sputtering method to obtain porous WC. The material was subjected to stability test between 0.6 and 1.8 V/RHE, and oxygen reduction reaction (ORR) activity was recorded before and after for both, Pt/WC and commercial catalyst, Pt/C. Interestingly, it was observed that Pt/WC was more stable and maintained its high ORR activity, while the conventional catalyst Pt/C lost its ORR activity rapidly. DC magnetron sputtering of W onto C proved to be a promising technique to generate high surface area WC, porous, and with good electrochemical stability against surface oxidation. Such results suggest that tailoring the structure of WC is very important to enhance its stability for use in PEMFC.

Furthermore, it has been reported that addition of Ta to W can lead to more corrosion-resistant carbides [72]. This can be explained from thermodynamic point of view, because the oxide layer of Ta has an excellent stability in potential window ranged between 0 and 1.5 V/SHE and over a wide range of pH [73], and as such the carbide alloys, TaWC, is expected to perform better than its analogue WC. However, it is very important to mention that corrosion also depends on the conductivity of the oxide layer, which in turn depends strongly on the content of Ta in the carbides alloys. In other words, if Ta is present as doped element, such as the

Table 23.2 Corrosion data for WC and TaWC supported on carbon KB [74]

Sample	Spec. charge (C/mg)	Weight change of sample (%)
30 % WC/KB	1.95	7.0 gain
30 % TaWC/KB (15 % W, 15 % Ta)	1.60	3.8 gain
30 % TaWC/KB (27 % W, 3 % Ta)	3.79	2.7 gain

composition $W_{90}Ta_{10}$, we expect the formation of a conductive oxide layer that may influence significantly the corrosion rate of TaWC alloys.

In this regard, Merzougui et al. have investigated the effect of carbide composition on corrosion behavior [74]. Results presented in Table 23.2 indicate that as the weight percentage of Ta changed from 15 to 3 %, significant increase in corrosion-specific charge passed at potential of 1.4 V/RHE and 80 °C. Atomic modeling of these specific compositions predicts that the alloy containing 3 % Ta and 27 % W did exist in solid solution, whereas the alloy with 15 % W and 15 % Ta reveals phase segregation. Such a difference in physical properties of alloy might explain the large increase in corrosion rate.

Interestingly, similar corrosion behavior was also observed with the bimetallic NbWC alloy. This confirms the role of alloying element in determining the corrosion behavior of a metal carbide alloy. Starting materials (precursors) do not seem to have any effect on corrosion behavior of formed carbides. As an example, corrosion rate of TaWC carbide, produced from both precursors, $Ta(o\text{-}CH(CH_3)_2)_5$ and oxide (Ta_2O_5), was found to be the same.

23.7 ORR Activity and Stability on Metal Carbide Supports

Practically, parents of metal carbides such as metal oxides offer a strong metal–support interaction (SMSI). However, their direct use in PEM fuel cell environments may create certain issues to fuel cell electrodes, because they are extremely hydrophilic and in most of the cases are nonconductive. Therefore, the strategy of using metal carbide-modified carbon as catalyst supports may circumvent these issues. Carbides are considered to offer a double role mechanism; on one hand they provide the SMSI property due to the formation of core–shell structure; the shell is basically a layer of oxide or oxo-carbides, which also participates in catalytic reactions. The shell plays vital role in providing interaction with supported metal catalysts (e.g., Pt), which results in a suitable change in surface of catalyst leading to enhanced ORR activity and stability. On the other hand, having metal carbides dispersed on high surface area carbon may reduce the degradation of carbon that usually occurs in the acidic environment at high potentials. As shown in Table 23.3, we regrouped ORR data obtained with metal carbide alloys supported Pt catalyst (carbides were synthesized via temperature-programmed reaction method on surface of Ketjenblack).

Table 23.3 ORR data for Pt catalyst supported on metal carbide-modified carbon supports [74]

Sample	% Pt (wt.)	ECA (m^2/g_{Pt})	Mass activity (A/mg_{Pt})	Charge ratio (Q_{Pt-OH}/Q_{Pt-H})
Pt/KB	40	92	0.14	1
Pt/WC/C	30	60	0.14	0.5
Pt/Ta–WC/C (Wt.15 % Ta, 15 % W)	40	45	0.16	0.7
Pt/Ta–WC/C (Wt. 3 % Ta, 27 % W)	40	65	0.2	0.5

All the above catalysts show low Pt-oxide formation as demonstrated from the charge ratio, Pt-Ox/Pt-H_{ads}, the charge ratio was estimated from cyclic Voltammograms (CVs) in nitrogen atmosphere at scan rate of 20 mV/s and in potential window between 0 and 1.2 V/RHE. The interesting finding was that the decrease in oxide surface of Pt was accompanied with a significant enhancement in ORR mass activity. Moreover, alloying the carbides seems to lead to better results, which we believe that in the mixture of metal carbides, there may be strong perturbation in Pt electronic environment weakening the binding of oxygen intermediates species to Pt surface. It is also believed that oxides adsorbed on Pt surface may spillover to the carbide supports under interaction mechanism [30]. In other words, the passive layer covering metal carbides core can act as a sink to absorb oxide species liberating more active sites for ORR. This may be the main reason that hydrogen peroxide formation on carbon support modified with metal oxides, such as WO_3, was much lower than that of unmodified [59].

Similar behavior was also reported by Popov group on doped metal oxide (Nb–TiOx) as catalyst support for Pt catalyst [60]. Thus, our observation with Pt/Ta–WC catalysts seems to be in good agreement with the work reported in literature, in particular the recent work by Ma et al. [75]. In this work, Pt supported on metal carbide alloys, such as Co–MoC synthesized by using an ion-exchange method, has demonstrated an excellent ORR activity. Mass activity at 0.9 V/RHE for this system Pt/Co–MoC was almost three times higher than that of conventional catalyst Pt/C. Authors attributed such an improvement in ORR activity to the synergic effect induced by Co–MoC support, which is believed to behave as an electron donor causing change in Pt surface. In addition, ORR activity on Co–MoC without Pt was also significant and confirmed the dual function of carbides (see Fig. 23.6). Furthermore, the system Pt/Co–MoC seemed to offer a better stability; after 1,000 cycles in $HClO_4$ solution between 50 and 1,100 mV/RHE, the shift in half-wave potential of ORR, $E_{1/2}$, was only 6 mV, while for conventional catalyst Pt/C, the shift was about 27 mV. Such phenomenon was also reported with WC nanofiber support, synthesized by electrospinning. The test of ORR in alkaline medium using RDE technique showed a good electrocatalytic activity, which is probably originated from the surface of WC nanofibers. Moreover, WC nanofiber electrocatalysts exhibited not only a good activity but also a good stability. Treatment with NH_3 was also found to be beneficial and led to further enhancement in catalyst properties [76]. Thus, all the results reported earlier clearly indicate that metal carbides possess a bifunctional property; they can play role of both, catalyst and catalyst support.

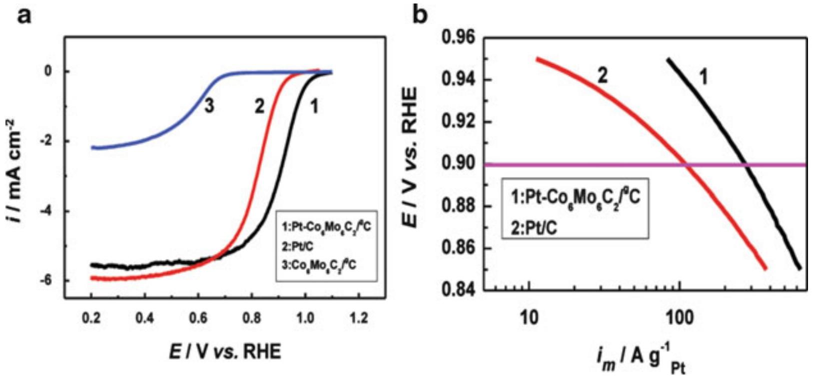

Fig. 23.6 (**a**) Linear potential sweep curves for the ORR on Pt$-$Co$_6$Mo$_6$C$_2$/C (1), Pt/C (2), and Co$_6$Mo$_6$C$_2$/C (3). (**b**) ORR mass activities for both catalysts, Pt–Co$_6$Mo$_6$C$_2$/C (1) and Pt/C (2) [75]

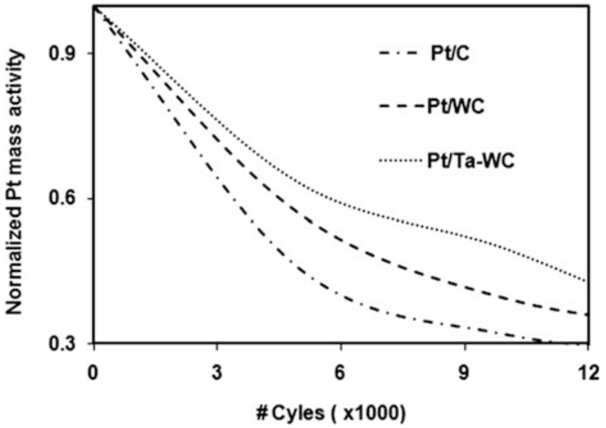

Fig. 23.7 Effect of potential cycling on Pt mass activity for ORR on different supports. Cycling condition, 0.1 M HClO$_4$; 0.6–1.2 V/RHE for 5 s; oxygen atm.; and 25 °C [74]

On the other hand, we have investigated the impact of metal carbides as advanced supports on catalyst durability. Samples listed in Table 23.3 were subjected to potential cycling between 0.6 and 1.2 V/RHE for 5 s in acid medium and at room temperature. Normalized ORR mass activities are plotted against number of cycles and illustrated in Fig. 23.7. As expected, catalysts based on metal carbide-modified carbon have shown a better retention in activity. Several techniques, such as NMR and XPS, can give insight into a clear understanding of the catalyst–support interaction mechanism. XPS analysis reveals a slight change in binding energy of Pt (4f$_{7/2}$, 4f$_{5/2}$) as follows: (71.2 eV, 74.2 eV) and (71.9 eV, 75.2 eV) for Pt/Ta–WC/C and Pt/C, respectively. This shift is not significant but it may indicate the tendency of electron-donor characteristic of Ta–WC support, in accordance with results and explanation of Ma et al. [75]. It is worth mentioning, however, that support–catalyst strain depends not only on type of metal carbides or

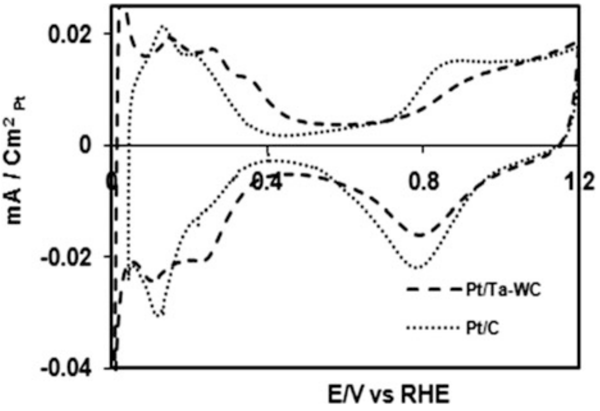

Fig. 23.8 Comparison of cyclic voltammograms of Pt supported on carbon and Ta–WC/KB. Conditions: 0.1 M $HClO_4$, N_2 atmosphere, and 25 °C [74]

oxides but also on the size of Pt particles. Of course, an extreme strain might result in a catalyst supported on carbides or oxides in a monolayer fashion as stated in Adzic work [77].

Such a strain between catalyst and support can also be verified by electrochemical technique. As illustrated in Fig. 23.8, the electrochemical behaviors of Pt/Ta–WC and Pt/C systems changed as result of the support effect; the intensity of oxidation peak corresponding to Pt–OH formation on Ta–WC support has suppressed (current intensities are normalized to real area of Pt and reported as mA/cm^2_{Pt}) and shifted toward positive potentials. Estimated charge ratio of oxide peak to hydrogen adsorption peak (Q_{Pt-OH}/Q_{Pt-H}) was largely reduced below the unity. In addition, the peaks in the hydrogen adsorption/desorption region seem not well defined in the case of Pt/C. Also they were shifted to more anodic potential. This kind of changes in cyclic voltammogram clearly put in evidence the synergic effect that metal carbides exerted upon Pt surface. In our view, the electrochemical data agreed with the slight shift in binding energy revealed by XPS; both techniques predict a donor effect of Ta–WC support, resulting into low concentration of oxide adsorbents, such as OH and O on Pt surface.

Hence, based on our studies and those reported in literature, it is clear that metal carbides play a dual role; on one hand, they act as a sink for oxides species generated on the surface of Pt leading to less peroxide formation and subsequently enhanced ORR activity. On the other hand, they can slow down the movement of Pt particles leading to less agglomeration as metal carbides have the tendency to form oxide layer that enhances interaction between support and Pt. Also, due to oxocarbide and/or oxide layers, metal carbides supports can protect carbon from severe corrosion, especially during high potential excursion of cathode in the start-up and anode starvation in PEMFCs.

In order to take advantages of the high stability and metal–support interaction properties of metal carbides, it is necessary to develop them with high surface areas and preferably dispersed on carbon black uniformly. Practically, this approach is attracting more attention and some studies have already been reported [46, 47].

23.8 Conclusion

In this chapter, we have given a broad overview on metal carbides as catalyst support for fuel cell cathode reactions. In particular, the role of WC as a support for Pt and others metal catalysts was reviewed. It has been found that ORR activity using metal carbide supports could be improved significantly as compared to conventional catalyst (e.g., Pt/C). Moreover, supports based on metal carbide alloys have shown further improvement in ORR. Furthermore, metal carbides when used as support have been found to improve the stability of catalysts. A bifunctional mechanism seems to be evident for carbides—on one hand, they play a role of a support and, on the other hand, they can contribute in catalyzing ORR. Most studies, however, attribute such a dual function of carbides to their synergetic effect that can trigger surface change of metal catalyst, since carbides have a tendency to form oxide and/or oxocarbide layers and thereby facilitates the interaction between catalyst and support, leading to less movement of catalyst particles which results in more stable and active ORR catalyst.

In conclusion, metal carbides as bifunctional materials have a great potential which can minimize the Pt utilization while maintaining or improving the cathode performance in PEFMCs.

References

1. Antolini E, Gonzalez ER (2009) Ceramic materials as supports for low-temperature fuel cell catalysts. Solid State Ionics 180(9–10):746–763
2. Sasaki K, Shao MH, Adzic RR (2009) Dissolution and Stabilization of Platinum in Oxygen Cathodes. In: Buchi FN, Inaba M, Schmidt J (eds) Proton exchange membrane fuel cell durability. Springer, New York, pp 7–28
3. Kinoshita K (1988) Carbon: electrochemical and physicochemical properties. Wiley, New York
4. Mathias MF, Makharia R, Gasteiger HA, Conley JJ, Fuller TJ, Gittleman CJ, Kocha SS, Miller DP, Mittelsteadt CK, Xie T, Yan SG, Yu PT (2005) Two fuel cell cars in every garage. Electrochem Soc Interface 14(3):24–35
5. Fuller TF, Gray G (2006) Carbon corrosion induced by partial hydrogen coverage. ECS Trans 1:345–353
6. Reiser CA, Bregoli L, Patterson TW, Yi JS, Yang JD, Perry ML, Jarvi TD (2005) A reverse-current decay mechanism for fuel cells. Electrochem Solid State Lett 8(6):A273–A276
7. Tang H, Qi ZG, Ramani M, Elter JF (2006) PEM fuel cell cathode carbon corrosion due to the formation of air/fuel boundary at the anode. J Power Sources 158:1306–1312
8. Swathirajan S, Merzougui B, Yu PT Fuel cell and method for reducing electrode degradation during startup and shutdown cycles. US patent US 2008/0166599 A1
9. Meng H, Shen PK (2006) Novel Pt-free catalyst for oxygen electroreduction. Electrochem Comm 8:588–594

10. Dembinska B, Kulesza P (2009) Multi-walled carbon nanotube-supported tungsten oxide-containing multifunctional hybrid electrocatalytic system for oxygen reduction in acid medium. Electrochim Acta 54:4682–4687
11. Izhar S, Nagai M (2009) Transition metal phosphide catalysts for hydrogen oxidation reaction. Catal Today 146:172–176
12. Nallathambi V, Lee JW, Kumaraguru SP, Wu G, Popov BN (2008) Development of high performance carbon composite catalyst for oxygen reduction reaction in PEM Proton Exchange Membrane fuel cells. J Power Sources 183:34–42
13. Serov A, Min M, Chai G, Kang S, Kwak C (2008) Preparation, characterization, and high performance of RuSe/C for direct methanol fuel cells. J Power Sources 175:175–182
14. Shao M, Sasaki K, Marinkovic NS, Zhang L, Adzic RR (2007) Synthesis and characterization of platinum monolayer oxygen-reduction electrocatalysts with Co-Pd core-shell nanoparticle supports. Electrochem Commun 9(12):2848–2853
15. Lefevre M, Proietti E, Jaouen F, Dodelet JP (2009) Iron-based catalysts with improved oxygen reduction activity in polymer electrolyte fuel cells. Science 324:71–74
16. Gong K, Du F, Xia Z, Durstock M, Dai L (2009) Nitrogen-doped carbon nanotube arrays with high electrocatalytic activity for oxygen reduction. Science 323(5915):760–764
17. Gang Wu G, More KL, Johnston CM, Zelenay P (2011) High-performance electrocatalysts for oxygen reduction derived from polyaniline, iron, and cobalt. Science 332:443
18. Grubb WT, Mckee DW (1966) Boron carbide, a new substrate for fuel cell electrocatalysts. Nature 210:192
19. Honji A, Mori T, Hishinuma Y, Kurita K (1988) Platinum supported on silicon carbide as fuel cell electrocatalyst. J Electrochem Soc 135:917–918
20. Jalan V, Frost DG (1989) Fuel cell electrocatalyst support comprising an ultra-fine chainy-structured titanium carbide. US Patent 4,795,684
21. Chhina H, Campbell S, Kesler O (2008) High surface area synthesis, electrochemical activity, and stability of tungsten carbide supported Pt during oxygen reduction in proton exchange membrane fuel cells. J Power Sources 179(1):50–59
22. Hwu HH, Chen JG (2005) Surface chemistry of transition metal carbides. Chem Rev 105: 185–212
23. Serov A, Kwak C (2009) Review of non-platinum anode catalysts for DMFC and PEMFC application. Appl Catal B Environ 90:313–320
24. Weigert EC, Stottlemyer AL, Zellner MB, Chen JG (2007) Cyclic voltammetry and X-ray photoelectron spectroscopy studies of electrochemical stability of clean and Pt-modified tungsten and molybdenum carbide (WC and Mo_2C) electrocatalysts. J Phys Chem C 111: 14617–14620
25. Chhina H, Campbell S, Kesler O (2007) Thermal and electrochemical stability of tungsten carbide catalyst supports. J Power Sources 164(2):431–440
26. Santos LGRA, Freitas KS, Ticianelli EA (2007) Electrocatalysis of oxygen reduction and hydrogen oxidation in platinum dispersed on tungsten carbide in acid medium. J Solid State Electrochem 11(11):1541–1548
27. Wang Y, Song S, Maragou V, Shen PK, Tsiakaras P (2009) High surface area tungsten carbide microspheres as effective Pt catalyst support for oxygen reduction reaction. Appl Catal B Environ 89(1–2):223–228
28. Wang Y, Song S, Shen PK, Guo C, Li CM (2009) Nanochain-structured mesoporous tungsten carbide and its superior electrocatalysis. J Mater Chem 19:6149–6153
29. Wang Y (2009) DOE Hydrogen and Vehicle Technologies Annual Review, Arlington
30. Zellner MB, Chen JG (2005) Surface science and electrochemical studies of WC and W_2C PVD films as potential electrocatalysts. Catal Today 99:299–305
31. Opalka S, Belabbes M, Shao MH (2010) Alternative catalyst supports based on metal carbides. In: 139th TMS meeting, Seattle
32. Meng H, Shen PK (2005) Tungsten carbide nanocrystal promoted Pt/C electrocatalysts for oxygen reduction. J Phys Chem B 109(48):22705–22709

33. Nie M, Shen PK, Wei Z (2007) Nanocrystalline tungsten carbide supported Au–Pd electrocatalyst for oxygen reduction. J Power Sources 167(1):69–73
34. Meng H, Shen PK (2005) The beneficial effect of the addition of tungsten carbides to Pt catalysts on the oxygen electroreduction. Chem Commun 35:4408–4410
35. Binder H, Kohling A, Sandstede G (1969) On the performance of WC electrodes upon oxidation of hydrogen, hydrazine, and formaldehyde, http://www.anl.gov/PCS/acsfuel/preprint%20archive/Files/13_3_NEW%20YORK_09-69_0099.pdf
36. Armstrong RD, Douglas AF, Keene DE (1971) The anodic oxidation of hydrogen in aqueous acids by conducting compounds of the transition elements. J Electrochem Soc 118:568
37. Bennett LH, Cuthill JR, McAlister AJ, Erickson NE, Watson RE (1974) Electronic structure and catalytic behavior of tungsten carbide. Science 184(4136):563–565
38. Bronoel G, Museux E, Leclercq G, Leclercq L, Tassin N (1991) Study of hydrogen oxidation on carbides. Electrochim Acta 36(10):1543–1547
39. Pei LZ, Tang YH, Chen YW, Guo C, Li XX, Yuan Y, Zhang Y (2006) Preparation of silicon carbide nanotubes by hydrothermal method. J Appl Phys 99(11):114306
40. Hu FZ, Chan C, Hui M, Wang R, Kang RP, Fu SH (2011) Oxygen reduction electrocatalysis enhanced by nanosized cubic vanadium carbide. Electrochem Commun 13(8):763–765
41. David AW, Edmond IK (1995) Preparing catalytic materials by the sol-gel method. Ind Eng Chem Res 34(2):421–424
42. Hudson MJ, John WP, Peter JFH (2005) Low-temperature sol-gel preparation of ordered nanoparticles of tungsten carbide/oxide. Ind Eng Chem Res 44(15):5575–5578
43. Yao W, Makowski P, Giordano C, Goettmann F (2009) Synthesis of early-transition-metal carbide and nitride nanoparticles through the urea route and their use as alkylation catalysts. Chem Eur J 15(44):11999–12004
44. Giordano C, Antonietti M (2011) Synthesis of crystalline metal nitride and metal carbide nanostructures by sol–gel chemistry. Nano Today 6(4):366–380
45. Volpe L, Boudart M (1985) Compounds of molybdenum and tungsten with high specific surface area: I. Nitrides. J Solid State Chem 59(3):332–347
46. Shao M, Merzougui B, Shoemaker K, Stolar L, Protsailo L, Mellinger ZJ, Hsu IJ, Chen JG (2011) Tungsten carbide modified high surface area carbon as fuel cell catalyst support. J Power Sources 196(18):7426–7434
47. Shen KP, Yin S, Li Z, Chen C (2010) Preparation and performance of nanosized tungsten carbides for electrocatalysis. Electrochim Acta 55(27):7969–7974
48. Zhang H, Li F, Jia Q, Ye G (2008) Preparation of titanium carbide powders by sol–gel and microwave carbothermal reduction methods at low temperature. Sol-Gel Sci Technol 46(2): 217–222
49. Seong HK, Choi HJ, Lee SK, Lee J, Choi DJ (2004) Optical and electrical transport properties in silicon carbide nanowires. Appl Phys Lett 85:1256
50. Sundaresan SG, Davydov AV, Mark D, Vaudin MD, Levin I, Maslar JE, Tian YL, Rao MV (2007) Growth of silicon carbide nanowires by a microwave heating-assisted physical vapor transport process using group VIII metal catalysts. Chem Mater 19:5531–5537
51. Chung CK, Wu BH (2006) Thermally induced formation of SiC nanoparticles from Si/C/Si multilayers deposited by ultra-high-vacuum ion beam sputtering. Nanotechnology 17: 3129–3133
52. Xu M, Ng VM, Huang SY, Long JD, Xu S (2005) Growth of SiC nanoparticle films by means of RF magnetron sputtering. IEEE Trans Plasma Sci 33(2):242–243
53. Claridge JB, York APE, Brungs AJ, Green MLH (2000) Study of the temperature-programmed reaction synthesis of early transition metal carbide and nitride catalyst materials from oxide precursors. Chem Mater 12(1):132–142
54. Hara Y, Inami N, Itagaki H (2007) Synthesis and characterization of high-surface area tungsten carbides and application to electrocatalytic hydrogen oxidation. Appl Catal A Gen 323:86–93
55. Ross PN, Stonehart P (1977) The relation of surface structure to the electrocatalytic activity of tungsten carbide. J Catal 48(1–3):42–59

56. Delannoy L, Giraudon MJ, Granger P, Leclercq L, Leclercq G (2002) Chloropentafluoroethane hydrodechlorination over tungsten carbides: influence of surface stoichiometry. J Catal 206(2): 358–362
57. Yin S, Cai M, Wang C, Shen PK (2011) Tungsten carbide promoted Pd–Fe as alcohol-tolerant electrocatalysts for oxygen reduction reactions. Energy Environ Sci 4:558
58. He G, Yan Z, Ma X, Meng H, Shen PK, Wang C (2011) A universal method to synthesize nanoscale carbides as electrocatalyst supports towards oxygen reduction reaction. Nanoscale 3(9): 3578–3582
59. Trogadas P, Ramani V (2008) Pt/C-WO_3 electrocatalysts for degradation mitigation in polymer electrolyte fuel cells. J Electrochem Soc 155(7):B696–B703
60. Ganesan P, Huang S, Popov BN (2008) Preparation and characterization of Pt/Nb-TiO2 cathode catalysts for unitized regenerative fuel cells (URFCs). ECS Trans 16(2):1143–1150
61. Hu Z, Chen C, Meng H, Wang R, Shen PK, Fu H (2011) Oxygen reduction electrocatalysis enhanced by nanosized cubic vanadium carbide. Electrochem Commun 13:763–765
62. Esposito DV, Chen JG (2011) Monolayer platinum supported on tungsten carbides as low-cost electrocatalysts: opportunities and limitations. Energy Environ Sci 4:3900–3912
63. Hsu IJ, Hansgen DA, McCandless BE, Willis BG, Chen JG (2011) Atomic layer deposition of Pt on tungsten monocarbide (WC) for the oxygen reduction reaction. J Phys Chem C 115: 3709–3715
64. Kitchin JR, Norskov JK, Barteau MA, Chen JG (2004) The role of strain and ligand effects in the modification of the electronic and chemical properties of bimetallic surfaces. Phys Rev Lett 93(15):156801–156804
65. Hsu IJ, Kimmel YC, Dai Y, Chen S, Chen JG (2012) Rotating disk electrode measurements of activity and stability of monolayer Pt on tungsten carbide disks for oxygen reduction reaction. J Power Sources 199:46–52
66. Zhang J, Sasak K, Sutter E, Adzic RR (2007) Stabilization of platinum oxygen-reduction electrocatalysts using gold clusters. Science 315:220
67. Sui S, Ma L, Zhai Y (2011) TiC supported Pt–Ir electrocatalyst prepared by a plasma process for the oxygen electrode in unitized regenerative fuel cells. J Power Sources 196:5416–5422
68. Zhang S, Zhu H, Yu H, Hou J, Yi B, Ming P (2007) The oxidation resistance of tungsten carbide as catalyst support for proton exchange membrane fuel cells. Chin J Catal 28(2): 109–111
69. Halalay I, Swathirajan S, Merzougui B, Balogh M, Garabedian G, Carpenter M (2011) Anode materials for mitigating hydrogen starvation effects in PEM fuel cells. J Electrochem Soc 158(3): B313–B321
70. Ganesan R, Lee JS (2005) Tungsten carbide microspheres as a noble-metal-economic electrocatalyst for methanol oxidation. Angew Chem Int Ed 44(40):6557–6560
71. Ganesan R, Ham JD, Lee JS (2007) Platinized mesoporous tungsten carbide for electrochemical methanol oxidation. Electrochem Commun 9(10):2576–2579
72. Lee K, Ishihara A, Mitsushima S, Kamiya N, Ota K (2004) Stability and electrocatalytic activity for oxygen reduction in WC + Ta catalyst. Electrochim Acta 49(21):3479–3485
73. McCafferty E (2010) Introduction to corrosion science. Springer, London
74. Merzougui B, Shoemaker K, Shao M, Protsailo L, Chen J (2009) Electrochemical behavior of metal carbides modified high surface area carbon. Unpublished work
75. Ma X, Meng H, Cai M, Shen PK (2012) Bimetallic carbide nanocomposite enhanced Pt catalyst with high activity and stability for the oxygen reduction reaction. J Am Chem Soc 134(4):1954–1957
76. Zhou X, Qiu Y, Yu J, Yin J, Gao S (2011) Tungsten carbide nanofibers prepared by electrospinning with high electrocatalytic activity for oxygen reduction. Int J Hydrogen Energy 36(13):7398–7404
77. Sasaki K, Zhang L, Adzic RR (2008) Niobium oxide-supported platinum ultra-low amount electrocatalysts for oxygen reduction. Phys Chem Chem Phys 10:159–167

Chapter 24
Promises and Challenges of Unconventional Electrocatalyst Supports

Sujan Shrestha and William E. Mustain

Abstract One of the most significant roadblocks in the commercialization and widespread implementation of proton exchange membrane fuel cells is the identification of low-cost, high-stability, high-activity electrocatalysts. An overwhelming amount of the work that has been done in this area has targeted the electrochemically active material, which has been the focus of much of this book. However, a key component to any catalyst is its support. Interaction between the catalyst and support dictates some of the most critical parameters for fuel cell performance including catalyst dispersion, particle size, faceting, and stability. Some supports, like graphitic carbon, interact very weakly with Pt and have a limited influence on catalyst activity and stability. On the other hand, recent work by several groups has shown that a strongly interacting support can drastically impact both catalyst activity and stability.

24.1 Introduction

Graphitic acetylene carbon blacks manufactured by pyrolysis are the most widely used supports in electrochemical applications due to their (1) tolerance to acidic and alkaline media; (2) complex microporous structure, yielding high catalyst layer porosity and high specific surface area; (3) high electronic conductivity; and (4) low cost. Of the many commercially available carbon blacks, the most commonly employed carbons for proton exchange membrane fuel cell (PEMFC) catalyst applications are Vulcan XC-72R (Cabot Corporation) and TKK (Tanaka Kikinzoku Kogyo K.K.) HSAC, which are used either directly or following activation or preprocessing steps [1].

S. Shrestha • W.E. Mustain (✉)
Department of Chemical and Biomolecular Engineering, University of Connecticut,
191 Auditorium Rd., Unit 3222, Storrs, CT 06269-3222, USA
e-mail: mustain@engr.uconn.edu

M. Shao (ed.), *Electrocatalysis in Fuel Cells*, Lecture Notes in Energy 9,
DOI 10.1007/978-1-4471-4911-8_24, © Springer-Verlag London 2013

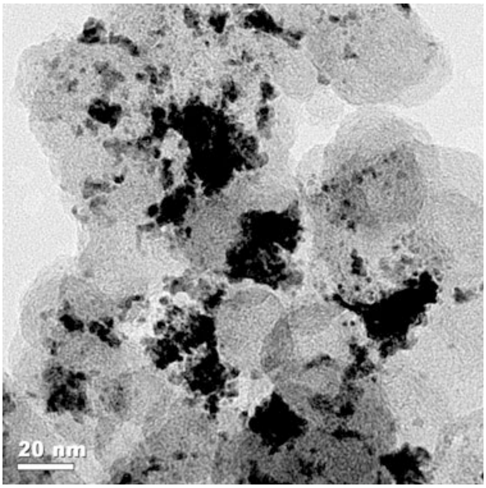

Fig. 24.1 TEM image of platinized Vulcan XC-72R without pretreatment

Preprocessing of the carbon support is done to aid in the dispersion of catalytically active Pt nanoparticles, which are typically 2–5 nm in diameter [2, 3], and/or improve catalyst support durability. A typical TEM image for a Pt/Vulcan electrocatalyst using non-modified Vulcan XC-72R® is shown in Fig. 24.1.

For non-modified carbon, the Pt cations that approach the surface during the deposition process, typically a polyol process where ethylene glycol acts as both the solvent and kinetically slow reducing agent, mostly encounter a graphitic π-stabilized sp^2-bonded structure with completely saturated valences and nearly zero unpaired surface electrons. Thus, on non-modified carbon, platinum tends to deposit almost exclusively at defect or edge sites that have free electrons in bonding orbitals, which are located at the interfaces (kinks, folds, etc.) between carbon particles.

Carbon modification is typically achieved through two primary methods: graphitization and chemically induced surface modification. Graphitization of the carbon support is achieved by exposure to extreme temperatures (2,600–3,000 °C) in inert atmosphere (He); when this is done to Vulcan, it is referred to as Vulcite®. Graphitization has some advantages, including a reduction in the number of edge and defect sites and an increase in the length of graphitic carbon domains, which is believed to increase the electrochemical stability of carbon. However, there are a few disadvantages, including a lowering of the specific surface area [4] and a further reduction in the number of deposition sites for Pt. Therefore, these materials typically require chemically induced surface modification to make Pt deposition with good dispersion possible.

Chemical modification of the carbon support surface is accomplished by exposure to a highly caustic aqueous environment, either by thermal treatment in air or chemical oxidation (typically a concentrated HNO_3/H_2SO_4 solution). Nearly all highly graphitic supports are pretreated; however, it is also common to pretreat non-graphitized supports [5] to improve Pt dispersion. The purpose of such a treatment is to disrupt the sp^2 hybridization of the support surface through the introduction of

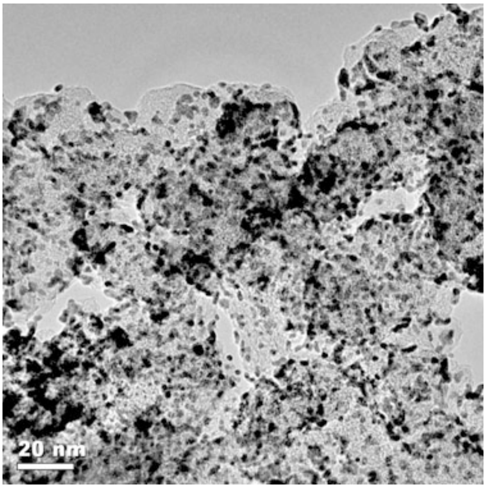

Fig. 24.2 Highly dispersed Pt nanoparticles deposited on acid-oxidized Vulcan XC-72R

oxygen functional groups such as carboxyl (COOH), hydroxyl (COH), and carbonyl (C=O) [6]. The presence of surface functional groups improves the dispersion of Pt on the support surface considerably. This is shown by the TEM image for a surface-modified Pt/Vulcan XC-72R electrocatalyst in Fig. 24.2. The catalyst loading is ca. 50 wt%, the same as Fig. 24.1.

The enhanced Pt dispersion has been shown to lead to Pt electrocatalysts with high activity for the oxygen reduction reaction (ORR), Eq. (24.1).

$$O_2 + 4H^+ + 4e^- \rightarrow H_2O, \quad E^0 = 1.23\,\mathrm{V} \tag{24.1}$$

The ORR is of particular interest to PEMFC researchers since it is the performance-limiting reaction, requiring four proton and electron transfer steps and the breaking of the O=O bond. The mass activity (A/mg$_{\mathrm{Pt}}$) of Pt/Vulcan and Pt/TKK catalysts is typically reported between 0.16 and 0.20 A/mg$_{\mathrm{Pt}}$ @ 0.9 V vs. NHE [1], with the Pt/TKK catalyst being considerably better at high Pt loadings (~50 % Pt/C) than Pt/Vulcan.

Though these catalyst systems show reasonable activity (catalysts with activities closer to or exceeding commercial and government targets employ Pt-alloy catalysts, with their own limitations, for the ORR [7]), the durability of these materials for thousands of hours of operation is limited by the stability of both the Pt catalyst and the carbon support material. Stability concerns for Pt and carbon-based supports will be detailed in Sects. 24.1.1 and 24.1.2, respectively.

24.1.1 Stability of Pt Nanoparticles Supported on Carbon

Perhaps the most pressing issue with regard to ORR electrocatalysts for PEMFCs is the slow, but drastic, decrease in the Pt mass activity with time, which has been

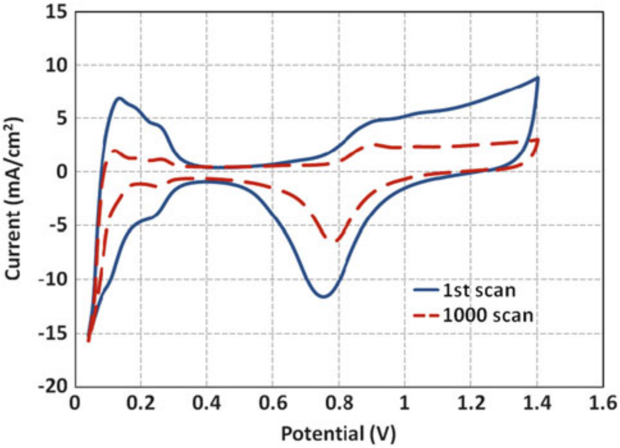

Fig. 24.3 Cyclic voltammogram of a 5 cm^2 PEMFC with a Pt/Vulcan anode and cathode, Nafion® 117 electrolyte; 80 °C

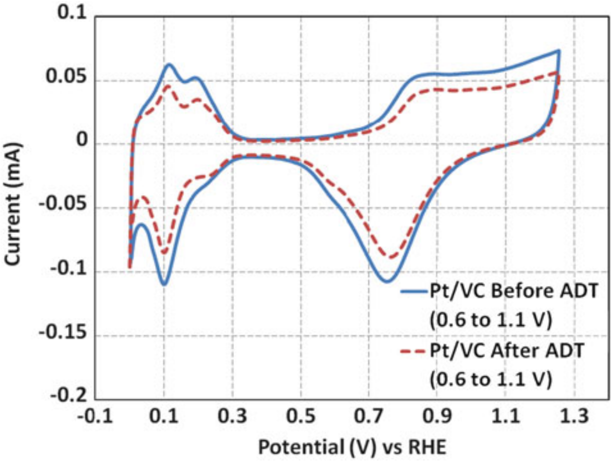

Fig. 24.4 Cyclic voltammograms for Pt/Vulcan electrocatalyst deposited on a glassy carbon disk electrode in 0.1 M $HClO_4$ thermostated at 25 °C

confirmed both in situ (PEM stack testing) and ex situ (three-electrode testing). An example of an in situ test is shown in Fig. 24.3, where Pt/Vulcan was loaded into a 5 cm^2 PEMFC single-cell stack and exposed to 1,000 harsh voltammetric cycles between 0.0 and 1.4 V.

The loss of electrochemically active surface area (ECA) for the cell shown in Fig. 24.3 was 77 % over the experimental period. Even a less harsh ex situ cycling test in 0.1 M $HClO_4$ at 25 °C between 0.6 and 1.1 V vs. NHE revealed significant losses in the ECA, approximately 31 % over 1,000 cycles, which is shown in Fig. 24.4.

Fig. 24.5 SEM images of Pt/HOPG (**a**) before and (**b**) after electrochemical cycling

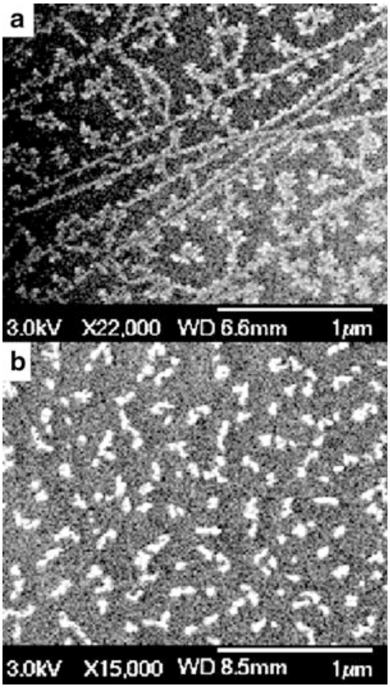

The loss in ECA can be coupled to significant changes in the catalyst structure over time. This is well shown by Pt nanoparticles evaporated onto highly ordered pyrolytic graphite (HOPG). Pt/HOPG is an interesting system since it consists of nearly defect-free carbon, showing the true interaction of Pt with oxygen-free C. A SEM image of newly prepared Pt/HOPG and electrochemically treated HOPG are shown in Figs. 24.5a and 24.5b, respectively; the data and images were collected in collaboration with Prof. Brian Willis at the University of Connecticut. Following preparation, the Pt/HOPG catalyst was exposed to 0.1 M $HClO_4$ and cycled between 0.6 and 1.2 V vs. NHE for 100 cycles. Post-cycling, the supported Pt particles appear to have both agglomerated and grown in size.

Shao-Horn and coworkers recently summarized the possible pathways for Pt ECA loss on Pt/C electrocatalysts, Fig. 24.8 [8]. It was shown that four primary mechanisms are active: (a) Pt nanoparticle growth via modified Ostwald ripening, (b) coalescence via crystal migration, (c) detachment from the support, and (d) dissolution and precipitation in the ion conductor. The most widely cited evidence for the crystal migration mechanism is the particle-size distribution following lifetime chronoamperometric testing [9, 10]. Following electrochemical treatment, the observed Pt particle-size distribution was asymptotic and showed a distinct tail at large particle sizes. In previous heterogeneous catalysis studies, this particle-size distribution was considered consistent with growth via crystal migration [11]. However, one critical aspect of Pt ECA loss that this mechanism is not able to explain is its potential dependence, which has been observed by several researchers [12]. Evidence for Pt detachment from the support, either through carbon degradation or limited bonding/interaction of Pt with the support, was recently reported by Mayrhofer et al. using a TEM gold finder grid to make observations on the same Pt/C ORR catalyst before and after electrochemical treatment in a three-electrode cell [13, 14]. They concluded, however, that the overall mechanism was not necessarily dominated by detachment and varied with the type and severity of the electrochemical treatment.

The potential dependence of ECA loss for Pt/C ORR electrocatalysts has led most researchers to point toward modified Ostwald ripening as the dominant mechanism for performance loss at the PEMFC cathode. Here, Pt ions result from the dissolution of metallic and oxidized platinum surface species, which are subsequently redeposited onto larger particles due to the highly reducing environment of the PEMFC cathode and its operating electrode potential [15].

Currently, the most widely accepted mechanism for Pt detachment was proposed by Meyers and Darling [16, 17] who considered two processes in a simplified model: dissolution of metallic Pt (Eq. 24.2) and oxidation of metallic Pt by water followed by the chemical dissolution of the surface oxide in acidic media (Eqs. 24.3 and 24.4).

$$\mathrm{Pt} \leftrightarrow \mathrm{Pt}^{2+} + 2\mathrm{e}^{-} \tag{24.2}$$

$$\mathrm{Pt} + \mathrm{H_2O} \leftrightarrow \mathrm{PtO} + 2\mathrm{H}^{+} + 2\mathrm{e}^{-} \tag{24.3}$$

$$\mathrm{PtO} + 2\mathrm{H}^{+} \leftrightarrow \mathrm{Pt}^{2+} + \mathrm{H_2O} \tag{24.4}$$

Equations (24.2)–(24.4) all have a Nernstian dependence; this is shown for the dissolution of metallic platinum in Eq. (24.5).

$$\mathrm{Pt} \leftrightarrow \mathrm{Pt}^{+2} + 2\mathrm{e}^{-}; \quad \log\left[\mathrm{Pt}^{+2}\right] = \frac{2F}{2.303RT}\left(E - E^{*}\right) \tag{24.5}$$

where F is Faraday's constant, R is the ideal gas constant, T is the temperature, E is the electrode potential, and E^* is the formal potential for the reaction of interest. The potential dependence for the other steps can be found in ref. [15]. Pt^{2+} is then plated either elsewhere within the cathode or even in the proton exchange membrane (mechanism d in Fig. 24.6). Of course, deposition of Pt^{2+} onto larger Pt particles is thermodynamically favored because of their lower surface free energy due to reduced lattice strain. Since Pt oxidation occurs at ORR-relevant potentials ($0.6 < E < 0.8$ V vs. NHE), the Pt dissolution mechanism is always active on Pt/C catalysts, which facilitates rapid Pt ECA loss.

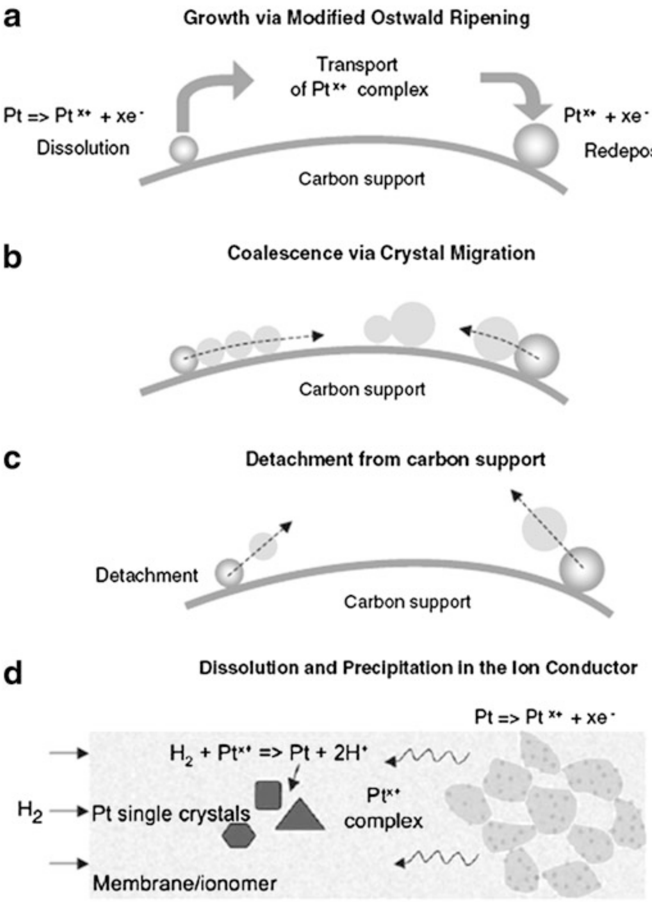

Fig. 24.6 Illustration of the possible mechanisms for Pt ECA loss in the PEMFC cathode (reproduced with permission from [8])

24.1.2 Electrochemical Stability of Carbon

Though less important during steady state cell operation, the oxidation of the carbon support is a significant issue for PEMFCs during startup and shutdown, which is particularly important for automotive and other mobile applications. During these transient states, a large hydrogen concentration gradient and air/fuel boundary are established, which very quickly drives the anode potential positive, causing the cell polarity to switch. In turn, the oxygen electrode potential also rises to potentials in excess of 1.5 V, where the only fuels available for oxidation are the graphitic carbon support and water [18]. Though water electrolysis is the dominant reaction, as the potential rises, carbon corrosion becomes more competitive. This is shown by chronoamperometric experiments performed by Maass and coworkers in

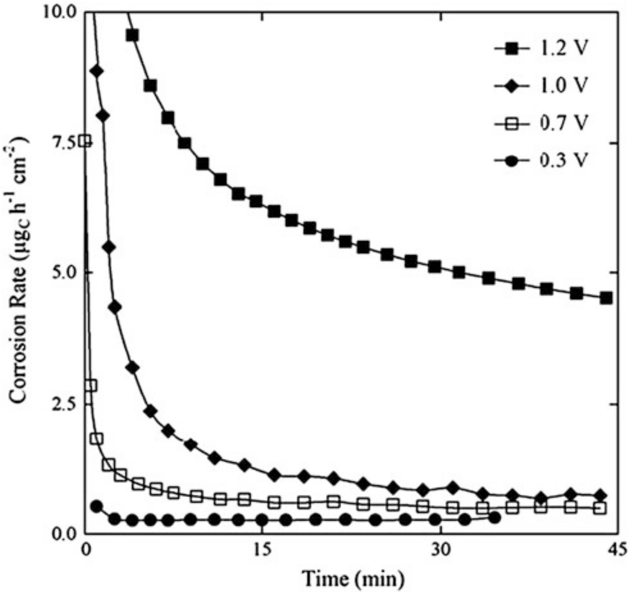

Fig. 24.7 Potential dependence of the specific carbon (Ketjenblack EC300J) corrosion current as a function of electrode potential vs. RHE (reproduced with permission from [19])

Fig. 24.7 where the specific corrosion rate (μg C/h/cm^2) was increased by orders of magnitude from 0.3 to 1.2 V vs. a quasi RHE [19].

At elevated potential, surface carbon atoms are activated through a simple one electron oxidation, Eq. (24.6). Following activation, the resulting carbon species participates in consecutive reactions with water to yield CO_2, which are shown as Eqs. (24.7) and (24.8) [20, 21]. The overall reaction is given as Eq. (24.9).

$$C_s \rightarrow C_s{}^+ + e^- \tag{24.6}$$

$$C_s{}^+ + H_2O \rightarrow C_sO + 2H^+ + e^- \tag{24.7}$$

$$C_sO + H_2O \rightarrow CO_2(g) + 2H^+ + 2e^- \tag{24.8}$$

$$C + 2H_2O \rightarrow CO_2(g) + 4H^+ + 4e^-; \quad E^0 = 0.207\,\text{vs. NHE} \tag{24.9}$$

It has also been shown that the Pt acts as a carbon corrosion catalyst [1, 2], which likely localizes a significant portion of the carbon loss to areas in direct contact with Pt. Localized degradation has the potential to orphan Pt particles and expedite their dissolution, leading to severe decreases in the ECA and cell performance with time, akin to Fig. 24.3 where the electrode potential was forced to similarly high potentials.

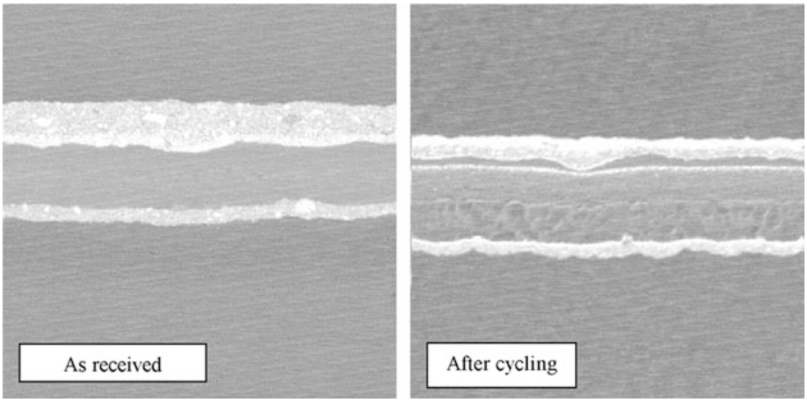

Fig. 24.8 Cross-sectional electron micrographs taken before and after electrochemical cycling of a PEMFC MEA [22]

In addition to orphaning Pt particles and a reduction in the ECA, carbon support degradation also disrupts the delicate microstructure that is engineered within the catalyst layer during membrane electrode assembly (MEA) fabrication. As the support is oxidized to CO_2, the structure collapses under stack compression. This is shown in Fig. 24.8 where electron micrographs of PEMFC MEAs before and after testing by Myers and Darling are shown [22]. In Fig. 24.8, the cathode layer (top) has clearly collapsed under the compressive loading of the cell stack. This can have severe implications on cell/stack performance as mass transfer in/out of the cathode layer can lead to oxygenate starvation and flooding.

24.1.3 Alternatives to Pt/Carbon Black Supports

The stability limitations for traditional Pt/C electrocatalysts have led researchers to suggest that new electrocatalyst supports should be designed that:

- Have enhanced intrinsic stability compared to Vulcan and TKK
- Possess a more complex, controllable microstructure
- Interact more strongly with Pt than graphite to:
  - Improve Pt dispersion
  - Reduce Pt surface mobility
  - Enhance the intrinsic electrochemical activity or specific activity (A/cm^2_{Pt}) of Pt

To date, there have been two notable approaches: (1) highly graphitic sp^2-like support materials (often with a microstructure very much different than Vulcan/TKK) that include the synthesis of adatom (N, S, B, and P)-functionalized carbons and (2) non-carbon support materials, which are typically electrically conductive ceramics (oxides, carbides, nitrides). Both of these approaches, along with their promises and challenges, will be discussed in Sects. 24.2 and 24.3, respectively.

24.2 "Advanced" Carbon Supports

Application of carbon as a catalyst support can be traced back as early as 1934, when it was shown that catalyst supported on charcoal could be used for the conversion of sulfur-containing naphthalene to tetrahydronaphthalene [23]. In the 1980s and 1990s, scientists at Los Alamos National Laboratory (LANL) were able to reduce the Pt loading in the PEMFC cathode to 0.4 mg/cm^2, which was considerably lower than the Pt loading of 4 mg/cm^2 used in early PEMFCs by NASA for the Gemini space flights in 1960s by using proton conducting ionomer infused carbon black (Vulcan XC-72R) as a support for platinum electrocatalyst [24]. Still today, platinum supported on carbon black is considered the standard catalyst for PEMFCs. This signifies the prominent role carbon has in R & D of heterogeneous catalysis and in low-temperature PEMFCs.

Over the past decades, an extensive body of work has been carried out to reduce the loading of supported catalysts, which are usually expensive transition or noble metals. To reduce loading and increase active surface area, the catalyst particle size has been reduced to the nanometer scale. To accommodate such small nanoparticles with high dispersion, high-surface-area supports are preferred. High-surface-area supports help to increase catalyst utilization by reducing particle agglomeration and coarsening, which demands that the nanoparticles be dispersed uniformly. As such, various methods for ultralow loading of Pt nanoparticles (NPs) on carbon black have been developed for PEMFC applications [25, 26]. Carbon also acts as the current collector in PEMFC electrodes and provides the microstructure for mass transfer of reactants and products.

24.2.1 Surface Chemistry, Porosity, and Metal Deposition

The microstructure of carbon blacks consists of carbon crystallites of varying sizes, which are arranged in a disordered fashion. Each crystallite is composed of polyaromatic layers of carbons in hexagonal rings with sp^2 hybridization. The half-filled p orbitals provide e-conductivity through mobile π electrons. For catalysis, the most interesting regions of the carbons are the edge and defect sites where the carbon has unfilled valence orbitals or dangling bonds, making these edge and defect sites reactive. Heteroatoms such as H, N, and O can form bonds with carbon atoms at these sites, and the chemical nature of the carbon can be significantly influenced by these heteroatoms. The basal planes, sections of hexagonal rings of carbon, are less active than the edge or defect sites; the edge plane of a graphene sheet has a maximum heterogeneous electron transfer rate constant of 0.01 cm/s, while the basal plane has a maximum transfer rate of 10^{-9} cm/s [27]. These edge/defect sites, along with steps, are believed to be the active sites on carbon [28]. Hence, carbons with a higher ratio of edge/defect sites to basal planes are preferred for catalysis.

Porosity and surface area are also very important. For a catalyst support, high surface area is a desired quality. High surface area is typically the result of a high concentration of micropores, which are voids between carbon structures having a diameter less than 2 nm. Micropores have been found to greatly affect the dispersion and activity of the catalyst [28]. On the other hand, they hinder mass transfer. In contrast, mesopores (2–50 nm) and macropores (>50 nm) provide efficient pathways for mass transfer. Therefore, accessibility of the micropores through a network of mesopores and macropores greatly impacts the performance of the carbon blacks. Unfortunately, the pore structure and network of carbon blacks have not been well defined to date. Hence, studying the relationship between micropores and activity is often difficult. Moreover, measuring the effective porosity and surface area depends on the size of the probe molecules. Larger molecules do not infiltrate smaller pores and might provide an underestimation of the pore volume or be unable to register the existence of pores below a certain size. On the other hand, smaller molecules might infiltrate pores that are not available to the substrates involved in the reaction, providing a high surface area that may not be utilizable for the targeted application.

Surface oxides present on graphitic surface have been extensively studied. Three types of surface oxides have been identified, which are shown in Fig. 24.9: acidic, basic, and neutral. Acidic surface oxides are formed by oxidizing agents at room temperature or when carbon is treated with oxygen up to 400 °C. Carboxyl, lactones, anhydrides, hydroxyl, and lactol groups are the most common acidic surface oxides. Carboxylic groups are especially acidic, though they are thermally unstable and decompose at 300–800 °C under vacuum or inert atmosphere. Basic (pyrone, chromene, and quinine) surface oxides are formed when oxidized carbon is freed from surface oxides at high temperature in vacuum or inert atmosphere and exposed to air after cooling down to low temperature. Neutral surface oxides are formed at the unsaturated sites ($>C{=}C<$) by irreversible adsorption of oxygen molecules. The concentration and nature of surface oxides depends on the carbon, the oxidizing reagent, and the oxidizing procedure. Furthermore, the oxidation of carbon can change porosity, surface area, crystallite size, resistivity, and wettability. A mild oxidation may increase surface area through the opening of pores; however, if the carbon is highly graphitic, or if the fine pores are in close proximity, oxidation can have a negligible or reverse effect.

These oxide groups are generally believed to act as nucleation sites for Pt growth during metal deposition, making control over the support surface chemistry critical. For optimal dispersion and a narrow particle-size distribution, nucleation sites should be evenly distributed on the support surface, and metal growth should take place at a similar rate at all sites without planar movement of the supported atoms. Either of these mechanisms would lead to a large particles and a heterogeneous particle-size distribution.

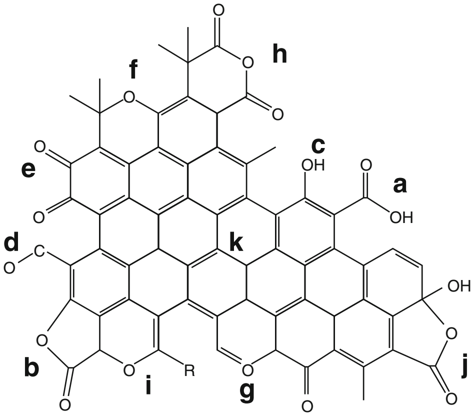

Fig. 24.9 Oxygen functionalities of carbon: (a) carboxyl, (b) lactone, (c) hydroxyl, (d) carbonyl, (e) quinine, (f) ether, (g) pyrone, (h) carboxylic anhydride, (i) chromene, (j) lactol, and (k) π-electron density [29]

In PEMFCs, where carbon also acts as the primary electron transport media, efficient electron transfer between the catalyst and carbon is critical and can only occur if the catalyst particle is present at edge/defect sites where the heterogeneous electron transfer rate is higher. Whether interaction at these active sites can increase catalyst activity fundamentally through geometric and electronic modification will be discussed later. For example, using a colloidal method for Pt deposition on graphitic carbon, where reduced colloids of Pt salt are mixed externally with high-surface-area carbon, does not utilize the surface properties of carbon to control the electron transfer site. Thus, researchers typically yield highly dispersed Pt/C catalysts with very poor ORR activity [30]. This is an interesting example where an electrocatalyst activity toward the ORR is not limited by the catalytic activity of the electroactive material, but by electron transfer between the catalyst and support.

The dispersion of supported metal particles not only depends on the physico-chemical properties of carbon but also on the deposition technique. Generally, higher surface-area supports result in higher dispersion of metal nanoparticles (though this effect is muted for ultra high-surface-area carbons, >200 m^2/g [21]). One of the simplest procedures for Pt deposition is impregnation. First, a metal precursor (commonly H_2PtCl_6) solution is impregnated into the pores of carbon by capillary action. Next, the solvent is evaporated, leaving precipitates that are reduced in a subsequent step. In this process, adsorption of the catalyst salt ion is crucial, but before that, the metal salt solution must wet or penetrate the entire available surface. This makes oxidative pretreatment an essential step prior to deposition. Supercritical deposition methods tend to wet the pores more completely than atmospheric aqueous approaches [25]. Of course, porosity also plays an important role in this case, which is why mesopores are believed to provide better dispersion.

In 1978, Brunelle showed that Pt could be efficiently dispersed through ion exchange with surface functionals on silica [31]. He showed that when the pH of the impregnating solution is higher than the isoelectric point (IP) or point of zero charge (PZC), the surface amphoteric oxides are negatively charged. Cationic precursors (i.e. $Pt(NH_3)_4^{2+}$) are attracted to these negatively charged sites. On the other hand, if the pH is lower than the IP or PZC an anionic precursor (i.e. $PtCl_6^{2-}$) should be selected. Though this work focused on silica and alumina supports, it has been extended to carbon as well [32], and several models exist describing Pt precursor adsorption on carbon [33]. These models claim that basic oxygen groups (or electron rich π-sites) are stronger anchoring sites than the acidic surface oxides.

On pregraphitized carbon blacks, Coloma et al. concluded that surface oxygen groups assist in wetting the surface and act as primary anchor sites [34]. However, whether the metal interacts directly with the surface oxygen groups has not been rigorously verified experimentally. Generally, enhanced dispersion is used as the primary indicator for improved metal–support interaction. However, as discussed above, improved dispersion after oxidation can be caused by a number of factors that are difficult to decouple. Physical changes in the carbon due to oxidation might help in metal dispersion rather than formation of surface oxide groups. Some oxide groups (i.e., C=O) can hinder surface diffusion of the supported catalyst particles, which might affect particle growth and agglomeration. In addition, the effect of heat treatment during reduction should be considered when analyzing the final metal dispersion. If heat treatment is carried out to reduce metal precipitates, thermally unstable oxygen groups can decompose, which will remove any interaction between Pt and surface oxygen groups. Upon heat treatment in H_2, weak acidic surface oxygen groups decompose, and Pt particles interact mainly with π-sites, which are delocalized areas on graphitized carbon surface with high π-electron density. The remaining stable oxygen groups decrease Pt interaction with the π-sites through an electron-withdrawing effect. Moreover, it can be difficult to study the effect of surface oxygen groups experimentally as the surface is almost always in flux during metal deposition where various surface oxides are formed or converted from one form to another. For example, anhydrides can be converted to carboxylic groups [32]. In addition, some researchers have reported oxidative treatments that do not yield better dispersion [33].

24.2.2 Carbon Nanotubes

Carbon nanotubes (CNTs) are the most popular advanced carbon support for Pt NPs. CNTs can be classified as single-walled carbon nanotubes (SWCNTs) or multiwalled carbon nanotubes (MWCNTs) depending on the number of graphene walls. They are also characterized by their geometry as armchair, zigzag, and chiral depending on the arrangement of carbon bonds on the curved graphene surface. The surface area of CNTs depends on the number of graphene sheets that comprise the walls: 1,315 m^2/g for single wall, 580–680 m^2/g for two walls, 295–430 m^2/g for five walls, and so on [35]. CNTs act as both metal and semiconductor depending on the arrangement of carbon atoms. The electronic conductivity is very high (10^8/ohm-m) in metallic CNTs as scattering does not occur [36, 37].

Since pristine CNTs are very difficult to disperse in solution because of their high graphiticity, surface functionalization is often carried out to prepare the surface for metallization. There are various methods of surface functionalization, one of the simplest one being chemical oxidation [38–40]. Besides chemical oxidation, other methods such as sonochemical treatment and microwave irradiation can also introduce oxygen groups on CNTs. By avoiding high heat and using proper reducing agents such as ethylene glycol (EG), sintering during the reduction step can be avoided. Surprisingly, reduction of the metal precursor can also take place on SWCNT in the absence of a reducing reagent. Choi et al. reported spontaneous reduction of $PtCl_4^{2-}$ and $AuCl_4^{-1}$ on SWCNTs, which they attributed to the formation of redox pairs where the Fermi level of the SWCNT was greater than the reduction potential of $PtCl_4^{2-}$ and $AuCl_4^{-1}$ [41]. In another interesting study, Sheng et al. showed that on amine-functionalized MWCNTs, even after heat treatment from 200 to 600 °C, the particle size of Pt NPs remained constant at 2 nm [42]. Hence, like in carbon blacks, surface functionalization and catalyst deposition method influence both metal dispersion and metal–support interaction.

There have been some promising studies showing that CNT-supported Pt shows enhanced ORR specific activity than that of conventional Pt/C. Against 40 wt% Pt/Vulcan (E-TEK), Kongkanand et al. demonstrated that the onset potential of Pt/SWCNT shifted 10 mV positive to Pt/C despite the ESA of the Pt/SWCNT being lower (17.8 m^2/g_{Pt} vs. 33.5 m^2/g_{Pt}) than Pt/C. Recently, Kim et al. deposited Pt on amine-functionalized MWCNT treated with HCl and heated at 220 °C in air, both for 2 h [42]. The intrinsic activity of such Pt/MWCNT was 0.95 mA/cm^2_{Pt}, higher than that of as-prepared Pt/MWCNT (0.40 mA/cm^2_{Pt}), acid-treated Pt/MWCNT (0.75 mA/cm^2_{Pt}), and 46 wt% Pt/TKK (0.36 mA/cm^2_{Pt}). On a similar catalyst, Sheng et al. reported comparable specific activity compared to Pt/C [42]. However, from these studies it is not clear if the enhanced specific activity was achieved through strong interaction with the support. For the study by Kongkanand et al., the enhancement was very small, while for Kim et al. the enhancement could be due to their resulting Pt nanostructure where Pt particles blanketed the CNTs.

Numerous studies have shown that CNT-supported Pt catalysts exhibit higher electrochemical stability under accelerated degradation test than that of carbon black-supported Pt. A major source of this stability is likely enhanced stability of the support itself caused by its highly graphitic nature compared to carbon black. In addition, authors have given credit to the strong interaction between Pt NPs and CNTs, though the nature of this interaction is ambiguous and has not been studied with sufficient detail. Furthermore, Pt/MWCNTs have been reported to be more stable than Pt/SWCNTs. Wang et al. has reasoned that the top layers of the MWCNT act as a protective sheath for inner layers, which then have fewer sites for corrosion [43].

24.2.3 Graphene

Graphene is a 2D crystal of sp^2-hybridized carbon atoms. In this form, carbon exhibits unusual electronic properties. For instance, the charge carriers on a single-atomic graphene sheet are massless Dirac fermions with speeds 300 times smaller than the speed of light [44]. The electronic properties of graphene change drastically even with addition of one additional layer; bilayer graphene can act as tunable gap semiconductor [45]. With ten or more layers, layered graphene acts as a thin film of graphite [46]. It also has robust mechanical features like extremely high breaking strength (~40 N/m) and Young's modulus (~1.0 TPa) [47]. The theoretical specific surface area of single-plane graphene is 2,630 m^2/g [35–48]; however, utilizing the full surface area is very challenging as they tend to aggregate due to van der Waals forces. Bulk produced graphenes by chemical or thermal exfoliation of HOPG are usually a few layers thick. In addition, its properties differ considerably depending on the oxidation/reduction treatment, making reproducibility a potential issue. Thus, graphene as a carbon support is promising, but research in this area is not mature enough. Pt on wrinkled graphene sheets prepared by thermal exfoliation of chemically oxidized graphite flakes was shown to have higher mass activity and stability by Kou et al., but the authors did not present any data on specific activity [49].

24.2.4 Graphitic Nanofiber/Carbon Nanofiber

While graphene and CNTs are single to few layers of simple graphene structure, carbon nanofiber (CNF) or graphitic nanofiber (GNF) have a multilayer complex graphene structure, which makes it a very interesting alternative support. CNF has been classified into fishbone (herringbone) with graphene layers at an acute angle to the growth axis, platelet (deck of cards) with graphene layers perpendicular to the growth axis, and tubular (parallel) with graphene layers parallel to the growth axis. Although the tubular CNF has similar arrangement to the graphitic planes of MWCNT, the former has a solid core in contrast to the hollow core of the latter [50]. However, some authors do not make such a distinction [51]. It can also have different structures such as bidirectional, helical, twisted, and branched [52]. The diameter of the CNF (2–100 nm) depends on the size of the catalyst that catalyzes its growth [40, 52]. Like CNTs and graphene, surface functionalization must be carried out to achieve acceptable dispersion of metal particles.

The most attractive feature of CNF is the exposed graphitic edge planes on the surface. The fishbone CNF (f-CNF) and platelet CNF (p-CBF) have a very high edge to basal plane ratio, while tubular CNF (t-CNF) has a very high basal to edge plane ratio. Hence, catalyst particles on f-CNF and p-CNF are expected to have higher ORR activity than that of t-CNF. Researchers have shown that metal-free f-CNF and p-CNF are more active than on t-CNF [53, 54]. Also, Zheng et al. concluded that 5 wt% Pd on f-CNF and p-CNF has higher ORR activity than that on activated carbon [55]. The unique arrangement of sp^2 planes in f-CNF and p-CNF also allow for a unique pathway for electron conduction that occurs by hopping along the a-axis (basal plane) and c-axis (perpendicular to the basal plane) [56, 57]. However, Yoon et al. showed that the microstructure of CNF is more complex than a planar or conical stack of graphene as previously assumed [58, 59]. They found

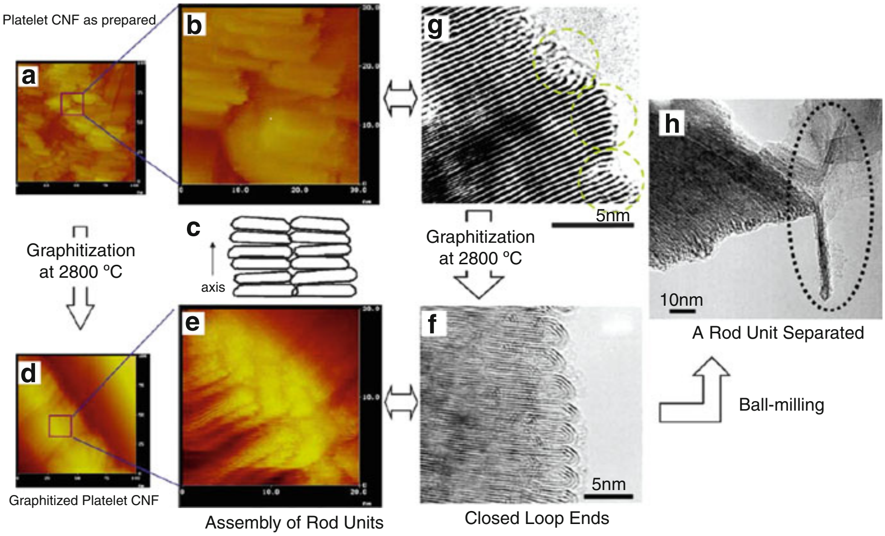

Fig. 24.10 STM images of platelet CNF before (**a**, **b**) and after (**d**, **e**) graphitization, HR-TEM pictures of as platelet CNF before (**g**) and after (**f**) graphitization, HR-TEM image of isolated rod like graphitic unit (**h**), and schematic showing stacking of rod like unit [59]

that the basic structural unit of the CNFs to be carbon nano-rods, 2.5 nm in diameter and varying lengths, consisting of a few graphene layers with open edges at low temperature that close at high graphitization temperature (2,800 °C, used by authors) to conical or pyramidal caps (Fig. 24.10). They proposed that these rods arrange in carbon nano-plates, the stacking of which gives rise to fishbone or platelet or tubular structures. This finding demands a closer experimental and theoretical look into structure and properties of CNFs.

24.2.5 Carbon Aerogel

Carbon aerogel is a pyrolyzed organic aerogel usually synthesized using resorcinol–formaldehyde (RF) sol-gels. In a typical synthesis [60, 61], a mixture of resorcinol (R) and formaldehyde (F) in a certain molar ratio is base or acid catalyzed to form a colloidal sol, which is converted to a gel by slow heating to promote cross-linkage. At this stage, the aqueous solvent can be exchanged with an organic solvent. Then, the gel is dried subcritically in air/nitrogen to produce a xerogel, supercritically in CO_2 to produce an aerogel, or freeze-drying to produce a cryogel. The latter two drying methods prevent collapse of the structure by avoiding formation of a liquid–vapor interface, retaining high porosity. The surface area, mesoporosity/microporosity, pore-size distribution, surface texture, and carbon particle size can be modified by controlling reactant ratio (R/F), gel pH, catalyst, curing and drying process, and carbonization temperature. The microstructure of the carbon aerogel consists of slightly overlapping carbon nanospheres in a continuous chain giving arise to a porous 3D interconnected network [62]. Aerogels are attractive for PEMFCs because of their mesoporosity; high mesoporosity can be obtained independent of micropores [62]. In addition, by molding, the aerogels can be produced in various shapes such as monoliths, beads, and thin films [63]. The performance of carbon aerogel-supported Pt catalysts was reported in a PEMFC by Smirnova and coworkers [64]. During 60 h of operation, the cell showed good ECA retention. Unfortunately, the cell performance was hindered significantly by mass transfer limitations, though correction for IR, and mass transport resistances showed good catalyst activity.

24.2.6 Ordered Mesoporous Carbon

Ordered mesoporous carbon (OMC) was first reported by Ryoo et al. which they called CMK-1 with mesopores of 3 nm diameter [65]. CMK-1 was synthesized in a MCM-48 silica template with cubic (*Ia3d*) symmetry, though precise control over its microstructure was difficult since CMK-1 is not an exact inverse replica of MCM-48. OMC displaying exact inverse replication of its template was made by Jun et al. using SBA-15 with hexagonal (*p6mm*) symmetry [66]. This was possible because the periodic mesopores in SBA-15 are interconnected through pores in the walls of the template [67, 68].

The field of ordered mesoporous carbon has seen tremendous growth since then; the pore structure can be modified, the particle morphology can be controlled, the carbon fibers can be graphitized, and the synthesis procedure has been greatly simplified such that OMC can be synthesized without a hard silica template by cooperative assembly between resol (phenol/formaldehyde) and the Pluronic triblock copolymer [67]. Furthermore, a rational pathway to control pore size has been developed using boric acid as the pore-expanding agent in the silica template where the pore size depends on the carbon precursor/boric acid molar ratio [69]. The boric acid phases out during carbonization and forms a layer between the carbonized precursor and the walls of the template. Great interest in OMC was sparked by a paper in *Nature* by Joo et al. [70] where they showed that the mass activity of 33 wt% Pt/OMC (0.1 A/mg$_{Pt}$) was 10× higher than that of 33 wt% Pt/carbon black (<0.01 A/mg$_{Pt}$) in O_2-saturated 0.1 M $HClO_4$ at 10,000 RPM with a scan rate of 50 mV/s (Fig. 24.11).

10,000 RPM is an unusually high rotation rate to report catalyst activity since any wobble in the RDE will cause significant turbulence at the electrode surface, which will disrupt the streamlines that are key to performance deconvolution and Levich analysis. In addition, 50 mV/s is not generally considered to be a reliable scan rate to determine catalyst activity since the system is not operating at steady state. To the author's knowledge, similar success has not been replicated in situ, even in a laboratory-scale PEMFC [71]. It is believed that the uniform pore-size distribution with good interconnectivity has the potential to reduce mass transfer

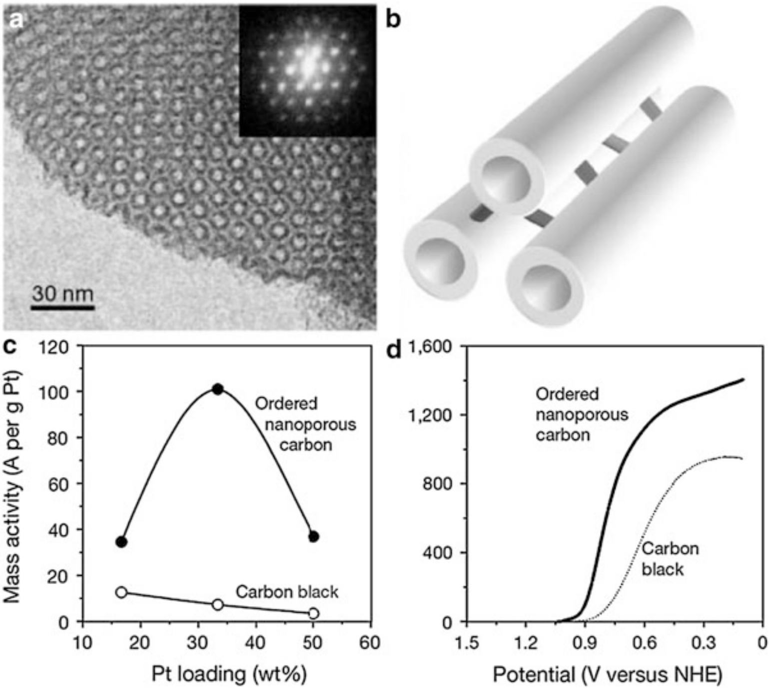

Fig. 24.11 TEM image of ordered nanoporous carbon (ONC) and its Fourier diffraction (**a**), schematic of ONC (**b**), mass activities of Pt on ONC and carbon black depending on the Pt loading (**c**), and ORR polarization curves measured in O_2-saturated 0.1 M $HClO_4$ at 10,000 RPM (**d**) [70]

through proper alignment in the direction of mass transfer [72]. Unlike carbon black, the defined pore structure and network allows for controlled study of such parameters on catalyst performance.

24.2.7 Hierarchically Ordered Mesoporous Carbon

Hierarchically ordered mesoporous carbons (HOMC) are attractive as a support for fuel cell applications because of their interconnected bimodal pore-size distribution. Both pore systems can be mesoporous or one can be mesoporous while other can be macroporous. While a mesoporous pore structure imparts high surface area and uniform distribution of catalyst particles, macropores provide efficient mass transfer. Of course, the interconnectivity between pores has a significant role in realizing the advantages of both pore structures. Also, a novel feature about these structures is that the two pore structures can be adjusted independently, allowing for good control over their porosity [73, 74]. Like OMC, controllable pore structure, and carbon microstructure and surface chemistry, makes them an attractive support for fuel cell catalysis. Fang et al. have shown that Pt on hollow core/mesoporous shell (HSMC) and ordered hierarchical nanostructured carbon (OHNC) outperforms Pt/Vulcan in single-cell fuel cell tests [75–77], which might be due to better mass transport; however, the authors did not discuss or present data supporting such hypothesis.

24.2.8 Carbon–Pt Interaction

The bonding of metal with carbon takes place by exchanging electrons between π-sites of carbon and vacant d-orbitals of metals. Metals lacking vacant d-orbitals such as Cu, Ag, Au, and Al have negligible interaction, while metals having large number of vacant d-orbitals such as Ti, V, and Nb form carbides. Metals with few vacant d-orbitals such as Fe, Co, and Ni dissolve carbon. In that respect, Pt has the fewest possible vacant orbitals. Hence its interaction with carbon is expected to be very weak. Indeed, first-principle studies have shown that the binding energy between Pt and graphene is low [78, 79]. However, the surface of synthesized carbons is not smooth; it has defects and edges, which have dangling bonds, and many theoretical studies have shown that Pt has higher adsorption energies at these sites [80–84]. In addition, surface curvature can induce stronger bonding by rehybridization of bonding orbitals like in CNTs. In CNTs, depending on their diameter, stronger metal interaction can occur relative to a flat graphene layer. Also, microstructural spatial constraints can cause geometric strain, which may positively affect activity.

The magnitude of the metal–support interaction also depends on the catalyst particle size. In a first-principle study by Okazaki-Maeda et al., the shape of Pt clusters ($n < 10$) appeared to depend on their size [85]. For a Pt cluster size $3 \leq n \leq 7$, vertical planar adsorption was stable, and for $n \geq 7$ adsorption as a parallel planer was energetically favorable. Their calculations showed that the interaction energy decreased as cluster size increased. Yamakawa et al. modeled Pt nucleation on graphene using a phase–field method coupled with first-principle calculations [86]. They demonstrated that as the coordination between Pt atoms increases, the interaction between Pt and graphene decreases. Their results support a Volmer–Weber (island) growth mode, which occurs when adsorbate–adsorbate interaction overcomes adsorbate–substrate interaction combined with lattice mismatch that cannot be compensated by structural relaxation alone [87]. They also point out that obtaining a uniform size distribution depends on the competing nucleation and growth. Instantaneous nucleation leads to homogeneous particle growth, while progressive nucleation leads to heterogeneous particle growth. This has been experimentally supported by Zoval et al. [88] who employed noncontact AFM and TEM to analyze Pt particles deposited on clean HOPG by pulsed potentiostatic deposition. They discovered that spontaneous deposition of Pt was taking place onto HOPG without application of any voltage. Moreover, most of the observed deposition was concentrated at step edges. According to the authors, the spontaneous reduction was caused by reducing equivalents such as aldehydes,

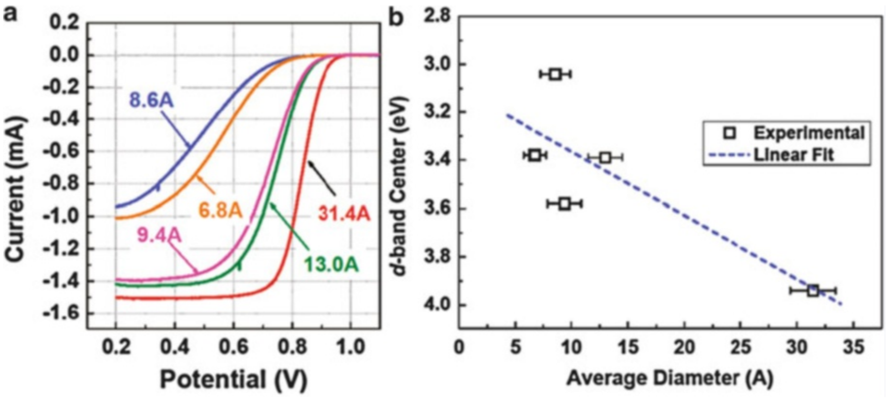

Fig. 24.12 ORR polarization curves of Pt with different sizes on glassy carbon electrode (**a**) and relation of Pt cluster size and d-band center (**b**) [89]

alcohols, and ketones on defect and edge sites. They also found that preoxidation of HOPG decreases the amount of Pt deposited by spontaneous reduction. This led the authors to anodically protect their electrode during pulsed electrodeposition, which resulted in a narrow particle-size distribution, though the distribution broadened as the average particle size increased from 2.6 to 7.2 nm.

Jinnouchi et al. showed that not only does the binding energy per Pt atom between graphene and Pt decrease as the particle size increases, the d-band center also lowers with respect to Fermi level. The lowering of d-band center was also correlated with an increase in the dissolution potential [90]. Toyoda et al. correlated the d-band center of Pt particles ranging from 6.8 to 31.4 Å deposited on a glassy carbon electrode using an arc plasma gun to their specific ORR activity [89]. As the Pt size increases, the d-band center increases or moves away from the Fermi level, and ORR activity increases accordingly (Fig. 24.12). This was also verified by X-ray photoelectron spectroscopy (XPS) as the binding energies of the Pt valence band and core 4f shifted closer to that of polycrystalline Pt as the particle size increased, though a perfect fit with the theoretical prediction was not obtained, which the authors ascribed to final state effects.

24.2.9 Nitrogen-Doped Carbons

In 1996, Roy et al. reported an enhancement in ORR activity when carbon black (Vulcan XC-72R) was doped with sulfur and nitrogen [91]. They attributed this enhancement to a decrease in Pt particle size on the doped carbon black at the same Pt loading, yielding a high specific surface area. However, the data they reported has a wide margin of error. In a series of papers by Ye et al. around the same time, ORR activity for Pt on carbon aerogel made from PAN was reported, which had significant nitrogen content [92–96]. Based on a XPS study of the N 1s peak, they suggested formation of a charge transfer complex between Pt and pyridinic nitrogen, though they did not observe any shift in the binding energy of the Pt 4f peak [96]. Also, they did not suggest that such an interaction may have an effect on the ORR activity of the supported Pt.

Metal-free carbon nanostructures doped with nitrogen (N) have also been investigated as ORR electrocatalysts, showing some activity in alkaline media. The ORR activity of these materials has led some to suggest that in metallized N-doped carbon, the catalyst may only catalyze the formation of active nitrogen-containing active sites [97], though this is unlikely, especially in acid media where the activity is very poor. A breakthrough in this field was obtained by Gong et al. who demonstrated nitrogen-doped vertically aligned carbon nanotubes (VACNTs) with higher ORR activity and stability than commercial Pt/C [98]. Same group reported remarkable ORR activity and stability for N-doped graphene [99]. Similarly, a number of metal-free nitrogen-doped carbon nanostructures have shown ORR activity [71, 100]. Interestingly, activity is higher when the carbon nanostructure is highly graphitic. A more detailed discussion on metal-free catalysts can be found in Chap. 12 of this book. Experimental and theoretical studies have shown that nitrogen doping induces both electronic and structural changes in carbon. The type of nitrogen defect, its concentration, and distribution can have significant effect on electronic and transport properties of CNT which is a subject of intense research. It has been suggested that doping with nitrogen may increase the metallic properties of CNTs [101]. Also, incorporation of nitrogen during the CNT growth can bring about significant structural changes. Ma et al. reported the formation of bamboo-like CNTs when mixture of CH_4 and N_2 were used as precursors over mesoporous silica plates containing Fe and Ni nanoparticles in a microwave plasma-assisted chemical vapor deposition [102]. Likewise, Kurt et al. reported vermicular CNTs decorated graphene sheets perpendicular to the surface with bias-enhanced hot-filament CVD using CH_4 and N_2 precursors [103]. Other groups have reported graphene basal plane distortions in carbon nanostructures doped with nitrogen during synthesis [104, 105]. This is probably caused by buckling around pentagonal defects, which is stabilized by the presence of N atoms [104, 106]. Hence, carbon nanostructures with nitrogen atoms doped during synthesis clearly have more structural deformations, distortions, or dislocations compared to their non-doped analogs. This can significantly impact NP nucleation, growth, distribution, and the structure of (electronic/geometric) supported Pt NPs, which requires further research.

Four types of nitrogen functionalities have been identified by XPS, which are illustrated in Fig. 24.13: pyridinic (N_{Py}), pyrrolic (NH), quaternary (NQ), and an unknown (N-X). N-X is assigned mainly to pyridine N-oxides, but can also be nitro, nitroso groups, or shake-up satellite peaks [107]. N_{Py} ($\approx$399.0 eV) donates one p-electron, while NH ($\approx$400.3 eV) donates two p-electrons. NQ, also called graphitic nitrogen, has a formal positive charge [107]. NQ exists in-plane, while N_{Py} and NH are edge structures. However, NQ can also be protonated N_{Py} and NH could also be pyridone, a hydroxylated pyridine. In addition, substitutional, interstitial, and sp^3-bonded N could also be present. This already intricate picture is

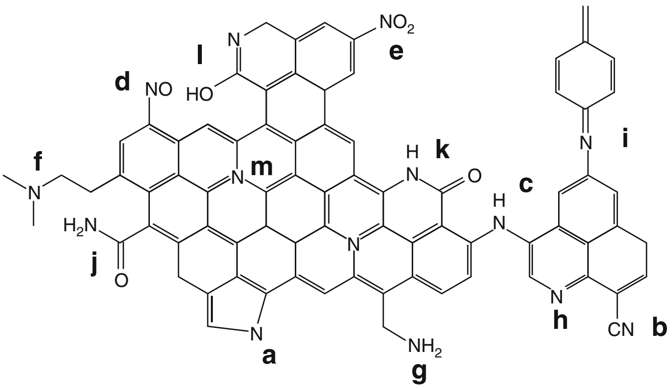

Fig. 24.13 Nitrogen functionalities of carbon: (a) pyrrole-like N, (b) nitrile, (c) secondary amine, (d) nitro group, (e) nitroso group, (f) tertiary amine, (g) primary amine, (h) pyridine-like N, (i) imine, (j) amide, (k) lactam, (l) pyridone, and (m) quaternary amine [29]

further complicated by tendency of these defects to group together [108]. Typically, pyridinic nitrogen is associated with the activity and dispersion of catalyst nanoparticles, though its exact role is unknown.

Computational studies have suggested that the nitrogen sites do not directly bond Pt atoms; N likely disrupts the π-electron distribution in the graphene layer by drawing electrons from carbon to itself [108, 109]. This is not unexpected as atomic N has higher electronegativity compared to C (3.04 vs. 2.55 P.U.). Thus, carbon atoms adjacent to surface N groups are localized low-electron-density sites, which likely act as electron transfer sites for Pt during deposition, leading to stronger Pt–support interactions than functional-free C. Electron transfer between the catalyst and support has the potential to enhance the intrinsic electrocatalytic activity of Pt for the ORR by shifting the d-band center relative to the Fermi level. The increase in dispersion of Pt on N-doped carbon due to enhanced nucleation rate is well established experimentally [110]. However, convincing experimental evidence showing significant electron transfer for Pt nanoparticles supported on N-functionalized carbon has yet to be presented. This may be due to the large Pt particles that are typically supported on these groups (~5 nm), which would have several atomic layers between the support and electrocatalyst surface. Besides, based on strong ORR performance of metal-free nitrogen-doped carbon nanostructures, a complementary cocatalyst role of nitrogen group has been speculated on Pt-decorated N-doped carbon support [110].

24.2.10 Carbons Doped with Boron, Sulfur, and Phosphorous

Besides nitrogen, carbons can be doped with other heteroatoms such as boron, sulfur, and phosphorous. Among these heteroatoms, boron has been the most widely investigated. Boron-doped diamond has been explored as an electrocatalyst support for fuel cell applications [111]. Boron primarily increases the electronic conductivity of the diamond. Recently, a number of publications have reported metal-free boron-, sulfur-, or phosphorous-doped advanced graphitic carbons such as CNTs, graphene, and CNF to be highly ORR active in alkaline electrolyte [112–115]. Also, Wang et al. showed Pt on boron-doped carbon seems to have good stability which is also supported by theoretical studies that shows Pt on boron-doped carbon to have high binding energy [116–120]. In addition, the presence of sulfur or boron or phosphorous with nitrogen was found to increase catalytic activity of metal-free doped carbon supports [120–123]. Thus, carbons doped with heteroatoms, single or in combination, may be promising candidates as electrocatalyst supports. However, at this point, their chemical state, interaction with metal nanoparticles, and chemical and microstructural changes brought about by these heteroatoms are unknown.

24.3 Non-carbon Supports

Despite improvements in the dispersion and stability of Pt nanoparticles on advanced carbons, they still suffer from three significant limitations that make their long-term implementation in PEMFCs questionable: (1) their oxidation remains thermodynamically favored over the entire ORR operating window and kinetically facile under startup/shutdown conditions; (2) the complex microstructures that are necessary to extended their sp^2 structure with high surface area have not been shown to improve performance in PEMFCs. Failure to reproduce the enhanced ORR activity that was observed ex situ may be due reduced proton mass transfer within the manufactured nanostructure or differences in reactant mass transport on the electrode scale; and (3) the interaction of Pt with these support materials mostly occurs through van der Waals forces and electrostatic interaction at sp^2 sites, though some weak covalent bonding is possible in adatom-doped carbon and edge and defect sites on traditional carbons, which limits the ability of carbon-based supports to improve the intrinsic activity of Pt nanoparticles. Therefore, there exists a groundswell of researchers who aim to replace carbon supports with electrically conducing ceramic materials that have the ability to undergo strong covalent metal–metal bonding with the Pt clusters. It has been hypothesized that this enhanced interaction can further improve Pt nanoparticle dispersion and stability as well as improve their ORR activity. Several supports have been proposed in the literature, though only a few have been studied with enough detail to make reasonable conclusions regarding their potential application as supports for Pt ORR electrocatalysts.

24.3.1 Tungsten Carbide

Both stoichiometric (WC) and sub-stoichiometric (W_2C) tungsten carbide have recently been investigated as ORR electrocatalyst support materials for Pt. Though

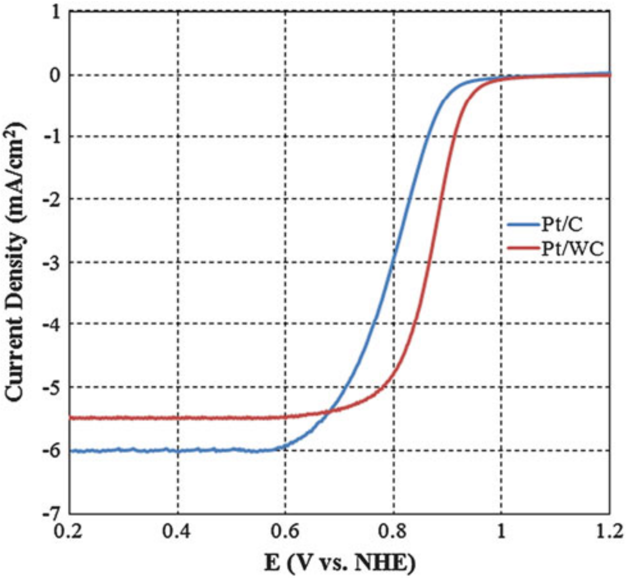

Fig. 24.14 1,600 RPM linear sweep voltammograms for Pt/C and Pt/WC electrocatalysts in perchloric acid electrolyte thermostated at 25 °C

Ganesan et al. found that W_2C supports improved the dispersion of Pt compared to commercial Pt/C [124], it has been shown that W_2C has extremely poor stability in acid media, undergoing both oxidation [125] and partial dissolution, which limits their application as a support in the PEMFC. In contrast, WC has shown very good chemical stability in acid media [126] and represents a better candidate support material for study.

A few groups have studied Pt/WC electrocatalysts for the ORR [127–132]. Though non-carbon support materials have traditionally suffered from low specific surface area, often 1–10 m^2/g [128, 133–135], three different studies have been reported for WC with very high surface area, as high as 256 m^2/g [127, 130, 131]. In general, authors have reported enhanced mass activity for Pt nanoparticles supported on WC, which is shown in Fig. 24.14 by a linear sweep voltammogram for Pt/Vulcan and Pt/WC electrocatalysts, prepared by the method outlined in ref. [127], dispersed on a glassy carbon disk electrode, and immersed in 0.1 M $HClO_4$ at 25 °C, rotating at 1,600 RPM. The results are reported versus a calibrated NHE.

The activity enhancement for Pt deposited onto WC was accompanied by a binding energy shift for Pt by XPS, which was not observed on Pt/C, which suggested significant bonding between Pt and WC. In addition, deconvolution of the rotating disk electrode (RDE) data in Fig. 24.14 yielded a Tafel slope of 120 mV/decade for the Pt/WC electrocatalyst over the entire voltage range. This is in contrast to Pt/C, where the typical 120 mV/decade Tafel slope was observed at low potentials where oxide-free Pt is present with a transition to a 60 mV/decade Tafel slope at high potentials. These results suggest that the enhanced ORR activity

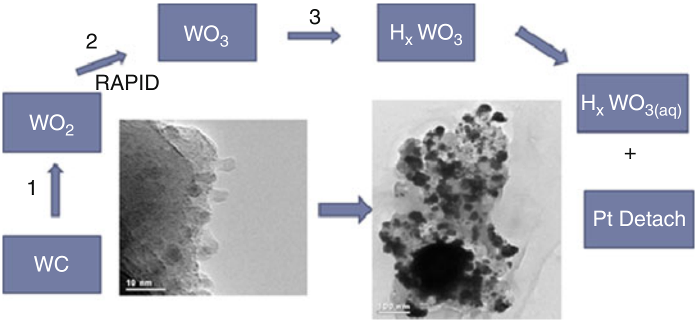

1 $WC(s) + 4H_2O \rightarrow WO_2(s) + CO_2(g) + 8H^+ + 8e^-$

2 $WO_2(s) + H_2O(l) \rightarrow WO_3(s) + 2H^+ + 2e^-$

3 $WO_3 + xH^+ + xe^- \rightarrow H_x WO_3$

Fig. 24.15 Mechanism for ORR activity loss and Pt agglomeration on Pt/WC electrocatalysts

for Pt/WC is caused primarily by pushing the onset potential of Pt surface oxidation higher, an indicator of electronic interaction between Pt and WC that has not been demonstrated on any known Pt/C electrocatalyst.

Unfortunately, the activity enhancement between Pt and WC has been shown to be short-lived [127] due to the oxidation of the WC support in the region relevant to the ORR to WO_2 at potentials > 0.8 V vs. NHE, followed by the facile oxidation of WO_2 to WO_3 [126, 127, 136]. In addition, surface oxidation of WC to WO_3 is followed by the formation of acid-soluble tungsten bronze species, H_xWO_3, which leads to Pt detachment and agglomeration. The agglomeration of Pt is accompanied by a total loss in activity enhancement, returning the activity of Pt to the same level as Pt/C as the catalytic clusters lose their interaction with the surface. The mechanism proposed by Liu for the WC instability and Pt activity loss is shown in Fig. 24.15.

This mechanism is also supported by a recent article by Esposito et al. who reported a pseudo Pourbaix diagram for WC, shown in Fig. 24.16 [126]. The slow dissolution of tungsten oxide also prohibits the use of WO_3 as an electrocatalyst support material for Pt ORR electrocatalysts, which has also been reported in the literature with initially positive outcomes [136–140], even suggesting electronic rearrangement through strong metal–support bonding [141, 142]. Though these catalysts have low stability in ORR-relevant environments, the pseudo Pourbaix diagram in Fig. 24.16 suggests that WC may be a high-stability electrocatalyst support at low potentials, which are relevant to the hydrogen oxidation (HOR) and hydrogen evolution (HER) reactions.

The discussion above also implies that the interaction between Pt and WC may improve the catalyst activity and stability. The activity and stability of Pt/WC electrocatalysts for the HOR/HER was recently probed by Liu and Mustain in acidic environments [143]. It was found that Pt/WC showed significantly improved

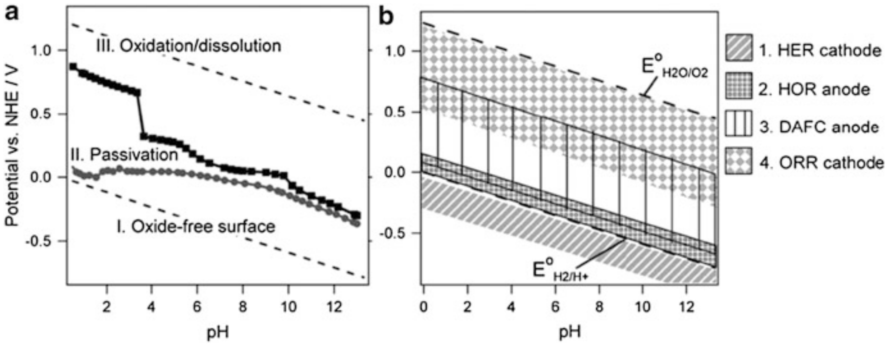

Fig. 24.16 Pseudo Pourbaix diagram for WC (**a**) and possible potential windows where WC could be employed as an electrocatalyst support for various low-temperature electrochemical applications (**b**) [126]

stability compared to Pt/C during electrochemical cycling; however, the authors found no evidence linking the WC support to enhanced Pt activity toward the HOR/HER.

Stability limitations of WC have led researchers to explore other possible carbides as electrocatalyst supports, such as Mo_2C. Similar to Pt/WC, Pt/Mo_2C showed very nice initial Pt dispersion and a positive shift in the ORR onset potential [144]; however, Mo_2C also has poor electrochemical stability [145].

24.3.2 Titania-Based Supports

TiO_2 is a wide bandgap semiconductor (4.85 eV) with extremely low electronic conductivity at 25 °C, 10^{-13} S/cm [146], making it unusable as an ORR electrocatalyst support in PEMFCs. However, researchers have recently been investigating methods to improve the electronic conductivity of titania while still taking advantage of its high chemical stability in acid media and proven ability to influence the activity of deposited noble metal nanoparticle catalysts [141, 142, 147–149], as well as its tolerance to high applied potentials. Much of this work has focused on two primary methods for conductivity enhancement: partial reduction to sub-stoichiometric oxides and transition metal doping.

Magnéli phase titanates, with the general formula Ti_xO_{2x-1} (where $4 < x < 10$), have received particular attention in the literature [150–152] with Ti_4O_7 being the most popular due to its unusually high electronic conductivity at room temperature, around 1,000 S/cm, which is comparable to graphitized carbon [153]. The most common sub-stoichiometric titania supports are available commercially through the Ebonex® brand name. The particle size for this material is large, >1 μm, shown in Fig. 24.17.

It has been shown that Ti_4O_7 has good stability when employed as an electrocatalyst support for Pt at the PEMFC cathode [150], significantly

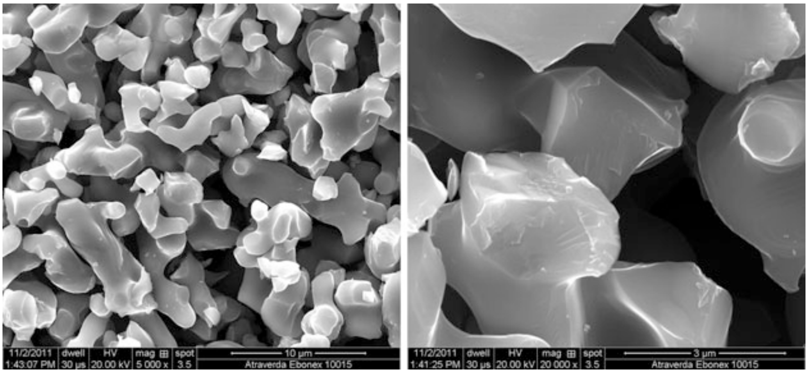

Fig. 24.17 SEM images (Prof. Radenka Maric, University of Connecticut) of Ebonex® powder dispersed on carbon tape

outperforming Vulcan XC-72R at electrode potentials in excess of 0.9 V [150, 154–156], while also increasing the electrochemically active area compared to Pt/C. In fact, rapid electrochemical oxidation of Ti_4O_7 was not observed until potentials greater than 1.6 V vs. NHE, where the onset potential for Vulcan was around 1.0 V. It should also be noted that Ti_4O_7 also oxidized chemically under oxygen rich conditions. Since the fully oxidized phase is chemically stable and the crystal structure deformation is not severe compared to the Magnéli phase, the supported Pt does not appear to detach readily, unlike WC, though the electronic conductivity near the active site decreases, which lowers the ECA over time [157]. Another issue with state-of-the-art Ti_4O_7 supports is the number of nucleation sites that are available for Pt deposition. The lack of surface sites leads to the deposition of larger than optimal Pt nanoparticle sizes, even at lower loadings than Pt/C catalysts. For example, Ioroi et al. recently reported that a 5 wt% Pt/Ti_4O_7 catalyst had a lower mass activity toward the ORR than 20 wt% Pt/Vulcan [150]. However, the specific activities were almost identical, suggesting that the lower ECA for Pt/Ti_4O_7, facilitated by a larger mean Pt cluster size, was responsible for the lower activity. Also, the larger Pt particle size would certainly mute any possible activity enhancements that may be realized through metal–metal bonding with the support.

Nb-doped TiO_2 has also been demonstrated as a possible electrocatalyst support for Pt. Nb is an n-type dopant in TiO_2 that is used to increase the number of free electrons in the crystal lattice. Pentavalent n-type donor atoms are incorporated into the titania matrix with a coordination number of 4. This leaves an excess electron whose energy level is much closer to the conduction band of the host material. Thus, the Fermi level is raised, significantly reducing the electron ionization energy, increasing the electronic conductivity of the semiconductor considerably. This effect is illustrated in Fig. 24.18 [158].

The ORR activity of Pt/Nb–TiO_2 electrocatalysts was reported by Park and Seol [159], who synthesized 40 wt% Pt/Nb–TiO_2 by hydrothermal synthesis at 120 °C using Ti(IV) isopropoxide and Nb(V) ethoxide as metal precursors. To activate the

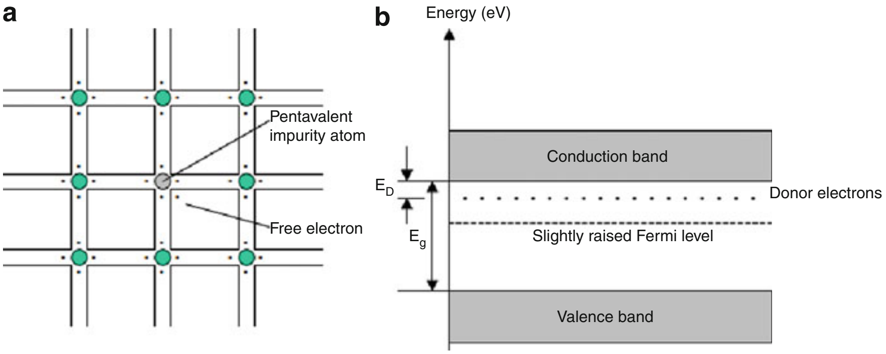

Fig. 24.18 Illustrations of (**a**) an n-type electron donator in a TiO_2 lattice and (**b**) the lowering of the electron ionization energy with a n-type donor [158]

Nb dopant in TiO_2, the nanoparticles were annealed at 400 °C for 2 h in a H_2 atmosphere. Pt nanoparticles were deposited by reduction with $NaBH_4$. The authors reported that Pt/Nb–TiO_2 possessed a higher activity for oxygen reduction than that of Pt/C prepared by the same method. Synchrotron XANES measurements of the Pt L edge on Pt/Nb–TiO_2 implied a shift in the electronic structure of Pt following deposition, which may be responsible for the improved ORR activity. PtRu/Nb–TiO_2 catalysts have also been studied for the ORR [157]. Here, the authors also reported very good activity and stability for $PtRu/Nb_{0.1}Ti_{0.9}O_2$. In addition, the authors compared this catalyst to Pt/Ti_4O_7 and found that it to be superior to the sub-stoichiometric oxide as Ti_4O_7 was oxidized during the electrochemical treatment to TiO_2 at a significant rate.

24.3.3 Tin and Indium Oxide Supports

Recent interest in tin oxide electrocatalyst supports for Pt ORR catalysts can be traced to Nakada et al. [160] who reported that oxide formation of Pt nanoparticles supported on nanosized SnO_2 was pushed to higher potentials, similar to WC. Pushing the oxide potential of Pt to higher potentials has the promise to improve the Pt mass activity toward the ORR by allowing the electron transfer process to occur on clean Pt in a PEMFC cathode at higher potentials. It also increases Pt stability since PtO is a key dissolution intermediate. In addition, this report showed that SnO_2 is stable to very high potentials (at least 1.5 V). Also, a recent study of Pt nanoparticles deposited on tin oxide nanowires by Saha and coworkers [161] reported an enhancement in ORR activity. However, one interesting limitation of these materials is their lower potential stability where Sn^{4+} is reduced to Sn^{2+} at potentials around 0.55 V vs. NHE. This may limit the support stability during high current operation, which suggests that a secondary dopant may help to improve the support stability. The introduction of a metal dopant may also simultaneously improve the electronic conductivity of SnO_2.

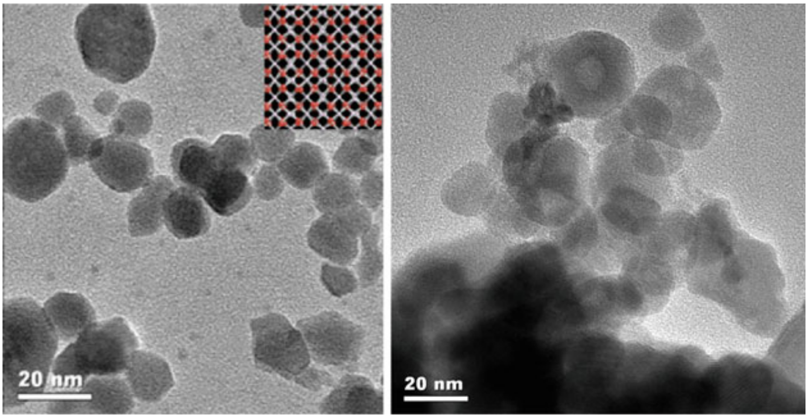

Fig. 24.19 TEM images for In_2O_3 (*left*) before and (*right*) after electrochemical cycling

Indium has been the most widely speculated material to use in combination with Sn, and several commercial indium–tin oxide (ITO) materials have been tested. However, these commercial materials are all predominantly In (90 %) with a cubic bixbyite structure consistent with In_2O_3, which is significantly different from the rutile structure of SnO_2. In addition, In will interact with Pt in a significantly different manner than Sn due to their drastic difference in electronic structure, preferred coordination, and oxidation state. Unfortunately, to the authors' knowledge, there are no reports for undoped Pt/In_2O_3 electrocatalysts in the literature, or a systematic study of the impact of Sn doping in In_2O_3, or In doping in SnO_2. These studies represent important holes in the analysis of ITO materials for the ORR.

That being said, Chang and coworkers [162, 163] reported improved activity for Pt/ITO for the ORR and the ferri/ferrocyanide (FEFI) redox couple, Eq. (24.10).

$$\mathrm{Fe(CN)_6^{3-}} + \mathrm{e^-} \leftrightarrow \mathrm{Fe(CN)_6^{4-}} \tag{24.10}$$

Pt/ITO showed nearly an order of magnitude decrease in R_{CT} for the FEFI, which suggested that the ITO support altered the intrinsic electron transferability of Pt. This result was echoed in the ORR where its half-wave potential was shifted slightly positive. Recently, Pt/Sn-doped In_2O_3 (5 % Sn) showed extremely high specific (75 $0\,\mathrm{mA/cm_{Pt}^2}$) and mass activity ($621\,\mathrm{mA/mg_{Pt}}$) with almost no loss in activity over 1000 cycles between 0.0 and 1.4 V vs NHE [168]. Additionally, Chhina [151] showed that Pt/ITO catalysts experience some degradation over the first 30 potential cycles between 0.0 and 1.8 V vs. NHE, followed by nearly no performance loss over an additional 70 cycles over the same potential window. This study also noted a new peak at low potentials for Pt/ITO that disappeared with cycling. Some of the ECA loss may be due to structural changes in the In_2O_3 structure during potential cycling where In can be reduced to In^{2+} at ca. 0.5 V vs. NHE. These structural changes are shown in Fig. 24.19 for In_2O_3 nanoparticles before and after cycling 300 times between 0.0 and 1.2 V vs. NHE. Interestingly, holes are observed in the cycled samples, which XPS measurements suggest are In_2O_3 even after cycling.

24.3.4 Tantalum Oxyphosphate

One of the highest activity electrocatalysts to be reported in recent years is Pt supported on tantalum oxyphosphate (TOPh)-coated Vulcan XC-72 [164]. This catalyst support is different than the others discussed above since TOPh has quite low electronic conductivity. It was suggested by Garsany and coworkers that the carbon core provides particle-to-particle electronic conductivity, while the very thin TOPh layer interacts with the Pt nanoparticles, manipulating their activity and stability. Linear sweep voltammograms for the Pt/TOPh/C electrode in O_2-saturated perchloric acid are shown in Fig. 24.20a.

Figure 24.20a shows that the Pt ORR activity was improved on Pt/TOPh compared to Pt/C, which is indicated by the increase in the half-wave potential and current density at 0.9 V. Using the current density at 0.9 V vs. NHE, the authors found a mass activity for Pt/TOPh of 0.46 A/mg_{Pt}, more than twice that of Pt/Vulcan and Pt/TKK. In addition, the ECA for Pt/TOPh was superior to Pt/Vulcan (Fig. 24.20b), though comparable to Pt/TKK. The durability of the Pt/TOPh during ex situ testing was also superior to Pt/Vulcan and Pt/TKK over 1,000 30 s pulse cycles of 0.6 and 1.2 V vs. NHE. The authors speculated that electron transfer between the catalyst and the TOPh shifted the Pt surface oxidation to more positive potentials. One possible limitation for the TOPh/C support is the carbon core, which will have the same thermodynamic limitations as conventional supports if poor TOPh coating is achieved or if the TOPh itself has poor cycling stability at higher potentials, which was not reported.

24.4 Trends and Opportunities for Next-Generation Electrocatalysts

A significant amount of work has been done in recent years to develop new electrocatalyst supports for Pt ORR electrocatalysts. It should be noted that the previous discussion was not intended to provide a comprehensive detailing of all of the work that has been done, but to provide examples of work that is currently being done and identify trends. For an additional level of detail, particularly regarding experimental procedures and conditions, differences in preparation methods, and a more quantitative discussion of results, we would like to point the reader to the following recent review articles [71, 111, 165].

For carbon-based electrocatalyst supports, there is no question that advanced supports have been made that enhance the dispersion of Pt nanoparticles. Much of the time, this advanced dispersion has led to higher ECA compared to Pt/Vulcan and Pt/TKK; however, this has not always translated into an increase in the Pt mass activity. Observations on Pt mass activity appear to be a balance between ECA and particle faceting, which plays a significant role in the ORR [166], as the particle size is altered at the same loading as Pt/C. In cases where the Pt mass activity was increased, the specific activity (when reported) always decreased, calling into

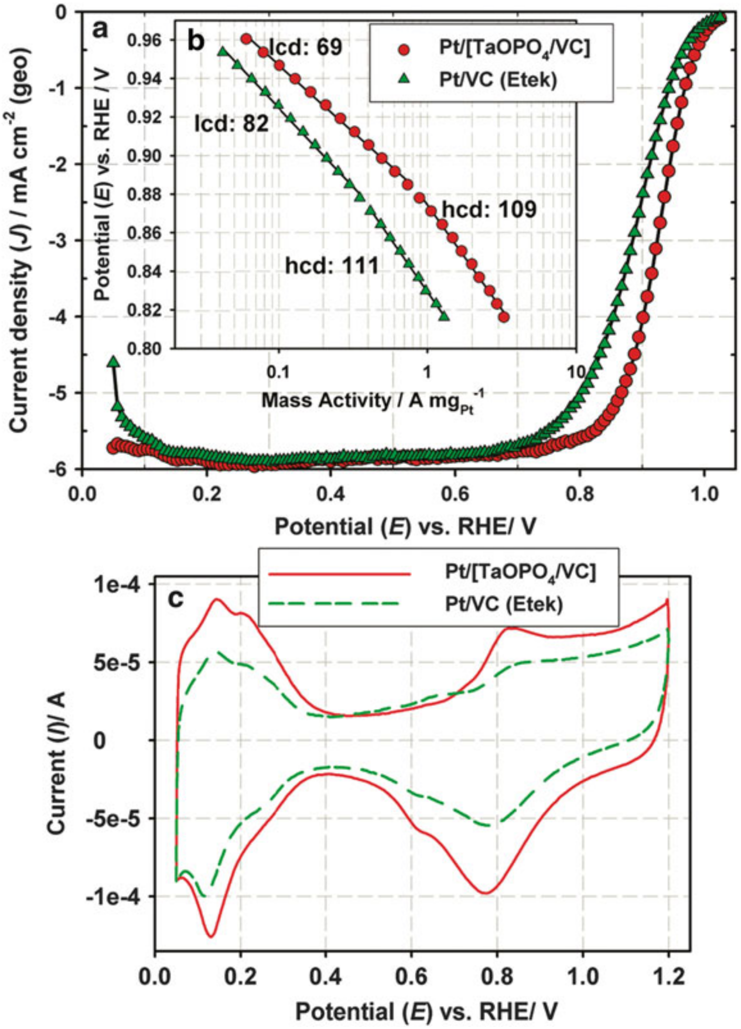

Fig. 24.20 (**a**) RDE ORR voltammograms and (**b**) Tafel plots for Pt/C (*triangles*) and Pt/TOPh/C electrocatalysts (*circles*) in O_2-saturated perchloric acid. (**c**) Cyclic voltammograms for Pt/C and Pt/TOPh/C in N_2-saturated 0.1 M $HClO_4$ [164]

question the ability of carbon-based supports to significantly impact the intrinsic activity of Pt. This suggests that the fairest comparisons for activity are not necessarily done at the same Pt loading, but at identical Pt particle sizes. There is also enough evidence to assert that functional groups on carbon (even oxygen groups) have the potential to improve the stability of Pt during operation.

The proposed next-generation carbon-based materials typically have complex microstructures that extend their sp^2 structure with high surface area. In general, methods to prepare these carbon materials allow for nanometer length-scale control

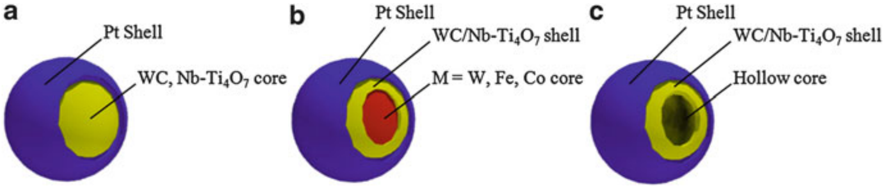

Fig. 24.21 Annotated conceptual illustrations of (**a**) Pt–WC and Pt–Nb-doped Ti_4O_7 core–shell catalysts, (**b**) Pt–WC–M dual-core catalysts, and (**c**) Pt–WC hollow-core catalysts

of their pore size and distribution. Platinum supported on many of these materials has been reported to have improved mass activity compared to conventional Pt/C catalysts; however, this level of structural control has not been translated into performance in an operating PEMFC to date, and there are currently no theoretically sound methodologies to systematically design or evaluate the support nanostructure and its role on catalyst performance. Performance differences between in situ and ex situ tests are most likely due to the difference between the flooded electrolyte conditions in ex situ experiments (where all of the active sites are accessible to the electrolyte) that are typically reported and the PEMFC cathode environment where the ionomer is needed to conduct protons and water must rapidly be removed from the active sites following the ORR.

Experiments regarding non-carbon support materials have suggested that, unlike carbon supports, there is an opportunity to alter the intrinsic activity of Pt, which represents a distinct advantage for the former over the latter. Unfortunately, all of the non-carbon supports that have been studied widely to date oxidize to their most stable form (i.e., WO_3 for WC and TiO_2 for Ti_4O_7), and most show poorer potential stability than carbon. One interesting opportunity to avoid support corrosion with non-carbon supports may be to mask the unstable support from the electrolyte. This can happen through at least two mechanisms. One such mechanism was proposed in DFT studies by Balbuena [167] who suggested Ir core/metal–carbide shell/Pt shell ORR electrocatalysts. DFT work has shown that Pt should be able to form and arrange itself as a true monolayer on clean WC [126]. Potential core–shell structures using WC/Ti_4O_7 support are illustrated in Fig. 24.21, though these materials have not yet been synthesized since oxide surface impurities act as Pt nanoparticle nucleation sites.

A second possible mechanism is controlled oxidation during synthesis or pretreatment. This may work best on nitride-based supports to form oxynitrides, though very few nitrides have been reported in the literature to date as electrocatalyst support, which is why no nitride supports were highlighted here. Additionally, researchers could utilize a highly stable, oxidizible metal (i.e., Al) in pure or alloy form that would form a simple monolayer of oxide while still maintaining its bulk composition and, thus, high electronic conductivity. Another important issue with ceramic supports is that they generally have a significantly higher density than carbon-based supports. Excess loading of these ceramics may result in increased stack weight, a negative for mobile applications. High density may also complicate catalyst dispersion in an ink, making MEA manufacturing by conventional methods difficult. Perhaps this is why almost no studies for platinum catalysts on non-carbon supports report PEMFC data.

Though literally thousands of articles have been published in recent years regarding the development of new catalysts, supports and methods for catalyst layer deposition, and their relationship to PEMFC performance, there are currently no guiding principles on what to make and in what architecture (micro-, meso-, macroscales). Researchers have a limited understanding on how metal–support interactions affect Pt nucleation and dispersion, as well as the degree of electron transfer between Pt and various supports and its effect on the Pt d-band structure (activity). Also, the impact of support microstructure on Pt utilization, Nafion® dispersion/impregnation, and both oxygen and proton mass transport are unclear. This makes the systematic design of the electrocatalyst and the MEA difficult at best.

References

1. Gasteiger HA, Kocha SS, Sompalli B, Wagner FT (2005) Activity benchmarks and requirements for Pt, Pt-alloy, and non-Pt Oxygen reduction catalysts for PEMFCs. Appl Catal B 56(1–2):9–35
2. Sheng W, Chen S, Vescovo E, Shao-Horn Y (2012) Size influence on the oxygen reduction reaction activity and instability of supported nanoparticles. J Electrochem Soc 159(2): B96–B103
3. Perez-Alonzo FJ, McCarthy DN, Nierhoff A, Hernandez-Fernandez P, Strebel C, Stephens IEL, Hielsen JH, Charkendorff I (2012) The effect of size on the oxygen electroreduction activity of mass-selected platinum nanoparticles. Angew Chem Int Ed 51(16):1–4
4. Yamamoto S (2006) US Patent 7022642
5. Bezerra CWB, Zhang L, Liu H, Lee K, Marques ALB, Marques EP, Wang H, Zhang J (2007) A review of heat-treatment effects on stability of PEM fuel cell catalysts for oxygen reduction reaction. J Power Sourc 173(2):891–908
6. Hernández-Fernández P, Montiel M, Ocón P, de la Fuente JLG, García-Rodríguez S, Rojas S, Fierro JLG (2010) Functionalization of multi-walled carbon nanotubes and application as a support for electrocatalysts in proton-exchange membrane fuel cell. Appl Catal B 99 (1–2):343–352
7. Antolini E, Salgado JRC, Gonzalez ER (2006) The stability of Pt-M (M = first row transition metal) alloy catalysts and its effect on the activity in low temperature fuel cells. J Power Sourc 160(2):957–968
8. Shao-Horn Y, Sheng WC, Chen S, Ferreira PJ, Holby EF, Morgan D (2007) Instability of supported platinum nanoparticles in low-temperature fuel cells. Top Catal 46(3–4):285–305
9. Wilson MS, Garzon FH, Sickafus KE, Gottesfeld S (1993) Surface area loss of supported platinum in polymer electrolyte fuel cells. J Electrochem Soc 140(10):2872–2877
10. Tada T (2003) High dispersion catalysts including novel carbon supports. In: Vielstich W, Lamm A, Gasteiger HA (eds) Handbook of fuel cells – fundamentals, technology and applications, vol 3. Wiley, New York
11. Eberl DD, Drits VA, Srodon J (1998) Deducing growth mechanisms for minerals from the shapes of crystal size distributions. Am J Sci 298(6):499–533

12. Ferreira PJ, la O' GJ, Shao-Horn Y, Morgan D, Makharia R, Kocha S, Gasteiger HA (2005) Instability of Pt/C electrocatalysts in proton exchange membrane fuel cells. J Electrochem Soc 152(11):A2256–A2271
13. Mayrhofer KJJ, Meier JC, Ashton SJ, Wiberg GKH, Kraus F, Hanzlikn M, Arenz M (2008) Fuel cell catalyst degradation on the nanoscale. Electrochem Commun 10(8):1144–1147
14. Mayrhofer KJJ, Ashton SJ, Meier JC, Wiberg GKH, Hanzlik M, Arenz M (2008) Non-destructive transmission electron microscopy study of catalyst degradation under electrochemical treatment. J Power Sourc 185(2):734–739
15. Borup R et al (2007) Scientific aspects of polymer electrolyte fuel cell durability and degradation. Chem Rev 107(10):3904–3951
16. Darling RM, Meyers JP (2003) Kinetic model of platinum dissolution in PEMFCs. J Electrochem Soc 150(11):A1523–A1527
17. Darling RM, Meyers JP (2005) Mathematical model of platinum movement in PEM fuel cells. J Electrochem Soc 152(1):A242–A247
18. Tang H, Qi Z, Ramani M, Elter JF (2006) PEM fuel cell cathode carbon corrosion due to the formation of air/fuel boundary at the anode. J Power Sourc 158(2):1306–1312
19. Maass S, Finsterwalder F, Frank G, Hartmann R, Merten C (2008) Carbon support oxidation in PEM fuel cell cathodes. J Power Sourc 176(2):444–451
20. Passalacqua E, Antonucci PL, Vivaldi M, Patti A, Antonucci V, Giordano N, Kinoshita K (1992) The influence of Pt pn the electroxidation behaviour of carbon in phosphoric acid. Electrochim Acta 37(15):2725–2730
21. Kinoshita K (1988) Carbon: electrochemical and physicochemical properties. Wiley, New York
22. Myers JP, Darling RM (2006) Model of carbon corrosion in PEM fuel cells. J Electrochem Soc 153(8):A1432–A1442
23. Rodríguez-Reinoso F, Sepúlveda-Escribano A (2009) Carbon as catalyst support. In: Serp P, Figueiredo JL (eds) Carbon materials for catalysis. Wiley, New Jersey
24. Costamanga P, Srinivasan S (2001) Quantum jumps in the PEMFC science and technology from the 1960s to the year 2000: Part I. Fundamental scientific aspects. J Power Sourc 102 (1–2):242–252
25. Esmaeilifar A, Rowshanzamir S, Eikani MH, Ghanzanfari E (2010) Synthesis methods of low Pt-loading electrocatalysts for proton exchange membrane fuel cell systems. Energy 35 (9):3941–3957
26. Wee JH, Lee KY, Kim SH (2007) Fabrication methods for low-Pt-loading electrocatalysts in proton exchange membrane fuel cell systems. J Power Sourc 165(2):667–677
27. Pumera M (2010) Graphene-based nanomaterials and their electrochemistry. Chem Soc Rev 39(11):4146–4157
28. Rodríguez-Reinoso F (1998) The role of carbon materials in heterogeneous catalysis. Carbon 36(3):159–175
29. Bandosz TJ (2009) Surface chemistry of carbon materials. In: Serp P, Figueiredo JL (eds) Carbon materials for catalysis. Wiley, New Jersey
30. Yoshitake T, Shimakawa Y, Kuroshima S, Kimura H, Ichihashi T, Kubo Y, Kasuya D, Takahashi K, Kokai F, Yudasaka M, Iijima S (2002) Preparation of fine platinum catalyst supported on single-wall carbon nanohorns for fuel cell application. Phys B 323 (1–4):124–126
31. Brunelle JP (1978) Preparation of catalysts by metallic complex adsorption on mineral oxides. Pure Appl Chem 50:1211–1229
32. Bitter JP, De Jong KP (2009) Preparation of carbon-supported metal catalysts. In: Serp P, Figueiredo JL (eds) Carbon materials for catalysis. Wiley, New Jersey
33. Yu X, Ye S (2007) Recent advances in activity and durability enhancement of Pt/C catalytic cathode in PEMFC: Part I. Physico-chemical and electronic interaction between Pt and carbon support, and activity enhancement of Pt/C catalyst. J Power Sourc 172(1):133–144

34. Coloma F, Sepúlveda-Escribano A, Fierro JLG, Rodríguez-Reinoso F (1994) Preparation of platinum supported on pregraphitized carbon blacks. Langmuir 10(3):750–755
35. Peigney A, Laurent C, Flahaut E, Bacsa R, Rousset A (2001) Specific surface area of carbon nanotubes and bundles of carbon nanotubes. Carbon 39(4):507–514
36. Baughman RH, Zakhidov AA, de Heer WA (2002) Carbon nanotubes-the route towards applications. Science 297(5582):787–792
37. Baxendale M (2003) The physics and applications of carbon nanotubes. J Mater Sci Mater Electron 14(10–12):657–659
38. Georgakilas V, Gournis D, Tzitzios V, Pasquato L, Guldi DM, Prato M (2007) Decorating carbon nanotubes with metal or semiconductor nanoparticles. J Mater Chem 17(26):2679–2694
39. Saha MS, Kundu A (2010) Functionalizing carbon nanotubes for proton exchange membrane fuel cells electrode. J Power Sourc 195(19):6255–6261
40. Lee K, Zhang J, Wang H, Wilkinson DP (2006) Progress in the synthesis of carbon nanotube- and nanofiber-supported Pt electrocatalysts for PEM fuel cell catalysis. J Appl Electrochem 36(5):507–522
41. Choi HC, Shim M, Bangsaruntip S, Dai H (2002) Spontaneous reduction of metal ions on the sidewalls of carbon nanotubes. J Am Chem Soc 124(31):9058–9059
42. Sheng W, Lee SW, Crumlin EJ, Chen S, Shao-Horn Y (2011) Synthesis, activity, and durability of Pt nanoparticles supported on multi-walled carbon nanotubes for oxygen reduction. J Electrochem Soc 158(11):B1398–B1404
43. Wang J, Yin G, Shao Y, Wang Z, Gao Y (2008) Electrochemical durability investigation of single-walled and multi-walled carbon nanotubes under potentiostatic conditions. J Power Sourc 176(1):128–131
44. Castro Neto AH, Guinea F, Peres NMR, Novoselov KS, Geim AK (2009) The electronic properties of graphene. Rev Mod Phys 81(1):109–162
45. Castro EV, Novoselov KS, Morozov SV, Peres NMR, Lopes dos Santos JMB, Nilsson J, Guinea F, Castro Neto AH (2007) Biased bilayer graphene: semiconductor with a gap tunable by the electric field effect. Phys Rev Lett 99(21):216802
46. Geim AK, Novoselov KS (2007) The rise of graphene. Nat Mater 6(3):183–191
47. Geim AK (2009) Graphene: status and prospects. Science 324(5934):1530–1534
48. Park S, Ruoff RS (2009) Chemical methods for the production of graphenes. Nat Nanotechnol 4(4):217–224
49. Kou R, Shao Y, Wang D, Engelhard MH, Kwak JH, Wang J, Viswanathan VV, Wang C, Lin Y, Wang Y, Aksay IA, Liu J (2009) Enhanced activity and stability of Pt catalysts on functionalized graphene sheets for electrocatalytic oxygen reduction. Electrochem Commun 11(5):954–957
50. Serp P, Corrias M, Kalck P (2003) Carbon nanotubes and nanofibers in catalysis. Appl Catal A 253(2):337–358
51. De Jong KP, Geus JW (2000) Carbon nanofibers: catalytic synthesis and application. Catal Rev Sci Eng 42(4):481–510
52. Rodriguez NM (1993) A review of catalytically grown carbon nanofibers. J Mater Res 8 (12):3233–3250
53. Biddinger EJ, Ozkan US (2010) Role of graphitic edge plane exposure in carbon nanostructures for oxygen reduction reaction. J Phys Chem C 114(36):15306–15314
54. Zheng JS, Zhang XS, Li P, Zhou XG, Yuan WK (2008) Microstructure effect of carbon nanofiber on electrocatalytic oxygen reduction reaction. Catal Today 131(1–4):270–277
55. Zheng JS, Zhang XS, Li P, Zhu J, Zhou XG, Yuan WK (2007) Effect of carbon nanofiber microstructure on oxygen reduction activity of supported palladium electrocatalyst. Electrochem Commun 9(5):895–900
56. Ngo Q, Cassell AM, Austin AJ, Li J, Krishnan S, Meyyappan M, Yang CY (2006) Characteristics of aligned carbon nanofibers for interconnect via applications. IEEE Electron Device Lett 27(4):221–224

57. Ngo Q, Yamada T, Suzuki M, Ominami Y, Cassell AM, Li J, Meyyappan M, Yang CY (2007) Structural and electrical characterization of carbon nanofibers for interconnect via applications. IEEE Trans Nanotechnol 6(6):688–695
58. Yoon SH, Lim S, Hong SH, Qiao W, Whitehurst DD, Mochida I, An B, Yokogawa K (2004) Carbon nano-rod as a structural unit of carbon nanofibers. Carbon 42(15):3087–3095
59. Yoon SH, Lim S, Hong SH, Qiao W, Whitehurst DD, Mochida I, An B, Yokogawa K (2005) A conceptual model for the structure of catalytically grown carbon nano-fibers. Carbon 43 (9):1828–1838
60. Al-Muhtaseb SA, Ritter JA (2003) Preparation and properties of resorcinol-formaldehyde organic and carbon gels. Adv Mater 15(2):101–114
61. Moreno-Castilla C, Maldonado-Hódar FJ (2005) Carbon aerogels for catalysis applications: an overview. Carbon 43(3):455–465
62. Gavalda S, Kaneko K, Thomson KT, Gubbins KE (2001) Molecular modeling of carbon aerogels. Colloids Surf A 187–188:531–538
63. Job N, Théry A, Pirard R, Marien J, Kocon L, Rouzaud JN, Béguin F, Pirard JP (2005) Carbon aerogels, cryogels and xerogels: influence of drying method on the textural properties of porous carbon materials. Carbon 43(12):2481–2494
64. Smirnova A, Dong X, Hara H, Vasiliev A, Sammes N (2005) Novel carbon aerogel-supported catalysts for PEM fuel cell application. Int J Hydrogen Energy 30(2):149–158
65. Ryoo R, Joo SH, Jun S (1999) Synthesis of highly ordered carbon molecular sieves via template-mediated structural transformation. J Phys Chem B 103(37):7743–7746
66. Jun S, Joo SH, Ryoo R, Kruk M, Jaroniec M, Liu Z, Ohsuna T, Terasaki O (2000) Synthesis of new, nanoporous carbon with hexagonally ordered mesostructure. J Am Chem Soc 122 (43):10712–10713
67. Lee J, Kim J, Kyeon T (2006) Recent progress in the synthesis of porous carbon materials. Adv Mater 18(16):2073–2094
68. Ryoo R, Joo SH, Kruk M, Jaroniec M (2001) Ordered mesoporous carbon. Adv Mater 13 (9):677–681
69. Lee HI, Kim JH, You DJ, Lee JE, Kim JM, Ahn WS, Pak C, Joo SH, Chang H, Seung D (2008) Rational synthesis pathway for ordered mesoporous carbon with controllable 30- to 100-Angstrom pores. Adv Mater 20(4):757–762
70. Joo SH, Choi SJ, Oh I, Kwak J, Liu Z, Terasaki O, Ryoo R (2001) Ordered nanoporous arrays of carbon supporting high dispersion of platinum nanoparticles. Nature 412(6843):169–172
71. Shrestha S, Liu Y, Mustain WE (2011) Electrocatalytic activity and stability of Pt clusters on state-of-art supports: a review. Catal Rev Sci Eng 53(3):256–336
72. Du CY, Yang T, Shi PF, Yin GP, Cheng XQ (2006) Performance analysis of the ordered and the conventional catalyst layers in proton exchange membrane fuel cells. Electrochim Acta 51(23):4934–4941
73. Fang B, Kim M, Kim JH, Yu JS (2008) Controllable synthesis of hierarchical nanostructured hollow core/mesoporous shell carbon for electrochemical hydrogen storage. Langmuir 24 (20):12068–12072
74. Gross AF, Nowak AP (2010) Hierarchical carbon foams with independently tunable mesopore and macropore size distributions. Langmuir 26(13):11378–11383
75. Fang B, Kim JH, Lee C, Yu JS (2008) Hollow macroporous core/mesoporous shell carbon with a tailored structure as a cathode electrocatalysts support for proton exchange membrane fuel cells. J Phys Chem C 112(2):639–645
76. Fang B, Kim JH, Kim M, Kim M, Yu JS (2009) Hierarchical nanostructured hollow spherical carbon with mesoporous shell as a unique cathode catalyst support in proton exchange membrane fuel cell. Phys Chem Chem Phys 11(9):1380–1387
77. Fang B, Kim JH, Kim M, Yu JS (2009) Ordered hierarchical nanostructured carbon as a highly efficient cathode catalyst support in proton exchange membrane fuel cell. Chem Mater 21(5):789–796
78. Khomyakov PA, Giovannetti G, Rusu PC, Brocks G, van den Brink J, Kelly PJ (2009) First-principles study of the interaction and charge transfer between graphene and metals. Phys Rev B 79(19):195425

79. Gong C, Lee G, Shan B, Vogel EM, Wallace RM, Cho K (2010) First-principle study of metal-graphene interfaces. J Appl Phys 108(12):123711
80. Kong KJ, Choi Y, Ryu BH, Lee JO, Chang H (2006) Investigation of metal/carbon-related materials for fuel cell applications by electronic structure calculations. Mater Sci Eng C 26 (5–7):1207–1210
81. Okamoto Y (2006) Density-functional calculations of icosahedral M13 (M = Pt and Au) clusters on graphene sheets and flakes. Chem Phys Lett 420(4–6):382–386
82. Wang JG, Lv YA, Li XN, Dong M (2009) Point-defect mediated bonding of Pt clusters on (5, 5) carbon nanotubes. J Phys Chem C 113(3):890–893
83. Yumura T, Kimura K, Kobayashi H, Tanaka R, Okumura N, Yamabe T (2009) The use of nanometer-sized hydrographene species for support material for fuel cell electrode catalysts: a theoretical proposal. Phys Chem Chem Phys 11(37):8275–8284
84. Qin W, Li X (2010) A theoretical study on the catalytic synergetic effects of Pt/graphene nanocomposites. J Phys Chem C 114(44):19009–19015
85. Okazaki-Maeda K, Morikawa Y, Tanaka S, Kohyama M (2010) Structures of Pt clusters on graphene by first-principles calculations. Surf Sci 604(2):144–154
86. Yamakawa S, Okazaki-Maeda K, Kohyama M, Hyodo S (2008) Phase-field model for deposition process of platinum nanoparticles on carbon substrate. J Phys Conf Ser 100:072042
87. Kolasinski KW (2008) Surface science: foundations of catalysis and nanoscience, 2nd edn. Wiley, Chichester
88. Zoval JV, Lee J, Gorer S, Penner RM (1998) Electrochemical preparation of platinum nanocrystallite s with size selectivity on basal plane oriented graphite surfaces. J Phys Chem B 102(7):1166–1175
89. Toyoda E, Jinnouchi R, Hatanaka T, Morimoto Y, Mitsuhara K, Visikovskiy A, Kido Y (2011) The d-band structure of Pt nanoclusters correlated with the catalytic activity for an oxygen reduction reaction. J Phys Chem C 115(43):21236–21240
90. Jinnouchi R, Toyoda E, Hatanaka T, Morimoto Y (2010) First principles calculations on site-dependent dissolution potentials of supported and unsupported Pt particles. J Phys Chem C 114(3):17557–17568
91. Roy S, Christensen PA, Hamnett A, Thomas KM, Trapp V (1996) Direct methanol fuel cell cathodes with sulfur and nitrogen-based carbon functionality. J Electrochem Soc 143 (10):3073–3079
92. Ye S, Vijh AK, Dao LH (1996) A new fuel cell electrocatalyst based on highly porous carbonized polyacrylonitrile foam with very low platinum loading. J Electrochem Soc 143 (1):L7–L9
93. Ye S, Vijh AK, Dao LH (1996) Oxygen reduction on a new electrocatalyst based on highly porous carbonized polyacrylonitrile microcellular foam with very low platinum loading. J Electroanal Chem 415(1–2):115–121
94. Ye S, Vijh AK, Wang ZY, Dao LH (1997) A new electrocatalyst consisting of a molecularly homogeneous platinum-aerogel nanocomposite. Can J Chem 75(11):1666–1673
95. Ye S, Vijh AK, Dao LH (1997) A new fuel cell electrocatalyst based on carbonized polyacrylonitrile foam. J Electrochem Soc 144(1):90–95
96. Ye S, Vijh AK, Dao LH (1997) Fractal dimension of platinum particles dispersed in highly porous carbonized polyacrylonitrile microcellular foam. J Electrochem Soc 144 (5):1734–1738
97. Matter PH, Ozkan US (2006) Non-metal catalysts for dioxygen reduction in an acidic electrolyte. Catal Lett 109(3–4):115–123
98. Gong K, Du F, Xia Z, Durstock M, Dai L (2009) Nitrogen-doped carbon nanotube arrays with high electrocatalytic activity for oxygen reduction. Science 323(5915):760–764
99. Qu L, Liu Y, Baek JB, Dai L (2010) Nitrogen-doped graphene as a efficient metal-free electrocatalyst for oxygen reduction in fuel cells. ACS Nano 4(3):1321–1326
100. Shao Y, Sui J, Yin G, Gao Y (2008) Nitrogen-doped carbon nanostructures and their composites as catalytic materials for proton exchange membrane fuel cell. Appl Catal B 79 (1):89–99

101. Czerw R, Terrones M, Charlier JC, Blasé X, Foley B, Kamalakaran R, Grobert N, Terrones H, Tekleab D, Ajayan PM, Blau W, Rühle M, Carroll DL (2001) Identification of electron donor states in N-doped carbon nanotubes. Nano Lett 1(9):457–460
102. Ma X, Wang E, Zhou W, Jefferson DA, Chen J, Deng S, Xu N, Yuan J (1999) Polymerized carbon nanobells and their field-emission properties. Appl Phys Lett 75(20):3105–3107
103. Kurt R, Karimi A (2001) Influence of nitrogen on the growth mechanism of decorated C:N nanotubes. Chemphyschem 2(6):388–392
104. Sjöström H, Stafström S, Boman M, Sundgren JE (1995) Superhard and elastic carbon nitride thin films having fullerenelike microstructure. Phys Rev Lett 75(7):1336–1339
105. Maldonado S, Stevenson KJ (2005) Influence of nitrogen doping on oxygen reduction electrocatalysis at carbon nanofiber electrodes. J Phys Chem B 109(10):4707–4716
106. Stafström S (2000) Reactivity of curved and planar carbon-nitride structures. Appl Phys Lett 77(24):3941–3943
107. Pels JR, Kaptejin F, Moulijn JA, Zhu Q, Thomas KM (1995) Evolution of nitrogen functionalities in carbonaceous materials during pyrolysis. Carbon 33(11):1641–1653
108. Holme T, Zhou Y, Pasquarelli R, O'Hayre R (2010) First principles study of doped carbon supports for enhanced platinum catalysts. Phys Chem Chem Phys 12(32):9461–9468
109. Groves MN, Chan ASW, Malardier-Jugroot C, Jugroot M (2009) Improving platinum catalyst binding energy to graphene through nitrogen doping. Chem Phys Lett 481 (4–6):214–219
110. Zhou Y, Neyerlin K, Olson TS, Plypenko S, Bult J, Dinh HN, Gennett T, Shao Z, O'Hayre R (2010) Enhancement of Pt and Pt-alloy fuel cell catalyst activity and durability via nitrogen-modified carbon supports. Energy Environ Sci 3(10):1437–1446
111. Antolini E (2009) Carbon supports for low-temperature fuel cell catalysts. Appl Catal B 88 (1–2):1–24
112. Sheng ZH, Gao HL, Bao WJ, Wang FB, Xia XH (2012) Synthesis of boron doped graphene for oxygen reduction reaction in fuel cells. J Mater Chem 22(2):390–395
113. Yang Z, Yao Z, Li G, Fang G, Nie H, Liu Z, Zhou X, Chen X, Huang S (2012) Sulfur-doped graphene as an efficient metal-free cathode catalyst for oxygen reduction. ACS Nano 6 (1):205–211
114. Yang L, Jiang S, Zhao Y, Zhu L, Chen S, Wang X, Wu Q, Ma J, Ma Y, Hu Z (2011) Boron-doped carbon nanotubes as metal-free electrocatalysts for the oxygen reduction reaction. Angew Chem Int Ed 50(31):7132–7135
115. Liu ZW, Peng F, Wang HJ, Yu H, Zheng WX, Yang J (2011) Phosphorous-doped graphite layers with high electrocatalytic activity for the O2 reduction in an alkaline medium. Angew Chem Int Ed 50(14):3257–3261
116. Wang J, Chen Y, Zhang Y, Ionescu MI, Li R, Sun X, Ye S, Knights S (2011) 3D boron doped carbon nanorods/carbon nanofiber hybrid composite: synthesis and application in highly stable proton exchange membrane fuel cell. J Mater Chem 21(45):18195–18198
117. Acharya CK, Turner CH (2006) Stabilization of platinum clusters by substitutional boron dopants in carbon supports. J Phys Chem B 110(36):17706–17710
118. Acharya CK, Sullivan DI, Turner CH (2008) Characterizing the interaction of Pt and PtRu clusters with boron-doped, nitrogen-doped, and activated carbon: density functional theory calculations and parameterization. J Phys Chem C 112(35):13607–13622
119. Acharya CK, Li W, Liu Z, Kwon G, Turner CH, Lane AM, Nikles D, Klein T, Weaver M (2009) Effect of boron doping in the carbon support on platinum nanoparticles and carbon corrosion. J Power Sourc 192(2):324–329
120. Deak DV, Biddinger EJ, Luthman KA, Ozkan US (2010) The effect of phosphorous in nitrogen-containing nanostructures on oxygen reduction in PEM fuel cells. Carbon 48 (12):3637–3659
121. Ozaki J, Kimura N, Anahara T, Oya A (2007) Preparation and oxygen reduction activity of BN-doped carbons. Carbon 45(9):1847–1853
122. Ikeda T, Boero M, Huang SF, Terakura K, Oshima M, Ozaki JI, Miyata S (2010) Enhanced catalytic activity of carbon alloy catalysts codoped with boron and nitrogen for oxygen reduction reaction. J Phys Chem C 114(19):8933–8937

123. Wohlgemuth SA, White RJ, Willinger MG, Titirici MM, Antonietti M (2012) A one-pot hydrothermal synthesis of sulfur and nitrogen doped carbon aerogels with enhanced electrocatalytic activity for oxygen reduction reaction. Green Chem 14:1515–1523
124. Ganesan R, Lee JS (2005) Tungsten carbide microspheres as a noble-metal-economic electrocatalyst for methanol oxidation. Angew Chem Int Ed 44(40):6557–6560
125. Zellner MB, Chen JG (2005) Surface science and electrochemical studies of WC and W2C PVD films as potential electrocatalysts. Catal Today 99(3–4):299–307
126. Esposito DV, Chen JG (2011) Monolayer platinum supported on tungsten carbides as low-cost electrocatalysts: opportunities and limitations. Energy Environ Sci 4(10):3900–3912
127. Liu Y, Mustain WE (2011) Structural and electrochemical studies of Pt clusters supported on high-surface-area tungsten carbide for oxygen reduction. ACS Catal 1(3):212–220
128. Chhina H, Campbell S, Kesler O (2007) Thermal and electrochemical stability of tungsten carbide catalyst supports. J Power Sourc 164(2):431–440
129. Chhina H, Campbell S, Kesler O (2008) High surface area synthesis, electrochemical activity, and stability of tungsten carbide supported Pt during oxygen reduction in proton exchange membrane fuel cells. J Power Sourc 179(1):50–59
130. Wang Y, Song S, Maragou V, Shen PK, Tsiakaras P (2009) High surface area tungsten carbide microspheres as effective Pt catalyst support for oxygen reduction reaction. Appl Catal B 89(1–2):223–228
131. Liang C, Ding L, Li C, Pang M, Su D, Li W, Wang Y (2010) Nanostructured WCx/CNT as highly efficient support of electrocatalysts with low Pt loading for oxygen reduction reaction. Energy Environ Sci 3(8):1121–1127
132. Hsu IJ, Hansgent DA, McCandless BE, Willis BG, Chen JG (2011) Atomic layer deposition of Pt on tungsten monocarbide (WC) for the oxygen reduction reaction. J Phys Chem C 115 (9):3709–3715
133. Li G, Ma C, Zheng Y, Zhang W (2005) Preparation and electrocatalytic activity of hollow global tungsten carbide with mesoporosity. Microporous Mesoporous Mater 85(3):234–240
134. Hara Y, Minami N, Matsumoto H, Itagaki H (2007) New synthesis of tungsten carbide particles and the synergistic effect with Pt metal as a hydrogen oxidation catalyst for fuel cell applications. Appl Catal A 332(2):289–296
135. Li G, Ma C, Tang J, Zheng Y (2007) Preparation of tungsten carbide porous sphere core wrapped by porous multiwall. Mater Lett 61(4–5):991–993
136. Liu Y, Shrestha S, Mustain WE (2012) Synthesis of nanosize tungsten oxide and its evaluation as an electrocatalyst support for oxygen reduction in acid media. ACS Catal 2(3):456–463
137. Chhina H, Campbell S, Kesler O (2007) Ex situ evaluation of tungsten oxide as a catalyst support for PEMFCs. J Electrochem Soc 154(6):B533–B539
138. Reichman B, Bard AJ (1979) The electrochromic process at WO3 electrodes prepared by vacuum evaporation and anodic oxidation of W. J Electrochem Soc 126(4):583–591
139. Chen KY, Tseung ACC (1996) Effect of nafion dispersion on the stability of Pt/WO3 electrodes. J Electrochem Soc 143(9):2703–2707
140. Raghuveer V, Viswanathan B (2005) Synthesis, characterization and electrochemical studies of Ti-incorporated tungsten trioxides as platinum supports for methanol oxidation. J Power Sourc 144(1):1–10
141. Timperman L, Lewera A, Vogel W, Alonso-Vante N (2010) Nanostructured platinum becomes alloyed at oxide-composite substrate. Electrochem Commun 12(12):1772–1775
142. Lewera A, Timperman L, Roguska A, Alonso-Vante N (2011) Metal-support interactions between nanosized Pt and metal oxides (WO3 and TiO2) studied using X-ray photoelectron spectroscopy. J Phys Chem C 115(41):20153–20159
143. Liu Y, Mustain WE (2012) Evaluation of tungsten carbide as the electrocatalyst support for platinum hydrogen evolution/oxidation catalysts. Int J Hydrogen Energy 37(11):8929–8938
144. Pang M, Li C, Ding L, Zhang J, Su D, Li W, Liang C (2010) Microwave-assisted preparation of Mo2C/CNTs nanocomposites as efficient electrocatalyst supports for oxygen reduction reaction. Ind Eng Chem Res 49(9):4169–4174

145. Weigert EC, Esposito DV, Chen JG (2009) Cyclic voltammetry and X-ray photoelectron spectroscopy studies of electrochemical stability of clean and Pt-modified tungsten and molybdenum carbide (WC and Mo2C) electrocatalysts. J Power Sourc 193(2):501–506
146. Hayden BE, Malevich DV, Pletcher D (2001) Electrode coatings from sprayed titanium dioxide nanoparticles – behaviour in NaOH solutions. Electrochem Commun 3:390–394
147. Tauster SJ, Fung SC, Garten RL (1978) Strong metal-support interactions: group 8 noble metals supported on titanium dioxide. J Am Chem Soc 100(1):170–175
148. Tauster SJ, Fung SC, Baker RTK, Horsley JA (1981) Strong interactions in metal-supported catalysts. Science 211(4487):1121–1125
149. Hammer B, Norskov JK (2000) Theoretical surface science and catalysis-calculations and concepts. Adv Catal 45:71–129
150. Ioroi T, Siroma Z, Fujiwara N, Yamazaki SI, Yasuda K (2005) Sub-stoichiometric titanium oxide-supported platinum electrocatalyst for polymer electrolyte fuel cells. Electrochem Commun 7(2):183–188
151. Chhina H, Campbell S, Kesler O (2006) An oxidant-resistant indium tin oxide catalyst support for proton exchange membrane fuel cells. J Power Sourc 161(2):893–900
152. Smith JR, Walsh FC, Clarke RL (1998) Electrodes based on magnéli phase titanium oxides: the properties and applications of Ebonex® materials. J Appl Electrochem 28(10):1021–1033
153. Bartholomew RF, Frankl DR (1969) Electrical properties of some titanium oxides. Phys Rev 187(3):828–833
154. Graves JE, Pletcher D, Clarke RL, Walsh FC (1991) The electrochemistry of magnéli phase titanium oxide ceramic electrodes: Part I. The deposition and properties of metal coatings. J Appl Electrochem 21(10):848–857
155. Hu F, Ding F, Song S, Shen PK (2006) Pd electrocatalyst supported on carbonized TiO2 nanotube for ethanol oxidation. J Power Sourc 163(1):415–419
156. Shanmugam S, Gedanken A (2007) Carbon-coated anatase TiO2 nanocomposite as a high-performance electrocatalyst support. Small 3(7):1189–1193
157. Chen G, Bare SR, Mallouk TE (2002) Development of supported bifunctional electrocatalysts for united regenerative fuel cells. J Electrochem Soc 149(8):A1092–A1099
158. Chhina H (2009) Oxidation resistant catalyst support for proton exchange membrane fuel cells. Ph.D. Thesis, Mechanical and Industrial Engineering, University of Toronto
159. Park KW, Seol KS (2007) Nb-TiO2 supported Pt cathode catalyst for polymer electrolyte membrane fuel cells. Electrochem Commun 9(9):2256–2260
160. Nakada M, Ishihara A, Mitsushima S, Kamiya N, Ota K (2007) Effect on tin oxides on oxide formation and reduction of platinum particles. Electrochem Solid State Lett 10(1):F1–F4
161. Saha MS, Li R, Cai M, Sun X (2007) High electrocatalytic activity of platinum nanoparticles on SnO2 nanowire-based electrodes. Electrochem Solid State Lett 10(8):B130–B133
162. Chang G, Oyama M, Hirao K (2006) In situ chemical reductive growth on platinum nanoparticles on indium tin oxide surfaces and their electrochemical applications. J Phys Chem B 110(4):1860–1865
163. Chang G, Oyama M, Hirao K (2006) Seed-mediated growth of palladium nanocrystals on indium tin oxide surfaces and their applicability as modified electrodes. J Phys Chem B 110 (41):20362–20368
164. Garsany Y, Epshteyn A, Purdy AP, More KL, Swider-Lyons KE (2010) High-activity, durable oxygen reduction electrocatalyst: nanoscale composite of platinum-tantalum oxyphosphate on vulcan carbon. J Phys Chem Lett 1(13):1977–1981
165. Shao Y, Liu J, Wang Y, Lin Y (2009) Novel catalyst support materials for PEM fuel cells: current status and future prospects. J Mater Chem 19(1):46–59
166. Marković NM, Schmidt TJ, Stamenković V, Ross PN (2001) Oxygen reduction reaction on Pt and Pt bimetallic surfaces: a selective review. Fuel Cells 1(2):105–116
167. Ramirez-Caballero GE, Hirunsit P, Balbuena PB (2010) Shell-anchor-core structures for enhanced stability and catalytic oxygen activity. J Chem Phys 133(13):134705
168. Liu Y, Mustain WE (2013) High stability, high activity Pt/ITO oxygen reduction electrocatalysts. J Am Chem Soc 135:530–533

Index

M. Shao (ed.), *Electrocatalysis in Fuel Cells*, Lecture Notes in Energy 9,
DOI 10.1007/978-1-4471-4911-8,